Proceedings of the 1st International Conference on Diffusion in Solids and Liquids “DSL-2005”

Volume II

Editors:

Andreas Öchsner
José Grácio
Frédéric Barlat

Organising Committee

Andreas Öchsner (Chairman of the Organising Committee)
University of Aveiro, Portugal

José Grácio
University of Aveiro, Portugal

Frédéric Barlat
Alcoa Technical Center, USA
University of Aveiro, Portugal

Marcia Öchsner (Secretary)
University of Aveiro, Portugal

Honoury Chairman:

J. Ågren
KTH Royal Institute of Technology, Sweden

Scientific Committee:

F. Barlat
Alcoa Technical Center, USA
D. Beke
University of Debrecen, Hungary
A.R. Bennacer
Université de Cergy-Pontoise, France
J. Bernardini
Université Aix-Marseille III, France
B. Bokstein
Moscow Institute of Steel and Alloys, Russia
H. Bracht
University of Muenster, Germany
C.E. Campbell
National Institute of Standards and Technology, USA
M. Danielewski
AGH University of Science and Technology, Poland
M.A. Dayananda
Purdue University, USA
M.J.S. De Lemos
Instituto Tecnologico de Aeronautica - ITA, Brazil
A. Fishman
Ural Department of Russian Academy of Sciences, Russia
P. Gas, U 31.01.2005
CNRS - Universite Aix-Marseille 3, France
P. Heitjans
University of Hannover, Germany
Y. Iijima
Tohoku University, Japan
A.S. Khanna
Indian Institute of Technology, India
A.A. Kodentsov
Eindhoven University of Technology, The Netherlands
A.V. Kuznetsov
North Carolina State University, USA
J.L. Lage
Southern Methodist University Dallas, USA
D.N. Lee
Seoul National University, Korea
J.-Y. Lee
Korea Advanced Institute of Science and Technology, Korea
W.O.F. Lengauer
Vienna University of Technology, Austria
Y. Limoge
C.E. SACLAY, France
S. Linderoth
Riso National Laboratory, Denmark
T. Maruyama
Tokyo Institute of Technology, Japan
G. Martin
French Atomic Commission (CEA), France
M. McLean
Imperial College London, UK
H. Mehrer
University of Muenster, Germany
Y. Minamino

Osaka University, Japan
G. Mishuris
Rzeszow University of Technology, Poland
A.A. Mohamad
University of Calgary, Canada
T.V. Morosuk
Odessa State Academy of Refrigeration, Ukraine
G.E. Murch
The University of Newcastle, Australia
H. Numakura
Kyoto University, Japan
C.R. Picu
Rensselaer Polytechnic Institute, USA
E. Rabkin
TECHNION-Israel Institute of Technology, Israel
E. Rauch
Ecole Nationale Supérieure de Physique de Grenoble, France
A.H. Reis
University of Évora, Portugal
V.K. Sarin
Boston University, USA
J.-H. Schmitt
Ecole Centrale Paris, France
S. Seetharaman
Royal Institute of Technology, Sweden
K. Sefiane
The University of Edinburgh, UK
P. Seyffarth
SLV Mecklenburg-Vorpommern, Germany
L. Skerget
University of Maribor, Slovenia
E.H. Schindel-Bidinelli
Swiss Bonding (President), Switzerland
M.A.J. Somers
Technical University of Denmark, Denmark
A.C.M. Sousa
University of Aveiro, Portugal
S. Sridhar
Carnegie Mellon University, USA
F. Stella
Universita' degli Studi di Roma "La Sapienza", Italy
C. Tome
Los Alamos Natl Lab, USA
M. Uematsu
NTT Basic Research Laboratories, Japan
J.E.S. Venart
The University of New Brunswick , Canada
P.W. Voorhees
Northwestern University, USA
W.K. Wang
Chinese Academy of Sciences, China
L.C. Wrobel
Brunel University, UK
M. Zinigrad
College of Judea and Samaria, Israel

Industrial Committee:

T. Iung
IRSID, ARCELOR, France
C. Klinkenberg
Niobium Products Company GmbH, Germany
C. Lavoie
IBM Research, USA
J.-C. Zhao
General Electric Company, GE Global Research, USA
T. Matsumiya
Nippon Steel Corporation, Japan
N. Winter
eupec GmbH, Germany
J.-W. Yoon
Alcoa Technical Center, USA

ACKNOWLEDGEMENTS

The organisers gratefully acknowledge the support given to the conference by the following organisations:

Sponsors

Fundação Oriente	Hotel IMPERIAL	Rota da Luz Aveiro
Delta Cafés	Fundação Calouste Gulbenkian	Fundação Luso-Americana
Caixa Geral de Depositos	Cockburn's	Pastelaria LATINA
Herdade do Perdigão	Fundação para a Ciência e a Tecnologia	

Cooperating Institutions / Co-Sponsors

The Iron and Steel Institute of Japan	Sociedade Portuguesa de Química	The Japan Institute of Metals

PREFACE

These Proceedings contain the papers presented at the First International Conference on Diffusion in Solids and Liquids (DSL-2005) held in Aveiro, Portugal during the period 6th-8th July, 2005.

The goal of the conference was to provide a unique opportunity to exchange information, present the latest results as well as review the relevant issues on diffusion research today. Young scientists were especially encouraged to attend the conference and to establish international networks with well known scientists.

The need for two volumes emphasises the considerable academic and industrial interest in the conference theme. More than 200 papers were presented by scientists and researchers, joining together from more than 40 countries. The editors wish to thank the authors and delegates for their participation and cooperation, which made the conference possible.

The proceedings are directly printed from lithographs of the authors' manuscripts and the editors cannot accept responsibility for any inaccuracies, comments or opinions contained in the papers.

Finally, we wish to express our warm thanks and appreciation to our colleagues and associates for their sustained assistance, help and enthusiasm during the preparation of the conference.

Aveiro, June 2005

Andreas Öchsner
José Grácio
Frédéric Barlat

Already our earliest records on diffusion, more than 300 years ago, are related to practical issues; how to change the color of metals. Over the last century diffusional processes became of immense importance in many areas of practical interest, e.g. medicine, chemical engineering and processing and degradation of materials. At the same time there has been an impressive development in the science of diffusion yielding not only a deeper understanding and the discovery of new exciting phenomena but also a complex but rather rigourous theory. Todays computer technology is turning this theory into valuable tools for the engineer. It is thus evident that the interplay between practical and fundamental issues drives the field of diffusion. This is much reflected by the exciting content of this conference.

Prof. John Ågren
KTH Royal Institute of Technology, Sweden

Honoury Chairman of DSL-2005

CONTENTS

(alphabetic order of presenting author)

Proceedings of The 1st International Conference on **D**iffusion in **S**olids and **L**iquids
DSL-2005, July 6-8, 2005, University of Aveiro, Aveiro, Portugal

DIFFUSIONAL CONTROL OF THE NEAR-SURFACE MICROSTRUCTURE IN FUNCTIONAL GRADIENT HARDMETALS

Walter LENGAUER

Institute for Chemical Technologies and Analytics, Vienna University of Technology,
Getreidemarkt 9/164-CT, A-1060 Vienna, Austria

Fax: +43 1 58801 16199; Email: walter.lengauer@tuwien.ac.at

Abstract

The efforts of the last several years of a research cooperation on diffusional near-surface microstructure modification of hardmetals are summarised. This modification was performed with a reactive gas supplied within the sintering cycle so that functional gradient hardmetals, FGHMs, were obtained, which show a graded distribution of phases. They were optimised for increased wear resistance in metal cutting operations. The thermochemical and diffusional basics of two principally different FGHMs, one with an increased surface hardness and a decreased toughness (with 'regular gradient') and one with a decreased surface hardness but an increased toughness ('inverse gradient') are described in detail. Some of the developed grades were successfully tested and scaled up into industrial production. The FGHMs were found to outperform conventional hardmetals in certain machining tests (continuous turning as well as milling).

Keywords: Hardmetals; Cemented carbides; Diffusion; Gradient; Cutting

1 Introduction

After sintering, most of the hardmetals are subjected to a costly separate coating process in order to deposit layers with high hardness and wear resistance. The core of these hardmetals, which are mainly used for cutting operations, remains tough. The coating step amounts to about 20% of the total hardmetal costs. As an alternative, a one-step diffusion process can be applied under certain circumstances, which creates a surface-modified material already within the sintering cycle. Such an alternative route does not offer the great variability of the various coating processes, which can create multilayer of many different hard phases, but offers substantial benefit as compared to some as-sintered hardmetal grades without additional costs. In addition, the so-obtained material can also provide better substrate properties if a coated hardmetal is finally desired.

The microstructure of such hardmetals is modified in the near-surface region as compared to the core and shows a graded distribution of various phases. Such materials are thus called functional gradient hardmetals (FGHMs).

In our efforts of the last several years summarised here, two concepts were finally followed for preparation of FGHMs. One is an enrichment of hard phase particles at the surface in order to achieve a hardness increase and a toughness decrease of the cutting edge. This gradient is called 'regular gradient'. The second type of a functional gradient hardmetal shows a decrease in hardness and an increase in toughness in the surface zone but has a hard-particle-enriched zone in the interior. This type is called 'inverse gradient'.

The regular gradient was described by Japanese authors [1] without supplying much detail. In our own research of several years by means of laboratory experiments as well as experiments in industrial scale at Kennametal-Widia GmbH in Germany, the conditions of formation of near-surface microstructures was exhaustively studied. Substantial insight into the interdependency of composition, temperature and nitrogen pressure in order to create different microstructures in the near-surface region was obtained [2], including a classification of several types of hardmetals with nitride-enriched or nitride-depleted zones within the near-surface region. Some of these microstructures are favourable for the cutting performance of these hardmetals and were studied in more detail.

The formation of a de-nitrided zone on the surface of hardmetals is well know and was first described by Japanese authors [3], too. Following this, a more detailed investigation of the formation mechanism was described [4,5], which recently was also modelled by thermodynamic and diffusion software [6]. For the formation of a nitrogen-depleted zone nitrogen diffuses out of the material whereas titanium, with its high affinity towards nitrogen, diffuses inside the material. The surface zone it thus depleted in cubic carbides and carbonitrides such as Ti(C,N) and shows the typical microstructure of a pure WC-Co hardmetal. As will be shown later, such a type is the prerequisite for the formation of an inverse gradient, a most recent development.

2 Experimental procedure

For the preparation of hardmetals, powders of WC, (Ti,W)C, (W,Ti,Ta,Nb)C, (Ta,Nb)C, TiC, Ti(C,N), TiN and Co with a particle size on the order of 1-2µm were employed. The powders were mixed in an industrial state-of-the-art procedure, pressed to green bodies, de-waxed and pre-sintered.

The pre-sintered hardmetals were sintered in furnaces of industrial scale as well as in laboratory furnaces. This was performed mainly with N_2 addition. One laboratory furnace was equipped with a mass spectrometer in order to study the gas evolution behaviour of the hardmetals. Thermal dilatometry was performed in Ar as well as in N_2 atmosphere. The usual procedures were applied for XRD and metallographic investigations (SEM and light optical) to characterise the nature and distribution of phases.

Cutting tests were performed by turning (continuous cutting) and milling (interrupted cutting) on steel. The maximum width of the wear land (VB_{max}) as well as the crater depth (KT) was measured as a function of time.

3 Gas evolution and shrinkage

The process parameters of microstructural modification of the near-surface area must be compatible with the sintering cycle of the hardmetal, i.e. no procedure is applicable, which results in a detrimental amount of porosity or yields a high surface roughness. Therefore, basic investigations have been performed in order to study the gas evolution as well as the shrinkage behaviour in order to adjust the diffusional surface modification to the sintering cycle.

3.1 Gas evolution

An example of CO and N_2 evolution of an FGHM body is shown in Fig.1 for an alloy containing already some amount of a carbonitride [7]. CO evolution arises from the oxygen of the starting powders and occurs at different temperatures depending on the stabilities of the various oxides. The two CO peaks correspond to the reduction of WC (at lower T) and of Ti(C,N) (at higher T), respectively. The main nitrogen evolution occurs at higher temperatures than the CO evolution and it starts at around 1200°C, still in the solid regime. This onset coincides with the onset of the second evolution of CO, which reaches its maximum for the most part in the solid region. The maximum of nitrogen evolution occurs later at higher temperature in the liquidus region due to poorer wetting of nitride phases by the binder.

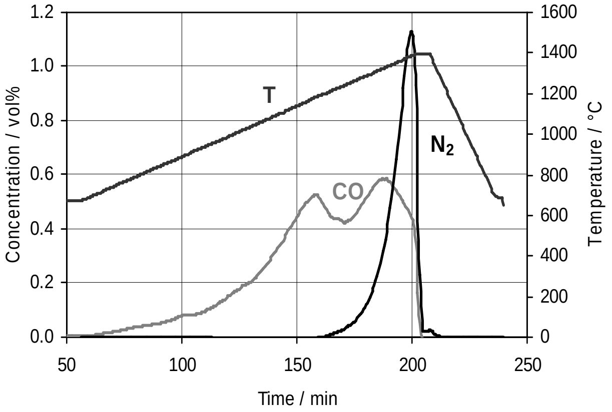

Figure 1: Gas evolution (CO and N_2) of an FGHM as a function of temperature (T).

The total of evolved nitrogen is dependent on the different phases in the starting formulation. If TiN is used instead of Ti(C,N), the amount of evolved nitrogen is larger due to the higher nitrogen equilibrium pressure of TiN as compared to Ti(C,N).

3.2 Shrinkage

A significant influence of the nitrogen partial pressure on the shrinkage behaviour was observed for some alloys [7]. If the amount of cubic phases reaches a certain amount the nitrogen pressure has a large influence on the location of the maximum shrinkage rate. The higher the nitrogen pressure, the more the maximum shifts towards lower temperatures (Fig.2). This is due to the interaction of nitrogen with Ti(C,N). If the nitrogen pressure is higher than the equilibrium pressure of Ti(C,N) carbon is replaced by nitrogen and excess carbon is supplied to the system which accelerates sintering by reducing the liquidus temperature. Corresponding behaviour can be found from thermal analysis, which yields lower liquidus temperatures for higher nitrogen pressures, as well as from specific saturation magnetisation measurements, which yield higher $4\pi\sigma$ values for higher nitrogen pressures.

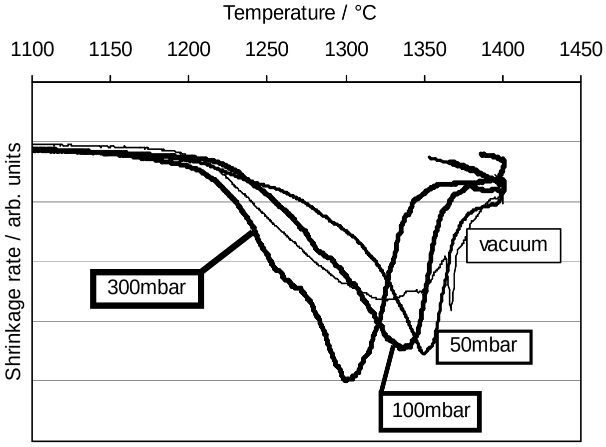

Figure 2: Shrinkage rate of an FGHM as a function of different nitrogen pressures. The maximum shifts to lower temperatures upon increasing pressures.

4 Thermochemistry of gradient formation

An important procedure for the sintering of nitride-containing hardmetal formulation is the introduction of nitrogen at specific positions in the sintering profile in order to (i) exactly compensate for nitrogen loss, (ii) overcompensate for nitrogen loss or (iii) taking some nitrogen loss into account. These procedures will give different near-surface microstructures, i.e. (i) a non-graded, (ii) a nitride-enriched and (iii) a nitride-depleted near-surface region. Such sub-processes were combined in the sintering process in order to arrive at specific microstructures, i.e. with a regular or an inverse gradient.

For a more detailed explanation of the combination of such sub-processes the general behaviour of nitrogen equilibrium pressure vs. temperature is given in Fig.3. Although some part of the sintering takes place a higher than liquidus temperature T_L, which is around 1320°C, $\ln(pN_2)$ of the solid carbonitride will behave almost linearly with temperature. If the nitrogen atmosphere of such a hardmetal formulation will be adjusted exactly as a function of this relationship no gradient formation will occur within sintering. This is a prerequisite for tailoring gradients by in-diffusion or out-diffusion of nitrogen. In-diffusion of nitrogen will occur if the temperature is lowered and the nitrogen pressure is kept constant or increased [8]. Out-diffusion will occur if the temperature is increased by keeping the nitrogen pressure constant or by lowering the nitrogen pressure (compare Fig. 3).

Within a sintering cycle the two principal diffusion directions can even be combined by adjustment of nitrogen pressure and temperature in order to arrive at specific gradients.

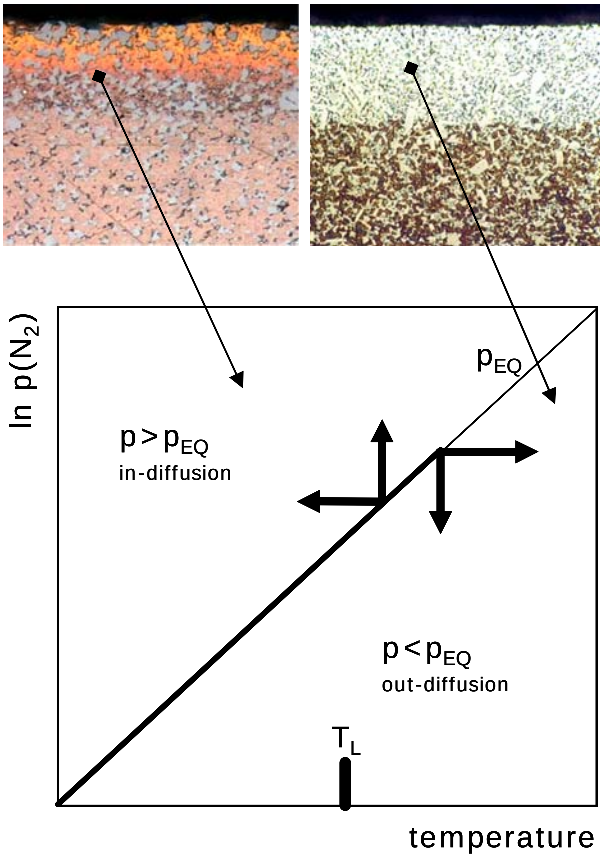

Figure 3: Bottom: Nitrogen equilibrium pressure as a function of temperature (diagonal). At higher pressure and/or lower temperature than equilibrium nitrogen in-diffusion and at lower pressure and/or higher temperature nitrogen out-diffusion takes place. Top: corresponding near-surface microstructures (left: nitride-enriched, above p_{EQ}; right: nitride-depleted surface zone, below p_{EQ}).

5 Preparation of specific FGHMs

5.1 FGHMs with a regular gradient [9]

For an enrichment of nitride or carbonitride phases the nitrogen pressure has to be kept above the equilibrium pressure. This procedure can be performed at some isothermal temperature in order to be able to easily establish a certain thickness of the zone by knowledge of the isothermal growth rate. The process can take place above or below the eutectic temperature T_L.

The path of an alloy with a regular gradient is indicated in Fig.4. The first sub-process (SP1) is a near-equilibrium dense sintering (at liquidus temperature) followed by diffusion annealing at 1200°C (SP2). The whole procedure can be performed in the same furnace or in two different furnaces.

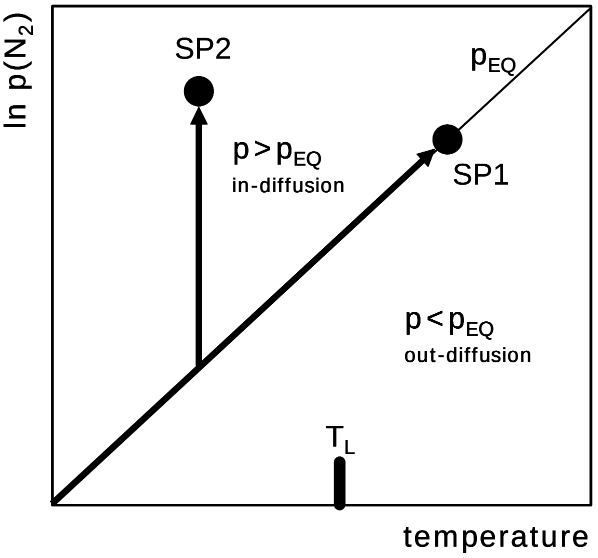

Figure 4: Preparation of an FGHM with a nitride-enriched surface by diffusion annealing at $T<T_L$. First step (SP1): liquid-phase equilibrium sintering, second step (SP2): solid-state sintering above p_{EQ}.

A microstructure of such an FGHM is presented in Fig.5, together with the corresponding element profiles [10]. Both, the increased nitrogen pressure and the lowered temperature, caused in-diffusion of nitrogen. Within the Ti(C,N)-enriched zone the outer region is higher in nitrogen content than the inside, which can be seen from the N/fcc ratio (Fig.5, bottom). Also some WC is formed outside due to the reaction $(Ti,W)C + N_2 \rightarrow Ti(C,N) + WC$, hence the W/fcc ratio is a large as in the bulk and shows that mainly the fcc phase is affected. This is due to the low temperature of SP2 and the reduced mobility of WC. If SP2 is performed at higher temperature WC will diffuse inside.

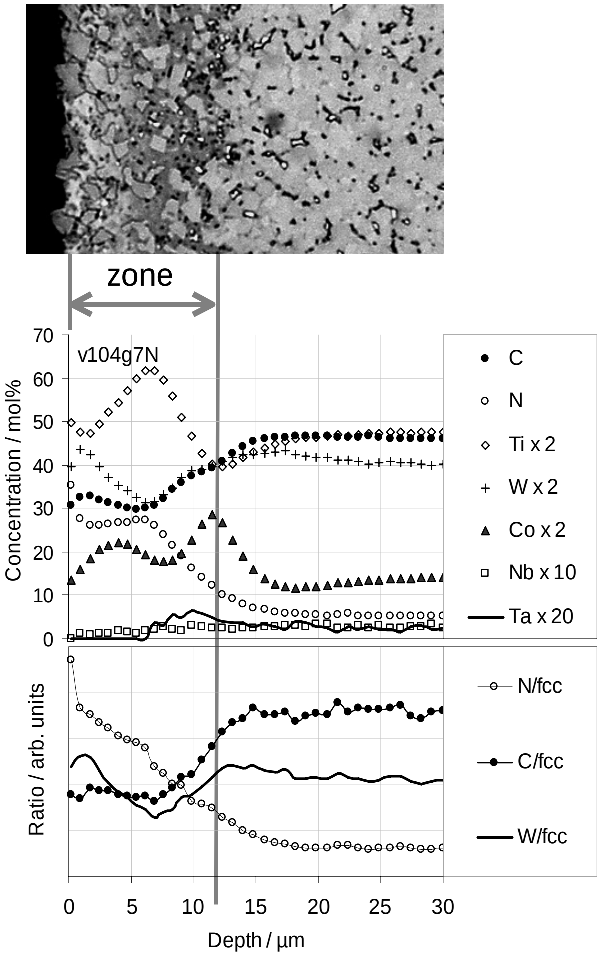

Figure 5: FGHM with a nitride-enriched surface zone (top), the corresponding GDOES element profiles (centre) and nitrogen, carbon and tungsten content vs. amount of fcc phase (bottom). The fcc phase is Ti(C,N).

By application of different annealing times the growth rate of the zone could be established, favourable for finding an optimum thickness in cutting experiments. This growth is parabolic, i.e. $d^2 = k \bullet t$ (d: zone thickness, t: time, k: constant) such as for diffusion layers of distinct nitride or carbide phases [11]. The growth rates are shown in Fig.6 for two nitrogen pressures (5 and 25bar N_2). The increase in growth rate upon higher nitrogen pressure corresponds approximately to the ratio of the square root of pressures $\sqrt{p(N_2)_{high}}/\sqrt{p(N_2)_{low}}$. At higher pressure a higher isothermal growth rate of the zone could be found which can be exploited if the annealing times should be kept short because of grain growth during annealing.

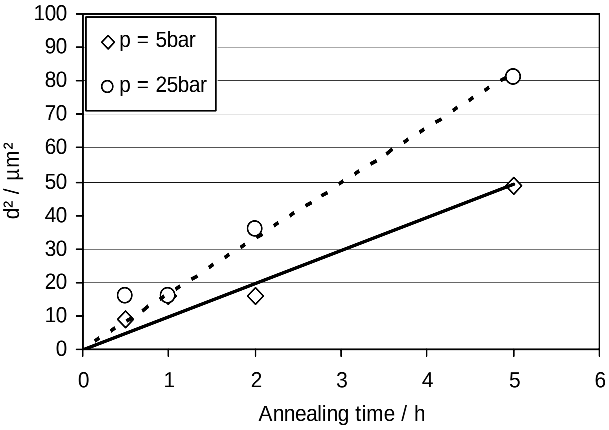

Figure 6: Growth of the nitride-enriched zone shown in Fig.5 indicating parabolic growth behaviour. Increased nitrogen pressure increases the growth rate [10].

5.2 FGHMs with inverse gradient [12]

If hardmetal alloys are sintered at a lower nitrogen pressure than their nitrogen equilibrium pressure, a nitride-depleted zone is achieved (Fig.3). During experiments it turned out that FGHMs with a Ti(C,N)-enrichment below the WC+Co zone shows excellent performance. Therefore, a procedure by which a Ti(C,N) diffusion zone forms below the WC+Co zone was designed and the according gradient called 'inverse gradient' because the outer hardness is lower than at some distance from the surface.

The nitrogen pressure vs. temperature behaviour of the sub-processes of this procedure is sketched in Fig.7. After equilibrium sintering (SP1), the nitrogen pressure is lowered and a WC+Co-rich outer zone is formed (SP2). Then the temperature is lowered and the nitrogen pressure increased relative to the equilibrium pressure. Hence, the main diffusion direction of nitrogen changes and nitrogen diffuses now inside (whereas titanium diffuses outside).

Although the second step of this procedure corresponds to the second step of the formation of a regular gradient (nitride enrichment), nitride particles are not created at the outside of the FGHM due to peculiarities in the occurring diffusional fluxes.

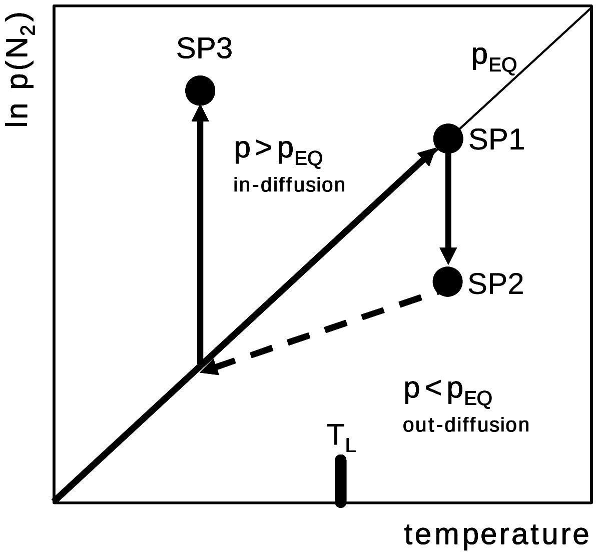

Figure 7: Sub-processes (SP1, SP2 and SP3) for the preparation of an FGHM with an inverse gradient (nitride-depleted surface zone and an inner nitride-enriched zone).

This is explained in Fig.8. First the hardmetal is sintered (SP1) and then a nitride-depleted surface zone is formed within SP2, Fig.8, top. The thickness of this zone can be adjusted by appropriate choice of the annealing conditions.

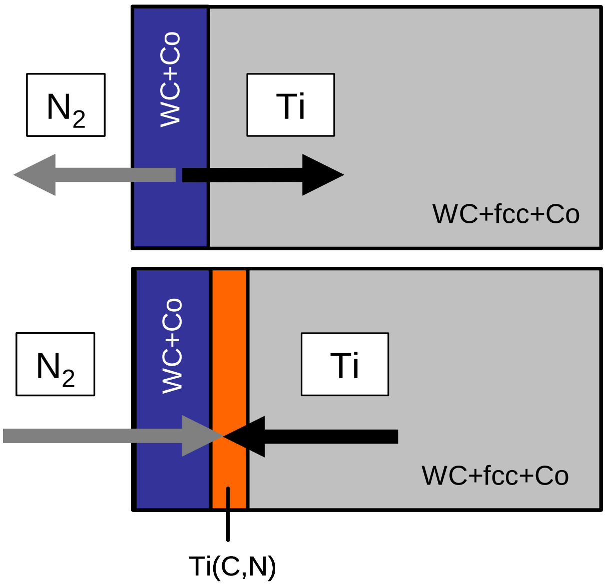

Figure 8: Formation of an inverse gradient, i.e. a nitride-enriched zone below the nitride-depleted zone. Top: the nitride-depleted surface is created in SP1 and SP2 (Fig.7). Bottom: nitrogen diffusion reverses and forms and inner nitride-enriched zone within SP3, Ti cannot diffuse outside through the WC+Co layer.

For the last step SP3 the temperature is lowered in order to arrive in the solid region and occasionally the nitrogen pressure is increased, corresponding to SP3 in Fig.7. Now nitrogen diffuses inside and titanium outside (Fig.8, bottom) but the latter cannot diffuse towards the outermost surface due to the much higher activation energy of Ti diffusion as compared to N diffusion. Thus, the WC+Co zone behaves like a membrane which allows for in-diffusion of nitrogen but not for out-diffusion of titanium. Because of the higher-than-equilibrium nitrogen pressure (or lower temperature) a Ti(C,N)-enriched zone forms inside the WC+Co zone.

Fig.9 shows a SEM microstructure of this region after SP2 (top) and after SP3 (bottom), corresponding to Fig.8. In these microstructures Ti(C,N) appears dark and WC bright.

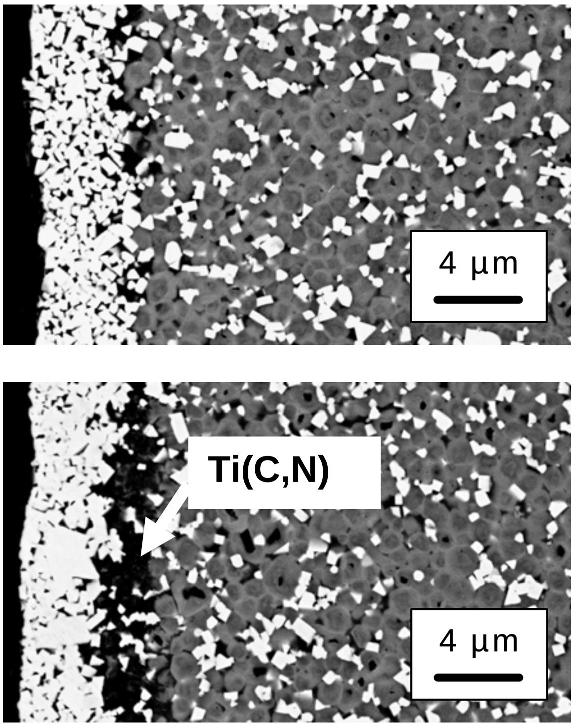

Figure 9: SEM-BSE microstructures corresponding to the sketch shown in Fig.8. Top: nitride-depleted WC+Co surface zone (bright), bottom: formation of nitride-enriched zone (dark) below WC+Co.

Also for the inner nitride-enriched zone parabolic growth was observed as for the outer Ti(C,N) zone in regular gradients (Fig.10). This was studied in the same material for which on one side the WC+Co surface zone was removed by grinding after SP2. The inner Ti(C,N) zone has a slightly smaller growth rate than the latter because the WC+Co zone reduces the diffusion flux to some extend. During SP3 the WC+Co zone does not grow so that it is possible to tailor the thicknesses of the WC+Co and the Ti(C,N) zone independently of each other within SP2 and SP3, respectively. This yields optimum thicknesses of both zones with respect to cutting performance.

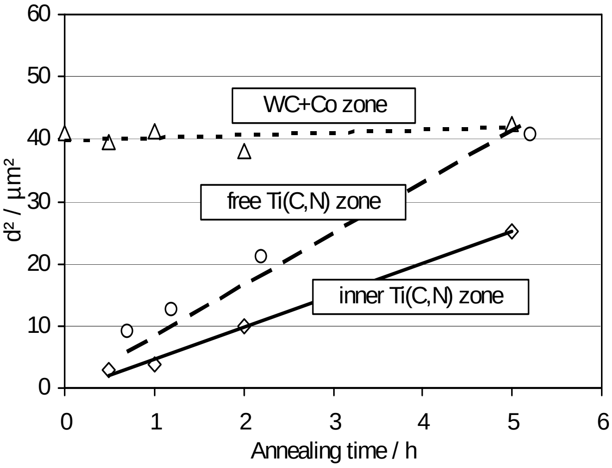

Figure 10: Parabolic growth of the inner and the outer ‘free’ Ti(C,N) zone, whereas the WC+Co zone remains at constant thickness. The outer nitride-enriched zone grows faster than the inner.

6 Cutting tests

In turning (continuous cutting) tests the crater depth KT and the maximum wear land VB_{max} at the flank side are measured as a function of time. This is shown in Fig.11. In milling (interrupted cutting) usually only the flank wear is recorded.

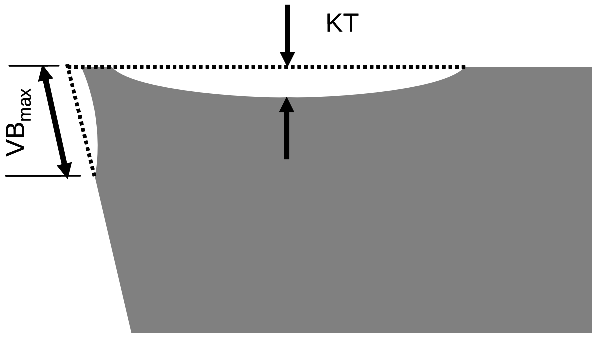

Figure 11: Schematic representation of wear on a cutting insert with crater depth KT and max wear land VB_{max}, which are measured as a function of time in cutting tests.

6.1 FGHMs with regular gradient

Fig.12 shows the turning performance of FGHMs with nitride-enriched surface zone. By changing diffusion time, different zone thicknesses of outer Ti(C,N) were obtained for the tests. A P25 type hardmetal was tested for comparison. It turned out that a Ti(C,N) zone thickness of about 9µm performs best, at smaller thicknesses wear becomes larger. There is no absolutely clear sequence with zone thickness but in any case the FGHMs performed much better than the uncoated commercial P25 type hardmetal.

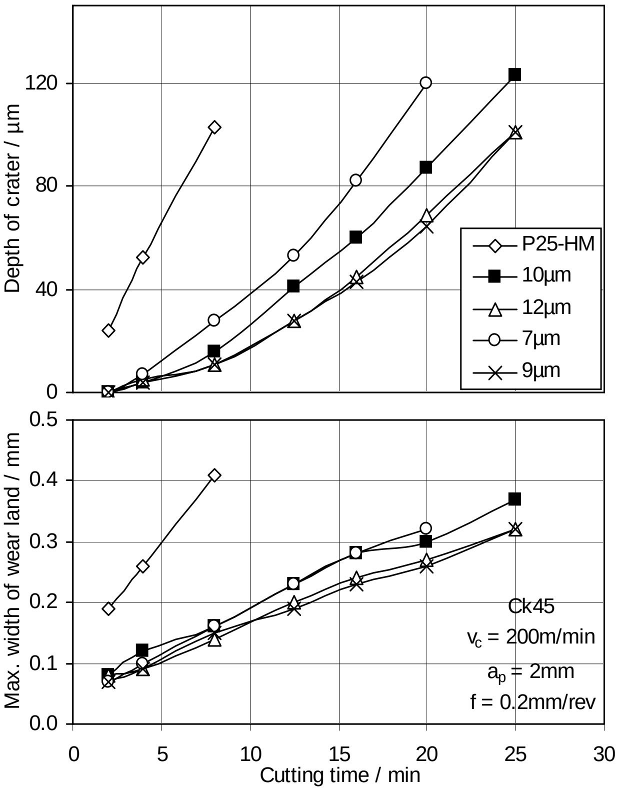

Figure 12: Turning test (top: crater depth, bottom: maximum wear land, compare Fig.11) of an FGHM with regular gradient of different thickness of the nitride-enriched zone (7-12µm) as compared to a commercial P25 hardmetal. Workpiece material: Ck45 steel. Cutting conditions on the lower right. Lifetime increase is more than fivefold.

6.2 FGHMs with inverse gradient

Due to the presence of a tough surface layer of FGHMs with inverse gradient it can be assumed that they are excellent materials for milling. As an example for the performance of such FGHMs Fig.13 shows a milling test [13]. Note that the cutting speed is at relatively high values (315 m/min). For comparison a TiAlN-coated P25 type hardmetal without gradient was tested within the same run. The milling performance of the inverse FGHMs was substantially better than that of commercial grade. The optimum is at an intermediate thickness of the inner Ti(C,N) zone ('inverse + 1h') as compared to thicker ('inverse + 5h') or thinner ('inverse') Ti(C,N) zones within the inverse gradient. Here, the wear is plotted as a function of tool path (instead of time as in Fig.12). A tool path of 6m corresponds to a cutting time of approximately 90min. Another favourable finding is that the wear of the best FGHMs shows only a small steady increase as a function of tool path.

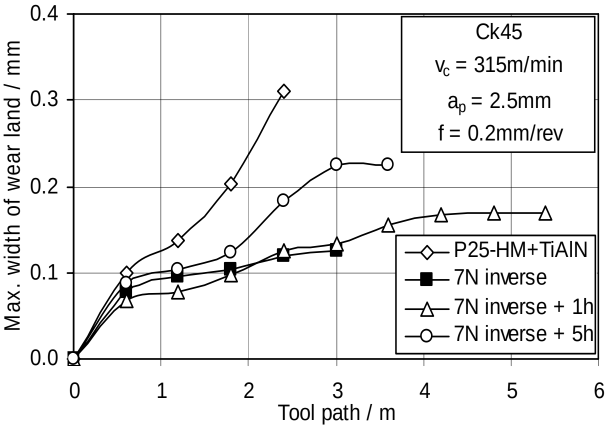

Figure 13: Milling test (only VB_{max} is recorded here) for FGHMs with inverse gradient. The inner nitride-enriched layer with intermediate thickness performed best. Comparison with a commercial coated P25 type hardmetal with TiAlN coating.

7 Conclusions

The near-surface region of hardmetals can be modified by means of diffusion processes to arrive at functionally graded hardmetals, FGHMs. The starting formulation must contain species which different affinity toward the reactive atmosphere. In such hardmetals Ti forms a very stable nitride whereas W does not. This is a necessary condition to establish a graded layer. Upon knowledge of the thermodynamic as well as diffusional properties of the compounds and constituents involved, an appropriate choice of process parameters is possible to tailor specific micro-structures.

The method was applied for hardmetals with both, a low and a high amount of Ti(C,N). The high amount is representative for a material which is intermediate between a hardmetal and a cermet. It was already applied for pure cermets, too (e.g. [14]).

Different types of gradients with respect to mechanical properties were designed, prepared and tested as a function of the established zone thicknesses. The so-called regular gradient consisted of a microstructure with a hardness increase and toughness decrease towards the surface, the other showed opposed mechanical properties, i.e. a maximum hardness in the interior of the hardmetal and a maximum in toughness outside. Both FGHMs have their field of application which was shown in cutting tests.

References

[1] Tsuda, K., Ikegaya, T., Isobe, K., Kitagawa, N.: Development of functionally graded sintered hard materials, *Powder Metallurgy* 39, pp. 296-300, 1996.

[2] Lengauer, W., Dreyer, K.: Functionally graded hardmetals. *J .Alloys Comp.*, 338(1-2), pp. 194-212, 2002.

[3] Suzuki, H., Hayashi, K., Taniguchi, Y.: The β-free layer formed near the surface of vacuum sintered tungsten carbide-β-cobalt alloys containing nitrogen. *Trans. Jap. Inst. Met.*, 22(11), pp. 758-764, 1981.

[4] Schwarzkopf. M., Exner, H., Fischmeister. H.: Kinetics of compositional modification of (W,Ti)C-WC-Co alloy surfaces. *Mater. Sci. Engin.,* A105/106, pp. 225-231, 1988.

[5] Gustafson, P., Östlund, Å.: Binder-phase enrichment by dissolution of cubic carbides. *Int. J. Refr. Met. & Hard Mater.*, 12, pp. 129-136, 1994.

[6] Ekroth, M., Frykholm, R., Lindholm, R., Andrén, H.-O., Ågren, J.: Gradient zones in WC-Ti(C,N)-Co-based cemented carbides: experimental study and computer simulations. *Acta mater.,* 48, pp. 2177-2185, 2000.

[7] Eder, A., Mauger, M., Königshofer, R., Lengauer, W., Dreyer, K., Kassel, D., Daub, H.-W., van den Berg, H.: Gas/solid interactions in the evolution of graded micro-structures in hardmetals. *Proc. EURO PM2003 Valencia*, EPMA, Shrewsbury, pp. 37-43, 2003.

[8] Lengauer, W., Thermochemistry of the Formation of nitrogen-rich diffusion layers on transition metal nitrides; a study of the $VN_{1-x}-N_2$ couple. *J. Phys. Chem. Solids* 52(2), pp. 393-399, 1991.

[9] Chen, L., Lengauer, W., Daub, H.-W., Dreyer, K., Kassel, D.: US 6,110,603, Hardmetal or cermet body, especially for use as a cutting insert. 29.08.2000.

[10] Königshofer, R., Eder, A., Lengauer, W., Dreyer, K., Kassel, D., Daub, H.-W., van den Berg, H.: Growth of the graded zone and its impact on cutting performance in high-pressure nitrogen modified functionally gradient hardmetals. *J. Alloys Comp.*, 366, pp. 228-232, 2004.

[11] Lengauer, W.: Handbook of Ceramic Hard Materials: Transition metal carbides, nitrides and carbonitrides. Wiley-VCH, Weinheim, Vol.1, Ch. 7, pp. 202-252, 2000.

[12] Lengauer, W., Ucakar, V., Dreyer, K., Kassel, D., Daub, H.-W.: WO 2005/026400 Hardmetal or cermet body and method for producing the same. 24.03.2005.

[13] Lengauer, W., Eder, A., Dreyer, K., van den Berg, H., Daub, H.-W., Kassel, D.: Functional gradient hardmetals for milling applications. *Proc.PM2004*, *Vienna,* EPMA, Shrewsbury, Vol. 3, pp. 487-494, 2004.

[14] Zackrisson, J., Rolander, U., Jansson, B., Andrén, H.-O.: Microstructure and performance of a cermet material heat treated in nitrogen. *Acta Mater.* 48, pp. 4281-4291, 2000.

Proceedings of The 1st International Conference on **D**iffusion in **S**olids and **L**iquids
DSL-2005, July 6-8, 2005, University of Aveiro, Aveiro, Portugal

SELF-DIFFUSION OF ADATOMS ON Pd (001) SURFACE STUDIED BY MOLECULAR DYNAMICS SIMULATION

Alexander EVTEEV, Alexander KOSILOV, Elena LEVCHENKO*, Sergey SOLYANIK

Department of Material Science and Metal Physics, Voronezh State Technical University,
Moskovsky Prospect 14, 394026 Voronezh, Russia

*Corresponding author. Fax: +7 0732 463277; Email: elevchenko@vmail.ru

---

Abstract

In this paper it has been shown by molecular dynamics simulation that the displacement of Pd adatoms on Pd (001) surface takes place mainly by means of “relay-race” mechanism with participation of the substrate atoms. Activation energy of the elementary act of “relay-race” self-diffusion has been calculated using a kinetic equation, which describes the concentration changes on the surface of “marked” at the initial instant of time adatoms.

Keywords: Calculation of diffusion coefficient; Molecular dynamics; Embedded atom method; Surface, Metals

---

1 Introduction

It is well known from Refs [1-6], that at the initial stages of a film forming from the gas phase on the crystal substrates a surface diffusion of adatoms is one of the most important factors for a nucleation and growth of the condensate.

It is commonly supposed (see for ex. Refs [1,2]) that an adatoms’ diffusion on the metallic surface takes place mainly by means of “rolling stone” mechanism, i.e. by sequential thermally activated transitions of adatoms from one stable state to another. This scheme of adatoms’ displacement on the singular part of surface was so evident that other (alternative) mechanisms of their diffusion were considered as unlikely. At the same time direct experimental methods of the observation on diffusion processes on a solid surface allow “to see” separate atoms, but these methods can fix atomic positions only before and after a diffusion act. And it is impossible to recognize after which processes the atom is located in a new position and to answer if it is the same atom, which was in the initial position. Only a computer experiment within the molecular dynamics (MD) method allows to observe the displacements of each atom in a system (including adatoms) during any moment of the studied diffusion process. In Ref. [7] during the diffusion investigation of Au, Ir and Pt adatoms on (110) Pt surface it has been shown by MD method using pair Lannard-Johnes potential, that diffusion of Ir and Pt atoms can occur also by “exchange” mechanism (extrusion atom from substrate by diffusing adatom). This process promotes a mutual atomic interfusion of condensed matter and substrate. Experimentally observed emergence effect of Cu atoms on the surface of growing Pd, Rh, Pt film [4] can indirectly argue a realization of this mechanism, which was unexplainable within the framework of volume heterogeneous diffusion model.

In the present paper the atomic mechanisms and kinetics of a self-diffusion of Pd adatoms on the surface of Pd (001) single-crystal substrate are investigated by MD method.

2 Model procedure

The substrate was simulated using the calculated cell consisting of eight planes Pd (001), each of them was a square with 48 atoms on side, i.e. 2304 atoms per plane. Periodical boundary conditions were imposed in [110] and $[1\bar{1}0]$ directions upon the system. Tree bottom layers were static and next five were dynamic. On the substrate’s surface 64 adatoms were arranged in a square lattice of 8×8 size. Then the static relaxation of the system was carried out. To describe interatomic interactions we used a many body potential calculated within the scope of the embedded atom method [8].

Adatoms and substrate atoms in dynamic layers had initial velocities defined by the Maxwellian distribution. Isothermal annealing of the system was carried out by MD method. The MD calculation procedure consisted of numerical integration of the motion equations with a time step of Δt = 1.5×10^{-15} s using the Verlet algorithm [9].

3 Results and discussion

It has been established, that during an isothermal annealing a diffusion displacement of adatoms on Pd (001) surface takes place mainly not by means of "rolling stone" mechanism from one stable position to another, but by "relay-race" mechanism, i.e. by replace adatom with an atom of the first substrate's layer under the simultaneous displacement of this atom onto the surface to the nearest stable position, which is the most distant position from the initial adatom's one, as shown in Fig. 1.

A result of such "relay-race" diffusion act in the case of one component system is the displacement of adatom in the direction ⟨100⟩ on a value of a lattice constant. In particular, in computer experiment carried out at 800 K in 3×10^{-11} s in the first Pd (001) substrate layer we observed 37 "marked" atoms from the initial 64 "marked" Pd adatoms. At the same time there was not any "marked" atom in the second or next substrate layers and none of the atoms from the first substrate layer and situated far from adatom was found on the surface.

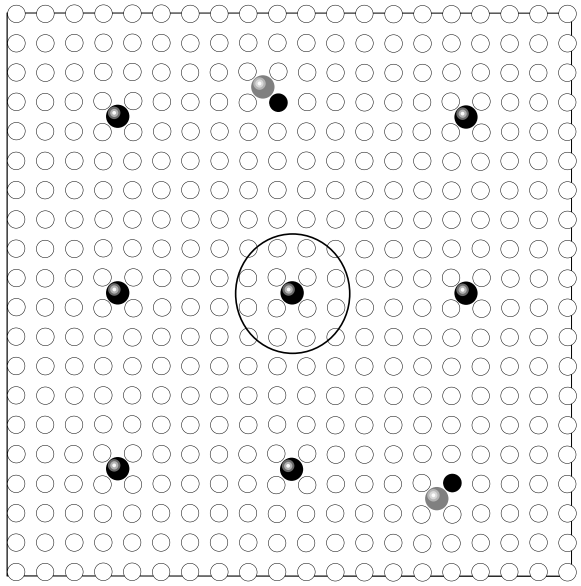

a)

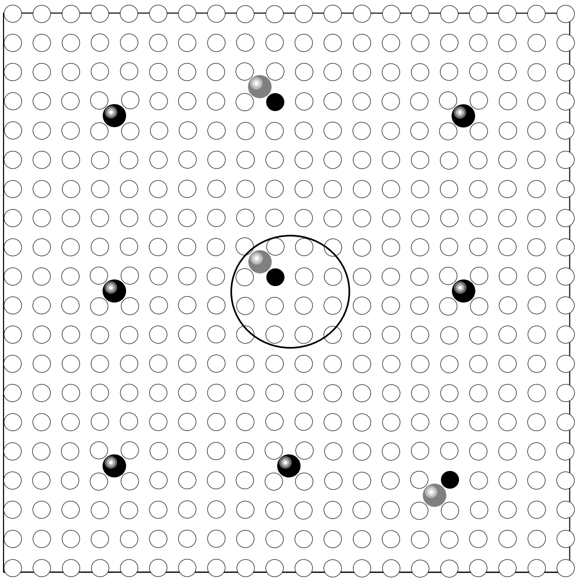

b)

Figure 1: Fragments of Pd (001) surface after annealing at 700 K during 1.5×10^{-11} s (a) and 3×10^{-11} s (b). In the ringed section an elementary act of "relay-race" self-diffusion mechanism is shown. Adatoms are given by large spheres and substrate atoms are shown by small circles. Adatoms "marked" at the initial time are given by black color.

Therefore, during the annealing a number of "marked" atoms increases in the first substrate layer and decreases on the surface of the sample. In this context due to the emergence of atoms of the first substrate layer to the surface a sum of adatoms is constant. However increment of the number of "marked" atoms in the first substrate layer results in an increase of a probability of their displacement to the sample surface again. With time a balance of the reverse streams of the "marked" atoms is setting up and their concentration on the surface is approaching to the equilibrium one.

The obtained data for the atomic mechanism of surface self-diffusion allow to describe kinetics of decreasing the number of "marked" at the initial instant of time adatoms n_0 under small coating density: $\theta = n_0/N$, where N is a total number of adsorption places on the surface. Using a scheme of relative position of the substrate atoms presented in Fig. 2, we consider all possibilities of adatom's displacements by "relay-race" mechanism. Assume that the "marked" adatom changed the initial position 0 to the position a on the substrate by "relay-race" diffusion, while substrate atom displaced from position *a* to the adatom's position 1. A probability of such process per time unite is determined as $\nu = \nu_0 \exp(-W/kT)$, where ν_0 is the frequency factor; W is the activation energy of elementary act of "relay-race" diffusion; k is the Boltzmann's constant; T is a temperature. Then two variants for adatom 1 can occur: (i) either to touch off to substrate atom to take up one of tree positions 2, (ii) or to oust "marked" atom from position *a* in order to return to the initial position. Probability for every of these acts is equal to $\frac{1}{4}$ (Fig.2). If adatom is in one of positions 2 (probability to be in each of them is $\frac{1}{3}$) then the following alternatives of displacements are possible: (i) either to occupy one among five positions 3_1 and one out of two 3_2 positions with probability $\frac{1}{3}\cdot\left(5\cdot\frac{1}{4}+2\cdot\frac{1}{4}\cdot 2\right)=\frac{3}{4}$, (ii) or to replace to the initial position 1 with probability $\frac{1}{4}$. Since the probability of displacement from position 2 to position 3_2 is twice as much as to the position 3_1, probabilities of adatom's location in one out of five positions 3_1 and two positions 3_2 are equal to $\frac{5}{9}$ and $\frac{4}{9}$ respectively. Then the probability of adatom's displacement from position 3 to position 2 is $\frac{5}{9}\cdot\frac{1}{4}+\frac{4}{9}\cdot\frac{1}{2}=\frac{13}{36}$. Variants discussed above of "relay-race" transition of adatoms among different positions under the small coating density (θ<<1) allow to construct a system of kinetic equations for adatoms in different positions. Suppose that at the time moment t we have n, n_1, n_2, *and* n_3 atoms in 0, 1, 2 and 3 positions respectively, then the equations will have the form

$$\begin{cases} \dfrac{dn}{dt} = -\nu n + \frac{1}{4}\nu n_1; \\ \dfrac{dn_1}{dt} = \nu n - \nu n_1 + \frac{1}{4}\nu n_2; \\ \dfrac{dn_2}{dt} = \frac{3}{4}\nu n_1 - \nu n_2 + \frac{13}{36}\nu n_3; \\ \dfrac{dn_3}{dt} = \frac{3}{4}\nu n_2 - \nu n_3. \end{cases} \tag{1}$$

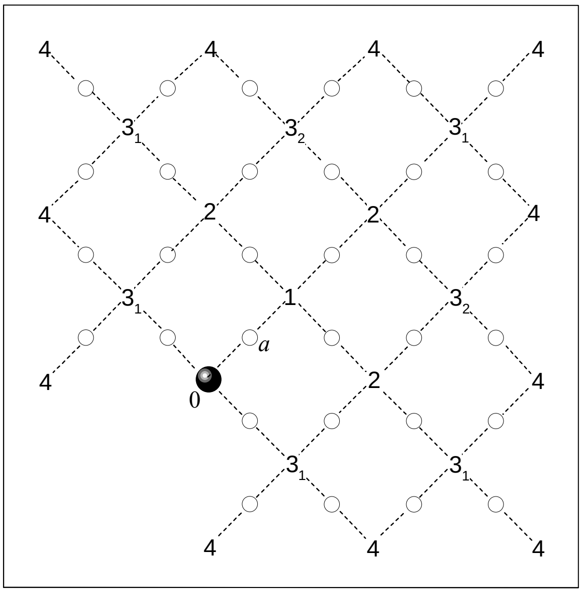

Figure 2: Scheme of substrates atoms (small circles) disposition and possible ways of adatoms displacements to the positions1, 2, 3_1, 3_2, 4 (dotted lines). Adatom "marked" in the initial position is shown by the large sphere.

Here it is suggested that the number of atoms in the positions 4 is so small that their stream in the position 3 can be ignored. Therefore, the system of kinetic equations (1) describes time dependence of concentration of the adatoms located in four positions (0, 1, 2, 3). It follows from Eq. (1) that if at the initial moment all adatoms were in 0 positions ($n(0) = n_0$) and they were marked, then a decrease of the concentration of "marked" adatoms as a function of time $c(t) = n/n_0$ can be described by the expression (2)

$$c(t) = \frac{1}{2}\exp(-\nu t)\left[\left(1-\frac{5\sqrt{133}}{133}\right)\mathrm{ch}\left(\frac{\sqrt{51}}{12}\sqrt{1+\frac{\sqrt{133}}{17}}\nu t\right) + \left(1+\frac{5\sqrt{133}}{133}\right)\mathrm{ch}\left(\frac{\sqrt{51}}{12}\sqrt{1-\frac{\sqrt{133}}{17}}\nu t\right)\right] \tag{2}$$

Figure 3 shows the results of computer simulations of the surface diffusion obtained at 700, 750, 800 and 850 K temperatures. The values of parameter ν for various temperatures were found by approximation of computer experiment data in correspondence with the expression (2). The obtained results allowed to determine the activation energy of an elementary act of "relay-race" diffusion of adatoms from the slope of ln(ν)-dependence of

1/*T* , which is shown in Fig. 4. A value of activation energy is 0.62±0.04 eV/at. A value of activation energy for “rolling stone” mechanism calculated in Ref. [2] equals 0.71–0.74 eV/at, i.e. it is larger than obtained in our experiment. This fact is an additional confirmation of the dominant role of “relay-race” diffusion mechanism.

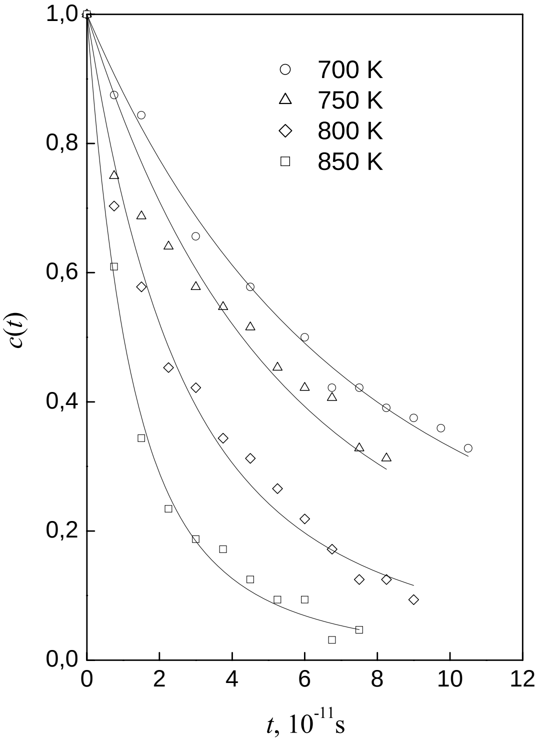

Figure 3: Concentration changes of “marked” adatoms during the annealing at various temperatures and results of the approximation by Eq. (2).

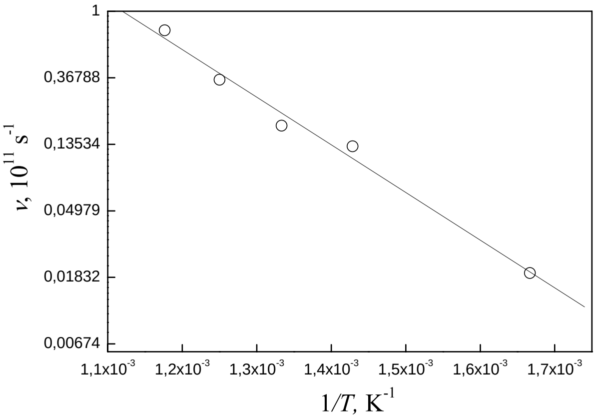

Figure 4: Temperature dependence of number of elementary acts of “relay-race” self-diffusion per time unit constructed on the "ln(ν) – 1/*T*" coordinates.

4 Conclusions

It is shown by means of made MD experiment that the self-diffusion of Pd adatoms on Pd (001) surface occurs mainly by “relay-race” mechanism with a participation of substrate atoms. The activation energy of an elementary act of the “relay-race” self-diffusion calculated from the obtained kinetic equation describing concentration changes of “marked” at the initial time adatoms on the surface, is equal to 0.62±0.04 eV/at.

In conclusion it should be noted that “relay-race” mechanism of adatoms’ diffusion on Pd (001) surface does not preclude the presence of other processes of surface self-diffusion, however their probability is considerably smaller as follows from our MD experiment. For example, during the time of computer experiment only at 850 K one elementary act of the self-diffusion by “rolling stone” mechanism was occurred.

References

[1] Zhdanov, V. P.: *Elementary Physicochemical Processes on the Surface*: *Nauka*, Novosibirsk, 1988 [in Russian].

[2] Liu, C.L., Cohen, J.M., Adams, J.B., Voter, A.F.: EAM study of surface self-diffusion of single adatoms of fcc metals Ni, Cu, Al, Ag, Au, Pd, and Pt. *Surf. Sci.*, 253, pp. 334-344, 1991.

[3] Li, H., Wu, S.C., Tian, D., Quinn, J., Li, Y.S., Jona, F.:Epitaxial growth of body-centered-tetragonal copper. *Phys. Rev. B*, 40, pp. 5841-5844, 1989.

[4] Graham, G.W., Schmitz, P.J., Thiel, P.A.: growth of Rh, Pd and Pt films on Cu(100). *Phys. Rev. B*, 41, pp. 3353-3359, 1990.

[5] Li, Y.S., Quinn, J., Li, H., Tian, D., Jona, F.: Large strains in the epitaxy of Cu on Pt(001). *Phys. Rev. B*, 44, pp. 8261-8265, 1991.

[6] Zeng, H., Vidali, G.: Measurement of growth kinetics in a heteroepitaxial system: Pb on Cu(100). *Phys. Rev. Lett.*, 74, 582-585, 1995.

[7] Garofalini, S.H., Halicioglu., T.: Mehanisms rof the self-diffusion of Au and Ir adatoms on Pt (110) surface. *Surf. Sci.*, 104, pp.199-204, 1981.

[8] Folies, S.M.: Application of method embedded atom to liquid transition of metals. *Phys. Rev. B*, 32, pp. 3409-3415, 1985.

[9] Verlet, L.: Computer experiments on classical fluids. I. thermodynamic properties of Lennard-Jonnes molecules. *Phys. Rev.*, 159, pp. 98-103, 1967.

Proceedings of The 1st International Conference on **D**iffusion in **S**olids and **L**iquids
DSL-2005, July 6-8, 2005, University of Aveiro, Aveiro, Portugal

MATLAB© IMPLEMENTATION OF INVERSE DIFFUSION METHODS

Afina LUPULESCU*, Christopher J. O'BRIEN[1], Martin E. GLICKSMAN[1], Wei YANG[1], Renaud L. HUBERT[2],

[1]Rensselaer Polytechnic Institute, Materials Science & Engineering Department, 110 8th Street, Troy, New York, 12180, USA
[2]Laboratoire d'Analyses par Réactions Nucléaires, Facultés Universitaires Notre-Dame de la Paix, 61 rue de Bruxelles, B-5000 Namur, Belgium

*Corresponding author. Fax: 518-276-2198; Email: lupula@rpi.edu

---

Abstract

One of the authors (CJO) developed a MATLAB© code called `Inversemethods`© to determine concentration–dependent diffusivities from experimental data. This software allows comparison between the diffusivities calculated with four numerical methods: a) Boltzmann-Matano (BM), b) Sauer-Freise-den Broeder (SFB), c) Fictitious image–source method (error function approximation), and 4) Fourier series image–source solutions. The choice of writing this code in MATLAB© was meeting the requirements for portability, as MATLAB© runs on various platforms and enables users to perform subsequent analyses on the data produced by this program. The BM and SFB methods are implemented following Simpson's rule to calculate the integrals, and employs a simple finite–difference method to calculate the derivatives. The software also implements a Savizky-Golay filtering algorithm that smoothes noisy penetration data by locally fitting a 3rd-order polynomial to 201 points. Such parameters were found to be most effective for noisy experimental data obtained using electron microprobe, proton-induced X-ray emission (PIXE), and Rutherford Back Scattering (RBS).

Keywords: Basics of Diffusion; Numerical Methods; Boltzmann-Matano; Sauer-Freise-Den Broeder; Fictitious Image Source; Fourier Series, Savizky-Golay

---

1 Introduction

Extracting diffusivities from experimental data is a challenging task. Usually, the diffusion coefficients are calculated by applying different solutions to Fick's second law. Composition-dependent diffusivities are encountered more often than are the simpler linear cases involving a constant diffusivity. This paper explains and demonstrates the development of the InverseMethods© program at Rensselaer Polytechnic Institute (RPI) to determine concentration–dependent diffusivities from experimental binary diffusion data [1,2,3]. This software first allows comparison between the diffusivities calculated from both the Bolztmann-Matano, and the Sauer-Freise-den Broeder methods [2,3]. The RPI MATLAB© code also produces the results of other solutions to the linear diffusion equation for semi-finite media: a) Fictitious image source method, and b) Fourier series source techniques. Using inverse methods to calculate diffusion coefficients is not original. However, the current study was undertaken with the goal of creating robust in–house software capable of comparing these four methods for extraction of binary interdiffusion coefficients.

2 RPI MATLAB© Code–`InverseMethods`©

The software extracts *D*-values and facilitates comparison among the diffusivities calculated using four different inverse methods for finding interdiffusion coefficients from penetration data measured in a binary diffusion couple. The concentration-dependent diffusivity, *D*(C), is calculated using the Boltzmann-Matano, and the Sauer-Freise-den Broeder methods. Output from the program is returned showing the values of the concentration-dependent interdiffusion coefficient in graphical and text form. The value of concentration-dependent diffusivity calculated for the Matano interface is given in order to aid in comparing these results with the single diffusivity calculated by the other two methods allowed (viz., Error function and Fourier series method). These last methods model the penetration curve in a binary diffusion couple with fictitious image sources and appropriate no-flow boundary conditions presumed to exist at the lateral extremes of the concentration data. Both the

Fourier and Error-function series approximations are used to determine diffusivity at the Matano interface. Diffusivity values and the concentration curves resulting from these values are shown along with the R^2 values. This code could be used as MATLAB© function or/and as a simple graphical interface (GUI). See Figure 1. Since the graphical interface is still in progress, we will discuss only the code as a MATLAB© function. The code was written for MATLAB© and is run by calling it as a function from the MATLAB© command line interface. The primary design is to be portable for use by students and researchers interested in finding concentration-dependent diffusion coefficients from binary couple data.

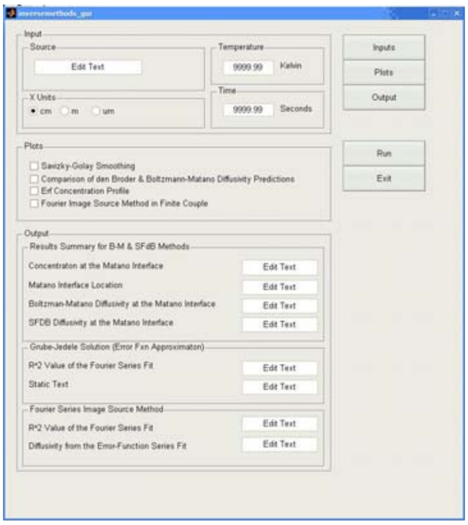

Temperature: 9999.99 Kelvin

Time: 9999.99 Seconds

X Units: ● cm ○ m ○ um

- ☐ Savizky-Golay Smoothing
- ☐ Comparison of den Broder & Boltzmann-Matano Diffusivity Predictions
- ☐ Erf Concentration Profile
- ☐ Fourier Image Source Method in Finite Couple

Results Summary for B-M & SFdB Methods
Concentraton at the Matano Interface
Matano Interface Location
Boltzman-Matano Diffusivity at the Matano Interface
SFDB Diffusivity at the Matano Interface

Grube-Jedele Solution (Error Fxn Approximaton)
R^2 Value of the Fourier Series Fit
Static Text

Fourier Series Image Source Method
R^2 Value of the Fourier Series Fit
Diffusivity from the Error-Function Series Fit

Figure 1: Graphical interface (GUI) for the RPI MATLAB© code, `InverseMethods`©. *In progress.*

The Boltzmann-Matano method is also implemented through the `InverseMethods`© program. The implementation uses the integro–differential form [2, 3] that can be expressed as

$$D(C^{'}) = \left(-\frac{1}{2t}\frac{dx}{dC}\right)_{C^{'}} \int_{C_R}^{C^{'}} \left(x - X_m\right)\, dC \tag{1}$$

The code also contains an algorithm to compute the location of the Matano interface by finding the minimum of the difference between the areas above and below the concentration curve, as implied by the integral form of the Matano interface condition,

$$\int_{-\infty}^{X_M} \left[C_L - C(x)dx\right] = \int_{X_M}^{\infty} \left[C(x) - C_R\right] dx \tag{2}$$

The Sauer-Freise-den Broeder method is implemented by using its integro-differential form that can be expressed as

$$D(C^{'}) = \frac{1}{2t\left(\frac{dC}{dx}\right)_{x^{'}}} \left[(1-\psi)\int_{x^{'}}^{\infty}\left(C^{'} - C_R\right)dx + \psi\int_{-\infty}^{x^{'}}\left(C_L - C^{'}\right)dx\right] \tag{3}$$

The integrals in Eqs.(1, 3) are calculated by using Simpson’s rule, and a and a finite-difference method for approximating the spatial derivatives of the concentration.

3 Running the program

`InverseMethods`© software was programmed as a MATLAB© function, which does not return arguments. It only displays a figure window. Additional output is returned to the screen that gives the numerical error and an estimate of the concentration at the Matano interface. These aid in locating the interface in the lower window of the displayed plot. The function requires three inputs where the function call is of the form `InverseMethods`© (concentration data, time, smoothing option) where concentration data is an *n* by 2 matrix with the second column containing the concentration values at the distances in the corresponding row of the first column. The time argument is the elapsed time (*t*) at which the concentration versus distance data were obtained. The smoothing option argument is an integer argument that may contain the values 0, 1, or 2. Three options are offered for subsequent interpolation and smoothing of the data:

1. The program will use the data without interpolating, smoothing, or otherwise altering the input. This option must be used with caution because the results are sensitive to the initial data. This option often results in significant numerical instability in the output. As a result of this sensitivity, however, this method is accurate to the fourth order of the step-size.

2. The program will implement a cubic-spline interpolation using the MATLAB© function spline to smooth and evenly sample the input data at evenly spaced intervals along the distance axis. The built-in default value for the number of sampling points is 2000; this default value may be changed in the code. The spline smoothing does not always improve the quality of the output. In fact, for already smoothed and evenly spaced data sets, spline interpolation can cause the appearance of numerical artifacts in the output.

3. This option also implements a cubic spline interpolation step to sample the data at 2000 uniformly spaced points. Interpolation is undertaken in order to convert originally unevenly spaced data into a form *usable by the algorithms provided by the software. This option also implements a Savizky-Golay filtering algorithm that smoothes noisy data by locally fitting a 3rd-order polynomial to 201 points. The procedure was found to be effective for noisy experimental data.*

Initially, the program displays a graph showing the input data and the results of smoothing, if employed. During execution, the user is prompted to enter the physical unit of distance used in the input concentration-distance data file. One enters the number that corresponds to the distance unit used as prompted. All diffusivity data for this program are given in units of (cm^2/s).

4 Methodology

Many programs that are capable of performing inverse diffusion coefficient extraction rely on a curve-fitting algorithm before performing the analysis. Curve fitting insures that the data are sufficiently well behaved, and have continuous first derivatives for subsequent use during numerical integration. The authors, however, felt that the quality of curves fit to some of the noisy and non-symmetric diffusion data used for testing this program fell short of what was desired. The authors felt that an alternative approach was needed that would better capture the nuances in diffusion profiles, especially those that arise in multicomponent diffusion, or non-symmetric data. The primary method for dealing with the compound problem of non-uniformly spaced, noisy data, was to interpolate the data to a high degree of accuracy using a cubic spline then taking uniformly spaced data and implementing a smoothing algorithm. The algorithm used to smooth the data is the well-known Savizky-Golay filter [4]. The Savizky-Golay filter is commonly employed in signal-processing as a low-pass filter capable of eliminating high-frequency noise while preserving the details of the underlying, lower frequency, signal. This two-fold method is offered as an option that may be employed if the user finds that it is required; otherwise, if the data is sufficiently smooth, the user may follow other options that request more of the original data.

5 Numerical Methods

Due to the need for integration and calculation of derivatives in both the Boltzmann-Matano method, and the Sauer-Freise-den Broeder method, Simpson's fifth-order 1/3 rule [1] was employed in all cases for integration, whereas derivatives were taken using fourth-order central-differences. Near the endpoints of the data, however, to avoid loss of accuracy in the derivatives, a forward or backwards difference method (also of fourth-order) was implemented to eliminate the need to truncate data near the end of its range. One minor simplification was incorporated into the program that resulted from a limitation of Simpson's 1/3 rule, which requires the number of data points to be even [1]. Consequently, the program truncates the last data point when the data contain an odd number of points. This simplification allowed for significantly simpler programming without loss of useful data. This simplification was justified because the data near its endpoints were already of questionable usefulness, due, in part, to numerical instabilities in both methods. These instabilities result from the need to divide small values of the derivative approaching zero, with small values of the area integrals that are also approaching zero.

6 Examples of the `InverseMethods`©

6.1 Rh–C Diffusion Couple: Smoothing procedure

These data were used to demonstrate the output of `InverseMethods`© software. First, the number of points at which the sampling occurs was intentionally chosen to be large in the program in order to obtain an accurate representation of the original data, which is then smoothed by the Savizky-Golay Filter. See Figure 2 for the graphical output.

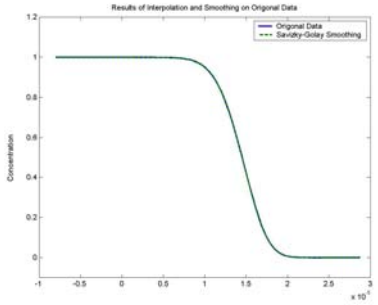

Figure 2: Original experimental versus data obtained smoothed by using Savizky-Golay filter.

6.2 Rh–C Diffusion Couple: Boltzmann-Matano and Sauer–Freise– Den Broeder graphical output

A second graphical and numerical output of the `InverseMethods`© software is represented by the diffusivities extracted using Boltzmann-Matano and Sauer-Freise-den Broeder methods.

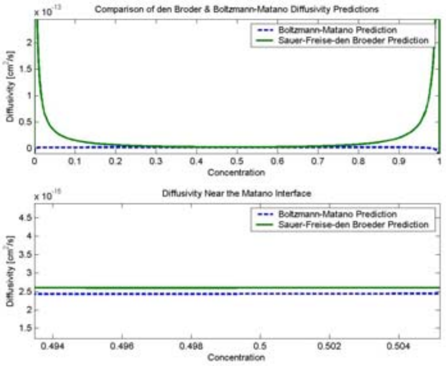

Figure 3: The diffusivities values obtained by `InverseMethods`© implementing Boltzmann-Matano and Sauer-Freise-den Broeder methods. *Upper frame:* a comparison of the results using two different methods. *Lower frame:* a comparison of the diffusivity results next to the Matano interface.

This output is composed of two frames: a) the upper frame represents an overall comparison of the two methods for all concentration-distance interval, b) the lower frame shows the detailed comparison of the two methods close to the Matano interface. See Figure 3.

6.3 Rh–C Diffusion Couple: Error function solution and Fourier series solution

The `InverseMethods`© allows the user to obtain both numerical and graphical results for the Grube-Jedele (error function approximation) solution as well as the Fourier series solution.

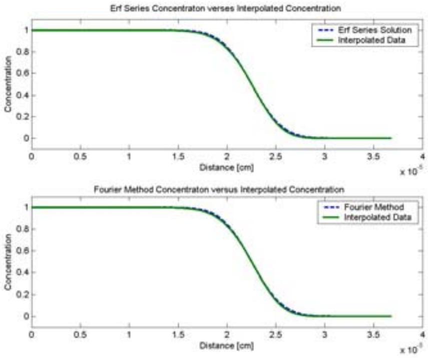

Figure 4: Error function versus interpolated concentrations. *Upper frame:* Grube-Jedele solution. *Lower frame:* Fourier's method.

Users could extract the diffusivities that appear in the numerical outputs produced by the `InverseMethods`© program, and proceed to show the results as Arrhenius plots. See Figure 5.

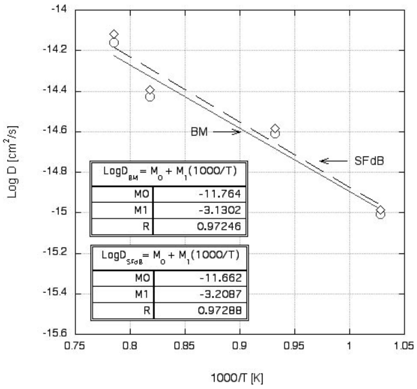

Figure 5: Arrhenius plot based on the numerical outputs obtained by using `InverseMethods`©. Comparison of the numerical results of the four methods: a) the Boltzmann–Matano, b) the Sauer–Freise–den Broeder.

These results are based on experimental data measured at different temperatures for a binary diffusion couple Rh-glassy C.

7 Conclusions

1) An original MATLAB© code named `InverseMethods`© has been developed at RPI.

2) The code and its graphical interface, or GUI, are user friendly. Some MATLAB© experience is recommended if you use the MATLAB© function.

3) Four different sets of diffusivity data for Rh-C are displayed as both numerical and graphical outputs.

4) These diffusivity data serve as a meaningful comparison between the four methods.

Acknowledgments

The authors are grateful for the support received from the John Tod Horton Chair in Materials Science and Engineering, Rensselaer Polytechnic Institute, and from the National Science Foundation under grant DMR-0303813.

References

[1] O'Brien, C.J.: *Original Notes-Diffusion in Solids Project*, Rensselaer Polytechnic Institute, 2004.

[2] Glicksman, M.E.: *Diffusion in solids: Field Theory, Solid-State Principles, and Applications*. John Wiley and Sons, New York, 2000.

[3] Glicksman, M.E., Lupulescu, A.: *Diffusion in Solids: Original Teaching Module, Rensselaer Polytechnic Institute*, Troy, NY, 2002.

[4] Jaluria, Y.: *Computer Methods for Engineering*, Taylor & Francis, Philadelphia, PA, 1996.

Proceedings of The 1st International Conference on **D**iffusion in **S**olids and **L**iquids
DSL-2005, July 6-8, 2005, University of Aveiro, Aveiro, Portugal

IMPLEMENTING THE SQUARE–ROOT DIFFUSIVITY METHOD

Afina LUPULESCU[1,*], Martin E. GLICKSMAN[1], Shrividya KAILASAM[2], Wei YANG[1]

[1]Rensselaer Polytechnic Institute, Materials Science & Engineering Department, 110 8th Street, Troy, New York, 12180, USA
[2]National Exposure Research Laboratory, US Environmental Protection Agency, Las Vegas, NV, 89119, USA

[*]Corresponding author. Fax: 518-276-2198; Email: lupula@rpi.edu

Abstract

Applying the theory of multicomponent diffusion and solving Fick's second law is a challenging task, even for cases of linear diffusion. Fortunately, most of the tedious mathematical aspects can be eliminated by employing programs that efficiently handle the various linear algebraic steps. In 1986, Morral and Thompson [1, 2] developed a systematic methodology for constructing linear, one-dimensional, single-phase, multicomponent diffusion solutions, now referred to as the "square-root diffusivity method." Implementing the square-root diffusivity method for multicomponent alloys was made convenient through the computer program, *Profiler©,* developed by Morral and Stalker [3, 4]. Here we discuss an educational code based on the *MatLab©* computing platform. The new code combines original features available in *Profiler©* as well as those added by Glicksman and Lupulescu [5] to evaluate multicomponent diffusion in single-phase solid-solution alloys to study the kinetics of zero-flux planes (ZFP's).

Keywords: Basics of diffusion; Numerical methods; Multicomponent diffusion; Zero flux plane; Square-root diffusivity method

1 Introduction: Multicomponent diffusion software

There are some well-known computer programs and mathematical packages that handle the mathematical requirements encountered in multicomponent diffusion problems. A brief summary of available numerical approaches follows.

MultiDiflux©: This program is based on an analysis developed by M.A. Dayananda [6, 7, 8, 9]. called *MultiDiflux©*, which consists of two versions: 1) an educational and research computer program being developed for interdiffusion calculations of multicomponent diffusion couples. *MultiDiFlux©* smoothes the raw penetration-distance data measured from concentration profiles using Hermite interpolation polynomials. The program calculates the locations of the Matano planes for each component and evaluates the profiles of all the corresponding fluxes directly from the smoothed profiles. *MultiDiFlux©* also provides estimates of the ternary interdiffusion coefficients over selected concentration ranges along the diffusion zone.

DICTRA©**:** *DICTRA©* is an unique engineering [10] software for simulations of DIffusion Controlled TRAnsformations in multicomponent alloys. *DICTRA* coupled with the thermodynamic data base, *Thermo-Calc©*, provides a powerful tool for simulating diffusion in a wide variety of scientific and industrial applications. *DICTRA©*, which started out as a Ph.D. dissertation, evolved to a commercial system developed by John Ågren, KTH, Stockholm, Sweden.

Profiler**©** [3, 4]: *Profiler©* provides a systematic method for obtaining one-dimensional, single-phase, multicomponent (up to seven components), diffusion solutions. The methodology behind it was outlined in a series of papers by Morral and Thompson [1, 2], and is often referred to as the *"square-root diffusivity method."* The multicomponent concentration field for a linear diffusion couple with a constant *D*-value consists of a sum of linearly independent error functions. Thompson and Morral's published solution yields the concentration *differences* for each component around a diffusion couple's average concentration, expressed as a sum of error function complements, and appearing as Eqs.(3) and (4) in [1, 2].

2 RPI's MatLab© Code

Both Profiler© and MultiDiflux© are designed for, and operate on, DOS-based PCs. Many students have a difficult time returning to command-line MS-DOS. Consequently, we developed an educational Matlab© code to model a wider range of diffusion effects occurring in multicomponent alloys. This code implements all the equations used in Profiler© [3] plus those derived subsequently by Glicksman and Lupulescu for analyzing the component diffusion fluxes [5, 11, 12, 13]. Input required from the user are the elements of the interdiffusion coefficients matrix, [D_{ij}], with their values given in CGS units. See Figure 1. The interdiffusion matrices may be obtained using MultiDiFlux© or DICTRA© software. The new code is flexible in choosing diffusion time and temperature, and chemical compositions of the end-members as an Euler angle(s) in composition space. There are two main options: a) selecting a ZFP angle for users interested in obtaining the zero flux Euler angles, and corresponding plots, and b) selecting any composition (Euler angle) of interest and the corresponding plots.

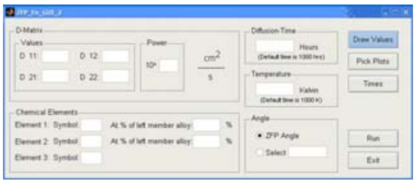

● ZFP Angle

Figure 1: First screen of the graphical interface (GUI) for the RPI Matlab© code.

The plots and their names are listed in the middle section of the graphical interface. The user can select any of the desired figures mentioned on the list. The figures obtained follow the logical order presented by Glicksman and Lupulescu [5].

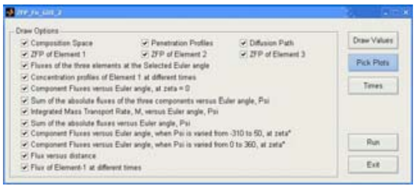

☑ Composition Space ☑ Penetration Profiles ☑ Diffusion Path
☑ ZFP of Element 1 ☑ ZFP of Element 2 ☑ ZFP of Element 3
☑ Fluxes of the three elements at the Selected Euler angle
☑ Concentration profiles of Element 1 at different times
☑ Component Fluxes versus Euler angle, at zeta = 0
☑ Sum of the absolute fluxes of the three components versus Euler angle, Psi
☑ Integrated Mass Transport Rate, M, versus Euler angle, Psi
☑ Sum of the absolute fluxes versus Euler angle, Psi
☑ Component Fluxes versus Euler angle, when Psi is varied from -310 to 50, at zeta*
☑ Component Fluxes versus Euler angle, when Psi is varied from 0 to 360, at zeta*
☑ Flux versus distance
☑ Flux of Element-1 at different times

Figure 2: Second screen of the graphical interface (GUI) for the RPI Matlab© code.

Basically, one can predict the behavior of any ternary alloy if one knows the interdiffusion coefficient matrix. See Figure 2. The user could choose the times of interest for the selected plots by opening the 3rd screen of the graphical interface. If the new times are not implemented, the code will select the indicated default times. See Figure 3.

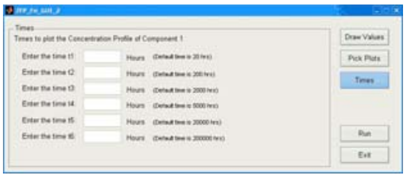

Figure 3: Third screen of the graphical interface (GUI) for the RPI Matlab© code.

To determine the concentrations of the first component in the right-hand end-member alloy, the cosines of angles ranging from 0° to 359° incremented by 1° are added to the concentration of the first component in the left-hand end-member alloy. The composition of any right-hand end-member alloy may be determined from the composition space plot, once the Euler angle is known. See Figure 4.

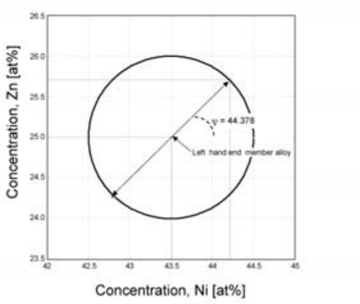

Figure 4: Composition space for the left-hand end-member alloy Ni–43.5at.%, Zn–25at.%, Cu–31.5at%, and all other right-hand end-members that differ by 1At.% in their composition vectors.

The code extracts the concentration profiles of the chosen ternary alloy. See Figure 5. The MatLab© code produces all plots based on Eqs. 23-25 from [5]. Component fluxes are calculated at $\zeta=0$, where $\zeta=x/\sqrt{(4E_i t)}$ is the scaled diffusion length, x is the distance from the Matano plane, E_i is one of the N-1 eigenvalues of the diffusion matrix for an N-component alloy, and t is the diffusion time. Figure 6 illustrates the individual flux lines that are computed at a 0.5 increment. It also verifies the close correspondence between individually computed data, based on Eq. 23 from [5], and their analytical representation.

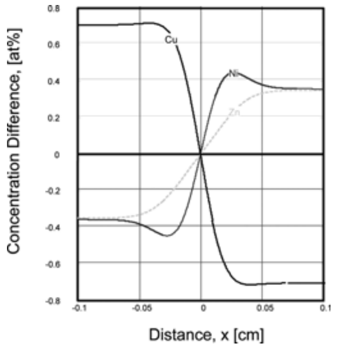

Figure 5: Concentration profiles for the left-hand end-member alloy Ni–43.5 at.%, Zn–25at.%, Cu–31.5at%, obtained by using the RPI Matlab© code.

The stationary ZFPs occur precisely at the angles calculated using Eqs. 15-17 [5] and represent the roots of these flux curves. There are in principle six stationary ZFPs for Ni, Zn, and Cu, shown in Figure 6 [4, 11, 12, 13].

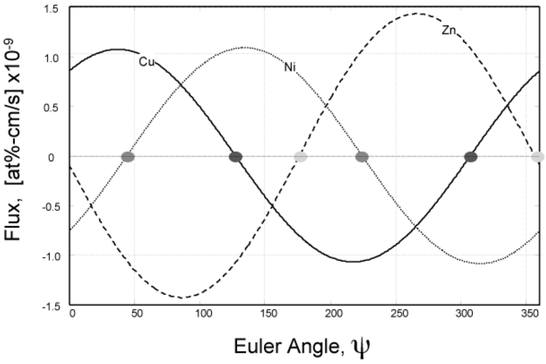

Figure 6: Component fluxes versus Euler angle, at $\zeta=0$ in the ternary alloy 43.5 at%-Ni, 25 at%-Zn, 31.5 at%-Cu.

The RPI Matlab© code calculates these fluxes as explained, by using Eqs. 25-27 [5], and demonstrates the narrowing trend of the fluxes for any ternary system approaching ψ^* or ψ_{minor}. As it is clearly demonstrated in Figures 7 and 8, the width of the flux distribution narrows substantially where the composition vector is oriented near the critical values of ψ_{minor}=-29.0° and ψ_{minor} =69.81°, respectively. This critical angle may be found for any ternary alloy system using the relation given in [1, 2, 4, 5]. For the case of the two Cr-Al-Ni couple [5], the width and spreading rates of the ternary diffusion zones can be reduced by about 50% by adjusting the composition vector's orientation to be near the Euler angle for the minor eigenvector. For the ternary alloy illustrated in Figure 8, the flux near to the critical Euler angle is decreased 80%.

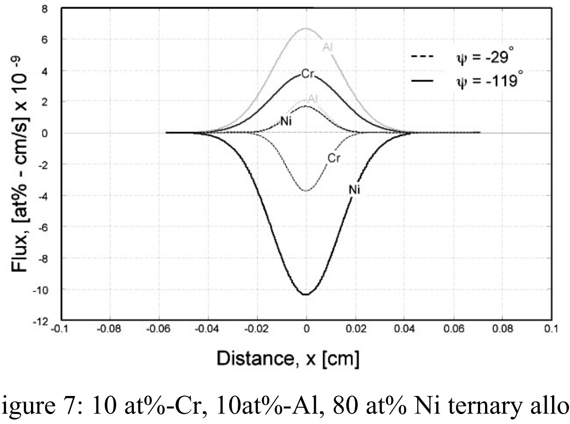

Figure 7: 10 at%-Cr, 10at%-Al, 80 at% Ni ternary alloy fluxes calculated at two different orientation in composition space.

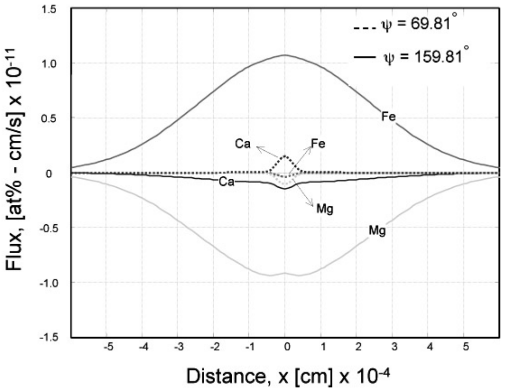

Figure 8: 32.39at%-Fe, 49.41at%-Mg, 18.20at%-Ca ternary alloy fluxes calculated at two different orientations in composition space. Dashed lines represent the fluxes for Ca, Mg, Fe next to the critical angle ψ_{minor} =69.81°.

Figures 9 and 10 show the absolute sum of the component fluxes (AFS) and the integrated atomic transport, *M*, across the diffusion zone, plotted against the Euler angles of the specified couples. The total atomic transport rate across the diffusion zone, was calculated according to Eq. 29 from Glicksman and Lupulescu [5] using the $[A_{ij}]$ matrix. For a specified diffusion time, *t*, these amplitudes were calculated for all the Euler angles, along with the elements of the $[D_{ij}]$ matrix, and the major and minor eigenvalues, e_1, and e_2. It is apparent from Figures 9 and 10 that the integrated atomic transport rate, *M*, for all of the diffusing components moving throughout the couple is sharply reduced over a narrow range of compositions, for which the couple's Euler angles correspond closely with the orientation angle of the minor eigenvector.

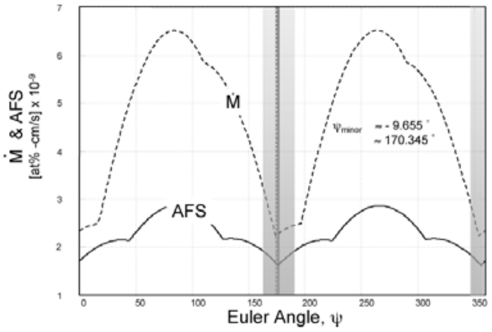

Figure 9: Absolute sum of fluxes, AFS, and integrated mass transport, M, versus Euler angles for couples with the fixed end-member ternary alloy Ni–43.5at.%, Zn–25at. %, Cu–31.5at%.

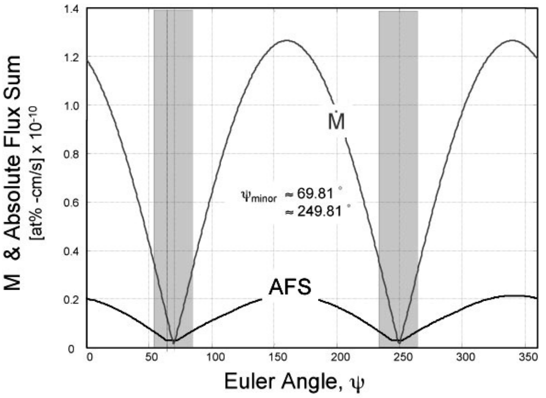

Figure 10: Absolute sum of fluxes, AFS, and integrated mass transport, *M*, versus Euler angles for couples with the fixed end-member ternary alloy 32.39at%-Fe, 49.41at%-Mg, 18.20at%-Ca.

Conclusions

1) A new MatLab© code was developed to understand multicomponent diffusion in various single-phase alloy systems.

2) The numerical data obtained upon running the MatLab© script was compared during the initial stages of this work with the output provided by Profiler©. Subsequent output, such as fluxes and integrated transport could not be checked as Profiler© does not these plots generated by this script.

3) The script was also tested by comparing the plots with those obtained independently using Kaleidagraph©, a spread-sheet based plotting program.

4) MatLab© proved to be an efficient tool in modeling diffusion across thick diffusion couples. The script can be run by a single command and the plots are generated within minutes. As the software can handle large volumes of data, it was possible to achieve high resolution in the plots.

5) The RPI MatLab© code was tested for different ternary alloys. The diffusive spreading is markedly reduced for multicomponent couples located in composition space close to the minor eigenvectors of the diffusion matrix.

Acknowledgments

The authors are grateful for the partial support received from the John Tod Horton Chair in Materials Science and Engineering, Rensselaer Polytechnic Institute, and from the National Science Foundation under grant NSF-DMR-0303813.

References

[1] Thompson, M.S., Morral, J.E.: *Acta Metallurgica*, 34, p. 339, 1986.
[2] Thompson, M.S., Morral, J.E.: *Acta Metallurgica*, 34, p. 2201, 1986.
[3] Stalker M.K., Morral, J.E.: *Acta Metall. Mater.,* 38, 439, 1990.
[4] Glicksman, M.E.: *Diffusion in Solids: Field Theory, Solid-State Principles, and Applications,* John Wiley & Sons Inc., New York, 2000.
[5] Glicksman, M.E., Lupulescu, A.O.: *Acta Materialia,* 51, p. 1181, 2003.
[6] Dayananda, M.A., Kim, C.W.: *Metall. Trans. A*, 10A, p. 1333, 1979.
[7] C.W. Kim, M.A. Dayananda, *Metall. Trans. A*, 15A, p. 649, 1984.
[8] Dayananda, M.A., Sohn, Y.H.: *Metall. Trans.*, 30A, p. 537, 1999.
[9] https://engineering.purdue.edu/MSE/Research/MSE.
[10] http://www.thermocalc.com/Products/Products.html.
[11] Lupulescu, A., Glicksman, M.E., Kailasam, S.: *Journal of Defect and Diffusion Forum, Trans Tech Publications Ltd.,* 237-240, p. 230, 2005.
[12] Lupulescu, A., Glicksman, M.E., Kailasam, S., Yang, W.: *TMS Letters,* TMS (The Minerals, Metals & Materials Society), 2005.
[13] Vielzeuf, D., Lupulescu, A., Perchuk, A., Laporte, D., Baronnet, A., Ahmad, A.: *TMS Letters,* TMS (The Minerals, Metals & Materials Society), 2005.

Proceedings of The 1st International Conference on **D**iffusion in **S**olids and **L**iquids
DSL-2005, July 6-8, 2005, University of Aveiro, Aveiro, Portugal

NON-LINEAR VICOPLASTIC POLYCRYSTALLINE INTERMEDIATE MODELING FOR TEXTURE EVOLUTION IN FCC METALS: COMPRESSION TEST

Said AHZI[1], Siham M'GUIL[1,*], Hiba YOUSSEF[1], Mohammad KHALEEL[2], José GRACIO[3]

[1]Université Louis Pasteur – IMFS – UMR 7507 CNRS
2, rue Boussingault, 67000 Strasbourg, France
[2]Pacific Northwest National Laboratory
Computational Sciences and Mathematics Division
Richland, WA 99352, USA
[3]Department of Mechanical Engineering,
University of Aveiro, Portugal

[*]Corresponding author. Fax: +33 (0) 388 614 300; Email: siham.mguil@ipst-ulp.u-strasbg.fr

---

Abstract

In this paper, we report predicted results for texture evolution in FCC metals under uniaxial compression test. These results are computed using a newly developed nonlinear rigid viscoplastic crystal plasticity model based on an intermediate interaction law. This interaction law is formulated by the minimization of a normalized error function which combines the local fields' deviations, from the macroscopic ones, obtained by the classical upper bound (Taylor) and lower bound (Sachs) models. This interaction law leads to results lying between the upper and lower bound approaches by simply varying a scalar weight function ϕ ($0<\phi<1$). A simple interaction law based on the linear mixture of the fields from the Taylor and Sachs models is also used. The results from these both the linear and nonlinear intermediate approaches are shown in terms of texture evolution under uniaxial compression. These results are discussed in comparison with the well known experimental textures in compressed FCC metals. Finally, we show that the linear intermediate approach yields fairly acceptable texture predictions under compression and that the fully non-linear approach predicts much better results.

Keywords: Crystallographic Texture; *Polycrystalline plasticity; Intermediate linear and non-linear models*

---

1 Intermediate modeling

1.1 Single Crystal Behavior

We assume plasticity to occur by crystallographic slip only and use the classical viscoplastic power law at the slip system level. The constitutive law for rigid viscoplastic behavior of the single crystal is given by the following non linear relationship between the plastic strain rate tensor D and the deviatoric Cauchy stress tensor S:

$$D = \dot{\gamma}_0 \sum_{\alpha} R^{\alpha} \cdot \dot{\gamma}^{\alpha} \equiv M(S) \cdot S \qquad (1)$$

In Equation (1), $\dot{\gamma}^{\alpha}$ is the shear rate for the slip system α, $\dot{\gamma}_0$ is a reference shear rate and R^{α} is the symmetric part of Schmid tensor. Here, *M(S)* represents the fourth order compliance tensor which depends on the stress tensor S.

1.2 Macroscopic Behavior

The macroscopic behavior can be described by a similar relationship to (1). If we denote by $\overline{D}$, $\overline{S}$ and $\overline{M}$ the macroscopic plastic strain rate, the deviatoric stress and compliance tensors, respectively, we can then write:

$$\overline{D} = \overline{M} \cdot \overline{S} \qquad (2)$$

The global (consistency) conditions are given by the following averaging conditions:

$$< D >= \overline{D} \quad \text{and} \quad < S >= \overline{S} \qquad (3)$$

Here, < > designates the volume average over the entire volume of the considered polycrystal.

1.3 Concentration tensors – Interaction laws

1.3.1 Linear formulation for rigid viscoplastic deformation

Linear combination of the Taylor and Sachs models was proposed by Gambin and Barlat [1] for rigid viscoplastic case and was extended to the elastic viscoplastic behavior by Ahzi et al. [2, 3]. Following these works, we used the classical rigid viscoplastic Taylor ($D = \overline{D}$) and Sachs ($S = \overline{S}$) hypotheses for estimating a linear intermediate interaction law. This is simply carried out by combining the local fields obtained from the bounds (Taylor and Sachs) using a single weight parameter ϕ that varies from zero to unity:

$$R^{\phi} = (1-\phi) \cdot R^{t} + \phi \cdot R^{s} \tag{4}$$

Here, R represents the local field (stress, strain rate or spin) and the superscripts ϕ, t and s designate the intermediate Taylor and Sachs models, respectively.

1.3.2 Non-linear formulation for rigid viscoplastic deformation

Based on our recent work [4-6] a quadratic error function E is defined:

$$E = (1-\phi) \cdot E_d + \phi \cdot E_s \tag{5}$$

This error combines the normalized deviation of the single crystal strain rate from the macroscopic one, represented by E_d, and that of the single crystal stress and the macroscopic one E_s. The weight parameter ϕ varies between 0 (for Taylor) and 1 (for Sachs). By minimizing this error function E, we obtain the following highly non-linear dual interaction laws [6]:

$$D = A \cdot \overline{D} \quad \text{or} \quad S = B \cdot \overline{S} \tag{6}$$

The fourth order interaction tensor A (or B) is a function of the local and macroscopic compliance tensors and of ϕ (Details are given in ref. [6]):

$$A = \left[(1-\phi) I + \frac{\phi}{n} M^{-1} M^{-1} \right]^{-1} \cdot \left[(1-\phi) I + \frac{\phi}{n} M^{-1} \overline{M}^{-1} \right] \tag{7}$$

$$B = \left[(1-\phi) M + \frac{\phi}{n} M \right]^{-1} \cdot \left[(1-\phi) \overline{M} + \frac{\phi}{n} M \right] \tag{8}$$

We note that A reduces to the identity tensor if we take $\phi = 0$. In the same way, the interaction tensor B reduces also to the the identity for the lower bound case ($\phi = 1$). In the above equations, n is the inverse rate sensitivity coefficients (used in the viscoplastic power law).

2 Results: uniaxial compression test

2.1 Used polycrystal

We considered the axisymmetric compression tests for the comparison between these two approaches. We imposed a fully prescribed macroscopic velocity gradient corresponding to a compression test. The used FCC polycrystal is represented by 100 randomly–oriented crystals as shown in Figure 1. The rate sensitivity coefficient is taken as: n = 13. We neglected the strain hardening.

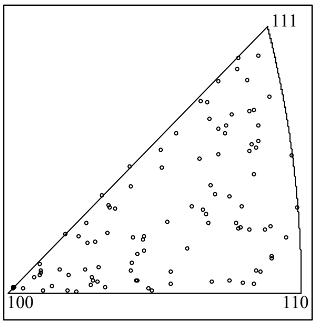

Figure 1: Inverse pole figure for 100 randomly oriented crystals (initial texture).

To be able to quantitatively evaluate these two intermediate models, we also present a statistical analysis of the texture deviation from the expected fiber <110> component. This deviation is schematically explained in figure 2.

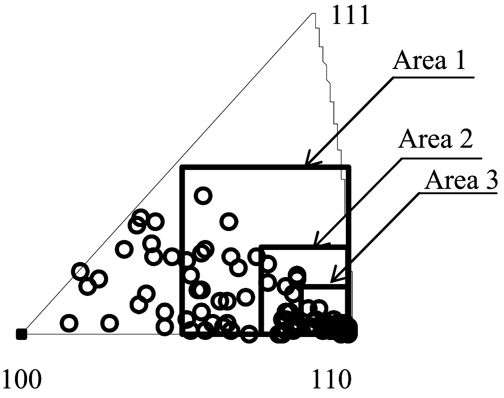

	Area 1	Area 2	Area 3
Δα	19.35°	9.67°	5.37°

Figure 2: Representation of the deviation of texture components from the fiber <110>.

2.2 Results obtained from the pure Taylor and Sachs models

The textures obtained by the pure Taylor and Sachs models and the textures obtained by the non-linear model with the parameter ϕ very close to 0 or very close to 1, give the same results. It is a first numerical validation of the non-linear intermediate model. We choose to plot the inverse pole figures obtained in the case of rigid viscoplastic deformation for three deformation levels: 30%, 70% and 100%. The textures obtained by the Taylor and Sachs models are used as references and are also linearly combined to get the results for the linear intermediate model.

It is well known, from the literature, that the compression texture in FCC metals such as copper show a strong intensity around the <110> component fiber (see for instance Ref. [7]). We can notice that the Taylor results deviate from the <110> fiber and that the Sachs results show that a fairly important number of crystals deviate also from the <110> fiber. These are well established results. Tables 1, 2 and 3 shows the deviations from the fiber <110> for both Taylor and Sachs models at different levels of strain.

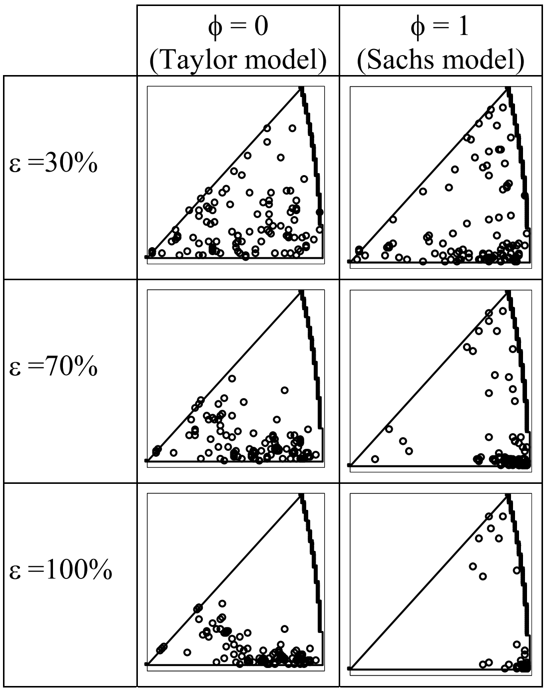

Figure 3: Inverse pole figure in the case of Taylor and Sachs models at ε =30%; 70% and 100%.

Table 1: Deviation of the texture component from the <110> fiber (values in the table represent the number of orientations percent) at 30%.

		$\phi = 0$ (Taylor)	$\phi = 1$ (Sachs)
<110>	Area 1	57	69
	Area 2	21	38
	Area 3	3	12

Table 2: Deviation of the texture component from the <110> fiber (values in the table represent the number of orientations percent) at 70%.

		$\phi = 0$ (Taylor)	$\phi = 1$ (Sachs)
<110>	Area 1	64	88
	Area 2	30	79
	Area 3	7	53

Table 3: Deviation of the texture component from the <110> fiber (values in the table represent the number of orientations percent) at 100%.

		$\phi = 0$ (Taylor)	$\phi = 1$ (Sachs)
<110>	Area 1	74	94
	Area 2	40	91
	Area 3	10	87

2.3 Comparison between the linear and the non-linear approach

2.3.1 Comparison in terms of inverse pole figure

Now, we compare the results from the linear and the non-linear intermediate models. We select for this comparison three deformation levels of 30%, 70 % and 100%. In figures 4, 5 and 6, we plot the inverse pole figures for these two approaches for different values of ϕ (ϕ=0.3, ϕ=0.5 and ϕ=0.7).

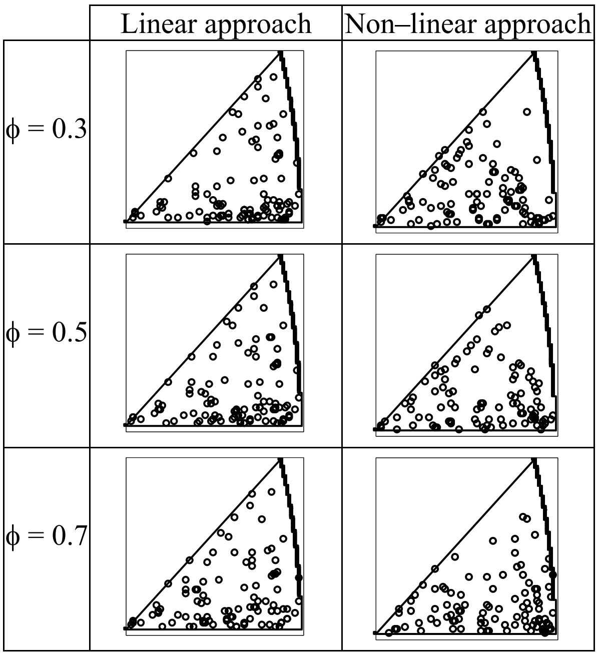

Figure 4: Comparison of the linear and the non-linear models under compression at ε = 30%.

Table 4: Deviation of the texture component from the <110> fiber (values in the table represent the number of orientations percent) at 30%.

			ϕ=0.3	ϕ=0.5	ϕ=0.7
<110>	Area 2	Non-linear	27	33	36
		Linear	21	26	29
	Area 3	Non-linear	8	9	14
		Linear	3	5	7

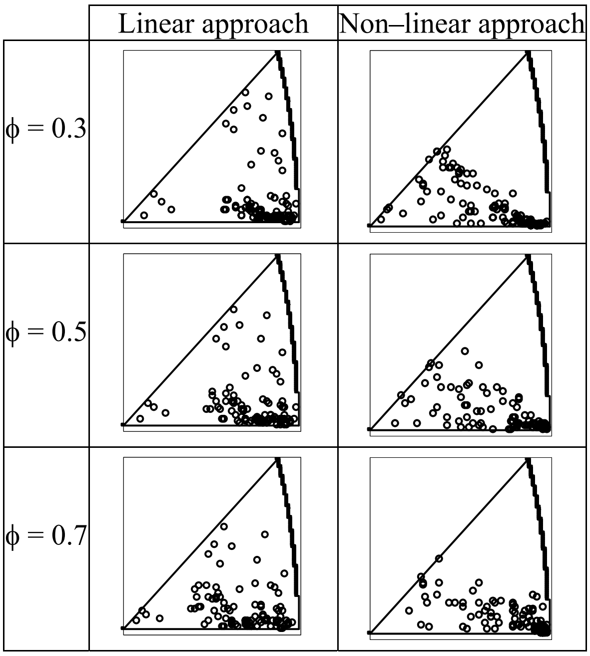

Figure 5: Comparison of the linear and the non-linear models under compression at ε = 70%.

Table 5: Deviation of the texture component from the <110> fiber (values in the table represent the number of orientations percent) at 70% strain.

			ϕ=0.3	ϕ=0.5	ϕ=0.7
<110>	Area 2	Non-linear	47	59	65
		Linear	42	51	64
	Area 3	Non-linear	14	38	41
		Linear	11	18	22

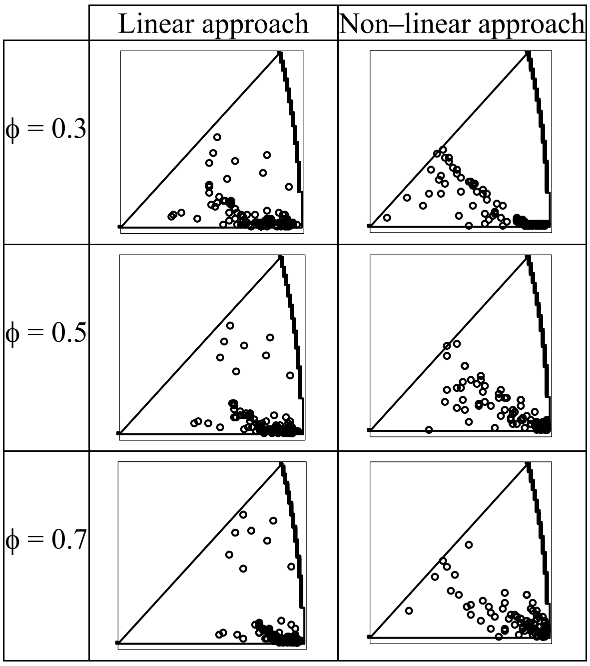

Figure 6: Comparison of the linear and the non-linear models under compression at ε = 100%.

Table 6: Deviation of the texture component from the <110> fiber (values in the table represent the number of orientations percent) at 100%.

			ϕ=0.3	ϕ=0.5	ϕ=0.7
(110)	Area 2	Non-linear	59	69	81
		Linear	54	67	87
	Area 3	Non-linear	38	50	50
		Linear	17	26	41

In Tables 4, 5 and 6, we report the corresponding (to figures 4-6) deviations from the fiber <110> From these results, one can see a difference in texture results depending on the value of ϕ The following remarks can therefore be made:

- at 30%, figure 4 and table 4
For low level of strain, we begin to see the migration of the crystal orientations towards the <110> fiber for the two approaches. This observation is more pronounced with the non-linear model.

- at 70%, figure 5 and table 5
For high values of strain, the two approaches seem to predict the fiber component <110>. However, the percent of crystals with orientation close the <110> fiber is higher for the non linear intermediate model and for higher values of ϕ .

- at 100%, figure 6 and table 6
At 100% strain, both models predict fairly good <110> fiber texture particularly for the value of ϕ=0.5 and 0.7 .

In figure 7 we show the number of crystals with <110> orientation ϕ=0.3. This result shows that with the non-linear model the crystals converge more quickly towards the fiber <110>. A stronger <110> fiber is therefore obtained by the non linear approach.

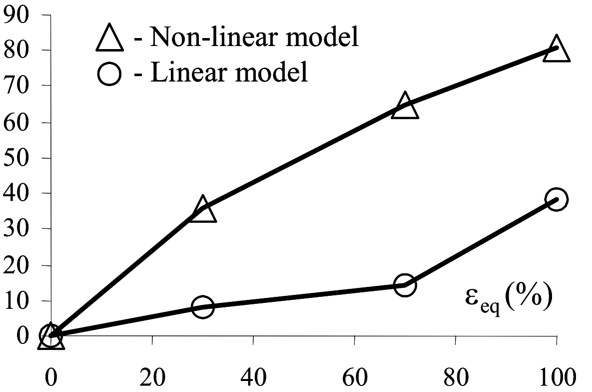

Figure 7: Number of oriented crystals in the <110> direction for the linear and non-linear models, for ϕ = 0.3, as function of strain (%).

2.3.2 Comparison in term of stress/strain curves

The stress-strain curves obtained with the linear and the non-linear intermediate models are very close, that is why, we decide to plot only the results obtained with the linear approach. Figure 8 shows the stress-strain curves for different values of ϕ without strain hardening in the case of linear formulation. One notes, in this figure, that the stress-strain responses for different value of ϕ fall between the Taylor and Sachs estimates for both the linear and non–linear model.

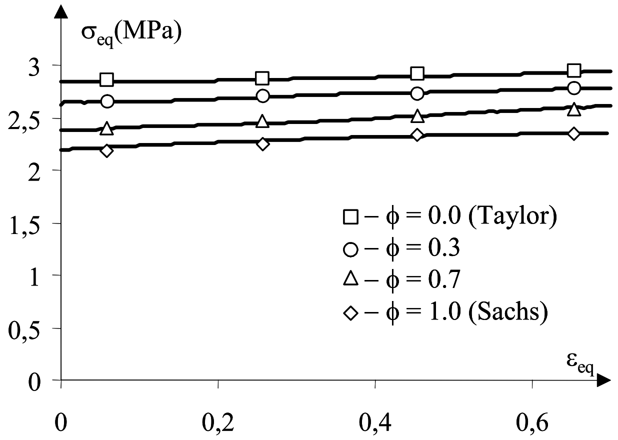

Figure 8: Stress-Strain curves obtained for different values of ϕ for uniaxial compression.

3 Conclusions

Both the linear and the non-linear viscoplastic intermediate models predict a texture transition between the Taylor and the Sachs type textures. For the case of uniaxial compression, the crystal orientations converge more rapidly towards the

<110> fiber by the use of the non-linear approach. At high strains, it is clear that the predicted <110> fiber is stronger for the non-linear approach than for the linear one. This permits us to state the non linear intermediate approach yields better texture predictions than the linear one. This is also true under uniaxial tension test for which the results are reported elsewhere (see [4-6]).
To improve our proposed non-linear intermediate modeling, we need to link the interaction law to some physical insights. For instance, the parameter ϕ must be interpreted in terms of microstructural and physical grounds of the material (stacking fault energy, crystal shape and size…).

References

[1] W. Gambin, F. Barlat, 1997, *International Journal of Plasticity*, Vol. 13, p. 75.

[2] S. Ahzi, S. M'Guil and A. Agah-Tehrani, 2002, *Mater. Sci. Forum*, Vol. 408-412, p. 463.

[3] S. Ahzi, S. M'Guil, 2004; Trans Tech Publications Inc. Periodical *Solid State Phenomena*; as a part of the *Inter. Conf. Texture and Anisotropy of Polycrystals*, July 2004 Metz (France). In press.

[4] S. M'Guil, S. Ahzi, H. Youssef, M.A. Khaleel and J. Gracio, 2005, *Proceedings of McMat2005*, Baton Rouge, Louisiana, June 2005. In press.

[5] S. Ahzi, S. M'Guil and M.A. Khaleel, 2005; *Materials Science Forum*; As part of *ICOTOM 14*, Leuven, July 2005 (Belgium). In press.

[6] S. Ahzi, S. M'Guil, M.A. Khaleel and J.J. Gracio, *Manuscript in preparation* (2005).

[7] C. S. Barett, L. H. Levenson, *Trans. AIME*, 137, pp. 112, 1940.

SILICIDE $NiSi_2$ FORMATION REGULARITIES IN Ni(10 nm)/Si(001) THIN FILM

Svetlana VOLOSHKO[1], Yurij MAKOGON[1,*], Elena PAVLOVA[1], Sergej SIDORENKO[1],
Sergej ZAMULKO[1], Anna MOGILATENKO[2], Gunter BEDDIES[2]

[1]National Technical University of Ukraine "KPI", Kiev, Ukraine
[2]Institute of Physics, Chemnitz University of Technology, Germany

[*]Corresponding author. Fax: +38 044 241 76 18; Email: makogon@users.ntu-kpi.kiev.ua

---

Abstract

Thermally induced solid state reactions in the Ni(10 nm)/Si(001) film system that occur under the annealings in the nitrogen ambient were researched. It was established that the final product of solid state reactions (that is $NiSi_2$) process consists of several steps, namely: a) Si and Ni interdiffusion via a lattice mechanism results in formation of the NiSi polycrystalline silicide layer; b) Si atoms along grain boundaries go out on the surface and accumulate; c) $NiSi_2$ islands form and laterally grow on the surface; d) islands normal growth is accompanied by "diffusion dilution" of the NiSi layer; i) spherical $NiSi_2$ inclusions form in the Si-matrix. A mathematical model was suggested that describes spherical inclusions growth in the finite size areas of the supersaturated solid solution Ni-Si. Approximate solutions of the start-edge task for the second Fick's equation in terms of suggested diffusion model and computer simulation results allow to establish the most important parameters that control mass transfer processes. According to computer simulation results a diffusion coefficient of Si at 950°C is $6.5 \cdot 10^{-11}$ cm^2/s.

Key words: Reactive diffusion, Silicide, Annealing, Inclusion, Diffusion model

---

1 Introduction

Today new material engineering and technology problems arise from problems of the further miniaturization, development of the nanotechnology. Investigations of the formation mechanisms of the silicide nanostructures during development of the solid state reactions in the thin metal layers deposited on the Si are very important. Diffusion processes are already developing at deposition, directly after deposition and during nature aging due to peculiarities of the "evaporation-condensation" process and great degree of the nonequilibrium of the "film-substrate" system, Ref. [1]. External surface essentially has effect on the development of the structure and phase reformation processes at thermal treatment. One plays role of "diffusion pump" that stimulates diffusion mass transfer expansion of Si atoms across metal layer via grain boundary mechanism, Ref. [2]. These effects show itself for "metal film (100-200nm)- monocrystalline Si" system. But the silicide phases formation regularities and the kinetics of the solid state reactions development in the systems with thin metal layers (< 10nm) on the Si can be substantially different.

In this connection the purpose of this study was experimental investigation and computer simulation of the processes of the thermally induced reactive diffusion during $NiSi_2$ inclusions formation in the Ni(10nm)/Si(001) thin film system in the temperature range 500-1000^{0}C.

2 Experimental procedures

Ni film 10 nm was deposited by magnetron sputtering with a deposition rate of 0.3 $nm \cdot s^{-1}$ onto room-temperature boron-doped substrate Si of (001) orientation. The Ar pressure was kept at 10^{-1}Pa during the deposition. The samples were annealed in the temperature range 500-1000^{0}C during 30 s in a N_2 ambient. Thermally induced solid state reactions in the Ni(10 nm)/Si(001) film system have been investigated by the methods of cross-section transmission electron microscopy (XTEM) in a Philips CM20 FEG. The surface morphology has been studied by the scanning electron microscopy (SEM) in a SEMMA-100.

3 Results and discussion

The XTEM micrograph (Fig. 1, a) of an as-deposited sample shows a 6 nm thick amorphous interlayer Ni_xSi_y at the interface of the Ni layer to Si.

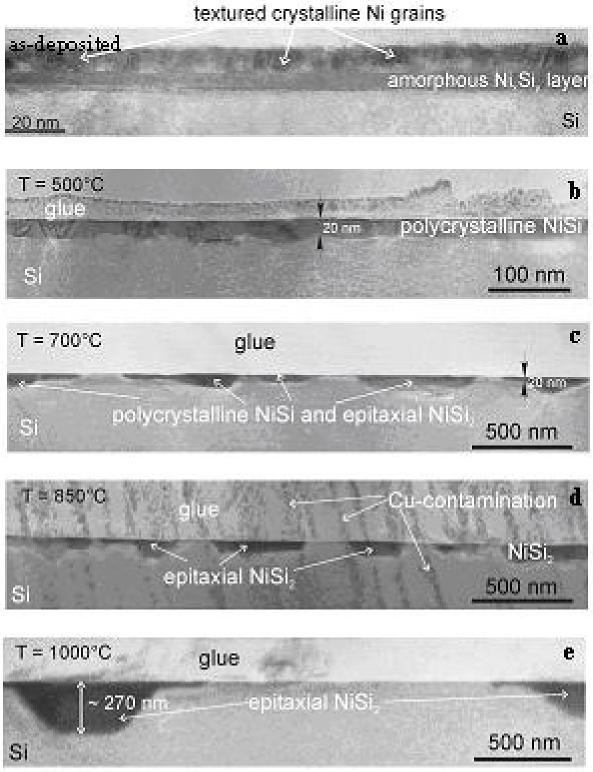

Figure 1: Influence of the annealing temperature on the layer structure of the Ni(10nm)/Si(001) thin film.

Therefore it is suggested that a quantity of Si penetrates in the Ni top layer with (Ni+Si) solid solution formation during condensation-stimulated diffusion and directly. The formation of the solid solutions with diffused substance concentration which exceeds equilibrium from phase state diagram due to increase in the solubility in the thin film state was obtained for many "metal film (100-200 nm) – Si" system. For example, solid solution at the interface forms in the as-deposited Mo(200nm)/Si system. And Si concentration in the one is from 0.1 to 13 at. % along of the transitional layer thickness, Ref. [3]. Formation of the metastable substitutional solid solution was observed in Ref. [4] for Ti(200nm)/Si(111) system by x-ray diffraction (increase in the elementary cell volume of the Ti crystal lattice). Si maximum concentration in the solid solution is ~ 7 weight % and greatly exceeds Si solubility in Ti for bulk state.

Annealing at a temperature below of 500°C results in formation of the continuous film of the NiSi polycrystalline silicide of thickness ~ 20 nm (Fig. 1, b).

Under rise in temperature Si diffusion occurs already to the NiSi silicide phase. The Si atoms come out on the external surface along grain boundaries and accumulate on the surface and near-surface region. At the same time the role of the external surface becomes decisive and causes the primary mass transfer in the Ni(10 nm)/Si(001) film system. Si concentration is a maximum in the places where grain boundaries come out to the surface and inclusions formation of the $NiSi_2$ epitaxy phase occurs (Fig. 1, c). In other words nucleation process of the new phase particles is heterogeneous.

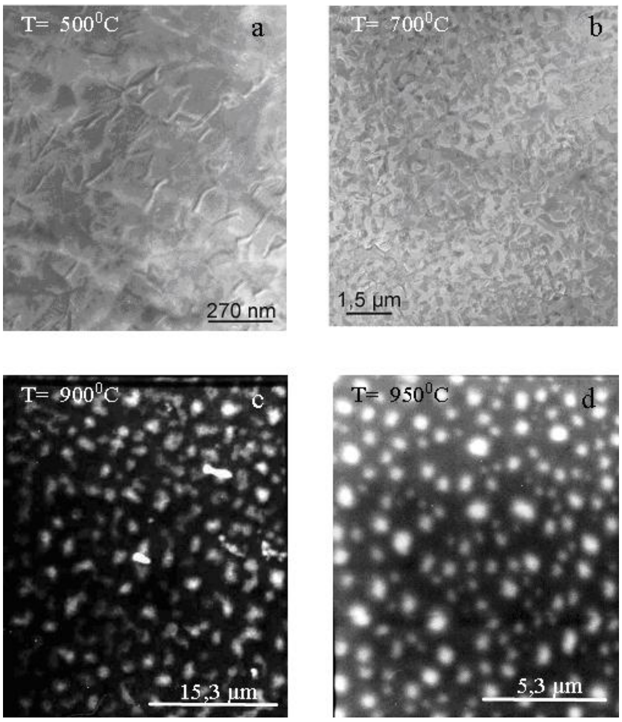

Figure 2: Influence of the annealing temperature on the structure morphology of the Ni(10nm)/Si(001) thin film.

We think the formation of the $NiSi_2$ phase islands begins already at 500°C. They have lamellar shape and average size about 140 nm (Fig. 2, a).

In accordance with reactive diffusion model further islands growth must result in formation new phase layer, Ref. [5]. Really, if Ni layer thickness is 100 nm the formation of the $NiSi_2$ continuous layer is observed. But in our case Ni quantity is insufficient for formation such continuous layer. That is why attachment of the $NiSi_2$ separated inclusions causes. Diffusion redistribution of Ni from NiSi silicide to $NiSi_2$ inclusions finish by total "solution" of the NiSi layer. In other words consistent reconstruction of the island structure occurs in $NiSi_2$ volumetric inclusions in the Si matrix that consume all Ni (Fig. 1, e).

At first new phase islands growth laterally: at 700°C islands size on the surface is ~ 230-350 nm (Fig. 2, b); at 900°C one is ~ 850-1000 nm (Fig. 2, c). At temperatures above 700°C also consistent growth begins in the line of normal to surface (Fig. 1, d). This process is continuing as long as the inclusion is acquiring spherical shape.

The radius $NiSi_2$ inclusions which are situated in Si-matrix is ~280-380 nm at 950°C (Fig. 2, d). One is smaller than inclusions radius at 900°C but greatly exceed initial thickness of Ni layer. Decrease of inclusions size of the silicide phase with increase of the annealing temperature is observed other researchers, Ref. [6,7]. We think that reconstruction of the island surface structure in volume spherical inclusions promotes decrease their size.

It is known in particular that condition of the elastic energy minimum define shape of the separate particles during new phase formation in solid state. If elastic properties of matrix and inclusion are close separations of the new phase have lamellar shape. If new phase is harder than matrix concentration of elastic field inside particle become unprofitable and new phase has round shape. This theory result is confirmed in our case. Harder $NiSi_2$ phase (H_v= 10.2 ± 0.3 GPa at loading of 50 g) is in soft matrix NiSi (H_v = 4 ± 0.5 GPa at loading of 50 g). Therefore harder phase gradually become itself spherical. H_v significances are represented in Ref. [8].

Thus our investigation demonstrates that formation process of the $NiSi_2$ silicide phase particles in Ni(10 nm)/Si(001) thin film at annealings above 500°C is multi-step (Fig. 3) and occurs in following consistency:

- Si and Ni interdiffusion via a lattice mechanism results in formation of the NiSi polycrystalline silicide layer;
- Si atoms along grain boundaries go out on the surface and accumulate;
- $NiSi_2$ islands form and lateral growth on the surface;
- Islands normal growth is accompanied by "diffusion dilution" of the NiSi layer;
- Spherical $NiSi_2$ inclusions form in the Si-matrix.

A mathematical model was suggested that describes spherical inclusions growth in the finite size areas of the supersaturated solid solution Ni-Si, Ref. [9]. Approximate solutions of the start-edge task for the second Fick's equation in terms of suggested diffusion model and computer simulation results allow to establish the most important parameters that control mass transfer processes. It is established that calculated value of the $NiSi_2$ inclusion radius is agree with experimental (335 nm) if supersaturation degree in the Ni-Si solid solution is 20 at. % and a diffusion coefficient of Si is $6.5 \cdot 10^{-11}$ cm^2/s. Maximum radius of inclusion at 950°C is 431 nm after annealing for 142 s.

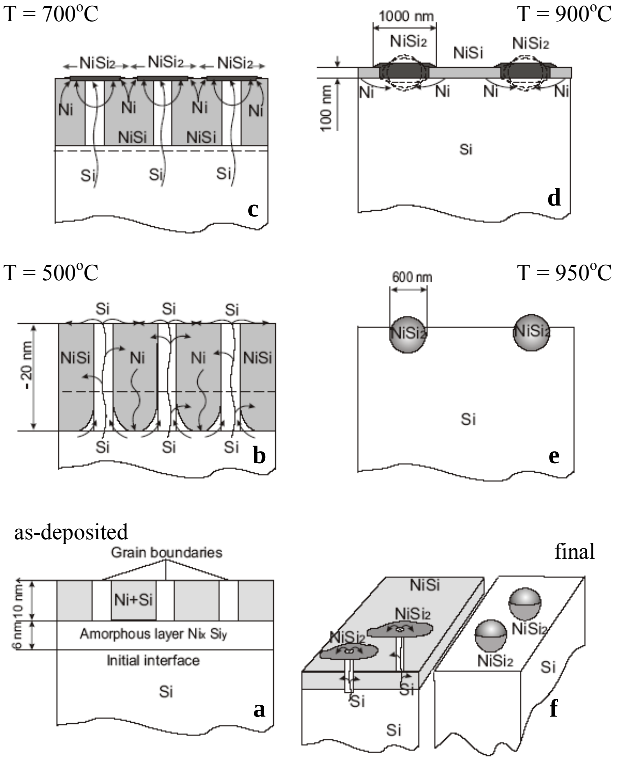

Figure 3: Model of the formation mechanism of the $NiSi_2$ inclusions in the Ni(10nm)/Si(001) thin film at the annealings.

This work was performed in the frame of the Project 2469 of the Science and Technology Center in Ukraine.

References

[1] Sidorenko, S.I., Makogon, Yu.N, Voloshko, S.M.: *Material Science of Thin Films Nanostructures. Diffusion and Reactions*. Kiev, 2000.

[2] Voloshko, S.M., Sidorenko, S.I., Tcherkatschenko, Yu.V,, Lutsenko, G.V.: "Oxygen pump" model at diffusion in the thin films. *Met. Phys. Adv. Tech.*, 21**,** No. 9, pp. 67-70, 1999.

[3] Makogon, Yu.N., Sidorenko, S.I., Yaremenko,

N.N.: Impurities role at formation of the Mo thin film silicides. *Fizika i khimiya obrabotki materialov*. 3, pp. 60-63, 1990.

[4] Makogon, Yu.N. Treatment influence on the phase composition of the Ti films on the Si substrate. *Izvestiya AN SSSR, seriya Neorganicheskie materialu*. 27, No 1, pp. 18-24, 1991.

[5] Larikov, L. N. Mechanisms of the reactive interdiffusion. *Met. Phys. Adv. Tech*., 16**,** No. 9, pp. 3-25, 1994.

[6] Poate, J.M. *Thin Film - Interdiffusion and reactions.* Moscow, 1982.

[7] Teichert, S., Bretschneider, W., Helms, H., Beddies, G., Franke, Th., Lange, Chr. Epitaxial $NiSi_2$ films on Si(100). *J. Thin Solid Films*. 229, pp. 137-139, 1993.

[8] Maex, K., Van Rossum, M. *Properties of metal silicides.* Belgium: IMEC, 1995.

[9] Sidorenko, S.I., Voloshko, S.V., Berezovskij, A.A., Zamulko, S.A., Konorev, S.I. Mathematic model of the spherical inclusions growth of the new phase in the supersaturation solid solutions. *Met. Phys. Adv. Tech*., 25, No. 4, pp. 431-443, 2003.

Proceedings of The 1st International Conference on **D**iffusion in **S**olids and **L**iquids
DSL-2005, July 6-8, 2005, University of Aveiro, Aveiro, Portugal

ANNEALING AMBIENT EFFECT ON THE PHASE FORMATION IN THE Ti(10 nm)/Ni(10 nm)/C(2 nm)/Si(001) THIN FILM SYSTEM

Yuij MAKOGON[1,*], Gunter BEDDIES[2], Anna MOGILATENKO[2], Elena PAVLOVA[1],
Olena CHUKHRAI[1]

[1]National Technical University of Ukraine "KPI", Kiev, Ukraine
[2]Institute of Physics, Chemnitz University of Technology, Germany

[*]Corresponding author. Fax: +38 044 241 76 18 ; Email: makogon@users.ntu-kpi.kiev.ua

---

Abstract

Annealing ambient effect on the phase formation in Ti(10 nm)/Ni(10 nm)/C(2 nm)/Si(001) thin film system obtained by sequential sputtering of C, Ni and Ti targets without vacuum breaking was under investigation. Specimens were annealed in the vacuum at pressures of about $1.3\cdot10^{-4}$ Pa in the temperature range 400-1000°C for 30 s. Thermally activated solid-state reactions that occur as the result of interdiffusion processes between layers under investigations were examined by methods of X-ray- and electron diffraction, Rutherford backscattering spectroscopy and resistivity measurements. NiSi formation starts at 550°C, but $NiSi_2$ growth was observed at 600°C. After annealing at 1000°C film system consists of $TiSi_2$ and $NiSi_2$ disilicide. Structure of thin film system remains continuous.

Keywords: Phase transformations, Film, Silicide, Phase, Phase composition, Annealing

---

1 Introduction

Transition metal silicides are widely used as functional elements in silicon microelectronic technology. It is permits to increase integration level and operating speed of the devices. Silicide thin films reduce contact resistance on the active parts of the transistors of the storage devices. One of the advantages of silicides is possibility to obtain of their by various ways during microdevices manufacturing.

Using of $TiSi_2$ and $CoSi_2$ silicides for functional elements with thickness less than 0.15 microns is limited. Among silicides, which are used in superscale integration technology in particular for transistors with dimensions less than 0,1 microns, NiSi is the most attractive. It is formed at a relatively low temperature (350^oC) and has low resistivity (~10 μkΩ·cm) at the temperatures above 600°C [1]. But at 750°C NiSi transforms in high resistivity $NiSi_2$ [1-5].

The purpose of the present work is investigation influence of titan as top layer and influence of carbon as barrier layer on passing of thermally activated solid-state reactions in Ti(10nm)/Ni(10nm)/C(2nm)/Si(100) thin film system at the annealing in a vacuum.

2 Experimental details

The researched Ti(10nm)/Ni(10nm)/C(2nm)/Si(100) film system was obtained by magnetron sputtering of C, Ni and Ti targets. Layers of carbon, nickel and titan were deposited sequentially onto (001) Si in Ar ambient at pressures of about 10^{-1} Pa without vacuum breaking. Layers of the titan and nickel were deposited with rate of 2-3 Å/s and a layer of carbon - 0,1 Å/s. Specimens were annealed in the vacuum at pressures of about $1.3\cdot10^{-4}$ Pa in the temperature range 400-1000°C for 30 s. The phase identification was analyzed using X-ray- and electron diffraction. Rutherford backscattering spectroscopy (RBS) was performed using 1,7 MeV He^+ in order to determine the layer composition of the samples. Resistivity of film was measured using a four-point probe.

3 Results and discussion

The data of the phase identification both as-deposited sample and annealed samples of the Ti(10nm)/Ni(10nm)/C(2nm)/Si(001) thin film system are shown in the Table 1.

Table 1: X-ray and electron diffraction analysis.

Temp. (°C)	Method of the investigation	
	x-ray diffraction	electron diffraction
20	Ni +Ti	Ti
400-500	Ni +Ti	TiO_2+Ti
550	NiSi +Ti	
600-750	Ti	TiO_2 + Ti +Ni_3Ti (NiTi)
800		TiO_2 +Ni_3Ti (NiTi)
850		TiO_2 + TiSi + Ni_3Ti (NiTi)
900		TiO_2 + $TiSi_2$ + NiTi (Ni_3Ti)
950	$TiSi_2$	
1000	$TiSi_2$	TiO_2 + $TiSi_2$ + NiTi (Ni_3Ti) +$NiSi_2$

RBS analysis of as-deposited sample demonstrates that metal layers are imperfect.

It is established solid-state reactions are not observed in the film system after vacuum annealings in temperature range from 400 to 500˚C (Fig. 1, Table 1).

After annealing at 500˚C it was found the presence of oxygen in a superficial layer of sample. According to electron diffraction results oxygen interacts with titan formed TiO_2 layer of (3-6) nm thickness (Table 2). Resistivity measurements shown resistivity of film is not changed as compared with one after deposition (Fig. 2).

Interdiffusion between both Ti, Ni, C layers and Si substrate occurs at the annealings above 500˚C and is accompanied by solid-state reactions (Table 1).

According to X-ray and RBS analysis NiSi phase is formed at 550˚C. As the annealing temperature is increased to 550°C resistivity of the film drops too though NiSi has low resistivity (Fig. 2). It points to occurred changes of the structure and phase composition of the thin film. RBS analysis shows formation of the Ni-Ti compound (NiTi) due to intermixing of Ni and Ti.

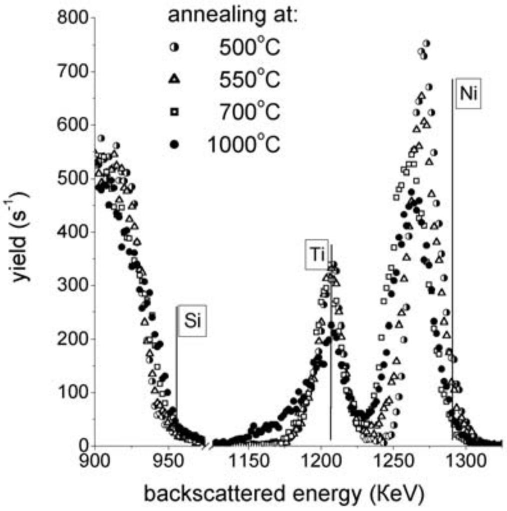

Figure 1: Backscattering spectra of the Ti(10nm)/Ni(10nm)/C(2nm)/Si(001) samples.

Table 2: Theoretical phases and their corresponding thicknesses by RBS analysis.

Temp. (°C)	Model of layers by RBS		Phase
	Thickness, (nm)	Atomic composition	
500	3	Ti:O=1:2	TiO_2
	9	Ti	Ti
	10	Ni	Ni
	substrate	Si	Si
550	3	Ti:O=1:2	TiO_2
	9	Ti	Ti
	2	Ni:Ti=1:1	NiTi
	20	Ni:Si=1:1	NiSi
	substrate	Si	Si
700	3	Ti:O=1:2	TiO_2
	9	Ti	Ti
	38	Ni:Si=1:2	$NiSi_2$
	substrate	Si	Si
1000	5	Ti:O=1:2	TiO_2
	12	Ti:Si=1:2	$TiSi_2$
	38	Ni:Si=1:2	$NiSi_2$
	substrate	Si	Si

Increasing the annealing temperature from 600°C till 800°C causes further changes of the phase composition (Table 1). According to RBS analysis film consists of layers of titan oxide (3 nm), unreacted titan (9 nm), $NiSi_2$ disilicide (38 nm) (Fig. 1, Table 2). Presence of the unreacted Ti was also observed by methods of x-ray and electron diffraction (Table 1).

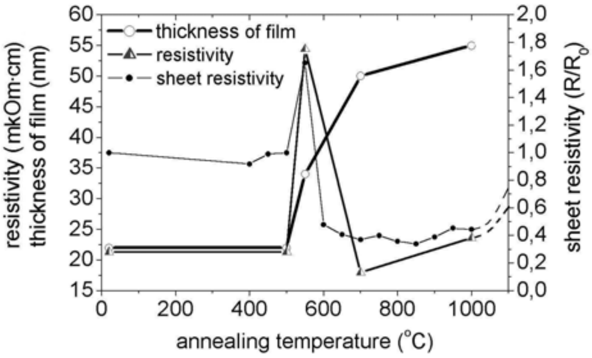

Figure 2: Resistivity, sheet resistivity and thickness of film system as a function of annealing temperature.

From the results of resistivity measurements resistivity of the film increases (Fig. 2). It may be caused by formation of $NiSi_2$ that has the higher resistivity among the Ni silicides. This conclusion follows also from comparison of the our experimental results with ones of the investigations of Ni(10-20nm)/Si(001) thin film systems by method of resistometry [6].

X-ray diffraction analysis didn't show $NiSi_2$ formation. This indicates that $NiSi_2$ grow epitaxially on Si (001) [7-10].

According to electron diffraction data the superficial layer of thin film system consists of titan, titan oxide (TiO_2) and Ni-Ti compounds (Ni_3Ti and NiTi) (Table 1). In this temperature range of annealings phase Ni_3Ti dominates at the lower temperatures and phase NiTi dominates at the higher temperatures. At increasing the annealing temperature the titan layer is gradually consumed due to passing of the solid-state reactions with formation Ti-riched Ni-Ti compounds.

During an annealing step in the temperature range from 850˚C to 1000˚C it was observed formation of the titan silicide together with earlier formed Ni-Ti compounds and $NiSi_2$. In this case the thin film system consist of top layer of TiO_2 (5 nm) and subsequent layers of Ni-Ti compounds (2 nm), disilicides of $TiSi_2$ (12 nm) and $NiSi_2$ (38 nm) (Table 2).

It is important to note that film system after annealing at the temperature of 1000˚C is continuous without breaks. It is confirmed the smooth shape of RBS spectrum and low resistivity (~ 20 μΩ·cм) (Fig. 1, Fig. 2).

To explain continuity of the film it is necessary to investigate the change of RBS spectrum from titan top layer. It is known titan is a good getterer of oxygen from ambient. It connects oxygen with formation of TiO_2 at the low temperatures of annealing protecting reactions from contaminations. TiO_2 is preserved till the annealing temperature of 1000°C. Interaction between titan and silicon begins at the temperatures above 850°C with formation TiSi and $TiSi_2$ (Fig. 1, Table 2). Thus we may conclude the titan top layer promotes preservation of structure continuous of the thin film system till the temperature of 1000°C at annealing in the vacuum. It prevents outcrop of substrate silicon on the surface of the film system and breaking of its.

Diffusion of carbon was not observed by used methods of investigations. Earlier it has been established that carbon is not built in formed silicide film and replaced to surface of film system [11-14].

Sequence of the solid-state reactions in the Ti(10nm)/Ni(10nm)/C(2nm)/Si(001) thin film system after vacuum annealings in the researched temperature range is shown in the Table 3.

Table 3: Phase composition of the Ti(10nm)/Ni(10nm)/C(2nm)/Si(001) film system after vacuum annealings.

Temp. (˚C)	Phase composition
400	TiO_2+Ti+Ni
550	TiO_2+Ti+(Ni_3Ti+NiTi)+NiSi
600	TiO_2+Ti+(Ni_3Ti+NiTi)+$NiSi_2$ (ep.)
800	TiO_2+(Ni_3Ti+NiTi)+$NiSi_2$ (ep.)
850	TiO_2+ (NiTi +Ni_3Ti)+TiSi+$NiSi_2$ (ep.)
900	TiO_2+ (NiTi +Ni_3Ti)+$TiSi_2$+$NiSi_2$ (ep.)
1000	TiO_2 + (Ni_3Ti+NiTi) +$TiSi_2$ +$NiSi_2$

4 Conclusion

Diffusion interactions between deposited layers and silicon substrate in the Ti(10nm)/Ni(10nm)/C(2nm)/Si(001) thin film system are registered after vacuum annealing at 500°C and are accompanied by solid-state reactions. Titan oxide forms in the superficial layer of film and preserves till the temperature of 1000°C. Formation both NiSi silicide and Ni-Ti compounds (Ni_3Ti, NiTi) begins after annealing at 550˚C. Formation of $NiSi_2$ disilicide occurs after annealing at 600˚C. $TiSi_2$ disilicide forms after annealing at 900˚C. Thus we may conclude the titan top layer promotes preservation of structure continuous of the Ti(10nm)/Ni(10nm)/C(2nm)/Si(001) thin film system till the temperature of 1000°C at annealing in the vacuum. Additional layers of Ti and C decrease the NiSi stability

Acknowledgments

The authors would like to express the gratitude Prof. H.-J. Hinneberg for possibility to carry out this work

We wish to thank Mr. L. Budzinski for helpful discussion concerning the RBS measurements.

References

[1] Brandes, E.A., Brook, G.B.: *Smithells Metals Referense Book.* Butterworth-Heinemann Ltd , USA, 1992.

[2] Hirose, K., Hanta, A., Uda, M.: Initial stage of room temperature reaction at Ni/Si (111)-H interfaces. *J. Appl. Surface Science,* Vol.162-163, pp.25-29, 2000.

[3] Gregoratti, L., Gunther, S., Kovac, J., Marsi, M., Kiskinova, M.: Intermediate phases and mass transport during interaction of a thin Ni film with a laterally heterogeneous Ni-Si(111) interface. *J. Surface Science,* 439, pp. 120-130, 1999.

[4] Meyer, B., Gottlieb, U., Laborde, O., Yang, H., Lasjaunias, J.C., Sulpice, A., Madar, R.: Some electrounic properties of single crystalline NiSi. *J. Microelectronic Engineering*, 37/38, pp. 523-527, 1997.

[5] Teodorescu, V., Nistor, L., Bender, H., Steegen, A., Lauwers, A., Maex, K., Van Landuyt, J.: In situ transmission electron microscopy study of Ni silicide phases formed on (001) Si active lines. *Journal of Applied Physics*, V.90, pp.167-174, 2001.

[6] Teichert, S., Falke, M., Geisler, H., Beddies, G., Hinneberg, H.-J.: Allotaxy in the Ni-Si system. *Thin Solid Films*, Vol.336, pp.222-226, 1998.

[7] Magnelinck, D., Gas, P., Gay, J.M., Pichaud, B., Thomas, O.: Effect of Co, Pt, and Au additions on the stability and epitaxy of $NiSi_2$ films on (111) Si. *Journal of Applied physics*, Vol.84, pp. 2583-2590, 1998.

[8] Cheng, L.W., Cheng, S.L., Chen, L.J., Chien, H.C., Lee, H.L., Pan, F.M.: Formation of Ni silicides on (001) Si with a thin interposing Pt layer. *J. Vac. Sci. Techn*, Vol. A.18 (4), pp. 115-152, 2000.

[9] Magnelinck, D., Dai, J.Y., Pan, J.S., Lahiri, S.K.: Enhancement of thermal stability of NiSi films on (100) Si and (111) Si by Pt addition. *Journal of Applied physics*, Vol.75, pp. 1736-1738, 1999.

[10] Sidorenko, S.I., Tu, K.N., Makogon, Yu.N., Pavlova, E.P., Verbitskaya, T.I., Nesterenko, Yu.V.: Solid-state reactions in Ti/Ni thin film system on silicon single crystal (in Russian). *J. Metallofizika i noveishie tekhnologii*, Vol. 25, №5, pp. 613-620, 2003.

[11] Makogon, Yu.N., Ostapchuk, A. I., Sidorenko, S.I., Smiyan, O.D.: Role of the impurities (O, C) during formation of the crystal structure of titan disilicide films (in Russian). *J. Metalls*, Vol.2, pp.187-192, 1993.

[12] Firstova, I.S., Sidorenko, S.I., Makogon, Yu.N., Adeev, V.M.: Influence of technology and heat treatment on the structure and composition of the molybdenum disilicide films (in Russian). *J. Metallofizika i noveishie tekhnologii*, Vol.23, №4, pp.459-464, 2001.

[13] Dub, S.N., Makogon, Yu.N., Pavlova, E.P., Sidorenko, S.I., Zelenin, O.V.: Influence of structure-phase composition of the tantalum disilicide thin films on their mechanical properties (in Russian). *J. Metallofizika i noveishie tekhnologii,* Vol.24, №1, pp. 61-73, 2002.

[14] Makogon, Yu.N., Sidorenko, S.I: Silicides Formation in Metal-Silicon Film-Systems: the Role of Impurities. *Electronic Packaging for High Reliability; Low Cost Electronics, Proceedingsof the NATO Advanced Research Workshop on the Electronic Packaging for High Reliability; Low Cost Electronics,* Tummala, R., Kosec, M., Jones, W., Belavic, D. (Eds), NATO ASI Series 3. High Technology, Vol.57, pp. 91-98, 2000.

Proceedings of The 1st International Conference on **D**iffusion in **S**olids and **L**iquids
DSL-2005, July 6-8, 2005, University of Aveiro, Aveiro, Portugal

MICROSTRUCTURE DEVELOPMENT IN IONIC CRYSTALLINE MEMBRANE UNDER DIFFUSIONAL MASS TRANSPORT: CHEMICAL POTENTIAL DISTRIBUTION AND VOID FORMATION

Toshio MARUYAMA*, Mitsutoshi UEDA, Kenichi KAWAMURA

Department of Metallurgy and Ceramics Science, Tokyo Institute of Technology,
S8-11, 2-12-1, O-okayama, Meguro-ku, Tokyo, 152-8552, Japan

*Corresponding author. Fax: +81 3 5734 3136; Email: maruyama@mtl.titech.ac.jp

Abstract

In many high-temperature processes, ionic materials such as metal oxides are exposed under chemical potential gradients. The typical processes are a gas separation with an ion-permeable membrane and high temperature oxidation of metals. The ionic constituents are driven by the electrochemical potential gradients and diffuse through the oxide. The metal ion diffuses from the lower oxygen potential side to the higher side. The oxide ion diffuses to the opposite direction. The diffusion of metal ion governs the displacement of the membrane. The microstructure of oxides develops under the ionic flow. In the high temperature oxidation, voids are frequently observed in growing scale. The void formation in the membrane for gas separation is a crucial issue.

This paper described the quantitative expression of displacement of and void formation in a membrane under the assumption of non-zero divergence of ionic flux.

Keywords: Mathematical modelling; Microstructual and crystallographic texture evolution; Void formation; Chemical potential distribution; Divergence

1 Introduction

In many high-temperature processes, ionic materials such as metal oxides are exposed under chemical potential gradients. The typical processes are a gas separation by an ion-permeable membrane and high temperature oxidation of metals. In high temperature gas separation with a metal-oxide membrane, the metal-oxide is exposed to chemical potential gradients. The ionic constituents are driven by the electrochemical potential gradients and diffuse through the oxide. The metal ion diffuses from the lower oxygen potential side to the higher side. The oxide ion diffuses to the opposite direction. The diffusion of metal ion governs the displacement of the membrane. The oxide scale growth in high temperature oxidation of metals is almost the same phenomena except the metal ion is continuously supplied at the lower oxygen potential side. The microstructure of oxides develops under the ionic flow. The quantitative understanding of microstructure evolution such as void formation in the growing scale requires the consideration with the ionic flux. In the high temperature oxidation, voids are frequently observed in the growing scale. The void formation in the membrane for gas separation is a crucial issue.

Wagner [1] presented the rigorous expression of the parabolic rate constant for high temperature oxidation of metals, which expression was implicitly assumed the steady state diffusion with the divergence to be zero. However, the formation of voids and the additional oxide growth within the scale are caused by the non-zero divergence of fluxes of constituent ions.

The authors [2] have predicted the void formation in the growing scale of magnetite during high temperature oxidation of iron under the preliminary assumption in which the major stationary flux of iron ion determines the chemical potential distribution and the resulting flux of oxide ion and its divergence is a measure of the void formation.

This paper described the improved analytical expression of mass transport in an ionic crystalline membrane under the consideration of non-zero divergence. It may help to understand the displacement of a membrane and the void formation in a membrane under chemical potential gradients.

2 Mass Transport in an Ionic Compound of $\mathrm{M}_a^{Z_\mathrm{M}}\mathrm{X}_b^{Z_\mathrm{X}}$ under Chemical Potential Gradients

2.1 General Background

In the ionic crystalline compound of $\mathrm{M}_a^{Z_\mathrm{M}}\mathrm{X}_b^{Z_\mathrm{X}}$, there are charged species of the metal cation with the ionic charge of Z_M (positive integer), the non-metal anion with Z_X (negative integer), excess hole with Z_h (= +1) and excess electron with Z_e (= -1). The following three relations are existed.

$$aZ_\mathrm{M} + bZ_\mathrm{X} = 0 \tag{1}$$

$$c_\mathrm{M}Z_\mathrm{M} + c_\mathrm{X}Z_\mathrm{X} = 0 \tag{2}$$

$$\frac{c_\mathrm{M}}{a} = \frac{c_\mathrm{X}}{b} = c^*(=\mathrm{const.}) \tag{3}$$

where c is the concentration (mol m^{-3}).

If the compound is placed under the chemical potential gradients as shown in Fig. 1, the electrochemical potential gradients appear through the compound. The charged species in the electrochemical potential field are driven and forced to move.

The cation and anion flow toward the left and right, respectively. During the mass transport process, the stoichiometric ratio of cation and anion, i.e. the ratio of sublattice sites shall be maintained so that the divergences of ionic fluxes are related in the following manner.

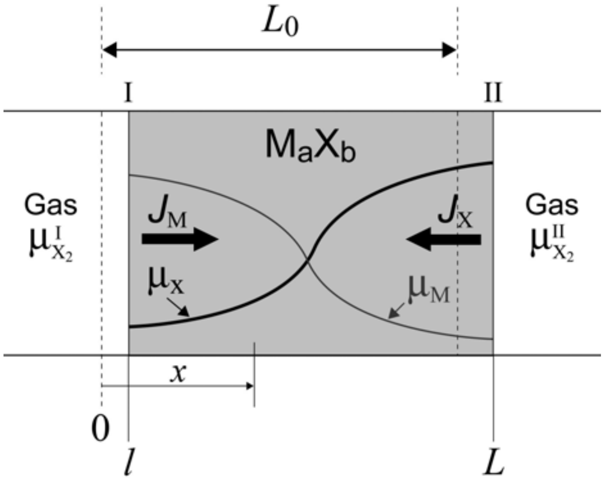

Figure 1: The ionic compound under the chemical potential gradients.

$$\frac{\partial n_{\mathrm{M}_a\mathrm{X}_b}}{\partial t} = -\frac{1}{a}\frac{\partial J_\mathrm{M}}{\partial x} = -\frac{1}{b}\frac{\partial J_\mathrm{X}}{\partial x} \tag{4}$$

where the left-hand term is the change in number of mole of the compound, $\mathrm{M}_a^{Z_\mathrm{M}}\mathrm{X}_b^{Z_\mathrm{X}}$, and , J_i (mol m^{-2}s^{-1}) is the flux of a species, i.

The flux of a species is expressed as follows.

$$J_\mathrm{i} = -c_\mathrm{i}B_\mathrm{i}\frac{\partial \eta_\mathrm{i}}{\partial x} \tag{5}$$

where B the absolute mobility (molJ^{-1}m^{2}s^{-1}), η (Jmol^{-1}) the electrochemical potential and x the coordination (m). The Nernst-Einstein relation gives

$$B_\mathrm{i} = \frac{D_\mathrm{i}}{RT} \tag{6}$$

where D is the self diffusion coefficient (m^{2}s^{-1}), R the gas constant (8.31 Jmol^{-1}K^{-1}) and T the absolute temperature (K). The electrochemical potential is defined as

$$\eta_\mathrm{i} = \mu_\mathrm{i} + Z_\mathrm{i}F\phi \tag{7}$$

where μ is the chemical potential (Jmol^{-1}), F the Faraday constant (96500 C), and ϕ the electrostatic potential (V).

Through the oxide, the following electro-neutrality condition shall be maintained.

$$Z_\mathrm{M}J_\mathrm{M} + Z_\mathrm{X}J_\mathrm{X} + Z_\mathrm{h}J_\mathrm{h} + Z_\mathrm{e}J_\mathrm{e} = 0 \tag{8}$$

2.2 Chemical potential distribution in the compound, $\mathrm{M}_a^{Z_\mathrm{M}}\mathrm{X}_b^{Z_\mathrm{X}}$

From Eq. (4), one can obtained as

$$-\frac{\partial(\frac{J_\mathrm{M}}{a})}{\partial x} = -\frac{\partial(\frac{J_\mathrm{X}}{b})}{\partial x} \tag{9}$$

The integration of Eq. (9) gives

$$\frac{J_\mathrm{M}}{a} = \frac{J_\mathrm{X}}{b} + I \tag{10}$$

where I is the constant and independent of x.

Based on Eqs. (7) and (1), the thermodynamic relation for metal and non-metal elements is

$$\begin{aligned} &a\eta_{\mathrm{M}} + b\eta_{\mathrm{X}} = a(\mu_{\mathrm{M}} + Z_{\mathrm{M}}F\phi) + b(\mu_{\mathrm{X}} + Z_{\mathrm{X}}F\phi) \\ &= (a\mu_{\mathrm{M}} + b\mu_{\mathrm{X}}) = \mu^{\circ}_{\mathrm{M}aXb} \end{aligned} \qquad (11)$$

where the following relation of chemical potentials is used

$$a\mu_{\mathrm{M}} + b\mu_{\mathrm{X}} = \mu^{\circ}_{\mathrm{M}aXb} \qquad (12)$$

Differentiation of Eq. (11) by x and introduction of Eq. (7) lead

$$\begin{aligned} &a\frac{\partial \eta_{\mathrm{M}}}{\partial x} + b\frac{\partial \eta_{\mathrm{X}}}{\partial x} = -(\frac{aJ_{\mathrm{M}}}{c_{\mathrm{M}}B_{\mathrm{M}}} + \frac{bJ_{\mathrm{X}}}{c_{\mathrm{X}}B_{\mathrm{X}}}) \\ &= -\frac{1}{c^{*}}(\frac{J_{\mathrm{M}}}{B_{\mathrm{M}}} + \frac{J_{\mathrm{X}}}{B_{\mathrm{X}}}) = 0 \end{aligned} \qquad (13)$$

and

$$\frac{J_{\mathrm{M}}}{B_{\mathrm{M}}} + \frac{J_{\mathrm{X}}}{B_{\mathrm{X}}} = 0 \qquad (14)$$

Introduction of Eq. (10) into (14) gives

$$(bB_{\mathrm{M}} + aB_{\mathrm{X}})J_{\mathrm{X}} = -abB_{\mathrm{X}}I \qquad (15)$$

Using Eq. (5), the electrochemical potential gradient of non-metal is

$$\begin{aligned} &\frac{\partial \eta_{\mathrm{X}}}{\partial x} = \frac{abI}{c_{\mathrm{X}}(bB_{\mathrm{M}} + aB_{\mathrm{X}})} \\ &= \frac{b{Z_{\mathrm{X}}}^{2}I}{Z_{M}^{2}c_{\mathrm{M}}B_{\mathrm{M}} + {Z_{\mathrm{X}}}^{2}c_{\mathrm{X}}B_{\mathrm{X}}} = \frac{b{Z_{\mathrm{X}}}^{2}I}{\alpha} \end{aligned} \qquad (16)$$

For the sake of brevity, the following simplification is made

$$\alpha = Z_{M}^{2}c_{\mathrm{M}}B_{\mathrm{M}} + {Z_{\mathrm{X}}}^{2}c_{\mathrm{X}}B_{\mathrm{X}} \qquad (17)$$

One rewrite Eq. (8) with Eq. (10) to

$$\begin{aligned} &Z_{\mathrm{M}}J_{\mathrm{M}} + Z_{\mathrm{X}}J_{\mathrm{X}} = Z_{\mathrm{M}}(\frac{aJ_{\mathrm{X}}}{b} + aI) + Z_{\mathrm{X}}J_{\mathrm{X}} \\ &= \frac{1}{b}(aZ_{\mathrm{M}} + bZ_{\mathrm{X}})J_{\mathrm{X}} + aZ_{\mathrm{M}}I \\ &= -bZ_{\mathrm{X}}I = J_{\mathrm{e}} - J_{\mathrm{h}} \end{aligned} \qquad (18)$$

In this derivation, Eqs. (1) and (2) are used

The reaction between excess electron and hole is expressed as

$$\text{null} = \mathrm{e}' + \mathrm{h}^{\cdot} \qquad (19)$$

The sum of electrochemical potentials of hole and electron is equal to the sum of the both chemical potentials as shown in the following equation.

$$\eta_{\mathrm{e}} + \eta_{\mathrm{h}} = (\mu_{\mathrm{e}} - F\phi) + (\mu_{\mathrm{h}} + F\phi) = \mu_{\mathrm{e}} + \mu_{\mathrm{h}} = \text{const.} \qquad (20)$$

The differentiation of Eq. (20) gives

$$\frac{\partial \eta_{\mathrm{h}}}{\partial x} = -\frac{\partial \eta_{\mathrm{e}}}{\partial x} \qquad (21)$$

and one can rewrite Eq. (18) as

$$\begin{aligned} &-bZ_{\mathrm{X}}I = J_{\mathrm{e}} - J_{\mathrm{h}} = -c_{\mathrm{e}}B_{\mathrm{e}}\frac{\partial \eta_{\mathrm{e}}}{\partial x} + c_{\mathrm{h}}B_{\mathrm{h}}\frac{\partial \eta_{\mathrm{h}}}{\partial x} \\ &= -(c_{\mathrm{e}}B_{\mathrm{e}} + c_{\mathrm{h}}B_{\mathrm{h}})\frac{\partial \eta_{\mathrm{e}}}{\partial x} = -\beta\frac{\partial \eta_{\mathrm{e}}}{\partial x} \end{aligned} \qquad (22)$$

For the sake of brevity, the following simplification is made

$$\beta = c_{\mathrm{e}}B_{\mathrm{e}} + c_{\mathrm{h}}B_{\mathrm{h}} \qquad (23)$$

The ionization of non-metal is

$$\mathrm{X} + |Z_{\mathrm{X}}|\mathrm{e} = \mathrm{X}^{Z_{\mathrm{X}}} \qquad (24)$$

and the thermodynamic relation is

$$\mu_{\mathrm{X}} + |Z_{\mathrm{X}}|\eta_{\mathrm{e}} = \mu_{\mathrm{X}} - Z_{\mathrm{X}}\eta_{\mathrm{e}} = \eta_{\mathrm{X}} \qquad (25)$$

The differentiation of Eq. (25) gives

$$\frac{\partial \mu_{\mathrm{X}}}{\partial x} = \frac{\partial \eta_{\mathrm{X}}}{\partial x} + Z_{\mathrm{X}}\frac{\partial \eta_{\mathrm{e}}}{\partial x} \qquad (26)$$

and the introduction of Eqs. (16) and (22) into Eq. (26) gives the chemical potential gradient of non-metal.

$$\frac{\partial \mu_{\mathrm{X}}}{\partial x} = \frac{b{Z_{\mathrm{X}}}^{2}I}{\alpha} + \frac{b{Z_{\mathrm{X}}}^{2}I}{\beta} = \frac{b{Z_{\mathrm{X}}}^{2}(\alpha + \beta)I}{\alpha\beta} \qquad (27)$$

Integration of Eq. (27) from ℓ (μ_X^{I}) to L (μ_X^{II}) gives

$$\int_{\ell}^{L} I\partial x = \frac{1}{bZ_X^{2}}\int_{\mu_X^{I}}^{\mu_X^{II}} \frac{\alpha\beta}{\alpha+\beta}\partial\mu_X = k(=\text{const.}) \qquad (28)$$

and

$$I(L-\ell) = k \qquad (29)$$

On the other hand, integration of Eq. (27) from ℓ (μ_X^{I}) to x (μ_X) gives

$$\int_{\ell}^{x} I\partial x = I(x-\ell) = \frac{1}{bZ_X^{2}}\int_{\mu_X^{I}}^{\mu_X} \frac{\alpha\beta}{\alpha+\beta}\partial\mu_X \qquad (30)$$

One obtains the chemical potential distribution by dividing Eq. (30) by Eq. (28)

$$\frac{x-\ell}{L-\ell} = \frac{\int_{\mu_X^{I}}^{\mu_X} \frac{\alpha\beta}{\alpha+\beta}\partial\mu_X}{\int_{\mu_X^{I}}^{\mu_X^{II}} \frac{\alpha\beta}{\alpha+\beta}\partial\mu_X} = \frac{\int_{\mu_X^{I}}^{\mu_X} \frac{\alpha\beta}{\alpha+\beta}\partial\mu_X}{bZ_X^{2}k} \qquad (31)$$

.

2.3 Chemical potential gradient

The introduction of Eq. (29) into Eq. (27) gives

$$\frac{\partial\mu_X}{\partial x} = \frac{(\alpha+\beta)bZ_X^{2}k}{\alpha\beta(L-\ell)} \qquad (32)$$

2.4 Electrochemical potential gradient

The combination of Eqs. (16), (29) and (32) gives the electrochemical potential gradient as

$$\frac{\partial\eta_X}{\partial x} = \frac{bZ_X^{2}I}{\alpha} = \frac{\beta}{(\alpha+\beta)}\frac{\partial\mu_X}{\partial x} = t_e\frac{\partial\mu_X}{\partial x} \qquad (33)$$

where t_e is the electronic transference number.

2.5 Electrostatic potential gradient

Using Eqs. (7) and (33), the electrostatic potential gradient is obtained as

$$\begin{aligned}\frac{\partial\phi}{\partial x} &= \frac{1}{Z_XF}\left(\frac{\partial\eta_X}{\partial x} - \frac{\partial\mu_X}{\partial x}\right) \\ &= -\frac{1}{Z_XF}\frac{\alpha}{(\alpha+\beta)}\frac{\partial\mu_X}{\partial x} = -\frac{1}{Z_XF}t_i\frac{\partial\mu_X}{\partial x}\end{aligned} \qquad (34)$$

where t_i is the electronic transference number. This equation is the well-known Nernst equation.

3 Membrane for Gas Separation

In this section, mass transport and void formation in the membrane are treated. The membrane with the thickness of L_0 is placed between x=0 and x= L_0 at the beginning (t=0). After the certain time, the interface I is exist at x= ℓ and the interface II is at x= L (Fig. 1).

3.1 Permeation of non-metal of X through the membrane of $M_a^{Z_M}X_b^{Z_X}$.

From Eqs. (5) and (33), the flux of X injected into the membrane at the interface II is expressed as

$$J_X^{II} = -c_X^{II}B_X^{II}\left(\frac{\partial\eta_X}{\partial x}\right)^{II} = -\frac{bkZ_X^{2}c_X^{II}B_X^{II}}{\alpha^{II}(L-\ell)} \qquad (35)$$

and that released from membrane at the interface I is

$$J_X^{I} = -c_X^{I}B_X^{I}\left(\frac{\partial\eta_X}{\partial x}\right)^{I} = -\frac{bkZ_X^{2}c_X^{I}B_X^{I}}{\alpha^{I}(L-\ell)} \qquad (36)$$

The Eq. (36) indicates the amount of the gas permeated, and the difference of Eqs. (36) and (35) is related to formations of void and additional compound in the membrane.

3.2 Displacement of interfaces I and II

The velocity of displacement of the interface II is described as

$$\frac{dL}{dt} = V_{MaXb}\left(\frac{1}{a}\right)J_M^{II} = \frac{V_{MaXb}k}{(L-\ell)}\frac{Z_M^{2}c_M^{II}B_M^{II}}{\alpha^{II}} \qquad (37)$$

where the Eqs. (14) and (35) are used and V_{MaXb} is the molar volume of $M_a^{Z_M}X_b^{Z_X}$. The velocity of the interface I is

$$\frac{d\ell}{dt} = V_{MaXb}\left(\frac{1}{a}\right)J_M^{I} = \frac{V_{MaXb}k}{(L-\ell)}\frac{Z_M^{2}c_M^{I}B_M^{I}}{\alpha^{I}} \qquad (38)$$

The ratio of the velocities is

$$\frac{\frac{\mathrm{d}\ell}{\mathrm{d}t}}{\frac{\mathrm{d}L}{\mathrm{d}t}} = \frac{c_{\mathrm{M}}{}^{\mathrm{I}} B_{\mathrm{M}}{}^{\mathrm{I}} \alpha^{\mathrm{II}}}{c_{\mathrm{M}}{}^{\mathrm{II}} B_{\mathrm{M}}{}^{\mathrm{II}} \alpha^{\mathrm{I}}} = r_{\mathrm{m}} \left(= \text{const.}\right) \tag{39}$$

The ratio of the velocities is fixed only by the kinetic factors at interfaces

3.3 Dimensional stability of the membrane

The change in thickness of the membrane is

$$\frac{\mathrm{d}(L-\ell)}{\mathrm{d}t} = \frac{\mathrm{d}L}{\mathrm{d}t} - \frac{\mathrm{d}\ell}{\mathrm{d}t}$$

$$= \frac{V_{\mathrm{M}a\mathrm{X}b} k}{(L-\ell)} \left(\frac{Z_{\mathrm{M}}{}^{2} c_{\mathrm{M}}{}^{\mathrm{II}} B_{\mathrm{M}}{}^{\mathrm{II}}}{\alpha^{\mathrm{II}}} - \frac{Z_{\mathrm{M}}{}^{2} c_{\mathrm{M}}{}^{\mathrm{I}} B_{\mathrm{M}}{}^{\mathrm{I}}}{\alpha^{\mathrm{I}}} \right) \tag{40}$$

$$= \frac{V_{\mathrm{M}a\mathrm{X}b} k \alpha^{\mathrm{II}}}{(L-\ell) Z_{\mathrm{M}}{}^{2} c_{\mathrm{M}}{}^{\mathrm{II}} B_{\mathrm{M}}{}^{\mathrm{II}}} (1 - r_{\mathrm{m}}) = \frac{k_{\mathrm{p}}^{\mathrm{mem}}}{(L-\ell)}$$

where

$$k_{\mathrm{p}}^{\mathrm{mem}} = \frac{V_{\mathrm{M}a\mathrm{X}b} k \alpha^{\mathrm{II}}}{Z_{\mathrm{M}}{}^{2} c_{\mathrm{M}}{}^{\mathrm{II}} B_{\mathrm{M}}{}^{\mathrm{II}}} (1 - r_{\mathrm{m}}) \tag{41}$$

Integration of Eq. (40),

$$\int_{L_0}^{L-\ell} (L-\ell) \mathrm{d}(L-\ell) = k_{\mathrm{p}}^{\mathrm{mem}} \int_0^t \mathrm{d}t \tag{42}$$

gives

$$(L-\ell)^2 = L_0{}^2 + 2 k_{\mathrm{p}}^{\mathrm{mem}} t \tag{43}$$

The thickness increases at r_{m} <1 ($k_{\mathrm{p}}^{\mathrm{mem}}$ >0) where voids may form in the membrane. When r_{m} >1 ($k_{\mathrm{p}}^{\mathrm{mem}}$ <0), it may decrease creating new lattice sites in the membrane, in which case a compressive stress must be generated and large plastic deformation or fracture are expected. Only the case of r_{m} =1 ($k_{\mathrm{p}}^{\mathrm{mem}}$ =0) allows the stable situation to the membrane.

3.5 Position at which voids form

The flux of non-metal in the membrane is expressed as

$$J_{\mathrm{X}} = -c_{\mathrm{X}} B_{\mathrm{X}} \left(\frac{\partial \eta_{\mathrm{X}}}{\partial x} \right) = -\frac{bkZ_{\mathrm{X}}{}^{2} c_{\mathrm{X}} B_{\mathrm{X}}}{\alpha (L-\ell)} \tag{44}$$

Using Eqs. (44) and (32), the divergence of the flux is expressed as

$$-\frac{\partial J_{\mathrm{X}}}{\partial x} = \frac{bkZ_{\mathrm{X}}{}^{2} c_{\mathrm{X}}}{(L-\ell)} \frac{\partial (\frac{B_{\mathrm{X}}}{\alpha})}{\partial \mu_{\mathrm{X}}} \frac{\partial \mu_{\mathrm{X}}}{\partial x}$$

$$= \frac{(\alpha+\beta)(bkZ_{\mathrm{X}}{}^{2})^2 c_{\mathrm{X}}}{\alpha\beta (L-\ell)^2} \frac{\partial (\frac{B_{\mathrm{X}}}{\alpha})}{\partial \mu_{\mathrm{X}}}$$

$$= \frac{(\alpha+\beta)(bkZ_{\mathrm{X}}{}^{2} Z_{\mathrm{M}})^2 c_{\mathrm{X}} c_{\mathrm{M}} B_{\mathrm{M}} B_{\mathrm{X}}}{\alpha^3 \beta (L-\ell)^2} \left(\frac{1}{B_{\mathrm{X}}} \frac{\partial B_{\mathrm{X}}}{\partial \mu_{\mathrm{X}}} - \frac{1}{B_{\mathrm{M}}} \frac{\partial B_{\mathrm{M}}}{\partial \mu_{\mathrm{X}}} \right) \tag{45}$$

The term in the bracket on the right hand side, is modified to

$$\frac{1}{B_{\mathrm{X}}} \frac{\partial B_{\mathrm{X}}}{\partial \mu_{\mathrm{X}}} - \frac{1}{B_{\mathrm{M}}} \frac{\partial B_{\mathrm{M}}}{\partial \mu_{\mathrm{X}}} = \frac{\partial \ln B_{\mathrm{X}}}{\partial \mu_{\mathrm{X}}} - \frac{\partial \ln B_{\mathrm{M}}}{\partial \mu_{\mathrm{X}}} \tag{46}$$

Using Eq. (6) and

$$2 \mathrm{d}\mu_{\mathrm{X}} = \mathrm{d}\mu_{\mathrm{X}_2} = RT \mathrm{d} \ln P_{\mathrm{X}_2} \tag{47}$$

Eq. (46) is rewritten as

$$\frac{\partial \ln B_{\mathrm{X}}}{\partial \mu_{\mathrm{X}}} - \frac{\partial \ln B_{\mathrm{M}}}{\partial \mu_{\mathrm{X}}} = \frac{2}{RT} \left(\frac{\partial \ln D_{\mathrm{X}}}{\partial \ln P_{\mathrm{X}_2}} - \frac{\partial \ln D_{\mathrm{M}}}{\partial \ln P_{\mathrm{X}_2}} \right) \tag{48}$$

Therefore, one can evaluate the sign of the divergence of the Eq. (45) if the chemical potential dependence of the diffusivities of constituent ions and evaluate the position at which voids form. Voids form at positions where

$$\frac{\partial \ln D_{\mathrm{X}}}{\partial \ln P_{\mathrm{X}_2}} < \frac{\partial \ln D_{\mathrm{M}}}{\partial \ln P_{\mathrm{X}_2}} \tag{49}$$

and additional compound forms in the membrane at positions where

$$\frac{\partial \ln D_{\mathrm{X}}}{\partial \ln P_{\mathrm{X}_2}} > \frac{\partial \ln D_{\mathrm{M}}}{\partial \ln P_{\mathrm{X}_2}} \tag{50}$$

The condition at which the membrane is stable is established in the case of

$$\frac{\partial \ln D_{\mathrm{X}}}{\partial \ln P_{\mathrm{X}_2}} = \frac{\partial \ln D_{\mathrm{M}}}{\partial \ln P_{\mathrm{X}_2}} \tag{51}$$

This equation gives

$$\frac{D_{\mathrm{X}}}{D_{\mathrm{M}}} = \text{const.} \tag{52}$$

This relation indicates that both the diffusivities must have the same chemical potential dependence. The situation is generally impossible because defect chemistry does not allow it. Only the case is the diffusivity to be independent of chemical potential. The heavy doping may offer this situation, giving the extrinsic defect concentrations.

4 Conclusion

This paper offered the analytical equations for elucidation of microstructure development, especially of void formation in a binary ionic compound under chemical potential gradients.

The divergence of ionic flux is a measure of the void formation. The chemical potential dependence of ionic diffusivity is a key factor to understand the microstructure development in the gas separation membrane.

Acknowledgement

The present work was supported in part by the Grant-in-Aid for Scientific Research on Priority Area, “Nanoionics (439) by the Ministry of Education, Culture, Sports, and Technology”

References

[1] Wagner, C.: Beitrag zur Theorie des Anlaufvorgangs, Z. Physik. Chem., 21, pp. 25-41, 1933.

[2] Maruyama T., Fukagai N., Ueda M, Kawamura K.: Chemical potential distribution and void formation in magnetite scale formed in oxidation of iron at 823K, Materials Science Forum, 461-464, pp. 807-814, 2004.

Proceedings of The 1st International Conference on **D**iffusion in **S**olids and **L**iquids
DSL-2005, July 6-8, 2005, University of Aveiro, Aveiro, Portugal

GRADED STRUCTURE FORMED BY SEDIMENTATION OF ATOMS IN Se-Te SOLID SOLUTION

Tsutomu MASHIMO[1,2,*], Xinsheng HUANG[1], Hideto UENO[1], Ono MASAO[2]

[1]Shock Wave and Condensed Matter Research Center, Kumamoto University,
2-39-1 Kurokami, Kumamoto 860-8555, Japan
[2]Advanced Science Research Center, Japan Atomic Energy Research Institute,
Tokai-mura, Nakagun, Ibaraki 319-1195, Japan

*Corresponding author. Fax: 81-96-342-3293, Email: mashimo@gpo.kumamoto-u.ac.jp

---

Abstract

An atomic scale graded structure was formed in an all-proportion miscible $Se_{70}Te_{30}$ semiconductor by sedimentation of substitutional solute atoms under an ultra-strong gravitational field (1,020,000 G in maximum acceleration, 260 ºC (below melting point), 100 hours). The Te content increased along the direction of gravity from about 0 to 60 at.%, while the Se content decreased from about 100 to 40 at.%. The lattice constants of the hexagonal structure continuously increased as the gravitational field increased. This showed that the graded structure was continuous on atomic scale and the sedimentation of substitutional atoms occurred. In the graded structure region, the crystal growth along the direction of gravity was observed. The XPS spectra of Se showed the binding energies of Se 3d electrons continuously decreased in the direction of gravity for the whole specimen,

Keywords: Atom sedimentation; Atomic-scale gradient; Gravitational field; Crystal growth

---

1 Introduction

Materials science research under a very strong gravitational field of up to higher than 1,000,000 G (1 G = 9.8 m/s^2) has now remained as an unexploited field. Unlike under high pressures, under a gravitational field, each atom is displaced by one-dimensional body force, and as a result, a unique molecular-crystal state of one-dimensional displacement or sedimentation of atoms can be realized. Such strong gravitational field has direct effects in atomic scale such as sedimentation or structure change [1]. It is suggested that the sedimentation of atoms based on differences in atomic weight and volume will be used as a new materials processing, to concentrate elements or even isotopes, and to form an atomic-scale graded structure or nano-mezo composite structure in condensed matter, and so on. However, the sedimentation of atoms is very difficult to realize in solids or liquids, because the chemical potential of the atoms is usually much greater than the mechanical energy.

To study the sedimentation of atoms or crystal-chemical instability in solids under a strong gravitational field, we developed two ultracentrifuge apparatuses in Kumamoto University [2] and Japan Atomic Energy Research Institute (JAERI) [3], which can generate an acceleration of over 1 million G for a long time at high temperature. The new developed ultracentrifuge apparatus in JAERI can generate a larger potential energy of over two times and a wider temperature range up to over 500 ºC compare with that in Kumamoto University [3], to expand the investigation of a variety of materials and phenomena. We previously formed atomic-scale graded structures in a Bi-Sb alloy [4, 5] and an In-Pb alloy [6], etc. by sedimentation of substitutional solute atoms.

In this study, we performed the ultra-strong gravitational field experiment on the all-proportion miscible selenium (Se)-tellurium (Te) system (70:30 in at.%) semiconductor, to form an atomic scale graded structure with a graded band gap structure.

2 Experimental Procedure

The $Se_{70}Te_{30}$ alloy lump was prepared by melting the pure Se and the pure Te shots in a

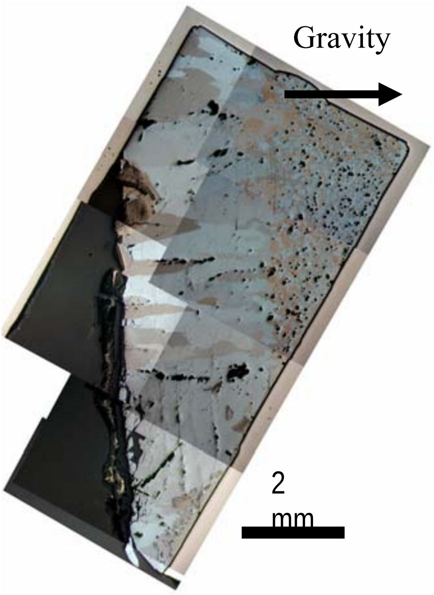

Figure 1: Polarmicroscope photograph of the polished surface cut at a plane containing the rotation axis of the ultracentrifuged $Se_{70}Te_{30}$ specimen (1,020,000 G, 260 ºC, 100 hours).

Pyrex test tube at about 640 ºC for 30 minutes under an argon atmosphere. The purities of Se and Te shots were 99.99%. The lump was crushed to a powder and was melted again at about 430 ºC under vacuum in a hollow glass rod with an inner diameter of 4 mm for several minutes. The uniformity of the specimen was confirmed by the EPMA analysis. The specimen was cut to be a column shaped piece with a height of about 5 mm, and was set into a SUS304 capsule with an inner diameter of 4 mm. The rotation of the rotor was stopped after the temperature of the rotor dropped to less than about 80 ºC.

The ultracentrifuge experiment was performed by the new developed ultracentrifuge apparatus in JAERI. For the $Se_{70}Te_{30}$ specimen, the ultracentrifuge experiment was performed at a rotation rate of 160,000 rpm and a temperature of 260 ºC for a long time of 100 hours. The experimental temperature was below the melting point of the starting sample, which is about 280 ºC [9]. The acceleration field at the maximum distance (35.8 mm) from the rotor axis in the specimen was 1,020,000 G. For the ultracentrifuged specimen, the composition analysis was carried out using an electron probe micro analyzer (EPMA) apparatus. Micro-area x-ray diffraction (XRD) analysis was carried out for the specimen to investigate the change in crystal structure. The diameter of the x-ray beam was 100 μm, and the distance between the measured spots was 300 μm. The high resolution XPS spectra of Se core levels were obtained after cleaning the surfaces of the specimens by sputtering using an argon ion beam.

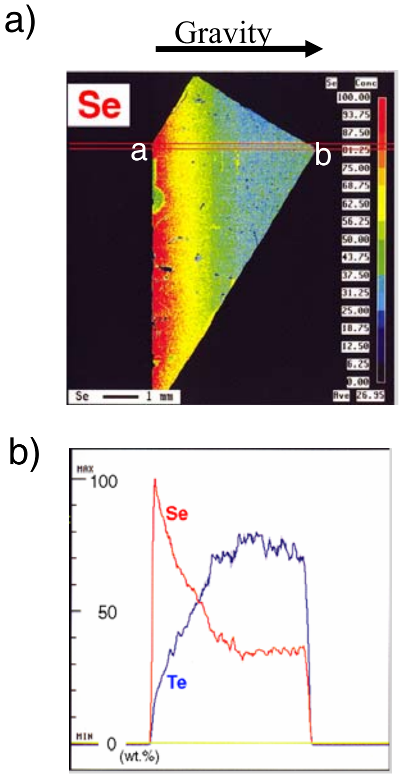

Figure 2: Color composition mapping of Se (a) and the linear composition profiles of Se and Te along a straight line a-b in the direction of gravity (b).

3 Results and Discussion

The polarmicroscope photograph of the polished surface cut at a plane containing the rotation axis of the ultracentrifuged $Se_{70}Te_{30}$ specimen is shown in Fig. 1. The composition mappings of Se and the linear composition profiles of Se and Te along a straight line a-b in the direction of gravity are shown in Fig. 2. The maximum acceleration field at the right edge of the specimen was 1.02×10^6 G, and the minimum one at the left edge of the specimen was about 0.9×10^6 G. In the low gravity field region of the ultracentrifuged specimen, the content of Te with a heavier atomic weight (127.6 g/mol) greatly

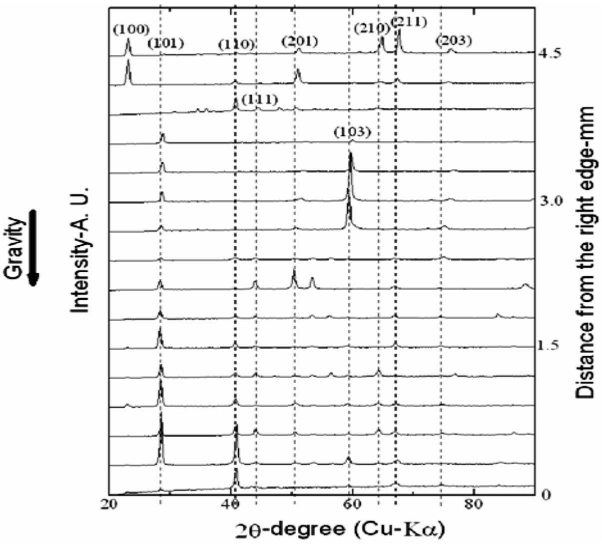

Figure 3: Micro-area XRD patterns of the ultracentrifuged $Se_{70}Te_{30}$ specimen, which were obtained along the straight line a-b in the direction of gravity shown in Fig. 2.

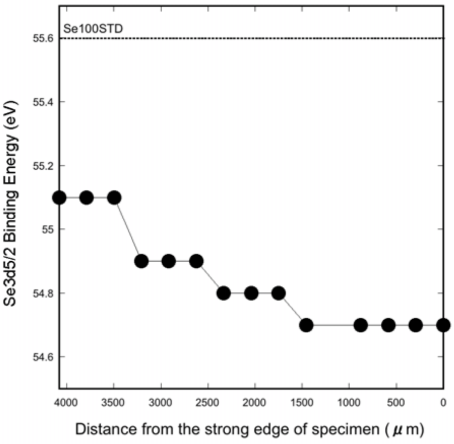

Figure 4: The change in the binding energy of Se electron as a function of the ultracentrifuged $Se_{70}Te_{30}$ specimen (XPS result).

increased in the direction of gravity from about 0 to 60 at.%, while the content of Se with a lighter atomic weight (79.0 g/mol) greatly decreased from about 100 to 40 at.%. The large composition gradient was obtained in the low gravity region, which might be due to the change in the diffusion coefficient. In the low gravity region, the diffusion coefficient became larger with the increase of the content of Se because the melting point of Se is lower than that of Te. Therefore, the sedimentation proceeded faster in the low gravity region than that did in the high gravity region. If the ultracentrifugation was continued, the sedimentation might progress in the high gravity region as well.

The large and long crystals oriented along the direction of gravity can be observed in the low gravity field region. The grain sizes of the large and long crystals were several mm long and hundreds of μm wide, while those of the small crystals in the high gravitational field region were tens of μm. This crystal growth might be related to the ultra-strong gravitational field because the orientation of the long grown crystals was consistent with the direction of gravity. The large composition gradient was observed even in the large grown single crystals. The boundary between the large crystals in the low gravity region and the small crystals in the high gravity region coincided with that of the region where the composition changed greatly. This indicated that the crystal growth in the solid state was strongly correlated with the sedimentation of atoms.

Figure 3 shows the micro-area XRD patterns of the ultracentrifuged $Se_{70}Te_{30}$ specimen, which were obtained along the straight line a-b in the direction of gravity shown in Fig. 2. The crystal structure in all areas was confirmed to be hexagonal. In the low gravity region, all peaks shifted to higher angles with the increase in distance from the right edge of the specimen, where received the strongest gravitational field. As the gravitational field increased, the lattice parameters, a_0 and c_0, continuously increased from 0.44079 nm to 0.44467 nm, and from 0.49669 nm to 0.51368 nm, respectively, while a_0 and c_0 of pure Se and Te are 0.43662 and 0.49536 nm, and 0.44579 and 0.59270 nm, respectively. The lattice parameter of the area near to the top-free surface of the specimen was approximately same as that of the pure Se. This means the Se component was concentrated to about 100 at.% at the top-free surface of the specimen. This result was consistent with the EPMA result. Thus a nonequilibrium Se-Te solid solution with continuously changes in composition and lattice parameter was formed. The change in lattice parameter exactly showed the graded structure was formed on the atomic scale. This also showed that the sedimentation of substitutional atoms occurred in this solid solution.

Figure 4 shows the change in the binding energy of Se electron as a function of the distance from the spot with a maximum rotation radius for the ultracentrifuged $Se_{70}Te_{30}$ specimen, which were obtained from the high resolution XPS spectra of Se and Te core levels using linear analysis. The binding energy of Se 3d electron greatly decreased linearly from 55.1 to 54.7 eV in the direction of gravity for the whole specimen. The chemical shifts might be due to the different chemical environments, which were caused by rearrangement of the charge distribution of valence electrons in the Se-Te solid solution. These results showed that the electronic state changed after ultracentrifugation, and the band structure should be also continuously changed along the direction of gravity for these specimens.

4 Summary

An atomic-scale graded structure was formed in all-proportion miscible Se-Te system (70:30 in at.%) semiconductor by the sedimentation of substitutional solute atoms under an ultra-strong gravitational field of 1 million G level at 260 ºC. The crystal growth along the direction of gravity was observed, while it is difficult to grow a single crystal in this system alloy by ordinary method [11]. The graded band gap structure can be expected because of the semiconductor property of the Se-Te system solid solution. The functionally graded material in atomic scale is expected to show unique electronic or optical properties [12, 13]. It is expected that the strong gravitational field will offer us new and powerful options in materials science.

Acknowledgments

This work was partially supported by a grant-in-aid from the Mitsubishi Foundation.

References

[1] Mashimo, T.: Exploitation of new materials processing in a mega-gravity field. *Acta. Astronautica*, 48, 145-151, 2001.

[2] Mashimo, T., Okazaki, O., Shibazaki, S.: Ultracentrifuge apparatus to generate a strong acceleration field of over 1,000,000 g at high temperature in condensed matter. *Rev. Sci. Instrum.*, 67, 3170-3174, 1996.

[3] Mashimo, T., Huang, X.S., Osakabe, T., Ono, M., Nishihara, M., Ihara, H., Sueyoshi, M., Shibasaki, K., Shibasaki, S., Mori, N.: Advanced high-temperature ultracentrifuge apparatus for mega-gravity materials science. *Rev. Sci. Instrum.*, 74, 160-163, 2003.

[4] Mashimo, T., Okazaki, S., Tashiro, S.: Sedimentation of atoms in solid under a strong acceleration field of around 1 million G. *Jpn. J. Appl. Phys.*, 36, 498-500, 1997.

[5] Mashimo, T., Ikeda, T., Minato, I.: Atomic-scale graded structure formed by sedimentation of substitutional atoms in a Bi-Sb alloy. *J. Appl. Phys.*, 90, 741-744, 2001.

[6] Mashimo, T., Ono, M., Kinoshita, T., Huang, X.S., Osakabe, T., Yasuoka, H.: Sedimentation of substitutional atoms and phase change in an In-Pb alloy under an ultrastrong gravitational field. *Phillos. Mag. Lett.*, 83, 687-690, 2003.

[7] Mashimo, T.: Self-consistent approach to the diffusion induced by a centrifugal field in condensed matter: sedimentation. *Phys. Rev. A*, 38, 4149-4154, 1988.

[8] Mashimo, T.: Sedimentation of atoms in condensed matter: theory. *Philos. Mag. A*, 70, 739-760, 1994.

[9] Hansen, M., Anderko, K.: *Constitution of Binary Alloy*, 2nd ed., Genium Publication, New York, p. 332, 1991.

[10] Ono, M., Mashimo, T.: Sedimentation process for atoms in Bi-Sb system alloy under a strong gravity field: a new type of diffusion of substitutional solutes. *Philos. Mag. A*, 82, 591-600, 2002.

[11] Shiosaki, T., Kawabata, A.: Single Crystal Growth of Se-Te Alloys onto Tellurium from the Melt. *J. Appl. Phys.*, 10, 1329-1336, 1971.

[12] Mahan, G.D.: Inhomogeneous thermoelectrics. *J. Appl. Phys.*, 70, 4551-4554, 1991.

[13] Indradev, L.J., Ruyven, V., Williams, F.: Growth and Electrical Properties of Zinc-Cadmium Sulfide Graded-Band-Gap Crystals. *J. Appl. Phys.*, 39, 3344-3348, 1968.

Proceedings of The 1st International Conference on **D**iffusion in **S**olids and **L**iquids
DSL-2005, July 6-8, 2005, University of Aveiro, Aveiro, Portugal

ANALYSES OF DIFFUSION RELATED PHENOMENA IN STEEL PROCESS

Tooru MATSUMIYA

Technical Development Bureau, Nippon Steel Corporation
20-1 Shintomi, Futtsu-city, Chiba-prefecture, 283-9511 Japan

*Corresponding author. Fax: +81 439 80 2769; Email: matumiya@re.nsc.co.jp

---

Abstract

In steel production process, there are various diffusion-related phenomena and these are controlled to obtain required steel quality. In the refining process slag-metal reaction controlled by diffusion of various reactants and products in boundary layers in both slag and metal side along the slag-metal interface are analyzed by coupled reaction model. Solidification microsegregation is controlled by the solute diffusion in liquid and solid phase and various analytical microsegregation models have been proposed. Tertiary precipitation of non-metallic inclusions is also affected by solute diffusion in solid phase and analyzed by coupled precipitation model, modified solidification segregation model. Formation of carbon rich band structure along the centreline of steel plates and welding cracking are also prevented by regulating the diffusion of carbon by accelerated cooling and encouraging hydrogen diffuse-out by preheating the weld part, respectively. A key element of intra granular ferrite precipitation for ferrite grain refinement is the formation of manganese-depleted zone by slow manganese diffusion around a precipitate.

Keywords: Mathematical modelling; Industrial applications; Phase transformations; Multiphase diffusion systems; Reactive diffusion

---

1 Introduction

Steel product qualities are obtained by controlling chemical reactions, phase transformation, precipitation, segregation, etc. in steel production and fabrication processes. Diffusion plays pivotal roles in these processes in many cases. Therefore, proper control of the processes can be done by the proper use of the effect of the diffusion. In the following examples of the diffusion involved processes are mentioned. They are demanganization process of hot metal, segregation and precipitation during solidification processing, diffusion controlled transformation process, welding and coating process.

2 Refining Process

The refining of steel is conducted mainly by the use of slag/metal reaction and injection metallurgy. In both cases chemical reaction occurs between liquid metal and refining agents, that is frequently, liquid oxides. The slag/metal refining process can be analyzed by coupled reaction model developed by D. G. C. Robertson, et al. [1]. The reaction between injected flux and metal can be analyzed in the same manner. Figure 1 shows the schematic view of the model. In the model, thermodynamic equilibrium for each component oxide in the slag and solutes in metal is assumed at slag/metal interface and double diffusion layers are considered along the slag/metal interface. Chemical compositions in the bulk metal and the bulk slag outside the boundary layers are treated as uniform with respective concentrations. Concentrations in slag and metal at the slag/metal interface are calculated by the use of flux conservation equations of metal components and oxygen across the double boundary layers and thermodynamic equilibrium equations for component oxides with solute contents in the metal at the interface. In the case of carbon (C), a rate equation of carbon monoxide (CO) evolution is applied at the slag/metal interface instead of the local thermodynamic equilibrium, $\underline{C}+\underline{O}=CO$, and a mass balance equation for C between C flux from the metal and the CO evolution rate is considered.

Once the interfacial concentrations are determined, the flux of each component metal and oxygen from the bulk metal to the bulk slag, or vice versa, and CO evolution rate, decarburization

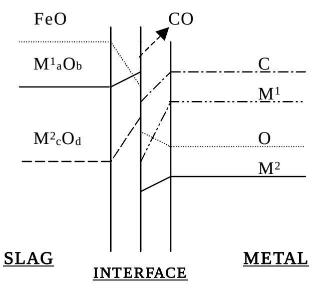

Fig.1: Schematic diagram of the coupled reaction model

rate, are obtained and chemical composition changes in both the bulk slag and metal are calculated.

This model was applied to optimize demanganization process of hot metal, where iron oxide powder is injected in a hot metal through an immersed nozzle [2]. The chemical composition change of the injected powder is analyzed with the model. The results are shown in Fig. 2. Silica concentration increases and iron oxide concentration decreases monotonically, while manganese oxide concentration reaches its maximum and decreases as time elapses after the powder is injected. This is because oxygen potential in the powder is not enough to oxidize manganese in hot metal after the manganese oxide reaches its maximum and manganese oxide is reduced back to hot metal. Therefore, from the viewpoint of efficient demanganization the injected powder is desired to float up to the top slag when the manganese concentration in the powder reaches the maximum. Since the time at the maximum manganese concentration becomes longer as demanganization process proceeds due to less concentration in silicon and manganese in hot metal, the depth of nozzle immersion should be increased accordingly to realize efficient demanganization. According to this result, the demanfanization process is operated successfully.

3 Solidification Microsegregation

Depending on the degree of solute diffusion, several approximations can be made for the description of solidification microsegregation. Local thermodynamic equilibrium at the solid/liquid (S/L) interface and complete mixing of solute in liquid phase are always assumed in sections *3.1* through *3.4*.

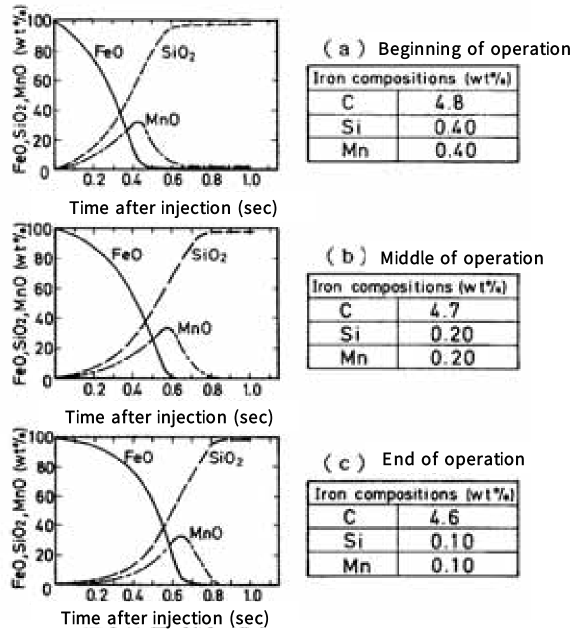

Fig.2: Chemical composition changes in the refining powder after it is injected to hot metal in demanganization and desiliconization process [2].

3.1 Equilibrium solidification

When solute is uniformly distributed over respective solid and liquid phases, that is, whole system is in thermodynamically equilibrium, solute concentration in solid C_S is calculated by the following equation:

$$C_S=kC_0/\{1-(1-k)f_S\} \quad (1)$$

where, C_0 is average solute concentration, k is equilibrium solid/liquid partition coefficient and f_S is fraction solid.

3.2 Scheil's Equation

When the diffusion in solid is completely neglected and complete mixing of solute in liquid is assumed, Scheil's equation applies [3]:

$$C_S=kC_0(1-f_S)^{k-1} \quad (2)$$

Where, C_S is the concentration in solid at the S/L interface.

3.3 Brody-Fleming's Equation

When back diffusion of solute into the solid phase from the S/L interface is considered, following Brody-Flemings's equation is delived [4]:

$$C_S=kC_0\{1-(1-2\alpha k)f_S\}^{(k-1)/(1-2\alpha k)} \qquad (3)$$

where α is called as solidification parameter and defined as $D_S t_S/L^2$. D_S is diffusion coefficient in the solid phase, t_S is local solidification time and L is half of secondary arm spacing. In the delivation of Eq. (3), the amount of back diffusion is approximately calculated by $D_S(dC_S/Ldf_S)dt$ and time increment dt is replaced by $2t_S f_S df_S$ assuming the parabolic growth law, $f_S=(t/t_S)^{1/2}$.

3.4 Clyne-Kurz's Equation

Clyne and Kurz corrected the overestimation of back diffusion in Brody-Flemings's equation and proposed the following equation replacing the solidification parameter α by Ω[5]:

$$C_S=kC_0\{1-(1-2\Omega k)f_S\}^{(k-1)/(1-2\Omega k)} \qquad (4)$$

where Ω is defined by the Eq. (5):

$$\Omega=\alpha\{1-\exp(-1/\alpha)\}-1/2\exp(-1/2\alpha) \qquad (5)$$

Ω tends to 1/2 as α tends to infinity, that is, diffusion is complete and Eq. (4) becomes Eq. (1). Ω tends to α and then to 0, as α approaches to 0. That is, Eq. (4) tends to Eq. (3) and then to Eq. (2). Therefore, Eq. (4) qualitatively covers all situations ranging from complete to zero mixing in solid.

3.5 Effective Partition Coefficient

When the complete mixing in the liquid cannot be assumed and the diffusion boundary layer along the S/L interface is considered, the effective S/L partition coefficient k_e is calculated as follows:

$$k_e=k/\{k+(1-k)\exp(-R\delta/D_L)\} \qquad (6)$$

where δ is the thickness of the diffusion boundary layer, R is the advancement velocity of S/L interface and D_L is diffusion coefficient in liquid. As δ approaches 0 and infinity, k_e approaches to k and 1, respectively.

3.6 Microsegregation Analysis by Finite Difference Method

For quantitative preciseness, finite difference method (FDM) was applied to analyze microsegregation. Transverse cross-section of a dendrite is approximated as hexagonal shape and a double-triangle section as shown in Fig. 3 is chosen for analysis considering the symmetry of diffusion and neglecting the diffusion along the axial direction of dendrite. The double-triangle section is divided into finite segments and solute diffusion in the radial direction is calculated by the use of FDM. Solute content in each segment is up-dated and thermodynamic equilibrium calculation is conducted in each time step in the segment where solid and liquid coexist using the up-dated average content. The calculated fractions of liquid and solid give the interface location. Figure 4 shows the simulated results of manganese concentration in comparison with microsegregation values calculated by other model equations mentioned above [6].

By the use of similar analysis method with consideration of solid-to-solid transformation, i.e., δ-γ transformation as well as liquid-to-solid transformation [7-8], solidification structure of

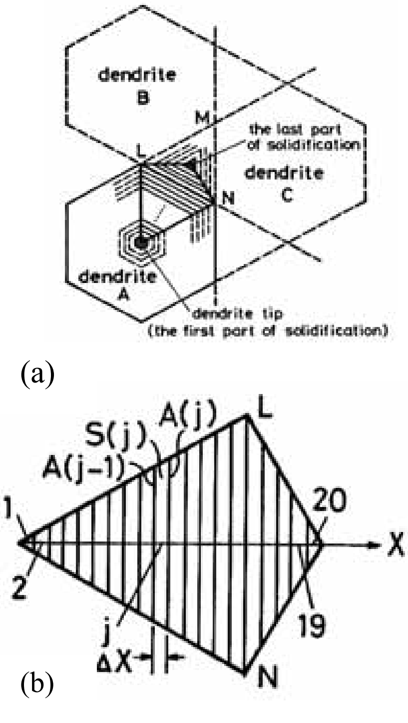

Fig.3: Model for transverse cross-section of dendrite (a) and portion for analysis selected from the dendrite section (b)[6].

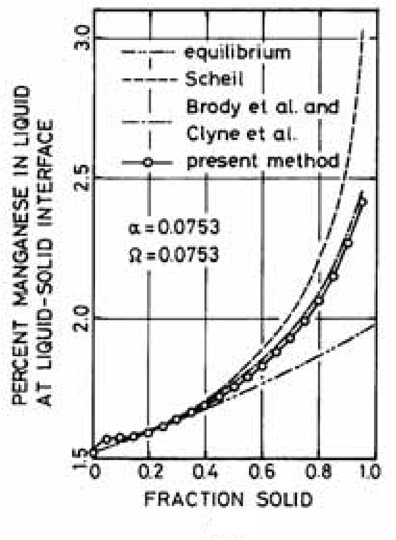

Fig.4: Comparison of dendrite segregation calculated by various analytical methods [6].

welding of stainless steels was analyzed and residual δ fraction, which affects the welding cracking, was estimated in agreement with observations as shown in Fig. 5 [8].

Regarding diffusion controlled transformation and precipitation analysis DICTRA [9] is one the integrated analytical software based on the combinations of multi-component diffusion analysis by FDM and local thermodynamic equilibrium analysis at the interfaces.

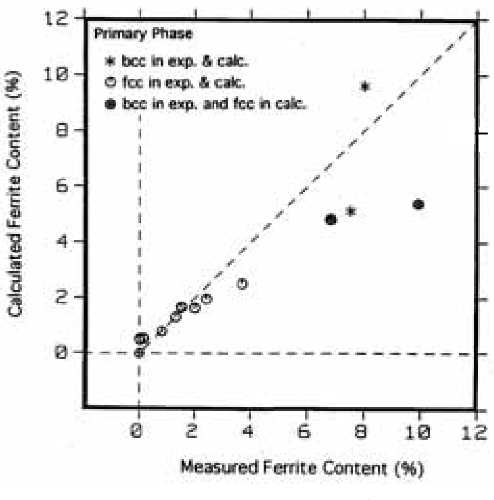

Fig.5: Comparison of retained δ ferrite content between calculation and measurement [7].

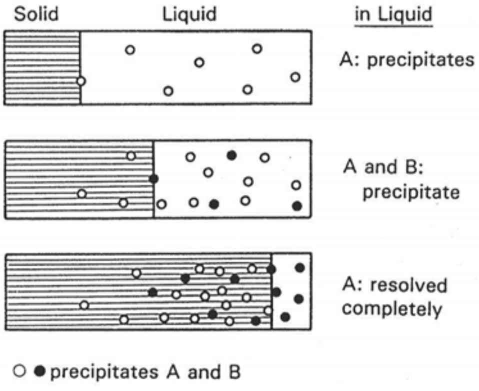

Fig.6: Schematic diagram of coupled precipitation model [9]

4 Precipitation of Nonmetallic Inclusions

Coupled precipitation model [10] was developed to analyze chemical composition change of nonmetallic inclusions during solidification of steels. Basic equations are as follows:

$$(1-k)C_L^i df_S=\{1-(1-2\,\Omega^i k^i)f_S\}dC_L+\sum_j R_{ij}dP_j \quad (7)$$

Where super suffix i indicates the kind of solute, R_{ij} is moles of element i in the precipitate j and P_j is concentration of precipitate j. If the last term in Eq. (7) is omitted, Eq. (7) becomes the solute conservation equation, which derives Eq. (4).

Equation (7) is solved with mass action equation of precipitation:

$$\prod_i a_i^{R_{ij}}/a_j=K_j \quad (8)$$

Where a_i is activity of element i, a_j is activity of precipitate j and K_j is the equilibrium constant of precipitate j. That is, in the coupled precipitation model solidification microsegregation is analysed with consideration of back diffusion of solutes into solid and local thermodynamic equilibrium is assumed in the residual liquid including the precipitation of non-metallic inclusions (Fig. 6).

The model was applied to the analysis of sulphide shape control in steel for line pipe. When manganese sulphide (MnS) precipitates at the spot-like segregation along the centreline in the slab of this steel, it is elongated during plate rolling and film-like MnS is resulted in the thickness center of the line pipe produced, which acts as initiation site of hydrogen induced cracking (HIC). In order to prevent from MnS precipitation, calcium is added to capture sulphur in the form of calcium sulphide (CaS).

Figures 7 and 8 compare the calculated results of chemical composition change of non-metallic inclusions during the solidification of spot like segregation with a diameter of 100 μ and 1000 μ. Spot-like segregation is formed by the localization of solute enriched liquid along the centreline in the slabs, which is squeezed out from the inter-dendrite region by slab bulging and solidification shrinkage. The average concentrations at the spot-like segregation are approximately the solute concentrations in the residual liquid between the dendrites at fraction solid of 0.9. Table 1 lists the average concentrations of line pipe steel and the concentrations at the spot-like segregation.

Table 1: Chemical compositions of anti-HIC steel on average and in the residual liquid of growing dendrite at fraction solid of 0.9 (calculated value) [10].

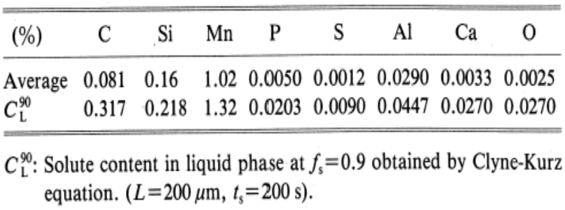

(%)	C	Si	Mn	P	S	Al	Ca	O
Average	0.081	0.16	1.02	0.0050	0.0012	0.0290	0.0033	0.0025
C_L^{90}	0.317	0.218	1.32	0.0203	0.0090	0.0447	0.0270	0.0270

C_L^{90}: Solute content in liquid phase at $f_s=0.9$ obtained by Clyne-Kurz equation. ($L=200\,\mu$m, $t_s=200$ s).

At the beginning of solidification of a spot-like segregation with a diameter of 100 μ, oxygen (O) is mostly trapped as the form of calcium-aluminate (C-A) and the rest of calcium (Ca) is used up for capturing sulphur (S) as calcium sulphide (CaS). Dissolved O content is less than 1ppm and dissolved Ca is around 1/100ppm. Dissolved aluminium (Al) content is about 200ppm and dissolved S content is about 70ppm. As solidification proceeds, segregating S decompose calcia (CaO) in C-A forming CaS and decomposed O is trapped by dissolved Al forming alumina (Al_2O_3). As the result, Al_2O_3 content in C-A and CaS concentration increase as fraction solid increases. Since CaO in C-A does not decompose completely even at the end of solidification, segregating S is captured as CaS throughout the solidification and precipitation of MnS is prevented in this case.

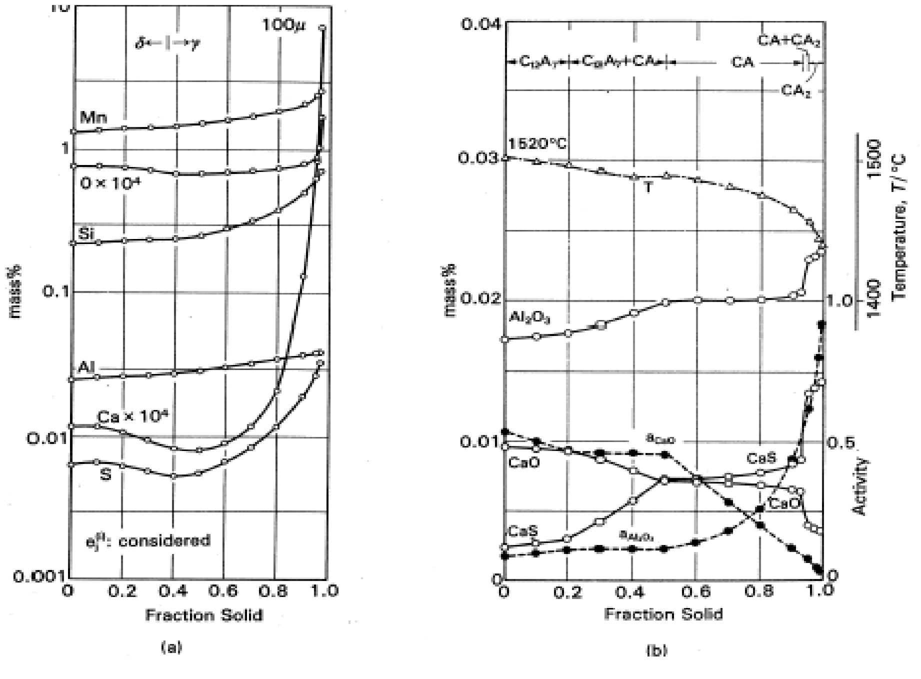

Fig.7: Changes of the amount of dissolved solutes (a) and non-metallic inclusions (b) in the residual liquid during solidification of a spot like segregation with a diameter of 100 μ (calculated values) [9].

In the case of solidification of a spot-like segregation with a diameter of 1000 μ the general behaviour of chemical composition change of non-metallic inclusions are quite the same as that in the case of spot-like segregation with a diameter of 100 μ. However, CaO decomposes completely at the very end of solidification. After that, there is no source of Ca for capturing segregating S and as the result MnS precipitates at the end. Sulphide shape control is not successful in this case. Since the back diffusion of sulphur is smaller, S enrichment in the residual liquid is severer, consuming CaO in C-A faster in the case of a larger spot-like segregation than in smaller one. In order to prevent from MnS precipitation, size of spot-like segregation should be regulated as well as proper amount of Ca addition, which can be done by minimization of slab bulging and soft reduction of slab thickness near the crater end to compensate thermal and solidification shrinkage.

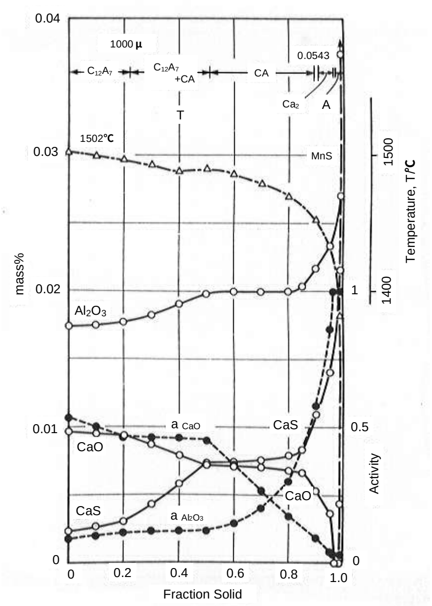

Fig.8: Calculated change of amounts of non-metallic inclusions in the residual liquid during the solidification of a spot-like segregation with diameter of 1000 μ [10].

5 Transformations in Solid Phase

5.1 Band Structure Formation

Since austenite (γ) to ferrite (α) transformation takes place from the outside of steel plate during thermo-mechanical processing carbon ejected at the γ/ α transformation front diffuses into residual γ phase and carbon content in the thickness centre of plate, the last part of γ/ α transformation, becomes extremely high and forms perlite band when the cooling rate of the plate is low during the γ/ α transformation. By the use of accelerated cooling during this period, the inward diffusion of carbon is regulated and by stopping the accelerated cooling above the martensite transformation temperature, the formations of perlite band and martensite along the thickness centre of produced plates are prevented, which is favourable for prevention of crack propagation and initiation [11].

5.2 Intra Granular Ferrite Precipitation

In the γ/ α transformation temperature range ferrite precipitates at a titanium oxide inside a γ grain as shown in Fig. 9 [12], which is intra granular ferrite (IGF) precipitation and realizes ferrite grain refinement and production of steel

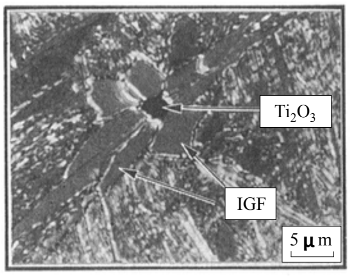

Fig.9: Intragranular ferrite precipitation at Ti_2O_3 [12].

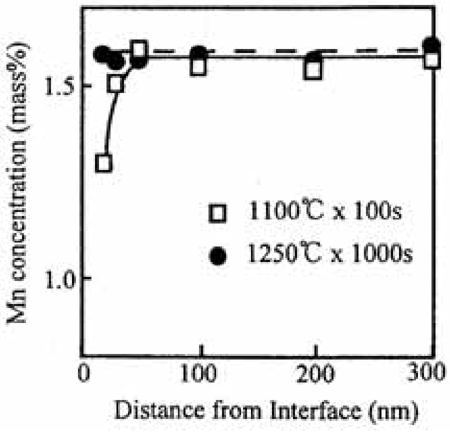

Fig.10: Mn concentration near MnS/ α-Fe interface [13].

plates with high strength and high toughness. The conditions for IGF are providing of heterogeneous nucleation site and carbon or manganese depleted zone, which is favourable for ferrite stability.

G. Shigesato, et al. showed the existence of Mn depleted zone around MnS in a properly heat treated steel which acts as IGF precipitation site (Fig. 10) [13].

6 Welding

Since welding pool temperature reaches 10,000°C, hydrogen from ambient atmosphere and rust dissolves into the pool. Apparent activity coefficient of hydrogen after the welding varies from location to location depending on the stress and strain field, i.e., dislocation distribution, formed during solidification and cooling. Figure 11 shows the calculated hydrogen distribution near the weld part with consideration of them [14]. The calculated results indicate hydrogen enrichment in the heat-affected zone (HAZ) where high micro-void density is assigned. By this reason welding cracking propagates along the HAZ. However, when preheating is conducted in advance of welding, the cooling rate of the weld part is reduced, concomitantly, out-diffuse of hydrogen is encouraged during the cooling, hydrogen concentration in the HAZ is lowered and welding cracking is prevented.

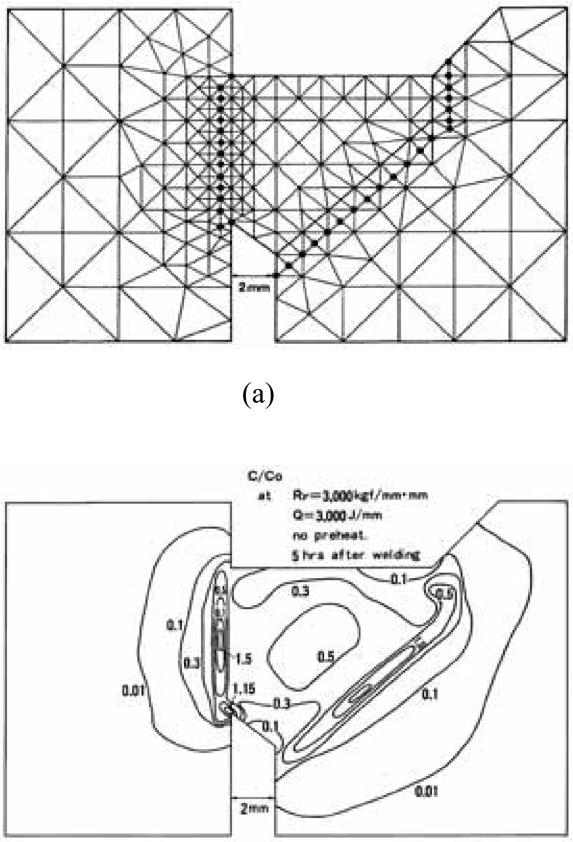

(a)

(b)

Fig.11: Element system for hydrogen diffusion in a weld by FDM (a) and calculated hydrogen distribution (b)[14].

7 Zinc Alloy Coating

Since zinc (Zn) η phase has tendency to stick to metal mould during the sheet pressing, a Fe-Zn inter-metallic compound phase δ, which has less sticking tendency and is rather lubricative against the press mould, is preferred for the coating surface of steel sheets. This phase can be produced by Fe-Zn inter diffusion during the heat treatment after Zn coating on steel sheets. Since another Fe-Zn inter-metallic compound Γ richer in Fe than δ phase is brittle and causes powdering during the forming of coated sheets, Fe-Zn inter diffusion should be regulated not to form this phase while forming δ phase. Although the inter diffusion and formation of various inter-metallic phase is thought to be analyzed simply as shown in Fig. 12, the situations that interface energy between various

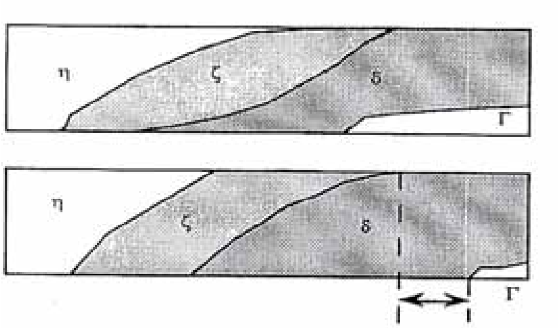

Fig.12: Schematic view of inter diffusion and phase transformation in Zn coating during heat treatment.

phases affects the nucleation of new phase, that the interface energy and growth rate of various phases have crystal orientation dependency and that grain boundary diffusion affects the reaction make the analysis much complicated.

References

[1] Robertson, D.G.C., Deo, B., Oguchi, S.: Muticomponent mixed-tarsport-control theory for kinetics of coupled slag/metal and slag/meta/gas reactions: application to desulphurization of molten iron. *Ironmaking and Steelmaking*, 11, pp.41-55, 1984.

[2] Kitamura, T., Shibata, K., Sawada, I., Kitamura, S.: Optimization of Refining Process by Computer Simulation. *Bulletin of Japanese Institute of Metals*, 28, pp.310-312, 1989.

[3] Scheil, E.: *Z.Metallk.*, 34, pp.70-, 1942.

[4] Brody, H.D., Flemings, M.C.: Solute redistribution in dendritic solidification. *Trans. Metall. Soc. AIME*, 236, pp.615-634, 1966.

[5] Clyine, T.W., Kurz, W.: Solute Redistribution During Solidification with Rapid Solid State Diffusion. *Metall. Trans. A*, 12A, pp.965-971, 1981.

[6] Matsumiya, T., Kajioka, H., Mizoguchi, S., Ueshima, Y., Esaka, H.: Mathematical Analysis of Segregation in Continuously-cast Slabs. *Trans. ISIJ*, 24, pp.873-882, 1984.

[7] Ueshima, Y., Mizoguchi, S., Matsumiya, T., Kajioka, H.: Analysis of Solute Distribution in Dendrites of Carbon Steel with δ / γ Transformation during Solidification. *Metall. Trans. B*, 17B, pp.845-859, 1986.

[8] Koseki, T., Matsumiya, T., Yamada, W., Ogawa, T.: Numerical Modeling of Solidification and Subsequent Transformation of Fe-Cr-Ni Alloyes. *Metall. Trans. A*, 25A, pp.1309-1321, 1994.

[9] Agren, J.: Numerical Treatment of Diffusional Reaction in Multicomponent Alloys. *J. Phys. Chem. Solids*, 43, pp.385-391, 1982

[10] Matsumiya, T.: Mathematical Analyses of Segregations and Chemical Compositional Changes of Nonmetallic Inclusions during Solidification of Steels. *Trans JIM*, 33, pp.783-794, 1992.

[11] Tamehiro, H., Habu, R., Yamada, N., Matsuda, H., Nagumo, M.: Properties of Large Diameter Line Pipe Steel Produced by Accelerated Cooling After Controlled Rolling. *Proceedings of the International Symposium on Accelerated Cooling of Steel*, Southwick, P.D. (Ed), AIME, pp.401-413, 1986.

[12] Takamura, J., Mizoguchi, S.: Role of Oxides in Steels Performance -Metallurgy of Oxides in Steels –1 -. *Proceedings of the 6th International Iron and Steel Cingress*, ISIJ, pp.591-597, 1990.

[13] Shigesato, G., Sugiyama, M., Aihara, S., Uemori, R., Furutani, H.: Influence of Mn-Depleted Zone on Intragranular Ferrite Formation in HAZ of Low Alloy Steel (2). *CAMP-ISIJ*, 12, p.1294, 1999.

[14] Yurioka, N., Ohshita, S., Nakamura, H., Asano, K.: An Analysis of Effects of Micro-structure, Strain and Stress on the Hydrogen Accumulation in the Weld Heat-Affected Zone. *IIW Doc*. 1X-1161-80, 1980.

Proceedings of The 1st International Conference on **D**iffusion in **S**olids and **L**iquids
DSL-2005, July 6-8, 2005, University of Aveiro, Aveiro, Portugal

DEVELOPMENT OF AN EXPERIMENTAL TECHNIQUE FOR THE STUDY OF THERMODIFFUSION IN BINARY MIXTURES

Alexander MIALDUN*, Valentina SHEVTSOVA, Frank DUBOIS
Microgravity Research Center, Université Libre de Bruxelles,
Av. F.D. Roosevelt, 50, CP 165/62, 1050, Bruxelles

*Corresponding author. Fax: +32 02 650 3126; Email: amyaldun@ulb.ac.be

Abstract

The measurement technique of thermodiffusion in binary mixtures is considered. The experimental cell, the vibration stimuli and the optical system of observation are designed and adjusted. The developed experimental approach is aimed at the future space experiment. The preliminary results coming from the ground-based experiment demonstrate positive feature of the existing design, and generate ideas for the set-up improvement.

The diffusion of components, the mass fraction of which differs by 1%, was successfully observed in the laboratory tests using digital optical interferometry. These excellent results provide good expectations for the future measurements, when the mass fraction will differ by only 0.1%. The ground measurements of the thermodiffusion water-isopropanol mixture display the existence of the external heat flux at the corners of the cell, which leads to the deleterious convection. On the one hand, it emphasizes the relevance to the microgravity environment; on the other hand, it causes necessity of improving the thermal design.

Keywords: Experimental methods; Diffusion; Vibration; Soret effect; Interferometry; Binary mixture

1 Introduction

Molecular diffusion occurs when a concentration gradient exists in a mixture: there is a net mass flux that tends to decrease the magnitude of this concentration gradient. To describe the effect of temperature gradients on separation of components in liquids, the thermodiffusion process, also called Soret effect, is considered. This effect is usually small but can be quite important in the analysis of the distributions of components in oil reservoirs. The Soret coefficient $S_T = D_T/D$ measures the separation of the components of a mixture subjected to a temperature difference. Because of buoyancy-induced convection in the gravitational field, accurate measurements of the Soret coefficient in a multi-component system are a quite complicated problem.

The microgravity environment minimizes the effect of gravity and allows the true diffusion limit to be achieved. Therefore performing experiments in space to measure coefficients of diffusion and thermo diffusion is looking as a promising option.

The background g-jitter encountered in many space experiments may alter the benefits of the microgravity environment. Trembling of the space vehicle, onboard machinery, and crew's activity generate these vibrations. A detailed study of the residual accelerations on Foton-12 is given by Shevtsova *et al.* [1]. Although g-jitter seems to have a major impact on diffusion coefficient measurements, very few experimental studies addressed this topic. Previous experiments on-board the Mir station using the Canadian MIM platform indicated that diffusion coefficients in dilute binary metallic alloys depend upon the residual accelerations and the quality of microgravity. Thus, a study of the effects of controlled vibrations on the measurements of diffusion and Soret coefficients in liquid systems could be beneficial.

Chacha *et al*. [2,3] numerically investigated the thermal diffusion in binary mixtures subject to g-jitters with moderately high frequency. The numerical study reveals that the residual gravity and g-jitter reduce the compositional variation due to the increased convection.

Shevtsova *et al*. [4] studied the effect of residual acceleration on the flow in a side-heated rectangular cell. To capture many of the essential characteristics of the convective flow, a new approach was suggested, based on the observation of tracer particles trajectories.

In the limit of high frequencies and small amplitude, the method of averaging can be efficiently applied: governing equations are derived describing the mean field [5,6]. The analysis of mean fields reveals the additional destabilizing effect.

In the frame of ESA Physical Sciences project "Diffusion and Soret Coefficient Measurements for Improvement of Oil Recovery", the discussed experiment is planned to examine the influence of vibration stimuli on the diffusive phenomena. Ground-based experiments should be undertaken to test and improve the data acquisition technique.

2 Experiment

An optical method was chosen to measure diffusion and thermodiffusion in a liquid mixture, as it is fast, sensitive, non-contact and well established. By an appropriate choice of specific technique, it is possible to measure local gradients in the refractive index of the fluid, both steady-state and dynamic. The image formed by a wide laser beam contains information on the continuous refraction profile over the entire span of the fluid. When corrected for thermal effects, this profile represents a continuous measure of the concentration gradient in the fluid at every point along the axis between the thermal boundaries. Thus, the diffusion can be monitored in real-time, and the diffusion coefficient calculated from the measured results.

2.1 Interferometer

Two beams Mach-Zehnder interferometer designed for diffusion measurements is illustrated in Fig. 1.

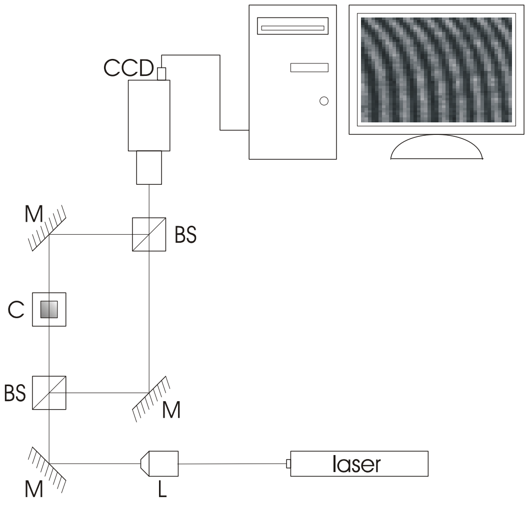

Figure 1: Mach-Zehnder interferometer for real-time diffusion measurements.

The beam of CW He-Ne laser (wavelength λ=632.8 nm) is diverged by the microscope objective (L) and then being passed through the system of two beam splitters (BS) and two mirrors (M), as well as through the cell (C) in the object interferometer branch. It is finally captured by the CCD camera (1280 x 1024 pixels sensor; image scale is approximately 50 pixels/mm).

2.2 Cell and liquid mixture

Heat and mass transfer with Soret effect are considered in a cubic cell 10mm × 10mm × 10mm (Fig. 2) filled with a binary mixture of water-isopropanol.

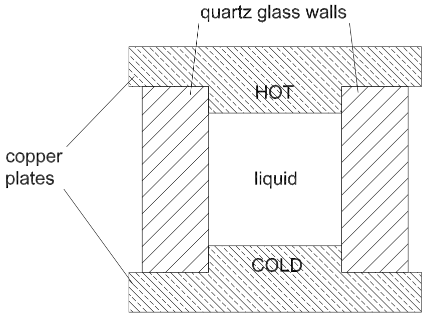

Figure 2: Sketch of the diffusion cell; vertical cross-section.

The sidewalls of the cell made from *Quarzglas Suprasil*, which are 5 mm thick, have special coating providing clear optical view through the cell. The top and bottom are kept at constant temperatures (T_{top} and T_{bot}, respectively) by Peltier elements with accuracy 0.01°C.

Particularly for this mixture, the sign of the Soret effect is strongly dependent on the concentration: the Soret effect is positive $S_T>0$ if the isopropanol content is larger than 25wt.%, otherwise the Soret effect is negative, $S_T<0$ (Fig. 3). Thus a rich variety of phenomena can be studied using the same mixture.

The first experimental results of the dependence of S_T on the mass fraction of water, shown in Fig. 3, were reported in 1974 by Poty *et al.* [7]. Since that time, the main attention was focused on measuring S_T in the vicinity of the point with mass fraction ~ 0.9, e.g. see Ref. [8]. Note that the Soret coefficient is also temperature dependent, and the major part of available experimental data is located inside the oval region in Fig. 3.

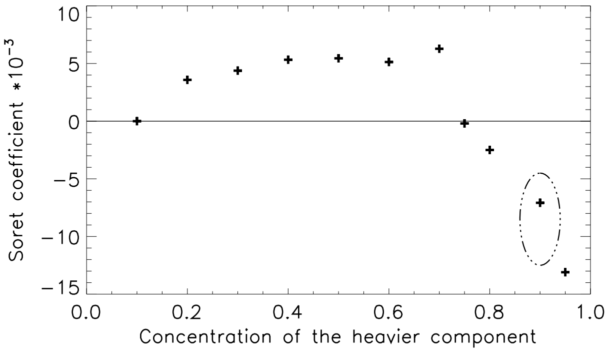

Figure 3: Dependence of the Soret coefficient on the mass fraction of water in water-isopropanol binary mixture.

Our experiments will be done for a few different mass fractions including mass fraction ~ 0.9.

The refractive index variations with temperature and concentration are assumed constant in the narrow *T*-*C* region under investigation ($\Delta T < 10^{o}$C, $\Delta C < 1$ wt.%). The corresponding values are $(\partial n/\partial T)_{\mathrm{To,Co}} = -1.3\times10^{-4}$ 1/K, $(\partial n/\partial C)_{\mathrm{To,Co}} = -8.7\times10^{-4}$ 1/wt.%.

2.3 Fringe analysis

Interferograms are recorded with a specified rate during observation of processes in liquid. An important step is recording the so called reference interference pattern before the start of the experimental run. The reference phase shift, caused only by the optical elements of the system, is then subtracted from all the following processed phases.

Each individual interferogram is reconstructed by first performing a 2-D Fourier transform of the fringe image, filtering a selected band of the spectrum, and then performing an inverse 2-D Fourier transform of the filtered result. Thus, one gets a spatial distribution of total phase shift in the object beam. To consider the phase shift caused only by the change of liquid properties, it is necessary to subtract reference phase shift as shown in Fig. 4.

The methods used for phase unwrapping were either simplest growing pixel method, or quality guided path unwrapping technique [9]. The latter is slower, but more robust in case of some occasional defects in the field of view.

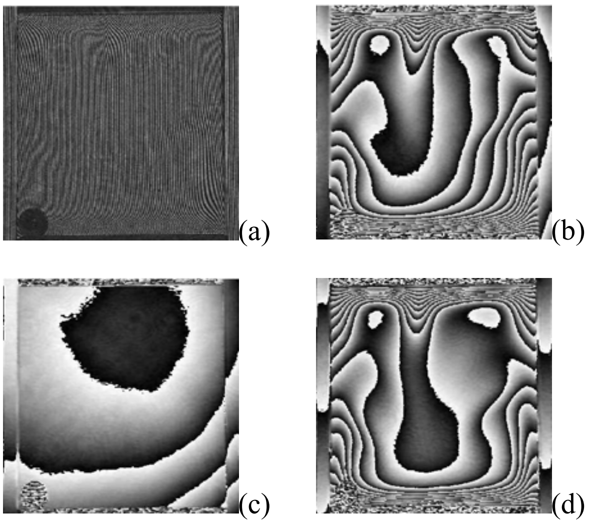

Figure 4: Example of extracting the total phase change (b) from initial fringes (a) and subtracting the reference phase change (c) to get a liquid-induced one (d). Water, T_{top}-T_{bot}=-10^{o}C.

The refractive index gradient Δn is computed from the unwrapped phase φ by

$$\frac{2\pi}{\lambda}\cdot\Delta n\cdot L=\phi, \qquad (1)$$

where *L* is the length of optical path in liquid.

In case of a single-component liquid, the refractive index gradient is simply converted into temperature distribution by

$$T(x,z)-T_0=\Delta T(x,z)=\Delta n(x,z)\Big/\left(\frac{\partial n}{\partial T}\right)_{T_0,C_0}, \qquad (2)$$

with the following adjustment to the known temperature of top and bottom plates.

In case of thermodiffusion, the observation of the procedure becomes more complex since it requires a correction of this thermal effect. This correction can be done by finding “reference” temperature distribution obtained by Eq. 2 with assumption of much faster thermal stabilizing in comparison with the diffusive one. Then the concentration gradient can be obtained by using

$$\Delta n(x,z)=\Delta T_{ref}\left(\frac{\partial n}{\partial T}\right)_{T_0,C_0}+\Delta C\left(\frac{\partial n}{\partial C}\right)_{T_0,C_0}. \qquad (3)$$

2.4 Modelling diffusion data

A solution of the diffusion equation $\frac{\partial C}{\partial t} = D\frac{\partial^2 C}{\partial z^2}$ for this finite media with a constant diffusion coefficient and no-source diffusion (with boundary conditions $\partial C/\partial z = 0$) yields the equation

$$C(z,t) = \frac{1}{8(\pi D t)^{3/2}} \int C_0 \exp\left(-\frac{(z-z')^2}{4Dt} \right) dz \ . \quad (4)$$

The Eq. 4 is applied to fit all measured concentration profiles using D as free parameter.

2.5 Strategy of experiment

Since very different time scales are involved in the process, the complexity of the investigation can be reduced. Starting with an isothermal homogeneous binary mixture and applying a temperature gradient, a concentration profile will set up due to thermodiffusion (Soret effect). Thermal equilibrium will be established within a characteristic time which depends on the size L of the experimental cell and the thermal diffusivity κ of the binary mixture: $\tau_{\text{th}} \approx L^2/\kappa \approx 770$ s.

Simultaneously, mass separation occurs along the temperature gradient. However, mass transport is significantly slower than the thermal process; its characteristic time is usually two orders of magnitude larger than the thermal time τ_{th}; $\tau_{\text{D}} \approx L^2/D \approx 115 \cdot 10^3$ s. The viscous time, which is taken into account in the gravity conditions, is even shorter than the thermal time, $\tau_{\text{v}} \approx L^2/\nu \approx 70$ s. Applied external vibrations will introduce an additional characteristic time - a period of oscillations τ_{os} that varies in wide range.

The fact that $\tau_{\text{th}} << \tau_{\text{D}}$ actually makes possible obtaining and using the reference temperature distribution for the concentration extracting, without significant reduction of accuracy.

The experiments are suggested to be performed in two steps. During the first step, a concentration gradient is established by imposing a temperature gradient along the experimental cell that is filled with a homogeneous binary mixture. Due to the Soret effect, the binary mixture tends to separate with time. At the second step, the system is reverted to an isothermal case, and molecular diffusion will progressively reduce the previously established concentration gradient as depicted in Fig. 5.

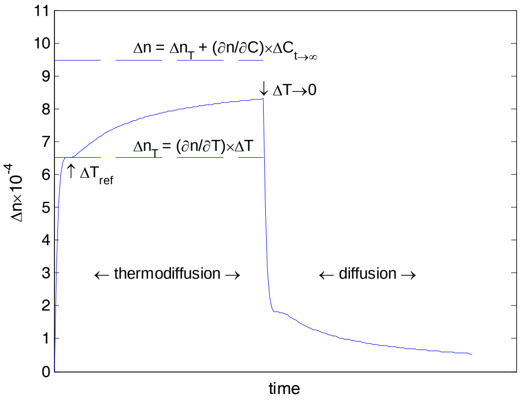

Figure 5: Soret effect and diffusion in liquid mixture: experimental scenario. Refractive index variation estimated assuming mixture of 90 wt.% of water with applied $\Delta T = 5^{\circ}$C.

Thus there is an exceptional opportunity to measure the Soret coefficient during the first step and the molecular diffusion coefficient during the second step. One of the significant benefits of this scheme is the absence of mechanically driven parts in contact with the liquid (no valves, curtains, etc.). Moreover, such an approach allows repetition of the experiments to study exactly the same system with identical or different vibration parameters. In this way, the reliability of the experiments will be improved by statistical processing.

The experimental sequence can also be coupled to a vibration stimulus, thus investigating the influence of a well-known vibration spectrum on the diffusion process.

3 Results

Preliminary ground-based study was carried out to clarify time constraints and transitory factors to be accounted in future space experiments.

3.1 Thermal stabilizing time

To find a typical time required for establishing temperature distribution within the liquid, the cell was first thermostabilized at some intermediate temperature. Then the temperature gradient was instantaneously applied to the cell, by lowering the temperature of the bottom plate and rising the temperature of the top plate. The time interval of the interferogram record was 5 s. Vertical temperature distribution is fully formed 3-5 min after the gradient application (Fig. 6a).

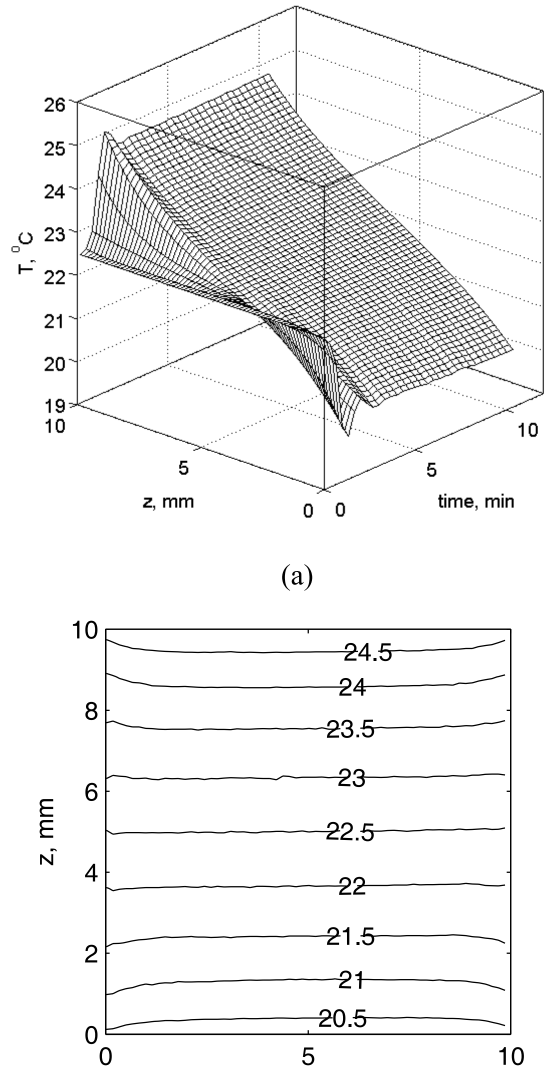

(a)

(b)

Figure 6: Results of time-domain measurement of vertical temperature distribution in the cell (a) and observed stabilized (“reference”) temperature distribution over the cell (b).

Evident temperature overshooting at the very beginning is due to PID regulators behaviour, which cannot be completely avoided.

Final stabilized 2-D temperature distribution in liquid for this case is shown in Fig. 6b.

3.2 Characteristic diffusion timescale

To estimate a characteristic time scale for molecular diffusion, the situation with stable density gradient was created. The cell was initially filled with a solution of 90 wt.% of water. After getting a reference phase image, the solution of 91 wt.% of water was injected into the cell through the bottom inlet to replace half of the initial solution which was expelled through the top outlet. Careful injection allows the initial mixing minimization to create a nearly two-layer system. Time interval between recorded interferograms was 5 min in this case.

Initial distribution of water concentration measured soon after heavier solution injection is shown in Fig. 7a.

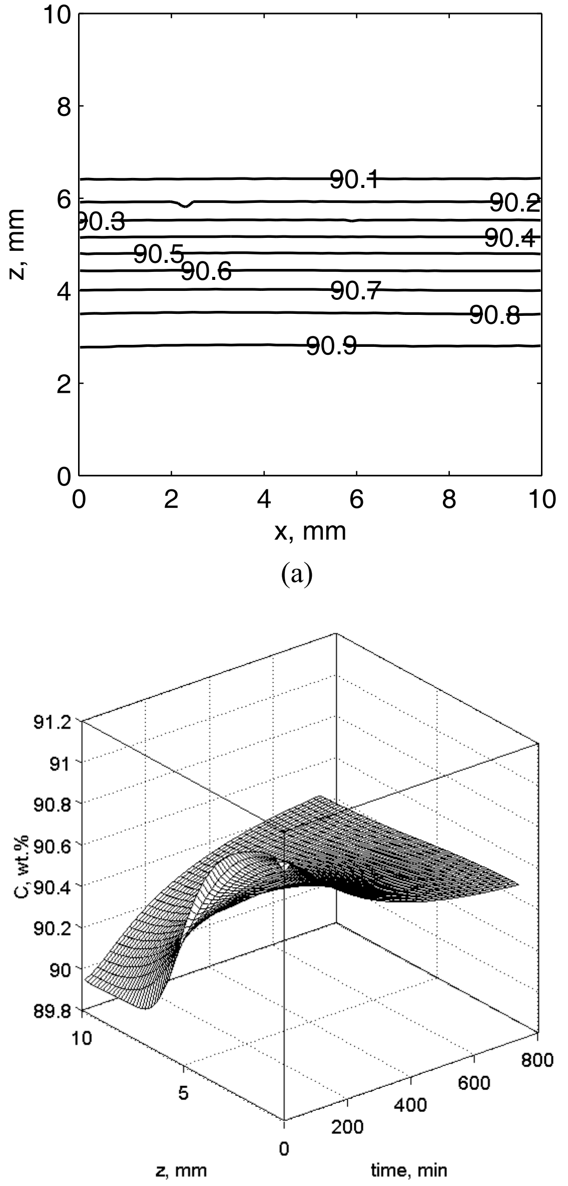

(a)

(b)

Figure 7: Initial concentration distribution over the cell (a) and experimental results on time evolution of vertical concentration distribution (b).

There was no necessity of reference temperature subtracting in this case, because of isothermal condition, and therefore the Eq. 3 only containing the concentration term.

With this experiment, the ability of the established technique to catch small concentration variation caused by diffusion was clearly demonstrated.

Time duration suitable for diffusion measurement as it is seen in Fig. 7b is around 10 hours for the studied mixture.

3.3 Thermodiffusion test

The procedure of reference temperature getting and subtracting was implemented in some test experiments to observe the thermodiffusion.

These ground-based measurements faced certain difficulties. An additional investigation was undertaken to clarify the problems. In the corners of the cell was found convective vortexes even at stable temperature stratification (heating from above).

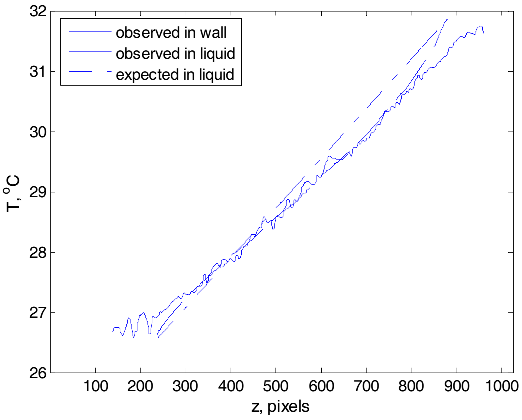

Figure 8: Vertical temperature profiles measured in lateral wall and in liquid near glass-liquid interface.

The most probable reason is illustrated in Fig. 8: the evident deviation of the temperature from linear profile in liquid and in glass wall takes place at the bottom and top corners of the cell.

Thus the continuation of the present study is first aimed at the improvement of the thermal design of the cell, especially for ground-based experiments.

4 Conclusions

The objective of the study is to improve our understanding of the kinetic mechanisms that are driven by diffusion and thermodiffusion in presence of vibrations. The important part of future investigations will be devoted to theoretical developments and numerical modelling. In this way, the new data from the ground and space experiments will validate the theoretical models applicable for diffusion.

Microgravity experiments appear to be the most reliable way to get reference values of Soret coefficient.

Acknowledgments

We are indebted to Prof. J.C. Legros for helpful discussions and creating the academic environment that made this research possible. A Belgian PRODEX Program financially supported this work.

References

[1] Shevtsova, V.M., Melnikov, D.E. and Legros, J.C.: *Report for ESA*, ESTEC, Noordwijk, The Netherlands, p. 135, 2002.

[2] Chacha, M., Faruque, D., Saghir, M.Z., Legros, J.C.: *Int. J. Thermal Science*, 41, pp. 899-911, 2002.

[3] Chacha, M., Saghir, M.Z.: *Int. J. Thermal Science*, 44, pp. 1-10, 2005.

[4] Shevtsova, V.M., Melnikov, D.E. and Legros, J.C.: *Microgravity Sci. Technol.*, XV-1, p.49, 2004.

[5] Gershuni, G.Z., Kolesnikov, A.K., Legros, J.C. and Miznikova B.I.: *J. Fluid Mech.*, 330, pp. 251-269, 1997.

[6] Zebib, A.: *Physics of Fluids*, 13, pp. 1829-1832, 2004.

[7] Poty, P., Legros, J.C., and Thomaes, G.: *Z. Naturforsch.*, 29A, pp. 1915-1916, 1974.

[8] Platten, J.K., Dutrieux, J.F. and Chavepeyer, G.: *Lecture Notes in Physics*, 584, p.313, 2002.

[9] Herraez, M.A., Burton, D.R., Lalor, M.J., and Gdeisat, M.A.: *Appl. Opt.*, 41, pp. 7437-7444, 2002.

Proceedings of The 1st International Conference on Diffusion in Solids and Liquids
DSL-2005, July 6-8, 2005, University of Aveiro, Aveiro, Portugal

COUNTER-CURRENT DIFFUSION PROCESSES DURING OSMOTIC DEHYDRATION OF FOOD MATERIALS USING SALT AND SUGAR SOLUTIONS

Ramón MOREIRA*, Francisco CHENLO, Christian FERNÁNDEZ-HERRERO, Gonzalo VÁZQUEZ

Departament of Chemical Engineering, University of Santiago de Compostela,
Escola Técnica Superior de Enxeñería, Av. Lope Gómez de Marzoa, s/n, E-15782, Santiago de Compostela (Spain)

*Corresponding author. Fax: +34 981 528 050; Email: eqmoncho@usc.es

Abstract

Osmotic dehydration of foodstuffs (using sugars or salt as osmotic agent) was analyzed in order to obtain effective diffusion coefficients for water and solute. Chestnut (*Castanea sativa Mill.*) was the food material used in the assays. These effective coefficients are determined by assuming an ideal geometry for the samples, and supposing homogeneity and isotropicity of the food material during the osmotic process (this means constant diffusion coefficients). However, these data were very useful, as they have allowed modeling satisfactorily the mass transfer processes implied in the osmotic dehydration. In this way, water loss and solids gain data were successfully fitted by the diffusional model proposed. The results from these assays showed the evidence of a dehydration front moving into the product as the osmotic dehydration proceeds.

Keywords: Porous media; Dehydration front; Chestnut; Sodium chloride; Modelling

1 Introduction

If two solutions of different concentration are separated by a semi-permeable membrane which is permeable to the smaller solvent molecules but not to the larger solute molecules, then the solvent will tend to diffuse across the membrane from the less concentrated to the more concentrated solution. This process is called osmosis and the energy which drives the process is usually discussed in terms of osmotic pressure. This phenomenon is of great importance in biological processes where the solvent is water, because the transport across biological membranes is essential to many processes in living organisms.

In this work, osmotic dehydration of foodstuffs was analyzed in order to obtain effective diffusion coefficients for water and solute. These coefficients are determined by assuming an ideal geometry for the samples, and supposing homogeneity and isotropicity of the food material during the osmotic process (this means constant diffusion coefficients). However, these data are very useful, as they have allowed modeling satisfactorily the mass transfer processes implied in the osmotic dehydration [1, 2]. In this way, water loss and solids gain data were successfully fitted by the diffusional model proposed. European chestnut (*Castanea sativa Mill.*) was the food material used for the assays, as it is a product of great economical importance in many regions of Spain and the north of Portugal and because it has a high porosity but low initial moisture content (about 50 % of the initial weight).

Solute choice and concentration depend on several factors, namely the effect on organoleptic quality properties, solute solubility, cell membrane permeability, its stabilising effect and cost [3, 4]. The two most common solute types used for osmotic treatments are sugars and salts. In this work, three different solutes were used: two sugars (glucose and sucrose) with high molecular weight, and sodium chloride, which is a chemical species with significantly lower molecular weight but with stronger chemical potential when is dissolved in water.

2 Material and methods

2.1 *Sample preparation*

Chestnut samples of uniform quality were purchased in a local market and selected for the experiments according to a similar size (average weight of 9 g) and ripeness. Chestnuts were stored in a cold chamber at 4 ºC until use, and their initial moisture content, X_0, was (56.2 ± 2.1) %, expressed in wet basis.

For the assays, whole chestnuts were used as samples, and after hand-peeling, the internal pellicle (tegument or episperm) was carefully removed with a cutter in order to obtain a homogeneous surface to contact the osmotic solutions.

2.2 Osmotic solutions

The osmotic solutions were made using commercial sucrose (table sugar, 98 % minimum purity), glucose (reagent grade, 99 % minimum purity), table salt (98 % purity) and distilled water. The solute concentrations used were 40.0, 50.0 and 60.0 % (w/w) for sucrose; 40.0, 50.0 and 56.5 % (w/w) for glucose; and 17.0, 22.0 and 26.5 % (w/w) for sodium chloride. The systems were assayed at three different values of temperature, *T* (25, 35 and 45 ºC), which was kept constant by means of a laboratory oven (Selecta Digitheat 2001245).

2.3 Experimental procedure

Chestnuts, once weighed, were introduced into beakers and immersed into the corresponding osmotic media, being removed from them at different time intervals (0.5, 1, 2, 4, 6 and 8 hours). After that, the samples were blotted in order to remove the excess of osmotic solution over the chestnut surface and then weighed using an analytical balance, Mettler AJ 150 (accuracy: ±0.0001 g). No shaking was used in any of the assays, and the ratio solution/foodstuff was kept over 10 in order to guarantee that the concentration change of the osmotic media could always be neglected. Five chestnut samples were employed for osmotic dehydration kinetics.

The final dry basis after the osmotic process was attained by means of a vacuum oven, Heraeus Vacutherm VT 6025, at 70 ºC and less than 100 mm Hg of pressure following a standard procedure [5]. In order to follow adequately the osmotic dehydration kinetics, individual analysis for each sample were carried out and from these, weight reduction (*WR*), solids gain (*SG*), water loss (*WL*) and normalized moisture content (*NMC*) data were obtained at different times of operation, according to Eqs. (1) - (4) [6]:

$$WR = \frac{M_0 - M}{M_0} \tag{1}$$

$$SG = \frac{m - m_0}{M_0} \tag{2}$$

$$WL = WR + SG \tag{3}$$

$$NMC = \frac{1 - m/M}{1 - m_0/M_0} = \frac{X}{X_0} \tag{4}$$

where *M* represents the total mass of a sample, *m* is the mass of the solids contained in that sample and a zero subindex means the initial conditions previous to the osmotic treatment.

2.4 Mass transfer models

Mass transfer kinetics during osmotic treatments has been successfully modeled using second Fick's law of diffusion [7]. The analytical solutions for the differential equations obtained from these microscopical models always need equilibrium values which are used to normalize data and make them dimensionless. Osmotic dehydration assays are often problematic in obtaining such values, as the foodstuff composition and structure can be severely affected after the long operation times required to reach equilibrium, making the data obtained not reliable. In order to solve this problem, a *LDR* (logistic-dose response) model has been used to estimate the necessary equilibrium values using the experimental data from the kinetic assays [8]. This model makes possible to estimate kinetic parameters for any osmotic solute concentration, operating temperature and contact time.

$$P_{t,T,C} = \frac{a}{\left[1 + \left(\frac{t}{b}\right)^{-c}\right]\left[1 + \left(\frac{C}{d}\right)^{-c}\right]} \tag{5}$$

In the Eq. (5), *P* represents *WL* or *SG* and also (1-*NMC*). Analysing the model, the values at equilibrium conditions $P_{eq,T,C}$ can be obtained as:

$$P_{eq,T,C} = \frac{a}{\left[1 + \left(\frac{C}{d}\right)^{-c}\right]} \tag{6}$$

The estimated equilibrium values can now be used to obtain transport coefficients from an analytical solution of the Fick's law. In order to do that, considering external resistance to mass transfer negligible against the internal resistance (this assumption means that the characteristic values of the dimensionless mass Biot number are less than 0.1) and considering the chestnuts as spheres (chestnuts have a high sphericity, $\phi > 0.9$) the analytical solution of the difusional Fick's law comes given as [9]:

$$W_{w\,or\,s} = \frac{6}{\pi^2}\sum_{n=1}^{\infty}\frac{1}{n^2}\,exp\left(\frac{-D_{eff}\,n^2\pi^2 t}{r^2}\right) \qquad (7)$$

where $D_{eff} \cdot t/r^2$ constitutes the dimensionless Fourier number, D_{eff} the effective coefficient of diffusion considered constant, t the osmotic operation time, r the average radius of the chestnuts considered as spheres calculated by:

$$r = \sqrt[3]{\frac{3M_0}{4\pi\rho}} \qquad (8)$$

where ρ is the bulk density of the chestnut which value was determined employing volumetric displacement based on Archimedes' principle. [1, 2]. Finally, $W_{w\ or\ s}$ is the dimensionless parameter for water loss (*w*) or net solids gain (*s*), respectively, defined as:

$$W_{w\,or\,s} = \frac{P_t - P_{eq}}{P_0 - P_{eq}} \qquad (9)$$

3 Results and discussion

The diffusional model, Eq. (7), was developed employing the equilibrium values given by the logistic model (Eq. (5)). The model is satisfactory for all the solutes employed (Figure 1), but several deviations between experimental and calculated data can be observed. These results indicate that considering a constant effective coefficient of diffusion for the chestnut is not adequate at all.

This is motivated by the mechanism of mass transfer during osmotic dehydration for cellular biological materials where the physical structure of the material changes with progress of the mass transfer.

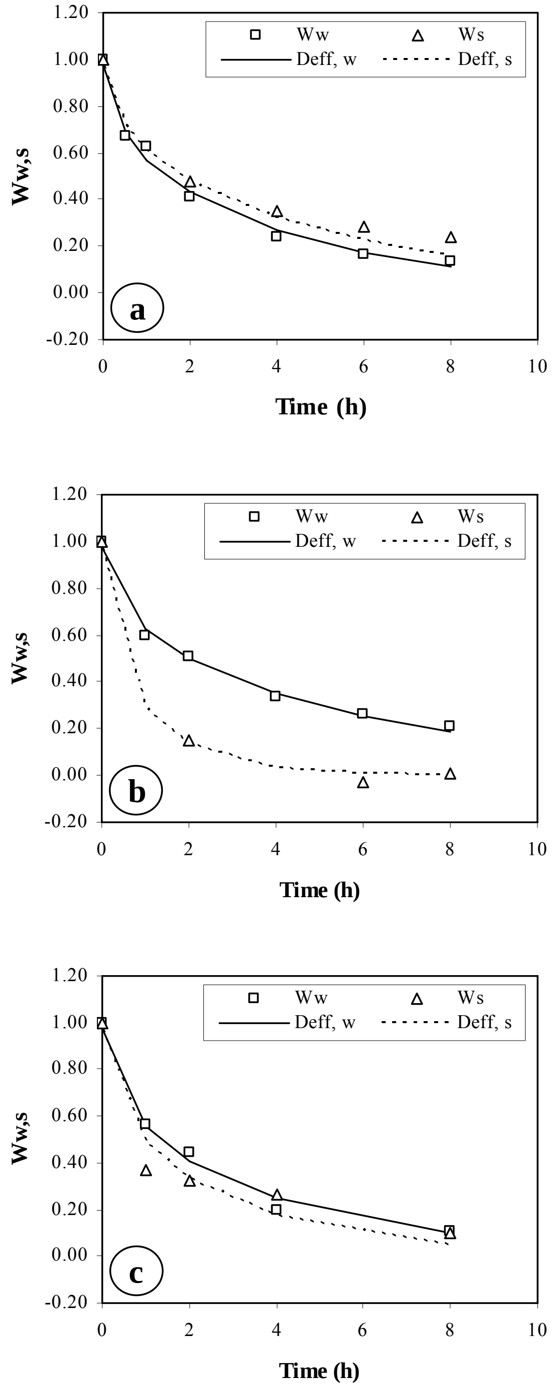

Figure 1: Experimental data of W_w and W_s and diffusional model for osmotic dehydration of chestnut at 25 ºC. (a) NaCl, 22.0 % (w/w); (b) Glucose, 56.5 % (w/w); (c) Sucrose, 60.0 % (w/w).

A dehydration front moves during osmotic operation from the surface towards the centre of the material carrying out the moisture removal and the solute acquisition, changing the composition

[7]. In this way, water transport can be considered in different zones: first the diffusion from the core of the material to the dehydration front, later diffusion across the front and diffusion through the osmotically treated material. Obviously, the effective coefficient of diffusion can change its value in each region and the consideration of a constant value for the whole operation time is actually a simplified method to describe the mass transfers.

The values of these coefficients of diffusion are collected in Table 1 and are within the range obtained for other products [10]. Obviously, taking into account the previous assumptions, the values of the effective coefficients of diffusion are valid in the range of temperatures assayed and the variations with the osmotic concentration only mean an indirect measurement of the osmotic dehydration rate.

Table 1: Effective coefficients of diffusion for water, D_w, and solids, D_s, obtained during osmotic dehydration of chestnut from 25 ºC up to 45 ºC.

Solute concentration (% (w/w))	D_w (10^{-9} $m^2 \cdot s^{-1}$)	D_s (10^{-9} $m^2 \cdot s^{-1}$)
NaCl, 17.0%	0.95	1.22
NaCl, 22.0%	0.90	0.72
NaCl, 26.5%	1.04	1.64
Glucose, 40.0%	0.56 - 0.87	1.37 - 2.62
Glucose, 50.0%	0.61 - 0.95	2.15 - 3.10
Glucose, 56.5%	0.67 - 0.97	2.62 - 3.47
Sucrose, 40.0%	0.57 - 0.79	1.00 - 1.54
Sucrose, 50.0%	0.70 - 0.89	1.11 - 1.96
Sucrose, 60.0%	0.93 - 0.99	1.37 - 2.32

No significative temperature effect was observed during the osmotic dehydration with salt. However, sugar difussion coefficients were clearly influenced by operating temperature. Comparing the values of effective coefficients of diffusion at the same concentration expressed as molality (mol/kg), it can be said that osmotic dehydration with sucrose leads to higher water diffusivities than glucose and sodium chloride while solid diffusivities are very close to the values obtained with other solutes.

Acknowledgements

The authors acknowledge the MCyT (Spain) and the FEDER the partial support with the project (AGL2002-00255).

References

[1] Chenlo, F., Moreira, R., Fernández-Herrero, C., Vázquez, G.: Mass transfer during osmotic dehydration of chestnut using sodium chloride solutions. *J. Food. Eng.*, (in press), 2005.

[2] Chenlo, F., Moreira, R., Fernández-Herrero, C., Vázquez, G.: Experimental results and modelling of the osmotic dehydration kinetics of chestnut with glucose solutions. *J. Food. Eng.*, (in press), 2005.

[3] Shi, J., Le Maguer, M.: Osmotic dehydration of foods: Mass transfer and modeling aspects. *Food Rev. Int.*, 18, pp. 305–335, 2002.

[4] Sereno, A.M., Moreira, R., Martínez, E.: Mass transfer coefficients during osmotic dehydration of apple in single and combined aqueous solutions of sugar and salt. *J. Food. Eng.*, 47, pp. 43-49, 2001.

[5] AOAC: *Official Methods of Analysis*. Association of Official Analytical Chemists International, Washington, 1995.

[6] Lerici, C.R., Pinnavaia, T.G., Dalla Rosa, M., Bartolucci, L.: Osmotic dehydration of fruit: Influence of osmotic agents on drying behavior and product quality. *J. Food Sci.*, 50, pp. 1217-1226, 1985.

[7] Rastogi, N.K., Raghavarao, K.S.M.S., Niranjan, K., Knorr, D.: Recent developments in osmotic dehydration: methods to enhance mass transfer. *Trends Food Sci. Tech.*, 13, pp. 48-59, 2002.

[8] Streibig, J.C., Rudemo, M., Jensen, J.E.: *Dose-response curves and statistical models*. Herbicide bioassays (pp. 30-55). CRC Press, Florida, Boca Raton, 1993.

[9] Crank, J.: *The mathematics of diffusion*. Second ed. Clarendon Press, Oxford, 1975.

[10] Mayor, L., Moreira, R., Chenlo, F., Sereno, A.M.: Kinetics of osmotic dehydration of pumpkin with sodium chloride solutions. *J. Food Eng.*, (in press), 2005.

Proceedings of The 1st International Conference on **D**iffusion in **S**olids and **L**iquids
DSL-2005, July 6-8, 2005, University of Aveiro, Aveiro, Portugal

FICKIAN EFFECTIVE COEFFICIENTS OF DIFFUSION OF WATER DURING DRYING OF CHESTNUTS TAKING INTO ACCOUNT SAMPLE SHRINKAGE

Ramón MOREIRA*, Francisco CHENLO, Lívia CHAGURI, Gonzalo VÁZQUEZ

Departamento de Enxeñaría Química, Escola Técnica Superior de Enxeñaría, Universidade de Santiago,
Rúa Lope Gómez de Marzoa s/n, E-15782 Santiago de Compostela, Spain

*Corresponding author. Fax: +34 981 528 050; Email: eqmoncho@usc.es

---

Abstract

Drying kinetics of chestnuts were experimentally determined. The experiments were carried out in a dryer, pilot-plan scale, with an air closed circuit and assisted by a heat pump. Several experimental conditions were designed varying temperature, relative humidity of the air, and air velocity. Chestnuts were put in contact with the convective air in several dispositions as were the presence of pericarp (external shell), endocarp (internal skin) or without these natural resistances (previous careful peeling). The results show drying kinetics are faster when the driving force is higher and the physical resistances are eliminated. A proposed model involving a water effective coefficient of diffusion (varying from 0.029 up to $0.381\cdot10^{-9}$ $m^2\cdot s^{-1}$) and food shrinkage (volumetric shrinkage depends linearly on normalised moisture content) has been successfully tested to simulate the drying kinetics. It was determined that the most important resistance to water removal is found in the rough surface of the chestnut.

Keywords: Porous media; Shells; Shrinkage; Mass transfer rate; Spherical geometry

---

1 Introduction

Chestnut (*Castanea sativa Mill.*) is a traditional product with an important role in the economy in the Mediterranean countries where is mainly consumed unprocessed, but nowadays its presence in stores, in many different ways of production such as *marron glace*, purees, flours, as a pre-cooked products and even as frozen products [1] is proved. Their worldwide production is around 250,000 ton/year).

Studies about drying processes are numerous because it is one of the most common industrial operations and involves high energetic consumptions, 10-25 % of the total energy used in the manufacturing process worldwide.

Chestnuts have been dried introducing the food material into a hot air convection chamber, in which air heat is transferred by convection to the material to dry. In order to avoid energy losses and to guarantee low physical damages, a close air drying chamber system was used with air at low temperature using a heat pump system as it was previously described [2].

The aims of this work are to evaluate the influence of some operational factors on drying kinetics of chestnut, drying time, temperature, and relative humidity of drying air, as well as, the influence of resistances such as the natural chestnut shells (internal tegument or endocarp and external skin or pericarp) on drying kinetics, which protect it from external damages, but their presence can reduce water removal rates. By other hand, the mechanism of water movement is not yet clear enough [3], but water diffusion by the existence of moisture gradients in the bulk of the food material is the most accepted theory that is successfully employed in the corresponding modeling for many foodstuffs. Other objective is to propose a diffusional model involving shrinkage of the chestnut to obtain the modeling of the drying kinetics.

2 Modelling

Dehydration operation can be considered at isothermal conditions because heat transfer is faster than mass transfer. In this way, Fick's second law of the unsteady state diffusion can describe the water transport in the falling rate period of drying. Assuming spherical geometry for chestnut (evaluating the corresponding equivalent radius, r (m)) and only radial diffusion of water an analytical solution relating moisture content, X_t (kg water/kg dry basis), and drying time, t (s), can be obtained if uniform initial moisture distribution and surface moisture as equilibrium moisture content, X_e (d.b), with the air conditions are considered [4]:

$$X_t = X_e + (X_o - X_e)\frac{6}{\pi^2}\sum_{n=1}^{\infty}\frac{1}{n^2}exp\left(\frac{-n^2\pi^2 D_{eff}\,t}{r^2}\right)$$

(1)

where D_{eff} (m^2/s) is the water effective coefficient of diffusion. As the samples change their dimensions (shrinking) during drying, the volume was determined employing a heptane displacement technique at several drying times. To evaluate the characteristic length, the chestnut was assumed as a sphere obtaining the corresponding equivalent radius as follows:

$$r = \sqrt[3]{\frac{0.75\,m}{\pi\rho}}$$

(2)

where m (kg) is the weight of the samples and ρ (kg/m^3) the bulk density is determined as:

$$\rho = \frac{m}{V} \qquad (3)$$

and the sample volume, V (m^3), is determined as:

$$V = \frac{m - m_{heptane}}{\rho_{heptane}} \qquad (4)$$

where $m_{heptane}$ (kg) is the weight of the sample immersed in heptane and $\rho_{heptane}$ (kg/m^3) is the density of the fluid. In this way, introducing in Eq. (1) the experimental data obtained at determined time interval (X, t and r) and other values as initial moisture content (X_o) and the bibliographic value of equilibrium moisture content (X_e), [5], it is possible to obtain the effective coefficient of diffusion as lumped parameter that allows the modeling of the experimental data.

3 Methods and materials

3.1 Materials

Chestnuts were purchased at a local market and selected for the experiments according to weight (10 g approximately) with a similar size and ripeness. Chestnut were stored in a cold chamber at 4 ºC until use, and the average initial moisture content for these experiments was 55.4 ± 1.8 % expressed in wet basis.

Three different chestnut varieties (*Judia, Longal* and *Famosa*) used in the Galician food processing industry were dried under different conditions and drying kinetics were determined (no significant differences during drying processes between them were found and the analysis is carried out indistinctly). Chestnut samples (a variable number among four and six unities) were introduced in drying chamber in several ways, with and without natural skins (internal (endocarp) or external (pericarp)). In this paper, when both skins are removed the chestnut will be denoted as “peeled”. Also, with some chestnuts the tissue of external surface was removed with a knife (to determine the influence of the rough surface of the chestnut during drying process), and these samples will be denoted as “cut”.

3.2 Air drying experiments

Convective drying with hot air of chestnut experiments were carried out using a pilot-scale close circuit drying plant was used. The plant comprises three basic units: the drying chamber, the heat pump and a control and data processing unit [2]. Drying experiments were carried out at three different temperatures (45, 55, and 65 ºC) and three relative humidities of air (20, 30, and 40 %). The air velocity was also variable from 1.8 up to 2.7 m/s. In all cases kinetics were monitoring by samples weight at different drying times (Scaltec SBA 41) with an accuracy ± 0.001 g, being the whole process for 24 hours. The moisture content was determined using a vacuum oven (<15 kPa) and 70 ºC (Heraeus Vacutherm VT650) getting samples up to constant weight. For each run, the initial moisture content of some chestnut samples was determined as control.

In order to determine the volume of the samples, they were weighted on air and immersed into heptane contained in a vessel at 20 ºC ($\rho_{heptane}$: 710 kg/m^3) taking into account the volumetric displacement on Archimedes’ principle (Eq. (4)). With this data is obtained the bulk density of chestnut at different moisture content (Eq. (3)).

4 Results and discussion

4.1 Chestnut shrinkage

Volumetric shrinkage of chestnut during drying was slightly larger than the equivalent volume of evaporated water. This behaviour means that a light structure collapse takes place and can partially explain the difficulty for rehydrating the dried chestnut taking into account the results found with potato by other researchers.

Several models are proposed in the bibliography to evaluate the volumetric shrinkage with moisture content [6]. One of the simplest is a linear relationship successfully applied to several starchy foods. The following relationship for chestnuts was obtained (with an average coefficient of regression, $R^2 = 0.998$) after analyzing around 100 chestnuts (with different ways of peelings) dehydrated at different conditions assayed in this work:

$$\frac{V}{V_o} = 0.611\frac{X}{X_o} + 0.366 \tag{6}$$

The volume data calculated with Eq. (6) are employed in the Eq. (2) to obtain the characteristic length (equivalent radius) considering the chestnut as a sphere that allows taking into account the shrinkage during drying to obtain the effective coefficient of diffusion.

4.2 Drying kinetics at different air conditions

The relative humidity of the air showed slight effect on drying kinetics. For example, in the case of cut chestnut when 0.6 of driving force is attained the same drying times independently of relative humidity are necessary; and when 0.4 of driving force is attained, the difference between drying times is one hour among them.

The influence of the drying air velocity on drying kinetics was determined employing as conditions of temperature 65 ºC and relative humidity at 20 %. The highest effect relative of air velocity is proved during initial drying period when water evaporation takes place at the surface resulting less important after this period because water diffusion from the interior of the product processes governs the process.

The effect of air temperature on drying kinetics is shown in Fig. 1 for cut chestnuts, as an example. As expected, there is an important acceleration of the drying process due to the increase of the drying temperature from 45 up to 65 ºC. In this case, three times reduction in the driving force takes places when temperature increases from 45 up to 65 ºC after 8 hours of operation time, and a reduction to the half when the temperature increases form 45 ºC to 55 ºC.

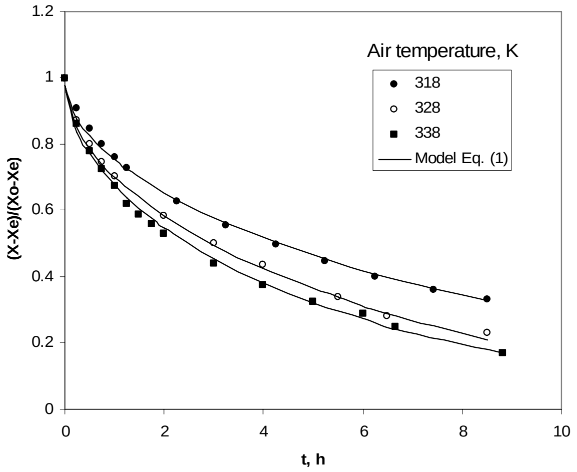

Figure 1: Air temperature effect on drying kinetics at relative humidity 20% and velocity 2.7 m/s (cut chestnuts) of the air.

4.3 Drying kinetics using peelings of chestnut

Fig. 2 shows, an example at determined air conditions, drying kinetics obtained for whole chestnut (presence of endocarp and pericarp), with only endocarp, peeled (removal of both skins) and cut chestnuts (removal of the both skins and the rough external surface). Each chestnut barrier has a relevant effect on drying kinetics. The presence of the internal tegument causes an important decrease on water removal rate. The pericarp, external shell, shows a slight additional resistance because it is more rigid and partial fractures appear during drying process allowing the water transport easily through it. Finally, the removal of rough external surface of the peeled chestnut also means an appreciable increment on drying rate. Chemical substances related with adhesives substances present in the endocarp skin and also other substances for protection (surface of chestnut peeled is darker than the internal tissue) and the particular texture (harder than the internal tissue) can be the responsible of this effect on mass transfer.

4.4 Drying kinetics modelling: effective coefficient of diffusion

Experimental drying curves showed the typical falling-rate drying behaviour under all run conditions and constant rate-drying period was not observed, meaning that the internal mass transfer controls the process, proposing for the modelling of the drying of the chestnut a diffusional model that involves a constant lumped parameter denominated effective coefficient of diffusion.

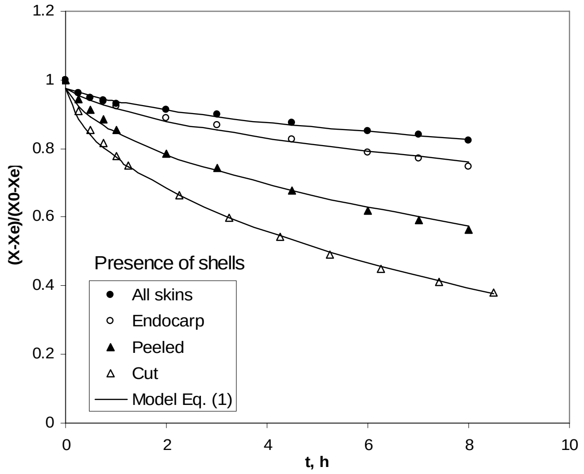

Figure 2: Effect of pericarp, endocarp, and rouge surface on drying kinetics at 45 ºC and air relative humidity at 30 %.

This assumption implies the diffusion as the predominant mechanism, but other water transports can be expressed in the same mathematical way that Fick's Law and therefore are included in the coefficient value. Analyzing the effect of operation variables, we can conclude that the most important effects are air temperature and the different peelings (excepting the pericarp removal) of the chestnut. Figs 1 and 2 show with lines the simulated drying kinetics obtained employing the proposed model (Eq. (1)). It is observed that model successfully fits the experimental values in all cases considering the shrinkage of chestnut during drying, confirming that the model is adequate. Effective coefficients of diffusion are correlated with temperature using linear and exponential relationships:

$$D_{eff} = a + bT \tag{7}$$

$$ln D_{eff} = ln D_o - \frac{E_a}{RT} \tag{8}$$

The first one gives better results (Table 1), but the second one is the most usual way for relating the coefficient with the reciprocal of the absolute temperature and the parameters can compared with the obtained for other products. Obtained values for the energy of activation are within the range 12.7-110 kJ/mol reported for many food materials [7].

Table 1: Parameters of Eqs. (7) and (8).

	Linear (Eq 7)		
	a	b	R^2
Chestnut	(m^2/s)	(m^2/sK)	
Whole	-115.6	0.370	0.994
Peeled	-220.4	0.733	0.993
Cut	-310.0	1.032	0.998
	Exponential (Eq 8)		
	$D_o(10^3)$	E_a	R^2
	(m^2/s)	(kJ/mol)	
Whole	69.4	57.0	0.982
Peeled	0.084	34.5	0.971
Cut	0.081	35.4	0.994

Acknowledgments

The authors acknowledge the Spanish MCyT and FEDER the project (Project AGL2002-0255).

References

[1] Pinnavaia, G.G., Pizzirani, S., Papotto, E.G.: Study of the production feasibility of a extruded chestnut flour product. *Industria Alimentari*, 34: pp. 977-984, 1995.

[2] Vázquez, G., Chenlo, F., Moreira, R., Cruz, E.: Grape drying in a pilot plant with a heat pump. *Drying Technol.*, 15: pp. 899-920, 1997.

[3] Aguilera, J.M.: Why food microstructure? *J. Food Eng.*, 67, pp. 3-11, 2005.

[4] Crank, J.: *The mathematics of diffusion.* Second ed., Oxford University Press, New York, 1975.

[5] Vázquez, G. Chenlo, F., Moreira R.: Modeling of desorption isotherms of chestnut: Influence of temperature and evaluation of isosteric heats. *Drying Technol.*, 19, pp. 1189-1199, 2001.

[6] Mayor, L., Sereno, A.M.: Modelling shrinkage during convective drying of food materials: a review. *J. Food Eng.*, 61, pp. 373-386. 2004.

[7] Zogsas, N., Maroulis, Z., Marinos-Kouris, D.: Moisture diffusivity data compilation in foodstuffs. *Drying Technol.*, 14, pp. 2225-2253, 1996.

Proceedings of The 1st International Conference on **D**iffusion in **S**olids and **L**iquids
DSL-2005, July 6-8, 2005, University of Aveiro, Aveiro, Portugal

THERMOECONOMIC ANALYSIS OF ABSORBER OF WATER-AMMONIA REFRIGERATION MACHINE

Tatiana MOROSUK

Refrigeration Machines Department, Institute for Low Temperature,
Odessa State Academy of Refrigeration, Dvorianskaya 1/3, Odessa 65026, Ukraine

Fax: +38 0482 238931; Email: morosuk@paco.net

Abstract

Subject of author's research is absorption refrigeration machines. Traditionally first stage of absorption machine design is idealized processes calculation; further enter correction factors for the coordination theoretical and experimental data. Such method does not allow predicting exact data of working fluid (i.e. concentration of mixture "agent - absorbent") and temperatures of the flows without preliminary experimental data. For absorption process calculation only conditions of heat transfer take into account in first stage of the analysis. Really, there is complex process as sum of heat and mass transfer between cold vapor of agent from evaporator and hot weak solution from generator. The correct definition of "moving force" of absorption is the basic point as it influences simultaneously values of investment and operational costs on absorber in absorption refrigeration machine. The author examines bases for design of an absorber by thermoeconomic methods with using minimally experimental data.

Keywords: Ab-sorption; Heat-mass transfer; Refrigeration machine; Thermoeconomic analysis

---

1 Introduction

Thermoeconomic (exergoeconomic) analysis is connection of the First (Second) Law of Thermodynamics and Theory of Cost. Thermoeconomics (exegoeconomics) as a direction in modern applied thermodynamics is the powerful tool for analysis, evaluation and optimization of energy conversion systems. This analysis gives possibility of determination of the efficiency of system by analysis of each element of this system. The cost formation process throughout system from the 'fuel' to the final 'product' is made transparent with the aid of a thermoeconomic analysis. The cost is associated with the thermoeconomic inefficiencies occurring in each detected system component [1].

The object of the author's scientific researches is absorption refrigeration machine. Basic elements of this machine are *four heat exchangers* (Fig. 1a): generator, absorber, condenser and evaporator. A lot of schematic solutions of absorption refrigeration machines are formed as addition of auxiliary elements to the minimal number of basic elements. For theses machines auxiliary elements are also heat-mass exchangers (regeneration heat exchangers, additional absorbers and generators etc.).

Numerous researches in area of absorption refrigeration machines especially for future thermoeconomic analysis the following dependences have revealed:

- technical function of absorption machine by [2] as logical equation is

$$[TV] \equiv [COP]^{l} \times [\Delta\Theta]^{m} \times \left[\frac{COE}{H_S}\right]^{n} \qquad (1)$$

with limitations

$$l+m+n=1$$

and

$$0 < l < 1;\ 0 < m,\ 1;\ 0 < n < 1,$$

where COP is coefficient of performance of refrigeration machines, $COP = Q_E / Q_G$; $\Delta\Theta_k$ is temperature difference of all absorption refrigeration machine, $\Delta\Theta = \Theta_A - \Theta_E$. Value Θ_k can be determined by Carnot's temperature factor $\Theta_k \equiv 1 - T_o/T$; COE/H_S is specific exergy contain of mixture "agent – absorbent".

On the basis of the experimental data for water-ammonia refrigeration machine received in the Odessa State Academy of Refrigeration the following equations were accepted:

$$COP = f\,(COP_{max}\,,\ \Theta_{\Sigma}) \qquad (2)$$

where COP_{max} is maximal value for theoretical cycle; Θ_Σ is temperature differential of a heating source in the generator of absorption machine, $\Theta_\Sigma = T_{hot,max} - T_{hot,theory}$;

The value Θ_Σ can be determined as

$$\Theta_\Sigma = \Theta_2 + \alpha(\Theta_W + \Theta_4) + \beta(\Theta_W + \Theta_6) + \Theta_H \quad (3)$$

where there are temperature differentials: Θ_2 - on "hot end" of the generator; Θ_3 - on "cold end" of regeneration heat exchanger; Θ_4 - the "cold end" of the absorber; Θ_6 – on the "cold end" of the condenser; $\Theta_W = T_{env}^{max} - T_{env}^{min}$ – between outlet and inlet of the cooling environment in the condenser (cooling of an absorber and the condenser is accepted consecutive); α - coefficient which is taking into account influence of change of pressure from P_E up to P_A on temperature difference in absorber at giving difference of concentration $(X_R - X_R^t)$; β - similar coefficient for the generator $(P_G - P_C)$. Values α and β were determined experimentally and maximal deviation of their change is ~10-15 %.

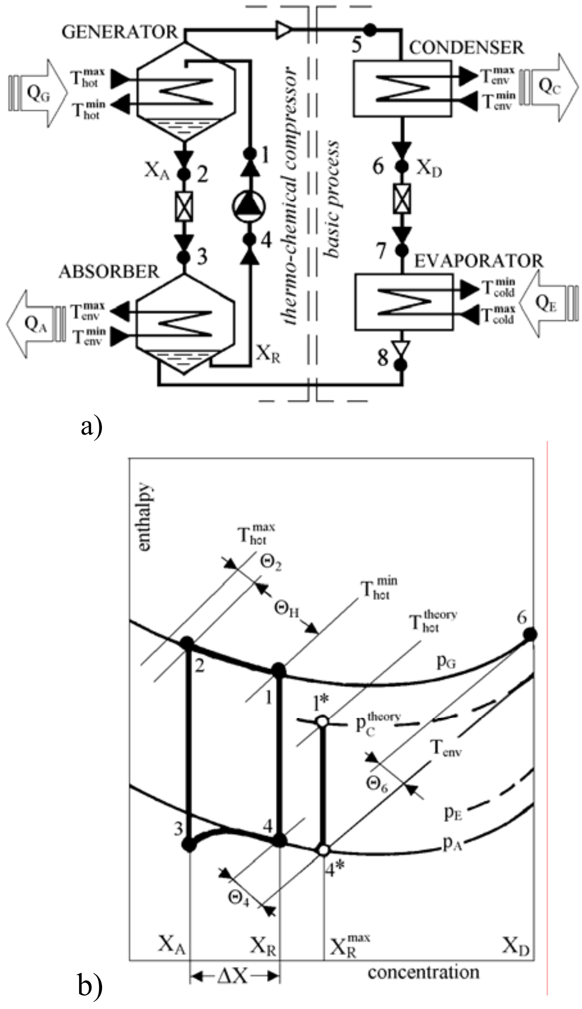

a)

b)

Figure 1: Absorption water-ammonia refrigeration machine: a) schema; b) cycle of thermochemical compressor in the diagram '*enthalpy-concentration*' (*h-X*).

Analysis of the eq. (3) shows, that the set of temperature differences is interconnected. Mathematical modeling of this interrelation and its influence on characteristics of absorption refrigeration machine was described in detail in the author's work [3].

Mass transfer process complicates the heat transfer process in generator and absorber. It is taken into account for calculation. In this paper author shows it for water-ammonia absorption refrigeration machines on example of correct value Θ_4 definition.

2 Theory of the absorption process

Fig.2a presents the basic scheme of simple absorber of water-ammonia refrigeration machine. The solution flowing down by a thin film is in the overcooled condition and it reaches a condition of saturation on the interface of phases only. So complex process at variable temperature with phase transitions on two zones can be divided: *adiabatic stabilization of absorption* (absorption process without cooling) and *actually absorption* (absorption process with cooling) [6].

One of conditions of mathematical model creation (and thermoeconomic analysis and optimization also) is replacement of one complex process to a set of elementary processes with condition that set of elementary processes gives the same effect as complex process. The equivalent of the elementary absorber is present in Fig. 2b. Note, that it is impossible to idealize process of absorption only by heat transfer even at level of simplifications.

Impossibility of full saturation of strong solution ΔX_{liq} (Fig. 2c) usually not take into account for calculation of absorption refrigeration machine cycle. Many authors prefer replaced value ΔX_{liq} by value Θ_4=3 … 7°.

Calculation data in Table 1 shows that the error at various calculations is ~300 %. The first variant is corresponding to limit of workable machine but the second one is corresponds to the machine with impossible real cycle.

Table 1: Influence of value Θ_4 to calculation data.

	T_{env}^{min} n, °C	T_4, °C	X_A, kg/kg	X_R, kg/kg	$f=\frac{X_D-X_A}{X_R-X_A}$, kg/kg	ΔX, %
$\Theta_4=0$ (theory)	25	25	0,142	0,204	13,8	7,2
$\Theta_4=7$	25	32	0,142	0,160	47,7	2,1

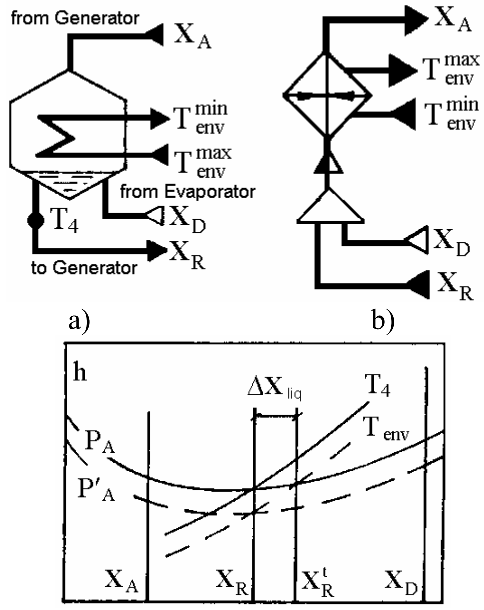

a) b)

c)

Figure 2: Absorber: a) schema; b) schema-equivalent; c) absorption process in the diagram *h-X*.

It is recommended (by results of the experimental data in [8]) impossibility of full saturation of strong solution to take into account as difference of pressure in absorber P_A and partial pressure $P_{A'}$ corresponding to an equilibrium condition of a strong solution at T_4. This difference is determining as *moving force of absorption* and recommend to equal 40kN/m^2 for traditional design of heat-mass surfaces of absorber and 20kN/m^2 for new ones. Calculation data show that this case is equivalent to a choice of value Θ_4 within in diapason of 10 … 15°.

If value Θ_4 or value (P_A- $P_{A'}$) is preliminary knows then the mass-transfer process is included to the heat transfer process.

3 Experimental data

Experimental research of absorber as element of water-ammonia absorption refrigeration machines was made in Refrigeration Machines Department at Odessa State Academy of Refrigeration [9].

Experimental data was accepted at the following variation by initial characteristics:

- Temperature of strong solution $T_4 = 25\ldots37^{\circ}$C;
- Heat of absorption process $Q_A = 8\ldots30$ kW;
- Rate of strong solution circulation $f = 5 \ldots 20$.

Let us analyze experimental data (Fig. 3). It is visible that in large diapason of absorption pressure change (P_A = 140…550 kN/м^2) value of *moving force of absorption* tends growth with delay. This corresponds to value T_4 also. Thus, experimental data deny preliminary author's opinion about obligatory increase of value Θ_4 at growth of value P_A.

For examine of features of absorption process by experimental data let us comparison experimental data and calculation data with using widely calculation methodic [8].

Calculation data of moving force of absorption of vapor into liquid phases exceed the experimental one. Significant difference is take place for high concentration of ammonia in water-ammonia mixture. It testifies that well-known calculation methodic does not take into account a high degree of saturation of strong solution that is very important for modern water-ammonia absorption refrigeration machines [9].

For the analysis experimental regimes 146 and 153 was accepted because there are the most removed from middle one (regime 125).

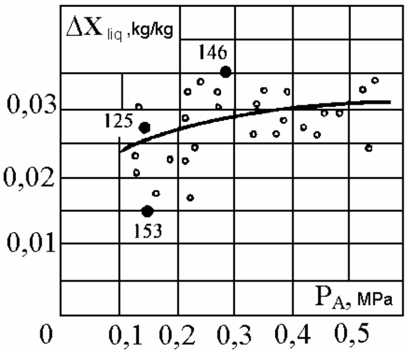

Figure 3: Experimental data of moving force of absorption process $\Delta X_{liq}=f(P_A)$.

The difference between values of moving force of absorption in a liquid phase is 15-20 % that it is possible to recognize as good. Thus, calculation of mass-transfer process is expedient for carrying out only for a liquid phase.

4 Definition of moving force of absorption

Let us influence of external operation factors on value of moving force of absorption based on calculation methodic (Table 2).

Moving force of absorption by mass concentration is

$$\Delta X_{liq} = \frac{\Delta C_{liq}}{\rho_{liq}} = \frac{G_A}{\rho_{liq}\beta_{liq}F_A} \quad , \tag{4}$$

where

$$\beta_{liq} = \frac{D_{liq}}{\nu} Nu_{liq} , \tag{5}$$

$$Nu_{liq} = 0.888\, Re_{liq}^{0.24} \left(Pr_{liq}\right)^{0.5} \left[\frac{\nu}{h}\right]^{0.5} , \tag{6}$$

finally,

$$\Delta X_{liq} = \frac{0.414}{D_{liq}} \cdot \frac{G_a}{F_A} \cdot \frac{h^{0.5}}{\Gamma^{0.45}} \cdot \frac{\eta_{liq}^{0.28}}{\rho_{liq}^{0.83}} . \tag{7}$$

Value D_{liq} can be determined from the equation

$$D_{liq} = D_{293}\left[1 + \frac{0.2\eta_{239}^{0.5}}{\rho_{293}^{0.33}}\left(T_{liq} - 293\right)\right], \tag{8}$$

and for absorption of ammonia by water-ammonia mixture at following regime T_{liq} = 20°C (293K), D_{293} = 0,176·10^{-8}m^2/s; ρ_{293} = 850 kg/m^3; η_{293} = 1 N·s/m^2

$$\Delta X_{liq} = M \frac{\eta_{liq}^{0.28}}{\rho_{liq}^{0.83}} , \tag{9}$$

where

$$M = \frac{10^4}{\left[1 + 0.022\left(T_{liq} - 239\right)\right]^{0.5}} \cdot \frac{G_a}{F_A} \cdot \frac{h^{0.5}}{\Gamma^{0,45}} . \tag{10}$$

The value M depends from operation temperature regime and an absorber design; the complex $\eta_{liq}^{0,28} / \rho_{liq}^{0,83}$ is depend on parameters of a mixture (Fig. 4).

The values which are included in value M are not independent variables; therefore, it is possible to find other equations using connections between them.

Let us use eqs. (11)-(13)

$$F_A = \pi d l i n_{h_l} \tag{11}$$

$$\Gamma = G_a f \left(2li\right)^{-1} \tag{12}$$

$$h = d n_h \tag{13}$$

where d, l, i, n_h are value of absorber design geometry for eq.(10), thus

$$M = \frac{4340}{\left[1 + 0.022\left(T_{liq} - 293\right)\right]^{0.5}} \times \frac{G_a}{l^{0.55} d^{0.5} f^{0.45} i^{0.55} n_h^{0.5}} \tag{14}$$

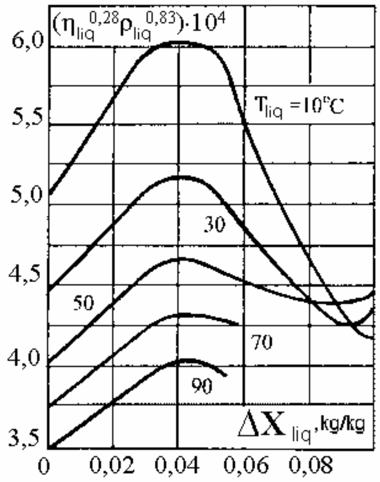

Figure 4: Complex $\eta_{liq}^{0,28} / \rho_{liq}^{0,83} = f(\xi_{liq}, T_{liq})$.

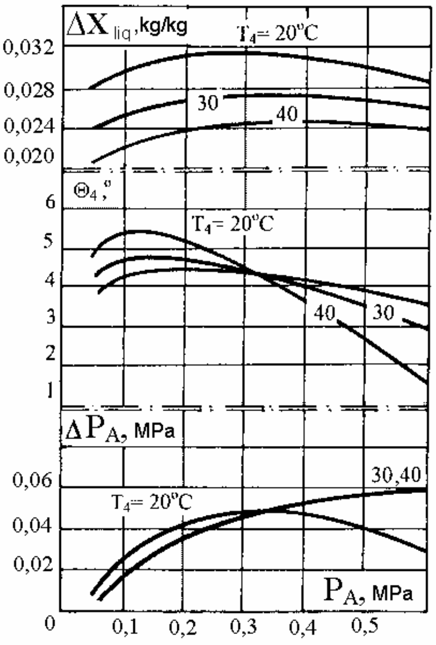

Figure 5: Experimental data at f =14.

Table 4: Mathematical model and experimental data of absorption process for thermoeconomic analysis.

Values		Regime 125	Regime 153	Regime 146
Experimental data				
Mass flow of vapor from evaporator	G_A, kg/s	0,00866	0,00750	0,0108
Heat of absorption process	Q_A, kW	13,6	16,6	21,2
Absorption pressure	P_A, kN/m^2	179	160	268
Concentration of week solution	ξ_A, kg/kg	0,242	0,246	0,295
Temperature of start of absorption process	T'_3,°C	52	46	51
Concentration of strong solution	ξ_R, kg/kg	0,348	0,360	0,424
Temperature of strong solution	T_4,°C	32	20	25
Concentration of vapor from evaporator	ξ_D, kg/kg	0,999	0,999	0,999
Temperature of vapor	T_9,°C	20	20	20
Circulation ration of strong solution	f, kg/kg	7,15	7,65	5,45
Consumption of environment cooling (water)	G_{env}, kg/s	0,93	1,2	0,873
Temperature of environment cooling (water) in inlet of absorber	T_{env}^{min}, °C	27,4	22,3	20,8
Temperature of environment cooling (water) in outlet of absorber	T_{env}^{max}, °C	30,9	25,6	26,6
Characteristics of heat-mass transfer surface of absorber (by experiment)				
Linear solid irrigate density	Γ, kg/m s	0,00298	0,00186	0,00164
Heat transfer coefficient from film of water-ammonia mixture to cooling environment with take into account of fouling in heat-mass transfer surface	k_A, kW/m^{2}K	0,234	0,206	0,204
Middle temperature difference	Θ_A, grad	10,8	9,8	11,2
Surface of absorber	F_A, m^2	5,6	8,2	9,3
Moving force of absorption				
Mass transfer coefficient in vapor phase	β_{vap}, kg/m^{2}s	0,0171	0,0161	0,0132
Moving force of absorption in vapor phase	ΔX_{vap}, kg/kg	0,086	0,051	0,047
Nusselt number for liquid phase	Nu_{liq}	0,90	0,76	0,86
Mass transfer coefficient in liquid phase	β_{liq}, kg/m^{2}s	$0{,}5\cdot10^{-4}$	$0{,}406\cdot10^{-4}$	$0{,}455\cdot10^{-4}$
Moving force of absorption in liquid phase	ΔX_{liq}, kg/kg			
• calculation data		0,035	0,020	0,030
• experimental data		0,028	0,015	0,035

The analysis of the eq. (14) shows, that redistribution of number of pipes in vertical or horizontal lines (heat-mass transfer surface design of absorber) gives small influence to the value ΔX_{liq}. Increasing of number of pipes in horizontal lines nevertheless allows reducing a small value ΔX_{liq}.

If height of an irrigated surface to present as

$$h = \frac{F_A}{\pi \cdot l \cdot i} \qquad (15)$$

then

$$M = \frac{8000}{\left[1+0.022\left(T_{liq}-293\right)\right]^{0.5}}\left(\frac{G_a}{F_A f}\right)^{0.5}\cdot \Gamma^{0.05} \qquad (16)$$

The value Γ changes in diapason from 0,03 up to 0,01, hence, $\Gamma^{0,05}$ changes from 0,89 up to 0,80. Let us use this value for eq. (13)

$$M = \frac{6500}{\left[1+0.022\left(T_{liq}-293\right)\right]^{0.5}}\cdot\left(\frac{G_a}{F_A f}\right)^{0.5} \qquad (17)$$

Each of eqs. (14), (16), (17) for value M definitions can be useful depending of giving data for the analysis.

Fig. 5 presents values of moving force of absorption ΔX_{liq}, super-cooling of strong solution at outlet from absorber ΔT_4 and difference of pressure ΔP_A at various T_4. It is visible that there is small change value ΔX_{liq} at change in wide interval of pressure P_A and temperature T_4. Middle value of ΔX_{liq} is ΔX_{liq} =0,028 kg/kg. The value $\Delta T_4 < 5^{\circ}$ at low values ΔP_A.

The temperature difference in absorber can be determined as function of moving force of absorption

$$\Theta_A = \Theta_{A_0} - \mu \Delta X_{liq} \qquad (18)$$

where Θ_{Ao} is temperature difference at ΔX_{liq}=0;
μ is coefficient, $\mu = \Delta T_4 / \Delta X_{liq}$ = 120…180°.

The value Θ_A by eq. (18) gives the possibility to determine mass of heat-mass surface of absorber that is very important characteristic for future thermoeconomic analysis

$$G = \frac{Q_A}{k_A \Theta_A} g_A \qquad (19)$$

The mass of heat-mass surface of each element of any machine is determined investment cost. Thus occurrence of new designs of heat-mass surface (for absorber, for example) will give influence only for value g_A but all analysis is actual.

5 Conclusion

There is more than 100 years of history of research, design and operation of absorption refrigeration machines. However, till now these machines are calculating approximately, independent of the calculation forms (by software or by "hand" with diagrams using). Traditionally first stage of design is calculation of idealized process. Author proposed even in level of idealized process calculation (i.e. pre-design analysis) to include mass transfer influence to the heat transfer process in generator and absorber. Correct describing heat- and mass transfer process in the absorber is manly that in the generator from point of view of cycle creation of absorption refrigeration machine.

In the present work is basic for design of absorption refrigeration machines by thermoecinomic method with use of minimally sufficient experimental data.

Acknowledgments

The author grateful acknowledges the financial support by Alexander von Humboldt Stiftung (IV-UKR/1117838 STR).

References

[1] Bejan, A., Tsatsaronis, G., Moran, M.: *Thermal Design and Optimization*, J.Wiley, New York, 1996.

[2] Le Goff, P., Ramadane, A., Jeday, M., Ranger, P.: Procee pour la revalorisation d'une energie thermique, son application a des pompes a chaleur et appareillage pour la mise en œuvre, *Brevet CNRS* 870211, 1987.

[3] Morosuk, T.V.: Choice of the optimal temperature drop in apparatus of the absorption water-ammonia thermotransformers, *Proceedings of the 13-th International Congress of Chemical and Process Engineering*, Praha, CD-ROM, P-1.138, 1998.

[4] Feidt, M.: Thermodynamic and optimization of reverse cycle machines, refrigeration, heat pumps, air conditioning, cryogenics, *Proceedings of NATO ASI "Thermodynamics and the optimization of complex energy systems"*, Neptun, pp. 205-230, 1998.

[5] Mihaila, C.C., Chiriac, F.N., Sota, I.D., Baltaretu, F.I.: The modeling of a film absorber with ammonia-water solution, *Proceedings of 19-th International Congress IIR/IIF*, The Haag, vol.III, pp. 154-160, 1995.

[6] Morosuk, T.V., Minkus, B.A., Morosuk, L.I.: L'intensification des processus dans les thermotransformers d'absorption par la saturation du melange riche, *Proceedings of 19-th International Congress IIR/IIF*, The Haag, vol.III a, p. 161-168, 1995.

[7] Schulz, S.: Die Berechnung und Optimizirung von Absorptionskaltemachinen-prozessen mit Hilfe von Edv-Anlagen, *Kaltetechnik-Klimatisierung*, no.24, pp.181-188, 1972.

[8] Niebergall, W.: *Sorption-Kaeltemaschinen*, Berlin, Springer, 1959.

[9] Morosuk, T.: *Water-ammonia thermotransformers (theory, analysis, synthesis, optimization).* Thesis of professor dissertation, Odessa State Polytechnic University, Ukraine, 2001.

ADHESION AND INTERFACIAL REACTIONS ON METAL/OXIDE INTERFACE DURING PLASTIC DEFORMATION AT ROOM TEMPERATURE

Faina MUKTEPAVELA[1,*], Georgy BAKRADZE[1], Vera SKVORTSOVA[1], Edmunds TAMANIS[2], Sara STOLYAROVA[3]

[1]Institute of Solid State Physics, University of Latvia,
Kengaraga 8, LV1063, Riga, Latvia
[2]Daugavpils University,
Parades 1, LV5400, Daugavpils, Latvia
[3]Technion, Solid State Institute,
Technion-City, 32000, Haifa, Israel

[*]Corresponding author. Fax: +371 7132778; Email: famuk@latnet.lv

Abstract

Properties of interfaces in solid state metal/oxide joints (Al/SiO$_2$, Al/MgO, Al/glass, Mg/MgO, Mg/SiO$_2$, In/glass etc.) are reported. The interfaces were formed at plastic deformation of metal on the oxide surface at room temperature. Their structure, chemical composition, and micromechanical properties were studied by the AFM, X-ray diffraction, SIMS, optical microscopy, and precision microindentation techniques. A noticeable adhesion was observed for metals with high affinity for oxygen and only in the regions of the maximum shear stress. Formation of a interfacial reaction zone with an oxygen concentration gradient is detected. In this zone metals are nanostructured and noticeably hardened. The effect of mechanoactivation is considered as a result of physical and chemical interaction and formation of nanostructures in deformed metal/oxide systems.

Keywords: Metal/oxide interfaces; Adhesion; Interfacial reaction; Mechanoactivation; Nanostructure

1 Introduction

Metal/oxide interfaces play a crucial role in many important present-day technological applications such as optoelectronic and microelectronic systems, heterogeneous catalysis, oxide dispersion-strengthened alloys, powder materials, solid state joint devices, anticorrosion and thermal insulation coating industry, etc.; moreover, they have found important applications in medicine Ref. [1-3]. Strong interfaces between dissimilar materials, such as metal and metal oxide, are also critical for future nanotechnology development. In such applications, frequently the properties of the heterophase interface, but not of the bulk materials, determine behaviour of the system. Mechanical properties, structure, and adhesion strength on metal/oxide interfaces are of the greatest concern. Most of studies in this area have been performed at high temperatures and are devoted to the role of diffusion processes in the formation of the structure and adhesion bonds Ref. [2-5]. At the same time, comparatively little attention has been paid to the obtaining of metal-oxide composites at room temperature, when thermoactivation of adhesion is negligible. Only few sources of detailed information in literature on this problem provide evidence of such possibility Ref. [6-8]. According to some theoretical works Ref. [9,10], it is possible to enhance adhesion at metal/oxide interfaces at room temperature by introducing the structural defects into oxide surface layers.

The question about the role played by structural defects in the formation of a chemical bond at the solid-state interfaces is still controversial. On the one hand, there are considerations about active centres of adhesion such as dislocations and vacancy groups Ref. [11]. On the other, experimental data on atomically-clean metal/metal, metal/Si and metal/Ge interfaces have shown that under the conditions of full contact atomic interaction occurs with formation of chemical bonds and no further activation of the surfaces is needed Ref.

[12-14]. In this case, the thermodynamically gain in surface energy (ΔF) of two fully contacting materials could be expressed as follows:

$$\Delta F = \gamma_o^A + \gamma_o^B - \gamma_{ib}^{AB},$$

where γ_o^A is the surface energy of the contacting metal A; γ_o^B is the surface energy of the contacting metal B (or semi-conductor); and γ_{ib}^{AB} is the interphase boundary energy. Evidently, the ΔF values for such systems as metal/metal, metal/Si and metal/Ge are high enough to form chemical bonding between the contacting surfaces. For the systems metal/oxide the influence of the oxide surface activation on the adhesion strength could be expected. One of the possible activation means is the mechanoactivation of oxide surface layers by plastic flow of metals. However, experimental data on metal/oxide solid state joining at room temperature are seldom met in the literature.

In the present work, the properties of interfaces in solid state joints of metal/oxide (Al/SiO_2, Al/MgO, In/glass, Mg/SiO_2, and others) formed by plastic flow of metals at room temperature are investigated.

2 Experimental procedure

The metal/oxide solid-state joints were obtained by static compression of freshly prepared metal and oxide surfaces at room temperature. The contact experiments with atomically-clean surfaces were performed in high vacuum (10^{-6}Pa) and in air by the controlled rupture/cleaving of the samples. Right after the rupture of samples the surfaces of metal and oxide were brought into contact with each other. The interfaces were formed under the conditions of plastic flow of metal on oxide surface. For our studies, polycrystalline simple metals (Al, Sn, Pb, Mg, Cd, In), boron-silica glass, and single crystal oxides (SiO_2, Al_2O_3, MgO) were chosen. The adhesion strengths of joints were determined in pull-off tests. The fracture mode was examined after the tests.

The structure and composition of fracture surfaces were studied by optical microscopy (NEOPHOT 30), AFM (Nanoscope), X-ray diffraction (DRON-3M), SIMS (Secondary Ion Mass Spectrometry). For the SIMS method, Ar^+ ions with energy of 6keV were used, the ion sputtering rate being 0.01-0.02μm/min. The peak intensity (I^+, arb.units) of the investigated elements served as a working standard.

The microhardness was determined by a tester with original self-adjusting loading device, allowing carrying out the precision microhardness measurements at very small loading (starting from 1.5 mN) Ref. [15]. The indentor was a Vicker's diamond pyramid. To reveal the presence of dislocations in MgO single crystals the chemical etchant: 5 parts of saturated NH_4Cl solution, one part of H_2SO_4 and one part of distilled water - was used.

3 Results and discussion

The results of mechanical tests and data on fracture mode are presented in Table 1. As can be seen the metals Al, In and Mg have the good adhesion to the oxides. Fractures of these joints occurred with the transfer of metal to the surface of oxide, being the evidence of a strong chemical bonding at the metal/oxide interfaces. The adhesion strength of Sn, Cd, Pb was much smaller than in the case of aluminium, indium or magnesium, and in many cases fractures occurred along the metal/oxide interfaces without transfer of metal to the oxide.

Table 1: Adhesion strength (σ, MPa), and transfer of metal (+ or –) to oxide surfaces in pull-off tests of metal/oxide joint.

Oxide / Metal	σ, MPa			
	Glass	SiO_2	Al_2O_3	MgO
Al	60 +	62 +	65 +	60 +
In	25 +	20 +	18 +	18 +
Mg	22 +	15 +	20 +	25 +
Sn	2 +	10 +	0 –	10 +
Cd	2 –	0 –	5 +	5 +
Pb	2 –	2 +	0 –	5 –

Apparently metals with high affinity for oxygen (Al, In, Mg) form stronger bonds with oxides. The observed distinction in adhesion strength between the investigated metals may be explained in terms of the thermodynamics of chemical interaction between metals and oxygen of the oxide.

As a parameter for our estimate of chemical interaction between metal and oxide we have chosen metal oxide formation energies (Gibbs' free energy ΔZ). Table 2 shows that the oxide formation energy increases from aluminium to lead. Evidently, that metals with high affinity for oxygen form stronger adhesive bonds with the surface of oxides.

Table 2: Metal oxide formation energies Ref. [11].

Metal oxide	$-\Delta Z_{293}\cdot 10^{-6}$, J/kmol
Al_2O_3	1675
In_2O_3	926
MgO	602
SnO_2	581
CdO	260
PbO	219

This result is in agreement with the experimental data obtained by other authors who studied the adhesion on thin-film metals/oxide systems after the activation by electron or ion beam and in wetting experiments Ref. [16].

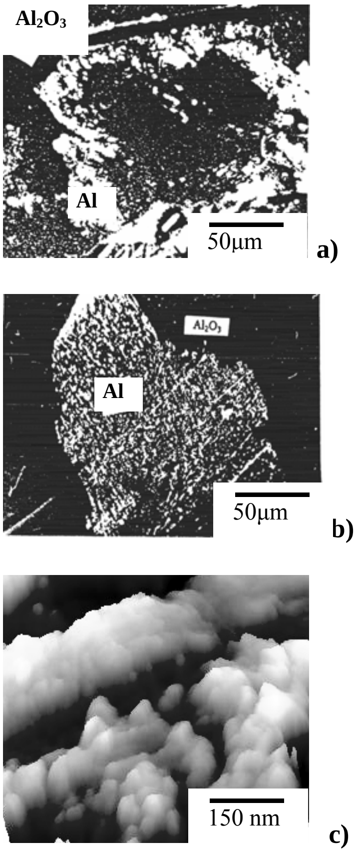

Figure 1: Micrographs of the fracture of metal/oxide joints: transferred Al to Al_2O_3 at normal contact (a) and at friction scheme (b), dark field; AFM image of transferred Al to glass (c).

However, in our case the formation of strong adhesion in these systems occurs not over the whole contact area, but only in the regions of the maximum shear stress (Fig. 1, a), where fracture occurs along bulk metal. At the centre, where the metal first makes contact with the surface of oxide, there is no detectable transfer.

Special experiments with the Al/glass system were performed so that plastic flow of Al on the surface of glass could be obtained under friction. In this case strong adhesion is observed over the whole surface of oxide (Fig. 1, b). The AFM studies of surfaces show that the transferred metals (Al in this case) have a nanostructure with a grain size from 30 to 100 nm (Fig. 1, c), though the nanostructure is not homogeneous. This result was confirmed by X-ray diffraction patterns and, in addition, it shows that the nanostructure of the transferred Al is stable after annealing in vacuum. Thus, the action of the maximum shear stress leads to the formation of nanostructure in metal near the interface. The raised density of defects on the grain boundaries characterizes this strongly deformed state of metal. It could be assumed that the metals with high affinity for oxygen and having nanostructured state form chemical bonds with the oxides more easily.

If we consider the obtained result for some processes on the oxide surface, we can explain the metal/oxide chemical bonding at room temperature by mechanoactivation of the oxide surface. Also, the possibility exists of such mechanoactivation by plastic flow of metal. Point defects and dislocations may be treated as the main influencing structural factors. The energy of point defect formation in oxide is insignificant (≈ 2 eV). Therefore, it is possible to assume with confidence that point defects form in near-surface layers of oxide even at room temperature under the active plastic flow of all investigated metals. On the other hand, it was interesting to find out the role of dislocations of oxide in the formation of adhesive bonds. If dislocations cause the occurrence of adhesive bonds between metal and oxide, then by chemical etching it would be possible to reveal this defects in the contact zone. We have studied the role of dislocations in In/MgO and Pb/MgO systems with different adhesion strengths and thermodynamically parameters of metal/oxygen interaction. As it was shown above in Table 1 and Table 2 indium has strong adhesion to a crystal with transfer of metal to the MgO surface at the testing of joints. At the same time, adhesion of lead did not exceed the level of physical adsorption, and no transfer of metal was observed. Furthermore, the hardness of soft In (about 16 MPa) was smaller than the value of starting stress for dislocations in MgO ($\tau_0 \approx 28$-30 MPa, Ref. [17]), whereas the hardness of Pb (30 MPa) should be sufficient to create fresh dislocations in MgO. In Fig. 2 are shown micrographs of etched MgO surface, after contact with In (Fig. 2, a) and Pb (Fig. 2, b). Etching experiments on the MgO crystal did not reveal the presence of new dislocations around and inside the area of the transferred In (Fig. 2, a).

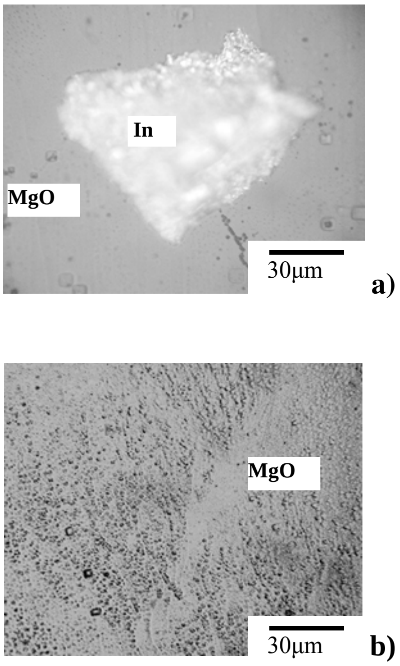

Figure 2: Micrographs of the etched MgO surface after contact with In (a), Pb (b).

As concerns lead, groups of fresh dislocations are clearly visible in the field of its contact with the crystal in the area of the maximum shear stress in MgO, but without any trace of adhesion of Pb to MgO (Fig. 2, b). So, at present there is sufficient evidence that dislocations do not play any significant role in the formation of chemical bonding between metal/oxide interfaces.

Apparently, the high concentration of point defects on oxide surface can be the primary mechanoactivation factor of adhesion with metals. We can assume that the presence of point defects facilitates the formation of metal-oxygen complexes on the interfaces. The leading role of oxygen and point defects in the formation of metal/oxide adhesion is confirmed by theoretical data on adsorption and by the experimental data on thin film adhesion in metal/oxide systems Ref. [9,10,18]. To verify this hypothesis in our case the chemical compound of the metal transferred to oxide was experimentally traced level-by-level by the SIMS method.

Here, as an example, the result obtained for aluminium transferred to glass is given in Fig.3, which shows the presence of oxidized aluminium near the metal/oxide interface. This result testifies about the formation of a reaction zone Me-MeO (with a size of 0.5-1.0 µm) spreading in the metal, with a gradient of oxygen concentration. The formation of such interfacial reaction zone is possible only for metals with a high activity to oxygen and also because of many deformation defects and the nanostructure of metals.

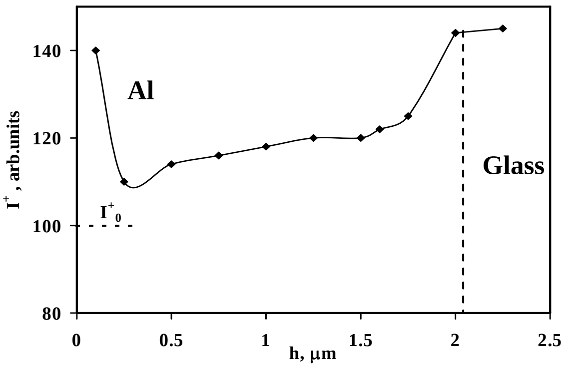

Figure 3: Depth profile of the intensity of SIMS-signal of Al^+ in the Al transferred to glass. Intensity of non-oxidized Al pointed as I^+_0.

The grain boundary diffusion coefficients in nanomaterials synthesized by means of severe plastic deformation are known to be by an order of magnitude higher than in classical polycrystals Ref. [19,20]. Thus, in the regions of maximum shear stress the processes of atomic diffusion of oxygen and formation of metal-oxygen complexes can take place. In turn, a change in the mechanical properties of metals near the interface can also be expected. The presence of metal oxide – even nonstoichiometric one – should increase the hardness of metals. We can compare the mechanical properties of metals on the fracture surfaces at metal/oxide joints with those of deformed bulk metals. The data on Al and In are presented in Table 3.

Table 3: Microhardness (H, MPa, load P = 50 mN) and strength (σ, MPa) of deformed bulk metals and metals transferred to SiO_2 .

	H, MPa		σ, MPa	
	bulk metal	transferred metal	bulk metal	transferred metal
Al	400	700	200	62
In	16	150	9	20

As it is seen, the microhardness of the two metals is noticeably increased in the fracture zone. At the same time, the strength value for aluminium decreases, while in the case of indium it remains high. It can be assumed, that a brittle Al–Al_xO_y composite is formed at Al/oxide interface. Al_2O_3 is known to be a very hard and brittle material. For In_2O_3 these properties are expressed weaker, and formation of this oxide causes increase both in hardness and in strength.

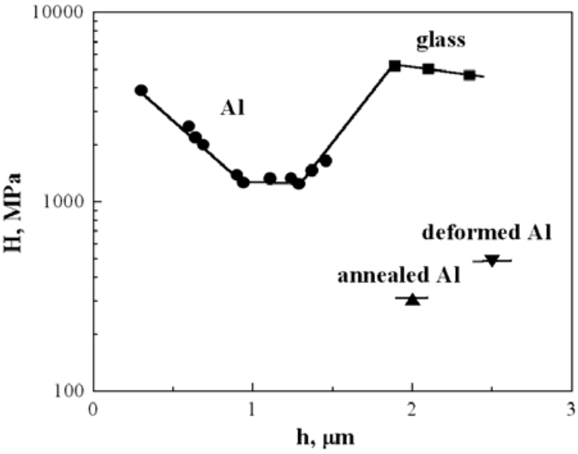

Figure 4: Dependence of transferred Al microhardness on indentation depth. Load range P = 1.5 mN – 2 N.

Let as consider the change of microhardness values in depth of Al left adhering to glass at friction scheme in air. The dependence of microhardness on indentation depth is given in Fig.4.

Microhardness of transferred Al has different values in depth (1.5-4 GPa). There is significant hardening up to 4.5 GPa in the surface layer (0.1-0.5 μm), which is caused by the presence of strongly oxidized surface layers. The increase in hardness values at deeper indentation depth values is caused by the influence of hard substrate. This result shows, that the transferred metal is a new material with the mechanical properties different from properties of pure aluminium in both annealed and deformed state.

The change of mechanical properties of metal near the metal/oxide interface corresponds to the SIMS data and testifies to the formation of a reaction zone under plastic deformation of metal on the oxide surface.

From SIMS and microhardness data we can estimate the mutual diffusion coefficient (D) of oxygen in nanostructured Al or Al in glass in the interfacial reaction zone. Assuming, that reaction zone ($x \approx 2$ μm) is equal to the diffusion length, then according to the equation

$$x = \sqrt{D \cdot t} ,$$

where t is contact time in solid state joint ($t \approx 60$ s), D is equal to about $7 \cdot 10^{-10}$ cm^2/s. This result is seems to be reasonable and is in good agreement with the known diffusion coefficients for Al/quartz systems in wetting experiments at high temperatures (700-800 °C) Ref. [21]. Such correspondence can be explained with the high density of point defects in the surface layers of oxide and formation of nanostructure in metal during plastic flow.

4 Conclusion

The investigation carried out by us allows the conclusion to be drawn that a strong chemical adhesion arises on the metal/oxide interface under plastic deformation of metal at room temperature. Mechanoactivation of the adhesion occurs in the metals with low oxide formation energies only in the regions of the maximum shear stress. Formation of a interfacial reaction zone with an oxygen concentration gradient is detected. In this zone metals are nanostructured and noticeably hardened. Influence of dislocations on oxide surface was found to be insignificant; at the same time the nanostructured state of metal together with the high concentration of point defects in surface layer of oxide can be the primary factors of interfacial chemical interaction in metal/oxide systems.

References

[1] Ernst, F.: Metal-oxide interfaces. *J. Mat. Sci. Eng.,* R14, pp. 97-156, 1995.

[2] Lojkowski, W., Fecht, H.-J.: The structure of intercrystalline interfaces. *Prog. Mater. Sci.*, 45, pp. 339-568, 2000.

[3] Sinnott, S.B., Dickey, E.C.: Ceramic/metal interface structures and their relationship to atomic- and mesoscale properties. *Mater. Sci. Eng. R-Reports,* R43, pp. 1-59, 2003.

[4] Wagner, M., Wagner, T., Caroll, D.L., Marien, J., Bonnell, D.A., Rühle, M.: Model systems for metal-ceramic interface studies, *MRS Bulletin*, 22, pp. 8-15, 1997.

[5] Akatsu, T., Hosoda, N., Suga, T., Rühle, M.: Microstructure of Al/□-Al$_2$O$_3$ interface fabricated by surface activated bonding at room temperature. *Mat. Sci. Forum,* 329, pp. 294-297, 1999.

[6] Keino, M., Shinichiro, F.: Microstructure and adhesion mechanism of mechanically prepared composite particles. *J. Mater. Sci. Eng. B,* 10, pp. 139-147, 1991.

[7] Muktepavela, F., Manika, I., Kalnacs, J.: Investigation of mechanically alloyed metal/oxide coatings by SIMS method. *Latv. J. Phys. Techn. Sci.,* 6, pp. 141-144, 2000.

[8] Bailey, F. P., Black, K.J.T: Au/Al$_2$O$_3$ solid state reaction. *J. Mat. Sci.*, 13, pp. 1045-1050, 1978.

[9] Zhukovskii, Yu.F., Kotomin, E.A., Jacobs, P.W.M., Stoneham, A.M., Harding, J.H.: Modelling of silver adhesion on MgO(100) surface with defects. *J. Phys.: Condens. Matter.,* 12, pp. 55-66, 2000.

[10] Duffy, D., Harding, J., Stoneham, A.M.: The energies of point defects near metal/oxide interfaces. *J. Appl. Phys*., 76, pp. 2791-2798, 1994.

[11] Krasulin, Ju. L.: *Interaction of Metal with Semiconductor in Solid State.* Nauka, Moscow, 1971. (in Russian).

[12] Upit, G.P.: Bonding of juvenile surfaces of Al with Si. *Izvestija AN Latv.SSR, ser. fiz-teh. Nauk,* 1, pp. 22-25, 1971. (in Russian).

[13] Muktepavela, F., Maniks, J.: Mechanical properties and accommodation processes on metallic interfaces. *Nanostruc. Mater.,* 10(3), pp. 479-484, 1998.

[14] Buckley, D.H.: *Surface Effects in Adhesion Friction, Wear and Lubrication.* Elsevier, Amsterdam, 1981.

[15] Muktepavela, F., Manika, I., Mironovs, V.: Structure and mechanical properties of Al-B composite powder. *Mat. Design,* 18, pp. 257-259, 1997.

[16] Woirgard, J., Cabioc, T., Riviere, J.P., Dargenton, J.C.: Nanoindentation characterization of SiC coatings prepared by dynamic ion mixing. *Surf. Coat. Tech*., 100-101, pp. 128-131, 1998.

[17] Sangwal, K., Sanz, F., Gorostiza, P.: Study of the surface morphology of the (100) cleavage planes of MgO single crystals by atomic force microscopy. *Surf. Sci.,* 424, pp. 139-144, 1999.

[18] Netzer, F.P.: Interfacial oxide layers at the metal-oxide phase boundary. *Surf. Rev. & Let.,* 9, pp. 1553-1563, 2002.

[19] Paritskaya, L.N., Kaganovskii, Yu., Bogdanov, V.V.: Size-dependent interdiffusion in nanomaterials. *Sol. St. Phen.,* 101-102, pp. 123-130, 2005.

[20] Valiev, R.Z., Alexandrov, I.V., Islamgaliev, R.K.: Processing and properties of nanostructured materials prepared by severe plastic deformation. *Nanostructured materials*, Chow, G.M., Noskova, N.I. (Eds), NATO ASI series 50, pp. 121-142, 1998.

[21] Trifonova, E.P, Lasarova, V., Spassov, L., Efremova, N.: Composite microhardness of quartz-Al structures. *Cryst. Res. Technol.*, 34(3), pp. 391-395, 1999.

Proceedings of The 1st International Conference on **D**iffusion in **S**olids and **L**iquids
DSL-2005, July 6-8, 2005, University of Aveiro, Aveiro, Portugal

SUM-RULE RELATIONSHIPS AMONG PHENOMENOLOGICAL COEFFICIENTS: SIMPLIFICATIONS FOR THE ANALYSIS OF SEGREGATION AND CHEMICAL DIFFUSION

Irina V. BELOVA[1,*], Graeme E. MURCH[1]

[1]Diffusion in Solids Group, School of Engineering,
The University of Newcastle, Callaghan, New South Wales 2308, Australia

[*]Corresponding author. Fax: +61 2 49216946; Email: Irina.Belova@newcastle.edu.au

---

Abstract

In this review paper, we first introduce the phenomenological transport coefficients and relationships between them and the tracer diffusion coefficients. Next, we discuss a sum-rule relating phenomenological coefficients themselves in the random alloy model. We then consider several applications of the sum-rule to diffusion problems. These applications include intrinsic diffusion in multicomponent alloys, chemical diffusion in strongly ionic mixed cation crystals and the segregation (demixing) of cations in mixed oxides in an oxygen potential gradient and/or an electric field. In each case a substantial simplification is possible as a result of the sum-rule.

Keywords: Phenomenological transport coefficients; Multicomponent alloys; Mixed oxides; Intrinsic diffusion coefficients; Demixing; Segregation;Ttracer diffusion coefficients; Darken Relations; Manning Relations

---

1 Introduction

It is well known that an implication of Fick's First Law is that once the concentration gradient for the diffusing species *i* reaches zero, the flux of species *i* must also cease. Whilst frequently true, it is in fact a too restrictive condition for equilibrium. In general, the net flux of a diffusing species ceases only when all direct and indirect forces on that species are zero. The Onsager flux equations of irreversible processes achieve this through the postulate of linear relations between the fluxes and the driving forces, see for example [1,2]:

$$J_i = \sum_j L_{ij} X_j \qquad (1)$$

where the L_{ij} are the phenomenological transport coefficients and the X_j are the driving forces. The matrix of phenomenological transport coefficients is frequently simply called the ***L*** matrix. The Onsager flux equations have been used very extensively in theoretical treatments of collective diffusion problems such as chemical diffusion and ionic conductivity especially in multicomponent systems. The great importance of the phenomenological transport coefficients stems from their independence of driving force. Although highly desirable on this account, unfortunately, the experimental determination of the *L* matrix is most difficult for the solid state because of the difficulty in measuring chemical potential gradients, the usual solid state driving forces. Gaining access to diffusion coefficients is much more straightforward because concentrations (and their gradients) are of course readily measurable. Accordingly, this has first of all prompted interest in finding relations between the phenomenological coefficients and the (measurable) diffusion coefficients.

2 Relations between phenomenological coefficients and tracer diffusion coefficients

The first relations between the phenomenological transport coefficient and tracer diffusion coefficients were the Darken Relations [3]. In essence, the Darken assumption is the neglect of any off-diagonal phenomenological transport coefficients. The remaining diagonal phenomenological transport coefficients are then related to the corresponding tracer diffusion coefficients; for example, in a binary *AB* alloy, L_{AA}

is then simply related to the tracer diffusion coefficient of A, D_A^*:

$$L_{AA} = C_A D_A^* / kT\,, \tag{2a}$$

$$L_{AB} = 0 \tag{2b}$$

In principle, the off-diagonal phenomenological transport coefficients can make a large difference to the value of a given flux, and can even change the sign. Accordingly, whether the neglect of the off-diagonal phenomenological transport coefficient is a reasonable thing to do or not depends very much on the context. In highly ordered stoichiometric AB intermetallic compounds, where it is believed there are concatenated sequences of jumps (an example is the six-jump cycle [4]), it is known that the off-diagonal phenomenological transport coefficients take values that are very close to zero anyway [5], and so ignoring them is not likely to make much difference. In other situations such as the 'five-frequency' model for a solute in an electric field, ignoring the off-diagonal phenomenological transport coefficient can in principle give the wrong direction for the solute flux. It is generally accepted however that as a first rough approximation it is not unreasonable to ignore the off-diagonal phenomenological transport coefficients.

The second set of relations between the phenomenological transport coefficients and tracer diffusion coefficient are the Manning Relations [6] that were developed originally for the random alloy in which the various atomic species and the isolated vacancy are randomly mixed and where the atom-vacancy frequencies depend only on the identity of the atom jumping. In the Manning Relations, the phenomenological transport coefficients are directly related to the tracer diffusion coefficients by the expressions:

$$L_{ii} = \frac{C_i D_i^*}{kT}\left(1 + \frac{2C_i D_i^*}{M_0 \sum_k C_k D_k^*}\right), \tag{3a}$$

$$L_{ij} = \frac{2C_i D_i^* C_j D_j^*}{kT(M_0 \sum_k C_k D_k^*)}, \quad \text{for } i \neq j. \tag{3b}$$

where $M_0 = 2f_0/(1-f_0)$ and f_0 is the geometric tracer correlation factor for the lattice, e.g. f_0=0.78146… for the f.c.c. lattice [7]. The extra factor in Eq. 3a compared with Eq. 2a should be noted. It is worth noting too that the Manning Relations can also be obtained on the basis of two somewhat intuitive assumptions without recourse to the random alloy model [8], thereby suggesting that they have rather more general validity than the random alloy model might suppose. That this is indeed the case has been shown in various computer simulations even for ordered alloys, at least at low levels of order before concatenated mechanisms such as the six-jump cycle [4] start to become important [9-11]. The Manning Relations have also been re-derived specifically for the ordered alloy [12].

The self-consistent theory of Moleko, Allnatt and Allnatt [13] also provides relations between the phenomenological coefficients and the tracer diffusion coefficients for the random alloy model, but these relations are not expressible in a convenient closed form. Nonetheless, it is still possible to use straightforward numerical methods to find all of the L_{ij} from a given set of tracer diffusion coefficients for all of the atomic species [14]. Computer simulations [15] have shown these relations to be considerably more accurate than those provided by Manning described above. The differences between the results of the self-consistent theory and the Manning theory are mainly apparent at more extreme ratios of the atom-vacancy exchange frequencies.

The third relation between the phenomenological transport coefficients and the tracer diffusion coefficients is the Heumann relation [16] that was determined after consideration of the five-frequency model, see also [1]. This model, which was first proposed by Lidiard [17], is very useful for describing solute and host diffusion kinetics in f.c.c. metals and f.c.c. sublattices in ionic crystals when the vacancy-solute interaction is localized. The five frequencies in the model refer to the following: a vacancy-host atom (A) exchange frequency w_0, a vacancy-host (A) exchange frequency w_1 referring to a 'rotational jump' around a solute atom i.e. from one nearest neighbour site to another of the solute, a vacancy-solute (B) exchange frequency w_2, a vacancy-host (A) atom exchange frequency w_3 that brings the vacancy to a site neighbouring to the solute atom (this is usually called the 'associative jump'), and finally a vacancy-host atom (A) exchange frequency w_4 that is the reverse of the w_3 jump (this is usually called the 'dissociative jump'). It can be shown that for a dilute alloy in the limit where the solute concentration $C_B \rightarrow 0$, the ratio of $L_{AB}(0)$ / $L_{BB}(0)$ is given by [16]:

$$\frac{L_{AB}(0)}{L_{BB}(0)} = \frac{D_A^*(0)}{D_B^*(0)} \left(f_0^{-1} - \frac{D_A^I(0)}{D_A^*(0)} \right) \quad (4)$$

where $D_A^*(0)$, $D_B^*(0)$ are the tracer diffusion coefficients of A and B and $D_A^I(0)$ is the intrinsic diffusion coefficient of A in the dilute alloy at the limit $C_B \rightarrow 0$.

3 Relations among Phenomenological coefficients: the sum-rule

Various relations have been identified between the phenomenological coefficients themselves in randomly mixed systems, in effect reducing the number of independent coefficients. These are of great interest, first of all because the assumption of random mixing in diffusion problems is a very common one indeed in solving diffusion problems analytically. Second, experience gained from many Monte Carlo computer simulations indicates that a non-random distribution of components does not actually change the basic diffusion kinetics behaviour very much unless long range order or clustering is present. In other words, the effect on the jump frequency and the correlation factors, tracer or collective, of a non-random distribution itself is relatively small. Indeed, the main effect of a change in the distribution of the components is in fact in the thermodynamic factor that typically appears in expressions for the chemical diffusion coefficient. This factor can in general be factored out and treated quite separately from the jump frequency and correlation parts. It has been found that a considerable simplification is often possible in collective diffusion problems through the use of such relations. The first of these relations was the exact sum-rule identified in 1988 by Moleko and Allnatt [18] for the multicomponent random alloy with the monovacancy mechanism operating at arbitrary vacancy concentration. This sum-rule was implied in earlier diffusion kinetics work on the random alloy model at a very low vacancy concentration; see, for example, the Manning formalism [6] of the early 1970s, but was simply not identified as such at the time.

As an aside we note that the random alloy model is a very important model because it is a convenient vehicle for describing the diffusion kinetics in concentrated multicomponent alloys and also for sublattices in compounds that exhibit random mixing of two or more components. In its original form, the vacancy concentration was infinitely small. In its more general form where the vacancy concentration can be arbitrary (and where it is often called the lattice gas) the model is useful for describing the mobile sublattice of a fast ion conductor or a mixed adsorption system. In the random alloy model, the atom-vacancy exchange frequencies, w_i, can be considered in two rather different ways. In the first way, the frequencies can be classified simply as explicit frequencies that depend only on the species of the atom and not the surroundings. For example, in the binary random alloy, w_A then simply represents the A atom vacancy exchange frequency of a given A atom at all compositions and environments. In the second and more general way, one considers that the w_i represent an *average* frequency of species i at a given composition. For example, in the binary random alloy, w_A would then represent the *average* frequency of a given A atom as it migrates through the lattice sampling the various environments. Since the average environment of an atom will obviously change with composition, then the w_i can also be expected to change with composition, see for example [19].

Moleko and Allnatt identified the following sum-rule for the M-component random alloy with the vacancy mechanism operating and at arbitrary vacancy concentration [18]:

$$\sum_{i=1}^{M} L_{ij} w_j / w_i = A c_V w_j C_j\,, \quad i,j=1,\ldots,M \quad (5)$$

where A is given by $A = z\, a^2/6kT$ (z is the coordination number and a is the jump distance for a vacancy jump and k and T have their usual meanings) and c_V is the vacancy fraction. In effect, the sum-rule relates the phenomenological coefficients to the vacancy-atom exchange frequencies and, in so doing, reduces the number of independent phenomenological coefficients. For example, in the binary random alloy, there is only one independent phenomenological coefficient and not three.

Thus in the binary alloy AB the sum-rule relation is:

$$L_{AA}+\frac{w_A}{w_B}L_{AB}=L_{AA}^{(0)}=c_V C_A w_A A\,, \qquad (6a)$$

$$L_{BB}+\frac{w_B}{w_A}L_{AB}=L_{BB}^{(0)}=c_V C_B w_B A\,, \qquad (6b)$$

For the case of the very frequently used hopping model, where the atoms thermalize with the surroundings between hops or jumps, the phenomenological transport coefficients can be conveniently partitioned into a correlated part (a correlation function, frequently called the collective correlation factor because of its similarity to a tracer correlation factor) and an uncorrelated part (principally containing the jump frequency):

$$L_{ij}=f_{ij}^{(j)}L_{jj}^{(0)} \qquad (7)$$

where $f_{ij}^{(j)}$ is the collective correlation factor and $L_{jj}^{(0)}$ is the uncorrelated phenomenological transport coefficient.

The sum-rule can then also be restated in terms of these collective correlation factors as:

$$\sum_{i=1}^{M} f_{ij}^{(j)} w_j / w_i = 1\,,\ j=1,\ldots,M \qquad (8)$$

The derivation of this sum-rule is beyond the scope of this overview but we can describe it qualitatively. We consider a random alloy with the vacancy mechanism operating. We assume that an atom of species *i* has just made a jump. We accept this jump as the initial point in time and take a 'snapshot' of the system. Then, for each quantity like L_{ij}, we need to consider how the system changes from the initial configuration (after the jump of the *i* atom) during the jumping of the vacancies: i.e. after the first jump, the second jump and so on. At each moment in time we choose a vacancy randomly from the current configuration (there is a specific probability for the system to get to this configuration starting with the initial one), then we choose a *random direction* and find an atom of some type (or another vacancy). Accordingly, for each direction there is a defined probability that the vacancy makes an exchange with the atom there. If this is an atom of species *j* then a contribution to the cosine between the first jump of the *i* atom and the final jump of the *j* atom (the basic quantity in L_{ij} see Equations 14, 15) is equal to the probability for a system to get to the current configuration multiplied by the vacancy concentration and multiplied by the vacancy-atom *j* exchange frequency (and divided by the co-ordination number). Therefore each contribution of this type for a different atomic species *j* differs from one another only by the corresponding exchange frequency. After all the summations are done we end up with the sum-rule relation as shown in Eq. 5.

Since the discovery of the first sum-rule, various other closely related sum-rules have been identified for a number of other mechanisms and situations including the dumb-bell interstitial mechanism in the binary random alloy [20], the divacancy mechanism in the f.c.c. random alloy [21], the vacancy-pair mechanism in strongly ionic materials with randomly mixed cations [22], the vacancy mechanism for a model of an intermetallic compound (with randomly mixed sublattices) and certain parts of a reduced five-frequency model for solute and solvent diffusion in the f.c.c. lattice with the vacancy mechanism operating [23,24]. In the remainder of this review we review some of the applications of the first sum-rule to collective diffusion problems.

4 The Sum-Rule and the Intrinsic Diffusion Coefficients in Multicomponent Alloys.

In this example, we consider intrinsic diffusion in a random N-component alloy with the vacancy mechanism operating. We write the driving forces X_i as $-\nabla\mu_i$ where μ_i is the chemical potential of species i (we assume there are no external driving forces) and we make the usual assumption that sources and sinks of vacancies are sufficiently numerous that the gradient of the chemical potential of the vacancies $\nabla\mu_V \approx 0.0$ and that there are no external forces).

Using the Gibbs-Duhem relation we can then readily transform Eq. 1 into:

$$J_i=-\sum_{j=1}^{N-1} nD_{ij}^{N}\nabla c_j\,, \quad i=1,\ldots,N, \qquad (9)$$

where D_{ij}^{N} are the intrinsic diffusion coefficients.

For binary *AB* alloys, the ratio of the intrinsic diffusivities D_A and D_B can be expressed in terms of the phenomenological coefficients in the usual way; see, for example, [1]:

$$\frac{D_A}{D_B} \equiv \frac{c_B L_{AA} - c_A L_{AB}}{c_A L_{BB} - c_B L_{AB}} \qquad (10)$$

Application of the sum-rule (Eq. 5) to Eq. 10 immediately gives the surprisingly simple and exact result for the binary random alloy model [25]:

$$\frac{D_A}{D_B} = \frac{w_A}{w_B} \qquad (11)$$

It is seen that despite the appearance of the off-diagonal phenomenological coefficients in Eq. 10 *no* correlation factors or vacancy wind factors appear in Eq. 11. Similarly, for ternary *ABC* alloys, the sum-rule gives that [25]:

$$\frac{D_{BA}^C D_{CB}^C - D_{BB}^C D_{CA}^C}{D_{AA}^C D_{BB}^C - D_{AB}^C D_{BA}^C} = \frac{w_C}{w_A} \qquad (12a)$$

$$\frac{D_{AB}^C D_{CA}^C - D_{AA}^C D_{CB}^C}{D_{AA}^C D_{BB}^C - D_{AB}^C D_{BA}^C} = \frac{w_C}{w_B} \qquad (12b)$$

where D_{AA}^C etc are the ternary intrinsic diffusivities in the *ABC* ternary alloy and *C* is, by convention, the dependent concentration variable.

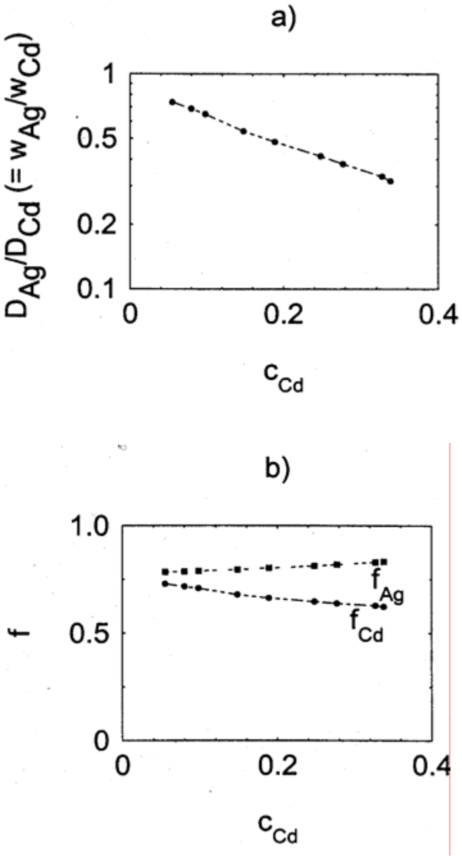

Figure 1: a) The ratio D_{Ag}/D_{Cd} (= w_{Ag}/w_{Cd}) as a function of c_{Cd} at 873K [26]; b) corresponding tracer correlation factors using the Moleko *et al.* [13] self-consistent formalism for the random alloy.

The general expression (for an *N* atomic component alloy) can be written as:

$$\mathbf{D}^{-1} \times \begin{bmatrix} D_{N1}^N \\ D_{N2}^N \\ \dots \\ D_{NN-1}^N \end{bmatrix} = \begin{bmatrix} w_N / w_1 \\ w_N / w_2 \\ \dots \\ w_N / w_{N-1} \end{bmatrix} \qquad (13)$$

where **D** is a matrix with elements D_{kl}^N and $k,l \neq N$.

There has been a very long tradition in solid-state diffusion research to gain access to the tracer correlation factors, if possible, because these factors give rather direct information on the relative degrees of correlation in the random walks of the various atomic species. It is well known that tracer correlation factors in materials can frequently be inferred directly from isotope effect experiments [27] and, for ionic conductors, from measurements of the Haven Ratio [28]. It is a rather less well-known that tracer correlation factors can also be obtained in concentrated disordered alloys, specifically from ratios of the *tracer* diffusivities and the value of the geometric tracer correlation factor f_0 using a diffusion kinetics theory in the random alloy model, such as that of Manning [6] or the more recent self-consistent theory of Moleko *et al.* [13]. However, it can now be seen that tracer correlation factors can also be obtained by way of the ratio of the intrinsic diffusivities in the random alloy and one of the diffusion kinetics theories just cited. As an example of this, in Fig.1a we show the ratio of the atom-vacancy exchange frequencies as deduced directly from the measured intrinsic diffusivities (Eq. 11) in the *Cd-Zn* system at 873K [26] and in Fig. 1b we show the corresponding tracer correlation factors obtained from the ratio of the exchange frequencies by way of the Moleko *et al.* diffusion kinetics theory [13]. It can be seen that at low *Cd* compositions the tracer correlation factors are similar, indicating that the *Ag* and *Cd* atoms are similarly correlated in their motion. As the *Cd* composition increases *Ag* atoms have the higher tracer correlation factors (they have the lower atom-vacancy exchange frequencies) indicating they are less correlated in their motion than the *Cd* atoms.

5 The Sum-Rule and Chemical Diffusion in Strongly Ionic Randomly Mixed Crystals

In this example, we consider chemical diffusion in strongly ionic mixed cation crystals *(A,B)Y*. We assume Schottky disorder and that the cations *A* and *B* diffuse by monovacancies on the cation sublattice (with exchange frequencies w_A and w_B) whilst the anions *Y* diffuse independently by single vacancies on the anion sublattice (with exchange frequency w_Y). The flux equations are (we assume for convenience here that the charges on the ions are simply related by $q_A = q_B = -q_Y$):

$$\begin{aligned} J_A &= L_{AA}X_A + L_{AB}X_B; \\ J_B &= L_{AB}X_A + L_{BB}X_B; \\ J_Y &= L_{YY}X_Y. \end{aligned} \qquad (14)$$

where for the internal driving forces we have that:

$$\begin{aligned} X_A &= -\nabla\mu_A + q_A E; \\ X_B &= -\nabla\mu_B + q_B E; \\ X_Y &= -q_Y E. \end{aligned} \qquad (15)$$

where E is the internal (Nernst) electric field. Upon application of the electro-neutrality conditions and the Gibbs-Duhem relation we find that [29]:

$$J_A = -D_A N\nabla c_A \, , J_B = -D_B N\nabla c_B \qquad (16)$$

where the intrinsic diffusion coefficients D_A and D_B are given by:

$$D_A = \frac{\alpha kTc_Y}{Nc_Ac_B}\left(\frac{L_{AA}L_{BB} - L_{AB}^2 + L_{YY}(L_{AA}c_B - L_{AB}c_A)/c_Y)}{L_{AA} + L_{BB} + 2L_{AB} + L_{YY}}\right) \qquad (17a)$$

$$D_B = \frac{\alpha kTc_Y}{Nc_Ac_B}\left(\frac{L_{AA}L_{BB} - L_{AB}^2 + L_{YY}(L_{BB}c_A - L_{AB}c_B)/c_Y)}{L_{AA} + L_{BB} + 2L_{AB} + L_{YY}}\right) \qquad (17b)$$

and α is a thermodynamic factor. On substitution of the sum-rule (Eq. 5), we soon find that the ratio of these intrinsic diffusion coefficients is given in this case by [29]:

$$\frac{D_A}{D_B} = \frac{w_A(w_B + w_Y)}{w_B(w_A + w_Y)} \qquad (18)$$

where w_Y is the anion vacancy exchange frequency. For the limiting case $w_Y >> w_A$ (w_B), i.e. the anion mobility is very high compared with the cation mobility, Eq. 18 shows that the ratio of the intrinsic diffusion coefficients is simply given by w_A/w_B. This is of course exactly the same result obtained for the ratio of the intrinsic diffusivities for the components *A* and *B* in the binary metallic alloy described above (Eq. 11). This equivalence comes about because the mobility of the vacancies on the anion sublattice is so high that it cannot determine the rate of cation vacancy mobility and therefore cation interdiffusion. This is analogous to noting that the free electrons in the metallic alloy have no influence on the diffusion rate of the atoms themselves. On the other hand, for the other limiting case where $w_Y << w_A$ (w_B), i.e. the anion mobility is now very low compared with the cation mobility, Eq. 18 then shows that the ratio of the intrinsic diffusion coefficients is simply unity, i.e. the two intrinsic diffusion coefficients are now required to be equal. This can be understood as follows. In the interdiffusion experiment with a diffusion couple *AY-BY* an essentially immobile *Y* anion sublattice means there is no anion vacancy mobility. The cation vacancies are restricted in their motion in the sense there can be no cation vacancy flux. The fluxes of the *cations A* and *B* must then be exactly equal and opposite. Therefore there would be no Kirkendall shift. The intrinsic diffusivities of the cations *A* and *B* are thus equal and of course equal to the interdiffusion coefficient too.

6 The sum-rule and cation segregation (demixing) of mixed oxides in an oxygen potential gradient and/or an electric field

In this example, we consider the segregation or demixing of cations in an oxygen potential gradient and/or an electric field of the cations of a mixed oxide *(A,B)O* taking the rock-salt structure. We consider the oxygen potential gradient and the electric field together in the analysis. In these oxides, the oxygen ions are essentially immobile at the temperatures of interest and act as 'spectators' for the cation diffusion processes.

Consider that one end of the sample is exposed to a higher oxygen partial pressure (which determines the (higher) cation vacancy composition at this end) whilst the opposite end is exposed to a lower oxygen partial pressure, which again determines the (lower) cation vacancy composition. At high temperatures where the cations are mobile, there is a resulting vacancy flux across the sample and a cation flux in the opposite direction. Alternatively, a vacancy flux can be obtained by applying an electric field: at high current conditions there is a cation flux in direct response to the field and a vacancy flux in the opposite direction. In general, the two cations *A* and *B* in *(A,B)O* will have different mobilities, i.e. they have different exchange rates with the vacancies *V*. As the species of cation diffuse in the flux of vacancies there will be a demixing of the cations across the sample.

The usual assumption in addressing this problem is to assume that the electronic mobility is far greater than the atomic mobilities and therefore is not rate determining in the diffusion of the cations. We also assume that the cations are randomly mixed, i.e. the cation sublattice is a binary 'random alloy'. The Onsager flux equations (Eq. 1) for the cation sublattice system with vacancies can be written as [30]:

$$J_i = -\sum_j L_{ij}(\nabla\mu_j - \nabla\mu_V - F_j), \quad i,j=A,B \qquad (19)$$

where the F_j are the electrical driving forces (= qE, where q is the charge on the cation and E is the electric field). For convenience here we will assume that $F_A = F_B = F$.

Once steady state demixing of the cations has been achieved, the crystal moves with a steady state velocity, v, with respect to the laboratory frame (which is fixed at an oxygen lattice plane). The condition that leads to steady state can be expressed as [31]:

$$J_i - vc_i N = 0 \qquad i = A,B \qquad (20)$$

where c_i is the composition of component i (with respect to the cation sublattice so that $c_A + c_B + c_V = 1.0$) and N is the number of lattice sites per unit volume. Eqs. 19 and 20 lead to the result:

$$\begin{bmatrix}\nabla(\mu_A - \mu_V - F)\\ \nabla(\mu_B - \mu_V - F)\end{bmatrix} = \begin{bmatrix} L_{AA} & L_{AB}\\ L_{AB} & L_{BB}\end{bmatrix}^{-1}\begin{bmatrix}-c_A vN\\ -c_B vN\end{bmatrix} \qquad (21)$$

Eq. 21 is the principal demixing equation. We can now make use of the sum-rule (Eq. 5) and then Eq. 21 reduces to:

$$\nabla(\mu_i - \mu_V) = -\frac{vc_iN}{L_{ii}^{(0)}} + F = -\frac{vNkT}{w_i c_V K} + F, \quad i = A,B \qquad (22)$$

As in the previous examples, the formal absence of any correlation factors or vacancy-wind factors is especially noted. Next, after converting the chemical potential gradients to composition gradients and assuming thermodynamic ideality (the random mixing model where $\mu_i - \mu_V = kT\ell n(c_i/c_V)$). This leads to the following coupled set of ordinary differential equations describing the steady-state composition profiles of the two cations and the vacancies:

$$\frac{dc_i}{d\xi} = \frac{c_i vN}{c_V K}\left(\sum_j \frac{c_j}{w_j} - \frac{1}{w_i}\right) + \frac{c_i c_V F}{kT}, \qquad (23a)$$

$$\frac{dc_V}{d\xi} = \frac{vN}{K}\sum_i \frac{c_i}{w_i} - \frac{c_V(1-c_V)F}{kT}, \quad i=A,B \qquad (23b)$$

where ξ represents a coordinate along the length of the moving sample. Eq. 23 describes the steady state composition profiles for cations and vacancies generally i.e. with, in principle, either an oxygen potential gradient, an electric field operating, or both. Eq. 23 is readily solved using standard numerical methods to provide the steady state atom (and vacancy) composition profiles themselves across the sample.

7 Conclusions

In this overview, we have discussed the sum-rule for diffusion via vacancies in the random alloy model and considered several applications of the sum-rule to collective diffusion problems. These applications included intrinsic diffusion in a multicomponent alloy, chemical diffusion in strongly ionic mixed cation crystals and demixing in an oxygen potential gradient and/or electric field of cations in mixed oxides. In each case a substantial simplification was possible as a result of the sum-rule.

Acknowledgements

We wish to thank the Australian Research Council (Discovery Project Grants Scheme) for its support of this research. One of us wishes to thank the Australian Research Council for the award of an Australian Professorial Fellowship (I.V.B).

References

[1] Philibert, J*., Atom Movements: Diffusion and Mass Transport in Solids,* Editions de Physique, Les Ulis, 1991.

[2]Allnatt, A.R. and Lidiard, A.B., *Atomic Transport in Solids*, Cambridge University Press, Cambridge 1993.

[3] Darken, L.S., *Trans. Am. Inst. Min. (Metall.) Engrs.*, 175, p. 184, 1948.

[4] Huntington, H.B., Miller, N.C. and Nersis, V., *Acta Met*., 9 , p. 749, 1961.

[5] Belova, I.V. and G. E. Murch, G.E., *Defect Diffusion Forum*, 213/215, p. 95, 2003.

[6] Manning, J.R., *Phys. Rev. B*, 4, p. 1111 (1971).

[7] Manning, J.R., *Diffusion Kinetics for Atoms in Crystals*. Van Nostrand, Princeton, NJ, 1968.

[8] Lidiard, A.B., *Acta Metall.,* 34, p.1487, 1986.

[9] Zhang, L., Oates, W.A. and Murch, G.E., *Phil. Mag. B,* 60, p. 277, 1989.

[10] Belova, I.V. and Murch, G.E. *J. Phys. Chem. Solids*, 60, p. 2023. 1999.

[11] Belova, I.V. and Murch, G.E. *Phil. Mag. A*, 78, p. 1085, 1998.

[12] Belova, I.V. and Murch, G.E., *Phil. Mag. A*,

[13] Moleko, L.K., Allnatt, A.R. and Allnatt, E.L., *Phil. Mag. A*, 59, p. 141, 1989.

[14] Belova, I.V., Allnatt, A.R. and Murch, G.E., *J. Phys: Condens. Matter,* 14, p. 6897, 2002.

[15] Belova, I.V. and Murch, G.E., *Phil. Mag. A*, 80, p 599, 2000.

[16] Heumann, Th., *J. Phys. F: Metal Physics*, 9, p. 1997, 1979.

[17] Lidiard, A.B., *Phil. Mag.* 46, p. 1218, 1955.

[18] Moleko, L.K. and Allnatt, A.R., *Phil. Mag. A,* 58, p. 677, 1988.

[19] Murch, G.E. and Belova, I.V., *Mass and Charge Transport in Inorganic Materials II*, V P. Vincenzini, P. and V. Buscaglia, V. (Eds), Techna, Faenza, Italy, p. 99, 2003.

[20] Sharma, S., Chaturvedi, D.K., Belova, I.V. and Murch, G.E., *Phil. Mag. Lett.*, 80, p. 65, 2000.

[21] Belova, I.V. and Murch, G.E., to be published.

[22] Belova, I.V. and Murch, G.E., *Phil. Mag.*, 34, p. 3637, 2004

[23] Belova, I.V. and Murch, G.E., *Defect Diffusion Forum,* 194/199, p. 547, 2001.

[24] Allnatt, A.R., Belova, I.V. and Murch, G.E., to be published.

[25] Belova, I.V. and Murch, G.E., *Phil. Mag. Lett.,* 81, p. 661, 2001.

[26] Iorio, N.R., Dayananda, M.A. and Grace, R.E., *Metall. Trans*., 4, p. 1339, 1973.

[27] Peterson, N.L., *Diffusion in Solids: Recent Developments*, Nowick, A.S. and Burton, J.J. (Eds), Academic Press, New York 1975, p. 115.

[28] Murch, G.E., *Solid State Ionics*, 7, p. 177, 1982.

[29] Belova, I.V. and Murch, G.E. *Phil. Mag.*, 84, p. 2139, 2004.

[30] Belova, I.V., Brown, M.J. and Murch, G.E. *Solid State Ionics*, 167, p. 175, 2004.

[31] Schmalzried, H., Laqua, W. and Lin, P.L., *Z. Naturforsch*., 34a, p. 192, 1979.

Proceedings of The 1st International Conference on **D**iffusion in **S**olids and **L**iquids
DSL-2005, July 6-8, 2005, University of Aveiro, Aveiro, Portugal

COBALT DIFFUSION IN POLYCRYSTALLINE CVD DIAMON GROWN ON PURE COBALT SUBSTRATES

Miguel A. NETO*, Estela PEREIRA

Department of Physics, University of Aveiro, 3810-193 Aveiro, Portugal

*Corresponding author. Fax: +351 234 424 965; Email: mangelo@fis.ua.pt

Abstract

We have used an MPCVD reactor to grow relatively thick polycrystalline diamond films on highly pure cobalt substrates. With well controlled growth conditions we were able to grow free-standing samples with thickness ranging from a few microns to a couple of hundreds. The films morphology and impurity content were accessed by the usual SEM, XRD, Raman and EDS techniques.

SEM analysis conducted on the films growth surface revealed the presence of grain boundaries inclusions, which were subsequently identified by EDS as been made of cobalt. The surface density evolution of these inclusions with film thickness was compared with the average crystallite size. XRD spectra help us to identify dominant crystallographic planes during several stages of the film growth. At the end we present a model for the incorporation of cobalt in the films during the CVD process.

Keywords: Diffusion in crystalline and amorphous materials; polycrystalline CVD diamond; cobalt; surfaces; inclusions

1 Introduction

Nowadays polycrystalline diamond films are one of the most promising materials for a number of applications from the mechanical, electrical and optical to electronics. However, their characteristic low crystallographic order, structural imperfections and impurity content, limits the range of possible applications. On the other hand, there are cases where the incorporation of special impurities could benefit diamond (i.e. incorporation of boron to give *p-type* semiconductor). In the case of polycrystalline CVD diamond films very few elements were successfully incorporated into the diamond lattice (i.e. H, N, O, B, Si). Other elements, like nickel and cobalt have only been detected in HPHT diamond when they are present in the solvent catalyst. In the particular case of cobalt, it was found that it is preferentially incorporated in the lattice in [111] sectors [1]. Furthermore, it is also optically active [2] and can bind to nitrogen to form complex optical centres similar to those due to nickel [3, 4] observed either by photoluminescence and cathodoluminescence.

It is known that impurity incorporation in growing CVD diamond films can be achieved by two distinct processes: one is aggregation from the gas phase that contains the impurity element and the other by diffusion phenomena. However due to the lattice energy barrier of diamond at characteristic CVD temperatures, diffusion is extreme difficult. Exceptions must be taken for hydrogen, nitrogen and boron, as they can diffuse at CVD growth temperatures. In the particularly case of polycrystalline materials diffusion can be divided in two major processes: lattice diffusion and inter-granular (or grain boundary - GB) diffusion [5]. Also, because these two processes are very much dependent on the growth temperature and on the material's lattice parameters [6] it is expected that GB diffusion will be the dominant process in polycrystalline CVD diamond.

There have been several studies on the growth of diamond films on cobalt containing substrates as WC-Co hard metal substrates containing up to 12wt.% Co [7-15] and on pure cobalt substrates [16,17]. It is well established that the Co contained in the binder phase of the hard metal is detrimental to the deposition of diamond films [9-13] as it inhibits the growth of very thick and adherent films. To overcome these problems several substrate pre-treatments were suggested. These pre-treatments are usually aimed to deplete Co in the substrate surface by selective chemical etching [18-21] and formation of intermediate layers of Co compounds such as borides, silicides and aluminides [22-25]. Some of these studies also report that cobalt migration form drops on the substrate surface frequently observed during the diamond deposition [26-28]. They are primary formed on the hard metal substrate interface but can also be observed on the films growth surface. The way they appear on the growth surface is not yet fully understood.

Besides the detection of Co on the film growth and substrate surfaces, there is almost no information about the presence of this element inside the film. With this work we hope to clarify if cobalt can really diffuses into the films during growth. Its distribution along the films growth direction will also be studied. At the end we propose a model that could explain the dominant mechanisms for the cobalt incorporation – lattice, GB diffusion or aggregation from the gas phase.

2 Experimental details

In order to study the incorporation of cobalt during the CVD process, the films were grown directly on high purity (99.9%) cobalt substrates (5x5x1mm) using ASTeX PDS 18 MPCVD reactor with well adjusted growth conditions as described in our previous work [16]. The films were all grown with the same growth conditions, namely: 470 sccm H_2, 35 sccm CH_4, 2400 W of microwave power and a pressure of 90 Torr. To enhance the density of nucleation sites, a polishing technique was applied on all substrates: first they were polished with a sequence of SiC sand papers with 600, 1200 and 2400 grid; after the substrates were polished with 3 μm diamond paste and then ultrasonic cleaned in acetone; finally and before the deposition the substrates were again polished with an 3 μm diamond powder and ultrasonic cleaned in the same acetone solution. Although the substrates were subject to such abrasive pre-treatments no other method was used on the substrate surface [18-25]. Any other method would strongly reduce Co mobility as well as its vapour pressure in the deposition chamber [29].

X-ray diffraction (XRD) analysis was used to confirm the synthesis of diamond and identify the dominant crystallographic growth planes. It was carried out on a Philips X'Pert equipment with a scanning step of 0.05° and 0.5 s of integration time. The films morphology and crystallite size were examined by scanning electron microscopy (SEM) using a FEG-SEM Hitachi S4100 system. The presence of cobalt in these films was studied by energy disperse X-ray spectroscopy (EDS) available in the SEM system. Prior to SEM analysis, the films were coated with carbon and in a few cases with Pt/Au, in order to avoid charge effect. Finally the presence of diamond and other forms of carbon was studied by micro-Raman analysis with the use of a Jobin Yvon T64000 spectrometer, with a spectral resolution of 0.45 cm^{-1} and with an Ar^+ laser using the 514.5 nm excitation line with 2 mW laser power on the sample.

3 Results and discussion

Several polycrystalline diamond films with different thickness, ranging from a few microns to a couple of hundred microns, were obtained (table 1).

Table 1: Growth time, film thickness and growth rate of the free-standing films.

Film Ref.	Growth time (hr)	Thickness (μm)	Growth-rate (μm/hr)
Co1	3	6	2
Co2	5	18	3.6
Co3	25	65	2.6
Co4	68	190	2.8

After post-deposition cooling to room temperature they all self delaminated from the substrates. This observation is consistent with our previous work [16] and other observations on WC/Co substrates [9-13], and can be explained by the absence of carbide formation and for both lattice and thermal expansion coefficient mismatch. The Co at the substrate surface catalyses the formation of non-diamond carbon phases, which are deposit at the interface and reduce the adhesion [12]. In fact Raman spectra taken on the films back surface shows the characteristic D and G bands of graphite (fig. 1a) meaning that indeed a graphitic layer was formed at the initial stages of film growth. Even after a 3 hour etching in H_2 environment this layer was not completed removed (fig. 1b). Taking into account the typical H_2 etching efficiencies the thickness of this layer was estimated to be in the range of 1-3 μm.

The presence of cobalt in the films was accessed by SEM and EDS analysis on the films back and growth surfaces. EDS spectra taking on the films substrate surface indicate that cobalt is homogeneous distributed, even after almost all graphite was removed (fig. 2). This means that carbon diffuses through the substrate until saturation creating a layer of graphite, amorphous carbon and cobalt before diamond nucleation takes place.

As with CVD diamond films grown on cobalt containing cemented WC substrates [26-28], we observe the same cobalt drops, homogeneously distributed on the films growth surface (fig.3).

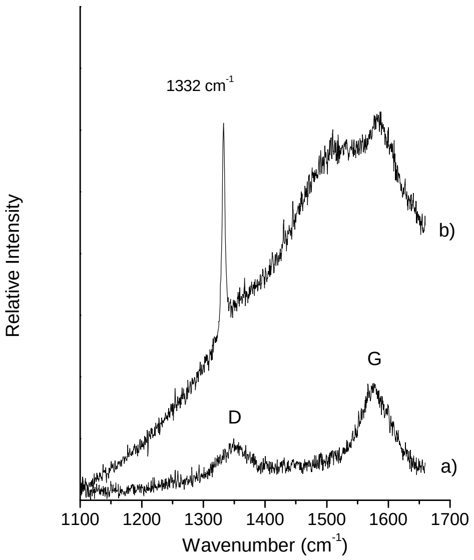

Figure 1: Typical Raman spectra of films back surface: a) after growth; b) after 3 hours H_2 etching.

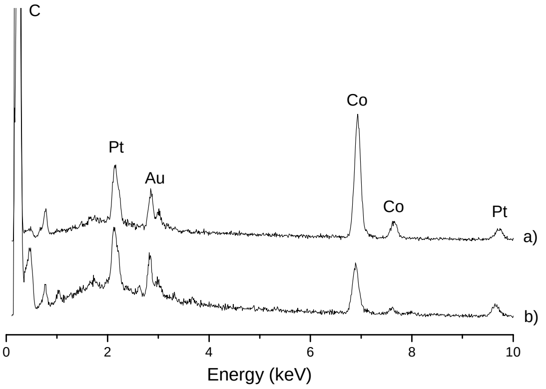

Figure 2: Typical EDS spectra taken on films back surface: a) after growth; b) after 3 hours H_2 etching.

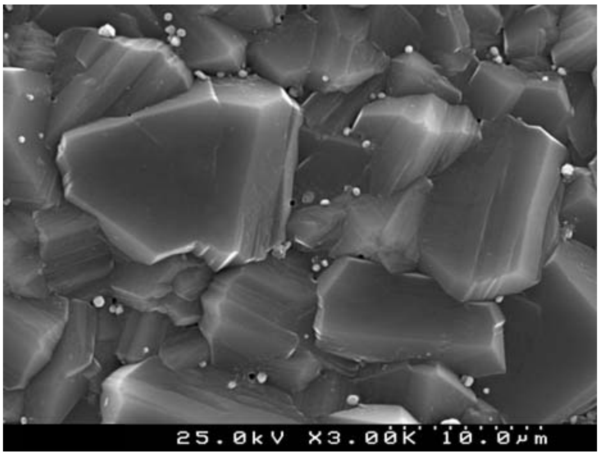

Figure 3: SEM image of sample Co2 with cobalt drops (white dots) on the growth surface.

However these drops are not really bounded to diamond, because they can be easily removed with a simple solution of acetone in an ultrasonic bath. Due to cobalt's vapour pressure the presence of these drops could be attributed to aggregation of cobalt present in the plasma. This is consistent with the darkening of the reactor's windows during growth.

SEM images were taken on the films growth surface and are presented in figure 4.Nanometer sized spots (dark spots - DS) are observed on the growth surface at the crystallites grain boundaries. It is clear that they decrease in number as the film thickens.

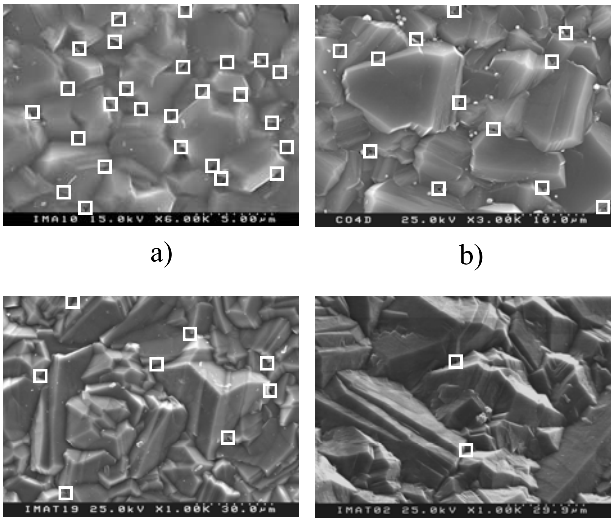

a) b)

c) d)

Figure 4: SEM images of films growth surface: a) Co1; b) Co2; c) Co3 and d) Co4. Dark spots (DS) identified with □.

Table 2 shows the surface density (σ) of these DS. Its behaviour with film growth is illustrated by fig. 5 where we compare it with the crystallites average size. The correlation between these two quantities is indication that the DS are only dependent of the crystallites GB. The coalescence of the crystallites during growth reduces the number of GB consequently reducing the number of DS. High magnification SEM analysis on DS revealed a tunnel like shape in all the films (fig. 6). To access the chemical nature of these DS, EDS analysis was performed inside (I) and outside (O) of such spots (fig. 6). We conclude that they are essentially made of cobalt and silicon. The origin of this silicon can be attributed to unavoidable contamination from the reactor's windows and walls (the reactor is mainly used for deposition on silicon substrates). Moreover, we observed that silicon is detected only in samples grown on cobalt substrates. In films grown on silicon, copper and molybdenum substrates and in the same reactor, silicon is found to lie below EDS detection limit. This suggests that cobalt could act as a catalyst for silicon incorporation.

Table 2: DS surface density (σ) on the films growth surface.

Film Ref.	Thickness (μm)	Surf. density σ ($\times 10^4$ cm^{-2})	Error Δσ ($\times 10^4$ cm^{-2})
Co1	6	861,1	78,3
Co2	18	156,5	19,6
Co3	65	9,8	2,2
Co4	190	2,0	1,0

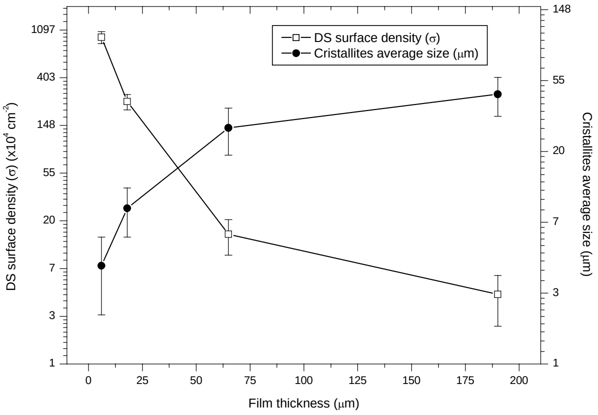

Figure 5: Correlation between DS surface density (σ) and crystallites average size for different film thickness.

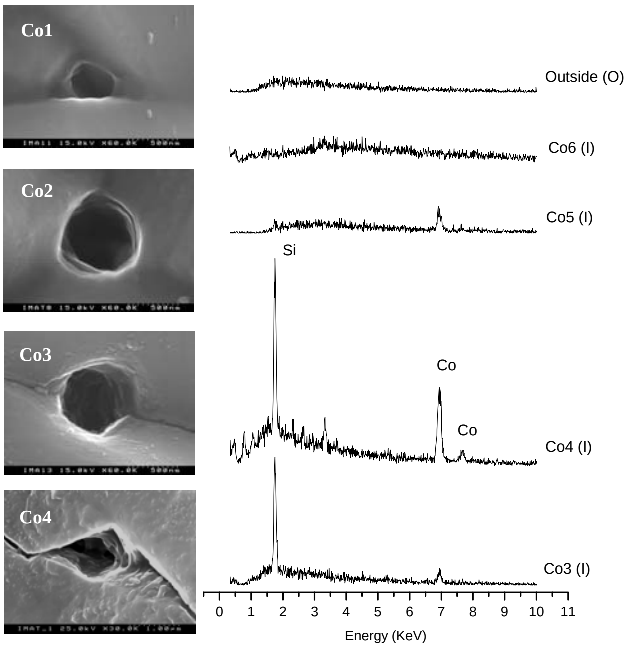

Figure 6: High magnification SEM images of films DS and typical EDS spectra inside (I) and outside (O) of these DS.

The analysis of sample Co1 cross-section (fig. 7) and the films DS (fig. 8) illustrates how cobalt and silicon concentrations vary with film growth. In the initial stages of film growth corresponding to the graphitic layer, a high decrease of cobalt incorporation is observed reaching a minimum around 3 μm. This thickness corresponds more or less to the stage when diamond starts to grow (considering the typical graphitic layer thickness). The slight increase in cobalt incorporation accompanied by the same corresponding increase in silicon content, between 3.5 and 6 μm can be explained by preferential aggregation of cobalt and silicon present in the plasma. In fig. 8 EDS have shown that cobalt incorporation depend on the film thickness. After an initial increase, as observed when comparing samples Co1 and Co2, a decrease is detected for samples Co3 and Co4. Silicon concentration presents a steady decrease.

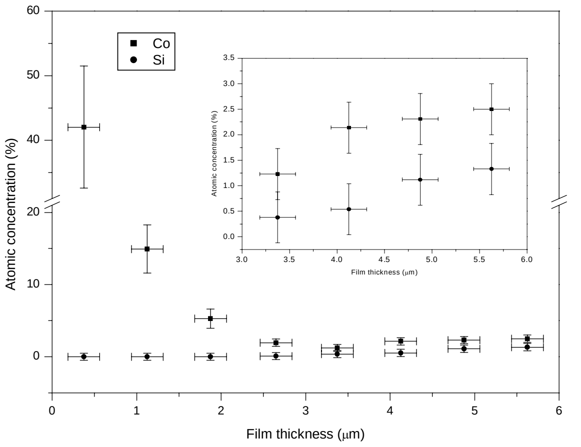

Figure 7: EDS analysis at the film Co1 cross-section at different positions from the back surface.

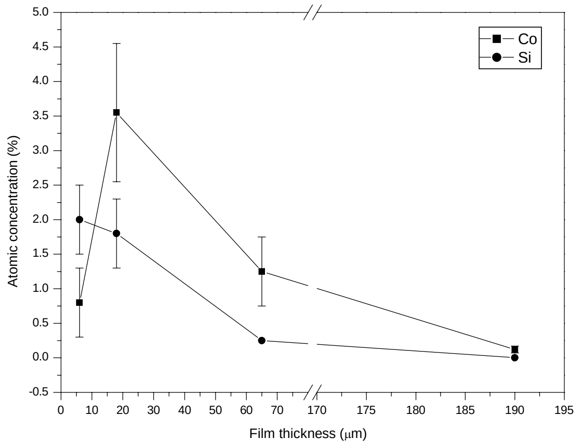

Figure 8: Evolution of cobalt and silicon concentrations with film thickness at the films DS.

XRD analysis presented in fig.9 indicates that Co1 have preferential (111) growth planes while the thicker films have a misture of (111), (220) and (311). The increase in Co incorporation in Co1 can probably be explained by preferential Co incorporation in (111) planes similar to what is observed in HPHT grown diamonds. Thicker films have (220) and (311) morphologies. This fact explains the decrease in Co incorporation. Another effect contributes to this decrease: during the deposition process, the remaining cobalt present in the plasma will gradually deposit on the reactors windows and walls blocking the silicon and reducing the amount of these elements incorporated in the films. High magnification SEM images for the thicker samples (fig. 6a) shows empty DS.

3.1 Proposed model

A proposed model will now be presented for the formation of such DS. The CVD process starts after the surface seeding of the substrate with diamond powder during the described abrasive pre-treatment. Then, and before nucleation takes place a layer of graphite and cobalt is formed between the substrate and the film, due to the carbon diffusion in the substrate. At the same time some cobalt easily evaporates to the plasma in the deposition chamber. So, before nucleation occurs, there are two competitive diffusion phenomena: one the diffusion carbon that goes into the substrate and the easily evaporating cobalt to the chamber. As shown by Raman scattering, after a certain time we have progressive transformation of graphite sp^2 bounding to diamond sp^3 by atomic hydrogen, that in some extent block further cobalt evaporation to the deposition gas. Nevertheless the surface thereby obtained, consists of diamond nucleation sites separated by cobalt reactive regions with estimated surface density of the order of 10^7 cm^{-2}. At this stage the silicon incorporation is very low.

The beginning of film growth is characterized by very small crystallites, high grain disorder and high cobalt content in the deposition chamber. So, it is most likely that the doping process responsible for the formation of such spots at the initial stages of film growth is cobalt aggregation at the grain boundaries. The proof comes from the detection of silicon and cobalt in those DS, which is indication of cobalt aggregation with these elements present in the plasma. When crystallites with preferential (111) growth planes are detected by XRD, the percentage of cobalt increased in these regions. At this time diffusion takes the lead in incorporating cobalt. At the same time the remaining cobalt present in the plasma goes to the reactor's windows and walls blocking the silicon leading to a decrease of this element in the film. Further growth, change the crystallographic planes, which in turn results in lower incorporation efficiency. Now aggregation is again the major doping process, but less important due to lower percentage of atomic cobalt present in the deposition chamber, as the substrate becomes covered with diamond. Therefore the film will present a polycrystalline structure where the GB are filled with cobalt to a certain height.

4 Conclusions

In this work, we present evidence of cobalt incorporation in polycrystalline CVD diamond films during growth. In this case cobalt incorporation is mainly achieved by two distinct ways: one through the diamond lattice only at the early stages of film growth (i.e. 3-4 µm deep) were cobalt easily diffuses trough the forming graphite; another at the crystallites grain boundaries in the shape of cylindrical spots similar to tunnels that grow with the film. Besides cobalt these spots also contain silicon, due to contamination of the deposition chamber. Its presence clearly indicates aggregation phenomena characteristics of cobalt that possibly bounds to silicon forming some cobalt silicites (i.e. CoSi) [30]. In fact, these silicites are

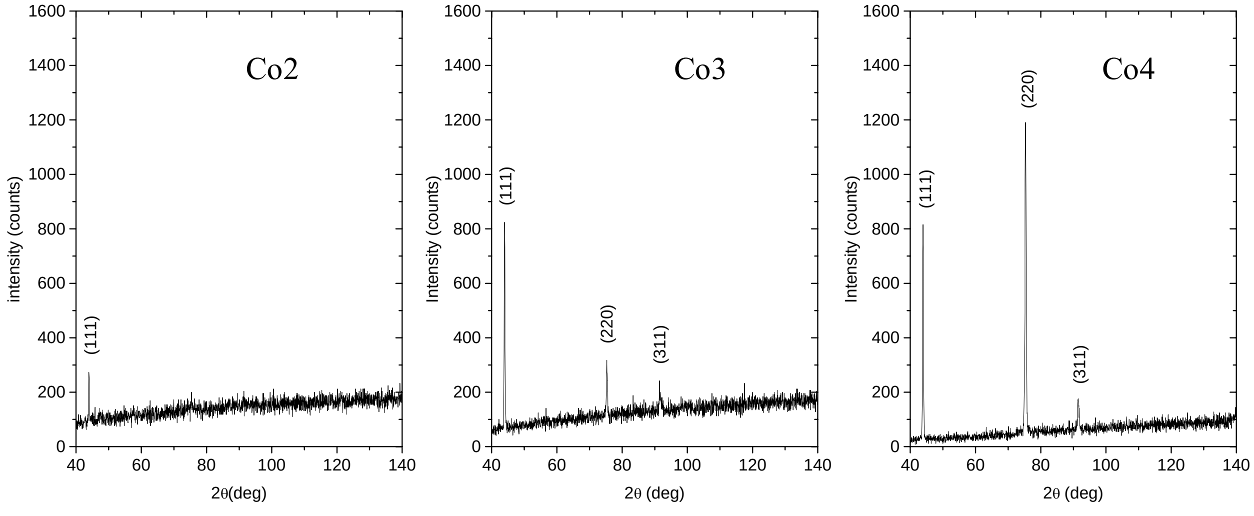

Figure 9: X-ray diffraction spectra for the free-standing CVD samples.

stable under diamond deposition conditions [22].

We believed that formation and growth of such DS is divided in three major phases: 1) cobalt aggregation from the gas phase to the surface cobalt reactive sites immediately after nucleation; 2) cobalt diffusion in these spots when there are dominant (111) crystallographic planes; 3) further cobalt aggregation of the remaining cobalt present in the plasma.

With the results presented here we show that incorporation of cobalt in polycrystalline CVD diamond films occurs, whether by aggregation from the gas phase or diffusion at the crystallites grain boundaries.

Further analysis is needed to clarify the importance of silicon in the diffusion process of cobalt.

Acknowledgements

Miguel A. Neto thanks FCT – Fundação para a Ciência e a Tecnologia for the grant PRAXIS XXI/BD/16161/98. The authors would like to acknowledge A. J. S. Fernandes for the precious help on the CVD equipment and any relevant discussions.

References

[1] X. Jia, H. Kagi, S. Hayakawa, M. Wakatsuky, and Y. Gohshi, in Advances in *New Diamond Science and Technology*, edited by S. Saito, N. Fujimori, O. Fukunaga, M. Kamo, K. Kobashi, and M. Yoshicawa (MY, Tokyo, 1994), p.525.

[2] S.C. Lawson, H. Kanda, K. Watanable, I. Kiflawi, Y. Sato, *J. Appl. Phys.*, 79 (8), 4348 (1996).

[3] A.T. Collins, H. Kanda, R.C. Burns, *Philos. Mag. B* 61 (1990).

[4] S.C. Lawson, H. Kanda, *J. Appl. Phys.* 73 (1993) 3967.

[5] I. Kaur, W. Gust, *Fundamentals of grain and interphase boundary diffusion*, (1988).

[6] M. Stanislau, *Defects and diffusion in solids: an introduction*, (1980).

[7] M. Murakawa, S. Takeuchi, *Surf. Coat. Technol.*, 49 (1991) 359.

[8] J. Oakes, X. X. Pan, R. Bichler, R. Haubner, B. Lux, *Surf. Coat. Technol.*, 47 (1991) 600.

[9] R. Haubner, B. Lux, *Journal de Physique* C5 (1989) 169.

[10] R. Haubner, A. Lindlbauer, B. Lux, *Diamond and Related Materials* 2 (1993) 1505.

[11] R. Haubner, S. Kubelka, B. Lux, M. Griesser, M. Grasserbauer, Journal de Physique C5 (1995) 753.

[12] H. Matsubara, J. Kihara, *Science, Technology of New Diamond*, KTK Scientific Publishers, Tokyo (1990) S. Saito, O. Fukunaga, M. Yoshikawa Eds., pp. 89-93.

[13] T. H. Huang, C. T. Kuo, C. S. Chang, C. T. Kao, H. Y. Wen, *Diamond and Related Materials*, 1 (1992) 594.

[14] R. Cremer, R. Mertens, D. Neushütz, O. Lemmer, M. Frank, T. Leyendecker, *Thin Solid Films*, 355-356 (1999) 127.

[15] A. Fernandes, A. Neves, R. F. Silva, M. H. Nazaré, *Diamond and Related Materials* 6 (1997) 769.

[16] M.A. Neto, Qi Hua Fan, E. Pereira, *Diamond and Related Materials* 10 (2001) 316-321.

[17] Wei Liu, Denise A. Tucker, Peichun, Yang, and Jeffrey T. Glass, *J. Appl. Phys.* 78 (2), 1291 (1995).

[18] A. K. Mehlmann, S. F. Dirnfeld, Y. Avigal, *Diamond and Related Materials* 1 (1992) 600.

[19] K. Shibuki, M. Yagi, K. Saijo, S. Takatsu, *Surf. Coat. Technol.* 36 (1988) 295.

[20] X. X. Pan, *Doctoral Thesis*, Technical University of Vienna (1989).

[21] B. S. Park, Y. -J. Baik, K. -R. Lee, K. Y. Eun, D. H. Kim, *Diamond and Related Materials* 2 (1993) 910.

[22] S. Kubelka, R. Haubner, B. Lux, R. Steiner, G. Stingeder, M. Grasserbauer, Diamond and Related Materials 3 (1994) 1360.

[23] W. G. Moffat, *The Handbbok of Binary Phase Diagrams*, Genium Publishing Corporation, New York, USA.

[24] J. Karner, E. Bergmann, et al, *Int. Patent* WO 95/12009 (1995).

[25] R. Cremer, R. Mertens, D. Neushütz, O. Lemmer, M. Frank, T. Leyendecker, *Thin Solid Films*, 355-356 (1999) 127.

[26] D. Satrapa, *Doctoral Thesis*, University of Thecnology Vienna (1993).

[27] A. K. Mehlmann, A. Fayer, S. F. Dirnfeld, Y. Avigal, R. Porath, A. Kochman, *Diamond and Related Materials* 2 (1993) 317.

[28] N.M. Everitt, R.F. Silva, J. Vieira, C.A. Rego, C.R. Henderson, P.W. May, *Diamond and Related Materials* 4 (1995) 730-734.

[29] R. Haubner, W. D. Schrubert, B. Lux, *Proceedings of the 14th International Plansee Seminar*, Eds. G. Knermger, P. Rödhammer, P. Wilhartitz, Plansee AG, Reutte(1997) Vol. 3.

[30] A. P. Horsfield, H. Fujitani, *Physical Review B* 63 (2001) 235303-1(6).

Proceedings of The 1st International Conference on **D**iffusion in **S**olids and **L**iquids
DSL-2005, July 6-8, 2005, University of Aveiro, Aveiro, Portugal

PROBING DIFFUSIONAL JUMPS IN ORDERED COMPOUNDS BY ANELASTIC RELAXATION SPECTROSCOPY

NUMAKURA Hiroshi*

Department of Materials Science and Engineering, Kyoto University,
Sakyo-ku, Kyoto 606–8501, Japan

*Corresponding author. Fax: +81 75 753 4978; Email: hiroshi.numakura@materials.mbox.media.kyoto-u.ac.jp

Abstract

Intrinsic point defects may give rise to anelastic relaxation effects in ordered compounds in which some of the sublattice sites have lower symmetry than the host lattice. Detailed experiments have been carried out on one of such effects: the relaxation effect in Ni_3Al, which was interpreted to be due to stress-induced reorientation of antisite Al atoms in the Ni-sublattice (Numakura et al. 1999), focussing on the effects of deviation of composition from stoichiometry. The relaxation strength has been found to increase sensitively with increasing Al concentration, supporting firmly the earlier interpretation. The observed relaxation rates have been analysed on the basis of the mechanism of atomic diffusion (Numakura et al. 1998) to evaluate the diffusion coefficient of Al in Ni_3Al for various compositions.

Keywords: Anelastic relaxation; Mechanical spectroscopy; Internal friction; Point defects; Intermetallic compounds

1 Introduction

Anelastic relaxation due to point defects provides a unique means of investigating elementary processes of diffusion, i.e. atomic jumps, in solids. Measurements of relaxation rates at low frequencies are particularly useful as they allow determination of very small diffusion coefficients that are not accessible by other conventional methods. However, conversion of the relaxation rate to the diffusion coefficient may not be straightforward; it is possible only if the detailed mechanism is known.

Ni_3Al, an intermetallic compound with the $L1_2$ ordered structure, exhibits a well-defined anelastic relaxation effect [1–4], which can be interpreted to be due to stress-induced reorientation of antisite Al atoms in the Ni sublattice [5]. In this paper we first review earlier observations and the proposed mechanism. Next we show the results of new measurements by isothermal mechanical spectroscopy. Then we discuss how the diffusion coefficient can be evaluated from the rate of the anelastic relaxation effect, with an aid of the knowledge on the mechanism of diffusion in Ni_3Al [6,7], and the diffusion coefficient of Al is derived. Applications of the method to study diffusion in other materials are discussed.

2 Relaxation effect in Ni_3Al

Gadaud and Chakib [1,2] studied anelastic behaviour of Ni_3Al by isothermal mechanical spectroscopy and discovered a well-defined Debye type relaxation peak at intermediate temperatures. Mourisco et al. [3,4] reported a similar relaxation peak in Ni_3Al containing a small amount of Ta ($Ni_{75}Al_{24}Ta_1$). The latter is believed to be the same effect as the former, i.e., it is not due to Ta solutes but intrinsic defects, from the close similarities between the two. The characteristic features of the relaxation effect are summarized as follows:

(i) The shape of the peak is close to that of a Debye type relaxation peak with a single relaxation rate.

(ii) The relaxation rate obeys the Arrhenius law,

$$\tau^{-1} = \tau_0^{-1} \exp\left(-\frac{E}{kT} \right), \tag{1}$$

with the activation energy E of about 3 eV and a pre-exponential factor τ_0^{-1} of the order of 10^{17} s^{-1}. In the above, k is the Boltzmann constant and T is temperature.

(iii) In measurements in torsional vibration using single crystal specimens, the relaxation magnitude is the largest in specimens whose torsional axis is oriented to ⟨111⟩, while it is very small in those oriented to ⟨001⟩.

The values of the activation parameters suggest a Zener-type mechanism, namely stress-induced reorientation of substitutional-defect complexes, as the activation energy of 3 eV is close to the activation energy of the diffusion of Ni in Ni_3Al [8,9].

3 Relaxation mechanism [5]

3.1 Defect symmetry

Figure 1 (a) shows the unit cell of an A_3B ordered alloy of the $L1_2$ structure, in which the majority species A occupies the face-centre sites (α sublattice sites) and the minority species B occupies the cube-corner sites (β sublattice sites). Figures 1 (b) and 1 (c) illustrate the atomic arrangement about an A atom and about a B atom, respectively. From these illustrations one sees immediately that the symmetry of the α sublattice site is tetragonal, while that of the β sublattice site is cubic. An atomic defect at an α sublattice site thus forms a point defect of tetragonal symmetry in a crystal of cubic symmetry, which fulfils the condition for an anelastic relaxation effect to take place [10]. In fact, the variation of the relaxation magnitude with the stress axis, item (iii) in the previous section, is what expected for relaxation due to tetragonal defects. As the effect occurs in binary Ni_3Al, it is attributed to intrinsic atomic defects on α sublattice sites: either vacancies, V_α, or antisite B atoms, B_α.

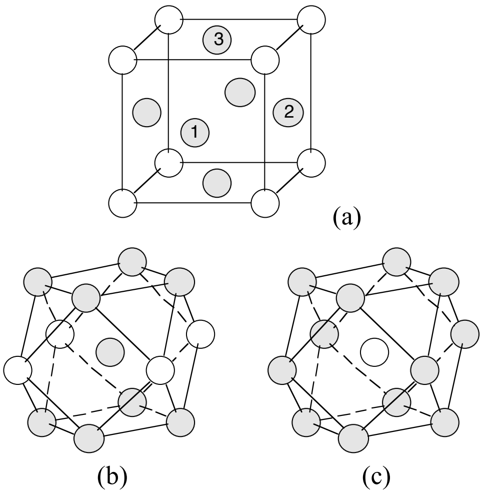

(a)

(b) (c)

Figure 1: (a) The unit cell of the $L1_2$ ordered structure, the atomic arrangements (b) around an A atom (shaded circles) and (c) around a B atom (open circles).

3.2 Relaxation rate

The rate of anelastic relaxation due to reorientation of tetragonal defects in a cubic crystal is generally written as

$$\tau^{-1} = 3\nu, \tag{2}$$

with ν the rate of reorientation from one orientation to another. Figure 2 illustrates the reorientation processes of V_α and B_α. If the relaxation is due to reorientation of V_α, its rate equals to $4w_0$, with w_0 being the jump frequency of a vacancy in the α sublattice, as there are four possible paths for the defect of orientation 3, for example, to reorient either to orientation 1 or to orientation 2. The relaxation rate is thus given by

$$\tau^{-1} = 12w_0. \tag{3}$$

In the case of reorientation of B_α, for the atom to change its position the destination site must be a vacancy. Thus, the reorientation rate is given by $4w_2C_1$, where w_2 is the exchange frequency of a V_α and a neighbouring B_α, and C_1 is the probability that an α sublattice site next to B_α is vacant. This leads to the following expression for the relaxation rate:

$$\tau^{-1} = 12w_2C_1. \tag{4}$$

If the defect species responsible for the relaxation is V_α, the activation energy is that of w_0, namely, the migration energy of vacancies in the α sublattice. On the other hand, if it is B_α, the activation energy is the sum of the activation energy of w_2, i.e. of $B_\alpha \leftrightarrow V_\alpha$ exchange, and the formation energy of a vacancy. The vacancy migration energy in Ni_3Al was evaluated to be 1.2 eV [11], to which the activation energies of w_0 and w_2 must be similar in magnitude. The vacancy formation energy was reported to be 1.8 eV [12]. As their sum is very close to the activation energy of the relaxation rate found for Ni_3Al ($\approx$ 3 eV), the relaxation effect is most probably due to reorientation of B_α.

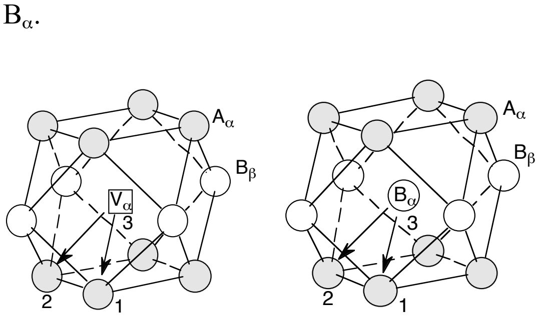

(a) (b)

Figure 2: Reorientation of (a) a vacancy, V_α, and (b) an antisite B atom, B_α, in the α sublattice.

3.3 Relaxation magnitude

The strength of anelastic relaxation, Δ, is defined as the relative change in the elastic compliance. In the case of measurements under shear stress, it is written as

$$\Delta = \frac{\delta G^{-1}}{G^{-1}}, \tag{5}$$

where G^{-1} denotes the shear compliance and δG^{-1} its variation associated with the relaxation. For the case of relaxation due to reorientation of defects of tetragonal symmetry in cubic crystals, it is given by

$$\delta G^{-1} = \frac{4}{3}\frac{c\Omega}{kT}|\lambda_1 - \lambda_2|^2 \Gamma , \tag{6}$$

where c is the defect concentration (in mol fraction), Ω the molar volume of the host crystal, λ_1 and λ_2 are the principal values of the characteristic strain tensor of the defect, and Γ is the so-called orientation factor, which is given from the direction cosines between the stress axis and the crystal axes as

$$\Gamma \equiv \gamma_2{}^3\gamma_3{}^3 + \gamma_3{}^3\gamma_1{}^3 + \gamma_1{}^3\gamma_2{}^3. \tag{7}$$

The relaxation strength in a single-crystal specimen of composition $Ni_{75.5}Al_{24.5}$ with $\Gamma = 0.1$ was measured under forced torsional oscillation to determine the magnitudes of the key factors in Eq. (6): the quantity $c|\lambda_1 - \lambda_2|^2$ was evaluated to be 1×10^{-4} at 950 K [5]. The equilibrium concentrations of intrinsic point defects in Ni_3Al were calculated using the Bragg–Williams model [5,6]: the concentration, c, at 950 K is estimated to be in the range from 10^{-9} to 10^{-8} and from $10^{-3.6}$ to $10^{-1.6}$ for V_α and B_α, respectively. The anisotropy in the characteristic strain, $\lambda_1 - \lambda_2$, was evaluated separately by molecular statics simulation [13]: +0.3 for V_α and –0.2 for B_α. For the two possible defect species, therefore, the product is predicted as follows:

Defect	$c\,|\lambda_1 - \lambda_2|^2$
V_α	10^{-10} to 10^{-9}
B_α	10^{-5} to 10^{-4}

It is the latter that agrees well with the experimental value, 1×10^{-4}. Thus, the magnitude of the relaxation also indicates that the observed effect is due to reorientation of antisite Al atoms on the Ni sublattice.

4 New experimental results

Detailed measurements of the relaxation have been carried out by isothermal mechanical spectroscopy by the sub-resonance forced vibration method on polycrystalline Ni_3Al of various compositions, from 24.1 to 26.4 mol % Al. No relaxation peak was detected for specimens of 24.1% Al, while the others, of 25.1, 25.8, 26.1 and 26.4% Al, exhibited the relaxation effect with varying magnitudes. Figure 3 shows the relaxation spectra of specimens of 25.8 and 26.1% Al. The solid curves in the figure are the Debye functions

$$J/J_U = 1 + \Delta \frac{1}{1+(\omega\tau)^2} \tag{8a}$$

$$\tan\phi = \Delta \frac{\omega\tau}{1+(\omega\tau)^2}, \tag{8b}$$

where J is the shear compliance, J_U is the unrelaxed compliance at a high-frequency limit, $\omega = 2\pi f$ is the angular frequency (with f being the frequency of forced vibration), and ϕ is the phase lag. For the spectrum at each temperature, Eq. (8b) is fitted to the data points of tan ϕ to determine the relaxation strength Δ and the relaxation time τ, and using these parameters the curve for the compliance is drawn according to Eq. (8a) to confirm the consistency.

The relaxation strength of each specimen at temperatures around 950 K are shown in Fig. 4 as a function of composition. Equation (6) predicts that the relaxation strength is proportional to the concentration of the responsible defect species. The observed magnitude increases with increasing Al concentration, in qualitative agreement with the prediction, as the concentration of the antisite atoms of Al, i.e., B_α, must exhibit the same trend. The absence of relaxation in specimens of 24.1% Al is understood that the magnitude is too small to be detected. In the same figure is displayed the concentration of B_α calculated by a simple statistical thermodynamic model (the Bragg–Williams approximation) with parameters chosen for Ni_3Al [6]. It turns out that the observed relaxation strength varies much more sensitively with the composition than the calculated concentration of antisite atoms. The dissociation between the experiment and theory at large deviations from stoichiometry may be attributed to reduced accuracy of the Bragg–Williams approximation at low degrees of order. This point will be discussed in more detail in a forthcoming paper.

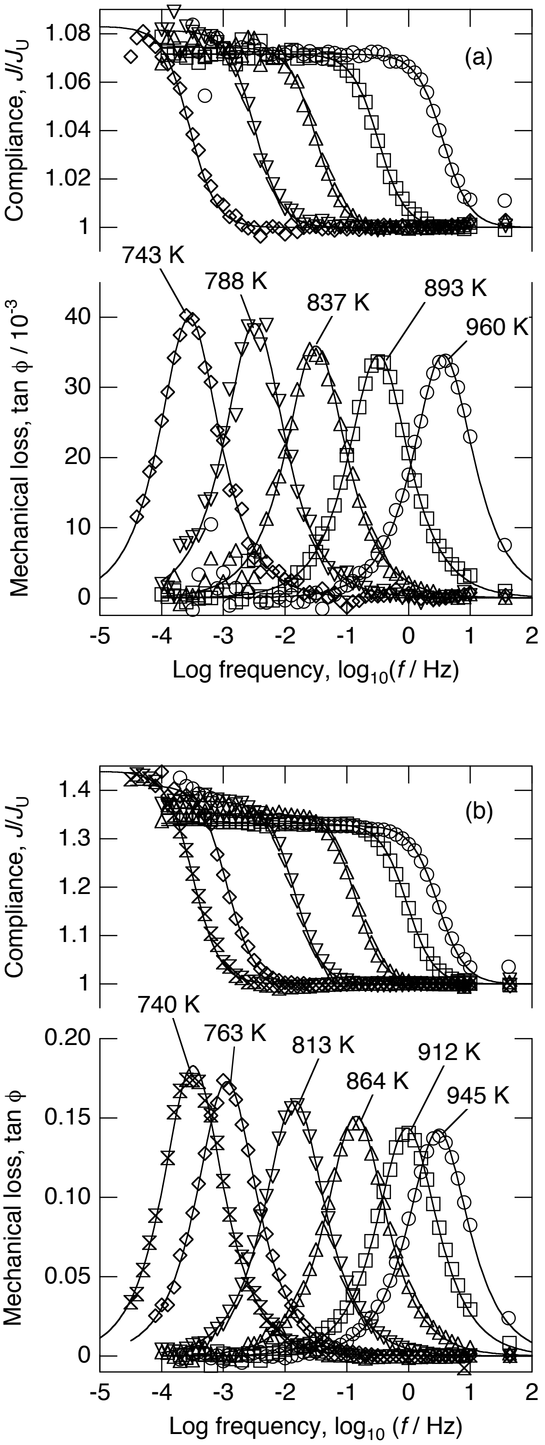

Figure 3: Isothermal relaxation spectra of polycrystalline Ni_3Al of (a) 25.8% Al and (b) 26.4% Al.

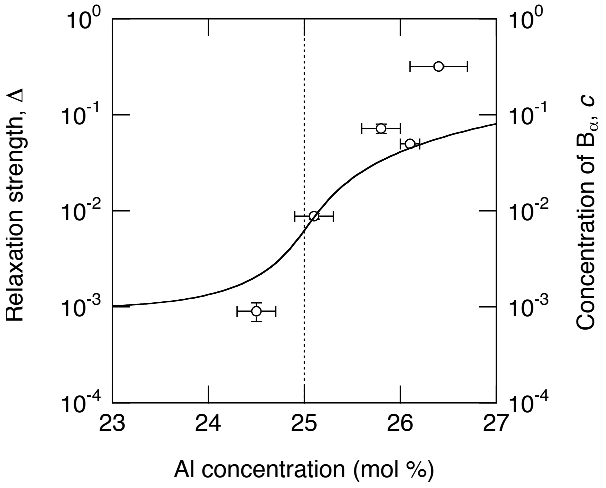

Figure 4: Relaxation magnitude in Ni_3Al at 950 K.

Figure 5 shows Arrhenius plots of the values of the relaxation time obtained by these measurements and those from measurements of logarithmic decrement in free-decay of resonance vibration at 40–70 Hz, together with those for a specimen of 24.5% Al [5]. The activation parameters evaluated by linear regression are summarized in Table 1. Note that the values of the last set are distinctly different from the present results for the hyper-stoichiometric alloys. By reference to Eq. (4), this is attributed to the variations of the activation energy of the jump frequency w_2 and the vacancy formation energy with composition. While the former may be assumed to be rather insensitive to composition, the latter is known to increase with increasing the concentration of Al [6,12], which is in agreement with the observation.

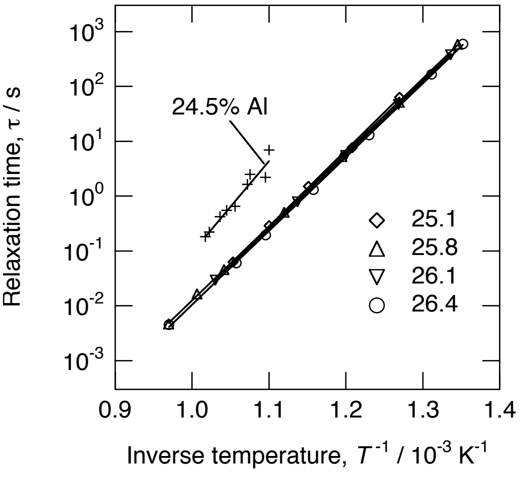

Figure 5: Arrhenius plots of the relaxation time in Ni_3Al of various compositions.

Table 1: Activation parameters of the relaxation time in Ni_3Al of composition x (mol % Al).

x	$\log_{10}(\tau_0 / \mathrm{s})$	E / eV
24.5 ± 0.2	−17.7 ± 0.4	3.31 ± 0.07
25.1 ± 0.2	−15.8 ± 0.6	2.75 ± 0.11
25.8 ± 0.2	−15.37 ± 0.07	2.673 ± 0.012
26.1 ± 0.1	−15.37 ± 0.08	2.665 ± 0.014
26.4 ± 0.3	−15.43 ± 0.09	2.669 ± 0.014

5 Diffusion coefficient

In the $L1_2$ ordered structure, atoms of the majority species are expected to diffuse in their own sublattice by the ordinary vacancy mechanism, as the α sublattice sites at nearest-neighbour distances are 'connected' to form a continuous network. On the other hand, since each β sublattice has no sites of the same type at the nearest-neighbour distance, a nearest-neighbour jump of a B atom out of a β sublattice site leads to a formation of an antisite defect, disrupting, even though locally and momentarily, the ordered atomic arrangement. It is to be noted, however, that such antisite atoms are present in thermal equilibrium even in a material of stoichiometric composition. Those atoms may then contribute to long-range diffusion of the minority species by migrating through the α sublattice by the vacancy mechanism as impurity diffusion [6].

Figures 6 (a) and 6 (b) show some of the atomic jumps relevant to the diffusion of A atoms and B atoms, respectively, mediated by vacancies in the α sublattice. The diffusion coefficients of the two species of atoms by these mechanisms are expressed, by assuming the five-jump frequency model for the impurity diffusion for the latter, as

$$D_A^* = \frac{2}{3} a^2 C_1 w_0 f_0, \tag{9a}$$

$$D_B^* = \frac{2}{3} a^2 C_1 \frac{w_4}{w_3} w_2 f p_\alpha, \tag{9b}$$

where a is the lattice parameter, f_0 is the correlation factor for the vacancy mechanism in the α sublattice (which is equal to 0.689), w_3 and w_4 are the jump frequencies of V_α that associates and dissociates a nearest-neighbour pair of V_α and B_α (w_4 is the reverse jump of w_3 and is not displayed explicitly in the figure), and f is the correlation factor for impurity diffusion in the α sublattice, which is a function of all of the five frequencies, including w_1, which does not appear directly in Eq. (9b). The last factor p_α is the fraction of antisite B atoms defined as follows, and is related to the long-range order parameter η as

$$p_\alpha \equiv \frac{N_{B_\alpha}}{N_{B_\alpha} + N_{B_\beta}} = \frac{3}{4}\left(1 - \frac{\eta}{4x_B}\right), \tag{10}$$

with N_i being the number of species i and x_B the bulk composition, i.e. the mol fraction of B.

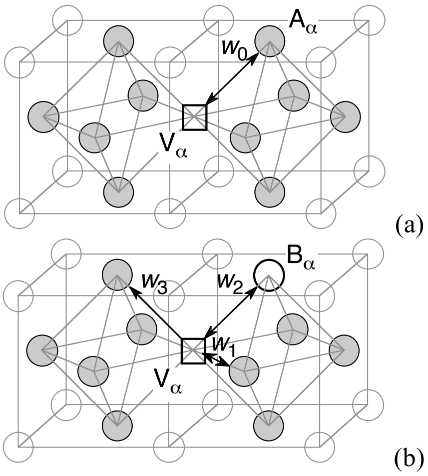

Figure 6: The diffusion of A atoms (a) and B atoms (b) mediated by vacancies in the α sublattice. The jump frequencies are denoted using the convention in the five-jump frequency model for impurity diffusion.

If the α sublattice vacancy mechanism is operative for the diffusion of B species, the jumps of antisite B atoms that give rise to the anelastic relaxation, which are depicted in Fig. 2(b), constitute the elementary process of the diffusion. In that case the relaxation rate can be related to the diffusion coefficient by substituting Eq. (4) into Eq. (9b),

$$D_B^* = \frac{1}{18} a^2 \frac{w_4}{w_3} f p_\alpha \tau^{-1}. \tag{11}$$

Although it is not generally easy to determine the jump frequencies w_3 and w_4 by experiment or even the ratio w_4/w_3, which is the Boltzmann factor for the binding of a nearest-neighbour pair of V_α and B_α, it is possible to estimate them by theoretical calculation or computer simulation, which was in fact done for Ni_3Al [13]. Then the correlation factor f, which is a function of those jump frequencies, can also be calculated [13]. The fraction of antisite B atoms, p_α, can be evaluated with the aid of a statistical thermodynamic model [6]. Thus, the diffusion coefficient of the B species can be derived from the rate of the anelastic relaxation using Eq. (11).

Figure 7 shows the tracer diffusion coefficient of Al in Ni_3Al evaluated by this procedure. The diffusion coefficient of Al turns out to be larger at higher Al concentrations. It is understood naturally in terms of the variation of the concentration of antisite Al atoms with composition, or the factor p_α, which increases significantly with the increase in the bulk concentration of Al over the stoichiometric composition. In the same figure are shown the tracer diffusion coefficient of Ni in Ni_3Al [8,9] and that of Al at the stoichiometric composition estimated from the chemical diffusion coefficient in Ni_3Al [14]. The latter is about 1/3 in magnitude of the former at the temperature of $0.85T_m$, or 1400 K.

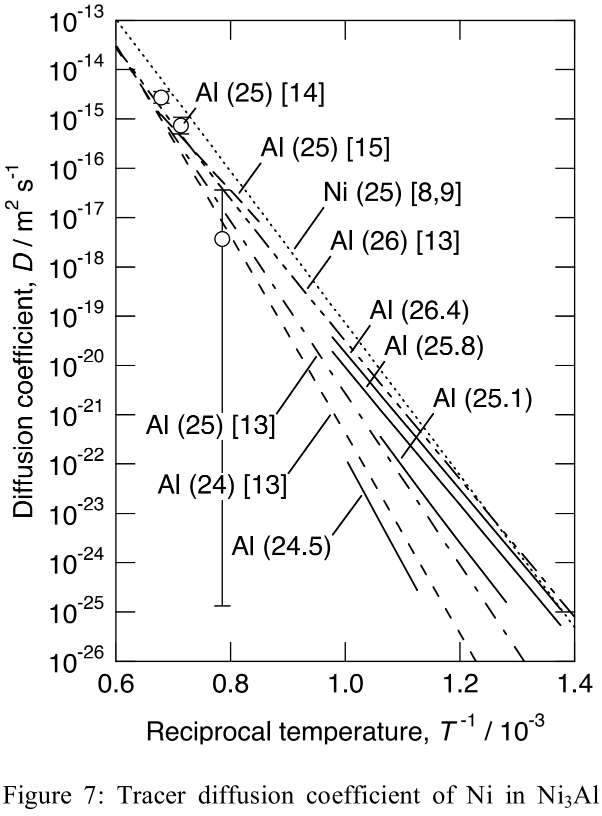

Figure 7: Tracer diffusion coefficient of Ni in Ni_3Al [8,9], that of Al in Ni_3Al calculated on the basis of the results of computer simulation [13], those estimated from the chemical diffusion coefficient [14,15], and those obtained from the rate of the anelastic relaxation in the present work (solid lines). Numbers in parentheses are compositions in mol% Al.

When the values of the diffusion coefficient of Al determined from the relaxation rate are compared with an extrapolation of the diffusion coefficient of Ni, the value for 27% Al is about half an order of magnitude smaller, while that for 24.5% Al is much smaller, by nearly three orders of magnitude. This can be interpreted as the effect of rapid decrease in the antisite atom concentration at compositions below the stoichiometry, particularly at low temperatures. As expected from the expressions for the diffusion coefficients, Eqs. (9a) and (9b), the activation energy of the diffusion of the minority species must be larger than that of the majority species by the temperature dependence of the antisite atom concentrations.

5 Importance and utility of relaxation measurements

Anelastic relaxation effects due to redistribution of point defects can prove a method for determining the diffusion coefficient, and for the case of low-frequency measurements the range of the magnitudes of the diffusion coefficient is commonly below 10^{-14} m^{2}s^{-1}, which are difficult to obtain by conventional methods of diffusion measurements. As mentioned in Introduction, however, the conversion from the relaxation rate to the diffusion coefficient is possible only if the mechanisms of the relaxation and diffusion are both known. Now that it appears highly probable that the relaxation is due to reorientation of antisite Al atoms in Ni_3Al and at the same time the diffusion of Al occurs mostly by the α sublattice vacancy mechanism. One can therefore calculate one quantity from the other the relation, Eq. (11), although evaluating the quantities involved in the relation is not straightforward.

Clearly it is possible to apply this relation to any material of the $L1_2$ structure, provided that the α sublattice vacancy mechanism is operative. A work is now in progress to find a corresponding relaxation effect in ordered alloys and intermetallic compounds of the $L1_2$ structure. Note, however, that it is not guaranteed whether one can observe the relaxation effect due to the reorientation; even if the relaxation is taking place, the magnitude of the relaxation, which is governed by the anisotropy of the strain field around the defect, $|\lambda_1-\lambda_2|$, may be too small to be detected. Nevertheless, the relation between the relaxation rate and the diffusion coefficient is particularly useful for the case of $L1_2$ ordered alloys and compounds with Al as the minority species, Ni_3Al as a representative example, in view of the fact that radioactive tracers of Al suitable for tracer diffusion experiments are hardly available. In fact, while several sets of data have been reported for the tracer diffusion of Ni in Ni_3Al, there are no reliable data of the tracer diffusion of Al. In this respect, relaxation experiments provide an important means of determining the diffusion coefficient of Al.

Similar relaxation effect is expected to occur in compounds of the structure in which the point symmetry of the site of one of the constituents is lower than the symmetry of the host lattice, and in that case a relation between the relaxation rate and the diffusion coefficient of the defect on that site may be established. An example is ternary ABX_3 compounds of the $E2_1$ (perovskite) structure. It is actually a structure derived from $L1_2$; it is formed by introducing the species A at the body-centred site of the cubic unit cell of the $L1_2$ structure of a binary compound BX_3. There are a number of transition metal oxides of this structure, where important applications may be found; it will be a unique tool for measuring the diffusion of oxygen vacancies in those oxides that are, for instance, candidates for oxygen conductors in solid oxide fuel cells. As the operating temperature of the fuel cells is desired to be as low as possible, the method, which is applicable to measuring diffusion at low temperatures where conventional radiotracer experiments are difficult, should find its utility.

6 Summary and conclusions

The results of detailed measurements confirm that the anelastic relaxation effect observed for Ni_3Al is due to stress-induced reorientation of antisite Al atoms in the α sublattice. On the assumption of the α sublattice vacancy mechanism, the tracer diffusion coefficient of Al in Ni_3Al has been derived from the relaxation rate. The calculated values appear to be consistent with those at high temperatures estimated from chemical diffusion experiments. Since this relaxation effect can occur in principle in any compounds or alloys of the same structure and also in materials of related structures, it provides a useful means of determining the relevant diffusion coefficient, in particular that of very small magnitude, by anelastic relaxation measurements.

Acknowledgements

The author wishes to thank Dr P. Gadaud, Messrs Uedi T. and Nishi K. for collaboration. This work was supported by Grant-in-Aid for Scientific Research by the Japanese Ministry of Education, Science, Culture and Sports (Basic Research B 13559004 and Basic Research C 17560584), Materials Science Research Foundation, Tokyo, Japan, and Iketani Science and Technology Foundation, Tokyo, Japan.

References

[1] Gadaud, P., Chakib, K.: *Mater. Sci. Forum*, 119–121, p. 397, 1993.

[2] Chakib, K.: Thesis, University of Poitiers, 1993.

[3] Mourisco, A., Baluc, N., Bonneville, J., Schaller, R.: *J. Phys.* (Paris) IV, Colloque 8, p. C8-235, 1996.

[4] Mourisco, A., Baluc, N., Bonneville, J., Schaller, R.: *Mater. Sci. Eng.* A, 239–240, p. 281, 1997.

[5] Numakura, H., Kurita, N., Koiwa, M., Gadaud, P.: *Phil. Mag.* A, 79, p. 943, 1999.

[6] Numakura, H., Ikeda, T., Koiwa, M., Almazouzi, A.: *Phil. Mag.* A, 77, p. 887, 1998.

[7] Numakura, H., Ikeda, T., Nakajima, H., Koiwa, M.: *Mater. Sci. Eng.* A, 312, p. 109, 2001.

[8] Frank, S., Södervall, U., Herzig, C.: *Phys. Stat. Sol.* (b), 191, p. 45, 1995.

[9] Shi, Y., Frohberg, G., Wever, H.: *Phys. Stat. Sol.* (a), 152, p. 361, 1995.

[10] Nowick, A. S., Berry, B. S.: *Anelastic Relaxation in Crystalline Solids*, Academic Press, New York, 1972.

[11] Wang, T.-M., Shimotomai, M., Doyama, M.: *J. Phys.* F: *Met. Phys.*, 14, p. 37, 1984.

[12] Badura-Gergen, K., Schaefer, H.-E.: *Phys. Rev.* B, 56, p. 3032, 1997.

[13] Numakura, H., Kurita, N., Koiwa, M.: *Solid-Solid Phase Transformations PTM'99*, Edited by M. Koiwa, K. Otsuka and T. Miyazaki, The Japan Institute of Metals, Sendai, p. 465, 1999.

[14] Ikeda, T., Almazouzi, A., Numakura, H.,

Koiwa, M., Sprengel, W., Nakajima, H.: *Acta Mater.*, 46, p. 5369, 1998.

[15] Cserháti, C., Paul, A., Kodentsov, A. A., van Dal, M. J. H., van Loo, F. J. J.: *Intermetallics*, 11, p. 291, 2003.

Proceedings of The 1st International Conference on Diffusion in Solids and Liquids
DSL-2005, July 6-8, 2005, University of Aveiro, Aveiro, Portugal

DIFFUSION IN THE Ir–Nb SYSTEM

WATANABE Tatsuru[1], UCHIDA Makoto[1], NUMAKURA Hiroshi[1,*],
YAMABE-MITARAI Yoko[2], BANNAI Eisuke[2]

[1] Department of Materials Science and Engineering, Kyoto University, Sakyo-ku, Kyoto 606–8501, Japan
[2] National Institute for Materials Research, Sengen 1–2–1, Tsukuba 305–0047, Japan

[*]Corresponding author. Fax: +81 75 753 4978; Email: hiroshi.numakura@materials.mbox.media.kyoto-u.ac.jp

---

Abstract

The diffusion behaviour of Ir-rich Ir–Nb alloys has been studied by interdiffusion experiments. The chemical diffusion coefficient has been measured in the Ir-rich fcc solid-solution and the $L1_2$ ordered compound Ir_3Nb has been measured in the temperature range between 1750 and 1950°C, using Ir / Ir–8%Nb and Ir–26%Nb / Ir–28%Nb single-phase diffusion couples, respectively. While the diffusion coefficient in the solid-solution phase turns out to be similar in magnitude to the tracer self diffusion coefficient in pure iridium, the diffusion in the $L1_2$ compound has been found to be extremely slow: the diffusion coefficient is about 1/20. The low diffusion rate in the compound phase must be beneficial for high-temperature performance of refractory superalloys based on the Ir–Nb system.

Keywords: Refractory superalloys; Chemical diffusion; Single-phase interdiffusion; Electron-probe microanalysis

---

1 Introduction

Alloys based on iridium, rhodium and platinum are attracting growing interest recently as ultra-high-temperature materials, aiming at operating temperature far exceeding those of current nickel-base superalloys [1]. While the microstructure, mechanical properties and their relationships have been studied extensively [2,3], much work is needed on the basic material properties, including atomic diffusion, which controls stability and performance at elevated temperatures.

In the present investigation we have studied the diffusion in the constituent phases of the two-phase (A1 + $L1_2$) Ir–Nb alloys, which is a leading candidate for *refractory superalloys* of the next generation. The chemical diffusion coefficient in the A1 (fcc solid-solution) and the $L1_2$ ordered compound phases has been measured by single-phase interdiffusion experiments. Part of the present work has been published elsewhere [4].

2 Experimental

2.1 Specimens

Single crystals and coarse-grained polycrystals of pure iridium, Ir–8Nb, Ir–26Nb and Ir–28Nb alloys were used, where the numbers denote the concentration of Nb in mol per cent. They were rods of about 5 mm in diameter and 20 mm in length grown by optical floating-zone melting. The exact compositions of the alloys were later determined by electron-probe microanalysis.

Discs of about 3 mm in thickness were sectioned by spark erosion. After polishing the surfaces, every pair discs, either of Ir / Ir–8Nb or of Ir–26Nb / Ir–28Nb, was diffusion-bonded at 1400 or 1500°C, for 1 h in a vacuum, under compressive stress of 10 MPa. Each pair was then cut perpendicularly to the bonded interface into four pieces. The diffusion couples thus prepared were diffusion-annealed in a vacuum furnace maintained below 5×10^{-4} Pa.

2.2 Measurements of concentration profiles

Composition versus distance profiles were measured by wavelength dispersive electron-probe microanalysis with acceleration voltage of 15 kV, beam current of 10 nA and probe size of about 1 μm. Intensities of Ir Mα and Nb Lα characteristic X-rays were measured by step-sweeping across the bonded interface over a distance of about 10 times the expected diffusion distance. The composition at each point was calculated with the standard ZAF correction [5] using pure iridium and pure niobium as reference materials. At least three profiles were obtained and were averaged to reduce statistical errors.

3 Results and discussion

3.1 Determination of diffusion coefficient

Figures 1 (a) and 1 (b) show the averaged concentration profiles in diffusion couples of the A1 solid-solution phase and of the $L1_2$ phase, respectively, annealed at 1900°C. The annealing time was 64 h for the former and 192 h for the latter. It is immediately apparent that the diffusion is much slower in the $L1_2$ compound phase than in the A1 solid-solution phase; the extent of the diffusion zone in Fig. 1 (b) is about 1/4 of that in Fig. 1 (a) in spite of the longer annealing time.

The chemical diffusion coefficient, D, has been evaluated by fitting the standard error-function profile to the measured data,

$$c(x,t) = \frac{c_1 + c_2}{2} - \frac{c_1 - c_2}{2} \operatorname{erf}\left(\frac{x - x_0}{2\sqrt{Dt}} \right), \tag{1}$$

with four adjustable parameters, c_1, c_2 (the terminal concentrations), x_0 (the co-ordinate centre) and $2\sqrt{(Dt)}$ (the diffusion distance, with t the annealing time). In none of the experimental data has been found significant deviation from a symmetrical profile described by Eq. (1); D can therefore be assumed constant. The values of D thus obtained are summarized in Table 1.

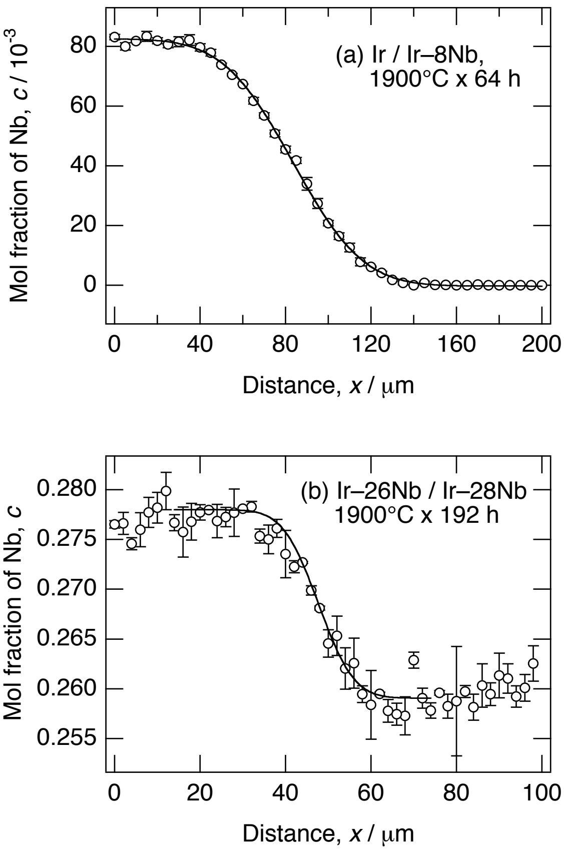

Figure 1: Concentration profiles in diffusion couples of (a) Ir / Ir–8Nb and (b) Ir–26Nb / Ir–28Nb. The circles and the solid curve show measured concentrations and the fitted error-function profile, respectively.

Table 1: Chemical diffusion coefficient D in the A1 solid-solution and $L1_2$ ordered phases of Ir–Nb alloys obtained from Ir / Ir–8Nb and Ir–26Nb / Ir–28Nb diffusion couples annealed at temperature T for time t.

Phase	T / °C	t / h	D / m^2s^{-1}
A1	1650	672	$(4.05 \pm 0.23) \times 10^{-17}$
	1700	312	$(8.82 \pm 0.75) \times 10^{-17}$
	1750	168	$(1.89 \pm 0.10) \times 10^{-16}$
	1850	96	$(7.30 \pm 0.51) \times 10^{-16}$
	1900	64	$(1.49 \pm 0.05) \times 10^{-15}$
$L1_2$	1750	408	$(4.9 \pm 1.3) \times 10^{-18}$
		1128	$(4.2 \pm 0.9) \times 10^{-18}$
	1800	96	$(9.5 \pm 2.9) \times 10^{-18}$
		384	$(9.0 \pm 2.9) \times 10^{-18}$
	1850	96	$(1.9 \pm 0.5) \times 10^{-17}$
		288	$(2.0 \pm 0.4) \times 10^{-17}$
	1900	192	$(3.1 \pm 0.9) \times 10^{-17}$
		192	$(3.6 \pm 0.9) \times 10^{-17}$
	1950	96	$(5.1 \pm 1.0) \times 10^{-17}$

3.2 Temperature dependence of diffusion

Figure 2 shows Arrhenius plots of the chemical diffusion coefficients in the two phases obtained in this work and the tracer self-diffusion coefficient in pure iridium in the literature [6]. Both the plots can be expressed by the Arrhenius-type formula,

$$D = D_0 \exp(-Q/kT), \tag{2}$$

with the pre-exponential factor $D_0 = 10^{-2.80 \pm 0.41}$ m^2s^{-1} and the activation energy $Q = 5.19 \pm 0.17$ eV for the A1 solid-solution phase, with $D_0 = 10^{-5.3 \pm 1.1}$ m^2s^{-1} and $Q = 4.83 \pm 0.44$ eV for the $L1_2$ compound phase (with k the Boltzmann constant). The Arrhenius parameters for the tracer self-diffusion coefficient of iridium are $D_0 = 10^{-4.44}$ m^2s^{-1} and $Q = 4.548$ eV.

According to the empirical rule for the self-diffusion in pure metals [7], the tracer self-diffusion coefficient at the melting temperature T_m takes a similar value for the same class of metals and the activation energy is roughly proportional to the melting temperature. For the particular case of metals of the A1 structure, the rules can be expressed as

$$D(T_m) \approx 10^{-12.26}\ m^2s^{-1}\,, \tag{3a}$$

$$Q \approx 18.4\ kT_m\,. \tag{3b}$$

The diffusion properties of pure iridium and the Ir–Nb alloys are compared in Table 2 in reference to these relations. (This comparison is, however, tentative because chemical diffusion coefficient has never been in the scope of the rule and, moreover, chemical diffusion is a complex phenomenon and may not obey the Arrhenius law). The self-diffusion behaviour of pure iridium conforms well to the empirical rule. We find here that the activation energies in the A1 and $L1_2$ phases of the Ir–Nb alloys agree fairly well with the rule, Eq. (3b). On the other hand, the absolute magnitude of the diffusion coefficient at the melting temperature is notably small for the $L1_2$ phase. As it is already obvious in the original experimental data presented in Fig. 2, the slow diffusion in the $L1_2$ compound is due largely to the small pre-exponential factor, $10^{-5.3}$ m^{2}s^{-1}, in comparison to the value of $10^{-4.3}$ m^{2}s^{-1} lead from Eqs. (3a) and (3b). In any case, the slow diffusion in the $L1_2$ phase must be a good advantage for high-temperature performance: microstructural stability and resistance to diffusional creep deformation.

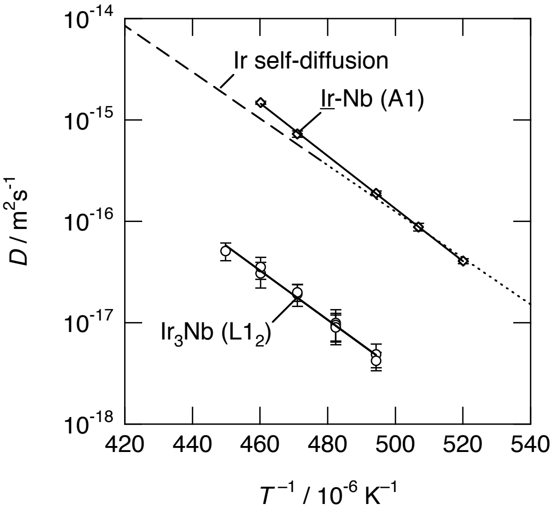

Figure 2: Arrhenius plots of the chemical diffusion coefficients of Ir–Nb alloys of the A1 solid-solution phase and of the $L1_2$ compound phase. The dashed line shows the tracer self-diffusion coefficient of pure iridium [6], and the dotted line is its extension.

Table 2: Characteristics of the tracer self-diffusion of iridium, chemical diffusion of Ir–Nb alloys in reference to the empirical rule.

Phase	T_m / K	$\log_{10}$ ($D(T_m)$ / m^{2}s^{-1})	Q/kT_m
Ir, self (A1)	2720	−12.87	19.40
Ir–Nb (A1)	2693*	−12.5 ± 0.7	22.4 ± 0.7
Ir_3Nb ($L1_2$)	2708	−14.3 ± 1.9	20.7 ± 1.9

* The solidus temperature of Ir–4%Nb.

3.3 Chemical diffusion and tracer diffusion

The chemical diffusion coefficient in a binary solid-solution alloy is related to the tracer diffusion coefficient of constituent species, D_1^* and D_2^*, by the formula derived by Darken [8] and later modified by Manning [9], namely,

$$D = (D_1^* N_2 + D_2^* N_1)\ \Phi\ S, \tag{4}$$

where N_1 and N_2 are mole fractions of the constituents 1 and 2, respectively, Φ is the thermodynamic factor and S is the vacancy wind factor. Recent discussion suggests that this relation is applicable to $L1_2$ and some other ordered alloys [10,11].

Because of the reciprocal arithmetic average in Eq. (4), the chemical diffusion coefficient in the Ir / Ir–8Nb solid–solution diffusion couples depends primarily on the tracer diffusion coefficient of Nb in the alloy, for which no experimental data have been reported. According to a preliminary thermodynamic assessment of the Ir–Nb system [12], the thermodynamic factor Φ in the temperature range of the present measurements varies from 1 to 3 with increasing the Nb concentration up to 8%. The tracer diffusion coefficient of Nb in the solid solution phase is thus suggested to be slightly smaller in magnitude than the chemical diffusion coefficient and decreasing with Nb concentration, since the chemical diffusion coefficient turned out to be independent of composition. (The effect of the vacancy wind factor S is generally small and may be ignored except for detailed analyses.)

In comparison to solid-solution alloys the role of the thermodynamic factor is in general much more pronounced in ordered alloys: Φ can be much larger than in the solid-solution phase and may exhibit a sharp maximum at the stoichiometric composition in chemically stable compounds. The magnitude of Φ in the range of 26–28% Nb has been estimated to be about 20 [12]. Variations of the diffusion coefficient with composition may not be detected in the present measurements, on the other hand, since the range of compositions is in the same side of off-stoichiometry and is limited to only 2%. The Darken–Manning equation thus suggests that the tracer diffusion coefficients of Ir and Nb, the latter in particular, in Ir_3Nb are further smaller than the chemical diffusion coefficient by more than an order of magnitude.

In a foregoing report of the chemical diffusion in Ir_3Nb [4], the diffusion rates in the A1 and $L1_2$ phases that constitute nickel-base superalloys and Ir–Nb alloys of the same design were compared in a homologous scale of temperature. While the self-diffusion of nickel and iridium are similar in magnitude to each other and the chemical diffusion in Ni_3Al falls in the same range, the chemical diffusion in Ir_3Nb is slower by more than an order of magnitude. It is interesting to explore the remarkably slow diffusion in Ir_3Nb: whether or not the mechanism is similar to the case of Ni_3Al and related compounds [13], and how chemical stability influences atomic diffusion in ordered compounds.

4 Summary and concluding remarks

Chemical diffusion coefficients in Ir–Nb alloys of the A1 solid-solution and $L1_2$ ordered compound phases have been measured by single-phase interdiffusion experiments. The diffusion coefficient in the A1 phase (from 0 to 8 mol % Nb) is roughly equal to the tracer self-diffusion coefficient of pure iridium, while it is about 1/20 in the $L1_2$ phase.

Refractory superalloys are tailored to consist of the two-phases, A1 and $L1_2$, with cuboidal microstructure. While the slow diffusion in the compound phase is advantageous for high-temperature applications, the diffusion behaviour of the solid-solution alloy is not unusual. Since the creep resistance of solid-solution Ir–Nb alloys is in fact much lower than $L1_2$ compounds [14], it is desired to work on a design for lowering the diffusion rates in the A1 phase to improve further the overall performance at elevated temperatures.

Acknowledgments

This work is partly supported by Grant-in-Aid for Scientific Research, Basic Research (C), 1756-0584, from the Ministry of Education, Culture, Sports, Science and Technology, Japan. The financial support for the participation of the author in the conference by Iketani Science and Technology Foundation, Tokyo, Japan, is gratefully acknowledged.

References

[1] See, e.g., *JOM*, 56 (9), 2004, and *Metall. Mater. Trans.* A, 36A (3), 2005.

[2] Yamabe-Mitarai, Y., Ro, Y., Maruko, T., Harada, H.: *Metall. Mater. Trans.* A, 29A, 537, 1998.

[3] Yamabe-Mitarai, Y., Gu, Y., Harada, H.: *Metall. Mater. Trans.* A, 34A, 2207, 2003.

[4] Uchida, M., Numakura, H., Yamabe-Mitarai, Y., Bannai, E.: *Scripta Mater.*, 52, 11, 2005.

[5] Goldstein, J. I., et al.: *Scanning Electron Microscopy and X-ray Microanalysis*, 2nd edition, Plenum Press, New York and London, 1992.

[6] Mehrer, H.: *Diffusion in Solid Metals and Alloys*, Landolt-Börnstein New Series, Group III, vol. 26, Springer Verlag, Berlin, 1990.

[7] Brown, A. M, Ashby, M. F.: *Acta Metall.*, 28, 1085, 1980.

[8] Darken, L. S.: *Trans. AIME*, 175, 184, 1948.

[9] Manning, J. R.: *Acta Metall.*, 15, 817, 1967.

[10] Belova, I. A., Murch, G. E.: *Phil. Mag.* A, 78, 1085, 1998.

[11] Ikeda, T., Almazouzi, A., Numakura, H., Koiwa, M., Sprengel, W., Nakajima, H.: *Acta Mater.*, 46, 5369, 1998.

[12] Abe, T.: private communication, 2005.

[13] Numakura, H., Ikeda, T., Nakajima, H. Koiwa, M.: *Mater. Sci. Eng.* A, 312, 109, 2001.

[14] Yamabe-Mitarai, Y., Harada, H., Gu, Y., Huang, C.: *Metall. Mater. Trans.* A, 36A, 547, 2005.

Proceedings of The 1st International Conference on **D**iffusion in **S**olids and **L**iquids
DSL-2005, July 6-8, 2005, University of Aveiro, Aveiro, Portugal

POSITRON LIFETIME MEASUREMENT ON CENTRIFUGED Bi_3Pb_7 INTERMETALLIC COMPOUND

Masao ONO[1,*], Xinsheng HUANG[2], Yasuhiro SHIBATA[2], Yusuke IGUCHI[2],

Seiji SAKAI[1], Masaki MAEKAWA[1], Z. Q. CHEN[1], Toyotaka OSAKABE[1],

Atsuo KAWASUSO[1], Hiroshi NARAMOTO[1], Tsutomu MASHIMO[1, 2, *]

1 Advanced Science Research Center, Japan Atomic Energy Research Institute,
Tokaimura, Nakagun, Ibaraki Prefecture 319-1195, Japan
2 Shock Wave and Condensed Matter Research Center, Kumamoto University,
2-39-1 Kurokami, Kumamoto 860-8555, Japan

* Corresponding author. Fax: +81-29-282-5927; E-mail: masao@popsvr.tokai.jaeri.go.jp
mashimo@gpo.kumamoto-u.ac.jp

Abstract

Recently, we formed atomic-scale graded structures in some miscible alloys and observed the decomposition in Bi_3Pb_7 intermetallic compound by sedimentation of atoms under strong gravitational field. In this study, we measured positron lifetime of centrifuged Bi_3Pb_7, in which the composition change was very small as it was treated at low temperature. It was found that the positron lifetime became longer than that of starting state. This indicated that the point defects (vacancy or divacancy) increased in the sample by centrifugal treatment.

Keywords: Diffusion in crystalline and amorphous materials; Sedimentation; Positron lifetime; Ultracentrifuge; Intermetallic compound

---

1 Introduction

Sedimentation of atoms in condensed matter can be used to control the composition and structures, based on difference in atomic weight and volume. These materials are expected to show unique electric and optical properties. However, sedimentation of atoms is very difficult to realize in solids or liquids, because the chemical potential of the atoms is usually much greater than the mechanical energy. No sedimentation of substitutional solute atoms in alloys or compounds has ever been reported until our previous study.

To study sedimentation of atoms or crystal-chemical instability in solids under a strong acceleration field, we had developed two types of ultracentrifuges that can generate an acceleration of over $1x10^6$ g for long time duration at elevated temperature [1,2]. Using these apparatus, we formed atomic-scale graded structures in some miscible alloys and observed the decomposition in Bi_3Pb_7 intermetallic compound by sedimentation of atoms under strong gravitational field [3-7]. It was also found that the sedimentation of atoms under strong gravitational field was very fast [6,8]. This indicates that the diffusion mechanism of the sedimentation should be different from the conventional one. About the sedimentation mechanism, we are still under investigation.

In this study, the ultra-centrifuge experiments were performed on an intermetallic compound of Bi-Pb system alloy (Bi_3Pb_7). And, we measured the positron lifetime of the sample and investigated the point defects to get some information to discuss the mechanism of sedimentation of atoms.

Table 1: Positron lifetime of samples (Bi-Pb system).

Samples		Annealing (h)	Centrifugation (h)	Life Time (ps)
Standard	0%Bi	24	0	187.7
	20%Bi	24	0	194.0
	Bi_3Pb_7	24	0	199.0
	60%Bi	24	0	209.6
	100%Bi	24	0	216.6
Centrifuged (Bi_3Pb_7)	A side	24h before centrifugation	100	210.0
	A' side			199.3

2 Experimental procedure

We used an ultracentrifuge of *JAERI* one (*JAERI* Facility) for centrifugal treatment. The samples were contained in a rotor with an outer diameter of 80.4 mm made of a titanium alloy. The maximum distance from the axis of rotation in a specimen was about 35.8 mm.

The Bi_3Pb_7 lump shaped starting sample was prepared by melting the Bi and Pb shots (composition: 30:70 mol%, atmosphere: 10^{-4}Pa, purity: 5N, temperature: 450°C), and by annealing it for 24 hours. The sample was cut into a plate with a diameter of 5 mm, and was set into SUS304 made capsule with an inner diameter of 5 mm. The sample can be lay perpendicular to the centrifugal force with a capsule as shown in Fig.1-a). The plate shaped sample helped us to demonstrate the positron annihilation lifetime measurement (PAL) as we need to sandwich the radiation sauce with two samples and set detectors on the other sides.

The ultracentrifuge experiments were performed at a rotational speed of around 15,1000 rev.min^{-1} i.e. 812,000G and a temperature of 120°C for 100 hours. It was not expected remarkable composition change same as the previous work at the temperature [7]. Usually, the composition profiles influence on positron lifetime in bulk body. We need centrifuged sample that has small composition change to avoid the composition change influencing on positron lifetime.

PAL is suitable for discovering open-volume defects in the bulk body such as vacancies. If there are vacancies and positrons trap in them, the lifetime becomes longer than that of annihilating in prefect crystal. More over, positron lifetime in an open-volume defect depends on how many vacancies compose the defect. That is, the positron has different lifetime in a vacancy or a divacancy or a void [9,10]. So we can identify what kind of point defects are distributing in the sample by PAL. Positron lifetime in bulk body will be influenced not only by point defects but also by composition profiles. The average positron lifetime in standard samples with different composition are summarised in Table 1. The higher the composition of Bi becomes, the longer the positron lifetime becomes in this system.

3 Results and Discussions

Fig. 1-b) is the SEM image of the cut plane of the sample and the composition profiles by EPMA line analysis on A-A' in the figure. The component analysis was carried out using the EPMA (JXA-8900R (JEOL Ltd., Tokyo, Japan). The change of composition profiles was very small form starting state of Bi:Pb=70:30 at.%. We performed the PAL measurement on both surface that were perpendicular to A-A'. The average positron lifetime in the centrifuged sample were summarised in Table 1.

At the surface of maximum gravity side (A'), the average positron lifetime was 199.3ps almost the same as starting state. It showed that the concentration of vacancies around the area was almost the same as starting state. On the contrary,

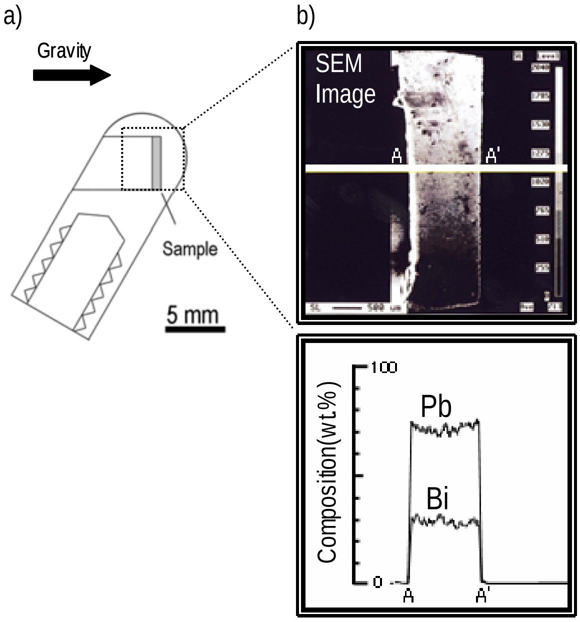

Figure 1: a) Sample image in a capsule, b) SEM image and EPMA line analysis.

at the surface of minimum gravity side (A), the average positron lifetime was 11ps longer than that of starting state. The lifetime of 210ps at A was almost same as 60 at.% Bi alloy. In this case, the long averaged lifetime was not due to the composition change as it was very small but due to point defects. Detector had counted the lifetime of 300ps at A. The positron lifetime in divacancy in metal was around 300ps [9]. So, it was found that divacancis distributed around A, in other word, the concentration of vacancies around the area was higher than that of starting state.

We performed PAL measurement not under centrifugal treatment but after centrifugation. It was considered that there had been more point defects under centrifugal treatment because high temperature should have lead high concentration of thermal vacancies. The relationship between the increase of point defects and sedimentation of atoms are now under investigation.

Acknowledgments

This work was partially supported by Grant-in-Aid for Scientific Research and The Mitsubishi Foundation.

References

[1] Mashimo, T., Okazaki, S., Shibazaki, S.: Ultracentrifuge apparatus to generate a strong acceleration field of over 1,000,000 g at high temperature in condensed matter: *Rev. Sci. Instr.*, 67, pp. 3170-3174, 1996.

[2] Mashimo, T., Huang, X.S., Osakabe, T., Ono, M., Nishihara, M., Ihara, H., Sueyoshi, M., Shibasaki, K., Shibasaki, S., Mori, N.: Advanced high-temperature ultracentrifuge apparatus for Mega-gravity materials science: *Rev. Sci. Instr.*, 74, pp. 160-163, 2003.

[3] Mashimo, T., Okazaki, S., Tashiro, S.: Sedimentation of atoms in solid under a strong acceleration field of around 1 million g: *Jpn. J. Appl. Phys.*, 36, pp. 498-500, 1997.

[4] Mashimo, T., Ikeda, H., Minato, I.: Atomi-scale graded structure formed by sedimentation of substitutional atoms in a Bi-Sb alloy: *J. Appl. Phys.*, 90 pp. 741-744, 2001.

[5] Mashimo, T., Ono, M., Kinoshita, T., Huang, X.S., Osakabe, T., Yasuoka, H.: Sedimentation of substitutional atoms and phase change in an In-Pb alloy under an ultrastrong gravitational field: *Philos. Mag. Lett.*, 83, pp. 687-690, 2003.

[6] Ono, M., Kinoshita, T., Ueno, H., Huang, X.S., Osakabe, T., Mashimo, T.: Sedimentation of Substitutional Solute Atoms in In-Pb System Alloy under Strong Gravitational field: Experiments and Simulations: *Mat. Trans.*, 46, No.2, pp. 219-224, 2005.

[7] Ono, M., Huang, X.S., Ueno, H., Kinoshita, T., Osakabe, T., Mashimo, T.: Sedimentation of substitutional atoms in intermetallic compound of Bi-Pb system under ultra-strong gravitational field: *Deffect and Diffusion Forum*, 237-240, pp. 1101-1107, 2005.

[8] Ono, M., Mashimo, T.: Sedimentation process for atoms in a Bi-Sb system alloy under a strong gravitational field: a new type of diffusion of substitutional solutes: *Philos. Mag. A*, 82, pp. 591-600, 2002.

[9] Kawasuso, A., Hasegawa, M.: Defect in Bulk Semiconductors, *Materia Japan.*, 35, No.2,

pp. 130-139, 1996.

[10] Mäkinen, J., Corbel, C., Hautojärvi, P., Moser, P., Pierre, F.: Positron trapping at vacancies in electron-irradiated Si at low temperatures, *Phys. Rev. B*, 39, No.14, pp. 10162-10173, 1989.

Proceedings of The 1st International Conference on **D**iffusion in **S**olids and **L**iquids
DSL-2005, July 6-8, 2005, University of Aveiro, Aveiro, Portugal

DIFFUSION OF IMPURITIES IN LIQUID GERMANIUM

Eduard PASTUKHOV[1,*], Lyubov ANTONOVA[2], Victor DENISOV[2]

[1]Institute of Metallurgy of the Urals Division of Russian Academy of Sciences,
101 Amundsen Str., Yekaterinburg 620016, Russia
[2]Krasnoyarsk State University,
Svobodny Av. 79, Krasnoyarsk 660041, Russia

[*]Corresponding author. Fax: +7(343) 267 89 18; Email: past@imet.mplik.ru

Abstract

Diffusion of Cu, Ag, Au, Pt, Pd, Fe, Co and Ni in liquid germanium within temperature range 1223-1383 K stepping by 3-5 K was studied by a capillary method in a version of diffusion from a changeable source into semi-infinite medium. It was shown that diffusion constants D can not be described by the single equation $D=D_o\exp(-E_D/RT)$ in the whole temperature range. Two segments (1223-1323 K and 1323-1383 K) with different D_o and E_D are observed on $D=f(T)$ curves. Presence of a break on the curves was associated with the change of structure of liquid germanium.

Keywords: Experimental Methods; Diffusion in Liquids; Diffusion Constants; Impurities; Structure

The study of the particles transportation in liquid metals and semiconductors is one of the physico-chemical analysis methods, which promote revealing of special features of particles interaction in melts. The information on diffusion in germanium-based melts is of interest for many industries operating germanium and its alloys. We've studied diffusion of Cu, Ag, Au, Pt, Pd, Fe, Co and Ni in liquid germanium within the temperature range 1223-1383 K stepping by 3-5 K.

When carrying out experimental determination of diffusion constants D in germanium one should take into account the following phenomenon. D values for some impurities are close enough to each other in liquid and solid Ge. After in-depth consideration of methods of diffusion constants determination in molten metals and semiconductors, we came to the conclusion that capillary method in a version of diffusion from an unsteady source into semi-infinite medium is the most suitable one for the systems under study.

Special experimental cell was developed allowing to set a contact between analyzed impurity and liquid germanium at a given temperature and to perform a quenching after homogenizing annealing. All this made it possible to eliminate the effect of solid-state mass-transfer and to reduce significantly an error in D determination.

The cell was made of spectral pure graphite, i.e. there was no contamination with uncontrollable impurities at high temperatures. Moreover, liquid germanium does not interact with graphite at the temperatures of experiment. The solubility of carbon in liquid germanium at melting point of the latter is 10^8 atoms/cm^3 [1].

Experiments were carried out as follows. Beforehand prepared alloy of germanium with the appropriate chemical element was placed on a bottom of a capillary having diameter about 0.6-1.0 mm. The certain amount of germanium was put into the container of such a volume that could be emptied completely after filling a capillary with germanium. Some of such cells were introduced into a quartz reactor, which was vacuumized. The furnace was heated up to the predetermined temperature. By this time germanium in the container melted and became liquid. The same happened with the alloy on the bottom of a capillary. After establishment of the proper temperature and subsequent ~30 minutes exposure the gaseous argon was let into a quartz reactor and simultaneously the timer was switched on. Then liquid germanium filled a capillary and process of diffusion of analyzed substance along a capillary began. After homogenizing annealing, which duration was selected by practical consideration, the quartz reactor was taken out from the furnace and quenched in ice-cold water. All this had allowed to eliminate an influence of solid state mass transfer and to reduce considerably an error of estimation of D.

Afterwards germanium capillary was taken out from a cell and was divided into parts about 1-2 mm. Concentration of an analyzed impurity was measured with the help of atomic absorptive spectrophotometer. It gave an opportunity to reject application of isotopes on the one hand and to increase quickness of determination without loss in accuracy of the analysis on the other hand.

If the addition of a studied impurity is insignificant, the solution of the Fick's second law for constant factor of diffusion

$$\frac{\partial C}{\partial \tau} = D\frac{\partial^2 C}{\partial l^2} \tag{1}$$

is [2]:

$$C(l,\tau) = \frac{C_{tot}}{2\sqrt{\pi D\tau}}\exp\left(-\frac{l^2}{4D\tau}\right), \tag{2}$$

where $C(l, \tau)$ is concentration of an impurity along the length l of a capillary; τ is duration of homogenizing annealing; C_{tot} is total amount of an impurity. Typical distribution of copper content along a sample is shown in Fig. 1.

Equation (2) is linear in $\ln C - l^2$ coordinates:

$$\ln C = A_C - l^2/(4D\tau), \tag{3}$$

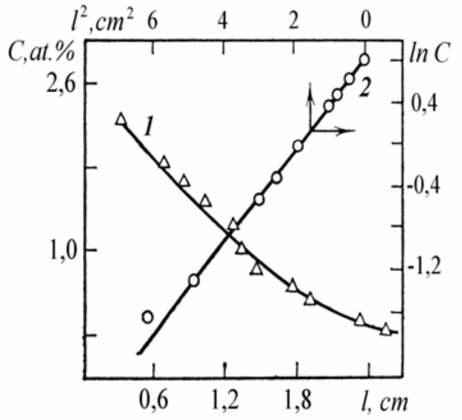

Figure 1: Distribution of copper along a capillary (*1*) and dependence of ln C on l^2 (*2*) (T = 1260 K, τ = 1200).

where A_C is constant.

One can derive D from the graph using slope ratio of a straight line which is $D = 1/(4\tau \mathrm{tg}\alpha)$ (α is angular slope of a straight line). The relative error of D determination did not exceed 10%.

Experiments demonstrated that D values for the whole range of studied temperatures couldn't be described by single exponential equation:

$$D = D_o \exp\left(-E_D/RT\right) \tag{4}$$

which is valid for hole mechanism of diffusion [3]. At lower temperatures (1223-1250 K) experimental data follow one exponential Eq. (4), but at the higher temperatures 1250–1383 K they are described by another equation. The data on diffusion of Cu in liquid Ga and Ge and in alloy Ge + 60 at. % Ga are shown as an example in Fig 2 (*a, b, c*). For the diffusion of Au and Pd in Ge this data can be expressed by the following equations:

$$\lg D_1^{Au} = (-5.813 \pm 0.219) - (2187 \pm 163)/T, \tag{5}$$

$$\lg D_2^{Au} = (-2.922 \pm 0.158) - (5824 \pm 66)/T, \tag{6}$$

$$\lg D_1^{Pd} = (-6.936 \pm 0.281) - (1367 \pm 101)/T, \tag{7}$$

$$\lg D_2^{Pd} = (-5.006 \pm 0.199) - (3250 \pm 69)/T. \tag{8}$$

The same results were observed for the other studied systems.

Practice of representation of diffusion data as parameters of Eq (4) was repeatedly criticized in Refs. [4–6]. The basic objection against use of the Eq. (4) consists in significant structural changes in liquid metals and semiconductors with growth of temperature (see for example Ref. [7]) whereas factors of diffusion poorly vary with temperature. Therefore selection of the relationship for description of $D = f(T)$ dependence in the form of Eq. (4) is justified only for small temperature intervals.

Let's notice that the author of Ref. [8] when solving a problem of deriving specific equation of diffusion for the non-uniform medium with any distribution of temperature has come to a conclusion that the universal kind of the equation of diffusion does not exist.

When the diffusion obeys fluctuation but not vacancy mechanism the temperature dependence of diffusion constants can be described by Swalin's equation [9]:

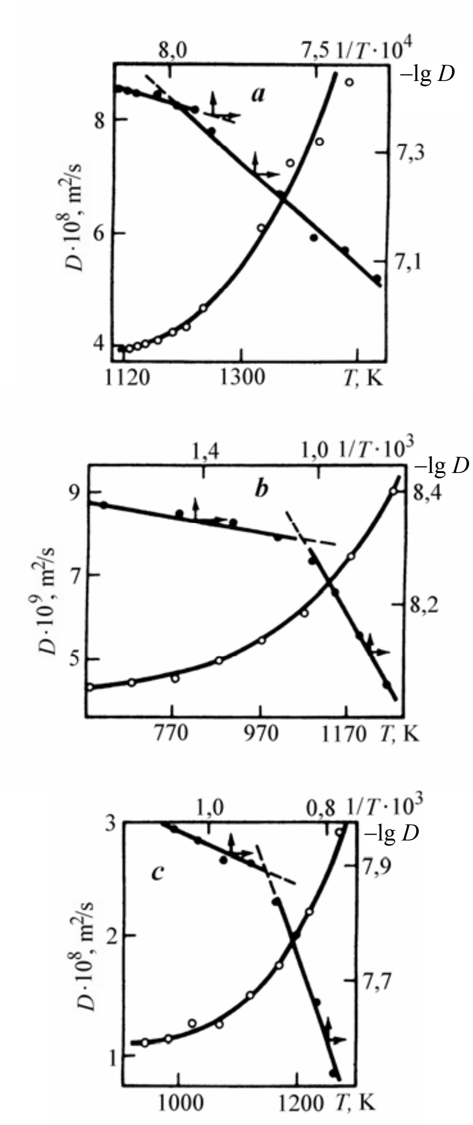

Figure 2: $D = f(T)$ and $\lg D = f(1/T)$ dependencies for copper in liquid Ge (*a*), Ga (*b*) and Ge + 60 at.% Ga alloy (*c*)

$$D = 3Z^2 N_A k_B^2 T^2 / 96\Delta H_v \cdot h \cdot \beta^2 = bT^2, \quad (9)$$

where Z is coordination number, N_A is Avogadro constant, k is Boltzmann's constant, ΔH_v is the heat of vaporization, h is Planck's constant, β is related to the curvature of the potential vs distance curve.

The analysis of temperature dependence of factors of diffusion in metal melts was done in Ref. [10]. It was marked that the hard spheres model of a liquid is most suitable one for the description of diffusion in liquid metals. At the same time the data on diffusion of cobalt in liquid tin can not be described well neither by the Eq. (4), nor by the hard spheres model of a liquid.

It was revealed that D value in the studied temperature range for all the considered impurities doesn't follow the Eq. (9). Experimental values of D are growing faster than it can be predicted using fluctuation theory.

Analysis of impurity atoms diffusivity dependence on their properties in solid spheres model of liquid phase is based on the equation [11]:

$$\frac{D_1}{D_2} = \frac{4}{\sqrt{2}} \frac{\left(1 + m_1/m_2\right)^{1/2}}{\left(1 + \sigma_{22}/\sigma_{11}\right)^2}, \quad (10)$$

in which D_1 and D_2 are self-diffusivity and diffusivity of impurity respectively, m_1 and m_2 are masses of atoms of corresponding elements, σ_{11} and σ_{22} are diameters of solid spheres. It was found that $(D_2/D_1)_{\text{theor}}$ is 1.5-2 times higher than $(D_2/D_1)_{\text{exp}}$ for metals of the 8th group and at the same time it is 2 times lower than $(D_2/D_1)_{\text{exp}}$ for metals of the 1st group. These discrepancies between calculated and experimental values of (D_2/D_1) are apparently caused by special structural features of liquid Ge and Ge-based alloys. X-ray diffraction studies of structure of Ge-based liquid alloys carried out by us and by other authors showed that there are microheterogeneities in these alloys with a low content of elements of the 1st and the 8th groups. This fact is probably resulted in special features of diffusion in the systems under study [1, 7]. It is necessary to note that the break of $D = f(T)$ curve occurs at such a temperatures where a shoulder on the right branch of the 1st diffractional maximum of liquid germanium disappears and temperature dependence of kinematic viscosity $\nu = f(T)$ changes sharply [1].

Diffraction examinations [7] have shown, that short-range order in molten Ge (as well as in Si) is arranged on the base of white tin structure having atomic coordination 6 (4+2), typical metallicity and the nearest interatomic distance considerably exceeding those in crystalline germanium with diamond-like structure. The similar phenomenon is observed in the course of crystalline germanium and silicon conversion into β-Sn structure under 13 and 12 GPa pressures, which is accompanied by arising of a metallic conductivity due to sp^3-covalent links destruction and by valence electrons collectivization.

Calculations show that silicon and germanium after melting keep certain memory about structure of a crystalline state. That is the minor part of atoms has diamond-like short range ordering but the major one is ordered according to white tin structure. The best agreement between simulation and experimental diffraction curves is achieved for superposition of these structures with 0.2 and 0.8 weight factors respectively.

Experimental study of temperature influence on diffusion constants of Cu in liquid Ga (Fig. 2) and In was performed to find out whether the revealed course of $D = f(T)$ dependence is a special feature of liquid Ge or such a phenomena are observed in other melts. These melts were chosen because they are in the same group of periodical system. Moreover, Ga (as well as Ge) is the metal with a loose atom packing in solid state whereas In belongs to metals with close atom packing. It was found out that complex temperature dependence of D in these melts within the temperature range 573-1273 K results from their structural changes with temperature growth.

Thus the development of a precision method of measurement of diffusion constants in molten metals and semiconductors allowed establishing distinct interrelation between diffusion constants and melts structure.

The influence of 5th group elements on Cu and Ag diffusion in Ge and of Bi on Cu diffusion in Ge was studied. The systems Cu – (Ge–Ga), Cu – (Ge–In), Cu – (Ge–Sn), Cu – (Ge–Pb), and Ni – (Ge–Cu) were also examined. It was determined that the changes of $D = f(T)$ for all the melts under study are also associated with structural changes in the melts. D isotherms in these systems have a shape of smooth curves, which have no extremums of any kind. In all the cases D values decreases from pure Ge with the growth of third component content in alloy. Comparison of D isotherms with liquidus lines of corresponding phase diagrams allowed to make the conclusion that there is no correlation between them.

D dependencies on concentration in Ge-based systems were analyzed using the equation:

$$D_A(A-B) = [D_A(A)]^{C_A}[D_A(B)]^{C_B}, \qquad (11)$$

in which $D_A(A–B)$, $D_A(A)$, $D_A(B)$ are self-diffusivities of element A in A-B alloy and in pure metals A and B, C_A and C_B are concentrations of corresponding elements. It was showed that in some cases (e.g. Ag – (Ge–Sb)) Eq. (11) describes experimental results quite well.

Certain shape of D isotherms for specified melts was associated with size effect: In, Sn, Pb, Bi and Sb addition to germanium increases the number of larger particles. That results in decreasing of free volume and therefore in increasing of energy consumption for diffusion in these systems.

For Ge-Pb system the difference between D values calculated using Eq. (11) and experimental results is 19 %. But for the other studied systems it is 9-16 %. That's why it was assumed that Eq. (11) is not universal.

References

[1] Denisov V.M., Istomin S.A., Podkopaev O.I. et all. *Germanium, its compounds and alloys*. Ur. Div. RAS, Yekaterinburg, 2002. (In Rus.).

[2] Zhukhovitsky A.A., Belashenko D.K., Bokshtein B.S. et all. *Physicochemical principles of metallurgical processes.* Publishing House "Metallurgia", Moscow, 1973. (In Rus.).

[3] Frenkel Ya.I. *Kinetic theory of liquids.* Publishing House "Nauka", Leningrad, 1975. (In Rus.).

[4] Nachtrieb N.H. *Advances Phys.* Vol.16, No 62, pp. 309–323, 1967.

[5] Nachtrieb N.H. *Propert. Liquid Metals. Proc. 2nd. Int. Conf.* Tokyo, 1972, London, 1973, pp. 521–535.

[6] Rigny D.F. *Liquid metals.* Publishing House "Metallurgia", Moscow, 1980. (In Rus.).

[7] Pastukhov E.A., Vatolin N.A., Lisin V.L. et all. *Diffraction studies of high-temperature melts structure*. Ur. Div. RAS, Yekaterinburg, 2003. (In Rus.)

[8] Van Kampen N.G. *Zs. Phys.* A 68, No 2-3, pp. 135–138, 1987.

[9]. Swalin R.A. *Acta Metalurg.* Vol. 7, No 11, pp. 737-740, 1959.

[10]. Ogloblya V.I., Lozovoy V.I., Chumakov A.G. *Metallophysics.* Vol. 9, No 3. pp. 62-67, 1987. (In Rus.).

[11] Khar'kov E.I., Yakushevsky S.Yu., Onoprienko G.I. *Ukr. Phys. Journal.* Vol. 25, No 2, pp. 277-280, 1980. (In Rus.)

Proceedings of The 1st International Conference on **D**iffusion in **S**olids and **L**iquids
DSL-2005, July 6-8, 2005, University of Aveiro, Aveiro, Portugal

DIFFUSION OF GOLD IN ALPHA-Zr

Rodolfo A. PÉREZ,[*], Fanny DYMENT
Departamento de Materiales, Comisión Nacional de Energía Atómica, Av. del Libertador 8250, 1429 Buenos Aires, Argentina.
Members of the Carrera del Investigador - CONICET

[*]Corresponding author. Email: rodperez@cnea.gov.ar

Abstract

Diffusion coefficients of *Au* in α-*Zr* between 800 and 1081 K were measured in samples of *Zr* with three different impurities content, in particular *Fe*. An enhancement in the diffusion coefficient related to the total amount of *Fe* present in the *Zr* matrices was measured. A non Arrhenius plot was observed in the three matrices; two regions, above and below 900K, with different diffusion parameters were introduced in order to model this behaviour.

Keywords: Basics of diffusion, Diffusion in crystalline materials, Zirconium, Gold, Diffusion, RBS, Ultra-fast impurities.

---

1 Introduction

Zr belongs to the group IV B of the Periodic Table and presents a bcc (β) structure at high temperature and an hcp (α) structure at low temperature. The transformation temperature $T_{\alpha\beta}$ is 1136 K (0.6 $T_{m\alpha}$) where $T_{m\alpha}$ is the hypothetical melting temperature of the α phase.

α-*Zr* shows self -diffusion parameters that are not consistent with the so-called "normal behaviour" and a downward curvature in the Arrhenius plot was observed not only for self-diffusion [1] but also for *Hf* [2] and *Pb* [3] diffusion in pure α-*Zr*.

It is well known that transition metal elements with small size such as *Fe, Co* and *Ni* are fast diffusers in α-*Zr*. The curvature for self-diffusion is followed by *Fe* [4] and *Co* [5] diffusion in α-*Zr* and there is some experimental evidence [6] that little amounts (as a few ppm) of these impurities in the *Zr* matrix, could modify the diffusion behaviour of substitutional diffusers.

Different models [7, 8] try to explain this curvature; all of them are based in the influence of these fast diffusers. These models take only the *Fe* in solution as the responsible for the enhanced diffusion process. They explain the curvature in the Arrhenius plots observed in the diffusion studies performed in the α-*Zr* matrix as a consequence of *Fe* precipitation at low temperatures. For a complete analysis of these models see Ref. [9].

The present study deals with the diffusion of *Au* in α-*Zr* samples with different amounts of *Fe* as impurity, measured using Rutherford Backscattering Spectrometry techniques to obtain the diffusion profiles.

The goal of this work is to perform the measurements of *Au* diffusion in *Zr* samples with different amounts of Fe as impurity even at temperatures below 900 K, where the *Fe* solubility is almost null, in order to determine if the enhancement proceeds or, as predicted by the mentioned models, the precipitation of *Fe* inhibit this effect.

2 Experimental procedure

The α-*Zr* samples used in this work were slabs of about 5 mm thickness. Three different kinds of samples, with different amounts of impurities, in particular *Fe*, were used. Samples A with 20, B with 50 and C with 150 μgr/gr.

In order to achieve the final large, stabilised grain size, the samples underwent three annealing cycles of 1 h at 1473 K, followed by 10 days at 1133 K.

The samples were mechanically polished to a flat surface for *Au* implantation. The final polish was done on a metallurgical cloth with the use of an increasingly diluted mixture of ignited ammonium dichromate and a 0.5 per cent aqueous solution of HF. The samples were then pre-annealed in sealed quartz tubes under high purity *Ar*, for 1 day at 1133 K. They were wrapped with *Ta* foils in order to prevent reactions between the *Zr* and the quartz tube.

Au was ion beam implanted using the 500 kV ion implanter at the Instituto de Física, Universidade Federal de Rio Grande do Sul (IF-UFRGS), Porto Alegre, Brazil, with an implantation energy of 30 keV and 1 10^{15} at/cm^2 fluence. RBS measurements show that the as implanted profile has a gaussian shape with about 10 nm width.

The diffusion anneals were performed in sealed quartz tubes. When samples with different amount of impurities were studied at the same temperature, they were annealed all together, in the same sealed tube, in order to minimise the influence of systematic errors in the determination of the diffusion coefficients. The temperatures were controlled within ± 1K.

Ion beam analysis techniques were used in the measurements of the diffusion profiles.

At low temperatures the diffusion profiles were obtained using the RBS technique. A ^{2}He ion beam from the IF-UFRGS TANDETROM accelerator was used. The backscattered α particles were detected using a Si surface-barrier detector, located at a scattering angle of 170°. The electronic resolution of the system was better than 13 keV, which implies a depth resolution of around 10 nm.

At higher temperatures the Heavy Ion RBS (HIRBS) technique was used. The use of a heavier ion beam at higher energies increases the mass resolution and depth of the analysis. The experiments were performed in the TANDAR accelerator at the Departamento de Física – Comisión Nacional de Energía Atómica, using a ^{9}F 38 MeV ion beam. The experimental set-up implies a depth resolution of around 30 nm.

In both cases, the conversion of the spectrum to diffusion profile was made according to the algorithm developed in [10].

3 Results

After *Au* implantation the shape of the initial profile is a Gaussian function centered at x_0 = 10 nm corresponding to the implantation depth for *Au* peak and with a $\sigma = 2\ \Delta R_p \equiv 4Dt_0$, where ΔR_p is the lateral straggling and t_0 is a fictitious time magnitude, defined in order to fit the as implanted initial profile. Then, the solution of Fick's equation is also given by a Gaussian function. So, each diffusion profile can be fitted by:

$$C(x) = \frac{C_0}{\sqrt{\pi D(t+t_0)}} \exp\left(\frac{-(x-x_0)^2}{4D(t+t_0)} \right) \quad (1)$$

where *C* is the Au concentration at depth *x*, C_0 is the initial amount of *Au*, *D* is the diffusion coefficient at the studied temperature, *t* is the annealing time and x_0 and t_0 are obtained from the as implanted initial peak and width, respectively.

Typical penetration profiles (ln [*C(x)*] against $(x\text{-}x_0)^2$) are displayed in Fig. 1 for 3 samples with different amount of impurities annealed at the same temperature and time. Straight lines were obtained, so Eq. (1) is followed.

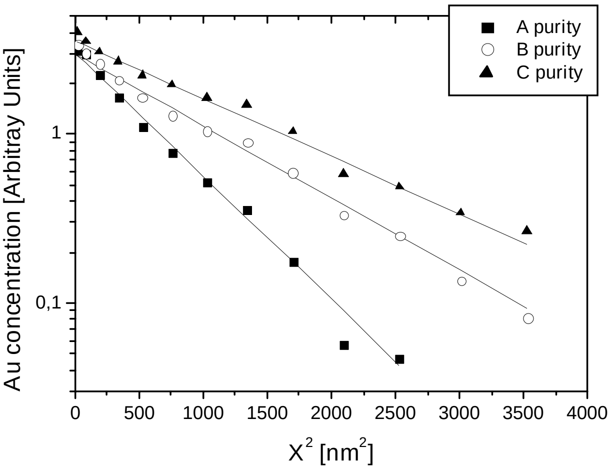

Figure 1: Diffusion profiles at 800 K for the three kinds of samples

The diffusion coefficients obtained for *Au* diffusion in *α-Zr* are listed in the Table 1 together with temperatures and annealing times and the impurity quality of the samples.

An Arrhenius plot with these results is shown in Fig. 2 together with the self-diffusion data [1] for comparison.

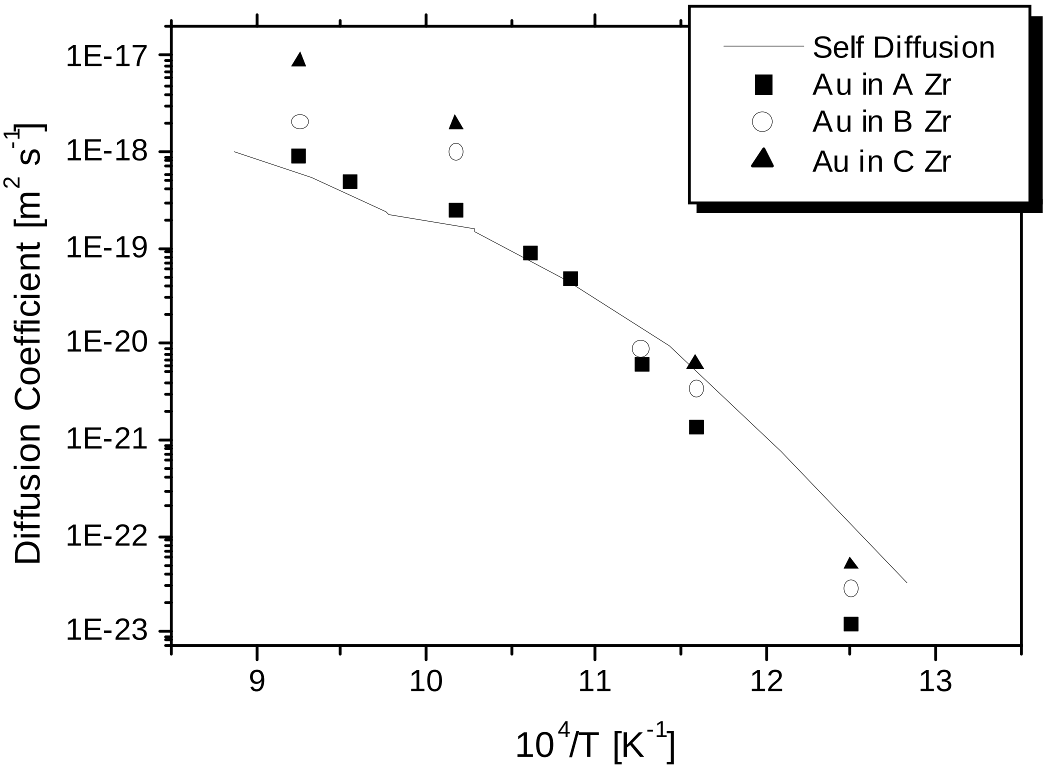

Figure 2: Arrhenius plot

Table 1: Diffusion coefficient of *Au* in *α-Zr* measured in the three kinds of samples.

Temperature (K)	Time (10^4 sec)	D [m^2 s^{-1}] Purity A	B	C
800	552.96	$1.2 \cdot 10^{-23}$	$2.8 \cdot 10^{-23}$	$5 \cdot 10^{-23}$
863	1814.40	$1.4 \cdot 10^{-21}$	$3.5 \cdot 10^{-21}$	$6.2 \cdot 10^{-21}$
888	216.00	$6.0 \cdot 10^{-21}$	$9.0 \cdot 10^{-21}$	-
922	25.92	$4.7 \cdot 10^{-20}$	-	-
943	120.96	$9.0 \cdot 10^{-20}$	-	-
983	86.40	$2.5 \cdot 10^{-19}$	$1.0 \cdot 10^{-18}$	$2.0 \cdot 10^{-18}$
1048	0.09	$5.0 \cdot 10^{-19}$	-	-
1081	0.18	$8.9 \cdot 10^{-19}$	$2.1 \cdot 10^{-18}$	$9.0 \cdot 10^{-18}$

4 Discussion

The simple inspection of Fig. 2 shows two remarkable points: first, the diffusion coefficient does not follow an Arrhenius law. In particular, for the purest samples (kind A), which impurity content is similar to the one used for the self-diffusion measurements [1], the variation of D with the temperature could be fitted by a downward curvature or by two different straight lines. One line above 900K, with low diffusion parameters $Q = 130$ kJ mol^{-1} and $D_0 \approx 10^{-12}$ m^2 s^{-1} and the other one below this temperature, with high parameters $Q = 360$ kJ mol^{-1} and $D_0 \approx 20$ m^2 s^{-1}. This behaviour is similar to the observed one not only for self-diffusion, but also for other substitutional diffusers like *Hf* [2] and *Pb* [3].

The second point is that the *Fe* enhanced diffusion takes place even at the lowest temperature measured, when the solubility of *Fe* in *α-Zr* is almost zero. Besides, the amount of *Fe* as impurity in the samples B and C is higher than the maximum solubility reported in [11], so the amount of *Fe* in solution in both kinds of samples is the same. If only the Fe in solution is responsible for the enhanced diffusion, as proposed in the literature [7, 8], the diffusion coefficients in samples B and C must be the same, which is not the behaviour observed in this work.

The models proposed in order to explain the curvature observed in the self-diffusion Arrhenius plot [7, 8] postulate that it was caused by a solute-enhanced diffusion process due to the presence of small amounts, as a few tenths of ppm, of ultra-fast impurities like Fe and that this enhancement diminish, and finally ceases at lower temperatures, when the impurities precipitate from solution. So they propose that this precipitation must be the responsible for the break in the Arrhenius plot close to 900K.

This idea is not supported by the present results, since the break at 900K is observed in the *Au* diffusion in *α-Zr* but below this temperature an enhancement of the diffusion coefficient is measured despite of the almost null solubility of *Fe* in the matrix.

Two regions (above and below 900 K) with different diffusion parameters (activation energy and pre-exponential factor) seem to be a better approximation to the results obtained for self and substitutional diffusion in *α-Zr* instead of a curve fit in the Arrhenius plot if the gradual variation of the diffusion enhancement is disregarded. The diffusion parameters values are summarised in Table 2.

Table 2: Diffusion parameters for self and substitutional diffusers in *α-Zr*

	High temp		Low temp	
	Q(kJmol^{-1})	D$_0$ (m^2 s^{-1})	Q (kJmol^{-1})	D$_0$ (m^2 s^{-1})
Zr	336	1.1	125	$6\ 10^{-13}$
Pb	319	0.05	225	$2\ 10^{-7}$
Hf	343	2.1	188	$5\ 10^{-9}$
Au	360	20	130	$1\ 10^{-12}$
Proposed as normal value			320	$5\ 10^{-5}$

Finally, if these two regions with different thermodynamic properties are an intrinsic property of pure *α-Zr* or a property of the dilute *Zr-Fe* alloys is still and open question. Nevertheless since the variation of thermodynamic properties in a non-magnetic matrix with a non ordered arrangement of magnetic spins is a well known effect, the hypothesis that the observed break in the dependence of the diffusion coefficients with the temperature is a property of diluted *Zr-Fe* alloys seems to be the more probable hypothesis.

Moreover, experimental Mössbauer data [12] obtained on recoil implantation of Coulomb-excited ^{57}*Fe* into *α-Zr* at 24 K shows that almost 30 % of the implanted atoms sit at "off-center" (asymmetrical) positions around the octahedral interstitial cage (see Fig. 3). At high temperature the *Fe* interstitials can jump among these equivalent positions (in the "cage").

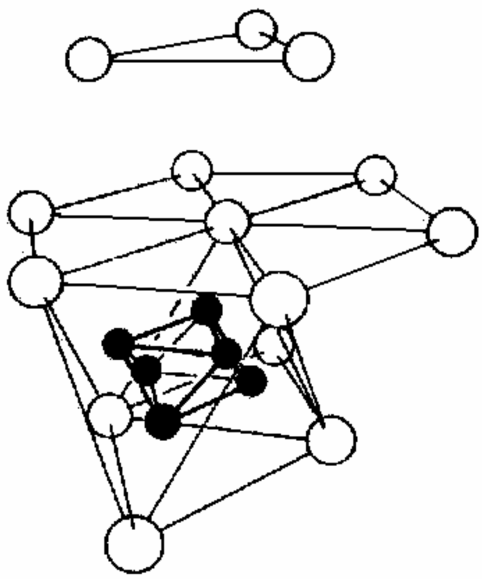

Figure 3: Octahedral interstitial cage in an hcp cell.

This *Fe* position, neither in a substitutional nor in a symmetric octahedral site, could be related to an interaction among the *4s* electrons of the *Fe* with the *4d* electrons of the *Zr*, so strong that, at least partially, this electrons are shared between both atoms and the *Zr* atom is shifted from the lattice node. This shift could be extended to several *Zr* atoms giving origin to different arrangements as the ones shown in Fig. 4. These arrangement of three *Zr* atoms surrounding two *Fe* (above) or six *Zr* close to one *Fe* atoms (below) correspond to the Zr_3Fe structure and so, they are the candidates to have the lower associated configuration energy, being

Zr_3Fe the first intermetalic that appears in the *Zr* reach part of the binary phase diagram.

Let's call one of these possible complexes as Zr_3Fe embryo. So, the *Fe* is not in solid solution, thinking it as in a pure substitutional or pure interstitial site, but forming one of those embryos. This idea is supported by the variation in the values obtained for the *Fe* solvus line among different authors [6, 11, 13] and the segregation to the surface and precipitation of Zr_3Fe second phase [6] even in *Zr* samples with a *Fe* content lower than the value proposed as limit of solubility.

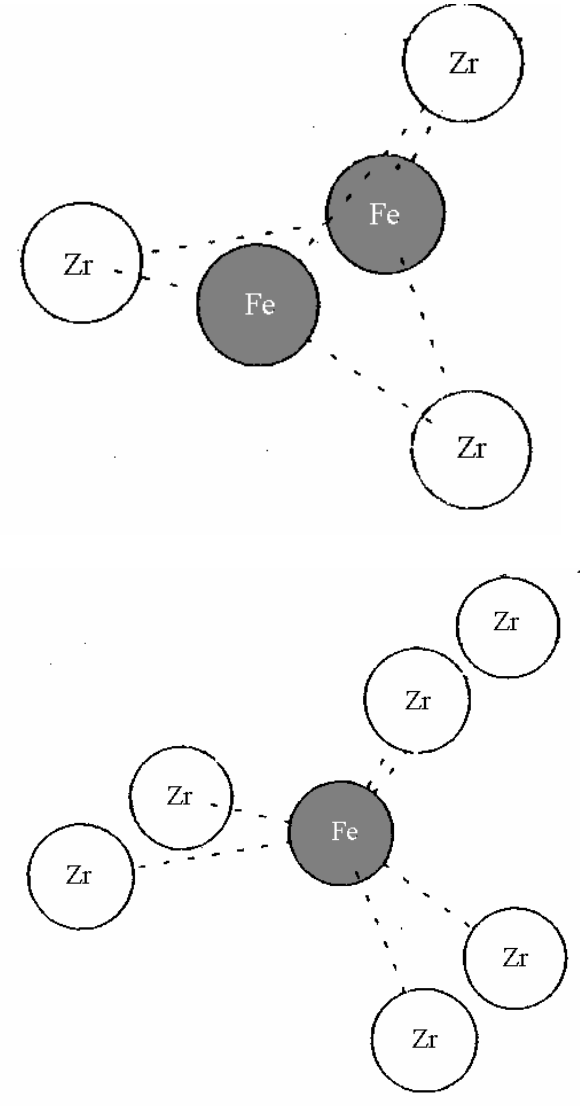

Figure 4: Different arrangements corresponding to the Zr_3Fe structure.

The presence of these mobile embryos gives origin to a more open structure than the pure *Zr* hcp one, so an enhancement in the diffusion coefficient could happen. The total number of the embryos is proportional to the total amount of *Fe*, not to the *Fe* in solution, if any solubility at all exists.

A variation on the mobility and the properties of these kinds of embryos above and below 900K could be responsible for the variation in the thermodynamic properties of the diluted α-*Zr-Fe* alloys.

5 Conclusions

Diffusion coefficient between 800 and 1081 K for *Au* in α-*Zr* matrices with different amounts of ultra-fast impurities were measured.

The Arrhenius law was not observed, even for the purest A samples. The deviation from the Arrhenius law is similar to the observed in self-diffusion and other substitutional diffusers.

Enhancement on the diffusion coefficient induced by the total amount of *Fe* present in the samples was measured, even at the lowest temperatures, despite of the postulated dependence with the amount of *Fe* in solution proposed in the literature.

Acknowledgments

The authors wish to thank Dr. M.Behar for his collaboration with the RBS measurements, to Drs. G.García Bermúdez and D. Abriola for their collaboration with the HIRBS measurements.

References

[1] Horvát, J., Dyment, F. and Mehrer, H.: "Anomalous Self-Diffusion in a single crystal of α-Zirconium" *J. Nucl. Mater.* 126, pp. 206-214, 1984.

[2] Hood, G.M., Zou, H., Schultz, R.J., Roy, J.A. and Jackman, J.A.: "Hf diffusion in pure and ultrapure α-Zr" *J. Nucl .Mater.* 189, pp.226-230, 1992.

[3] Pérez, R.A. and Dyment, F.: "Lead diffusion in α-Zr". *Appl. Phys. A.* 68, pp. 667-671, 1999.

[4] Nakajima, H., Hood, G.M. and Schultz, R.J.: "Diffusion of ^{59}Fe in single-crystal α-Zr" *Philos. Mag. B* 58, pp.319-337, 1988.

[5] Kidson, G.V.: "The diffusion of ^{58}Co in oriented single-crystals of α-zirconium" *Philos. Mag. A* 44, pp.341-355, 1980.

[6] Zhou, H., Hood, G.M., Roy, J.A., Schultz, R.J. and Jackman, J.A.: "The solid solubility of Fe in α-Zr: a secondary ion mass spectrometry study" *J. Nucl. Mater.* 210, pp. 239-243, 1994.

[7] Hood, G.M.: "The anomalous self-diffusion in α-Zr" *J. Nucl. Mater.* 135, pp. 292-295, 1985.

[8] Frank, W.: "Rapid-pair-enhanced diffusion in α-Zr and its integration into the point-defect scenario in hcp metals" *Philos. Mag. A* 63, pp. 897-913, 1991.

[9] Pérez, R.A., Nakajima, H. and Dyment, F. "Diffusion in α-Ti and Zr" *Mater. T JIM* 44, pp.2-13, 2003.

[10] Pérez, R.A., Bermúdez, G.G., Abriola, D., Dyment, F., Somacal, H.: "Use of HIRBS in diffusion measurements" *Defect Diffus Forum* 143-147, pp 1335-1340, 1997.

[11] Borelly, R., Merle, P. and Adami, L.: "Study of the solubility of iron in zirconium by thermoelectric power" *J. Nucl. Mater.* 170, pp.147-156, 1990.

[12] Yoshida, Y., Menningen, M., Sielemann, R., Vogl, G., Meyer, G. and Schroder, K.: "Local Atomic-Jump Process of Iron in *alpha* –Zr" *Phys. Rev. Lett.* 61, pp.195-198, 1988.

[13] Arias, D. and Abriata, J.P.: "Fe-Zr (Iron-Zirconium)". Binary Alloy Phase Diagram, 2nd edition, pp. 1798-1800, ed.by T.B.Massalski Eds. ASM International, USA, 1990.

Proceedings of The 1st International Conference on **D**iffusion in **S**olids and **L**iquids
DSL-2005, July 6-8, 2005, University of Aveiro, Aveiro, Portugal

ANALYTICAL INVESTIGATION OF THERMAL CHARACTERISTICS OF COMPOSITES WITH DIFFERENT TOPOLOGY: EFFECT OF PERTURBATIONS

Ekaterina PESETSKAYA[1,*], Thomas FIEDLER[1], Andreas ÖCHSNER[1,2], José GRÁCIO[1,2]

[1]Centre for Mechanical Technology and Automation, University of Aveiro,
Campus Universitário de Santiago, 3810-193 Aveiro, Portugal
[2]Department of Mechanical Engineering, University of Aveiro,
Campus Universitário de Santiago, 3810-193 Aveiro, Portugal

*Corresponding author. Fax: ++351 234 370 953; Email: epesetskaya@mec.ua.pt

Abstract

The effective thermal conductivity of 2D composite materials with finite number of circular reinforcements inside periodic cells is analytically investigated. The cases of symmetric and nonsymmetric location of reinforcements in a cell are considered. The effect of increasing of the effective conductivity in the case of small perturbation of reinforcements for structures with different arrangements is shown.

Keywords: Composite materials; Effective conductivity; Boundary value problems; Functional equations; Perturbed reinforcements

1 Introduction

This paper is devoted to the investigation of the effective conductivity of two-dimensional composite materials with a quasi periodic structure, i.e. consisting of periodically located cells occupied by a finite number of circular disjoint reinforcements generating quasi periodical structures inside each cell. Under a quasi periodical structure, a small perturbation of reinforcements in a periodic arrangement is understood (cf. Figure 1). In the case of a larger number of microscopical components of a composite, its averaging can be done by using homogenisation concepts [2]. These concepts allow to consider composites with above described structures and to determine the effective characteristics of materials.
From a mathematical point of view, a definition of physical-mathematical fields in periodic piece-wise homogenised structures is reduced to the solution of boundary value problems of the potential theory for infinitely connected domains. In particular, macroparameters of a structure can be explicitly defined as some functionals on the solutions of functional equations for an appropriate boundary value problem. The interpretation of the macroparameters as functionals containing all necessary information about the structure gives ways for construction of real composite materials.

In this case, a boundary value problem for multiple connected domains is analytically solved by the method of functional equations [5]. As a result, a simple algorithm containing elliptic functions which are well-studied and readily available for computing is obtained [8]. The effective conductivity λ_e is found as a power series in the reinforcement concentration ν [1]. Coefficients of the series are calculated by means of this algorithm. The derived numerical values of the effective conductivity as a function of the concentration are compared with numerical values obtained using the finite element method [9].

A random perturbation of the reinforcements in a cell is considered. It is assumed that each disk (reinforcement) lies in a prescribed part of the original cell and does not cross and touch another disk. It is shown for structures with different topology (cf. Figure 1) that composite materials with symmetrical position of the reinforcements possess the minimal effective conductivity in comparison with materials having perturbed position of the reinforcements.

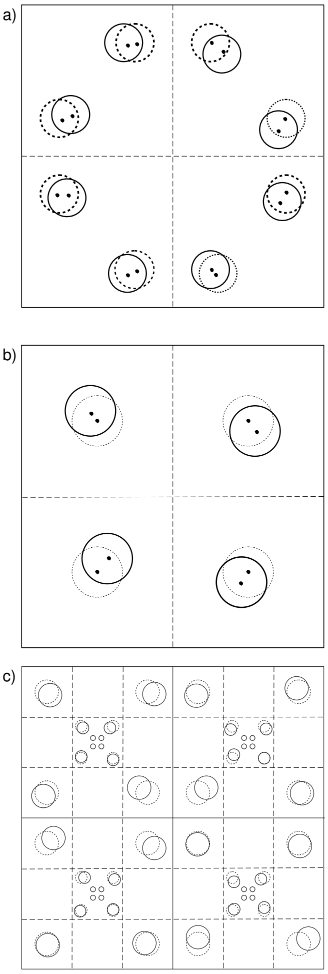

Figure 1: a) Diagonal arrangement; b) square arrangement; c) fractal arrangement.

2 Effective conductivity of composites

A lattice L which is defined by the two fundamental translation vectors 1 and $\imath$ ($\imath^2 = -1$) in the plane $\mathbb{C} \cong \mathbb{R}^2$ of the complex variable $z = x + \imath y$ is considered. The fundamental cell $Q_{(0,0)}$ is the square

$$\{ z = t_1 + \imath t_2 \in \mathbb{C} : -\frac{1}{2} < t_p < \frac{1}{2}, p = 1, 2\}.$$

Let $\mathcal{E} := \bigcup\limits_{m_1,m_2} \{m_1 + \imath m_2\}$ be the set of the lattice points, where $m_1, m_2 \in \mathbf{Z}$. The cells corresponding to the points of the lattice $\mathcal{E}$ are denoted as

$$Q_{(m_1,m_2)} = Q_{(0,0)} + m_1 + \imath m_2 :=$$
$$\{z \in \mathbb{C} : \; z - m_1 - \imath m_2 \in Q_{(0,0)}\}.$$

First, the situation when N mutually disjoint disks of equal radii

$$D_k := \{z \in \mathbb{C} : |z - a_k| < r\} \, (k = 1, 2, \ldots, N)$$

are located inside of fundamental cell $Q_{(0,0)}$, and periodically repeated in all cells $Q_{(m_1,m_2)}$ is considered. The boundary of the corresponding reinforcements is denoted by

$$T_k := \{z \in \mathbb{C} : |z - a_k| = r\} \, (k = 1, 2, \ldots, N),$$

and considered the connected domain

$$D_0 := Q_{(0,0)} \setminus (\bigcup_{k=1}^{N} D_k \cup T_k)$$

obtained by removing of the reinforcements from the fundamental cell $Q_{(0,0)}$.
The problem is to define the effective conductivity of the doubly periodic composite material with the matrix

$$\mathcal{D}_{per} = \bigcup_{m_1,m_2} ((D_0 \cup \partial Q_{(0,0)}) + m_1 + \imath m_2)$$

and reinforcements

$$\mathcal{D}_r = \bigcup_{m_1,m_2} \bigcup_{k=1}^{N} (D_k + m_1 + \imath m_2)$$

occupied by materials of conductivities λ and $\lambda_1 > 0$, respectively. This problem is equivalent to the determination of the potential of the corresponding field, i.e. to find a function $u(z)$ satisfying the Laplace equation in each component of the composite material:

$$\nabla^2 u = 0, \quad z \in \mathcal{D}_{per} \bigcup \mathcal{D}_r, \tag{1}$$

and conjugation conditions:

$$u^+(t) = u^-(t), \; \lambda \frac{\partial u^+}{\partial n}(t) = \lambda_1 \frac{\partial u^-}{\partial n}(t), \tag{2}$$

$$t \in \bigcup_{m_1,m_2} T_k, \quad k = 1, 2, \ldots, N,$$

where $\frac{\partial}{\partial n}$ is the outward normal derivative and

$$u^+(t) := \lim_{z \to t, z \in D_0} u(z), \quad u^-(t) := \lim_{z \to t, z \in D_k} u(z),$$

$$t \in \bigcup_{m_1,m_2} T_k, \quad k = 1, 2, \ldots, N.$$

The first equality in (2) describes the temperature balance. The second one describes the flux balance. Together they form so-called ideal contact conditions.

The quasi periodicity conditions are also imposed on $u(z)$, where $u(z)$ has a constant jump in the direction of each fundamental translation vector:

$$u(z+1) = u(z) + 1, \quad u(z+\imath) = u(z). \tag{3}$$

Furthermore, the complex potentials $\varphi(z)$, $\varphi_k(z)$ which are analytic in D_0 and D_k and continuously differentiable in the closures of D_0 and D_k, respectively, are introduced. The harmonic potential u and complex analytic potentials φ and φ_k are related by the equalities

$$u(z) = \begin{cases} \Re\left(\varphi(z) + z\right), & z \in D_0, \\ \frac{2\,\lambda}{\lambda+\lambda_1}\,\Re\varphi_k(z), & z \in D_k, \end{cases} \tag{4}$$

$$k = 1, 2, \ldots, N.$$

Conditions (2) can be rewritten following [1] in terms of the complex potentials

$$\varphi(t) = \varphi_k(t) - \rho\ \overline{\varphi_k(t)} - t, \ \ |t - a_k| = r, \tag{5}$$

$k = 1, 2, \ldots, N$. The problem (5) is a particular case of so-called $\mathbb{R}$-linear conjugation problem.
To determine the flux $\nabla u(x,y)$, it is necessary to obtain the derivatives of the complex potentials:

$$\begin{aligned} \psi(z) &:= \tfrac{\partial\varphi}{\partial z} = \tfrac{\partial u}{\partial x} - \imath\tfrac{\partial u}{\partial y}, && z \in D_0 \\ \psi_k(z) &:= \tfrac{\partial\varphi_k}{\partial z} = \tfrac{\lambda_1+\lambda}{2\,\lambda}\left(\tfrac{\partial u}{\partial x} - \imath\tfrac{\partial u}{\partial y}\right), && z \in D_k. \end{aligned} \tag{6}$$

Differentiating (5), the following problem is obtained

$$\psi(t) = \psi_k(t) + \rho\left(\frac{r}{t-a_k}\right)^2\overline{\psi_k(t)} - 1, \tag{7}$$

$$|t - a_k| = r, \ \ k = 1, 2, \ldots, N,$$

which can be solved by the method of functional equations [1], [5]. $\psi_k(z)$ is expressed in the form of series in r^2 [1]:

$$\psi_k(z) = \psi_k^{(0)}(z) + r^2\,\psi_k^{(1)}(z) + r^4\,\psi_k^{(2)}(z) + \ldots, \tag{8}$$

where each term in (8) is expanded into a Taylor series

$$\psi_k^{(s)}(z) = \sum_{l=0}^{\infty}\psi_{lk}^{(s)}(z - a_k)^l.$$

The method of functional equations allows to find a simple recursive algorithm [1] which defines the flux $\nabla u(x,y)$ in terms of Eisenstein's functions $E_l(z) = \sum\limits_{m_1,m_2,m_1+\imath m_2\neq 0}(z - m_1 - \imath m_2)^{-l}$ of order l, modified Eisenstein's functions $\sigma_l = E_l(z) - z^{-l}$ of order l, properties of which are studied in [8] in detail, and the contrast parameter $\varrho = \frac{\lambda_1-\lambda}{\lambda_1+\lambda}$, which expresses the difference between the conductivity of both materials:

$$\begin{aligned} &\psi_m^{(0)}(z) = 1 \\ &\psi_m^{(1)}(z) = \rho\Big[\sum_{k\neq m}^{N}\overline{\psi_{0k}^{(0)}}E_2(z-a_k) + \overline{\psi_{0m}^{(0)}}\sigma_2(z-a_m)\Big] \\ &\psi_m^{(2)}(z) = \rho\Big[\sum_{k\neq m}^{N}\overline{\psi_{0k}^{(1)}}E_2(z-a_k) + \overline{\psi_{0m}^{(1)}}\sigma_2(z-a_m) \\ &\qquad + \sum_{k\neq m}^{N}\overline{\psi_{1k}^{(0)}}E_3(z-a_k) + \overline{\psi_{1m}^{(0)}}\sigma_3(z-a_m)\Big] \\ &\ldots \end{aligned} \tag{9}$$

$$\begin{aligned} \psi_m^{(p+1)}(z) = \rho\Big[&\sum_{k\neq m}^{N}\overline{\psi_{pk}^{(0)}}E_{p+2}(z-a_k) \\ &+\overline{\psi_{pm}^{(0)}}\sigma_{p+2}(z-a_m) + \sum_{k\neq m}^{N}\overline{\psi_{p-1,k}^{(1)}}E_{p+1}(z-a_k) \\ &+\overline{\psi_{p-1,m}^{(1)}}\sigma_{p+1}(z-a_m) + \ldots + \\ &+\sum_{k\neq m}^{N}\overline{\psi_{0k}^{(p)}}E_2(z-a_k) + \overline{\psi_{0m}^{(p)}}\sigma_2(z-a_m)\Big]. \end{aligned} \tag{10}$$

The effective conductivity of an isotropic composite material with N identical reinforcements is given by the equality [1]

$$\lambda_e = \lambda + 2\lambda\rho\nu\sum_{p=0}^{6}A_p\nu^p + o(\nu^8), \tag{11}$$

where $\nu = N\pi r^2$ is the concentration of reinforcements, and the coefficients

$$A_p = \frac{1}{\pi^p N^{p+1}}\sum_{m=1}^{N}\psi_m^{(p)}(a_m), \ \ p = 0, 1, 2, \ldots, \tag{12}$$

are represented in

$$A_0 = 1,$$

$$A_1 = \tfrac{\rho}{\pi N^2} X_2,$$

$$A_2 = \tfrac{\rho^2}{\pi^2 N^3} X_{22},$$

$$A_3 = \tfrac{1}{\pi^3 N^4}[-2\rho^2 X_{33} + \rho^3 X_{222}],$$

$$A_4 = \tfrac{1}{\pi^4 N^5}[3!\rho^2 X_{44} - 2!\rho^3[X_{332} + X_{233}]$$
$$+\rho^4 X_{2222}],$$

$$A_5 = \tfrac{1}{\pi^5 N^6}[-4!\rho^2 X_{55} + 3!\rho^3[X_{442} + X_{343} + X_{244}]$$
$$-2!\rho^4[X_{3322} + X_{2332} + X_{2233}] + \rho^5 X_{22222},$$

$$A_6 = \tfrac{1}{\pi^6 N^7}(5!\rho^2 X_{66} - 4!\rho^3[X_{255} + X_{354} + X_{453}$$
$$+X_{552}] + 3!\rho^4[X_{2244} + X_{2343} + X_{3333} + X_{2442}$$
$$+X_{3432} + X_{4422}] - 4!\rho^5[X_{22233} + X_{22332}$$
$$+X_{23322} + X_{33222}] + \rho^6 X_{222222}) \ldots \tag{13}$$

with $X_{p_1,\ldots,p_M}$ defined as

$$X_{p_1} := \sum_{m=1}^{N} \sum_{k \neq m} E_{p_1}(a_m - a_k) + \sigma_{p_1}(0)$$

$$X_{p_1,p_2} := \sum_{m=1}^{N} \Bigg(\sum_{k \neq m} \sum_{k_1 \neq k} E_{p_1}(a_m - a_k) \overline{E_{p_2}(a_k - a_{k_1})}$$
$$+\sigma_{p_2}(0) \sum_{k \neq m} E_{p_1}(a_m - a_k) + \sigma_{p_1}(0)\sigma_{p_2}(0) \Bigg)$$

and so on.

Numerical investigations of the effective conductivity of composites with square arrangement (cf. Figure 1b) were carried out using the finite element method. The basic idea of the finite element method is the decomposition of a domain with a complicated geometry into geometrically simple elements, such that the governing differential equation (e.g. describing a temperature field) can be solved approximately for these finite elements. The single element solutions are then assembled to obtain the complete system solution using given boundary conditions. The assembly process uses appropriate balance equations at the nodes which are used to define the elements and serve also as connection points between the elements. In the scope of the finite element approach, three different geometries have been considered (square arrangement of reinforcements for $\nu = 0.1, 0.3, 0.5$). Results obtained from both approaches are presented in Figure 2, and a good correlation of the results is found.

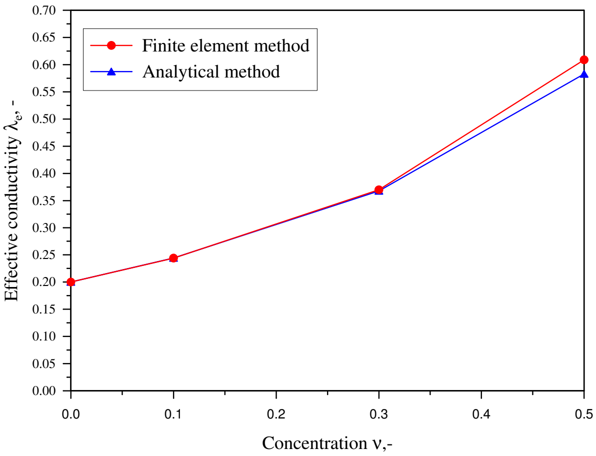

Figure 2: Effective conductivity λ_e in dependence on the concentration ν.

An analytical formula for the effective conductivity of composite materials with a fractal arrangement has the form (11), where coefficients $A_s, s = 1, 2, \ldots,$ are defined as follows [6]

$$A_s = \frac{1}{16^{s+1}\pi^s (\sum\limits_{g=1}^{G} \frac{1}{9^{g-1}})^{s+1}} \times \tag{14}$$
$$\times \sum_{g=1}^{G} \sum_{h=1}^{4} \sum_{k=1}^{4} \frac{1}{9^{g-1}} \psi_{ghk}^{(s)}(a_{ghk}).$$

For a fractal structure, it is considered that the cell $Q_{(0,0)}$ is divided by four equal parts which are numbered in the counter-clock wise direction (cf. Figure 1c). Thus, g denotes the generation of disk set, G is the number of the generations, h is the number of the part of the cell $Q_{(0,0)}$, k is the number of the disk at a generation on the part of $Q_{(0,0)}$.The radius of a disk of the g generation

$$D_{ghk} := \{z \in \mathbb{C} : |z - a_{ghk}| < r_g\}$$
$$(g = 1, \ldots, G, \;\; h, k = 1, \ldots, 4)$$

is defined by the following relation

$$r_g = \frac{1}{3^{g-1}} r_1,$$

where r_1 is the radius of a disk of the first generation. The concentration is defined as

$$\nu = \sum_{g=1}^{G} \nu_g = 16\pi r_1^2 \sum_{g=1}^{G} \frac{1}{9^{g-1}}.$$

For coefficients $A_s,\ s = 0,1,2,\ldots,$ the functions $\psi_{ghk}^{(s)}(z)$ are calculated by the recursive algorithm (9).

3 Effective conductivity of composites with perturbed structures

First, the case of N circular reinforcements of equal radii in the cell $Q_{(0,0)}$ is considered. Let $b_1, b_2, \ldots, b_N$ be the centres of these reinforcements. It is assumed that points $b_1, b_2, \ldots, b_N$ form a symmetric array in $Q_{(0,0)}$. N identically distributed random variables $\boldsymbol{d}_1, \boldsymbol{d}_2, \ldots, \boldsymbol{d}_N$ with uniform distribution inside the disk $|z| < d$ are considered, i.e. they have the probability density

$$f_k(z) := \begin{cases} \frac{1}{\pi d^2}, & |z| < d, \\ 0, & |z| \geq d. \end{cases}$$

Let $\boldsymbol{a}_1, \boldsymbol{a}_2, \ldots, \boldsymbol{a}_N$ be the random variables defined by formula $\boldsymbol{a}_k = \boldsymbol{d}_k + \boldsymbol{b}_k,\ k = \overline{1, N}$, where the variables $\boldsymbol{b}_k$ possess the constant values b_k. In the following, the values of the above introduced random variables $\boldsymbol{a}_k$ are denoted by a_k. Thus, the disks $D_k = \{z : \ |z - b_k| < d\}$ are randomly distributed inside the unit periodic cell $Q_{(0,0)}$. It is assumed that $d + r < \frac{1}{\sqrt{N}}$. This means that each disk lies in the prescribed part of the original square cell and does not cross or touch the boundary of corresponding part. Below, the dependence of the effective conductivity upon the random positions of the reinforcements in the symmetric array is investigated.

For the sake of simplicity, each coefficient $\mathbf{A}_p$ in the representation λ_e is decomposed as follows

$$\mathbf{A}_p = A_p^{(0)} + \widetilde{\mathbf{A}}_p, \tag{15}$$

where $A_p^{(0)}$ corresponds to the deterministic periodic structure ($d = 0$) and $\widetilde{\mathbf{A}}_p$ is the correction due to randomness of the positions of a_k. The expected value from the last equality is

$$\langle \mathbf{A}_p \rangle = A_p^{(0)} + \langle \widetilde{\mathbf{A}_p} \rangle. \tag{16}$$

Since λ_e is linear in A_p, the same decomposition for λ_e: $\lambda_e = \lambda_e^{(0)} + \widetilde{\lambda}_e$ is obtained. Calculating the expected value from the latter relation, one gets

$$\langle \lambda_e \rangle = \lambda_e^{(0)} + \langle \widetilde{\lambda_e} \rangle. \tag{17}$$

The part $\lambda_e^{(0)}$ corresponds to the deterministic symmetric structure. The case of a single reinforcement in a square periodicity cell has been calculated in [3], [4]. The expected value of $\langle \widetilde{\lambda_e} \rangle$ is defined by the formula:

$$\langle \widetilde{\lambda_e} \rangle = 2\rho\nu[\langle \widetilde{\mathbf{A}_0} \rangle + \langle \widetilde{\mathbf{A}_1} \rangle \nu + \langle \widetilde{\mathbf{A}_2} \rangle \nu^2 + \ldots]. \tag{18}$$

By definition

$$\langle \widetilde{\mathbf{A}_p} \rangle := \int\limits_{[Q_(0,0)]^N} \widetilde{\mathbf{A}_p}(a_1, ..., a_N) \prod_{k=1}^{N} f_k(a_k)\ (d\sigma)^N, \tag{19}$$

where $p = 0, 1, 2, \ldots$. Here, the integration is performed with respect to the complex-valued variables $a_k = x + \imath y\ \ (k = 1, 2, ..., N)$ which are the values of random variables $\boldsymbol{a}_k$.

It is shown in [7] that the expected values of the random correction of the coefficients $\mathbf{A}_p$ in the representation (18) are non-negative

$$\langle \widetilde{\mathbf{A}_p} \rangle \geq 0, \qquad p = 0, 1, 2, 3, \ldots \tag{20}$$

for contrast parameter $\rho > 0$.

For composite materials with fractal structure identically distributed random variables a_{ghk} have uniform distributions inside the disk $|z| < d_g$, i.e. the probability density has a form

$$f_{ghk}(z) := \begin{cases} \frac{1}{\pi d_g^2}, & |z| < d_g, \\ 0, & |z| \geq d_g. \end{cases}$$

In this case, equalities (15), (16), (18), (19) hold. It is also shown in [6] that the expected values of $\mathbf{A}_p$ are non-negative for contrast parameter $\rho > 0$.

It follows from the inequalities (17), (18), (20) that a symmetric structure with circular reinforcements has a lower effective conductivity than any nonsymmetric structure which consists of reinforcements distributed in an arbitrary way. Thus, the effective conductivity λ_e attains its minimum when $d = 0$.

Table 1: Effect of a small perturbation on the effective conductivity ($\lambda_1 = 190,\ \lambda = 0.2$).

Concentration ν	Symmetric structure	Perturbed structure
diagonal arrangement		
0.1	0.24401	0.24493
0.2	0.29974	0.30849
0.3	0.38093	0.42979
0.4	0.52602	0.72485
0.5	0.82138	1.46112
square arrangement		
0.1	0.24425	0.24444
0.2	0.29892	0.29998
0.3	0.3679	0.37139
0.4	0.45822	0.46783
0.5	0.58292	0.60713
fractal arrangement		
0.1	0.2438	0.24401
0.2	0.29678	0.29788
0.3	0.36198	0.36504
0.4	0.44426	0.45118
0.5	0.55145	0.56542

Conclusions

The effective conductivity of 2D composite materials with different topology is analytically investigated. Obtained values for the effective conductivity as a function of the concentration ν are compared with the values independently obtained by the numerical finite element method. An excellent correlation is shown in Figure 2.

A small perturbation of the reinforcement position is also considered. It has been proven for different arrangements that for $\rho > 0$ (i.e. the reinforcements conductivity is more than the matrix conductivity) and disjoint reinforcements a small perturbation increases the effective conductivity.

References

[1] Berlyand, L., Mityushev, V.V.: Generalized Clausius-Mossotti formula for random composite with circular fibers. *Journal of Statistical Physics*, 102, No. 112, pp. 115-145, 2001.

[2] Jikov, V.V., Kozlov, S.M., Olejnik, O.A.: *Homogenization of Differential Operators and Integral Functionals.* Springer Verlag, Berlin, 1994.

[3] McPhedran, R.C.: Transport properties of cylinder pairs and of the square array of cylinders. *Proc. Roy. Soc. Lond. Ser. A*, 408, pp. 31-43, 1986.

[4] Mityushev, V.V.: Transport properties of regular arrays of cylinders. *ZAMM* 77, pp. 115-120, 1997.

[5] Mityushev, V.V., Rogosin, S.V.: *Constructive Methods for Linear and Nonlinear Boundary Value Problems for Analytic Functions. Theory and Application.* Boca Raton-London-New York-Washington: Chapman & Hall/CRC Press, 2000.

[6] Pesetskaya, E.V.: Effective conductivity of composite materials with random position of circular inclusions of different radii. Finite number inclusions in the cell. *Proc. Inst. Math.* v. 12, No. 1, pp. 117-122, 2004.

[7] Pesetskaya, E.V.: Effective conductivity of composite materials with random position of circular inclusions. Finite number inclusions in the cell. *Applicable Analysis, in press.*

[8] Weil, A.: *Elliptic Functions According to Eisenstein and Kronecker.* Springer Verlag, Berlin, 1976.

[9] Zienkiewicz, O.C., Taylor, R.L.: *The Finite Element Method.* Butterworth-Heinemann, Oxford, 2000.

STRUCTURAL AND CHEMICAL DISORDER IN LASER- AND MECHANICALLY-INDENTED INSB PROBED BY RAMAN SCATTERING

Paulo S. PIZANI[1,*], Miryam R. JOYA[1], Francesco LANCIOTTI[1], Renato G. JASINEVICIUS[2], Ricardo E. SAMAD[3], Wagner de ROSSI[3], Anderson Z. FREITAS[3], Nilson D. VIEIRA JUNIOR[3]

[1]Departamento de Física, Universidade Federal de São Carlos, C. P. 676, 13565-905 São Carlos, SP, Brasil
[2]Escola de Engenharia de São Carlos, Universidade de São Paulo, C. P. 369, 13 560-970 São Carlos, SP. Brasil
[31]Centro de Lasers e Aplicações, Instituto de Pesquisas Energéticas e Nucleares, Cidade Universitária, Av. Lineu Prestes, 2242, 05508-900 São Paulo, SP, Brasil

[*]Corresponding author. Fax: (55) 16 3361 4835; Email: pizani@df.ufscar.br

Abstract

In the present paper we report on the structural and chemical disorder effects caused by mechanical and laser indentations in indium antimonide by means of a tomograph and topograph Raman scattering analysis. In the mechanical indentation, it was observed three main effects: amorphization, structural pressure induced phase transition from zinc blende to wurtzite structure at the centre of the face fingerprint and the presence of both compressive and tensile residual strains. In the laser indentations was observed an intense irreversible chemical disorder, the main effect being the segregation of crystalline antimony to the surface of the fingerprint.

Keywords: Phase transformation; Mechanical indentation; Laser indentation; Disorder effects

1 Introduction

In the majority of the cases, Vickers indentations are used to determine the hardness of materials. However, the process of indentation involves interesting physical transformations as pressure induced structural phase transition, plastic flow of matter, amorphization, and structural defect generation. For brittle materials a detailed analysis of the response to mechanical indentations serves as a guide to define the best conditions for machining in ductile regime, in a single point diamond turning machines for example. This mechanical process of matter removal can be used as an alternative to machine special surface forms, such as aspherical_silicon lenses for infrared region.

More recently, another process applied to obtain special surface forms uses fusion by means of a high power pulsed laser as the main material removal mechanism. In this case the vaporized material during a few picoseconds is removed by a gas flow. These two essentially different processes of matter removal - one purely mechanical and other purely thermal - lead both nevertheless to damages to the worked surface.

In the present paper we performed a detailed Raman scattering study on the structural and chemical disorder effects produced into and around the fingerprint of Vickers micro-indentation and indentation by using a high power pulsed laser in crystalline indium antimonide, InSb. The choice for InSb is that between the III-V semiconductors it is one that has the lowest transition pressure value, a important parameter that determines the conditions to machine in the ductile regime. A topographic study was performed by taken Raman spectra since the centre of the fingerprint up to several microns far form the indentation and a tomographic study by taken the Raman spectra with several different exciting wavelength with the penetration deep of the light varying from 8 to 14 nm.

2 Experimental Details

The samples used in this study were wafers of commercial InSb single crystals grown in the [001] direction. This direction was choose because in the backscattering configuration with the incident and scattered light along [001] direction, the Raman spectrum presents only a single peak at 190 cm^{-1} due to the light scattering by the longitudinal optical (LO) phonon, as previewed by the Raman selection rules for the zinc blende structure of InSb. The presence of the peak at 180 cm^{-1} due to the light scattering by the transverse optical phonon (TO) and the broadening of the Raman peaks indicate structural disorder. So, the intensity ratio between the TO and LO Raman peaks can be used to probe the structural disorder of InSb. Furthermore, residual strains can be probed by the shift of the Raman peaks: positive (negative) shifts indicate compressive (tensile) residual strain.

The Raman scattering measurements were performed using a micro-Raman spectrometer with a triple monochromator and a CCD detector. As exciting wavelengths were used the 488, 514, 568 and 647 nm lines of an Ar ion laser, focussed on the sample as a spot of about 1 micron square by a microscope with a 100X objective. The light penetration depths of these lines are about 8, 9, 12 and 14 nm, respectively for crystalline InSb [1]. Finally, all measurements were performed at room temperature, with the laser power kept at about 1 mW at the entrance of the microscope to avoid thermal effects on the spectra. All results were obtained from fitting the Raman peaks using Lorentzian line shapes.

The micro indentation tests were performed in a VMHT MET Leica (Leica Mikrosysteme**,** Gmbh**;** A-1170, Vienna, Austria) micro indentation apparatus using a Vickers pyramidal indenter. The indentation loads used in the tests were varied between the range of 10 g, 25 g, 50 g and 100g. The micro indentation test was performed on 12 mm x 12 mm square, 0.5 mm thick samples of monocrystalline (001)-oriented InSb. The majority of the results presented in this work were performed mainly on the indentations with 25 g, with 10 x 10 microns size.

The laser indentations were performed using an ultrashort laser pulses from a Quantronix Odin CPA system seeded by a Coherent Mira-SEED. Only one laser pulse was used for each indentation; the temporal pulse width was 60 fs and its energy E = 167 mJ. The laser pulse was focused on the crystal surface by an f=90mm converging lens to produce a spot with approximated intensity of 7,3 TW/cm2. The experiment, which was performed in air, produces a 10 x 30 microns alonged "scratch" into the surface of the sample.

3 Results and Discussions

3.1 Mechanical indentations

Figure 1 shows a sequence of Raman spectra performed on points at the centre of the fingerprint, (Fig. 1 a), at the centre of the face (Fig. 1 b), at the border (Fig. 1 c) and far from the fingerprint (Fig. 1 d), using the line 458 nm, whose penetration is about only 8 nanometers. From the spectra, it can be seem several different effects: the excitation of the TO mode of the InSb inside the indentation with the simultaneous broadening of the LO peak, the amorphization of InSb in the region around the centre, denounced by the presence of the broad band at 185 cm^{-1} (the optical band, which reflects the optical vibrational density of states), positive and negative frequency shifts of both LO and TO modes and the appearance of new Raman peaks at the centre of the face of the fingerprint.

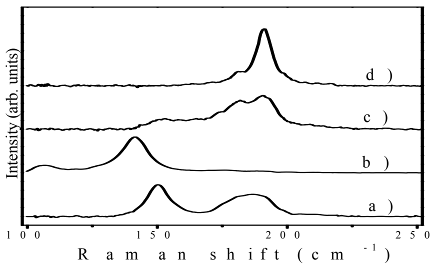

Figure 1: Raman spectra performed on points at the centre of the fingerprint, a), at the centre of the face b), at the border c) and far from the fingerprint d) using the 458 nm exciting wavelength.

The activation of the TO peak and the broadening of the LO indicate high structural disorder due to the defects generation driven by the high pressure with high shear components applied by the indenter. At the centre of the indentation, where the pressure applied reaches its maximum value, it can be observed a complete amorphization of the material.

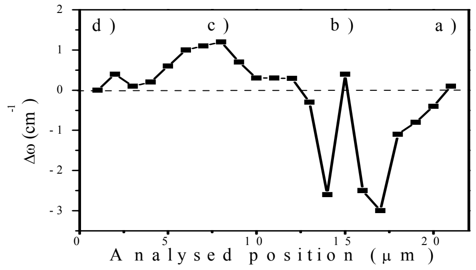

Figure 2. Frequency shift of the LO mode for several positions as indicated in Fig. 1 from a) to d).

Relationship to the residual strains, denounced by the shifts of the Raman peaks, there are an interesting behaviour of InSb which shows positive and negative frequency shifts along the indentation face, similar to that also observed in GaAs, but completely different from the Si case, in which was observed only compressive residual strains, with very high values at the border of the indentation [2, 3]. Figure 2 displays the relative frequency shift of the LO mode $\Delta\omega$ (= ω_0 - ω, ω_0 is the frequency of the LO mode far from indentation) for several different positions: from outside towards the centre of the indentation. At the centre of the face there is an inversion of the sign of $\Delta\omega$, the residual strain changing from compressive to tensile.

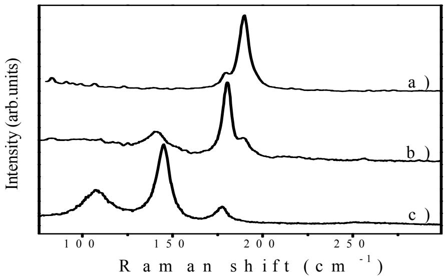

Figure 3: Raman spectra of InSb sample submitted to mechanical impact.

At this region two new features appears in the Raman spectra at about 145 and 175 cm^{-1}, suggesting that a structural phase transition occurred. Similar features was also observed by Gogotsi in indented InSb but only in cases where the decompression rate was intentionally increased, contrary to our case[4] These features are indicative of the occurrence of a pressure induced structural phase transition from zinc blende to wurtzite structure.

Guided by the theoretical studies of Wang [5] that have predicted this transition at about 1.85 GPa, we searched to detect it via Raman scattering by carefully applying hydrostatic pressure using a diamond anvil cell. All attempts to observe this specific phase transition were unsuccessful.

To corroborate the assumptions that the compression rate and shear components induce the phase transition, we applied to one sample a rapid impact, where the shear components and the compression/decompression rates are very high. The resulting spectra are shown in figure 3. Among several visual different regions produced by the rapid impact imposed on the sample, there are some whose Raman spectrum is that from InSb in the wurtzite structure, as showed in figure 3-c). It seems indeed that the existence of shear component simultaneous to a high compression/decompression rate is primordial to produce this transition from zinc blende to wurtzite structure.

Figure 4 shows the same sequence of Raman spectra showed in Fig. 1, but now using the 647 nm as excitation line, with a penetration deep of about 14 nm. It can be noticed that the LO Raman peak at about 190 cm^{-1} is always more intense than the TO one, indicating that the structural disorder decrease increasing the deep, being

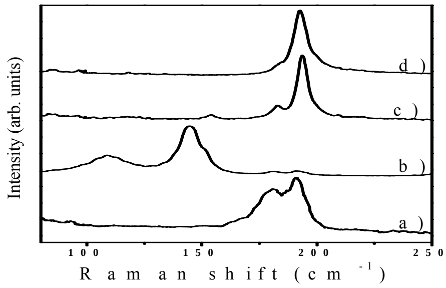

Figure 4: Raman spectra performed on points at the centre of the fingerprint, a), at the centre of the face b), at the border c) and far from the fingerprint d), using the 647 nm as exciting wavelength.

than the TO one, indicating that the structural disorder decrease increasing the depth, being localized mainly into the first 8 nm. The Raman peaks of the wurtzite phase are still present at the centre of the face. Figure 5 shows the Raman spectra taken at the same point of the indentation, but with three different exciting wavelengths. It is clear that the disorder effects are localized into the surface.

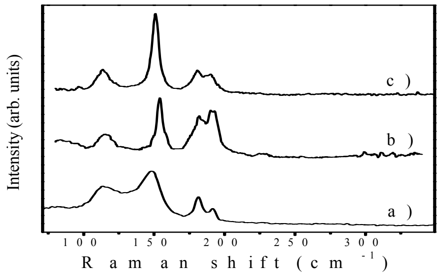

Figure 5: Raman spectra at the centre of the fingerprint at three different exciting wavelengths: a) 458 nm, b) 488 nm and c) 514 nm.

3.2 Laser indentations

Figure 6 shows a sequence of Raman spectra along a line starting at points far from up to the centre of the laser indentation. The Raman peaks at 150 and 190 cm^{-1} indicate the presence of crystalline antimony and the peak at 180 cm^{-1} due to the TO mode simultaneous to the broadening of the LO one indicate high structural disorder. This topographical study reveals that the effect of the laser is to promote both chemical and structural disorder.

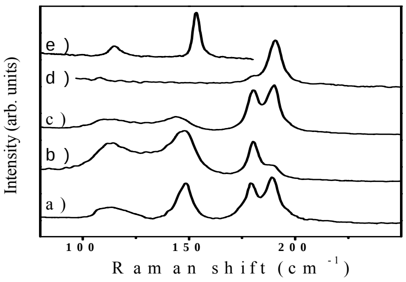

Figure 6: Sequence of Raman spectra along a line starting at the centre, a) to points far from d) the centre of the laser indentation. e) is the Raman spectrum of crystalline Sb

Figure 7 shows a sequence of Raman spectra taken at the same point of the indentation with different excitation wavelengths. It is interesting to notice the increase of the intensity of the A_{1g} and E_g Raman peaks of antimony relative to that of InSb decreasing the excitation wavelength that is, decreasing the probed deep. This result indicate that the localization of the antimony mainly into the surface. Similar results were observed in GaAs and GaSb submitted to thermal treatment in conventional furnace, with the migration of the V element to the surface [6].

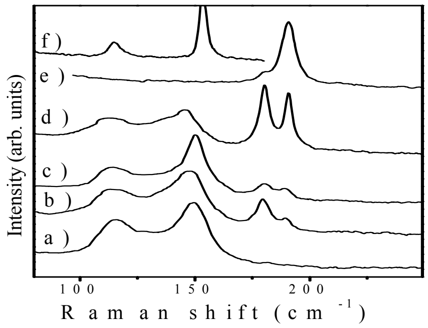

Figure 7: Raman spectra taken at the same point of the laser indentation with different excitation wavelengths: a) 466, b) 488, c) 514, d) 568, e) 647 nm. f) is the Raman spectrum of crystalline Sb.

4 Conclusions

We have performed a detailed Raman scattering study on the effects of the indentation of InSb using two different processes: mechanical indentation (Vickers) and thermal fusion using a high power pulsed laser. Our Raman results showed that the mechanical process lead to high structural disorder, localized mainly into the first 8 nm into the surface and a complete amorphization at the centre of the indentation. At the centre of the face, there are two very interesting effects: an inversion of the sign of the residual strain, changing from compressive to tensile and a pressure induced phase transition from zinc blende to wurtzite structure. This phase transition was only reproduced on samples submitted to high impact, it was not observed by applying hydrostatic pressures using a diamond anvil cell. This means that high components of shear and high compression/decompression rates are need to induce zinc blende to wurtzite structural phase transition in InSb. Relationship to the laser indentations, our Raman results indicate that the thermal process produces both structural and chemical disorder, with the migration of the antimony to the surface. Finally, our results indicate that the both mechanical and thermal process lead always to disorder effects, with may be a limiting factor to the use of the mechanical and thermal machining of special surfaces in III-V semiconductors.

Acknowledgments

The authors would like to thank the Brazilian funding agencies FAPESP, CAPES and CNPq.

References

[1] Aspnes, D. E and Studna A. A.: Dielectric functions and optical-parameters of Si, Ge, GaP, GaAs, GaSb, InP, InAs, and InSb from 1.5 to 6.0 eV., *Phys. Rev. B* **27**, 985 (1982).

[2] Puech, P., Demangeot, F., and Pizani, P. S.: Strain determination around Vickers indentation on silicon surface by Raman spectroscopy. *J. Mater. Res.*, 19, pp.1273-1280, 2004.

[3] Puech, P., Demangeot, F., Pizani, P. S., Wey, S., and Fontaine, C.: Strain field in indented GaAs, *J. Mater. Res.*, 18, pp.1474-1480, 2003.

[4] Kailer, A., Nickel, K. G., and Gogotsi, Y. G.: Raman microspectroscopy of nanocrystalline and amorphous phases in hardness indentations. *J. Raman Spectrosc.*, 30, pp. 939-U7, 1999.

[5] Wang, S. Q. and Ye, H. Q.: A plane-wave pseudopotential study on III-V zinc-blende and wurtzite semicondutors under pressure.. *J. Phys.: Condens. Mater*, 14, pp. 9579-9587, 2002.

[6] Campos, C. E. M. and Pizani, P. S.: Morphological studies of annealed GaAs and GaSb surfaces by micro-Raman spectroscopy and EDX microanalysis. Appl. Sur. Sci., 200, pp. 111-115, 2002.

Proceedings of The 1st International Conference on **D**iffusion in **S**olids and **L**iquids
DSL-2005, July 6-8, 2005, University of Aveiro, Aveiro, Portugal

ALTERNATIVE APPROACH TO DESCRIBE THE OXIDATION BEHAVIOUR OF BINARY ALLOYS

Gabriel PLASCENCIA[1,2,*], Torstein UTIGARD[2], Juliana GUTIÉRREZ[3]

[1]CIITEC – IPN,
Cerrada Cecati s/n, 02250, México. D.F., México
[2]Department of Materials Science & Engineering, University of Toronto,
184 College St., M5S 3E4, Toronto, ON, Canada
[3]UAM – Azcapotzalco,
Sn. Pablo 180, 02200, México. D.F., México

[*]Corresponding author. Fax: +(5255) 5561-7536; Email: g.plascencia@utoronto.ca

---

Abstract

A new model to describe the formation of the internal oxidation layer during the oxidation of binary A - B alloys (where A is the host metal and B is the solute and more active metal) is presented. The model assumes a linear oxygen concentration profile within the internal oxidation layer, while it neglects the diffusion of the solute metal through the internal oxidation layer. As a result of such basic assumptions, we developed an equation equivalent to that formulated by Wagner almost fifty years ago. The main difference between our model and that by Wagner is that ours does not need accurate independent measurements of the concentrations of the different diffusing species. At the same time, the mathematics leading to Wagner's equation are complex and their physical meaning strongly depends on the measurements mentioned above. Another limitation of Wagner's model is that it was developed for cartesian coordinates, and there is no mention on the applicability of such model in non flat samples. Furthermore, our model can be used to estimate the solubility of oxygen in the host metal. Thermogravimetric experiments conducted in different dilute Cu - Al alloys showed that when the solubility limit is exceeded, there is formation of the internal oxidation layer, whereas when the concentration of oxygen in the host metal lies below its solubility limit, a protective layer of oxide is formed along the alloy surface.

Keywords: High Temperature Oxidation; Diffusion; Binary alloys; Solubility limit; Internal oxidation layer

---

1 Background

Wagner made the first attempt to describe the oxidation behaviour in binary (A-B) alloys. In his model [1,2] he assumed that alloy oxidation is similar to that of pure metals.

Wagner's model considers thermodynamic equilibrium between the oxidant medium and the alloy. He estimated the rate of transport of both the oxygen and the alloying element (B). This model only works if the solubility product of BOν oxide is very small. The model also requires that the concentrations of both oxygen and B at the oxidation front are insignificant.

In this treatment, when oxygen diffusion predominates, Wagner defined the depth of the internal oxidation layer as:

$$\xi^2 = 2 \cdot \frac{N_O^{(s)} \cdot D_O \cdot t}{\nu \cdot N_B^{(i)}} \tag{1}$$

Where $N_O^{(s)}$ is the concentration of oxygen at the alloy surface, $N_B^{(i)}$is the concentration of the solute B, D_O is the diffusion coefficient of oxygen in the host metal A, t is the time of exposure and ν is the stoichiometric coefficient in the BOν oxide.

Although equation (1) does not seem to be too complex, it involves very precise measurements of the concentrations of the different diffusing species. Such measurements are extremely difficult to perform due to limitations in the sensitivity of the measuring devices. In spite of such limitations, Gesmundo et al [3] modified Wagner's model. The main difference between Gesmundo and Wagner models relies on the estimation of the oxidation parameters. However, as in the case of Wagner's, Gesmundo's model needs, independent measurements of the concentrations of the different diffusing species which are difficult to make accurately. At the same time, the equations leading to equation (1) are complex and their physical meaning is strongly dependent on the measurements mentioned above.

On the other hand, Rhines et al [4,5] proposed a set of equations to estimate the rate of external and internal oxidation. Instead of approaching these equations analytically, Rhines et al inserted guessed values of the different oxides thicknesses and compared them to their experimental measurements. The expression developed for the internal oxidation layer is:

$$x^2 = \frac{2 \cdot N_O^{(s)} \cdot D_O}{\alpha} \cdot t \qquad (2)$$

Where x is the depth of the internal oxidation layer, α is a parameter determined experimentally and $N_O^{(s)}$, D_O and t have been already described.

2 Diffusion data in the Cu-Al system

To develop our model, we selected the Cu – Al system. Figure 1 shows data on the diffusivities of oxygen in copper [6, 7] and aluminium in copper [8]. The figure reveals that the diffusivity of oxygen in copper is three orders of magnitude higher than that of aluminium at 1000 ºC, whereas at 700 ºC, it is 5 orders of magnitude higher. Therefore it would be expected that oxidation always occurs since aluminium would not be able to diffuse at such rate that it would stop the oxygen from penetrating into the alloy. However, as it can be seen in Figure 2, if oxidation takes place, both aluminium and oxygen have to diffuse through the same path, and the molar fluxes are defined only by the product of their diffusivity and their solubility limit in copper. Since the solubility of oxygen in copper is very low and the absolute diffusion fluxes of both aluminium and oxygen are comparable, the oxidation can be explained by the kinetic model described in the next section.

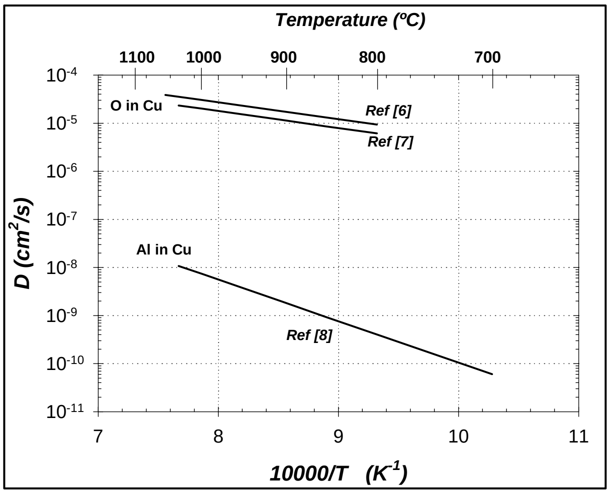

Figure 1: Diffusivities of oxygen and aluminium in copper as a function of temperature.

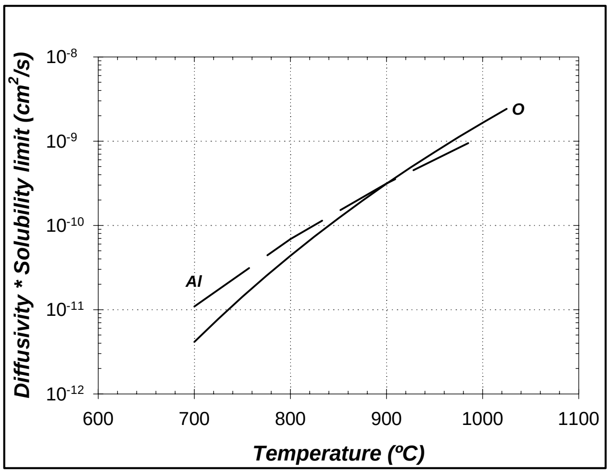

Figure 2: Product of the solubility limit and diffusivity of oxygen and aluminium in copper.

3 Model description

During oxidation, oxygen penetrates into the alloy where it reacts with the aluminium to form an oxide layer that may or may not serve as a diffusion barrier. Depending upon the alloying element content and the oxidizing conditions, the oxide layer may not be able to stop the oxygen uptake, allowing the base metal (copper) to be oxidized. To further improve the understanding of the oxidizing behaviour of dilute Copper –

aluminium alloys, we developed a kinetic model based on the following assumptions:

1. The concentration of oxygen in the unoxidized alloy is zero
2. The formation of CuO in the outer scale is neglected
3. Oxygen and copper concentration gradients in the external scale are linear.

Since aluminium has a greater affinity for oxygen than copper, it will be oxidized preferentially over copper, accordingly to the equation:

$$2\mathrm{Al} + {}^{3}/_{2}\,\mathrm{O}_2 = \mathrm{Al}_2\mathrm{O}_3 \tag{3}$$

From (3) we define the stoichiometric mass ratio:

$$R_S = \frac{O}{Al} = \frac{48}{54} \tag{4}$$

Since the samples used to probe this model are cylindrical, and assuming no concentration gradients in the z-direction, the number of moles of oxygen that penetrates into the alloy, forming the internal oxidation layer, is given by:

$$n_O = \frac{\pi \cdot R_S \cdot \rho_{Cu} \cdot \underline{Al} \cdot L \cdot \left(r_1^2 - r_2^2\right)}{16} \tag{5}$$

where R_S has been defined, ρ_{Cu} is the density of copper (g/cm^3), $\underline{Al}$ is the mass fraction of aluminium in the alloy, L is the cylinder length (cm), r_1 is the radius of the cylinder (cm) and r_2 is the radius of the un-oxidized alloy.

The molar rate of oxygen uptake is obtaining by deriving equation (5) with respect of time:

$$\frac{dn_O}{dt} = -2\pi L \cdot r_2 \cdot \frac{R_S \cdot \underline{Al} \cdot \rho_{Cu}}{16} \cdot \frac{dr_2}{dt} \tag{6}$$

where t is the oxidation time (s). Equation (6) represents the total amount of oxygen that can penetrate into the alloy as dissolved oxygen to oxidize the aluminium present in the copper matrix.

On the other hand, the oxygen uptake in the radial direction and the molar flux are given by:

$$\frac{dn_O}{dt} = 2\pi \cdot r \cdot L \cdot D_O \cdot \frac{dC_{\underline{O}}}{dr} \tag{7}$$

where $2\pi\ r\ L$ is the mass transfer area (cm^2), D_O is the diffusion coefficient of oxygen in copper (cm^2/s) and $dC_{\underline{O}}$ /dr is the concentration gradient of dissolved oxygen in the radial direction. This equation represents the concentration profile of the dissolved oxygen through the internal oxidation layer. Since basically all the oxygen diffusing into the alloy reacts with aluminium, equations (6) and (7) are equated, and since we are dealing with diluted copper alloys, $C_{\underline{O}}$ can be expressed in terms of the weight fraction (5) of oxygen ($\underline{O}$) in copper, thus we obtain:

$$-r_2 \cdot R_S \cdot \underline{Al} \cdot \frac{dr_2}{dt} = r \cdot D_O \cdot \frac{d\underline{O}}{dr} \tag{8}$$

The solution of equation (8) is:

$$\varepsilon(t) = \frac{r_1^2 - r_2^2}{2} - r_2^2 \cdot \ln\left(\frac{r_1}{r_2}\right) = 2 \cdot \frac{D_O \cdot \underline{O}}{R_S \cdot \underline{Al}} \cdot t \tag{9}$$

For more details in the development of this model, we refer the reader to literature [9]. Swisher and Fuchs [10], using slightly different assumptions arrived to the same equation.

4 Experimental

To verify the model above described, several dilute copper - aluminium (1 to 4 wt %) alloys were prepared in an electric furnace. High purity copper and aluminium were melted in a graphite crucible under an inert atmosphere to prevent oxygen pick up. Once melted, the alloys were cast into cylindrical graphite moulds; then the cylinders were machined to smaller cylinders with a diameter of 1.0 cm and height of 1.0 cm.

Before every oxidation test, each cylinder was ground with grit paper grade 800, water rinsed and pickled in an acidic solution. After pickling, the samples were rinsed in water and dried with air. Once cleaned every sample was measured and weighted. Finally every sample was placed into an alumina crucible to be oxidized in a muffle from 700 to 1000 ºC in air. Samples were taken out of the muffle at different times. Once cooled, the samples were weighted again, and then mounted for metallographic examination. In every case the mounted samples were ground with grinding paper (grades 180 to 1200) and polished with chromia to avoid alumina contamination. The samples were observed under an optical microscope and the thickness of the internal oxidation layer was measured by means of a grid.

Figures 3 and 4 show micrographs of two different alloys oxidized under the same conditions. The 2 wt% Al alloy developed both a thick external scale and the internal oxidation layer. The 2.25 wt% Al alloy only developed a not so thick external scale; such scale is the due to the oxidation of the copper in the alloy surface. There is no indication of the formation of the internal oxidation layer.

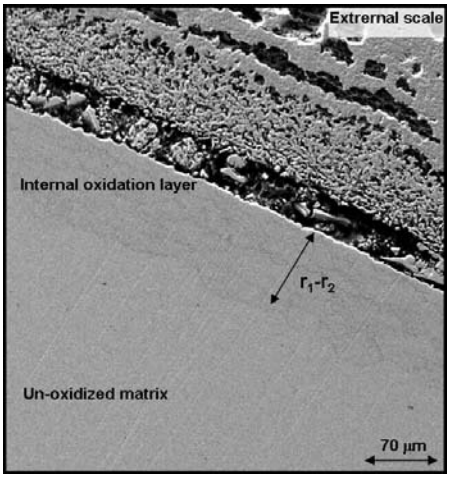

Figure 3: 2 wt% Al alloy oxidized in air at 850 ºC during 8 hrs.

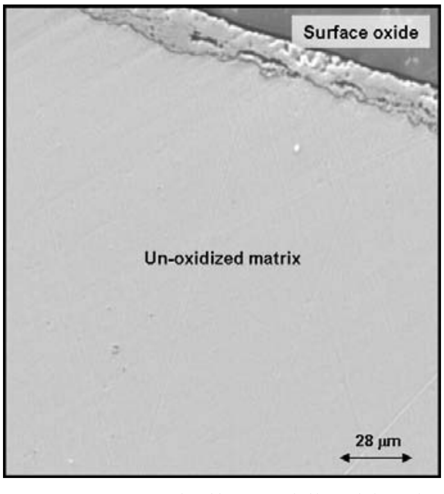

Figure 4: 2.25 wt% Al alloy oxidized in air at 850 ºC during 8 hrs.

5 Results

The thickness of the internal oxidation layer was used to estimate the difference in radii (r_1-r_2) in equation (9).

Equation (9) represents the penetration of oxygen in the alloy as a function of time. It has the shape of a straight line whose ordinate is time and its slope is the quotient on the right side term of equation (9). To estimate the amount of oxygen dissolved in the alloy, we used the measured depth and the average diffusion coefficient for oxygen in copper [6, 7]. Figure 5 shows plots of ε(t) versus time for the oxidation of the 2 wt % Al alloy at different temperatures. Table I summarizes the results for the different alloys tested.

It also must be noticed that the right hand side of equation (9) is equivalent to the ones in equations (1) and (2) respectively.

Thus by measuring the difference between r_1 and r_2, it is possible to indirectly measure the concentration of oxygen within the internal oxidation zone.

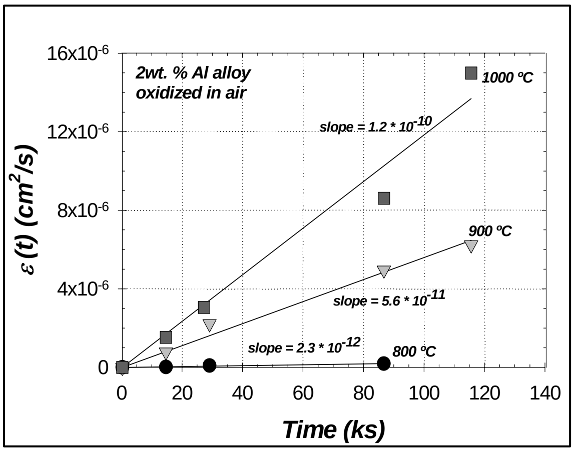

Figure 5: Depth of penetration of oxygen at different temperatures in the 2 wt% Al alloy.

Figure 6 shows a plot of the solubility of oxygen versus the reciprocal of temperature for different alloys. In the same figure, we compare our results to independent measurements of the oxygen solubility in copper [6, 7]. If the concentration of oxygen in any alloy exceeds its solubility limit in copper, the internal oxidation zone will lead to an external scale, whereas if the concentration of oxygen lies below the solubility limit, no external scale will be formed, so the amount of aluminium in the alloy is sufficient to protect copper from being oxidized.

Table 1: Depth of penetration of oxygen in the alloys tested at different temperatures.

Alloy	**Temperature (ºC)**	**D_O (cm^2/s)**	$2\times\frac{D_O \cdot O}{R_S \cdot \underline{Al}}$
1 wt. % Al	700	3.6×10^{-6}	5×10^{-12}
	800	7.8×10^{-6}	1×10^{-11}
	850	1.1×10^{-5}	1×10^{-10}
	1000	2.5×10^{-5}	2×10^{-10}
2 wt. % Al	700	3.6×10^{-6}	1×10^{-14}
	800	7.8×10^{-6}	2×10^{-12}
	850	1.1×10^{-5}	3×10^{-11}
	900	1.5×10^{-5}	6×10^{-11}
	1000	2.5×10^{-5}	1×10^{-10}
2.25 wt. % Al	800	7.8×10^{-6}	1×10^{-14}
	850	1.1×10^{-5}	1×10^{-13}
	900	1.5×10^{-5}	1×10^{-12}
	1000	2.5×10^{-5}	4×10^{-11}
2.5 wt. % Al	900	1.5×10^{-5}	1×10^{-14}
	1000	2.5×10^{-5}	1×10^{-11}

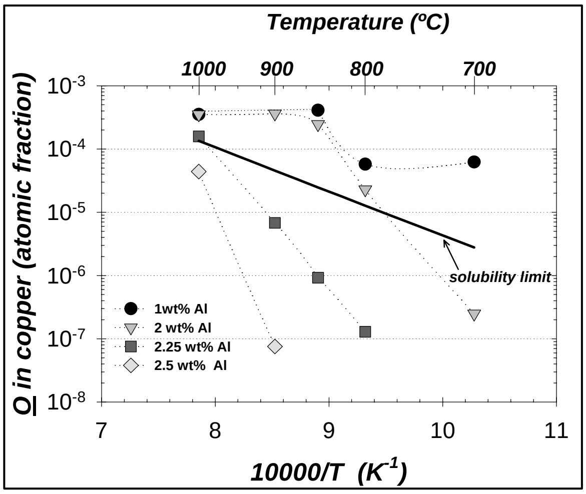

Figure 6: Oxygen content in copper for different alloys after being oxidized in air at different temperatures.

6 Future work

To verify the accuracy and precision of the model presented in this paper, we have started oxidation tests in copper base alloys: Cu-Ti, Cu-Cr, Cu-Si, Cu-Be and Cu-Zn. It is expected that these systems behave in a manner similar to the Cu-Al system. We also want to extend this approach to ternary and higher order alloy systems.

7 Conclusions

A new alternative kinetic model to describe the oxidation behaviour of dilute binary alloys has been proposed.

The model was set up by means of a mass balance and assuming a linear concentration profile of the different diffusing species within the alloy.

The model allows estimating the amount of oxygen that has penetrated into the alloy. When the amount of oxygen in the alloy exceeds its solubility limit in the base metal, the internal oxidation layer develops; consequently a thick external oxide layer develops as well. On the other hand, if the amount of oxygen within the alloy does not exceed the solubility limit, a dense compact layer of the most stable oxide (Al_2O_3 in this case) forms serving as a diffusion barrier; such barrier slows down the oxidation process. As more alloying element is added to the base metal (copper) the more likely the oxidation process will stop completely.

Acknowledgments

Funding for this project from CONACyT and CIITEC-IPN (México) and NSERC (Canada) is greatly appreciated

References

[1] Wagner, C.: Reaktionstypen bei der oxydation von legierungen, *Z. Elektrochem*, 63 (7), pp 772-790, 1959.

[2] Kofstad, P.: *High Temperature Corrosion*, Elsvier, Amsterdam, 1988.

[3] Gesmundo, F, Castello, P., Viani, F., Roos, C.: The effect of supersaturation on the internal oxidation of binary alloys. *Oxid.*

Met., 49 (3/4), pp. 237-260, 1998.

[4] Rhines, F.N.: A metallographic study of internal oxidation in the alpha solid solutions of copper, *Trans. Amer. Inst. of Mining and Metallurgical Engs.*, 137, pp. 246-290, 1940.

[5] Rhines, F.N., Johnson, W.A., Anderson, W.A.: Rates of high temperature oxidation of dilute copper alloys, *Trans. Amer. Inst. of Mining and Metallurgical Engs.,* 147, pp. 205-221, 1942.

[6] Pastorek, R.L., Rapp, R.A.: The solubility and diffusivity of oxygen in solid copper from electrochemical measurements, *Trans. Met. Soc. AIME*, 245, pp. 1711-1719, 1969.

[7] Narula, M.L., Tare, V.B., Worrell, W.L.: Diffusivity and solubility of oxygen in solid copper using potentiostatic and potentiometric techniques, *Met. Trans B,* 14B, pp 673-677, 1983.

[8] Askeland, D.R.: *The Science and Engineering of Materials,* PWS Publishing Co., Boston, USA, 1994.

[9] Plascencia, G., Utigard, T.: High temperature oxidation mechanism of dilute copper aluminium alloys. *Corr. Sci.*, 47 (5), pp. 1149-1163, 2005.

[10] Swisher, J.H., Fuchs, E.O.: Kinetics of internal oxidation of cylinders and spheres; properties of internally oxidized Cu-Cr alloys, *Trans. Met. Soc. AIME*, 245, pp. 1789-1794, 1969.

Proceedings of The 1st International Conference on **D**iffusion in **S**olids and **L**iquids
DSL-2005, July 6-8, 2005, University of Aveiro, Aveiro, Portugal

NUMERICAL SIMULATION OF CARBIDE AND NITRIDE PRECIPITATE EVOLUTION IN STEELS

Vladimir V. POPOV*, Igor I. GORBACHEV
Institute of Metal Physics, Ural Division of Russian Academy of Sciences,
S. Kovalevskaya str., 18, GSP-170, Ekaterinburg, RU620041, Russia

*Corresponding author. Fax: 7(343)374 52 44; Email: vpopov@imp.uran.ru

Abstract

A numerical method is described enabling to simulate the evolution of carbide and nitride precipitates ensemble in steels at isothermal annealing. This method is based on the mean field approximation and consideration of precipitate evolution in field cells. It is taken into account that this evolution includes not only the growth and dissolution of the particles existing, but nucleation of the new ones as well. This method enables to simulate the precipitate evolution at all the stages beginning from nucleation and up to stationary coarsening. The results of kinetic calculations of VC evolution in steels at different initial particle size distributions are presented and analyzed.

Keywords: *Numerical simulation; Growth; Dissolution; Coarsening; Precipitates; Steels; Carbides; Nitrides*

1 Introduction

Carbide and nitride particles may significantly affect the structure and properties of steels. The degree and character of the dispersed particles effect is determined by the state of the precipitate ensemble forming mainly at heat treatment.

In the development of the dispersed-hardened and ageing alloys it was impossible up to now to do without a great deal of experimental research on the state of precipitates forming in these materials. Recently however the situation substantially changed with the occurrence of opportunity to simulate precipitates behavior at heat treatment. It was due to two reasons, namely, an accumulation of a great volume of thermodynamic and diffusion data, and the development of high-productivity personal computers.

Nevertheless, as a rule, only different special cases are considered and various assumptions are made because of the complexity of this problem. Moreover, different models are usually used for different stages of precipitates evolution. In particular, in simulation of precipitate growth and dissolution it is usually assumed that all the particles are of the same form and sizes and are equally spaced to each other [1,2].

These assumptions are naturally not valid at simulation of coarsening. And in the latter case it is usually assumed that the equilibrium phase composition has been already attained [3-5], which makes impossible to apply this model for simulation of growth and dissolution.

In Ref. [6] we suggested a new numerical method enabling to simulate precipitate evolution in binary systems at different stages. Later this method was generalized to the case of multicomponent systems [7,8], and in Ref. [9] the formation of new nucleation centers was taken into account. In the present work the essence of this method is considered in brief, its capability is analyzed and the results of calculation of precipitate evolution in steels accomplished by means of this method are presented.

2 Numerical calculation techniques

Working out the model we did our best to make minimum assumptions, the following ones being used:

1. Particles are of a spherical form.
2. The precipitates composition is constant, and there is no diffusion in them.
3. The local thermodynamic equilibrium is established on precipitate/matrix interfaces.
4. Mass transfer is controlled by volume diffusion in a matrix.

These assumptions substantially simplify calculation only slightly lowering its commonness.

The volume fracture of precipitates (*F*) and particle size distribution (PSD) in the initial state served as the original data in simulation of precipitate ensemble evolution. The PSD was given by a histogram where the fraction of particles, n_k, falling into the interval from R_k-ΔR/2 to R_k+ΔR/2 was associated with this k-th interval of particles radii. Here R_k is an average radius of particles of the k-th size interval, and ΔR is the width of size intervals, this width being the same for all size intervals. Then a step-wise procedure was used, and based on the volume fracture and PSD at the moment of τ these parameters were calculated for $\tau+\Delta\tau$.

The method is based on the mean field approximation, where the concentrations of all elements at some distance from a particle are considered to be the same (equal mean surrounding). This approximation requires some assumptions associating the extension of particles transport fields (i.e. the sizes of spheres of their influence) with particles sizes and their volume fraction. The choice of possible field cell geometrical models was discussed in detail in Refs [6,10], and that is why it is not considered here. Note that in the present work the model from Ref. [10] is used, according to which the radius of a field cell of the k-th size interval (R_k^L) is proportional to the particle radius and inversely proportional to a cubic root of the precipitate volume fraction (*F*):

$$R_k^L = R_k \cdot F^{-1/3} \tag{1}$$

A quasi-stationary approximation was used for the calculation of the diffusing component concentration distribution, i.e. the time derivative was neglected in the diffusion equations. The mass transfer in a cell of the k-th size interval is thus expressed by the following equations:

$$\sum_{j=1}^{N} \widetilde{D}_{ij} \frac{\partial C_j^k}{\partial r} = \frac{K_i^k}{r^2} \tag{2}$$

where $C_j^k(r)$ is the concentration of the *j*-th component in a cell of the k-th size interval; $\widetilde{D}_{ij}$ are the partial interdiffusion coefficients; and K_i^k are the constants.

The mass balance conditions at an interface of a particle and the matrix from the k-th size interval are as follows:

$$\left[{}^{P}C_i\, \upsilon_m^M / \upsilon_m^P - {}^{M/P}C_i^k\right] \frac{dR_k}{d\tau} = \left.\frac{K_i^k}{r^2}\right|_{r=R_k} \tag{3}$$

where υ_m^P and υ_m^M are molar volumes of a precipitating phase and a matrix, respectively; and ${}^{M/P}C_i$ and ${}^{P}C_i$ are concentrations of the i-th component in a matrix/precipitate interface and in the precipitate itself, correspondingly.

The local thermodynamic equilibrium conditions at an interface of a carbide or nitride precipitate of the *k*-th size interval, *MX* (where X denotes carbon or nitrogen), and a matrix, with the correction for the interface curvature are as follows:

$$\overline{G}_M + \overline{G}_X - \frac{2\sigma\upsilon_m^P}{R_k} - G_{MX} = 0 \tag{4}$$

where $\overline{G}_M$ and $\overline{G}_X$ are chemical potentials of a carbide- or nitride-forming element and carbon or nitrogen in a matrix at an interface with the particle; σ is the specific surface energy of a precipitate/matrix interface; G_{MX} is the Gibbs energy of the *MX* formation.

Component concentrations at boundaries of all field cells should satisfy the boundary condition

$$C_i^k(r = R_k^L) = {}^{L}C_i \tag{5}$$

This boundary condition expresses the equality of component concentrations at boundaries of all field cells, i.e. the equal mean surrounding.

Besides, the usage of a quasi-stationary approximation makes it necessary to add to these equations the mass conservation condition to which the calculated component concentrations in a matrix should satisfy:

$$\alpha\, {}^{P}C_i + (1-\alpha)\overline{C}_i = C_i^0\,, \tag{6}$$

where α is a precipitate mole fraction, $\overline{C}_i$ is the average concentration of the dissolved component in a matrix, and C_i^0 is the dissolved component concentration in an alloy.

The average concentration of the dissolved component in a matrix is connected with concentration distributions in cells, and the precipitate mole fraction is associated with its volume fraction by the following equations:

$$\overline{C}_i = \frac{3\sum_{k=1}^{m} n_k \int_{R_k}^{R_k^L} C_i^k r^2 dr}{\sum_{k=1}^{m} n_k \left[(R_k^L)^3 - (R_k)^3\right]} \tag{7}$$

$$\alpha = \frac{F/\upsilon_m^P}{F/\upsilon_m^P + (1-F)/\upsilon_m^M} \tag{8}$$

With a knowledge of the particles volume fraction and PSD it is possible to calculate the interface rates for particles of all size intervals by the combined solution of equations (2)-(6) with the account for (7)-(8). These equations were solved numerically by Newton's method using the finite differences technique for calculation of the component concentration distributions in cells. The mobile spatial nets were constructed for field cells of all size intervals, their first node coinciding with an interface and the last one with a cell boundary, and the continuous component concentration distributions were replaced by net functions determined in discrete nodes of the spatial net.

In the algorithm suggested the state of the particles ensemble at a new time step, namely, their radii R'_k, volume fraction F' and PSD, is at first calculated by the following formulas without regard for nucleation processes:

$$R_k^{'} = R_k + \frac{dR_k}{d\tau}\Delta\tau \tag{9}$$

$$F' = \frac{\sum_{k=1}^{m} n_k \left(R'_k\right)^3}{\sum_{k=1}^{m} n_k \left(R_k^L\right)^3} \tag{10}$$

A special procedure, described in Refs [6,7] and based on the analysis of the amount of particles leaving the original size interval and falling into it from other intervals in the process of growth or dissolution, is used for PSD calculation at a new time step.

Then the critical nucleus radius ($R_{crit.}$) and the mean nucleation rate *(J)* were calculated based on the mean matrix composition. This calculation was carried out based on the classical nucleation theory using the method suggested in Refs [11,12]. Based on the obtained data the corrections on the volume fraction and PSD connected with the formation of new nucleation centers were calculated. The calculation procedure for a case when the formation of new nucleation centers is probable is described in more detail in Ref. [9].

The calculated values of volume fraction and PSD served as the initial data for calculations at a new time step. This procedure was repeated till the necessary time was reached.

In Refs [7-9] we compared the results of precipitate evolution calculations accomplished using this method with the available experimental data for different stages of precipitate evolution in steels of various composition. For all the cases considered a satisfactory agreement of calculations with experiment was obtained.

Thus, we have worked out a numerical method enabling to simulate precipitate evolution in steels at the stages of nucleation, growth, dissolution, coarsening and intermediate stages.

3 Analysis of the original PSD influence on the kinetics of precipitate evolution

Using the algorithm developed the influence of the original PSD on further precipitate evolution has been analyzed, the analysis having shown the strong dependence of particles ensemble evolution on the initial PSD. To illustrate that we present here the calculation results of simulation of vanadium carbides growth and dissolution in austenite for three original PSD:

1. A very narrow PSD (the width of 0.5 nm) given by a normal distribution with the center at 10 nm
2. A relatively wide PSD (the width of 5 nm) given by a normal distribution with the center at 10 nm
3. A bimodal PSD given by a sum of two normal distributions the width of 5 nm with centers at 9 and 70 nm. The volume fraction of particles corresponding to them was 0.99 and 0.01 respectively.

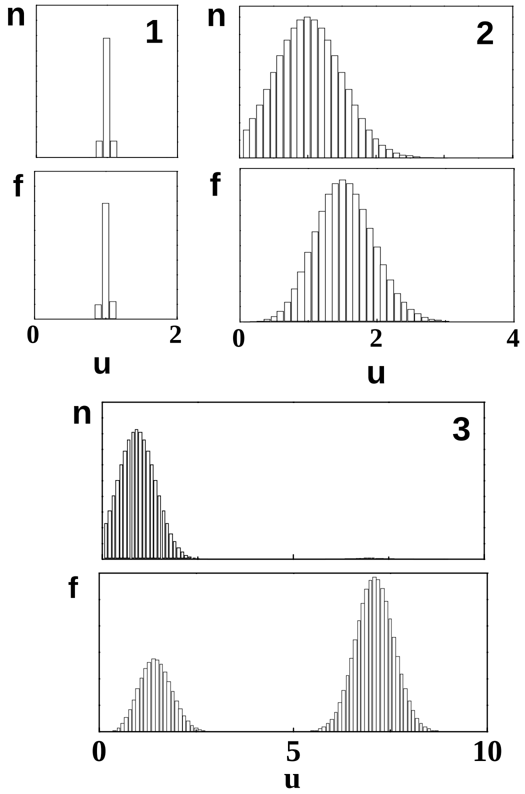

Figure 1: Three types of the initial PSD.

The average particle size for all the three types of PSD was the same and equaled to 10 nm. Figure 1 demonstrates the normalized histograms of the initial PSD, the upper ones for every PSD showing the number of particles (n), and the lower ones – the volume fraction of particles (f) corresponding to every size interval. The latter histograms show how the precipitates volume is distributed between the particles of different sizes.

Figure 2 presents dependences of VC average size, their volume fraction and PSD width on the annealing time at 900^0C for steel with 0.1 wt. % V and 1.0 wt. % C. The volume fraction of the precipitating phase was 0.0017 in the initial state, which corresponded to the maximal possible amount of VC in steel of composition considered and was substantially more than the equilibrium value. At heating of this steel up to 900^0C precipitates at first partly dissolve, and then the coarsening stage starts. At the dissolution stage the free energy of a system decreases mainly at the expense of its volume constituent through the reduction of the precipitate volume fraction. When phase composition approaches its equilibrium value, the coarsening stage starts.

At the dissolution stage the precipitates volume fraction reduces which is accompanied with particle size changes. In that case the initial PSD has a strong effect on precipitates average size and volume fraction temporal dependences.

In case of a narrow initial PSD (type 1) the dissolution process is the most rapid and is accompanied with the decrease of the precipitate average size. The precipitates dissolution results in the reduction of their volume fraction up to the value lower than the equilibrium one. This is due to the fact that in that case particles become very dispersed, and that is why their solubility increases.

Precipitate dissolution is accompanied by a noticeable grow of the PSD width, which may be explained as follows. Fine particles dissolve faster than the coarse ones, and, consequently, the narrow initial PSD substantially broadens.

In case of wide initial PSD (type 2) dissolution proceeds slower because in that case the main precipitate volume is concentrated in coarser particles, which dissolve slower. In spite of dissolution the average particles size at first does not change and at later steps even grows, because at dissolution not only particle sizes reduce, but the most dispersed particles completely disappear. The PSD width at precipitate dissolution in this case changes only slightly.

The dissolution is the slowest in case of the bimodal PSD (type 3). The most complicated dependences of the average size, volume fraction and PSD width on the annealing time are characteristic of this case. For understanding of these dependences one should remember that coarse particles dissolve much slower than small ones. At first small particles dissolve while the coarse ones only slightly reduce in sizes. The complete dissolution of fine particles results in the several times growth of the average size. At further annealing the precipitates average size slightly reduces due to their dissolution. After the complete dissolution of fine particles the process slows down, and a fold appears on the volume fracture temporal dependences. The PSD width at the step of fine particles dissolution at first increases due to the broadening of the initial distribution, and then drastically reduces at their full dissolution, and the distribution is no more bimodal. At further dissolution of coarse particles the PSD width grows again.

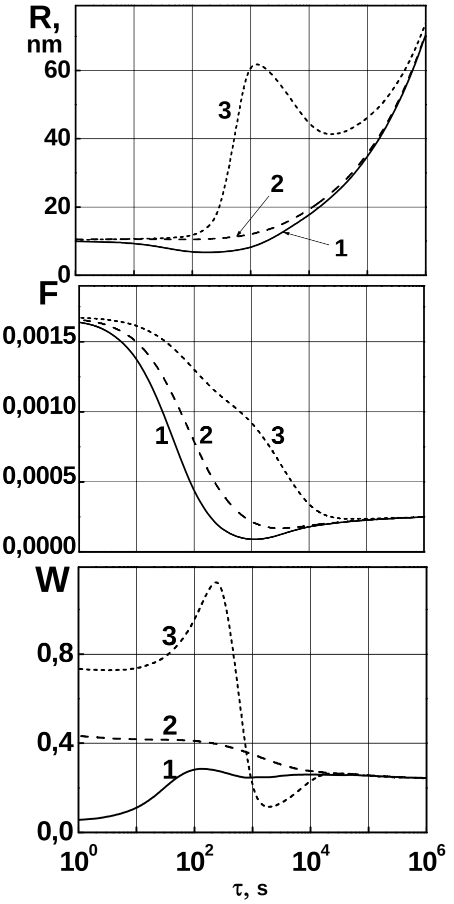

Figure 2: Variation of VC average radius (R), volume fraction (F) and PSD width (W) at 900^0C annealing of steel with 1 % C and 0.1 % V. $R_0 = 10$ nm, $F_0 = 0.0017$. Figures near curves denote the type of the initial PSD.

After dissolution the coarsening stage comes, at which the particles volume fracture is close to the equilibrium and only slightly changes with time, the cube of the average size linearly depends on time and the distribution width tends to an asymptotic value. At the coarsening stage the curves corresponding to different initial distributions flow together.

To illustrate the initial PSD influence on the particles growth kinetics the precipitate evolution in steel with 0.5 % V and 1.0 % C at 1000^0C has been simulated. The volume fracture of VC particles in the original state was taken 0.001, which is several times lower than the equilibrium value (0.00463). Figure 3 demonstrates the calculation results for three initial distributions. It can be seen that there are several areas corresponding to different stages of precipitate ensemble evolution in the curves presented. The first stage corresponds to the diffusion growth of precipitates, then some intermediate stage is observed and, finally, the coarsening stage starts. The solid solution supersaturation in the original state is not great in this case, and that is why the new nucleation centers formation is not well developed.

At the stage of growth the precipitates volume fraction rapidly increases practically achieving the equilibrium value. The phase transformation is the rapidest in case of narrow PSD (type 1), and the slowest at bimodal PSD (type 3). It is explained by the fact that the greater is the interface area, the faster is the phase transformation. This area is the greatest at PSD 1, when all particles are small, and the smallest at PSD 3, when more than a half of precipitates volume fraction is concentrated in coarse particles.

The initial PSD changes in the process of growth. In case of PSD 1 it slightly broadens, but nevertheless remains quite narrow at the entire stage of the diffusion growth.

At PSD 2 and 3 they just on the contrary get substantially narrower. Thus, the precipitate diffusion growth if it is not accompanied by noticeable nucleation promotes the formation of quite narrow PSD, which is due to the fact that fine precipitates grow faster than the coarse ones.

As the solute precipitates from the solid solution, and the precipitate volume fraction approaches to its equilibrium state, the possibilities for further decrease of the system's volume free energy are exhausted, the diffusion growth ceases and the following stage of the process starts. In the examples considered the stage of particle sizes stabilization set up after the end of the diffusion growth. By the beginning of this stage a narrow PSD has been formed as a result of the previous diffusion growth, and the precipitate volume fraction attains the value close to the equilibrium one and practically does not change at further annealing. It is the formation of the narrow PSD at the diffusion growth of precipitates that is the cause and the necessary condition for the realization of this stage, as the stability of a dispersed system to coarsening is the higher the lower is the particle size scattering. At this stage of the process the average particle size practically does not change, but the PSD broadens.

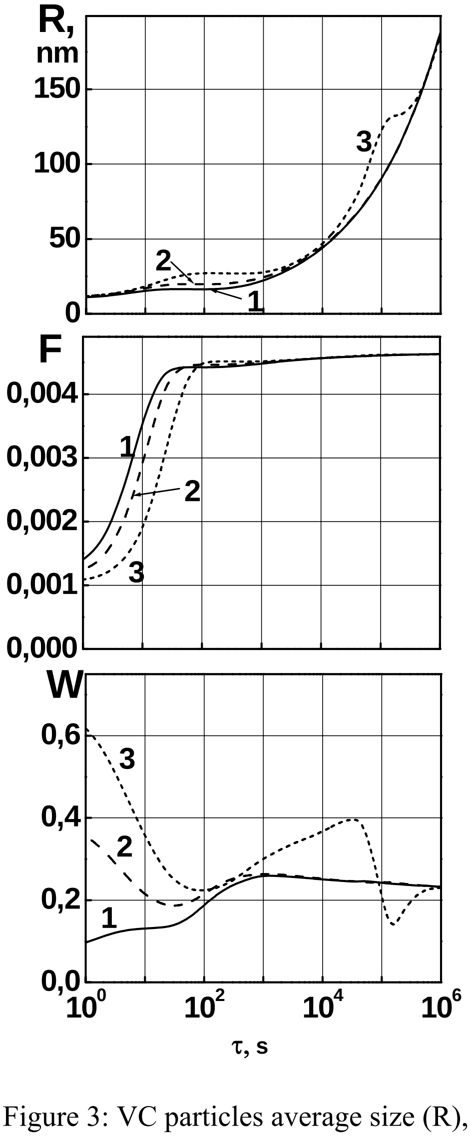

Figure 3: VC particles average size (R), their volume fraction (F) and PSD width (W) in steel with 1 % C and 0.5 % V versus the annealing time at 1000^0C. R_0 = 10 nm, F_0 = 0.001, figures 1, 2 and 3 denotes the initial PSD type.

When the distribution width attains a certain value (W ~ 0.21-0.22) the precipitate ensemble average size is capable to grow by dissolution of fine and growth of coarse particles, i.e. transition to the coarsening stage occurs.

In cases 1 and 2 the PSD is close to the universal Lifshitz-Slezov's distribution [13], and at further evolution the cube of the average particles size linearly changes with time, and PSD asymptotically approaches to the Lifshitz-Slezov's one.

In case of the initial PSD 3 the evolution at the coarsening stage substantially differs, as the particles are concentrated in two appreciably differing size intervals. At coarsening particles from large size interval grow at the expense of the small ones, and the average size grows with time faster than in cases 1 and 2. At the beginning of this stage the fraction of large size interval particles is small, and the main part of precipitates is concentrated in the interval of small sizes. As coarsening proceeds the number of particles in the small size interval decreases. This results at first in PSD broadening, but then, at full dissolution of fine particles, in its drastic narrowing. In that case the second interval of particles size stabilization is observed, at which the narrow PSD broadens and classical coarsening starts.

At certain isothermal annealing duration the average precipitate size dependences on time for the three initial distributions flow together.

4 Conclusion

An algorithm enabling to simulate the behavior of polydispersed carbide and nitride precipitates ensemble of constant composition at heat treatment has been worked out. The characteristic feature of this algorithm is that it accounts for the ensemble polydispersity and is valid for multicomponent systems, and describes such stages as growth, dissolution and coarsening in the framework of one model. Besides, it accounts for nucleation of new particles. Several assumptions and simplifications were made in working out this algorithm, which surely make the model less realistic and limit its application, but at further development of the algorithm the majority of them may be rejected. The analysis of the initial PSD effect on precipitate evolution accomplished with the algorithm suggested has shown that the original PSD type may substantially influence the heat treatment kinetics both at growth and dissolution of precipitates.

Acknowledgment

This work is supported by "MMK", "AUSFER" and "INTELS" foundations (Project No 11-03-02).

References

[1] Agren, J.: Numerical treatment of diffusion reactions in multicomponent alloys. *J. Phys. Chem. Sol.,* 43, No 4, pp. 385-391, 1982.

[2] Agren, J.: Kinetics of carbide dissolution. *Scand. J. Met.,* 19, No 1, pp. 2-8, 1990.

[3] Voorhees, P.W., Glicksman, M.E.: Solution to the multi-particle diffusion problem with applications to Ostwald ripening. *Acta Met*., 32, No 11, pp. 2001-2030, 1984.

[4] Enomoto, Y., Kawasaki, K., Tokuyama, M.: Computer modeling of Ostwald ripening. *Acta Met*., 35, No 4, pp. 907-913, 1987.

[5] Mandyam, H., Glicksman, M.E.: Late-Stage coarsening dynamics in phase-separating systems - simulation results. *Mater. Sci. & Eng.*, A238, No 10, pp. 121-127, 1997.

[6] Popov, V.V.: Numerical simulation of evolution of polydispersed ensemble of precipitates in a two-component alloy upon isothermal annealing. *Phys. Met. Metallogr.*, 87, No 5, pp. 379-386, 1999.

[7] Popov, V.V.: Simulation of dissolution and coarsening of MnS precipitates in Fe-Si. *Phil. Mag.,*. 82, No 1, pp. 17-27, 2002.

[8] Popov, V.V., Gorbachev, I.I.: Simulation of the evolution of precipitates in multicomponent alloys. *Phys. Met. Metallogr.*, 95, No 5, pp. 417-426, 2003.

[9] Popov, V.V., Gorbachev, I.I., Alyabieva, J.A.: Simulation of VC precipitates evolution in steels with consideration for the formation of new nuclei. *Phil. Mag*., in press.

[10] Tsumuraya, K., Miyata, Y.: Coarsening models incorporating both diffusion geometry and volume fraction of particles. *Acta Met*., 31, No 3, pp. 437-452. 1983.

[11] Liu, W.J., Jonas, J.: Characterization of critical nucleus/matrix interface: application to Cu-Co alloys and microalloyed austenite. *Sci. Tech*., 5, pp. 8-12, 1989.

[12] Liu, W.J., Jonas, J.: Nucleation kinetics of Ti carbonitride in microalloyed austenite. *Metall. Trans. A*., 20A, No 4, pp. 689-697, 1989.

[13] Lifshitz, I.M., Slyozov, V.V.: On the kinetics of the diffusion decomposition of supersaturated solid solutions. *Z. Exp. Teor. Fiz. (Russian J. Exp. and Theor. Phys)*, 35, No 2, pp. 479-492, 1958.

Proceedings of The 1st International Conference on **D**iffusion in **S**olids and **L**iquids
DSL-2005, July 6-8, 2005, University of Aveiro, Aveiro, Portugal

DIFFUSION MECHANISM AND SEGREGATION OF ^{119M}Sn IN POLYCRYSTALLINE Nb GRAIN BOUNDARIES

Vladimir KAIGORODOV, Vladimir POPOV*, Elena POPOVA,
Timofey PAVLOV, Svetlana EFREMOVA

Institute of Metal Physics, Ural Division of Russian Academy of Sciences,
S. Kovalevskaya str., 18, GSP-170, Ekaterinburg, RU620041, Russia

*Corresponding author. Fax: 7(343)374 52 44; Email: vpopov@imp.uran.ru

---

Abstract

The parameters of nuclear gamma-resonance (Mössbauer) spectra on ^{119m}Sn nuclei inserted in grain boundaries of polycrystalline Nb have been determined at the annealing temperatures of 680-994K (0.25-0.36T_m). Two components are observed in the emission NGR spectra at all the annealing temperatures considered. One of them (component 1) was found to result from the ^{119m}Sn atomic probes localized in grain boundary cores, while the other one (component 2) corresponds to that located in the near-boundary areas. Diffusion annealing temperature dependences of both components parameters have been analyzed. The coefficients and enthalpy of Sn grain-boundary segregation are determined based on this analysis, as well as the ratio of the diffusion pumping zone extention to the grain boundary width and the enthalpy of the atomic probes "pumping" from grain boundaries into the bulk.

Keywords: Grain boundaries; Grain-boundary diffusion; Segregation; Mössbauer spectroscopy

---

1 Introduction

The investigation techniques based on the use of the emission Mössbauer spectroscopy of radioisotope nuclei inserted into grain boundaries has been lately successfully applied to study the structure and physical properties of high-angle grain boundaries in a number of transition and noble metals [1-6 et al.]. This method of investigation of grain boundaries and the adjacent areas, developed by Klotsman and Kaigorodov [1-2], is as follows. The Mössbauer atomic probes capable of giving spectra information are diffusion inserted into a substance under investigation at such annealing conditions, which ensure their primary localization in grain boundary cores. The registered resonance γ-radiation gives information on the properties of those states, where the atomic probes appear to locate. In Refs [1-6 et al.] grain boundaries of a number of transition and noble metals were investigated using the ^{57}Co Mössbauer nuclei, while the ^{119m}Sn nuclei practically have not yet been employed to study internal interfaces, though in some cases it is of great importance to use those very nuclei.

The application of the emission Mössbauer spectroscopy on ^{119m}Sn nuclei is of special interest for the investigation of local structure, diffusion and physical properties of grain boundaries and adjacent areas in polycrystalline niobium, because the manufacture of superconducting Nb_3Sn-based bronze-processed composites is based on Sn penetration from Cu-Sn matrix into niobium filaments [7].

The main goal of the present study was to investigate grain boundaries in polycrystalline Nb by the method of the emission nuclear gamma-resonance (NGR) spectroscopy on ^{119m}Sn nuclei.

2 Experimental procedure

The research has been carried out on a high-purity polycrystalline niobium. The SIMS analysis with the CAMECA IMS-3f ion analyzer has shown the total concentration of substitution impurities to be about 5 at. ppm. The interstitial impurities concentration appeared to be substantially higher, namely, ~ 350 at. ppm O and ~ 100 at. ppm C. There was no texture in the specimens investigated, and an average grain size was about 50 µm.

To obtain a Mössbauer source, the ^{119m}Sn radionuclide (~ 80 MBq) was electrolytic deposited on a surface of a polycrystalline Nb sample the area of about 1 cm^2. To insert the ^{119m}Sn atomic probes into grain boundaries this sample was then annealed at 680K, 7h. After the annealing the residual undiffused ^{119m}Sn radionuclide was removed from the sample surface by a selective etchant (HCl).

The main rapid diffusion paths in Nb polycrystals of the recrystallization origin are common high-angle grain boundaries. Besides, the rapid diffusion is possible along dislocations and special boundaries. Diffusion coefficients along the latter defects of crystal structure are appreciably lower than that along the high-angle grain boundaries [8], and, respectively, they control a narrower diffusion zone. To exclude the effects of dislocations and special boundaries on the Mössbauer grain-boundary spectra, a layer of about 1 μm thick was removed from the sample surface by chemical polishing.

Along with the grain-boundary Mössbauer source, a bulk (standard) Mössbauer source was manufactured with the same techniques, with about 20 MBq of ^{119m}Sn deposited on a surface of a high-purity Nb single crystal. The latter was annealed at 1273R, 4h.

The NGR spectra were measured on a Mössbauer spectrometer operating in a constant rate regime. After the measurement of the NGR spectrum of polycrystalline Nb annealed at the lowest temperature, the latter was annealed at higher temperatures with 20-80K intervals and the same duration of 2h with subsequent taking of NGR spectra. All the measured isomer shifts are presented relatively to $BaSnO_3$. The emission NGR spectra expansion in constituents was accomplished with the specialized “Univem MS” program for the Mössbauer spectra treatment.

3 Results and discussion

Characteristic emission NGR ^{119m}Sn spectra in polycrystalline Nb after the annealing at different temperatures are shown in Fig. 1. It can be seen that at all the annealing temperatures there are two components in these spectra, the origin of which has been definitely established in Refs [1-6]. The more intensive at lower temperatures component 1 corresponds to the atomic probes localized in grain boundary cores. The quadrupolar splitting of this line (of about 0.44-0.48 mm/s) testifies that the ^{119m}Sn atomic probe positions in high-angle boundaries of polycrystalline Nb possess nonsymmetrical ion surroundings. This quadrupolar splitting is assumed to result from the distortions forming around relatively big Sn atoms. This assumption is supported by the fact that there is no quadrupolar splitting of component 1 when ^{57}Co atomic probes are employed [2-6].

The second line (component 2) is due to the ^{119m}Sn atomic probes localized in near boundary areas. It may be considered as a single but noticeably broadened line, its width being 2.59 mm/s after the annealing at 680K. Evaluations using the data of Ref. [9] on the volume diffusion of Sn in Nb show that the diffusion kinetic regime *C* is realized at 680-806K The calculation for the annealing at 806K, 2h gives the value of about 0.01 nm for the Sn volume diffusion effective depth.

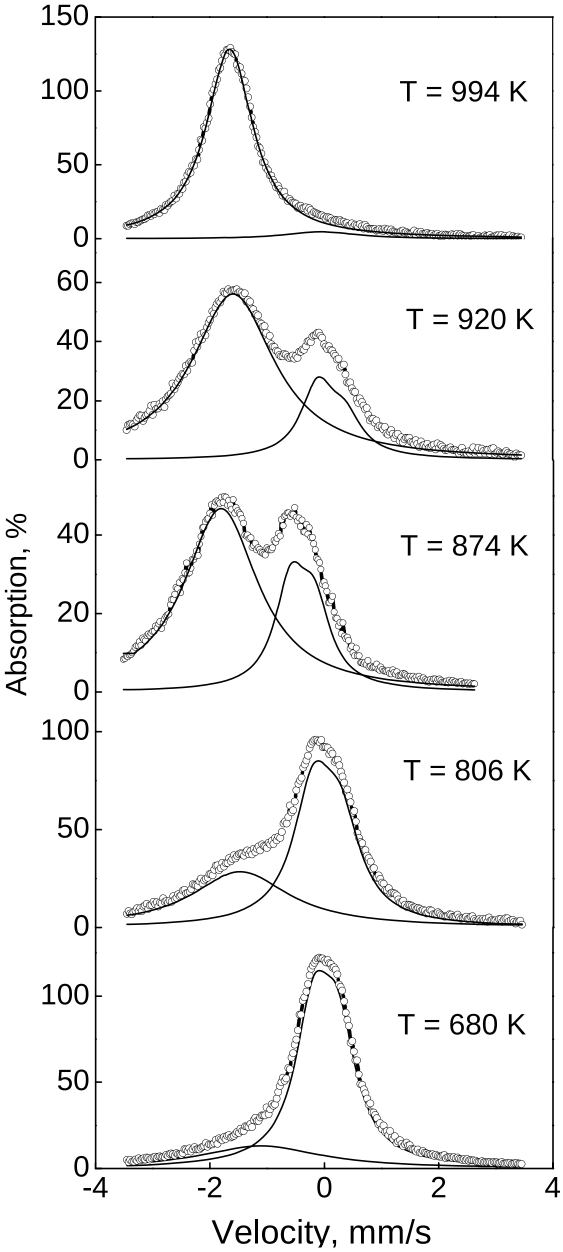

Figure 1: The expansion of NGR ^{119m}Sn spectra in polycrystalline Nb. The experimental spectrum is shown by markers, and the spectrum components – by solid lines. The annealing temperatures are indicated on the figure.

At the same time the presence of component 2 in the grain boundary spectrum testifies an appreciable penetration of the ^{119m}Sn atomic probes in the bulk of the polycrystalline Nb.

The analogous results were obtained at the Mössbauer investigation of grain boundaries of a number of polycrystalline metals employing ^{57}Co nuclei. This observation was one of the reasons to modify the classical Fisher's model [10]. Thus, in Refs [11,12] a hypothesis was suggested that between grain-boundary cores and crystallite volume there existed a so-called pumping zone of *l* width with high concentration of point defects, in which the diffusion coefficient D_{pump} satisfies the inequality:

$$D_V << D_{pump} << D_b\,, \qquad (1)$$

where D_V and D_b are the diffusion coefficients in the volume and grain boundaries, respectively.

The modified Fisher's model is schematically shown in Fig. 2, the following designations being used: C_b, C_{pump} and C_V are concentrations in grain boundary cores, pumping zone and crystallite volume, respectively.

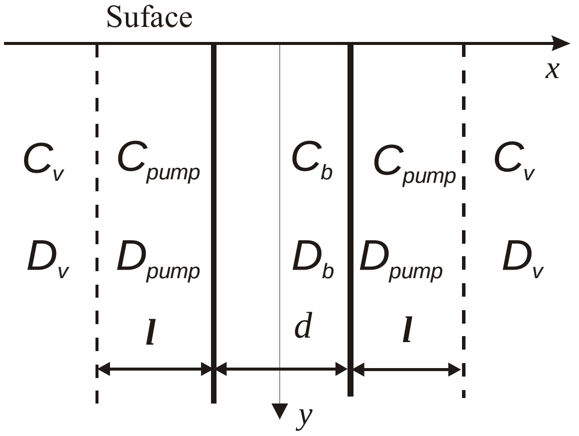

Figure 2: Scheme of the modified Fisher's model.

We further discuss the obtained results based on this model and its mathematical description presented in Refs [11-12]. According to this model, there are three temperature intervals of primary intercrystalline diffusion: (1) $D_{pump}t << l^2$ (the stage at which the pumping region is being filled with the atomic probes*); (2) $D_{pump}t \cong l^2$, but $D_Vt << l^2$ (the stage at which the pumping region is filled with the atomic probes); (3) $D_Vt > l^2$ (the stage at which the pumping front crosses the boundary between the pumping zone and the bulk of a crystallite).

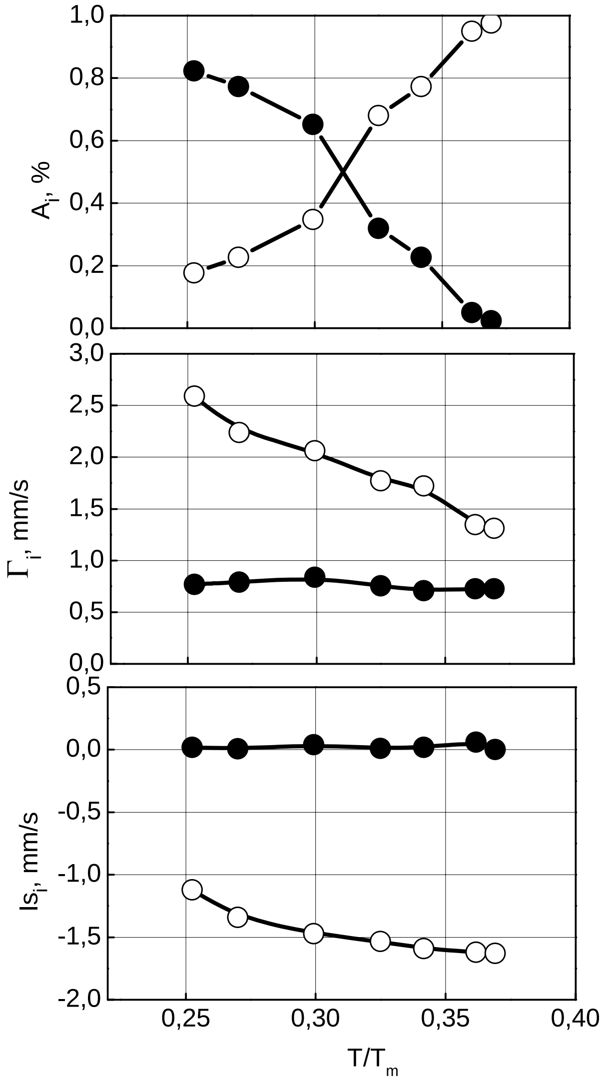

Figure 3: Dependences of NGR ^{119m}Sn spectra parameters on the annealing temperatures. Dark markers – component 1, light markers – component 2.

Figure 3 demonstrates the emission NGR ^{119m}Sn spectra parameters in polycrystalline Nb (where A_i are the relative squares, Is_i are isomer shifts and Γ_i are the component widths) on the temperature of isochronal annealing. There are two regions on the of relative areas dependences. At low temperatures (up to about 0.3 T_m) the A_i dependence on the annealing temperature is relatively weak. With the account for previous studies it may be concluded that this temperature interval corresponds to the stage of saturation of the high-concentration point defect zone with the diffusing impurity. At this stage the ^{119m}Sn atomic probes concentration in a

---

* This stage of the primary intercrystalline diffusion is commonly not possible to observe experimentally.

pumping zone reaches its equilibrium state, and the volume diffusion rate is still too low for Sn atoms to transfer from the pumping zone into the volume of crystallites.

In that case the diffusing impurity concentration in grain boundaries and in the pumping zone are related as follows:

$$C_{pump} = \frac{C_b}{s} \tag{2}$$

where s is the coefficient of the atomic probes segregation.

The segregation coefficient is expressed through the segregation enthalpy (Q_s) as follows:

$$s = \exp\left(\frac{Q_s}{RT}\right) \tag{3}$$

At the saturation stage the occupancies of states, q_i, are related to the grain boundary width *d*, the pumping zone width *l* and the segregation coefficient s by the following equation:

$$\frac{q_1}{q_2} = \frac{s}{2(l/d)} \tag{4}$$

From the temperature dependence of q_1/q_2 it is possible to determine the segregation enthalpy of the diffusing impurity:

$$Q_s = R\frac{\partial \ln\left(\frac{q_1}{q_2}\right)}{\partial\left(\frac{1}{T}\right)} \tag{5}$$

At this stage the relative occupancies of states are proportional to the relative areas of the spectra lines, because the probabilities of the Mössbauer effect for the states 1 and 2 at low annealing temperatures are approximately equal [4,5]. This enables to determine Q_s based on the temperature dependence of A_1/A_2 in the low temperature interval of 680-806R. Using the obtained value, $Q_s = 31 \pm 2$ kJ/mole, the values of *s* were calculated for different temperatures, and then the ratio of the pumping zone extension to the diffusion grain boundary width was determined to be $l/d = 30 \pm 6$.

At higher temperatures (above 0.3 T_m) the relative areas temperature dependences become steeper, testifying the stage of the crystallites volume occupation with the diffusing impurity.

Based on the temperature dependences of the occupancies of states at this stage, the activation enthalpy of the process controlling the Sn pumping to the grain volume was determined to be ~ 300 kJ/mole, which is close to the activation enthalpy of Sn volume diffusion in Nb (330 kJ/mole [9]). This makes possible to conclude that it is the volume diffusion that controls the pumping of atoms from a boundary into the volume. Besides, this suggests that the pumping zone does not decompose at the annealing temperatures of up to the highest of the investigated ones, 994K (0.36 T_m), at which the grain boundary component of the spectrum practically entirely vanishes.

The isomer shift of component 1 is close to zero and is substantially higher than that of the volume line measured on the Nb single crystal (-1.63 mm/s). This result shows that the electron density in the state 1 (that is in grain boundary cores) for the polycrystalline niobium is appreciably lower than in substitution positions of the Nb regular crystal lattice. Thus, after the diffusion annealing the ^{119m}Sn atomic probes locate in grain boundary cores in positions with the reduced atomic density, and these are the substitution positions in a high-angle boundary structure. Tin is an impurity with a big radius, its atomic volume being 23 % higher than that of niobium [13], and that is why Sn is not able to diffuse in a grain boundary core along its internodes, but only along vacancy-like positions of the same type with minimal energy barriers.

High-angle grain boundaries of polycrystalline niobium obtained by rolling and annealing of high-pure Nb single crystals were investigated employing the ^{57}Co (^{57}Fe) Mössbauer nuclei in [6]. There were also found two components in the emission Mössbauer spectrum of polycrystalline Nb, one of them formed by ^{57}Co (^{57}Fe) atomic probes located in grain boundary cores (component 1), and the other one – by ^{57}Co (^{57}Fe) atomic probes situated the Nb regular crystal lattice near boundaries (component 2). The isomer shift of component 1 was found to be higher than that of component 2. For the emission NGR spectroscopy on ^{57}Co(^{57}Fe) nuclei this result indicates the higher density of s-electrons of the ^{57}Co(^{57}Fe) nuclei located in grain boundary cores compared to the electron density of those atomic probes which are in the regular lattice node positions near boundaries. Based on that observation the conclusion about the internodes character of cobalt diffusion in high-angle grain boundaries of polycrystalline niobium was made in Ref. [6].

When the atomic volume of a diffusing impurity is larger than the atomic volume of a matrix (the case of Sn in Nb) or is commensurable with the latter (the case of Co in Cr [4]), the vacancy diffusion mechanism is realized in high-angle boundaries. In both ^{57}Co - Cr and ^{119m}Sn – Nb systems the Mössbauer impurity diffusion along high-angle polycrystal grain boundaries also occurs by the vacancy mechanism.

The isomer shift and the line width of component 1 change almost not at all with the annealing temperature indicating that the Sn atomic probes surroundings in polycrystalline Nb grain boundaries only slightly change with temperature.

Contrary to component 1, the component 2 parameters appreciably change with the annealing temperature. At the lowest investigated annealing temperature of Nb polycrystals (680K) the isomer shift of the volume line equals to -1.12 mm/s, which is substantially higher than that of the volume (standard) source (-1.63 mm/s). The higher isomer shift value is due to the lower electron density on ^{119m}Sn nucleus. The analogous effect, that is the lower electron density on nuclei in the pumping zone at low annealing temperatures ($T/T_m < 0,3$) compared to that in the volume was observed in other metals investigated using the ^{57}Co atomic probes [2-6]. The most probable cause of the isomer shift increase in the near-boundary pumping zone is segregation of interstitial impurities in this zone. The interstitial impurities in metals are known to result not only in shift, but also in broadening of spectral lines [14,15]. The number of interstitial atoms located closely to the ^{119m}Sn probe (in the first and second coordinate spheres) may be different which results in some distribution of isomer shifts and line widths. As a result, the experimental width of component 2 in polycrystalline Nb annealed at 680K is appreciably higher (2.59 mm/s) than the volume source line width (0.91 mm/s).

With growth of the annealing temperature the isomer shift decreases approaching to its value in the standard source. It is apparently explained by an increase of non-equilibrium vacancies and vacancy-impurity complexes concentration in the pumping zone. It was shown in [16,17] that vacancies and their complexes with interstitial impurities decrease the lattice period contrary to individual interstitial impurities. As a result, the electron density on ^{119m}Sn nuclei grows and, correspondingly, the component 2 isomer shift reduces with temperature growth. The growth of concentration of vacancies and their interstitial impurity complexes with the increase of the annealing temperature results in the decrease of individual interstitial impurities concentration and weakening of their influence on the component 2 width in NGR spectra of polycrystalline Nb. As a result, the width of the volume line reduces with the growth of the annealing temperature. The second possible reason for the decrease of the electron density on ^{119m}Sn nuclei and the volume line width with growth of the diffusion annealing temperature may be the withdrawal of interstitial impurities from the pumping zone.

4 Conclusion

The study of high-angle grain boundaries in polycrystalline Nb with the use of ^{119m}Sn Mössbauer nuclei inserted by the kinetic regime of *C* type has shown that the ^{119m}Sn atomic probes occupy two types of sites in the grain-boundary diffusion zone, namely, in grain boundary cores and in near boundary areas of regular lattice. The atomic ^{119m}Sn probes are located in grain boundary cores in positions with the reduced atomic density, which indicates the vacancy-type mechanism of Sn diffusion along the polycrystalline Nb high-angle boundaries. This results from the fact that ^{119m}Sn probe in Nb is a large-radius impurity, and it cannot diffuse along the internodes.

According to the character of temperature dependences of both components areas (occupancy of states) it has been shown that Sn in Nb enriches grain boundaries. The activation enthalpy of Sn segregation on high-angle grain boundaries of polycrystalline Nb is determined to be 31 ± 2 kJ/mole. The ratio of the extension of the high concentration point defect zone, l, to the diffusion width of a grain boundary, d, is shown to be $l/d = 30 \pm 6$.

In the investigated temperature interval the parameters of a grain boundary line in the emission NGR spectra (isomer shift, line width and quadrupole splitting) only slightly depend on the annealing temperature. This means that at these temperatures there are no appreciable changes either in composition or in concentration of the residual or alloying impurities as well as their complexes with vacancies in high-angle grain boundary cores of polycrystalline Nb. At the same time the parameters of the volume line (component 2) substantially change in the temperature interval considered. These peculiarities are apparently connected with differences in the atomic structure of grain boundary cores and near-boundary areas.

Acknowledgment

The work is supported by the Russian Foundation on Basic Research (RFBR) (grant No 04-03-32829) and by the Ural and Siberian Divisions of Russian Academy of Sciences (integration project No 28 - 2005)

References

[1] Klotsman, S.M.: Impurity states and diffusion in metal grain boundaries. *Uspehi Fiz. Nauk* (in Russian), 160, No 1, pp. 99-139, 1990.

[2] Kaigorodov, V.N., Klotsman, S.M.: Impurity states in the grain boundaries and adjacent to them crystalline regions. *Phys. Rev. B*, 49. No 14, pp. 9374-9399, 1994.

[3] Kaigorodov, V.N., Klotsman, S.M., Kurkin, M.I. et al.: Intercrystalline diffusion of cobalt in polycrystalline tungsten. II. Experimental study of diffusion in core of crystallite-conjugation regions and adjacent zones. *Phys. Met. Metallogr.*, 85, No 2, pp. 212-217, 1998.

[4] Kaigorodov, V.N., Klotsman, S.M., Zherebtsov, D.V.: Types and properties of states localized beyond the core of crystallite-conjugation regions and occupied by ^{57}Co during its intercrystalline diffusion in polycrystalline chromium. *Phys. Met. Metallogr.,* 85, No 3, pp. 348-354, 1998.

[5] Kaigorodov, V.N., Klotsman, S.M., Zherebtsov D.V.: Segregations of vacancy-interstitial impurity complexes in polycrystalline tantalum. *Phys. Met. Metallogr.,* 86, No 1, pp. 70-78, 1998.

[6] Kaigorodov, V.N., Klotsman, S.M., Koloskov, V.M., Tatarinova, G.N.: Nuclear gamma-resonance investigation of grain boundaries in niobium and molybdenum. *Phys. Met. Metallogr.,* 66, No 5, pp. 116-123, 1988.

[7] Popova, E.N., Romanov, E.P., Sudareva, S.V.: A15 superconducting composites and high-strength Cu-Nb conductors. *Phys. Met. Metallogr.,* 96, No 2, pp. 146-159, 2003.

[8] Kaur, I., Gust, W.: Fundamentals of grain and interphase boundary diffusion. Stuttgart, Ziegler Press, 1989.

[9] Askill, O.: Tracer diffusion of ^{113}Sn in niobium. *Phys. Stat. Sol.,* 9, No 3, pp. K167-K168, 1965.

[10] Fisher, J.C.: Calculation of diffusion penetration in curves of surface and grain boundary diffusion. *J. Appl. Phys.*, 22, No 1, pp. 74-77, 1951.

[11] Kurkin, M.I., Klotsman, S.M., Dyakin, V.V.: The effect of saturation of “pumping-out” zone upon ultrafast diffusion along grain boundaries in polycrystals. *Phys. Met. Metallogr.,* 81, No 4 pp. 366-373, 1996.

[12] Klotsman, S.M., Kurkin, M.I., Kaigorodov, V.N., Dyakin.: On the nature of states occupied by the atomic probes in the zone of intercrystallite diffusion: The case of extremely small bulk diffusion length. *Phys. Met. Metallogr.,* 82, No 4, pp. 419-426, 1996.

[13] Physical values: Reference book, Moscow, Energoatomizdat (in Russian), 1991.

[14] Sauer, Ch.: Messung der ruckstossfreien Resonaz – Absorption am 6,2 keV Niveau in ^{181}Ta. *Zs. Physik.,* 222, pp. 439-454, 1969.

[15] Klotsman, S.M., Kaigorodov, V.N., Kurkin, M.I. et al.: Regions of enhanced concentration of point defects localized near internal interfaces in condensed media. I. Types of solid solutions in Cr, Pd, Ta, W, Ir and Au. *Phys. Met. Metallogr.*, 93, No4, pp. 349-357, 2002.

[16] Klotsman, S.M., Kaigorodov, V.N., Ermakov, A.V., Rudenko, V.K.: Regions of enhanced concentration of point defects localized near internal interfaces in condensed media. III. Composition and structure of vacancy-oxygen complexes in regions of enhanced concentration of point defects in Pd, Ta, W, and Pt. *Phys. Met. Metallogr.*, 95, No 1, pp. 79-85, 2003.

[17] Klotsman, S.M., Kaigorodov, V.N., Ermakov, A.V., Rudenko, V.K.: Regions of enhanced concentration of point defects localized near internal interfaces in condensed media. IV. Ultra-high concentrations of vacancies and enthalpies of the enthalpies of their formation regions of enhanced concentration of point defects in Pd, Ta, W, and Pt polycrystals. *Phys. Met. Metallogr.*, 95, No 2, pp. 137-145, 2003.

Proceedings of The 1st International Conference on **D**iffusion in **S**olids and **L**iquids
DSL-2005, July 6-8, 2005, University of Aveiro, Aveiro, Portugal

THE INFLUENCE OF FLUID RADIATION IN MEASUREMENTS WITH THE TRANSIENT HOT-WIRE TECHNIQUE: N-PENTANE AND PROPANE

S. YAN[1], L. SUN[1], R. PRASAD[1,*], J. VENART[1,2]

[1]Department of Engineering, University of New Brunswick, Saint John Campus,
Saint John, NB, Canada E2L 4L5
[2]Department of Mechanical Engineering, University of New Brunswick,
Fredericton Campus, Fredericton, NB, Canada E3B 5A3

[*]Corresponding author: Fax; 506-648-5513, Email; prasad@unb.ca

Abstract

The transient hot-wire technique is widely used for absolute measurements of the thermal conductivity and thermal diffusivity of fluids. Both free convection and fluid radiation can significantly influence these measurements – especially those for thermal diffusivity. Corrections to account for these effects are seen in departures in linearity of the actual line source model temperature rise. In this paper the influence of free convection on measurements of thermal conductivity and thermal diffusivity for argon is shown; for comparison the influence of fluid radiation on some measurements of the thermal conductivity of n-pentane are also presented thus demonstrating the difference between the influence of natural convection and thermal radiation.

Keywords: n-pentane; Propane; Thermal radiation; Natural convection; Transient hot wire technique

1 Introduction

The transient line source instrument provides rapid and accurate measurements of fluid thermal conductivity utilising what is called the 'line-source' model. A series of corrections, however, must be made to account for differences between the actual and ideal heat transfer; free convection and thermal radiation are two of the necessary corrections. This paper summarises the development of the line source transient hot-wire technique and the potential influence both free convection and thermal thermal radiation can have on the measurement of fluid thermophysical properties.

2 Method

The transient hot-wire method is widely accepted as a primary instrument for accurate measurement of fluid thermal conductivity on a wide variety of fluids. Though theoretically feasible, practical simultaneous use for thermal diffusivity measurements has been limited due to the lack of reproducibility and a dependence of the results on the power employed. The instrument consists of a very thin and long wire vertically submerged in the test fluid. A constant current through the wire results in heat dissipation into the surrounding fluid and a transient temperature rise of the wire from which the thermal conductivity of the fluid can be determined. The working equation for thermal conductivity is based on the transient solution of Fourier's law for an infinite line source [4, 5]. The ideal temperature rise of the fluid, at the wire–fluid interface, *r=a*, at time *t* is

$$\Delta T = \frac{q}{4\pi\lambda(\rho,T)} \ln \frac{4\alpha t}{a^2 C} \tag{1}$$

where

$$\Delta T = \Delta T_w + \sum \delta T_i$$

and $\sum \delta T_i$ are appropriate corrections to the measured temperature rise, ΔT_w, q is the power per unit length applied to the wire, λ is the thermal conductivity, $\alpha = \lambda /(\rho C_p)$ is the thermal diffusivity, ρ is the density, and C_p is the isobaric heat capacity (all for the fluid), with *C=1.781…* the exponential of Euler's constant. One of the necessary corrections to ΔT_w accounts for thermal radiation δT_{rad}.

For fluids which absorb radiation, Nieto de Castro and fellow workers [6–8] have shown that the dominant correction term in the heat flux gradient arises from the emission of radiation by the heated fluid [9]. These considerations permitted an approximate analytical solution to the applicable energy equation. The temperature rise of the test fluid at the wire surface, *ΔT*, is given by [7]:

$$\Delta T_2 = \frac{q}{4\pi\lambda_2}\ln\frac{4\alpha_2 t}{a^2 C}\left(1+\frac{Ba^2}{4k_2}\right)-\frac{qBt}{4\pi\lambda_2}+\frac{qBa^2}{16\pi\lambda_2\alpha_2}+o\left(\frac{a^2}{\alpha_2 t},B^2t^2\right) \quad \ldots\ldots(2)$$

where

$$B=\frac{16Kn^2\sigma T_0^2}{\left(\rho C_p\right)_2}$$

and, the correction for radiation absorbing / emitting fluids is [11]:

$$\delta T_{rad} = -\frac{qB}{4\pi\lambda_2}\left[\frac{a^2}{4k_2}\ln\left(\frac{4k^2 t}{a^2 C}\right)-t+\frac{a^2}{4k_2}\right] \quad (3)$$

In this result, however, the wire itself was regarded as part of the fluid since the inner boundary condition was considered to be *r=0* and not *r=a*. To eliminate this inaccuracy, the following solution was obtained [1] using the correct inner boundary condition at *r=a*, with the thermophysical properties of the wire taken into account, i.e.;

$$\Delta T_1(a,t) = \Delta T_1(a,t)+\frac{fa^2 q\lambda_1\alpha_2}{8\pi\lambda_2^2\alpha_1}\ln\frac{4\alpha_2 t}{a^2 C}+$$

$$\frac{qfa^2}{16\pi\lambda_2}\left(\frac{-\pi^2}{6}+\ln^2\frac{4\alpha_2 t}{a^2 C}\right)-\frac{qf\alpha_2 t}{4\pi\lambda_2}-\frac{qfa^2}{8\pi\lambda_2} \quad (4)$$

where

$$f=\frac{B}{\alpha_2} \quad \text{and} \quad B=\frac{16Kn^2\sigma T_0^2}{\left(\rho C_p\right)_2}$$

The temperature rise *ΔT*$_w$ represents the corrected measured temperature difference (aside from fluid radiation) and *ΔT* the ideal, and now radiation-corrected temperature difference. *K* is the mean absorption coefficient, *n* the refractive index of the fluid (both considered temperature independent), σ the Stephan–Boltzmann constant, with subscript 1 referring to the properties of wire and subscript 2 referring to the properties of fluid.

For fluids transparent to thermal radiation, this can be corrected by [5].

$$\delta T_{rad} = \frac{8\pi a\varepsilon_p \sigma T_0^3 \Delta T^2}{q} \quad (5)$$

3 Experiment

A transient hot-wire instrument was modified to allow improved measurements of both thermal conductivity and thermal diffusivity [10–12]. Two vertical wires, each of different length, were used for end effect compensation (Fig. 1). The principle of the measurement and details of the apparatus are described elsewhere [10, 11]. The apparatus [11] includes a pressurising system and an isothermal block to maintain the test fluid at a desired pressure (up to 70 MPa) and temperature (120 K-500 K) for measurements.

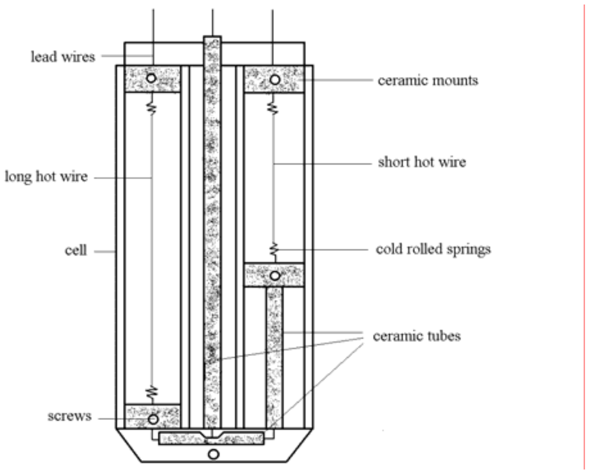

Figure 1: Schematic diagram of the hot-wire cell.

The measurement bridge used is shown in Fig. 2 [11]. It includes a data acquisition/control unit (HP3497A), a dc power supply (HP6625A), an integrating voltmeter (HP3458A) which provides integration from 0 to 16667 ms, an external trigger unit (HP3437A), and a C-MOS digital switch which is used to switch from the ‘‘dummy’’ to the ‘‘measurement’’ circuit. HP3497A is used to provide constant currents of 1, 0.1, and 0.01 mA when calibrating the wires and balancing the bridge, and also as an integrating voltmeter with integration times of 0.167, 1.67, and 16.67 ms along with digital switches used to monitor the circuit, under computer control, during the preliminary balancing as well as during the measurement process. HP6625A provides a high-stability fast response power supply with 0 to 16 VDC output to the hot-wire.

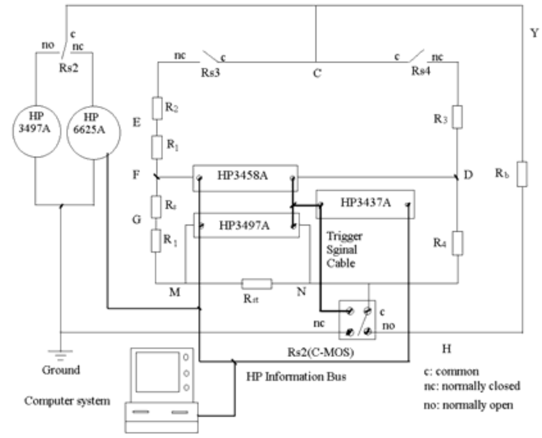

Figure 2: Electrical system for measurement of thermal conductivity and thermal diffusivity.

As indicated above, the HP3497A Data Acquisition System is used for several purposes. First, it provides a voltmeter to measure the voltage across the standard resistance, R_{st} , to accurately determine the current through the wires. Second, it also supplies 1-mA current used for balancing the bridge. Finally, it provides the digital switches for switching operations in the circuit. HP3458A is used to measure the transient imbalance of the bridge introduced by the temperature change of the hot wires and the voltages in every branch of the bridge. The methods of determining and correcting the bridge balance and the effective ‘‘zero’’-time residual bridge imbalance corrections are given elsewhere [10, 11].

The HP3437A is used to trigger HP3497A, HP3458A, and C-MOS switch to connect circuit components and to begin simultaneous measurements of both the current and the voltage across the bridge elements.

4 Results and discussion

For fluids which do not absorb or emit thermal radiation, for example argon, the plot of $\Delta T \sim$ *ln(t)* is shown in Fig. 3 [1]. A similar behaviour is observed with nitrogen. In these cases, a straight-line behaviour is observed from the very beginning. The deviation plot resulting from a linear fit to $\Delta T \sim$ *ln (t)* data shows a random behaviour without any definite trend up to the point where free convection commences. Fig. 4 [1] shows the deviation plot for argon at 323 K and 20.9 MPa.

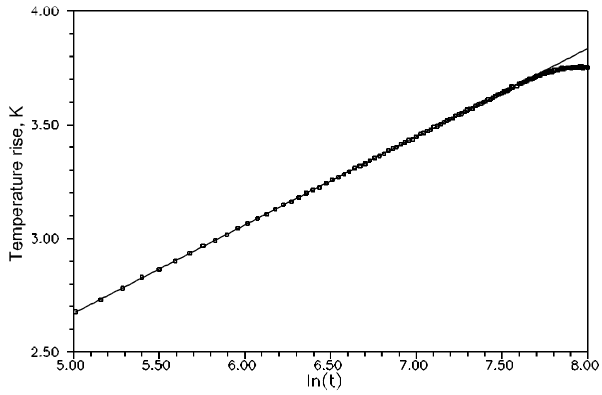

Figure 3: Temperature rise as a function of *ln (t)* for a measurement on argon at 323K and 20.9MPa.

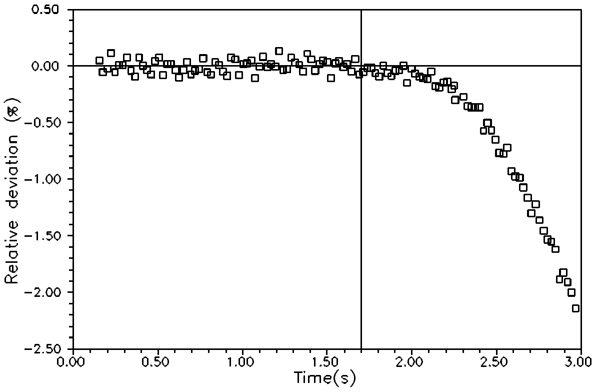

Figure 4: Deviations in the thermal conductivity of argon at 323K and 20.9MPa from the linear fit.

Table 1: Thermal conductivity of Argon at 323.56 K and 20.93 MPa with q=0.13915 W/m.

Time interval (s)	λ (W/m·K)	T_{ref}(K)
0.12-1.00	0.02857	326.53
0.12-1.70	0.02852	326.63
1.00-1.70	0.02852	327.07

For fluids which absorb and emit thermal radiation, such as pentane, a corresponding result is shown in Figs. 5, 6, and 7 [1]. The behaviour of $\Delta T \sim ln\ (t)$ data is observed to be nearly linear. However, due to emission, the straight line fit results in a deviation plot which indicates curvature. Figure 6 shows the deviation plot for the $\Delta T \sim ln\ (t)$ data corrected for all non-ideal effects aside for radiation. Fig. 7 shows the deviation plot of $\Delta T \sim ln\ (t)$ data for both the uncorrected and corrected influence of radiation using Eqs. (2) and (3) [1,3,11].

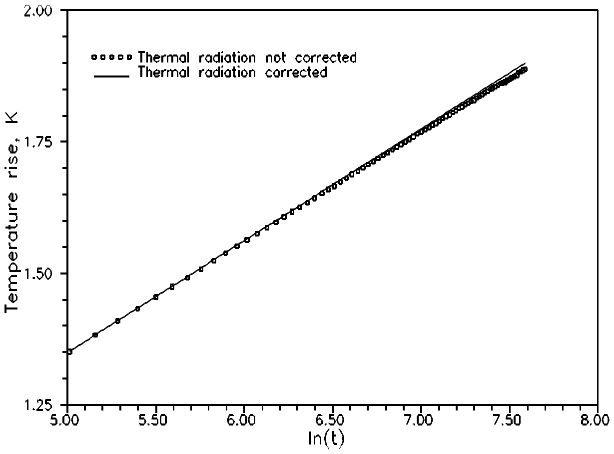

Figure 5: Temperature rise as a function of *ln (t)* before and after fluid thermal radiation corrections: normal pentane at 376K and 34.17MPa and a power of 0.28036W/m.

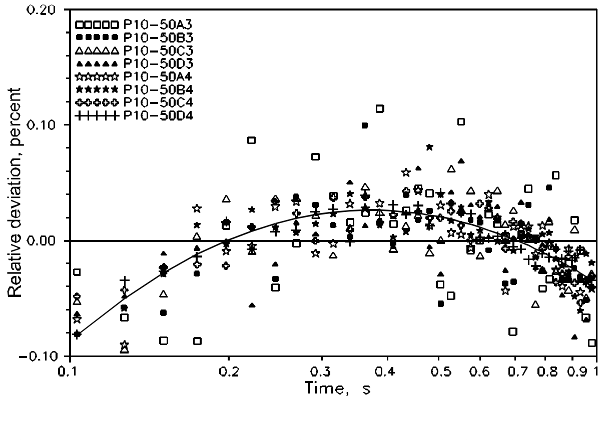

Figure 6: Deviation of the corrected (aside from fluid radiation) temperature differences from the best-fit straight line for a series of n-pentane experiments near 376K and 34.2MPa.

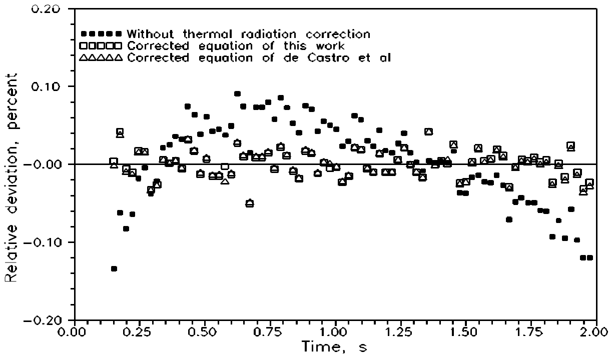

Figure 7: Deviation of uncorrected and fluid radiation-corrected temperature rise from the linear fit: normal pentane at 376K and 34.17MPa and a power of 0.28036W/m.

Table 2: Deviation of the corrected temperature rise from the best-fit straight line before and after correction for fluid radiation for a series of experimental runs near 376K and 34.2MPa.

ID	Power (W/m)	Std. deviation	
		before	after
50A3	0.15803	0.050	0.043
50B3	0.15802	0.034	0.030
50C3	0.21478	0.033	0.024
50D3	0.21500	0.032	0.025
50A4	0.28036	0.032	0.019
50B4	0.28029	0.027	0.014
50C4	0.35441	0.029	0.012
50D4	0.35452	0.025	0.011
Mean Std. deviation		0.033	0.022

The curvature observed with n-pentane in Fig. 6 and Fig. 7 is due to thermal radiation effect and not natural convection. This can be illustrated by comparing $\Delta T \sim ln\ (t)$ response for argon and n-pentane. The commencement of free convection is detected by a departure from the straight line of the corrected temperature difference, $\Delta T \sim ln\ (t)$ data provided it is remote from regions where outer boundary effects can be observed [5]. In Fig. 3 [1], measurement of corrected temperature difference over a 2-s period for argon at 323.56 K and 20.93 MPa ($\lambda_0 = 0.02852$W/m·*K*, $\alpha_0 = 12.35 \times 10^{-8}$m^2·s [10]) is shown. The deviation from a linear fit of the corrected temperature difference is indicated in Fig. 4 [1], where the departure from linearity after 1.7 s (Fig. 4) indicates the onset of convection. A comparison of these deviation plots (Fig. 6 and 7) with that for argon (Fig. 4) clearly establishes that the curvature trend observed with n-pentane is due to radiation effects. Table 1 [10] for argon indicates that as the time frame for the determination of λ from the data set is extended and/or contracted from 0.12 to 1 and then 1.7 s, there is no significant *($\leq 0.2\%$)* difference in the value of λ returned. The modified Raleigh number, $Ra = g\beta\Delta T\delta^3/(\nu\alpha)$, for the commencement of convection for this measurement is 1.3×10^5, a value that compares favourably with the predicted ''critical'' criterion $Ra \geq 10^5$ based upon the conduction layer thickness at time t [13].

The exact determination of the influence of fluid thermal radiation requires consideration of the full form of the appropriate integral-differential energy equation. Its numerical solution is reported by Menashe et al [9] for specified conditions and selected fluids in the *n*-alkane series. The deviation of the temperature rise of the hot wire was simulated for measurements in *n*-heptanes from the best-fit straight line. It is clearly indicated [Figure 6 of Ref. 9] that a curvature in $\Delta T \sim$ ln (t) deviation plot may be expected in these fluids.

A similar behavior is observed with n-pentane for a range of power levels (heat dissipation rate for the hot-wire into the surrounding test fluid) used in measurements. In this example, the corrected (aside from fluid radiation emission) $\Delta T \sim$ ln *(t)* data indicate, from the start, a consistent departure from linearity for all times with a shape that corresponds, almost exactly, to that indicated by Menashe et al [9]. However, in case of n-pentane [14] the same authors stated "that the effects of radiation introduce no significant curvature to the experimental line". Table 2 [1] illustrates that if the correction for fluid radiation to the *n*-pentane data of Fig. 6 is implemented, the goodness of fit, as expressed by the deviation plot, improves substantially, and thus indicates that the corrected measurements, especially at higher power levels, have a reproducibility of better than ±0.02%.

The full correction method [9] is time-consuming and computationally intensive and could not be directly applied to the experimental procedure. Nieto de Castro [7] showed that an approximate correction procedure could be implemented to account for the fluid radiation emission characteristics, although, as indicated earlier, the inner boundary condition was inappropriate. The revision of their analysis results in a correction only slightly different as illustrated in Figs. 5 and 6, where the uncorrected and fluid radiation-corrected temperature differences are shown as functions of time for *n*-pentane. In this example, the value of fluid radiation correction B necessary to restore linearity is 0.025s^{-1}, an empirical value determined through the use of Eq. (2.3). It should be noted that for the above measurement, *Ra* is only 8330 and there is no convection despite the extension of the measurement time to 2s.

Figure 1 and Table 1 (taken from reference [1]) illustrate that the differences between these two corrections are very small, less than 0.01% for thermal conductivity and less than 0.03% for thermal diffusivity.

As for the measurement of thermophysical properties of propane, to date the thermal conductivity measurements of propane using the transient hot-wire technique have been considered free of radiation effects. In this work, recent correction techniques have been applied to examine this assumption and correct, if necessary, for the influence of even weak radiation effects. Measurements at ambient temperature and pressures up to about 900kPa are proposed using a hot-wire instrument employing 12.7µm diameter platinum wires. Due to a break down of the instrument, the proposed measures have not as yet been completed. However, preliminary investigation has shown the existence of curvature in the $\Delta T \sim$ *ln (t)* deviation plots similar to Fig. 7 for n-pentane. Therefore, it is concluded that the radiation effect is present in measurements with propane.

Radiation also influences the measurement of thermal diffusivity for two reasons. One reason is that the radiation effect can influence the temperature rise of the hot wire and therefore move the intercept of the $\Delta T \sim$ *ln (t)* line, which always affects thermal diffusivity directly. The other reason is that radiation influences the conductivity value of the fluid. Therefore, thermal radiation has a significant influence on the measurement of thermal diffusivity (Eqn 7 of Ref [1]).

5 Conclusion

Thermal radiation is one of the main correction terms for the difference between the actual and the ideal model in the transient hot wire technique to measure the thermal conductivity and thermal diffusivity of fluids. It influences both transparent and absorbing fluids. For absorbing fluids, the main part of this influence comes from the radiation emitted by the fluid and not from its absorption. It is also necessary to distinguish between the influence of natural convection and radiation. Natural convection occurs only after a certain initial convection-free time has elapsed. This time is calculated by a *Ra* number criterion after which curvature may appear in the deviation plot. For argon at 323K and 20.9MPa, this criterion gives a convection-free time of 1.7s. The influence of radiation commences at the very beginning of the measurement process. Thus the curvature in the deviation plot can only be observed from the initial time. Our measurements to date on pentane and propane, which are both radiation absorbing and emitting fluids, indicate a significant influence by radiation emission on measurements of thermal conductivity and thermal diffusivity using the transient hot-wire technique.

Acknowledgement

This work was performed under a program of studies funded by the Natural Sciences and Engineering Research Council of Canada, under Grant numbers A8859 and A5477.

References

[1] L. Sun, J. E. S. Venart, and R. C. Prasad, The Thermal Conductivity, Thermal Diffusivity, and Specific Heat of Liquid n-Pentane. *Int. J. Thermophysics*, 23 (2002) 391.

[2] L. Sun and J. E. S. Venart, Thermal Conductivity, Thermal Diffusivity and Heat Capacity of Gaseous Argon and Nitrogen, *Int. J. Thermophysics*, 26(2005)1.

[3] L. Sun, J. E. S. Venart and R. C. Prasad, The Thermal Conductivity, Thermal Diffusivity and Isobaric Heat Capacity of Toluene and Argon, *Int. J. Thermophysics*, 23(2002)1487.

[4] H. S. Carslaw and J. G. Jaeger, *Conduction of Heat in Solids*, Clarendon Press, Oxford, 2nd Edn., 1959, 339.

[5] J. J. Healy, J. J. de Groot, and J. Kestin, The Theory of The Transient Hot Wire Method for Measuring Thermal Conductivity, *Physica*, 82C(1976) 393.

[6] C. A. Nieto de Castro, R. A. Perkins, and H. M. Roder, Thermal Conductivity Surface of Argon: A Fresh Analysis, *Int. J. Thermophysics*, 12(1991) 985.

[7] C. A. Nieto de Castro, S. F. Y. Li, G. C. Maitland, and W. A. Wakeham, Radiative Heat Transfer in Transient Hot-Wire Measurements of Thermal Conductivity, *Int. J. Thermophys,* 4(1983)344.

[8] R. A. Perkins, H. M. Roder, and C. A. Nieto de Castro, A High-Temperature Transient Hot Wire Thermal Conductivity Apparatus for Fluids, *Journal of Research of the National Bureau of Standards*, 96(1991)247.

[9] J. Menashe and W. A. Wakeham, Effect of Absorption of Radiation on Thermal Conductivity Measurements by the Transient Hot-Wire Method Technique*, Int. J. Heat Mass Transfer*, 25(1982) 661.

[10] L. Sun, J. E. S. Venart, and R. C. Prasad, The Thermal Conductivity, Thermal Diffusivity, and Heat Capacity of Gaseous Argon, *Int. J. Thermophysics*, 23(2002)357.

[11] L. Sun, Simultaneous measurement of Thermal Conductivity and Thermal Diffusivity, Doctoral Dissertation, University of New Brunswick, Fredericton, NB, Canada (2001).

[12] E. F. Buyukicer, J. E. S. Venart, and R. C. Prasad, An Apparatus for the Measurement of the Thermal Conductivity of Fluids*, High Temperature-High Pressure*, 18 (1986) 55.

[13] G. H. Wang, J. E. S. Venart, and R. C. Prasad, The Radiation Effect in the Transient Line-Source Technique for Thermal Properties Measurement, *Proceedings of 11th Symposium on Thermophysical Properties, June 23-27, 1991, Boulder, Colorado, USA*.

[14] J. Menashe and W. A. Wakeham, Absolute Measurements of the Thermal Conductivity of Liquids at Pressure up to 500 MPa, *Ber. Bunsenges. Phys. Chem.* 85 (1981) 340.

Proceedings of The 1st International Conference on **D**iffusion in **S**olids and **L**iquids
DSL-2005, July 6-8, 2005, University of Aveiro, Aveiro, Portugal

INFLUENCE OF TEMPERATURE AND SIZE OF NANOSCALE LIQUID LEAD INCLUSIONS CAPTURED BY DISLOCATIONS IN ALUMINUM ON THEIR DIFFUSION

Sergei PROKOFJEV[1,2*], Victor ZHILIN[1], Erik JOHNSON[2,3], Ulrich DAHMEN[4]

[1]Institute of Solid State Physics, Russian Academy of Sciences
Chernogolovka, Moscow distr., 142432, Russia
[2]Nano Science Center, NBI, University of Copenhagen
Universitetsparken 5, DK-2100, Copenhagen Ø, Denmark
[3]Materials Research Dept., RISØ National Laboratory
DK-4000, Roskilde, Denmark
[4]National Center for Electron Microscopy
Lawrence Berkeley National Laboratory
1 Cyclotron Road, Berkeley, CA 94720, USA

[*]Corresponding author. Fax: +7(096)5249701; Email: prokof@issp.ac.ru

---

Abstract

Diffusion of nanoscale liquid Pb inclusions in thin Al foils was investigated *in-situ* using transmission electron microscopy. Movement of the inclusions was examined quantitatively from their trajectories. The motion of Pb inclusions attached to dislocations was shown to be random but confined to close proximity of the dislocations. Longitudinal motion of the inclusions along the dislocation lines was used to study the effect of temperature and size on their diffusion coefficients, which were estimated using Smoluchowski's equation for Brownian motion in a harmonic potential. The similarity to the values found for free inclusions of similar sizes indicate that the same microscopic mechanism may be responsible for their motion. The Arrhenius plots of the diffusion coefficients are non-linear and the mobility of the inclusions can be associated with the two different activation enthalpies. The large values of the activation enthalpies and their dependence on inclusion size cannot be explained in terms of a single atom diffusion mechanism or a detachment of single Al atoms from the Al matrix as the controlling mechanism.

Keywords: Inclusions on dislocations; Random motion; Transmission electron microscopy; Diffusion coefficient; Effect of temperature and size

---

1 Introduction

The mobility of micro- and nano-sized pores, gas bubbles, liquid and solid inclusions in solid materials has a strong influence on the rate of evolution of the microstructure and properties, and hence on their lifetime [1,2]. The latter are affected by interactions of the pores, bubbles and inclusions with elements of the matrix microstructure e.g. dislocations, grain boundaries, interfaces, and etc. This makes it relevant to investigate the mechanisms controlling the bubble and particle mobility, the influence of the particle microstructure and morphology on their mobility, and the influence of the elements of the matrix microstructure on the kinetic behaviour and the mobility of the particles.

In this paper we present *in-situ* TEM studies of the motion of nanoscale liquid Pb inclusions attached to dislocations in aluminum thin foils for varying temperature and inclusion size.

The high mobility of liquid Pb inclusions in Al makes it possible to conduct accurate, quantitative *in-situ* TEM analyses of their motion and to investigate the impact of the microstructural elements on their motion [3-6]. Besides, 'Pb inclusions in Al' is an appropriate model system for examining of the morphological and structural properties of the inclusions [7-9].

2 Experimental

TEM samples of Al containing nano-sized Pb particles were prepared from high-purity ribbons of Al containing about 1 at.% Pb. The alloys were obtained by rapid solidification from a temperature above the Al-Pb liquid immiscibility gap. The samples were subsequently annealed in an Ar atmosphere to equilibrate their microstructure. *In-situ* TEM studies of the motion of the inclusions were carried out at temperatures around 700 K in a 200 kV Phillips CM 20 microscope using a single tilt heating stage (Gatan). The observations were recorded on videotape (25 video frames per second). The relative accuracy of the sample temperature control was around 1 K, while the temperature determination error is estimated to be around 5 K.

When the effect of temperature on the diffusion of the inclusions was studied, the experiments were always started at the highest temperature. At each temperature a video sequence was started after the sample was stabilized at the new temperature. Video sequences with duration from around 1 minute to more than 10 minutes were recorded from the same area at different temperatures.

Video sequences used for analysis were split into individual digitized images. Inclusion trajectories projected into the plane of view were obtained from measurements of the positions of the centers of the individual Pb inclusions corrected for sample drift. Average diameters d of individual inclusions have been determined using measurements conducted on many video frames.

3 Results and analysis

3.1 Kinetic behaviour of inclusions attached to dislocations

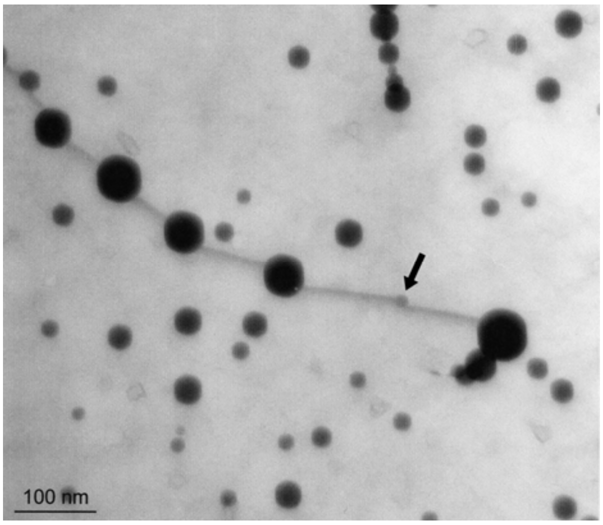

Figure 1: TEM micrograph of liquid Pb inclusions in the Al matrix at 703 K. The arrow points at one of attached to dislocations inclusions whose longitudinal motion is studied.

TEM observations show that most inclusions are attached to defects – dislocations and grain boundaries. The microstructure typical for TEM specimens is shown in Fig. 1. At elevated temperatures the liquid inclusions can be seen to move. Trajectories of inclusions attached to dislocations are localized in the vicinity of the dislocation lines. Their shape depends on the orientation of the dislocations relative to the image plane. Fig. 2 shows the trajectories of an ensemble of inclusions recorded at 681 K during an observation time of around 2.5 minutes. The elongated traces are from inclusions attached to dislocations sloped notably to the foil plane while the point-like traces are from inclusions attached to edge on dislocations.

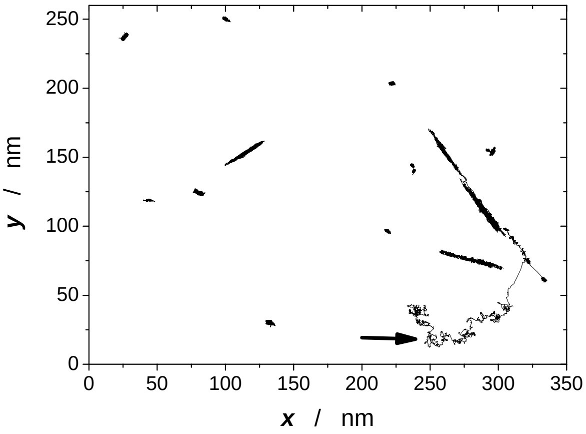

Figure 2: Trajectories of liquid Pb inclusions in Al at 681 K.

Sometimes a trapped inclusion detaches from the dislocation and moves freely for relatively short time until it either disappears at a free surface of the foil, coalesces with another inclusion, or becomes re-trapped by another defect. The arrow in Fig. 2 shows the trajectory of such an inclusion. The trajectories of inclusions attached to dislocations suggest that their movements are random oscillations with small amplitudes in a plane perpendicular to the dislocation line and with larger amplitudes along the direction of the dislocation. This can be seen in the time dependences of transverse and longitudinal displacements of inclusions shown in Fig. 3. From this behaviour it is anticipated that a fixed dislocation may act as an elastic string, returning the inclusions to their equilibrium positions where the dislocation has its minimal length. This model is shown schematically

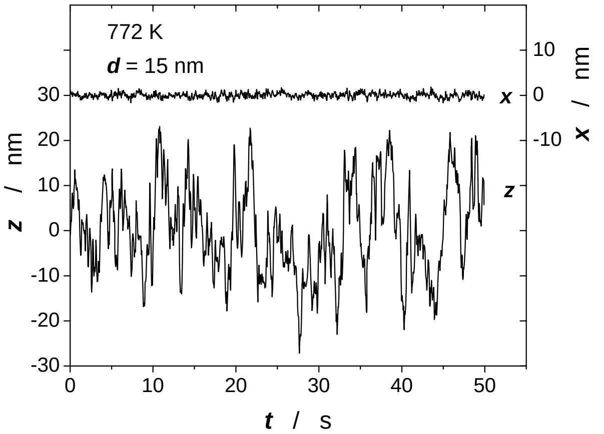

Figure 3: Time dependences of transverse (x) and longitudinal (z) displacements of inclusion.

in Fig. 4, where P is an inclusion attached to a dislocation segment of length $2L$, whose fixed ends lie on the Z-axis, ρ is the displacement of the inclusion from the straight dislocation geometry caused by thermal fluctuations and z stands for its distance from the midpoint 0 of the dislocation segment. The ρ-displacements give rise to a restoring force due to the line tension of the dislocation, the arrow $\boldsymbol{F}$ in Fig. 4. A projection of the force on the Z-axis produces repulsion of the inclusion from the nearest fixed end of the dislocation.

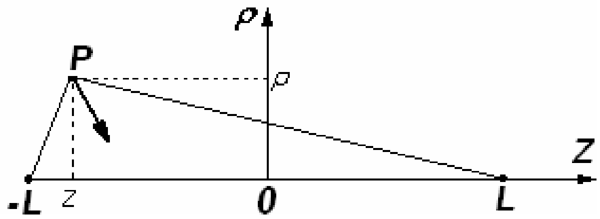

Figure 4: Schematic geometry of the 'dislocation–inclusion' system.

Using this model, the random oscillations of trapped inclusions can be analyzed as a random walk under an action of elastic force. The problem of one-dimensional Brownian motion of a particle under action of a restoring force $P = - f \cdot x$ (f is the force constant) was analyzed by Smoluchowski [10]. He has shown that the stationary distribution of the deviation of the particle from its equilibrium position $x = 0$ is a Gaussian with a standard deviation $\sigma_x = (kT/f)^{1/2}$, where k is the Boltzmann constant, and T is the temperature.

The distribution of the z-displacements in the longitudinal motion is a curve with well-defined maximum (Fig. 5) that corresponds to a spatially confined random motion. Quite often z-distributions obtained are described satisfactorily by a Gaussian, like in Fig. 5. It indicates that in our case a non-linear component in the elastic restoring force is weak. Indeed, the most significant deviation from linearity is expected near the ends of the dislocation, i.e. in the regions where the probability of finding of the inclusion is small because of the repulsion from its ends. This justifies the application of Smoluchowski's equation to determine diffusion coefficients of inclusions.

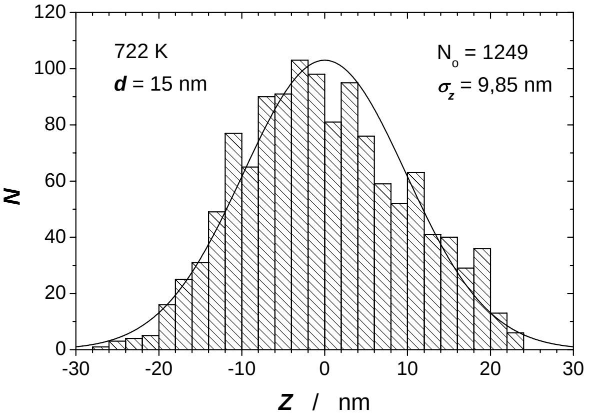

Figure 5: Probability distribution of positions of the inclusions along the dislocation line.

3.2 Determination of diffusion coefficients of inclusions attached to dislocations

Considering one-dimensional motion of a Brownian particle under action of a linear restoring force Smoluchowski has obtained the dependence of the mean squared displacement of particle $<\Delta x^2>$ from its initial position as a function of elapsed time Δt [11]:

$$<\Delta x^2> = 2\sigma_x{}^2[1 - exp(-D_p \Delta t / \sigma_x{}^2)] \quad (1)$$

The average is taken over the trajectory. As above $\sigma_x = (kT/f)^{1/2}$, and D_p is the diffusion coefficient of the particle. Here D_p can be determined from Eq. (1) if the particle trajectory is recorded with time steps that are small enough to obey the relation $D_p \Delta t / \sigma_x^2 \leq 1$. At $D_p \Delta t / \sigma_x^2 << 1$ Eq. (1) turns into Einstein's equation for one-dimensional diffusion [12].

We have utilized Eq. (1) for determination of the diffusion coefficients of trapped inclusions using one-dimensional trajectories of their longitudinal motion. Comparison between diffusion coefficients of trapped inclusions and those of free inclusions obtained using Einstein's equation for two-dimensional random walk shows good agreement [6].

Figure 6 shows the experimental result for the root mean squared longitudinal displacements $\sqrt{<\Delta z^2>}$ of the 15 nm inclusion as a function of elapsed time Δt at 722 K plotted in log - log coordinates. Its slope is close to ½ at small Δt indicating free random motion of the inclusion. At larger Δt the mean squared displacements become independent of Δt and approach a constant value as they should for confined random motion. The fitting by Eq. (1) gives a value for the diffusion coefficient of $D_p = 1.09 \cdot 10^{-16}$ m^{2}s^{-1}.

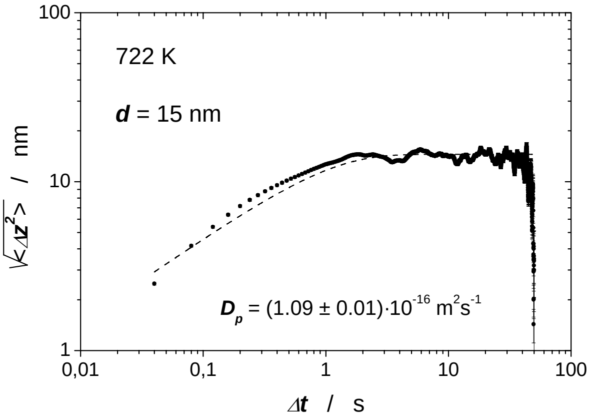

Figure 6: Log-log plot of the root mean squared longitudinal displacement of the inclusion as a function of elapsed time. The dashed line fit it by Eq. (1).

3.3 Effect of temperature on diffusion coefficient of inclusions

One might anticipate that the determination of diffusion coefficients of free inclusions using Einstein's equation would be somewhat more accurate than that of Smoluchowski's equation for a trapped inclusions. However, the lifetime of free inclusions is in most cases too short to use them for investigation of effect of temperature on the diffusion. Much longer lifetime of trapped inclusions would make such studies much easier.

Figure 7 presents the Arrhenius plots of the diffusion coefficient D_p of two inclusions with diameters of 16 nm and 23 nm respectively.

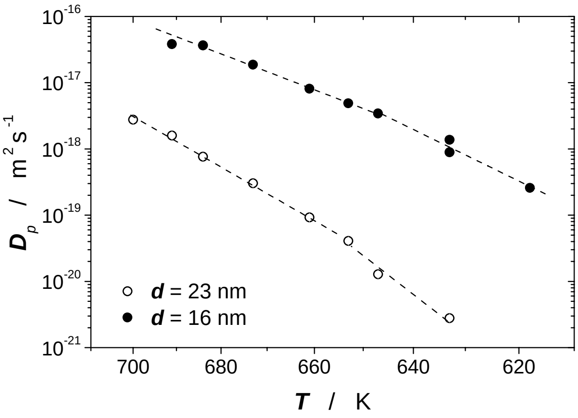

Figure 7: Arrhenius dependence of diffusion coefficient of 16 nm and 23 nm inclusions.

The plots are non-linear, and can be associated with two different activation enthalpies: 3.5 eV and 5.8 eV at low temperature and 2.5 eV and 3.5 eV at high temperature. The transition zone is around 650 K.

3.4 The size dependence of the activation enthalpy for diffusion of inclusions

In Fig. 8 activation enthalpies of diffusion of the liquid Pb inclusions in Al (circles) are shown as a function of their size. The solid symbols correspond to the high-temperature range (T > 650 K), and open symbols are used for the low-temperature range. Both dependences indicate an increase in the activation enthalpy with increasing inclusion size. For comparison the data on the enthalpies of the diffusion of He [13], Kr [14, 15] and Xe [16] bubbles in Al are shown in Fig. 8.

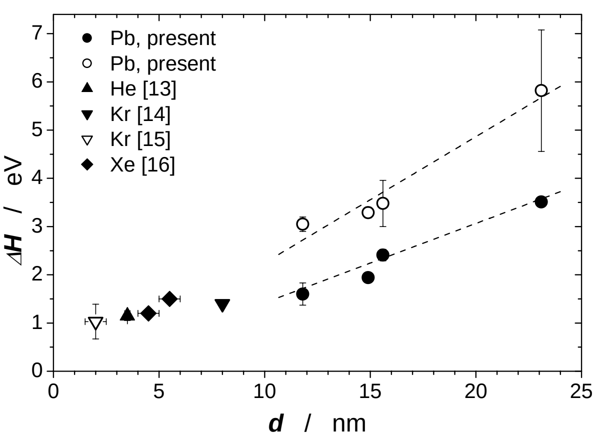

Figure 8: Activation enthalpy of diffusion of inclusions as a function of their size.

This plot shows that large differences in the activation enthalpies for diffusion of liquid Pb inclusions and noble gas bubbles in Al may be explained by the difference in their size. In other words, the activation enthalpy may be determined by Al matrix rather than by the nature of the inclusions or the bubbles.

4 Discussion

Motion of inclusions in a crystalline matrix is necessarily accompanied by a local destruction of the crystal lattice in the direction of the motion, and its recreation at the opposite side of the inclusion. Hence, the displacement of an inclusion is mediated by detachment of atoms from the matrix crystal, their consequent transfer and rejoining to the crystal lattice. Thus, the mobility is controlled either by crystal growth-dissolution at the crystal-liquid interface or by diffusion. The dependence $D_p \sim d^{-4}$ found for diffusion of liquid Pb inclusions in Al [6] indicates that their mobility is controlled by kinetic processes at the Pb/Al interface [17]. A similar size dependence is obtained for diffusion of He bubbles in Al [13].

The activation enthalpies of diffusion of liquid Pb inclusions in Al obtained in the present study reach values that significantly exceed the activation enthalpies of atomic transport processes in Al-Pb binary system related to single atom diffusion and, in particular, of diffusion along the Pb/Al interface. This suggests that the mobility is not governed by diffusion. The high values of the activation enthalpies also exceed the sublimation enthalpy of Al, which is equal to 3.36 eV [18]. This also discards the assumption that the mobility of liquid Pb inclusions in Al is controlled by detachment of single Al atoms from the Al matrix at the interface of the inclusions, which was made in our preceding work [6], where a smaller (12 nm) inclusion was studied. It was then assumed that the low-temperature activation enthalpy was related to detachment of Al atoms from {111} facets of the Pb/Al interface, and the high-temperature activation enthalpy to a similar detachment from the rough Pb/Al interface [6].

The high activation energies may be due to the control of the mobility of the inclusions by nucleation of steps on the Pb/Al interface as it was assumed in the model developed for facetted bubbles [19]. This model also predicts the linear relation between the activation enthalpy of the diffusion and the size of the inclusions seen in Fig. 8. Note, however, that the observed size dependence of the activation enthalpy in the high-temperature regime where Pb inclusions have a rounded shape is beyond the framework of the model [19].

A more accurate determination of the behaviour of the activation enthalpies with inclusion size is needed for better understanding of the process controlling the mobility of liquid Pb inclusions in Al.

5 Conclusions

1. Using Smoluchowski's equation the diffusion coefficients of trapped inclusions are determined from their one-dimensional trajectories of random oscillatory motion along the dislocation lines.

2. The non-linear Arrhenius plot of the inclusions can be associated with two different activation enthalpies at lower and higher temperature.

3. A linear increase in the low- and high-temperature activation enthalpies with increasing incluison size observed.

4. Single atom diffusion mechanisms and detachment of single Al atoms from Al matrix cannot explain the high values of the activation enthalpies and their size dependence, which we have observed.

Acknowledgments

The work was supported by the Russian Foundation for Basic Research (project 05-03-33141), by the Director, Office of Basic Energy Sciences, Materials Science Division, US Department of Energy, under contract DE-AC3-76SF00098, and the Danish Natural Sciences Research Council. We are grateful to P. Ochin and his group (CNRS-CECM) for providing rapidly solidified materials.

References

[1] Geguzin, Ya.E., Krivoglaz, M.A.: *Migration of macroscopic inclusions in solids*, Consultants Bureau, New York, 1973.

[2] Cottrell, G.A.: Void migration, coalescence and swelling in fusion materials. *Fusion Eng. Design*, 66-68, pp. 253-257, 2003.

[3] Prokofjev, S.I., Zhilin, V.M., Johnson, E., Levinsen, M., Dahmen, U.: Investigation of mobility of liquid nano-inclusions of lead in crystalline aluminum with dislocations. *Proc. 5th Int. Conf. Single Crystal Growth and Heat & Mass Transfer, Vol. 2*, Ginkin, V.P. (Ed.), Obninsk, Russia, 2003, pp. 487-496.

[4] Johnson, E., Andersen, J.S., Levinsen, M.T., Steenstrup, S., Prokofjev, S., Zhilin, V., Dahmen, U., Radetic, T. and Turner, J.H.: Random Vibrational Movements of Liquid Nanosized Pb Inclusions in Al. *Mater. Sci. Eng.* A, 375-77, pp. 951-555, 2004.

[5] Johnson, E., Levinsen, M.T., Steenstrup, S., Prokofjev, S., Zhilin, V., Dahmen, U., Radetic, T.: One-dimensional random walk of nano-sized liquid Pb inclusions on dislocations in Al. *Phil. Mag.*, 84, pp. 2663-2673, 2004.

[6] Prokofjev, S., Zhilin, V., Johnson, E., Levinsen, M.T., Dahmen, U.: In-situ TEM investigation of diffusion of nano-scale liquid Pb inclusions on dislocations and in bulk aluminium. *Def. Diff. Forum*, 337-340, pp. 1072-1077, 2005.

[7] Johnson, E., Johansen, A., Dahmen, U., Chen, S., Fujii, T.: Shapes and sizes of nanoscale Pb inclusions in Al. *Mater. Sci. Eng.,* A304-306, pp. 187-193, 2001.

[8] Gabrisch, H., Kjeldgaard, L., Johnson, E., Dahmen, U.: Equilibrium shape and interface roughening of small liquid Pb inclusions in solid Al. *Acta Mater.*, 49, pp. 4259-4269, 2001.

[9] Johnson, E., Andersen, H.H., Dahmen, U.: Nanoscale lead and noble gas inclusions in aluminium: structures and properties. *Microsc. Res. Techn.* 64, pp. 356-372, 2004.

[10] Smoluchowski, M.v.: Einige Beispiele Brown'scher Molekularbewegung unter Einfluβ äuβerer Kräfte. *Bull. Int. de l'Acad. de Cracovie, Classe de Sci. Math. et Nat., Serie A*, s. 418-434, 1913.

[11] Smoluchowski, M.V.: Studien uber Molekularstatistik der Emulsionen und deren Zussamenhang mit der Brown'schen Bewegung. *Sitzungsber. Kais. Akad. Wissensch. Wien* (IIa), 123, s. 2381-2405, 1914.

[12] Einstein, A.: Über die von der molekularkinetischen Theorie der Wärme geforderie Bewegung von in ruhenden Flüssigkeiten suspendierten Teilchen. *Ann. d. Phys.*, 17, s. 549-560, 1905.

[13] Ono, K., Furuno, S., Hojou, K., Izui, K., Kino, T., Mizuno, K., Ito, K.: In-situ observations of Brownian motion and diffusion of helium bubbles in aluminum. *Def. Diff. Forum*, 95-98, pp. 335-340, 1993.

[14] Takaishi, K., Kikuchi, T., Furuya, K., Hashimoto, I., Yamaguchi, H., Yagi, E., Iwaki, M.: Thermal extraction of krypton in aluminum using mass spectrometer. *Phys. Stat. Sol. (a)*, 95, pp. 135-139, 1986.

[15] Yamaguchi, H., Hashimoto, I., Mitsuya, H., Nakamura, K., Yagi, E., Iwaki, M.: The random motion of bubbles in krypton-implanted aluminum. *J. Nucl. Mater.*, 161, pp. 164-168, 1989.

[16] Alexander, D.E., Birtcher, R.C.: The effect of ion irradiation on inert gas bubble mobility. *Mat. Res. Soc. Symp. Proc.*, 235, pp. 545-550, 1992.

[17] Nichols, F.A.: Kinetics of diffusional motion of pores in solids. *J. Nucl. Mater.*, 30, pp. 143-165, 1969.

[18] *Metal Reference Book*, Smithells, C.J., Brandes, E.A. (Eds.), Butterworths, Boston, 1976.

[19] Wilertz, L.E. Shewmon, P.G.: Diffusion of helium gas bubbles in gold and copper foils. *Metall. Trans.*, 1, pp. 2217-2223, 1970.

Proceedings of The 1st International Conference on **D**iffusion in **S**olids and **L**iquids
DSL-2005, July 6-8, 2005, University of Aveiro, Aveiro, Portugal

THERMAL STABILITY AND STRENGTH OF POLYCRYSTALLINE NANOWIRES

Leonid KLINGER [1,*], Eugen RABKIN[1]

[1]Department of Material Engineering, Technion-Israel Institute of Technology, 32000 Haifa, Israel

[*]Corresponding author. Fax: +972 4 8295677; Email: klinger@tx.technion.ac.il

---

Abstract

We considered a polycrystalline cylindrical nanowire of the initial radius R_0 composed of identical cylindrical grains of the length L_0, strained uniaxially by an external stress P. At the temperatures at which some surface and grain boundary diffusion are allowed the thinning of the nanowire in the vicinity of grain boundaries occurs due to the phenomenon of grain boundary grooving. We calculated the equilibrium shapes of the nanowire achieved after long annealing times. Our calculations demonstrated that for any given L_0/R_0 ratio some critical value of the applied stress exists above which the nanowire is unstable and breaks down into the string of isolated spherical particles, in full analogy with the Rayleigh instability of long cylinders. The kinetics of the shape change was calculated numerically. It was shown that the rate of thinning of unstable nanowires diverges as the moment of breakdown is approached. We also demonstrated that the breakdown may occur even for nominally stable nanowires “on the way” to achieving their equilibrium shape. Therefore, the stability of nanowire is determined by a combination of geometric (L_0/R_0), thermodynamic (grain boundary energy), and kinetic (ratio of grain boundary and surface diffusivities) parameters. An application of external tensile stress accelerates the breakdown of nanowires.

Keywords: Nanowires; Bamboo microstructure; Surface diffusion; grain boundaries

---

1 Introduction

Semiconductor and metallic nanowires are considered to be important building blocks of the future microsystems. They can both provide interconnections between different functional blocks and can be designed as active elements, like gas sensors and transistors [1]. The unusual functional properties of nanowires result from their small diameter, which is usually in the range of nanometers. The same high aspect ratio of the nanowires which determines their useful functional and electrical properties entails, however, the danger of morphological instability at elevated temperatures, at which diffusional mobility of the atoms becomes important. It is well-established that semiconductor nanowires [1] and thin sub-micrometer metallic filaments in fibrous in-situ metal matrix composites [2] can break up into isolated particles by the mechanism of Rayleigh instability, in full analogy with the loss of stability of liquid jets [3]. While semiconductor nanowires are usually grown as single crystals, metallic nanowires are often polycrystalline and contain the grain boundaries (GBs) transversing the nanowire normal to its axis (bamboo microstructure). Similar microstructures with transverse heterophase boundaries are also obtained in longitudinal heterostructured semiconductor nanowires produced by switching between different materials during growth [4]. The interfaces in such structured nanowires provide an additional source of morphological instability at elevated temperatures. For example, it was shown recently that Cu nanowires break up along the transversal GBs during annealing at 400 °C [5]. The aim of the present work is to analyze the equilibrium shape of polycrystalline bamboo nanowires and determine their thermal stability and kinetics of break down under the assumption that the surface and GB diffusion are responsible for the changes in morphology and nanowire elongation, respectively. This assumption is certainly true for the relatively low temperatures of interest for microelectronics, at which surface and GB diffusion are many orders of magnitude faster than volume self-diffusion. It should be noted that the problem of equilibrium shape considered in the present work is mathematically similar to the problem of the shape of a fluid bridge attached to a pair of rigid parallel plates [6].

2 Governing equation

We will consider a cylindrical wire of initial radius R_0 with the periodic bamboo microstructure and grain size (length) of $2L$ (see Fig. 1) under the uniaxial load P.

The surface topography evolution of the wire controlled by surface diffusion is described by a function $R(X,t)$, where X is the distance along the axis of the wire and t is annealing time. Due to periodicity of the system we will consider only one half of the grain ($0 \le X \le L$) with $X = 0$ and $X = L$ corresponding to the GB plane and to the middle of the grain, respectively. Initially,

$$R(X,0) = R_0 \tag{1a}$$

We will suppose that a condition of mechanical equilibrium is fulfilled at the root of the GB groove:

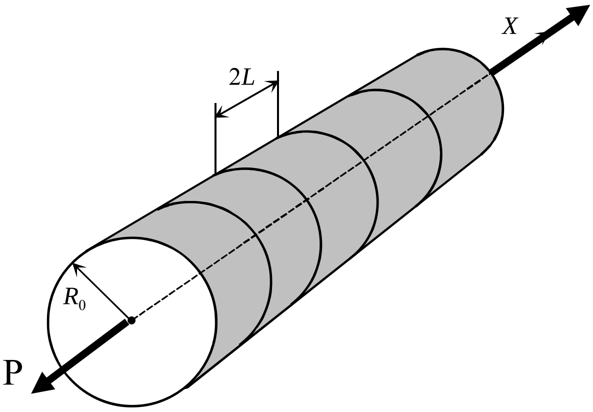

Figure 1: Schematic of bamboo-type polycrystalline cylindrical nanowire of initial radius R_0 and grain length $2L$ under uniaxial load P.

$$\partial_X R\big|_{X=0} \equiv m = \tan(\theta)\text{, with } \sin(\theta) = \frac{\gamma_{GB}}{2\gamma} \tag{1b}$$

and

$$\partial_X R\big|_{X=L} = 0\,, \tag{1c}$$

due to the symmetry of the problem. Here, γ_{GB} and γ are the Gibbsian energies of the GB and of a free surface, respectively.

2.1 Surface diffusion

Our main assumption is that surface diffusion is responsible for the radial shape change of the nanowire, while the grain boundary diffusion is responsible for the nanowire elongation. According to the Mullins' theory [7], the self-diffusion flux along the surface, J_s, is driven by the gradient of mean surface curvature, K:

$$J_s = -\frac{\delta_s D_s}{kT}\nabla_s \mu_s = -B\frac{1}{\sqrt{1+(\partial_X R)^2}}\partial_X K\,, \tag{2}$$

where B is Mullins coefficient

$$B = \frac{\delta_s D_s \Omega\gamma}{kT}\,, \tag{3}$$

and

$$K = -\frac{\partial_X^2 R}{\left(1+(\partial_X R)^2\right)^{3/2}} + \frac{1/R}{\left(1+(\partial_X R)^2\right)^{1/2}} \ . \qquad (4)$$

Here δ_s, D_s, μ_s and Ω are the thickness of surface layer in which the diffusion process occurs, surface self-diffusion coefficient, chemical potential of surface atoms and atomic volume, respectively. kT has its usual meaning. The governing equation for the function *R(X,t)* can be obtained from the condition of mass balance:

$$\partial_t R = -\frac{1}{R}\partial_X\left(RJ_s\right) = \frac{B}{R}\partial_X\left(\frac{R\partial_X K}{\sqrt{1+(\partial_X R)^2}}\right) \qquad (5)$$

We need solution of this equation with initial condition and boundary conditions (1). Additional boundary conditions follow from vanishing of the atomic flux at the middle of the grain

$$J_s\big|_{x=L} = 0\,, \qquad (6)$$

and a continuity of the atomic flux at the root of the GB groove

$$J_s\big|_{x=0} = 0.5J_{GB}\,, \qquad (7)$$

where J_{GB} is grain boundary diffusion flux at the root of the GB groove.

2.2 Grain boundary diffusion

Let us consider uniaxial tensile load applied to the wire. This load causes a driving force for atomic flux (from the surface of wire to its centre) along the GB, the accumulation of atoms at the GB caused by this flux being responsible for the elongation of the wire. The radial diffusion flux along the GB is proportional a gradient of normal stress

$$J_{GB}(r) = -\frac{\delta_{GB} D_{GB}\Omega}{kT}\partial_r\sigma \qquad (8)$$

We assumed a steady state distribution of the stresses along the GB, and thus a constant divergence of the grain boundary flux: $(1/r)\partial_r\left(rJ_{GB}(r)\right) = const$. It follows from this equation that steady state normal stress along the GB should be a parabolic function of radius: $\sigma(r) = ar^2 + b$. For finding the coefficients *a* and *b* the condition of continuity of the chemical potential at the root of the GB groove can be used:

$$\sigma(R_{\min}) = \gamma K_{\min} \qquad (9)$$

where R_{min} and K_{min} are a radius of the nanowire and mean surface curvature at the root of the groove. An additional condition is given by a force balance equation:

$$-P + \gamma 2\pi R_{\min}\cos\theta = 2\pi\int_0^{R_{\min}} r\sigma(r)dr \qquad (10)$$

where *P* is applied load. Using these conditions we can find the atomic flux at the root of the GB groove:

$$J_{GB} = -4\frac{\delta D_{GB}\Omega\gamma}{kTR_{\min}}\left(K_{\min} - \frac{2\cos\theta}{R_{\min}} + \frac{P}{\pi R_{\min}^2\gamma}\right) \ (11)$$

and the overall elongation rate of the nanowire

$$\partial_t L == 4\frac{\delta D_{GB}\Omega\gamma}{kTR_{\min}^2}\left(K_{\min} - \frac{2\cos\theta}{R_{\min}} + \frac{P}{\pi R_{\min}^2\gamma}\right) \ (12)$$

It should be noted that in the case of *fas*t GB diffusion the overall length of the grain changes even for $P = 0$.

3 Equilibrium shape of the nanowire

For the equilibrium state the mass flux in the system is nil everywhere, and thus the mean curvature is a constant along the surface: $K = const$. It should be noted that this is a universal condition of equilibrium that does not depend on dominating mass transport mechanism. Using Eq. (4) we can calculate the corresponding surface shape $R = R(X)$. Multiplying both sides of Eq. (4) by $R\partial_X R$ and performing an integration we obtain

$$\frac{R}{\sqrt{1+(\partial_X R)^2}} = \frac{K}{2}R^2 + const \qquad (13)$$

The integration constant and curvature K can be found from boundary conditions (1b), (1c). An additional boundary condition can be obtained from $J_{GB} = 0$:

$$P = \pi R_{\min}^2 \gamma \left(\frac{2\cos\theta}{R_{\min}} - K \right) \qquad (14)$$

These boundary conditions, together with a mass conservation law allow integrating the Eq. (13). The details of solution are given in Ref. [9].

Figure 2 shows the dependence of equilibrium grain length on applied load P for m=0.15. All lengths are normalized by $R_e \equiv \left(R_0^2 L_0\right)^{1/3}$, where $L_0 = L(t = 0)$. We see that for each applied load P there are two equilibrium grain lengths (and thus two equilibrium shapes of the nanowire surface). It can be shown, however, that the upper line only represents a stable shape. On the same figure the minimal radius of equilibrium grains is also shown.

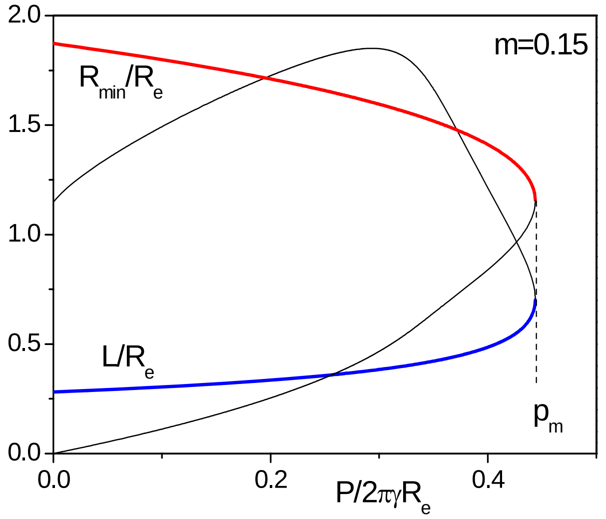

Figure 2: Length of the equilibrium grain as a function of the applied load. Equilibrium shape exists only for the loads below a threshold: $P/2\pi\gamma R_e < p_m \approx 0.444$ (for $m = 0.15$).

Therefore, it can be concluded that equilibrium shape of the grains of polycrystalline nanowire can be achieved only for the loads below a certain threshold:

$$p_0 \equiv \frac{P}{2\pi\gamma R_0} < p_m \left(\frac{L_0}{R_0} \right)^{1/3} \qquad (15)$$

($p_m = 0.444$ for m=0.15).

In the plane p_0 – (L_0/R_0) the equation (15) determines the border of the region where the equilibrium shapes of the grain exist. But not every equilibrium shape in this region can be actually achieved. We will demonstrate that a significant part of the region of allowed equilibrium shapes is not achievable due to kinetic reasons – the nanowire breaks down into individual grains before it arrives at the equilibrium shape.

4 Stability diagram

We have solved the equation (5) numerically. Details of the calculation procedure were described in [9]. The typical time dependences of the elongation, (L/R_0), and minimal radiuses, ($R_{\min}/R_0$), are presented in Fig. 3.

Two kinds of the kinetic curves can be distinguished in this Figure. In all cases the evolution of the grain shapes begins with the GB grooving and R_{min} decreases at this stage. For the curves of the first type (1, 2) this process slows down and later the shape of the grains slowly evolves toward the equilibrium one. For the curves of the second type (3, 4) the GB grooves develop with accelerating rate up to the full separation of the wire into individual grains. The time elapsed until separation is always finite. It is remarkable that the curve No. 3 corresponds to the nanowire inside the region where the equilibrium shapes of the grains exist.

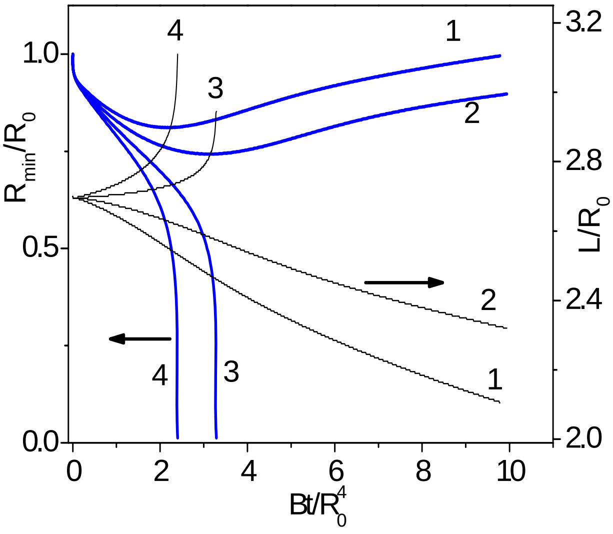

Figure 4: Typical kinetic curves.
$m = 0.15$, $L_0/R_0=2.7$, $D_{GB}/D_S = 0.01$.
$1 - p_0=0$, $2 - p_0=0.25$, $3 - p_0=0.5$, $4 - p_0=0.7$

In Fig. 4, the black line determines the border of the region in which the equilibrium grain shapes exist (see Eq. (15)), while the red line marks the sub-region inside this region where the equilibrium shape is achievable kinetically. The size of this sub-region depends on the ratio of GB and surface diffusivities, D_{gb}/D_s. In fact, the red line determines the region of stability of the nanowire, in which zero-creep experiments can be performed.

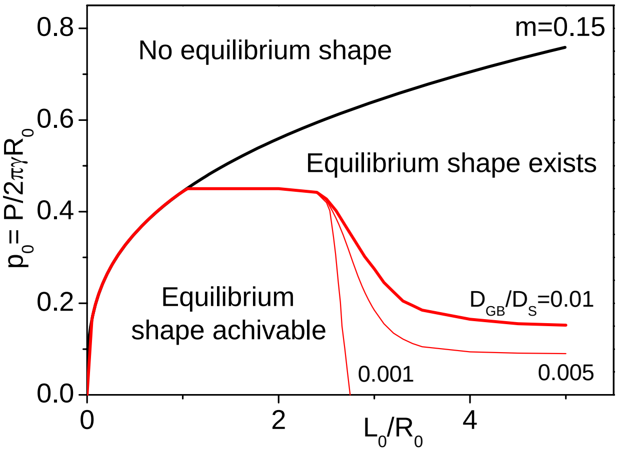

Figure 4: Stability diagram of the nanowire in the "stress-aspect ratio" space.

It follows from the above analysis that the equilibrium shape of the polycrystalline nanowire can be achieved only for certain grain sizes:

$$L_0/R_0 \le (L_0/R_0)_{\max}.$$

For $L_0/R_0 > (L_0/R_0)_{\max}$ the nanowire will break down with time into individual grains.

The range of stability depends on D_{gb}/D_s, see Fig. 5. It is interesting that for D_{gb}/D_s ratios larger than some critical value (0.0225 for $p_0 = 0$) the grain shape achieves an equilibrium one for *any* ratio

L_0/R_0. Similarly, for any applied load inside the equilibrium region the kinetic stability sub-region extends with increasing D_{gb}/D_s ratio.

Nevertheless, the kinetic stability sub-region is always smaller than the region where the equilibrium grain shapes exist: irrespectively of the L_0/R_0 ratio, the nanowire will break down with time into individual grains for p_0 larger then some critical value (≈0.45 for m=0.15). This break down will occur even for very high values of D_{gb}/D_s.

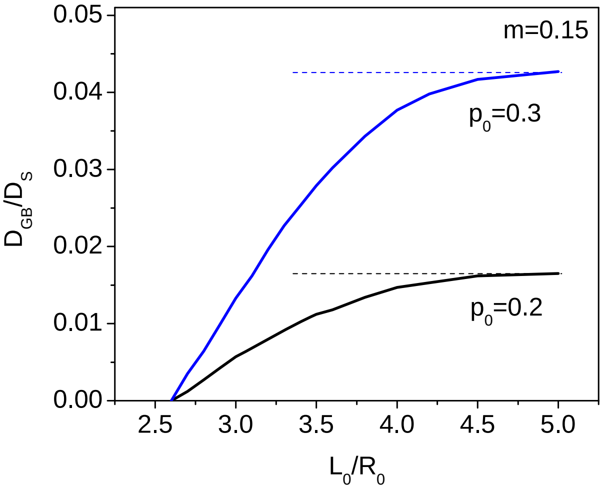

Figure 5: Effect of diffusivities ratio D_{gb}/D_s on the range of kinetic stability of the nanowire.

5 Conclusion

We have calculated the equilibrium shapes of polycrystalline nanowires with bamboo microstructure subjected to the external uniaxial stress. It was assumed that surface and GB diffusion represent the only mechanisms of the shape change of the nanowire. It was shown that for every initial aspect ratio of the grain, L_0/R_0, there is some critical value of the applied stress above which no equilibrium shape exists and the nanowire breaks down with time into individual isolated grains. The deformation kinetics accelerates dramatically as the moment of break-down is approached. Surprisingly, it was found that the break down can also occur for lower stresses, for which the equilibrium shape of the nanowire does exist. The region of kinetic stability of the nanowire in the parametric space "stress – aspect ratio" has been determined. The size of this region depends on the ratio of GB and surface diffusivities and on the relative GB energy.

References

[1] Th. I. Kamins, in "*The Nano-Micro Interface: Bridging the Micro and Nano Worlds*", H.-J. Fecht and M. Werner (Eds.), Wiley-VCH, Weinheim, Germany (2004) 195.

[2] D. Raabe, J. Ge, *Scripta mater.* 51 (2004) 915.

[3] Lord Rayleigh, *Proc. London Math. Soc.* 10 (1878) 4.

[4] P. Yang, *MRS Bulletin* 30 (2005) 85.

[5] M.E. Toimil Molares, A.G. Balogh, T.W. Cornelius, R. Neumann, and C. Trautmann, *Appl. Phys. Lett.* 85 (2004) 5337.

[6] W.C. Carter, *Acta metal.* 36 (1988) 2283.

[7] W.W. Mullins, *J. Appl. Phys.* 28 (1957) 333.

[8] L. Klinger and E. Rabkin, *Scripta mater.*, 2005, in press.

[9] L. Klinger and E. Rabkin, *Z. Metallkd.*, 2005, in press.

Proceedings of The 1st International Conference on **D**iffusion in **S**olids and **L**iquids
DSL-2005, July 6-8, 2005, University of Aveiro, Aveiro, Portugal

MICROSCOPIC APPROACH TO THE EVALUATION OF DIFFUSION COEFFICIENTS FOR SUBSTITUTIONAL F.C.C. SOLID SOLUTIONS

Taras RADCHENKO[1], Valentyn TATARENKO[1,*], Sergiy BOKOCH[2], Mykola KULISH[2]

[1]Department of Solid State Theory, G. V. Kurdyumov Institute for Metal Physics, N.A.S. of Ukraine,
36 Academician Vernadsky Boulevard, 03680 Kyyiv-142, Ukraine
[2]Department of Physics of Functional Materials, Taras Shevchenko Kyyiv National University,
6 Academician Glushkov Prospekt, 03650 Kyyiv-22, Ukraine

[*]Corresponding author. Fax: +380 44 4242561; Email: tatar@imp.kiev.ua

Abstract

The microscopic theory of atomic diffusion kinetics is used for f.c.c. substitutional solid solutions. Within this approach, the short-range order relaxation is due to the atomic migration. Experimental data on the time dependence of radiation diffuse scattering are used for the determination of microscopic characteristics of atomic migration. The model takes into account the discrete and anisotropic character of atomic jumps in a long-range field of the concentration heterogeneities of interacting atoms. Such a consideration is applied for a close-packed Ni–Fe solid solution. Atomic-jumps' probabilities are estimated that allows to determine the diffusion coefficients and activation energies. Independent kinetic experimental data about a time evolution of long-range order are also used to calculate diffusivities in $L1_2$-Ni–Fe alloy.

Keywords: Basics of diffusion; Short-range order kinetics; Diffuse scattering; Long-range ordering; Diffraction evolution

1 Introduction

It is well known that existing experimental methods for studying diffusion processes are based on the measurements in solid solutions where concentration heterogeneities have macroscopic spatial dimensions greatly exceeding the lattice parameters. The information available from these experiments gives only macroscopic diffusivities for continuous diffusion equations. Besides, such experiments are characterized by low rates of diffusion relaxation of macroscopic concentration heterogeneities. To reduce the measurement time, the relatively high temperatures should be used. This is why the conventional data predominantly concern the high-temperature diffusion characteristics.

However, some diffusion processes occur within the atomic-scale ranges and can be studied by the radiation diffraction technique. They are: spinodal decomposition, long-range order kinetics below the stability limits of the disordered phase, homogenization of the sandwich-like deposit structures, short-range order kinetics, and so on [1]. The first three processes should be described by the discrete theory of single-site probability kinetics (the theory of discrete diffusion), while a kinetics of the short-range order should be described by the discrete theory of two-site probability kinetics.

In fact, short-range order is the unique natural occurring concentration heterogeneity, whose dimensions are commensurate with lattice parameters of a solid solution. Kinetics of short-range order is determined by the microscopic diffusion over intersite distances. Therefore, kinetic measurements of its relaxation provide us with detailed information on the discrete diffusion mechanism such as a possibility to determine the microscopic characteristics of atomic migrations, including probabilities and types of atomic jumps, and activation energy of diffusion.

The most convenient instrument for the investigation of short-range order kinetics, that is elementary diffusion events, is relaxation of radiation (X-ray, thermal neutrons) diffuse scattering intensities [1–3]. Besides, discrete diffusion measurements can be performed at room temperatures, because of short time of elementary diffusion events. This means that results can be utilized to determine the low-temperature diffusivities and activation energies.

The goal of a present paper is to estimate the microscopic characteristics of diffusion elementary events in Ni–Fe solid solution: 'potential'-fields' distribution due to the concentration heterogeneities caused by the atom at zero ('central') site and probabilities of atomic jumps per unite time at arbitrary sites of f.c.c. lattice. Diffusion parameters are determined using experimental data [3] on thermal neutrons' diffuse scattering within the framework of first-order kinetics model. Microscopic values enable to calculate the macroscopic characteristics: diffusion and self-diffusion coefficients. On the other hand, we use independent experimental data [4] on long-range order relaxation kinetics to estimate the diffusivities in this alloy.

2 Model of diffuse-scattering kinetics

Let us consider a two-particle correlation function $P_{\alpha\beta}(\mathbf{R}-\mathbf{R}', t)$—probability to find simultaneously (at a given time t) atoms of α, β components at the sites $\mathbf{R}$, $\mathbf{R}'$ ($\mathbf{R}$, $\mathbf{R}'$—radius-vectors of Bravais lattice sites). For a binary substitutional solid solution, time dependence of its Fourier transforms,

$$\widetilde{P}_{\alpha\beta}(\mathbf{k},t) = \sum\nolimits_{\mathbf{R}-\mathbf{R}'} P_{\alpha\beta}(\mathbf{R}-\mathbf{R}',t)e^{-i\mathbf{k}\cdot(\mathbf{R}-\mathbf{R}')}, \qquad (1)$$

can be approximately represented as follows [1]:

$$\Delta\widetilde{P}_{\alpha\beta}(\mathbf{k},t) = a_{11}^{\alpha\beta}(\mathbf{k})e^{-2\lambda_1(\mathbf{k})t} + \\ + a_{22}^{\alpha\beta}(\mathbf{k})e^{-2\lambda_2(\mathbf{k})t} + a_{12}^{\alpha\beta}(\mathbf{k})e^{-[\lambda_1(\mathbf{k})+\lambda_2(\mathbf{k})]t}; \qquad (2)$$

$\Delta\widetilde{P}_{\alpha\beta}(\mathbf{k},t) = \widetilde{P}_{\alpha\beta}(\mathbf{k},t) - \widetilde{P}_{\alpha\beta}(\mathbf{k},\infty)$; $\widetilde{P}_{\alpha\beta}(\mathbf{k},\infty)$ is equilibrium value; $a_{11}^{\alpha\beta}(\mathbf{k})$, $a_{22}^{\alpha\beta}(\mathbf{k})$, $a_{12}^{\alpha\beta}(\mathbf{k})$—pre-exponential coefficients; $\{2\lambda_1(\mathbf{k})\}^{-1}$, $\{2\lambda_2(\mathbf{k})\}^{-1}$, $\{\lambda_1(\mathbf{k})+\lambda_2(\mathbf{k})\}^{-1}$ represent the possible relaxation times of three atoms'-configuration modes with a wave vector $\mathbf{k}$; $\lambda_1(\mathbf{k})$, $\lambda_2(\mathbf{k})$—eigenvalues of matrix

$$\widetilde{W}_{\alpha\beta}(\mathbf{k}) = \sum\nolimits_{\gamma}[\widetilde{L}_{\alpha\gamma}(\mathbf{k})/k_B T]c_\alpha c_\gamma \widetilde{\Psi}_{\gamma\beta}(\mathbf{k}). \qquad (3)$$

In the last equation, $\widetilde{L}_{\alpha\beta}(\mathbf{k})$ is Fourier transform of Önsager kinetic coefficient $L_{\alpha\beta}(\mathbf{R}-\mathbf{R}')$, which defines the exchange probability between a pair of α and β atoms at lattice sites $\mathbf{R}$ and $\mathbf{R}'$ per unit time; k_B—Boltzmann constant; T—temperature; c_α is the atomic fraction of the α-kind atoms; $\widetilde{\Psi}_{\alpha\beta}(\mathbf{k})$ is a Fourier transform of matrix

$$\Psi_{\alpha\beta}(\mathbf{R}-\mathbf{R}') \approx \left(\delta^2 F/[\delta P_\alpha(\mathbf{R})\delta P_\beta(\mathbf{R}')]\right)_{\substack{P_\alpha(\mathbf{R})=c_\alpha \\ P_\beta(\mathbf{R}')=c_\beta}} \qquad (4)$$

within the framework of the quasi-chemical approximation [1]. In Eq. (4), F—free energy of the equilibrium binary solid solution with one-particle probability $P_\alpha(\mathbf{R})$ to find the α-kind atom at the site $\mathbf{R}$ (in disordered state $P_\alpha(\mathbf{R}) \equiv c_\alpha$).

Diffuse scattering of radiations is caused by the atoms'-configuration fluctuations, *i.e.* short-range order of atoms. Short-range order relaxation 'promotes' the diffuse-scattering relaxation. In a reciprocal space, distribution of diffuse scattering intensity, $I_{\text{diff}}(\mathbf{k},t)$, is connected with two-particle correlation function [1, 2]:

$$\Delta I_{\text{diff}}(\mathbf{k},t) = \sum\nolimits_{\alpha,\beta} f_\alpha f_\beta \Delta\widetilde{P}_{\alpha\beta}(\mathbf{k},t); \qquad (5)$$

$\Delta I_{\text{diff}}(\mathbf{k},t) = I_{\text{diff}}(\mathbf{k},t) - I_{\text{diff}}(\mathbf{k},\infty)$, $I_{\text{diff}}(\mathbf{k},\infty)$—diffuse scattering intensity in the equilibrium solid solution, wave vector $\mathbf{k}$ characterizes distance of the point of measurement from the nearest site of reciprocal lattice in $\mathbf{k}$-space of crystal, f_α and f_β—atomic-scattering factors of α and β components.

Substituting Eq. (2) into (5) and assuming strict inequality $\lambda_1(\mathbf{k}) << \lambda_2(\mathbf{k})$, Eq. (5) results in

$$\Delta I_{\text{diff}}(\mathbf{k},t)/\Delta I_{\text{diff}}(\mathbf{k},0) \approx e^{-2\lambda_1(\mathbf{k})t},\ \tau \approx 1/[2\lambda_1(\mathbf{k})]. \quad (6)$$

This corresponds to the first-order kinetics model; τ is a relaxation time of intensity (in $\mathbf{k}$-space).

It is useful to express the Fourier component, $\lambda_1(\mathbf{k})$, in terms of function $\widetilde{\varphi}_1(\mathbf{k})$ [1] showing 'potential'-fields' action due to the concentration heterogeneities in solid solution:

$$\lambda_1(\mathbf{k}) \approx \lambda_1^0(\mathbf{k})[1+\widetilde{\varphi}_1(\mathbf{k})]; \qquad (7)$$

$\lambda_1^0(\mathbf{k})$ corresponds to the ideal solid solution. Function $\widetilde{\varphi}_1(\mathbf{k})$ is connected with Fourier transforms of interaction energies by means of $\widetilde{\Psi}_{\alpha\alpha}(\mathbf{k})$, $\widetilde{\Psi}_{\beta\beta}(\mathbf{k})$, $\widetilde{\Psi}_{\alpha\beta}(\mathbf{k})$ values [1] and is not vanishing in non-ideal solid solution only.

Thus, diffuse-scattering kinetics data enable to estimate the relaxation time τ and calculate $\lambda_1(\mathbf{k})$.

3 Determination of atomic jumps in f.c.c. lattice

Value of $\lambda_1(\mathbf{k})$ is also presented in equations of random-walk problem, which, in a case of long-wave approach, turn into diffusion equations. As shown in [1], using linear approximation within the framework of the first-order kinetics model, the time dependence of Fourier transform of one-particle probability $P_\alpha(\mathbf{R},t)$ (to find, at a time t, the atom α at a site $\mathbf{R}$ of the binary solution) can represented in a form of

$$\widetilde{P}_\alpha(\mathbf{k},t) \approx \widetilde{P}_\alpha(\mathbf{k},\infty) + a_1^\alpha(\mathbf{k})e^{-\lambda_1(\mathbf{k})t}. \qquad (8)$$

The last equation is valid for the real cases of substitutional diffusion, if the diffusion coefficients of components in binary solution are considerably different ($\lambda_1(\mathbf{k}) << \lambda_2(\mathbf{k})$). In such a case, one can suppose that 'fast' atoms (of β) form a quasi-equilibrium atmosphere around 'slow' atoms (of α). Therefore, the time evolution of the α-atoms should be only considered.

Krivoglaz [5] has considered the random walk of atoms. Solution of this problem has a form, which coincides with Eq. (8). In terms of [5], a value analogous with $\lambda_1(\mathbf{k})$ represents Fourier transform (with a sign 'minus') of atomic-jumps' probability for α component into a given site **R** in a unite time. Such a problem describes the process, which takes place in a 'gas' of non-interacting atoms and is connected with phenomenon of self-diffusion. So, if, for any **k** in Brillouin zone, $\tilde{\varphi}_1(\mathbf{k}) \equiv 0$, then $-\lambda^0_1(\mathbf{k})$ is a Fourier transform of α-atom-jumps' probability per unite time over sites $\{\mathbf{R}\}$ in ideal solid solution.

As follows from Eq. (7), the same equation describes random walks of atoms in non-ideal and ideal solid solutions, if formally assume that $-\lambda_1(\mathbf{k})$ is Fourier transform of jumps' probability for α-atoms over sites $\{\mathbf{R}\}$ per unite time.

If $\{-\lambda_1(\mathbf{k})\}$ are known, one can obtain their Fourier original, $-\Lambda_\alpha(\mathbf{R})$—jumps' probability of α-atoms per unit time into the given site **R** from the all surroundings sites $\{\mathbf{R}'\}$ in a field of interaction 'potential' $\psi_\alpha(\mathbf{R}')$. We assume that 'potential' $\psi_\alpha(\mathbf{R}')$ at the site $\mathbf{R}'$ is generated, if microscopic concentration heterogeneities take place in a solid solution, for instance, because of location of α-atom at the 'zero' site. Apparently, $\Lambda_\alpha(\mathbf{R})$ for any **R** (including a 'zero' site) of the lattice is proportional to values of all $\{\psi_\alpha(\mathbf{R}')\}$. Using inverse Fourier transformation into the **R**-space [6], $\Lambda_\alpha(\mathbf{R})$ can be written as:

$$\Lambda_\alpha(\mathbf{R}) \cong \sum\nolimits_{\mathbf{R}'} \Lambda^0_\alpha(\mathbf{R}-\mathbf{R}')\psi_\alpha(\mathbf{R}')[c_\alpha(1-c_\alpha)/k_BT], \quad (9)$$

where $-\Lambda^0_\alpha(\mathbf{R}-\mathbf{R}')$—jump probability of α-atom into the site **R** from any site $\mathbf{R}'$ per unit time. At a 'zero' site of the ideal solid solution, 'potential' is $\psi_\alpha(\mathbf{0}) \approx \psi_0 \equiv k_BT/c_\alpha(1-c_\alpha)$. Value of $\Lambda_\alpha(\mathbf{R})$ is dependent on the location of sites in a crystal of a given syngony, *i.e.* on the set of possible differences $\{\mathbf{R}-\mathbf{R}'\}$ for each **R**. We will also assume that region of 'potential'-field influence is bounded. This means that values of $\psi_\alpha(\mathbf{R})$ are non-zero for some co-ordination shells only.

In case of the vacancy mechanism of diffusion, we can take into account atomic jumps only over the nearest distances between the sites. When it is necessary to test the possibility of not only vacancy diffusion mechanism, but also more complex diffusion processes, then we have to consider several sets of values $\Lambda^0_\alpha(\mathbf{R}-\mathbf{R}'_{\mathrm{I}})$, $\Lambda^0_\alpha(\mathbf{R}-\mathbf{R}'_{\mathrm{II}})$, *etc.* Indexes I, II, *etc.* relate to the jumps to the site **R** from the nearest-neighbour sites $\{\mathbf{R}'_{\mathrm{I}}\}$, next-nearest-neighbour sites $\{\mathbf{R}'_{\mathrm{II}}\}$, *etc.* (Fig. 1).

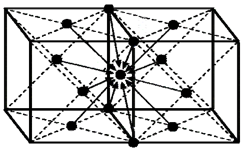

Figure 1: Atomic jumps into one of sites from nearest sites and next-nearest sites in f.c.c. lattice.

Analogous models have been considered in [6–8]. In Ref. [6], authors assumed atomic jumps within the first co-ordination shell only; in Ref. [7], scheme of studying microdiffusion has been proposed only, without estimation of diffusivities.

Let us assume that 'potential' field extends on the six co-ordination shells around the 'central' ('zero') site, and jump of α-atom is possible within the two co-ordination shells:

$$\Lambda^0_\alpha(R_{\mathrm{I}}) = \Lambda^0_{\alpha\mathrm{I}} \neq 0;\ \Lambda_\alpha(R_{\mathrm{II}}) = \Lambda^0_{\alpha\mathrm{II}} \neq 0;$$
$$\psi_\alpha(R_{\mathrm{I}}) = \psi_{\alpha\mathrm{I}} \neq 0;\ \psi_\alpha(R_{\mathrm{II}}) = \psi_{\alpha\mathrm{II}} \neq 0;$$
$$\psi_\alpha(R_{\mathrm{III}}) = \psi_{\alpha\mathrm{III}} \neq 0;\ \psi_\alpha(R_{\mathrm{IV}}) = \psi_{\alpha\mathrm{IV}} \neq 0;$$
$$\psi_\alpha(R_{\mathrm{V}}) = \psi_{\alpha\mathrm{V}} \neq 0;\ \psi_\alpha(R_{\mathrm{VI}}) = \psi_{\alpha\mathrm{VI}} \neq 0;$$

R_{I}, R_{II}, *etc.* are radii of the first, second, *etc.* co-ordination shells, respectively. If α-atom is located at the 'zero' site, other probabilities ($\Lambda^0_{\alpha\mathrm{III}}$, $\Lambda^0_{\alpha\mathrm{IV}}$, *etc.*) and 'potential' functions ($\psi_{\alpha\mathrm{VII}}$, $\psi_{\alpha\mathrm{VIII}}$, *etc.*) equal zero, then we can write the following equations with $\Lambda_\alpha(\mathbf{R}_n(lmn))$ (*lmn*—co-ordinates of sites in a usual system with basis vectors along [100], [010], [001] directions) for 8 nearest (with respect to 'zero' site) co-ordination shells only and for $\mathbf{R} = \mathbf{R}_0 = \mathbf{0}$ as well;

$$\Lambda_\alpha(\mathbf{R}_0(000)) \cong 12\Lambda^0_{\alpha\mathrm{I}}[\psi_{\alpha\mathrm{I}}/\psi_{\alpha0}] +$$
$$+ 6\Lambda^0_{\alpha\mathrm{II}}[\psi_{\alpha\mathrm{II}}/\psi_{\alpha0}] + \Lambda^0_{\alpha0},$$

$$\Lambda_\alpha(\mathbf{R}_{\mathrm{I}}(\tfrac{1}{2}\,\tfrac{1}{2}\,0)) \cong \Lambda^0_{\alpha\mathrm{I}} + 4\Lambda^0_{\alpha\mathrm{I}}[\psi_{\alpha\mathrm{I}}/\psi_{\alpha0}] +$$
$$+ 2\Lambda^0_{\alpha\mathrm{I}}[\psi_{\alpha\mathrm{II}}/\psi_{\alpha0}] + \Lambda^0_{\alpha\mathrm{I}}[\psi_{\alpha\mathrm{III}}/\psi_{\alpha0}] + 2\Lambda^0_{\alpha\mathrm{I}}[\psi_{\alpha\mathrm{II}}/\psi_{\alpha0}] +$$
$$+ 4\Lambda^0_{\alpha\mathrm{I}}[\psi_{\alpha\mathrm{IV}}/\psi_{\alpha0}] + \Lambda^0_{\alpha0}[\psi_{\alpha\mathrm{I}}/\psi_{\alpha0}],$$

$$\Lambda_\alpha(\mathbf{R}_{\mathrm{II}}(100)) \cong 4\Lambda^0_{\alpha\mathrm{I}}[\psi_{\alpha\mathrm{I}}/\psi_{\alpha0}] + \Lambda^0_{\alpha\mathrm{II}} +$$
$$+ 4\Lambda^0_{\alpha\mathrm{II}}[\psi_{\alpha\mathrm{III}}/\psi_{\alpha0}] + 4\Lambda^0_{\alpha\mathrm{I}}[\psi_{\alpha\mathrm{IV}}/\psi_{\alpha0}] +$$
$$+ \Lambda^0_{\alpha0}[\psi_{\alpha\mathrm{II}}/\psi_{\alpha0}] + \Lambda^0_{\alpha\mathrm{II}}[\psi_{\mathrm{VI}}/\psi_{\alpha0}],$$

$$\Lambda_\alpha(\mathbf{R}_{\mathrm{III}}(1\,\tfrac{1}{2}\,\tfrac{1}{2})) \cong \Lambda^0_{\alpha\mathrm{I}}[\psi_{\alpha\mathrm{II}}/\psi_{\alpha0}] + 2\Lambda^0_{\alpha\mathrm{I}}[\psi_{\alpha\mathrm{III}}/\psi_{\alpha0}] +$$
$$+ 2\Lambda^0_{\alpha\mathrm{I}}[\psi_{\alpha\mathrm{I}}/\psi_{\alpha0}] + \Lambda^0_{\alpha\mathrm{II}}[\psi_{\alpha\mathrm{I}}/\psi_{\alpha0}] + 2\Lambda^0_{\alpha\mathrm{I}}[\psi_{\alpha\mathrm{IV}}/\psi_{\alpha0}] +$$
$$+ 2\Lambda^0_{\alpha\mathrm{II}}[\psi_{\alpha\mathrm{IV}}/\psi_{\alpha0}] + \Lambda^0_{\alpha\mathrm{I}}[\psi_{\alpha\mathrm{V}}/\psi_{\alpha0}] + \Lambda^0_{\alpha0}[\psi_{\alpha\mathrm{IV}}/\psi_{\alpha0}],$$

$$\Lambda_\alpha(\mathbf{R}_{\mathrm{IV}}(110)) \cong \Lambda^0_{\alpha\mathrm{I}}[\psi_{\alpha\mathrm{I}}/\psi_{\alpha0}] + 2\Lambda^0_{\alpha\mathrm{II}}[\psi_{\alpha\mathrm{II}}/\psi_{\alpha0}] +$$
$$+ 4\Lambda^0_{\alpha\mathrm{I}}[\psi_{\alpha\mathrm{IV}}/\psi_{\alpha0}] + 2\Lambda^0_{\alpha\mathrm{II}}[\psi_{\alpha\mathrm{V}}/\psi_{\alpha0}] + \Lambda^0_{\alpha0}[\psi_{\alpha\mathrm{III}}/\psi_{\alpha0}],$$

$$\Lambda_\alpha(\mathbf{R}_{\mathrm{V}}(1\tfrac{1}{2}\,\tfrac{1}{2}\,0)) \cong \Lambda^0_{\alpha\mathrm{I}}[\psi_{\alpha\mathrm{II}}/\psi_{\alpha0}] + \Lambda^0_{\alpha\mathrm{I}}[\psi_{\alpha\mathrm{III}}/\psi_{\alpha0}] +$$
$$+ \Lambda^0_{\alpha\mathrm{II}}[\psi_{\alpha\mathrm{I}}/\psi_{\alpha0}] + \Lambda^0_{\alpha\mathrm{I}}[\psi_{\alpha\mathrm{IV}}/\psi_{\alpha0}] + \Lambda^0_{\alpha\mathrm{I}}[\psi_{\alpha\mathrm{VI}}/\psi_{\alpha0}],$$

$$\Lambda_\alpha(\mathbf{R}_{\mathrm{VI}}(111)) \cong 3\Lambda^0_{\alpha\mathrm{II}}[\psi_{\alpha\mathrm{III}}/\psi_{\alpha0}] +$$

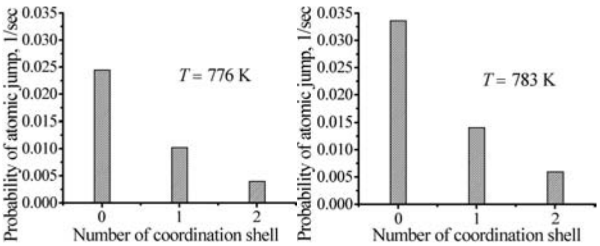

Figure 2: Jumps' probabilities for α-atoms within the two co-ordination shells (numbered by n = 0, 1, 2) per unite time, $-\Lambda^0_\alpha(R_n)$, in 'ideal' f.c.c.-$Ni_{0.765}Fe_{0.235}$-type solution.

$$+3\Lambda^0_{\alpha\mathrm{I}}[\psi_{\alpha\mathrm{IV}}/\psi_{\alpha0}]+\Lambda^0_{\alpha0}[\psi_{\alpha\mathrm{V}}/\psi_{\alpha0}],$$

$$\Lambda_\alpha(\mathbf{R}_{\mathrm{VII}}(1\tfrac{1}{2}\,1\,\tfrac{1}{2}))\cong\Lambda^0_{\alpha\mathrm{I}}[\psi_{\alpha\mathrm{III}}/\psi_{\alpha0}]+\Lambda^0_{\alpha\mathrm{I}}[\psi_{\alpha\mathrm{IV}}/\psi_{\alpha0}]+$$

$$+\Lambda^0_{\alpha\mathrm{II}}[\psi_{\alpha\mathrm{IV}}/\psi_{\alpha0}]+\Lambda^0_{\alpha\mathrm{I}}[\psi_{\alpha\mathrm{V}}/\psi_{\alpha0}],$$

$$\Lambda_\alpha(\mathbf{R}_{\mathrm{VIII}}(200))\cong\Lambda^0_{\alpha\mathrm{I}}[\psi_{\alpha\mathrm{VI}}/\psi_{\alpha0}]+\Lambda^0_{\alpha\mathrm{II}}[\psi_{\alpha\mathrm{II}}/\psi_{\alpha0}];$$

here $-\Lambda^0_{\alpha0}$—probability of α-atom to stay *in situ* (at a given site) per unite time, $\psi_{\alpha0}$—'potential' function at the 'zero' site. Values of $\Lambda_\alpha(\mathbf{R}_n(lmn))$ are obtained for disordered f.c.c.-$^{62}Ni_{0.765}Fe_{0.235}$ solution from inverse Fourier transformation using experimental data [3] by the estimated values of $\lambda_1(\mathbf{k})$ on a basis of kinetic model (6). Fourier original of probability to jump into the site **R** of a cubic lattice is as follows:

$$\Lambda_\alpha(\mathbf{R})=K(lmn)\times$$
$$\times\sum_{h_1h_2h_3}\lambda_1(h_1h_2h_3)\cos(2\pi h_1 l)\cos(2\pi h_2 m)\cos(2\pi h_3 n),$$

where K—geometrical coefficient, which is dependent on the co-ordinates of vector $\mathbf{R}(lmn)$.

Jumps' probabilities of 'slow' α-atoms (*i.e.* conditionally 'slow' Fe atoms within the 'coat' of 'fast' Ni atoms [9]) within the first two co-ordination shells in 'ideal' $Ni_{0.765}Fe_{0.235}$-type alloy for temperatures 776 K and 783 K are presented in Fig. 2. The first column in both figures means a probability (per unite time) of 'slow' atom to stay *in situ* at a given site. Magnitude of this probability (≈ 0.024 sec^{-1} and 0.033 sec^{-1} for 776 K and 783 K, respectively), just as two another probabilities for the first and second co-ordination shells, is, for example, smaller than for f.c.c.-Ni–Mo (≈ 0.6 sec^{-1} [8]).

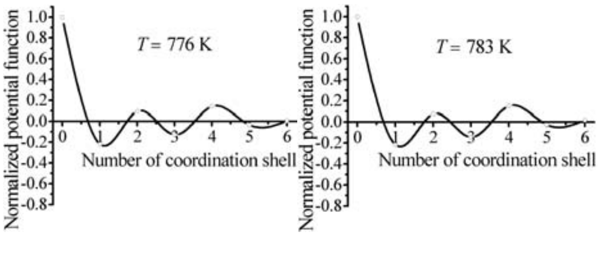

Figure 3: Normalized values of 'potential' functions, $\psi_\alpha(R_n)/\psi_{\alpha0}$ (produced by the α-atom at the 'zero' site) at different co-ordination shells (n = I, …, VI) in f.c.c.-$^{62}Ni_{0.765}Fe_{0.235}$ for two temperatures.

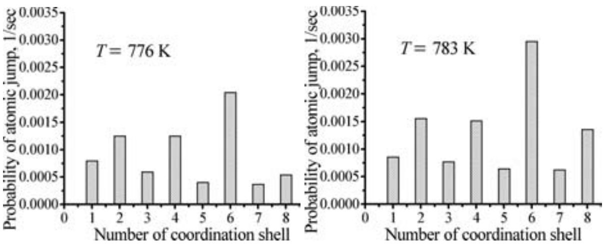

Figure 4: Jumps' probabilities of α-atoms into the site $\mathbf{R}_n$ per unite time, $-\Lambda_\alpha(R_n)$ (n—number of co-ordination shell), in non-ideal disordered f.c.c.-$^{62}Ni_{0.765}Fe_{0.235}$.

Caused by microscopic heterogeneity, 'potential' function of R_n (Fig. 3) determines the atomic jumps (Fig. 4) during short-range order relaxation. It has oscillating character, and its absolute value decreases as a whole with increasing distance from the concentration heterogeneity at the 'zero' site (Fig. 3).

4 Calculation of diffusivities

Atomic-jumps' probabilities enable to calculate macroscopic diffusion characteristics, *i.e.* diffusion and self-diffusion coefficients of 'slow' α-atoms.

Equation (7) is analogue to the Darken formula:

$$D_\alpha=D^*_\alpha[1+(d\ln\gamma_\alpha)/(d\ln c_\alpha)]; \qquad (10)$$

here D_α, D^*_α, γ_α—diffusion, self-diffusion and activity coefficients, respectively, for α-atoms. So realising long-wave limit transition from discrete to continual process and comparing Eq. (7) with Eq. (10), we obtain the following relationship between the diffusion micro- and macroparameters:

$$\lambda_1(\mathbf{k})\approx D_\alpha|\mathbf{k}^2|,\ \lambda^0_1(\mathbf{k})\approx D^*_\alpha|\mathbf{k}^2|,\ \tilde{\varphi}_\alpha(\mathbf{k})\cong\frac{d\ln\gamma_\alpha}{d\ln c_\alpha} \quad (11)$$

(for $\mathbf{k}\to\mathbf{0}$) neglecting Kirkendall effect, at least. By definition, value $\lambda_1(\mathbf{k})$ is connected with jumps' probability $-\Lambda_\alpha(\mathbf{R}_n)$ of α-atoms per unit time:

$$\lambda_1(\mathbf{k})=-\sum_{n=\mathrm{I}}^{\infty}\sum_{\mathbf{R}_n}\Lambda_\alpha(\mathbf{R}_n)[1-\exp(-i\mathbf{k}\cdot\mathbf{R}_n)]. \quad (12)$$

For $\mathbf{k}\to\mathbf{0}$, expanding $\exp(-i\mathbf{k}\cdot\mathbf{R}_n)$ in a series and retaining first nonzero terms ($\lambda_1(\mathbf{0})=0$), we obtain [1]:

$$\lambda_1(\mathbf{k})\approx-(1/6)\sum_{n=\mathrm{I}}^{\infty}\Lambda_\alpha(R_n)R_n^2Z_n|\mathbf{k}|^2, \quad (13)$$

Z_n—co-ordination number for a n-th co-ordination shell. Comparison of Eq. (13) with (11) yields formula for diffusivity in non-ideal cubic solution:

Table 1: Vacancy-controlled diffusion (D_{Fe}), self-diffusion (D^{*}_{Fe}), and interdiffusion (D) coefficients for $^{62}\mathrm{Ni}_{0.765}\mathrm{Fe}_{0.235}$.

T, K	D_{Fe}, cm^2/sec	D^{*}_{Fe}, cm^2/sec	D, cm^2/sec [3]
776	$4.49\cdot10^{-17}$	$1.81\cdot10^{-17}$	$2.49\cdot10^{-18}$
783	$6.90\cdot10^{-17}$	$2.55\cdot10^{-17}$	$3.56\cdot10^{-18}$

$$D_{\alpha} \approx -(1/6)\sum\nolimits_{\mathrm{n=I}}^{\infty}\Lambda_{\alpha}(R_{\mathrm{n}})R_{\mathrm{n}}^{2}Z_{\mathrm{n}}. \qquad (14)$$

Similarly, for ideal solid solution,

$$D^{*}_{\alpha} \approx -(1/6)\sum\nolimits_{\mathrm{n=I}}^{\infty}\Lambda^{0}_{\alpha}(R_{\mathrm{n}})R_{\mathrm{n}}^{2}Z_{\mathrm{n}}. \qquad (15)$$

In a given model, we assume that atomic jumps into the sites within the same co-ordination shell (with respect to the 'zero' site) are equiprobable.

Diffusion and self-diffusion coefficients of Fe atoms in f.c.c.-$^{62}\mathrm{Ni}_{0.765}\mathrm{Fe}_{0.235}$ solution calculated from Eqs. (14), (15) are listed in Table 1. In the last column, interdiffusion coefficients extrapolated from the high-temperature measurements [3] are presented too. Total activation energies of vacancy-mediated diffusion and self-diffusion of Fe atoms are also calculated: 2.13 and 3.47 eV, respectively.

Now let us consider the case of exchange mechanism governing the diffusion in $\mathrm{Ni}_3\mathrm{Fe}$ alloy (which is similar by the composition to $\mathrm{Ni}_{0.765}\mathrm{Fe}_{0.235}$ solid solution) at temperatures below the temperature of order–disorder phase transformation. Atomic distribution function in this ordering alloy can be represented as a superposition of the static concentration waves (SCW) [1]. Using SCW approach along with self-consistent-field approximation, one can consider the differential kinetic equation for relaxation of long-range order parameter η [1] of $L1_2$-type $\mathrm{Ni}_3\mathrm{Fe}$:

$$\frac{d\eta}{dt} = \frac{3\widetilde{L}_{\alpha\alpha}(\mathbf{k}_X)}{16}\left[\frac{\eta\widetilde{w}(\mathbf{k}_X)}{k_BT} + \ln\frac{(1+3\eta)(3+\eta)}{3(1-\eta)^2}\right]. \quad (16)$$

In the last equation, $\mathbf{k}_X = (100)$—wave vector (in a first Brillouin zone of f.c.c. lattice), which generates the $L1_2$-type superstructure, $\widetilde{L}_{\alpha\alpha}(\mathbf{k}_X)$—Fourier transform of Önsager kinetic coefficients, $\widetilde{w}(\mathbf{k}_X)$—Fourier component of pairwise-interaction 'mixing' energy between Ni and Fe atoms; magnitudes of $\widetilde{w}(\mathbf{k}_X)$ for $\mathrm{Ni}_3\mathrm{Fe}$ alloy with different temperatures were estimated in [7]. An implicit solution $t = t(\eta)$ of Eq. (16) is given by the following equation:

$$\int\limits_{\eta_0}^{\eta} d\eta\left[\frac{\eta\widetilde{w}(\mathbf{k}_X)}{k_BT} + \ln\frac{(1+3\eta)(3+\eta)}{3(1-\eta)^2}\right]^{-1} = \frac{3\widetilde{L}_{\alpha\alpha}(\mathbf{k}_X)t}{16}, \quad (17)$$

where η_0—initial magnitude of the long-range order parameter (at $t = 0$). Assuming atomic jumps between nearest-neighbour sites only and using condition that the total number of atoms in a system is conserved, for f.c.c. lattice, we can write

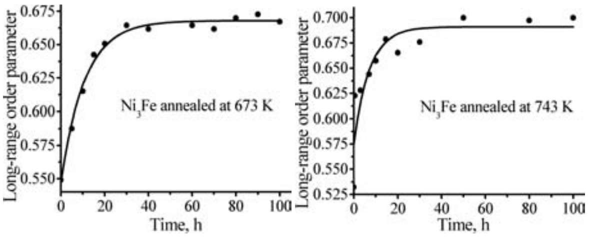

Figure 5: Time dependence of long-range order parameter in $L1_2$-type $\mathrm{Ni}_3\mathrm{Fe}$ alloy; ●—experimental data [4].

$$\widetilde{L}_{\alpha\alpha}(\mathbf{k}) \approx -4L_{\alpha\alpha}(R_{\mathrm{I}})[3 - \cos\pi h_1\cdot\cos\pi h_2 - \\ -\cos\pi h_2\cdot\cos\pi h_3 - \cos\pi h_3\cdot\cos\pi h_1], \qquad (18)$$

where $L_{\alpha\alpha}(R_{\mathrm{I}})$ is proportional to the jump probability of a pair of atoms at nearest-neighbour sites $\mathbf{R}$ and $\mathbf{R}'$ per unite time ($R_{\mathrm{I}} = |\mathbf{R} - \mathbf{R}'|$). Using experimental data [4] (Fig. 5) and Eqs. (17), (18), we obtain roughly averaged values: $\langle L_{\alpha\alpha}(R_{\mathrm{I}})\rangle \approx 4\cdot10^{-8}$ sec^{-1} for $T = 673$ K and $\langle L_{\alpha\alpha}(R_{\mathrm{I}})\rangle \approx 7\cdot10^{-8}$ sec^{-1} for $T = 743$ K. Substituting $L_{\alpha\alpha}(R_{\mathrm{I}})$ instead of $-\Lambda^{0}_{\alpha}(R_{\mathrm{n}})$ in equation similar to Eq. (15), exchange diffusive mobilities of 'slow' Fe atoms in $L1_2$-type $\mathrm{Ni}_3\mathrm{Fe}$ alloy may be coarsely estimated by averaging data of Table 2 over annealing times: $\langle D^{0}_{\mathrm{Fe}}\rangle \approx 1.03\cdot10^{-22}$ cm^2/sec for $T = 673$ K and $\langle D^{0}_{\mathrm{Fe}}\rangle \approx 1.78\cdot10^{-22}$ cm^2/sec for $T = 743$ K. Accordingly estimated diffusion migration energy of Fe atoms is 0.34 eV.

5 Discussion of results and conclusions

Obtained microparameters of diffusion, $-\Lambda^{0}_{\alpha}(R_{\mathrm{n}})$ and $-\Lambda_{\alpha}(R_{\mathrm{n}})$, are estimated on the basis of available experimental data about diffuse-scattering kinetics, which is caused by the short-range order relaxation in the solid solution. Thus, obtained 'microdiffusivities' determine the short-range order changes and give information about their kinetics.

For 'ideal' f.c.c.-$\mathrm{Ni}_{0.765}\mathrm{Fe}_{0.235}$-type solid solution, probability of atomic jumps into a given site $\mathbf{R}$ of the nearest-neighbour shell around a 'zero'-site heterogeneity is less than $-\Lambda_{\alpha}(\mathbf{0})/2$, and of the next-nearest-neighbour sites—considerably less than $-\Lambda_{\alpha}(\mathbf{0})/2$ (Fig. 2). This stands for the predominance of atomic

Table 2: Exchange diffusive mobilities in $L1_2$-type $\mathrm{Ni}_3\mathrm{Fe}$ alloy for different annealing times and temperatures.

	$T = 673$ K	$T = 743$ K
t, h	D^{0}_{Fe}, cm^2/sec	D^{0}_{Fe}, cm^2/sec
100	$8.99\cdot10^{-23}$	$1.26\cdot10^{-22}$
90	$1.04\cdot10^{-22}$	$1.55\cdot10^{-22}$
80	$1.15\cdot10^{-22}$	$2.52\cdot10^{-22}$

jumps within the first co-ordination shell that is mainly governed by the vacancy mechanism of diffusion within the commonly accepted interpretation.

Dependence of normalized 'potential' function on a radius of co-ordination shell, R_n, is non-monotone (Fig. 3). For some R_n, function value is positive, for another one—negative. This determines thermodynamic 'disadvantage' or 'advantage' of 'slow' α-atom to stay in corresponding sites $\{\mathbf{R}_n\}$.

Probability of an α-atom jump into the site **R**, $-\Lambda_\alpha(\mathbf{R})$, in a field caused by the α-atom excess at the 'zero' site is determined by the value of this field at a site **R**. That is why the jumps' probability of α-atoms into the site **R** is non-monotone (Fig. 4): it is higher at sites, where arrangement of α-atom is more energy-wise preferable.

If we put Fe-atom at a cube corner of an f.c.c.-lattice conditional unit cell, then, in a presence of the short-range order of $L1_2$(Ni_3Fe)-type, Fe-atoms will try to occupy predominantly the cube corners (*viz.* sites within the II-nd, IV-th, VI-th, VIII-th co-ordination shells around a 'zero' site, which coincides with one of the cube corners), and Ni-atoms will be localized at the face centres of cubic unit cells. So, in our case, a short-range order of $L1_2$-type is characterized by the arrangement of Ni atoms at the face centres that is more energy-wise preferable for Ni. Evidently, that is why jumps' probabilities of α-atoms (Fe) into the sites $\{\mathbf{R}_{II}\}$, $\{\mathbf{R}_{IV}\}$, $\{\mathbf{R}_{VI}\}$, $\{\mathbf{R}_{VIII}\}$ (Fig. 4) are higher than jumps' probabilities into the sites $\{\mathbf{R}_{I}\}$, $\{\mathbf{R}_{III}\}$, $\{\mathbf{R}_{V}\}$, and $\{\mathbf{R}_{VII}\}$. These jumps into the sites of the II-nd, IV-th, VI-th, VIII-th co-ordination shells with respect to the cube-corner 'zero' site have to be realised mainly as nearest-distance jumps from the sites, where arrangement of α-atoms (Fe) is less energy-wise 'advantageous', that is from the sites of the I-st, III-rd, V-th, VII-th co-ordination shells with respect to the cube-corner 'zero' site. Thus, n-dependent probabilities presented in Fig. 4 do not contrary to the vacancy mechanism of diffusion in alloy at issue.

It is quite clear that, if temperature increases, all probabilities increase as well (Figs. 2, 4).

Total activation energies of diffusion and self-diffusion of 'slow' Fe atoms in disordered alloy $^{62}Ni_{0.765}Fe_{0.235}$ are 2.13 eV and 3.47 eV, respectively. Exchange-diffusion migration energy of Fe atoms in long-range ordered Ni_3Fe proves to be 0.34 eV. The first two values are higher than the third one because the latter does not involve the energy of vacancy formation; migration energy in Ni_3Fe is evaluated within the alloy model without vacancies. Vacancy formation energy in a former model is 84–90%.

Diffusive mobilities listed in Table 2 are lower than diffusivities in Table 1 because of some reasons. Firstly, because of temperature- and concentration-dependent statistical-thermodynamic factor (of $\{c_\alpha c_\gamma \tilde{\Psi}_{\gamma\beta}(\mathbf{k})/(k_B T)\}$-type; see Eqs. (3), (9)). Secondly, below the order–disorder transformation temperature, the diffusion mechanism in long-range ordering alloys may be modified, and this will affect the value of D in the direction of observed variation; in fact, the probability of exchange ('ring') mechanism of diffusion is small; it is proved by the magnitude of Önsager kinetic coefficient. Thirdly, because of temperature is decreased.

A given paper shows the possibility evaluating 'macrodiffusivities' by means of 'microdiffusivities' from the independent data on short- or long-range order kinetics. The presented scheme can be used for multicomponent systems based on f.c.c. lattice as well.

Acknowledgements

One of authors (T.R.) is grateful for the NATO Reintegration Grant support under reference RIG 981326.

References

[1] Khachaturyan, A.G.: *Theory of Structural Transformations In Solids.* John Wiley & Sons, New York, 1983.

[2] Krivoglaz, M.A.: *Diffuse Scattering of X-Rays and Neutrons—Fluctuations in Solids.* Springer, Berlin, 1996.

[3] Bley, F., Amilius, Z., Lefebvre, S. *Acta metall.*, 36, pp. 1643–1652, 1988.

[4] Goman'kov, V.I., Puzey, I.M., Rukosuev, M.N. *Ordering of atoms and its influence on properties of alloys. Metallofizika,* Vol. 20. Naukova Dumka, Kiev, 1968.

[5] Krivoglaz, M.A. *Zh. Ehksp. Teor. Fiz.*, 40, pp. 1812–1824, 1961.

[6] Naumova, M.M., Semenovskaya, S.V., Umanskiy, Ya.S. *Fiz. Tverd. Tela,* 12, pp. 975–982, 1970.

[7] Tatarenko, V.A., Radchenko, T.M. *Metallofiz. Noveishie Tekhnol.*, 24, pp. 1335–1350, 2002.

[8] Bokoch, S.M., Kulish, M.P., Tatarenko, V.A., Radchenko, T.M. *Metallofiz. Noveishie Tekhnol.*, 26, pp. 541–558, 2004.

[9] Caplain, A., Chambron, W. *Acta metall.*, 25, p. 1001, 1977.

Proceedings of The 1 st International Conference on Diffusion in Solids and Liquids
DSL-2005, July 6-8, 2005, University of Aveiro, Aveiro, Portugal

DIMENSIONAL ANALYSIS IN THE GROWTH KINETICS OF FeB AND Fe_2B LAYERS DURING THE BORIDING PROCESS

Rodrigo TORRES [1], Iván CAMPOS [1]*, Oscar BAUTISTA [1], Giselle RAMÍREZ [2], Paulina ZÚÑIGA [1]

[1] Tecnológico de Monterrey, Campus Ciudad de México. Mechanical Department. Calle del Puente 222 Col. Ejidos de Huipulco., México D.F. 14380. México.
[2] IPN-SEPI-ESIME. U.P. Adolfo López Mateos, Zacatenco. México D.F. 07738. México
* Corresponding author. Fax: (+52)(55)54832195; Email: ivan.campos@itesm.mx

Abstract

Dimensional analysis is presented as a powerful tool in the study of paste boriding. In particular, a non dimensional method is used to study the growth kinetics of the boride layers FeB and Fe_2B. Experiments were performed in AISI 1045 steel and AISI M2 steel to prove the suggested model. Samples of 1045 steel were prepared and treated using 3 – 5 mm of boron paste thickness, at temperatures of 1193, 1223 and 1273 K, for exposure times of 2, 4 and 6 h . The M2 specimens had 3 and 4 mm of boron paste thickness and, temperatures of 1223, 1253 and 1273 K for 2 and 6 h. It was found that the layers growth obeys potential laws of the form $y = \alpha x^{\beta}$, where α and β constants are a function of the material and the interface of interest. Validation of the model was made using experimental data with an average error percentage of 7.6% for Fe_2B in 1045 steel; 15.8% for FeB and 3.4% for Fe_2B in M2 steel.

Keywords: reactive diffusion; dimensional analysis; growth kinetics; paste boriding process; boride layers

1 Introduction

Dimensional analysis is a method that reduces the number and complexity of experimental variables affecting a physical problem, by using compacting techniques Ref. [1]. If a phenomenon depends on *n* dimensional variables, dimensional analysis can reduce the problem to only *k* dimensionless variables, where the subtraction *n* – *k* = *1, 2, 3,* or *4* depends only on the process complexity. Generally, n – k is equivalent to the number of fundamental dimensions that govern the problem. One of the most important benefits of dimensional analysis is the generation of a model, based on scaling laws, that groups every experimental aspect used during the process. In the same way, it helps to predict the behavior of physical phenomena in similar conditions, under the same experimentation range Ref. [2].

There are different methods to reduce the number of variables into a lower number of dimensionless groups; Buckingham Pi Theorem is one of the most applied. The fundamentals of the theorem are based on the creation of groups of variables in a power product form. Essentially, these are dimensionless variables (Π_1, Π_2, Π_3, etc.), that represent the most important parameters of the process. In this way, a lower number of experiments are assured, as well as the optimization and automation of the physical phenomena. During this study, dimensional analysis was applied to the paste boriding process. Via this surface hardening technique, boron atoms are diffused into the surface of several types of ferrous and non-ferrous alloys. Thus, the formation of iron borides causes an increment of engineering components exposed to corrosion and wear Ref. [3, 4].

Inside the paste boriding process, there are three important parameters to be controlled: time, temperature and the boron potential that surrounds the material surface. Boron potential is closely related to the paste amount that covers the steel sample; as paste thickness increases, boron diffusion velocity is greater over the formed phases in the surface. Likewise, boride growth kinetics increases, while the activation energy required for transport phenomena to occur is reduced Ref. [5]. In contrast, boron potentials involved in the process can create two characteristic phases at the surface: Fe_2B, body-centered lattice structure, convenient for industrial applications; and the outermost phase, FeB, with an orthorhombic crystalline structure, which is not desired in engineering components, due to its high fragility Ref. [3-5]. Also, these phases are formed according to the present alloying elements in the material. It is more likely to have Fe_2B growth in low carbon and low alloy steels, with a columnar morphology. In contrast, fronts of flat growth of a bi-phase FeB/Fe_2B are formed when the substrate has an increment in carbon and alloying elements such as: molybdenum, tungsten, vanadium and chromium Ref. [6].

This study considers the most important variables in the paste boriding process; such as, boron paste thickness, treatment time, iron boride layer thickness, growth constant, and boron concentration at the substrate surface and at the FeB/Fe_2B interface. The purpose is to group these variables in a dimensionless form to generate a tentative model containing the experiments carried out at work temperatures. The validity of the model is done in AISI 1045 and M2 steels, (under different experimental conditions) where the main influence is given by the boron paste thickness.

2 Model

The objective in dimensional analysis is to reduce the mass diffusion problem into a function that depends only on a single independent variable. Reducing the number of independent variables, the experimental process can be optimized. This method not only reduces the number of experiments, but also demonstrates which parameters are the simplest to modify.

2.1 Assumptions

- It has been considered that the growth of borided phases in the paste boriding process is a function of: the initial amount of boron paste h_o, growth constant k, the treatment time T, the boron concentration at the surface C_s, and the concentration in present interphases C_o.
- The growth of iron boride layers obeys a potential law, in the form of $y = \alpha x^{\beta}$, where α and β are constants that depend on the process parameters.
- The phase growth is unidirectional.

2.2 Non-dimensional method

The independent and dependent parameter units are defined as: u $[L]$ indicating average thickness of layer FeB and Fe_2B; t $[T]$ corresponding to treatment time; h_o $[L]$ equivalent to an initial amount of boron paste at the substrate surface; growth constant defined as k $[L^cT^1]$; and C_s and C_o with units of the form $[ML^{-3}]$ are described as the boron concentration at the material surface and in present interphases. Dimensionless numbers are found through the classical method application of a dimensionless solution, as proposed in Ref. [1].

For the first dimensionless parameter (Π_1), the terms h_o, t, C_s and u are grouped, resulting in the following expression:

$$L^X T^Y \left(ML^{-3}\right)^Z L = M^0 L^0 T^0 \tag{1}$$

where $x = -1$, $y = 0$, $z = 0$. Finally, according to (1), the dimensionless parameter Π_1 is defined as:

$$\Pi_1 = \frac{u}{h_o} \tag{2}$$

Π_2 groups h_o, k, t, C_s in the form:

$$L^X T^Y \left(ML^{-3}\right)^Z \left(L^c T^{-1}\right) = M^0 L^0 T^0 \tag{3}$$

$x = -C$, $y = 1$, $z = 0$. Under these circumstances, Π_2 results in:

$$\Pi_2 = \frac{kt}{h_o{}^c} \tag{4}$$

where c is the inverse of the proposed exponent. Lastly, the dimensionless parameter Π_3, considers the variables ho, t, C_s and C_o :

$$L^X T^Y \left(ML^{-3}\right)^Z \left(ML^{-3}\right) = M^0 L^0 T^0 \tag{5}$$

where $x = 0$, $y = 0$, $z = -1$. Equation (5) is then expressed as:

$$\Pi_3 = \frac{C_s}{C_o} \tag{6}$$

The relationship of interest is the iron boride layer thickness as a function of dependent parameters, so:

$$\Pi_1 = f\left(\Pi_2, \Pi_3\right) \tag{7}$$

$$\frac{u}{h_o} = f\left(\frac{kt}{h_o{}^c}, \frac{C_s}{C_o}\right) \tag{8}$$

It is assumed that boron concentration on the surface and interfaces remain constant during the treatment.

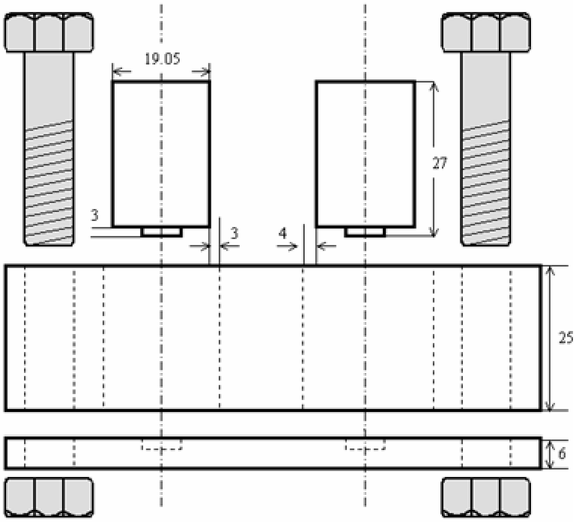

Figure 1: Scheme of covering process with boron paste at the metal surface. Scale in mm.

3 Experimental procedure

Samples of M2 steel were machined and recrystallized for 1 h at 923K. Afterwards, the samples were placed in acrylic molds (Fig.1), in order to control boron paste thickness. The water/paste ratio was 0.2. To eliminate water residues on paste, samples were put in a conventional furnace for 20 minutes at 373 K. Boriding in 1045 steel was done at 1193, 1223 and 1273 K. Different treatment times were used: 2, 4, and 6 h, modifying boron potentials in a range of 3, 4 and 5 mm of boron paste. For M2 steel, treatment was carried out at temperatures of 1223, 1253 and 1273 K, and exposure times of 2 and 6 h for each temperature. Under these different conditions, samples of 3 and 4 mm of boron paste thicknesses were treated under a pure argon atmosphere. After the treatment, the pieces were quenched in oil and cross-sectioned by electrical discharge machining, Roboform 20A. After the metallographic preparation, the thickness of the boride layers was measured by means of optical microscopy (in each sample, a minimum of 25 measurements were done at different points of the layer). Then, obtained images were analyzed with MSQ PLUS software for the phase identification in the sample surface.

4 Results and discussions

The growth of iron borides obeys a controlled diffusion process in the form of $y = \alpha x^{\beta}$, where β represents the major adjustment in experimental data used within the process. Using the parabolic growth hypothesis, β exponents for FeB and Fe_2B phases are 0.7 and 0.53, respectively, in M2 steel. For Fe_2B the dispersion was 0.99 and 0.96 for FeB. To improve the data dispersion, the FeB growth was adjusted only to potential functions, with 0.7 as an exponential of growth. The previous modification was done using a generalized parameter of dimensionless growth $\frac{kt}{h_o^{\,c}}$, where c is the inverse of the proposed exponent. It was found that the dimensionless growth adjusted to a β exponent worth 0.799, with a dispersion value of 0.986. A subsequent iteration was performed fitting the FeB phase growth to 0.8, resulting in a dimensionless growth exponent of 0.83 with a data dispersion of 0.99.

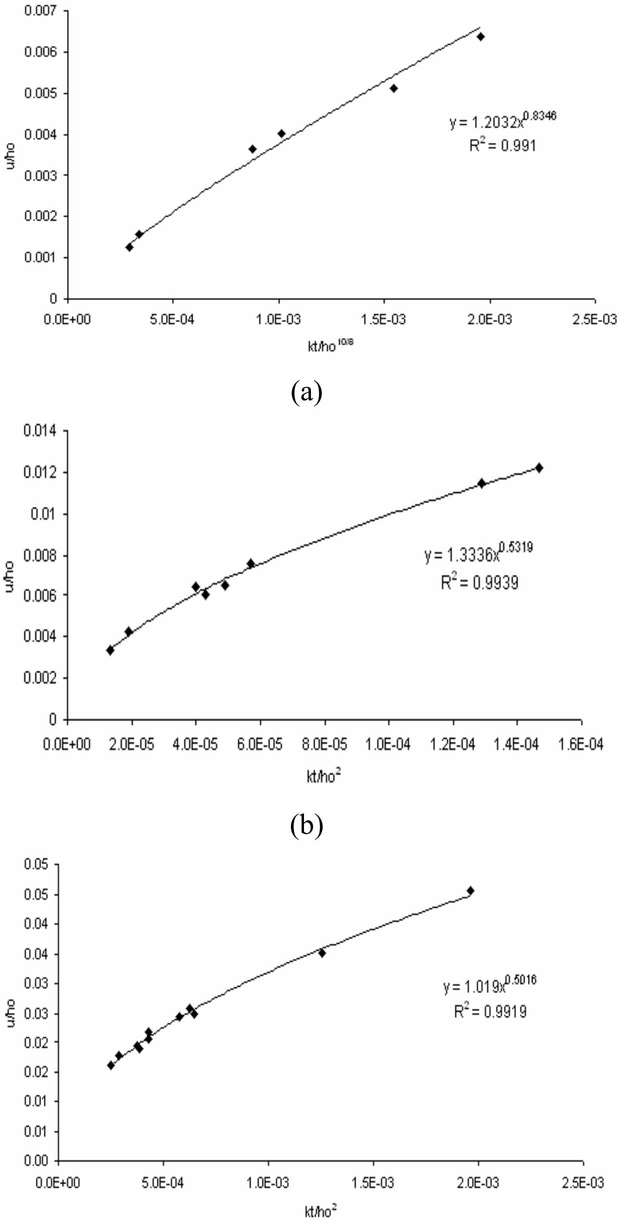

(a)

(b)

(c)

Figure 2: Dimensionless growth of iron boride layers on M2 steel (a) FeB, (b) Fe_2B. 1045 steel reflects a Fe_2B phase growth on (c).

The dimensionless growth for the Fe_2B phase in 1045 steel adjusted the experimental data with a β value equal to 0.50 with a 0.99 dispersion. Figure 2 presents the obtained curves for M2 and 1045 steel, with the dimensionless variable group shown in Eq. (8). These data represent the experiment set done with 3 and 4 mm of boron paste thickness, for both steels below 6 h of treatment. Fe_2B and FeB phases in M2 steel showed a preferential growth, but only Fe_2B showed a preferential growth in 1045 steel. This proves the influence of alloying elements in steel such as chromium, molybdenum, vanadium and high contents of carbon, within the formation of the FeB phase in the substrate Ref. [7].

However, the morphology of the formed layers in M2 steel (dependent of alloying elements) is less saw-toothed and more compact against the morphology of Fe_2B in 1045 steel (Fig.3). The dimensionless parameter $\frac{kt}{{h_o}^c}$, used in graphics of Fig. 2, is below the dimensionless values to the unit. By maintaining α constant along the used values, the curve $y = \alpha x^{\beta}$ grows in a slower way when β parameter increases, inverting this kinetics for greater values than the unit. With the proposed experiments for the M2 steel, the dimensionless potential growth reflects, on the β exponent, a slower dynamic growth of the FeB phase, compared with the Fe_2B phase. Also, the Fe_2B phase growth for both steels indicates a controlled and preferential growth, according to the β values obtained in the experimental data adjustment.

The resulting expressions for M2 steel, according to the dimensional analysis are:

$$\frac{u_{FeB}}{h_o} = 1.2032\left(\frac{kt}{{h_o}^{10/8}}\right)^{0.8346} \tag{9}$$

$$\frac{u_{Fe_2B}}{h_o} = 1.3336\left(\frac{kt}{{h_o}^{2}}\right)^{0.5319} \tag{10}$$

For Fe_2B phase growth in 1045 steel, the equation results into:

$$\frac{u_{Fe_2B}}{h_o} = 1.019\left(\frac{kt}{{h_o}^{2}}\right)^{0.5016} \tag{11}$$

Comparing (10) and (11), for dimensionless growths of Fe_2B phase in both steels, it is evident that the process is much faster in 1045 steel. As presented by Carbucicchio et al. Ref. [8], the alloying elements, i.e. Mo, V, Cr, contained in M2 steel, are introduced in a substitutional manner, and tend to concentrate in the serration limit of the boride layer. As a consequence, the active boron flux is reduced in this zone and the columnarity of the generated fronts is lowered in the Fe_2B/substrate interface. The same phenomenon is presented in the FeB/Fe_2B interface.

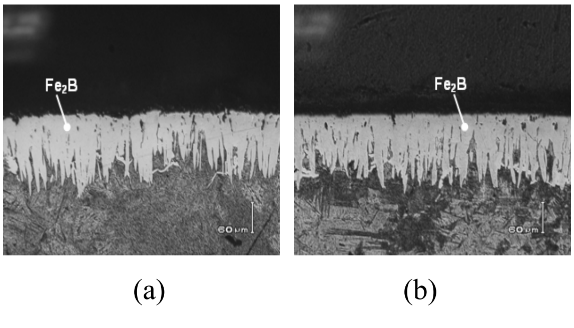

(a) (b)

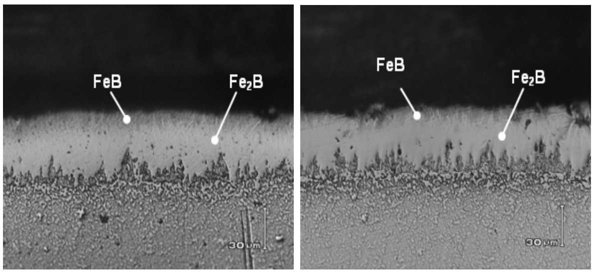

(c) (d)

Figure 3: Cross-sectional view of paste borided samples on AISI M2 and AISI 1045 steel at 1273 K with 6 h of treatment. (a) and (b) for 1045 steel with boron potentials of 3 and 4 mm of paste thickness; (c) and (d) for M2 steel under the same boron paste thicknesses.

The influence of temperature is also studied with dimensional analysis and is presented in Fig. 4. The growth kinetics shown in dimensionless parameter β, establishes that between temperatures of 1223 and 1253 K, the kinetics is greater than in extreme temperatures of 1193 K for 1045 steel and 1223 for M2 steel, as well as for 1273 K in both steels. This could indicate an optimal process temperature, where the growth kinetics of the borided phases has its maximum value. Likewise, when work temperature increases, β value converges into values equivalent to 0.5.

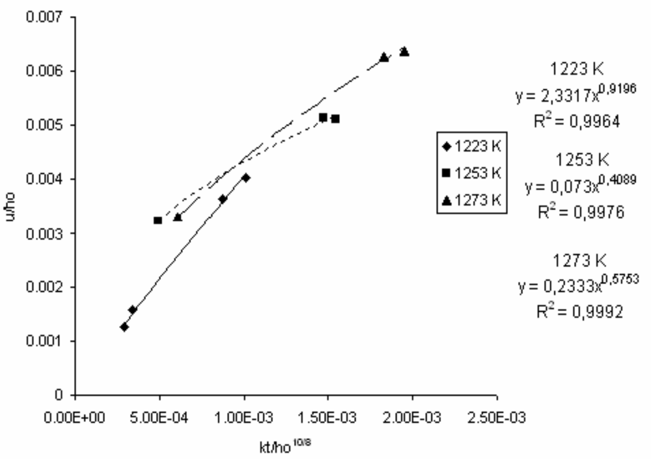

(a)

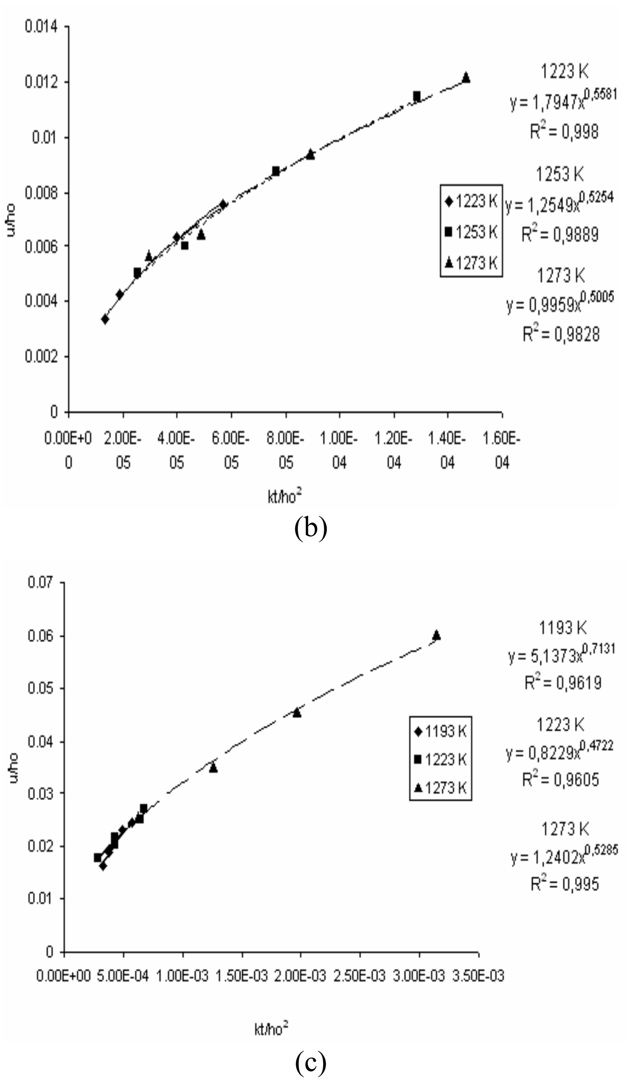

(b)

(c)

Figure 4: Temperature influence on β dimensionless parameter for borided phases growth. M2 steel (a) FeB , (b) Fe_2B. 1045 steel (c) Fe_2B.

The validity of the dimensionless model was done with experimental data, using a work temperature range of $1223K \leq T \leq 1273K$, which was not used for the initial adjustment of the model. Table 1 shows the error percentage obtained in the model, according to the growth data of FeB and Fe_2B for both steels. The average error of FeB phase in M2 steel is approximately of 16%, and it is lower than 10% for Fe_2B phase in both steels.

5 Conclusions

The following conclusions were established:

a) The use of dimensional analysis reduces the mass diffusion problem into a function than depends only on an independent variable. The reduction of independent variables optimises the experimental procedure, minimizing the number of tests, in addition to the indication of the modified parameters.

b) The regression of the dimensionless variables showed that the dimensionless growths of the FeB and Fe_2B layers follow potential laws within the form $y = \alpha x^{\beta}$, where constants α,β are a function of the substrate, and the generated layers at the material surface.

c) Dimensionless value β reflects a slower growth kinetics than FeB phase in M2 steel; in the case of Fe_2B phase, dimensionless growth kinetics is faster in 1045 steel than in M2 steel. This is due to alloying elements in this last steel, which slows the phase growth, creating less columnar coverings.

d) Dimensional analysis showed that boride phase growth, does not necessarily follow a parabolic growth, because dimensionless growth obeys potential laws, which demonstrates a minor dispersion of dimensionless points, and into an error percentage of the dimensionless model.

e) The dimensionless β parameter shows the influence of the process temperature in the borided phases growth. It is possible that the kinetics growth of the iron borides in the substrate surface might be higher in the range of $1223K \leq T \leq 1253K$.

Acknowledgements

This work has been supported by research grant no. 42883/A-1 of the *Consejo Nacional de Ciencia y Tecnologia at Mexico.* I. Campos thanks the *"Cátedra de Investigación en Materiales,"* supported by *Centro Regional de Investigacion en Materiales* of the *Sistema Tecnologico de Monterrey*. The authors wish to thank Mr. Isaac Aguilar Ventura and Mr. Jorge Hadad Bellamy for their valuable cooperation.

Table 1: Validity of dimensionless model for phases (a) FeB, (b) Fe_2B in M2 steel; (c) Fe_2B for 1045 steel

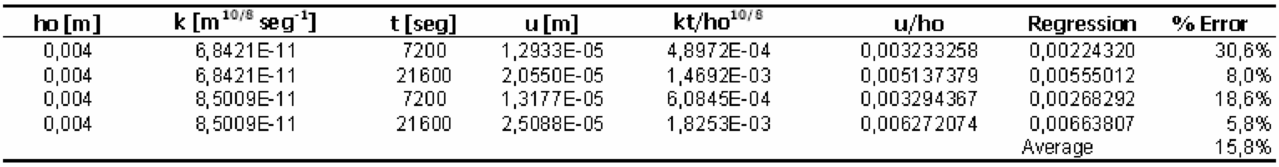

ho [m]	k [$m^{10/8}$ seg^{-1}]	t [seg]	u [m]	kt/$ho^{10/8}$	u/ho	Regression	% Error
0,004	6,8421E-11	7200	1,2933E-05	4,8972E-04	0,003233258	0,00224320	30,6%
0,004	6,8421E-11	21600	2,0550E-05	1,4692E-03	0,005137379	0,00555012	8,0%
0,004	8,5009E-11	7200	1,3177E-05	6,0845E-04	0,003294367	0,00268292	18,6%
0,004	8,5009E-11	21600	2,5088E-05	1,8253E-03	0,006272074	0,00663807	5,8%
						Average	15,8%

(a)

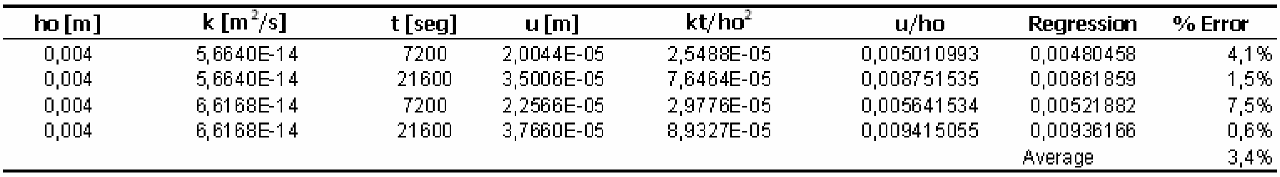

ho [m]	k [m^2/s]	t [seg]	u [m]	kt/ho^2	u/ho	Regression	% Error
0,004	5,6640E-14	7200	2,0044E-05	2,5488E-05	0,005010993	0,00480458	4,1%
0,004	5,6640E-14	21600	3,5006E-05	7,6464E-05	0,008751535	0,00861859	1,5%
0,004	6,6168E-14	7200	2,2566E-05	2,9776E-05	0,005641534	0,00521882	7,5%
0,004	6,6168E-14	21600	3,7660E-05	8,9327E-05	0,009415055	0,00936166	0,6%
						Average	3,4%

(b)

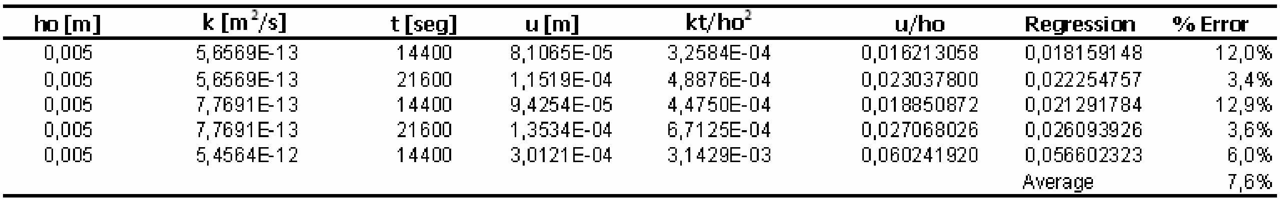

ho [m]	k [m^2/s]	t [seg]	u [m]	kt/ho^2	u/ho	Regression	% Error
0,005	5,6569E-13	14400	8,1065E-05	3,2584E-04	0,016213058	0,018159148	12,0%
0,005	5,6569E-13	21600	1,1519E-04	4,8876E-04	0,023037800	0,022254757	3,4%
0,005	7,7691E-13	14400	9,4254E-05	4,4750E-04	0,018850872	0,021291784	12,9%
0,005	7,7691E-13	21600	1,3534E-04	6,7125E-04	0,027068026	0,026093926	3,6%
0,005	5,4564E-12	14400	3,0121E-04	3,1429E-03	0,060241920	0,056602323	6,0%
						Average	7,6%

(c)

References

[1] Barenblatt, G. I.: *Scaling, self.similarity, and intermediate asymptotics, Cambridge Texts in Applied Mathematics*, 2002.

[2] Barabási, A. L., Stanley H. E.: *Fractal Concepts in surface growth, Cambridge University Press*, 1995.

[3] Graf von Matuschka, A., *Boronising*, (1980), Carl Hanser Verlag, Munich, FRG.

[4] Sinha A.K.: *Boronizing, ASM Handbook*, OH, USA, J. Heat Treat. 4 (1991) 437.

[5] Campos, I., Bautista, O., Ramírez, G., Islas, M., De la Parra, J., Zúñiga, L., *App. Surf. Sci*. 243 (2005) 429-436.

[6] Chatterjee-Fischer, R. and Schaaber, O., *Proceedings of Heat Treatment '76, The Metals Society, 1976, p. 27-30.*

[7] Kunst, H., Schaaber O.: *HTM 22* (1967) 4, 275-292.

[8] Carbucicchio, M., Palombarini, G.: *Mater J.. Sci. Lett.* 6 (1987) 1147-1149.

Proceedings of The 1st International Conference on **D**iffusion in **S**olids and **L**iquids
DSL-2005, July 6-8, 2005, University of Aveiro, Aveiro, Portugal

COUPLED MICROSTRUCTURAL OBSERVATIONS AND LOCAL TEXTURE MEASUREMENTS WITH AN AUTOMATED CRYSTALLOGRAPHIC ORIENTATION MAPPING TOOL ATTACHED TO A TEM

Edgar F. RAUCH[1,*], Muriel VERON[2]

[1]Laboratoire GPM2 - ENSPG, BP 46 38402 Saint Martin d'Hères, France
[2]LTPCM/ENSEEG, Domaine Universitaire, BP75 38402, Saint Martin d'Heres, France

[*]Corresponding author. Fax: +33 4 76 82 63 82; Email: edgar.rauch@inpg.fr

Abstract

The development of an automated crystal orientation mapping tool attached to a transmission electron microscope is described. The electron beam displacement is controlled by a remote computer while thousands of diffraction patterns are recorded with an external CCD camera and analysed with a dedicated software. The work being mainly concerned with severely deformed metals, spot patterns rather that Kikuchi lines are considered in this approach. The capabilities and the sensitivity of template matching techniques for orientation identification are stressed. To locate precisely the scanned area on TEM pictures, a pseudo-bright field image reconstruction procedure is proposed. A simple procedure to eliminated some orientation ambiguities is described.

Keywords: *TEM; Spot patterns; Electron diffraction; Pattern recognition*

1 Introduction

Transmission electron microscopy remains one of the main characterization tools to infer at a nano scale the physical processes controlling the electrical, magnetic or mechanical properties of most of the materials. Coupled with X rays or electron detectors and considering the multiple observation modes available (bright/dark fields, diffraction, high resolution, convergent beam, nano beam, etc), it offers a unique source of information on the substructure, misorientations, local chemical gradients, especially for crystalline materials. For the image or chemical aspects, the adequate accessories have reached impressive resolutions and rapidity. By contrast, for crystallographic orientations there are only very few attempts to promote fast and reliable tools to record complete orientation maps at a nano scale. It is worth recalling that it has been demonstrated in the past that the task is fully achievable on TEM [1-3]. The present paper describes the current state of the development of a hardware and software package dedicated to automated crystallographic orientation mapping. The initial objective was to analyse in details the misorientations related to severe plastic deformation. But the device is believed to have high potential fields of utilisation in all metallurgical problems that necessitate nano scale analysis.

2 Orientation identification principle

Basically, the crystallographic orientation is contained in the diffraction pattern. The latter includes Kikuchi lines and/or individual spots. Kikuchi lines are usually preferred presumably because they permit intrinsically a sub-degree orientation accuracy. They were made popular with the famous EBSD (Electron Backscattered Diffraction) attachments that are quite common on modern scanning electron microscopes. Extension for TEMs are also under development (e.g.: Morawiec and co-authors [3,4]). For studies that involve large strains, the spot patterns are preferred. Indeed, they are known to be less sensitive to the internal stresses resulting from severe plastic deformations.

The procedure necessitates (i) fast acquisitions of spot patterns and (ii) reliable orientation identification. This supposes hardware equipments and software developments that will be briefly described before discussing some particular issues of the technique.

2.1 Spot patterns acquisition

The work was performed on a JEOL 3010 TEM operating at 300 kV. The beam size is decreased down to the adequate diameter. A compromise between the beam intensity and spatial resolution must be found. Typically, beam sizes of 20 to 50 nm are used on the microscope that is equipped with a LaB_6 filament. As for EBSD attachments on SEM, the procedure requires a full control of the beam displacement and rapid capture of the diffraction patterns. Both functions are performed thanks to a remote computer equipped with a D/A board that generates a software controlled signal over four channels connected to the electron microscope shift and twist deflecting coils. As in the pionner work of Schwarzer [5], an external CCD camera is used for the acquisition. It collects the patterns at a rate of 25 frames per second through the frame grabber. The 758x486 sensor size is reduced mainly by binning to an area of interest of typically 150x150 pixels [6].

2.2 Identification through template matching

The usual way to extract the orientation from a spot pattern consists in locating the intense spots and to compare their relative positions (angle and distance from the transmitted beam) to values pre-calculated for a given material and known observation conditions. The present approach differs significantly from this scheme [6,7]. Firstly, the spot patterns for all the possible sets of Euler's angles (in the limits of the crystal symmetry) are entirely generated and stored in a database. Then, every pattern is compared to the real one through template matching and the most adequate is selected.

The degree of matching for a given template is characterised by the correlation index that writes:

$$Q(i)=\frac{\sum_{j=1}^{m}P(x_j,y_j)T_i(x_j,y_j)}{\sqrt{\sum_{j=1}^{m}P^2(x_j,y_j)}\sqrt{\sum_{j=1}^{m}T_i^2(x_j,y_j)}}$$

where the pattern is represented by the intensity function P(x,y) while every template i is given by the function $T_i(x,y)$. The highest Q value corresponds to the solution. The efficiency of the technique is due to the very limited number m of triplets (positions x and y, intensity) that compose the templates: usually around 50 dots are sufficient and therefore only 50 products are computed for every orientation. Moreover, because the values are compared for a given picture, the first part of the denominator is merely omitted in the calculation. A typical example of pattern matching is shown on Fig. 1. The recorded pattern, here for a b.c.c. material, is first numerically filtered to enhance the spot intensity and to locate the transmitted beam. Then, the correlation index is calculated for every possible orientation and the best one is selected. Finally, the solution is superimposed to the pattern on the figure.

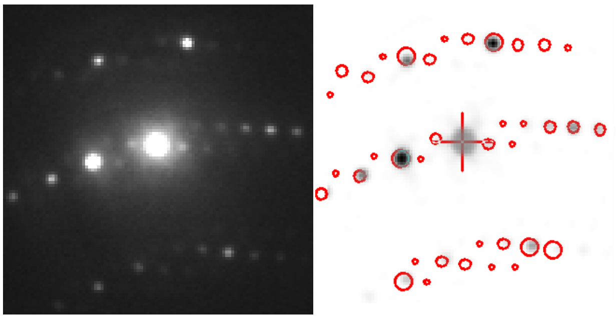
a) b)

Figure 1: Example of pattern matching for a random orientation of an α Fe grain a) as acquired, b) filtered image with the selected template superimposed.

The Q values for a given pattern may be visually compared. This is performed on Fig. 2 that shows the so-called correlation indexes map (Q map) related to the pattern of Fig. 1. This is the portion of the stereographic projection that cover all the possible orientations for the given crystal symmetry. For the b.c.c. example considered here, the area is bounded by the [001], [111] and [1-11] directions. The orientation step between two successive templates being one degree, less than 1500 templates are required to cover all the possibilities. On Fig. 1, the correlation indexes, divided by the highest one, are converted in grey levels. The selected orientation corresponds to the darkness point on the map.

This map is particularly useful to estimate the reliability of the solution. A single dark area means that the solution is safe; the appearance of extra dark spots on the map indicates that other orientations may be valid and therefore that the solution must be rejected [7]. As a consequence, the reliability may be weighted by the index R that is defined as:

$$R=100\left(1-\frac{Q_2}{Q_1}\right)$$

where Q1 and Q2 are the correlation indexes for the two highest and distinct maxima. If R vanishes, the identification is insecure. This occurs when the pattern is of poor quality either because the intensities of the spots are not high enough or merely because two patterns are superimposed as at grain boundaries. The reliability is also quite poor if the pattern has a 180° ambiguity. This particular problem will be discussed in detail in section 5.

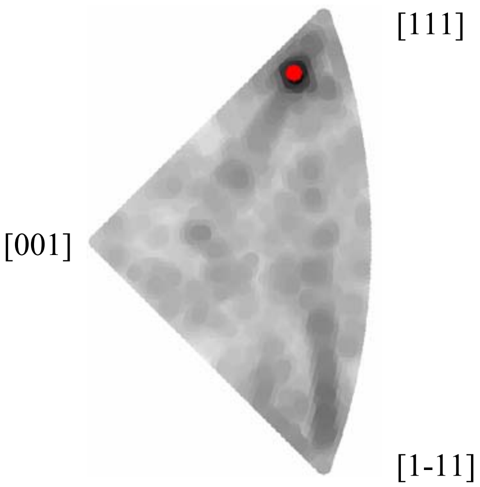

Figure 2: Correlation indexes map (Q map) with the selected orientation that is close to the [658] axis as indicated by the red dot.

2.3 Software settings optimization

The efficiency of the present procedure to select the adequate orientation is such that part of the identification parameters may be optimized automatically by considering the evolution of Q. This is illustrated with the camera length selection. Usually the value is given by the TEM settings but it may vary in a limited way inducing inconsistencies in the solution. Therefore the following procedure proves useful: on Fig. 3, the indexes are calculated for increasing camera lengths. More precisely, the best match is estimated while all the templates are expanded (or contracted) homothetically.

For every camera length some degree of matching may be fortuitously found and the corresponding solution, merely indicated by its number, is given on the plot. These correlations are poor and consequently for two different expansion factors the selected patterns are quite different (Fig. 3). The feature of interest is that the real solution is unambiguously recognised thanks to a sharp increase of the index when the camera length approaches the adequate one. For the present case the camera length is equal to 21 (arbitrary units).

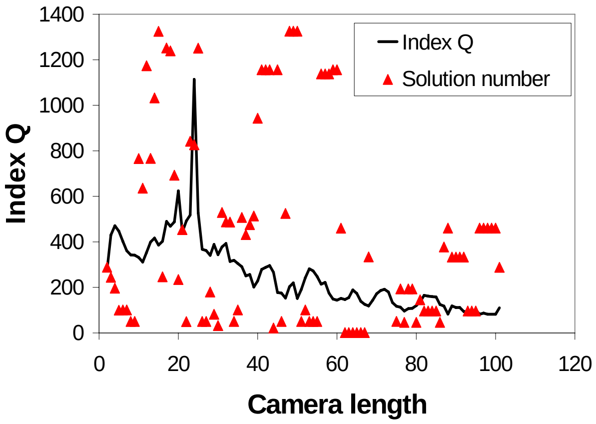

Figure 3: Correlation indexes in arbitrary units and the corresponding solutions indicated by their numbers for increasing camera lengths. The real camera length coincides with the peak value.

This procedure may also be used to select the adequate indexing parameters when a diffraction pattern with unknown observation conditions is analysed. It may be easily understand that the strong sensitivity of the template matching technique on the degree of similarity between the template and the actual diffraction pattern can also be used to distinguish say a b.c.c. pattern from a f.c.c. one. Phase identification performed with the present tool will be discussed in a devoted paper.

3 Misorientations in severely deformed steel

Figure 4 shows an orientation map and the corresponding highest index values (Q_{max} map) measured for low carbon steel subjected to alternated simple shear up to a cumulated shear strain of 18. A step size of 20 nm was used for the acquisition. Despite the high dislocation density, the orientation is determined in 96% of the cases.

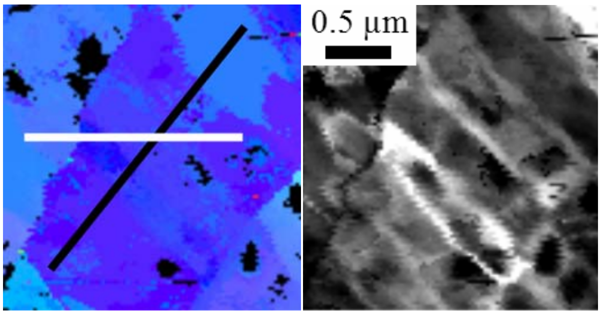

Figure 4: Orientation and Q_{max} maps for a low carbon steel severely deformed.

As expected, the observed structure is rather complex. Nevertheless, a rather uniform colour is obtained for the orientation map meaning that the normal axis is nearly the same for the whole area. The average orientation is close to the one given on Fig. 2. To analyse more precisely the area, misorientations along the two lines drawn on Fig. 4 are plotted on Fig. 5. The substructure appears to be composed of a mixture of cell and grain boundaries that are characterized thanks to the knowledge of the local crystallographic orientation. Of interest is the fact that on the TEM picture the boundaries are quite visible (Fig. 7), but it is hard to notice on the image if a boundary separates cells or grains. As noticed on Fig. 5, the horizontal line cross a grain boundary (20° misorientation) whereas the other line does not.

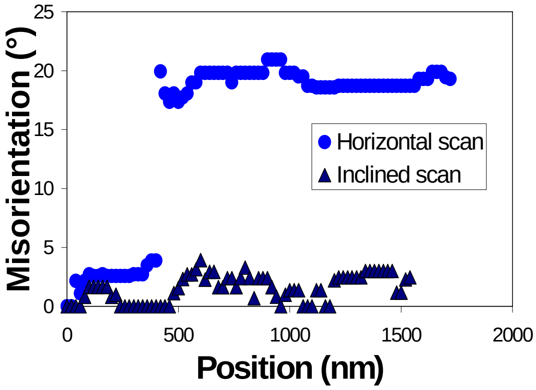

Figure 5: Misorientations calculated with respect to the first point for the white and black lines drawn on Fig. 3. A grain boundary is detected from the former.

It should be mentioned that unfortunately the Q_{max} map does not give a good picture of the sample substructure. Indeed, the correlation index is sensitive to the similarity between the pattern and the selected template but also to the pattern quality that differs substantially from place to place. As a consequence, it is frequently difficult to recognize with the contrast given by the Q indexes, the area that was really scanned. An alternative technique is used for this purpose and is detailed in section 4.

4 Pseudo bright field image

One of the advantages of the present technique with respect to EBSD attachments on SEM is that both orientation map and TEM picture may be recorded together. This supposes that the area scanned for orientation identification is easily located. The task is simplified by the construction of a pseudo bright field image.

As for the standard STEM mode, it is possible to reconstruct a bright field image of the object by plotting the intensity of the transmitted beam while the area of interest is scanned. In the present case, the diffractions patterns being recorded at every step, it is possible to calculate the average intensity in a disc that surrounds the transmitted beam. This is entirely equivalent to the introduction of a virtual aperture in the beam trajectory as shown on figure 6.

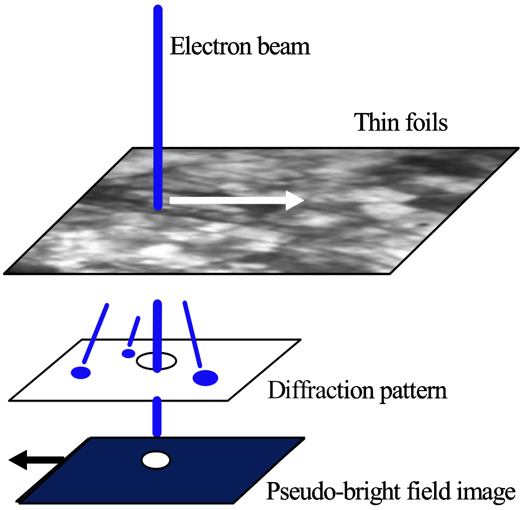

Figure 6: Pseudo bright field construction. Only the transmitted beam is numerically selected and plotted on the image

The pseudo bright field image is obtained by plotting the fluctuating intensity with the same scanning rate and steps than the real one. An example of such a construction is shown on figure 7 that corresponds to the same area as

Fig. 4. It can be noted that the pseudo bright field image is for far better that the Q_{max} one to recognize the scanned area. This type of information is particularly useful to detect any unexpected drift of the beam during the sampling time that is, for 25 frames per second, typically one hour for a full map. Indeed, the beam stability is never perfect mainly because the temperature of the TEM coils is hardly constant. For example, a close inspection of Fig. 7 denotes a small alternating shift of the beam in the lower part of the image.

Concerning the spatial resolution, it should be mentioned that for the present reconstructed images, the virtual aperture has to be larger than the transmitted beam. This is because the inner part of the transmitted beam saturates and only the outer part contains contrast information. Therefore, as for STEM mode, it is mainly the beam diameter that delimits the pseudo bright field image resolution.

Of course, the virtual aperture may be displaced on the diffraction pattern and consequently any pseudo dark field image may be constructed in the same way. Of particular interest is the fact that the diffraction patterns being recorded these reconstructions may be performed off line.

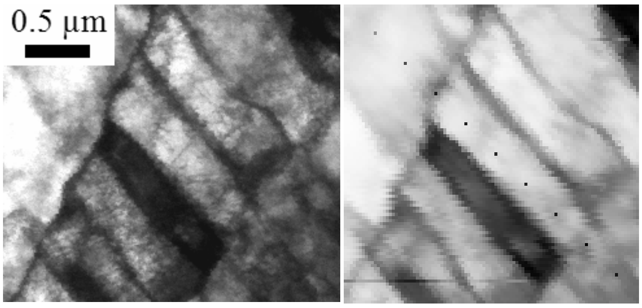

Figure 7: Real and Pseudo bright field images of the area analysed on Fig. 4.

5 Orientation ambiguity

The reliability of the orientation identification from diffraction spot patterns is limited by the well-known 180° ambiguity [8]. A typical example is the [111] pattern for b.c.c. materials that have sixfold symmetry instead of the crystal threefold symmetry. This occurs when there is no spot from the higher order Laue zones. The problem is encountered quite frequently and has to be surmounted by extracting more information from the patterns. Dedicated methods, which concern the equipment itself, are under development but are not running at date. Meantime a very simple procedure is used in order to exploit properly the available orientation maps. Basically, the method consists in extracting the adequate information from a collection of patterns. Indeed, if a single a highly symmetric pattern can not be resolute, the association of hundred of adjacent patterns is less problematic.

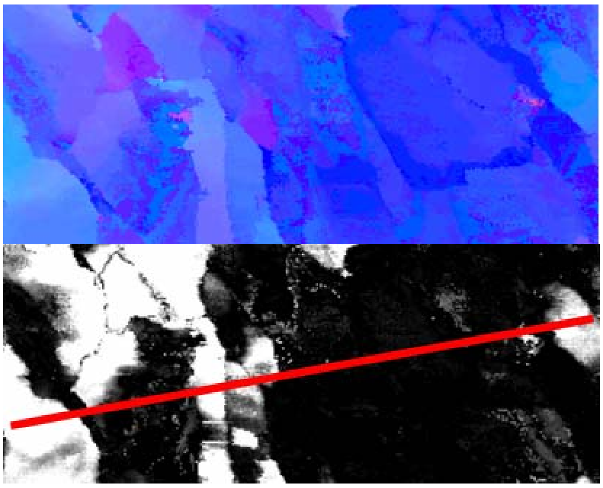

Figure 8: Orientation map and reliability map (R map) for a low carbon steel. R vanished in the black areas.

All the orientations sensitive to the 180° ambiguity are known a priori and have definite signatures. Consequently, it is possible to correct the local orientation by considering the two following facts:

- the ambiguities are related to some particular misorientations (e.g. 60° around the normal axis for [111] patterns). The noisy nature of the patterns leads to alternate orientations that are easily detected (Fig. 9)
- small misorientations always exists from one pixel to another and consequently the most ambiguous orientation is surrounded by more reliable ones.

The simplest way to reduce the ambiguity for a given point is to allow the crystal to rotate 180° and to select the orientation that is the closest from the adjacent pixels. In other words the alternated rotations that are related to the ambiguities are merely not permitted. The effective orientation is deduced from the safest point in the neighbourhood (the one that exhibits the highest R value).

Figure 8 gives a typical example of the lack of reliability that arises from the 180° ambiguity in ferrite. The steel was deformed up to a total strain of 7 through Equal Channel Angular Extrusion and large misorientations are recorded (Fig. 9). The orientations being close to the [111] axis over the whole area, the reliabilities are poor. This is illustrated by the R map, given also on Fig. 8, where it may be seen that more than half of the identifications are unsafe (black areas). Consequently, the misorientation evolution is jerky with frequent jumps up to 60° (Fig. 9).

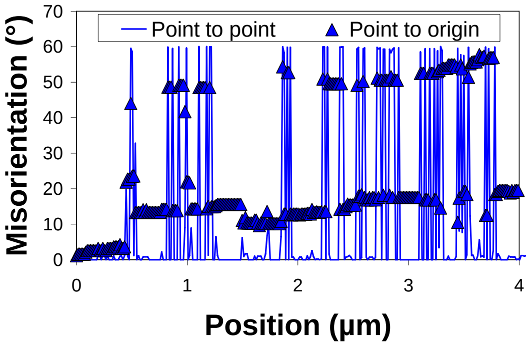

Figure 9: Misorientations calculated for the line drawn on Fig. 8. A jerky behaviour is observed when the line crosses an unreliable area.

For each pixel the selected orientation is rotated 60° around the [111] axis (from symmetry this is equivalent to a 180° rotation) and the one that correspond to the lowest misorientation with respect to the neighbourhood is selected. Of course, if the resulting misorientation is higher than a threshold value the correction is not performed (grain boundary).

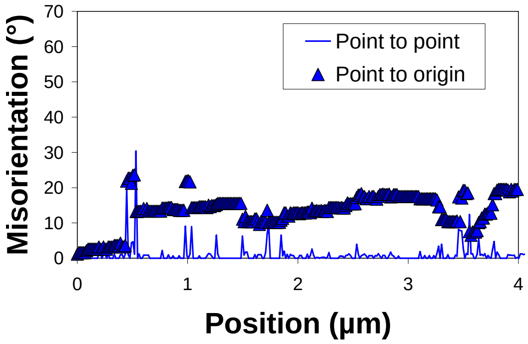

Figure 10: Same as Fig. 9 but after correction (see the text for details).

The corrected misorientation evolution for the same line as for Fig. 9 is shown on Fig. 10. Grain boundaries (point to point misorientation higher than 15°) are now easily distinguished.

6 Conclusions

Template matching algorithms are well adapted for the identification of spot diffraction patterns of randomly oriented crystals. Coupled with a fast image grabber hardware they constitute an efficient tool for the substructure characterisation of non trivial objects like severely deformed metals. The pseudo bright field image procedure as well as the ambiguity post treatment described in the previous sections constitute valuable complements to the procedure.

References

[1] Schwarzer, R.A., Sukkau, J.: *Mater. Sci. Forum*, Vols. 273-275, pp. 215-222, 1998.

[2] Zaefferer, S.: *J. Appl. Cryst*., 33; p.10, 2000.

[3] Morawiec, A.: J. *Appl. Cryst*., 32, pp.788-798, 1999.

[4] Fundenberger, J.-J., Morawiec, A., Bouzy, E., Lecomte, J.S.: *Ultramicroscopy*, 96, pp.127-1379, 2003.

[5] Schwarzer, R.A., Zaefferer, S.: *Mater. Sci. Forum*, Vols. 157-162, pp. 189-194, 1994.

[6] Rauch, E.F., Duft, A., to be published in *Proc. of 14th ICOTOM*, Leuven, Belgium, July 11-15, 2005.

[7] Rauch, E.F., Dupuy, L.: *Arch. Metall. Mater*., 50, pp. 87-99, 2005.

[8] Edington, J.W.: *Practical Electron Microscopy in Materials Science*, MacMillan, Philips Technical Library, vol. 2, p.27, 1991.

Proceedings of The 1st International Conference on **D**iffusion in **S**olids and **L**iquids
DSL-2005, July 6-8, 2005, University of Aveiro, Aveiro, Portugal

SIMULATION OF STRUCTURAL PHASE TRANSFORMATION IN SEMICONDUCTORS

Denilson S. BORGES[1,2], José Pedro RINO[*]

[1]Universidade Federal de São Carlos, Departamento de Física,
Caixa Postal 676, 13565-905, São Carlos, SP, Brazil
[2]Colégio Militar de Manaus – CMM, Rua José Clemente, 0157,
Centro – 69010-070, Manaus – AM, Brazil

[*]Corresponding author. Fax: +55 16 3361 4835; Email: djpr@df.ufscar.br

Abstract

An effective interaction potential consisting of two-body and three-body covalent interactions is proposed for zinc telluride semiconductor. This interaction potential is used to performed isothermal-isenthalpic molecular dynamics simulations of structural and dynamics correlation, in ZnTe, as a function of temperature and pressure. The cubic zinc blende zero pressure structure and the reversible transformation induced by pressure between the four-fold coordinated zinc blende structures to the six-fold coordinated rock salt structure are correctly described, in excellent accord with x-ray absorption spectroscopy results. The vibrational density of states for different temperature and pressure was obtained and the shift of the optical modes as a function of pressure was analyzed.

Keywords: Molecular dynamics; Structural transformation; ZnTe; Phase transition

1 Introduction

Atomistic simulation is a very important tool for describe and understand physical and chemical properties of materials. It bridges the gap between the laboratory experiments and analytical theories. In this paper we deal with classical simulations, *i. e.*, systems in which the dynamics of the constituent particles are governed by classical mechanics.

Visible light emitting devices are now a reality with the use of semiconductors of type II-VI, such as zinc telluride, ZnTe, [1, 2]. Besides its use for optical devices, substrates, and heterostructures, ZnTe for itself has been subject of several studies in order to characterize its different phases as a function of applied pressure, [3-7]. From the stable zinc blende structure at ambient conditions, ZnTe, under pressure, change to a cinnabar structure around 9 GPa and to *Cmcm* after 15GPa. [6] Above 90 GPa a new structure has been reported, but not yet determined. At high temperature and pressure a stable rock salt structure has been found, [3, 8].

In this paper we performed a molecular dynamics atomistic simulation (MD) in which an effective interaction potential is proposed for describe structural correlations and structural phase transformation under pressure in this particular semiconductor.

2 The interaction potential

A molecular dynamics technique (MD) is a method capable to generate the phase space trajectory for a given number of atoms which interacts with each other through a certain interaction potential. In this paper we propose an effective interaction potential in which two- and three-body interaction are considered, [9, 10]. The two body effective interaction potential takes into account size effects of the atoms, Coulomb interaction due to charge transfer between ions, charge-induced dipole interaction due to large electronic polarizability of anions, and induces-dipole induced dipole (van der Waals) interactions. These two-body effective potential is given by:

$$V^{(2)}(r) = \frac{H_{\alpha\beta}}{r^{\eta_{\alpha\beta}}} + \frac{Z_{\alpha\beta}e^{-r/\lambda}}{r} - \frac{D_{\alpha\beta}e^{-r/\xi}}{2r^4} - \frac{W_{\alpha\beta}}{r^6}. \quad (1)$$

Due to the long-range character of the Coulomb and the charge-dipole interactions, screening are introduced, so there is no need to perform Ewald sum, and an O(N) algorithm, necessary to integrate the equations of motion, could be used. These two-body potential was also truncated at r_c, and in order to prevent discontinuity in the potential and its first derivative at r_c the shifted potential approach was applied, [11].

A three-body interaction potential is necessary in order to describe the covalent character of the semiconductors. We proposed a modified Stillinger-Weber [12] type interaction potential to taken into account bond-bending and bond-stretching effects. In the expression below B_{jik} is the strength of the three body interaction, $\Theta(r_0 - r_{ij})$ are step functions, and $\bar{\theta}_{jik}$ is a constant. θ_{jik} is the angle between $\vec{r}_{ij}$ and $\vec{r}_{ik}$, and $r_{ij} = |\vec{r}_i - \vec{r}_j|$.

$$V^{(3)}\left(r_{ij},r_{ik}\right) = B_{jik}\exp\left(\frac{\gamma}{r_{ij}-r_o}+\frac{\gamma}{r_{ik}-r_o}\right) \times \frac{\left(\cos\theta_{jik}-\cos\bar{\theta}_{jik}\right)^2}{1+C\left(\cos\theta_{jik}-\cos\bar{\theta}_{jik}\right)^2} \times\Theta\left(r_o-r_{ij}\right)\Theta\left(r_o-r_{ik}\right) \qquad (2)$$

The parameters in these effective interaction potentials were chosen in order to have length scale, energy scale, and some mechanical property correctly describe. In Table 1 we summarize a comparison between simulated and experimental results for a selected quantity.

Table 1: MD and experimental results for lattice constant, bulk modulus, elastic constants, and cohesive energy of the zinc blende phase.

	MD	Experiments (Ref.14)
Cohesive energy (eV/particle)	2.30	2.28
Lattice Constant (Å)	6.10	6.1037
Bulk Modulus (GPa)	50.97	50.90
Elastic Constants (GPa)		
C_{11}	71.0	71.3
C_{12}	40.3	40.7
C_{44}	46.0	31.2

In conventional molecular dynamics simulations the observed quantities are measure in micro-canonical ensemble where the system is considered isolated. In this case the volume, energy and number of particles of the system are constants. In order to study structural phase transformation, with molecular dynamics techniques, it is necessary to use appropriate ensemble where the size and shape of the system can adequately respond to external sources. In this work we used the isenthalpic-isobaric (HNP) ensemble originally proposed by Parrinello and Rahman, [13]. In this ensemble the box of the system is considered as dynamical variables which allows to change in size and shape under conditions of constant stress or hydrostatic pressure. Temperature effects in the properties of the structural and dynamical, at zero apply pressure, were studied for systems with 1000, 27000, 64000, and 175 616 particles. The results for applying hydrostatic pressure was analysed at a fixed temperature for system with 1000 particles. The classical equations of motion were integrated using the velocity Verlet algorithm with a time step of 2.18fs. For each temperature and/or pressure, the system was always thermalized for at least 20000 time steps, and averages taken over additional 20000 time steps.

3 Results

The atomic trajectories generated from molecular dynamics simulations are used to calculate several structural, dynamical and thermo dynamical properties for the system.

3.1 Energies of crystalline structures

Zinc telluride can be found in several different crystalline structures when submitted to hydrostatic pressure. Figure 1 depicted the total energy per particle as a function of density for zinc-blende, cinnabar, and rock-salt structures

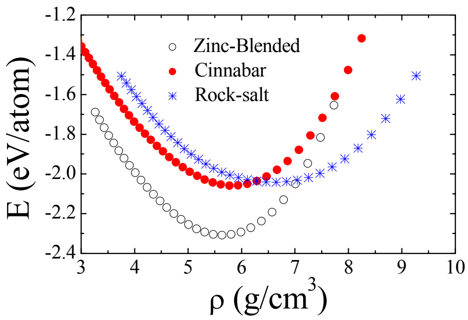

Figure 1: Total energy per particle as a function of density for three structures.

From a common tangent between zinc blende and rock salt structures we can infer the pressure of transformation to be 10.4 GPa. Experimentally the sequence of structural transformation, as a function of the applied hydrostatic pressure measured by x-ray diffraction techniques, is zinc-blende to cinnabar to *Cmcm* structure, and to rock salt at high temperatures, [6, 15]. The minimum energy for each structure described in Fig. 1 occurs at 5.64, 6.17, and 6.58 g/cc, in good agreement with the densities of 5.65, 6.36, and 6.91 g/cc calculated from lattice parameters measured by x-ray and extrapolated to zero pressures, for zinc-blende, cinnabar and *Cmcm* structures, respectively.

3.2 Temperature effects

Keeping null the external pressure, the zinc blende structure was heated with a heating rate of 4.59 K/ps. In Fig. 2 we show the volume ratio as a function of temperature.

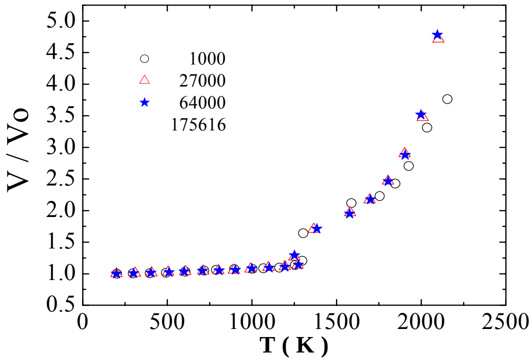

Figure 2: Volume fraction, V/V_0, as a function o temperature. The discontinuity around 1330K determines melting temperature.

The temperature at the discontinuity determines the melting temperature to be 1330±50 K, and no size effect was observed. The linear thermal expansion coefficient was obtained both from the temperature dependence of the first peak position of $g_{Zn\text{-}Te}(r)$ (partial pair correlation function) and from a linear approximation of the V/V_0 curve in the range of 200 to 700K. It was found to be, respectively, α=8.97x10^{-6} K^{-1} and α=7.83x10^{-6} K^{-1} in very good agreement with experimental value, 8.4x10^{-6} K^{-1}, [14].

3.3 Effect of Hydrostatic Pressure

Since the effective interaction potential could correctly describe melting temperature, cohesive energy, bulk modulus, elastic constants, and vibrational density of states (not shown), we kept the same set of parameters and study the effect of applied hydrostatic pressure. Starting from a system at 1000K the external pressure was applied in steps of 1 GPa every 30000 time steps up to 30 GPa. The temperature was kept constant at 1000K by scaling the velocities every 10 time steps. In Fig. 3 we display the time evolution of the MD cell vectors and the angles between them. Each plateau in this figure correspond to the same apply pressure during 65.3ps.

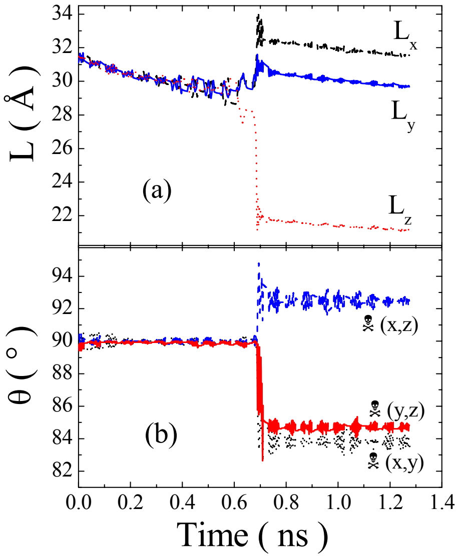

Figure 3: (a) Evolution of the MD cell vectors and (b) the angle between them. Each plateau corresponds to an external applied pressure.

Increasing the external pressure continuously we observe that around 12 GPa the system undergoes a structural phase transition.

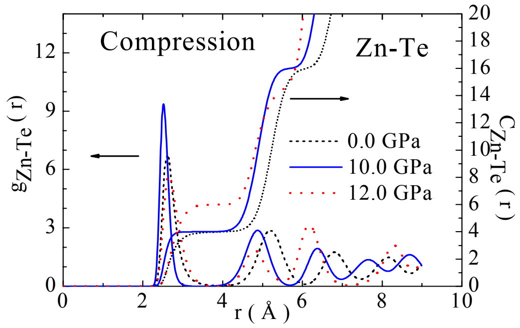

Figure 4: Zn-Te pair correlation function and coordination number for three applied pressures. At ambient condition, just before and after the structural phase transformation.

The two body correlations described by partial pair correlation function and coordination numbers and three body correlations given by the bond angles where calculated. In Figs. 4 we confirm that the system has change from a four-fold to a six-fold coordinated one. Up to 10 GPa the system remain in its original zinc blende structure four-fold coordinated displaying a simple elastic compression. Above this pressure a six-fold coordination number was observed followed by an increase of the bond length while the bond angles change from 109º (internal tetrahedral) to 90º and 180º characteristic of the rock salt structure.

The bond distances as a function of pressure is shown in Fig. 6 along with EXAFS data, [3].

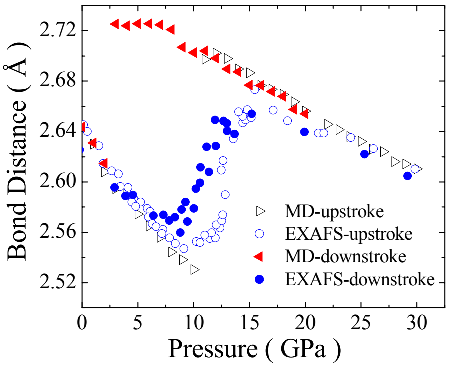

Figure 6: MD and EXAFS results for bond distance, Zn-Te, as a function of pressure.

Not only the dependence of the bond distance with pressure, both before and after the transition, is in good agreement with EXAFS results, but also the volume compression just before the transition. After the transition the MD result for the relative change in volume is also in agreement with experimental results, [3].

In conclusion, the proposed interaction potential could describe very well the properties of the semiconductor ZnTe.

Acknowledgments

This work was supported by Fundação de Amparo à Pesquisa do Estado de São Paulo – SP and Conselho Nacional de Desenvolvimento Científico e Tecnológico – CNPq, Brazil.

References

[1] Haase, M.A., Qiu, J., DePuydt, J.M., and Cheng, H., *Appl. Phys. Lett.*, 59, 1272, 1991.

[2] Kinto, H., Yagi, M., Tanigashira, K., Yamada, T., Uchiki, H., and Iida, S., *J. Cryst. Grow.*, 117, 348, 1992.

[3] San-Miguel, A., Polian, A., Gauthier, M., and Itié, J.P., *Phys. Rev. B,* 48, 8683, 1993.

[4] Camacho, J., Loa, I., Cantarero, A., and Syassen, K., *High Pressure Res.,* 22, 309, 2002.

[5] Camacho, J., Loa, I., Cantarero, A., and Syassen, K., *J. Phys.: Cond Matter,* 14, 739, 2002.

[6] Nelmes, R.J., McMahon, M.I., Wright, N.G., and Allan, D.R., *Phys. Rev. Lett.,* 73, 1805, 1994.

[7] Nelmes, R.J., McMahon, M.I., Wright, N.G., and Allan, D.R., *J. Phys. Chem. Solids,* 56, 545, 1995.

[8] Shimimura, O., Utsumi, W., Urakawa, T., Kikegawa, T., Kusaba, K., and Onodera, A., *Rev. High Pressure Sci. Technol.,* 6, 207, 1997.

[9] Rino, J.P., Chatterjee, A., Ebbsjö, I., Kalia, R.K., Nakano, A., Shimojo, F., and Vashishta, P., *Phys. Rev. B,* 65, 195206-1, 2002.

[10]Shimojo, F., Ebbsjö, I., Kalia, R.K., Nakano, A., Rino, J.P., and Vashishta, P., *Phys. Rev. Lett.,* 84, 3338, 2000.

[11]Allen, M.P. and Tildesley, D.J., *Computer Simulation of Liquids.* Clarendon Press, Oxford, 1990.

[12]Stillinger, F.H. and Weber, T.A., *Phys. Rev. B* 31, 5262, 1985.

[13]Parrinello, M. and Rahman, A., *Phys. Rev. Lett.* 45, 1196, 1980; *J. Appl. Phys*., 52, 7182, 1981.

[14]*Numerical Data and Functional Relationship in Science and Technology*, O. Madelung, , M. Schulz, and H. Weiss (Eds.), Landolt-Börnstein, New Series, Group III, Springer-Verlag, Berlin, Vol. 17a, p. 159, 1982.

[15]Camacho, J., Parlinski, K., Cantarero, A., and Syassen, K., *Phys. Rev. B.,* 70, 033205-1, 2004.

THE MODEL OF LIQUID GROOVE GROWTH WITH EXCESSIVE CHEMICAL POTENTIAL AS A DRIVING FORCE

Alexey RODIN
Moscow Steel and Alloys Institute (Technological University), 4, Leninsky pr-t, Moscow, 119049, Russia

Fax: +7 095 2368738; Email: rodin@misis.ru

Abstract

This paper is devoted to description of liquid groove growth at grain boundaries of solid polycrystalline metal in contact with liquid one. To describe the properties of atoms on grain boundary and on the surface excessive chemical potential ($\Delta\mu$) as compared with bulk is used. It includes excessive energy of grain boundary, coherent strain energy, but does not include a curvature of the surface. In dependence on type of $\Delta\mu$ (x) function the different morphology and growth kinetics of channels can be obtained. In the case when $\Delta\mu$ acts at GB only, two limit cases were analysed. If The first derivative of y on x y'<<1 the Mullins solution was obtained. In the second case (y'>>1) thin (2-3 interatomic distances) films can grow with constant rate. The triangle shape of the groove with constant growth rate corresponds to constant excessive chemical potential along solid liquid interface.

Keywords: Groove; Excessive chemical potential; Driving force

1 Introduction

This work is connected with description of liquid metal groove formation and their growth. This process can occur if grain boundary (GB) cross external surface, while there is a liquid in contact with the solid polycrystalline material. Both experimental and theoretical studies in this direction started more than 40 years ago Ref. [1,2]. But up to date there is no common theory, which describes the different morphological type of the channels. However, several models, included different driving forces (e.g. coherent stress, non-compensated surface tension etc) were published last several years Ref. [3-5]. That is clear that the groove growth is a complicated process, including several different stages. Each of them can control the total process. However, for most part of metallic systems (may be excluding pure Al-liquid Ga) it has some common features.

At low temperature the curvature of external surface plays the most important role. The kinetics can be different. It changes from $t^{1/4}$ up to $t^{1/2}$. This kinetics was predicted by Mullins Ref. [6] who constructed the theory of thermal groove growth and adapted it to the liquid groove. For example, in the case of mass transfer by evaporation-condensation mechanism (for thermal grooves) or dissolution-precipitation mechanism (for the liquid grooves) it gives us the following equation of groove deepening:

$$y = -2m(At)^{1/2}\,\mathrm{ierfc}\{x/2(At)^{1/2}\},$$

where m is liquid-solid/GB surface tension ratio and A is a constant depending mainly on diffusion coefficient in liquid and liquid-solid surface tension. The walls of the grooves are upward curved.

At higher temperature the morphology can change. The groove became more deep and narrow, the curvature became close to zero but the width became even less than at low temperatures. They have a wedge like shape. Sometimes one can see even downward curvature of the walls.

That means that for the same systems different type of the grooves can be observed in dependence on temperature and GB characteristics. Such a results (Fig. 1) was published for Al-based alloy-Ga Ref. [7], for pure Al-Sn Ref. [8], Cu-Bi Ref. [9] systems.

2 Model

Let's suppose that main mass transfer takes place through the liquid phase. To describe the process let's introduce a term "excessive chemical potential" $\Delta\mu$ of the atom of solids. It can change along the liquid-solid interface and its nature can be different.

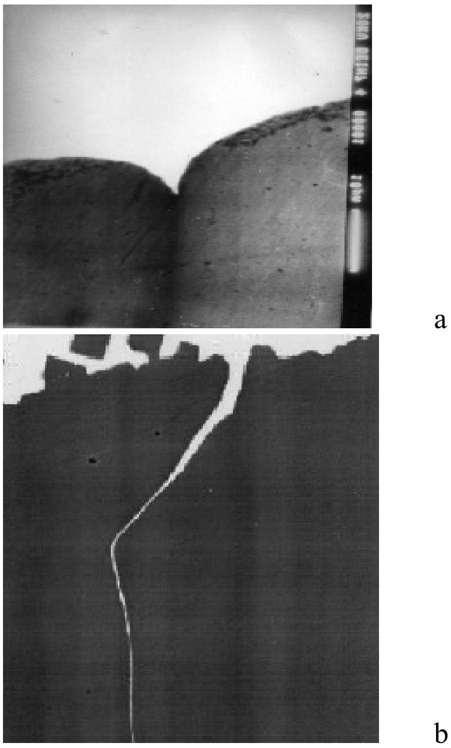

Figure 1: Different morphology of liquid grooves in Cu-Bi system Ref. [9]. a-curvature is clearly seen; b- triangle type groove.

“Excessive” means that atoms of solid have a higher potential at the surface or adjacent to the surface region than in liquid contacted with plate plane. What is the reason of that? First of all we have to mention that GB is non-equilibrium defect and at the point where GB is in contact with liquid the chemical potential is determined by the nature of grain boundary. In fact it corresponds to the GB surface tension recalculated per atom. It acts in the region $-\delta/2<x<\delta/2$ according to Fig. 2, where δ is GB width.

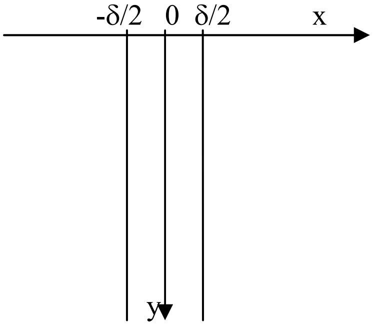

Figure 2: Geometry of GB.

If liquid metal is not saturated by the solid, the $\Delta\mu$ value is determined by the term $RT\ln(C/C_0)$, where C and C_0 are concentration at given moment and saturation concentration in liquid phase. Note that in some systems (e.g. Al-Sn, Cu-Bi) the equilibrium concentration depends strongly on temperature and any temperature fluctuation leads great difference between C and C_0 Ref. [10].

There are other reasons influenced on $\Delta\mu$: the coherent stress energy Ref. [11] linked with atomic size difference, the curvature (K), which change the concentration of saturation near the curved surface.

Thus we can introduce some function $\Delta\mu(x)$, which determines the equilibrium between solid and liquid phases. Supposing that local equilibrium is reached between solid and liquid phases, the equilibrium concentration of atom of solid in liquid phase at the point with coordinate x – C(x) can be written with the use the Gibbs-Thomson equation.

$$\frac{C(x)-C_0}{C_0}=\frac{\Delta\mu(x)}{RT} \tag{1}$$

To separate the curvature from other reasons let us write the following equation:

$$\frac{C_K(x)-C_0}{C_0}=K\frac{\gamma\Omega}{RT} \tag{2}$$

where C_K is saturated concentration on the surface with curvature K; γ is solid- liquid surface tension; Ω is molar volume of solid.

Let us write the equation for flux from surface. Supposing that liquid is of sufficient quantity and the diffusion coefficient is high, the following equation can be written:

$$j=D\frac{C(x)-C_0}{b} \tag{3}$$

Where j is a flux density; D is diffusion coefficient in liquid; b is a distance from the surface where concentration become equal to C_0.

Taking into account that the concentration C(x) is determined by curvature and excessive chemical potential, the total flux can be written as a sum of fluxes due to linearity:

$$j=j_1+j_2 \tag{4}$$

where

$$j_1=D\frac{C_0}{b}\frac{\Delta\mu(x)}{RT} \tag{5}$$

$$j_2=D\frac{C_0}{b}\frac{\gamma\Omega}{RT}K \tag{6}.$$

Rewriting the flux in terms of deepening of the channel we can write:

$$j=-\frac{1}{a\sqrt{1+y'^2}}\frac{\partial y}{\partial t} \tag{7}$$

Where a is an interatomic distance.

Substituting the curvature in accordance with its definition $K = -\frac{y''}{\left(1+y'^2\right)^{3/2}}$ and summarizing (4)-(6) and (7) we arrive to:

$$-\frac{1}{\sqrt{1+y'^2}}\frac{\partial y}{\partial t} = DC_0\frac{a}{b}\left(\frac{\Delta\mu(x)}{RT} - \frac{y''}{\left(1+y'^2\right)^{3/2}}\frac{\gamma\Omega}{RT}\right) \quad (8)$$

Equation (8) can be rewritten as:

$$\frac{\partial y}{\partial t} = -DC_0\frac{a}{b}\left(\sqrt{1+y'^2}\frac{\Delta\mu(x)}{RT} - \frac{y''}{\left(1+y'^2\right)}\frac{\gamma\Omega}{RT}\right) \quad (9)$$

3 Discussion

Let us discuss some simple cases. First of all we discuss the Mullins grooves growth Ref. [6].

For that we use only two sources of excessive chemical potential corresponding to GB ($\Delta\mu_{gb}$) and to the curvature. To write $\Delta\mu_{gb}$ in equation we use the Dirack δ-function defined as follow:

$$\delta(x) = \begin{cases} 0 \; x \neq 0 \\ \infty \, x = 0 \end{cases} \quad (10)$$

Excessive chemical potential can be written as

$$\Delta\mu(x) = \Delta\mu_{gb}\delta\delta(x) \quad (11)$$

Using the approximation that the slope is small $y' \ll 1$ we can write the equation (9) as:

$$\frac{\partial y}{\partial t} = DC_0\frac{a}{b}\frac{\gamma\Omega}{RT}y'' - DC_0\frac{a}{b}\frac{\Delta\mu(x)}{RT} \quad (12)$$

We can write now the full problem with boundary condition

$$\begin{cases} \frac{\partial y}{\partial t} = A\gamma\Omega y'' - A\Delta\mu_{gb}\delta\delta(x) \\ A = DC_0\frac{a}{b}\frac{1}{RT} \\ y(0,t) = 0 \\ y'(0,t) = 0 \end{cases} \quad (13)$$

The solution of the problem is:

$$y(x,t) = -\sqrt{\frac{A}{\pi\gamma\Omega}}\int_0^t \frac{\Delta\mu_{gb}\delta}{\sqrt{t-\tau}}exp\left\{-\frac{x^2}{4A\gamma\Omega(t-\tau)}\right\}d\tau \quad (14)$$

Let us compare this equation with Mullins solution.

$$y(x,t) = -\sqrt{\frac{A}{\pi}}\int_0^t \frac{m}{\sqrt{t-\tau}}exp\left\{-\frac{x^2}{4A(t-\tau)}\right\}d\tau$$

where $m = \frac{\gamma_b}{\gamma}$, and γ_b is a GB surface tension.

One can see that the difference is only in substitution of m by $\Delta\mu_{gb}\delta/\gamma\Omega$ and A by $A\gamma\Omega$. This substitution is just the recalculation of surface energy per unit area (surface tension) to the value per mol (chemical potential).

As it was mentioned above, such situation can be seen at relatively low temperature. In experiments it is often happens that $y' \geq 1$ or even $y' \gg 1$. In the last case second term in Eq. (9) vanishes. Neglecting this term we can rewrite Eq. (14)

$$y = -DC_0\frac{a}{b}\frac{\Delta\mu_{gb}}{RT}t \quad x \in (-\delta/2;\delta/2) \quad (15)$$

That means the formation of nanometric thin liquid film along GB with width of the same order as GB width.

But neglecting the curvature we can not neglect the other sources of the excessive chemical potential. In the region out of GB we have to take into account, for example, the coherency strain energy.

Let us use again two sources. The first one is the excessive chemical potential of GB $\Delta\mu_{gb}$ and the second is coherent stress energy $\Delta\mu_{coh}$.

$$\Delta\mu(x) = \begin{cases} \Delta\mu_{gb} \; x \in (-\delta/2;\delta/2) \\ \Delta\mu_{coh} \, x \notin (-\delta/2;\delta/2) \end{cases} \quad (16)$$

Supposing that $y' \gg 1$ in all region out of GB we receive instead Eq. (9)

$$\frac{\partial y}{\partial t} = -DC_0\frac{a}{b}\left(\sqrt{1+y'^2}\frac{\Delta\mu(x)}{RT}\right) \quad (17)$$

The equation (17) can be rewritten as a system of two equations: for region

$(-\delta/2; \delta/2)$ $y' = 0$

$$\frac{\partial y}{\partial t} = -DC_0\frac{a}{b}\frac{\Delta\mu_{gb}}{RT} \quad (18)$$

at other surface $y' \gg 1$.

$$\frac{\partial y}{\partial t} = -DC_0\frac{a}{b}\frac{\Delta\mu_{coh}(x)}{RT}y' \quad (19)$$

Resolving these two equations, we will find the solution for Eq. (18):

$$y = -DC_0\frac{a}{b}\frac{\Delta\mu_{gb}}{RT}t \; x \in (-\delta/2;\delta/2) \quad (20)$$

and for Eq. (19)

$$y = -Bt + Kx \;\; x \notin (-\delta/2;\delta/2) \quad (21)$$

Coefficient $K = \frac{\Delta\mu_{gb}}{\Delta\mu_{coh}}$ and finally

$$y = -DC_0\frac{a}{b}\frac{\Delta\mu_{gb}}{RT}t + \frac{\Delta\mu_{gb}}{\Delta\mu_{coh}}x \quad (22).$$

Thus we have received the solution with linear growth rate and constant angle at the tip of the groove.

Because of the mathematical difficulties we have not solved the equation than neither y'' nor y' can be neglected. But from analysis of equation we can see that there is a passage from the zone with zero slope to the zone with some constant slope. In fact it means that there is some region with positive second derivative and downward curvature.

Also we can create the combination between several solutions. That is the reason why we often observe some downward curvature at the level of initial surface and almost vertical walls at the tip (Fig. 3) In this case the real time dependence will be different from exact value and will be described by some low between $t^{1/2}$ and t.

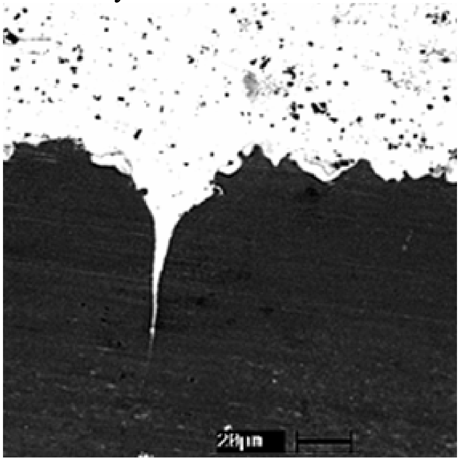

Figure 3: The groove with well-seen curvature on the upper part of the groove and almost triangle form at the tip (system Al (7010)-Ga) Ref. [7].

Acknowledgments

This work is made with financial support of Russian Foundation for Basic Research grant # 04-03-32800-a.

References

[1] Joseph B., Picat M., Barbier F. Liquid metal embrittlement: a state-of-the-art appraisal. *Eur. Phys. J. AP.* -vol.5 pp. 19-31, 1999.

[2] Bishop G.H. Grain Boundary Penetration and Embrittlement of Nickel Bicrystals by Bismuth. *Transactions of the Met. Soc. of AIME*, v.242, July, 1968.

[3] Fradkov V.E. Rapid Liquid Metal Corrosion along Grain Boundary, *Scripta Met.et Mat*, v.32, N12, 1599-1603, 1994.

[4] Glikman E., Nathan M., On the kinetic mechanism of grain boundary wetting in metals *J. Appl. Phys*., 85 (6), 3185-91, 1999.

[5] Vilenkin A. Grain boundary segregation and grain boundary Wetting. *Def. And Diff. Forum*, Vol. 216-217, pp. 191-195, 2003.

[6] W.W. Mullins. Theory of thermal groove. *J. Appl. Phys.*, 28, 333-338, 1957.

[7] Brechet Y., Rodin A., Veron M., Peron S. and Deschamps A., Examples of liquid metal embrittlement in industrial aluminium alloys. *J. Phys. IV France*, 12, pp. 263-276, 2002.

[8] Bokstein B., Kostel'tseva N., Peteline A., Rakov S. and Rodin A. Grain Boundary Liquid Grooving in Metals, *Defect and Diffusion Forum*, Vols. 237-240, pp. 756-762, 2005.

[9] Apykhtina I.V., Bokstein B.S., Ostrovsky A.S., Petelin A.L., Rodin A.O., Srolovitz D.J. Grain Boundary Wetting: Diffusion or Non-Diffusion Mechanism *Mat. Sci. For.*, Vol. 194-199, p. 1273-1296, 2001.

[10] Massalski T.B. a.o. *Binary Alloys Phase Diagrams.* Ohio: American Society for Metals, Metal Park, 1986.

[11] Rabkin E. Coherency strain energy as a driving force liquid grooving at grain boundaries. *Scr. Met.,* Vol. 39 N 6, p.685-691, 1998.

Proceedings of The 1st International Conference on **D**iffusion in **S**olids and **L**iquids
DSL-2005, July 6-8, 2005, University of Aveiro, Aveiro, Portugal

COMPLEX-ANALYTIC METHODS FOR THE STUDY OF THE EFFECTIVE CONDUCTIVITY OF COMPOSITE MATERIALS

Sergei ROGOSIN[1,*], Marina DUBATOVSKAYA[1],
Svetlana MAKARUK[2], Ekaterina PESETSKAYA[1,3]

[1]Department of Mathematics and Mechanics, Belarusian State University,
Fr. Skaryny ave, 4, 220050 Minsk, Belarus
[2]Department of Mathematics, Brest State Technical University,
Moskovskaya str., 267, 224017 Brest, Belarus
[3]Department of Mechanical Engineering, University of Aveiro,
Campus Universitário de Santiago, 3810-193 Aveiro, Portugal

*Corresponding author. Fax: +375 17 209 54 47; Email: rogosin@bsu.by

Abstract

The effective conductivity of 2D composite materials is discussed on the base of the complex-analytic methods. Main attention is paid to the application of the methods of boundary value problems for harmonic and analytic functions and functional equations for composite materials having multiply connected circular structure. The problems of new type are posed.

Keywords: 2D composite material; Effective conductivity; Analytic functions; Boundary Value Problems; Circular multiply connected domains; Functional equations

1 Introduction

In this report we describe a number of constructive methods for analytic functions following the ideas of the book [1] and recent papers. These methods extend the possibility of using mathematical constructions within different directions of mathematics, as well as mechanics, physics, chemistry, biology, economics etc. This field is too wide to be presented in a short paper. Thus we restrict ourselves by boundary value problems for analytic functions and some related problems of porous media mechanics and composite materials. As illustration of the mathematical constructions we present certain models for composite materials.

What is for us the meaning of the expression *explicit* or *closed form solution*? To get the closed form solution one have to construct the formula which contains a finite set of elementary and special functions, arithmetic operations, compositions, integrals, derivatives and even series. Besides all the objects in the formula ought to have precise meaning. At last, domains for parameters, as well as all functions, integrals, derivatives etc. have to be explicitly determined. It should be shown also that these domains and (if necessary) their intersections are non-empty.

This approach seems to be slightly nontraditional. For instance, in the classical books a form in series is not supposed to be a closed one. At the same time these books allow to have special functions in the solutions' formulas. But not all such functions has integral representations.

2 Method of functional equations

We describe first the main idea of the method of functional equations on the base of its application to the Dirichlet problem for a doubly connected domains.

Let us consider two discs $\mathbb{D}_k := \mathbb{D}(a_k, r_k) = \{z \in \mathbb{C} : |z - a_k| < r_k\}$ $(k = 1, 2)$, $cl\mathbb{D}_1 \cap cl\mathbb{D}_2 = \emptyset$, and the doubly connected domain $\mathbb{D} := \widehat{\mathbb{C}} \backslash (cl\mathbb{D}_1 \cup cl\mathbb{D}_2)$ on the extended complex plane $\widehat{\mathbb{C}}$. The orientation chosen on $\mathbb{T}_k := \{z \in \mathbb{C} : |z - a_k| = r_k\}$ leaves $\mathbb{D}$ to the left. The Dirichlet problem for the domain $\mathbb{D}$ consists in the following. Given Hölder continuous functions $f_k(t)$ on $\mathbb{T}_k$ $(f_k(t) \in \mathcal{H}(\mathbb{T}_k),\ k = 1, 2)$, find a function $u(z)$ harmonic in $\mathbb{D}$ and Hölder continuous on $cl\mathbb{D}$

satisfying the boundary condition

$$u(t) = f_k(t), \ t \in \mathbb{T}_k, \ k = 1, 2. \tag{1}$$

Using the Logarithmic Conjugation Theorem for a doubly connected domain we look for $u(z)$ in the following form

$$u(z) = \Re\left(\phi(z) + A \log \frac{z - a_1}{z - a_2}\right), \tag{2}$$

where the function $\phi(z)$ is analytic in $\mathbb{D}$ and Hölder continuous on $cl\mathbb{D}$, i.e., $\phi \in \mathcal{H}_{\mathcal{A}}(\mathbb{D})$, A is an unknown real constant. Let us choose a curve L_1 connecting the points $z = a_1$ and infinity, which has no common points with $\mathbb{T}_1$. Suppose that $\log(z - a_1)$ is a fixed analytic branch of the multi-valued logarithm in $\widehat{\mathbb{C}} \backslash L_1$. The function $\log(z - a_2)$ is defined in a similar way. Let us denote

$$z^*_{(k)} := z^*_{\mathbb{T}_k} = \frac{r_k^2}{\overline{z - a_k}} + a_k$$

the inversion with respect to the circle $\mathbb{T}_k$. We have $t^*_{(k)} = t$ on $|t - a_k| = r_k$. A function $\varphi(z)$ is analytic in $|z - a_k| < r_k$ if and only if $\overline{\varphi\left(z^*_{(k)}\right)}$ is analytic in $|z - a_k| > r_k$ (see Section 2.1). Using the Decomposition Theorem we find the function $\phi(z)$ in the form

$$\phi(z) = \overline{\phi_1\left(z^*_{(1)}\right)} + \overline{\phi_2\left(z^*_{(2)}\right)}, \tag{3}$$

where the function $\phi_k(z)$ is analytic in $|z - a_k| < r_k$ and Hölder continuous on $|z - a_k| \leq r_k \ (k = 1, 2)$, i.e., $\phi_k \in \mathcal{H}_{\mathcal{A}}(\mathbb{D}_k)$. Substituting (3) in (2) and using (1) we arrive at the following boundary conditions

$$\Re\overline{\phi_1\left(t^*_{(1)}\right)} + \Re\overline{\phi_2\left(t^*_{(2)}\right)} + A \log \left|\frac{t - a_1}{t - a_2}\right| = f_k(t), \quad t \in \mathbb{T}_k, \ k = 1, 2. \tag{4}$$

It is easily seen that

$$\begin{aligned} \phi_1(z) + \overline{\phi_2\left(z^*_{(2)}\right)} &= g_1(z) + \\ +A\left[\log(z - a_2) - \log r_1\right], \ & z \in cl\mathbb{D}_1. \end{aligned} \tag{5}$$

Similar arguments for the second relation (4) yield

$$\begin{aligned} \phi_2(z) + \overline{\phi_1\left(z^*_{(1)}\right)} &= g_2(z) - \\ -A\left[\log(z - a_1) - \log r_2\right], \ & z \in cl\mathbb{D}_2, \end{aligned} \tag{6}$$

where the known function g_2 belongs to $\mathcal{H}_{\mathcal{A}}(\mathbb{D}_2)$. The equalities (5) and (6) constitute a system of two functional equations with respect to the functions $\phi_1(z)$ and $\phi_2(z)$. Excluding $\overline{\phi_2\left(z^*_{(2)}\right)}$ from equality (5) we obtain the simple functional equation

$$\phi_1(z) = \phi_1[\alpha(z)] + g(z), \ z \in cl\mathbb{D}_1, \tag{7}$$

where the known function $g(z)$ belongs to $\mathcal{H}_{\mathcal{A}}(\mathbb{D}_1)$. The pure imaginary constant $i\gamma$ contains the additive constants $i\gamma_1$ and $i\gamma_2$ appearing in the definition of $g_1(z)$ and $g_2(z)$. The conformal mapping

$$\alpha(z) := \left(z^*_{(2)}\right)^*_{(1)} = \frac{r_1^2(z - a_2)}{r_2^2 + \overline{(a_2 - a_1)}(z - a_2)} - a_1$$

maps the closed disc $|z - a_1| \leq r_1$ into the open one $|z - a_1| < r_1$.

Now we outline some notations and facts of the general theory of the functional equation which are connected with those equations appearing at the study of boundary value problems. In particular we need the following

Theorem 1. (Denjoy–Wolff) *Let* f *be an analytic function in the unit disc* $\mathbb{U}$ *mapping* $\mathbb{U}$ *into itself (but not a Möbius transformation of* $\mathbb{U}$ *onto* $\mathbb{U}$*). Then there exists a point* z_0, $|z_0| \leq 1$, *such that the sequence of iterations* $f^n(z)$ *converges to* z_0 *uniformly on each compact subset of* $\mathbb{U}$. *Moreover, if* $|z_0| = 1$, *then* $\lim_{r \to 1-0} f(rz_0) = z_0$ *and* $s := \lim_{r \to 1-0} f'(rz_0)$ *exists and* $0 < |s| \leq 1$.

Theorem 2. *Let a function* $f \in \mathcal{C}_{\mathcal{A}}(cl\mathbb{U})$ *be mapping the closed unit disc* $cl\mathbb{U}$ *into the open unit disc* $\mathbb{U}$. *Then* f *has a unique fixed point* z_0 *in* $\mathbb{U}$ *and* $|f'(z_0)| < 1$. *The sequence* $f^n(z)$ *converges uniformly in* $|z| \leq 1$ *to the point* z_0.

The point z_0 is called *the attractive point* of $f(z)$.

Theorem 3. *The operator* $\varphi \mapsto \varphi[f(z)]$ *is compact in the spaces* $\mathcal{H}_{\mathcal{A}}(\mathbb{U})$, $\mathcal{C}_{\mathcal{A}}(\mathbb{U})$ *and in the Hardy space* $\mathcal{H}_p(\mathbb{U})$, $1 < p < +\infty$.

Theorem 4. *Let* $G, g \in \mathcal{C}_{\mathcal{A}}(\mathbb{U})$. *If* $G(z_0)\left[f'(z_0)\right]^k \neq 1$ *for all* $k = 0, 1, 2, \ldots$, *then the functional equation*

$$\varphi(z) = G(z)\varphi[f(z)] + g(z), \ |z| \leq 1 \tag{8}$$

has a unique solution $\varphi \in \mathcal{C}_{\mathcal{A}}(\mathbb{U})$. *If for some* k *we have* $G(z_0)\left[f'(z_0)\right]^k = 1$, *then (8) has a solution in* $\mathcal{C}_{\mathcal{A}}(\mathbb{U})$ *if and only if a solvability condition on* $G(z)$ *and* $g(z)$ *is fulfilled. If so then the general solution of (8) depends on an arbitrary complex constant.*

These results constitute a base of solvability theory for functional equations. The crucial idea is that if the mapping $\alpha(z)$ in the equation (7) maps its domain into itself then this equation can be solved in corresponding spaces by the method of successful approximation. In particular such situation appears at the study of several boundary value problems for analytic functions in a multiply connected circular domain.

3 Effective conductivity of composite materials

3.1 Optimal design

We refer to optimal design problems when it is necessary to determine an optimal composite in a given class of admissible composites. The investigation of optimal design problems for composite conductive materials is of mathematical and practical interest. The problems for optimal composites are usually formulated as variational problems of minimization of stored energy in the composite material (see, *e.g.* [2], [3], [6], [7] and papers cited therein). If unknown variables (*e.g.* the form of inclusions, their locations, size etc.) and/or constrains have geometric nature we deal with shape optimization problems (or optimal design problems). Typical physical constrains are the given conductivities of the components, condition of ideal contact on the boundary matrix-inclusions, the external field outside the composite. The latter two conditions can be represented in the form of the boundary value problems for certain potentials.

For periodic composites the optimal design problems coincide with the problem of optimization of effective conductivity tensor [7] in so called representative cell. We have to mention also a number of approaches which are devoted to the study of laminate composites (see e.g. [13]), fibre composites (see e.g. [9]), composites with the reach microstructure (see e.g. [16]), nanocomposites (see e.g. [14], [15]) etc.

This paper contains the description of a new approach in the study of optimal effective properties of the plane composite materials. In contrast to highly developed theory based on the weak and variational statement of the corresponding problems, this approach is oriented on the construction of the analytic solutions and even (when it is possible) the closed form solution. To show the perspectivity of this approach we use very simple examples, although several situations of more general type were considered recently as well.

We propose another statements of optimal design problems. The principal difference is that we fix shape and size of the inclusions. In particular, we consider a bounded domain occupied by a host material with N inclusions (N can be equal to unity). Hence, each inclusion has a positive concentration in the bulk material. It is known that if the characteristic size ε of the inclusion tends to zero (simultaneously N tends to infinity with fixed concentration of inclusions), the homogenization theory [8] can be applied. Such approach is not working for our model.

We also discuss optimal design problems for unbounded domains. In this case for simple external field the considered problem is equivalent to the problem of optimization of the effective conductivity of dilute composite materials, when concentration of inclusions is sufficiently small. Anyway the problem we arrive at could'not be handled via homogenization method.

The main mathematical difficulty we try to overcome is that for the moment an analytic solution of R-linear boundary value problem (Markushevich's problem in another sources) is not known. Moreover, the physically relevant statement of the optimal design problem in potential case leads to the mixed boundary conditions (different kind of boundary value problems on each component of the boundary). By using our approach we could overcome these difficulties at least in the case of very important model situations. Among the achievements presented in the paper we ought to mention the discovered phenomena of "packing" of inclusions in the optimal composites.

Our study is useful in technical applications, because this problem corresponds to the following engineering task. A designer has in his disposal a material of the given shape on the boundary of which a prescribed external field is applied. Let the designer also has inclusions of the given shape and size. It is necessary to locate these inclusions with a fixed concentration in such a way that the conductivity in the fixed direction will be maximal (minimal). So using our formulas a designer can project complex fibre composite materials to reach optimal properties.

We consider here the problems of two types.

First type problem. Bounded composite material.

Let Q be a bounded domain in the complex plane $\mathbb{C}$ encircled by a simple piece-wise smooth Lyapunov curve $\Gamma = \partial Q$. Let $h(t)$, $q(t)$ be given continuous functions on Γ. Let $g(z)$ be a given continuous function in the domain Q.

The question is to find a piece-wise smooth curve L, consisting of a finite number of connected components $L = \bigcup\limits_{k=1}^{n} L_k$, $L \subset \overline{\operatorname{int}\Gamma}$ (Γ è L_k, which have at most finite number of common points, and piece-wise harmonic function u,

$$\Delta u(z) = 0,\, z \in D^+ \cup D_k, \tag{9}$$

in $D_k = \mathrm{int} L_k$, $D^+ = Q \backslash \overline{\mathrm{int} \bigcup_{k=1}^{n} L_k}$, boundary conditions on the curve $L = \bigcup_{k=1}^{n} L_k$:

$$u^+(t) = u^-(t),\, \lambda_m \frac{\partial u^+}{\partial n}(t) = \lambda_i \frac{\partial u^-}{\partial n}(t), \tag{10}$$

or

$$u^+(t) - u^-(t) = g(t),\, \lambda_m \frac{\partial u^+}{\partial n}(t) = \lambda_i \frac{\partial u^-}{\partial n}(t), \tag{11}$$

and one of the following boundary conditions

$$\frac{\partial u^+}{\partial n}(t) = 0,\, t \in \Gamma, \tag{12}$$

$$u^+(t) = h(t),\, t \in \Gamma, \tag{13}$$

$$\frac{\partial u^+}{\partial n}(t) = q(t),\, t \in \Gamma, \tag{14}$$

on Γ, such that the effective conductivity functional λ_e possesses the maximal or minimal value.

Second type problem. Unbounded composite material.

$Q = \mathbb{C}$, thus the external boundary Γ is absent. Condition on Γ is replaced by certain condition at ∞. It is described by a single-valued analytic function $f(z)$ in $\mathbb{C}$, having isolated singularity at ∞.

The problem is to find a piece-wise smooth curve $L = \bigcup_{k=1}^{n} L_k$, having at most finite number of common points, and the potential u, satisfying the Laplace equation in D_k and in $D^+ = \mathbb{C} \setminus \bigcup_{k=1}^{n} \overline{D_k}$, which has the singularity of a prescribed type at ∞, and satisfies boundary condition (10) (or (11)) on L, such that the effective conductivity functional λ_e possesses the maximal or minimal value.

3.2 *The Schwarz boundary value problem for a pseudo-fractal domain*

One of the suitable methods for the study of 2D composite materials is the complex analytic approach. In the potential case the effective conductivity of the composite is described by the boundary value problems for harmonic or analytic function. We have to study the boundary value value problems (usually of mixed type) for multiply connected domains on the boundary of inclusions (and on the outer boundary of matrix if the composite is bounded). The model problem we start with is the so called Schwarz boundary value problem. The solvability of this problem was studied intensively. But the question of the exact analytic representation of the solution remains to be a difficult problem far from the finite description.

Among the investigations in this area we have to point out the work by Villat (1916, an analytic solution to the Schwarz problem for concentric annulus), Aksent'ev (1963-1967), Aleksandrov & Sorokin (1972), Mityushev (1985-1998). All these studies deal with multiply connected circular domains.

In our work we use the formula for the solution of the Schwarz problem for the multiply connected circular domains presented e.g. in [1].

This formula is a sum of certain series. Convergence of this series in the spaces of functions analytic on a bounded domains and continuous up to their boundaries was established earlier. Our main interest is in the description of components of this series in certain concrete cases.

Such aim follows from the possible applications of this construction. In particular, we use it in the study of the effective conductivity of composite materials having so called pseudo-fractal structure. Pseudo-fractal and fractal structures are of great importance for the composite materials with compound structure. The most investigated cases of composite materials of such a type are those periodic or doubly periodic (see e.g. contributions by Adler, Mityushev, Grigolyuk & Filshtinskii and others).

The problem we stated is based on the following ideas:

1) the most natural model for the composite with a compound structure could be a model which leads to the boundary value problem on a general infinitely connected domains. The theory of such problems is not too developed at the moment. Pseudo-fractals constitute a good approximation of the above said domains.

2) nowadays there are stated the problems of constructing composites for which the mixing is performed on the molecular level. It is known that such structure usually has the self-similarity property.

We consider on the complex plane $\mathbb{C}$ a multiply connected domain D whose boundary consists of a family of circles

$$|z| = \frac{1}{3}, \quad \left| z - 2\sum_{j=1}^{m} \frac{e^{\frac{\pi i}{3}k_j}}{3^j} \right| = \frac{1}{3^{m+1}}, \quad m \in \mathbb{N}.$$

This family has the self-similarity property (fractal structure). If we put $m = 1, 2, \dots, P$, where $P \in \mathbb{N}$ is a fixed positive integer number, then it is said that the considered family has the pseudo-fractal structure.

In our work [17] we construct an approximate solution to the Schwarz problem in a pseudo-fractal domain D. This problem is to find a function Ψ analytic in the domain D continuous up to the boundary of this domain, satisfying the boundary condition

$$\begin{cases} \mathrm{Re}\,\Psi(t) = q(t), \quad t \in \partial\, D, \\ \\ \mathrm{Im}\,\Psi(z_0) = 0, \end{cases} \tag{15}$$

where f is a given on $\partial\, D$ Hölder-continuous function, z_0 is a given point in D.

Solution to the problem (15) for multiply connected circular domains can be represented in the form of series in the Schottky group generated by symmetries with respect to the boundary curves. In our work we describe the structure of the group for the domain D. Its lower elements are given in the explicit form.

Similar problems for another types of fractal and pseudo-fractal domains were studied by Adler & Mityushev in connection with the calculation of the effective conductivity of composite materials possessing self-similarity property.

Let $\mathbb{D} \equiv \widehat{\mathbb{C}} \setminus \left(\bigcup\limits_{k=1}^{n} \mathrm{cl}\,\mathbb{D}_k \right)$ be a multiply connected circular domain, $\mathbb{D}_k \equiv \{z \in \mathbb{C} : |z - a_k| < r_k\}$. Let the following formula

$$z^*_{(k_m,k_{m-1},\dots,k_1)} = \left(z^*_{(k_{m-1},\dots,k_1)} \right)^*_{(k_m)} \tag{16}$$

be determined the successful symmetries with respect to the circles $\mathbb{T}_{k_1} = \partial\,\mathbb{D}_{k_1}, \dots, \mathbb{T}_{k_m} = \partial\,\mathbb{D}_{k_m}$. If in the sequence $k_m, k_{m-1}, \dots, k_1$ no two neighboring indexes are equal, then the number m is called a *level* of the mapping $z \mapsto z^*_{(k_m,k_{m-1},\dots,k_1)}$. If m is even then the corresponding mappings are simply Möbius transformations. If m is odd then the corresponding mappings are Möbius transformations with respect to $\overline{z}$. For each fixed domain $\mathbb{D}$ the family of successful symmetries generates so called Schottky group of symmetries $\mathcal{K}$. Denote by $\mathcal{G}$ the subgroup of all even elements of the group $\mathcal{K}$, and by $\mathcal{F}$ - the family of all elements of odd order (a conjugate class).

The solution $\Psi(z) \equiv \mathbf{T}(\mathbb{D}, \mathbf{q})(z)$ to the Schwarz problem (15) for a multiply connected circular domain $\mathbb{D} \equiv \widehat{\mathbb{C}} \setminus \left(\bigcup\limits_{k=1}^{n} \mathrm{cl}\,\mathbb{D}_k \right)$ can be represented in the form of series in the above described Schottky group (see [1, Thms. 4.11, 4.12]).

The series converge on each compact subset $\mathrm{cl}\,\mathbb{D} \setminus \{\infty\}$.

3.3 *Random composite materials*

We investigate also the effective conductivity of two-dimensional composite materials with the quasi periodic structure, i.e. it consists of periodically located cells occupied by a finite number of circular disjoint inclusions generating the quasi pseudofractal structure inside each cell. Under the quasi pseudofractal structure we understand a random “shaking” of inclusions about the pseudofractal array.

To study the effective conductivity of such composite we should average characteristics describing the material as a whole. This idea is realized by applying of the homogenization method [8].

The effective conductivity of composites with the pseudofractal structure was investigated by Adler and Mityushev [18], [19]. The “shaking” idea was first used by Berlyand and Mityushev and applied to circular inclusions which form the periodic square array [5]. In this paper we assume that the presented fundamental unit cell is divided into four parts each of which has the pseudofractal structure. We apply the “shaking” method to the given array, where each inclusion of certain level shakes in its own zone, the size of which proportionally depends on the level.

This approach is described in the papers [20], [21].

Acknowledgments

S.R. is grateful to organizers of the 1st International Conference DSL-2005, especially to Prof. J.J. de Almeida Grácio, for their hospitality during his stay at Aveiro.

The work is partially supported by the Belarusian Fund for Fundamental Scientific Research.

References

[1] Mityushev, V.V., Rogosin, S.V.: *Constructive Methods for Linear and Nonlinear Boundary Value Problems for Analytic Functions. Theory*

and Applications. Monograph and Surveys in Pure and Applied Mathematics, v. 108. Chapman & Hall / CRC, Boca Raton - London etc., 1999.

[2] Barbarosie, C.: Optimization of perforated domains through homogenezation. *Struct. Optim.* 14, pp. 225-231, 1997.

[3] Berdichevskij, V. L.: *Variational Principles of Continuum Mechanics.* Nauka, Moscow, 1983 (in Russian).

[4] Bergmann, D. J.: The dielectric constants of a composite material - a problem in classical physics. *Phys. Rep. C.* 43, pp. 377-407, 1978.

[5] Berlyand, L., Mityushev, V.: Generalized Clausius-Mossotti formula for random composite with circular fibers. *J. Statist. Phys.* 102, N 1/2, pp. 115-145, 2001.

[6] Buttazzo, G.: On the existence of minimizing domains for some shape optimization problem. *ESIAM: Proceedings.* Actes du 29ème Congrès d'Analyse Numerique: CANum'97. Paris. 3, pp. 51–64, 1998.

[7] Cherkaev, A. V.: *Variational Methods for Structural Optimization.* Springer Verlag, New York, 2000.

[8] Jikov, V. V., Kozlov, S. M. and Oleinik, O. A.: *Homogenization of Differential Operators and Integral Functionals.* Springer Verlag, Berlin, 1994.

[9] McPhedran, R. C., Milton, G. W. Transport properties of touching cylinder pairs and the square array of touching cylinders. *Proc. Roy. Math. Soc. London.* Ser. A. 411, pp. 313-326, 1987.

[10] Makaruk, S. F.: Mixed boundary value value problem for analytic functions with a free part of the boundary. *Proc. Inst. Math. (Minsk)*, 9, pp. 101-104, 2001 (in Russian).

[11] Makaruk, S. F.: Jump boundary value problem for a multiply connected domain with optimal location of internal domains. *Vesti of Academy of Sci. Belarus.* No. 3, pp. 26-29, 2003 (in Russian).

[12] Mityushev, V. V.: Transport properties of doubly periodic arrays of circular cylinders and optimal design problems. *Appl. Math. and Optimization.*, 44, pp. 17-31, 2001.

[13] Pobedrya, B. E.: *Mechanics of composite materials.* Moscow State Univ., Moscow, 1984 (in Russian).

[14] Slepyan, G. Ya., Maksimenko, S. A., Kalosha, V. P., Hoffmann, A. and Bimberg, D.: Effective boundary conditions for planar quantum dot structures. *Phys. Rev.* B. 64, p. 125326, 2001.

[15] Slepyan, G. Ya., Maksimenko, S. A., Hoffmann, A. and Bimberg, D.: Exitonic composites. *Advances in Electromagnetics of Complex Media and Metamaterials.* S. Zouhdi et al. (Eds.), Kluwer AP, Amsterdam, pp. 385-402, 2003.

[16] Sokolowski, J., Zolesio, J. P.: *Introduction to Shape Optimization.* Springer Verlag, Berlin, 1992.

[17] Dubatovskaya, M. V., Rogosin, S.V.: On an exact description of the Schottky group of symmetries. *Math. Modelling and Anal.* 9, No 1. pp. 32-46, 2004.

[18] Adler, P.M., Mityushev, V.V.,: Conductivity of a Sierpinski Carpet. *M*insk: Trudy Inst. Math. 9, pp. 7-15, 2001.

[19] Adler, P.M., Mityushev, V.V.: Schwarz Problem for Multiply Connected Domains and its Application to Diffusion Around Fractals. *C*omplex Variables. 47, No 4, pp. 303-324, 2002.

[20] Peseteskaya, E.V.: Effective conductivity of composite materials with random positions of cylindrical inclusions: finite number inclusions in the cell. *Proc. Inst. Math. (Minsk).* 12, No. 1, pp. 117-122, 2004.

[21] Peseteskaya, E.V.: Effective conductivity of composite materials with random position of circular inclusions of different radii. Finite number inclusions in the cell. *Applic. Anal.* pp. 1-23, 2005 (to appear).

Proceedings of The 1st International Conference on **D**iffusion in **S**olids and **L**iquids
DSL-2005, July 6-8, 2005, University of Aveiro, Aveiro, Portugal

DIFFUSION OF NANOPARTICLES IN GASES AND LIQUIDS

Valery RUDYAK[*], Aleksandr BELKIN, Serge KRASNOLUTSKII

Novosibirsk State University of Architecture and Civil Engineering,
630008, Novosibirsk, Leningradskaya, 113, Russia

[*]Corresponding author. Fax: +007 383 2664083; Email: rudyak@sibstrin.ru

---

Abstract

The present paper is devoted to a study of the nanoparticles relaxation and their diffusion in gases and liquids. It is shown that the interaction of a nanoparticle with a carrier fluid is collective in all cases. A molecule of the carrier rarefied gas interacts with all atoms of the nanoparticle. Such an interaction is described by the special potential [1]. In a condensed medium the nanoparticles relaxation is caused by the interaction with microfluctuations of the carrier fluid velocity and density. The results of molecular dynamics calculations are presented. The density, size and carrier fluid temperature dependences of the nanoparticles diffusion coefficient in a fluid are discussed.

Keywords: Multiphase systems; Diffusion coefficient; Nanoparticle; Kinetic Theory; Computer simulation

---

1 Introduction

Rapid development of nanotechnologies has defined the importance of the investigation of transport processes of nanoparticles in fluids. To control these processes it is necessary to study mechanisms of the velocity relaxation of nanoparticles in gases and liquids. There are some different approaches to describe the nanoparticles diffusion. On the one hand, it is believed, that the diffusion of nanoparticles may be described in the same manner as ordinary Brownian particles. On the other hand, attempts were made to describe the diffusion of nanoparticles using some kinetic theories, the modified Enskog theory for example.

Strictly speaking, there are no grounds to describe the diffusion of nanoparticles in either one of these ways. The nanoparticles size is of the order of hydrodynamic infinitesimal scale. Therefore we cannot use the hydrodynamic description. We cannot also apply the ordinary kinetic theory of gases because the molecule–particle interaction is collective one. The gas molecule interacts simultaneously with all atoms (or molecules) of the nanoparticle. Nanoparticles diameters range from the molecules diameters to the large dispersed particle ones. Therefore gas nano-suspensions (gas + nanoparticles) and nano-suspensions (liquid + nanoparticles) differ essentially from gas mixtures, ordinary gas suspensions and suspensions.

In the present paper the review of studying of the nanoparticles diffusion in fluids, received recently by the authors is made. The question of the relaxation mechanisms of nanoparticles is in detail considered. In particular, (i) diffusion of nanoparticles in rarefied, dense gases and in liquids is investigated, (ii) mechanisms of nanoparticle relaxation in the condensed medium are investigated, (iii) this paper present the molecular dynamics simulations data about the interaction processes of the nanoparticle and the carrier fluid microfluctuations, (iv) the diffusion coefficients of a nanoparticle in gases and liquids are discussed.

2 Kinetic theory of nanoparticles diffusion in rarefied gases

The small sizes of nanoparticles do not allow describing their motion in gases and liquids by the hydrodynamic methods. In rarefied gases the characteristic sizes of nanoparticles are much less than mean free path of a carrier gas molecules. One can show, that the dynamics of rarefied gas nanosuspensions is described by the system of the Boltzmann kinetic equations in this case [2–4]

$$\frac{\partial f_g}{\partial t} + \mathbf{v}_g \cdot \frac{\partial f_g}{\partial \mathbf{r}} = J_B^{gg} + J_B^{gp},$$

$$\frac{\partial f_p}{\partial t} + \mathbf{v}_p \cdot \frac{\partial f_p}{\partial \mathbf{r}} = J_B^{pp} + J_B^{pg}. \qquad (1)$$

Here, f_g and f_p are the distribution functions of the carrier gas molecules and the nanoparticles pseudo-gas respectively.

As was mentioned in the Introduction, the interaction of carrier gas molecules with a particle is collective, molecules interact simultaneously with all atoms (or molecules) of the particle. When such an interaction is described by the Lennard-Jones 6–12 potential the nanoparticle-molecule interaction is described well by the following pair potential [1,5]

$$\Phi(r) = \Phi_9(r) - \Phi_3(r)\,, \qquad (2)$$

$$\Phi_i(r) = C_i\left\{\left[(r-R)^{-i} - (r+R)^{-i}\right] - a_i\left[(r-R)^{-(i-1)} - (r+R)^{-(i-1)}\right]\right\}.$$

Here, $C_9 = 4\pi\varepsilon_{ij}\sigma_{ij}^{12}/(45V)$, $C_3 = 2\pi\varepsilon_{ij}\sigma_{ij}^{6}/(3V)$, $a_9 = 9/(8r)$, $a_3 = 3/(2r)$, V is the effective volume per molecule of a dispersed particle, ε_{ij} and σ_{ij} are the parameters of the Lennard-Jones 6-12 potential describing the interaction between molecules of the carrier gas and each molecule (atom) of the nanoparticle.

Solving Eqs. (1) by the ordinary Chapman-Enskog procedure [6] one can show that the diffusion coefficient of nanoparticles in rarefied gases is described by the following equation (in the first approximation of the expansion in the Sonin polynomials)

$$D = 3\sqrt{2\pi\alpha kT}\,/(16\,n\alpha\pi\,R^2\Omega_{ij}^{(1,1)*})\,, \qquad (3)$$

where m, M denote masses of gas molecule and nanoparticle respectively, n is the density of carrier gas, T is the temperature, $\Omega_{nm}^{(i,j)*}$ are Ω-integrals which are calculated by the equation (2). As a result we studied the dependence of diffusion coefficient on the particle size and carrier gas temperature. It was shown [5, 7, 8] that the dependence of the nanoparticle diffusion coefficient calculated by means of kinetic theory on a particle radius is well coincided with different experimental data in all range of nanoparticle sizes (see Fig. 1). The nanoparticle diffusion is described neither the Einstein–Langevin theory, nor the well known Cunningham–Millican–Davies (CMD) experimental correlation. The essential difference between the CMD–correlation and data of our kinetic theory is appeared in range of small values of the nanoparticle diameters d < 10 nm. This difference can exceed 100% (see Fig. 1). The traditional methods of the diffusion coefficient and sizes measurement in gases (DMA–method, diffusion battery etc.) lead to the systematic errors if the CMD–correlation is used for the interpretation of experimental data.

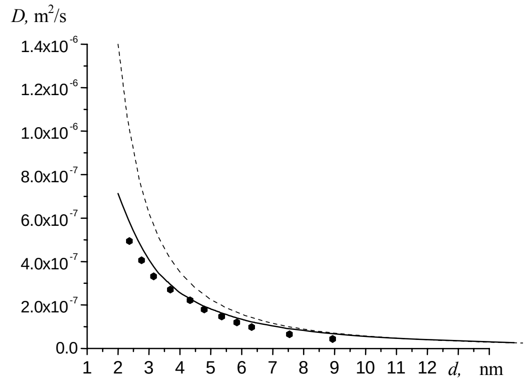

Figure 1: Diffusion coefficients *D* of the particle *AlO* in *N* vs. nanoparticle diameter *d*. The solid line is our theory, the dotted line is the CMD-correlation, and black points are the experimental values [7].

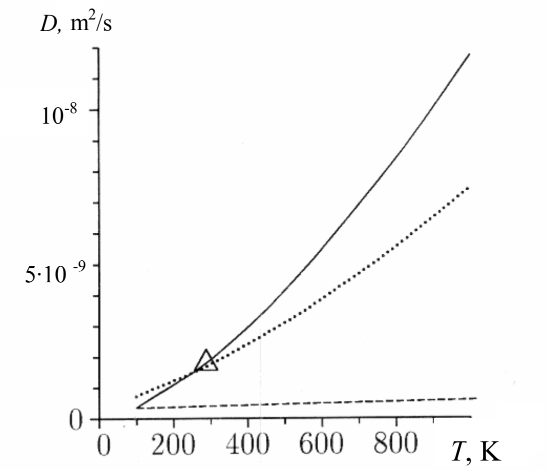

Figure 2: Diffusion coefficient of condensation kernels vs. carrier gas temperature *T*. The solid line is our theory, the dotted line is the CMD-correlation, the dashed line is the Einstein theory, and the triangle point is the experimental data [9].

Note that the diffusion coefficient of nanoparticles (in contrast to the Browinian particles), essentially depends on the temperature of the carrier medium. The CMD–correlation does not describe this dependence (see Fig. 2).

3 Mechanisms of a nanoparticle relaxation in a condensed media

There are no kinetic equations for the description of nanoparticles dynamics in dense gases and liquids because the characteristic size of the particle is comparable with the mean free path of a carrier medium molecule. In this case the particle interacts simultaneously with many molecules of a medium. Moreover, it's impossible here to deduce the kinetic equation for the one-particle distribution functions [4]. In this situation it is naturally to use the molecular dynamics method for the studying of the dynamics of heterogeneous system with nanoparticles. The brief review of received here results would be submitted in this section.

We used the hard spheres law for the simulation of an interaction of the nanoparticle with carrier fluid molecules. The diameter of the nanoparticle was equal $d = \sigma \div 5\sigma$, the mass relation ranged from $M = m$ to $M = 300m$ (here σ is the diameter of a carrier fluid molecule, m is their mass). The ordinary molecular dynamics method algorithm was used. The cubic cell contained N molecules and one nanoparticle. The density of this medium was defined by the parameter $\alpha = \left(V - V_p\right)/V_0$, here V is the cell volume, V_p is the nanoparticle volume, $V_0 = N\sigma^3/\sqrt{2}$ is the close-packed volume of molecules. Parameter α was varied from 1.5 to 80.0. The periodic boundary conditions are used to compensate the finite molecules number.

The diffusion coefficient of a nanoparticle is related to its velocity autocorrelation function (VAF) by the Kubo formula

$$D = \frac{1}{3}\int_0^\infty dt\,\chi(0,t). \tag{4}$$

Therefore in order to investigate the diffusion of a nanoparticle it is necessary to study the evolution of the VAF, which was calculated by the formula

$$\chi = \frac{1}{KN}\sum_{i=1}^{N}\mathbf{V}(i\Delta t)\mathbf{V}(t + i\Delta t),$$

where $\mathbf{V}$ is the velocity of a nanoparticle, and K is the number of realisation.

The molecular dynamics calculations have shown, that this function is described well by the sum of two exponents [10]

$$\chi_{\mathrm{vv}} = b_1 \exp(-t/\tau_1) + b_2 \exp(-t/\tau_2)\,. \tag{5}$$

Here $\tau_{1,2}$ are some relaxation times and $b_{1,2}$ are some coefficients. It was shown that the processes of relaxation of a nanoparticle velocity in equilibrium or nonequilibrium conditions are identical [11]. The function (5) has two different branches. One can call the first the "kinetic branch". The respective relaxation time τ_1 is well described by the kinetic theory of dense gas (precisely, by the modified Enskog theory). This time increases almost linearly with the increases of the nanoparticle mass M up to the values of $M/m \sim 50$, and then this rate slows down. This factor is affected by the fact that the individual interactions with molecules cannot change appreciably the behaviour of the nanoparticles relaxation when $M/m \sim 50$.

The second branch of the VAF relaxation is caused by the interaction of nanoparticle with the nonequilibrium microfluctuations of density and momentum of a carrier fluid which particle generates at moving in the molecular medium.

To study the influence of the nanoparticle motion on the velocity distribution of carrier fluid molecules we investigated the behaviour of the space-time correlation function [12]

$$\psi(t,r) = \left[\mathbf{V}(0)\cdot\sum_{i=1}^{N}\mathbf{v}_i(t,r)\right]\left(N < \mathrm{V} >< \mathrm{v} >\right)^{-1}, \tag{6}$$

where r is the distance from the nanoparticle to the i-th molecule, $\mathbf{v}_i$, $< \mathrm{v} >$ are the velocities of carrier gas molecule and its average velocity respectively. The typical behaviour of the function (6) is shown in Fig. 3 (here $d = 4\sigma$ and $M = 100m$, the time is measured in molecular mean free path times, and the distance is measured in molecular radii). The function (6) has two maximums; the velocity of the first maximum propagation coincides with sound velocity in the fluid. A decrease in nanoparticle mass results in a decrease of the second maximum. Therefore the nanoparticle generates in a carrier fluid the sound wave, which creates the local fluctuations of the density and the velocity of molecules. The perturbed medium molecules transmit the disturbance to enclosing molecules and interact with the particle again. This is the reason of the second maximum of the correlation function in Fig. 3.

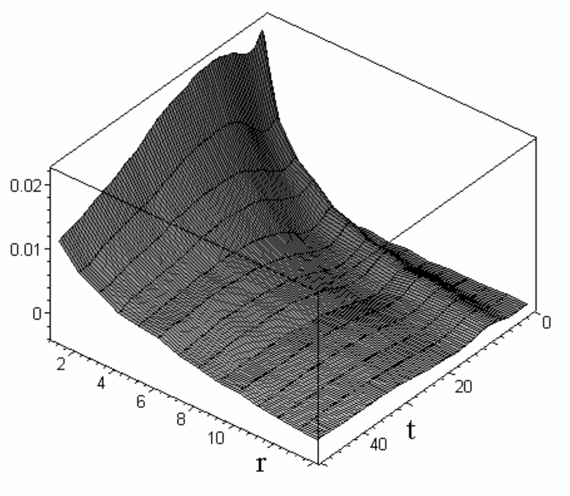

Figure 3: The space-time correlation function of a nanoparticle.

The dynamics of nanoparticles is described by the general Langevin equation

$$\dot{\mathbf{V}} = -\frac{1}{MkT}\int_0^t d\tau \chi_{ff}(\tau)\mathbf{V}(t-\tau) + \mathbf{f}(t),$$

where χ_{ff} is the autocorrelation function of force $\mathbf{f}$ acting on nanoparticle. One can show that this function is described by the following function

$$\chi_{ff}(t) = D\,\delta(t) + a\exp(-\beta t) \qquad (7)$$

when VAF has the form (5). The second term in Eq. (7) is caused by interaction of nanoparticle with microfluctuations of the velocity and the density of a carrier fluid.

The nanoparticle-molecules velocity correlations are small enough. However their relaxation time is of the order of a dozen of the mean free path time of carrying medium molecules. Namely these correlations affect the long-time "tails" of the VAF of nanoparticles. These processes bring therefore the essential contribution to the transport coefficients of nanoparticles in liquids and dense gases.

4 Diffusion coefficients of nanoparticles in dense gases and liquids

The diffusion coefficient *D* was determined by the VAF of nanoparticle using relation (4). Obtained data are given in Table 1, here α=4.8. The values of diffusion coefficient D_k received by the modified Enskog theory (actually it is semi-empirical correlation) are given here for comparison. The Einstein diffusion coefficient D_E is independent on the particle mass.

Table 1: Diffusion coefficients of nanoparticles.

M/m	1	10	50	100	300
D/D_E	1.20	0.94	0.95	0.96	0.96
D_k/D_E	0.67	0.50	0.49	0.49	0.49

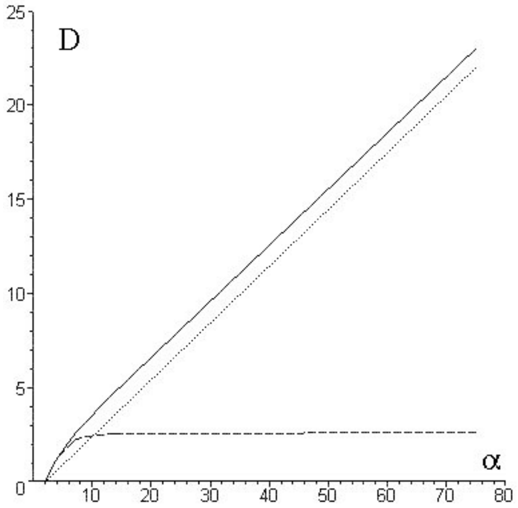

Figure 4: The dependence of the diffusion coefficients of a nanoparticle on α: D_E (dotted curve), D_h (dashed curve), D(solid curve).

The Enskog diffusion coefficient is almost always twice lower than the calculated value. There is a simple explanation of this fact. The kinetic and Einstein relaxation mechanisms are two limiting cases with essentially different relaxation times. The one more intermediate characteristic relaxation time appears in nanodispersed systems. Namely the relaxation processes connected with this time gives the basic contribution to the diffusion coefficient of nanoparticles. Probably there is one more diffusion relaxation process determining the behaviour of long-time "tails" of VAF, whose time evolution is described by the $t^{-3/2}$ law. However its contribution to the diffusion coefficient is very small.

In contrast to the Einstein diffusion coefficient, which is almost independent of the carrier fluid density at α>20, the diffusion coefficient of nanoparticles increases linearly with parameter α when the density decreases (Fig. 4).

5 Influence of the rotational degrees of freedom.

Molecules and nanoparticles have rotational degrees of freedom in real liquids, which can be described by the classical mechanics at the ordinary temperature. It's clear, that this property can change the values of the diffusion coefficient. To take into account the influence of the rotational degrees of freedom we use the model of rough hard spheres [6]. The test calculations have shown, that the molecular dynamics method allows studying diffusion even in such complex liquid as benzene for this model [13].

The dependence of the self-diffusion coefficient on density parameter $\xi = \pi n d^3 / 6$ for elastic smooth and rough spheres shown in Fig. 5. Here n is the numerical density of a fluid. The curve 1 corresponds to the elastic smooth spheres; square labels are obtained for the rough spheres. The calculation were performed for $k = 4I / md^2 = \; = 0.4$, where I is the moment of inertia of molecule. We see that these results diverge systematically at high system densities ($\xi > 0.15$). Observable reduction of the self-diffusion coefficient of rough spheres compared with that of smooth spheres is caused by negative 'tail' of VAF for rough spheres at $\alpha \le 2$. The rough spheres are more correlated than the smooth ones

Note, that our results submitted in Fig. 5 are described well by the following correlation (the curve 2 in Fig. 5)

$$D / D_k = 1 + 1.14468\xi + 1.04802\xi^2 - 11.37528\xi^3 .$$

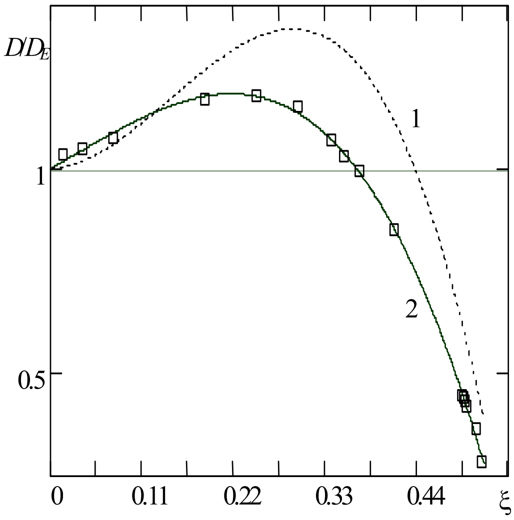

Figure 5: The dependence of the self-diffusion coefficient on density for the elastic smooth and the rough spheres.

6 Conclusion

The nanoparticles size is of the order of $1 \div 100$ nm. Clusters, fullerenes, and large organic molecules can be usually considered as such particles. They occupy the intermediate position between ordinary molecules and large disperse particles. Such a position determines the new, yet not investigated physics of their behavior in gases and liquids. Now it is possible to establish, that the basic mechanisms of the nanoparticles relaxation and their transport in gases and liquids became clear. Below we summarize briefly main received results.

- The Boltzmann kinetic theory with the pair particle-molecule potential (2) has been proved to describe well the transport processes of nanoparticles in rarefied gases.
- The dynamics of a nanoparticle has been proved to differ essentially from the dynamics of the Brownian particles in liquids. We cannot use the hydrodynamic methods for the description of their transport processes in fluid.
- The nanoparticle diffusion is described neither the Einstein–Langevin theory, nor well known CMD experimental correlation The essential difference between the CMD–correlation and the data of our kinetic theory is appeared in range of small values of diameters (d < 10 nm). This difference can exceed 100%.

- The traditional methods of measurement of the diffusion coefficient and the diameter of nanoparticles in gases (DMA–method, diffusion battery etc.) lead to the systematic errors if CMD–correlation is used.
- The diffusion coefficient of nanoparticles (in contrast to the Browinian particles), depends essentially on the temperature of the medium.
- The relaxation of a nanoparticle in the condensed medium is caused by its interaction with microfluctuations of fluid density and velocity fields which the particle generates at movement. The velocity of the generating disturbances propagation is of the order of the velocity of sound of a carrier fluid.

Acknowledgments

This work was supported in part by the Russian Foundation for Basic Researches (grant No. 04-01-00106) and the grant of the President of the Russian Federation for Support of Leading Scientific Schools (project No. NSh-964.2003.1).

References

[1] Rudyak V. Ya., Krasnolutskii S. L. The interaction potential of dispersed particles with carrier gas molecules. *Proceedings of the XXI Intern. Symp. on Rarefied Gas Dynamics.* Gépadués-Éditions, Toulouse, Vol. 1, pp. 263–270, 1999.

[2] Rudyak V.Ya. Kinetic description of rarefied finely dispersed gas suspension. *Sov. Tech. Phys. Lett.* Vol. 18, No. 10, pp. 681–682, 1992.

[3] Gladkov M. Yu., Rudyak V.Ya. Kinetic equations for a highly dispersed gas suspension *Tech. Phys,* Vol. 39, No. 4, pp. 441–443, 1994.

[4] Rudyak V. Ya. The kinetic equation of rarefied gas suspensions. *Proceedings of the XXI Intern. Symp. on Rarefied Gas Dynamics.* Gépadués-Éditions, Toulouse, Vol. 1, pp. 271–278, 1999.

[5] Rudyak V.Ya., Krasnolutskii S.L. Diffusion of nanoparticles in a rarefied gas. *Technical Phys.*, Vol. 47, No. 7, pp. 807–813, 2002.

[6] Chapman S. and Couling T.G. *The mathematical theory of non-uniform gases.* Cambridge, Cambridge Univ., 1952.

[7] Rudyak V.Ya., Krasnolutskii S.L. Kinetic description of nanoparticle diffusion in rarefied gas. *Doklady Physics*, Vol. 46 No. 12, pp. 897–899, 2001.

[8] Rudyak V.Ya., Krasnolutskii S.L., Nasibulin A.G., Kauppinen E.I. Methods of measuring of the diffusion coefficient and sizes of nanoparticles in a rarefied gas. *Doklady Physics*, Vol. 47, No. 10, pp. 758–761, 2002.

[9] Nolan J.J., Guerrini V.H. The determination of the mass and size of atmospheric condensation nuclei. *Trans. Faraday Soc.,* Vol. 32, pp. 1175–1179, 1936.

[10] Rudyak V.Ya., Kharlamov G.V., Belkin A.A. Diffusion of nanoparticles and macromolecues in dense gases and liquids. *Hihg Temperature*, Vol. 39, No. 2, pp. 264–271, 2001.

[11] Rudyak V.Ya., Belkin A.A. Nanoparticle velocity relaxation in a condensed carrying medium. *Tech. Phys. Lett,* Vol. 29, No. 7, pp. 560–562, 2003.

[12] Rudyak V.Ya., Belkin A.A. Mechanisms of collective nanoparticles interation with a condensed solvent. *Thermophysics and Aeromechanics,* Vol. 11, No. 2, pp. 243–252, 2004.

[13] Dubrovin A.A., Rudyak V.Ya., Kharlamov G.V. Simulation of molecular diffusion in liquids taking into account rotational degrees of freedom. *Russian J. Phys. Chem.,* Vol. 76, No. 5, pp. 767–772, 2002.

Proceedings of The 1st International Conference on **D**iffusion in **S**olids and **L**iquids
DSL-2005, July 6-8, 2005, University of Aveiro, Aveiro, Portugal

APPLICATION OF TRITIUM RADIOLUMINOGRAPHY TO THE DETECTION OF HYDROGEN DIFFUSION IN Ti-Cr ALLOY

Hideyuki SAITOH[1,*], Hirofumi HOMMA[1,2]

[1]Department of Materials Science and Engineering, Muroran Institute of Technology,
27-1 Mizumoto, Muroran 050-8585, Japan
[2]Present Address: Hydrogen Isotope Research Center, Toyama University,
3190 Gofuku, Toyama 930-8555, Japan

[*]Corresponding author. Fax: +81 143 46 5654; Email: saitoh@mmm.muroran-it.ac.jp

Abstract

Tritium radioluminography has been applied to determine the hydrogen diffusion coefficient in $Ti_{50}Cr_{50}$ and $Ti_{40}Cr_{60}$ alloys with two-phase structure of BCC phase and Laves phase. By the radioluminography, hydrogen distribution in them has been observed and hydrogen penetration profile has been measured. The tritium diffusion coefficients in the $Ti_{50}Cr_{50}$ and $Ti_{40}Cr_{60}$ alloys have been successfully determined by analysing the tritium penetration profiles to be 3.3×10^{-12} m^2/s and 1.3×10^{-12} m^2/s, respectively. These values suggest that the hydrogen diffusion in the Laves phase is slower than that in the BCC phase. It is also suggested that hydrogen diffuses by short-circuiting diffusion through the interface between BCC phase and Laves phase.

Keywords: Experimental method; Hydrogen diffusion coefficient; Tritium radioluminography; Laves phase

1 Introduction

Tritium radioluminography [1] is a useful technique to visualize hydrogen distribution in materials. In this method, imaging plate (IP) is used as a detector for tritium because of its higher sensitivity and wide dynamic range for radiation rays [2,3]. In our previous works, we performed a quantitative observation of hydrogen distribution in pure vanadium [1,4], vanadium based alloys [5-8] and Ti-Cr alloy [9,10] by the tritium radioluminography, and showed the effect of microstructure or constituent element on the tritium distribution in these materials. In one of the above experiments, we performed a cross sectional observation of hydrogen in the V-5 mass%Fe alloy [6], and obtained a concentration profile in equilibrium distribution due to the higher hydrogen diffusivity in it. This result suggests that if the hydrogen diffusion in an alloy system is slower to obtain a gradually decreased concentration profile by using the tritium radioluminography, it is possible to determine the hydrogen diffusion coefficient by analyzing the concentration profile.

In a Ti-Cr system, hydrogenation property was investigated for the $TiCr_2$ Laves phase with C14 type or C15 type structure [11,12] and Ti-Cr alloy with BCC structure [13]. We examined a relation between the hydrogen distribution and the microstructure in them by the tritium radioluminography [9]. In this experiment, hydrogen diffusion seems to be slow in comparison with the vanadium alloys. Thus, in the present work, we intend to apply the tritium radioluminography to obtain a hydrogen diffusion coefficient in the Ti-Cr binary alloys with BCC phase and Laves phase.

2 Experimental Procedure

$Ti_{50}Cr_{50}$ and $Ti_{40}Cr_{60}$ alloys in nominal composition were prepared by arc-melting titanium (99.9%) and chromium (99.9%) in high purity argon atmosphere, and were cut to make rectangular block specimens 5 mm × 5 mm × 10 mm in size. Hydrogen (protium and tritium) addition into the specimen was performed by an electrochemical cathodic charging method at room temperature. The electrolyte was 0.1 $kmol/m^3$ NaOH aqueous solution containing tritium of 1.9 PBq/m^3. The current density and charging period were 400 A/m^2 and 4 h, respectively. Before hydrogen addition, the specimens were covered with epoxy resin except for the hydrogen added surface. The hydrogen added specimens were kept at room temperature for 24 h, and were cut along the long transverse direction, which is the hydrogen diffusion direction, to observe a cross sectional distribution of tritium. Then the specimens were put on an IP, Fujix TR2040, and the radioactivity of the tritium recorded in the IP was measured by means of an IP-reader (Fujix FDL5000) as the intensity of photo-stimulated luminescence (PSL). The detail of the quantitative analysis of the surface tritium concentration was described elsewhere [4]. The PSL intensity was repeatedly measured in every 24 h to examine the time dependence of cross-sectional distribution of tritium. After the radioluminography, tritium concentration profile along the diffusion direction was measured and diffusion coefficient was determined.

3 Results and Discussion

Figure 1 (a) and (b) show X-ray diffraction profiles of the $Ti_{50}Cr_{50}$ and $Ti_{40}Cr_{60}$ specimen, respectively. Both specimens consist of BCC phase and C-14 type Laves phase. The ratio of the amount of the Laves phase to the BCC phase in the $Ti_{40}Cr_{60}$ specimen is higher than that in the $Ti_{50}Cr_{50}$ specimen.

Figure 2 (a) shows a tritium radioluminograph of the $Ti_{50}Cr_{50}$ specimen three days passed at room temperature after the hydrogen addition, cross-sectional tritium distribution being observed. In this figure, white contrast means higher hydrogen concentration as indicated by a scale bar. The hydrogen concentration is higher at the left hand side (hydrogen added surface) and gradually decreases to the right hand side of the specimen. This shows that the tritium penetrates into the interior of the specimen. Fig. 2 (b) show a cross-sectional tritium distribution in the $Ti_{50}Cr_{50}$ specimen nine days passed after the hydrogen addition, indicating that hydrogen penetrates more deeper into the specimen. Fig. 2 (c) shows concentration profiles of tritium in the specimens three and nine days passed after the hydrogen addition. The concentration profiles show Gaussian-like curves. However, the concentration profiles slightly deviate downward from the Gaussian curve near the hydrogen added surface of the nine days passed specimen. This is thought to be attributed that the hydrogen existed near the surface escapes to the outside the specimen.

Figure 3 (a) and (b) show cross-sectional tritium distributions of the $Ti_{40}Cr_{60}$ specimen three days and nine days passed after the hydrogen addition, respectively. These figure show that hydrogen penetrates from the hydrogen added surface to the interior of the specimen, and the penetrate distance increases as the increase of diffusion time. However, hydrogen penetration distance in the $Ti_{40}Cr_{60}$ specimen is not so longer compared with that in the $Ti_{50}Cr_{50}$ specimen. This suggests that the hydrogen diffusion in the $Ti_{40}Cr_{60}$ specimen is slower than the $Ti_{50}Cr_{50}$ specimen.

For one-dimensional volume diffusion of a tracer from an infinitesimally thin surface layer into a sufficiently long rod, a solution of Fick's second law is given by [14]

$$C_T(X,t) = \left[M/\sqrt{\pi D t}\right]\exp\left(-X^2/4Dt\right) \qquad (1)$$

where $C_T(X, t)$ is the concentration at the distance X from the surface after the diffusion time t, D the diffusion coefficient and M the total amount of the tracer before diffusion. Therefore, we can obtain a diffusion coefficient from the gradient of the $\ln C_T$ vs. X^2 plots. Fig. 2 (d) and Fig. 3 (d) show

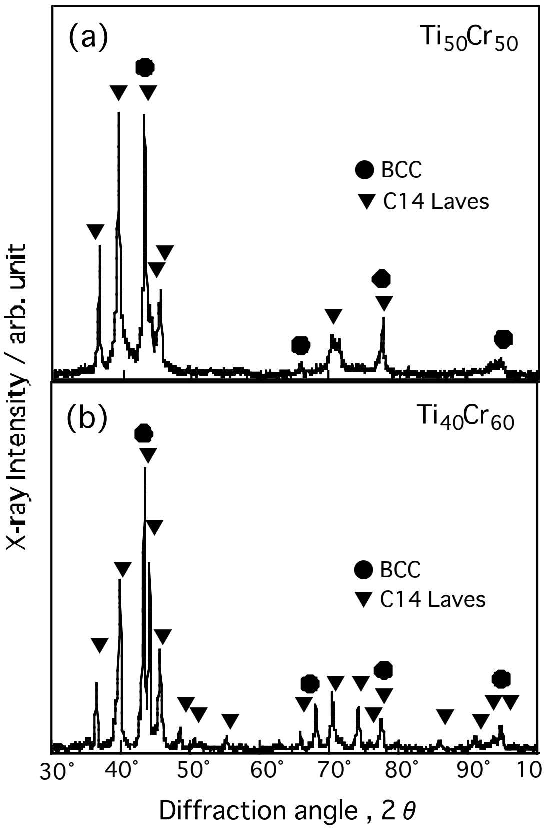

Figure 1: X-ray diffraction profiles of as-cast specimens. (a) $Ti_{50}Cr_{50}$ specimen, (b) $Ti_{50}Cr_{50}$ specimen.

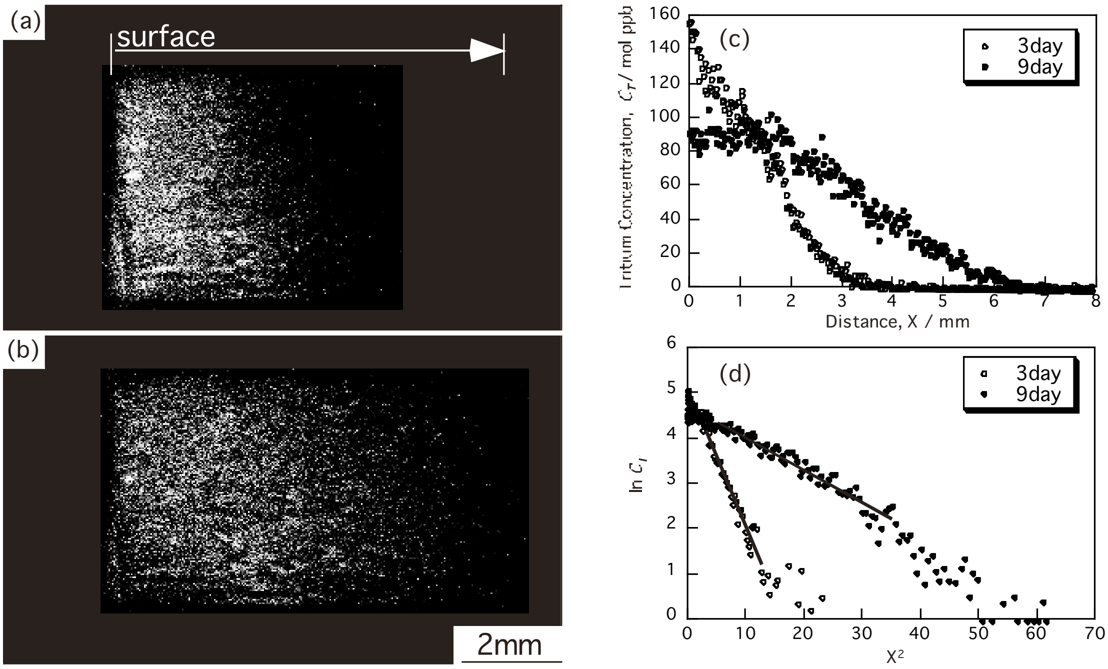

Figure 2 : Tritium radioluminographs of $Ti_{50}Cr_{50}$ as-cast specimen, (a) three days and (b) nine days passed after tritium addition. (c) tritium concentration profiles on the cross-section of (a) and (b). (d) $\ln C_T$ (X, t) vs. X^2 plots of (c).

$\ln C_T$ vs. X^2 plots for the $Ti_{50}Cr_{50}$ and $Ti_{40}Cr_{60}$ specimen, respectively, of the three days and nine days diffusion period. In these figures, the three regions are recognized, that is, the region that is affected by the backward diffusion near the hydrogen added surface, the region of volume diffusion and the region which is dropped to background. We use the region of volume diffusion for calculation of hydrogen diffusion coefficient. Both in Fig. 2 (d) and Fig. 3 (d), the $\ln C_T$ vs. X^2 plots shows linearity, indicating the eq. (1) hold. From the slopes of the plots, tritium diffusion coefficients are determined. For the $Ti_{50}Cr_{50}$ specimen, tritium diffusion coefficients are 3.3×10^{-12} m^2/s and 5.1×10^{-12} m^2/s for three days and nine days of diffusion periods, respectively. As the same way, tritium diffusion coefficients in the $Ti_{40}Cr_{60}$ alloy are determined to be 1.3×10^{-12} m^2/s and 1.7×10^{-12} m^2/s for the three days and nine days of diffusion periods, respectively. It is found that the diffusion coefficient in the $Ti_{40}Cr_{60}$ alloy is smaller than that in the $Ti_{50}Cr_{50}$ alloy.

These specimens are two-phase mixture of BCC phase and Laves phase with C14 type structure, and that the amount of Laves phase in the $Ti_{40}Cr_{60}$ alloy is larger than in the $Ti_{50}Cr_{50}$ alloy, as mentioned above. The present tritium diffusion coefficient in the $Ti_{40}Cr_{60}$ alloy is smaller than that in the $Ti_{50}Cr_{50}$ alloy, that is, the tritium diffusion coefficient decreases with increasing the amount of Laves phase. Therefore, we conclude that the hydrogen diffusion in the Laves phase is slower than that in the BCC phase.

Finally, we examined an effect of heat treatment on hydrogen diffusion. The specimens were heat treated at 1573 K for 8 h and then water quenched. It is expected by this heat treatment that the ratio of the BCC phase increases and the microstructure develops. The tritium diffusion coefficients of the heat treated specimens are determined to be 2.1×10^{-12} m^2/s for $Ti_{50}Cr_{50}$ alloy and 1.0×10^{-12} m^2/s for $Ti_{40}Cr_{60}$ alloy. Both values are slightly smaller than that obtained from the specimen without heat treatment. The diffusion coefficient decreases by the heat treatment. This means that the hydrogen diffusion coefficient decreases when the specimen has coarse microstructure. This seems to be attributed to the short-circuiting diffusion of hydrogen in the boundary region between the BCC phase and the Laves phase.

4 Conclusion

Tritium radioluminography was applied to examine hydrogen diffusion in Ti-Cr alloys with two-phase structure of BCC phase and Laves

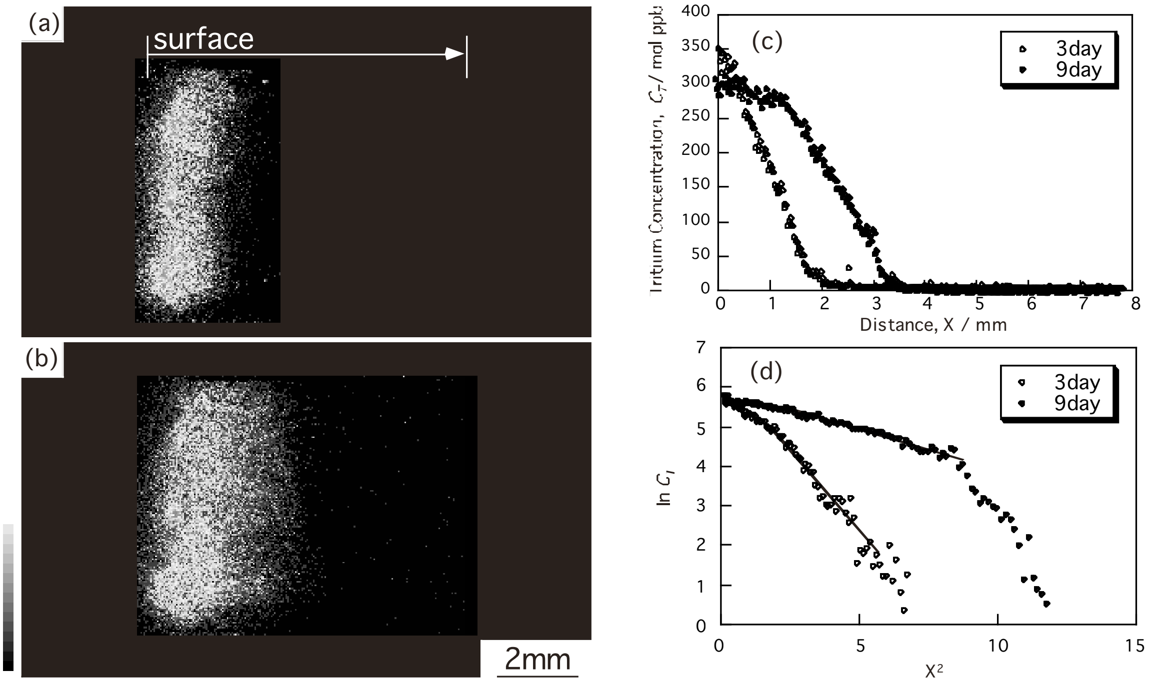

Figure 3 : Tritium radioluminographs of $Ti_{40}Cr_{60}$ as-cast specimen, (a) three days and (b) nine days passed after tritium addition. (c) tritium concentration profiles on the cross-section of (a) and (b). (d) lnC_T (X, t) vs. X^2 plots of (c).

phase. It is shown that the tritium radioluminography can be applicable to determine the tritium diffusion coefficient. From the cross sectional observation of hydrogen distribution, hydrogen concentration profile was measured and the hydrogen diffusion coefficient was obtained. The determined tritium diffusion coefficients in the $Ti_{40}Cr_{60}$ and $Ti_{50}Cr_{50}$ alloys were determined to be 3.3×10^{-12} m^2/s and 1.3×10^{-12} m^2/s, respectively, suggesting that the hydrogen diffusion in the Laves phase is slower than that in the BCC phase. These diffusion coefficients decreased by the heat treatment.

Acknowledgement

This work was supported by a Grant-in-Aid for Scientific Research (B) 15360360 from the ministry of Education, Culture, Sports, Science and Technology of Japan.

References

[1] Saitoh, H., Hishi, T., Misawa, T., Ohnishi, T., Noya, Y., Matsuzaki, T., Watanabe, T. : *J. Nucl. Mater.* 258-263, pp.1404-1408, 1998.

[2] Miyahara, J., Takahashi, K., Amemiya, Y., Kamiya, N., Satou, Y. : *Nucl. Instrum. Methods*, A246, pp.572-578, 1986.

[3] *BAS Technical Information* No.2, Fuji Photo Film Co. Ltd., Bio-Imaging Analyzer Group.

[4] Saitoh, H., Misawa, T., Noya, Y., Ohnishi, T. : *Mater. Trans. JIM*, 40, pp.692-695, 1999.

[5] Homma, H., Saitoh, H., Misawa, T., Ohnishi, T. : *Mater. Trans.*, 43, pp.1111-1114, 2002.

[6] Saitoh, H., Homma, H., Noya, Y., Ohnishi, T. : *Fusion Science and Technology*, 41, pp.536-541, 2002.

[7] H. Saitoh, H. Homma, T. Misawa and T. Ohnishi : *Mater. Trans.*, 42, pp.399-402, 2001.

[8] Homma, H., Saitoh, H., Misawa, T., Ohnishi, T. : *Mater. Trans.*, 43, pp.451-454, 2002.

[9] Homma, H., Saitoh, H., Kamegawa, A., Okada, M. : *Mater. Trans.*, 43, pp.2741-2747, 2002.

[10] Saitoh, H., Homma, H. : *Materials Science Forum*, 475-479, pp.2513-2516, 2005.

[11] Johnson, J.R., Reilly, J.J. : *Inorg. Chem.*, 17, pp.3103-3108, 1978.

[12] Kabutomori, T., Tanaka, H., Wakisaka, Y. Ohnishi, K. : *J. Alloys and Compounds*, 231, pp.528-532, 1995.

[13] Okada, M., Chou, T., Kamegawa, A., Tamura, T., Takamura, H., Matsukawa, A., Yamashita, S. : *J. Alloys and Compounds*, 356-357, pp.480-485, 2003.

[14] Crank, J. : *The Mathematics of Diffusion*, Clarendon Press, Oxford, 1975.

Proceedings of The 1st International Conference on **D**iffusion in **S**olids and **L**iquids
DSL-2005, July 6-8, 2005, University of Aveiro, Aveiro, Portugal

ADHESION PROCESS AT THE PHASE BOUNDARIES OF POLYMER/MTAL LAYERS - APPLICATION IN BONDLINE AND ELECTRO CORROSION

ALUMINIUM VAPOUR COATING OF POLYMER SURFACES-BAYBLEND

Eduardo H. SCHINDEL-BIDINELLI

Swibotech GmbH-Swiss Bonding,President
Swibotech GmbH, P.O.Box 35,CH-8180 Bülach/ZH Switzerland

Fax: +49 (0)7633-923-3561; Email: swissbonding-schindel@t-online.de

Abstract

Industries such as electro-engineering, electronics and microelectronics fields experience an amalgamation of application technique and the chemistry of adhesives and coatings. Conventional application technique are now becoming miniaturized as high-tech procedures classical backbone polymers are linked to adduct in order to improve the properties of final product, allowing entirely new application. Electrically conducting polymers are now breaking previous limits in contact corrosion.
However, the ageing of these new electrically conducting adhesives has been largely ignorised. The system is referred to as bondline corrosion / electro corrosion and involved a conducting alloy vapour coated surface with gold contact using silver filled epoxies and acrylates.The results clearly show the great risk of electro and bondline corrosion on vapored metal surfaces such as copper, aluminium and silver.

Introduction

For decades transformers have been polymer-dipped for protection. A whole array of new adhesives have been introduced to the field of electronics- electrically and thermally conducting as well as insulating adhesives applied in high tech industries. Adhesives technologies are focussing on the interactions of research, methodology, project scheming, applications techniques and the requirement profiles of the adhesives. Adhesives which are currently in usage are based on epoxies, polyesters, methylmethacrylates, diacrylates, polyurethane, silicones and cyanoacrylates; they are either warm-cold or IR-UV cured and either one ore two components formulations. The contents of this presentation is to illustrate a widely unknown case of the failing of a conductive adhesion joints on the base of ageing processes. It is not yet clear whether bondline or electro - corrosion trigger the destruction of the bond. The evaluation of the failure behaviour is expressed as composite fracture. Firstly, we accounter a failure of adhesion as separation at the interfaces of the two materials. High and low temperature storage had no negative effects on the adhesives joints. Modifications of surfaces resistance were insignificant. The humidity and weather- ability test revealed an increase of the surface resistance for both types of adhesives. Humidity storage was interrupted after 270 days, because the electrical resistance had reached values in the k-ohm-domain and because visually detectable, small black polymer beads had formed, i.e. perforation of the conduction layer. Acrylate showed a lower degree of corrosiveness than epoxy adhesives. The onset of corrosion and the increase of electrical resistance were lower.

For same storage times was shown that different mechanisms of corrosion were acting in acrylate and epoxy adhesives. The results clearly show the risks of electro- and bondline corrosion. An investigation of the QS-problem audit was carried out on the failure of deflection of leakage currents. Optical changes and technically measurable modifications were only detectable after nine months. It can be concluded that quality assessment programs as well as constant control of ageing processes of novel adhesives joints are inevitable in the electronics fields if one wants to avoid quality deficiencies and failure.

Function of Adhesion and State of the Art

Function of adhesives in the electronic industry

How and in which other domains can adhesives be employed other than for joining two materials

Function for adhesives

-joint formation, hard or elastic
-thermal conductivity, supply or deflection of heat
-thermal insulation
-electric conductivity, low-Ohmage or high-Ohmage
-electric insulation, dielectric features
-transparency, opacity, colour
-all resistance, ageing, humidity, UV-radiation, strong radiation, chemicals
-supreme electric features over long period
-dielectric loss factors, dielectric strength
-unchanging resistance, corrosion resistance

Adhesives can be employed for temporary (mounting aids for SMD) or permanent junction. Adhesives are being employed in the rapidly developing fields of electronics, electro-engineering, SMD technique, in-line assembly, encapsulation.

Adhesives for these purposes should be designed to fulfil the necessary requirements. Large quantity production, high productivity, high precision, joining conducting materials.

Compilling a requierement profile determing factors

1. Function of adhesion, state of the art
2. Combination of materials
3. Adhesive thickness
4. Room conditions/pretreatments
5. Static profile/testing criteria
6. Adhesive selection/ data sheets
7. Adhesive application
8. Adhesive curing systems
9. Aftertreatments

This system allows to avoid errors. An adhesive is sought which conducts electricity and deflects leakage currents on surfaces. The surface resistance may not exceed 10 mili-Ohm and should not change during storage and application. Commercial adhesives fulfill these requirements as stated in the pertinent data sheets.

The following parameters are known to have an effect on the electric conductivity.

Filler amount in conducting elements
Filler type
Base materials of resin, purity adhesive contents of Na, Ka, Cl, NH, Kations/ Ions
Curing time, rate of orientation of the molecules. (Ballconcentration)
Curing temperature
Glass transition temperature Tg
Motility of molecules with the filler
Metallization of substrates
Metal type
Adhesive thickness
Ration of inviduel components/curing ratio
Humidity uptake

Materials Used

A. Bayblend aloy vapor coated surface 3 microne, ohmage 10-15 of the conducting surface for leakage currents.
B. Gold-plated copper wire as a contact unit, 3 micron Argentum Au

Adhesive Used

2-components silver filled Epoxy adhesive
2-components silver filled Acrylate

Room Conditions for Bonding

Room temperature 24 °C
Air humidity: less than 30%
Dust-free according to U.S.Fed. Standard 209b, 100.000 P/m

Aftertreatments 60°C/24h after curing and conditionating to room temperature was necessary to make sure that curing had fully completed.

Examination / Testing Criteria

A. Storage 72h at 70°C, to RT within 12h.
B. Storage 72h at-25°C, to RT within 12h
C. Storage 72h at -40°C,to RT within 12h
D. Shock temperature test, cycle RT to 25°C 1h, (20min) 70°C/1h, 100cycles were performed, conditioning to RT/12h
E. Shock temperature test; -25°C to 70°C Immediate hold 1h; 1000 cycles were performed. Conditioning to RT/12h.

F. Humidity test;40°C/92% rel. humidity
1h, 10h, 1 day– 270 days, out door stor.

The humidity storage/ageing tests are calculated as short-terms test figures. Measurements of the resistance at the vapor coated surfaces and at the bonded gold contact lever were carried out after each weatherability test. Alternation of the Ohmage was determined for A, B, C, D, and E. The determined values showed a minor decrease of resistance. An increase of resistance was recorded for F where the ohmage increased from m-Ohm to k-Ohm.

The transmission resistance of the conducting adhesive is mainly dependant on the internal potential differences.

(Brunner H, University of Munich) Evaluations of short-term experiments must take into account that the test results ar only a preliminary indication of the ageing resistance of the adhesive joints.

Short-term experience test 1h to 10.000hrs
Long-term exp.- test 10000 -10.000.000hrs

As the present tests were long term it was possible to determine long-term effects at the metal/polymer interface at the end of 270 days period. Normally humidity and diffusion effects at the interface are not measurable in short term tests, and thus as long term effects of the mechanism can not be postulated from such results. It should be noticed that that there is no reliable test system for short term experiments on ageing processes which could be used to make predictions on possible long term effects on stability and ageing. In addition to resistance measurements mode of failure and corrosion behaviour were optically investigated.

Results

The evaluation of the failure behaviour is expressed as composite fracture. Firstly we encounter a failure of adhesion as a separation at the interface of the two materials. High- and low-temperature storage had no negative effects on the adhesive joints. Modifications of surface resistance were insignificant. The humidity and weatherability tests releaved an increase of the surface resistance for both types of adhesives. Humidity storage was interrupted after 270 days, because the resistance had reached values in the K-Ohm domain, visually detectable, small black polymerbeads had formed, i.e. perforation of the conducting layer. Acrylate adhesives showed a lower degree of corrosiveness than epoxy adhesives. The onset of corrosion and increase of resistance is lower. For same storage times it was shown that different mechanisms of corrosion were acting in acrylate and epoxy resins.

All ten measurements showed similar behaviour. As of yet, it was assumed that the bonding process was not source of the deficiency, e.g. through air bulbs inclusion or incorrect mixed rature. After 6 month in humidity storage (F) the contact zone were investigated; perforation corrosion was microscopically detected in the aluminium vapor-coated layer. The deflection of leakage currents was no longer guarenteed. Ageing processes take place in the adhesion-adhesive layer and the metal/polymer interface uptake by humidity. This leads to a stability deficit to the point of complete failure of the adhesive joints by perforation corrosion. The processes can be explained on the base of two separate mechanisms.

The Bond-line corrosion and the electro-corrosion. (Humidity tests)

During the ageing process we got 4 phases.

Phase 1

The excess amine monomers react with the OH group of water at the interface. Ageing is initiated: the first corrosion effect is an attack on the protruding tips of the aluminium oxide surface. First minute perforations develop; this still does not interfere with the stability of the bonded joints. The pH at the interface boundary becomes more basic character and the oxide layer dissolves. Just now, urgently the rate ageing process started.

Phase 2

Oxygen and humidity attack the aluminium layer and the adhesive. After dissolution of the oxide layer another chemical reaction in initiated at the polymer/metal/adhesive interface. AL and NH(OH)- react into amphoric hydroxide and further to aluminate Al(OH)- . Hydrogen- absorbing compounds are formed, e.g. ammonia NH + H NH, aluminium metahydroxyde AlO(OH). This process continues until water and excess monomer have been consumed

Phase 3

From bondline – to electro-corrosion. The subsequent steps are linked to electro-corrosion via the electric potential. The electrical potential and differences in the oxygen concentration at the adhesive boundary leads to a potential difference which further increases the progression rate of the corrosion process of metals (Breuel).

Phase 4

Cathodic Corrosion

A cathodic and a anodic domain develops a a result of the oxygen concentration and the electric potential of the aluminium vapor coated layer and the silver or gold filled adhesive. The electric potential difference of Al-Au, Al-Gold accelerated the electrochemical corrosion processes. This becomes evident through the rapid increase of resistance.

Summary

Which measures can be taken in order to prevent the aforementioned corrosion processes?

General, all material surfaces should be coated with anti corrosives, to slow down the cathodic and anodic reaction and preventing the onset of the corrosion cycle.

Electrically conducting adhesives, it is recommended to use pure, low corrosion adhesives, esp. phenoxy resins, the content of Cl, NH, K, Na should not exceed 50ppm. Ion concentration should be measured by the Cooker test. Complete avoidance of electro corrosion in electrically conducting adhesives is only possible in the absence of any kind of potential difference between adhesives and metal. This means that for conducting surfaces only compatible materials should be used as conducting components, e.g. gold vapor coated layer and gold or carbon filled adhesives. The adhesive joints should extend beyond the edges and be sealed with silicone rubber(primer) to prevent contact with humidity. The results clearly show the great risk of electric corrosion and bondline corrosion in the application of conducting adhesives on metal surfaces with high different electrical potential. This effect of E-corrosion and bondline corrosion occur simultaneously. Air humidity, electrical potential difference, as well as cathodic and anodic conditions at the interface lead to delamination of the bonded joint. This mechanism was first recognized in 1981 in the cours of investigations on the ageing of electrically conducting surfaces current-deflecting substrate/polymers.

The work of G. Breuel, W. Brockmann, L. Dorn, H. Käufer and H. Kollek have encouraged me to publish the present results.

It confirms my theory of the inter-relationship of electro-corrosion and bond- line corrosion and the stimulation of the corrosion processes through electric Potential differences.

References

Brockmann W. Adhäsion zwischen AL-Polymeren,S.134-154,Sonderdruck, 2.Arbeitsdiskussion Adhäsion 15.-18.Mai 85 Mühlhausen DDR AKDW
Brockman,W.Dorn,L. Käufer, H.
Kleben von Kunststoff mit Metall Springer Verlag 1989
E. Schindel-Bidinelli
1993 Oxford Brooks University, Adhesion Congress Prof. K. Allen
1998 CCA Conference Beijing P.R. China
2001 CSB Congress Beijing P.R. China

Proceedings of The 1st International Conference on **D**iffusion in **S**olids and **L**iquids
DSL-2005, July 6-8, 2005, University of Aveiro, Aveiro, Portugal

ON THE DIFFUSION-EVAPORATION EFFECTS IN THE WETTING MECHANISMS OF BINARY VOLATILE DROPLETS

Khellil SEFIANE[1,*], Gail DUURSMA[1]

[1]School of Engineering and Electronics, THE UNIVERSITY *of* EDINBURGH,
The King's Buildings Mayfield Road, Edinburgh, EH9 3JL, UK

[*]Corresponding author. Fax: +44 (0) 131 6506551; Email: ksefiane@ed.ac.uk

Abstract

In this paper the experimental results on the wetting behaviour of volatile binary sessile drops are reported. The evaporation rate is varied through the control of the ambient total pressure. The dynamic wetting contact angle of an evaporating Water-Ethanol drop is investigated at various sub-atmospheric pressures. The wetting properties (contact angle, shape and volume) are monitored in time using a drop shape analysis instrument. The results show that the evaporation of the binary droplet takes place in two stages: the first stage where the wetting behaviour is very similar to the pure ethanol case and a second stage where the behaviour is very similar to the pure water case. The effect of varying the evaporation rate is found to shift the observed stages. The analysis of these results shows that it seems that in these conditions the evaporation proceeds such that in a first stage where mostly the more volatile component evaporates and a second stage where mostly the less volatile component evaporates. It appears however that during these evaporation stages there can be an evaporation of both components in different proportions. This is clearly influenced by the total evaporation rate and the diffusion from the bulk to the interface.

Keywords: Wetting; Evaporation; Diffusion; Concentration gradients; Capillary

1 Introduction

Wetting phenomena play a crucial role in a wide range of technological applications. Spreading of liquids on solids involving phase change is encountered in many areas ranging from biological systems to industrial applications. Ring formation from evaporating drops and its use for thin films coating [1], and DNA chains elongation using a drying sessile droplet are examples of new developments and identify a need for the understanding of the process of evaporating droplets [2]. Extensive work can be found in the literature dedicated to understanding the fundamentals of this process, [3]-[6].

Although wetting and evaporation of binary mixtures is an important case to many applications, little work has been done to investigate the fundamentals of the problem. There are many possible applications to which understanding of evaporation and wetting behaviour of binary mixtures can be applied.

In wastewater treatment plants, knowledge of surface tension behaviour is used to monitor concentrations of volatile organic compounds such as benzene, toluene and trichloroethylene (TCE) to ensure that levels do not exceed safety limits. In the microelectronics field, recent trends towards technologies with high power dissipation and density have resulted in the need for the design of more effective thermal management systems. The traditional methods of air cooling and direct immersion cooling may no longer provide a sufficient level of heat removal from the circuitry. A promising solution to the cooling of high density microelectronic applications is the process of spray evaporative cooling. This involves the spraying of a dielectric liquid directly onto the circuitry. The liquid will absorb the heat from the circuitry, and then evaporate, thereby cooling the electronic components. The evaporative process and therefore the effectiveness of cooling will be governed by the wetting behaviour of the sprayed liquid. In a study by Rowan et al. [7] the wetting behaviour of a 1-propanol and water mixture were observed. Contact angle and base width measurements of the droplet were made for a variety of compositions at 21˚C and ambient pressure. The results of this paper show two distinct trends of wetting behaviour: one for mixtures with mole fractions of less than 0.39 propanol and one for mixtures with mole fractions more than 0.39 propanol. For mixtures containing more than 0.39 mole fraction propanol, it was fount that the contact angle decreased at a steady rate for the period required for total evaporation (90 s), whereas the base width measurement was steady for about 60 s before decreasing at a fast rate. Additionally, the droplet maintained a rough spherical cap-type shape throughout the evaporation process. For mixtures containing less than a 0.39 mole fraction of propanol, the behaviour observed was markedly different. Initially, for a short period of time, the contact angle decreased. After this however, contact angle measurements were found to be unobtainable due to instabilities around the droplet periphery. The droplet was then observed to spread and break into several smaller droplets, eventually leading to the formation a single new droplet.

A likely explanation for this behaviour has to do with the azeotropic nature of the propanol/water mixture. The azeotropic composition at the conditions of the experimental studies was externally verified to be 0.41 which is so close to the margin at which the trend of wetting behaviour changes. Therefore, when the mixture contains a water in excess of the azeotropic composition ($x_{propanol} < 0.41$), evaporation will result in a residual liquid that tends to pure water as the propanol is preferentially absorbed at the interface. The combined effects of the preferential absorption of propanol and also the cooling caused by evaporation induce local surface tension minima and maxima, leading to the instabilities observed. When most of the propanol has evaporated, the dynamic surface tension observed will tend to that of pure water, which is verified by the higher contact angles detected in the latter stages of the experiment.

Again, although a quantitative reasoning is given to explain the dynamic surface tension behaviour of the propanol/water droplet, it is essential to produce a more rigorous physical approach which will include mathematical modelling of the absorption and evaporation dynamics to verify the experimental findings. The aim of this paper is to present the findings of an experimental investigation of the evaporation and wetting behaviour of ethanol/water droplets. The effect of concentration and evaporation rate has been investigated and the role of diffusion in the liquid and gas phases is discussed.

2 Experimental Setup and Procedure

The experimental equipment used to carry out the evaporation of sessile droplets under various pressures consists of:- a computer with FTA200 package (contact angle analysis software), a CCD camera, a cell of dimension 4x4x3 cm, an injection pump, an aluminium/PTFE substrate of dimension 2.5x6 cm. The FTA200 package evaluates the contact angle, volume, height, diameter and surface tension of the sessile drops. The sessile drop and its contact angle is highly influenced by the surface finish and the presence of impurities on the substrate. For that reason, surface preparation techniques such as polishing, and cleaning in ultrasound bath were used, prior to the experiments, in an attempt to obtain a clean and homogenous surface. Substrates were pictured by the Atomic Force Microscope, (AFM). The analysis performed by the AFM was completed by the use of a Zygo profilometer to evaluate the roughness of the substrate. The resulting profile indicated that the PTFE substrate can be considered as relatively rough.

Some preliminary exploratory tests have been performed in order to select the binary system as well as the substrate. In order to select a binary mixture to demonstrate the coupling between volatility and surface tension, water, ethanol and methanol were investigated independently.

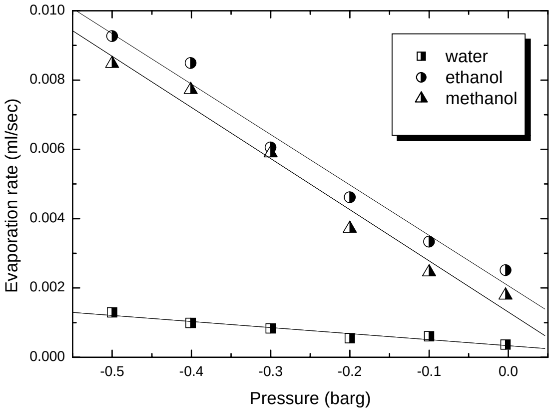

Figure 1: Evaporation of water droplet on aluminium and PTFE substrates.

The evaporation of the three liquids under reduced pressure has been investigated (Fig. 1). For these pure substances, evaporation rate increased linearly with decreasing pressure, with water having a much lower rate and pressure dependence than ethanol or methanol, which is consistent with its lower vapour pressures. Water and ethanol was chosen for the experiments with mixtures because pure water and pure ethanol have similar contact angle trends with time during evaporation.

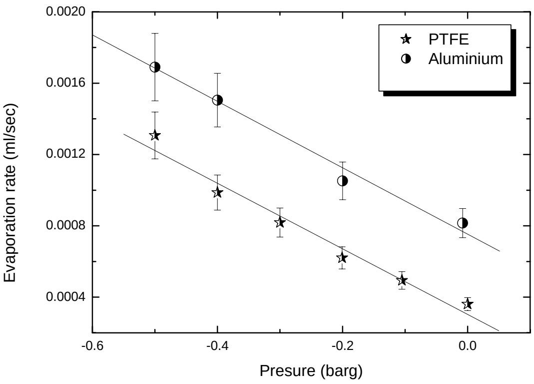

Figure 2: Evaporation of water droplet on aluminium and PTFE substrates.

Fig. 2 shows evaporation of a water droplet on both the PTFE substrate and Aluminium substrates. The evaporation rate is higher for the Aluminium substrate because the droplet spreads more on this surface, giving rise to a larger surface area. The PTFE substrate has lower thermal conductivity which could have reduced heat transfer for the energy required for evaporation in addition to the spreading effect.

However, the slopes of both lines are similar, indicating that heat transfer limitation is unlikely. The PTFE substrate was chosen because its high surface energy gave rise to larger and hence more readily measurable contact angles for ethanol.

3 Results

Evaporation rates for pure water and pure ethanol and a range of mixtures of these is given in Fig. 3 at various (sub)atmospheric pressures. The evaporation rate is observed to increase linearly with decreasing pressure for each substance. Increasing the ethanol concentration increases the overall evaporation rate consistently. In order to facilitate analysis of our results, some further data are presented in dimensionless form. The contact angle, base width and drop volume are normalized to the initial values, while time is normalized to the lifetime of the drop.

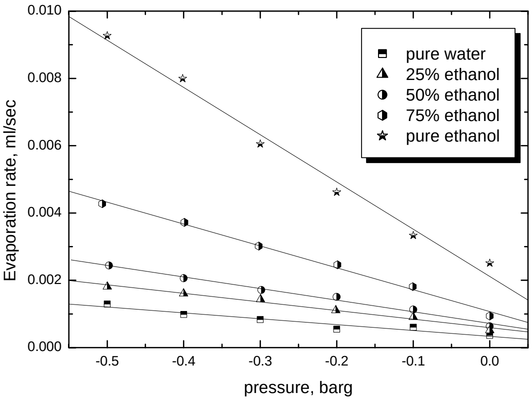

Figure 3: Overall evaporation rates of pure and mixtures at various sub-atmospheric pressures.

The normalised curves show two types of behaviour depending on the drop concentration regardless the parameter studied (drop volume, contact angle, drop base width). For pure substances, the normalised curves show almost a similar trend. The drop volume and the base width decrease monotonically for all the evaporation duration. For mixtures, the normalised curves reveal different behaviours from the pure substances. For small concentration (25 %) of the volatile liquid, the droplet characteristics evaporation is globally close to pure substances. As the volatile liquid concentration increases in the drop, the drop volume variation deviates significantly from the pure substances. This leads to the observation that the evaporation mechanisms for the mixtures differ from the pure ones. The present results show that for binary mixtures the wetting behaviour of evaporating drops deviates from the known pure component trends. In all performed experiments we found that on the rough surface we used, the contact angle decreases which suggests that pinning of the contact line may occur; however, base width measurements (Fig. 9) show a slow decrease for all tests except that of pure water. The evaporation sequence of an ethanol-water droplet did not display similar characteristics to either of the two pure components. There was a well defined two-phase evaporation sequence identified, which became more defined as the ethanol concentration increased (see Fig. 4). If pinning occurs an initial extra phase is observed – see Sefiane et al. [11].

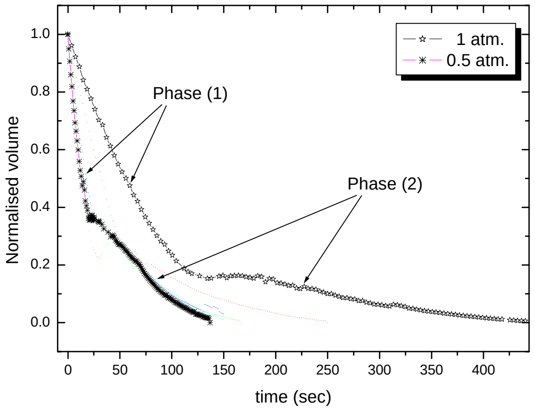

Figure 4: Identification of the two stages in the evaporation of water-ethanol mixtures at two pressures.

The duration of phase 1, compared to the entire evaporation time, increases with increasing ethanol concentration. The volume evaporated during phase 1 appears to be very close to the volume of ethanol in the droplet mixture. This indicates that it is likely that the ethanol, with its higher vapour pressure evaporates preferentially, though some small amount of water will evaporate too. Similarly the duration of phase 2 corresponds to the volume of water in the droplet and evaporates at a much lower rate than phase 1. This corresponds roughly to the evaporation of almost pure water.

The evaporation rates of phase one and phase two identified previously are compared to the evaporation rates of pure components. This comparison shows that on one hand, for the mixtures, the magnitude of the evaporation rate of phase one is very close to the one of pure ethanol. On the other hand the magnitude of the evaporation rate of phase two is close to the one of pure water. This corroborates the idea that the more volatile component evaporates mainly during the first phase while the less volatile one evaporates in the last phase.

When the evaporation occurs, the dynamic contact angle is correlated to the drop volume. The wetting angle varies continuously with the drop volume for pure substances. For mixtures this behaviour is different. For high ethanol concentration (75 %), the initial contact angle is close to that of pure ethanol for a wide range of drop volumes. The contact angle at some point increases rapidly to the contact angle of pure water and subsequently follows the behaviour of pure water for the rest of the drop lifetime. This 'jump' in contact angle is a key feature of evaporation of rich mixtures of ethanol. There is a corresponding reduction in base width of the droplets (see Fig. 8) and the drop height also increases.

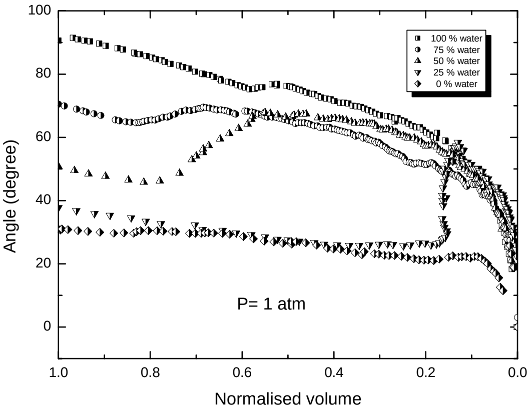

Figure 5: Evolution of the contact angle versus the drop volume for various initial concentrations at P = 1 atm.

The location of the jump in contact angle varies with reducing pressure, occurring at progressively lower normalised volumes, as shown in figures 5, 6, 7 and 10. From the results presented it is clear that the wetting behaviour strongly depends on the initial concentration of ethanol.

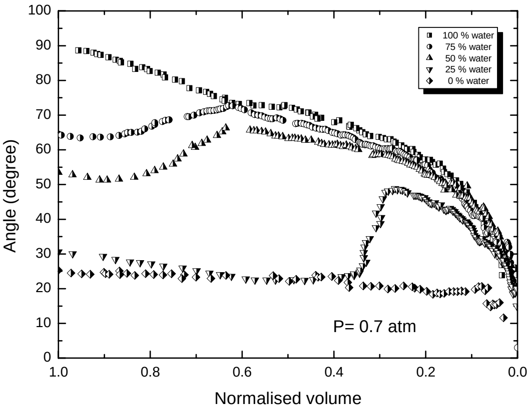

Figure 6: Evolution of the contact angle versus the drop volume for various initial concentrations at P = 0.7 atm.

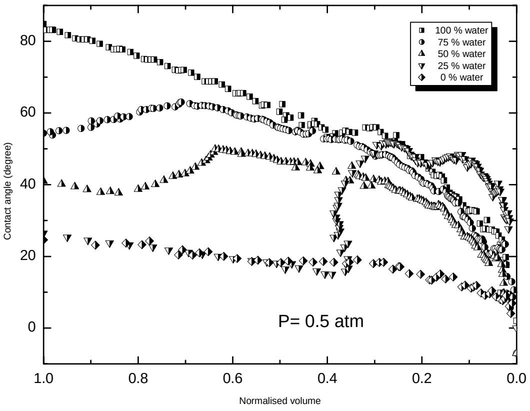

Figure 7: Evolution of the contact angle versus the drop volume for various initial concentrations at P = 0.5 atm.

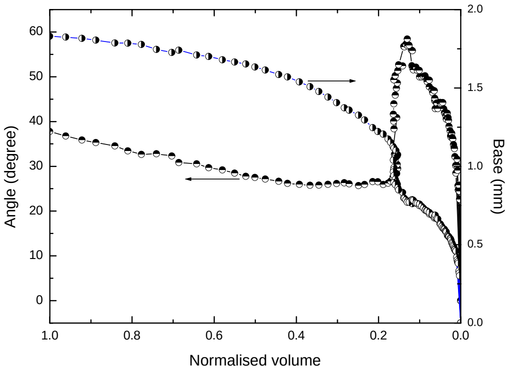

Figure 8: Depinning of the contact line during contact angle jump.

4 Discussion of mechanism

For mixture droplets, the overall rate of the evaporative process can be thought of as consisting of the following stages in series:

(a) diffusion (or more generally mass transfer) of the more volatile component to the surface of the drop;

(b) evaporation of both species from the surface according to their vapour pressures and droplet surface phenomena;

(c) diffusion of both species through quiescent air above the droplet in the cell.

The energy loss brought about by evaporation must be accounted for in stage (b) and, if not provided for entirely by heat transfer through the substrate, this heat transfer limitation must be modelled too.

Diffusivities of ethanol in water are significantly lower than those of either ethanol or water vapour in air. An estimate of the diffusive flux of ethanol from the base of the drop to the surface is much lower than the observed evaporation rate. This indicates that there are other mass transfer processes occurring in the drop. Circulation within evaporating drops has been observed [9] and it appears that this, which would replenish lost surface ethanol, is sufficient to keep the surface layer as ethanol rich as possible during preferential evaporation. Over time the ethanol concentration will decline. The contact angle is fairly insensitive to changes in concentration until the ethanol concentration has reduced to about 20 % (see Fig. 11), whereafter a rapid change in contact angle with further evaporation of ethanol would be expected; this appears to be the cause of the jump in contact angle seen. This insensitivity to ethanol concentration for rich mixtures also explains why the initial contact angle for these mixtures is close to that of ethanol.

The variation of location of the contact angle jump with pressure may be explained when considering the effect of pressure on evaporation of the mixture. The vapour pressure data (see Fig. 11 and [10]) suggest that the effect of reduced pressure is proportionately greater on ethanol evaporation than on that of water, leading to a transition to phase 2 earlier in normalised time the lower the system pressure.

The effects of dynamic surface phenomena on the evaporation rate has not yet been considered nor any surfactant-type behaviour. Incorporation of an energy balance into a model of the mass transfer phenomena explained above would be needed to accurately represent the system as would the dynamics of depinning of the droplet. Evaporation is not expected to be uniform along the surface.

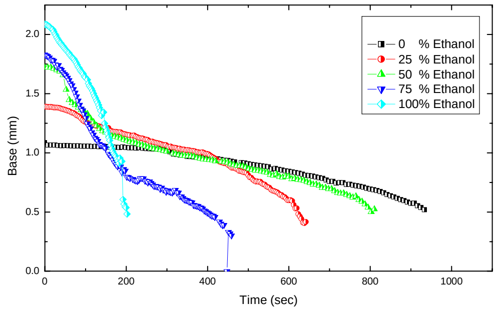

Figure 9: Evolution of the drop base versus time for various initial concentrations at P = 1 atm.

Many investigators see e.g. [1], have demonstrated that evaporation is larger near the contact points. This is a complicated system to represent accurately though the preliminary explanation provided here is in agreement with major observations.

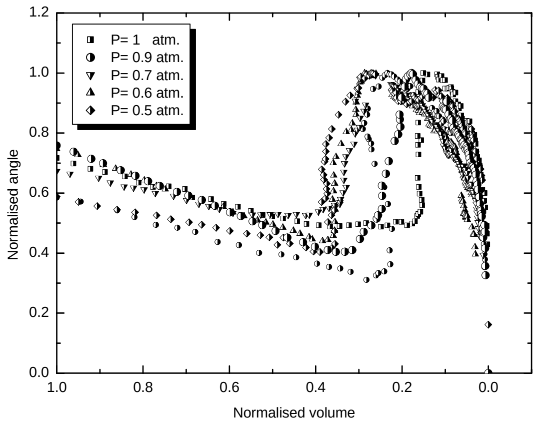

Figure 10: Evolution of the contact angle versus the drop volume for an initial concentrations of 75 % ethanol at various pressures.

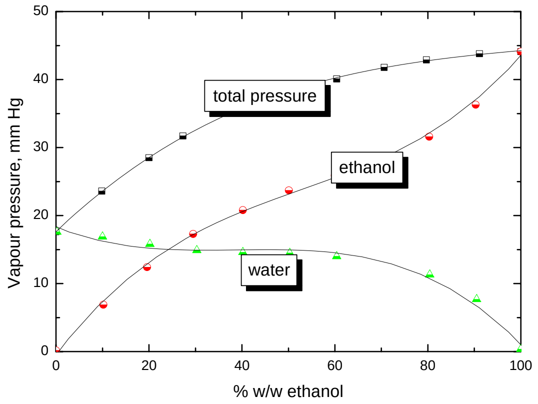

Figure 11: Vapour pressure of ethanol-water mixture.

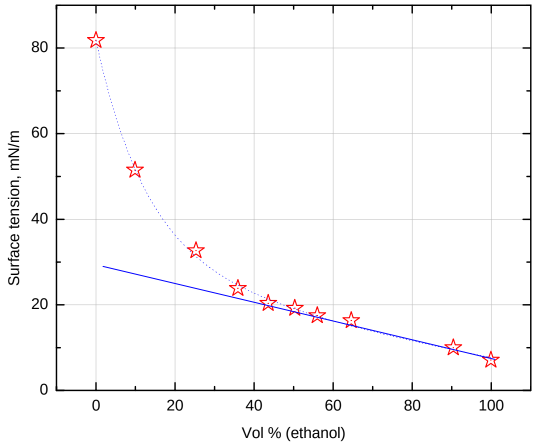

Figure 12: Surface tension of ethanol-water mixture.

4 Conclusions

It appears that the mechanisms which govern the evaporation of a binary sessile droplet are coupled mass transfer and evaporation together with surface-tension-determined contact angle and depinning. Ethanol evaporates preferentially during the first phase whereas second phase evaporation is similar to that of water. For initially ethanol-rich mixtures there is an observable jump in contact angle, which occurs earlier at lower system pressures and can be explained by surface tension phenomena.

.

References

[1] Deegan, R.: Pattern formation in drying drops. *Physical Review E*, 61(1): pp. 475-485, 1998.

[2] Hu, H. and R.G. Larson: Evaporation of a Sessile Droplet on a Substrate. *Journal of Physical Chemistry B*, 106: pp. 1334-1344, 2002.

[3] Pickenett, R. and R. Bexon: The Evaporation of Sessile or pendant Drops in Still Air. *Journal of Colloid and Interface Science*, 61(2): pp. 336-350, 1977.

[4] De-Gennes, P.: Wetting: statistics and dynamics. *Rev. Mod. Phys*., 57: pp. 827-863, 1985.

[5] Blake, T. and J. Haynes, *J. Colloid Interface Sci*., 30: pp. 421, 1969.

[6] Shanahan, M. and A. Carre: Viscoelastic dissipation in wetting and adhesion phenomena. *Langmuir*, 11: pp. 1396-1402, 1995.

[7] Rowan S. M., Newton M.I., Driewer F.W., McHale G.: Evaporation of microdroplets of azeotropic liquids, *J. Phys. Chem. B*, 104, pp. 8217-8220, 2000.

[8] Vasques G., Alvarez E., Navaza JM.: Surface tension of Alcohols+water from 20 to 50 C, *J. Chem. Eng. Data*, pp. 611-614, 1995.

[9] Hegseth, J.J., N. Rashidnia, and A. Chai: Natural convection in droplet evaporation. *Physical Review* E, 54(2): pp. 1640-1644, 1996.

[10] O' Hare KD., Spedding PL.: *the Chemical Engineering Journal*, 48, pp. 1-9, 1992.

[11] Sefiane K., Tadrist L., Douglas M.*: Int J. of Heat and Mass Transfer*, 46, pp. 4527-4534, 2003.

Proceedings of The 1st International Conference on **D**iffusion in **S**olids and **L**iquids
DSL-2005, July 6-8, 2005, University of Aveiro, Aveiro, Portugal

VAPOUR DIFFUSION EFFECT DURING EVAPORATION OF LIQUIDS IN CAPILLARY TUBE: A THERMAL ANALYSIS

Cosimo BUFFONE[1], Khellil SEFIANE[2,*]

[1]Thermacore Europe Ltd., Wansbeck Business Park, Ashington, Northumberland, NE63 8QW, UK

[2]School of Engineering and Electronics, THE UNIVERSITY of EDINBURGH,
The King's Buildings Mayfield Road, Edinburgh, EH9 3JL, UK

[*]Corresponding author. Fax: +44 (0) 131 6506551; Email: ksefiane@ed.ac.uk

Abstract

In this work the results about the evaporation of a volatile liquid in a capillary tube is reported. The strong evaporation near the contact line induces a cooling effect. The temperature near the contact line is measured using an infra-red camera. The evaporation rate from the meniscus is measured as this latter recedes inside the tube. The evaporation in this specific case is found to be diffusion limited, the IR temperature measurements near the contact line show clear correlation with the evaporation process. A theoretical model is developed to describe the evaporation and diffusion of vapour through the tube. The results show fairly good agreement with the experimental data.

Keywords: Evaporation; Diffusion; Interface; Temperature; Evaporative cooling

1 Introduction

Heat and mass transfer in micro-channels has attracted considerable attention both from academia and industry as micro-scale offers many advantages with a large area to volume ratio ultimately enhancing heat transfer and producing considerable saving of material. This trend is also driven by the need of packaging in areas such electronics cooling and biomedical. Another important factor that has certainly contributed to the wide interest in the micro-scale area is the rapid advances in sophisticated manufacture and measurement techniques such as MEMS and Selective Laser Melting, micro-PIV (Santiago et al. (1998), [1]) and many other processes.

The scale involved with the contact line region is so small (usually below few microns) that even most of the advanced measurements techniques become unusable either because of the inappropriate resolution or the contact/destructive nature of the techniques used. Therefore a lot of work is needed to access this region and understand the basic mechanisms of heat and mass transfer. Away from the contact line region diffusion can become important at micro-scale; and sometimes, as in the present case, can play a fundamental role.

This paper describes the evaporation of ethanol in a capillary tube closed at one end and open at the opposite one. It is worth mentioning that similar experiment (WIKELMANN) has for long been used to measure diffusion coefficients for gases (Coulson and Richardson (1999), [2]). By visualization and using an Infrared camera the meniscus movement has been tracked and the triple line temperature measured. It will be shown that diffusion of vapour into the tube becomes the limiting factor as the meniscus recedes inside the tube.

2 Experimental arrangement

The arrangement is depicted in Figure 1. More detailed information on the specific components of this setup can be found in a previous work (Buffone and Sefiane (2004), [3]). The measurement on the meniscus position inside the tube has been performed separately from the infrared (IR) measurement of the capillary tube wall, this has been dictated by the compactness of the experimental setup. The IR experimental arrangement has been described in details in a previous work [3] and will not be repeated here.

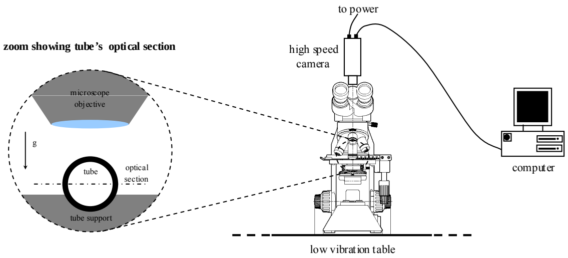

Figure 1: Schematic of the visualization experimental setup.

Worth of mention is the fact that both experiments have been repeated and consistency was found in the data collected. The borosilicate glass capillary tube is horizontally positioned on the stage and filled from one end with a micro-syringe until the liquid-vapour interface is positioned at the opposite tube end. At this point the operator stops acting on the syringe and either the CCD high speed camera or the IR camera are triggered to start recording.

3 Results presentation and discussion

Figure 2 shows the meniscus position inside the capillary tube versus time. The distance reported is from the tube mouth. The presented results are for liquids of different volatilities. The extracted velocity of the interface shows the stages of evaporation. Essentially, the slopes of the curves decrease as the meniscus moves deeper inside the tube confirming that the evaporation is basically dictated by the diffusion of vapour in the freed tube space.

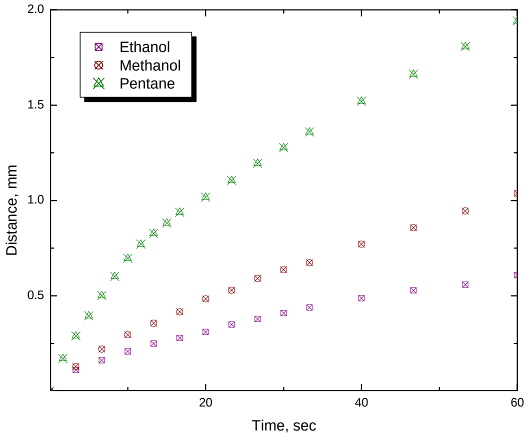

Figure 2: Meniscus position inside the capillary measured from the tube mouth, results for three different liquids.

In what follows we perform a thermal analysis for the case of Ethanol in a capillary tube of 900 μm in diameter. Figure 3 reports the temperature evolution of the meniscus triple line. As evaporation evolves mass is lost and the meniscus moves deeper in the tube. This movement is characterized by two stages. During the fist stage the large adhesion forces keep the meniscus anchored at the capillary mouth and the meniscus changes shapes. When then the receding contact angle is reached (Buffone and Sefiane (2004a)) the meniscus detaches and moves deeper inside the tube. The detachment event can be clearly seen in Figure 3 after which the triple line experiences a steep increase of temperature.

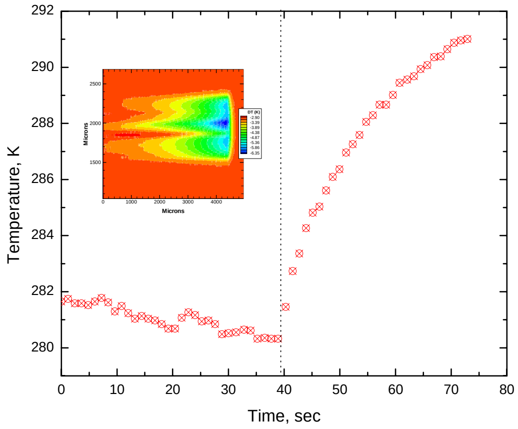

Figure 3: Temperature evolution of triple line as the meniscus moves deeper inside the tube extracted from IR measurements.

4 Theoretical model

In the following an attempt will be made to calculate the temperature at the triple line region by a heat diffusion model. Evaporation takes place along the meniscus interface producing a local drop in temperature. A heat transfer mechanism is induced and heat is transferred from the environment outside the tube to the meniscus interface, passing through the tube walls and the thin liquid layer. This heat is necessary to sustain the evaporation process. For an order of magnitude analysis, it is reasonable to neglect the heat conducted along the tube walls and the vapour can be assumed to be “passive” (Davis (1987) [4] and Pratt and Hallinan (1997)) [5], which means that no convection is present in the vapour, because it has negligible viscosity, density and thermal conductivity compared to the liquid.

Therefore we can reasonably assume that what evaporates from the meniscus interface is diffused in the gas phase. For diffusion through stagnant gas (the liquid-vapour interface is impermeable to air) the evaporation flux can be expressed as follows:

$$\dot{m} = \frac{M}{L} D C_{sat} \qquad (1)$$

Where M is the vapour molecular weight, D is the diffusion coefficient, C_{sat} is the surface vapour concentration of the volatile liquid in air at the triple line, assumed to be the saturation one, and L is the meniscus distance from the tube mouth.

As shown by many authors along the meniscus interface most of the evaporation takes place in the meniscus micro-layer region. This layer is of paramount importance in the heat and mass transfer from a meniscus interface as shown by different authors (Derjaguin (1965) [6], Moosman and Homsy (1980) [7], and Park and Lee (2003)) [8]; this layer has a thickness of the order of δ = 5-15 μm and is extended for levap = 17.5 μm (see Park and Lee (2003)). The local energy balance at the surface of the conductive layer region of the meniscus reads:

$$\dot{m} \frac{\Delta H}{M} A_{diff} = \kappa_l \vec{\nabla} T_l . \vec{1} A_{evap} \qquad (2)$$

Where ΔH is the latent heat of evaporation, k_l is liquid thermal conductivity, is the temperature gradient, is the unity vector, the $A_{evap} = 2\pi Ri\ l_{evap}$ and $A_{diff} = \pi Ri^2$. Equation (2) states that all that evaporates at the meniscus triple line has to diffuse through the cross section of the tube. Assuming 1-D conduction in the radial direction, the normal component of the heat flux can be then written as:

$$\dot{m} \frac{\Delta H}{M} A_{diff} = \kappa_l \frac{T_a - T_c}{\delta} A_{evap} \qquad (3)$$

where δ is the mean thickness of the conductive layer (assumed for calculation purposes in the model as δ = 10 μm), T_c is the temperature at the meniscus wedge and Ta is the wall temperature, this last being assumed to be the ambient air temperature for a conducting wall. Combining Eqs. (2-4) one gets:

$$D \frac{C_{sat}}{L} \Delta H \frac{A_{diff}}{A_{evap}} = \kappa_l \frac{(T_a - T_c)}{\delta} \qquad (4)$$

The saturation concentration can be written as:

$$C_{sat} = \frac{P}{\Re T_c} X(T_c) \qquad (5)$$

Where P is the pressure of the gas phase (air-vapour), is the molar ideal gas constant and X is the mole fraction of vapour into air. Clausius-Clapeyron relation is used to find the mole fraction as function of temperature:

$$X(T_c) = \exp\left[-\frac{\Delta H}{\Re}\left(\frac{1}{T_c} - \frac{1}{T_b}\right)\right] \qquad (6)$$

where Tb is the liquid boiling temperature. Equ. (4) can thus be re-written as follows:

$$D \frac{P}{\Re T_c} \frac{\Delta H}{L} \exp\left[-\frac{\Delta H}{\Re}\left(\frac{1}{T_c} - \frac{1}{T_b}\right)\right] \frac{A_{diff}}{A_{evap}} = \kappa_l \frac{(T_a - T_c)}{\delta} \qquad (7)$$

Solving the above equation will give the temperature of the interface at the meniscus triple line. Defining a dimensionless length as $\widetilde{L} = \frac{\delta}{L}$ and introducing $\frac{A_{diff}}{A_{evap}} = \frac{R_i}{2 l_{evap}}$, Equ. (7) is written as follows:

$$\frac{D \Delta H P}{\Re \kappa_{l\,l}} \frac{R_i}{2 l_{evap}} \widetilde{L} \exp\left[-\frac{\Delta H}{\Re}\left(\frac{1}{T_c} - \frac{1}{T_b}\right)\right] = T_c (T_a - T_c) \qquad (8)$$

Table 1 shows the results giving the temperature T_c, near the triple line as the meniscus recedes inside the capillary ($\widetilde{L}$ diminishes). According to Table 1 the temperature (T_c) increases to near ambient temperature after $\widetilde{L}$ = 0.01 (corresponding to L = 1 mm), therefore the driving force is weakened as the meniscus moves deeper inside the tube and the convection slows down; this is in agreement with the experimental results shown on Figures 3. Results of Table 1 are reported graphically in Figure 4 for clarity.

Table 1: Corner temperature vs. meniscus position, @ $T_a = 292\,K$ and $\delta = 10\,\mu m$.

$\widetilde{L} = \delta/L$	L, mm	T_c, K
1	0.01	283.6
0.9	0.011	284.2
0.5	0.02	287
0.4	0.025	287.8
0.3	0.033	288.7
0.2	0.05	289.7
0.1	0.1	290.8
0.05	0.2	291.3
0.0333	0.3	291.5
0.025	0.4	291.6
0.02	0.5	291.6
0.01	1	291

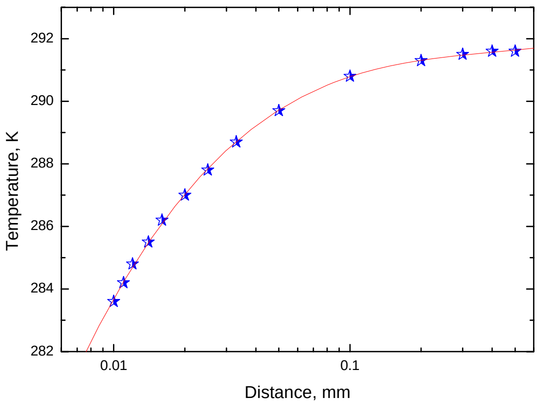

Figure 4: Temperature of triple line versus distance as the meniscus recedes, calculated from Eq. 8.

The calculated temperatures in Table 1 according to the formulated model describe the temperature in the corner of the meniscus on the liquid-vapour interface. The model as introduced in previous section does not account for the thermal resistance outside the tube in the air side. It is believed that after the first transient time the temperature on the outside of the tube will be very close to the one on the liquid side, because of the good thermal conductivity of liquid/glass media. The main resistance will be in an air boundary layer outside the tube where the environment is at ambient temperature. The estimated temperatures from the model will be a good estimate of the wall temperature as measured by the IR camera. The comparison between the estimated temperatures and the measured ones show a good agreement. The comparison between Table 1 and Figure 3 shows that the model describes well the magnitude of temperature change as well as the distance over which this change takes place (Figure 4).

5 Conclusion

This paper describes the evaporation of ethanol in a horizontally oriented capillary tube (900 microns ID) with one end open to ambient. Through the use of visual observation and an IR camera it has been possible to characterize the evaporation process and draw some useful conclusions. Both experimental techniques confirm that the evaporation in the described case is controlled by diffusion of vapour from the interface to the tube mouth. Additional confirmation is given by the analytical model developed. The estimation of the triple line temperature through this model is then compared to experimental measurements and a fairly good agreement is found.

References

[1] Santiago J.G., Wereley C.D., Meinhart C.D., Beebe J.D. and Adrian R.J.: A particle image velocimetry system for microfluids, *Experiments in Fluids*, Vol. 25, pp. 316-319, 1998.

[2] Coulson J.M. and Richardson J.J.: *Chemical engineering*, 6th Edition, Volume 1, Butterworth Heinemann, Elsevier, New York, 1999.

[3] Buffone C. and Sefiane K.: IR measurements of interfacial temperature during phase change in a confined environment, *Exp. Thermal and Fluid Science*, 29 (1), pp. 65-74, 2004.

[4] Davis S. H.: Thermocapillary instabilities, *Annual Review of Fluid Mechanics*, Vol. 19, pp. 403-435, 1987.

[5] Pratt D.M. and Hallinan K.P.: Thermocapillary effects on the wetting characteristics of a heated meniscus, *Journal of Thermophysic Heat Transfer*, Vol. 11, No. 4, pp. 519-525, 1997.

[6] Derjaguin B.V.: Definition of the concept of disjoining pressure and its role in the statics and kinetics of thin layers of liquids, *Colloid Journal USSR* (Engl. Transl.), Vol. 17, pp. 191-198, 1965.

[7] Moosman S. and Homsy S.M.: Evaporating menisci of wetting fluids, *Journal of Colloid and Interface Science*, Vol. 73, pp. 212-223, 1980.

[8] Park K. and Lee K.: Flow and heat transfer characteristics of the evaporating extended meniscus in a micro-capillary channel, *International Journal of Heat and Mass Transfer*, Vol. 46, pp. 4587-4594, 2003.

Proceedings of The 1st International Conference on **D**iffusion in **S**olids and **L**iquids
DSL-2005, July 6-8, 2005, University of Aveiro, Aveiro, Portugal

DEVELOPING CORRELATION FOR THREE-PHASE FLOW BOILING IN A CIRCULATING FLUIDIZED BED

Michael ARUMEMI-IKHIDE, Khellil SEFIANE*

School of Engineering and Electronics, University of Edinburgh
Kings Buildings, Edinburgh, UK

*Corresponding author. Fax: 0131 650 6551; Email: ksefiane@ed.ac.uk

Abstract

Fouling of heat transfer surfaces is a frequent engineering problem which is much more severe during subcooled flow boiling, due to the mechanisms of bubble formation. Thus, in response, our endeavours concern the investigation of boiling heat transfer enhancement and fouling prevention characteristics of a (vapour-liquid-solid) three-phase circulating fluidized bed. Experiments are performed at atmospheric pressure, using distilled water as the working fluid. The test unit consist of a glass riser column of square cross sectional area 21.5x11mm, height 1000mm, fitted with an electrically heated cartridge heater rod of 8mm diameter x 730mm length. Results show that higher heat transfer coefficients are achieved in three-phase flow boiling, compared with two-phase flow boiling. Based on the analysis of the governing heat transfer mechanisms, a boiling heat transfer correlation has been derived for the prediction of heat transfer in our three-phase circulating fluidized bed system; a favourable agreement between the derived three-phase boiling correlation, and our empirically obtained results is demonstrated.

Keywords: Heat transfer; Boiling; Fluidized beds; Heat transfer enhancement; Multiphase flow

1 Introduction

Three-phase flow boiling enhancing and limiting heat transfer effects have been experimentally determined. The heat and mass transfer processes causing these effects have also been visualised and clearly connected to the heat transfer data, resulting in a comprehensive theory regarding the heat transfer mechanisms of vapour-liquid-solid flow boiling. Some of our main findings can be stated as follows: (a) Compared with vapour-liquid two-phase flow boiling, the addition of solid particles enhances the three-phase flow boiling heat transfer. (b) Particle physical properties, e.g. density and size, influence the measured three-phase flow boiling heat transfer.

However, the ultimate objective of any fundamental approach to the problem of heat transfer in three-phase fluidized bed systems is to be able to predict the boiling heat transfer coefficient for a given condition through a knowledge and understanding of the processes involved. Due to the paucity of experimental data – borne from the complex nature of the three phase flow boiling system - correlations for the prediction of vapour-liquid-solid heat transfer appear fleeting within the available literature. Of the few studies undertaken, the work of Li Xiulun et al [1], [2] features most prominently. For our particular test geometry and investigated parametric range, analysis of both experimental and visualisation results, has lead to some novel conclusions (previously unreported) regarding the behaviour of the multiphase flow system. For instance, across our stipulated flow range (1 m/s to 2m/s), the measured three-phase flow boiling heat transfer coefficient exhibits non-linear functionality with fluid superficial velocity; a finding which stands in contrast to the work(s) of the aforementioned authors Li Xiulun et al, for an investigated velocity range of 0.5 m/s up to 1 m/s. Presumably the dissimilarity between our examined fluid velocity range accounts for such discrepancies

Thus in this paper, we aim to reflect some of these important experimental findings in the development of a modified approach for predicting our measured three-phase flow boiling heat transfer coefficients. As a consequence, both our experimental and theoretical heat transfer results can be compared and an analysis made regarding the accuracy and validity of the presented three-phase flow boiling correlation

2 The Three-Phase Flow Boiling Model

Excluding the addition of solid particles, there is no essential fundamental difference between the boiling regimes of two-phase and three-phase flow boiling. However, the presence of solid particles does affect the levels of both nucleation and convection. Thus based on the two-phase flow boiling asymptotic model introduced by Steiner et al [3], the proposed general equation describing the vapour-liquid-solid flow boiling coefficients, can be predicted as:

$$h_{\mathrm{CALC}} = \left[\left(h_{\mathrm{CB}}\right)^k + \left(h_{\mathrm{NB}}\right)^k \right]^{1/k}$$

$$h_{\mathrm{CALC}} = \left[\left\{h_{\mathrm{LS}} F_{\mathrm{CB}} \mathrm{f(u)}\right\}^k + \left\{\left(h_{\mathrm{nb,p}} F_{\mathrm{NB}}\right)^{b_{\mathrm{E}}}\right\}^k \right]^{1/k} \qquad (1)$$

The exponent k dictates the range of transition between the convective and nucleate components. $k = 3$.

2.1 Correlating Convective Contribution, h_{CB}

In Eq. (1) above, h_{LS} is the convective heat transfer coefficient, which accounts for heat transfer in the forced convective (i.e. liquid-solid only) region of three-phase circulating fluidised bed boiling. A satisfactory correlation as proposed by Jamialahmadi et al [4] was used in our developments:

$$h_{\mathrm{LS}} = h_L + \frac{6(1-\varepsilon)}{d_p} . \frac{D_e}{4} . \frac{n_p}{N} . \left(h_p - h_L\right) \qquad (2)$$

h_L is the heat transfer coefficient from the 'liquid flow only' zone of the heat transfer surface, and can be calculated from the Gnielinski correlation [5]:

$$h_L = \frac{\lambda_L}{D_e} . \frac{\frac{f_i}{8}(Re - 1000)Pr}{1 + 12.7\sqrt{\frac{f_i}{8}}\left(Pr^{2/3} - 1\right)} \left[1 + \frac{1}{3}\left(\frac{D_e}{L}\right)^{1/3} \right] \qquad (3)$$

The heat transfer coefficient for the particle controlled area, h_p, can be derived from the equation of Jamialahmadi et al., given as:

$$h_p = \left(\frac{2}{\sqrt{\pi}} \sqrt{\lambda_L \, \rho_L \, C_{p,L}} + R\sqrt{\lambda_p \, \rho_p \, C_{p,p}} \right) \sqrt{f} \qquad (4)$$

R is a constant taking into account the relative area of contact between particles and heat transfer surface and is equal to 0.0705 for spherical particles. f represents the frequency of the collisions experienced on the heat transfer surface by the action of fluidized particles and can be predicted according to Martin [6], [7]:

$$f = 0.3354 \sqrt{\frac{g}{d_p}\left(\frac{\rho_p - \rho_L}{\rho_p}\right) \frac{\varepsilon - \varepsilon_{pk}}{\left(1 - \varepsilon_{pk}\right)\left(1 - \varepsilon\right)}} \qquad (6)$$

Returning to Eq. (1), F_{CB} (i.e. the three-phase enhancement factor to the convective h_{LS} value, accounting for the improvement of the coefficient in the vapour-liquid-solid flow) can be derived as a function of the vapour quality x and the ρ_L / ρ_G ratio, according to Steiner et al [3]:

$$F_{\mathrm{CB}} = \left[(1-x)^{1.5} + 1.9(x)^{0.6} \left(\frac{\rho_L}{\rho_G} \right)^{0.35} \right]^{1.1}_{x \le 0.6} \qquad (7)$$

To account for the observed novel non-linear relationship between superficial velocity and our measured three-phase flow boiling coefficient, we have modified the three-phase model by including a convective velocity adjustment factor, f(u). This new correction factor (established via best fitting curve method) influences the dependency of h_{CB} on flow velocity.

2.2 Correlating Nucleate Contribution, h_{NB}

h_{NB} is based on Yang and Maa's correlation [8] for nucleate pool boiling heat transfer of water with suspended particles, $h_{\mathrm{nb,p}}$, compared with nucleate pool boiling of pure water, h_{nb}:

$$\frac{h_{\mathrm{nb,p}}}{h_{\mathrm{nb}}} = \left[1 + \beta \left(\frac{q}{q_{\mathrm{cr}}} \right)^{-\gamma} \right]^{-1} \left(\frac{\lambda_M}{\lambda_L} \right)^{\xi} \qquad (8)$$

According to Li XiuLun et al [2], Eq. (8) can be simplified to:

$$\frac{h_{\mathrm{nb,p}}}{h_{\mathrm{nb}}} = \left(\frac{\lambda_M}{\lambda_L} \right)^{1.7} \qquad (9)$$

For the prediction of h_{nb}, the physical properties based method of Stephan and Preusser [9] is used

Referring to Eq. (1), F_{NB}, is the three-phase nucleate flow boiling correction factor to $h_{\mathrm{nb,p}}$, which compensates for differences between pool and flow boiling conditions and is correlated by Steiner et al as:

$$F_{\mathrm{NB}} = f(m,x)F_{\mathrm{pf}}\left(\frac{q}{q_0}\right)^r F(d)F(R_a)F(M) \qquad (10)$$

To facilitate a true prediction of our experimental data, a new nucleate boiling enhancement exponent, b_E, is introduced to improve the calculated value of h_{NB}, thus increasing the dependency of the predicted three-phase boiling coefficient on heat flux. In the presented three-phase model b_E is a constant, established via the best-fitting curve method and identified as: $b_E = 4.43$.

3 Comparison between Predicted and Experimental Boiling Coefficient

The experimentally obtained heat transfer data has been compared with the model calculation for vapour-liquid-solid three-phase flow boiling. The heat transfer coefficients proposed by the presented correlation have been calculated across our given heat flux and flow velocity range.

Figure 1-3 presents results comparing the correlated and experimental three-phase flow boiling coefficient(s), for three different stainless steel particle sizes (d_p = 1.5, 2.0 and 2.5 mm). The graphs prove that the proposed correlation is able to describe the experimental data within a maximum deviation of 20 % for all employed particle sizes.

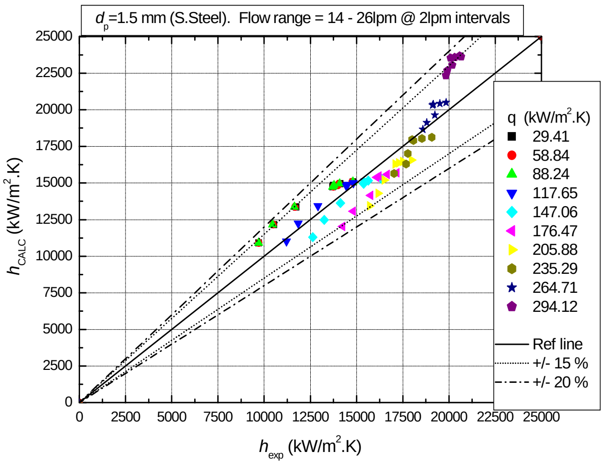

Figure 1: Comparison between calculated and experimental heat transfer coefficient for three-phase flow boiling, using 1.5 mm stainless steel particles

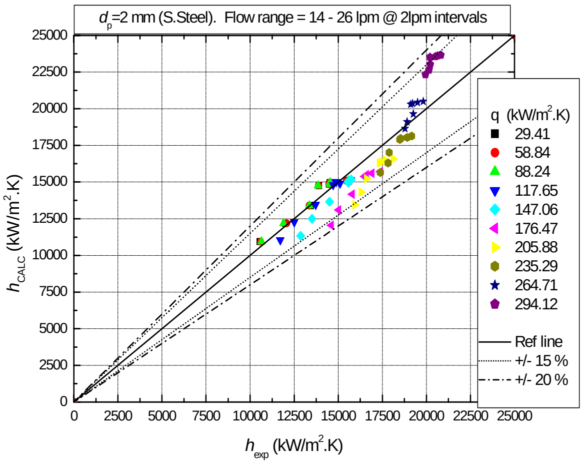

Figure 2: Comparison between calculated and experimental heat transfer coefficient for three-phase flow boiling, using 2.0 mm stainless steel particles

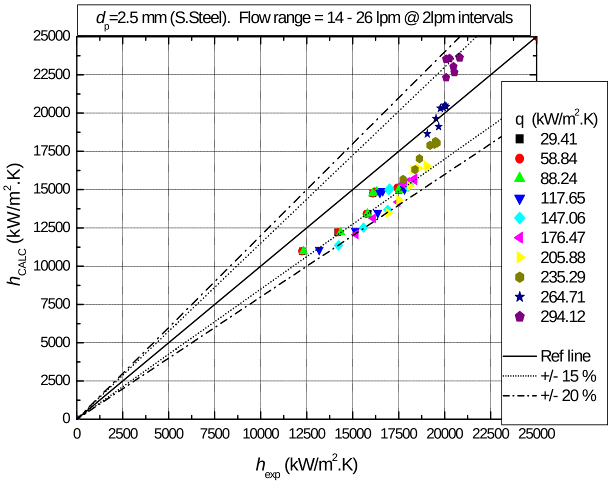

Figure 3: Comparison between calculated and experimental heat transfer coefficient for three-phase flow boiling, using 2.5 mm stainless steel particles

4 Conclusion

In this paper an equation has been developed for the prediction of three-phase flow boiling heat transfer coefficients. The models ability to predict experimental data has been successfully demonstrated.

Acknowledgments

The support of *Hansworth Limited* is recognised

Nomenclature

b_E	Nucleate boiling enhancement exponent
C_p	Specific heat capacity, (kJ/kgK)
d_p	Particle diameter (mm)
D_e	Equivalent bed diameter (m)
F(d)	Tube diameter factor
F(M)	Fluid molecular weight factor
F(Ra)	Surface roughness factor
F_{CB}	3-phase convective factor
F_{NB}	3-phase nucleate flow boiling factor
F_{pf}	Pressure factor
$f(m, x)$	Mass velocity & vapour fraction function
f_i	Friction factor
f	Collision frequency (s^{-1})
f(u)	Convective velocity adjustment factor
g	Acceleration due to gravity (ms^{-1})
h_{CALC}	Predicted 3-phase coefficient (kW/m^2K)
h_{CB}	Convective contribution ($kW/m^2.K$)
h_{exp}	Measured 3-phase coefficient (kW/m^2K)
h_{NB}	Nucleate boiling contribution (kW/m^2K)
h_{LS}	Liquid-solid flow coefficient (kW/m^2K)
$h_{nb,p}$	L-S pool boiling coefficient (kW/m^2K)
h_{nb}	Liquid pool boiling coefficient (kW/m^2K)
k	Flow boiling transition exponent
L	Bed height (m)
n_p	No. of particles contacting heater surface
N	Total number of particles
Pr	Prandtl number
q	Heat flux (kW/m^2)
q_{cr}	Heat flux at critical conditions (kW/m^2)
r	Nucleate flow boiling q exponent
R	Constant
Re	Reynolds number
x	Vapour quality

Greek Letters

β	Dimensionless number
γ	Dimensionless number
ε	Bed voidage
ξ	Dimensionless number
λ	Thermal conductivity (W/mK)
ρ	Density (kg/m^3)

Subscripts

G	Gas phase
L	Liquid phase
M	Solid-liquid mixture
p	Solid phase
o	At normalised conditions
pk	Packed bed

References

[1] Jianping, W., Huai, Z., Xiulun, L.: Performance of a new vapour-liquid-solid three-phase circulating fluidized bed evaporator. *Chemical Engineering and Processing,* 43, pp. 49-56, 2004.

[2] Xiulun, L., Jianping, W., Junjie, G.: Flow boiling heat transfer with fluidized solid particles. *Chinese J. of Chem. Eng.,* 3(3), pp. 163-170, 1995.

[3] Steiner, D., Tarborek, J.: Flow boiling heat transfer in vertical tubes correlated by an asymptotic model. *Heat transfer Engineering,* vol. 13, no. 2, pp. 43-69, 1992.

[4] Jamialahmadi, M., Malayeri, M.R., Müller-Steinhagen, H.: Prediction of heat transfer to liquid-solid fluidized beds. *The Canadian Journal of Chemical Engineering,* vol. 73, August 1995.

[5] Gnielinski, V.: Wärmeübertragung in Rohren, *VDI-Wärmeatlas, 5th ed.,* VDI-Verlag, Düsseldorf, 1986.

[6] Martin, H.: Fluid bed heat exchangers-a new model for particle convective energy transfer, *Chem. Eng. Comm.,* vol. 13, pp. 1-16, 1981.

[7] Martin, H.: Fluidized beds, *Heat exchanger design handbook,* Hemisphere publishing corporation, Washington DC, pp. 2.8.4.1-2.8.4.14, 1990.

[8] Yang, Y.M., Maa, J.R.: Boiling of suspension of solid particles in water, *Int. J. Heat Mass Transfer,* vol. 27, pp. 145-147, 1984.

[9] Stephan, K., Preusser, P.: Wärmeübergang beim Behältersieden, *Chem. Ing. Tech., Int. J. Heat Mass Transfer,* vol. 51, pp. 649-679, 1979.

SEMICONDUCTING PROPERTIES OF OXIDE/SULPHIDE LAYERS FORMED ON NICKEL-CHROMIUM ALLOYS AND THEIR RELEVANCE TO HOT CORROSION

César A.C. SEQUEIRA

Department of Chemical Engineering, Instituto Superior Técnico, Av. Rovisco Pais 1, 1049-001 Lisboa, Portugal

Fax +351 21 7783594; Email: cesarseq@mail.ist.utl.pt

Abstract

Electrochemical Impedance Spectroscopy (EIS) was used to analyse the semiconducting properties of oxide-layers formed on specimens of Ni, Ni-0.1 at% Cr, Ni-1 at% Cr, Ni-10 at% Cr, Ni-20 at% Cr, Ni-50 at% Cr, and Cr oxidized in O_2 / SO_2 atmospheres at 600 ºC for 6 and 24 hours.

Three different electrical behaviours were observed. Firstly, specimens mainly forming NiO and/or Cr_2O_3 exhibit only p-type character, secondly specimens mainly forming Ni_3S_2 and or Cr_2S_3 with only n-type properties and thirdly, specimens forming nickel-cromium oxide/sulphide scales, which exhibit both p- and n-type conduction. These mixtures of Ni, Cr oxysylphides show very complex behaviour in terms of degree of doping and flat-band potential.

Keywords: Semiconductivity; Oxide films; Sulphide films; Nickel-chromium alloys; High-temperature corrosion

1 Introduction

Metal oxides and sulphides are usually ionic crystals. A perfect ionic crystal would be an insulator since place exchange between ions of equal charge cannot lead to transport of ions and electrons. But electrolytic conduction actually measured for ionic crystals compares well with the values calculated from ionic mobilities obtained from diffusion measurements. Pioneer experiments by Wagner et al. have shown that the measured oxidation rates of Cu to Cu_2O, Cu to CuI, Ag to Ag_2S, and Ag to Ag Br, which depend on the diffusion of cations through the growing layer, are in good agreement with the rates calculated from the electrical conductivities of the products and transport numbers of the cations through them, which were measured for the purpose as functions of the partial pressure of the coexisting gas phase over a wide range. Wagner [1] has shown that both diffusion and ionic conduction can be attributed to the presence and migration of lattice defects, and defects are, in turn, related with the semiconducting properties of metal oxides and sulphides [1,2]. Film growth (or corrosion rate) in high temperature solid/gas reactions, therefore, can occur because of such a defect nature in the film formed and the consequent diffusion which can take place through it.

Hot corrosion is the term by which is recognised the in-service scaling produced on superalloy components of aero and marine gas turbines. Nickel and chromium are two of the principal metals which form the well known superalloys group. In the hot corrosion of Ni-base alloys, nickel- and chromium oxides and sulphides are formed, as well as mixed nickel-chromium oxides/ sulphides. It is therefore of great interest to study the role of the semiconducting properties of these films on the corrosion performance of different nickel-chromium alloys, and to map out the conditions at which the different films are formed.

NiO, Cr_2O_3, Ni_3S_2 and Cr_2S_3 are four of the main corrosion products observed in hot corrosion. They are non-stoichiometric Wagner-model semiconductors exhibiting n- and p-type behaviour [3,4]. This fact is of concern when it comes to hot corrosion of Ni-Cr alloys in O_2/SO_2 atmospheres, and deserves further consideration.

In aqueous corrosion, Electrochemical Impedance Spectroscopy (EIS) has been used to investigate the semiconducting properties of oxides, both synthetic oxide layers and oxides grown from metal-substrates electrochemically [5,6]. One approach used is to introduce the Mott-Schöttky relation [7] and examine the potential dependence of the capacitance of the oxide layer. By assuming a depletion of charge carriers in the oxide interface the semi-conducting properties can be obtained by measuring the capacitance of the space charge region as a function of potential. Information about the density of charge carriers, type of semi-conductor and flat-band potential might be extracted from the Mott-Schöttky relation:

$$\frac{1}{C_{SC}^2} = \frac{2}{\varepsilon\varepsilon_0 q N_q A^2}\ (E - E_{FB} - \frac{kT}{q}) \qquad (1)$$

where A is the area, N_q is the donor concentration, E is the applied potential, E_{FB} is the flat-band potential, ε is the relative permitivity of the film, ε_0 is the permitivity of vacuum, q is the charge of the electron, and kT / q is about 25 mV at room temperature.

This paper reports the results from electrochemical measurements made on Ni, Cr and Ni/Cr alloys corroded in O_2/SO_2 mixtures at 600 ºC for 6 and 24 hours and correlates the observed capacitance-potential behaviour with the semiconducting properties of the produced corrosion films.

2 Experimental

2.1 Alloy preparation

Nickel was obtained as spectrographically standardised metal in 3 mm diameter rod from Metals Research Ltd. with Mn, Mg, Al, Zn, P and Cr less than 50 ppm each, Si, Cu, Fe and oxygen less than 100 ppm each, and S 10 to 20 ppm. Chromium was obtained as flakes of purity 99.999 % from Halewood Chemicals Ltd.

The weight proportions of nickel and chromium for the 5 studied alloys were as follows:

Alloy, at% Cr	Wt. of Cr, g	Wt. of Ni, g
0.1	0.0443	49.9557
1	0.4434	49.5567
10	4.4797	45.5203
20	9.0637	40.9363
50	23.4838	26.5162

Weighed amounts of nickel and chromium pieces for the appropriate alloy were induction melted, at 1600 ºC, in an alumina crucible held loosely in a graphite susceptor. The resulting alloy, about 5 cm long and 1.2 cm dia., was found to be uniformely mixed on metallographic test. Specimens were cut from each cast alloy rod and their nominal compositions were confirmed by EPM analyses. No dissolved Al was detected in the alloys. The final specimen size was 10 x 10 x 2 mm^3. Specimens were then freshly polished on a series of Oakey polishing papers to Grade 4/0, washed with soap and water and degreased in redistilled acetone.

2.2 Alloy oxidation

Specimens were corroded in a conventional quartz helix microbalance in O_2/SO_2 mixtures in the ratios 1/0, 1/2, 1/12, 9/1 and 0/1 with actual flow rates 100/0, 33.3/66.6, 6/72, 135/15 and 0/100 mL/min., respectively. The specimen was initially located well above the hot zone (600 ºC) in the reaction furnace until the required reaction conditions had been established and then was winched down into the furnace. After the corrosion run had been continued for the required time (6 or 24 hours), the furnace was lowered, and the specimen unloaded.

2.3 Corrosion products characterization

Crystalline corrosion products were characterized by: visual observations; macro-, micro- and stereoscan micrography using a Reichert Universal Kamera Mikroskop "Mef"; X-ray studies, by the Debye-Sherrer method in a Philips type PW 1009 X-ray unit; and, electron probe results with a JEOL electron probe analyser with a 25 KW beam.

2.4 EIS Measurements

A three-electrode cell with a large concentric platinum counter electrode was used in the experiments. The electrolyte was a non-aggressive deaerated borate buffer with pH 9.22. Impedance measurements were first obtained at the open circuit potential in a large frequency range from 100 kHz to 1 mHz. The data were fitted to an appropriate equivalent circuit. Thereafter, impedance measurements were run at constant applied potentials in a sequence starting at the most positive potential. The frequency range was limited to two decades. The potential dependent capacitance was determined by fitting the data to the equivalent circuit. By this procedure, the change in capacitance with frequency, due to frequency dispersion, was eliminated.

The steady state current was measured at each potential to assure that the change in capacitance could be related only to the electric properties and not to the reduction/oxidation of metal-ions in the oxides/ sulphides and/or H_2/O_2 formation.

3 Results and discussion

3.1 Alloy oxidation and characterization

As reported in sections 2.2 and 2.3, the reaction of O_2/SO_2 mixtures, and oxygen/sulphur dioxide alone with Ni, Cr and Ni-Cr alloys at 600ºC for two corrosion durations, led to 70 different corrosion kinetics results.

The Ni-corroded sample was generally dark greenish-grey and heavily nodular, corrosion being particularly severe in 24 hours experiments. The main corrosion product was NiO.

The corrosion rate of Cr in O_2/SO_2 was low, exfoliation being observed particularly in 24 hours experiments. In some cases, red, blue and yellow areas were seen beneath the exfoliated layer, and, in O_2/SO_2 : 1/12, a relatively adherent layer was visible in 6 hours experiments.

The corrosion rates of 0.1, 1 and 10 % Cr alloys were found to conform equally well to both parabolic and linear rate relationships. The corroded samples were predominantly nodular, and the corrosion rate generally decreased with increase of the Cr content in the alloy but, between 0.1 and 1% Cr alloys, the posi-

positions reversed at times with the latter showing a higher corrosion. The corrosion layers were not always protective, and in the 24 hours experiments the metal could easily be cracked out of the corrosion layer. The change of corrosion rates between 10 and 20 % Cr alloys was very marked and the 50 % Cr alloy was similar to Cr in most respects. The corrosion layer built up in a O_2/SO_2 : 1/2 mixture on the 20 % Cr alloy could be broken off in chips. It was grey-green and nodular at the coat/gas interface, and shiny silver-grey on the metal/coat interface. Corrosion was very low in pure SO_2 ; the other two gas ratios 1:12 and 9:1 caused nodular growth but with lower corrosion rates. The 1:12 ratio gave an interesting multi-coloured surface underneath the nodules.

The attack of the 50 % Cr alloy by pure SO_2 was negligible; in general, there was exfoliation of the corrosion products, and a dull grey surface underneath the exfoliated layers, was always observed.

In general, the visual observations of the corroded samples showed that the polished surface of the sample went through several orders of interference colours (at least two sequences of blue-green-yellow-red) before becoming grey. Spallation and breakaway corrosion were also observed in several situations, and only the samples exhibiting compact layers with homogeneous thickness were selected for the EIS measurements.

X-ray analyses and electron probe detected NiO, Ni_3S_2, Cr_2O_3, CrS, Cr_2S_3, $NiCr_2O_4$, as main corrosion products. In the cross section micrography, Ni_3S_2 appeared yellowish white, NiO appeared lavender grey, and Cr_2O_3 was also grey but quite distinct from the grey NiO.

Ni corroded in pure O_2 developed a NiO layer; Cr corroded in pure O_2 developed a Cr_2O_3 layer; Ni corroded in pure SO_2 developed a thin Ni_3S_2 layer, that converted to a grey-black Ni_3S_2 – NiO twin layer with the duration of corrosion; Cr corroded in pure SO_2 for 6 hours, developed a Cr_2S_3 layer, that converted to a Cr_2S_3-CrS-Cr_2O_3 layer for 24 hours corrosion.

For the Ni-Cr alloys in O_2/SO_2 mixtures, NiO was the main corrosion product for all the alloys except the 50 % Cr alloy that contained essentially Cr_2O_3. Table 1 shows X-ray data for the scale on 20 % Cr alloy in O_2/SO_2 : 1/2, for 6 hours duration. As expected, the corrosion products are a complex mixture of Ni/Cr oxides and sulphides or, in other words, in electronic words, the corrosion products contain n-type and p-type semiconducting films, thus their semiconducting nature should oscillate between the p-type and the n-type.

3.2 Mott-Schöttky analysis

To obtain meaningfull results from the Mott-Schöttky analysis on our oxides, we followed the procedure described in section 2.4 and selected 4 samples with one single corrosion product (NiO, Cr_2O_3, Ni_3S_2, Cr_2S_3), and 3 samples with mixed oxide/sulphide layers. The plots were normalized against the maximum value of C^{-2} to facilitate comparison between the various corroded samples. Both Cr_2O_3 and NiO are p-type oxides [8-10] with predominant cationic diffusivity. Ni_3S_2 and Cr_2S_3 are n-type sulphides [11,12] with predominant anionic diffusivity. As expected, pure NiO (a) and Cr_2O_3 (b) samples showed p-type properties (Fig. 1); and pure Ni_3S_2 (c) and Cr_2S_3 (d) samples showed n-type properties (Fig. 1). The single NiO developed on Ni in pure SO_2; the single Cr_2O_3 developed on Cr in pure O_2; curve (c) corresponds to Ni_3S_2 most probably contaminated with NiO, and was developed on Ni in pure S_2; for the Cr_2S_3 layer developed on Cr in pure SO_2, again a Cr_2S_3-CrS-Cr_2O_3 contamination is to be considered.

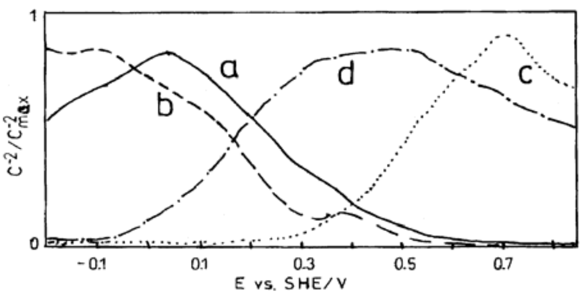

Figure 1: Mott-Schöttky results for nearly pure oxides and sulphides. (a) NiO (—); (b) Cr_2O_3 (---); (c) Ni_3S_2 (·····); (d) Cr_2S_3 (-·-·-·).

The three samples showing more complex behaviour are represented in Fig. 2. The 50 % Cr alloy corroded in 1/2 : O_2/SO_2 mixture for 6 hours, whose main corrosion product was Cr_2O_3, showed p-type behaviour like pure Cr_2O_3 (Fig. 2, a). The 20 % Cr alloy corroded in 1/2 : O_2/SO_2 mixture for 6 hours, showed a complex behaviour (Fig. 2, b) with more p-type properties than n-type properties, accompanied by changes in the charge.carrier concentration and shifts in the flat-band potentials. This seems to be due to the complex behaviour of the corroded layers, as shown in Table 1; furthermore, more recent results (not included in this paper) are showing that the protective properties of the external scale have a strong contribution to this behaviour, independently of the semiconductivity itself of the different constituents of the corrosion layers(s). Again, the 10 % Cr sample corroded in 1/12 : O_2/SO_2 mixture for 6 hours showed a complex behaviour (Fig. 2, c), with a predominance of the n-type behaviour (the main corrosion product was Ni_3S_2).

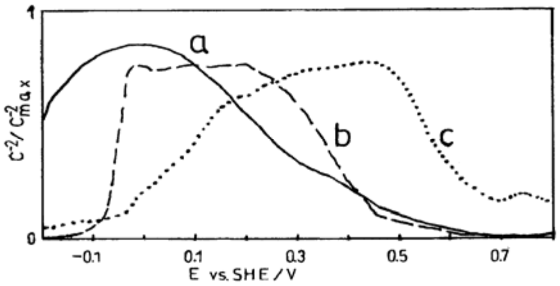

Figure 2: Mott-Schöttky results for mixed oxide-sulphide films. (a) 50 % Cr in 1/2 : O_2/SO_2; (b) 20 % Cr in 1/2 : O_2/SO_2; (c) 10 % Cr in 1/12 : O_2/SO_2.

To summarize, EIS used in combination with corrosion studies showed to be a very sensitive tool to determine electronic changes between p- and n-type properties as the chemical content of the formed corrosion layers changes. Further studies are necessary and would be published shortly

Table 1: X-ray data for scale on 20 % Cr alloy in O_2/SO_2 : 1/2, at 600 ºC, for 6 hour duration.

Intensity (visual)	d (Å)	Compounds
s	4.11	Ni_3S_2
w	3.63	Cr_2O_3
s	2.88	Ni_3S_2
vw	2.67	Cr_2O_3
vw	2.48	Cr_2O_3
vs	2.41	NiO, Ni_3S_2
vw	2.18	Cr_2O_3
vvs	2.09	NiO
w	2.04	Ni_3S_2, Cr_2O_3
m	1.83	Ni_3S_2, Cr_2O_3
m	1.81	Ni_3S_2, Cr_2O_3
vw	1.67	Ni_3S_2, Cr_2O_3
m	1.66	Ni_3S_2
vvs	1.475	NiO, Cr_2O_3
vw	1.29	Cr_2O_3, Ni_3S_2
s	1.26	NiO
vw	1.23	Cr_2O_3
vw	1.22	Ni_3S_2
s	1.21	NiO, Cr_2O_3
vw	1.13	Ni_3S_2
w	1.09	Ni_3S_2, Cr_2O_3
m	1.08	Ni_3S_2, Cr_2O_3
m	1.04	NiO, Cr_2O_3
w	1.02	Ni_3S_2
m	0.959	NiO, Ni_3S_2
s	0.934	NiO, Ni_3S_2
vs	0.854	NiO
s	0.805	NiO

References

[1] Wagner, C.: *Z. Phys. Chem*, B21, 25, 1933.

[2] Wagner, C.: *Prog. in Solid-State Chemistry*, 10, 3, 1975.

[3] Kofstad, P.: *High-Temperature Corrosion*, Elsevier Applied Science, London, 1988.

[4] Gleitzer, C.: *Key Eng. Mat*., 125-126, 355, 1997.

[5] Hakiki, N.E., Boudin, S., Rondot, B., Da Cunha Belo, M.: *Corros. Sci*., 37, 1809, 1995.

[6] Virtanen, S., Schmuki, P., Bhöni, H., Vuoristo, P., Mäntylä, T.: *J. Electrochem. Soc*., 142, 3067, 1995.

[7] Schöttky, W.: *Z. Phys*., 118, 539, 1941.

[8] Kröger, A.: *The Chemistry of Imperfect Crystals*, North-Holland, Amsterdam, 1974.

[9] Mrowec, S.: *Defect and Diffusion in Solids*, Elsevier, Amsterdam, 1980.

[10] Wagner, J.B.: *Solid State Ionics*, 12, 527, 1984.

[11] Gilewiez-Wolter, J., Zurek, Z., Ochoński, A.: *Solid State Communications*, 102, 397, 1997.

[12] Boutbila, My.A., Rasneur, J., Aatmani, M.El.: *J. Alloys and Compounds*, 283, 88, 1999.

Proceedings of The 1st International Conference on **D**iffusion in **S**olids and **L**iquids
DSL-2005, July, 6-8, 2005, University of Aveiro, Portugal

A STUDY OF THE REDOX CHEMISTRY OF ANTHRAQUINONE 2,7-DISULPHONATE

César A.C. SEQUEIRA[1,*], Rui F. LOBO[2], Giorgios ANASTASSAKIS[3]

[1] Instituto Superior Técnico, Av. Rovisco Pais 1, 1049-001 Lisboa, Portugal
[2] Grupo de Nanotecnologia, Faculdade de Ciências e Tecnologia, Universidade Nova de Lisboa, 2829-516 Caparica, Portugal
[3] National Technical University of Athens, Department of Mining and Metallurgical Engineering, 9 Heroon Polytechniou str., 15780 Zographou, Greece

[*]Corresponding author. Fax: +351 21 7783594; Email: cesarseq@mail.ist.utl.pt

Abstract

The redox chemistry of anthraquinone 2,7-disulphonate (AQ27DS) in alkaline aqueous solutions is studied. Cyclic voltammetry and exhaustive electrolysis indicated that AQ27DS was reversibly reduced in a two electron, one proton process at a variety of electrode surfaces:

$$\mathrm{AQ27DS} + \mathrm{H^+} + 2\mathrm{e^-} \rightarrow \mathrm{AQ27DSH^-}$$

From limiting current results at a rotating disc electrode, the diffusion coefficient of AQ27DS was calculated to be 3.37×10^{-10} m^2s^{-1}. The presence of a strong ESR signal from the reduced solution showed that $\mathrm{AQ27DSH^-}$ existed in equilibrium with the radical species, $\mathrm{AQ27DS}\overset{-}{\bullet}$. From an analysis of the voltammetric peak separation, the comproportionation constant for the AQ27DS/ $\mathrm{AQ27DS}\overset{-}{\bullet}$ equilibrium was estimated to be in the range 0.2 to 4.

Keywords: Anthraquinone disulphonate; Electrochemical reduction; Alkaline aqueous solutions; UV-visible spectrophotometry; ESR spectroscopy

1 Introduction

The anthraquinone disulphonate (AQDS) is an isomer mixture, but the most active isomers are believed to be the 2,7 and 1,5 disulphonates, of which AQ27DS is the most active (Fig. 1).

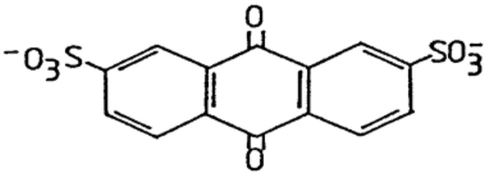

Figure 1: Anthraquinone 2,7-disulphonate (AQ27DS).

In this paper, its redox chemistry was investigated using cyclic voltammetry, at stationary and rotating disc electrodes, and controlled potential coulometry was conducted. The reduction products and intermediates were analysed by UV-Visible spectrophotometry and ESR spectroscopy.

2 Experimental

2.1Purification of AQ27DS

The purification of AQ27DS and the analysis of the purified AQ27DS solid were performed as described elsewhere [1]. The purification procedure led to a yield of 52%. High Pressure Liquid Chromatography (HPLC) showed that the pure 2,7 isomer contained 99.1% AQ27DS. The ^{13}C NMR spectrum was also recorded, and showed six distinct carbon resonances, which is consistent with the structure of AQ27DS.

2.2 Voltammetry

Solutions of AQ27DS (in the range 1-5 mol m^{-3}) were prepared by dissolving the appropriate mass of the sodium salt conducting carbonate buffer (0.059 kmol Na_2CO_3 m^{-3}, 0.223 kmol $NaHCO_3$ m^{-3}, 0.10 kmol Na_2SO_4 m^{-3}: pH 9.3). All working solutions were freshly prepared on the day of the experiment and were nitrogenated for two hours before use with white spot grade nitrogen (BOC plc).

Cyclic voltammograms were recorded using a conventional electrochemical cell design and a saturated calomel reference electrode (SCE electrode).

Either a hanging mercury drop electrode (HMDE), a gold flag or a platinum foil was used as the working electrode.

All experiments were conducted using an EG&G Princeton Applied Research M273A potentiostat/ galvanostat driven by M270 software and Powersine in the package of Powersuite.

2.3 Exhaustive Electrolysis

In order to determine the number of electrons involved in the reduction of AQ27DS and to provide a supply of the reduced compound, exhaustive electrolysis was performed as described previously [1].

2.4 UV-Visible Spectrophotometry

Observation of the electrode surface during cyclic voltammetry revealed that a deep red-brown colour was produced on the negative going scan; this colour was discharged on the return scan. This suggested that the production of the quinol (AQH_2) could be followed spectrophotometrically.

An apparatus was assembled to continuously monitor the UV-Visible spectrum of a $Na_2AQ27DS$ solution throughout its reduction, by pumping the solution through a flow-through UV cell. The apparatus is shown in Fig. 2.

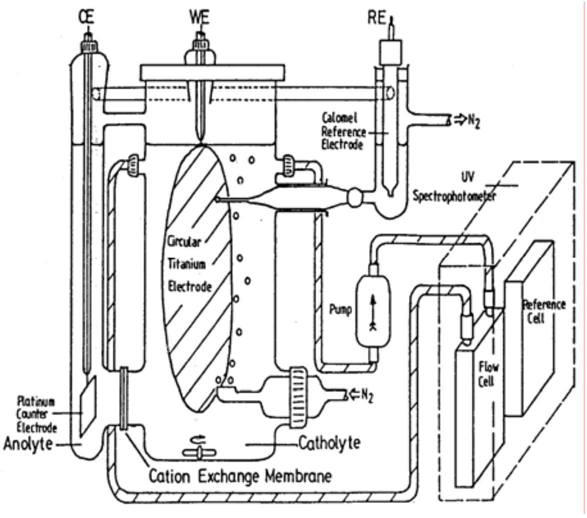

Figure 2: Electrolysis with Linked UV-Visible Spectrophotometry.

2.5 ESR Spectroscopy

The peak separation shown by voltammetry and the UV-Visible results indicated that the radical anion, $\mathrm{AQ27DS}\overset{-}{\bullet}$, was produced during the reduction of AQ27DS, even though the major product was $AQ27DSH^-$. If the radical anion was present, then the solution would show a strong ESR signal. The following experiment was designed to detect any ESR signal produced during the reduction of the anthraquinone.

Solutions of 1 and 5 mol AQ27DS m^{-3} were prepared by dissolving the appropriate mass of the sodium salt in conducting carbonate buffer (pH 9.3), then the solutions were deoxygenated by passing purified nitrogen through them.

The deoxygenated solution was loaded into the drive syringe of the electrochemical ESR apparatus shown in Fig. 3.

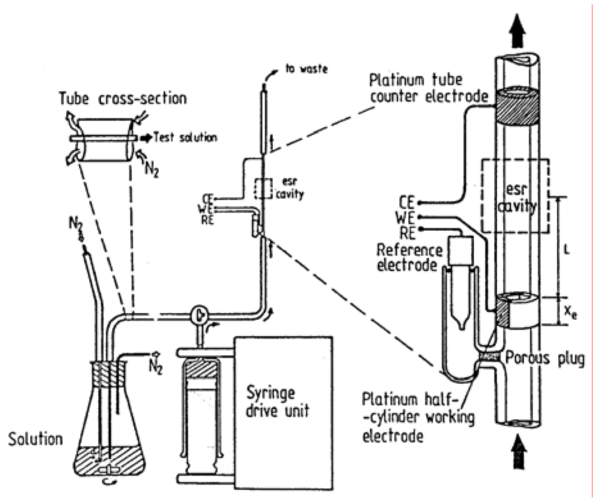

Figure 3: Electrochemical ESR apparatus.

3 Results and Discussion

3.1 Voltammetry and Exhaustive Electrolysis

Cyclic voltammetry and exhaustive electrolysis indicated that the anthraquinone was reversibly reduced in a two electron, one proton process at a hanging mercury drop electrode (HMDE), a gold flag, and a platinum foil electrode:

$$AQ27DS + H^+ + 2e^- \rightarrow AQ27DSH^-$$
(1)

From limiting current results at a rotating gold disc electrode the diffusion coefficient of AQ27DS was calculated to be $3.73 \times 10^{-10}\ cm^2s^{-1}$ [1].

3.2 UV-Visible Spectrophotometry

The UV-Visible spectra taken at approximately 15C charge intervals are shown in Fig. 4.

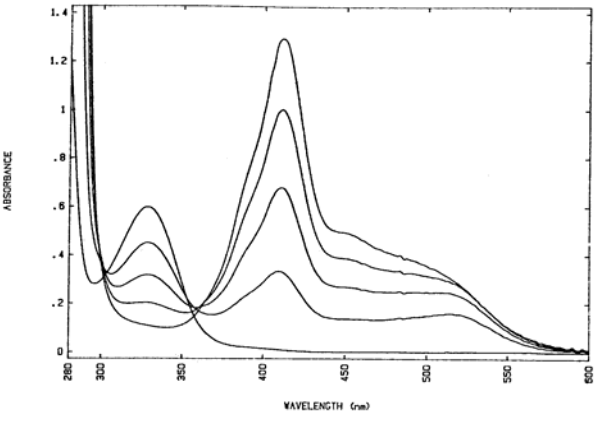

Figure 4: Spectra taken at 15 C Charge Intervals during AQ27DS Reduction. Concentration = 1.392 mol^{-3}. Path length = 1 mm. pH = 9.3

It can be seen that the peak at 330 nm, due to AQ27DS, decreased and two new peaks appeared as the reduction proceeded: a sharp peak at 410 nm and a broad shoulder at 520 nm. By measuring the absorbances at 330 nm of solutions containing different concentrations of AQ27DS, it was shown that the Beer-Lambert law was followed, and so the absorbance at 330 nm could be used to monitor the AQ27DS reduction.

The absorbance at 330 nm decreased linearly with charge passed as the AQ27DS was reduced (deviations were seen as the reduction neared completion, when the charge correction due to oxygen diffusion became very important). The charge taken to reduce the absorbance to half its initial value was 32.3 C, corresponding to 1.04 F $\mathrm{mol^{-1}}$. This suggests that a two electron process is required to achieve complete reduction, a conclusion in agreement with earlier results. The starting material, AQ27DS, shows absorbances at 330 nm ($\varepsilon = 460\ \mathrm{m^2mol^{-1}}$) and 258 nm ($\varepsilon = 4450\ \mathrm{m^2mol^{-1}}$) in the UV spectral region. The reduction product at pH 9.3 is believed to be AQ27DSH$^-$, and so the absorbances at 410 nm ($\varepsilon = 980\ \mathrm{m^2mol^{-1}}$) and 277 nm ($\varepsilon = 104\ \mathrm{m^2mol^{-1}}$) are attributed to this species. Here, ε is the extinction coefficient.

Work done by McQuillan [2] has shown that the $\mathrm{AQ27DS}\overset{-}{\bullet}$ radical anion can be produced by controlled potential electrolysis of AQ27DS at pH 13.2 in a solution containing 0.5 kmol $\mathrm{m^{-3}}$ tetraethyl ammonium hydroxide. In such a solution two reduction waves can be seen in a cyclic voltammogram, corresponding to two successive one electron reductions:

$$\mathrm{AQ27DS} + e^- \rightarrow \mathrm{AQ27DS}\overset{-}{\bullet}$$

(2)

$$\mathrm{AQ27DS}\overset{-}{\bullet} + e^- \rightarrow \mathrm{AQ27DS^{2-}}$$

(3)

By applying a potential sufficient to achieve only one electron reduction, McQuillan produced a solution containing $\mathrm{AQ27DS}\overset{-}{\bullet}$ as the major species, and therefore was able to measure its UV-Visible spectrum [2]. He found absorbances at 403 and 525 nm. It is likely that the shoulders at around 390 nm and 520 nm observed in Fig. 4 are due to $\mathrm{AQ27DS}\overset{-}{\bullet}$.

At more negative potentials, McQuillan reduced the di-anion AQ27DS^{2-} which absorbed at 454 and 540 nm. The pKa of AQ27DSH$^-$ is 10.8 [2], and so at pH 9.3 approximately 3 % of AQ27DSH$^-$ would be present as the di-anion. Therefore, the shoulder observed at 450 nm in Fig. 4 is likely to be due to AQ27DS^{2-}, present as a minor component. As the reduction proceeds, protons are consumed and, despite the buffering of the solution, the pH is likely to rise slightly. Calculations show that a change of only 0.3 of a pH unit would double the equilibrium concentration of the di-anion. This explains why the shoulder at 450 nm became more pronounced as the reduction progressed.

3.2 ESR Spectroscopy

The flow-through tube electrode provides a well defined mass transport rate, and the mass transport limited current at a half-cylinder electrode should be directly proportional to the third root of the flow rate, V_f / $\mathrm{m^3s^{-1}}$ [3]; of course, the slope of a graph of i_{lim} vs. $V_f^{1/3}$ would give an estimate of the diffusion coefficient, D_o, of AQ27DS.

Radical species produced at the tubular electrode are carried into the ESR cavity, but the velocity profile across a section of tube is parabolic and not uniform, with the flow slowest near the walls.

The radicals produced at the tube edge, diffuse towards the centre of where the flow is fastest. Thus, the number of radicals within the ESR cavity is dependent on the flow velocity profile across the tube and the rate of radial diffusion towards the centre. This combination has been considered by Compton [3] who found that the resulting ESR signal was given by equation:

$$S = \frac{S_o\,(\pi/4)^{2/3}\,l^{2/3}\,r^2\,i_{lim}\,I_{k'}}{zFD_o^{1/3}\,V_f^{2/3}\,I_k}$$

(4)

where

S = ESR signal strength,

S_o = ESR signal strength for one mole of spins within cavity,

l = length of ESR cavity / m,

r = radius of the tube / m,

I_k and I_k’ are sensitivity factors, and are constant for a given geometry.

Thus, the normalised signal strength (S/i_{lim}) should be directly proportional to $V_f^{-2/3}$.

Such a plot is shown in Fig. 5

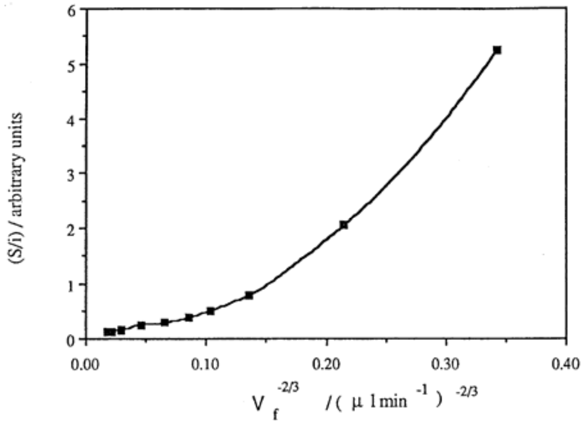

Figure 5: Normalised ESR signal (S/i_{lim}) vs. $V_f^{-2/3}$.

As can be seen, the resulting plot is not linear, showing a signal enhancement at low flow rates. This is consistent with a mechanism of radical production as follows:

$$\mathrm{AQ27DS} + 2e^{-} + H^{+} \rightarrow \mathrm{AQ27DSH}^{-}$$

(5)

$$\mathrm{AQ27DSH}^{-} \leftrightarrow \mathrm{AQ27DS}^{2-} + H^{+}$$

(6)

$$\mathrm{AQ27DS}^{2-} + \mathrm{AQ27DS} \leftrightarrow 2\ \mathrm{AQ27DS}\overset{-}{\bullet}$$

(7)

The electrochemical reduction results in the formation of the protonated di-anion (5) which exists in equilibrium with the unprotonated form (6); this then reacts with the starting material to produce the radical anion (7).

If the flow rate is slow, the reduced material undergoes greater radial diffusion, towards a region of high AQ27DS concentration, which will shift the equilibrium (7) to the right, and result in an increased ESR signal.

Using a concentration of 5 mol AQ27DS m^{-3} enabled a partially resolved ESR spectrum to be obtained. This was consistent with the radical structure shown below (Fig. 6).

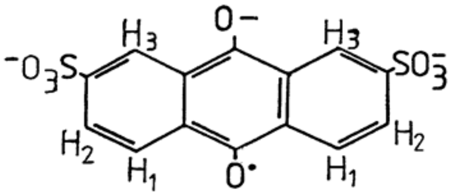

Figure 6: Structure of AQ27DSH$\overset{-}{\bullet}$

There are three groups of equivalent protons, labelled H_1, H_2 and H_3. This would be expected to produce 27 resonances, but spectral overlap and line broadening will reduce this number.

In summary, the ESR signal strength variation with flow rate showed that the radical was not produced directly at the electrode in a one electron process, but was formed via a comproportionation reaction between the di-anion and the AQ27DS starting material:

$$\mathrm{AQ27DS} + \mathrm{AQ27DS}^{2-} \leftrightarrow 2\ \mathrm{AQ27DS}\overset{-}{\bullet}$$

(8)

The peak separation from voltammetry enabled the comproportionation constant (K_c) to be estimated, and it was found to be in the range 0.2 to 4.

References

[1] Sequeira, C.A.C., Lobo, R.F., Anastassakis, G.: *Electrochemical Reduction of AQ27DS in Aqueous Solution*. Materials Science Forum, in press, 2005.

[2] McQuillan, A.J.: Private communication, Chemistry Dept., University of Otago, New Zealand, 1997.

[3] Compton, R.G.: *Electrochemical ESR*. Ph.D. Thesis, University of Oxford, U.K., 1980.

RING-DISC STUDIES OF OXYGEN REDUCTION AT LANTHANUM CALCIUM MANGANATE IN ALKALINE MEDIUM

César A.C. SEQUEIRA[1,a], Diogo M.F. SANTOS[1,b], Walmar BAPTISTA[2,c]

[1]Instituto Superior Técnico, Av. Rovisco Pais 1, 1049-001 Lisboa, Portugal
[2]Centro de Pesquisas e Desenvolvimento (CENPES), Cidade Universitária Quadra 7,
Ilha do Fundão, Rio de Janeiro, RJ, Brasil, CEP21941-598

[a]cesarseq@mail.ist.utl.pt; [b]di-santos@yahoo.com; [c]walmar@petrobras.com.br

---

Abstract

The electrocatalysis of the oxygen reduction reaction by lanthanum calcium manganate, ($La_{0.5}Ca_{0.5}MnO_3$) (LCM) has been studied by cyclic voltammetry using the rotating ring-disc electrode technique (RRDE) in alkaline medium. From the ring-disc data and other kinetic parameters it has been assumed that the oxygen reduction occurs by dissociative chemisorption at low overpotentials. At higher overpotentials, the formation of hydrogen peroxide has been observed on this electrocatalyst. The apparent exchange current density value for oxygen reduction on LCM has been found to be 5 x 10^{-8} Acm^{-2}, while the corresponding Tafel slope is 0.115 V per decade. The possible reaction mechanism for electroreduction of oxygen on this oxide catalyst has been discussed.

Keywords: Fuel cell; metal-air battery; lanthanum calcium manganate; oxygen reduction

---

1 Introduction

Fuel cells and metal-air batteries are energy generators that hold considerable potential for future efficiency and relatively clean generation of electricity. These electrochemical devices transform fuel energy into electricity without the need for a thermal cycle. One of the major concerns of fuel cells research is the development of good electrocatalysts for the oxygen reduction reaction. Platinum group metal electrodes, activated carbons, semiconducting mixed metal oxides, among others, are low cost materials that have been shown to possess good catalytic activity for oxygen reduction at low temperature [1].

In the present communication, the electrocatalysis of the oxygen reduction reaction by lanthanum calcium manganate, $La_{0.5}Ca_{0.5}MnO_3$ (LCM) has been studied by linear sweep cyclic voltammetry (LSCV) using the rotating ring-disc electrode technique (RRDE) in alkaline medium.

2 Experimental

The method of preparation of the LCM was similar to that described in the literature [2] using La, Ca and Mn oxides obtained by the decomposition of their salts. These oxides were mixed and sintered at 1000º C, showing a specific resistance of 1.2 ohm.cm at 1.5 $tons.cm^{-2}$. Their composition could be formulated as

$$La^{3+}_{(1-x)}\ Ca^{2+}_{x}\ Mn^{3+}_{(1-x+2y)}\ Mn^{4+}_{(x-2y)}\ O^{2-}_{(3-y)}\ \left(V_{O''}\right)_y$$

where $\left(V_{O''}\right)$ are the oxygen vacancies required for charge compensation. The electrochemical measurements have been carried out with PAR equipment and a conventional three-compartment cell. The catalyst was coated onto the gold-plated Pt-disc electrode, and the bright Pt ring was platinised. The electrolyte was prepared from pure KOH and bidistilled water, and the potentials were measured against a Hg/HgO reference electrode. The collection efficiency, N, for the RRDE system was calculated from the geometry of the ring-disc electrodes and found to be N ≅ 0.58 [2].

3 Results and Discussion

The catalyst coated on glassy carbon electrode (GCE) has been studied for its electrochemical behaviour in solutions deaerated with N_2 gas in the potential region of 0.1 V to –0.6 V and 0.8 V to –0.6 V, the results of which are shown in Fig. 1 (curves a,b).

The voltammograms obtained for GCE without catalyst coating are shown in Fig. 1b. The voltammograms show that in the cathodic region, the oxides are quite stable, unlike some of the systems which get reduced [1,3]. In the anodic potential region also, the catalyst maintains its stability and the evolution of oxygen is observed at a potential of about 0.6 V.

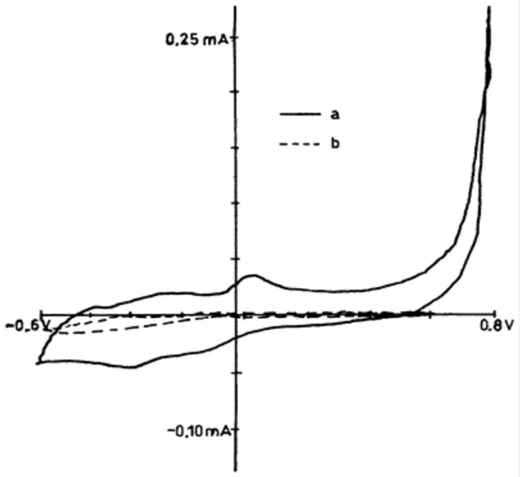

Figure 1: Linear sweep cyclic voltammograms of LCM and GCE (curves a, b, respectively) in 1M KOH solution deaerated with N_2 gas, at a sweep rate of 10 mV.sec.$^{-1}$.

The disc and ring currents as a function of the disc potential for oxygen reduction on LCM in KOH solution at different speeds in the range of 470 to 2300 rotations per minute are shown in Fig. 2.

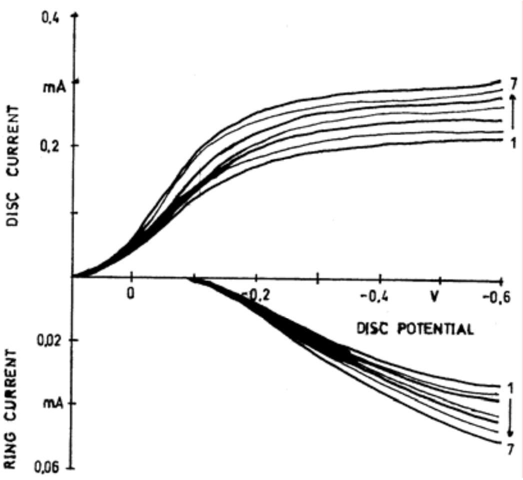

Figure 2: Oxygen reduction currents at LCM disc and H_2O_2 oxidation currents at a Pt/Pt ring in 1M KOH solution saturated with O_2 gas at different rotation speeds of (1) 470 (2) 670 (3) 950 (4) 1500 (5) 1670 (6) 1850 and (7) 2300; sweep rate is 10 mV.sec.$^{-1}$.

From this figure, it is observed that the ring current, indicating the formation of HO_2^- at the disc electrode is negligible in the potential region up to about –0.2 V starting from the rest potential of 0.1 V on the oxide catalyst. Above this potential there appears a small ring current I_r which gradually increases as the disc potential is made more cathodic up to the –0.6 V studied. The ring currents as well as the disc currents are dependent on rotation speed (ω) of the electrode.

The plot of limiting disc current density as a function of $\omega^{-1/2}$ for LCM shows straight lines which pass through the origin (figure not shown).

The oxygen reduction reaction on the LCM oxide is a mixed controlled process, i.e. controlled by both kinetic and diffusion up to a certain potential above which the process becomes more and more of diffusion controlled.

Plotting disc current values against rotation speed at different potentials and extrapolating them to $f \rightarrow \infty$ makes the determination of the kinetic current $I_k = nFkC_{bulk}$ possible. These plots are linear but not parallel to each other which probably indicates that the oxygen reduction is not first order with respect to dissolved oxygen. The mass transfer corrected I_d is then used for plotting Tafel lines (figure not shown) for the LCM electrocatalyst in 1M KOH solution at 27° C. These plots show Tafel slopes of 0.115 mV per decade. Deviation from Tafel linearity begins at a potential of about –0.2 V for the LCM system. The corresponding exchange current density value is 5 x 10^{-18} A.cm^{-2}.

The deviations from the Tafel lines are caused most likely by the occurrence of parallel sequential reactions as the potential where the deviation occurs corresponds to the beginning of ring current.

Plots of I_d / I_r vs $\omega^{-1/2}$ obtained from the experimental data of the present study for the LCM catalyst at various electrode potentials have been drawn (Fig. 3).

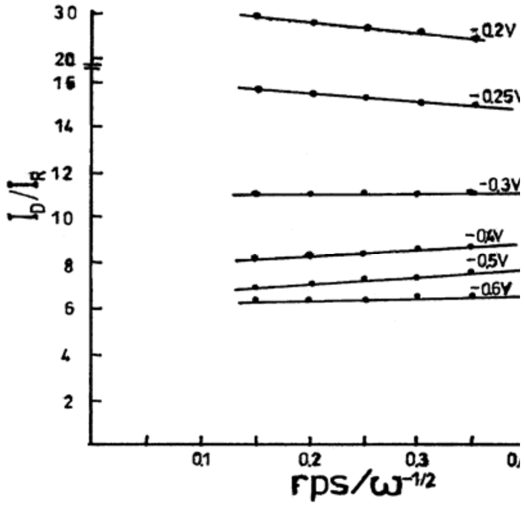

Figure 3: Plots of I_d / I_r vs. $\omega^{-1/2}$ obtained at various potentials in O_2-saturated 1M KOH solution at a LCM electrode.

From the plots of I_d / I_r vs $\omega^{-1/2}$ it can be concluded that the reaction mechanism undergoes a change as the electrode potential is shifted towards the negative direction. This becomes obvious if one examines the potential dependence of the intercepts and of the slopes of the obtained straight lines. In the lower overpotential region, the curves have negative slopes. As the potential is increased, the curves slowly become horizontal and at higher overpotentials, the curves show positive slopes. In all the cases, the value of intercept decreases with increase of overpotential. This indicates that in the lower overpotential region, the major reaction is that of the reduction of oxygen to hydroxyl ion without the formation of peroxide ion intermediate.

Literature survey indicates that a simple reaction model [4] is consistent with many of the reported experimental results. But in view of the present RRDE data in which one observes that the end product depends on the applied potential, it has been assumed that HO_2^- ion maintains an adsorption-desorption equilibrium and this equilibrium constant is dependent on the potential of the electrode. The reaction model can be written as:

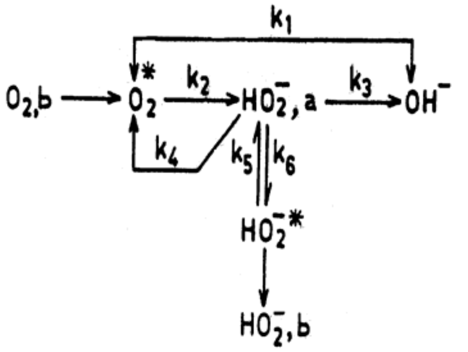

Here, k_1 represents the direct reduction to OH^- ion, i.e. without the formation of an intermediate that can be desorbed and detected on the ring of a rotating ring disc electrode experiment; k_1 will describe equally well any reaction in which the reductive splitting of the O – O bond occurs entirely in the adsorbed state, and the RRDE diagnostic criteria will not allow a distinction to be made between an electrochemical reductive cleavage and dissociative chemisorption of oxygen molecule. The routes shown in the above scheme are therefore relative to the possibilities offered by the RRDE method, and although this may appear to be a limitation, its usefulness has been repeatedly demonstrated. The factor k_2 is an overall rate constant for the formation of adsorbed peroxide, and may involve other rate constants that are related to both the intermediate formation of adsorbed super oxide and the disproportionation reaction; k_3 is the rate constant for reduction of peroxide, k_4 refers to the dismutation of adsorbed peroxide, and k_5 and k_6 represent rate constants for the process of desorption and adsorption of peroxide.

It has also been shown [4] that the expression for the calculation of rate constants may be written as:

$$\frac{I_d}{I_r} = \frac{I + 2k_1 / k_2}{N} + \frac{2\,(1 + k_1 / k_2)}{N_2} k_3\, \omega^{-1/2}$$

(1)

which can be modified as:

$$I_d / I_r = (1 + x) / N$$

(2)

when $\omega^{-1/2} \rightarrow 0$. Here, $x = 2\, k_1 / k_2$.

From the present experimental results of RRDE, it has been calculated that the value of x becomes 10 and above, at a potential of about –0.2 V for the oxide catalyst which is the value for the ratio of the partial current at the disc electrode due to the reduction of oxygen to OH^- ion, and partial current at the same electrode due to reduction to HO_2^-. As the potential is made more and more cathodic, current for oxygen reduction to HO_2^- increases comparatively. As the slopes of the lines increase with increasing electrode potentials, it follows that k_3 increases with increasing potential, and hence at these potentials, peroxide ion intermediate reduces further to hydroxyl ion at a rate that increases with increasing overpotential. But even at these potentials the value of k_1 does not become zero. At the intermediate potentials where the slope is nearly zero, the rate constant k_3 for the reduction of peroxide ion is small. Peroxide ion formed at these potentials is not further reduced to hydroxyl ion at a rate comparable with that by which it is produced.

Accordingly, we can conclude that the main reaction at lower overpotential region is O_2 reduction to OH^- ion directly, but as the potential is made cathodic, O_2 reduction to HO_2^- gradually begins which reduces slowly to OH^- ion and at still higher cathodic potentials reduction to OH^- ion through the formation of HO_2^- intermediate takes place at comparatively higher rates.

The "pseudo" splitting theory predicts that for every molecule of oxygen chemisorbed "side-on", there will be two-electron transfer centres. Thus the rate of oxygen chemisorption should be directly proportional to the square root of oxygen partial pressure. To verify this and to determine the value of n in the general relation $I = kp^n$, oxygen reduction on RDE (of RRDE) has been studied at different partial pressures of oxygen, by diluting it with nitrogen, and at a constant rotation speed of 2300 rpm. After correcting for the residual current, log I vs. log P_{O2} plots have been drawn at different potentials in the range of -0.05 to -0.25 V for the oxide system (figure not shown). The slopes have been observed in the range 0.45 – 0.55, up to a potential of about -0.15 V, and above this potential the value was found to increase with increase of overpotentials. This value indicates that dissociative chemisorption of oxygen molecule takes place in this low overpotential region on the surface of the catalyst. Similar type of observations have been reported [5] for the oxide catalysts for oxygen reduction reaction.

The RRD results and kinetic parameters observed for the O_2 reduction on the studied catalyst cannot be explained by considering the conventional models mentioned for these systems [6].

The zero ring current and the effect of partial pressure of O_2 on the rate at low overpotentials can be explained by considering either Griffith's model or Bridge model. To distinguish the possible adsorption of oxygen from these two models one may have to consider the interatomic distance of the transition metal ions of dual valencies. As the atoms of oxygen molecule can possibly adsorb on the two different valence ions, the bridge model appears probable in the case of our oxide catalyst.

References

[1] Brito, P.S.D., Sequeira, C.A.C.: *J. Power Sources*, 52, 1, 1994.

[1] Brito, P.S.D., Antunes, R.M.M., Sequeira, C.A.C.: *Técnica*, 3/95, 43, 1995.

[3] Matsumoto, M., Sato, E.: *Electrochim. Acta*, 25, 585, 1980.

[4] Damjanovic, A, Genshaw, M.A., Bockris, J.O'M.: *J. Chem. Phys*., 45, 4057, 1966.

[5] Yeung, K.L.M., Tseung, A.C.. *J. Electrochem. Soc*., 125, 878, 1978.

[6] Yeager, E.: *Proc. Electrochem. Soc. Symp*., 77-6, 149, 1977.

Proceedings of The 1st International Conference on **D**iffusion in **S**olids and **L**iquids
DSL-2005, July, 6-8, 2005, University of Aveiro, Portugal

INGRESS OF HYDROGEN IN HASTELLOY C

Yun CHEN[1,a], César A.C. SEQUEIRA[2,b], Xueyan SONG[3,c]

[1] Department of Engineering Physics, University of Wisconsin-Madison, Madison 53706, USA
[2] Instituto Superior Técnico, Av. Rovisco Pais 1, 1049-001 Lisboa, Portugal
[3] Applied Superconductivity Center, University of Wisconsin-Madison, Madison, USA

[a,c]chen2@wisc.edu; [b]cesarseq@mail.ist.utl.pt

Abstract

The ingress of hydrogen in Hastelloy C exposed to an acetate electrolyte (1 mol L^{-1} HAc/1 mol L^{-1} NaAc where Ac is the acetate ion) was studied using a potentiostatic pulse technique. The data were shown to fit a diffusion/trapping model under interface control, and values were determined for the irreversible trapping constants (k) and the flux of hydrogen into the alloy. The material was characterized by two trapping constants; one is associated with quasi-irreversible traps that saturate, leaving only irreversible traps. The density of irreversible traps was shown to agree with the concentration of phosphorus segregated at grain boundaries. The irreversible trapping constants for this alloy are consistent with its susceptibility to hydrogen embrittlement.

Keywords: Hydrogen ingress; Hastelloy C; Electrochemical techniques; Hydrogen diffusion; Irreversible trapping.

---

1 Introduction

The interaction of hydrogen with heterogeneities in alloys strongly influences the susceptibility of the alloys to hydrogen embrittlement. The heterogeneities provide trapping sites for diffusing hydrogen and the binding energy of these traps determines their reversible or irreversible character. By using models for the diffusion and trapping of hydrogen atoms, it is possible to identify the dominant types of irreversible traps in metals and alloys [1-5].

One model is used to analyze data obtained with a potentiostatic pulse technique in which a test electrode is charged with hydrogen at a constant potential (E_c) for a time (t_c). The potential is then stepped to a more positive value, E_A (10 mV negative of the open-circuit potential, E_{oc}), resulting in an anodic current transient with a charge q_a. Hydrogen ingress in all alloys studied so far has been found to occur under interface control in which the rate of ingress is controlled by the flux accross the interface rather than by diffusion in the bulk metal [1]. In the case of interfacial control, the total charge passed out is given in nondimensional form by

$$Q'(\infty) = \sqrt{R}\ \{1 - e^{-R} / \sqrt{(\pi R)} - [1 - 1/(2R)]\ \mathrm{erf}\sqrt{R}\} \quad (1)$$

The nondimensional terms are defined by

$$Q = q / [\ FJ \sqrt{(t_c / k_a)}] \quad \text{and} \quad R = k_a t_c$$

where q is the dimensionalized charge in C cm^{-2}, F is the Faraday constant, and J is the ingress flux in mol $cm^{-2}s^{-1}$. The charge $q'(\alpha)$ corresponding to $Q'(\infty)$ is equated to q_a. k_a is an apparent trapping constant measured for irreversible traps in the presence of reversible traps and is given by $k / (1 + K_r)$, where k is the irreversible trapping constant and K_r is an equilibrium constant for reversible traps.

Data for the anodic charge were obtained by integration of the current transients for different charging times and were fitted to Eq. (1) to determine k_a and J. The irreversible trapping constant (k) can then be obtained from the apparent trapping constant using the lattice and apparent diffusivities (D_L and D_a, respectively) of hydrogen according to Eq. (2)

$$k = k_a D_L / D_a \quad (2)$$

The density of irreversible traps (N_i) can be evaluated directly from the apparent trapping constant (k_a) by using a model based on spherical traps of radius d [2]

$$N_i = k_a a / 4 \pi d^2 D_a \quad (3)$$

where a is the diameter of the metal atom. The calculation of N_i requires a value for d, and therefore a knowledge of potential irreversible traps in terms of dimensions of heterogeneities in the alloy of interest. The dominant irreversible trap can then be identified by comparing the trap density with the concentrations of potential traps in the alloy.

The potentiostatic pulse technique and diffusion/trapping model have been applied to several nickel-containing alloys (for example, Inconel 718, Incoloy 925, and 18Ni maraging steel) and have now been extended to Hastelloy C.

The hydrogen ingress and trapping characteristics were obtained for the cold-worked alloy and used to identify the dominant type of irreversible trap. The study expanded the range of microstructures treated using the diffusion/trapping model and allowed a wider comparison of the trapping capability of alloys in terms of their resistance to hydrogen embrittlement.

2 Experimental

The composition of the alloy was provided by the manufacturer and is given in Table 1. The rod material (with diameter 1.27 cm) was received in a hot finished and annealed condition. The alloy was cold worked 27% to obtain its final yield strength of 1225 MPa.

.

Table 1: Hastelloy C composition (wt %).

Element	%
Al	0.10
C	0.05
Co	0.90
Cr	15.50
Fe	5.55
Mn	0.35
Mo	16.80
Ni	56.37
P	0.01
S	0.02
Si	0.05
V	0.15
W	4.15

The presence of particles in the samples was investigated using SEM. Scanning electron micrographs showed rare submicron spots that were assumed to be particles but were too small to identify by EDX, and it was concluded that there were a negligible number, if any, carbide-type particles in the Hastelloy.

The test electrodes of the alloy consisted of a 5-cm length of rod press-fitted into a Teflon sheath so that only the planar end surface was exposed to the electrolyte. The surface was polished with SiC paper followed by 0.05 μm alumina powder. The electrolyte was an acetate buffer (1 mol L^{-1} acetic acid / 1 mol L^{-1} sodium acetate) containing 15 ppm As_2O_3 as a hydrogen entry promoter. The electrolyte was deaerated with argon for 1 h before measurements began and throughout data acquisition. The potentials were measured with respect to a saturated calomel electrode (SCE). All tests were performed at 25 ± 2ºC.

The test electrode was charged with hydrogen for charging times from 0.5 to 50 s for each E_c. Anodic current transients were obtained for each charging time over a range of overpotentials ($\eta = E_c - E_{oc}$). The open-circuit potential of the test electrode was sampled immediately before each charging time and was also used to monitor the stability of the surface film.

3 Results

Typical anodic current transients for Hastelloy C are shown in Fig. 1. The charge associated with the adsorbed layer of hydrogen (q_{ads}) was shown to be negligible in all cases, and so q_a was assumed to be associated entirely with absorbed hydrogen. Data for q_a could be analysed in terms of the interface control model using Eq. (1) to obtain values of k_a and J that were independent of charging potential (E_c) and charging time (t_c), respectively. In accordance with our practice, the data analysis was restricted to charging times ≥ 10 s.

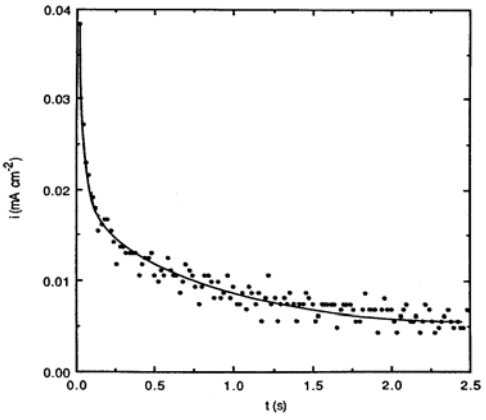

Figure 1: Anodic transient for Hastelloy C in acetate buffer. $t_c = 10$ s; $E_c = -0.725$ V (SCE). The full transient is not shown.

Significant trapping in this alloy is not observed before the surface film is reduced. After film reduction, the open-circuit potential remained steady over the range of charging times for each subsequent overpotential. Data were fitted to the interface control model, and values determined for k_a and J are given in Table 2.

Table 2: Values of k_a and J for Hastelloy C.

Test	η (V)	E_c (V/SCE)	K_a (s^{-1})	J (nmol cm^{-2} s^{-1})
1	-0.25	-0.748	0.061	0.27
2	-0.10	-0.593	0.025	0.06
	-0.15	-0.658	0.033	0.08
	-0.20	-0.725	0.023	0.04
	-0.30	-0.851	0.020	0.01
	-0.35	-0.895	0.026	0.02
3	-0.25	-0.754	0.041	0.22
	-0.30	-0.813	0.049	0.12
4	-0.20	-0.702	0.036	0.17
	-0.25	-0.762	0.041	0.12
	-0.30	-0.848	0.037	0.06

The high trapping constants for tests 1, 3, and 4 are thought to represent a combination of irreversible and quasi-irreversible traps, so k_a can be separated into two components, k'_a and k''_a, respectively. The total trapping constant was determined as the mean of the results from tests 1, 3, and 4, giving $k_a = 0.044 \pm 0.007\ s^{-1}$. The apparent rate constant for irreversible trapping was obtained as the mean of the results from test 2, so k'_a = $0.025 \pm 0.003\ s^{-1}$, and therefore $k''_a = 0.019 \pm 0.010 s^{-1}$. A comparison of calculated and experimental data for q_a (η = -0.20 V in test 2) in Fig. 2 again indicates that the derived values of k_a and J are independent of charging time over the range studied.

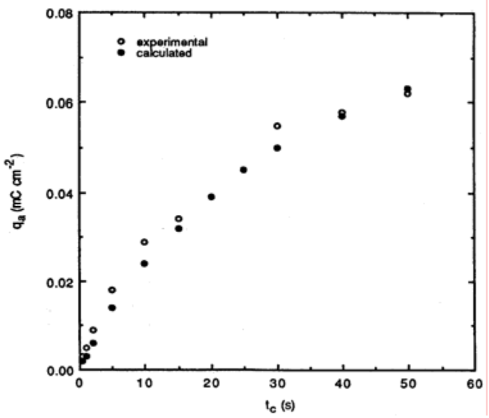

Figure 2: Comparison of experimental and calculated charge data for Hastelloy C in acetate buffer. E_c = -0.725 V (SCE).

4 Discussion

4.1 Irreversible trapping constant

The apparent diffusivity of hydrogen in 27% cold-worked Hastelloy C at 25ºC was estimated to be $(2.2 \pm 0.2) \times 10^{-15} m^2 s^{-1}$ from data for the annealed and 60% cold-worked forms of the alloy [6]. The most appropriate data for D_L corresponding to the pure Ni-Cr-Mo alloy are those for 76% Ni – 16% Cr – 8% Fe. Thus, by using $D_L = (7.9 \pm 1) \times 10^{-15}\ m^2 s^{-1}$ and $D_a = (2.2 \pm 0.2) \times 10^{-15}\ m^2 s^{-1}$ [7], K_r was calculated to be 2.7 ± 0.7 and, therefore, $k' = 0.095 \pm 0.027\ s^{-1}$ and $k'' = 0.070 \pm 0.048\ s^{-1}$.

4.2 Identification of quasi-irreversible traps

The behaviour of k_a is consistent with the formation of an unstable hydride during charging of this alloy as found by Lunarska-Borowiecka and Fiore [8]. The evidence therefore suggests that the apparent rate constant for quasi-irreversible trapping reflects hydrogen trapping via hydride formation. However, although the Hastelloy is believed to form an alloy hydride, the trap density cannot be determined because of a lack of information on the specific nature of the alloying component in the hydride.

4.3 Identification of irreversible traps

The susceptibility of Hastelloy C-276 to hydrogen embrittlement has been correlated with the concentration of phosphorus segregated at grain boundaries [9], so grain boundary phosphorus is assumed to provide the irreversible traps in this case. If hydrogen also segregates to the grain boundaries as in nickel [10], the grain boundary phosphorus is expected to provide the traps predominantly encountered by hydrogen in the Hastelloy.

In earlier work by Mezzanotte et al. on the C-276 alloy [6], trapping surprisingly appeared to be absent because permeation results failed to show any effect of an increase in the charging potential. The difference in trapping behaviour may have been due to differences in either the sensitivity between the pulse and permeation techniques or phosphorus levels at grain boundaries.

The density of irreversible traps was calculated on the basis of atomic phosphorus using $k'_a = 0.025\ s^{-1}$ in Eq. (3). The diameter of the metal atom in the Hastelloy was taken as the weighted mean of the atomic diameters of Fe, Ni, Cr, Mo, and W.

By using d = 110 ppm, $D_a = 2.2 \times 10^{-15}\ m^2 s^{-1}$, and a = 252.5 ppm, the density of irreversible traps was found to be $1.9 \times 10^{22} m^{-3}$. The phosphorus content of the alloy was taken as 0.01 wt% (see Table 1), which corresponds to a concentration of 2.2×10^{25} atoms m^{-3} that is clearly far greater than the calculated trap density. However, phosphorus at grain boundaries is considered more likely to interact with diffusing hydrogen than that in the bulk alloy and therefore to dominate the irreversible trapping.

Phosphorus in unaged Hastelloy C-276 with a bulk concentration of 0.006-0.008 at.% (0.003-0.004 wt.%), was previously found to be enriched to 0.3 at.% on the surface of grain boundaries [9]. If the surface phosphorus is assumed to lie in the first monolayer and a monolayer is taken as ~10^{19} atoms m^{-2}, the surface of the grain boundary is found to contain ~3×10^{16} P atoms m^{-2}. An estimate of the amount of grain boundary phosphorus distributed per unit volume is $6/b^3$, so the concentration of grain boundaries is $3/b^3$. Therefore, the total grain boundary area per unit volume is 3/b, and the amount of grain boundary phosphorus per unit volume (C_b) is given by $9 \times 10^{16}/b$ atoms m^{-3}.

Mezzanotte et al. determined the grain size for the annealed alloy and found it to vary from 30 to 50 μm. As found by these workers, cold work produced an elongated grain structure in the Hastelloy. Hence, the value of b corresponding to the grain size for the cold-worked alloy (non-annealed) in this study was estimated to be 10 μm, and therefore, C_b was found to be ~9×10^{21} P atoms m^{-3}. The close agreement between the values C_b and N_i is somewhat fortuitous but demonstrates that it is reasonable to consider phosphorus atoms at grain boundaries rather than in the bulk alloy to be the effective primary irreversible traps.

5 Summary

The ingress of Hastelloy C was shown to fit a diffusion/trapping model under interface control. The alloy is characterized by an unidentified quasi-irreversible trap and an irreversible trap thought to be phosphorus segregated at grain boundaries. The irreversible trapping constants (0.095 s^{-1} and 0.07 s^{-1}) are consistent with its susceptibility to hydrogen embrittlement, in parallel with test results for its cracking susceptibility.

References

[1] McKibbin, R., Harrington, D.A., Pound, B.G., Sharp, R.M., Wright, G.A.: *Acta metall.,* 35, 253, 1987.

[2] Pound, B.G., Sharp, R.M., Wright, G.A.: *Acta metall.*, 35, 263, 1987.

[3] Krom, A.H.M.: *Met. and Mat. Trans.*, B 31, 1475, 2000.

[4] Valentini, R., Solina, A., Tonelli, L.: *J. Nucl. Mater.*, 233, 1123, 1996.

[5] Ningshen, S., Uhlemann, M., Schneider, F.: *Corros. Sci.*, 43, 2255, 2001.

[6] Mezzanotte, D.A., Kargol, J.A., Fiore, N.F.: *Metall. Trans.*, 13A, 1181, 1982.

[7] Cornet, M, Bertrand, C., da Cunha Belo, M.: *Metall. Trans.*, 13A, 141, 1982.

[8] Lunarska-Borowiecka, E., Fiore, N.F.: *Metall. Trans.* 12A, 101, 1981.

[9] Berkowitz, B.J., Kane, R.D.: *Corrosion*, 36, 24, 1980.

[10] Lassila, D.H., Birnbaum, H.K.: *Acta Metall.* 35, 1815, 1987.

Proceedings of The 1st International Conference on **D**iffusion in **S**olids and **L**iquids
DSL-2005, July 6-8, 2005, University of Aveiro, Aveiro, Portugal

DIFFUSION AND WETTING ON CONTAMINATED SOLIDS

Martin E.R. SHANAHAN

Centre des Matériaux (CMGD), Ecole des Mines d'Alès,
6 avenue de Clavières, 30319 Alès Cedex, France

Fax : +33 4 66 78 53 65 ; Email : Martin.Shanahan@ema.fr

Abstract

The wetting dynamics of a drop of liquid (1) deposited on a solid on which there is already a thin layer of liquid (2) (contaminant, or maybe a wetting agent) is considered. Diffusion of liquid 2 into liquid 1 by Fickian diffusion leads to evolving effective solid/drop interfacial free energy, occurring during spreading, and modifying wetting kinetics. Spreading rate is increased. Strange behaviour is predicted near equilibrium conditions. The wetting line may "overshoot", before receding asymptotically. The motion of a two-dimensional drop is modelled, assuming it is given a slight push to one side after deposition. We expect a regime of spontaneous translational drop motion due to asymmetry in capillary conditions at the two triple lines. Diffusional wetting is compared to reactive wetting.

Keywords: Interfaces; Contaminant; Drop-sliding; Spreading; Wetting (kinetics)

1 Introduction

Most wetting problems, be they static or dynamic, are treated assuming that the various surface (interfacial) tensions (free energies) and their diverse components (van der Waals, polar, acid/base contributions, etc.) remain constants for the system studied. Exceptions are the recently studied area of reactive wetting [1]–[6]. (Problems concerning colloid science and surface active agents constitute a theme on their own.) Nevertheless, many practical situations involve the presence of a third (or even fourth!) substance(s) (in very small quantities), in the vicinity of a given interface between two bulk phases. The sizing applied to fibres before their inclusion in composite materials is an example [7], as is the presence of a thin oil layer on steel sheet, and often not removed before adhesive bonding, as found in the automotive industry [8],[9]. Generally, overall airborne contamination, including such entities as hydrocarbons resulting from the incomplete combustion of fossil fuels, may be readily adsorbed on a material to be bonded or otherwise surface-treated, and thus modify interfacial behaviour. Irrespective of the context, the presence of small quantities of a third component may lead to significantly modified interfacial properties, and thus effective interfacial free energies. In this study, we are interested in the time dependence of such modifications. We consider a simplified situation which may nevertheless give some insight into more realistic systems. The dynamic wetting of a solid substrate, S, by a droplet of liquid 1, is modelled, assuming that the surface is initially, uniformly covered by a very thin layer of "contaminant", liquid 2, diffusing into the droplet during spreading

2 Definition of system

The solid surface, S, is considered ideal (homogeneous, isotropic, flat, smooth and rigid) except for being covered by a thin, continuous film of liquid 2, of constant thickness, h, (*ca.* 1μm). For normal, organic liquids, this corresponds to a surface coverage, M of *ca.*10^{-3}kg.m^{-2}. Gravity is assumed negligible (drop contact radius, r, < capillary length, κ^{-1}). Initially, any shear motion within the film will be neglected (we shall return to this point later).

A small, axisymmetric drop of liquid 1 (r = *ca.* 10^{-3}m) is deposited on the "contaminated" solid. The two liquids are supposed *reasonably* similar, *e.g.* both being organic. This implies that the value of the initial, *effective*, interfacial free energy between the drop and the (covered) solid is low, corresponding approximately to that of the liquid 1/liquid 2 interface. However, a certain miscibility of the liquids is assumed and thus, as time, t, progresses, there is diffusion of liquid 2 into the bulk of liquid 1. This favours direct contact between solid S and liquid 1, and if these two phases are of a very different nature (say, solid S being metallic), the solid/drop interaction, or interfacial free energy, $\gamma_{SD}(t)$, thus *increases* with time, t. Diffusion leading to increasing $\gamma_{SD}(t)$ may be considered as one-dimensional, with liquid 2 migrating into the bulk of liquid 1 perpendicularly to the solid surface (Fig.1). With liquid 2 being the less viscous of the two, the classic equations of Fickian diffusion [10] from a finite, planar source into a semi-infinite medium are valid, leading to the concentration, C (x, t), of liquid 2, in liquid 1:

$$C\ (x,t)=\frac{M}{(\pi\ D\ t)^{1/2}}\ \exp\left(\frac{-x^2}{4Dt}\right), \qquad (1)$$

where x is perpendicular distance from the interface (assumed infinitely thin), and D is the (constant) coefficient of diffusion. The drop is a "semi-infinite" medium, given the very small quantity of liquid 2 per unit surface. (This also implies that any subsequent variations of the surface free energy, γ, or of the viscosity of liquid 1, η, may be neglected.)

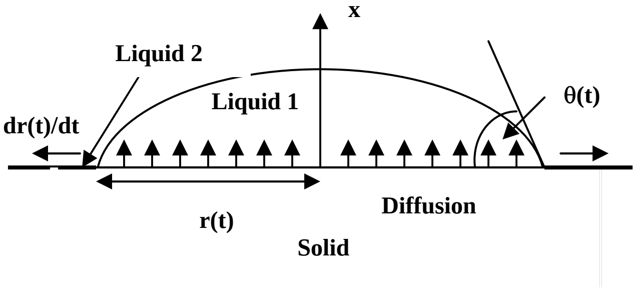

Figure 1: Axisymmetric drop of liquid 1 on solid surface, S, initially covered with thin film of liquid 2. Spreading and diffusion are concomitant.

The liquid 2 concentration at the interface, C (0, t), will modify $\gamma_{SD}(t)$. Realising that a singularity occurs for t = 0 (equation (1) assumes that all of M is concentrated in an infinitely thin plane at the origin for t = 0), we consider behaviour for times greater than an initial, short, period after drop deposition, δt:

$$C\ (0,t)=C\ (t)=\frac{M}{(\pi\ D\ t)^{1/2}}\ ;\ t\geq\delta t. \qquad (2)$$

$C\ (\delta t)$ really corresponds to the initial concentration. We assume that $\gamma_{SD}(t)$, the effective solid/drop interfacial free energy, increases with decreasing C (t) (increasing time) and thus a reasonable assumption, at least as a first approximation, is a linear dependence of $\gamma_{SD}(t)$ on C (t):

$$\gamma_{SD}(t)=\gamma_{SD}^{F}-\frac{C\ (t)}{C\ (\delta t)}\cdot\left[\gamma_{SD}^{F}-\gamma_{SD}^{I}\right];\ t\geq\delta t, \qquad (3)$$

where γ_{SD}^{I} and γ_{SD}^{F} represent, respectively, initial (i.e. at t = δt) and final ($t\to\infty$) values of $\gamma_{SD}(t)$. $\gamma_{SD}(t)$, as given by equation (3), assumes the same behaviour everywhere at the solid/drop interface. This should be a reasonable approximation provided initial spreading and diffusion rates are not too similar.

3 Spreading kinetics

Spreading of (small) drops is caused by an unequilibrated Young force [11] (per unit length of triple line), F_Y :

$$F_Y\ (t)=\gamma_S-\gamma_{SL}-\gamma\cos\theta(t)=\gamma\ (\cos\theta_o-\cos\theta(t)), \qquad (4)$$

where γ_S and γ_{SL} are solid and liquid free energies (we neglecting any potential adsorption of vapour by the solid), γ_{SL} is their common, interfacial free energy, and θ_o and $\theta(t)$ correspond to contact angles at equilibrium and at time t, respectively. γ_{SL} is represented by $\gamma_{SD}(t)$ in equation (3). Thus we have:

$$F_Y\ (t)=\gamma_S-\gamma\cos\theta(t)-\gamma_{SD}^{F}+\frac{C\ (t)}{C\ (\delta t)}\cdot\left[\gamma_{SD}^{F}-\gamma_{SD}^{I}\right]$$
$$=\gamma\ (\cos\theta_o-\cos\theta(t))+\beta\ t^{-1/2}, \qquad (5)$$

where γ_S here corresponds to the solid with its "contamination" layer and β is given by:

$$\beta=\frac{M.\Delta\gamma_{SD}}{(\pi D)^{1/2}.\ C\ (\delta t)}, \qquad (6)$$

where $\Delta\gamma_{SD}=\left[\gamma_{SD}^{F}-\gamma_{SD}^{I}\right]$. θ_o represents the contact angle at final equilibrium, satisfying Young's equation when $\gamma_{SD}=\gamma_{SD}^{F}$.

The dynamic frictional force (per unit length of triple line), F_F, resisting F_Y is given by [11]:

$$F_F(t)\approx\frac{3\eta\ell}{\theta(t)}\cdot\frac{dr}{dt}, \qquad (7)$$

where η is viscosity (liquid 1), ℓ is the natural logarithm of the ratio of drop contact radius and a microscopic cut-off (taken as constant given its weak r dependence), and dr/dt is spreading speed. Assuming θ small, allowing use of the approximation $\cos\theta\ (\approx 1-\theta^2/2)$. For a spherical cap drop, of volume $V\approx(\pi/4)\ r^3\theta$

and algebraic manipulation leads to:

$$\frac{dr}{dt} = \frac{32\ V^3 \gamma}{3\pi^3 \eta \ell} \left[\frac{1}{r^9} - \frac{1}{r^3 r_o^6} \right] + \frac{4V\beta}{3\pi\eta\ell r^3 t^{1/2}} \quad , (8)$$

where r_o is contact radius corresponding to θ_o.
We consider behaviour in three (simplified) stages. Simplifying, by defining a dimensionless drop contact radius as $y = r / r_o$, we find:

$$\frac{dy}{dt} = A \left[\frac{1}{y^9} - \frac{1}{y^3} \right] + \frac{B}{y^3\ t^{1/2}} \quad , \qquad (9)$$

where A and B are constants.
Expected behaviour is shown schematically in Fig. 2. We shall consider three stages.
(a) The first stage in drop spreading concerns short times, such that $\delta t \le t \le t_1$. Due to $t^{-1/2}$ being large, the second member on the right hand side of equation (9) is dominant. Neglecting the term with coefficient is A, we find:

$$y^3\ dy\ \approx\ B\ t^{-1/2}\ dt \quad , \qquad (10)$$

Leading to a scaling law of the form:

$$y \sim t^{1/8} \quad . \qquad (11)$$

For comparison, under similar conditions of y << 1, *without* diffusion of liquid 2, the equivalent behaviour is given by a scaling law of form $y\ \sim\ t^{1/10}$ [11]. This first regime is, however, very restricted, requiring $B\ y^6 / \left(A\ t^{1/2}\right) >> 1$, consistent with a large value of β.
(b) The second stage, corresponding to $t_1 \le t \le t_2$ with $y\ \left(t_2\right) \approx 0.8$, cannot be readily analysed (at least, to the author's knowledge). Qualitatively, however, it may be appreciated from equation (9) that the addition of a diffusion term can markedly increase the spreading speed, as given by dy/dt.
(c) The third stage, concerning behaviour near the equilibrium value of contact radius, r_o (y near unity), is perhaps the most interesting. Setting y = (1 – ε) leads to a simplified form of equation (9):

$$\frac{d\varepsilon}{dt} + 6A\varepsilon \approx \frac{-B}{t^{1/2}} \quad . \qquad (12)$$

Equation (12) may also be written as:

$$\varepsilon \approx -B\ \exp\left(-\ 6At\right) \int t^{-1/2} \exp\left(6At\right)\ dt\ , (13)$$

but even in this form, the integral yields only an unwieldy series solution! However, the salient points of the behaviour associated with equation (12) can be appreciated without complete solution. At the onset of stage (c), when y < 1 but approaching unity, dy/dt is positive (i.e. dε/dt negative). At y = 1 (ε = 0), dy/dt is still positive: the drop spreads *beyond* its equilibrium value. (In the absence of diffusion, y = 1 is the asymptotically attained spreading limit.) At this time, $t = t_3$, $dy / dt = B / t_3^{1/2}$. The values of dy/dt (and t_3) thus depend on B which in turn depends on the previous history (initial contact radius and concentration).

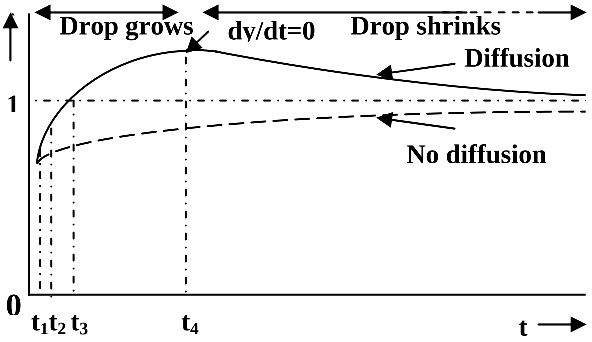

Figure 2: Qualitative spreading behaviour: normalised drop radius, y, vs time, t, (solid line). (Broken line: behaviour without diffusion effects.)

However, at t_3, spreading *speed* is decreasing, to reach a value of zero, at say, $t = t_4$, $\left(dy / dt = d\varepsilon / dt = 0\right)$. The maximum extent of spreading, at t_4, is given by $y = 1 + B / \left(6At_4^{1/2}\right)$ or, defining a time constant as $\tau = \left(6A\right)^{-1}$, at $y\ =\ 1\ +\ B\ \ \tau\ \ t_4^{-1/2}$. The drop has spread beyond final equilibrium at y = 1, the actual extent being intrinsically related to the ratio $B/(6A) = \beta / \left(3\ \gamma\ \theta_o^2\right)$. Thus, again, the "overshoot" depends on previous history, but also, note that a low value of θ_o favours the effect.
For $t > t_4$, the wetting front recedes. For large t, y tends asymptotically to unity, for $r = r_o$ and $\theta\ (t \to \infty) = \theta_o$, when liquid 2 has totally diffused into liquid 1.
Fig. 2 summarises the overall behaviour of the advancing wetting front, "overshoot" beyond the

equilibrium spreading position and, finally, asymptotic decay to equilibrium.

4 Lubrication

We assumed above that shear of liquid 2 parallel to the solid surface during spreading was negligible. Is this a reasonable assumption? Fig.3 represents the dynamic situation near the triple line. The spreading force, per unit length of triple line, F_Y, has two effects, *viz.* true spreading of liquid 1, and also Poiseuille shear in the (thin) layer of liquid 2.

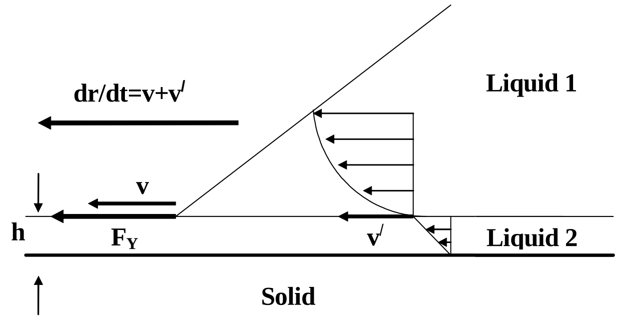

Figure 3: Lubrication effect near wetting front. Drop of liquid 1 spreading at speed v on thin layer of liquid 2, itself in shear parallel to the solid surface at (surface) speed v'.

For the layer of liquid 2, force F_Y corresponds to an average stress integrated over a distance comparable to drop contact radius, r, leading to a rate of displacement, v', of the upper surface of liquid 2 with respect to its lower surface. With simple shear flow in liquid 2 (viscosity η'), we find:

$$\frac{3\ \eta\ \ell\ v}{\theta} \sim \frac{\eta'\ r\ v'}{h}, \qquad (14)$$

where v is the spreading speed of liquid 1 *on* layer liquid 2 and h is the (average) layer thickness. Equation (14) is an average stress balance. The actual spreading rate of liquid 1 with respect to the solid surface, dr/dt, is given by $\left(v+v'\right)$. An energy balance between work done by F_Y and dissipation occurring in liquids 1 and 2, gives:

$$F_Y \cdot \frac{dr}{dt} \approx \frac{3\ \eta\ \ell\ v^2}{\theta} + \frac{\eta'\ r\ v'^2}{h}, \qquad (15)$$

leading to :

$$\frac{dr}{dt} \approx F_Y \left(\frac{\theta}{3\ \eta\ \ell} + \frac{h}{\eta'\ r}\right). \qquad (16)$$

The relative importance of the contributions v and v' to the overall spreading speed, dr/dt, is directly linked to the first and second members, respectively, in brackets on the right hand side of equation (16), and we find :

$$\frac{v'}{v} \approx \frac{3\ \eta\ \ell\ h}{\theta\ \eta'\ r} \approx \frac{3\ \pi\ \eta\ \ell\ h\ r^2}{4\ \eta'\ V}, \qquad (17)$$

For reasonable values: $\eta \approx 5\eta'$, $\ell \approx 10$, $h \approx 10^{-6}$ m, $r \approx 2x10^{-3}$ m and $V \approx 5x10^{-9} m^3$, we obtain $v'/v \approx 0.1$. Thus neglect of shear in liquid 2 is reasonable, at least in this case. However, note that v'/v increases with r^2, and thus for a given example, the assumption of neglecting shear in liquid 2 will become less acceptable as spreading ensues, although the effect will be to some extent offset by a decreasing value of h as absorption of liquid 2 by liquid 1 continues.

5 Crawling drop

Suppose the liquid be regarded as a ribbon of constant, circular section: the problem resembles that posed by the behaviour of a braid of adhesive applied to an oily steel sheet [12],[13]. With simplifying two-dimensional geometry, we assume that a ribbon of liquid 1 has been deposited on the "contaminated" solid surface, and inadvertently given a slight "nudge" to the right (Fig.4). The problem is similar to that in reactive wetting [1 - 4]. Due to variable interfacial free energy beneath liquid 1, the drop will move. Consider steady state behaviour [3], neglecting the start-up process [4]. With motion to the right in Fig.4, we set abscissa, z, with origin at the trailing edge, T, and in the frame of the drop. Leading edge, L, is at z = d. With steady state motion at speed U, the leading triple line has just contacted the contaminated solid: the value of (effective) solid/ drop interfacial free energy is $\gamma_{SD}\left(t = 0 \approx \delta t\right) = \gamma_{SD}^{I}$. At the trailing edge, contact time is d/U and the effective interfacial free energy $\gamma_{SD}\left(t = d/U\right)$.The two *equilibrium* contact angles, θ_L and θ_T respectively, at the leading and trailing edges should be different, but due to the equilibrating Laplace pressure in the drop, the two angles will be the same, θ, with $\theta_L < \theta < \theta_T$ [3]. Thus two unequilibrated Young forces act at the leading, F_L, and trailing, F_T, edges, making the drop move. (γ_S^I is the *initial* value of solid surface free energy with "contamination" layer (previously written simply as γ_S) and $\gamma_S(d/U)$ is the equivalent value after diffusion process has occurred for time (d/U).

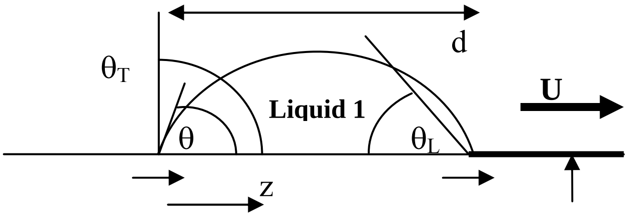

Figure 4: Two-dimensional drop of liquid 1 sliding on "contamined" solid, due to different capillary equilibria at leading (L) and trailing (T) edges.

We define $\Delta\gamma_S = \left[\gamma_S^F - \gamma_S^I\right]$, with γ_S^F the final value of solid surface free energy after total absorption of liquid 2 (for t →∞). The behaviour of $\gamma_S(t)$, where t = (d/U), is assumed to be analogous to that given by equation (3) for $\gamma_{SD}(t)$ leading to:

$$F(total) = \left(\Delta\gamma_{SD} - \Delta\gamma_S\right)\left[1 - \frac{M\,U^{1/2}}{(\pi Dd)^{1/2}.C(\delta t)}\right], \quad (18)$$

where we have made use of equations (2) and (3). Overall frictional force resisting F is $2F_F$, from equation (7), since two triple lines exist, resulting in:

$$\frac{6\,\eta\,\ell\,U}{\theta} \approx \left(\Delta\gamma_{SD} - \Delta\gamma_S\right)\left[1 - \frac{M\,U^{1/2}}{(\pi Dd)^{1/2}.C(\delta t)}\right], \quad (19)$$

We consider the two limiting cases corresponding essentially to high values of D, and to low values. For high values of D, the last term of equation (19) tends to zero and we obtain:

$$U \approx \frac{\left(\Delta\gamma_{SD} - \Delta\gamma_S\right).\ \theta}{6\,\eta\,\ell}\ . \qquad (20)$$

Here, D is sufficiently high for total absorption to have occurred at z = 0. Speed U depends on the difference between final and initial values, $\left(\Delta\gamma_{SD} - \Delta\gamma_S\right)$. As an example, we take $\left(\Delta\gamma_{SD} - \Delta\gamma_S\right) \approx 5\ \text{mJm}^{-2}$, $\theta \approx 0.5$ radian, $\eta \approx 0.1$ Pa.s and $\ell \approx 10$, giving a value of U of ca. 4 x 10^{-4} ms^{-1} for the "crawling" rate. The virtual independence of drop width (for small drops as studied here) is a well-known consequence of the fact that most viscous energy dissipation occurs near the triple line(s) [11].

For low values of D, the right hand member of equation (19) tends to zero (the term in brackets cannot become negative). Thus the translational speed U →0. Diffusion is so slow that both leading and trailing edges of the drop are on similar surfaces and no net force results. Behaviour of the drop for intermediate values of D requires detailed solution of equation (19). As the drop moves on, it encroaches upon fresh "contaminated" solid and absorbs more and more of liquid 2, leading finally to saturation and the drop stops. During absorption, but before saturation, the drop slows down as the effective value of the diffusion coefficient, D, decreases. Note, that if $\left(\Delta\gamma_{SD} - \Delta\gamma_S\right)$ is negative, drop "crawling" cannot occur, at least as a steady state.

6 Discussion

We have considered a simplified model of a solid surface, S, covered uniformly by a thin layer of a liquid 2 and onto which a small (negligible gravitational effects) axisymmetric drop of a liquid 1 is deposited. The assumption is made that liquid 2 diffuses into liquid 1 (the quantity of the former per unit area of substrate is vastly inferior to that of the latter) by simple Fickian diffusion, governed by equation (1). A possible refinement to this assumed behaviour would be to consider liquid 2, more realistically, as a finite source. This treatment would, however, involve use of a rather intractable form for C (x, t) involving a series of error-function complements [10]. The basic features of the concentration gradient are similar. Nevertheless, this feature could be retained for a more detailed model, albeit at the expense of mathematical simplicity.

Another simplification of the model involves use of equation (3). The actual microscopic behaviour leading to an effective value for $\gamma_{SD}(t)$ could well be complex, involving amongst other things, surface roughness and effects of disjoining pressure on equilibrium contact angle, via the Frumkin-Derjaguin equation [14], (both neglected here).

We have assumed that Fickian diffusion leads to an *increased*, *effective*, interfacial free energy between the drop and the solid. Thus, spreading of the drop towards equilibrium is modified by a varying value of the drop/substrate interaction. If the final equilibrium contact angle is finite, the spreading behaviour is accelerated by diffusion. Of most interest is the regime when the drop contact radius is near its final equilibrium value (i.e. when all of liquid 2 has successfully diffused into liquid 1). The triple line advances towards equilibrium, then, "overshoots" due to diffusion, reaching a maximum coverage, and then recedes asymptotically towards equilibrium. This phenomenon is rather similar to drop shrinking as expected in reactive wetting and reported elsewhere [4]. It is tentatively suggested here that this "overshoot" phenomenon may possibly be exploited in various industrial (and possibly biological?) situations ; in fact this may already be the case, such as in the application of adhesives to oil-contaminated steel sheet [13]. If the adhesive gels at maximum "overshoot", before solidification, then better coverage may be obtained (although, of course, in practice, other considerations such as applied pressure and temperature complicate the problem).

There is a possibility that spreading of liquid 1 may be modified by shearing of the thin layer of liquid 2. This would modify equation (8) and its subsequent solution near the equilibrium contact radius. We have considered the relative importance of this lubrication effect to give some idea about under what conditions it may be neglected. An aspect we have not considered here, however, is the potential role played by long range forces if the layer of liquid 2 is exceedingly thin (see above).

7 Conclusion

Wetting phenomena are often treated as though the three interfacial free energies associated with a given solid/ liquid/ fluid system are constants of the system in question. However, many practical situations involve a fourth (or further) component, often present in small quantities, which may be considered as a "contaminant", or in some cases as an aid to wetting and therefore surface coverage (e.g. fibre sizing).

A simple model is presented to account for behaviour resulting when a drop of liquid spreads on a solid surface initially covered with a thin layer of a second liquid. Assuming (a) Fickian diffusion of the thin layer into the first liquid, and (b) that this diffusion results in increased, effective interfacial free energy between drop and solid, we arrive at the following conclusions:

(i)The drop will initially spread following a scaling law in $t^{1/8}$, then after a transition period, it will “overshoot” its equilibrium contact radius before finally shrinking asymptotically back to its equilibrium configuration.

(ii) A lubrification effect may exist, in which the drop “slides” to some extent on the liquid film.

(iii) Analysis of a two-dimensional drop suggests that if motion is initiated by a slight “nudge”, the intrinsic asymmetry may lead to spontaneous movement, or “crawling”.

References

[1] Bain, C.D., Burnett-Hall, G.D., Montgomerie, R.R. : *Nature*, 372, p.414, 1994.

[2] Domingues dos Santos, F., Ondarçuhu, T. : *Phys. Rev. Lett.*, 75, p.2972, 1995.

[3] Brochard-Wyart, F., de Gennes, P.G. : *C.R. Acad. Sci.*, 321(IIb), p.285, 1995.

[4] Shanahan, M.E.R., de Gennes, P.G. : *C.R. Acad. Sci.*, 324(IIb), p.261 (1997).

[5] de Gennes, P.G. : *Physica*, A249, p.196, 1998.

[6] Ybarra, R.M., Neogi, P., Elroy, J.M.D.: *Ind. Eng. Chem. Res.*, 37, p.427, 1998.

[7] Khazanov, V.E., Kolesov, Yu. I., Trofimev, N.N.: *Fibre Science and Technology*, Kostikof, V.I. (Ed.), Chapman and Hall, London, p.147, 1995.

[8] Commerçon, P., Wightman, J.P.: *J. Adhesion*, 22, p. 13, 1987.

[9] Ogawa, T., Hongo, M.: *J. Adhesion Sci. Technol.* 11, p.1197, 1997.

[10] Crank, J.: *The Mathematics of Diffusion*, Clarendon Press, Oxford, 1956.

[11] de Gennes, P.G.: *Rev. Mod. Phys.*, 57, p.827, 1985.

[12] Shanahan, M.E.R.: *C.R. Acad. Sci.*, 1 (IV), p.347, 2000.

[13] Greiveldinger, M., Shanahan, M.E.R.: *J. Adhesion*, 75, p.161, 2001.

[14] Starov, V.M.: *Adv. Coll. Interface Sci.*, 39, p.147, 1992.

Proceedings of The 1st International Conference on **D**iffusion in **S**olids and **L**iquids
DSL-2005, July 6-8, 2005, University of Aveiro, Aveiro, Portugal

THERMAL ANALYSIS AND MICROSTRUCTURAL EVALUATION OF THE CONVENTIONAL AND DEVELOPED HIGH SPEED TOOL STEELS

Ali SHOKUHFAR[1],*, Tolou SHOKUHFAR[2]

[1]Division of Materials Engineering, Azad University, Karadj, Iran
[2]Department of Materials Science and Engineering
K.N.Toosi University of Technology, Tehran, Iran

*Corresponding author. Fax:+9821 7334338; Email: shokuhfar@kntu.ac.ir

---

Abstract

Thermal analyses and microstructural evaluation were carried out for the conventional M2 and M10 high speed steels as well as for alloys with varying Nb and/ or Ti contents to asses their liquidus, solidus and other high temperature reactions. It has been found that the slope change of cooling curves marks the formation of MC type carbides, while the break is due to the crystallization of delta ferrite and much larger volume fraction of different type of carbides including M6C mostly by eutectic reactions. Results show that the formation of dendrites is the most basic characteristic of the solidification process for the M2 and M10 alloys but for the steels containing niobium and/or titanium carbides, these primary carbides insert an inoculating effect and modify the coarse dendritic structure.

Keywords: Liquid phase; Thermal analysis; Solidification; Microstructure; High Speed Steel

---

1 Introduction

The properties of high speed steel are dependent on a variety of structural changes produced by heat and mechanical treatment. Structural changes including phase transformation, solid state decomposition, etc. are based upon atomic diffusion [1-2]. The constitution and freezing sequences of high speed steels have been qualitatively and quantitatively studied by many investigators [3-6]. Among the earlier works in the field of the constitution of alloy steels were those carried out by Takeda on the studies of the ternary alloys of the Fe-W-C phase diagram [3], although his work was continued by others [4-5], leading to the modification of the introduced phase diagram, but the basis concept remain unchanged and still serve as a useful guideline for the investigation of the present available high-speed steels. The solidification of conventional high speed steels was also studied by some researches [6-9] and would be expected to involve the formation and growth of dendrites early in the freezing sequence, the rejection of the solutes and their accumulation within the interdendritic liquid.

Purpose of the present investigation is to investigate the effects of solidification variables on phase relationships and microstructures in M2 and M10 high speed steel and a number of derivative materials in the cast state. If the resulting structures prove suitable it should be possible to produce any required tool by casting directly close to finish form using established casting processes, so combining reduced production costs with enhanced performance.

2 Experimental procedure

Several steels have been investigated . The experimental alloys were of the well known standard M2 and M10 HSS which have the compositions shown in Table1.

Experiments were first designed to investigate the freezing sequence and the microstructures of cast steels. The base composition were then subjected to melt treatments designed to develop additional primary carbide dispersions. The produced steels designated as MD1 and MD2 were those with conventional composition modified with primary NbC, Titanium was added to MD2 in order to find out the mechanism of NbC and TiC formation simultaneously and the steel named as MD3.For reducing chemical composition complexity, MD1,MD2 and MD3 were subjected to amendment to the base composition and the modified steels designated as AS3 and AS4 developed high-speed steels. The results for these alloys will be presented later.

The experimental steels were air melted in a high frequency induction furnace and poured into the lost wax ceramic shell moulds for producing set of cast bars 110 mm length and in diameter from 2-36 mm.The bars were sectioned longitudinally for soundness examination as shown in Fig.1. Thermal analyses were carried out during the freezing of the experimental alloys using a Pt/Pt-10 %Rh thermocouple. Time-temperature charts such as those in Figs 2-4, were obtained from an adjustable-range strip chart recorder. By setting the recorder scale for 1000-1500 ºC the entire freezing ranges of the alloys were determined.

The bars were then sectioned transversely and mounted in Bakelite and mechanically polished to 1-micron meter using emery papers and diamond pastes. The specimens were first etched in 5 % nital solution for 1-3 minutes and then in Oberhoffer's reagent for 5-10 seconds. At this stage the dendritic structures were revealed. Some of the samples were deep etched for examination in the scanning electron microscope to reveal the nature of different carbides morphologies.

Figure 1: Longitudinal section of the casting.

3 Results and Discussion

Thermal analyses were carried out on the experimental steels to assess liquidus, solidus and other high temperature reactions. The freezing reactions would be accompanied by evolution of latent heat. This will cause breaks in the time-temperature curves, which can be seen in Fig. 2 for M2.

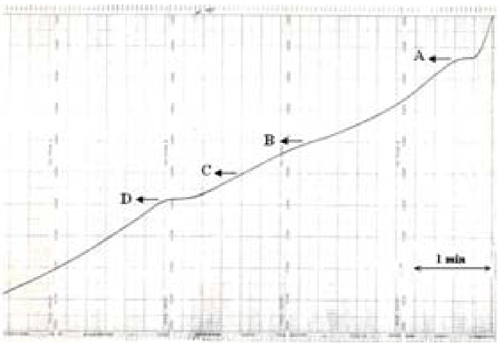

Figure 2: Cooling curve represent the solidification sequence for M2.

The curve shows four interruptions and slope changes; A, B, C and D, almost indicating the following reactions:

A) Liquid → delta ferrite, at 1428 ºC
B) Liquid + ferrit → austenite, at almost 1370 - 1302 ºC
C) Liquid + ferrite → austenite + carbides, at almost
1302 ºC-1220 ºC
D) Liquid → austenite + carbides, at 1220 ºC

The same sequence of reactions occurs for M10 steel but at lower temperatures as 1417 ºC, almost 1360 -1285 ºC, almost 1285 -1185 ºC, and 1185 ºC respectively.

The slope change marks the formation of small amounts of carbides, while the break is due to the crystallization of delta ferrite and much larger volume fraction of M6C (W4Fe2C) carbides.

In steels containing niobium and titanium the solidification sequence described above has been changed. Research is continue to find out what has happened during this complex freezing sequence, in cooling curve presented in figure 5 for MD1 steel, the marked slope change above liquidus temperature (1365 ºC) support the formation of primary NbC or TiC within the melt even before the actual solidification starts.

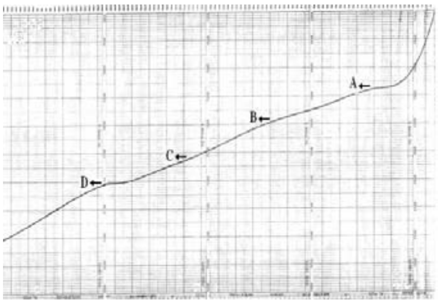

Figure 3: Cooling curve for MD1 steel.

The accuracy of the technique employed was checked by determining cooling curves for a Fe-Nb alloy of eutectic composition. For this purpose a charge of ferro-niobium and pure iron was melted and solidified under the same conditions as those used in the thermal analysis of the experimental steels. A pronounced thermal arrest was recorded at a temperature which gave reasonably good agreement with the eutectic temperature as indicated by the Fe-Nb phase diagram.

The formation of dendrites is the most basic characteristic of the solidification process for the M2 and M10 alloy. The dendritic structure of these steels are illustrated in Figs. 4 and 5.

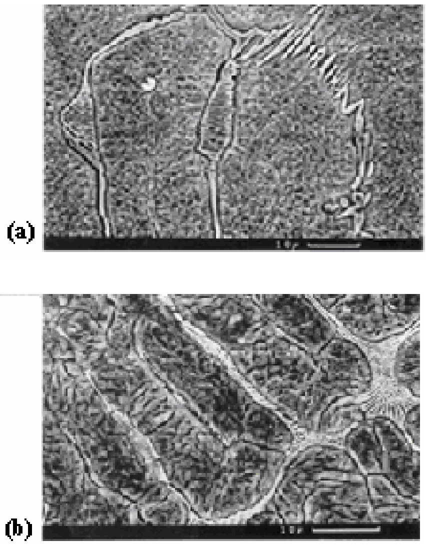

Figure 4: Scaning electron micrograph of (a) M10 and (b) M2.

Solidification of MD1 and other steels containing niobium and titanium carbide starts with many small delta ferrite grains that are nucleated by the primary particles similar to that shown in Fig.5.

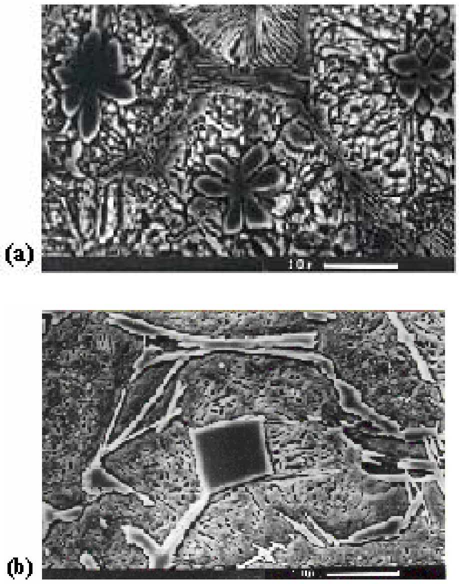

Figure5: Scanning electron micrograph (a) MD1 (4 mm) , (b)MD2 (16 mm).

These figures show the primary carbides particles surrounded by ferrite and or austenite rim, indicating the inoculating effect of NbC type primary carbides, and these approximately equiaxed pre-dendrites have no opportunity for dendritic growth, before this is arrested by peritectic reaction followed by impingement upon neighbouring grains more carbides are then formed. Resulting structures are similar to that shown in Figs. 5 (a) and (b). Although these figures clearly demonstrate the morphology of carbides as well as the inoculating effect of primary carbides, based on the atomic diffusion both in liquid and solid, the growth of NbC type carbides can also be seen , in thin samples similar to the powder particles [10], since there is not enough time for carbides to grow they freeze in the form of initial morphology (star shape) but for thick sections these star shape carbides grow to form compact idiomorphic morphology. In the solidification of MD3 contains titanium, the influence of titanium can be summarised as follows; similar to that for niobium, titanium is a grain refiner and strong carbide forming elements.

Table 1: Composition (wt %) of the experimental steels.

	C	Cr	Mo	W	V	Nb	Ti	other
M 10	0.92	4.13	8.11	----	2.13	----	----	traces
M 2	0.90	4.31	5.51	6.51	2.11	----	----	traces
M D 1	1.47	4.16	5.67	6.75	2.26	4.36	----	traces
M D 2	1.45	4.06	8.10	----	2.16	4.26	----	traces
M D 3	1.47	4.1	7.89	----	2.06	4.30	0.33	traces
A S 3	1.40	4.15	5.10	1.15	1.20	5.13	----	traces
A S 4	1.20	4.13	4.20	1.23	1.07	4.12	----	traces

The tendency of titanium to form titanium carbide or titanium carbonitride is so strong that even with a small titanium addition, titanium carbides have been formed within the melt and apparently provides a nucleating effect for the crystallization of the niobium carbides. Titanium may combine with niobium to form complex (TiNb) C carbide or in the presence of active element such as aluminium make an aggregate of TiC/Al2O3 even before the solidification starts.

Deoxidation of the melt with aluminium additions gives rise to the formation of aluminium oxide plus titanium carbide aggregates these aggregates are mostly appeared at the centre of the primary niobium carbides as shown in Fig.5.

4 Conclusion

- For the melt with the conventional M2 and M10 grades high speed steel the order of reactions take place during the solidification sequence were as follows:

Liquid → delta ferrite, at 1428 ºC for M2 and 1417 ºC for M10

Liquid + ferrite → austenite at ~ 1370 - 1302 ºC for M2 and 1360 - 1285 ºC for M10

Liquid + ferrite → austenite +carbides at ~1302 - 1220ºC for M2 and 1285 - 1185 for M10

Liquid → austenite + carbides at 1220 ºC for M2 and 1185 ºC for M10.

- The marked slope change above liquidus temperature (1365 ºC) for MD1 steel, suppor the formation of primary NbC or TiC within the melt even before the actual solidification starts.

- Due to the higher affinity of Ti for carbide formation, TiC particles may form even before NbC formation and the primary niobium carbides may be nucleated heterogeneously on particles pre-existing in the melt. Some of these have been directly observed and identified as an aggregate of titanium carbide with aluminium oxide.

References

1. Takamichi, Iida, Roderick, I.L.G.: *The Physical Properties of Liquid Metals*, Clarendon Press, Oxford, 1993.
2. Shewmon, P., *Diffusion in Solids*, Second ed., a Publication of TMS, 1989.
3. Takeda, S.; Metallographic Investigation of the Thermally Alloys of the Fe-W-C system, Technical reports, Tohoku univ, 9, pp.483-514, 1930, 10, pp.42-92, 1931.
4. Morakami, T. and Hatta, A.; Science Report Tohoku Imp. Univ. 1st ser., Hnda Anniversary Volume, pp. 882-895, 1936.
5. Grossman M. A., and Bain, E.C.; *High Speed Steel*, John Wiley and Sons, New York, pp. 100-116, 125-127, 1931.
6. McLaughlin, J. Kraft, R. W. and Goldstein J. I.; Characterization of the Solidification of the Structures within the Dendritic Core M2 High Speed Steel, *Met. Trans.*, Vol. 8, pp. 1787-1796, 1977.
7. Barkalow, R. H.: Kraft, R. W. and Goldstein, J. I: Solidification of M2 High Speed Steel, *Metall. Trans,* 3, pp. 919-927, 1972.
8. Boccalini M., and Goldenstein H.; Solidification of High Speed Steels., *International Material review*, No. 2, Vol. 46, pp. 92-109, 2001.
9. Fredriksson H., and Brising S.; The Formation of Carbide During the Solidification of High Speed Steels, *Scand. J. Metallurgy*, 5,pp. 268-276, 1976.
10. Kusy, M., Grgac, P., Behulova, M., Vyrostkova, A., Miglierini, M; Morphological variants of carbides of solidification origin in the rapidly solidified powder partices of hypereutectic iron alloy, *Mater. Scien. Eng. A* 375-377, pp. 599-603, 2004.

Proceedings of The 1st International Conference on **D**iffusion in **S**olids and **L**iquids
DSL-2005, July 6-8, 2005, University of Aveiro, Aveiro, Portugal

REACTION ENHANCED DIFFUSION IN SPHERICAL MEMBRANES

Vladimir M. SYSOEV[1], Serge SHPYRKO[1,2,*]

[1]Kiev National University, Physical Faculty, pr.Glushkova,6, Kiev, Ukraine
[2]Institute for Nuclear Research, Ukrainian Academy of Sciences, pr.Nauki,47, Kiev, Ukraine

*Corresponding author. Email: serge_shp@yahoo.com

Abstract

The reversible reactions like $A + B \leftrightharpoons C$ in the many-component diffusive system affect the diffusive properties of the constituents. The effective conjugation of irreversible processes of different dimensionality takes place due to the stationarity in the system and can lead to essential increase of the resulting diffusive fluxes. The exact equations for the spatial concentration profiles of the components are difficult to treat analytically. We solve approximately the equations for the concentration profiles of the reaction-diffusion components in the spherical geometry in the application to the problem of the enhanced oxygen transfer through a biological membrane and to the mathematically similar problem of surface diffusion in a solid body. In the latter case the spherical geometry can be an adequate tool for describing the surface of a real solid body which can be modeled as a fractal object formed of sequences of spherical surfaces with different radii.

Keywords: Enhanced diffusion; Transport phenomena; Thermodynamics; Membranes; Reversible chemical reactions

---

1 Introduction

The phenomenon of ”facilitated through chemical reaction diffusion” is familiar to various domains of science. Its essence consists in the diffusion enhancement through the intermittance of some chemical reaction involving the diffusive components. A straightfoirward example is the so called ”vacancy enhanced diffusion” of doped impurity into a solid body. Since long ago it was widely known that the presence of crystal imperfections is able to facilitate the impurity penetrating thus considerably enlarging the effective diffusion coefficient. From the thermodynamical point of view the facilitation comes from the presence of several fluxes of the diffusant (as if it were propagating through several different channels, or rather consist of several species having different diffusivity) and intervenience of the *reversible* chemical reaction between them. Thus, in a solid body the impurity atioms are known to reside either in the nodes of the crystalline lattice, (substitutional uimpurity) or in the space between nodes (interstitial impurity), the latter being fast diffusants and the former - slow ones. The reversible interchange of these two species tooks place and is facilitated by the presence of vacansies and eigen interstitial atoms of the matrix. An another example is taken from the biology domain and it concerns the phenomenon of the facilitated oxygen transfer through cellular membranes [1]. The principal reaction scheme consists in reversible ”tying” the ligande molecules by some slow macromolecular carrier. The facilitated transport of oxygen is possible via some fermentative kinetics (which should not however affect the chemical properties of O_2) and especially through reversible reaction with haemoglobine or myoglobine. In what follows we refer for concreteness to this example though our consideration can be applied to the vast variety of situations falling into the same reaction scheme.

The reaction process with Hb and oxygen can be (although very schematically) represented by the following expression

$$O_2 + Hb \rightleftharpoons HbO_2 \tag{1}$$

which means the formation of an (unstable) complex HbO_2; the rates of forward and reverse reactions are k_1 and k_-.

The system of balance equations for three constituents can be written as follows:

$$\begin{aligned} D\Delta c &= \rho + q \\ D_p \Delta c_p &= \rho \\ D_p \Delta c_c &= -\rho \end{aligned} \tag{2}$$

where c, c_p and c_c stand for concentrations of O_2,

Hb and complex HbO_2 respectively; D and D_p are diffusion coefficients for O_2 and Hb (assuming that both Hb and HbO-complex possess the same diffusion coefficients since the Hb molecule is much larger in size than oxygen one and both pure Hb and the complex HbO_2 must have similar diffusive properties). Instead Hb some other protein, e.g. Mb can appear. The consuming term q (here set to 0) should be added, for example, if treating the problem of muscular oxygen transport with myoglobine. The reaction rate ρ from elementary kinetics reads as follows

$$\rho = k_1 c c_p - k_- c_c \tag{3}$$

imposing minimal nonlinearity on the system.

2 Reaction-Diffusion System in Spherical Geometry

We start with considering the problem (2)-(3) within the spheroidal shell of internal and external radii a and b. The consideration of this problem within plain and cylindric geometry was performed not long ago [1] and was intended to describe the problem of oxygen saturation in the muscular tissue. Our choise of the spherical form of the membranes, besides purely mathematical interest, is motivated by several reasons. Besides the interest in elucidating the biological problem of facilitated oxygen transport in the (spherically shaped) alveols we refer also to the above mentioned diffusion problem in crystalline bodies. Usually the mathematical models of impurity diffusion use the plain geometry as a tool to represent the boundary of a solid body as the platform for the diffusion in a bulk. But the surface of a crystal is by no means plain, and its inhomogeneities can affect the diffusion effects (intuitively it is clear from the fact that merely the effective diffusive surface is bigger than the mathematical surface of the body). So, plain model for the boundary is an approximation which can be improved. Namely, it is possible to model the surface as a highly irregular sequence of spheres of different radii, perhaps, forming fractal structure. Therefore the consideration of the spherical geometry (on a single sphere) is believed to yield some improved approximation than just considering the straight plane.

So in the following we speak on the biological problem of oxygen transport and consider the spherical membrane. We assume the spherical symmetry so only one coordinate, namely r resides. As boundary conditions for the problem it is natural to take $c = c_a$ at $r = a$ and $c = c_b$ at $r = b$ and the zero flux of other components $dc_p/dr = dc_p/dr = 0$. But strictly speaking, the boundary conditions for all three constituents in real membranes *can not* be specified basing on a set of biological measurements [1]. As it can be demonstrated, the specification of one or other type of boundaries does not affect cardinally the shape of the solution across the whole width of the membrane exept thin layers at the edges. In any case at chosen way of handling the problem (see the next chapter) the set of boundary conditions should be included in the solution by some kind of self-matching procedure.

Integrating the sum of two last equations in (2) yields

$$c_p + c_c = const \equiv K \tag{4}$$

(the conservation of the protein content). If we introduce the new function

$$Y \equiv c_c/K \tag{5}$$

which has a meaning of the ferment saturation function the system of equations is cast as:

$$D \cdot \frac{1}{r^2}\frac{\partial}{\partial r}(r^2 \frac{\partial c}{\partial r}) = \rho \tag{6}$$

$$K \cdot D_p \cdot \frac{1}{r^2}\frac{\partial}{\partial r}(r^2 \frac{\partial Y}{\partial r}) = -\rho \tag{7}$$

with

$$\rho = k_1 K c - Y \cdot K(k_1 c + k_-) \tag{8}$$

Keeping in mind everything said about the boundary conditions specifications we now try to handle the problem setting

$$\begin{array}{ll} c_{|a} = c_a & c_{|b} = c_b \\ Y_{|a} = Y_a & Y_{|b} = Y_b \end{array} \tag{9}$$

where c_b and both Y_a, Y_b should be further determined basing upon restrictions imposed by the biological sense of the problem.

Using the boundary conditions add eqs (6-7) and integrate twice thus obtaining an expression relating $c(r)$ and $Y(r)$:

$$D\,(c_b - c(r)) + D_p\,K\,(Y_b - Y(r)) = \frac{b-r}{br}\cdot\frac{ab}{b-a}\cdot[D(c_b - c_a) + D_p\,K\,(Y_b - Y_a)] \tag{10}$$

3 External Solutions and Facilitated Transport

Expressing Y from (10) and inserting it into (6) and (8) following equation results:

$$\begin{aligned} D\frac{1}{r^2}\frac{\partial}{\partial r}(r^2\frac{\partial c}{\partial r}) = -\frac{k_-}{D_p}\cdot[Dc_b + Y_b K D_p] + \\ c\cdot\left\{\frac{k_- D}{D_p} - k_1 K[Y_b - 1 + \frac{D}{D_p K}c_b]\right\} - \quad (11) \\ \frac{b-r}{br}\frac{ab}{b-a}\left\{\frac{k_-}{D_p}[D(c_a - c_b) + D_p K(Y_a - Y_b)] - \right. \\ \left. \frac{k_1\cdot c}{D_p}[D(c_a - c_b) + D_p K(Y_a - Y_b)]\right\} + \frac{k_1 D}{D_p}c^2 \end{aligned}$$

The values Y_b, Y_a and c_b, c_a as said above should be determined from self-matching conditions.

The equation (11) is extremely difficult (if not impossible) to solve analytically. Instead of looking for its exact solution we notice that (11) can be cast (after scaling variables) as the equation in the form:

$$\varepsilon\Delta c = f(c, r),$$

and ε appears to be a small parameter ($\sim D/k_1$). This parameter is smaller if the reaction is more intensive; for biological issues its value varies within $10^{-4} - 10^{-6}$ [1], which allows approximate perturbative treatment of the problem. Since this parameter enters the equation near the term of the highest derivative, the problem appears to be that of the singular perturbation theory. Dropping out the ε term one gets so-called "external solution" to the problem. In general this equation of smaller order can't satisfy the boundary conditions and need "suturing" with the internal (exact) solution around the boundaries. The external solutions may suit for practical purposes within the bulk of the body, and would yield the desired solution of (11) provided that the constants (like Y_b, Y_a, c_b etc) are chosen properly, namely by means of the self-matching procedure. In this case (11) turns out to be an ordinary algebraic equation, whose coefficients depend on the values of Y_b, Y_a, c_b, c_a. But in fact these latter themselves are solutions to the equation at the boundaries. To ensure that this is the case one must set following self-matching conditions:

$$Y_b = \frac{k_1 c_b}{k_1 c_b + k_-}, \qquad Y_a = \frac{k_1 c_a}{k_1 c_a + k_-} \qquad (12)$$

(These expressions could be easily obtained from (8) setting $\rho = 0$ at the boundaries).

The variation of the saturation function and the total oxygen flux are:

$$Y_a - Y_b \equiv s = \frac{k_1 k_-(c_a - c_b)}{(k_1 c_a + k_-)(k_1 c_b + k_-)} \qquad (13)$$

and

$$\begin{aligned} F(r) \equiv -D\frac{\partial c}{\partial r} - K\cdot D_p\frac{\partial Y}{\partial r} \equiv \\ \equiv F_d + F_f = \frac{1}{r^2}\frac{ab}{b-a}\cdot[D(c_a - c_b) + \qquad (14) \\ D_p\cdot K\cdot\frac{k_1 k_-(c_a - c_b)}{(k_1 c_a + k_-)(k_1 c_b + k_-)}\Bigg] \end{aligned}$$

which is the sum of two terms, first of which, F_d is the ordinary diffusive flux, and the second one, F_f is the additional flux caused by the reaction.

The self-matching conditions yield two relations between four values c_a, c_b, Y_a and Y_b (or equally s). From the point of view of experimentalists these values are not treatable in the same fashion. Depending on whether we consider the biological problem of facilitated oxygen flux or mathematically similar problem of impurity diffusion, the set of good-to-operate values changes. For the oxygen transfer we can operate only the value c_a within wide range of magnitudes, and measure s, but this latter only for extremely big c_a, where it is known to tend to a constant $\bar{s}$ ($\sim 0.6 - 0.8$) [1]. And thus in order to get fluxes and concentrations within moderate c_a values one recurses to an interpolation which is expected to yield semi-quantitative results. Let us express c_b from (13):

$$c_b = \frac{k_{-1}c_a(1-s) - \frac{k_-^2}{k_1}s}{k_1 c_a s + k_-(1+s)}\,. \qquad (15)$$

This expression is exact. Hovewer the flux s is itself a function of c_a to be determined (only its value $\bar{s}$ at $c_a \to \infty$ is available), so let us go to the semiqualitative interpolation:

$$c_b \simeq \frac{k_- c_a(1-\bar{s})}{k_1 c_a \bar{s} + k_-(1+\bar{s})}\,. \qquad (16)$$

The expression (16): a) satisfies the limiting condition $c_b \to 0$ at $c_a = 0$; b) at big c_a ($k_1 c_a \gg k_-$) is consistent with (15). For intermediate c_a this is believed to be a plausible interpolation. So from (16) the approximate expression for saturation function is $s \equiv Y_a - Y_b$:

$$s \simeq \frac{k_1 c_a \bar{s}}{(k_1 c_a + k_-)} \cdot \left[\frac{k_1 c_a + 2k_-}{k_1 c_a + k_-(1+\bar{s})}\right] \tag{17}$$

From (16)-(17), substituting it into (14), we get the expression for the complete flux through a membrane. The flux at the external ($r = b$) layer equals

$$\begin{aligned} F = F_d + F_f \simeq \\ \simeq 4\pi \frac{a}{b}\frac{1}{b-a} \cdot c_a \bar{s}\,(k_1 c_a + 2k_-) \times \\ \left[\frac{D}{k_1 c_a \bar{s} + k_-(1+\bar{s})} + \right. \\ \left. + \frac{D_p K k_1}{(k_1 c_a + k_-)(k_1 c_a + k_-(1+\bar{s}))}\right] \end{aligned} \tag{18}$$

and is schematically depicted on Fig.1 where the ordinary diffusion flux and facilitated one are shown as functions of c_a.

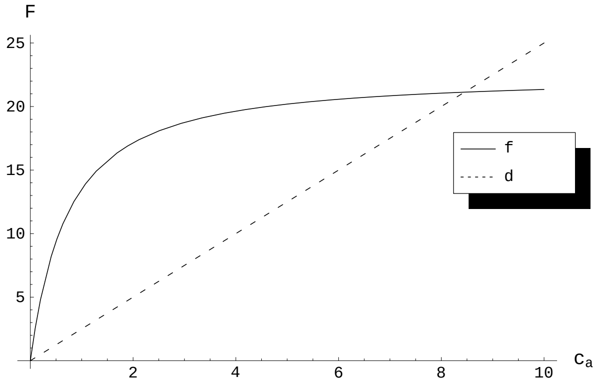

Figure 1: Diffusion and reaction facilitated oxygen flux as function of c_a (arbitrary units).

It is interesting to note different character of two fluxes from the latter formula and from Fig.1: at big c_a the diffusion flux grows linearly, but the flux component due to selfconjugation with reaction tends to a constant value. For both biological problem, and for the problem of vacansion diffusion enhancement this is clear intuitively: since the amount of carrier is limited at big values of c_a the substrate simply gets saturated. As to the moderate or small c_a the relation of two fluxes is

$$\frac{F_f}{F_d} = \frac{D_p K k_1}{D k_-}\,.$$

The value $D \gg D_p$ (since D stands for ”fast species”), but under condition $k_1 \gg k_-$ which is true far from chemical equilibrium, and if it is the case, the facilitated transport dominates over diffusion.

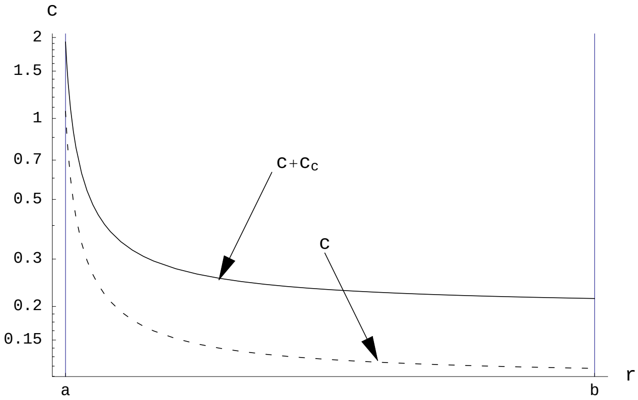

Figure 2: Space concentration of the free component $c(r)$ and total diffusion component $c(r) + c_c(r)$.

In the solid body physics the role of the reversible reaction is undertaken by the process of reversible transitions of impurity atoms between interstitial and substitution positions. The process of this interchange can be represented as the chemical reaction with vacancy:

$$I + V \rightleftharpoons S \tag{19}$$

(I and S standing for interstitial and substitutional impurities, V for vacancies). Thus vacansies can be formally understood as ”impurity carriers” like Hb complexes. Another mechanism is so called Watkins mechanism which also involves the interchange of fast and slow species, but by the intermittency of eigen interstitial atoms of the matrix. It is known (e.g., [2]) that such reversible reactions are crucial for understanding the impurity redistribution in the depth of a crystal. In order to handle analytically the impurity profile, the authors of [2] used similar assumptions of rapid chemical equilibrium establishing compared to the ordinary diffusion. In conclusion on Fig.2 we show the approximate solution for space oxygen concentration in a spherical slab (between inner a and outer b boundary). Shown are both diffusion $c(r)$ component and the value $c + c_c$, that is total oxygen concentration.

References

[1] Murray, J.D.: *Lectures in Non-linear Differential Equation Models in Biology*. Ed. Clarendon Press, Oxford, 1977.

[2] Loualiche, S., Lucas, C., Baruch, P., Gaillard, J.P., Pfister, J.C.: Theoretical model for radiation enhanced diffusion and redistribution of impurities. *Phys. Stat. Sol. (a)*, 69, pp. 663 – 676, 1982.

Proceedings of The 1st International Conference on **D**iffusion in **S**olids and **L**iquids
DSL-2005, July 6-8, 2005, University of Aveiro, Aveiro, Portugal

CALCULATIONS OF PHASE DIAGRAMS IN ASSOCIATED SOLUTION MODEL

Konstantin SHUNYAEV

Institute of Metallurgy, Ural's Division of Russian Academy of Sciences,
101, Amundsen Str., 620016, Ekaterinburg, Russia

Corresponding author. Fax: +7 343 267 89 18; Email: shun@ural.ru

Abstract

The review on authors' works on the development of a model variant of an ideal associated solution dealing with complexes of various compound, size and shape is presented. The model was used for calculation for thermodynamic characteristics and the liquidus line location of systems with a stable compound in a solid phase of binary eutectic mixings. In all cases the model parameters were not adjusted but were estimated from melting temperatures of individual substances. The last works are devoted to research of influence of associates by arbitrary stoichiometry on equilibrium thermodynamic properties of liquid alloys. The application of the model for eutectic systems and systems having an unlimited miscibility in solid and liquid states near to a liquidus was considered. It is shown that, for small difference in the melting temperatures of components, different types of fusibility diagrams is possible: eutectic diagrams, cigar-shaped diagrams or diagrams with upper or lower azeotropic points. Peritectic transformations can appear when there is a large difference in the melting temperatures of the components.

Keywords: Phase diagrams; Phase transformations; Association; Alloys; Thermodynamics

1 Introduction

There are many papers dedicated to the calculation of thermodynamic characteristics of binary alloys mixing in the frames of associated models [1-5]. Typically the model is applied to the systems having stable compound in solid state. Common theory of ideal associated solutions was developed for the associates with different compositions, sizes and shapes [1]. As the rule, the practical calculations are taking into account only those associates with minimum size and are ignoring the possibility of self-association. Though the theoretical analysis of the influence of self-association on thermodynamic functions of mixing behavior was carried out earlier [1, 6, 7], in practical calculations their influence is considered seldom [8, 9].

We had suggested earlier [10, 11] the variant of the model of associated solutions allowing to take into account the presence of associates of different sizes and shapes in the liquid phase. The calculation of the associate's energy was reduced to pair interaction of the nearest neighbors. This consideration was limited also by taking into account only configurational contributions into the entropy. It was found out that for such associate of infinite size as crystal it is possible to derive the energy parameter of the model from melting temperature of stable compound. Moreover, we succeeded to extend the number of properties, which are typically calculated in associated models on the base of melting characteristics, including diagrams of melting [10-18]. It was shown also that the taking of self-association into consideration allows applying the given model to any system including the eutectic one.

Successful use of self-associates for calculation of pure metals and simple eutectic properties allows to assume, that in multicomponent melts can exist also any stoichiometry associates. If such associates existence is supposed, than, it is obvious, that their influence first of all should have an effect in systems having unlimited solubility in solid and liquid states. However, for simple eutectic, as well as for systems with stable compounds in solid phase, the account of any stoichiometry associates, generally speaking, can have an effect on size of the calculated properties, as well as on qualitative picture of their behavior.

2 Theory

Let's consider binary system A_cB_{1-c}, which components in a liquid phase form a solution with complete mutual dissolution. Let's present it as ideal solution of associates A_n (i), B_n (j) and A_nB_m (i, j, q), (n, m - number of the appropriate atoms in a complex, i, j and q - number of nearest neighbours pairs such as AA, BB and AB in a complex, accordingly). Accepting the energy of a complex as determined by the pair's energy sum of nearest neighbours and limiting entropy only by configuration contributions, we obtain mole fractions of complexes related by following equations [19-20]:

$$x_{A_{n,i}} = K_{A_{n,i}} x^n_{A_1} = \exp\left(\frac{\alpha_A i}{kT}\right) x^n_{A_1}$$

$$x_{B_{n,j}} = K_{B_{n,j}} x^n_{B_1} = \exp\left(\frac{\alpha_B j}{kT}\right) x^n_{B_1}$$

$$x_{A_nB_m}(i,j,q) = K_{A_nB_m} x^n_{A_1} x^m_{B_1} = \exp\left(\frac{\alpha_A i + \alpha_B j + \alpha_{AB} q}{kT}\right) x^n_{A_1} x^m_{B_1}$$

(1)

Where $x_{A_{n,\text{ш}}}; x_{B_{n,j}}; x_{A_nB_m}; x_{A_1}; x_{B_1}$ - mole fractions of complexes $A_{n,\,i}$, $B_{\,n,\,j}$, A_nB_m and of single atoms A_1 and B_1, accordingly, α_A, α_B and α_{AB} – bond energy of nearest neighbours pairs AA, BB and AB taken with opposite sign, $K_{A_{n,i}}; K_{B_{n,i}}; K_{A_nB_m}$ - constants of appropriate equilibrium.

Then the balance equations system for definition of single atoms concentration in solution has the following form:

$$\sum_n\sum_i x_{A_{n,i}} + \sum_n\sum_j x_{B_{n,j}} + \sum_{n,m}\sum_{i,j,q} x_{A_nB_m} = 1$$

$$c = \frac{\sum_n\sum_i n x_{A_{n,i}} + \sum_{n,m}\sum_{i,j,q} n x_{A_nB_m}}{\sum_n\sum_i x_{A_{n,i}} + \sum_n\sum_j x_{B_{n,j}} + \sum_{n,m}\sum_{i,j,q} (n+m) x_{A_nB_m}}$$

(2)

The equations system solution (2) with the account of (1) allows finding mole fraction of single atoms in solution. Then it's easy to calculate the thermodynamic characteristics of system and melting diagram (see, for example, [1-3, 10-11, 18, 20-21]).

For realization of calculations it's necessary to know energy parameters α_A, α_B and α_{AB}, and also nearest neighbours pairs number of a various type in associates. The energy parameters α_A, and α_B can be estimated from pure components melting temperatures [14]. Then, as varied parameter remains only α_{AB}. It is possible to calculate total number of pairs in associate in assumption, that the appropriate crystal local structure remains the in a liquid. For the preliminary analysis of opportunities of model it is possible to choose linear chain approximation for associate structure, as it was done in [14] for simple eutectic. Such simplification allows to carry out summation in (2) easily. Thus, as shows the analysis, which has been carried out in [17], the accuracy loss for the calculated properties does not exceed 10 %.

3 Results

Parameters α_A, and α_B were determined from melting temperatures of components, and parameter W = [α_{AB} – 0.5(α_A + α_B)] was varied. As well as it was expected, the model allows to describe both positive, and negative deviations from ideality [19, 21]. Thus the negative deviations can be arbitrary large, and at the large positive W values behaviour of the mixture thermodynamic characteristics becomes same, as for systems with strong interaction of components. Other situation is observed at negative W values, i.e. when the formation of pairs such as AB is energetically unprofitable. The mixture enthalpy positive value growth takes place at small W values of is observed as long as the configuration entropy can compensate the energy loss. Mixture enthalpy begins to decrease at the further W values increase. Mixture entropy also passes through maximum, but at others, much smaller W values, while activity of components and mixture free energy change monotonously. Moreover, it has appeared, that the model allows to describe a situation, when mixture enthalpy is negative, and components activities deviations from the Raul law are the positive. It is an additional illustration of that circumstance, that the offered model, in spite of the fact that it contains only one varied parameter, such as interchange energy, is capable to explain much more various behaviour of properties, than other similar models. In difference, for example, from model of a regular solution, where the sign of all properties deviation from ideality is determined by energy parameter sign, in the model, considered in present work, such unequivocal dependence is not present. The value of property is defined as result from the several contributions, say, of direct pair contribution to energy and indirect configuration contribution. Thus the result depends on energy parameter value, melt temperatures and component melting temperature.

The case of the solution melting has been considered in [20]. As solid it is a regular solution with components having melting points at 700 and 1000 K respectively. As liquid this system presents an ideal associated solution, consisting of associates of various dimensions with arbitrary stoichiometry. It has been supposed, that energy parameter wasn't changing during melting, and so, there was only one model parameter to change. It has been shown in the model example that the type of an equilibrium diagram was depending on value and sign of the model parameter. There are 4 possible types of equilibrium diagrams in this case, namely eutectic, "cigar"- type and azeotropic type diagrams with both upper and lower azeotropic points.

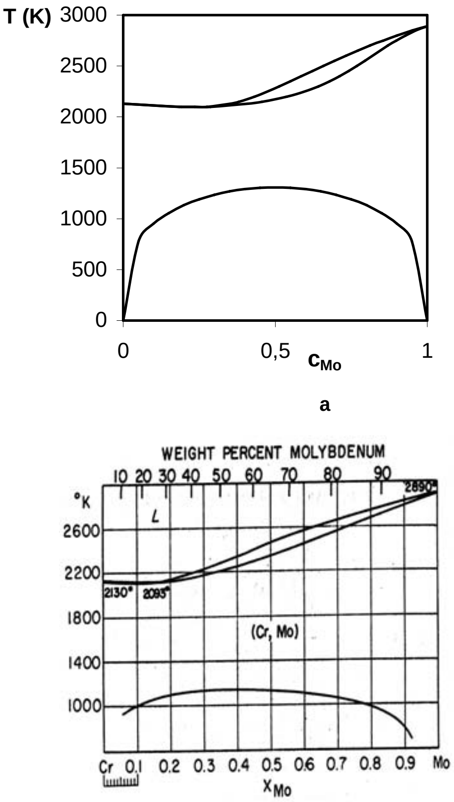

a

b

Figure 1: Calculated (a) and experimental [22] (b) Cr-Mo phase diagram.

In the case where the difference in the melting temperatures of components is rather high, the shape of phase diagram changes (for example, a strong increase in the "cigar" thickness is seen), and qualitatively new type of diagrams with peritectic equilibrium appears [21]. In this case a diagram of eutectic type and diagram with the lower azeotropic point are absent. It is possible to show, that peritectic equilibrium can appear only when a rather large difference in the temperatures of components exists ($T_B/T_A > 2.25$).

For demonstrating capabilities of the model the calculated phase diagram of Cr-Mo system with parameter W = -1300 J/mole is shown in a figure 1. It has appeared rather similar to experimental one [22] in the region of a melting. The calculated values of an azeotropic point are $c_{az} = 0.236$ and $T_{az} = 2097$ K, experimental values are $c_{az} = 0.125$ and $T_{az} = 2093$ K.

Acknowledgments

The work is under financial support of the Russian Foundation for Basic Research (grant № 04-03-33109) and Foundation "Leading Scientific Schools" (grant № 2022.2003.3)

References

[1] Prigogine I., Defay R. *Chemical thermodynamics*, Longmans Green and Co., London, 1954.

[2] Wasai K., Mukai K. Consideration of thermodynamic properties of binary liquid alloys with negative deviation of activities from Raoul't law based on associated solution model, *J. Jap. Inst. Metals,* 46, (3), pp. 266-274, 1982.

[3] Sommer F. Association model for the description of the thermodynamic functions of liquid alloys, *Z. Metallkunde*, 73, (2), pp. 72-86, 1982.

[4] C.Bergman, R.Castanet, H.Said, M.Gilbert, J.-C.Mathieu. Configurational entropy and the regular associated model for compound-forming binary systems in the liquid state, *J. Less-Common Metals*, 85, pp. 121-135, 1982.

[5] Schmid R., Chang Y.A. A thermodynamic study on an associated solution model for liquid alloys, *CALPHAD*, 9, (4), pp. 363-382, 1985.

[6] H.Kehiaian. Thermodynamics of chemically reacting mixtures. XII. Chemical equilibrium in ideal associated mixtures of in type $A+A_2+\ldots+A_l+B$, *Bull. Acad. Polon. Sci., Ser. sci. chim.*, 12, (7), pp. 497-501, 1964.

[7] Morachevsky A.G., Mokrievich A.G., Mayorova E.A. Analysis of behavior of thermodynamic functions based of ideal associated solution model. Systems $A_1+B_1+A_l$ and $B_1+Ai+A_lB_m$, *Journal of common chemistry*, 59, (9), pp. 1927-1934, 1989.

[8] Ivanov M., Thermodynamics of self-associated liquid alloys, *Z. Metallkunde*, 82, (1), pp. 53-58, 1991.

[9] Singh, R.N., Sommer F. A simple model for demixing binary liquid alloys, *Z. Metallkunde*, 83, (7), pp. 533-540, 1992.

[10] Tkachev N.C., Shunyaev K.Yu., Men A.N., Thermodynamic behavior of liquid alloys with stable compound of AB-type and size distribution of complexes. *Phys. Chem. Liquids*, 15, (4), pp. 271- 282, 1986.

[11] Shunyaev K.Yu., Tkachev, N.C., Men A.N., Thermodynamics of a ideal associated solution containing complexes of different sharp and size, *Rasplavy*, 2, (5), pp. 11-20, 1988.

[12] Tkachev N.C., Shunyaev K.Yu., Katznelson A.M., Krylov A.S., Men A.N., Kashin V.I., Estimation of configurational contribution in the melting entropy compounds with the fluorite-type structure, *Russian Journal of Physical Chemistry*, 63, (5), pp. 1372-1374, 1989.

[13] Tkachev N.C., Shunyaev K.Yu., Men A.N., Vatolin N.A., Configurational entropy of melting of body centred cubic and hexagonal metals, *Melts*, 2, (1), pp. 1-8, 1989.

[14] Tkachev N.C., Shunyaev K.Yu., Men A.N., Vatolin N.A., Mixing thermodynamics of liquid eutectic systems, *Reports of Academy of Science of USSR*, 302, (1), pp. 153-157, 1988.

[15] Tkachev N.C., Shunyaev K.Yu., Men A.N., Theoretical aspects of the associated liquid model, *High Temperatures-High Pressures*, 22, pp. 207-210, 1990.

[16] Shunyaev K.Yu., Vatolin N.A., Mixing thermodynamics and melting of liquid eutectic systems, *Reports of Academy of Science of USSR*, 332, (2), pp. 167-169, 1993

[17] Shunyaev K.Yu., Vatolin N.A., Calculation of thermodynamic characteristics of mixing and liqudus line location of simple eutectic, *Melts*, (5), pp. 28-34, 1993.

[18] Shunyaev K.Yu., Tkachev N.C., Vatolin N.A., Liquidus surface and association in eutectic ternary alloys, *Thermochimica Acta*, 314, pp. 299-306, 1998.

[19] Shunyaev K.Yu., Vatolin N.A., Lisin V.L. Influence of associates of the arbitrary stoichiometry on thermodynamics of mixture in liquid alloys, *Reports of Russian Academy of Science of USSR*, 386, (2), pp. 190-193, 2002.

[20] Shunyaev K.Yu., Vatolin N.A., Lisin V.L. Melting diagrams of an associating solution, *Reports of Russian Academy of Science of USSR*, 394, (1), pp. 46-49, 2004.

[21] Shunyaev K.Yu., Vatolin N.A., Lisin V.L. Phase diagram of a regular solid solution as a function of the character of association in the liquid phase, *Russian Metallurgy (Metally),* (5), pp. 445-451, 2004.

[22] Hultgren R., Desai P., Hawkins D., Gleiser M., Kelley K. *Selected values of the thermodynamic properties of binary alloys.* Metal Park; Ohio: ASM, 1973.

Proceedings of The 1st International Conference on **D**iffusion in **S**olids and **L**iquids
DSL-2005, July 6-8, 2005, University of Aveiro, Aveiro, Portugal

ON THE CONTRASTING BEHAVIOR OF DOUBLE-DIFFUSIVE SALT FINGERS AT HIGH AND LOW RAYLEIGH NUMBERS

Om Prakash SINGH[1,*], Sreenivas K. R[2], Jayaraman SRINIVASAN[1,2]

[1]Department of Mechanical Engineering, Indian Institute of Science,
Bangalore, Karnataka, India-560012
[2]Jawaharlal Nehru Centre for Advanced Scientific Research,
Jakkur, Bangalore-560064

*Corresponding author. Fax: +91 (80) 2360 0648; Email: ops@mecheng.iisc.ernet.in, osingh4@yahoo.com

---

Abstract

Double-diffusive finger convection at high and low Rayleigh numbers has been investigated with the help of laboratory experiments and numerical simulations. It has been found that finger zone sandwiched between two mixed layers is formed at high Rayleigh numbers only. Wide fingers are formed at low Rayleigh numbers which is consistent with the theory. However, wide fingers are diffusion dominated rather than advection dominated. Finger systems at low Rayleigh numbers, unlike high Rayleigh number systems, do not pass through quasi-equilibrium state but overturn completely during the latter part of their evolution.

Keywords: Basics of diffusion; Heat and mass transfer; Salt fingers; Rayleigh number; Mixed layer

---

1 Introduction

In a fluid system containing two diffusing substances with different molecular diffusivities e.g. heat and salt, instability can arise even if the overall stratification of the system is stable. When warm salty water overlies cool fresh water, the density is stably stratified in temperature (T) but unstably stratified in salinity (S). If the stabilizing temperature gradient ($\beta_T T_z$) or difference ($\beta_T \Delta T$) exceeds the destabilizing salt gradient ($\beta_S S_z$) or difference ($\beta_S \Delta S$), the convection takes the form of long, slender structures called as 'salt fingers' (see Fig. 1*b*).

Laboratory experiments (e.g. [1], [2], [3]) have consistently shown that salt fingers do not grow indefinitely but reach a finite amplitude sandwiched between two mixed layers from top and bottom. Salt fingers plays a vital role in controlling heat and salt fluxes in the ocean [4]. The common feature between the observations in the laboratory and the ocean is high Rayleigh number (Ra_T, defined latter). Rayleigh numbers in laboratory are typically 10^8 while those in ocean can go upto 10^{10} [5].

Many theories have been put forward for the finite amplitude finger convection e.g. collective instability theory [6], richardson number constraint [7], thermohaline intrusions [8], negative density diffusion [9] and flux ratio instability [10]. However, the scientific consensus on the mechanism for arresting the growth of salt fingers has not been reached [11].

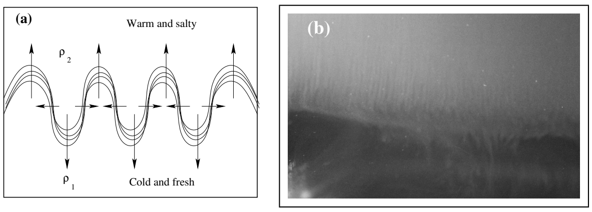

Figure 1: (a) Cartoon of salt fingering instability. Potential energy stored in the salinity field is released by faster the diffusion of temperature. (b) Thin fingers at $Ra_T = 3.80 \times 10^{11}$ and $Ra_S = 1.80 \times 10^{11}$. Sugar solution is denoted by lighter region and salt solution by darker region. Note how horizontal convection swipes away the ends of the fingers.

Interestingly, all these authors assumed thin and tall finger configurations in their analysis. Width of fingers varies as $Ra_T^{-1/4}$ [6] implying thin fingers at high Ra_T. System behavior at low Ra_T has not been studied so far.

Table 3 show the ranges of Ra_T covered in the laboratory and the numerical experiments to study the

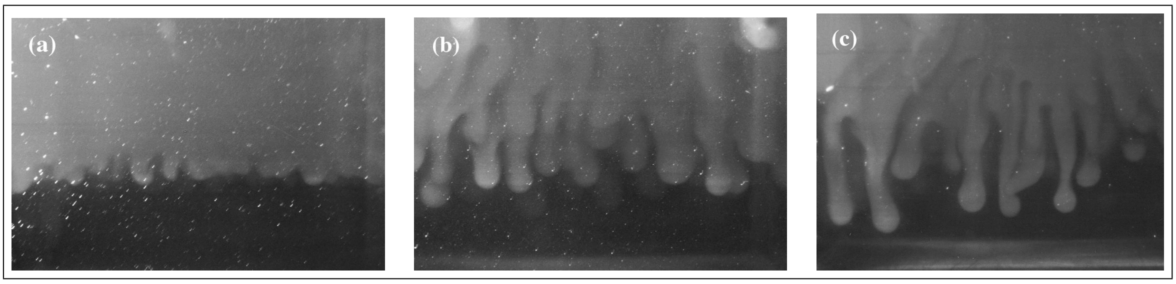

Figure 2: Time sequence of photographs showing the evolution of concentration fields at low Ra_T. Fingers width are of the order of 1cm. 0.25% CMC used for enhancing the viscosity. Parameters of the fluid are $Pr = 350$, $Ra_T = 4.6 \times 10^7$, $Ra_S = 1.0 \times 10^7$ and $R_\rho = 4.61$. The elapsed time of convection are (a) t = 15min (b) t = 22min and (c) t = 36min. Hot and sugary solution (top fluid) is denoted by lighter region and cold and fresh CMC solution by darker region.

system behavior. We will report how fingers of different width vary at different Ra_T. It is generally believed (e.g. [12], [13]) that density ratio (R_ρ) which defines the stability of the system, increases with time as the finger system runs down, thus implying that the system becomes more stable with time. We will show through simulations under what condition this observation is true. Further, it also believed that thick fingers, which forms at low Rayleigh numbers, are advection dominated and transports more heat and salt fluxes across the layers.

The rest of the paper is organized as follows: In section 2 we describe the experimental setup and finger structures. Numerical model is discussed in section 3 followed by results in section 4. Finally we conclude our findings in section 5.

2 Laboratory Experiments

We carried out a series of experiments to study the effect of Rayleigh numbers on finger convection. Experiments were performed in a transparent, 5mm thick glass, and doubly insulated tank of inner dimensions 19cm × 19cm × 19cm. An air gap of 5mm was provided with another tank enveloping the first one to prevent the heat losses from the sides of the tank. We conducted the experiments with heat-sugar system at low Rayleigh number. Sodium carboxy-methyl cellulose (CMC) was used for enhancing the fluid viscosity. CMC solution was prepared by adding CMC powder in distilled water. The advantage of using CMC is that it enhances viscosity exponentially with negligible effect on the density of the fluid. Viscosity of the fluid was measured by falling ball viscometer. Sodium fluorescent dye at a concentration of 1gm/lit was added to the sugary top solution which allowed us to distinguish between the two fluids during run down experiment. The evolution of the convective structures was recorded using a 35mm high-resolution camera. A 3mm thin sheet of light was projected from one side of the tank by passing focused 250W slide projector light beam through a slit.

2.1 Finger structures at high Ra_T

Figure 1(*b*) show the finger structures in salt-sugar system at high Rayleigh number. Thin and slender fingers which evolve remain in the system for many days. Heat-sugar or heat-salt systems at high Ra_T show similar features. Intense convection in finger zone caused by the deposition of sugar anomaly in the reservoir does not allow the fingers to grow indefinitely. Fingers get sandwiched between the mixed layers at the top and bottom boundaries. The vertical $\overline{T}$ and $\overline{S}$ profiles under such finger configuration measured by various researchers show mixed layers and gradient zone. This typical observation has been found by almost all researchers in laboratory and field experiments. Under what condition such profiles will form has never been answered satisfactorily.

2.2 Finger structures at low Ra_T

Figure 2 shows the evolution of fingers at low Rayleigh number. Low Ra_T was achieved by increasing the fluid viscosity. Wide and tall fingers evolve. There was no signature of large scale convection developing at the end of the finger zone which was an important factor in limiting the finger lengths at high Ra_T (see Fig. 1*b*). In many experiments conducted at low Rayleigh numbers, it was observed that large-scale convection layers above and below the fingering region get suppressed as Ra_T decreased. This allows the fingers to penetrate deep into the opposite reservoir and ultimately reach the system boundaries (Fig. 2*c*). As the system runs down in time, we observed complete overturning of the system i.e. initial top fluid occupy the place of initial bottom fluid and vice versa. There are many issues related to high and low Ra_T finger systems which is difficult to observe or measure in laboratory experiments. We will address some of the interesting aspects of finger convection through numerical simulation.

3 The numerical model

The conservation equations for two-dimensional salt fingers were non-dimensionalised using the following scaling: the depth of the total layer height H is chosen as the characteristic length, velocity (u, w), pressure (p), salinity (S) and temperature (T) are nondimesionalised respectively as $u = u^*/(k_T/H)$; $w = w^*/(k_T/H)$; $p = p^*/(k_T^2 \rho_0/H^2)$; $T^* = (T - T_B)/\Delta T$; $S^* = (S - S_B)/\Delta S$; $t^* = t/(H^2/k_T)$; respectively. T_B is the temperature of bottom layer. ΔT & ΔS are respectively temperature and salinity difference between top and bottom layers. The resulting equations in non-dimensional form are:

$$\frac{\partial u}{\partial x} + \frac{\partial w}{\partial z} = 0, \tag{1}$$

$$\frac{\partial u}{\partial t} + u\frac{\partial u}{\partial x} + v\frac{\partial u}{\partial z} = -\frac{\partial p}{\partial x} + Pr\left(\frac{\partial^2 u}{\partial x^2} + \frac{\partial^2 u}{\partial z^2}\right) \tag{2}$$

$$\frac{\partial w}{\partial t} + u\frac{\partial w}{\partial x} + w\frac{\partial w}{\partial z} = -\frac{\partial p}{\partial z} + Pr\left(\frac{\partial^2 w}{\partial x^2} + \frac{\partial^2 w}{\partial z^2}\right)\dots$$

$$+Ra_T Pr\, T - Ra_S Pr\, S \tag{3}$$

$$\frac{\partial T}{\partial t} + u\frac{\partial T}{\partial x} + w\frac{\partial T}{\partial z} = \left(\frac{\partial^2 T}{\partial x^2} + \frac{\partial^2 T}{\partial z^2}\right) \tag{4}$$

$$\frac{\partial S}{\partial t} + u\frac{\partial S}{\partial x} + w\frac{\partial S}{\partial z} = \frac{Pr}{Sc}\left(\frac{\partial^2 S}{\partial x^2} + \frac{\partial^2 S}{\partial z^2}\right) \tag{5}$$

The important dimensionless governing parameters emerges from the above equations are thermal Rayleigh number $Ra_T = g\beta_T \Delta T H^3/\nu k_S$, Prandtl number $Pr = \nu/k_T$ and Schmidt number $Sc = \nu/k_S$. Note that the definition of Ra_T and Ra_S is such that their ratio produces R_ρ i.e. $R_\rho = Ra_T/Ra_S$. R_ρ called as density stability ratio, defines the disequilibrium of the system. In a double-diffusive convection the density is a function of both temperature and salinity, i.e. $\rho = \rho_0(1 - \beta_T \Delta T + \beta_S \Delta S)$ where ρ_0 denotes the density of the fluid at room temperature. In the above equations, the Boussinesq approximation has been applied and β_T and β_S are defined as $\beta_T = -\frac{1}{\rho_0}\left[\frac{\partial \rho}{\partial T}\right]_{p,S}$, $\beta_S = -\frac{1}{\rho_0}\left[\frac{\partial \rho}{\partial S}\right]_{p,T}$ The equations were solved numerically using finite difference formulation, SIMPLER algorithm given by [14], along with Alternate Direction Implicit (ADI). The solutions were obtained by marching in time.

Since neither heat nor mass is allowed to cross the system boundaries, adiabatic and no mass flux boundary conditions was applied. Slip condition for the vertical velocity was imposed on the side walls. Initial condition for T and S was given a step profile similar to two layer laboratory experiments i.e. $[T, S] = [0, 0]$ for $z \in [0, 0.5]$ and $[T, S] = [1, 1]$ for $z \in (0.5, 1]$.

4 Results from numerical simulation

Figure 3 demonstrate the evolution of fingers at high and low Rayleigh numbers. The notable features are (i) thin and slender fingers are evolved at high Ra_T compared to tall and wide fingers at low Ra_T and (ii) mixed layers are formed above and below the fingering zone are high Ra_T, thus limiting the finger lengths. No such features are observed at low Ra_T (Fig. 3*b*). This is similar to what was observed in laboratory experiments (see Fig. 1*b* & 2).

Figure 4 compares the horizontally averaged mean profiles of $\overline{T}$ and $\overline{S}$ (or $< S >_H$) at high Rayleigh number corresponding to the salinity field shown in Fig. 3(*a*). Because of the mixed layers formation at high Ra_T, mean value of $\bar{S} \to 0.5$ in the region of $Y = [0, 0.2]$ & $Y = [0.8, 1]$ while rest of the region is isohaline. This is a king of typical profile which is most often observed in laboratory measurements. Mean $\overline{T}$ profile is reminiscent of a stable system in which the stabilizing anomaly diffuse laterally so that less of it is advected vertically by fingers.

Simulation at low Rayleigh numbers reveals interesting observations. Figure 5 shows the mean $\overline{T}$ and $\overline{S}$ profiles at $Ra_T = 7 \times 10^4$. Salinity field is advection dominated while temperature field is diffusion dominated. Strong thermal diffusion lead to

Table 1: Ranges of Ra_T used in the laboratory experiments and simulation. Values of Pr, Sc and τ used are respectively 7, 700 and 100 in all the cases, corresponding to heat-salt system.

Ra_T (lab) →	3.8×10^{11}	...	to →	...	...	1×10^5
Ra_T (sim) →	3.3×10^9	7×10^7	7×10^6	7×10^5	7×10^4	7×10^3

the establishment of linear temperature profile while mean $\overline{S}$ profile is clearly a manifestation of advection dominated system in which the salt is carried along with the fingers with little diffusion at the finger boundaries.

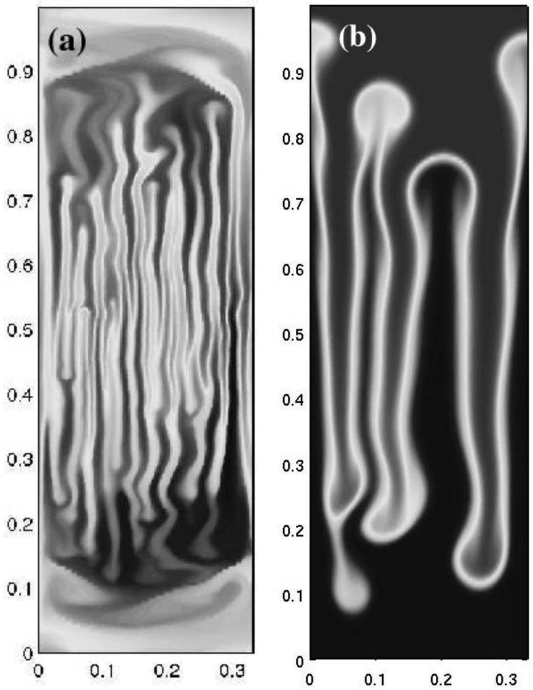

Figure 3: Evolution of concentration fields at high and low Rayleigh numbers (a) $Ra_T = 3.3 \times 10^9$, time t = 38m and (b) $Ra_T = 7 \times 10^6$, t = 57m 30s. Note the formation of large-scale convection layers above and below the fingering regions in (a).

Strong thermal diffusion at low Rayleigh numbers as observed above alter many local parameters of the system e.g. buoyancy ratio (R_ρ), one of the important parameter which controls the stability of the system. Figure 6 demonstrate the variation of local R_ρ with time at low and high Ra_T. When there is no convection (or instability) at the interface, diffusion dominates. During the diffusion period, local value of R_ρ drops below the initial value. R_ρ defined as: $R_\rho = \beta_T \Delta T / \beta_S \Delta S$. Because of the significant thermal diffusion, ΔT across the layers decreases at a faster rate compared to ΔS (see mean profiles in Fig. 5) and hence, R_ρ decreases locally.

How far will R_ρ drop below the initial value mainly depends upon the time during which the thermal diffusion dominates in the system. At high Ra_T, dominance of thermal diffusion lasts for less than a minute only (see Fig. 6*a*) while at low Ra_T it stretch upto more than 4.5 hours (Fig. 6*b*).

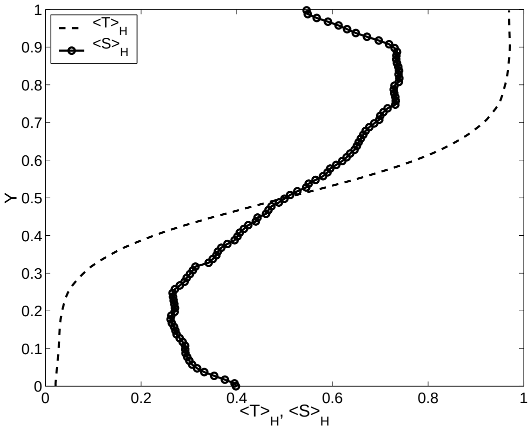

Figure 4: Vertical profiles of mean temperature and salinity at high Rayleigh number, $Ra_T = 3.3 \times 10^9$ corresponding to salinity field shown in Fig. 3*a*.

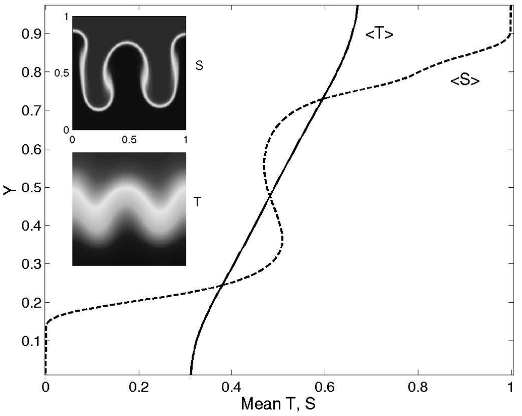

Figure 5: Mean $\bar{T}$ and $\bar{S}$ profiles at low Rayleigh number, $Ra_T = 7 \times 10^4$, $R_\rho = 6$ and time $t = 5\text{h}\,33\text{min}$. Shown in the inset are the corresponding T and S fields. Strong diffusion effect is clearly visible in T field making the mean $\bar{T}$ profile nearly vertical.

The consequence of this is that hardly 3% decrease in the initial value of R_ρ was observed at high Ra_T

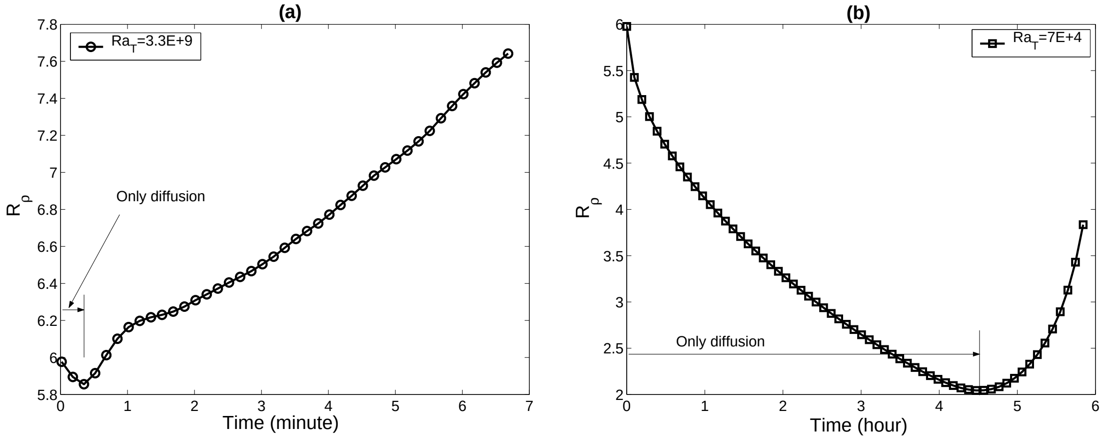

Figure 6: Local density stability ratio (R_ρ) as a function of time at high and low Rayleigh numbers (see legend). Initial $R_\rho = 6$. Note the time scales for both the cases during which the diffusion dominates at the interface. Diffusion results in the decrease of R_ρ below the initial value.

while it is around 70% at low Ra_T. This clearly indicate that finger systems at low Rayleigh numbers are diffusion dominated, contrary to the popular belief that wide fingers (i.e. at low Ra_T) are advection dominated which transports heat and salt across the layers at the same rate.

Value of R_ρ starts increasing after certain period of time, the time after which advection of salinity at the interface has began to overcome the effect of thermal diffusion. In short, it is the initial diffusion of temperature that allows the stored potential energy in the salinity field to be released and the convection takes the form of salt fingers. What happens to the finger structures when the initial diffusion time is long as in Fig. 6(*b*)? The ramification of diffusion dominated finger system at low Ra_T is demonstrated in the Fig. 7. It is evident that system has overturned (Fig. 7*b*).

4.1 *Why does the finger system overturn at low Rayleigh number?*

Salt finger convection rely on the faster diffusion of temperature which enables the unstably stratified salinity to release its potential energy. How potential energy will be released mainly depends upon two factors (i) finger width or Ra_T and (ii) initial diffusion period. Thin fingers evolve at high Ra_T and wide fingers at low Ra_T for any value of R_ρ. Further, we recall that fingers at low Ra_T fall near stable zone [15] which means that the onset of convection will be delayed and the system will be dominated by thermal diffusion (e.g. see Fig. 6*b*). Significant thermal diffusion for a longer period will make the whole system nearly isothermal and thus making the system susceptible to overturning. Further, at low Ra_T, wide fingers carry bulk of the salt anomaly with them (see Fig. 7*a*) making themselves more gravitationally unstable the consequence of which would lead the system to the final finger configuration as depicted in Fig. 7(*b*) i.e. complete overturning.

On the other hand, at high Ra_T, initial diffusion period is very small (Fig. 6*a*) and this is sufficient to trigger the instability. Thin fingers soon short-circuits the thermal anomaly between the upgoing and downgoing fingers resulting in the reorganization of stable thermal stratification (see Fig. 4). This regulates the releases the salt anomaly and the system passes through quasi-equilibrium state. R_ρ increases with time making the system more stable. No overturning of the system happens at high Ra_T, neither in laboratory experiments nor in numerical simulation.

5 Conclusions

Double-diffusive salt finger convection at high and low Rayleigh numbers was studied with the help of laboratory experiments and numerical simulations. Our results show that (i) fingers sandwiched between mixed layers from above and below forms at high Rayleigh numbers only (ii) finger systems at low Ra_T or wide fingers are diffusion dominated contrary to the notion that wide fingers are advection dominated which transports both heat and salt anomalies at a faster rates and (iii) all low Ra_T systems are vulnerable to overturning.

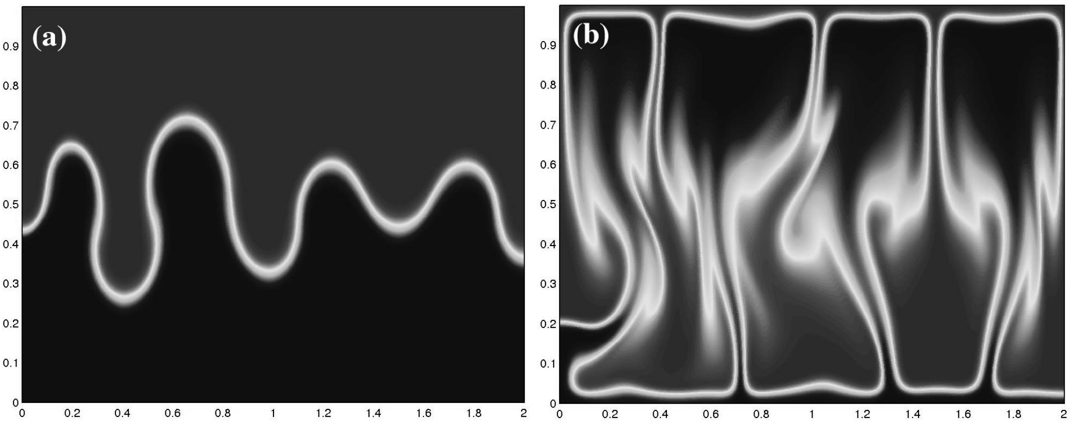

Figure 7: Evolution in time of salt fingers showing salinity fields at low $Ra_T = 7 \times 10^4$ and initial $R_\rho = 1.5$. The elapsed time of convection is (a) t = 1h 30m and (b) 2h 15m. Note that wide fingers evove in (a) and the system completely overturns during the latter part of the evolution in (b).

References

[1] Linden, P. F.: The formation of banded salt finger structure. *J. Geophys. Res.* 83, pp. 2902–2912, 1978.

[2] Taylor, J. & Veronis, G.: Experiments on double-diffusive sugar-salt fingers at high stability ratio. *J. Fluid Mech.* 321, pp. 315–333, 1996.

[3] Krishnamurti, R.: Double-diffusive transport in laboratory thermohaline straircases. *J. Fluid Mech.*, 483, pp. 287–314, 2003.

[4] Ruddick, B.: Enhanced: Sounding out ocean fine structure. *Science.* 301, 5634, pp. 772–773, 2003.

[5] Kelly, D.E.: Fluxes through diffusive staircases: A new formulation. *J. Geophys. Res* 95, pp. 3365–3371, 1990.

[6] Stern, M.E.: Collective instability of salt fingers. *J. Fluid Mech.* 35, pp. 209–218, 1969.

[7] Kunze, E.: Limits on growing, finite-length salt fingers: A Richardson number constraint. *J. Mar. Res.* 45, pp. 533–556, 1987.

[8] Schmitt, R.W.: Double-diffusion in oceanography. *Annu. Rev. Fluid Mech.* 26, pp. 255–285, 1994.

[9] Merryfield, W.J.: Origin of thermohaline staircases. *J. Phys Oceanogr.* 30, pp. 1046–1068, 2000.

[10] Radko, T.: A mechanism for layer formation in double-diffusive fluid. *J. Fluid Mech.* 497, pp. 365–380, 2003.

[11] Kunze, E.: A review of oceanic salt-fingering theory. *Prog. in Oceanogr.* 56(3-4), pp. 399–417, 2003.

[12] Taylor, J.: Laboratory experiments on the formation of salt fingers after the decay of turbulence *J. Geophy. Res.* 96, pp. 12497–12510, 1991.

[13] Özgökmen T.M, Esenkov, O.E, Olson, D.B.: A numerical study of layer formation due to fingers in double-diffusive convection in vertically-bounded domain. *J. Mar. Res.* 56, pp. 463–487, 1998.

[14] Patankar, S. V.: *Numerical heat transfer and fluid flow*, Hemisphere Publishing Company, 1980.

[15] Baines, P. G., Gill, A. G.: On thermohaline convection with linear gradients. *J. Fluid Mech.* 37, pp. 289–306, 1969.

Proceedings of The 1st International Conference on **D**iffusion in **S**olids and **L**iquids
DSL-2005, July 6-8, 2005, University of Aveiro, Aveiro, Portugal

BEM for the solution of natural convection in enclosure with large temperature gradients

Leopold Škerget*, Niko Samec, Jure Ravnik

Faculty of Mechanical Engineering, University of Maribor, Slovenia,

*Corresponding author. Fax: +386 2 220 7790; Email: leo@uni-mb.si

Abstract

The time dependent compressible and incompressible Navier-Stokes equations written in velocity-vorticity formulation are solved by the Boundary Element Method. The method is used to solve buoyancy driven flow in an 1:4 differentially heated enclosure under large temperature gradients. The ideal gas law is used and viscosity is given by the Sutherland law. Unsteady phenomena that occur at high Rayleigh number value ($Ra > 10^6$) are extensively studied and presented in the paper.

Keywords: heat and mass transfer; numerical methods; boundary element method; buoyancy driven flow; differentially heated enclosure;

1 Introduction

The discussion is focused to the study of a buoyancy driven air flow circumstances within a differentially heated enclosures subjected to extremely high temperature gradients [5]. The prevailing approaches to consider the natural convection in closed cavities are based on presuming the fluid is incompressible and viscous [3], [2]. Such an easy rheological model for the fluid flow is suitable for modelling of slow flows, or the flows with small pressure and temperature gradients or no chemical reaction, and therefore the velocity does not depend on the mass density. Pressure in the incompressible fluid flow model is not a thermodynamic state variable, but simply a force in the linear momentum balance equation.

The unsteadiness of natural convection flow are considered in an enclosure of aspect ratio $A = H/W = 4$, with height H and width W. It has been reported by [6] that for the Rayleigh number values less than $Ra = 10^5$ the steady state flow behavior is assumed and simulated, while for the Rayleigh number values greater than $Ra = 10^5$ the transition to unsteadiness is studied with numerical simulation. In the case of constant material properties, the transition takes place through a Hoph bifurcation with a critical Rayleigh number values of $3.2 \cdot 10^5 < Ra_c < 3.4 \cdot 10^5$, for a calculation performed on a 128×256 finite volume mesh [4]. Chaotic transient flow regimes occur for a long time until the periodic or steady-state flow regime sets in.

The velocity-vorticity formulation for the incompressible Navier-Stokes equations preserves distinct advantages over primitive velocity-pressure formulations. In the velocity-vorticity formulation of the time dependent dynamical set of equations the flow computation is partitioned into kinematic, kinetic and pressure computation aspects. The kinematics is given with the Poisson velocity vector equation, while the kinetics is represented with the vorticity transport equation. The evaluation of pressure field function is governed with Poisson scalar pressure equation. The accurate prediction of boundary vorticity values is given by the integral equation which conserve the vorticity field function globally [1], [7].

2 Conservation equations

2.1 Incompressible fluid model

The analytical description of the motion of a continuous viscous incompressible media is based on the conservation of mass, momentum and energy with associated rheological models and equations of state. The present development is focused on the laminar flow of incompressible isotropic fluid in a two-dimensional solution region Ω bounded by boundary Γ. The field functions of interest are velocity vector field $\vec{v}\,(\vec{r},t)$, scalar temperature field $T\,(\vec{r},t)$ and the vector vorticity field $\vec{\omega}\,(\vec{r},t)$, so that the mass, momentum and energy equations are given in non-dimensional form by

$$\nabla^2\vec{v} + \vec{\nabla}\times\vec{\omega} = 0, \quad (1)$$

$$\frac{\partial\omega}{\partial t} + (\vec{v}\cdot\vec{\nabla})\omega = Pr\nabla^2\omega + PrRa\vec{\nabla}\times T\frac{\vec{g}}{|\vec{g}|}, \quad (2)$$

$$\frac{\partial T}{\partial t} + (\vec{v}\cdot\vec{\nabla})T = \nabla^2 T, \quad (3)$$

where Pr is the Prandtl number, i.e. the ratio between viscosity and diffusivity of the fluid. In our calculations the Prandtl number value was set to $Pr = 0.71$. The Rayleigh number Ra is proportional to the thermal volume expansion coefficient, characterizing the Boussinesque approximation of the buoyancy force. The time derivatives were approximated with a second order three point formula $\frac{\partial u}{\partial t} \approx \frac{3}{2\Delta t}u^{n+1} - \frac{4}{2\Delta t}u^n + \frac{1}{2\Delta t}u^{n-1}$, where u are temperature and vorticity at the next time step ($n+1$), present time step (n) and previous time step ($n-1$).

2.2 Compressible fluid model

Differential description of the kinematic aspect of viscous compressible fluid motion can be expressed by the continuity equation written for the local expansion rate $\mathcal{D}$

$$\mathcal{D} = \vec{\nabla}\cdot\vec{v} = -\frac{1}{\rho}\left(\frac{\partial\rho}{\partial t} + (\vec{v}\cdot\vec{\nabla})\rho\right) \quad (4)$$

The kinematics deals with the relationship between the velocity filed at any given instant of time, the vorticity and mass density fields at the same time instant. By applying the curl operator to the vorticity definition one obtains the following elliptic Poisson equation for the velocity vector

$$\nabla^2\vec{v} + \vec{\nabla}\times\vec{\omega} - \vec{\nabla}\mathcal{D} = 0 \quad (5)$$

The kinetic aspect of the fluid motion is governed by the vorticity transport equation describing the redistribution of the vorticity in the fluid domain:

$$\frac{D\vec{\omega}}{Dt} = \nu_o\nabla^2\vec{\omega} + (\vec{\omega}\cdot\vec{\nabla})\vec{v} - \vec{\omega}\mathcal{D} + \frac{1}{\rho_o}\vec{\nabla}\times\rho\vec{g} + \frac{1}{\rho_o}\vec{\nabla}\times\vec{f}^m, \quad (6)$$

where $\vec{f}^m$ is the pseudo body force term. The heat transport equation is

$$\frac{DT}{Dt} = \alpha_0\nabla^2 T + \frac{S^m}{c_0}, \quad (7)$$

where S^m is the pseudo heat source term. See [8] for the detailed derivation of the above equations.
For a compressible fluid motion the Rayleigh number is defined as

$$Ra = Pr\,\frac{g\,\rho_o^2(T_h - T_c)\,W^3}{T_o\eta_o^2}, \quad (8)$$

where Pr is the characteristic non-dimensional Prandtl number, e.g. $Pr = 0.71$ for air, W is the width of the cavity, T_h and T_c are the hot and the cold wall temperatures respectively, T_o is a reference temperature defined as $T_o = (T_h - T_c)/2$, p_o is a reference pressure and $\rho_o(T_o, p_o)$ is a corresponding reference mass density. In our case we choose $T_o = 600K$ and $p_o = 101325Pa$. The temperature difference can be represented by a non-dimensional parameter ϵ, defined as

$$\epsilon = \frac{T_h - T_c}{2T_o}. \quad (9)$$

The heat transfer through the wall is represented by a local and an average Nusselt number, $Nu(y)$ and $\bar{N}u$ respectively, defined as

$$Nu(y) = \frac{\alpha(y)W}{k_o} = \frac{W}{k_o(T_h - T_c)}k(T)\frac{\partial T}{\partial x}\mid_w, \quad (10)$$

$$\bar{N}u = \frac{1}{L}\int_0^L Nu(y)\,dy, \quad (11)$$

where $k(T)$ is temperature dependent heat conductivity and $k_o = k(T_o)$. In the performed test cases the Pr number value is assumed to remain constant (0.71), the temperature dependence of the viscosity is given by the Sutherland's model

$$\frac{\eta(T)}{\eta^*} = \left(\frac{T}{T^*}\right)^{\frac{3}{2}}\frac{T^* + S}{T + S}, \quad (12)$$

and the heat conductivity is expressed as

$$k(T) = \frac{\eta(T)c_p}{Pr} \quad (13)$$

with $T^* = 273K$, $S = 110.5K$, $\eta^* = 1.68\cdot 10^{-5}kg/m/s$, $c_p = \kappa R/(\kappa - 1)$, $\kappa = 1.4$ and $R = 287.0\ J/kgK$. The influence of temperature on c_p is neglected. The parameters defining the problem are $\eta(\eta^*, S, T^*), R, \kappa, k, T_o, p_o, \epsilon, W$ and $\vec{g}$. The independent dimensionless parameters appearing in the problem are $\epsilon, \kappa, Pr, Ra, s/T^*, T_o/T^*$ and $\rho_o = p_o/RT_o$. The problem is completely defined by the Ra number value, the value of ϵ, a reference state p_o and T_o and initial conditions, e.g. $T(x,y) = T_o$, $p(x,y) = p_o$ and $\vec{v}(x,y) = 0$.

3 Numerical solution using the Boundary Element Method

The unique property and advantage of the boundary element method originates from the application of the Green fundamental solutions as particular weighting functions. Since the fundamental solutions only consider the linear transport phenomenon, an appropriate selection of a linear differential operator is of main importance in establishing a stable and accurate singular integral representation corresponding to the original differential conservation equation.
The non-linear character of the equations requires an iterative procedure for solving the coupled kinematics equation 1, vorticity transport equation 2 and the energy transport equation 3.

3.1 Solution algorithm

The solution algorithm can be described as follows:

1. Choose initial vorticity (ω_0) and velocity ($\vec{v}_0$) field, set initial time level $\tau = 0$, set initial nonlinear iteration level $i = 0$.
2. Time loop, $\tau := \tau + 1$.
3. Nonlinear iteration loop, $i := i + 1$.
4. Flow kinematics:
   (a) Solve equations (1) for boundary vorticities using internal vorticities from previous nonlinear iteration step using BEM.
   (b) Use explicit BEM calculation for domain velocities.
5. Flow kinetics; energy equation:
   (a) Solve energy equation (3) for domain and boundary temperatures according to known boundary conditions.
6. Flow kinetics; vorticity transport:
   (a) Solve vorticity transport equation (2) for domain vorticities, using the new velocity field and use boundary vorticities from kinematics as boundary conditions.
   (b) Use under-relaxation $0 < \phi \leq 1$ for computing new domain vorticity values $\omega_{i+1} := \phi\omega_{i+1} + (1-\phi)\omega_i$.
7. Check convergence:
   (a) Compute $error = ||\omega_{i+1} - \omega_i||_2/||\omega_{i+1}||_2$ and compute new under-relaxation ϕ.
   (b) If $error$ is greater then predefined ε go to step 3.
8. Finishing time loop:
   (a) Store time step values $\omega_\tau = \omega_{i+1}$, $\vec{v}_\tau = \vec{v}_{i+1}$.
   (b) If time step τ is less than maximum number of time steps NT go to step 2.
9. End of computation.

3.2 Solution of the kinematics equations by BEM

Incompressible fluid model The singular boundary integral representation for the velocity vector can be formulated by using the Green theorems for scalar functions, or weighting residuals technique, rendering the following vector integral formulation

$$c(\xi)\vec{v}(\xi) + \int_\Gamma \vec{v}\frac{\partial u^\star}{\partial n} d\Gamma = \int_\Gamma \frac{\partial \vec{v}}{\partial n} u^\star d\Gamma + + \int_\Omega \vec{\nabla} \times \vec{\omega} u^\star d\Omega, \qquad (14)$$

with $u^\star$ the elliptic Laplace fundamental solution. Numerical solution to this equation does not necessarily assure mass conservation, as discussed in [7]. In order to ensure mass conservation, the equation must be reformulated, see Škerget *et al.* [7], to give the final integral representation for the plane case as

$$c(\xi)v_i(\xi) + \int_\Gamma v_i \frac{\partial u^\star}{\partial n} d\Gamma = \int_\Gamma v_j \frac{\partial u^\star}{\partial t} d\Gamma - -e_{ij} \int_\Omega \omega \frac{\partial u^\star}{\partial x_j} d\Omega. \qquad (15)$$

Discretisation of this equation by means of boundary elements and internal cells is described in [7].

Compressible fluid model. The following form of the integral representation for the kinematics (5) is obtained by making use of the boundary element method [8]:

$$c\left(\xi\right)\vec{v}\left(\xi,t_F\right)+\int_\Gamma \vec{v}Q^\star d\Gamma=\int_\Gamma \frac{\partial \vec{v}}{\partial n}U^\star d\Gamma-$$
$$-\int_\Gamma \vec{\omega}\times\vec{n}U^\star d\Gamma+\int_\Omega \vec{\omega}\times\vec{Q}^\star d\Omega-$$
$$-\int_\Gamma \mathcal{D}\vec{n}U^\star d\Gamma+\int_\Omega \mathcal{D}\vec{Q}^\star d\Omega+\int_\Omega \vec{v}_{F-1}u^\star_{F-1}d\Omega,\ (16)$$

After the solution of the boundary velocities was obtained by BEM, we can calculate the domain velocities by means of explicit matrix vector products.

3.3 Solution of the kinetics equations by BEM

Incompressible fluid model Deriving integral representations of the vorticity transport equation (2) and heat transport equation (3), one has to consider the parabolic diffusion-convection character of the transport equation. The final integral statements are (Škerget et al. [7]):

$$c(\xi)\omega(\xi,t_F)+\nu\int_\Gamma\int_{t_{F-1}}^{t_F}\omega\frac{\partial u^\star}{\partial n}dtd\Gamma=$$
$$\nu\int_\Gamma\int_{t_{F-1}}^{t_F}\frac{\partial\omega}{\partial n}u^\star dtd\Gamma-\int_\Gamma\int_{t_{F-1}}^{t_F}\omega v_n u^\star dtd\Gamma$$
$$+\int_\Omega\int_{t_{F-1}}^{t_F}\omega v_j\frac{\partial u^\star}{\partial x_j}dtd\Omega+$$
$$e_{ij}\int_\Gamma\int_{t_{F-1}}^{t_F}n_i g_j F_B u^\star\ dtd\Gamma$$
$$-e_{ij}\int_\Omega\int_{t_{F-1}}^{t_F}g_j F_B\frac{\partial u^\star}{\partial x_i}\ dtd\Omega+\int_\Omega \omega_{F-1}u^\star{}_{F-1}d\Omega\ (17)$$

for the vorticity transport equation (2) and

$$c(\xi)T(\xi,t_F)+a\int_\Gamma\int_{t_{F-1}}^{t_F}T\frac{\partial u^\star}{\partial n}\ dt\ d\Gamma=$$
$$a\int_\Gamma\int_{t_{F-1}}^{t_F}\frac{\partial T}{\partial n}u^\star\ dt\ d\Gamma-\int_\Gamma\int_{t_{F-1}}^{t_F}Tv_n u^\star dtd\Gamma$$
$$+\int_\Omega\int_{t_{F-1}}^{t_F}Tv_j\frac{\partial u^\star}{\partial x_j}dtd\Omega+\int_\Omega T_{F-1}u^\star{}_{F-1}d\Omega,\ (18)$$

for the heat transport equation (3). In equations (17) and (18) the $u^\star$ is the parabolic diffusion fundamental solution and $\Delta t=t_F-t_{F-1}$ the corresponding time increment.

Compressible fluid model. The vorticity transport equation (6) is rewritten in the integral form:

$$c\left(\xi\right)\omega\left(\xi,t_F\right)+\int_\Gamma \omega Q^\star d\Gamma=$$
$$=\frac{1}{\eta_o}\int_\Gamma\left(\eta_o\frac{\partial\omega}{\partial n}-\rho_o v_n\omega+\rho g_t+f_t^m\right)U^\star d\Gamma+$$
$$+\frac{1}{\eta_o}\int_\Omega\left(\rho_o v_j\omega+\rho e_{ij}g_i+e_{ij}f_i^m\right)Q_j^\star d\Omega+$$
$$+\int_\Omega \omega_{F-1}u^\star_{F-1}d\Omega,\ (19)$$

where v_n, g_t and f_t^m are the normal velocity, and the tangential gravity and nonlinear material source components, respectively, e.g. $v_n=\vec{v}\cdot\vec{n}$, $g_t=\vec{g}\cdot\vec{t}=-e_{ij}g_i n_j$ and $f_t^m=\vec{f}^m\cdot\vec{t}=-e_{ij}f_i^m n_j$. The boundary integrals describe the total vorticity flux on the boundary, due to molecular diffusion, convection, and vorticity generation by a tangential force and source terms. The first domain integral gives the influence of force and natural convection, and nonlinear material behavior, while the last domain integral is due to initial vorticity distribution effect on the development of the vorticity field in subsequent time interval.

The integral form of the heat transport equation (7) is:

$$c\left(\xi\right)T\left(\xi,t_F\right)+\int_\Gamma TQ^\star d\Gamma=$$
$$=\frac{1}{k_o}\int_\Gamma\left(k\frac{\partial T}{\partial n}-cv_nT\right)U^\star d\Gamma-$$
$$-\frac{1}{k_o}\int_\Omega\left(\widetilde{k}\frac{\partial T}{\partial x_j}-cv_jT\right)Q_j^\star d\Omega+$$
$$+\frac{1}{k_o}\int_\Omega\left(Tv_j\frac{\partial c}{\partial x_j}+cT\mathcal{D}-\widetilde{c}\frac{\partial T}{\partial t}\right)U^\star d\Omega+$$
$$+\frac{1}{k_o}\int_\Omega\left(\Phi+S\right)U^\star d\Omega+\int_\Omega T_{F-1}u^\star_{F-1}d\Omega.\ (20)$$

The boundary integrals describe the total heat flux on the boundary, due to molecular diffusion and convection. The first domain integral gives the influence of the convection and the nonlinear diffusion flux, the second domain integral includes the nonlinear material effects, the third domain integral describes the Rayleigh dissipation and heat source term effects, while the last one is due to the initial temperature distribution effect on the development of the temperature field in subsequent time interval.

Further details of the Boundary Element Method applied to the vorticity - velocity formulation of Navier - Stokes equations can be found in [7] and [8].

4 Unsteady natural convection in an enclosed cavity

4.1 Incompressible fluid model

The numerical example investigated in this paper is the onset of unstable unsteady flow regime at high Rayleigh number values. The cavity width to height ratio is $1 : 4$. The left side of the cavity is heated and kept constant at $T_h = 1/2$, while the right side is cooled at $T_c = 1/2$. The bottom and top walls are adiabatic. The cavity was meshed with a structured mesh of 20x40 nine node Lagrange cells. The total number of nodes is 3321. The boundary conditions and the mesh are presented in Figure 1.

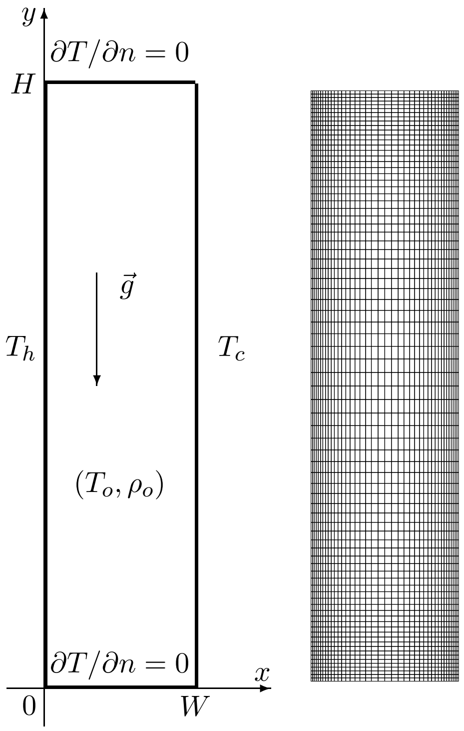

Figure 1: Presentation of the boundary conditions and of the 20x40 mesh.

The time step used in the calculation was $\Delta t = 10^{-4}s$. First we have investigated the phenomena at Rayleigh number value $Ra = 10^6$. After a quite long transition period, the flow becomes steady at this Rayleigh number. The temperature isolines, vorticity isolines and velocity vectors for steady state are presented in Figure 2.

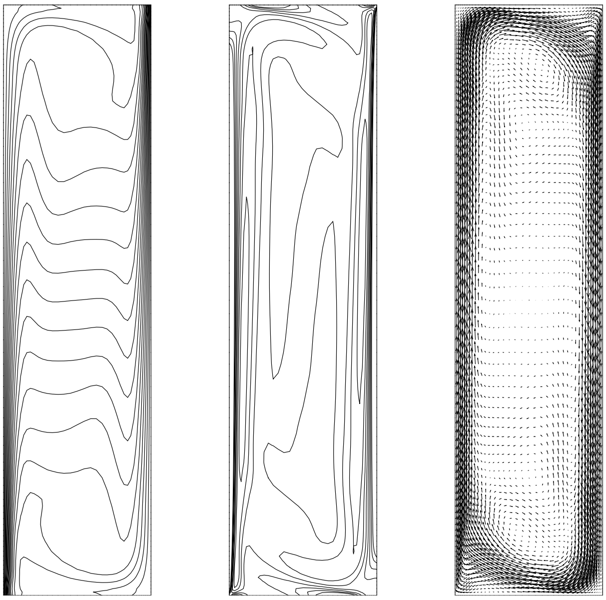

Figure 2: Temperature isolines (-0.45..0.45), vorticity isolines (-5000..5000) and velocity vectors in the steady solution at $Ra = 10^6$.

We can see that the boundary layer thickness is already very small. To characterize the transition period, we are showing the time dependance of the Nusselt number in Figure 3. We can observe that the Nusselt number value at steady state is 6.86. Table 1 summarizes Nusselt number values for Rayleigh number values form $Ra = 10^3$ to $Ra = 10^7$ Figure 4 shows temperature vs. time graph for node 701 (see coordinates in Table 2).

Table 1: Average Nusselt number $\bar{N}u$ values for different Rayleigh number values for incompressible fluid model.

Ra	10^3	10^4	10^5	10^6	10^7
Nu	1.112	2.112	3.873	6.86	12.323 ± 0.038

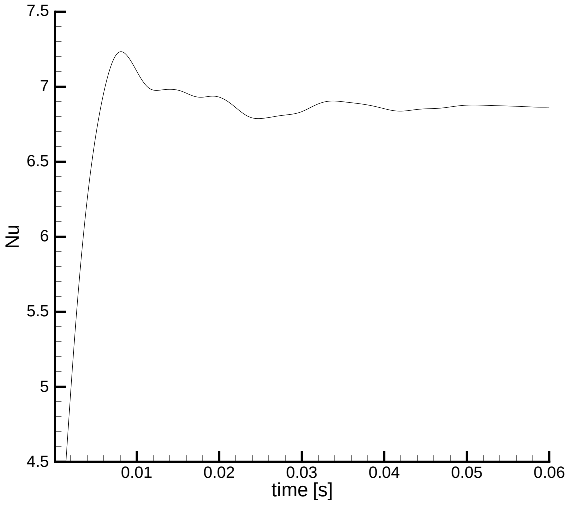

Figure 3: Time dependance of the Nusselt Nu number value for $Ra = 10^6$.

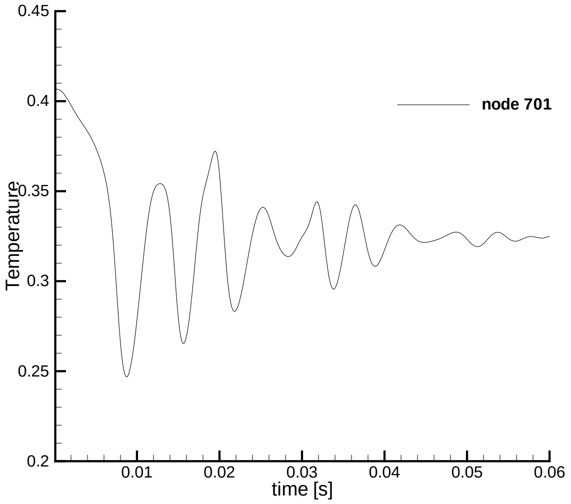

Figure 4: Temperature variations for $Ra = 10^6$.

True unsteady phenomena were observed at Rayleigh number value $Ra = 10^7$. After a transition period vortices are forming in the boundary layer and are transported up along the hot wall and down along the cold wall. Figure 5 shows temperature isolines at $t = 0.0700, 0.0705, 0.0710$. Node the vortices forming at upper right and lover right and upper left corner of the cavity.

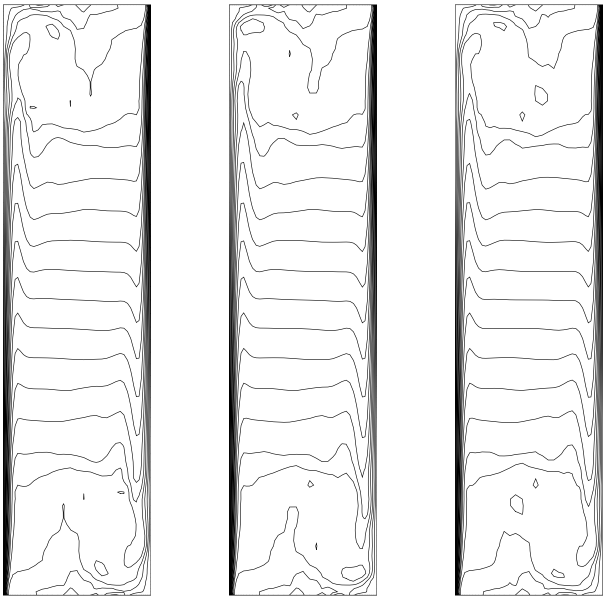

Figure 5: Temperature isolines (-0.45..0.45) at $Ra = 10^7$ and $t = 0.0700, 0.0705, 0.0710$.

Figure 6 shows vorticity isolines at $t = 0.0700, 0.0705, 0.0710$, while Figure 7 shows velocity vectors at the same time instant. The time instants were chosen in such manner to show the formation and convective transport of small vortices forming at lover right and upper left corner of the cavity.

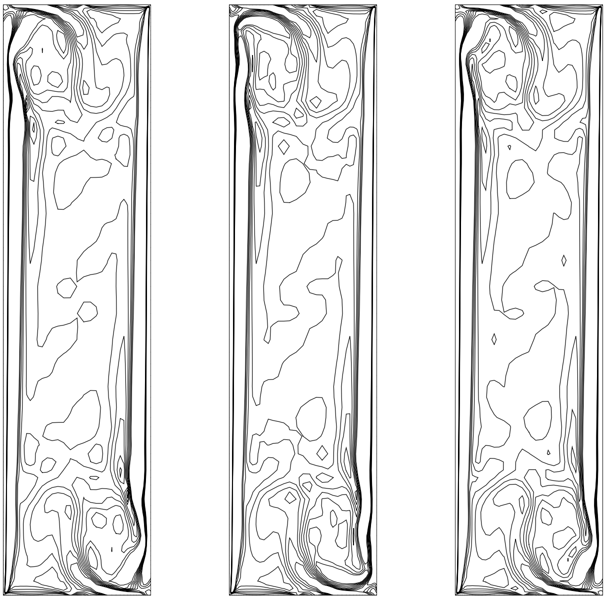

Figure 6: Vorticity ω_z isolines (-5000..5000) at $Ra = 10^7$ and $t = 0.0700, 0.0705, 0.0710$.

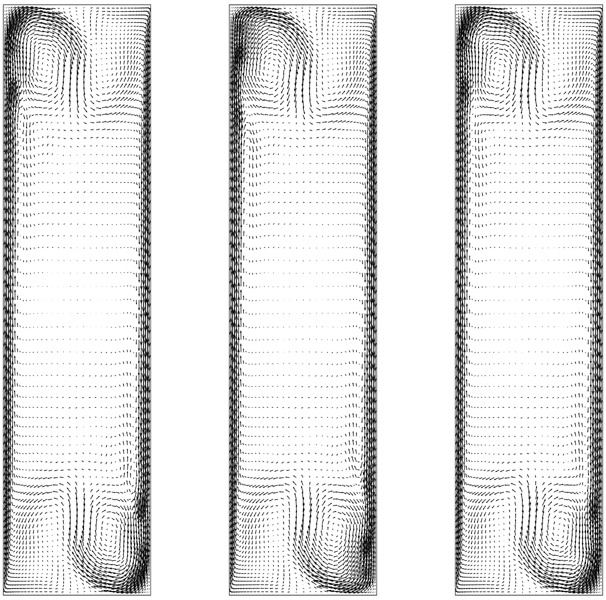

Figure 7: Velocity vectors at $Ra = 10^7$ and $t = 0.0700, 0.0705, 0.0710$.

In order to show the unsteady behavior of the flow we chose three nodes in the cavity (see coordinates in Table 2), where we present the time dependance of the temperature in Figure 8. The time dependance of the Nusselt number value for $Ra = 10^7$ is presented in Figure 9. We can readily observe oscillations in temperature as well in the Nusselt number value.

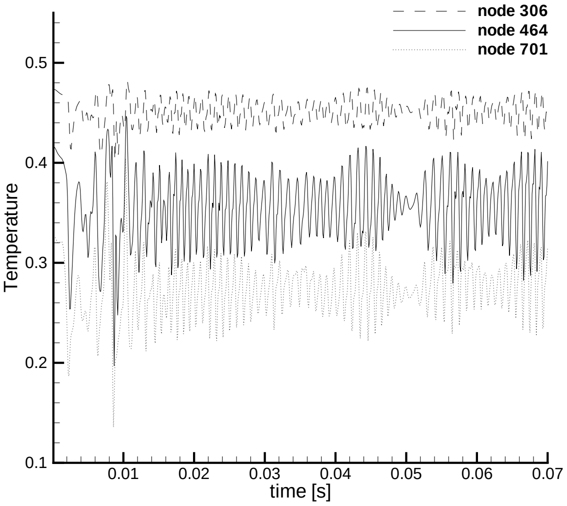

Figure 8: Temperature oscillations for $Ra = 10^7$.

Table 2: Node coordinates.

node	x	y
node 306	0.01135	3.59638
node 464	0.03595	3.59638
node 701	0.08011	3.59638

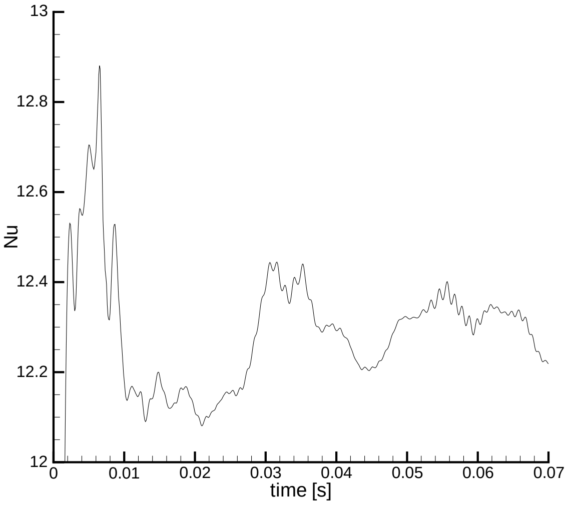

Figure 9: Time dependance of the Nusselt Nu number value for $Ra = 10^7$.

4.2 *Compressible fluid model*

The computations of compressible natural convection in a 1:4 enclosure were performed for $Ra = 10^3$, $Ra = 10^4$, $Ra = 10^5$, with temperature difference parameter $\epsilon = 0.6$, a result of imposed $T_h = 960K$ and $T_c = 240K$. The boundary conditions and mesh are presented in Figure 1.

Due to an increased nonlinearity of the compressible fluid flow model as opposed to the incompressible model, we were unable to make calculations for Rayleigh number value higher than 10^5, and hence were unable to detect unstable chaotic behavior with the compressible fluid model. We believe that the reason for divergence of the model for higher Rayleigh number values is the low computational mesh density. In future, these simulations will be repeated on a finer mesh, resulting with no doubt in a chaotic flow regime.

Flow reached steady state at all Rayleigh number values simulated $Ra = 10^3$, $Ra = 10^4$, $Ra = 10^5$. The average Nusselt number values for compressible fluid model are presented in Table 3. Figures 10 and 11 show steady state temperature and velocity fields respectively.

Table 3: Average Nusselt number $\bar{N}u$ values for different Rayleigh number values for compressible fluid model.

Ra	10^3	10^4	10^5
Nu	1.140	2.103	3.880

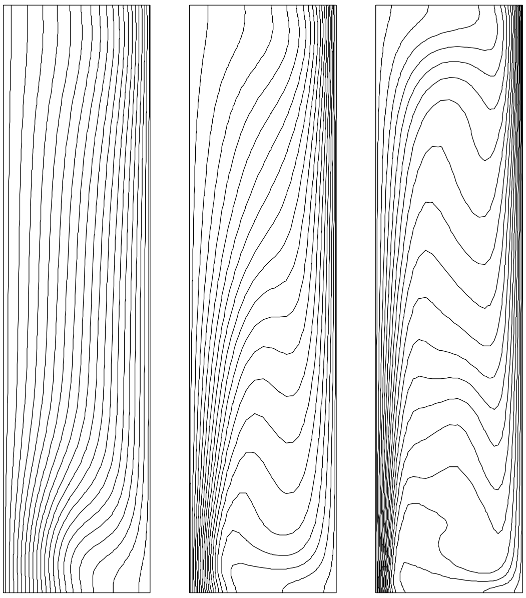

Figure 10: Temperature isolines, compressible flow: steady state results for $Ra = 10^3, 10^4, 10^5$, left to right.

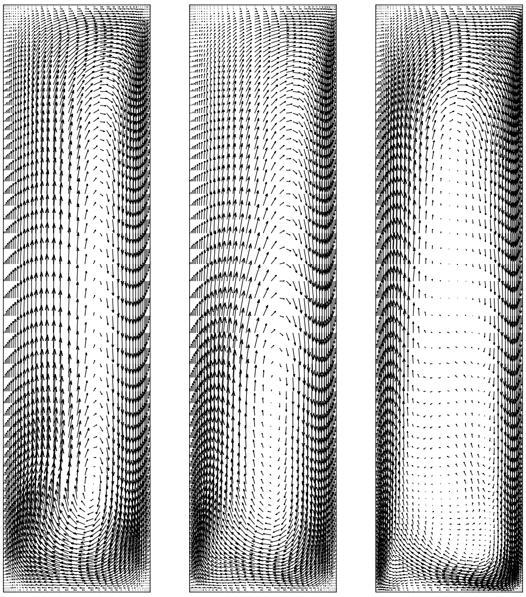

Figure 11: Velocity field, compressible flow: steady state results for $Ra = 10^3, 10^4, 10^5$, left to right.

5 Conclusions

We have shown that the flow in a differentially heated $1 : 4$ enclosure becomes unsteady at high Rayleigh number values ($Ra \geq 10^7$). Vortices are formed in the boundary layer and transported by convection up along the hot wall and down along the cold wall. The observed behavior is not oscillatory but chaotic, which can be observed from the time dependance of the Nusselt number value. Other researchers [6], [4] reported the onset of chaotic regime at a lower Rayleigh number value $Ra \approx 10^5$ working with higher density meshes.

Due to low mesh density we were not able to simulate compressible fluid flow at Rayleigh number value larger than $Ra \geq 10^5$. Although proof of chaotic compressible fluid behavior in and $1 : 4$ encloser will require additional computations on finer meshes, we are sure of its existence.

References

[1] Wu, J.C. (1982) : Problems of general viscous fluid flow. *Developments in BEM*, Vol. 2, Ch. 2, Elsevier Appl. Sci. Publ., London and N.Y.

[2] De Vahl Davis, G. (1983) : Natural convection of air in a square cavity: A bench mark numerical solution. *Int. J. for Num. Meth. in Fluids,* Vol.3, pp. 249-264.

[3] Le Quere, P. (1991): Accurate solutions to the square thermally driven cavity at high Rayleigh number. *Computers Fluids* , Vol. 20,No. 1, pp. 29-41.

[4] Weisman, C., Calsyn, L., Dubois, C.,Le Quere, P. (2001): Sur la nature de la transition a l'instationare d'un ecoulement de convection naturelle en cavite differentiellement chauffee a grands ecarts de temperature. *Comptes rendus de l'academie des sciences* Serie II b, Mecanique, pp. 343-350, Elsevier.

[5] Vierendeels, J., Merci, B., Dick, E. (2001): Numerical study of the natural convection heat transfer with large temperature differences. *Int. J. Numer. Meth. for Heat* & *Fluid Flow*, Vol.11, pp. 329-341.

[6] Ingber, M.S. (2003): A vorticity method for the solution of natural convection flows in enclosures. *Int. J. Numer. Meth. for Heat* & *Fluid Flow*, Vol.13, pp. 655-671.

[7] Škerget L, Hriberšek M, Žunič Z. Natural convection flows in complex cavities by BEM *Int. J. Num. Meth. for Heat & Fluid Flow* 2003;13(6):720-735.

[8] Škerget, L., Samec, N. : BEM for the two-dimensional plane compressible fluid dynamics. *Eng. Anal. Bound. Elem.*, Vol. 29, pp. 41-57, 2005

Proceedings of The 1st International Conference on **D**iffusion in **S**olids and **L**iquids
DSL-2005, July 6-8, 2005, University of Aveiro, Aveiro, Portugal

GRAIN BOUNDARY SEGREGATION EFFECT ON GRAIN BOUNDARY DIFFUSION IN BINARY ALLOYS WITH RESTRICTED SOLUBILITY

Boris BOKSTEIN*, Andrey SMIRNOV, Sergey ZHEVNENKO

Moscow Steel and Alloys Institute (Technological University), 4, Leninsky pr-t, Moscow, 119049, Russia

*Corresponding author. Fax: +7 095 2368738; Email: bokst@misis.ru

---

Abstract

This paper comments the possible effect of the phase transition in grain boundary with formation of 2D grain boundary (segregation) phase on the effective coefficient of grain boundary diffusion.

Keywords: Diffusion; Segregation; Grain boundaries

---

1 Introduction

The solute in a solid solution with restricted solubility can "choose" between three possibilities: to stay inside a solution (in a grain), to move to a grain boundary (GB) and segregate in it, or, a solubility in grain to be reached, to form the nearest (by composition) bulk phase in grain (chemical compound, other solid solution, pure component). GB segregation strongly influences on GB diffusion and diffusion related phenomena Ref. [1].

Recently Ref. [2] it was supposed that in the case of preferential attractive interaction between solute atoms, above critical value of solute concentration in grain, the phase transition in GB from one solid solution to the other, nearly saturated solution, occurs. This transition is accompanied by the gap in adsorption isotherm, the change of the slope ($d\gamma/\mu_2$) in the GB tension (γ) isotherm (μ_2 is a solute chemical potencial) and the formation of the new 2D grain boundary (segregation) phase (GBP).

Many approaches relevant to the nature of GBP were considered. The main idea Ref. [3] was that the nucleuses of this phase have atomic configuration, electronic structure and chemical bonds Ref. [4-11] which are very similar to the phase in grain.

This paper comments the possible effect of such phase transition on GB diffusivity.

2 Grain boundary adsorption isotherm

McLean's isotherm Ref. [12] is used commonly for grain boundary adsorption (segregation) description in ideal solutions, both in grain and in GB. It takes form

$$\frac{X_b}{X_b^0} = \frac{bX}{1 - X + bX} \qquad (1)$$

where X_b and X are atomic fractions of solute in GB and in grain, X_b^0 is a saturation value of X_b, or atomic fraction of available sites in GB, and b is enrichment coefficient which has a physical meaning of a solute segregation equilibrium constant. For a dilute solutions:

$$\frac{X_b}{X_b^0} = \frac{bX}{1 + bX} \qquad (2)$$

Obviously $X_b^0 \leq 1$.

$X_b(X)$ dependence in accordance with (2) is shown in Fig.1. It is clearly seen that at $b >> 1$, X_b reaches the saturation value X_b^0 long before X attains the solubility X_0.

Let us now take into account that B atoms in GB interact with A atoms. In zeroth-order quasichemical approximation (or regular solution model) this interaction may be characterized by a constant heat of mixion (E), which includes binding energy between pairs of nearest neighbor atoms, according to Fowler-Guggenheim isotherm Ref. [13]

$$\theta = \frac{bX\exp(\gamma\theta)}{1+bX\exp(\gamma\theta)} \qquad (3)$$

were $\gamma = E / RT$, T is temperature and R is a gas constant. In Eq. (3) it was supposed that a heat of adsorption is proportional to the coverage θ.

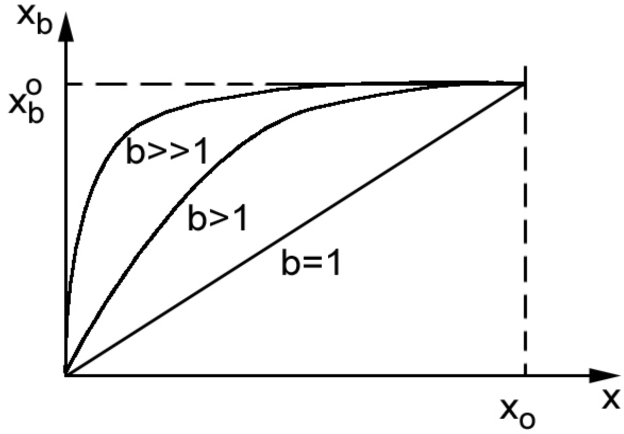

Figure 1: Dependence of solute GB atomic fraction (X_b) on atomic fraction in grain (X) for different b. X_0 is a solubility in grain; X_b^0 is a saturation value of X_b.

Now we would try to join two assumptions: the first one – about the interaction between the adsorbate and adsorbent atoms (Fowler) and second – about the limited number of available for adsorption sites in GB ($X_b^0 \leq 1$; McLean). The new hybrid isotherm for regular solution in GB and dilute ideal solution in grain is as follows

$$\frac{\theta}{\theta_0} = \frac{X_b}{X_b^0} = \frac{bX\exp(\gamma\theta)}{1+bX\exp(\gamma\theta)} \qquad (4)$$

where θ_0 is a coverage, corresponding to a saturation.

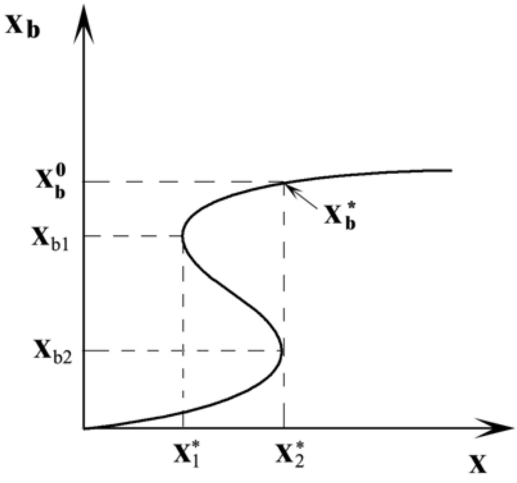

Figure 2: $X_b(X)$ dependence according to adsorption isotherm Eq. (4).

It is well known that at $\gamma > 2$, i.e. in the case of preferential attractive interaction between solute atoms, one can see a gap in the $X(X_b)$ dependence which is shown schematically in Fig. 2. Position of the extrema in $X(X_b)$ curve depends only on γ

$$(\theta/\theta_0)_{1,2} = (X_b/X_b^0)_{1,2} = 1/2(1 \pm \sqrt{1-2/\gamma}) \quad (5)$$

Unlike, the value of the extrema depends both on b and γ:

$$X_{1,2}^* = \frac{\theta_{2,1}\exp(-\gamma\theta_{2,1})}{b(1-\theta_{2,1})} \qquad (6)$$

As an example, Eq. (6) gives at γ = 5 and b = 10, $X_1^* = 0.007$, $X_2^* = 0.01$, $X_{b1} / X_b^0 = 0.72$ and $X_{b2} / X_b^0 = 0.28$; at γ = 6 and b = 100, $X_1^* = 0.0003$, $X_2^* = 0.0007$, $X_{b1} / X_b^0 = 0.79$ and $X_{b2} / X_b^0 = 0.21$.

Let us call your attention to the fact that a gap in the $X(X_b)$ dependence occurs at a very small values of X. Hence usually we deal with a second, ascending branch of a curve in Fig. 2, following a gap.

As solute content in alloy increases, the nucleuses of GB phase form. At the same time solute concentration in GB $X_2 = X_2^*$ = const and solute concentration in GB solution X_b reaches its saturation value (X_b^*) and remains constant. The composition of GB phase is also constant and close to the composition of the phase in grain X_p but its value increases to the certain extent. Hence, during this transformation three phases coexist with constant compositions: solid solution in grain (X_2^*), solid solution in GB (X_b^*; possibly X_b^* is closed to X_b^0; the fraction of GB area, occupied by solid solution, decreases during transformation) and GB phase (X_{GBP}; possibly X_{GBP} is closed to X_p, the fraction (α) of GB area, occupied by GB phase, increases tending to the limit α_0).

It could be written that

$$X_b^0 = X_p\alpha_0 + X_b^*(1-\alpha_0) \qquad (7)$$

It appears that $\alpha_0 \leq 1$, thus $X_b^0 \leq X_p$.

Analysis of our own experimental data obtained by the use of Auger spectroscopy for Cu-Sb Ref. [14, 15] and Sn-Bi Ref. [17] systems, and data of Ref. [18] for Fe-P system showed that the ratio of X_b^0 to X_p changes in the range from 0.5 to approximately 1. Let us remind that the phases in grain are in these systems Cu_3Sb, Fe_3P and pure Bi.

3 Qualitative estimations

Based on the reasons given above, we can consider GB as a two phase region partly occupied by GBP (α_0) and partly by saturated solution. Model of diffusion in such two phase system was proposed by Hart Ref. [19]. According to Hart, the effective diffusion coefficient (D_{eff}) may be entered as

$$D_{eff} = \alpha_0 D_p + (1 - \alpha_0) D_b^* \qquad (8)$$

In Eq. (8) α_0 has the same meaning as in Eq. (7), D_p and D_b^* are diffusion coefficients in GBP, which is similar to phase in grain, and in GB saturated solution. Of course, we do not know exact values neither for D_p, nor for D_b^*. But from Eq.(8) it can be said that the sign of $\Delta D = D_{eff} - D_b$ depends on the value of D_p. $\Delta D > 0$ if $D_p > D_b$ and the reverse. Therewith we assumed that D_b does not depend on the coverage. Hence, $D_b = D_b^*$ at every concentration in grain.

Unfortunately, direct GB diffusion data for above mentioned systems are absent. But started from common diffusion regularities we can say with reasonable confidence that Cu GB diffusion in Bi is faster while in Cu_3Sb – slower than Cu GB selfdiffusion. The last case is more often. Respectively, in frame of discussed model, GB segregation, as a rule, moderates GB diffusion.

4 Connection between two segregation coefficients

It is clearly seen from Fig. 2 that the gap in the $X_b(X)$ dependence occurs at a very small values of X. Hence we deal with a second, ascending branch of the curve in Fig. 2. This branch follows the gap. It can easily be shown that this branch of adsorption isotherm is obeyed to McLean's equation (2) and can be used, if it is obtained on the base of spectrometric data, for determination of X_b^0, the saturation value of X_b. Appropriate procedure is described in details in Ref. [14, 15].

It was underlined in Ref. [20] that GB segregation is usually characterized by one of the following coefficients: either b, which is used in McLean's and other isotherms of equilibrium adsorption, or s, which can be determined as a ratio of GB and bulk solute concentration in immediate vicinity of GB. The last one can be obtained in diffusion experiments carried out in so-called B and C regimes Ref. [21].

In a limit of dilute solution in grain ($X \ll 1$) Eq. (2) gives

$$X_b / X_b^0 \approx bX \qquad (9)$$

and

$$\frac{X_b}{X} = bX_b^0 \qquad (10)$$

On the other hand, from a definition of s it follows that

$$s = Lim(X_b / X) \text{ at } x \to 0 \qquad (11)$$

where x is a coordinate directed by the normal to GB plane, and x = 0 corresponds to this plane, i.e. the fracture surface after GB fracture was done.

From Equations (10) and (11) we can receive a connection between b and s:

$$bX_b^0 = s \text{ or } b = \frac{s}{X_b^0} \qquad (12)$$

As it was noted above, using quasi – stationary solution of Fisher model the triple product $P_i = s\delta D_{ib}$ can be determined in B – regime (index i relates to the i – th solute) and double product δD_{ib} - in C – regime (at lower temperatures). At last

$$\frac{P_i}{\delta D_{ib}} = s_i \qquad (13)$$

The set of such experiments was fulfilled by Chr. Herzig and his coauthors (see, for example, Ref. [8, 22]).

Unfortunately, both adsorption coefficients were measured only for one system, namely Ag – Cu. With sufficiently high reliability we can state that for all systems investigated b ≥ s. As is evident from our data, X_b^0 changes in the range 0.5 – 1.0 in a good agreement with the conlusion : b ≥ s.

5 Conclusion

Two phase GB model is considered. It follows from this model that acceleration or moderation of GB diffusion due to GB segregation can be observed. It depends on the coefficient of the solvent diffusion in the phase IN GRAIN which precipitates when solubility limit is reached.

Acknowledgements

The authors are grateful for financial support provided by Russian Foundation for Basic Researches (project N 04-02-26747a, project N 05-03-32910a) and program “Russian Universities” (program N 2367-05).

References

[1] Bokstein B. and Balandina N. (Ed). Grain Boundary Diffusion and Grain Boundary Segregation. *Defect and Diffusion Forum*, 1998. 156. 276 P.

[2] Bokstein B.S., Rodin A.O. and Smirnov A.N.. *Zt. für Metkunde*, 96 (2005).

[3] Guttman M.: *Metall. Trans*. 8A (1977) 1383.

[4] Bokstein B.S., Gel’tser I.S., Glickman E.E., Nikolsky G.S.: Reports Voronez Polytech. Inst., Voronez, 1988 (in Russian).

[5] Briant C.: *Met. Trans*. 21A (1990) 2339.

[6] Treglia G., Legrand B., Eugene J., Aufray B., Cabane F.: *Phys. Rev*. 44B (1991) 5842.

[7] Bernardini J., Gas P.: *Def. and Dif. Forum* 95 – 98 (1993) 393.

[8] Mishin Y., Herzig Chr.: *Mat. Sci. and Eng*. 260A (1999) 55.

[9] Hashimoto M., Wakayama S., Yamamoto R., Doyama M.: *Acta Met*. 32 (1984) 13.

[10] Losch W.: *Acta Met*. 27 (1979) 1885.

[11]Briant C.L., Banerji S.K.: *Metall. Trans*. 10A (1979) 1729.

[12]McLean D.: *Grain Boundaries in Metals*, Clarendon Press, Oxford, 1957.

[13] Fowler R.H., Guggenheim E.A.: *Statistical Thermodynamics*, University Press, Cambridge (1960).

[14] Bokstein B.S., Smirnov A.N.: Reports of High School. Nonferrous Met. 2 (2004) 64 (in Russian).

[15] Smirnov A.N.: Surface 1 (2005) 109 (in Russian).

[16]Bokstein B.S., Smirnov A.N.: *Materials Letters* 57 (2003) 4501.

[17] Bokstein B.S., Podgornyi D.A., Smirnov A.N.: Reports of the Russian Academy of Science, ser. Phys. 9 (2005) 2224 (in Russian)

[18] Erhart H., Grabke H.J.: *Metal Science* 15 (1981) 401.

[19] Hart E.W.: *Acta Met*. 5 (1957) 597

[20] Bokstein B.S., Razumeiko B.G. and Rodin A.O.: *Def. and Dif. Forum* 216 – 217 (2003) 231.

[21]Atkinson A. and Taylor R.I.: *Phil. Mag.* 43A (1981) 979.

[22] Divinsky S., Lohman M. and Herzig Chr.: *Acta Mat*. 49 (2001) 249.

Proceedings of The 1st International Conference on **D**ifusion in **S**olids and **L**iquids
DSL-2005, July 6-8, University of Aveiro, Aveiro, Portugal

KINETICS OF MICROSTRUCTURE EVOLUTION DURING GASEOUS THERMOCHEMICAL SURFACE TREATMENT

Marcel A.J. SOMERS*, Thomas CHRISTIANSEN

Department of Manufacturing Engineering and Management,Technical University of Denmark,
Kemitorvet b.204, DK-2800 Kgs. Lyngby, Denmark

*Corresponding author. Fax: +45 45936213; Email: somers@ipl.dtu.dk

---

Abstract

The incorporation of nitrogen or carbon in steel is widely applied to provide major improvements in materials performance with respect to fatigue, wear, tribology and atmospheric corrosion. These improvements rely on a modification of the surface adjacent region of the material, by the (internal) precipitation of alloying element nitrides/carbides or by the development of a continuous layer of iron-based (carbo-) nitrides. The evolution of the microstructure during thermochemical treatments is not only determined by solid state diffusion, but in many cases also by the kinetics of the surface reactions and the interplay with mechanical stress.

In the present article a few examples, covering research on the interaction of carbon and/or nitrogen with iron-based metals, are included to illustrate the various aspects of gas-metal interactions.

Keywords: Layer growth kinetics; Diffusion modeling; Nitriding; Nitrocarburizing; Expanded austenite

---

1 Introduction

Gaseous thermochemical surface treatments as nitriding and nitrocarburizing belong to the most versatile surface engineering processes of steels and allow improvement of the performance of components with respect to fatigue, wear and atmospheric corrosion. In principle during treatment the case developing can be subdivided in a surface layer consisting of compounds as nitrides and carbonitrides and a diffusion zone underneath, consisting of alloying element (carbo)nitrides or a supersaturated interstitial solution of nitrogen in a metallic matrix. In the present article the various aspects of the kinetics of microstructure evolution during gas-solid interactions during thermochemical treatment are dealt with. These aspects involve the implication of the competition between surface reaction kinetics and solid state diffusion and on nucleation of a compound at a surface and compound layer growth, the competition between carbon and nitrogen uptake during nitrocarburizing and the modelling aspects of the growth of expanded austenite during nitriding of austenitic stainless steel.

1.1 Gas-solid interactions [1]

The gas solid interactions to be discussed are essentially simple and concern nitriding in NH_3/H_2 and nitrocarburizing in $NH_3/CO_2/H_2$. In all cases atmospheric pressure applies. Dissociation reactions at the surface provide the atomic species adsorbed at the surface, which subsequently may be incorporated into the solid state or leave the surface again. For nitriding in NH_3/H_2, adsorbed nitrogen atoms can diffuse into the solid phase ϕ:

$$NH_3 \rightleftarrows N_{ad} + \tfrac{3}{2}H_2 \qquad \text{(Ia)}$$

$$N_{ad} \rightleftarrows [N]_\phi \qquad \text{(Ib)}$$

or, upon development of molecular nitrogen, leave the surface:

$$N_{ad} + N_{ad} \rightleftarrows N_2 \qquad \text{(Ic)}$$

For nitrocarburizing a competition between a carburizing and a nitriding reaction occurs. Because of the presence of hydrogen, carburizing according to the following scheme is kinetically preferred:

$$CO_2 + H_2 \rightleftarrows CO + H_2O \tag{IIa}$$

$$CO + H_2 \rightleftarrows C_{ad} + H_2O \tag{IIb}$$

$$\mathrm{C}_{ad} \rightleftarrows [C]_{\phi} \tag{IIc}$$

2 Nucleation of iron nitride at an iron surface during nitriding [2]

On gaseous nitriding of iron the first phase developing at the surface is γ'-Fe_4N_{1-x}, which nucleates upon exceeding the maximum solubility of nitrogen in iron in the region adjacent to the surface. The incubation time for the nucleation of γ' nitride depends on the competition between the flux of nitrogen atoms arriving at the surface and the fluxes of nitrogen atoms leaving the surface. The flux of arriving nitrogen atoms is controlled by ammonia dissociation (reaction (Ia); the fluxes of nitrogen atoms leaving the surface are due to the development and desorption of N_2 (reaction (Ic) and diffusion of nitrogen atoms into the solid state (reaction (Ib)). For an iron plate of infinite length and width with finite thickness (L) and a uniform, initial nitrogen distribution (C_0), the fluxes of nitrogen atoms associated with the dissociation reaction of ammonia at the surface, J_{diss}, the desorption of molecular nitrogen from the surface, J_{des}, and solid state diffusion into the substrate, J_{diff}, are given by (cf. Refs. [2] and [3]):

$$J_{diss} = k \cdot \left(C_{eq} - C_S\right) \tag{1}$$

$$J_{des} = -k_2 \cdot \frac{K_S \cdot C_S^2}{1 + K_S \cdot C_S} \tag{2}$$

$$J_{diff} = J\big|_{z=0} = -D_N^{\alpha} \left.\frac{\partial C_N}{\partial z}\right|_{z=0} \tag{3}$$

where k is the reaction rate constant for ammonia dissociation, C_{eq} is the nitrogen concentration in α-iron for equilibrium with the gas phase, C_S is the actual concentration of nitrogen in the solid state adjacent to the surface, k_2 is a rate constant of the formation of molecular nitrogen, K_S is the equilibrium constant of segregation of nitrogen atoms at the iron surface and *z=0* indicates the position of the surface. In order to obtain the nitrogen depth distribution as a function of nitriding time Fick's 2nd law ($\frac{\partial C_N}{\partial t} = D_N^{\alpha} \frac{\partial^2 C_N}{\partial z^2}$) has to be solved for the set of boundary conditions given by Eqs.(1-3). At the time where the surface concentration C_S exceeds the solubility limit for nitrogen in α-Fe a driving force for the nucleation of γ'-Fe_4N_{1-x} is established. This nitriding time is taken as the incubation time for iron nitride nucleation. In Fig. 1a the incubation time, thus calculated is given as a function of the nitriding potential[1], K_N, for nitriding temperatures ranging from 743 K to 863 K (details of the calculations and the data used are given in Refs. [2] and [3]). Evidently, the incubation time decreases with increasing nitriding potential. It follows from Fig. 1a that the formation of N_2 only affects the calculated incubation time for nitriding potentials just beyond the critical nitriding potential where ferrite can be stable. The effect of N_2 formation is a prolongation of the incubation period by maximally 10% (at 863 K) and decreases dramatically with decreasing temperature. The experimental investigation of the development of iron nitrides at a ferrite surface was carried out with light microscopy of polished the as-nitrided surface. Identification of the nitride phases was done with X-ray diffraction analysis.

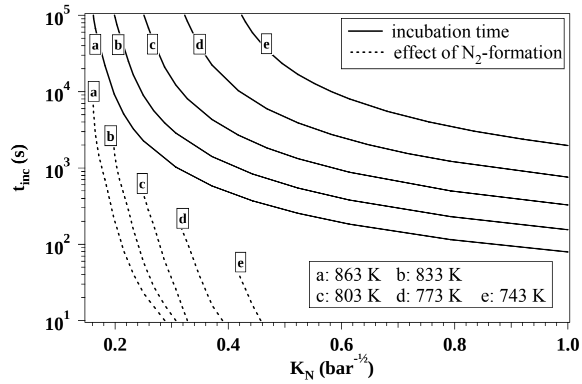

Figure 1:

a. Calculated incubation time for establishing a driving force for the nucleation of γ'-Fe_4N_{1-x} on pure iron. The dashed curves represent the additional incubation time due to N_2 development at the surface.

---

[1] Nitriding potential is proportional to the nitrogen activity in the solid state for equilibrium with the gas phase: $K_N = \frac{p_{NH_3}}{p_{H_2}^{3/2}}$

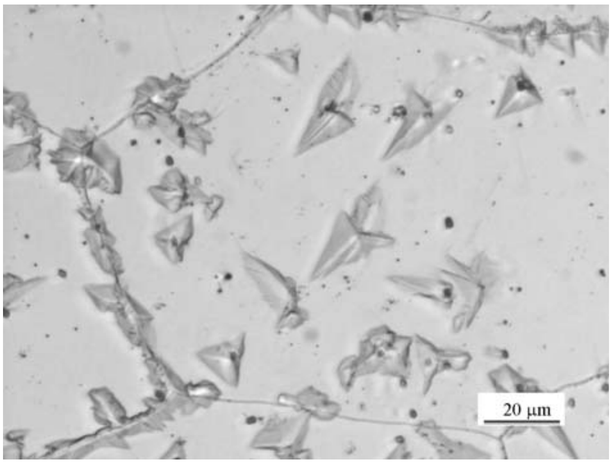

Figure 1:

b. Light microscopy of polished surfaces H_2-reduced and nitrided. Nitriding was performed at 833 K at nitriding potential K_N=0.38 $bar^{-1/2}$ (=1.2 10^{-3} $Pa^{-½}$) for 20 minutes.

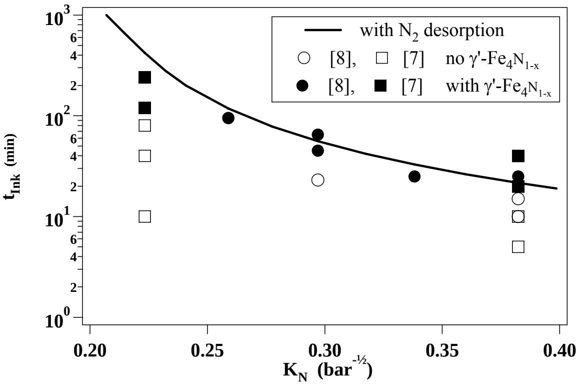

Figure 1

c. Comparison of experimental and calculated incubation times at 833 K.

The development of nitrides on grain surfaces rather than at grain boundaries (cf. Fig. 1b) was taken as a criterion for successful nucleation, because the calculations do not take the occurrence of grain boundaries into account. The experimental incubation times for γ'-Fe_4N_{1-x} nucleation are generally shorter than the times calculated for attaining the maximum lattice solubility of nitrogen in ferrite, i.e. establishing a driving force for nitride nucleation (Fig.1c). These systematic differences are attributed to differences in the surface conditions (composition and topography) of the samples used in the present experiments and those used in the experiments from which the rates of the surface reactions were assessed [2].

3 Nitride layer growth under combined surface reaction and diffusion control [4]

On nitriding the growth kinetics of the compound layer during nitriding is usually assumed to be controlled by solid-state diffusion of nitrogen through the phases constituting the compound layer; the diffusion of Fe atoms can be neglected [5]. The growth of γ'-Fe_4N_{1-x} monolayers or the ε-Fe_2N_{1-z} /γ'-Fe_4N_{1-x} double layers on ferrite can be evaluated from considering the fluxes entering and leaving the sublayers (for mathematical descriptions see Ref. [5]). The assumptions usually made to arrive at a mathematical description of the growth kinetics involve local equilibrium at the solid/solid interfaces as well as at the surface. It can be assumed that the composition in each of the sublayers changes linearly with depth, provided that the composition-dependent diffusion coefficients D_N^{φ} are replaced by the composition-weighted (effective) diffusion coefficient, $\left\langle D_N^{\varphi} \right\rangle$, for each of the sublayers [5]:

$$\left\langle D_N^{\phi} \right\rangle = \int_{y_{N,\varphi}^{\min}}^{y_{N,\varphi}^{\max}} \left(D_N^{\phi} \right)^* \cdot \frac{d \ln a_N}{d \ln C_N} \cdot dy_{N,\varphi} \qquad (4)$$

with $\left(D_N^{\varphi} \right)^* = RT\left(1 - y_{N,\varphi}\right) M_N^{\varphi}$

where $\left(D_N^{\varphi} \right)^*$ is the tracer diffusion coefficient of nitrogen in phase φ, $y_{N,\varphi}^{\min}$ and $y_{N,\varphi}^{\max}$ are the minimum and maximum occupancies of the interstitial sublattice in phase φ and M_N^{φ} is the mobility of nitrogen atoms in phase *φ*. The thermodynamic factor dln a_N/dln C_N in Eq. (4), where a_N is the activity of nitrogen and C_N the concentration of nitrogen, follows directly from the thermodynamics of the phases involved (cf. Refs. [5]-[7] and references therein). For ε/γ' double layers the assumption of local equilibrium at the gas/solid interface is clearly in conflict with experimental findings (cf. Fig. 2 [2,7]); local equilibrium at solid/solid interfaces appears to be in good agreement with experimental results. Generally, the nitrogen content in the ε phase close to the surface is significantly lower than the content corresponding to local equilibrium with an imposed nitrogen activity. This lower nitrogen content is attributed to the competition between the relatively slow kinetics of ammonia dissociation, the desorption of molecular nitrogen gas from the surface and solid-state diffusion into ε nitride (cf. the discussion in the previous chapter).

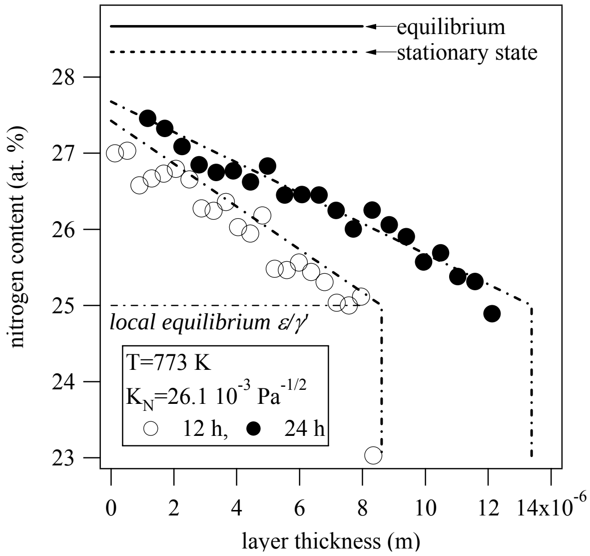

Figure 2: Comparison of experimental and modelled nitrogen profiles for the case of a dynamic state at the surface [4,7].

A model assuming local equilibrium at the solid/solid interfaces in the compound layer and a dynamic situation at the gas/solid interface is presented in Fig. 3. Analogous to the case of nucleation, the dynamic situation at the surface is described by Eqs. (1)-(3). The equations describing double layer growth under the condition of no local equilibrium at the surface were published elsewhere [8].

The evolution of the layer thicknesses of ε-phase and γ'-nitride were described mathematically by the model in Fig. 3 under the above conditions, adopting k, k_2, K_S for ε-phase and $\left(D_N^{\gamma'}\right)^*$ and M_N^{ε} as fit parameters. Layer growth kinetics at 773 K at a relatively high nitriding potential is shown in Fig. 4. The dashed lines represent the simulated layer growth kinetics if the model from Ref. [10] is adopted, which presumes local equilibrium at all interfaces, including the surface, and only one fit parameter ($\left\langle D_N^{\varepsilon}\right\rangle$ or M_N^{ε}). The model in Fig. 3 provides a better description of the evolution of the layer thickness than the model presuming local equilibrium at the surface (Fig. 4) and, perhaps more convincingly, the evolution of the nitrogen depth profile (Fig. 2).

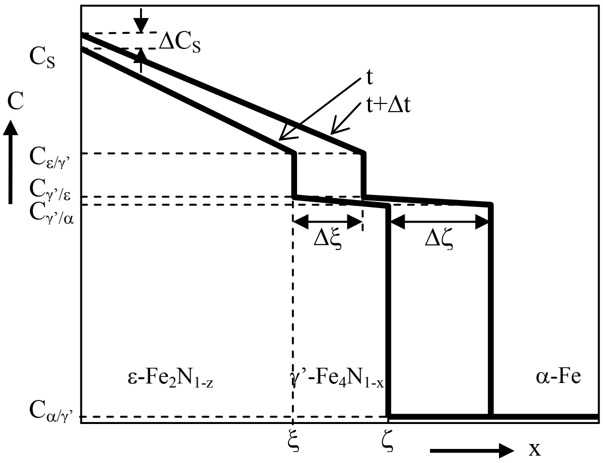

Figure 3: Model for double layer growth. Local equilibrium prevails at all solid/solid phase boundaries. For a time increment dt the sublayers increase in thickness by dξ and dζ, whilst the surface concentration increases by ΔC_S. Linear concentration profiles are assumed in the sublayers.

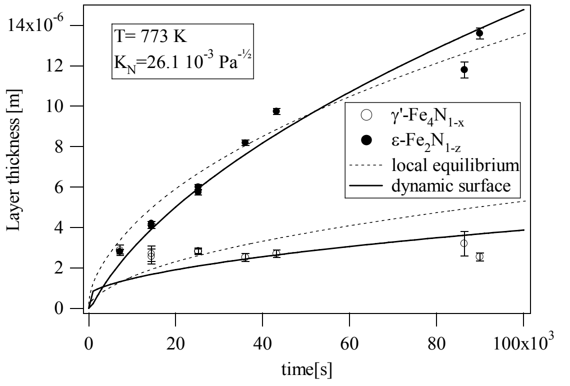

Figure 4: Results of modelling double layer growth for the cases of local equilibrium (dashed lines) and a dynamic state (solid lines) at the surface.

The major discrepancy between the modeled and experimental data in Fig. 4 concerns the thickness of the γ'-layer for relatively short nitriding times. Further improvement of describing the evolution of this part would involve incorporation of the nucleation of the γ'-layer at the surface, which was left out of the present model in order keep the number of fitting parameters as low as possible. Furthermore, it was found that, upon exceeding the maximum solubility of nitrogen in ferrite, the γ'-

layer does not form instantaneously as a layer, but by nucleation and subsequent coalescence (cf. Ref. [2,5] and references therein). As a consequence nitrogen incorporation can occur through both ferrite and the γ'-nuclei, resulting in a thicker γ' layer than would be obtainable for diffusion through a γ' layer only (as reflected by the experimental data in Fig.4). Another issue that deserves future attention is the occurrence of compositionally induced compressive stress profiles in the two nitride layers (cf. Ref. [8] and references therein). This topic will be dealt with in chapter 7.

5 Microstructural evolution of the compound layer during nitrocarburizing [10]

On gaseous *nitrocarburizing* the nucleation of the phases constituting the compound layer depends on the competition of the surface reactions (I) and (II). The carburizing reaction proceeds much faster than the nitriding reaction. Hence, the carbon solubility in the substrate is exceeded earlier than the nitrogen solubility and carbide or a carbonitride would be expected to nucleate. The nucleation of γ' iron nitride is suppressed, because of the low solubility of carbon in this phase. On nitrocarburizing pure iron the first phase appearing at the surface was observed to be cementite (θ-Fe_3C) for various combinations of nitriding and carburizing activities [10]. A first appearance of the carbonitride phase ε-$Fe_2(N,C)_{1-z}$ in the compound layer was observed to be promoted by a high nitriding potential and to be retarded by a high carburizing activity, but was never observed to nucleate as the first phase.

In the sequel the microstructural evolution of the compound layer is discussed for the following combination of nitrogen and carbon activities: a_N=753; a_C=1.37. The morphological and compositional evolution of the compound layer on iron during nitrocarburizing under these conditions is presented in Fig. 5. After the initial development of cementite, the ε-phase becomes dominant in the compound layer on prolonged treatment. The content of cementite decreases and, eventually, becomes zero. Concurrently, the amount of γ' phase increases (see Fig. 5), particularly in the part of the compound layer adjacent to the substrate. The evolution of the composition depth profiles shows that the nitrogen content at the surface increases with time, while the carbon content at the surface decreases complementarily (Fig. 6). This relatively slow increase of the nitrogen content is consistent with the observation of a continuously increasing nitrogen content in ε-phase on nitriding (cf. the previous chapter), due to the relatively slow kinetics of ammonia dissociation at (and nitrogen desorption from) the iron surface, which allowed an initially strong absorption of carbon. Needless to say that modeling of the microstructure evolution of the compound layer during nitrocarburizing is currently not possible, since it involves nucleation and dissolution of phases as well as composition changes. Most parameters necessary for such modeling are (as yet) quantitatively undetermined.

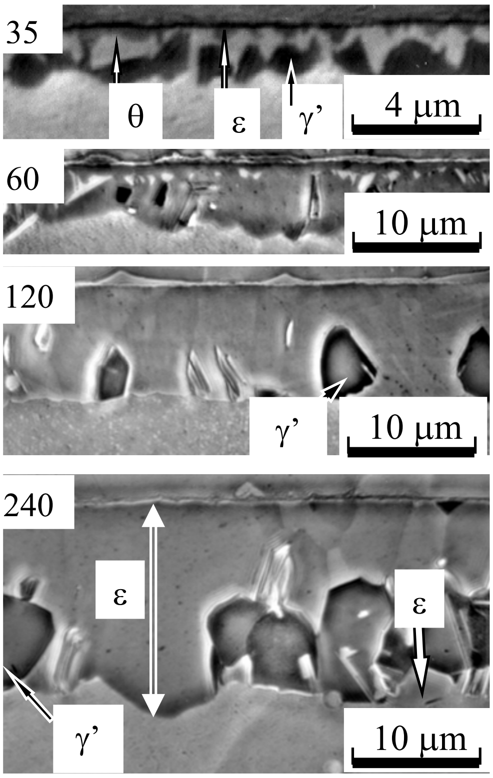

Figure 5: Light microscopy of polished surfaces H_2-reduced and nitrided. Nitriding was performed at 833 K at nitriding potential K_N=0.38 bar$^{-1/2}$ (=1.2 10^{-3} Pa$^{-½}$) for 15 minutes.

A very first attempt to model the growth kinetics of the compound layer during nitrocarburizing for a simple phase constitution of the compound layer and local equilibrium at the surface and solid/solid interfaces was presented in Ref. 11.

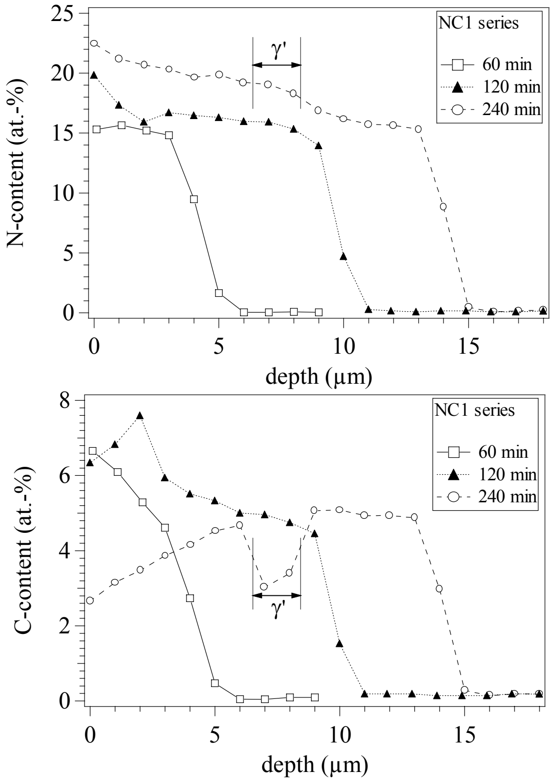

Figure 6: EPMA nitrogen and carbon depth profiles determined on cross sections of the samples in Fig.5 for 60, 120 and 240 minutes.

6 Dissolution of nitrogen in austenitic (f.c.c.) stainless steel [12]

A very recent development in the thermochemical treatment of iron-based materials is nitriding of stainless steel, with the purpose of improving the surface's wear performance without impairing the excellent corrosion properties. This can only be achieved when the hardening process does not hinder Cr atoms from forming the self repairing Cr-based oxide layer that provides corrosion resistance. Since Cr has a relatively strong affinity for forming nitrides, the temperature should be low to prevent Cr atoms from diffusing to nucleation sites for Cr-nitrides (surface, grain boundaries, dislocations). Accordingly, a metastable equilibrium between nitrogen in the gas phase and nitrogen in the solid state can be achieved, so-called expanded austenite (or S-phase), where nitrogen is interstitially dissolved in the strongly oversaturated f.c.c. lattice. The nitrogen occupancy of the interstitial f.c.c. lattice can be as high as $y_N=0.61$, which is higher than the nitrogen contents hitherto reported to be achievable for iron nitrides under gaseous nitriding conditions. In micrographs expanded austenite is typically recognized as a featureless surface layer (cf. Fig. 7) with a high hardness.

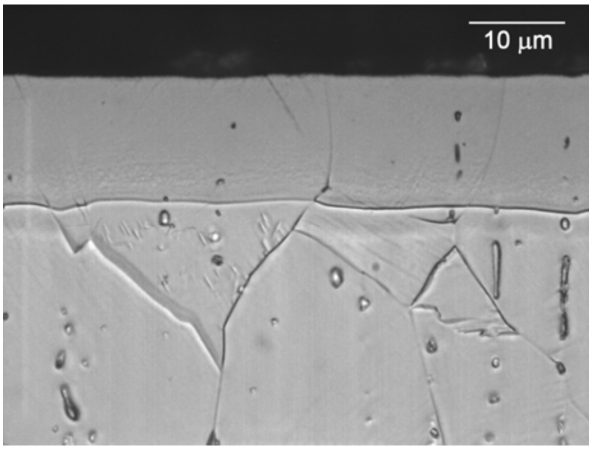

Figure 7: Layer of expanded austenite obtained by nitriding stainless steel (AISI 316) at 718 K for 22 hours in 60 % NH_3/40 % H_2 [12].

The nitrogen contents dissolvable in (stress-free) expanded austenite are colossal and can be controlled by adjusting the nitrogen activity in the gas phase (Fig. 8a). Experimentally the data in Fig. 8a were obtained thermogravimetrically by nitriding of thin coupons (5-7.5 μm) in pure NH_3 and thereafter equilibrating the coupons in a NH_3/H_2 mixture with known nitrogen activity a_N; the lowest a_N was obtained in pure H_2.

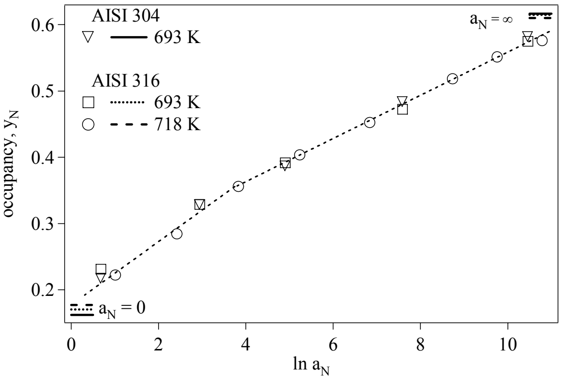

Figure 8a: Nitrogen occupancy, y_N, of the interstitial f.c.c. lattice of expanded austenite as a function of the imposed nitrogen activity, a_N, in the NH_3/H_2 gas mixture.

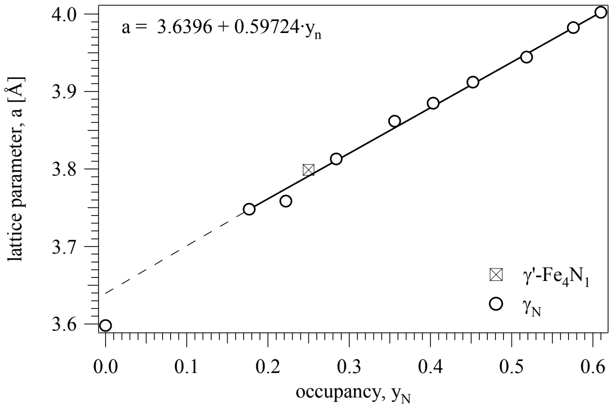

Figure 8b: Lattice parameter of expanded austenite versus occupancy of the interstitial f.c.c. lattice.

The lattice expansion associated with interstitial dissolution of nitrogen in the austenite lattice (Fig. 8b) implies the occurrence of large stresses and steep stress gradients over a growing layer of expanded austenite. Compressive stresses of the order of several GPa's and stress gradients of the order of a 10^{15} Pa.m^{-1} are no exception [12]. Consequently, the assessment of nitrogen diffusion coefficients from layer-growth kinetics experiments can only lead to stress-affected diffusion coefficients without general validity. Another complication in the determination of diffusion coefficients of nitrogen from the evolution of the nitrogen concentration profile is the occurrence trapped nitrogen in expanded austenite. As shown in Fig. 8a the nitrogen occupancy of the interstitial lattice obtained for a_N=0 leaves about a nitrogen content conforming to y_N=0.17 in the sample, which corresponds to the chromium content. This strongly suggests that a nitrogen content corresponding to Cr:N=1:1 is strongly bound in the sample. To be able to distinguish between the diffusion of strongly bound and less strongly bound nitrogen atoms the following method was applied for the determination of the concentration dependent diffusion coefficient of nitrogen in expanded austenite.

As mentioned above thin coupons were nitrided in a thermobalance for continuous monitoring of the change of the sample weight and thus the nitrogen content. After equilibrating in pure NH_3 the samples were equilibrated at a slightly lower a_N, by adjusting the composition of the NH_3/H_2 gas mixture. Consequently, the sample weight decreases by denitriding until a new stationary state (metastable equilibrium) between gas and sample is attained. The kinetics of weight decrease were described mathematically with the equation for desorption from a plate, taking the diffusivity as a constant fitting parameter. By repeating this procedure for a range of a_N values, a range of effective values for the diffusion coefficients in the composition ranges for the actual denitriding steps is obtained. The influence of stress (gradients) on these values is considered small.

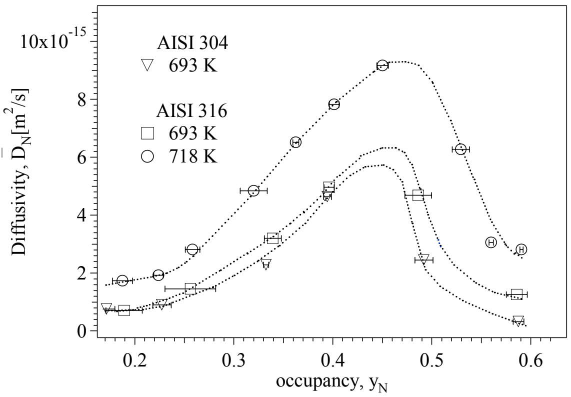

Figure 9: Effective diffusion coefficients of nitrogen in expanded austenite (both AISI 304 and 316) versus nitrogen occupancy of the interstitial f.c.c. lattice.

The effective diffusivities thus obtained are depicted in Fig. 9. Evidently, the diffusion coefficient of nitrogen in expanded austenite is concentration dependent and has a maximum value for nitrogen occupancies of about y_N=0.45. Qualitatively, these results can be reasoned as follows. The expansion of the austenite lattice by dissolution of nitrogen is likely to facilitate the transfer of a nitrogen atom from an octahedral interstitial site of the f.c.c. lattice to a tetrahedral site, which can be considered the activated state for interstitial diffusion in f.c.c. lattices. Thus, the activation energy for diffusion of nitrogen is reduced. With increasing nitrogen content the occupancy of the interstitial lattice increases, which reduces the probability that a nitrogen atom in the activated state can jump to an unoccupied octahedral site. Consequently, the diffusion coefficient is reduced. Evidently, for nitrogen contents exceeding y_N=0.45 the latter reduced probability for diffusion outweighs the reduced activation energy.

6.1 Calculation of nitrogen profiles in nitrided austenite

On the basis of the composition-dependent diffusivity of nitrogen in expanded austenite it is possible to estimate the evolution of the nitrogen concentration profile as a function of the nitriding parameters temperature, gas composition and time. In the modeling of nitrogen diffusion in expanded austenite it is assumed that nitrogen up to y_N=0.17 is immobile and does not contribute to long range diffusion (cf. Fig. 8a). A similar assumption was recently done for modeling the diffusion of nitrogen in ferritic Fe-Cr alloys [13,14], where distinction was made between so-called mobile and immobile excess nitrogen atoms [14]: all nitrogen atoms, including excess nitrogen, dissolved in the expanded ferrite lattice was considered mobile and contributed (solely) to the development of the nitrogen concentration profile, whilst (excess) nitrogen atoms residing in CrN and at the interface between CrN platelets and ferrite were considered immobile. In the present case of nitrogen in expanded austenite all nitrogen atoms are in solid solution, but evidently the chemical environments are different.

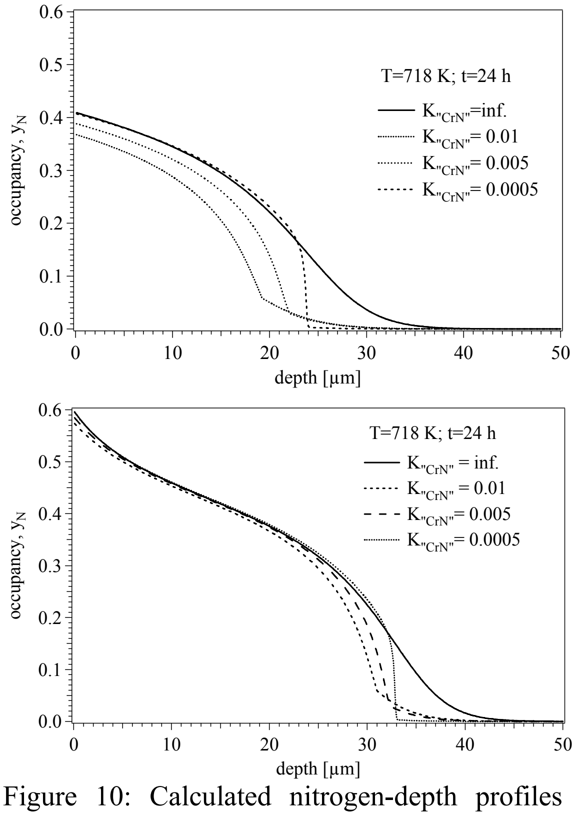

Figure 10: Calculated nitrogen-depth profiles in stainless steel AISI 316 after nitriding at 718 K for 24 hours at a nitriding potential K_N=1.39 bar$^{-1/2}$ (above) and 595 bar$^{-1/2}$ (below). Various values of the solubility product $K_{\text{"CrN"}}$ were chosen.

The first results of our calculations, with a model similar to that in Ref. [13,14], but with a concentration dependent nitrogen diffusion coefficient (Fig. 9) and immobile nitrogen considered as nitrogen trapped by Cr atoms (not as nitrides!) in the expanded austenite lattice are given in Fig. 10. The solubility product, $K_{\text{"CrN"}}=y_{Cr}.y_N$, of chromium and nitrogen in the austenitic lattice, i.e. the combination of chromium and nitrogen contents below which no trapping occurs, is not known for the present temperature. Therefore various values were considered in our calculations. The solubility product, $K_{\text{"CrN"}}$ effectively governs the trapping behavior of nitrogen. For a $K_{\text{"CrN"}}$ value of nil, infinitely strong trapping of nitrogen at the trap sites occurs. Conversely, an infinitely high value of $K_{\text{"CrN"}}$ implies that trapping does not occur at all.

The calculated profiles show a striking qualitative resemblance with those presented in the literature and are in qualitative agreement with the observation of a thin diffusion zone in front of the expanded austenite layer (cf. Fig.7). Further refinement of the model appears necessary, because the effects of compositionally-induced stresses as well as the effect of the kinetics of the surface reaction(s) were omitted in the present modeling. Furthermore, the diffusivity of nitrogen for compositions conforming to y_N<0.17 is not known and was estimated by an extrapolation of diffusivities determined at higher nitrogen contents (Fig. 9).

6.2 Residual stress in expanded austenite layers

Stress-depth distributions over expanded austenite layers were determined with X-ray diffraction analysis and successive removal of very thin sub-layers. It was recognized that the simultaneous occurrence of a stress-depth profile and a composition profile demands unraveling of the influences of stress (lattice strain) and composition on the lattice spacing and can lead to the occurrence of ghost stresses after data evaluation [15]. For the present case of residual stress in expanded austenite the ghost stresses can easily exceed 1 GPa [16]. Depth profiles of the strain free lattice spacing in expanded austenite (which is directly proportional to the interstitial atom content) and residual stress are given in Fig. 11 for two expanded austenite layers obtained by nitriding or carburizing. Compressive stresses were obtained in all investigated samples (see Ref. [12]). Typically, the compressive stresses in γ_N and γ_C layers are of the order of several GPa's, up to 7-8 GPa compression in γ_N layers. The very high compressive stresses are caused by the compositionally induced expansion of the austenite lattice (cf. Fig. 8b). However the residual stress values expected from pure elastic accommodation of the expanded austenite lattice, as reflected by the strain-free lattice parameter (Fig. 11b), are twice as high. This discrepancy can be explained from an anticipated change of the elastic constants with interstitial atom content (which was not taken into account) and the occurrence of plastic deformation in the layers during growth. Evidently, the part of the lattice expansion that is accommodated elastically in the γ_N layer shown in Fig. 11 changes close to the surface, because the (elastic) stress value decreases towards the surface, whilst the lattice expansion due to the nitrogen content has its maximum value at the surface. This is explained from pushing individual grains out of the surface and possibly local crack formation.

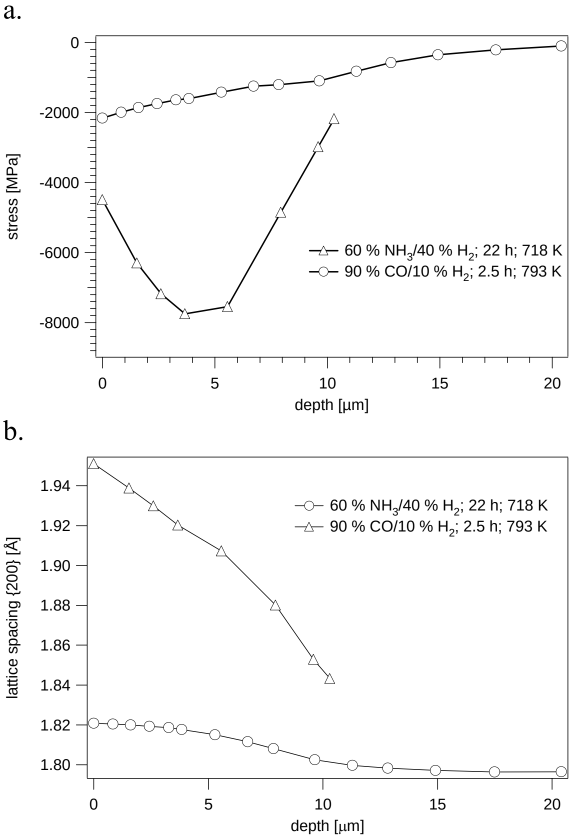

Figure 11: Residual stress (a.) and strain-free lattice spacing (b.) profiles for γ_N and γ_C layers obtained under the nitriding and carburizing conditions as given in the legend. Stress and lattice spacing were obtained by X-ray diffraction.

7 Interaction of stress and kinetics of microstructure evolution

Qualitatively, the occurrence of compositionally induced stresses in the growing layers has the following implications for the layer growth kinetics:

- a situation of local equilibrium at the surface is no longer given by absorption isotherms as determined for homogeneous stress free samples (cf. [5,6] and Fig. 8a), but should also take elastic strain energy into account [17]. For the present case of compressive stresses at the surface, this leads to lower nitrogen contents than reflected by the current (stress free) thermodynamic data.
- a compressive stress has a pressure effect on the diffusion coefficient [18]. In principle, this implies that the effective diffusivities/ mobilities obtained as fit parameters in Section 4 (Fig. 4) are affected by this pressure effect and have no general validity.
- a stress gradient, such that the maximum compressive stress occurs at the surface, provides an extra driving force for nitrogen atoms to diffuse to larger depth. This also implies that effective diffusivities/ mobilities obtained from fitting layer thickness data are affected by the compositionally induced stresses.

For the present cases of nitrogen and carbon diffusion in Fe-based interstitial systems the effects of compositionally induced stress appear to be of considerable importance, most specifically for the case of expanded austenite where exorbitantly high compressive stresses of 7-8 GPa were found (Fig. 11 and Ref. [12]). For the present interstitial systems the strategy to be followed for quantifying the effect of stress on diffusion and vice versa is combining experiments on thin foils, for determining the stress unaffected diffusion coefficients as a function of composition. Thereafter, the kinetics of the incorporation of nitrogen (or carbon) into bulk samples, as studied by weight gain (in situ), layer growth kinetics and evolution of the composition profile can be compared with the predictions on the basis of the stress unaffected thermodynamics and diffusion parameters as well as with a model that incorporates the stress and the kinetics of surface reaction(s).

8 Conclusion

The kinetics of gas-metal interactions in Fe-based interstitial systems is not exclusively controlled by solid state diffusion of the interstitial elements as might be expected at first consideration. It was demonstrated for the case of nitriding of iron that the kinetics of surface reactions can have a strong influence too. In the case of nitrocarburizing a competition between nitriding and carburizing is initially (kinetically) won by carburizing, but on prolonged time the nitriding reaction dominates thermodynamically. The case of the growth of expanded austenite in austenitic stainless steel was addressed. In all evaluations up to now the role of compositionally-induced residual stresses on the description of the thermodynamics and the diffusion coefficients was omitted. Nevertheless, compositionally induced stress values of several GPa's can result for interstitial systems, as shown for nitrogen and carbon in expanded austenite Future research should focus on the role of stress on diffusion.

References

1. Grabke, H.J.: *Mater. Sci. Forum*, 154, pp.69-85, 1994.
2. Friehling, P.B., F.W. Poulsen, M.A.J. Somers: *Z. Metallkde.*, 92, pp. 589-595, 2001.
3. Rozendaal, H.C.F., E.J. Mittemeijer, P.F Colijn, P.J van der Schaaf: *Metall. Trans. A,* 14, pp. 395-399, 1983.
4. Somers, M.A.J., P.B. Friehling: *Härterei-Tech. Mitt,.*57, pp.415-420, 2002.
5. Somers, M.A.J., E.J. Mittemeijer: *Metall. Mater. Trans. A*, 26, pp. 57-74, 1995.
6. Somers, M.A.J.: *Heat Treat. Met.,* 27, pp.92-102, 2000.
7. Mittemeijer, E.J., M.A.J. Somers: *Surf. Eng.,* 13, pp. 483-497, 1997.
8. Friehling, P.B.: Ph.D. Thesis, Technical University of Denmark, 2000.
9. Somers M.A.J.: *J. Phys. IV France,* 120, pp.21-33, 2004.
10. Du, H., M.A.J. Somers, J. Ågren: *Metall. Mater. Trans. A*, 31, pp.195-211, 2000.
11. Du , H., J. Ågren: *Metall. Mater.Trans. A*, 27, pp.1073-1080, 1996.
12. Christiansen, T., M.A.J. Somers- *in preparation*, see also Christiansen, T.: Ph.D. thesis Technical University of Denmark, 2004.
13. Sun, Y., T. Bell: Mater. Sci Eng. A, 224, pp. 33-47, 1997.
14. Schacherl, R., P.C.J. Graat, E.J. Mittemeijer: *Metall. Mater. Trans.*, 35A, pp. 3387-3398, 2004.
15. Somers, M.A.J., E.J. Mittemeijer: *Metall. Trans.*, 21A, pp. 189-204, 1990.
16. Christiansen, T., M.A.J. Somers: *Mater. Sci. Forum,* 443-444, pp.91-94, 2004.
17. Li, J.C.M.: *Metall. Trans. A*, 9, pp. 1353-1380, 1978.
18. Beke, D.L., I.A. Szabó, Z. Erdélyi, G. Opposits: *Mater. Sci. Eng.* A, 387–389, pp. 4–10, 2004.

Proceedings of The 1st International Conference on **D**iffusion in **S**olids and **L**iquids
DSL-2005, July 6-8, 2005, University of Aveiro, Aveiro, Portugal

MODELING OF MULTIPHASE FLOW WITH PHASE CHANGE IN POROUS MEDIA – A CASE STUDY

Jana ŠELIH[1,2], Antonio C.M. SOUSA[3,4,*]

[1]National Building and Civil Engineering Institute, Ljubljana, Slovenia
[2]Faculty of Civil and Geodetic Eng, University of Ljubljana, Slovenia
[3]Department of Mechanical Engineering, University of New Brunswick, Canada
[4]Department of Mechanical Engineering, University of Aveiro, Portugal

[*]Corresponding author. Fax: +1 506 4535025; Email: asousa@unb.ca

Abstract

A general numerical model developed to simulate the time-dependent changes of moisture content, temperature and pore pressures is proposed for a porous material. The model is based on a coupled heat and mass transfer mathematical formulation. The model's validation is conducted using experimental data for concrete. The gravimetric technique is used to obtain the experimental data on moisture content in cylinders made up of fully saturated concrete exposed to drying. Further to demonstrate the applicability of the model, it is also studied the moisture migration, temperature development and thermal stresses in a concrete element exposed to fire. The obtained results indicate that during fire, several degradation phenomena are taking place at the same time. Thermal stresses developed by the temperature differential, especially when temperature-dependent material properties are taken into the account, along with the increase of pore pressures, may contribute to structural failure.

Keywords: Concrete; Drying; Fire; Numerical modeling; Gravimetric technique

1 Introduction

Concrete is selected as the porous material of reference for the present study. Concrete has a wide range of applications, and concrete structures may be exposed to a variety of environmental conditions in their service life, which can influence the moisture content distribution in the material. Moisture affects the mechanical properties of concrete and its durability; in drying, one of the most common causes for moisture migration in concrete structures, the pore water is forced to move towards the surface of drying, which yields space and time dependent moisture content. Fire exposure is as an extreme case of drying, which has a strong effect not only upon the moisture but also upon temperature, pore pressure and thermal stress distribution in the concrete element.

Several mechanical properties, such as the modulus of elasticity, and the tensile and compressive strength, which are determinant to structural safety, are influenced by the moisture content in concrete due to the interaction of the solid matrix and the water in the pores [1]. Another phenomenon closely related to moisture content changes is drying shrinkage, which is associated with the removal of more tightly bound pore water, and tends to occur after a certain period of drying time, when moisture content decreases below the threshold level [2, 3]; moisture is also critical in determining corrosion of reinforced concrete [4]. The onset and the rate of several other deterioration processes associated with freezing/thawing and high temperature exposure [5] are also associated with moisture content levels in concrete.

Accurate determination of the saturation levels in concrete is a prime requirement for the improved assessment of concrete vulnerability to deterioration processes. This information can establish adequate preventative strategies in the design stage and to enable development of appropriate maintenance and repair actions which would take place during the service life of a structure. Therefore, a simulation model capable of predicting moisture content changes in concrete during various exposure types would be an invaluable asset for material behavior assessment.

Two distinct periods can be observed during drying of a saturated porous medium [6]. The majority of water is transported out of the material during the first period at a constant rate. During the second period, saturation levels are much lower, and drying rate is decreasing with time. The complete information on the drying process can be obtained only when spatial moisture content distribution and its change with time are known.

This paper presents a numerical model for simulation of mass transfer in initially saturated concrete during drying and validation of this model by comparing its predictions to experimentally obtained values. Furthermore, the model use is extended to the case of initially saturated concrete subjected to fire.

Concrete consists of two porous components, the aggregate and the cement matrix, in which the aggregates are embedded. Both components and their interaction influence significantly the structure, physical characteristics and behavior of this composite material [7].

A wide distribution of pore size is therefore encountered in concrete. A large proportion of mesopores in hydrated cement paste with pore size ranging from 10 to 250 Å results in a specific area of the order of magnitude of 10 m^2/g [8], and a permeability with typical values ranging from 10^{-16} to 10^{-15} m^2 for normal weight concrete [9]. Due to the large specific internal area, a large proportion of liquid water is in the adsorbed state. A physically realistic mathematical formulation for mass and heat transfer in concrete should therefore be able to describe free water flow, adsorbed (bound) water movement, and water vapor and air diffusion. In addition, effects of water phase change should be accounted for. Perre and Degiovanni [10] extended Whitaker's formulation [11] for drying by including bound water movement. This formulation meets the requirements specified above, and the numerical model presented in this study is based on a similar concept [12, 13].

2 Mathematical formulation of heat and mass flow in porous media

The fundamentals of the mathematical formulation developed to describe heat and mass transfer in concrete are described in [12], therefore only the distinguishing features are given here. The volumetric fractions (ε) for the liquid (*l*), bound (*b*), gaseous (*g*) and solid (*s*) phase are linked by the volumetric constraint:

$$\varepsilon_l + \varepsilon_g + \varepsilon_b + \varepsilon_s = 1 \tag{1}$$

The solid phase is assumed constant in the mass transfer calculation.

Conservation of mass for the liquid and bound water and water vapor requires

$$\begin{aligned}&\frac{\partial}{\partial t}(\rho_l \quad (\varepsilon_l + \varepsilon_b) + \varepsilon_g \overline{\rho}_1^g) + \\ &+ \nabla(\rho_b \overline{\mathbf{v}}_\mathbf{b} + \rho_l \overline{\mathbf{v}}_\mathbf{l} + \overline{\rho}_1^g \overline{\mathbf{v}}_\mathbf{1}) = 0\end{aligned} \tag{2}$$

where $\overline{\mathbf{v}}_\mathbf{l}$ indicates the averaged velocity vector, and ρ_l the density of the liquid phase. $\overline{\rho}_1{}^g \overline{\mathbf{v}}_1$ is the mass flux of the water vapor, and $\rho_b \overline{\mathbf{v}}_\mathbf{b}$ the mass flux of the bound phase. $\overline{\rho}_1{}^g$ is the intrinsic average of the partial water vapor density over the gaseous phase.

The continuity equation for water vapor is written as

$$\frac{\partial}{\partial t}(\overline{\rho}_1^g \varepsilon_g) + \nabla(\overline{\rho}_1^g \overline{\mathbf{v}}_\mathbf{1}) = \overline{m}_l + \overline{m}_b \tag{3}$$

where $\overline{m}_l$ is the evaporation rate of the liquid, and $\overline{m}_b$ the evaporation rate of the bound phase. Darcy's law is used to describe the velocities of both liquid and gas phase, and with low relative values of the water vapor partial pressure as compared to those for the total gaseous pressure, the assumption that the mixture behaves as an ideal gas is adopted.

The thermal energy equation that includes the term describing the phase change and convective heat transfer is formulated as

$$\begin{aligned}&(\rho c_p)\frac{\partial \overline{T}}{\partial t} + ((c_p)_l \rho_l \overline{\mathbf{v}}_\mathbf{l} + (c_p)_l \overline{\rho}_b \overline{\mathbf{v}}_b + \\ &\quad + \rho_g^g c_p^g \overline{\mathbf{v}}_\mathbf{g}) \cdot \nabla \overline{T} + \Delta h_{vap}(\overline{m}_l + \overline{m}_b) + \\ &\quad + h_s \overline{m}_b - \overline{\rho}_b \overline{\mathbf{v}}_b \cdot \nabla h_s = \nabla(\lambda_{eff} \nabla \overline{T})\end{aligned} \tag{4}$$

where Δh_{vap} is the specific heat of evaporation, h_S the differential heat of sorption, λ_{eff} the effective thermal conductivity, and ρc_p represents the averaged product of the density by the specific heat.

The exchange coefficients of heat and mass transfer, α and β, are taken as constant, and the total heat flux on the drying surface can be written as

$$((\lambda_{eff}\nabla\overline{T}) + \Delta h_{vap}(\rho_l\overline{\mathbf{v}}_{\mathbf{l}} + \overline{\rho}_b\overline{\mathbf{v}}_b) - \overline{\rho}_b\overline{\mathbf{v}}_b \cdot h_s)\cdot\mathbf{n}_{\mathbf{boun}} = \\ = \alpha(\overline{T} - T_\infty) \tag{5}$$

where $\mathbf{n}_{\mathbf{boun}}$ is the unit vector normal to the boundary surface, and T_∞ the ambient temperature. A similar convective type of boundary condition is used for the mass flux, namely:

$$(\rho_l\overline{\mathbf{v}}_{\mathbf{l}} + \overline{\rho}_b\overline{\mathbf{v}}_b + \overline{\rho}_1^g\overline{\mathbf{v}}_1)\cdot\mathbf{n}_{\mathbf{boun}} = \\ = \beta(\overline{\rho}_1^g - \rho_{1\infty}) \tag{6}$$

$\rho_{1\infty}$ is the partial water vapor density of the ambient.

The total gaseous pressure at the drying surface is taken as equal to the atmospheric pressure. In the beginning of the process, temperature and gas phase pressure are assumed to be uniform throughout the specimen, and initial saturation distribution satisfies the condition of hydrostatic equilibrium.

2.1 Discretization of governing equations

The control volume formulation with 2nd order and 1st order approximations for space and time, respectively, is employed to discretize the governing differential equations; a fully implicit scheme is employed for the integration in time [12]. The coefficients appearing in the governing equations are strongly dependent upon the variables to be computed, therefore, an iterative procedure is required within each time step. The set of linearized equations is solved in each sweep of the iterative procedure by using the alternating direction block iterative method, and the tridiagonal matrix algorithm is used as a segregated solver for each equation [12]. Results of the code are generated in terms of spatial distribution of temperature, saturation and total pressures of the gaseous phase at a pre-specified time.

3 Case study 1: drying

3.1 Experimental procedure

Most methods for measuring moisture content in porous media are only applicable to low levels of moisture; the gravimetric method is one of the few that can be employed at high moisture content levels, and was used in the present experimental study.

Measurements of moisture content were performed on normal weight concrete cylinders with length varying from 100 to 200 mm. Water to cement ratio (w/c) of concrete employed was 0.4 and 0.6, respectively. Volumetric proportion of the coarse aggregate is 0.34, and volumetric fractions of the fine aggregate are 0.31 and 0.36 for w/c of 0.4 and 0.6, respectively. Natural crushed aggregate with the maximum size of 12.5 mm is used as the coarse aggregate, and natural sand as the fine aggregate. Normal Portland cement DSA A-5 type 5 was used.

Concrete was cast into plastic moulds with diameter of 100 mm and lengths 100, 150 and 200 mm. The cylinders were then covered with plastic sheet for 12 hours to prevent the evaporation of water from unhardened concrete. After 12 hours, they were placed in the moist curing room with relative humidity no less than 95%. Moist curing time varied from zero to 28 days, and when the predetermined moist curing period has elapsed, the cylinders were exposed to drying on the top surface at constant temperature of 22±1°C and relative humidity of 50±5%. The “zero days” refers to moist cured concrete, which was exposed to drying immediately after removing the plastic sheet. Cylinders were placed vertically with the drying surface on the top. During drying, as well as during moist curing, the moulds were not removed. The side and bottom surfaces of the cylinder can therefore be considered sealed against moisture flow. This configuration forces the moisture flow to be unidirectional along the longitudinal axis of the cylinder. Cylinders were dried out for 0, 1, 3, 7, 28 and 90 days.

Local contents of moisture were measured by splitting the cylinder into discs with thickness of 25 mm. After splitting the cylinder, each disc was weighed, dried out at 95°C in the oven for 3 days, and re-weighed. Subsequent weighing, after 3 days of oven drying, showed no more than 0.1% of change of dry weight. The difference between the wet and the dry weight was taken as the amount of moisture in a disc, and was considered to represent the local moisture content of the cylinder. Moisture content distribution along the longitudinal axis of the cylinder, x, can be established for each predetermined drying time. As depicted in Figure 1, the x-axis is arbitrarily oriented from the insulated end (x=0) towards the drying surface (x=L).

Moisture content is expressed in mass of water per unit volume of concrete, w:

$$w = (W_{wet} - W_{dry}) / V_{wet} \tag{7}$$

where W_{wet} and W_{dry} are the wet and dry weight, respectively, and V_{wet} is the wet volume.

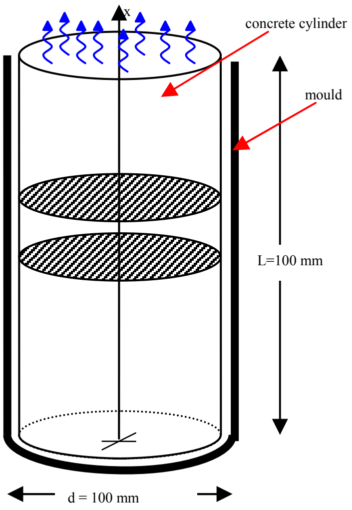

Figure 1: Schematic presentation of the cylinder tested.

3.2 Experimental and numerical simulation results

3.2.1 Material parameters and constitutive relations

The dependence of capillary pressure upon saturation was formulated based on the Leverett approach, as described in [14]. Relative permeabilities of the gas and liquid phase are taken from [14], with a modification in the high saturation domain, suitable for concrete, as suggested in [15], which, for this region, proposed a small non-zero value of relative gas permeability.

The relationship between partial water vapor pressure and saturation, the so-called sorption isotherm, is taken as proposed in [11]. The effective diffusion coefficient of water vapor in the porous medium is assumed to be proportional to the coefficient of pure molecular diffusion, D_{free}, and to the relative gas permeability. Therefore, it can be expressed as

$$D_{eff}^{1} = f_{att}\, k_g\, D_{free} \tag{8}$$

The attenuation factor, f_{att}, accounts for the resistance to the diffusion due to the pore structure, and is taken as 10^{-5} in the present work..

The bound water diffusion coefficient is a function of the activation energy of bound water [16] and can be expressed as a function of saturation and temperature.

The functions for the sorption isotherm and for the bound water diffusion coefficient are selected in such a way that they depend on one single parameter, irreducible saturation. The two constitutive relations do not contribute significantly to moisture movement in the initial stage of drying, which is the primary focus in this paper; therefore, it is justifiable to describe them with functions depending only on one parameter.

Measured values of concrete intrinsic permeability differ depending on the selection of the permeating fluid (gas or liquid) in average by a factor of 10 due to gas slippage [17]. Values selected in present work for normal weight concrete are based on measurements of Dhir *at al* [19], who used water as a permeating fluid. They are collected in Table 1. It can be seen that permeability decreases with increasing moist curing time and decreasing water to cement ratio.

Values of porosity employed in the numerical simulation of drying are determined as weighed averages of concrete constituents' porosities. Porosity of cement paste depends strongly upon moist curing time and water to cement ratio, and is taken as proposed in [18]. Porosity of normal weight aggregate is taken as 3% [9].

Irreducible saturation is the level of saturation above which free liquid exists, and therefore presents a boundary between free liquid flow and predominating water vapor / bound water flow. It depends upon the proportion of large capillary pores in which free liquid water can be present, and therefore increases with increasing moist curing time and decreasing water to cement ratio. Values for irreducible saturation employed in this study are estimated from current experimental data.

The mass transfer coefficient, β, is used to describe the rate of moisture exchange between the porous medium and the environment adjacent to the drying surface. It depends upon pore structure and ambient conditions, such as ambient temperature, relative humidity and wind velocity [19]. Mass transfer coefficient is estimated with the help of boundary conditions (5) and (6).

Initial water contents are obtained from experimental data. Selected values of material parameters defining porous structure, i.e. of permeability, porosity, irreducible moisture content, initial moisture content are also given in Table 1.

Table 1: Values of specific permeability, porosity, mass transfer coefficient, irreducible saturation and initial saturation employed in the numerical analysis.

w/c	moist curing time	K	ε_s	β	W_o	W_{irr}
	(days)	(10^{-17} m^2)	(-)	(10^{-5} m/s)	(kg/m^3)	
0.4	0	3.2	0.79	84	175	143
	1	1.6	0.82	20	175	143
	3	0.4	0.82	20	175	143
	7	0.24	0.85	9	145	135
	28	0.11	0.85	4	145	135
0.6	0	22.0	0.79	102	180	135
	1	11.0	0.80	80	180	135
	3	3.0	0.81	72	150	130
	7	1.4	0.83	26	150	130
	28	1.0	0.85	26	150	130

3.2.2 Results and discussion

The numerical computations were performed for all types of concrete with respect to water to cement ratio and moist curing time for cylinder length of 0.10 m. Typical results for 1 day moist cured concrete with w/c of 0.4 are presented in Figure 2. Good agreement between the experimental and numerical data is observed for all cases analyzed. In general, it can be observed that in the beginning of drying, moisture content distribution keeps its initial shape with time, while the overall values decrease. Rapid changes of moisture content and therefore large drying rates are observed in the first days of drying. Such behavior indicates there is free liquid water present in the pores. Capillary flow is the predominant mechanism of mass transport during this period. The shape of moisture content profile starts changing at approximately 7 days, when increased moisture content gradients appear in the vicinity of the drying surface. The corresponding drying rates significantly decrease, indicating that capillary flow of free liquid water is no longer present in the porous medium, and water moves due to the concentration gradient.

Temperature gradients are negligibly small throughout the drying process. A small decrease in temperature is observed throughout the cylinder as a result of the energy required for the evaporation of the liquid water in the initial stage of drying. When all liquid water is removed from the pores, the temperatures start increasing towards the ambient value.

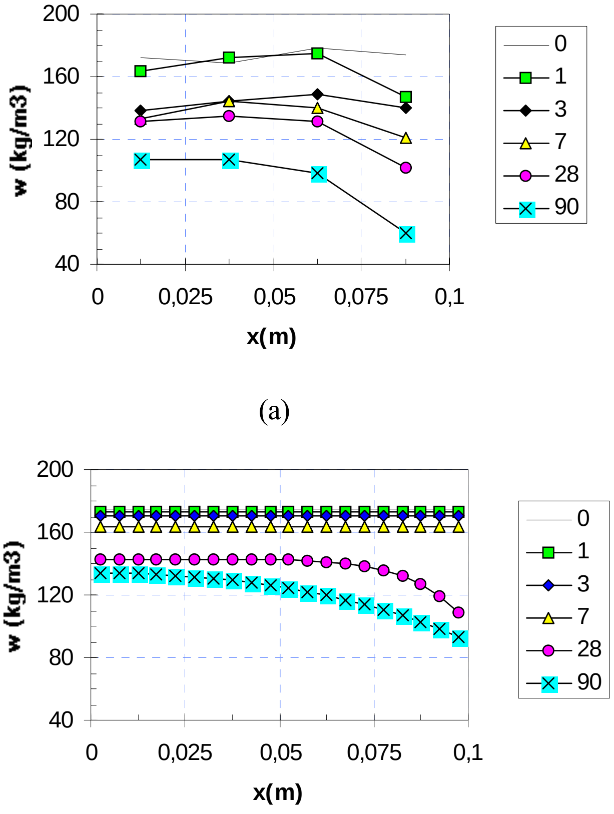

(a)

(b)

Figure 2: (a) experimental and (b) numerical moisture content distribution in the cylinder with length 0.10 m with 1 day moist cured concrete with water to cement ratio (w/c) of 0.4 for 0, 1, 3, 7, 28 and 90 days of drying.

4 Case study 2: fire exposure

Fire is one of the most devastating causes for the structural failure, as the occurring elevated temperatures may impose high thermal loads to the structural elements. Concrete structures exposed to fire deserve special attention as concrete is weak in tension, and the stresses which develop as a result of the non-uniform temperature distribution may cause serious material failure [20]. There is also experimental evidence of explosive spalling of concrete subjected to fire ([21, 22]) confirming the danger of fire.

The numerical model described in the previous section was extended to describe the behavior of concrete exposed to elevated temperatures due to fire. The existing numerical tool [23] was enhanced by a calculation procedure for the thermal stresses within a concrete wall, as proposed by Lenczner [24].

Combustion in a closed compartment, as it occurs during a fire in a building, involves highly complex mechanisms. As a first approximation, the heat transfer from the fire to the adjacent structure can be expressed by a time-dependent fire temperature. Several time-dependent relations to describe this temperature have been proposed in the literature (e.g. [25]). In the present work, numerical predictions are obtained for a fire temperature model obtained by using an overall energy balance equation for the fire compartment [26], the so-called *short duration high intensity fire* (SDHI) temperature model. In this model the temperature is described by a curve that exhibits an early peak followed by a decaying period.

Elevated temperatures occurring in a concrete structure during fire affect moisture migration within the porous material. Heat supplied from the fire is being partly absorbed by the evaporation of the liquid water, and when the evaporation rate is higher than that of the vapor migration, high pore pressures may develop.

4.1 Calculation of thermal stresses

To calculate the thermal stresses in the concrete wall, the cross-section is divided into n layers as shown in Figure 3. It is assumed that the vertical movement of each layer is prevented.

The layer i has a thickness Δx_i, and its stress is determined as

$$\sigma_{1,i} = -\alpha_{T,i}\, E_i\, (T_i - T_i^0) \qquad (9)$$

where $\alpha_{T,i}$ is the thermal expansion coefficient, E_i modulus of elasticity, and T_i and T_i^0 current and initial temperature of layer i, respectively.

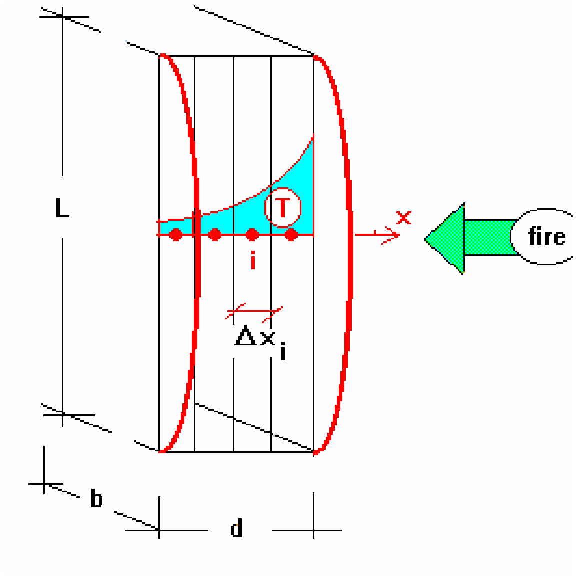

Figure 3: Schematic depiction of the wall exposed to fire.

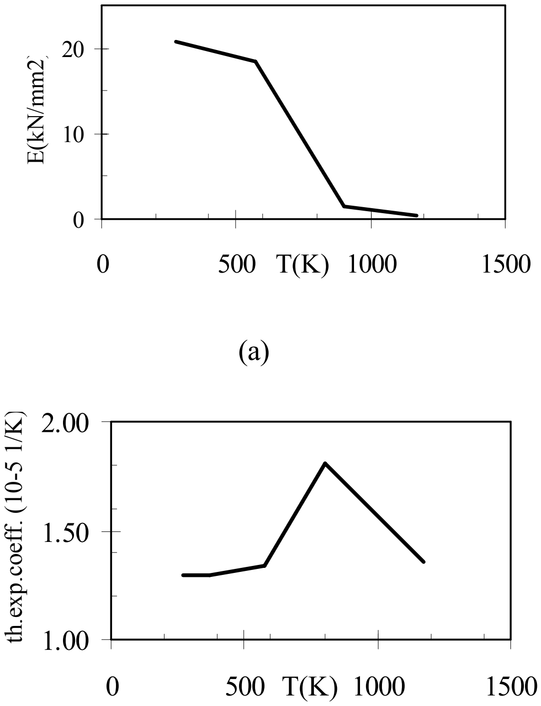

(a)

(b)

Figure 4: Dependence of modulus of elasticity (a) and thermal expansion coefficient (b) upon temperature [27].

Vertical movement is prevented, therefore the force acting on the entire cross-section is

$$F = -\Sigma\, \sigma_i A'_i = \sigma_2 A' \tag{10}$$

where A'_i is the reduced area of the layer i, $A'_i = b\,\Delta x_i \xi_i$, and A' the total area of the cross-section, $A' = \Sigma A'_i$. Externally applied stress $\sigma_2 = F/A'$ is acting on each layer, and ξ_i represents the reduction factor that accounts for the changes of modulus of elasticity due to the temperature changes,

$$\xi_i = E(T_i)/E_{ref}\,. \tag{11}$$

E_{ref} denotes the reference modulus of elasticity at 20°C. The moment of inertia of the entire reduced cross-section is

$$I = \sum_i (A'_i y_i^2 + \Delta x_i^{\;2} \xi_i b/12) \tag{12}$$

where y_i is the distance from the layer i to the centre of gravity,

$$y_i = \left| x_{CG} - x_i \right| \;. \tag{13}$$

The distance to the centre of gravity, x_{CG}, is determined with

$$x_{CG} = (\Sigma A'_i x_i)/A' \tag{14}$$

where x_i is the distance to the layer i.

The additional bending moment, *M*, defined with

$$M = \sum_i (\sigma_{1,i} + \sigma_2)\, y_i A'_i \tag{15}$$

yields the stress condition

$$\sigma_{3,i} = \frac{M y_i}{I} \tag{16}$$

The total stress due to the non-uniform temperature distribution in the layer i can be defined as

$$\sigma_i = \sigma_{1,i} + \sigma_2 + \sigma_{3,i} \tag{17}$$

4.2 Results and discussion

To demonstrate the capability of the numerical model, the analysis was performed for a 0.2 m thick wall made of concrete exposed to SDHI fire as depicted in Figure 3. The initial ambient temperature and relative humidity are taken as 20°C and 30%, respectively, on both sides of the wall. Ambient conditions adjacent to the wall not exposed to fire are assumed constant, and at the fire-exposed side, the ambient temperature increases according to the selected fire exposure curve.

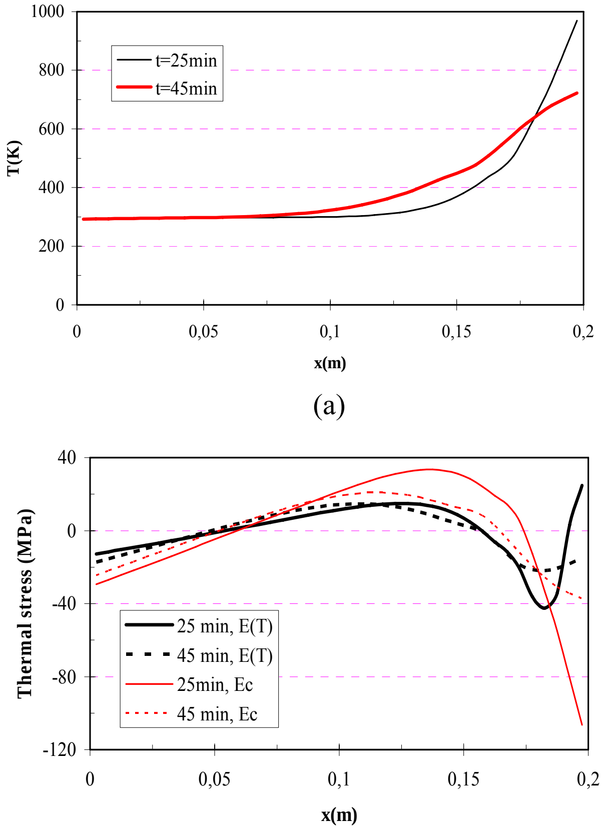

(a)

(b)

Figure 5: (a) temperature and (b) thermal stress distribution in the cross-section of the wall after 25 and 45 minutes of SDHI fire exposure, respectively; stresses are calculated for constant (Ec) and temperature-dependent (E(T)) modulus of elasticity.

The mass transfer coefficient is taken as 0.01 m/s, and the heat transfer coefficient and emissivity on both sides of the wall have the value of 20 W/(mK) and 0.5, respectively. The initial saturation and temperature in the wall are 90% and 25°C. The details on the selection of the constitutive relations, mass transfer coefficient, permeability, porosity and irreducible saturation levels are given in [23]. The dependence of the modulus of elasticity, *E(T),* and thermal expansion coefficient, α_T , upon temperature, is shown in Figure 4 (a) and (b) as reported in [27].

Figure 5 presents the temperature and corresponding thermal stress distribution in the wall exposed to SDHI fire for exposure times of 25 and 45 minutes. The analysis considers both the constant and the temperature-dependent modulus of elasticity. The SDHI fire temperature [26] T_{fire}, Figure 6 (a), exhibits a peak value after approximately 20 minutes of fire exposure. Maximum temperatures in the cross-section of the wall are obtained approximately after 25 minutes of fire exposure. Figure 5 (b) clearly shows the importance of taking into account the reduction of the modulus of elasticity at high temperatures.

At peak temperatures, a thin layer of the wall next to the exposed surface is in tension due to the reduced modulus of elasticity; however, when a constant modulus of elasticity was assumed in the calculation of stresses, the above mentioned layer was under compression. The central part of the wall is in tension while both sides of the wall are in compression due the large increase of the temperature combined with the assumption of elastic strains in the thermal stresses calculation. The assumption of a constant modulus of elasticity yields higher stresses in both tensile and compressive region at equal exposure times.

Temperature and thermal stress development with time is presented in Figure 6. Several typical sections of the wall are analyzed. It can be seen that for the time domain under consideration, the temperatures at the unexposed side of the wall (x=0.0075m) and at mid-plane (x=0.0975m) increase slowly. Close to the fire-exposed surface (x=0.1925m), significant temperature increase can be observed with peak temperature value of 867 K achieved after 25 minutes of exposure. A temperature-dependent modulus of elasticity has a pronounced influence upon the development of both stresses and deflection with time. Thermal stresses are larger when constant modulus of elasticity is taken into the account throughout the time domain analyzed.

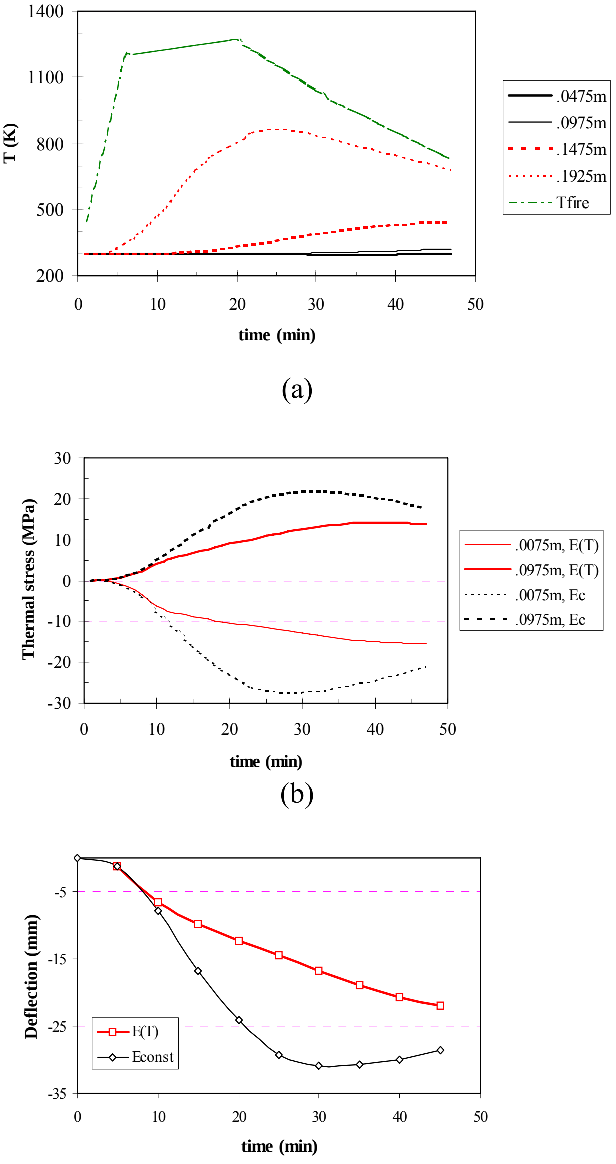

(a)

(b)

(c)

Figure 6: Effect of temperature on the modulus of elasticity: (a) temperature development in characteristic points (x=.0475, .0975, .1475, .1975 m) and time development of SDHI fire temperature [5], (b) thermal stress development in time for 2 characteristic points, x=.075 and .0975 m, (c) total deflection of the wall.

Deflection calculated with constant modulus of elasticity as presented in Figure 6 (c) starts decreasing once temperatures and temperature gradients within the wall start decreasing, which is not the case when temperature-dependent E is taken into account.

To fully evaluate the structural integrity of the element, thermal stresses obtained with the formulation described above have to be considered concurrently with the pore pressures of the saturated medium, which, in this case, is concrete. Numerical predictions of spatial pore pressure distribution and its change with time have been comprehensively discussed in [23]. Pore vapor pressures induced by the elevated temperatures can be as high as 9 bar, if concrete is saturated [28]; therefore, they can not be neglected.

5 Concluding remarks

The numerical model developed uses a generalized formulation for moisture migration in a porous media, and it is presented within the context of drying of initially saturated concrete. The predictions are reported for two case studies: ambient drying at constant environmental temperature and relative humidity, and accelerated drying due to fire.

For the first case, the numerical results are compared against experimental gravimetric data with good agreement. For the second case, simulations are conducted for a concrete wall with different thicknesses subjected to short duration high intensity (SDHI) type of fire. These extreme conditions demonstrate the robustness of the numerical model and algorithm, and its capability of providing time-dependent data for heat and mass transfer in concrete combined with corresponding thermal stresses. The results show that the occurring thermal stresses in the wall are significant, and they may affect seriously its structural integrity, i.e. the predicted values may be larger than typical concrete compressive or tensile strength, respectively. For these particular conditions the simplification of a linear stress-strain relationship may be suitable, since it leads to stress distributions far more conservative than those obtained with the temperature-dependent Young’s modulus. Altogether, the formulation presented seems to be a reliable and useful numerical tool to analyze a wide range of engineering situations dealing with moisture migration in porous media.

Acknowledgement

The authors gratefully acknowledge the financial support received from NSERC (Natural Sciences and Engineering Research Council of Canada) - Discovery Grant 12875 (ACMS) and from Slovenian Ministry of Science Research Program - Grant No.P2-0273 (JS).

References

[1] Hanson, J.A.: Effect of curing and drying environments on splitting tensile strength of concrete. *ACI Journal*, 65, pp.535-543, 1968.

[2] Bazant, Z.P., Kim, J.: Consequences of diffusion theory for shrinkage of concrete, *Mater Struct*, 24, pp.323-326, 1991.

[3] Bolander Jr., J.E., Berton, S.: Simulation of shrinkage induced cracking in cement composite overlays, *Cement Concrete Comp*, 26, pp.861-871, 2004.

[4] Bary, B., Sellier, A.: Coupled moisture-carbon dioxide-calcium transfer model for carbonation of concrete, *Cement Concrete Res*, 34, pp.1859-1872, 2004.

[5] Xu, Y., Wong, Y.L., Poon, C.S., Anson, M.: Impact of high temperature on PFA concrete, *Cement Concrete Res,* 31, pp.1065-1073, 2001.

[6] McCabe W.L., Smith J.C.: *Unit Operations of Chemical Engineering*, McGraw Hill, New York, NY, 1968.

[7] van Breugel, K., Koenders, E.A.B., Guang, Y., Lura, P.: Modelling of Transport Phenomena at Cement Matrix-Aggregate Interfaces, *Interface Sci,* 12, pp.423-431, 2004.

[8] Daian, J.F.: Condensation and isothermal water transfer in cement mortar: Part I - pore size distribution, equilibrium water condensation and imbibition, *Transport Porous Med*, 3, pp.563-589, 1988.

[9] Mehta, P.K.: *Concrete: structure, properties and materials*, Prentice Hall Inc., Englewood Cliffs, NJ., 1986.

[10] Perre, P., Degiovanni, A.: Simulation par volumes finis des transférts couplés en milieux poreux anisotropes: séchage du bois à basse et à haute temperature, *Int J Heat Mass Tran*, 33, pp.2463-2478, 1990.

[11] Whitaker, S.: Simultaneous heat, mass, and momentum transfer in porous media: a theory

of drying, *Advances in Heat Transfer*, Vol.13, pp.119-200, 1977.

[12] Šelih, J., Sousa, A.C.M., Bremner, T.W.: Moisture transport in initially saturated concrete during drying, *Transport porous med*, 24, pp.81-106, 1996.

[13] Salagnac, P., Glouannoc, A., Lecharpentier, D.: Numerical modeling of heat and mass transfer in porous medium during combined hot air, infrared and microwaves drying, *Int J Heat Mass Tran*, 47, pp.4479-4489, 2004.

[14] Scheidegger, A.E.: *The physics of flow through porous media*, University of Toronto Press, Toronto, Canada, 1974.

[15] Volkwein, A.: *Untersuchungen uber das Eindringen von Wasser und Chlorid in Beton*, Dokt. Dissertation, Technische Universitat Munchen, Munchen, Germany, 1991.

[16] Skaar, C., Siau, J.F.: Thermal diffusion of bound water in wood, *Wood Sci Technol*, 15, pp.105-112, 1981.

[17] Dhir, R.K, Hewlett, P.C., and Chan, Y.N.: Near surface characteristics of concrete: intrinsic permeability, *Mag Concrete Res*, 41, pp.87-97, 1989.

[18] Roy, D.M., Idorn, G.M.: *Concrete Microstructure*, Stategic Highway Reasearch Program, Report No. SHRP-C-340, National Research Council, Washington, DC (180 pp.), 1993.

[19] Masmoudi, W., Prat, M.: Heat and mass transfer between a porous medium and a parallel external flow. Application to drying of capillary porous materials, *Int J Heat Mass Tran*, 34, pp.1975-1989, 1991.

[20] Ali F., Nadjai, A, Silcock, G., Abu Tair, A.: Outcomes of a major research on fire resistance of concrete columns, *Fire Safety J*, 39, pp.433-445, 2004.

[21] Peng, G.F., Chan, S.Y.N., Yan, J.H., Liu, Y.F., Yi, Q.X.: Characteristics of crack growth in high performance concrete subjected to fire, *J Mater Sci Technol* 21, pp.118-122, 2005.

[22] Georgali, B., Tsakiridis, P.E.: Microstructure of fire-damaged concrete. A case study, *Cement Concrete Comp*, 27, pp.255-259, 2005.

[23] Šelih, J., Sousa, A.C.M., Bremner T.W.: Moisture and heat flow in concrete walls exposed to fire, *J Eng Mech- ASCE*, 120, pp. 2028-2043, 1994.

[24] Lenczner, D.: *Movements in buildings*, Pergamon Press, New York, 1981.

[25] "*Standard test methods for fire test of building construction and materials*", ASTM Standard E-119, ASTM, Philadelphia, Pa., 1989.

[26] Ellingwood, B.R.: Impact of fire exposure on heat transmission in concrete slabs, *J Struct Eng- ASCE*, 117, pp.1870-1875, 1991.

[27] Keats, C.: *Effect of elevated temperature on concrete*, M.Sc. Thesis, University of New Brunswick, Fredericton, NB, Canada, 1994.

[28] Copier, W.J.: The spalling of normal weight and lightweight concrete exposed to fire, *Fire safety of concrete structures, ACI Publication SP-80*, American Concrete Institute, Detroit, Mi, pp.219-237, 1983.

SEGREGATION OF OXYGEN AT METAL/OXIDE-INTERFACES: EFFECT OF KINETICS AND PRECIPITATE DISTRIBUTION

Michal STASIEK[1,*], Andreas ÖCHSNER[1,2], José GRÁCIO[1,2]

[1]Centre for Mechanical Technology and Automation, University of Aveiro,
Campus Universitário de Santiago, 3810-193 Aveiro, Portugal
[2]Department of Mechanical Engineering, University of Aveiro,
Campus Universitário de Santiago, 3810-193 Aveiro, Portugal

*Corresponding author. Fax: +351 234 370 953; Email: mstasiek@mec.ua.pt

Abstract

A numerical approach for the segregation of atomic oxygen at metal/oxide-interfaces is presented. A general segregation kinetics is considered and the coupled system of partial differential equations is solved due to a one-dimensional finite difference scheme. Based on model oxide distributions, the influence of kinetics and the oxide distribution is numerically investigated. The results for non-equidistant distributions are compared with the solution for equidistant arrangements. The numerical approach allows for the consideration of general boundary conditions, specimen sizes and time-dependent material and process parameters.

Keywords: Segregation; Metal-oxide interfaces; Mathematical modelling; Numerical modelling; Finite difference method

1 Introduction

Metal-ceramic phase boundaries are of great importance for many applications in materials science technology [1, 2], e.g. to thin solid films, coatings, electronic packaging, supported catalysts, and fibre-reinforced metal-matrix composites. In many dispersion-hardened materials, metal-oxide interfaces are involved in strengthening mechanisms. They are also included in microminiature electronic devices, e.g. MOSFETs.
The presence of solute atoms at internal metal-oxide interfaces influences the physical properties of the interfaces and this, in turn, may affect the bulk properties [3]. Therefore, it is an important task to accurately predict and measure the level of equilibrium solute-atom segregation at internal interfaces. In the presented work, the segregation of oxygen at Ag/MgO interfaces is numerically simulated whereas a general segregation kinetics which incorporates adsorption and desorption of oxygen is considered. The numerical approach results in a coupled system of partial differential equations. This general approach allows for the consideration of general boundary conditions, specimen sizes and time-dependent (e.g. temperature dependent) material and process parameters. A schematic sketch of the problem is shown in Fig. 1.

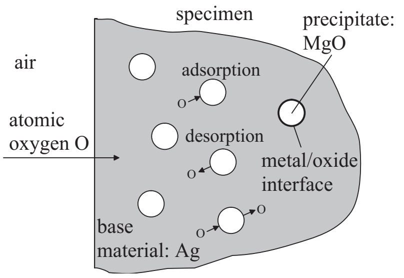

Figure 1: Schematic description of the problem.

2 General kinetics of segregation

The kinetics of oxygen segregation at metal/oxide-interfaces can be described based on Fick's second law of diffusion for the oxygen mole fraction ψ_{O} as

$$\frac{\partial \psi_{\mathrm{O}}}{\partial t} = \mathrm{div}\,(D_{\mathrm{O}}\,\mathrm{grad}\,\psi_{\mathrm{O}}) + a \cdot \gamma_{\mathrm{O}}\,, \qquad (1)$$

where D_{O} denotes the diffusion coefficient of oxygen in the alloy and div and grad are the divergence and gradient operator, respectively. The material depending factor $a = M_{\mathrm{tot}}/(N_A \cdot \rho_{\mathrm{tot}} \cdot V_{\mathrm{tot}})$ in Eq. (1) ensures unit consistency for the general source expression γ_{O} [4, 5] which involves adsorption (index a) and desorption (index d) at time t as:

$$\gamma_{\mathrm{O}} = (1-\Theta)^{\alpha}\cdot\psi_{\mathrm{O}}\cdot\nu_{\mathrm{a}}\exp\left(-\frac{E_{\mathrm{a}}^{0}}{\bar{R}T}\right)\exp\left(-\frac{a\Theta}{\bar{R}T}\right) - \Theta^{\beta}\cdot\nu_{\mathrm{d}}\exp\left(-\frac{E_{\mathrm{d}}^{0}}{\bar{R}T}\right)\exp\left(\frac{b\Theta}{\bar{R}T}\right) = \frac{\partial\Theta}{\partial t}, \quad (2)$$

where the oxygen surface coverage Θ is the fraction between the actual amount of segregated oxygen atoms at the metal/oxide interface and the maximum possible amount $(0 \leq \Theta \leq 1)$. Constants α and β denote the kinetic order and ν the frequency of the ad- and desorption process [5]. It is important for the numerical approach to underline that the general source expression given in Eq. (2) depends not only on Θ but also on the oxygen mole fraction ψ_{O}.

3 Numerical approach

3.1 Equidistant Grid Distribution

The numerical approach is based on the one-dimensional model shown in Fig. 2 which reduces the dimensionality of the problem in order to minimise the computing time for such problems. In the presented model, the content of MgO precipitates is equally distributed to the grid points of the equidistant finite difference discretisation. However, the conversion from a three- or two-dimensional structure to a one-dimensional problem requires some procedures in order to incorporate the information of the spatial distribution of the precipitates in the reduced model. A numerical procedure to convert two-dimensional microstructures into representative one-dimensional distributions is described e.g. in [6].

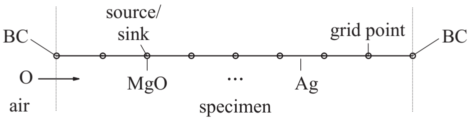

Figure 2: 1D modeling approach (Ag/MgO).

The solution of the coupled problem is found as follows: The update of the oxygen mole fraction ψ_{O} is based on the following Crank-Nicolson scheme (n denotes the grid point, $0 \leq n \leq N$, and k the time step, $k \geq 0$)

$$\psi_{\mathrm{O},n}^{k+1} = \psi_{\mathrm{O},n}^{k} + \frac{\Delta t}{\Delta x^2}\frac{1}{2}\cdot\Big[D^{k+1}\psi_{\mathrm{O},n+1}^{k+1} + D^{k}\psi_{\mathrm{O},n+1}^{k} - 2\left(D^{k+1}\psi_{\mathrm{O},n}^{k+1} + D^{k}\psi_{\mathrm{O},n}^{k}\right) + D^{k+1}\psi_{\mathrm{O},n-1}^{k+1} + D^{k}\psi_{\mathrm{O},n-1}^{k}\Big] + \Delta t a\gamma_{\mathrm{O},n}^{k}, \quad (3)$$

which results finally in a system of equations with a tridiagonal coefficients matrix. The solution can be easily obtained based on the classical Thomas algorithm, [7]. Then, Eq. (2) represents for known ψ an ordinary differential equation with respect to Θ. The update of the surface coverage Θ requires an indirect scheme (internal iteration loop variable: j) which incorporates linearisation of the right-hand side of Eq. (2) in order to ensure convergence of the solution:

$$\Theta_{n(j+1)}^{k+1} - \Theta_{n}^{k} = \Delta t\Big[\gamma_{\mathrm{O}}\left(\psi_{\mathrm{O},n}^{k+1}, \Theta_{n(j)}^{k+1}\right) + \frac{\partial}{\partial\Theta}\gamma_{\mathrm{O}}\left(\psi_{\mathrm{O},n}^{k+1}, \Theta_{n(j)}^{k+1}\right)\cdot\left(\Theta_{n(j+1)}^{k+1} - \Theta_{n(j)}^{k+1}\right)\Big]. \quad (4)$$

Iteration of the scheme given in Eq. (4) is stopped as soon as the difference of two iteration loops is smaller than a certain tolerance ε, i.e. $\Theta_{n(j+1)}^{k+1} - \Theta_{n(j)}^{k+1} < \varepsilon = 0.01$.

3.2 Non-Equidistant Grid Distribution.

The update of the oxygen mole fraction is obtained as [8]:

$$\psi_{\mathrm{O},n}^{k+1} = \psi_{\mathrm{O},n}^{k} + \Delta t\frac{D^{k+1}}{2}\left(l_{n+1}\psi_{n+1}^{k+1} - l_n\psi_n^{k+1} + l_{n-1}\psi_{n-1}^{k+1}\right) + \Delta t\frac{D^{k}}{2}\left(l_{n+1}\psi_{n+1}^{k} - l_n\psi_n^{k} + l_{n-1}\psi_{n-1}^{k}\right), \quad (5)$$

where the coefficients l_n are defined as

$$l_{n+1} = \frac{1}{2h_n}\left(\frac{1}{h_n} + \frac{1}{h_{n-1}}\right), \quad (6)$$

$$l_{n-1} = \frac{1}{2h_{n-1}}\left(\frac{1}{h_n} + \frac{1}{h_{n-1}}\right), \quad (7)$$

$$l_n = \frac{1}{2}\left(\frac{1}{h_n} + \frac{1}{h_{n-1}}\right)^2, \quad (8)$$

and $h_{n-1} = x_n - x_{n-1}$ and $h_n = x_{n+1} - x_n$ (cf. Fig. 3).

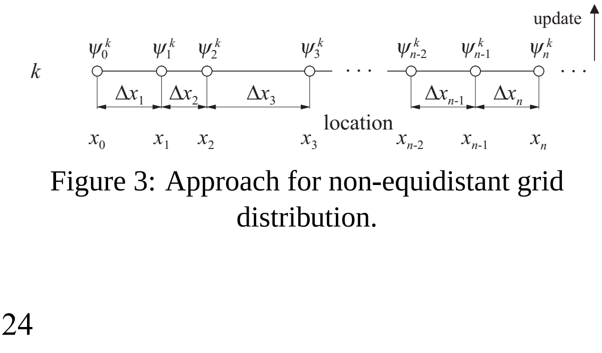

Figure 3: Approach for non-equidistant grid distribution.

4 Results

4.1 Effect of kinetics

In the following, the results for different kinetics, i.e. ad- and desorption, pure adsorption and pure desorption (which corresponds to the case of pure diffusion without reaction) are presented. Figures 4 and 5 show the variation of the oxygen mole fraction ψ_{O} and coverage Θ_{O} with time t for a 30 μm thick specimen, an initial oxygen mole fraction of $\psi_{\text{O}}(x, t = 0) = 0$ and an initial oxygen coverage of $\Theta_{\text{O}}(x, t = 0) = 0$. The magnesium mole fraction ψ_{Mg} was equal to 0.03 and an oxygen diffusion coefficient of $D_{\text{O}} = 2.72 \cdot 10^{-2} \exp(-46055/(RT))$ mm^2/s was incorporated in the model simulation. Other parameters were assigned as follows: $\alpha = \beta = 1$, $\nu_{\text{a}} = \nu_{\text{d}} = 2 \cdot 10^7$ s^{-1}, $E^0_{\text{a}} = 10 \cdot 10^3$ J/(mol·K), $E^0_{\text{d}} = 85 \cdot 10^3$ J/(mol· K), T = 733 K, $a = 10^3$ J/mol, $b = 10^4$ J/mol, N = 200.

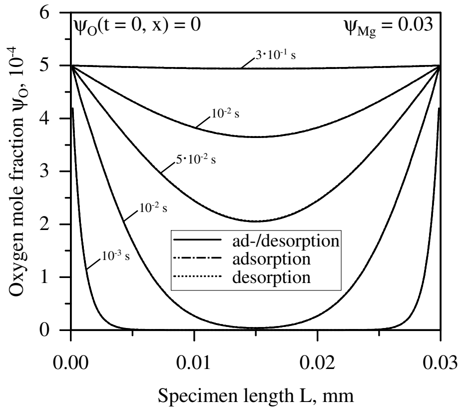

Figure 4: Variation of oxygen mole fraction with time.

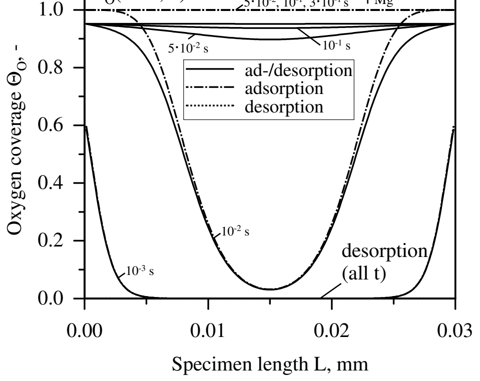

Figure 5: Variation of oxygen coverage with time.

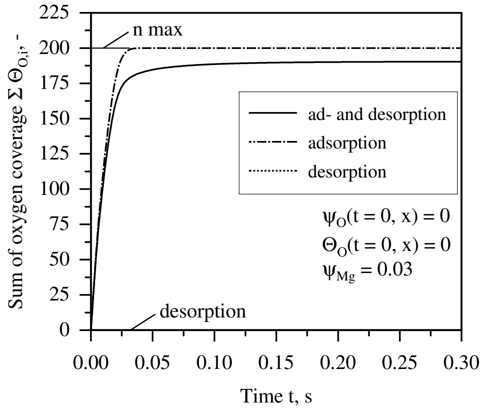

Figure 6: Variation of the sum of the oxygen coverage with time.

The sum of the surface coverage is shown in Fig. 6.

4.2 Effect of precipitate distribution

Here, the results for a homogenous and a non-homogeneous model oxide distribution (cf. Fig. 7) are presented. The grid was in the regions with high source gradients refined. Figures 8 and 9 show the variation of the oxygen mole fraction ψ_{O} and coverage Θ_{O} with time t for a 30 μm thick specimen, an initial oxygen mole fraction of $\psi_{\text{O}}(x, t = 0) = 0$ and an initial oxygen coverage of $\Theta_{\text{O}}(x, t = 0) = 0.2$. The magnesium mole fraction ψ_{Mg} was equal to 0.03 and an oxygen diffusion coefficient of $D_{\text{O}} = 2.72 \cdot 10^{-2} \exp(-46055/(RT))$ mm^2/s was incorporated in the model simulation. Other parameters were assigned as follows: $\alpha = \beta = 1$, $\nu_{\text{a}} = \nu_{\text{d}} = 2 \cdot 10^7$ s^{-1}, $E^0_{\text{a}} = E^0_{\text{d}} = 10 \cdot 10^3$ J/(mol·K), T = 733 K, $a = b = 10^3$ J/mol.

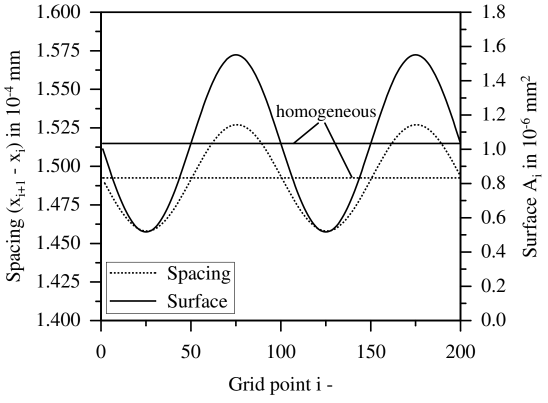

Figure 7: Variation of local grid spacing and local oxide surface.

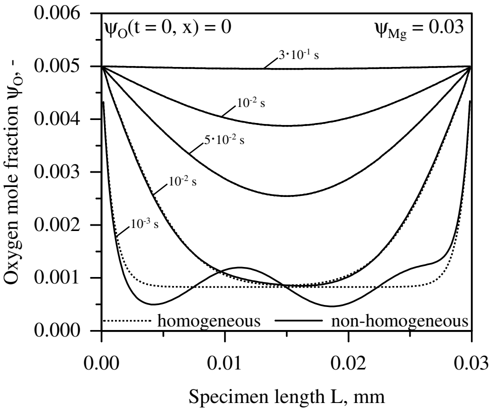

Figure 8: Variation of oxygen mole fraction with time.

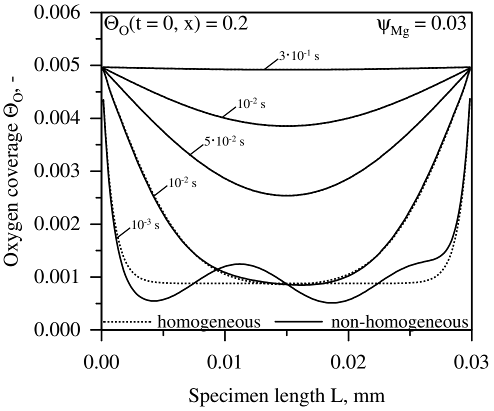

Figure 9: Variation of oxygen coverage with time.

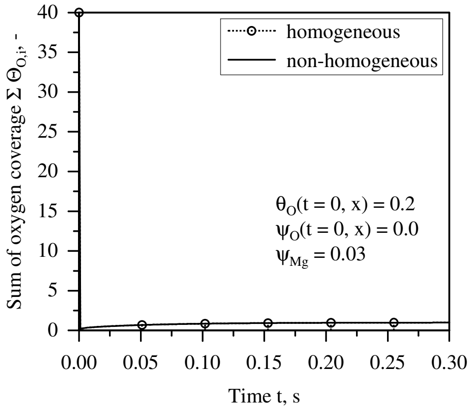

Figure 10: Variation of the sum of the oxygen coverage with time.

The sum of the surface coverage is shown in Fig. 10. It can the seen that the initial value of $200 \cdot 0.2 = 40$ significantly drops down at the beginning of the the simulation and converges then towards a maximum value of ~ 0.99 under the chosen model parameters.

5 Conclusions

A stable code based on a one-dimensional finite difference scheme has been developed for the description of the oxygen segregation at metal-oxide interfaces. The approach allows for the consideration of different boundary conditions, specimen sizes, time-depending material and process parameters and non-homogeneous oxide distributions. It is envisaged to extend the code in our future research work to consider concentration dependant properties (e.g. diffusion coefficient) and to expand the dimensionality of the code to 2D distributions.

Acknowledgments

A. Öchsner is grateful to Portuguese Foundation of Science and Technology for financial support. M. Stasiek is grateful to the European Union which supported this work in the framework of the ERASMUS/SOCRATES program. The authors are grateful to Professor G. Mishuris for helpful discussions.

References

[1] Gonis, A., and Tuchi, P. (ed.): *Stability of Materials. Structure-Property Relationship of Metal-Ceramic Interfaces*. Gordon & Breach, New York, 1996.

[2] Pippel, E., Woltersdorf, J., Gegner, J., and Kirchheim, R.: Evidence of Oxygen Segregation at Ag/MgO Interfaces. *Acta Mater.*, 48, pp. 2571-2578, 2000.

[3] Wolf, D., and Yip, S. (ed.): *Materials Interfaces*. Chapman & Hall, London, 1992.

[4] Aharoni, C., Tompkins, F.C.: Kinetics of Adsorption and Desorption and the Elovich Equation. *Advanc. Catalysis*, 21, pp. 1-49, 1970.

[5] Tompkins, F.C.: *Chemisoption of Gases on Metals*. Academis Press, London, 1978.

[6] Öchsner, A., Gegner, J., and Grácio, J.: Quantitative Determination of Microstructural Inhomgeneity for Directional Particle Distribution. *Prakt. Metallogr.*, 42, pp. 116-125, 2005.

[7] Anderson, D.A., Tannehill, J.C., and Pletcher, R.H.: *Computational Fluid Mechanics and Heat Transfer*, Taylor & Francis, New York, 1984.

[8] Öchsner, A., Stasiek, M., and Grácio, J.: Ad- and Desorption of Oxygen at Metal-Oxide Interfaces: Numerical Approach for Non-Homogeneous Oxide Distribution. *Defect Diffus. Forum*, accepted for publication, 2005.

Proceedings of The 1st International Conference on **D**iffusion in **S**olids and **L**iquids
DSL-2005, July 6-8, 2005, University of Aveiro, Aveiro, Portugal

THE INFLUENCE OF DOPING BY TRANSITION METAL ELEMENTS ON THE VACANCY FORMATION ENERGY IN FeAl B2 PHASE.

Angelica STRUTZ*, David FUKS, Arik KIV

Materials Engineering Department, Ben-Gurion University of the Negev,
P. O. Box 653, 84105 Beer Sheva, Israel

*Corresponding author. Fax: +972 86461 460; Email: strutza@bgu.ac.il

---

Abstract

Based on the *ab-initio* calculations for FeAl B2 phase with and without the vacancies we studied the influence of alloying by Ni, Cr and V on the energy of vacancy formation. We predict that the presence of these alloying elements in the vicinity of the vacancy on the Fe site increases the energy of the vacancy formation. We discuss the changes of the electron charge redistribution in the vicinity of the vacancy in FeAl alloyed with these transition metals and link the preference of their site occupation with the peculiarities of the electron density redistribution. In addition, we report on the results of calculations of different types of anti-site defects in FeAl, and show that the formation of the anti-site on the Al site is the energetically preferable configuration for this defect. Obtained results are in agreement with the experimental data.

Keywords: Vacancy formation; FeAl B2 phase; Alloying elements; Anti-site defects; Ab-initio calculations

---

1 Introduction

Several experimental together with the theoretical studies, in particular based on *ab initio* methods, concentrate their efforts on understanding the influence of point defects, such as vacancies and ternary additives, on the mechanical and on the electrical properties of the intermetallic compounds. It was shown that FeAl have a high concentration of point defects, one of the most prominent are thermal vacancies. Therefore many researches, since the pioneer works started in 1970's [1, 2, 3], were pointed to understand the influence of the vacancies formation on the properties of this intermetallic compound. For example, study of equilibrium point defects in FeAl and NiAl, [4] based on Local-Density Functional (LDF) equations within mixed-basis pseudopotential method, predicted strong tendency for vacancy clustering in FeAl and explained the different mechanical behaviour of FeAl and NiAl by shedding some light on the dissimilarity of the defects which formed in these intermetallics. Vacancies cause hardening [5, 6] and increase in their concentration depends on the temperature and on the aluminium concentration [4, 7]. Alloying of iron aluminides by Ni slows down the removal of thermal vacancies [8] In contrast, boron increases the rate of vacancy elimination [9]. The study of the site preference of ternary alloying additions, by *ab initio* calculations with a Local Density Functional (LDF), [10] shows that in FeAl Cr and Ti occupy the Al sublattice whereas Ni has a distinct preference for the Fe sublattice. Also using the TEM-based technique ALCHEMI (Atom Location by Channelling Enhanced Microanalysis) it was shown that in Fe-45at.%Al-5at.%Cu the Cu atoms occupy the Fe sublattice but Cr atoms mostly occupies the Al sublattice in Fe-45at.%Al-5at.%Cu and in Fe-40at.%Al-5at.%Cu [11]. Beyond other things, it was found that the strain-induced ferromagnetism in B2-structured FeAl is a function of composition and of deformation degree [12]. Other major structural defects in B2 type iron aluminides are anti-structure atoms which form on both sublattices [13-16] Since intermetallic compounds, and FeAl B2 phase in particular, are candidate high-temperature structural materials, diffusion in them and factors that affect diffusion mechanism have been actively investigated [17-19]. One of the conditions for the atom diffusion is a vacancy formation on nearest or second nearest neighbour site. Therefore diffusivity depends on the vacancy concentration [18].

Alloying elements affect the energy of the vacancy formation and therefore they influence the diffusion mechanics [20]. In the present paper we report the results of our study of the influence of Ni, Cr, and V on the energy of vacancy formation on both Fe and Al sites in FeAl.

2 Computational method

We perform *ab initio* calculations with density-functional-theory (DFT) in the generalized-gradient approximation (GGA) for the exchange-correlation functional [21]. It was found that *k-mesh* about 800 points in the first Brillouin zone makes the total energy independent on the number of *k*-points. The Augmented Plane Wave + local orbitals (APW+lo) basis for all valence orbitals was used. The basis-set size, $R_{mt}K_{max}$ = 6.5 was used, while a chosen radius of muffin-tin spheres, R_{mt} both for Fe and Al atoms, was taken equal to 2.2 a.u. The energy *cut-off*, separating core and valence states, was chosen equal to -7.0 Ry and the maximal wave vector G was taken equal to 14 (in units $2\pi/a$, where a is the lattice parameter). The WIEN2k package [22] was applied. All calculations were done in relativistic approximation for FeAl with and without defects.

Using the 54-atoms supercell as follows from our calculations changes the energy of vacancy formation in ~10% as compared with the results for 16-atoms supercell increasing drastically the computation time. This is why in our study, we use a 16-atoms supercell that includes one point defect of any kind (vacancy, anti-structure atom or ternary element).

3 Results

In the studies for simple metals it was shown that the vacancy formation is followed by significant shift of the atoms in the vicinity of the vacancies. In the case of intermetallic compounds not only metallic bonds (as in the case of a simple metals), but also 30%-40% of covalent bonds are present which are known to be much stronger than a metallic bonds. In our investigation we used *2x2x2* supercell, therefore we could check the displacements around the vacancy only of its first nearest neighbors. We found, that the local relaxation around the vacancy is an inward shift of the first neighbors of the vacancy. This value is 0.4% of equilibrium lattice parameter of the extended FeAl B2 phase with the vacancy. When this local relaxation is taken in account, the energy of vacancy formation is negligibly decreases in about 0.43%. This value is much smaller then values which had been reported for a simple metals. The reason for the small value of local relaxation in our case as compared with simple metals follows from the presence of highly localized covalent bonds in FeAl. The highly localized electronic charge makes the lattice of the intermetallic compound very rigid, only slightly sensitive with respect to formation of the hollow site. The elastic field around the vacancy in FeAl is rather short ranged. The elastic field has negligible effect on second neighbors of the vacancy on Fe site. Therefore we have omitted the local relaxations in our further calculations.

The quality of our calculations is shown in Table 1. The enthalpy of formation, ΔH, and the lattice parameter, *a*, are in good agreement with the calorimetric measurements [23, 24].

Table 1: The comparison of the calculated results for the enthalpy of formation, for the lattice parameter and for the energies of the vacancies formation, $E_v(A)$, on the A-atom site.

	ΔH (eV/atom)	a(Å)	$E_v(Fe)$ (eV)	$E_v(Al)$ (eV)
This work	-0.324	2.88	0.869	3.537
Exp.[23]	-0.33	---	---	---
Exp. [24]	-0.28	2.86	---	---
FLAPW [25]	---	---	0.82	4.00
Exp.[26]	---	---	0.85	---
Exp.[27]	---	---	0.934	---

The energies of the vacancy formation in stoichiometric FeAl B2 phase on the Fe and on the Al site, $E_v(Fe)$and $E_v(Al)$ respectively, are in good agreement with the calculated values by Full-Potential Linearized Augmented Waves (FLAPW) method with spin polarization [25] and with experimental measurements [26, 27].

3.1 The preference of site occupation of the alloying elements

We found that the preference occupation site of Ni in FeAl with and without the vacancies is Fe site. The analysis was based on a comparison of the mixing energies following the scheme presented in our previous work [20]. There was also reported that Cr and V occupy the Al site in the ideal FeAl B2 phase. In the case with vacancy on the Fe site in FeAl V occupies the Al site and Cr occupies the nearest Fe site to the vacancy.

3.2 Energy of vacancy formation

The vacancies in FeAl B2 phase are formed mainly on the Fe sublattice [20] therefore it is of interest to check the influence of the alloying transition metal (TM) on the preference site for the vacancy formation. The calculated results are summarized in Table 2.

Table 2: The energy of the vacancy formation, $E_v(A)$, at the *A*-atom site in FeAl without and with alloying elements in eV.

FeAl alloyed with :	$E_v(Fe)$	$E_v(Al)$
Without alloying element	0.869	3.537
Cr on the Fe site	0.910	4.510
Cr on the Al site	2.166	3.887
V on the Fe site	0.902	3.354
V on the Al site	1.261	3.963
Ni on the Fe site	1.928	4.848
Ni on the Al site	0.993	3.333

One can see that the energy of the vacancy formation on the Al site remains approximately four times higher than this on the Fe site also after alloying. Therefore the vacancies are formed mainly at Fe sites also when TM alloying elements present in their vicinity. In addition, alloying by Cr on the Al site and by the Ni on the Fe site doubles the energy of the vacancy formation on the Fe site. Alloying by V increases the energy of vacancy formation in 1.5 times.

3.3 Energy of anti-sites formation

Another structural defects that were studied, are anti-site defects on both sublattices. For FeAl we found relatively low anti-site formation energy at stoichiometry. Our calculated results are given in Table 3 and compared with other relativistic [25] and with non-relativistic *ab-initio* calculations [4, 28]. Our results of anti-site energy formation slightly differ from the previous *ab-initio* calculations. The previous results for the anti-site formation energies at the Fe and Al sublattices almost the same, while our calculations show much more significant difference in the formation energies of anti-sites at the Fe site and at the Al site. Our results are confirmed experimentally by Mössbauer spectroscopy experiments [29] and [30] that show that FeAl *B2* phase contains predominately anti-sites at the Al sublattice and vacancies at the Fe sublattice. Only negligible amount of defects such as anti-sites at the Fe sublattice and the vacancies on the Al sublattice were detected in these experiments.

Table 3: Anti-site formation energies (in eV) of FeAl at stoichiometry, $E_{anti}(A)$, at *A-atom* sites.

Method	$E_{anti}(Fe)$	$E_{anti}(Al)$
This work	1.054	0.699
FLAPW [25]	0.68	0.65
FLAPW [4]	1.03	0.95
Pseudopotentials [28]	0.99	0.99

It is interesting to note, that FeAl has relatively low anti-site formation energy at the Fe site, but very high vacancy formation at the Al sites. Therefore it is easier to add an Al atom than to remove an Al atom. Actually, the anti-site defects at the Fe sites become the dominant defect type for Al-rich FeAl. But for the Fe-rich FeAl the dominant defects are vacancies at the Fe sites and anti-sites at the Al sites.

3.4 Equilibrium lattice parameter

The total energies in the APW + lo calculations have been also minimized for the defect supercell systems. The corresponding equilibrium lattice constants are given in Table 5.3 and compared with the results of the previous TB-LMTO (Tight-Binding Linear Muffin-Tin Orbital) calculations.

Table 4: Equilibrium lattice constant (Å) for the FeAl supercell with defects.

	This work	TB-LMTO [31]
vacancy on Fe sublattice	5.715	5.719
vacancy on Al sublattice	5.715	5.716
Fe anti-structure atom	5.760	5.701
Al anti-structure atom	5.800	5.741

3.5 Charge distribution

To understand the preference of the alloying elements to occupy particular site in FeAl B2 with and without vacancies, the charge redistribution in the real space were studied. We compared the differential charge distribution (the difference between the electron distribution in the intermetallic compound and that of the constituent atoms) in FeAl, as shown on the Figs. 1 and 2.

For the case without the vacancy (Fig. 1) we compared the charge transfer in the vicinity of the alloying elements on the Fe site (Fig.1 (a-c)) and the same when the alloying elements occupy the Al site (Fig.1 (d-f)). Isodensity curves in Figs. 1 and 2 are drawn with increments of 0.001 $e/Å^3$.

When Cr or V occupies the Al site, Fig. 1 (d) and (f) respectively, the electron density between these ternary elements and their first nearest neighbours, the Fe atoms, is relatively high. In the case of Cr the value is 16 and in the case of V is 14(in units 0.001 $e/Å^3$ here and in further discussion). On the contrary when Cr or V occupies the Fe site the electron density is relatively low between ternary elements and their nearest neighbours, Al atoms. The corresponding values are 4 between Cr and Al, and 3 between V and Al atoms. Thus strong directional bonds are formed between these ternary elements and Fe atoms an therefore these ternary elements prefer to occupy the Al site in agreement with a result of the mixing energy [20]. When Ni occupies the Al site the value of the electron density in the vicinity of the ternary element is only 6. It means that no strong directional bonds are formed between Ni and its nearest neighbours, Fe atoms. When Ni occupies the Fe site the electron density in the vicinity of Ni is almost homogeneously distributed and relatively low, the differential charge distribution changes from 2 to 3. Therefore in this case the uniform distribution of the charge makes the compound more stable.

Similar comparison of the charge transfer has been done for the case with the vacancy on the Fe site in FeAl with alloying elements, Fig. 2. When the alloying elements occupy the Fe site, the second nearest neighbour of the vacancy (Fig. 2 (a-c)) the "vacancy pocket" is nearly symmetric. This symmetry is distorted when the alloying elements occupy the Al site, nearest vacancy neighbour (Fig. 2 (d-f)). In the cases of alloying by Cr and Ni (Fig. 2 (a, b)) the distortion is more pronounced than in the case of alloying by V (Fig. 2 (c)). When Cr or V atoms occupy the Al sites the high electron density was detected between these alloying elements and Fe atoms (Fig. 2 (d) and (f), respectively), the differential charge density is 16. This high charge density was not detected in the case with Ni as alloying element (Fig. 2 (e)). In this case the highest value of differential charge density between these atoms is 7. Similar to the case without the vacancy, when Ni occupies the Fe site, the electron density in its vicinity is relatively low. It is possible to explain the site preference of these alloying elements in FeAl with vacancies basing on the competition between the strong directional bond formation and the symmetry in charge distribution. When Cr or Ni occupies the Al site the symmetry distortion is very high and therefore these alloying elements prefer to occupy second nearest neighbor of the vacancy, the Fe atom. When V occupies the Al site the strong directional bonds are formed between TM. This effect compensates the distortion of differential charge density in the vicinity of the vacancy; therefore V prefers to occupy the Al site.

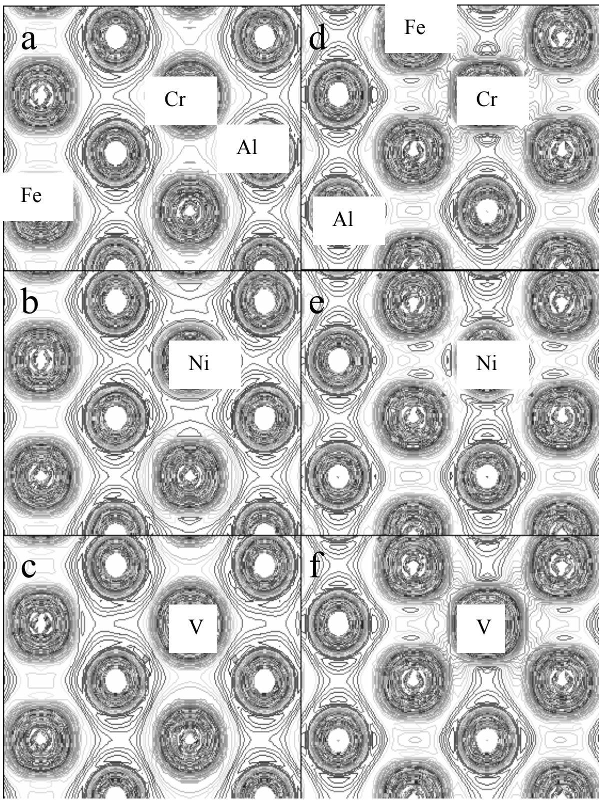

Figure 1: Differential charge distribution for electrons in spin-up state for the FeAl *B2* phase alloyed by (a) Cr, (b) Ni and (c) V on the Fe site and alloyed by (d) Cr, (e) Ni and (f) V on the Al site in the (110) plane.

Whatever the alloying elements occupy the Fe sublattice or Al sublattice the differential charge density in the center of the "vacancy pocket" in the cases with Ni and Cr is (-4) and in the case with V is (-3). In the vicinity of the Al atoms this value drops to (-6) in the cases with Cr and V and to (-7) in the case with Ni. Therefore we found here a charge transfer from Al atoms to TM atoms.

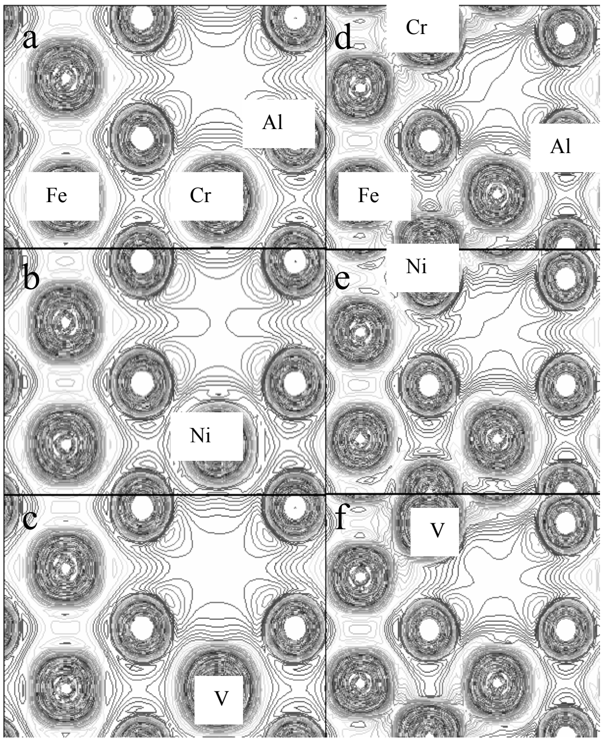

Figure 2: Differential charge distribution for electrons in spin-up state for the FeAl *B2* phase with the vacancy on the Fe site (the second nearest neighbor of the vacancy) alloyed by (a) Cr, (b) Ni and (c) V on the Fe site and alloyed by (d) Cr, (e) Ni and (f) V on the Al site in the (110) plane.

4 Summary

The energy of the vacancy formation increases when the alloying elements occupy the site in the vicinity of the vacancy on the Fe site. In addition, alloying of FeAl by Cr, Ni or V does not decrease the energies of the vacancy formation on the Al site. Therefore due to the high energies of vacancy formation in alloyed FeAl the vacancies are formed mainly on the Fe site.

The analysis of preference occupation site of Ni, V and Cr in FeAl was done on the basis of the study of electron density distribution. According to our results, Ni occupies the Fe sites both in ideal FeAl and in FeAl with the vacancy on the Fe site. Transition metals with lower than Fe atomic numbers, V and Cr occupy the Al sublattice in ideal FeAl in agreement with our previous work [20] where the analysis was performed on the basis of energy considerations.

We showed that Cr prefers to occupy the closest Fe site in FeAl with the vacancy on the Fe site. We link this amphoteric property of Cr with the peculiarities of the electron density distribution.

The calculated energies of the anti-site formation on the both sublattices are relatively low. The energy formation of the anti-site on the Al site is lower than that of the anti-site on the Fe site showing the preference of this configuration of defect in agreement with experiment.

Acknowledgments

This work was supported by the German-Israeli Foundation for Scientific Research and Development, grant N^0 G 617 - 16.10/1999. Authors are thankful to Prof. H. Mehrer for providing the experimental data and constant interest in their work.

References

[1] Junqua, N., Desoyer, J.C.,Moine, P.: Electron microscopy odservation of quenching defects in an ordered alloy of B2 type: Fe-40 at% Al. *Phys. Stat. Solidi A*, 18, pp. 387-395, 1973.

[2] Paris, D., Lesbats, P., Levy, J.: An investigation of the distribution of vacancies in an ordered Fe-Al alloy by field ion microscopy. *Scripta Metall.*, 9, pp. 1373-1378, 1975.

[3] Ho, K., Dodd R.A.: Point defects in FeAl. *Scripta Metall.*, 12, pp. 1055-1058, 1978.

[4] Fu C.L., Ye Y.-Y., Yoo M.H., Ho K.M.: Equilibrium point defects in intermetallics with B2 structure: NiAl and FeAl. *Phys. Rev. B*, 48, pp. 6712-6715, 1993.

[5] Chang, Y.A., Pike, L.M., Liu C.T., Bilbrey, A.R., Stone, D.S.: Correlation of the hardness and vacancy concentration in FeAl. *Intermetallics*, 1, pp. 107-115, 1993.

[6] Nagpal, P., Baker, I.: Effect of cooling rate on hardness of FeAl and NiAl. *Metall. Trans. A*, 21A, pp. 2281-2282, 1990.

[7] Schneibel, J.H., Pike, L.M.: A technique for measuring thermal vacancy concentration in stoichiometric FeAl. *Intermetallics*, 12, pp. 85-90, 2004.

[8] Schneibel, J.H.: Strengthening of iron aluminides by vacancies and/or nickel. *Mater. Science and Eng. A*, A258, pp. 181-186, 1998.

[9] Fraczkiewicz, A., Gay, A.S., Biscondi, M.: On the boron effect in FeAl (B2) intermetallic alloys. *Mater. Science and Eng. A*, A258, pp. 108-114, 1998.

[10] Fu C.L., Zou J.: Site preference of ternary alloying additions in FeAl and NiAl by first-principles calculations. *Acta Mater.,* 44, pp. 1471-1478, 1996.

[11] Anderson, I.M.: ALCHEMI study of site distributions of 3D transition metals in B2-ordered iron aluminides, *Acta Mater.*, 45, pp. 3897- 3909, 1997.

[12] Wu, D., Baker, I., Munroe, P.R.: The effect of substitutional elements on the strain-induced ferremagnetism in B2-structured Fe-Al single crystals. *Intermetallics*, 12, pp. 851-858, 2004.

[13] Kogachi, M., Tanahashi, T., Shirai, Y., Yamaguchi, M.: Determination of vacancy concentration and defect structure in the B2 Type NiAl β-phase alloys. *Scripta Mater.*, 34, pp. 243-248, 1996.

[14] Kogachi, M., Haraguchi, T., Kim, S.M.: Point defect behaviour in high temperature region in the B2-type intermetallic region compound FeAl. *Intermetallics*, 6, pp. 499-510, 1998.

[15] Kogachi, M., Haraguchi, T.: Possibilities of random vacancy distribution and antisite atom recovering in the point defect mechanism in B2-type intermetallics. *Intermetallics*, 7, pp. 289-300, 1999.

[16] Krachler, R., Ipser, H., Sepiol, B., Vogl, G.: Diffusion mechanism and defect consentrations in β'-FeAl, an intermetallic compound with B2 structure. *Intermetallics*, 3, pp. 83-88, 1995.

[17] Nakamura, R., Takasawa, K., Yamazaki, Y., Iijima, Y.: Single-phase interdiffusion in the B2 type intermetallic compounds NiAl, CoAl and FeAl. *Intermetallics*, 10, pp. 195-204, 2002.

[18] Kao, C.R., Chang, Y.A.: On the composition dependencies of self-diffusion coefficients in B2 intermetallic compounds, *Intermetallics*, 1, pp. 237-250, 1993.

[19] Mehrer, H., Eggersmann, M., Salamon, M., Sepiol, B.: Diffusion in intermetallic phase of the Fe-Al and Fe-Si systems. *Mater. Science and Eng. A*, 239-240, pp. 889-898, 1997.

[20] Fuks, D., Strutz A., Kiv, A.: Bonding of Cr and V in FeAl B2 phase., *Inter. J. Quan. Chem.*, 102, pp. 606-611, 2005.

[21] Perdew, J.P., Burke, S., Ernzerhof, M.: Generalized Gradient Approximation Made Simple , *Phys. Rev. Let.*, 77, pp. 3865-3868, 1996.

[22] Blaha, P., Schwarz, K., Madsen, G., Kvasnicka, D., Luitz, J.: *Computer code WIEN2k.* Inst. f. Materials Chemistry, TU Vienna, 2005.

[23] Hultgren, R., Desai, P.D., Hawkins, D.T., Gleiser, M., Kelley, K.K.: *Selected Values of the Thermodinamic Properties of Binary Alloys*; American Society for Metals, Metals Park, OH, 1973.

[24] Smithels, C.J.: *Metals Reference Book Vol. II*. Butterworth, London, 1962.

[25] Fu, C.L.: Origin of ordering in *B*2-type transition-metal aluminides: Comparative study of the defect properties of PdAl, NiAl, and FeAl, *Phys. Rev. B*, 52, pp. 3151-3158, 1995.

[26] Kerl, R.; Wolff, J.; Hehekamp, Th: Equilibrium vacancy concentration in FeAl and FeSi investigated with an absolute technique. *Intermetallics*, 7, pp. 301-308, 1999.

[27] Kass, M., Brooks, Ch.R., Falcon, D., Basak, D.: The formation of defects in Fe-Al alloys: electrical resistivity and specific heat measurements. *Intermetallics*, 10, pp. 951-966, 2002.

[28] Fähnle, M., Mayer, J., Mayer, B.: Theory of atomic defects and diffusion in ordered compounds, and application to B2-FeAl. *Intermetallics*, 7, pp. 315-323, 1998.

[29] Collins, G.S., Peng, L.S.J.: Point Defects in FeAl. *Il Nuovo Cimento*, 18D, pp. 329-337, 1996.

[30] Mayer, J., Elsässer, C., Fähnle, M.: Concentrations of atomic defects in B2-Fe_xAl_{1-x} An ab-initio study. *Phys. Stat. Sol. (b)*, 191**,** pp. 283-298, 1995.

[31] Kulikov, N.I., Postnikov, A.V., Borstel, G., Braun, J.: Onset of magnetism in *B*2 transition-metal aluminides. *Phys. Rev. B*, 59, pp. 6824-6833, 1999.

INFLUENCE OF GRAIN BOUNDARY INCLINATION ON THE GRAIN BOUNDARY AND TRIPLE JUNCTION MOTION IN Zn

Vera SURSAEVA*, Boris STRAUMAL

Institute of Solid State Physics, Russian Academy of Sciences, Chernogolovka, Moscow District, RU-142432, Russia

*Corresponding author: Fax: 7 096 52 49 701; E-mail: sursaeva@issp.ac.ru

---

Abstract

The experimental results of an investigation of the steady-state motion of individual grain boundaries (GBs) of natural deformation twin and individual twin GBs in bicrystals and tricrystals with triple junction (TJ) are obtained. For experimental observation of GB mobility from the dependence on GB inclination the Zn specimens with individual GBs and TJs were produced. The mobility of natural deformation twin GBs and twin GBs in bicrystals and tricrystals are compared in connection with the GB inclination.

Keywords: Grain Boundary; Triple Junction; Twin; Grain boundary Inclination; Coherent twin; incoherent twin

---

1 Introduction

It is known that the presence of special grain boundaries (GBs) in a material is desirable since the material as a whole would perform better in service [1]. GBs with markedly different properties than those of average GBs are known as 'special'. For many years the coincidence site lattice (CSL) model, which describes GBs in terms of the misorientation between neighboring grains, has been a cornerstone of GB research [2]. It was originally thought that any CSL GB with a low Σ value (where Σ is the reciprocal density of coinciding sites) had special properties. However Wolf indicated that a low-Σ CSL was a necessary but not sufficient criterion for specialness [3]. For instance the so-called "coherent twin" in fcc lattice is a $\Sigma3$ GB in {111} planes of both grains always possesses special properties whereas the so-called "incoherent twin" which is a $\Sigma3$ GB lying in a {211} plane may be characterized by "less special" behavior.

GBs can be classified using CSL which defines the periodicity, i.e. the degree of 'fit' between the two lattices which constitute GB. CSLs provide information on particular misorientation between two neighboring grains. Misorientation defines only three of the five degrees of freedom needed to describe GB structure. The other two degrees of freedom are obtained from GB plane orientation.

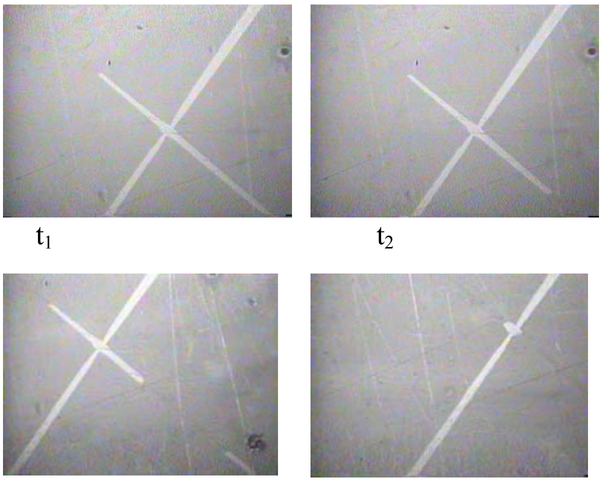

t_1 t_2

t_3 t_4

Figure 1: The line of intersection of the two deformation twins in zinc (99.995 at.%) is perpendicular to the plane of sample. ($t_4 > t_3 > t_2 > t_1$ are annealing times).

The importance of knowing GB plane indexes in addition to the misorentation are emphasizes by several researches [4-6]. We observed twin GBs in Zn with the same "matrix/twin" correlation and different space orientation demonstrating dissimilar rate of motion (Fig. 1).

The boundary plane geometry can be studied with the aid of bicrystals and tricrystals where all five degrees of freedom are predetermined. The use of fabricated bicrystals and tricrystals allows producing GB with specific plane configuration. Techniques for preparing bicrystals and tricystals are described in [7]. The main reason for using bicrystals and tricrystals is a possibility to measure mobility associated with precisely known GB geometries. In general, GB mobility depends both on GB misorientation and inclination. GB mobility is strongly depends on misorientation [8, 9]. An experimental study the mobility dependence on inclination of GB and TJ with fixed misorientation allows us to understand the inclination effect.

2 Experimental

2.1 Twin grain boundaries

Two kinds of twins exist in materials, namely mechanical (deformation) twins and grown (annealing) twins. The annealing twins are the main structural defects of polycrystals with low and medium stacking fault energy. The deformation twins are the main structural defects of deformed polycrystals. Deformation and grown twins have the same correlation “matrix/twin”. We can describe the grown twin GB in terms of axis and angle as GB generated by lattice rotation 86° about axis $[11\bar{2}0]$. Twin GB is special $[11\bar{2}0]$ tilt GB with $\Sigma = 15$.

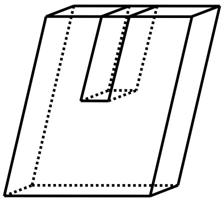

Fig.2: The scheme of specimen with twin.

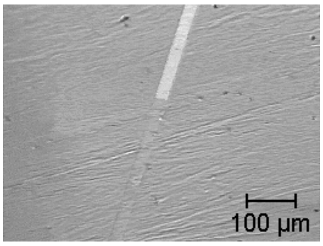

Fig. 3: Micrograph of a twin in zinc (99.995 at.%).

2.2 Deformation twin grain boundaries

Single crystals were grown by modified Bridgman technique using high purity (99.995 at.%) zinc. By means of an applied stress deformation twins were introduced into the single crystals and we have bicrystal in form of half-loop with two coherent and one incoherent GBs (Fig. 2 and Fig. 3). Coherent GB plane of deformation twin is $(10\bar{1}2)$. Incoherent GB plane as a rule consists of plane lattice facets with low indexes [10]. The using of deformation twins allows one to obtain relatively large driving forces, which is sufficient to force incoherent GB to move.

2.3 Grown twin grain boundaries

Twin GBs in Zn can be presented as the $[11\bar{2}0]$ tilt GBs with lattice rotation angle 86° (See section 2.1). The samples of the bicrystals of Zn (99.999at%) with a twin GB were grown by a modified Bridgman technique in a high purity argon atmosphere in a graphite crucible. Two reversed capillary techniques (Figs. 4 to 7), were used to investigate grown twin GB migration: under control variable driving force (“corner” method, Figs. 4 and 5) and under constant driving force (“half-loop” method, Figs. 6 and 7) [8, 11]. In first case the plane of grown twin GBs is under the angle α to basic plane (1000). The major advantages of first technique are the relative ease of manufacturing and preparation of specimen and the possibility to change the driving force by varying angle α to (1000) plane (Fig. 4). This technique allows one to obtain relatively large driving forces under small α. However we can get inclination dependence on GB mobility for low angle interval 0÷20º.

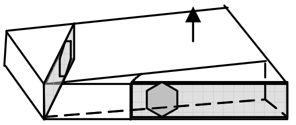

Fig. 4: The scheme for “corner method”.

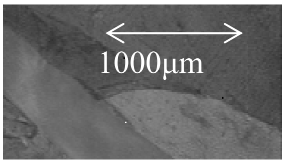

Fig. 5: Individual video frame of GB migration.

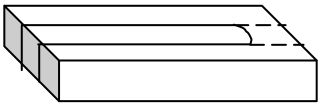

Fig. 6: The scheme for “half loop method”.

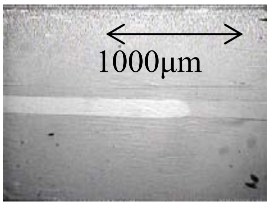

Fig. 7: Individual video frame of GB migration.

The major advantage of a technique with constant driving force is the possibility to change the inclination of grain boundary with the constant angle of misorientation. (Fig. 6). In this case the inclination angle changed between 0÷90º.

2.4 Grown twin grain boundaries with triple junction

The samples of the tricrystals of Zn (99.999 at. %) with TJs were grown by a modified Bridgman technique from single crystalline seeds in high purity argon atmosphere in a graphite crucible. In Fig. 9 the shape of moving GB system with TJ is shown. The sample contents two curved high angle tilt GBs, $[11\bar{2}0]$ 84° and $[11\bar{2}0]$ 87°, and a straight 3° tilt GB (not visible in the pictures, it ranges from the tip of the junction parallel to the straight part of the high angle GBs to the low right corner of the pictures).

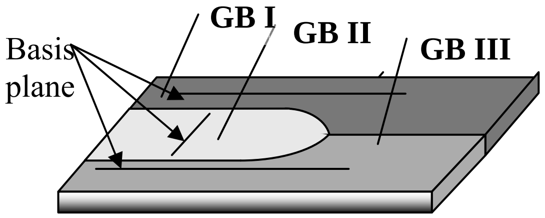

Figure 8: The geometry of tricrystalline specimen with TJ.

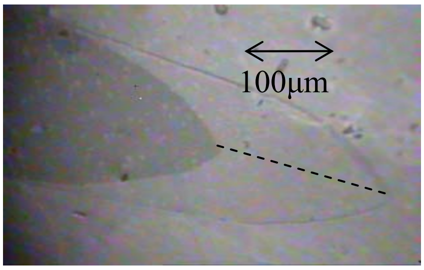

Figure 9: The shape of two moving GBs and TJ.

3 Results and discussion

To study *in-situ* the migration of twin GBs and system of twin GBs with TJ at elevated temperatures a modified optical microscope with polarised light and a hot stage was used. An additional polarisation filter applied in the reflected beam allows distinguishing the different orientations of the grains by the different intensity of the reflected light. By rotating the sample with respect to the incident beam the contrast was enhanced. The experiments were carried out in the temperature range 473 to 683 K. It is possible to determine the mobility of system from time dependence of GB or TJ displacement and a shape of moving GB or TJ at any moment. We consider the steady-state motion of GBs and TJs in the system of grown twin GBs. GBs and TJs in our configurations are straight and perpendicular to the plane of the diagram. Away from TJ all three GBs have to be planar and their planes are parallel to one another and perpendicular the plane of the diagram. This makes the problem quasi-two-dimensional.

The driving force was provided by reduction of the free energy of the boundaries and reads (per unit area):

$$p = \frac{2\sigma}{a} \ , \tag{1}$$

where σ is the surface tension of GB and a is the width of the shrinking grain. The mobility of GB is given by the ratio of velocity v and driving force p:

$$m = \frac{v}{p} = \frac{va}{2\sigma} \tag{2}$$

In our experiments we used the reduced mobility A [12]:

$$\mathrm{A} \equiv \frac{\mathrm{va}}{2} = \mathrm{m}\sigma = \mathrm{A_0 exp}\left(-\frac{\mathrm{H}}{\mathrm{kT}}\right) \tag{3}$$

where H is the activation enthalpy and A_O is the preexponential factor. The reduced mobility depends on activation enthalpy H and preexponential factor A_O. We suppose the inclination effects on H and A_O is different. We decided to divide the influence the inclination on H and A_O and to investigate the influence the inclination on parameter A_O. Fig. 10 shows the typical Arrhenius plot of the twin GB mobility. At low temperatures the motion is thermally activated process, at high temperatures the motion is athermal. The effect of the athermal grain boundary motion was observed in our early works in Zn only, the nature of the athermal motion was not clear [13, 14]. The influence of anisotropy is the one of the main reasons of athermal motion of grain boundaries in zinc [15].

Obviously it is best to study the inclination dependence of a boundary where the athermal motion is most marked. It has been found that effect is only observed in special GBs in Zn. We investigated the inclination dependence on the

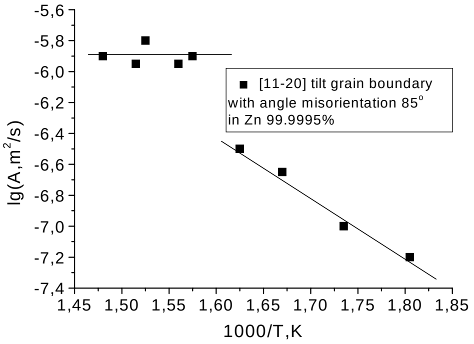

Figure 10: The temperature dependence of twin GB mobility in zinc bicrystal.

motion of natural deformation and grown twin GBs because twin GB is special. Moreover, we observe that twin GBs with the same "matrix/twin" correlation and different space orientation demonstrate dissimilar rate of motion (Fig. 1).

3.1 *Deformation twin grain boundaries motion*

Shrinkage of twin proceeds by incoherent twin GB motion along coherent twin GBs during annealing under high temperature. Large velocities of GB motion are obtained in motion under high driving force. Deformation twin GBs exhibit low mobility, it is necessary to create high driving force, i.e. very small dimension of half-loop (Fig. 2.) Athermal GB migration was experimentally observed for deformation twin GBs (Fig. 11). The temperature dependence of the mobility is characteristic for breakaway of migrating GB from its adsorbed impurities [16-19]. Essential new features are that before and after detachment from the impurity atmosphere the GB mobility is temperature independent. The motion of individual incoherent twin GB was investigated in the temperature interval between 473 and 681 K.

3.2 *Grown twin grain boundaries motion*

Fig.10. shows the temperature dependencies of the mobility of $[11\bar{2}0]$ tilt GBs, angle misorientation 86°±0.5°. Atermal GB migration was experimentally observed for grown twin GBs (Fig. 10). The temperature dependence of the mobility is characteristic for breakaway of migrating boundary from its adsorbed impurities [16-19]. An essential new feature is that GB mobility is temperature independent after detachment from the impurity atmosphere. The motion of individual grown twin GB was investigated in the temperature interval between 548 K and 681 K. A characteristic feature of the observed dependence is a drastic change of the GB mobility in a narrow temperature range. Below the breakaway region GB mobility demonstrates a usual Arrhenius-type temperature dependence Figs.10 and 11.

3.3 *Grown twin grain boundaries motion with triple junction*

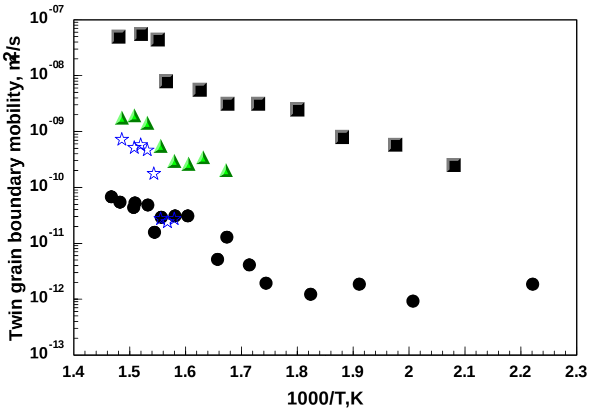

Figure 11: Temperature dependence of twin GB mobility and twin GB mobility with triple junction.

- ■ Grown twin GB
- ★ Triple junction with grown twin GBs($[11\bar{2}0]$ tilt GBs φ_1=82°, φ_1=80°,φ_1=2°)
- ▲ Triple junction with grown GBs ($[11\bar{2}0]$ tilt GBs φ_1=84°, φ_1=87°,φ_1=3°)
- ● Deformation twin GB

Fig. 11 shows the temperature dependencies of the TJ mobility. We observe the athermal TJ motion. It is known that the motion of GB systems with TJs in Zn can be controlled by slowly moving TJs and by GBs. The influence of TJs depends on temperature. It is particularly strong at temperatures below $0.85T_m$ in Zn (T_m is a melting temperature). In the temperature interval above $0.85T_m$ the motion of a connected GB system is less affected by TJ, and, therefore, effectively controlled by GB mobility [20, 21]. Contrary to the motion of an individual GB, there is new aspect of the problem where inclination influence can manifest itself, namely GB faceting in TJ, because the whole angle at triple point is 2π. The theories of inclination influence on GB motion also can be applied with certain corrections to TJ motion.

3.4 *The influence of inclination on twin grain boundaries motion and twin GBs motion with triple junction*

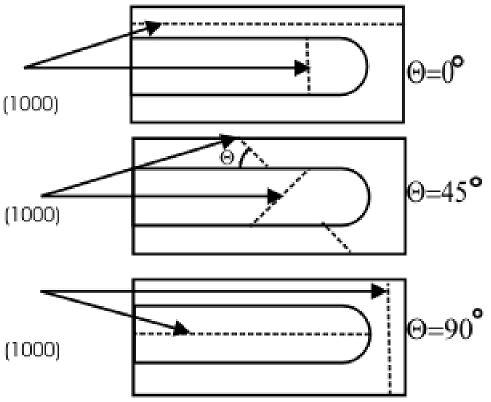

Figure 12: The scheme of bicrystals with grown twin GBs with different orientations of GB plane.

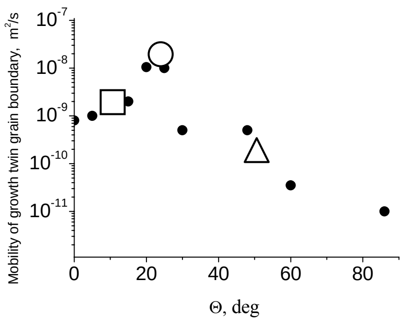

Figure 13: Dependence of twin GB mobility in bicrystals vs. inclination angle θ at 673 K. Open ring corresponds to the mobility of twin GB in a bicrystal measured by "corner method". Open square corresponds to the mobility of twin GB in a tricrystal measured from GBTJ experiments. Triangle corresponds to the mobility of deformation twin GB. Filled rings correspond to the mobility of twin GB in bicrystals with different inclination θ measured by a "half-loop".

It was found that kinetic parameters of GB depend strongly on GB inclination. There were observed three kinds of twin GB motion: **1.** Activated motion in a wide range of temperatures. **2.** Activation-less motion. **3.** Activated motion at low temperatures combined with activation-less motion at high temperatures. It has been established that the transition from activated to activation-less motion has a jump-wise character. The shape of a boundary will be a smooth curve as long as the boundary surface tension varies continuously. If, however, it changes discontinuously with GB inclination faceting of the moving grain boundary would occur [10, 18]. The scheme of bicrystals with grown twin GB with different orientations of GB plane and dependence of the twin GB mobility in bicrystals vs. inclination angle θ at 673 K are presented on Figs. 12 and 13. The angle of inclination θ was found as the angle between basic plane (1000) in one grain and the plane of GB. Fig. 13 shows experimentally determined curve of the GB mobility of tilt $[11\bar{2}0]$ GBs with misorienatation angle 86º on athermal intercept as a function of inclination θ (0, 4, 14, 19, 22, 30, 45, 60 and 90º). The angle of inclination θ was imparted in the process of fabricated GB. As we can see, the GB mobility varies non-monotonically with θ and amplitude is quite large

$$\frac{A(\theta = 20^o)}{A(\theta = 90^o)} \cong 10^3$$

The values of natural deformation twin GB mobility and TJ mobility coincide with this curve.

4 Conclusions

Twin GB motion has been observed.

1. The mobility of grown twin GB vs. inclination angle θ, measured by "half-loop method", the mobility varies non - monotonically with θ and amplitude is quite large $\cong 10^3$. The distinction may be attributed to structure variation of twin GB in dependence of the twin mode inclination. The experimental results show the strong effect of the inclination on kinetic properties of GBs and TJs in zinc.
2. It has been found that the mobility of GBs of deformation twin is 3 orders of magnitude less than the mobility of grown twin GBs (Fig. 11). It is a prove of the inclination influence.
3. GBs of deformation twin manifest athermal motion before and after detachment from impurity cloud. It is supposed that it is the result of low adsorption capacity of the different surfaces of twin misorientation. The temperature of detachment of deformation twin GB is 573 K.
4. It is known that the TJ mobility is controlled by GBs at high temperature, and TJ does not drag the motion of GBs system with TJ. It is suggested that the adsorption capacity of TJ line is low at temperatures more than $0.85T_m$. Therefore, it is supposed that the detachment of GBs from impurity cloud during GBs motion with TJ is observed. The additional prove is the same 643 K

of detachment for grown twin GB and for grown twin GBs connected by TJ.

5. It has been found that the mobility of grown twin GBs connected by TJ is lower by 2 orders of magnitude than the mobility of single fabricated twin GBs before and after detachment (Fig. 11). It is the influence the TJ.

6. The fabricated twin GBs connected by TJ manifest athermal motion after detachment from impurity cloud. It is supposed that this is the result of low adsorption capacity of the fabricated twin GB surface in system.

Acknowledgments

The financial support of Russian Foundation for Basic Research under contract 03-02-04000, 04-03-34982 and INTAS (contract 03-51-3779) is acknowledged.

References

[1] Watanabe, T., Fujii, H., Oikawa, H., and Arai, K.I.: *Acta metal.,* 37, pp. 941-952, 1989.

[2] Kronberg, M.I., Wilson, F.H.: *Trans AIME*, 185, pp. 501-510, 1949.

[3] Wolf, D.: *J. Phys.,* 46, pp. C4-197-204, 1985.

[4] Paidar, V., *Phys. Stat. Sol. (a),* 92, pp. 115-120, 1985.

[5] Priester, L., *Rev. Phys. Appl.,* 24, pp. 419-422, 1989.

[6] Leichek, P., Hofmann, S., *Mater. Sci. Forum*, 207-209, pp. 745-748, 1996.

[7] Sursaeva, V., Protasova, S., Kruz, S.: *Proceedings of the III International Conference "Crystals: growth, properties, real structure, applications",* Medovoi, A.I., Polyanskii, E.V. (Eds.) Russian Academy of Sciences, Alexandrov, Vol.2, pp. 143-154, 1997, in Russian.

[8] Sursaeva, V.G., Andreeva, A.V., Kopetskiy, Ch.V., Shvindlerman, L.S.: *Phys. Met. Metall.* 41, pp. 98-103, 1976.

[9] Kopetskiy, Ch.V., Sursaeva, V.G., Shvindlerman, L.S.: *Mobility of high angle tilt grain boubdaries in zinc.* ISSP RAN, Chernogolovka, 1979.

[10] Straumal, B.B., Sursaeva, V.G., Polyakov, S.A.: *Interface Sci.,* 9, pp. 275-281, 2001.

[11] Straumal, B.B., Sursaeva, V.G., Shvindlerman, L.S.: *Phys. Met. Metall.,* 49, pp. 102-107, 1980.

[12] Gottstein, G., Shvindlerman, L.S.: *Grain boundary migration in metals:* CRC Press, Boca Raton etc., 1999.

[13] Kopetskiy, Ch.V., Sursaeva, V.G., Shvindlerman, L.S.: *Sov. Phys. Solid State,* 21, pp. 238-240, 1979.

[14] Kopetskiy, Ch.V., Shvindlerman, L.S., Sursaeva, V.G.: *Scripta metal.,* 12, pp. 953-956, 1978.

[15] Sursaeva V.G.: *Mater. Sci. Forum,* Vols. 426-432, pp. 4411-4416, 2003.

[16] Aristov, Yu.A., Kopetskiy Ch.V., Sursaeva, V.G., Shvindlerman, L.S.: *Soviet Academy of Sciences Doklady*, 225, pp. 804-806, 1975, in Russian.

[17] Sursaeva, V.G.: Recrystallization and Grain Growth*, Proceedings of the Second International Conference in Recrystallization and Grain Growth, ReX&GG2.* Bacroix, B., Driver, J.H and etc. (Eds.), Trans Tech Publication, Uetikon, vol. 2, pp. 801-806, 2004.

[18] Tuflin, A.U., Sursaeva, V.G., Czubayko, U.: D*efect and Diffusion Forum,* Vols 194-199, pp. 1253-1258, 2001.

[19] Sursaeva V., Zieba P.: *Defect and Diffusion Forum,* Vols. 237-240, p.578-584, 2005.

[20] Czubayko, U., Sursaeva, V.G., Gottstein, G., Shvinderman, L.S.: *Acta mater.,* 46, pp. 5863-5871, 1998.

[21] Sursaeva, V.G., Gottstein, G.,.Shvinderman, L.S.: *Recrystallization and Grain Growth, Proceedings of the First Joint International Conference ,ReX&GG,* G.Gottstein and D.A.Molodov (Eds.) Springer-Verlag, Berlin, Vol.1, pp. 455-462, 2001.

Proceedings of The 1st International Conference on **D**iffusion in **S**olids and **L**iquids
DSL-2005, July 6-8, 2005, University of Aveiro, Aveiro, Portugal

THE INFLUENCE OF DIFFUSION ON HYDRATE GROWTH

Atle SVANDAL[1,*], Bjørn KVAMME[1]

[1]Department of Physics and Technology, University of Bergen, Allègaten 55, N-5007 Bergen, Norway

[*]Corresponding author. Fax: +47 55 58 94 40; Email: atle.svandal@ift.uib.no

---

Abstract

In this work we examine the rate limiting process for the formation of hydrate from aqueous solution of CO_2, and the rate limiting process when CO_2 hydrate dissociates towards pure water. A phase field theory is applied to model the growth and dissociation of the gas hydrate in a system consisting of an aqueous CO_2 phase, and an initial hydrate nucleus at constant pressure and temperature at 150 bar and 274.15 K. The diffusion of CO_2 in the aqueous phase is shown to be the governing parameter for the growth and dissociation rates. We investigate concentration profiles at the interface and shows that diffusion through Fick's law in the liquid can account for the behaviour of the system. We argue that the released heat has little or no effect on the kinetics of growth and dissociation for the systems in this study although we can not exclude the potential effect of released heat on the nucleation stage. Finally we also discuss the effects of anisotropic crystal growth on crystal morphology and kinetic rates of growth.

Keywords: Gas hydrate; Phase-field theory; Carbon dioxide; Diffusion; Nucleation

---

1 Introduction

Gas hydrates are crystalline structures in which water forms cavities that enclathrates small non-polar molecules, so called guest molecules, like for instance CO_2 or CH_4. Macroscopically the structure looks similar to ice or snow but unlike ice these hydrates are also stable at temperatures above zero °C. The enclathrated molecules stabilize the hydrate through their volume and interactions with the water molecules that constitutes the cavity walls. Hydrate can form and grow from aqueous solution of guest molecules if pressure, temperature and concentrations of these molecules are favourable. Historically the importance of hydrates has been dominated by the industrial problems related to hydrocarbon hydrate formation in equipment and pipelines during processing and transport. During more recent years the interest in hydrates has expanded in other directions. The total amount of energy related to hydrocarbons trapped in hydrate may be more than twice the amount of all known resources of coal and natural hydrocarbon sources. Historically some of the hydrate reservoirs have experienced catastrophic dissociations. One example is the Storegga slide. The largest slide in this area was created 7000 years ago and induced a tsunami that drowned Scotland. The second largest gas field outside Norway is located in the Storegga region and installation of equipment in sediments containing hydrate as well as drilling though hydrate sediments is another important issue related to hydrate stability. The stability and kinetics of hydrate depends, as indicated, on temperature and pressure as well as concentrations of all components involved the phase transition. In the present study the main focus is on growth of CO_2 hydrate from an aqueous solution and dissociation of CO_2 hydrate when exposed to pure water. This type of system is practically important for storage of CO_2 in cold aquifers. There are several regions around hydrocarbon fields with low seafloor temperatures and corresponding zones in the reservoir beneath that are inside hydrate stability. Potential leakage of CO_2 from reservoirs in these regions may be reduced by the formation of hydrate film on the interface between rising CO_2 plumes and groundwater. The kinetics and mechanisms of hydrate formation as well as hydrate dissociation towards pure water is essential in order to understand the potential leakage rates through the hydrate. Knowledge on the rate limiting mechanisms for the kinetics will make it possible to establish simplified correlations that can be implemented in reservoir modelling tools.

2 Phase field theory

A phase field theory has previously been applied to describe the formation of CO2 hydrate in aqueous solutions [1]. Here a similar version is applied to model the growth and dissociation of CO_2 hydrate. The solidification of hydrate is described in terms of the scalar phase field ϕ and the local solute concentration c. The field ϕ is a structural order parameter assuming the values $\phi = 0$ in the solid and $\phi = 1$ in the liquid. Intermediate values correspond to the interface between the two phases. Only a short review of the model will be given here. Full details of the derivation and numerical methods can be found elsewhere [1-4]. The starting point is a free energy functional:

$$(1) \qquad F = \int dr^3 \left[\frac{1}{2} \varepsilon^2 T |\nabla \phi|^2 + f(\phi, c) \right],$$

with ε a constant, T is the temperature and the integration is over the system volume. The phase field literature contains some ambiguities when it comes to the use of the terms concentration and mole fraction. In this paper we use c for concentration with units moles per volume, the mole fraction of CO_2 is termed x and is dimensionless. Assuming equal molar volume for the two components the following relation: $c = x/\nu_m$ can be applied, where ν_m is the average molar volume. The range of the thermal fluctuations is in the order of the interfacial thickness and, accordingly, ε may be fixed from knowledge of this thickness. The gradient term is a correction to the local free energy density $f(\phi,c)$. To ensure minimization of the free energy and conservation of mass, the governing equations can be written as

$$(2) \qquad \dot{\phi} = M_\phi \frac{\delta F}{\delta \phi}$$

$$(3) \qquad \dot{c} = \nabla \bullet \left(M_c \nabla \frac{\delta F}{\delta c} \right),$$

where M_c and M_ϕ are the mobilities associated with coarse-grained equation of motion, which in turn are related to their microscopic counterparts. To reproduce bulk fluid diffusion $M_c = Dx(1-x)/RT$, where $D = D_s+(D_l-D_s)p(\phi)$ is the diffusion coefficient with $D = 1.0 \cdot 10^{-9}$ m^2/s the diffusion coefficient in the liquid [5] and $D_s = 1.1 \cdot 10^{-12}$ m^2/s for the solid [6]. The local free energy density is assumed to have the form

$$f(\phi, c) = wTg(\phi) + [1 - p(\phi)] f_S(c) + p(\phi) f_L(c)$$
(4)

where the “double well” and “interpolation” functions have the forms $g(\phi) = 1/4\phi^2(1-\phi)^2$ and $p(\phi) = \phi^3(10-15\phi+6\phi^2)$, that emerge from the thermodynamically consistent formulation of the theory [4]. The parameter w is proportional to the interfacial free energy and can be deduced from experimental measurements [7] or predicted from molecular simulations of representative model systems [8]. Work along these lines is in progress [9] for the liquid water/hydrate interface. At present moment the applied value is
29.1 mJ/m^2 [7].

2.1 Fluid thermodynamics

The free energy density is calculated as

$$(5) \qquad \nu_m f_s = x \cdot g_{CO_2} + (1-x) g_w .$$

Here g_{CO2} and g_w are the partial molar free energies of CO_2 and water respectively. For the CO_2 we have

$$(6) \qquad g_{CO_2} = g^{\infty}{}_{CO_2}(T) + RT \ln\left(x \gamma_{CO_2}\right).$$

Here $g^{\infty}{}_{CO2}(T)$ is the partial molar free energy at infinite dilution, it is found from molecular dynamics simulations, and for 274.15 K it is $g^{\infty}{}_{CO2}$= -19.67 kJ/mole. R is the universal gas constant and γ_{CO2} is the activity coefficient of CO_2 in an aqueous solution in the asymmetric convention (γ_{CO2} is unity in the limit as x goes to zero) deduced from CO_2 solubility experiments and fitted to a logarithmic expansion in temperature [1]. For water we have

$$(7) \qquad g_w = g_w^{pure}(T) + RT \ln\left((1-x)\gamma_w\right)$$

Here $g^{pure}{}_w(T)$ is the partial molar free energy of pure water, Ref. [10] gives a value at 274.15 K of $g^{pure}{}_w$= -49.31 kJ/mole. The activity coefficient of water has been obtained through the Gibbs-Duhem relation.

2.3 Hydrate thermodynamics

The thermodynamics of the hydrate is based on the model by Kvamme and Tanaka [10] and van der Waals and Platteeuw [11]. The free energy is as for the liquid calculated as

$$(8) \qquad v_m f_S = x \cdot g^H_{CO_2} + (1-x) g^H_w \, .$$

The expressions for the partial molar free energies for water and CO$_2$ in hydrate are

$$(9) \qquad g^H_{CO_2} = \Delta g^{inc} + RT \ln\left(\frac{\theta}{1-\theta}\right)$$

$$(10) \qquad g^H_w = g^{0,H}_w + RT v_L \ln\left(1-\theta\right) .$$

The filling fraction of large cavities is given as $\theta = x/(v_L(1\text{-}x))$. From [10] the values of pure hydrate and partial molar inclusion of CO$_2$ at 274.15 K is $g_w^{0,H}$ = -48.46 kJ/mole and Δg^{inc} = -37.52 kJ/mole.

2.4 Saturation and equilibrium

Figure 1 shows the total molar free energies for solid and liquid as a function of the filling fraction. The coexistence point between the two phases can be calculated by the common tangent method. The same results can be obtained by solving the equations for equal chemical potential of each component in the two phases. The common tangent points thus correspond to the equilibrium mole fractions of each phase.

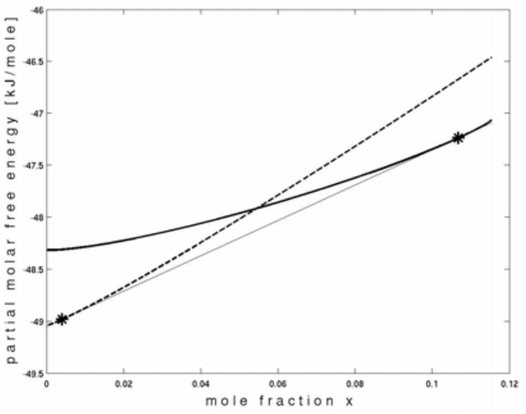

Figure 1: Molar free energies of the different phases involved in the phase transitions as function of mole-fraction CO$_2$. Solid line is hydrate, dashed line is liquid and thin line is the common tangent.

The mole fraction in the water under equilibrium is $x_a = 4.02 \cdot 10^{-3}$, and for the hydrate x_h = 0.107 marked by asterisks in Fig. 1. This defines the stability region in the mole fraction. Hydrate exposed to water within areas of stability with respect to temperature and pressure, with a higher mole fraction than x_a, will grow. Hydrate under the same condition but exposed to water with a lower mole fraction than x_a, will melt.

3 Hydrate growth and dissociation

3.1 Numerical results

The model has been implemented on a 1000x10 grid to simulate growth and dissociation of a planar surface, assuming fluxless boundary conditions at the walls. Pressure and temperature are assumed to remain constant in the system at 150 bars and 274.15 K respectively. The grid resolution is 4 Å, and the time step is $1.6 \cdot 10^{-12}$ s. Initially we start with a supersaturated CO$_2$-water solution and a hydrate film with thickness 16 nm for the growth simulation, and a 32 nm thick hydrate film exposed to pure water in the dissociation simulation. The supersaturated solution is x_s = 0.033 representing the meta-stable equilibrium between water and liquid-CO$_2$ [12]. The movement of the front is tracked by following the ϕ = 0.5 value, and the results are plotted in Fig. 2.

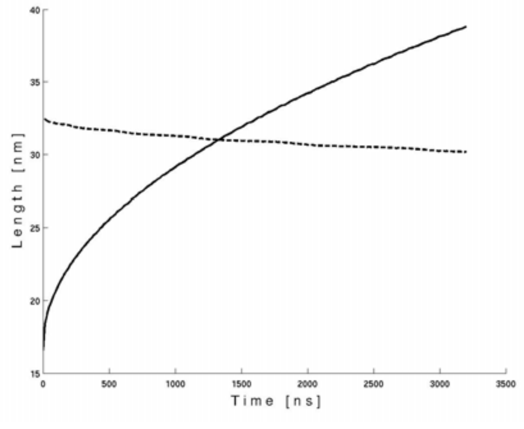

Figure 2: Position of the front as a function of time for the dissociation and growth simulation. Solid line is growth, dashed line is dissociation.

The interface under both simulations follows perfectly a power law $\propto t^{1/2}$, already indicating a diffusion controlled process. A square root function can be fitted to interpolate interface velocities at experimental time scales. After 1 s the growth rate following this function will be $v(1\text{s}) = 6$ μm/s, which is comparable to experimental results. Further discussion on this number is found in section 3.4.

3.2 Concentration profiles

To investigate further the diffusion dependence we take a closer look at the concentration profile near the interface Fig. 3 and Fig. 4.

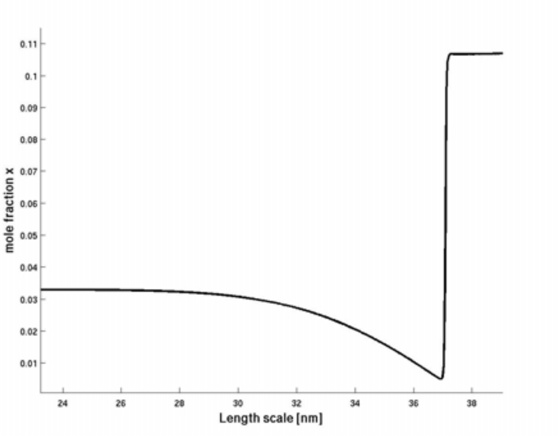

Figure 3: Concentration profile of the interface under growing conditions after 1 μs.

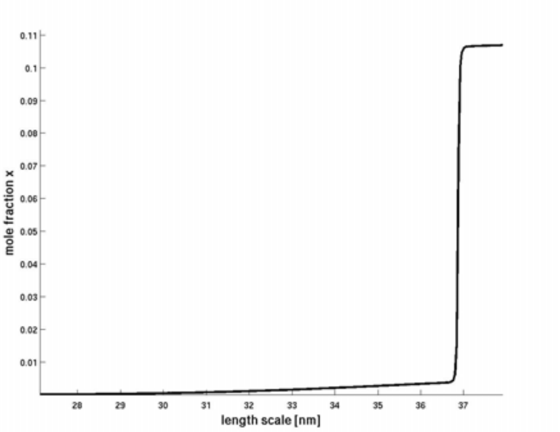

Figure 4: Concentration profile of the interface under dissociation conditions after 1 μs.

To the far left in the two figures the mole fraction equals the initial values; the CO_2 has not yet diffused to or from these regions. At the interface a minima very rapidly evolves for the growth simulation approximately at the hydrate equilibrium value x_a,. For the dissociation simulation the mole fraction in the solution approaches the x_a limit on the interface. The kinetics can be viewed as a moving local equilibrium interface where the velocity is determined by the transport of CO_2 towards or away from this interface. From the simulations we can calculate an effective flux using a Fick's law approach where the concentration gradient in the solution is used. According to Fick's law the flux can be calculated as

$$J = -D\frac{\Delta c}{\Delta x} \quad . \tag{11}$$

Taking the gradient close to the minima but in the liquid we obtain a velocity of the interface comparable to the simulated velocity. The result is shown in Fig. 5.

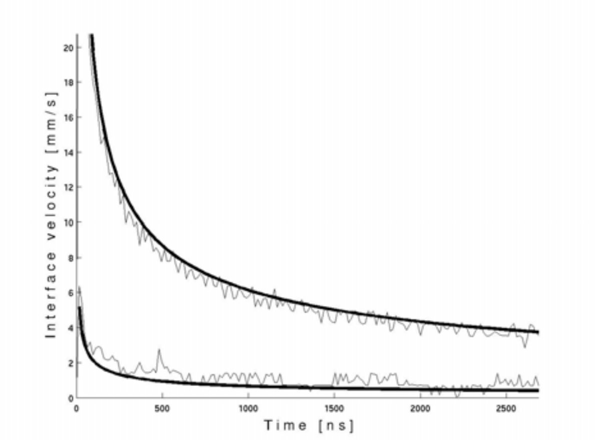

Figure 5. Absolute value of the interface velocity for the growth and dissociation simulation. Upper thick line is growth velocity, lower thick line is dissociation velocity, the thin lines are the calculated velocities.

The noise on the calculated curve is due to grid effects. These results seem to be able to account for the process of hydrate growth and dissociation, i.e. the limiting process for dissociation of hydrate is the transport of CO_2 away from the interface, likewise the growth is limited by the transport towards the interface. There are three terms in the expression for the flux in Eq. (11). The diffusion coefficient D_l in the solution is not dependent on mole fraction, we can also assume that the characteristic length Δx is the same for growth and dissociation. The difference in the concentration between the initial condition and the saturated x_a can be taken as the Δc term and will determine the flux. If we compare the growth and dissociation scenarios we see that for growth $\Delta c \propto x_s - x_a$, and for dissociation $\Delta c \propto x_a - 0$. Since $x_s > x_a$ with about one order of magnitude the growth rate should be larger than the dissociation rate, the results from Fig. 5 shows that this is a good relation giving a difference in interface velocity by the same order of magnitude. For growth or dissociation of hydrate exposed towards an aqueous solution of CO_2 and water the most important parameter then seem to be the initial fraction of CO_2 in the solution. Other parameters such as changes in driving force due to temperature or pressure changes are less important.

3.3 Temperature

The assumption of isothermal phase transition for the systems in this study is based on the relative magnitude of the thermal conductivity as compared to mass diffusivity. Some rough estimates can be made if we assume that the heat released through hydrate formation is converted into sensible heat according to Fourier's law. Our simulations are two-dimensional and if we assume that the growth is homogeneous in the direction perpendicular to the hydrate plane, z, we may write:

$$(12) \quad \frac{\partial T}{\partial z} = v_z \frac{\rho^H \Delta H}{k} \approx v_z \cdot 5.5 \cdot 10^{-7} \frac{K}{m},$$

where v_z is the hydrate growth velocity in the z direction and the approximate relationship on the right hand side is based on the following numbers and assumptions. ρ^H is the molar density of the hydrate which for complete filling is 49809 mole/m^3. ΔH is the enthalpy of the hydrate formation which is trivially calculated from the corresponding free energies of hydrate formation through standard thermodynamic relationships. The estimated value is 604 J/moles at the actual conditions, k is the thermal conductivity. The thermal conductivity of liquid water is 0.55 W/m·K at 1 °C. The value of the thermal conductivity of hydrate is similar in value. If the hydrate film is on the interface between liquid CO_2 and aqueous phase we may approximately assume heat flux only into the aqueous phase due to the low heat conductivity of CO_2. From the simulated results plotted in figure 2 the growth rate decays from 6 mm/s after 1 microsecond to 0.006 mm/s after 1 s. Within the approximate nature of these estimates the temperature change during the first 4 nm of hydrate growth is thus less than 10^{-16} K and even relatively smaller for subsequent stages of growth. The assumption of isothermal phase transitions for the systems presented in this study is therefore considered to be appropriate.

3.4 Anisotropy

In contrast to isotropic growth where the two model parameters ε and w are fixed through information on the interfacial properties there is no similar theoretical relationship to relate anisotropic crystal growth. On the other hand, at the cost of a few empiric model parameters the phase field approach has proven [2, 3] to be able to reproduce the growth of many experimentally observed crystal structures. The relative impact of these oriental effects on kinetic growth rates and kinetic limiting contributions is an important issue. For this purpose Eq (1) is extended with an oriental field [2], and the constant ε is assumed to be directional dependent, expressed as

$$(13) \quad \varepsilon \rightarrow \varepsilon' \left[1 + \frac{s_0}{2} \cos\left(n\vartheta - 2\pi\theta \right) \right].$$

Here s_0 is the anisotropic amplitude, n is the symmetry, θ is the introduced orientation field and $\vartheta = \arctan[(\nabla\phi)_y/(\nabla\phi)_x]$. Running the anisotropic simulation results in a dendritic structure shown in Fig. 8.

Figure 8: Anisotropic growth of hydrate.

The interface velocity for dendritic growth should theoretically approach a constant value. The results from our anisotropic simulations yield a faster growth rate than the isotropic deviating more and more from a square root law as the system evolves. The simulations are unfortunately computationally expensive, and we have not yet been able to achieve such convergence.

4 Conclusions

According to the results obtained from phase field simulations in this study, the growth and dissociation of carbon dioxide hydrates are shown to be governed by the diffusion of carbon dioxide in the aqueous phase. The most important parameters when it comes to the growth and dissociation rate will be the initial mole fraction of CO_2 in the aqueous phase. This result gives us a simple and valuable qualitative understanding of the process that should be taken into account when quantities as growth and dissociation rates are measured in experimental setups. These processes are also of particular interest relative to storage of CO_2 in cold aquifers where the formation of a hydrate film might induce extra stabilisation to the storage. The CO_2 leakage will then be determined by the dissociation of the hydrate film.

Acknowledgments

We thank Laszlo Granasy for sharing his experience and work on the phase field theory. We also like to thank Trygve Buanes and Joakim Hove for fruitful discussions. Financial support from the Norwegian Research Council through project 101204, and from Conoco-Phillips, is highly appreciated.

References

[1] Kvamme B., Graue A., Aspenes E., Kuznetsova T., Grànàsy L., Tòth G., Pusztai T. Tegze G.: Kinetics of solid hydrate formation by carbon dioxide; Phase field theory of hydrate nucleation and magnetic resonance imaging. *Phys. Chem. Chem. Phys.*, 6, 2327, 2004.

[2] Grànàsy L., Börzsönyi T., Pusztai T.: Nucleation and Bulk Crystallization in Binary Phase Field Theory, *Phys. Rev. Lett.,* 88, 206105, 2002.

[3] Warren J.A., Boettinger W.J.: Prediction of dendritic growth and microsegragation patterns in a binary alloy using the phase-field method. *Acta metall. Mater.,* 43, 689-703, 1995.

[4] Wang S.L., Sekerka R.F., Wheeler A.A., Murray B.T., Coriell S.R., Braun R.J., McFadden G.B.: Thermodynamically-consistent phase-field models for solidification. *Physica D*, 69, 189-200, 1993.

[5] Rehder G., Kirby S.H., Durham W.B., Stern L.A., Peltzer E.T., Pinkston J., Brewer P.G.: Dissolution rates of pure methane hydrate and carbon-dioxide hydrate in undersaturated seawater at 1000-m depth. *Geochemica et Cosmochimica Acta,* 68, 285-292, 2004.

[6] Radhakrishnan R., Demurov A., Herzog H., Trout B.L.: A consistent and verifiable macroscopic model for the dissolution of liquid CO_2 in water under hydrate forming conditions, *Energy Conversion and Management*, 44, 771-780, 2003.

[7] Hardy, S. C. *Philos. Mag*., 35, 471, 1977.

[8] Davidchack, R. L.; Laird, B. B. *J. Chem. Phys*, 108, 9452, 1998.

[9] Kuznetsova, T, Kvamme, B., *work in progress*, 2005

[10] Kvamme B., Tanaka H.: Thermodynamic Stability of Hydrates for Ethane, Ethylene, and Carbon Dioxide. *J. Phys. Chem.*, 99, 7114-7119, 1995.

[11] Waals, J.H.v.d., Platteeuw, J.C.: Clathrate solutions, *Advances in Chemical Physics*, 2, 1-57, 1959.

[12] Diamond L.W., Akinfiev N.N.: Solubility of CO_2 in water from -1.5 to 100 °C and from 0.1 to 100 MPa: evaluation of literature data and thermodynamic modelling. *Fluid Phase Equilibr.*, 208, 265-290, 2003.

Proceedings of The 1st International Conference on Diffusion in Solids and Liquids
DSL-2005, July 6-8, 2005, University of Aveiro, Aveiro, Portugal

THE ROLE OF GRAIN BOUNDARY DIFFUSION IN INITIAL SELECTIVE OXIDATION KINETICS OF A Mn/Al TRIP STEEL

Casper THORNING*, Seetharaman SRIDHAR

Department of Materials Science and Engineering
Carnegie Mellon University, Pittsburgh, PA 15213, USA

*Corresponding author. Email: ctmr@andrew.cmu.edu

Abstract

Confocal Scanning Laser Microscopy (CSLM) was used in real-time observation of alloy element oxidation of a Mn / Al TRIP steel. CSLM images reveal a marked role of grain boundaries in the overall initial oxidation kinetics of the alloy, and consequently in the morphology of the initial surface oxide. Changing *a):* the grain size and *b):* the oxidation temperature results in a change in the overall kinetics of selective oxidation and in the importance of oxidation at grain boundaries respectively. A combination of serial sectioning and Electron Back Scattering Diffraction (EBSD) mapping was employed to fully characterize the grain boundaries intersecting the surface over an area of the alloy. Subsequent CSLM observation of selective oxidation over the same area allowed quantification of oxidation kinetics as a function of individual grain boundary characteristics and grain orientation.

Keywords: TRIP-steel; Selective oxidation; Grain boundary

1 Introduction

The exposure of an alloy to an atmosphere containing oxygen (O) can generally be illustrated as in Fig. 1. The alloy consists of a base metal, A, with one or more alloying elements (B and C) in solid solution. The alloy is in contact with an atmosphere with an oxygen potential, pO_2. In the case that the pO_2 is high enough for oxides of all the elements A, B and C to form, the following mechanisms of formation of oxide compounds are possible.

The base metal, A, is in direct contact with the oxidizing gas and an oxide compound A_xO_y forms on the surface of the alloy. The rate limiting step is initially the supply of O from the surrounding atmosphere. As shall be discussed later, this supply may be controlled by the oxidation of B or C if any of these have a higher affinity to O than does A. When the oxide of A has grown sufficiently to form a coherent layer across the surface of the alloy, thus separating the unreacted A and O, diffusion of these species through the oxide layer becomes rate limiting to further growth.

Alloying elements B and C may form oxides on reaction with O, either externally at the surface of the alloy (B in Fig. 1) or internally, below the original surface of the alloy (C in Fig. 1). Whether an alloying element oxidizes internally or externally depends on: The pO_2 of the oxidizing gas, the concentration of the alloying element in the alloy, the diffusivity of O in the alloy and the diffusivity of the alloying element in the alloy.

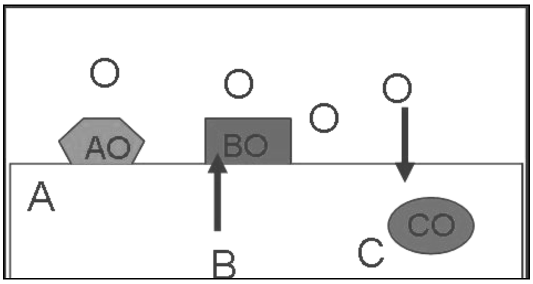

Figure 1: Schematic of alloys oxidation.

If we regard alloying element B, the criterion for external oxidation can be given as [1]:

$$N_B^{(0)} > \left[\frac{\pi g^*}{2\nu} N_O^{(S)} \frac{D_O V_m}{D_B V_{OX}} \right] \qquad (1)$$

Here, $N_B^{(0)}$ is the concentration of B in the alloy, $N_O^{(S)}$ is the solubility of O in base metal A, D_o and D_B are the diffusivities of O and B in A respectively, g^* a critical value of the volume fraction of oxide $g = f\left(\frac{V_{OX}}{V_m}\right)$, V_m is the molar fraction of oxide BO_υ in the internally oxidized zone. $N_O^{(S)}$ is directly related to pO_2 in the oxidizing atmosphere.

From Eq. 1, it can be predicted of how the exposure conditions affect the transition from internal to external oxidation: External oxidation may be promoted through increasing the concentration of the oxidizing element, $N_B^{(0)}$, increasing the diffusivity of the oxidizing element, D_B , and / or lowering the pO_2 (= lowering $N_O^{(S)}$). The former two measures increase the outward flux of B, while the latter reduces the inward flux of oxygen.

Increasing D_B has mainly been proposed through reducing the grain size of the alloy, thus increasing high diffusion grain boundary area. It is observed that substrate microstructure has a significant influence on selective oxidation kinetics [2-7]. In an interesting way, two opposite trends of this correlation are observed. In pure metals, oxidation rates increased in cold worked specimens, the increased being attributed to dislocations acting as vacancy sinks. In Fe based alloys containing Cr, decreased oxide growth rate is observed with decreasing grain size when oxidized at high temperature in atmospheres oxidizing both Fe and Cr [3-6]. An explanation for this observation is that the increased grain boundary area in the small grained samples, acting as high diffusion paths, offers an increased supply of Cr to the oxidation front. A protective layer of chromium oxide was then more rapidly established on the smaller grain samples, reducing the overall oxidation rate through suppression of oxidation of Fe. An identical conclusion was drawn from similar experiments on NiCrAlY alloys [2].

Several careful investigations have shown a heterogeneous oxidation behaviour of alloys, with oxidation at the grain boundaries of different chemistry and kinetics than that of the grain interior surfaces, leading to modifications of Eq. 1 to accommodate the greater D_B at grain boundaries [8]. One obstacle to such an analysis is the lack of data on the diffusivity of substitutional solutes in grain boundaries. As a further complication, solute diffusivity along grain boundaries is observed to be strongly dependent on the character of the grain boundary. Data that correlate the grain boundary character and diffusivity has been reviewed by Sutton and Balluffi [9], and has mainly been conducted for special types of grain boundaries, such as pure tilt or pure twist boundaries, where the atomic structure can be more readily understood. Grain boundary diffusivity is observed to decrease markedly at coincidence site lattice boundaries in fcc metals, where grain boundary energy and grain boundary free volume is low. However, diffusivity data is limited for random boundaries and for lattices other than fcc.

The purpose of the present investigation is to provide in situ observation of the relative kinetics of oxidation at grain boundaries and grain interior surfaces as a function of temperature and grain size in order to probe the mechanisms mentioned above. Further, an attempt is made to correlate the oxidation rate, as a measure of diffusivity, to grain boundary misorientation at a wide range of grain boundaries. Finally, a suggestion is given to how the methods employed in the present study may be expanded to correlate grain boundary diffusivity to the full characteristics of individual grain boundaries.

2 Experimental

2.1 Material Composition and history

A TRIP steel of composition, 0.144wt% C, 1.81 wt% Mn, 0.069 wt% Si and 1.57 wt% Al was melted in a vacuum furnace and cast into 5 x 12 in. steel molds. The steel was hot rolled in seven passes at 1280°C down to 1 inch thickness with the final pass temperature being about 900°C. Subsequent to hot rolling the sample was reduced in thickness by 25% by milling to avoid surface segregation effects. The steel was then cold rolled to a final thickness of 1.6 mm. The grain size of the specimens in this condition was approximately 5 micrometer and is referred to as fine grains below. In order to study the effect of grain size some specimens were annealed in H_2 at 1050°C for 2hrs. followed by furnace cool, resulting in a coarsening of the grain size to approximately 20 micrometers. These are referred to as coarse grains below.

2.2 Experimental procedure

Sample surface crystallography was measured in the coarse grain samples by EBSD at room temperature using a TSL system. A CSLM equipped with a gold-plated high temperature furnace was used to image oxide growth on the sample surface real-time. The specimens were heated in argon to 720°C at or 800˚C at 10°C / sec. and held. The pO_2 in the inlet and outlet gasses was measured to $10^{-4.8}$. CSLM combines confocal optics and He-Ne laser illumination to make possible observation of samples at high resolution at elevated temperatures. It has been described in detail in the literature previously [10]. The confocal optics enables the (i) detection of a strong signal from the focal plane while (ii) decreasing the intensity of signals not in the focal plane. Thus the contrast from surface topography is enhanced. The utilization of a laser results in high illumination intensity compared to the thermal radiation.

3 Results

3.1 Image analysis

Typical CSLM micrographs of the surface of an oxidizing specimen can be seen in Figs. 2a, 4, 5 and 6b. In order to properly interpret the developments that are shown in the images, an understanding of image formation in the CSLM is required. The CSLM makes use of the same optics and the same optical principles as a light optical microscope (LOM), but there are differences in the way contrast is formed. The more coherent laser light employed in the CSLM allows an accurate discrimination of reflected light. To this end, a plate with a pinhole is placed in front of the detector, which only allows light reflected from planes very close to the focal plane to pass and be detected. Light reflected from points on the specimen surface not in the focal place is excluded from the images, and such points appear black in the images, as opposed to LOM where objects away from the focal plane become increasingly diffuse. The resolution of this discrimination of reflected light is approximately 100 nanometers. The advantage of this method of contrast formation is that it becomes easy to observe the evolution of oxides that form as particles on the specimen surface. However, attention must be paid, as can be seen from a comparison between Fig. 2 a and b. The figures show a CSLM (2a) and a scanning electron (SEM) micrograph (2b) of the same area of a Mn/Al TRIP steel specimen oxidized under the above conditions. In Fig. 2a, all the boundaries appear dark compared to the grain interior, suggesting that a ridge of oxides exists along all boundaries, higher from the samples surface than the individual oxides in the grain interior surfaces. Comparison with Fig. 2b shows that this is not the case. Some of the boundaries that appear dark in the CSLM image have no oxide ridges along them, and indeed seem less oxidized that the bounding grain interior surfaces.

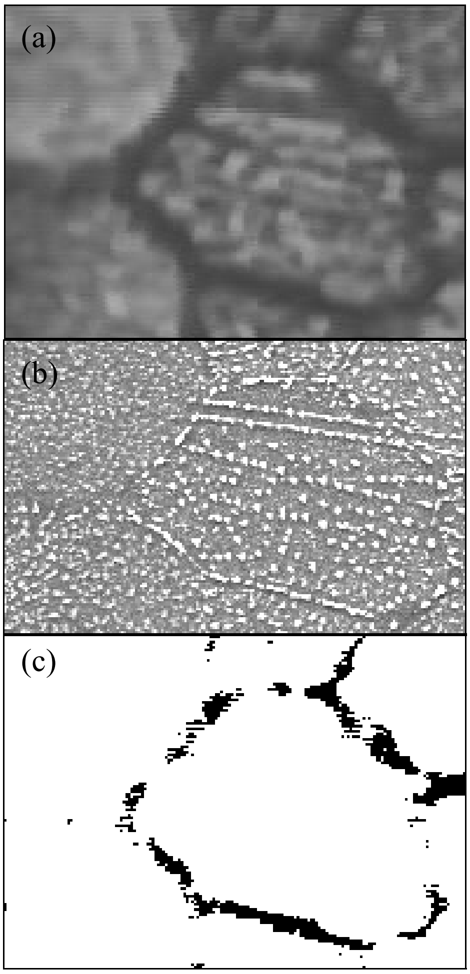

Figure 2: a) CSLM image of a coarse grained sample oxidized at 720˚C. b) SEM SE image of the area showed in a). c) Binarized version of a).

With the surrounding grain surfaces oxidized, the not oxidized GBs form a relative valley and, with the focal plane of the CSLM positioned to maximize reflection from the surface as a whole, they appear dark. The accurate relation between surface topography and image contrast may be exploited to distinguish between grain boundaries with oxide ridges and those without. Figure 2c shows a digitally binarized version of Fig. 2a. By choosing the correct brightness discriminator, only the grain boundaries show which can be identified as having oxide ridges in Fig. 2b. This method allows a faster way to identify oxidized grain boundaries and has been employed in obtaining the observations below in all cases where there was ambiguity. Comparison between figures 2 a,b and c further yields the observation that the topographical resolution is much greater in the CSLM micrographs (2a) compared to the SEM micrographs (2b). In the SEM micrographs, the difference in oxide particle height from the substrate between the oxide ridges on the GBs and the oxide particles in the grain interior surfaces is not well observable, whereas this difference stands out clearly in Fig. 2a and c.

3.2 Auger Electron Mapping

Auger electron maps of the surface chemistry of a typical (small) grain are provided in Fig. 3 along with a SEM secondary electron micrograph of the same area (Fig. 3a).

Elements Mn, Fe, Al and O are mapped in Figs. 3 b – e. The maps suggest a heterogeneous distribution of oxides across the specimen surface with Mn oxides forming oxide ridges on the grain boundaries and Fe oxides forming individual particles on the grain interior surfaces. An area of grain boundary at in Fig. 3a shows a high concentration of Mn although there is no oxide ridge observed on that part of the grain boundary, suggesting that the formation of Mn oxide ridges is preceded by an increase of Mn in the grain boundary or that the conditions allow internal oxidation of Mn at that part of the boundary. A fairly uniform distribution of Al across the surface suggests that none of the discreet particles on the specimen surface are Al rich compounds, but the relative weakness of the O signal in areas with high Mn or Fe would suggest that Al has formed an oxide, either internally or as a homogeneous layer below the particles of Mn oxides and Fe oxides.

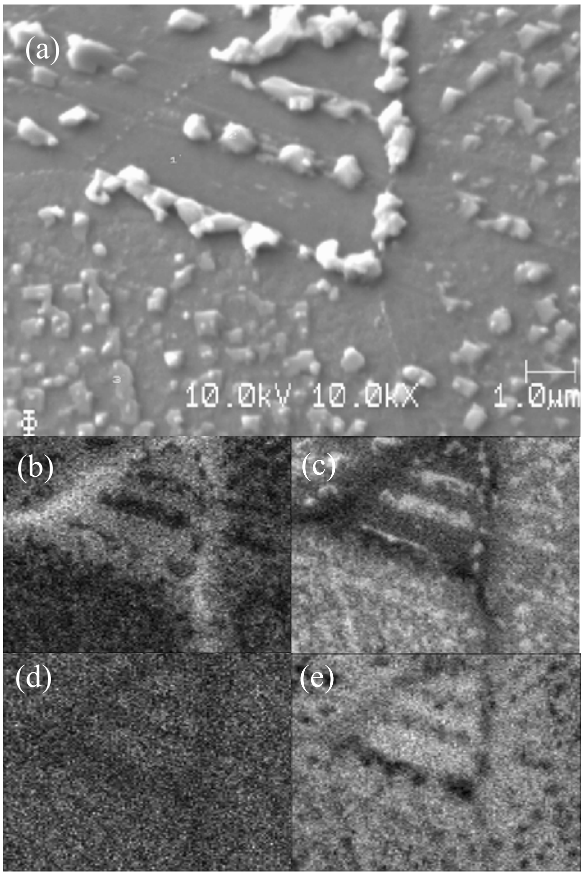

Figure 3: Auger Electron Maps of element distribution on the surface of a coarse grained samples oxidized at 720˚C. a) SEM SE image, b) Mn, c) Fe, d) Al, e) O.

3.3 Effect of temperature

Figure 4 a-c shows CSLM micrographs at 5 sec. intervals of a coarse grained sample oxidizing at approximately 810˚C. The formation of oxide ridges is observed at all grain boundaries, but obvious differences are observed in the kinetics and to some degree in the morphological development between the boundaries. In the first image (4a), no coherent oxide ridges are observed. In the second image (4b) detectable oxides appear on many, but not all boundaries. Fig. 4b shows how the oxides form as on the boundaries as individual particles first, and a comparison of Figs. 4 b and c shows the morphological development of grain boundary oxides from individual particles dressing the boundaries, then coalescing to form the coherent ridges observed in Fig. 4c.

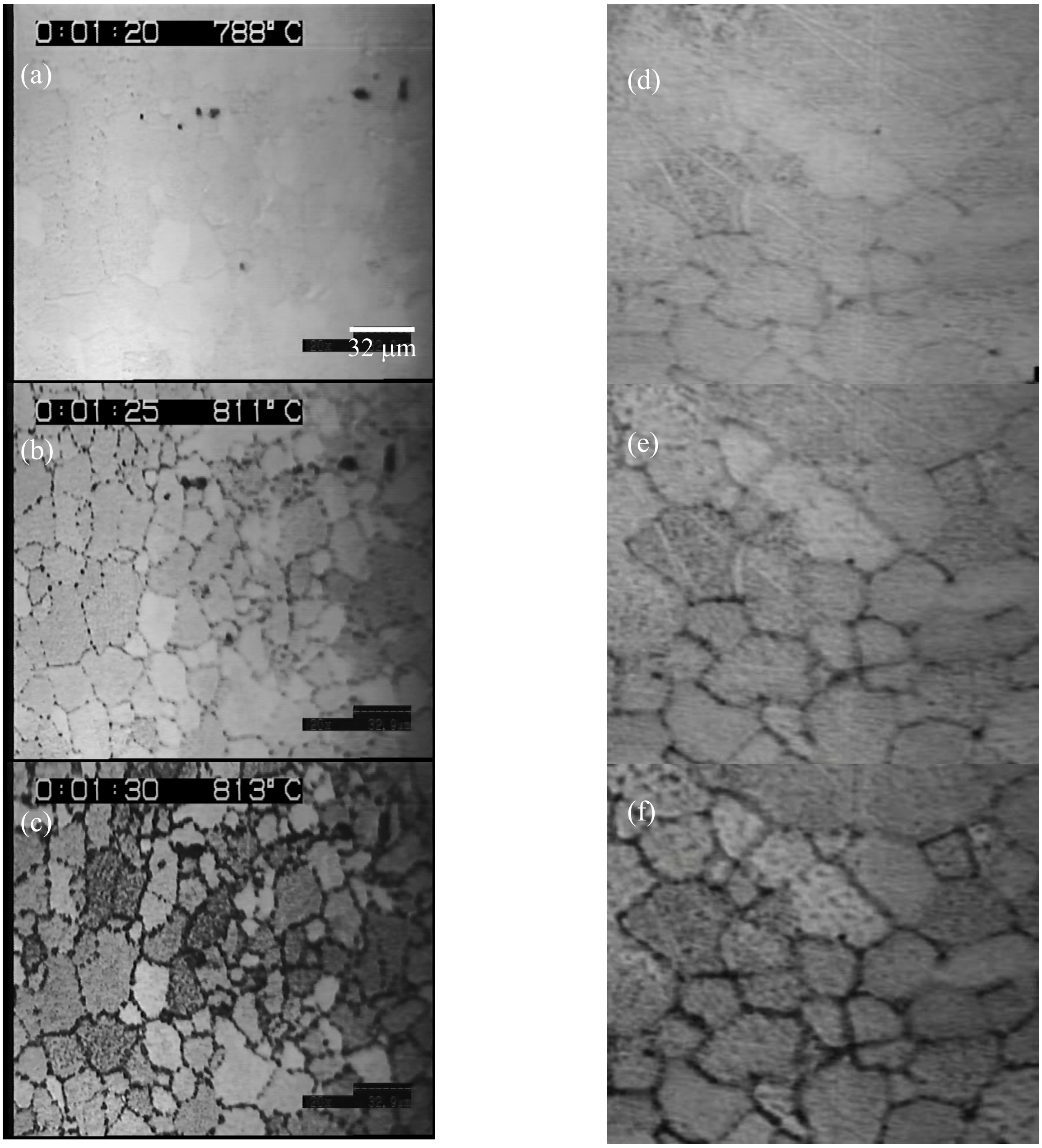

Figure 4: a – c show a coarse grained sample oxidizing at 800˚C, captured at 5 second intervals. d – f show a coarse grained sample oxidizing at 720 ˚C, captured at 50 second intervals.

In Fig. 4c, coherent ridges have not formed on all boundaries, some boundaries showing individual oxide particles.

Figure 4 d –f show CSLM micrographs at 50 sec. intervals of a coarse grained sample oxidizing at approx. 720˚ C. The overall kinetics of oxidation is observed to be slower than that observed in Fig. 4 a - c as might be expected. The morphological development of grain boundary oxidation observed in Fig. 4 d - f is similar to that observed in Fig. 4 a – c with oxidation starting at boundaries as discrete particles, which coalesce into coherent ridges. A marked difference between the behaviour observed in Fig. 4 a - cand that observed in Fig. 4 d - f is that in the latter, many boundaries are not dressed with oxides. Figure 6 c shows a binarized version of Fig. 4f, allowing easy identification of boundaries with oxides.

3.4 Effect of grain size

Figure 5 a – c shows CSLM micrographs at 30 and 20 second intervals of a cold rolled, fine grained sample oxidizing at 720˚C. The oxide development at the grain boundaries is markedly different in these images compared to that observed for the coarse grained samples above. While the development of oxides at the grain boundaries still appear in the form of particle growth and coalescence, only few boundaries show rich oxidation. The relative kinetics of oxidation at grain boundaries vs. grain interior surfaces is also different from that observed in Fig. 4 and 3.V. In Fig. 4, oxides appear at grain boundaries relatively late compared to oxides at the grain interior surfaces.

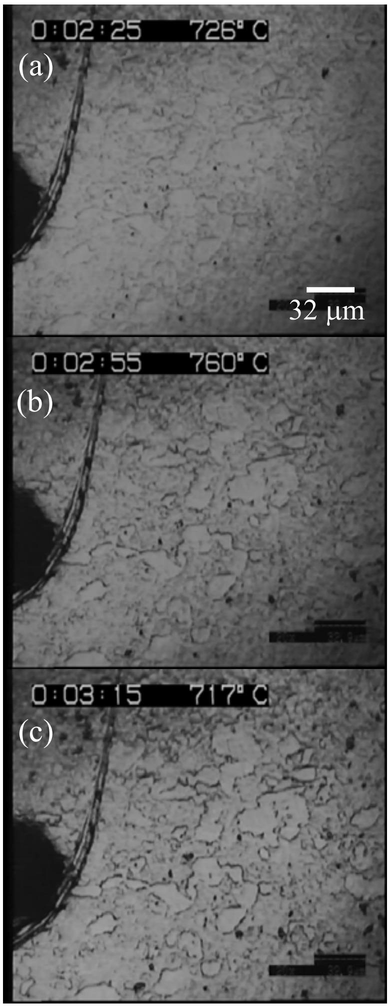

Figure 5: Fine grained specimen oxidizing at 720˚C.

X-Ray Diffraction analysis of fine grained specimens oxidized under the above conditions showed no presence of Fe – oxides, but marked peaks for MnO and Al_2O_3.

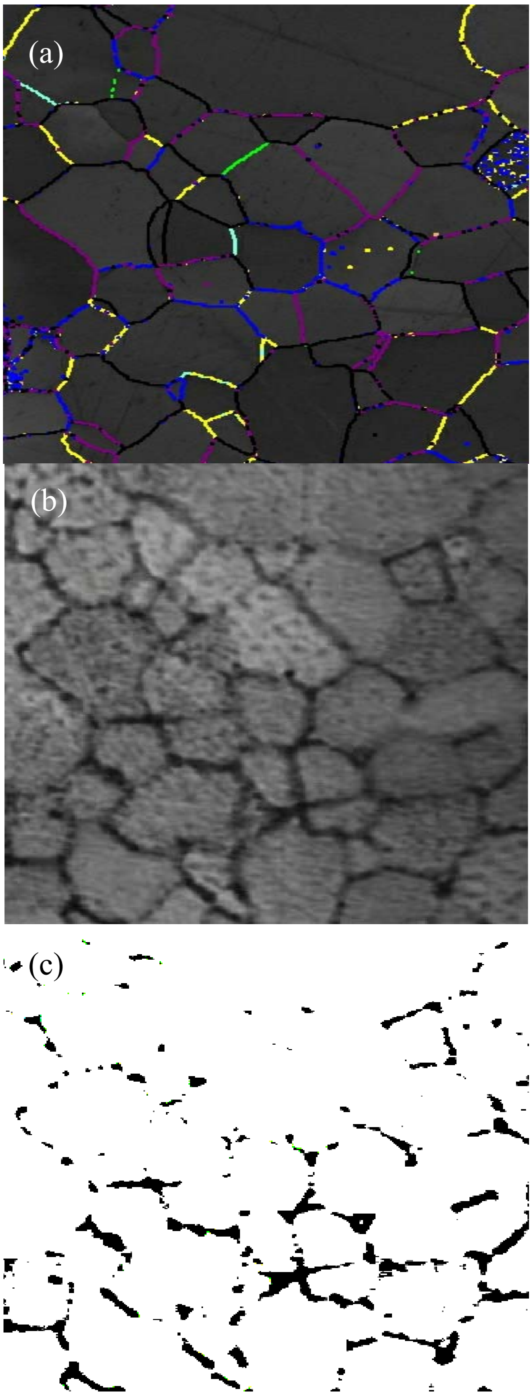

Figure 6 a) shows grain boundaries colored according to the misorientation that they represent in the following intervals: 5˚ - 10˚ green, 10˚ - 15˚ turquoise, 15˚ - 20˚ orange, 20˚- 30˚ yellow, 30˚- 40˚ blue, 40˚- 50˚ violet and 50˚ - 62.5˚ black
b): shows a series of CSLM micrographs of the TRIP steel during oxidation at 720˚C
c): shows a binarized version of b), allowing easy identification of boundaries with oxides.

3.5 Correlation between grain boundary oxidation and grain boundary misorientation.

Figure 6 a) shows a map of grain boundary misorientations in the specimen presented in fig. 4 d - f. No clear tendency can be derived from a correlation between the misorientation angle of a grain boundary and the oxidation at that boundary, except that no low angle boundaries (< 15˚) have oxide ridges forming at their intersection with the specimen surface.

4 Discussion

The above images provide in situ observation of the relative roles of selective oxidation through grain boundary diffusion and grain surface interior oxidation, and may in a broad sense confirm the mechanisms that have been proposed in literature [2-8].

The overall kinetics and morphological development of surface oxides appears heavily influenced by the grain boundary diffusion of solute elements to the alloy surface. A mechanism as illustrated in Fig. 7 may be derived from the observations in Fig. 4. Mn is brought to the surface almost exclusively through the grain boundaries, forming ridges of Mn oxides along the grain boundaries. Al oxidizes internally, leaving the alloy surface free for Fe oxides to be formed.

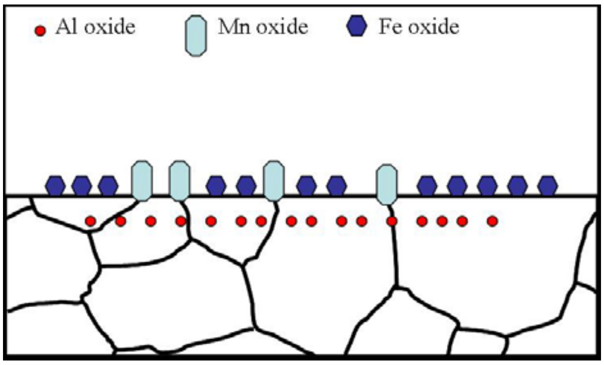

Figure 7: Schematic of possible oxide morphology.

Changing the grain size of a sample seems to have a pronounced effect, not only on the morphological distribution of the oxides, which would be expected if the mechanism in Fig. 5 was repeated for a smaller grain size, but also the chemistry of the oxide products that are formed in the fine grained alloy is different from the one in the coarse grained alloy, with no Fe oxides formed in the fine grained one. Alternative explanations can be offered for this observation. Close inspection of Fig. 5 reveals a pattern of oxidation in which ridges of Mn oxide enclose grains with entirely unoxidized surfaces. This suggests that a local equilibrium is established at the surface by the reaction of Mn and O. Due to the short distance between grain boundaries intersecting the surface in the fine grain sample, no place on the specimen surface is far enough removed from the reaction of Mn and O not to be affected by the local equilibrium. Thus Fe oxides can not form on the surface. The portions of the surface which shows some affect of oxidation outside the grain boundary ridges, may be Mn oxides appearing at the surface by diffusion through the lattice or dislocation pipes. However, a mechanism of local equilibrium would suggest that a similar absence of Fe oxides could be observed on the coarse grain specimens in Fig. 4 at least within a distance from the grain boundary oxide ridges corresponding to half the grain diameter in the small grain specimen. But no such Fe oxide depleted zone is observed in Fig. 4. Further, Fig. 6 shows no diffusion of Mn to the surface through low angle grain boundaries, which makes it unlikely that Mn oxides can account for the oxidation observed at grain interior surfaces in Fig. 3.4. An alternative explanation would be that the much increased grain boundary area in the small grain sample compared to the coarse grain sample changes the balance of internal and external oxidation for Al_2O_3, promoting external oxidation of Al according to equation 1. In this case the formation of Al oxide on the sample surface would prohibit the formation of Fe oxide.

Increasing the temperature of oxidation of the coarse grain sample results in an increase in the number of boundaries exhibiting oxidation. At 720 ˚C, the formation of Mn oxide ridges is absent at many boundaries. While this is not the case at 800 ˚C, a marked difference is observed between boundaries in the kinetics of Mn oxide ridge formation. This strongly suggests a correlation between grain boundary crystallography and grain boundary diffusivity in accordance with observations by other investigators [9]. Figure 6 demonstrates that one parameter of the grain boundary, the misorientation, is not enough to investigate the nature of such a correlation in the random boundaries present in these specimens, in contrast to the pure twist or pure tilt boundaries investigated in the past. We therefore propose an expansion of the current method of combined EBSD mapping and CSLM observation to include serial sectioning as described by Randle [11] in order to fully characterize the grain boundaries. Removal of a layer of well defined thickness parallel to the sample surface allows tracking of individual grain boundaries and the identification of the grain boundary inclination to the sample surface. Combined with identification of crystal orientation by EBSD, the full five parameters of the grain boundaries may be extracted. Subsequent observation of oxidation through CSLM, as above, is expected to enable correlation between grain boundary crystallography and grain boundary diffusivity. A similar approach has been successfully applied in the past to the study of wetting of grain boundaries in Fe with Cu [12].

5 Conclusions

The oxidation of Al-rich TRIP steel was investigated and the results suggest that:

1. Al_2O_3 forms internally, while Mn and Fe oxides form on the sample surface.
2. Mn-oxides form preferentially at certain grain boundaries as a result of rapid diffusion. Low angle boundaries appear to be less oxidized, especially at lower temperatures. No apparent correlation was found between grain boundary misorientation and oxidation kinetics for high-angle boundaries.
3. Grain boundary oxidation precipitates as discrete particles, which coalesce into coherent ridges.
4. Fe-oxides tend to form at grain interiors but to a lesser degree at a smaller grain size.

6 Acknowledgements

The research results presented in this paper were supported by funds from the National Science Foundation under grant DMR-0307188.

7 References

[1] N. Birks and G.H. Meier: *Introduction to High Temperature Oxidation of Metals*, Edward Arnold Ltd., London 1983.

[2] J.G. Goedjen and D. A. Shores: *The Effect of Alloy Grain Size on The Transient Oxidation Behavior of an Alumina-Forming Alloy*, Oxidation of Metals, Vol. 37, nos. 3-4, pp. 125 – 142, 1992.

[3] M. D. Merz, *The Oxidation Resistance of Fine-Grained Sputter Deposited 304 Stainless Steel*, Met. Trans. A, Vol. 10A, pp. 71-77, 1979.

[4] M.K. Hossian, *Effects of Grain Size on the High Temperature Oxidation of an Fe-10% Cr Alloy*, Corr. Sci., Vol 19, pp. 1031 – 1045, 1979.

[5] R.K. Singh Raman et al.: *Influence of Grain size on the Oxidation resistance in 2¼Cr – 1Mo Steel*, Oxidation of Metals, Vol. 37, nos. 1-2, pp. 1 – 12, 1992.

[6] D. R. Baer and M.D. Merz: Differences in Oxides on Large- and Small-Grained Stainless Steel, Met. Trans. A, Vol. 11A, pp. 1973 – 1980, 1980.

[7] D. Caplan and M. Cohen: *Scaling of Iron at 500 deg. C*, Corr. Sci., Vol. 3, pp. 139-143, 1963.

[8] J.M. Mataigne et al.: Selective Oxidation of Cold-Rolled Steel during Recrystallization Annealing, Developments in the Annealing of Sheet Steels, R. Pradhan and I. Gupta (eds.), TMMS, 1992.

[9] A.P. Sutton and R.W. Balluffi: *Interfaces in Crystalline Materials*, Oxford University Press, 1995.

[10] S. Sridhar, P.D. Lee and P. Rockett, *AFS Transactions*, 110, pp. 147-158, 2002.

[11] V. Randle: Crystallographic Characterization of Planes in the Scanning Electron Microscope, Mat. Char.. 34 (1): pp. 29-34, 1995.

[12] M. Takashami et al.: Correlation of Grain Boundary Character with Wetting Behavior, Interface Science, 8, pp. 351-361, 2000.

Proceedings of the 1st International Conference on **D**iffusion in **S**olids and **L**iquids
DSL-2005, July 6-8, 2005, University of Aveiro, Aveiro, Portugal

EFFECT OF ALKALI AND BORON CONTENT ON DIFFUSION OF CESIUM IN BOROSILICATE GLASS

Bhupendra S. TOMAR[1,*], Sumit KUMAR[1], Vijay K. MANCHANDA[1], Vilas K. SHRIKHANDE[2], Shobha MANIKANDAN[2], Govind P. KOTHIYAL[2]

[1]Radiochemistry Division, Bhabha Atomic Research Centre, Mumbai 400 085, INDIA
[2]Technical Physics and Prototype Engineering Division, Bhabha Atomic Research Centre, Mumbai 400 085, INDIA

*Corresponding author: Fax: 91-22-25505345; Email: bstomar@apsara.barc.ernet.in

Abstract

Diffusion coefficients for diffusion of cesium in borosilicate glasses of different sodium and boron contents have been measured by heavy ion Rutherford backscattering spectrometry using 30MeV ^{19}F beam. The activation energy (E_a) of cesium diffusion was found to be in the range of 10-22 kJmole^{-1}, with the E_a value decreasing with increasing sodium content. The results have been explained in terms of the ion exchange mechanism for leaching of metal ions from glass.

Keywords: Diffusion in crystalline and amorphous materials; Experimental methods; Heavy Ion Rutherford Backscattering Spectrometry; Cesium; Borosilicate glass; Accelerators

1 Introduction

Management of high level waste (HLW) generated during the reprocessing of spent nuclear fuel is one of the top priorities of nuclear industry the world over. One school of thoughts proposes to separate the long-lived radionuclides (particularly actinides) from HLW and transmute them into shorter lived fission products using the Accelerator Driven Subcritical (ADS) system [1]. However**,** the most accepted view has been to immobilize the long lived fission products, viz., ^{137}Cs, ^{90}Sr, ^{99}Tc, ^{129}I etc., and actinides viz., ^{237}Np, ^{239}Pu, ^{240}Pu, ^{241}Am, ^{243}Am, etc., into suitable glass matrix or synrock matrix, which after interim storage at the surface can be buried in deep geological repository so that the probability of leaching of these radionuclides into the environment is minimized [2]. Among the different glass matrices, borosilicate glass is considered to be one of the most suitable matrices for immobilization of long lived radionuclides [3]. However, the possibility of leaching of radionuclides due to the decay heat generated during the radioactive decay of these radionuclides cannot be ruled out. Diffusion of long lived radionuclides may be further enhanced by the defects created due to the alpha decay of actinides. Hence there is a need to study the long term behaviour of radionuclides in the glass matrix.

In the past studies on leaching behaviour of long lived radionuclides from glass matrix have been carried out using radiotracer technique [4], ion beam analysis [5], low energy ion scattering [6] and concentration couple method [7]. Though the radiotracer method is the most commonly used method for diffusion in solids, it requires the sectioning of the different layers of the glass sample to determine the depth profile of the radioisotope. In this method a thin layer of the radionuclide is generated near the surface either by drying the solution on the surface of the glass sample or ion implantation of the radionuclide. Another radiotracer method uses the generation of the radiotracer in-situ by irradiating the glass sample in a nuclear reactor and producing the radionuclide by (n,γ) reaction [8]. Recently we have used heavy ion Rutherford backscattering spectrometry (HIRBS) technique to study the diffusion of cesium in borosilicate glass of typical composition [9]. HIRBS has been used to study the diffusion of heavier elements in low Z matrices [10]. The methodology of HIRBS is based on applying a thin layer of the element of interest on the surface of the sample and annealing it at different temperatures for a fixed length of time. The depth profile of the diffusing element is measured by RBS using heavy ion as a beam. The HIRBS has advantages over conventional RBS that it provides better depth resolution (owing to higher linear energy transfer) and better mass resolution due to large variation in the kinematics factor (K) with mass number.

In the present paper we report the results of the measurement of diffusion coefficient of cesium in borosilicate glasses of varying sodium and boron content. According to the Doremus model [11] the leaching of soluble elements from glass is governed by inter diffusion between the soluble elements and hydrogen, which has been corroborated by the study of sodium diffusion in sodalime glasses by Landford et al. [12]. In order to optimize the composition of the borosilicate glass matrix it is important to understand the effect of the constituent elements on the rate of diffusion of the radioelement. Boron is a glass former and it reduces the glass transition temperature. On the other hand introduction of sodium is required to maintain the electrical neutrality of the matrix. However, excess of sodium may modify the structure of the glass and hence the rate of diffusion of cesium.

2 Experimental

Preparation of glass samples: Table 1 gives the composition of the glass samples studied.

Table 1: Composition (mol%) of the borosilicate glass samples.

Sample	Na_2O	B_2O_3	SiO_2	Al_2O_3	K_2O
A	5	22	69.0	1.1	2.9
B	12	15	69.0	1.1	2.9
C	22	5	69.0	1.1	2.9
D	12	20	64.0	1.1	2.9

The glass samples were prepared by weighing appropriate amounts of SiO_2, $NaNO_3$, B_2O_3, Al_2O_3 and KNO_3, which were then mixed thoroughly to form a homogeneous mixture. It was then calcined up to 750°C in a predetermined heating schedule, followed by grinding for homogenization. The calcined and ground charge is finally heated at 1550°C in a Rh/Pt alloy crucible for 1-2 hours. The melt is quickly poured into a preheated cylindrical graphite mould having diameter 22mm and is immediately transferred to a preheated furnace for annealing at 450°C for 3-4 hours. The resultant glass rod was clear transparent and bubble free. It was then cut into discs of thickness 1.5 mm using a precision cutting machine. One side of the glass samples was optically polished using fine alumina powder. The XRD of the powered samples was taken to ascertain the amorphous nature of the samples. The glass transition temperature (Tg) of the powdered samples was measured using differential scanning calorimetry and was found to be in the range of 350°-450°. A thin layer of about 500 A° of CsCl was vacuum evaporated on the polished surface of the glass samples. These samples were subsequently annealed at different temperatures between 100-350°C for about 12 hours in a furnace. During annealing the glass sample was stacked with another blank glass disc such that the CsCl layer was sandwiched between the two glass discs. The assembly was wrapper with tantalum metal foil during annealing.

RBS measurements: RBS measurements were carried out at the 14UD BARC-TIFR Pelletron accelerator at Mumbai. 30 MeV ^{19}F beam was used to bombard the glass samples. The beam intensity was 6pnA and the measurement time was about 500 seconds for each sample. The RBS spectra were measured using two 300μm thick surface barrier silicon detectors placed at 160° with respect to the beam direction on both sides of the beam. The solid angle subtended by the detectors at the target was 1.2msr. The data were collected in a multiparameter data acquisition system in singles mode with 8K ADC gain. The energy calibration of the system was carried out using a ^{239}Pu-^{241}Am mixed alpha source and silicon wafer having thin layers of Ag and Au (1000 A° each).During the analysis of RBS spectra the data were squeezed to 1K channels.

3 Results and discussion

Figure 1 shows the typical RBS spectra of the glass samples of a particular composition annealed at different temperatures between 100° and 350°C. The top most layer of the figure shows the RBS spectrum of the standard having thin layers of Au and Ag on thin silicon wafer as well as the alpha spectrum of the mixed alpha source of ^{239}Pu, ^{241}Am and ^{244}Cm, which was kept just above the standard in the target ladder. The counts under the RBS peak due to Au in the two silicon detectors were found to be within 5% of each other indicating that the ^{19}F beam was well focused at the center of the target. The RBS spectra due to cesium are clearly distinguished from the low energy spectrum due to low Z constituents, viz., Na, B, Si, O, Al and K. The increasing lower energy tail in the samples annealed at higher temperatures indicates the greater depth of diffusion of cesium.

The RBS spectra of cesium were transformed into depth profile using the slab method the details of which are given in [9].

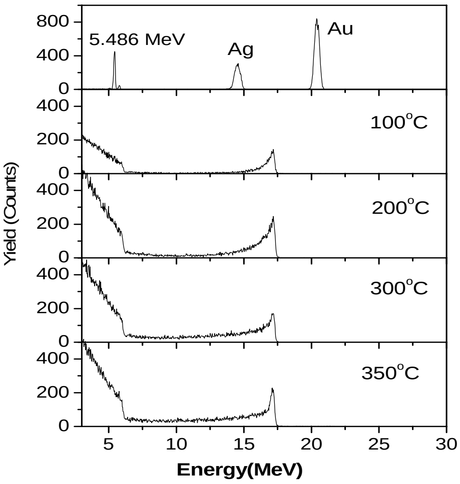

Figure 1: RBS spectra of glass samples.

The stopping power data for stopping of ^{19}F ions having energy in the range of 10-30 MeV in glass samples of different composition were calculated using the SRIM code of Ziegler et al. [13] which were fitted into the second order polynomial,

$$\frac{dE}{dx} = b_0 + b_1 E + b_2 E^2 \qquad (1)$$

The constants were supplied as input in the slab method of transforming the RBS spectrum into depth profile. Figure 2 shows the concentration of cesium as a function of the square of the depth of penetration of cesium. The solid lines are the linear fit to the log of concentration vs square of depth. The goodness of the fit indicates the validity of the thin film solution of the Fick's second law of diffusion, that is,

$$N(x,t) = \frac{M}{\sqrt{4\pi Dt}}\ e^{-x^2/4Dt} \qquad (2)$$

Where N is the concentration of the element at a particular depth (x), M is the concentration of the element present at the surface initially, D is the diffusion coefficient and t is the period of annealing. The depth profile of cesium in samples annealed at different temperatures was fitted into above equation to obtain the diffusion coefficient (D).

The diffusion coefficient when plotted as a function of 1/T were found to show Arrhenius behaviour as shown in figure 3.

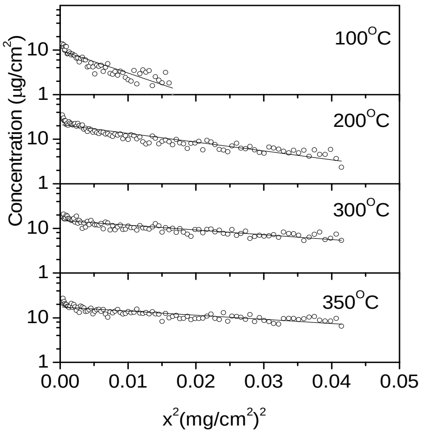

Figure 2: Concentration vs. square of depth profile.

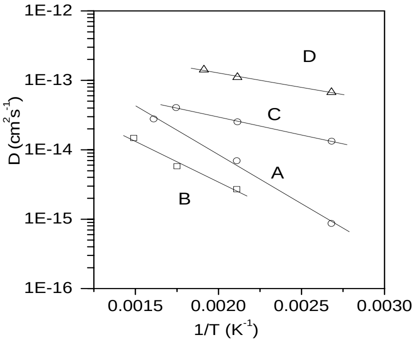

Figure 3: Plot of D vs (1/T).

The activation energies of diffusion obtained by fitting the D vs 1/T data into equation,

$$D(T) = D_0 e^{-\frac{E_a}{RT}} \qquad (3)$$

are shown in table-2 along with the D_0 values.

Table 2: Diffusion parameters for diffusion of cesium in borosilicate glass.

Sample	D_0 (m^2s^{-1})	E_a (kJ/mole)
A	7.03E-17	22.3 ± 3.6
B	6.06E-17	15.3 ±0.4
C	3.17E-17	9.8 ± 0.4
D	8.58E-17	8.0 ± 0.6

The data from previous study [9] are also shown. From the table it can be seen that for samples A, B and C the activation energy (E_a) is decreasing from 22 kJ/mile to 9 kJ/mole. The sodium content in the three glass samples is increasing from 5 to 22 mole percent while the boron content **is** decreasing from 22 to 5 mole percent. In the case of sample D, the E_a value is lower than that for sample C, though the sodium content is lower than that in sample C.

From the above observation it is apparent that the sodium content plays the dominant role in influencing the diffusion of cesium as compared to boron. In the case of sample D, the total mole percent of sodium and boron (32%) is higher than that for samples A, B and C and hence it is difficult to compare the data in terms of relative effect of sodium and boron.

Diffusion of alkali metals in glass has been explained by Doremus in terms of the interdiffusion between soluble elements viz., Na^+ with H^+ in sodalime glass. In the present study the diffusion of cesium is governed by ion exchange with sodium present in the bulk of the borosilicate glass, which is dependent upon the sodium concentration. Inman et al. [14], studied the concentration dependence of the interdiffusion between sodium and silver in sodium aluminosilicate glasses with varying alumina/soda ratios. As the sodium concentration increases these ions cluster around the non-bridging oxygen and the alkali rich regions may form channels along which cation transport may occur. This interaction leads to a strong electrostatic interaction between mobile cation, which varies with the cation species. As a result overall ion exchange process leads to concentration dependence of diffusion coefficient.

Acknowledgement

The authors wish to thank Dr. J V Yakhmi, Head, Technical Physics & Prototype Engineering Division, for his keen interest and encouragement during this work. Thanks are due to Shri Ajit Mahadkar and Mrs. Deepa Thapa for vacuum evaporation of CsCl on the glass samples and Mr Rakesh kumar for polishing the samples. The cooperation by Pelletron operating staff during the experiment is gratefully acknowledged.

References

1. Nifenecker, H., Meplan, O., David, S., Accelerator Driven Sub-critical Reactors, Series in *Fundamental and Applied Nuclear Physics*, 2003.
2. Design and operation of high level waste vitrification and storage facilities, *Technical Report Series No. 339, IAEA, Vienna,* 1992.
3. Audero, M.A., Bevilacqua, A.M., de Bernasconi, N.B.M., Russo, D.O., Sterba, M.E., *J. Nucl. Mater*, 223, 151, 1995.
4. Nonaka, K., Nakajima, H., Mitsui, S., Echigoya, J.I., *Mater. Trans*. 43, 654, 2002.
5. Hench, Lary L., Spilman, Derek B., Buonaquisti, A.D., *Nuclear and Chemical Waste Management*, 5, 75, 1984.
6. Kessel, O. Van, Brongersma, H.H., Holscher, J.G.A., Welzenis, R.G.Van, Ssangers, E.G.F., Janssen, E.J.J.F., *Nucl. Inst. Meth*. B64, 593, 1992.
7. Sangers, E.G.F., Janssen, F.J.J.G., Waal, H. de, in Scientific Basis for Nuclear Waste Management XIII, eds, V.M.Oversby and P.W.Brown, *Mater, Res. Soc. Symp. Proc.,* 176, 441, 1990.
8. Levi,H.W., Lutze, W., Malow, G., Sedighi, N., *Phys. Stat. Sol*.(a) 5, 617, 1971.
9. Tomar, B.S., Sumit Kumar, Shrikhande, V.K., and Kothiyal, G.P., *Nucl. Inst. Meth. B* 227, 391, 2005.
10. Perez, R.A., Bermudez, G.G., Abriola, D., Dyment, F., Somacal, H., *Defect and Diffusion Forum,* 143-147, 1335, 1997.
11. Doremus, R.H., *Treatise on Materials Science and Technology*, eds, Tomazawa, M, and Domerus, R.H., (Academic Press, NY) 17, 41, 1979.
12. Landford, W.A., in *Treatise on Heavy Ion Science, ed. Allan Bromley*, 1986, p363.
13. SRIM Code, *The Stopping and Range of Ions in Solid*, by Ziegler, J.F., Biersack, J.P., Littmark, U., Pergamon Press, New York, 1999.
14. Inman, J.M., Houde-Walter, S.N., McIntyre, B.L., B.L., Liao, Z.M., Parker, R.S., and Simmons, V., *J. Non-Cryst. Solids*, 194, 85, 1996.

MODELING COMPRESSION RELOADS IN COPPER PRE-STRAINED BY EQUAL CHANNEL ANGULAR EXTRUSION (ECAE)

Irene J. BEYERLEIN[1], Carlos N. TOMÉ[2,*]

[1]Theoretical Division
[2]Materials Science and Technology Division
Los Alamos National Laboratory, Los Alamos, NM 87545, USA

[*]Corresponding author: tome@lanl.gov

Abstract

When copper is deformed to large strains, as in Equal Channel Angular Extrusion (ECAE), its texture and microstructure change drastically and lead to plastic anisotropy upon reloading. In this work, we develop a multi-scale model that accounts for both texture and subgrain microstructural evolution. Specifically the evolution of directional anisotropy in the single crystals is induced by the formation of planar dislocation walls. The model successfully predicts the flow responses of copper strained by a single pass of ECAE and subsequently compressed in each of three orthogonal directions.

Keywords: Anisotropy; ECAE; Latent hardening; Strain path change; Copper

1 Introduction

When copper is deformed plastically to large strains it exhibits an anisotropic response in subsequent testing. Such anisotropy is the result of both, texture and microstructure, and depends much on prior straining. With small pre-strains the microstructures within the grains are weak, consisting mainly of dislocation cells with very low misorientations. In contrast, with large pre-strains, texture and subgrain microstructures become stronger and consequently both have a profound effect on the anisotropy. As a consequence, modeling anisotropy after large pre-strains requires describing the concurrent evolution of texture and dislocation structures inside the grains.

ECAE is a complex bulk forming process, which consists of extruding a material through a die formed by two channels with equal cross-section intersecting at an angle Φ ($\Phi = 90^{\circ}$ in our study). Each extrusion imparts roughly 100% strain. In a set of systematic studies [1,2], Cu samples extruded by ECAE were compressed in three orthogonal directions, one parallel to the extrusion direction (L), another parallel to the entry channel (T), and the third normal to the plane of the die (S). The experimental compression curves shown in Fig. 1 indicate strong anisotropy in the compression yield strength, with the out-of-plane response (S) much higher than the in-plane responses (T and L), (i.e. S > T > L). The hardening evolution differs with direction of straining as well: observe the marked jump in stress for the lateral compression (S) followed by a high degree of work softening over the first 15% compression, followed afterwards by a normal hardening rate.

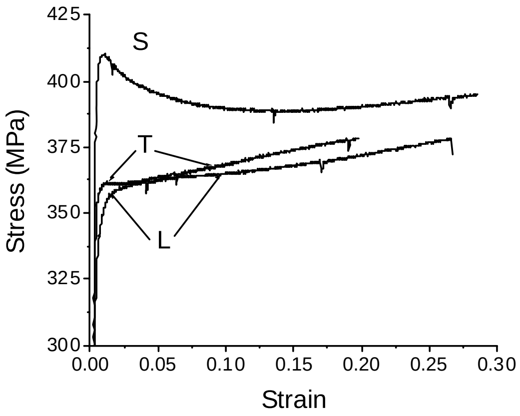

Figure 1: Compression stress-strain curves of the ECAE processed copper reloaded along the side (S), top (T) and length (L) orthogonal directions (experimental data from Ref. [2]).

The anisotropic response of ECAP Cu can be attributed to substantial texture and microstructural changes. After one ECAP pass, Cu grains can form deformation microstructures on two levels, shear and deformation bands [3,4] which are on the order of 10 to 10^2 μm apart, and finer dislocation structures organized into cellular or long planar walls, approximately 1 to 0.1 μm apart [3,5,6]. Both types can greatly induce directional anisotropy in slip which will manifest at the macroscale:

Anisotropic hardening caused by substructure development has been introduced in several ways: Hall-Petch hardening terms, dislocation density evolution laws, or latent hardening. The first two methods have been used in several recent efforts to model the role played by these planar boundaries on directional hardening in Al [7,8], bcc steels [9,10], and Cu [11] deformed either by rolling or simple mechanical tests. The method of latent hardening, which is the hardening of inactive slip systems by active ones, has been used recently to predict the anisotropic stress-strain responses of ECAE processed materials [12].

In this work we propose a multi-scale constitutive model for Cu which accounts for the build-up and disintegration of the finer scale dislocation sheets on crystallographic planes and which describes anisotropic single-crystal hardening as the interaction of slip systems with these dislocation sheets. To do this, we introduce a new model for latent hardening in fcc crystals, and a model for the cut-through and dissolution process which can result in work-softening.

We apply this multi-scale model to predict the stress-strain responses in reloading Cu after one ECAE extrusion. Compression of the ECAE Cu sample in each of three orthogonal directions corresponds to three separate strain path change experiments (Fig 1). The velocity gradient associated with ECAE is provided to the polycrystal plasticity code Visco-Plastic Self-Consistent (VPSC) [13] by an analytical flow model [14]. This flow model has proven to predict texture evolution quite well in many ECAE materials, even under simple crystal hardening models [15].

2 Modeling approach

VPSC is a rate-dependent polycrystal model that relates the plastic response of a polycrystalline material to the deformation of the individual grains [13]. The polycrystal is represented by a collection of grains each with a distinct crystallographic orientation, volume fraction, and shape. Each grain is modeled as an ellipsoid embedded in a homogeneous effective medium with the average properties of the aggregate. Usually, less than 5 independent slip systems are active in each grain. The rate-dependent visco-plastic constitutive law relating the grain strain rate D and grain stress σ is

$$D = D_0 \sum_{s=1}^{n_s} m_{ij}^{s} \left(\frac{m^{s} : \sigma}{\tau^{s}} \right)^{n} \qquad (1)$$

where D_0 is a normalizing strain rate, m^s is the Schmidt tensor for slip system s, $n=20$ is a model parameter, and n_s is the total number of slip systems. In fcc crystals there are 12 slip systems: 3 slip directions <110> on each of the four {111} slip planes. The threshold shears τ^s govern slip activation for each system and evolve with the accumulated strain in each grain Γ according to an extended Voce law which captures Stage II through Stage IV hardening [16]:

$$\tau_V^{s}(\Gamma) = \tau_0^{s} + \left(\tau_1^{s} + \theta_1^{s}\Gamma\right)\left[1 - \exp\left(-\theta_0^{s}\Gamma / \tau_1^{s}\right)\right] \qquad (2)$$

The four parameters in Eq. (2), $\tau_0^s, \tau_1^s, \theta_0^s, \theta_1^s$, are estimated using mechanical tests on the material of interest and depend on strain rate and temperature. The dependency of $\tau_V^s(\Gamma)$ on the accumulated slip in the grain Γ, rather than in the individual shears γ^s, introduces some degree of coupling between the slip systems and reflects that evolution of the τ^s is due to the storage of dislocations from other systems, not just its own.

2.1 Latent hardening model

The critical resolved shear stress for each system in the case of multiple slip, denoted as τ_h^s, is further coupled to the activities of other systems through latent hardening coefficients

$$\dot{\tau}_h^{s} = \Theta^{s}(\Gamma) \sum_r h^{sr} \dot{\gamma}^{r} \qquad (3)$$

where $\Theta^s(\Gamma) = \mathrm{d}\tau_V^s / \mathrm{d}\Gamma$ and h^{sr} is the hardening rate of system s due to slip taking place in system r. Usually $h^{sr} > 0$, meaning that even if some systems are inactive, their τ_h^s will still increase with straining. In our model, though, hardening criteria will be based on interactions between slip planes rather than individual slip systems. For this reason, we define Γ^{α}, the accumulated shear on slip plane α, where α = 1, 4, corresponds to the four slip planes, (111), $(1\bar{1}1)$, $(\bar{1}11)$, or $(\bar{1}\bar{1}1)$.

For fcc crystals it is common to consider h^{sr} between co-planar slip to be one and between non-planar slip to be a constant, $h^{sr}=h$, which is greater than one. However, in a previous study to model the anisotropy of ECAE-formed Cu seen in Fig. 1 using VPSC, only $h = 0.2$ reasonably predicted the degree of anisotropy seen in Fig. 1, while the $h \geq 1$ cases significantly underestimated it. Therefore, it was shown that while one can be successful in modeling monotonic straining with values of latent hardening in the range $1.4 < h < 0.2$, the correct representation of the evolution of latent hardening during straining really becomes apparent after a strain path change.

This suggests that latent hardening may evolve with straining. After small strains, the grain microstructure is relatively weak, consisting mainly of a three-dimensional network of cells with low misorientations. This structure will lead to isotropic hardening as all systems are likely to encounter resistance from them. After large strains, sheet-like dislocation boundaries form which will lead to anisotropic hardening as the most active systems encounter the most dislocation debris accumulated during deformation. To capture this influence of microstructural evolution on latent hardening we propose in [17] a more general form for the latent hardening parameter, denoted as $H(\delta)$, which evolves during the course of plastic straining and couples slip planes and not individual systems. The latent hardening between two planes α and β is

$$h^{\alpha\beta} \equiv H(\delta) = (1-h_s)e^{-\delta^{\alpha\beta}} + h_s \qquad (h_s \leq 1) \qquad (4)$$

where $\delta^{\alpha\beta}$ is a function of accumulated shear in planes α and β

$$\delta^{\alpha\beta} = \frac{\left|\Gamma^{\alpha} - \Gamma^{\beta}\right|}{\Gamma_0} \qquad (5)$$

In Eq. 4 $H(\delta)=1$ if $\alpha=\beta$, but $h_s \leq H(\delta) \leq 1$ for non-coplanar systems ($\alpha \neq \beta$). As plane α becomes more active with respect to β, $\delta^{\alpha\beta}$ increases, $H(\delta)$ decreases, and τ_h^s increases faster in the active than in the latent system. At most, $H(\delta)$ saturates to a value h_s, which falls between 0 and 1. These situation can promote activity in the latent systems because there is a built-in feed-back in the model that will promote non-coplanar slip and can evolve $H(\delta)$ back towards unity.

The parameters, h_s and v_0 depend on material properties, like stacking fault energy. The parameter v_0 governs how quickly stable planar substructure develops with strain. For Cu we assign $h_s = 0.2$ and $v_0 = 0.01$.

2.2 Cut-through model

Latent hardening alone cannot capture the ‘spike’ in flow stress followed by a negative hardening rate shown by the S compression in Fig. 1. The most likely explanation for this behavior is that new slip systems need to permeate and annihilate previously developed microstructure [9,10]. Once the structure is dissolved, these dislocations can propagate as usual and work-hardening recommences. While it is likely that both dislocation cells and planar dislocation boundaries are dissolved, the directionality of work-softening, as seen for instance in Fig. 1, suggests that the latter is the primary mechanism. In [17] we developed a cut-through model for directional hardening of slip systems to capture this phenomenon. This model builds upon continuum level formulations for the decay of a macroscopic strength component due to substructure dissolution [9], which have been successful at modeling work-softening in IF steels.

The basic idea of the cut-through model is that a barrier threshold stress

$$\tau_c^s = \tau_{c,0}^s\left(\Gamma_{prior}\right)\exp(-\omega\Gamma_{new}^{\alpha}) \qquad s \in s^{\alpha} \qquad (6)$$

is added to the τ_h^s of every slip system which must overcome a dislocation boundary. In Eq. 6 Γ_{new}^{α} is the shear on the plane α accumulated during the *new* deformation path, $\tau_{c,0}^s\left(\Gamma_{prior}\right)$ is the initial barrier stress required for dislocations associated with newly activated slip systems to overcome a dislocation boundary when a new straining direction is applied, and Γ_{prior} the value of Γ accumulated during the entire previous path. In [17] we derive the following expression for $\tau_{c,0}^s$:

$$\tau^{s}_{c,0}\left(\Gamma_{\mathrm{prior}}\right) = -k\mu k_{\rho}\sqrt{\Gamma_{\mathrm{prior}}}\,\ln\left(k_{\rho}\sqrt{\Gamma_{\mathrm{prior}}}\right) \qquad (7)$$

Here μ = 42 GPa is the shear modulus, k = 0.086 and k_ρ = 8.5 x 10^{-4}. Accordingly, the more active the new slip plane is, the more mobile dislocations are available for dissolving the boundary, and the more effectively it dissolves the boundary. The dissolution process in Eq. (6) will only remove at most the deformation resistance $\tau^{s}_{c,0}$ that is initially posed at the beginning of the cut-through process. So the higher Γ_{prior}, the 'stronger' the barrier $\tau^{s}_{c,0}$ (Γ_{prior}), and the more resistance that needs to be removed. The parameter ω in Eq. (6) reflects how effectively the material, through the activities Γ^{α}_{new} in newly activated planes, can dissolve dislocation barriers created during pre-load. For Cu at room temperature we set ω = 25.

3 Application to One-Pass ECAE Copper

We apply the modeling approach described above to predict the anisotropic plastic response of Cu in compression after a single pass of ECAE [1]. The prediction accounts for texture and grain shape evolution, interaction of each grain with the surrounding polycrystal, anisotropic hardening along active slip planes, and interactions between pre-existing and newly developing substructure.

The standard model for macroscale deformation during ECAE is simple shear localized at the intersection plane of the two channels in the ECAE die. Finite element models show that in most cases plastic deformation takes place in a 'plastic deformation zone' (PDZ), spread about the intersection plane. In Ref. [14] we propose an analytic form of the velocity gradients in the PDZ which amounts to deformation occurring by successive shearing on planes that rotate counterclockwise in the 1-2 plane of the die. The texture predicted with this model agrees well with measured textures [14].

For the VPSC forming simulations the Cu polycrystal is represented by 1500 weighted orientations assigened according to an OIM measurement of the initial texture. The latter is a weak fiber texture, axi-symmetric about the billet long axis. The Voce parameters in Eq. (2) are adjusted to reproduce the measured compression response of the starting annealed Cu. During the simulation, the parameters h_s and v_0 in $H(\delta)$ are set to 0.2 and 0.01, respectively. Figure 2 compares the measurements with the predicted response using the adjusted Voce parameters, ($\tau^{s}_{0}, \tau^{s}_{1}, \theta^{s}_{0}, \theta^{s}_{1}$) = (30, 250, 440, 23) MPa for all s. Because the annealed Cu was plastically isotropic, compression responses measured in the S, T, and L directions were practically the same. The predicted response follows the compression data very well. Beyond the data (~40% strain) the hardening rate decreases and remains constant up to a strain of 2. Such a response agrees well with measurements made on similar Cu compressed to large strains [23] and is consistent with the initial yield stresses obtained from S, T and L compression tests performed on the ECAE'ed Cu (shown as individual points in Fig. 2).

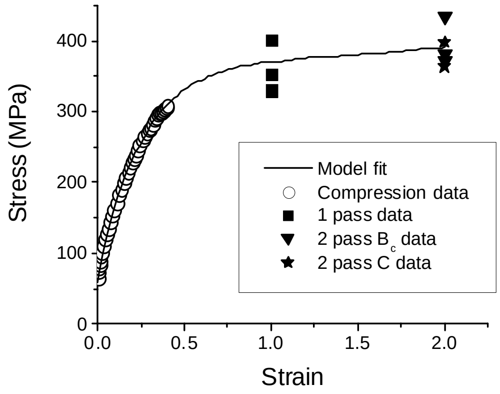

Figure 2: Comparison of predicted response of copper with compression data up to 45% strain and with measured yield stresses in the S, T, and L directions. (experimental data from Ref [2]).

The hardening stress Eq. (6) associated with cut-through is applied to active systems belonging to planes non-coplanar to the planes that were the most active in the primary path. The results therefore are affected by the definition of active planes for each grain. In the present calculations the previously first and second most active slip planes are defined as those that exhibit the two largest shears at the end of the ECAE pass. Newly activated systems upon reload must be non-coplanar to these boundaries to experience resistance τ^{s}_{c}.

The single crystal parameters presented above are used to simulate a single pass of ECAE immediately followed by compression testing in each of the three orthogonal directions. For subsequent compression testing we assume traction-free surfaces perpendicular to the direction of axial compression. VPSC calculates the resulting stress-strain response, texture and grain shape evolution, and slip activities.

Figure 3a compares the model predictions (symbols) using the latent hardening model only and Fig 3b the predictions using both, latent hardening and cut-through. Without the cut-through mechanism (Fig. 3a), we can see that the contribution to hardening from texture evolution and the Voce/*H*(δ) model for the evolution of τ_h^s predicts the right qualitative order (S > T > L), but fails to capture the small initial softening of the T test, and the large initial softening of the S test observed in the first 15% of straining. Past the 15% transient, the linear asymptotic response in the Voce/*H*(δ) law controls the stress evolution, while the texture effect governs the differences in slope between the S, L and T responses.

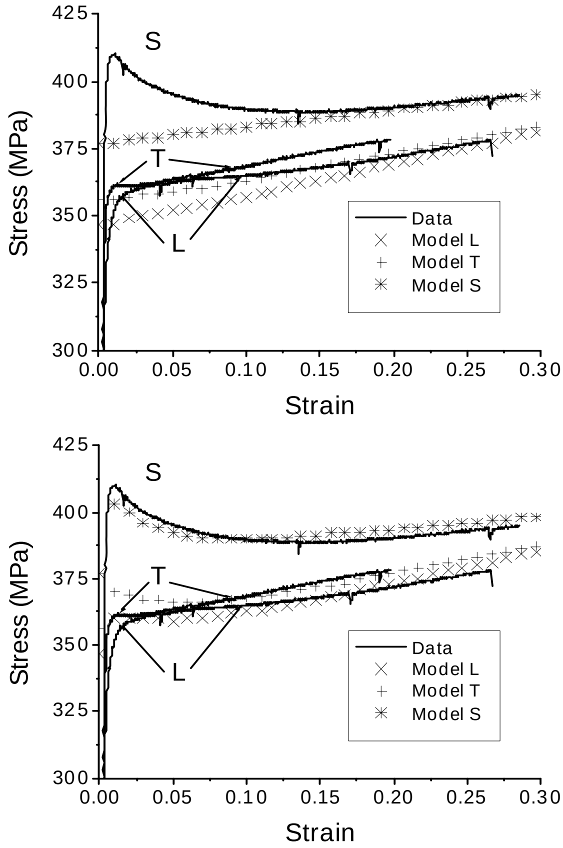

Figure 3: Comparison of the model predictions with experimental measurements reported in Fig. 1. The model utilized the Voce and *H*(δ) latent hardening laws (a) without the cut-through and (b) with the cut-through mechanism.

The cut-through process acts as a separate resistance to deformation which instantly hardens and then softens the previously latent systems. The deformation resistance due to cut-through is only invoked during the post compression testing. As shown in Fig. 3b, the incorporation of the cut-through mechanism removes most of the discrepancies associated with the *H*(δ) model alone. It captures reasonably well the large transient work-softening in S, suggesting that the key mechanisms are appreciated. The model also captures the characteristics of the T test: a small but noticeable jump in initial yield followed by a noticeable softening response.

Geometric hardening plays a large role in the strain hardening following the path change. When texture evolution and cut-through are suppressed during subsequent compression, the T and L responses have a significantly lower hardening rate (nearly flat) and the S response has a higher one by comparison with Fig. 3b. This result implies that texture evolution contributes a positive hardening rate to the total T and L responses and a negative one to the S response, as discussed in Ref. [1].

4 Discussion

Subgrain deformation microstructures play two roles in determining the directional anisotropy in single-crystal hardening. Regardless of which path in the straining sequence is being imposed, dislocations will tend to organize into substructures, which serve to increase the flow stress. The influence of their development with straining during any stage in the deformation is captured by the extended Voce model for single slip and the *H*(δ) model for coupling in multiple slip. Realistic hardening parameters, however, are better revealed by the strain path change (Fig. 3a). In contrast, the influence of new slip activity attempting to permeate and locally dissolve pre-existing structure is captured by the directional cut-through model. The model considers this second role of deformation microstructures to have a transient effect on the flow stress (Fig. 3b) and depending on the amount of new slip activity can be apparent in the event of a strain path change.

In light of these assumptions, agreement between the cut-through model and the data suggests that the cutting stress is proportional to the strength of the barriers and independent of the direction of the barrier relative to the new slip plane. The larger the pre-strains, the stronger barriers and the higher the cutting stresses. The more new systems a grain utilizes, the more slip systems are enhanced by a cutting stress. The more grains that are required to overcome these cutting stresses, the higher macroscopic stress response of the polycrystal (e.g. compare S to L in Fig. 3).

The dissolution scheme employed here assumes that the dissolution process occurs at a reduction rate proportional to the current slip activity $\Gamma_{\text{new}}^{\alpha}$ and the current strength of the boundary τ_c^s, $s \in s^{\alpha}$. Though simple, it captures two important dependencies: the dissolution rate varies among slip systems, from grain to grain, and with direction of straining. Some grains will have boundaries that dissolved relatively quickly while others will not completely dissolve the boundary before the end of straining and, finally some boundaries cannot be dissolved at all. If instead, over the polycrystal, all the boundaries were annihilated too fast or too slow, then work-softening will be too abrupt or not happen at all.

5 Conclusions

Modeling the anisotropy of an ECAE material in three orthogonal directions is the same as modeling simultaneously three two-stage strain path change experiments, each with very large pre-straining. We do so in this work with the introduction of two new single-crystal hardening models, and employing the same set of parameters throughout the entire deformation sequence. These models relate the substructure development and interactions to the critical resolved shear stresses for slip, which are then imported into a rate-dependent visco-plastic self consistent (VPSC) polycrystal model, so that the evolution of texture and grain shapes are accounted for simultaneously. Our model emphasizes the activity in and interaction between slip planes rather then the activity of individual slip systems. While we apply this to an ECAE material, we foresee that the model and concepts presented in this paper can be extended to improve predictive capability for general forming processes.

Acknowledgments

Research supported by a Los Alamos Laboratory-Directed Research and Development (Project No. 20030216) and Office of Basic Energy Sciences Project FWP 06SCPE401.

References

[1] Alexander, D. J., Beyerlein, I. J., in *Ultrafine Grained Materials III*, Y. T. Zhu et al., eds., TMS, Warrendale, PA, pp. 517-522, 2004.

[2] Alexander, D. J., Beyerlein, I. J., *Mats. Sc. and Engineering A*., in press, 2005.

[19] Beyerlein, I. J., Li, S., Alexander, D. J., *Mats. Sc. and Engineering A*, in press, 2005.

[9] Beyerlein, I. J., C. N. Tomé, C. N., *Mats. Sc. and Eng.* A380, pp. 171-190, 2004.

[22] Beyerlein, I. J., Tomé, C. N., submitted for publication.

[11] Hansen, N., Juul Jensen, D., *Acta Metall. Mater*. 40, pp. 3265-75, 1992.

[6] Huang, X., Borrego, A., Pantleon, W., *Mats. Sc. and Eng.* A319-321, pp. 237-241, 2001.

[7] Komura, S., Horita, Z., Nemoto, M., Langdon, T. G., *J. of Mats. Research* 14, pp. 4044-50, 1999.

[8] Lebensohn, R. A., Tomé, C. N., *Acta Metall. Mater*. 41, pp. 2611-24, 1993.

[10] Li, S., Beyerlein, I. J., Alexander, D. J., *Scripta Mater*. 52, pp. 1099-1104, 2005.

[17] Mahesh, S., Tomé, C. N., McCabe, R. J., Kaschner, G. C., Beyerlein, I. J., Misra, A., *Metall. Mater. Trans*. A35, 3763-74, 2004.

[4] McNelley, T. R., Swisher, D. L., in *Ultrafine Grained Materials III*, Y. T. Zhu et al., eds., TMS, Warrendale, PA, pp. 89-94, 2004.

[3] Miyamoto, H., Erb, U., Koyama, T., Mimaki, T., Vinogradov, A., Hashimoto, S., *Phil. Mag. Letters* 84, pp. 235-243, 2004.

[16] Peeters, B., Seefeldt, M., Teodosiu, C., Kalidindi, S. R., Van Houtte, P., Aernoudt, E., *Acta Mater*. 49, pp. 1607-19, 2001.

[14] Rauch, E. F., *Solid State Phenomena* 23-24, pp. 317-334, 1992.

[23] Tomé, C. N., Canova, G. R., Kocks, U. F., Christodoulou, N., Jonas, J. J., *Acta Metall.* 32, pp. 1637-53, 1992.

[13] Winther, G., *Scripta Mater*. 52, pp. 995-1000, 2005.

Proceedings of The 1st International Conference on **D**iffusion in **S**olids and **L**iquids
DSL-2005, July 6-8, 2005, University of Aveiro, Aveiro, Portugal

MECHANICAL PROPERTIES OF AUSTENITIC STAINLESS STEEL AFTER LOW TEMPERATURE N_2-H_2 PLASMA NITRIDATION

M. Cem İĞDİL, Levent TRABZON*

Department of Mechanical Engineering, Istanbul Technical University,
Materials Science Division, 80191 Istanbul, Turkey

*Corresponding author. Fax: +90 212 2450795; Email: levent.trabzon@itu.edu.tr

Abstract

A series of experiments are conducted to study the effect of low-temperature plasma nitridation on mechanical properties of austenitic stainless steel. The experiments were performed with a temperature range of 400 ^{0}C to 500 ^{0}C in a N_2 concentration of 5% to 25% and H_2 in the rest of the plasma ambient. The nitrided thin film was examined by glancing XRD measurements and the expanded austenite is grown at temperatures below 450 ^{o}C and/or in a gas composition of 10 % N_2, otherwise CrN is precipitated. The surface roughness is increased by duration of nitridation as well as by the N_2 content in the plasma ambient and by the processing temperature. The surface hardness is increased considerably by the formation of expanded austenite at the surface and the degree of hardness is dependent on the thickness of case depth. The modulus of elasticity is increased by 33 %, but the change of modulus of elasticity is independent of nitridation conditions.

Keywords: Nitridation; Austenitic Stainless Steel; Plasma

1 Introduction

The plasma nitriding has been extensively used to increase the hardness of surface for austenitic stainless steel by introducing nitrogen atoms into austenite matrix [1,2]. Stainless steel has superior corrosive properties, but the surface hardening is required under wear induced conditions. One of the possible ways of achieving the goal is doping the surface with nitrogen atoms at low temperatures in the plasma nitriding processing [3]. The presence of nitrogen atoms induces a lattice expansion, so that austenite matrix is transformed into phase called expanded austenite. The expanded austenite has very high hardness with excellent corrosion properties, so that there has been extensive research done in the last decade to understand its materials and mechanical properties. However, it is important to characterize the true nature of thin film that is doped by nitrogen on the surface. Otherwise, the materials and mechanical properties are underestimated due to contributions from the substrate. When there is a plasma nitriding with very short durations, the film developed after nitridation will be very thin. Thus, the characterization of the nitrided thin film should be performed with high precision.

In this study, we investigate mechanical properties of the plasma nitrided austenitic stainless steel. It is seen that the surface roughness is dependent on duration of nitridation, process temperature and ambient. The hardness of surface is increased by the nitridation as high as four times. The modulus of elasticity is observed to same constant in the different plasma nitriding conditions. The phases observed in the thin layer of nitrided layer are dependent on the temperature and the amount of nitrogen gas in the plasma ambient.

2 Experiments

The specimens used in the study were standard austenitic stainless steel that contains only 0.01% C by weight (316L). The samples were prepared in the sizes of 10x3x30 mm and they were cleaned in chemicals to free any kind of oil and dust. The plasma nitriding carried in a dc-discharge plasma system which is a 200-mm diameter quartz glass vacuum tube. Prior to locating the specimens on the cathode, 10x3x30 mm size of 316L samples were mechanically polished by using alumina slurry to obtain mirror-finished surfaces. Before starting nitridation, the samples were exposed to hydrogen (H_2) glow-discharge to clean the surfaces. The processing temperature was monitored by a thermocouple embedded in the system so that the nitridation started if the corresponding temperature was achieved on the specimen surface. The duration of processing is completed by the end of nitrogen contained (N_2) glow-discharge. Then the specimens were let cool down under a hydrogen gas ambient. The nitridation was conducted at 1300 Pa with different temperatures of 400, 450 and 500 ^{0}C with a maximum 2 kW and cathode current densities ranging from 0.75 to 2.5 mA/cm^2. In the experiments, the gas mixtures of 5%, 10%, and 25% nitrogen by volume and hydrogen in the rest were employed at all three temperatures. The experiments were also run for 15, 30, 60, 120 and 240 minutes with 4 samples in each case.

The glancing angle XRD measurements at a 2^o incoming angle to the surface was performed with Cu-Kα (λ = 1.542 nm) to determine phases in the nitrided thin film on the surface. The surface hardness is measured by a surface profilemeter and an atomic force microscopy (AFM). The Microhardness measurements were done by Shimadzu HMV-2 which has a load range of 100 mN – 20 N with a diamond indenter. A Vickers indenter, a four-sided diamond pyramid with a square base and a face angle of 136^0, was used for the measurements. To eliminate artifacts in the experiments due to surface roughness, the specimen were barely polished before measurements. All experiments were done at least 6 times and then evaluation of results was done by the average of measurements for each set. The modulus of elasticity was measured by Fischer HP100 ultra-microhardness tool which is characterized by a load range of 0.4–1000 mN, a load resolution of 0.2 mN, an indenter shift resolution of 2 nm and a stepwise increment of load.

3 Results and Discussions

The material properties of plasma nitrided 316L austenitic stainless steel are studied by glancing-angle XRD [4]. We found that the formation of only expanded austenite (γ_n) was seen at temperatures lower than 450 ^{0}C and with N_2 content of maximum 10% in the ambient. Otherwise, there is a precipitation of CrN in the plasma nitriding of 316L stainless steel as seen in the Fig. 1. The case-depth was seen to increase steadily by time as also seen in the XRD results [4].

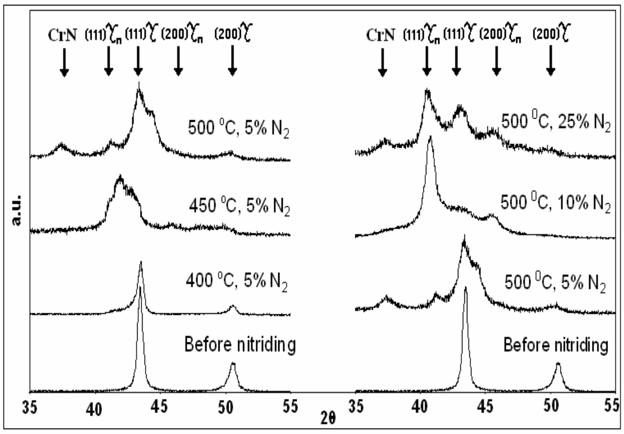

Figure 1: Glancing-angle at 2^0 XRD spectrum of nitrided samples under different conditions.

Fig. 2 shows the surface roughness of plasma nitrided 316L steel with 10% N_2 at 450 ^{0}C for one hour. It is very clear that the surface roughness is increased considerably. The island formation is seen on the surface. The surface roughness and the degree of island formation are also dependent on the duration of plasma nitriding. The average surface roughness can be as high as 600 nm with 10%N_2 at 450 ^{o}C for 240 min plasma nitriding (not shown here). Note that the average surface roughness of pristine sample is lower than 50 nm.

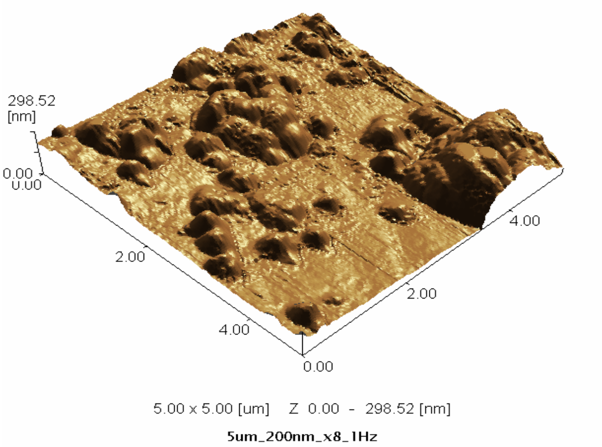

Figure 2: The Surface roughness measured by AFM on plasma nitrided samples with 10% N_2 at 450 ^{0}C for one hour.

Fig. 3 presents the variation of surface roughness on the process parameters. The surface roughness is clearly dependent on the temperature and the gas composition. The process temperature increases the surface roughness by five times as depicted in the 10% N_2 case. The amount of nitrogen gas by volume is also an effective parameter to induce an enhanced surface roughness. The observation may be related to degree of plasma nitriding conditions since there will be more different phases seen in the microstructure by higher temperature and higher N_2 content, as seen in the Fig. 1. Note that the measurements of surface roughness were performed on the samples that were barely polished. However, this little amount of polishing is not shadowing the trend in the surface roughness by the parameters of interest.

Fig. 4 and 5 show us the surface hardness by the Vickers Microhardness measurements for the samples plasma nitrided with 10 % N_2 at 450 ^{o}C for different plasma nitriding durations and the samples plasma nitrided with different gas compositions at the range of temperatures of 400 ^{o}C to 500 ^{o}C for one hour, respectively. The height of the square-base pyramid-Vickers diamond which is the penetration depth *h* of the Vickers indenter, has been calculated from geometrical calculations. Penetration depth, *h*, is equal to 1/2(*d*ctc68°) where d is the average of five measurements. The opposite edge angle of the indenter is 136°. Since there is no CrN formation seen in conditions depicted in Figure 1, the hardness is steadily increased by time at a given distance from the surface. It is a clear indication that there is a thicker formation of the nitrided thin film on the surface with a longer treatment time in the plasma nitriding, see Fig. 4. The surface hardness can be increased as high as four times. Note that with the formation of thicker nitrided thin film on the surface, the effect of substrate is reduced in the measurements. The hardness by depth in different treatment conditions for one hour is seen in Fig. 5. There is hardly formation of nitrided layer as depicted no measurable hardness at 400 ^{o}C with 5 % N_2 gas content. There is a grouping by temperature in hardness by depth regardless of N_2 content in the treatment ambient i.e. the higher the treatment temperature the higher the hardness at a given distance from surface. The formation of CrN in a given processing conditions (500 ^{o}C with any N_2 content) results in the higher surface hardness. The plasma nitridation with 25 % N_2 gas by volume in the treatment ambient at two different temperatures of 450 and 500 ^{o}C indicates that microstructure is not the only factor determining surface hardness, but treatment temperature and the amount of nitrogen in the plasma ambient play important roles. In both samples, there is a formation of CrN in the

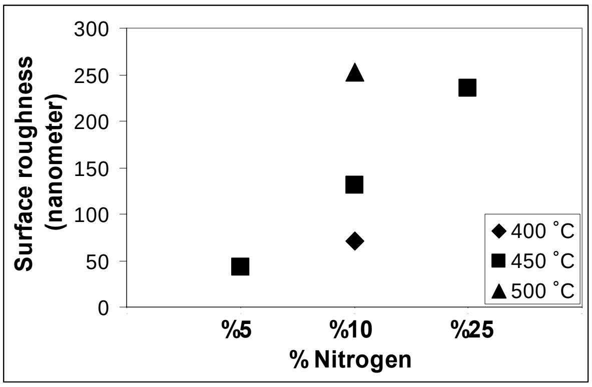

Figure 3: The Surface roughness measured by a Vickers Microhardness on plasma nitrided samples having different process duration and conditions.

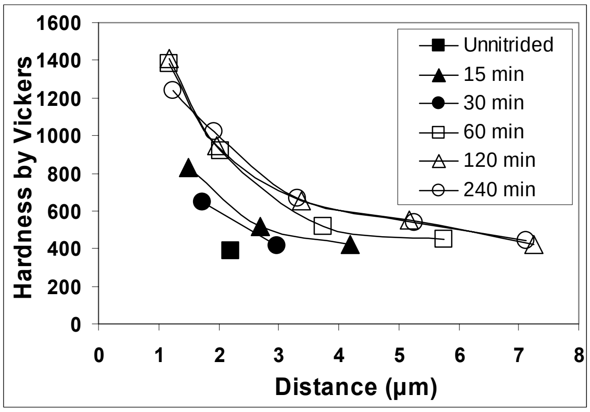

Figure 4: The Surface Hardness from Vickers microhardness measurements versus depth for samples nitrided at 450 ^{0}C and 10 % N_2 by volume in the treatment gas for different processing time.

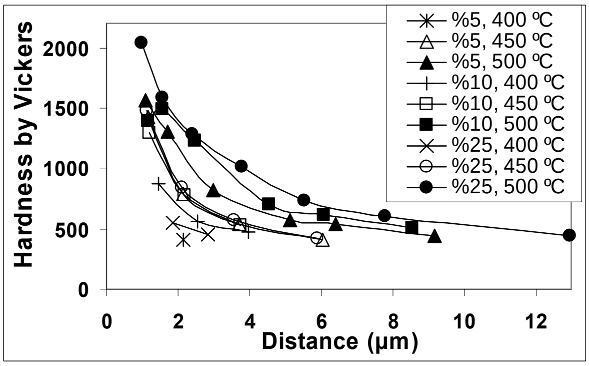

Figure 5: The Surface Hardness versus depth for samples nitrided under different plasma conditions for one hour.

microstructure, but the hardness by depth for the sample nitrided at 450 °C is not in the group of samples plasma nitrided at 500 ^{0}C. Temperature as driving nitrogen into austenite matrix is more facilitating for nitrogen atoms diffusing deeper so that the thickness of nitrided thin layer becomes thick enough to compensate substrate effect. The hardness of very-near surface, smaller than 1 µm from the surface, is also not detected by micro-hardness measurements due to difficulties in conducting experiments.

The modulus of elasticity is measured by Vickers ultra-microhardness measurements so that mechanical characteristics of coating-only nitrided thin film are possible [5]. The load applied on the surface is the 1/7 to 1/10 of nitrided layer thickness so that the penetration of Vickers indenter is not in the influence of the substrate. The change in the nature of lattice after plasma nitriding results in a modification of modulus of elasticity [4,6,7]. The modulus of elasticity is found to be increased by more than 50 % due to plasma nitriding and it is independent of processing conditions and depth of nitridation [8]. The modulus of elasticity is increased by almost 33% and it is independent of processing conditions, as seen in Fig. 6. However, the modulus of elasticity is higher in the samples containing CrN than the samples only containing expanded austenite. This point is required to be examined in more details.

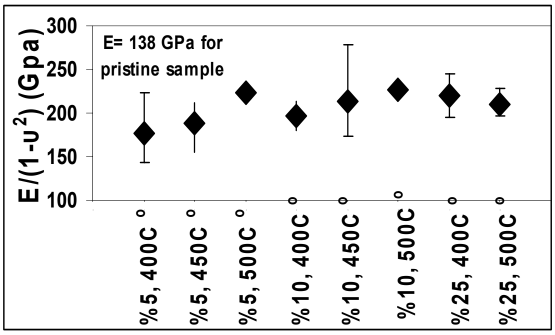

Figure 6: Reduced modulus of elasticity versus processing conditions for samples nitrided at 450 ^{0}C.

4 Conclusions

We found that there is an expanded austenite formation at temperatures lower than 450 °C and nitrogen content of lower than 10% in the plasma ambient conditions. The surface roughness after plasma nitriding is increased by time, temperature and N_2 content in the ambient as well as it is in the island form. The surface hardness is increased by 4 to 5 times after plasma nitridation. However, the substrate effect should be eliminated to observe coating-only hardness properties. The modulus of elasticity is seen to increase by 33% and it is independent of process parameters.

References

[1] Menthe, E., Bulak, A., Olfe, J., Zimmermann, A., Rie, K.-T.: Improvement of the mechanical properties of austenitic stainless steel after plasma nitriding. *Surf. Coat. Technol.* 133, pp.259-267, 2000

[2] Marot, L., Le Bourhis, E., Straboni, A.: Improved nitridation efficiency and mechanical property of stainless steel surface after N_2–H_2 plasma nitridation at low temperature. *Mater. Lett.* 56, pp. 76-79, 2002

[3] Czerwiec, T., Renevier, N., Michel, H.: Low-temperature plasma-assisted nitriding. *Surf. Coat. Technol.*131, pp. 267-272, 2000

[4] Trabzon, L., Igdil, C.M.: On the materials properties of thin film plasma nitrided austenitic stainless steel. To be published in *Surf. Coat. Technol.*, 2005

[5] Kazmanli, M.K., Rother, B., Urgen, M., Mitterer, C.: Identification of cracks generated by indentation experiments in hard-coating system. *Surf. Coat. Technol.* 107, pp. 65-71, 1998

[6] Mändl, S., Rauschenbach, B.: Anisotropic strain in nitrided austenitic stainless steel. *J. Appl. Physics* 88 (6), pp. 3323-3328, 2000

[7] Ledbetter, H.M., Austin, M.W.: Dilation of an fcc Fe-Cr-Ni alloy by interstitial carbon and nitrogen. *Mater. Sci. Techol.* 3, pp. 101-107, 1987

[8] Lin, J.F., Chen, K.W., Wei, C.C., Ai, C.-F.: The effects of differing nitrogen implantation conditions on penetration depth, mechanical properties, and tribological behavior of plasma-nitrided AISI 304 stainless steel. To be published in *Surf. Coat. Technol.* (2004)

EXPERIMENTAL CHARACTERIZATION AND COMPUTER-BASED SIMULATION OF THERMODYNAMICS AND KINETICS OF CORROSION OF STEELS AT HIGH TEMPERATURES

Vicente B. TRINDADE[1,*], Ulrich KRUPP[1], Hans J. CHRIST[1], Maurício J. MONTEIRO[2], Fernando C. RIZZO[2]

[1]Universität Siegen – Institut für Werkstofftechnik
Paul-Bonatz Str. 9-11, 57076-Siegen, Germany
[2]Pontificie Universidade Católica do Rio de Janeiro
Departamento de Ciência dos Materiais e Metalurgia / Brazil

[*]Corresponding author. Fax: +49 271 740 2545; Email: vicente@ifwt.mb.uni-siegen.de

---

Abstract

This study aims to an experimental and theoretical description of three different corrosion phenomena of steels during high-temperature exposure: (i) the effect of vanadium content during oxidation of tool steels, (ii) the grain size effect during oxidation of low-Cr boiler steels, and (iii) the carburization of austenitic steels. The experimental part was carried out by means of thermogravimetric measurements and scanning electron microscopy observations. Computational thermodynamics investigations were carried out by performing complex equilibrium calculations of the Fe-Cr-V-W-Mo-O-C system using the commercial software FactSage. The kinetics of oxidation and carburization processes were accounted for by solving the diffusion differential equation numerically (finite-difference method) taking the material's microstructure into consideration, by distinguishing between precipitation along the grain boundaries and within the grain interior as well as incorporating local thermodynamic equilibrium by means of the subroutine ChemApp, which works according to Gibbs energy minimization criteria.

Keywords: Tool steels; Low-alloy steels; Austenitic steel; Thermodynamic equilibrium; Finite-difference method; Oxidation; Carburization; Grain-boundary diffusion

---

1 Introduction

The present study aims to introduce a computer-based model for simulation of corrosion processes occurring during different high-temperature applications such as power plants, hot rolling processes and petrochemical industries.

The formation of a slow-growing chromium oxide scale (Cr_2O_3) on the surface of steels depends on the available amount of chromium on the sample surface for the formation of a continuous and dense oxide scale [1,2]. If a pure Cr_2O_3 scale formation is not possible due to the absence of a sufficient amount of chromium, iron will take part in the oxidation reactions forming fast-growing iron oxides and mixed (Fe,Cr) oxides (spinel phase). The oxidation rate decreases as the chromium content in the spinel phase increases [3,4].

Low-Cr steels are used for non-heated exit areas in superheater tubes and in reheater tubes as part of boiler components. The external surfaces of these tubes are exposed to air at temperatures between 400°C-600°C, which results in a loss of thickness of the tubes due to oxide formation.

Tool steels for hot rolling are usually used in a temperature range between 300°C and 700°C. Studies [5] have shown that the formation of an oxide scale on the surface of equipments used for forging, rolling and molding can be decisive for the in-service life of such equipments through its influence on the thermal, mechanical and thermomechanical properties. Elements such as vanadium have been used in order to improve the mechanical properties of tool steels by carbide formation [6]. However, the resistance to oxidation must also be considered properly.

In petrochemical industry, e.g., in pyrolysis furnaces, large hydrocarbon molecules are cracked into smaller molecules such as olefins, i.e., ethylene, propylene and butadiene. This gas-phase reaction takes place in metal alloy tubes within a fired furnace operating in a temperature range of 750°C-850°C. The high carbon activity on the tube surface shortens the tube life by carburization phenomena or under extreme conditions by metal dusting (carbon activity>1) [7].

This paper presents a computer-based simulation for the quantitative description of thermodynamics and kinetics of oxidation and carburization of three classes of steels (tool steels, ferritic boiler steels and austenitic steels) used in different high-temperature corrosive environments. Microstructual effects such as the influence of grain size on the degradation mechanisms are taken into consideration.

2 Material and Experimental Procedure

Three model tool steels (steels A, B and C), three low-Cr ferritic boiler steels (steel D, E and F) and one austenitic steel (steel G) were used in the present study (Table 1).

Table 1: Chemical composition (in wt.%) of the steels studied.

Material	C	Cr	Mo	W	V	Mn	Ni
steel A	2	4	2	2	5	---	---
steel B	2	4	2	2	6.5	---	---
steel C	2	4	2	2	8	---	---
steel D	0.07	0.55	---	---	---	1.01	---
steel E	0.06	1.44	---	---	---	0.59	---
steel F	0.09	2.25	1	---	---	0.59	---
steel G	0.04	17.5	---	---	---	1.84	10

The steels A-F were isothermally oxidized in air at different temperatures, i.e., tool steels at 650°C and the low-Cr ferritic steels at 550°C. The austenitic steel was exposed to atmosphere containing methane at 850°C. The mass change was recorded using a microbalance with a resolution of 10^{-5}g connected to a computer. The oxide phases were analyzed using scanning electron microscopy (SEM) in combination with energy-dispersive X-ray spectroscopy (EDX).

3 Results and Discussions

3.1 Tool steels

Figure 1 shows the oxidation rates of three tool steels with different V concentrations. It can be seen that the mass changes are strongly influenced by the V content during the initial stage of oxidation. It is also evident that the nucleation rate of oxide is accelerated (high oxygen uptake) due to V addition. This has been attributed to carbide formation by accelerating the oxide nucleation on the specimen suface.

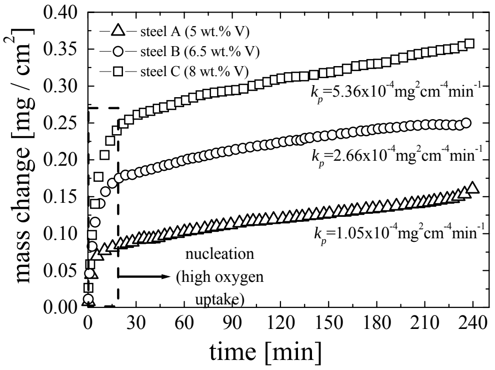

Figure 1: Measured mass change of the three investigated tool steels at 650°C in dry air.

Figure 2a shows the effect of V on the formation of carbides in steel with 4wt.% of Cr, 2 wt.% of Mo, 2wt.% of W and 2wt.% of C. As the V content increases, different carbide phases are formed at 650°C. Figure 2b shows an increase in the carbides based on V (VC+V_3C_2), which are formed as very fine precipitates as shown in Fig.3.

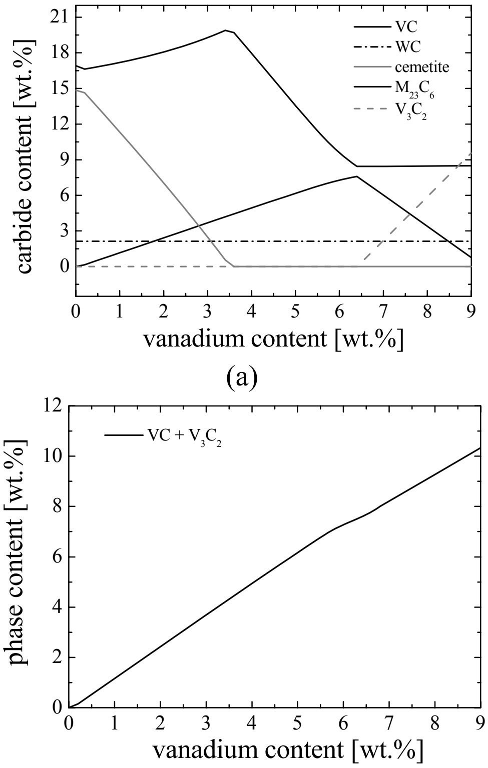

(a)

(b)

Figure 2: Thermodynamic calculations for the Fe-Cr-Mo-W-V-C system at 650°C using the software FactSage; (a) carbide phases and (b) V-carbide (VC + V_3C_2) content as a function of the initial V concentration.

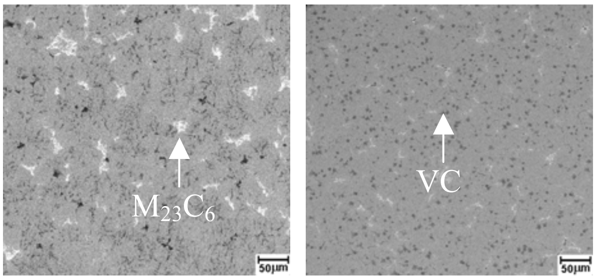

(a) (b)

Figure 3: Optical micrograph of the substrate (the bright phases are $M_{23}C_6$ carbide and the dark phases are vanadium carbides); (a) steel A and (b) steel C.

The slight difference in the oxidation rates after the nucleation time (after 1h) can be explained by an increasing amount of Cr in the $M_{23}C_6$ phase as the V content increases (Fig. 4). This decreases the amount of free Cr available in the matrix to diffuse towards the surface and to become enriched in the oxide phases. Consequently, it accelerates the diffusion of the species Fe and O within the oxide scale.

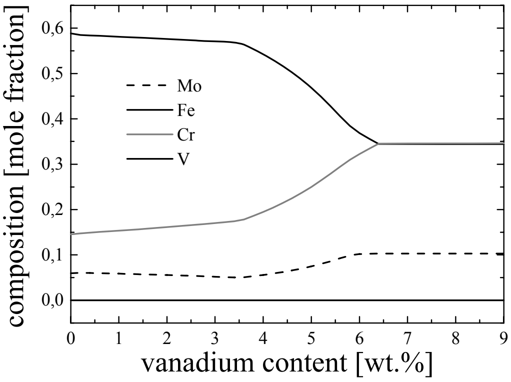

Figure 4: Composition of the $M_{23}C_6$ phase formed in Fe-Cr-Mo-W-V-C system at 650°C with varying V content.

3.2 *Oxidation of low-Cr boiler steels*

The low-Cr boiler steels exhibited a duplex oxide scale (Fig. 5) after 72h of oxidation at 550°C: an outer scale consisting of pure iron oxides (Fe_3O_4+Fe_2O_3) and an inner scale of Fe_3O_4 enriched with Cr. Thermodynamic equilibrium calculations for the Fe-Cr-O system (Fig. 5b) at 550°C revealed the oxide phase content as a function of the oxygen potential, which supports the experimental results regarding the phase identifications.

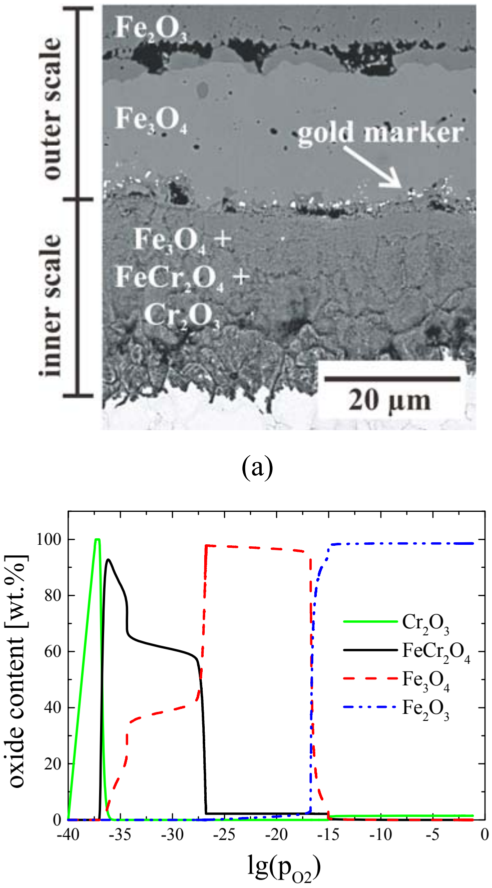

(a)

(b)

Figure 5: Oxide scale formed on the low-Cr boiler steel E at 550°C in air; (a) SEM cross section; (b) thermodynamic equilibrium calculation for the Fe-Cr-O system at 550°C.

Figure 6 shows that the kinetics of oxidation is accelerated by a decreasing grain size of the substrate. This phenomenon is supported by the idea that the inwards oxygen flux is increased for the fine-grained substrate due to the higher interface diffusivity along grain boundaries.

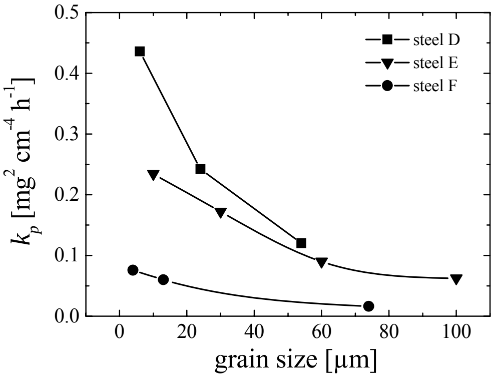

Figure 6: Oxidation rate of the low-Cr boiler steel at 550°C in laboratory air.

Calculation of oxide scale growth is possible through the combination of diffusion and local thermodynamic calculations. A computer-based model was used to calculate the growth of the inner scale in steels [8]. The diffusion of the species such as O and Cr is treated by solving numerically Fick's 2nd law applying the two-dimensional finite-difference method (Crank-Nicolson approach) [9]. This model distinguishes between diffusion in the bulk (lattice diffusion) and that along grain boundaries. The local thermodynamic equilibrium calculation is performed by calling interactively at every diffusion step the subroutine ChemApp, which is based on a numerical subroutine for Gibbs's energy minimization in combination with tailor-made data bases according to the Calphad methodology [10].

In order to avoid excessive computation time, the parallel-computing system PVM (parallel virtual machine) was used [9], i.e., the developed subroutine ThermoScript distributes the individual equilibrium calculations to thermodynamic workers according to the schematic representation in Fig. 7.

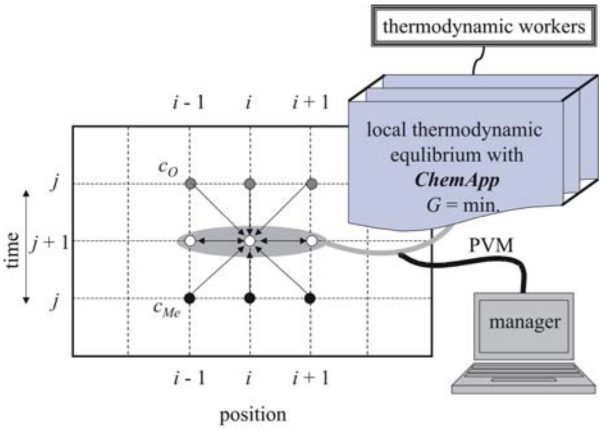

Figure 7: Schematic representation of the finite-difference technique (implicit Crank-Nicolson approach) in combination with thermodynamic subroutine ChemApp.

Figure 8a shows the two-dimensional calculation of the concentration profiles for Fe_3O_4 and $FeCr_2O_4$ formed on the steel E for a grain size of 10µm. The thermochemical database treats the Fe_3O_4 and $FeCr_2O_4$ phases separately, but as a coexisting phase ($FeFe_{2-x}Cr_xO_4$). Fig. 8b shows the calculated Cr gradient in the $FeFe_{2-x}Cr_xO_4$ spinel phase.

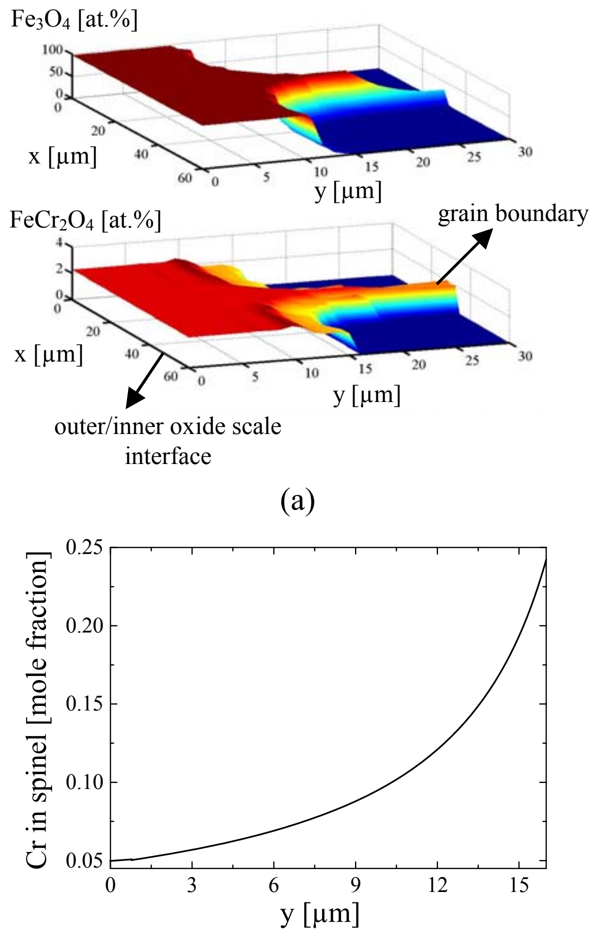

(a)

(b)

Figure 8: Simulated lateral concentration profiles of the oxide phase formed on the steel E; (a) Fe_3O_4 and $FeCr_2O_4$ concentration profiles, (b) Cr-gradient in the $FeFe_{2-x}Cr_xO_4$ phase within the grain.

3.3 Carburization of an austenitic steel

Cr is added in steels for different reasons such as (i) to increase the hardenability, (ii) to maintain mechanical resistance at high temperatures and (iii) to enhance to oxidation resistance. In austenitic steels, Cr as well as Fe have a strong affinity to carbon, and therefore the formed carbides are complex Fe-Cr carbides (solid solution). Figure 9a shows the different thermodynamically stable carbide phases for the Fe-Cr-Ni-C system at 850°C. The $M_{23}C_6$ is formed at low C and high Cr activities. This phase can be transformed into the M_7C_3 phase by increasing the C activity and this transformation is dependent on the temperature (see Fig. 9b).

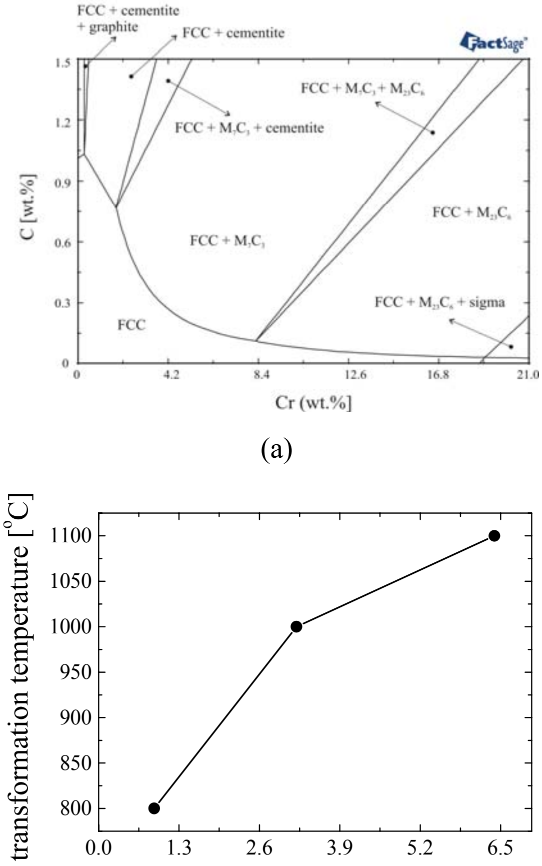

(a)

(b)

Figure 9: Thermodynamic equilibrium calculation for the system Fe-Cr-Ni-C; (a) map showing the stability of phases as a function of the Cr and C content at 850°C, (b) temperature for the transformation:
$M_{23}C_6 \leftrightarrow M_7C_3$.

Exposure of tubes with high Cr concentration to atmospheres containing oxygen and carbon leads usually to the formation of slow-growing chromia scales on the tube surfaces. Therefore, the carburization phenomenon is prevented. However, formation of local defects in the oxide scale allows carbon from the atmosphere to penetrate in the metal substrate and to dissolve in the metal phase [7]. Inward diffusion of the dissolved carbon leads to precipitation of carbides. The sequence of carbide phases precipitated depends on the flux of carbon in the substrate. This is determined by the diffusivity in the bulk (lattice diffusion) and the much higher diffusivity along grain boundaries.

Figure 10 shows $M_{23}C_6$ carbide formed along grain boundaries of the investigated austenitic steel at 850°C during the initial stage in a carburizing atmosphere containing methane.

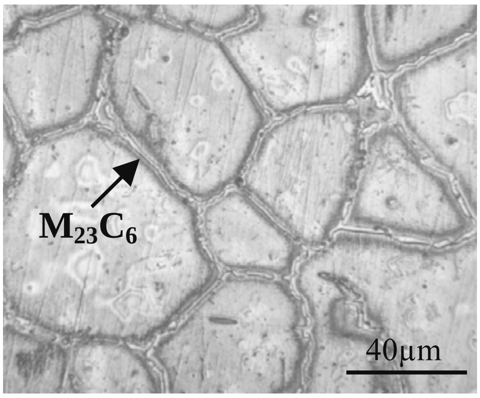

Figure 10: Micrograph showing intergranular $M_{23}C_6$ phase during carburization of an austenitic steel (steel G) at 850°C in the initial stage of exposure.

Using the computer-based model described in section 2.2 and in detail in [9], separation between carbon and Cr diffusion along the grain boundaries and the bulk was possible. The local thermodynamic equilibrium calculation was performed in the Fe-Cr-Ni-C system. Figure 11 shows the concentration profiles of the stable carbide phases. The more stable carbide ($M_{23}C_6$) starts to form on the reaction front, first along grain boundaries and it continuously transforms into M_7C_3 as the carbon potential increases.

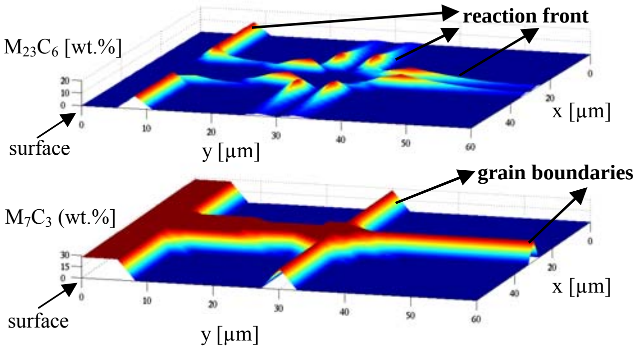

Figure 11: Concentration profiles of the carbides (M_7C_3 and $M_{23}C_6$) during carburization of an austenitic steel (steel G) with a grain size of 30µm at 850°C after 30h.

4 Conclusions

In this study three practical examples for corrosion attack of steels were presented and discussed. The mechanisms of high temperature material degradation caused by corrosion (oxidation and carburization) were demonstrated by experimental results. Computer-based simulation techniques were applied to understand the complex element and phase interactions under near-service conditions.

The presented computer-based model for the kinetics of oxidation processes of boiler steels and carburization of austenitic steels seems to be a powerful tool for service-life prediction, material selection and/or material development. In this model, complex diffusion calculations can be carried out that separate between diffusion along grain boundaries and diffusion in the bulk. This permits to predict precipitation along grain boundaries and within the grain interior. The implementation of local thermodynamic equilibrium calculations allow the assessment of complex phase transformations.

Acknowledgments

This research has been supported by the EU project OPTICORR and by the Brazilian Research Foundation (CAPES) through a fellowship to one of the authors (V. B. Trindade).

References

[1] Kofstad, P.: *High Temperature Oxidation of Metals*. First ed., Electrochemical Society, London, 1966.

[2] Trindade, V.B., Krupp, U., Wagenhuber, Ph.E.G., Christ, H.J: Oxidation Mechanism of Cr-Containing Steels and Ni-Base Alloys at High-Temperatures – Part I: The different role of alloy grain boundaries. *Materials and Corrosion*, in press, 2005.

[3] Töpfer, J., Aggarwal, S., Dieckmann, R.: Point defects and cation tracer diffusion in $(Cr_xFe_{1-x})_{3-\delta}O_4$ spinels. *Solid State Ionics,* 81, 251-266, 1995.

[4] Hay, K.A., Hicks, F.G., Holmes, D.R.: The transport properties and defect structures of the oxide $(Fe,Cr)_2O_3$ formed on Fe-Cr alloys. *Werkstoffe und Korrosion,* 11, 917-924, 1970.

[5] Hoyle, G.: *High speed steels*. First ed., Butterworths, London, 1988.

[6] A. P. Gulyaev, A.P.: Carbides in tool steels. *Metal Science and Heat Treatment*, 2, 127-129, 1960.

[7] Grabke, H.J.: Thermodynamics, mechanisms and kinetics of metal dusting. *Materials and Corrosion,* 49, 303-308, 1998.

[9] Crank, J.: *The Mathematics of Diffusion*, second ed., Clarendon Press, Oxford, 1986.

[8] Kupp, U., Trindade, V.B., Schmidt, P., Christ, H.J., Buschmann, U., Wiechert, W.: Oxidation Mechanism of Cr-Containing Steels and Ni-Base Alloys at High-Temperatures – Part II: Computer-based simulation. *Materials and Corrosion*, in press, 2005.

[10] Saunders, N., Miodownik, A.P.: *CALPHAD– Calculation of phase diagrams – A comprehensive guide*, Pergamon Materials Series, Pergamon, Guildford, 1998.

Proceedings of The 1st International Conference on **D**iffusion in **S**olids and **L**iquids
DSL-2005, July 6-8, 2005, University of Aveiro, Aveiro, Portugal

SELF-DIFFUSION AND IMPURITY DIFFUSION IN SILICON DIOXIDE

Masashi UEMATSU*

NTT Basic Research Laboratories, NTT Corporation,
3-1 Morinosato Wakamiya, Atsugi 243-0198, Japan

*Corresponding author. Fax: +81 46 240 4317; Email: uematsu@aecl.ntt.co.jp

Abstract

We present experimental and simulation results of silicon (Si) self-diffusion and boron (B) diffusion in silicon dioxide (SiO_2), and examine the effect of nitrogen (N) on diffusion in SiO_2. In order to elucidate the point defect that mainly governs the diffusion in SiO_2, the diffusion of implanted ^{30}Si in thermally grown $^{28}SiO_2$ is investigated. The experimental results show that Si self-diffusivity increases with decreasing distance between the ^{30}Si and Si/SiO_2 interface. We propose a model in which SiO molecules generated at the interface and diffusing into SiO_2 enhance Si self-diffusion, and the simulation results fit the experimental results. The B diffusivity also increases with decreasing the distance, which indicates that B diffusion is enhanced by SiO. In addition, we investigate the effects of B and N on SiO diffusion in SiO_2. We show that the existence of B increases SiO diffusivity and hence decreases the viscosity of SiO_2. On the other hand, the incorporation of N decreases SiO diffusivity, which reduces B diffusion in SiO_2 and increases the viscosity.

Keywords: Diffusion in crystalline and amorphous materials; Silicon dioxide; Boron; Oxynitride; Viscosity

1 Introduction

Silicon dioxide (SiO_2) is one of the most important materials in Si devices, especially for a gate insulator film of metal-oxide-semiconductor (MOS) transistors. With the scaling-down of MOS transistors, an ultrathin SiO_2 layer is demanded for the gate insulator. As the thickness of the SiO_2 layer decreases, atomic and molecular diffusion in SiO_2 becomes a fundamental issue. The diffusion in SiO_2 is also an important issue in high-k gate dielectrics because an interfacial SiO_2 layer forms between high-k gate films and Si substrates during post-annealing [1]. In addition, boron (B) penetration from the gate electrode through the thin SiO_2 layer into the Si substrate has been recognized as a serious problem [2]. It is well known that the incorporation of N into SiO_2, or using silicon oxynitride for the gate insulator, retards the B penetration [3]. Therefore, N atoms are also incorporated into the interfacial SiO_2 layer between high-k gate films and Si substrates [4]. However, the mechanism for the retardation of B diffusion in SiO_2 by the existence of N is not yet clear. Moreover, diffusion in SiO_2 is closely related to the viscosity of SiO_2, which is an important property of materials. The viscous flow of SiO_2 reduces the oxidation-induced strain, which is caused by a 125 % volume expansion, and therefore, plays an important role in thermal oxidation [5].

The present work investigates the mechanism of Si self-diffusion and B diffusion in SiO_2, and the effect of N on the diffusion. We observe Si self-diffusion and B diffusion in $^{28}SiO_2$ samples implanted with ^{30}Si and B, and based on the simulation, we show that SiO is the diffusing species that mailny governs the diffusion in SiO_2. In addition, the enhancement of SiO diffusion by the existence of high-concentration B is described. Moreover, we investigate the effect of N on SiO diffusion based on the simulation of the thickness in silicon thermal oxynitridation, where we show that SiO diffusion in SiO_2 is retarded by the incorporation of N.

2 Si self-diffusion

An isotopically enriched ^{28}Si single crystal epi-layer was thermally oxidized in dry O_2 at 1100 ˚C to form $^{28}SiO_2$ of thicknesses of 200, 300, and 650 nm. The samples were implanted with ^{30}Si at 50 keV to a dose of 2×10^{15} cm^{-2} and capped with a 30-nm-thick silicon nitride layer by rf magnetron sputtering. The as-implanted ^{30}Si profile is seen in the figures shown later. Samples were annealed at temperatures between 1100 and 1250 ºC. The depth profiles of ^{30}Si were measured by secondary ion mass spectrometry (SIMS). Figure 1 shows the experimental ^{30}Si depth profiles before and after annealing for 24 h at 1250 ˚C. The profiles demonstrate a strong dependence on the thickness of the ^{28}SiO$_2$ layer; the thinner the ^{28}SiO$_2$ layer is, the broader the diffusion profile becomes [6,7]. This result shows that the Si self-diffusivity increases with decreasing the distance between the diffusing ^{30}Si species and ^{28}Si/^{28}SiO$_2$ interface. This tendency was observed consistently in Si self-diffusion for other temperatures and annealing times employed in this study.

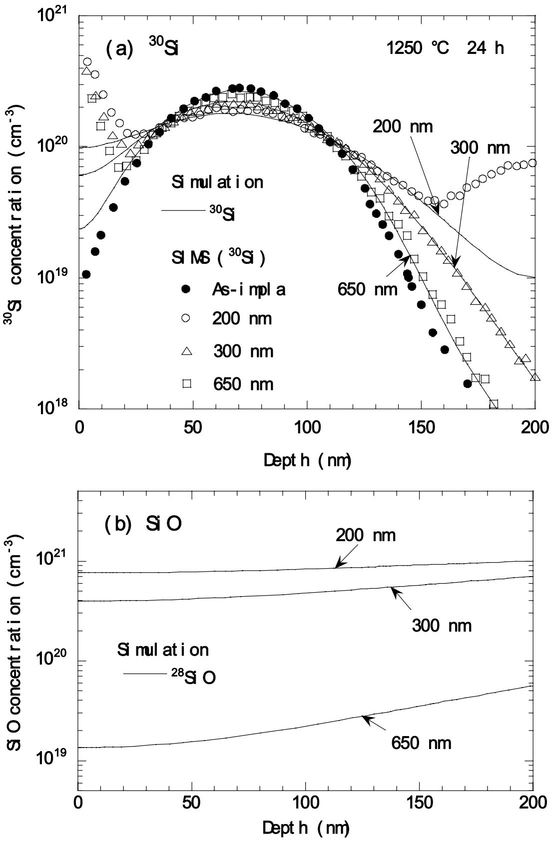

Figure 1: Experimental and simulated (a) ^{30}Si depth profiles and (b) simulated SiO profiles in SiO$_2$ samples with various thicknesses. Samples were annealed at 1250 ˚C for 24 h. The as-implanted ^{30}Si profile is shown as the initial profile. In SIMS data, the increase of ^{30}Si concentration deep in the bulk (> 150 nm) in the 200-nm-thick sample is ^{30}Si that diffused from ^{nat}Si substrates (800 nm below the ^{28}Si epi-layer) during the thermal oxidation to prepare the sample. (^{nat}Si refers to Si with the natural isotopic abundance.)

As the possible origins of the distance dependence of Si self-diffusion, we examined the effect of implantation damage, however, it is of no concern because the self-diffusivity of implanted Si in thick SiO$_2$ agrees with that obtained from damage-free CVD (chemical vapor deposition) SiO$_2$ [8,9] and remains unchanged for the doses between 1×10^{14} cm^{-2} and 2×10^{15} cm^{-2}. We also evaluated the stress due to a silicon-nitride capping layer; however, its effect is too small to induce the large enhancement of the Si self-diffusion (a factor-of-ten enhancement for the diffusion between 200 nm and 650 nm from the interface). Moreover, we have performed an experiment using CVD isotope heterostructures with a constant total oxide thickness, and Si self-diffusivity increases with decreasing the distance from the interface in the same way as that described above [10]. These results lead us to conclude that Si species generated at the Si/SiO$_2$ interface and diffusing into SiO$_2$ enhance Si self-diffusion. There have been a number of suggestions, based on experimental speculations and theoretical predictions, regarding emission of Si species from the Si/SiO$_2$ interface to SiO$_2$, and SiO generated at the Si/SiO$_2$ interface via the reaction Si + SiO$_2$ → 2SiO [11,12] is the most likely candidate as the dominant Si species. Consequently, we have proposed a model that SiO molecules, which are generated at the Si/SiO$_2$ interface and diffusing into SiO$_2$, enhance Si self-diffusion in SiO$_2$ via the reaction such that

$$^{30}\mathrm{Si(s)} + {}^{28}\mathrm{SiO} \Leftrightarrow {}^{28}\mathrm{Si(s)} + {}^{30}\mathrm{SiO} \qquad (1)$$

$$^{30}\mathrm{Si(s)} + {}^{28}\mathrm{Si(s)} \Leftrightarrow {}^{28}\mathrm{Si(s)} + {}^{30}\mathrm{Si(s)}\,. \qquad (2)$$

In these equations, Si atoms substituted in the Si sites of SiO$_2$ [denoted as (s)] diffuse via the kick-out reaction with diffusing SiO molecules. In addition, a simple mechanism of Si self-diffusion via Si interstitials or vacancies is taken into account for the thermal Si self-diffusion. This mechanism is described by Eq. (2), where SiO molecules are not involved in the diffusion. Evidence for the existence of two mechanisms (with and without SiO) is that very few SiO molecules arrive from the interface in the 650-nm-thick sample, as will be shown later by the simulation.

The above model leads to the following set of coupled partial differential equations to describe the diffusion of ^{30}Si in ^{28}SiO$_2$:

$$\frac{\partial C_{^{30}\mathrm{Si}}}{\partial t} = \frac{\partial}{\partial x}\left(D_{\mathrm{Si}}^{\mathrm{SD(th)}} \frac{\partial C_{^{30}\mathrm{Si}}}{\partial x} \right) - R \qquad (3)$$

$$\frac{\partial C_{^{30}\mathrm{SiO}}}{\partial t} = \frac{\partial}{\partial x}\left(D_{\mathrm{SiO}} \frac{\partial C_{^{30}\mathrm{SiO}}}{\partial x} \right) + R \qquad (4)$$

$$\frac{\partial C_{^{28}\mathrm{SiO}}}{\partial t} = \frac{\partial}{\partial x}\left(D_{\mathrm{SiO}} \frac{\partial C_{^{28}\mathrm{SiO}}}{\partial x} \right) - R\,, \qquad (5)$$

where R is the reaction term for Eq. (1) given by

$$R = k_{\mathrm{f}} C_{^{30}\mathrm{Si}} C_{^{28}\mathrm{SiO}} - k_{\mathrm{b}} C_{^{30}\mathrm{SiO}}\,. \qquad (6)$$

The Si self-diffusivity is, as a whole, described by

$$D_{\mathrm{Si}}^{\mathrm{SD}} = D_{\mathrm{Si}}^{\mathrm{SD(th)}} + D_{\mathrm{SiO}}^{\mathrm{SD}} \frac{C_{^{28}\mathrm{SiO}}(x,t)}{C_{\mathrm{SiO}}^{\mathrm{max}}}\,. \qquad (7)$$

In these equations, C_{x} is the concentration of the corresponding species in Eqs. (1) and (2), $D_{\mathrm{Si}}^{\mathrm{SD(th)}}$ the thermal Si self-diffusivity, D_{SiO} the diffusivity of SiO, and k_{f} and k_{b} are the forward and backward rate constants of Eq. (1). In Eq. (7), $D_{\mathrm{SiO}}^{\mathrm{SD}} = D_{\mathrm{SiO}} C_{\mathrm{SiO}}^{\mathrm{max}} / N_0$ is the Si self-diffusivity via SiO, where N_0 denotes the number of SiO$_2$ molecules in a unit volume of silicon oxide. Here, $C_{\mathrm{SiO}}^{\mathrm{max}}$ denotes the maximum SiO concentration in SiO$_2$ and is described as $C_{\mathrm{SiO}}^{\mathrm{max}} = 3.6\times10^{24}$ exp(-1.07 eV/kT) cm^{-3} [7]. In Eq. (3), the thermal Si self-diffusion [Eq. (2)] is represented by the diffusion term with $D_{\mathrm{Si}}^{\mathrm{SD(th)}}$, and $D_{\mathrm{Si}}^{\mathrm{SD(th)}} = 0.8$ exp(-5.2 eV/kT) cm^2/s [8] that was experimentally obtained is used for the simulation. In Eq. (7), $C_{^{28}\mathrm{SiO}}(x,t)$ depends on the depth and annealing times, which will be described below. The boundary condition for ^{28}SiO at the ^{28}Si/^{28}SiO$_2$ interface is given by $C_{^{28}\mathrm{SiO(x=interface)}} = C_{\mathrm{SiO}}^{\mathrm{max}}$ to describe the generation of SiO at the interface. The amount of ^{30}SiO arriving at the ^{28}Si/^{28}SiO$_2$ interface is so small that the mixing of ^{28}Si with ^{30}Si at the interface is neglected. The boundary condition at the nitride-capped surface is represented by a zero-flux condition because the cappings act as barriers. Reactions (1) and (2) are assumed to be so fast that the local equilibrium of the reaction is established, and hence the rate constants are set to be large enough. The parameters deduced from the simulation to fit the experimental profiles of ^{30}Si are $D_{\mathrm{SiO}}^{\mathrm{SD}}$, and we consistently obtained $D_{\mathrm{SiO}}^{\mathrm{SD}} = 4\times10^4$ exp(-6.2 eV/kT) cm^2/s for all samples. The $D_{\mathrm{SiO}}^{\mathrm{SD}}$ is comparable to the SiO diffusivities reported in Refs. 12 and 13. Equations (3) – (5) were solved numerically by the partial differential equation solver ZOMBIE [14].

Figure 1 shows the simulated ^{30}Si depth profiles after annealing for 24 h at 1250 ˚C together with the experimental profiles. For the simulated ^{30}Si profiles, the concentration of ^{30}Si(s) is shown because it is about two orders of magnitude larger than that of ^{30}SiO. The simulation results fit the experimental profiles of ^{30}Si for all ^{28}SiO$_2$ thicknesses using the same parameter values. This is in contrast to the Si self-diffusivity obtained by a simple fitting, or under the assumption of a constant diffusion coefficient for each profile, which increases with decreasing ^{28}SiO$_2$ thickness: 6×10^{-17}, 4×10^{-17}, 1×10^{-17} cm^2/s for 200, 300, 650 nm, respectively (the contribution from $D_{\mathrm{Si}}^{\mathrm{SD(th)}}$ at 1250 ˚C is 5×10^{-18} cm^2/s for all thicknesses). For other temperatures, the simulation results also fit the ^{30}Si profiles for all ^{28}SiO$_2$ thicknesses using the same parameter values for each temperature. In Fig. 1(b), the simulated SiO profiles are also shown (The concentration of ^{28}SiO is shown because it is a few orders of magnitude larger than that of ^{30}SiO). The SiO concentration in the ^{30}Si region increases with decreasing the ^{28}SiO$_2$ thickness. As expected from Eq. (7), SiO with higher concentration leads to larger enhancement of ^{30}Si diffusion. Therefore, the ^{30}Si self-diffusivity, assuming a constant diffusion coefficient, increase with decreasing ^{28}SiO$_2$ thickness. This thickness dependence arises because the SiO diffusion is so slow that the SiO concentration at the ^{30}Si region critically depends on the distance from the Si/SiO$_2$ interface, where the SiO is generated. In addition, the profile of SiO for the 650-nm-thick sample shows that the SiO concentration is so small that Si self-diffusion cannot be explained only by the kick-out diffusion via SiO [Eq. (1)]. This is the evidence for the existence of the two mechanisms (with and without SiO), as described above.

The time dependence of Si self-diffusion also shows the validity of our model. Figure 2 shows the experimental and simulated ^{30}Si profiles and the simulated SiO profiles in the 300-nm-thick sample for 6 h and 30 h at 1250 ˚C. The Si self-diffusivities, assuming a constant diffusion coefficient, show an enhancement of factor of 4.5 and are 1×10^{-17} cm^2/s for 6 h and 4.5×10^{-17} cm^2/s for 30 h. From the simulation, we found that the SiO concentration in the near-surface region becomes higher at longer annealing times until it reaches the maximum concentration. The time dependence arises because the SiO diffusion is so slow that more SiO molecules are arriving from the interface with time, and the self-diffusivity, assuming a constant diffusion coefficient, therefore increases for a longer annealing time. The simulated and experimental profiles almost coincide and this confirms the validity of our model. In addition, this result eliminates the concerns related to the strain or damage because Si self-diffusion would decrease with time if the diffusion were affected by the strain or damage, which should be gradually relieved or reduced by the anneals.

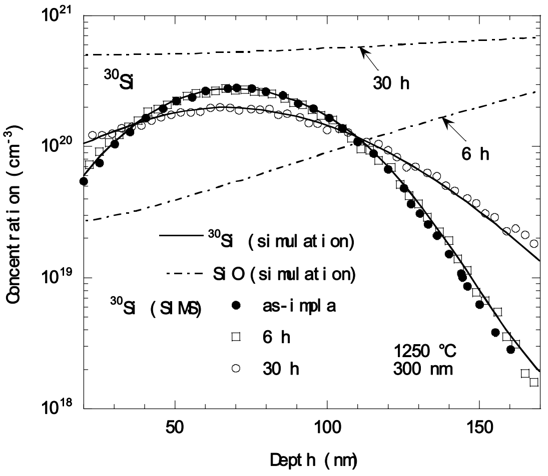

Figure 2: Experimental and simulated ^{30}Si depth profiles and simulated SiO profiles in the 300-nm-thick sample. Samples were annealed at 1250 ˚C for 6 and 30 h.

3 B diffusion

The ^{30}Si implanted samples mentioned in the previous section were subsequently implanted with ^{11}B at 25 keV to a dose of 5×10^{13} cm^{-2} or 3×10^{15} cm^{-2}, which will be referred to as low-dose and high-dose samples, respectively. Samples were annealed and the diffusion profiles of B and ^{30}Si were measured by SIMS. This simultaneous observation of B and ^{30}Si profiles allows us to investigate the B concentration effect on diffusion, as decribed in the next section. Figure 3 shows the experimental B profiles in low-dose samples with various thicknesses after annealing at 1250 ºC for 6 h. In the same way as Si self-diffusion, the B diffusion shows a clear dependence on the thickness of the $^{28}SiO_2$ layer; the shorter the distance from the Si/SiO_2 interface, the higher the B diffusivity in SiO_2 [15,16]. This tendency was also observed for the high-dose samples and other temperatures employed in this study. The distance dependence of B diffusivity indicates that the SiO molecules, which are generated at the Si/SiO_2 interface and diffusing into SiO_2, enhance not only Si self-diffusion but also B diffusion. In a similar manner to Si self-diffusion, B diffusion in SiO_2 is described by

$$B(s) + {}^{28}SiO \Leftrightarrow {}^{28}Si(s) + BO \qquad (8)$$

$$B(s) + Si(s) \Leftrightarrow Si(s) + B(s) . \qquad (9)$$

In Eq. (8), B atoms substituted in the Si sites of SiO_2 diffuse via the kick-out reaction with diffusing SiO. B diffusion via SiO is similar to B diffusion in Si via the kick-out mechanism, and BO may correspond to a complex of B-Si-O according to the first-principles calculation of B diffusion in SiO_2 [17]. In addition, a simple mechanism of B diffusion, where SiO molecules are not involved, is taken into account and is referred to as thermal B diffusion. Evidence for the existence of two mechanisms (with and without SiO) is that B diffusion occurs in the 650-nm-thick sample, where very few SiO molecules arrive from the interface, as described above.

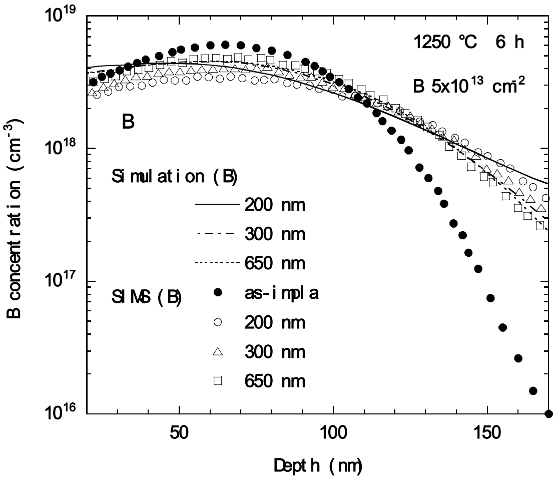

Figure 3: Experimental and simulated B depth profiles in SiO_2 samples with various thicknesses. Samples were implanted with B to a dose of 5×10^{13} cm^{-2} (low B dose) and annealed at 1250 °C for 6 h.

B diffusion in SiO_2 is simulated in a similar manner to Si self-diffusion by replacing ^{30}Si with B in Eqs. (1) and (2). Likewise, $D_{Si}^{SD(th)}$ should be replaced with $D_B^{eff(th)}$ (the effective diffusivity of thermal B diffusion), and D_{SiO}^{SD} with D_i^{eff} (the effective diffusivity of B diffusion via the kick-out mechanism with SiO). The total effective B diffusivity is expressed by

$$D_B^{eff} = D_B^{eff(th)} + D_i^{eff} \frac{C_{^{28}SiO}(x,t)}{C_{SiO}^{max}}. \qquad (10)$$

The experimentally obtained B diffusivity in thick (> 1 μm) SiO_2, $D_B^{eff(th)} = 3.12\times10^{-3}\exp(-3.93\ eV/kT)$ cm^2/s [18], which corresponds to the effective thermal B diffusivity, is used in our simulation. Consequently, the only parameter needed to fit the experimental B profiles in Fig. 3 is D_i^{eff}, and we consistently obtained $D_i^{eff} = 6.4\times10^{-2}\exp(-4.1\ eV/kT)$ cm^2/s for all samples.

Figure 3 shows the simulated B profiles after annealing for 6 h at 1250 °C. The simulation results fit the experimental B profiles for all the thicknesses using the same parameter values. This is in contrast to a simple fitting with a constant diffusivity, leading to 4×10^{-16}, 3×10^{-16}, 2×10^{-16} cm^2/s for 200, 300, 650 nm, respectively. For other temperatures, the simulation results also fit the B profiles for all $^{28}SiO_2$ thicknesses using the same parameter values for each temperature. In addition, the time-dependent B diffusion was also observed and simulated, in the same way as Si self-diffusion. These confirm the validity of our model that B diffusion in SiO_2 is enhanced by SiO. We mention that the effect of the Si/SiO_2 interface, which generates SiO molecules, should be taken into account for the analysis of diffusion in SiO_2. The D_{SiO} value deduced has the value of ~ 4×10^{-17} cm^2/s at 1100 °C, and the diffusion length for 10-second annealing is $2(D_{SiO}\times t)^{1/2}$ ~ 0.4 nm. This estimation indicates that SiO from the interface may affect the phenomena in the bulk when the material thickness is down to 1 nm.

4 Effect of high-concentration B

Figure 4 shows the depth profiles of ^{30}Si and B in the high-dose 200-nm-thick sample after diffusion anneal of 6 h at 1250 °C. The ^{30}Si depth profile of the annealed sample without B implantation is also shown. The profile of ^{30}Si in the high-dose samples shows larger diffusion than that without B [15,16]. On the other hand, the ^{30}Si profile of the low-dose samples (not shown in Fig. 4) showed no significant difference from that without B. In addition, for the high-dose sample, a significant decrease in the ^{30}Si concentration at its peak region was observed, where B concentration is high. In contrast, the tail region of ^{30}Si showed less significant diffusion, where B concentration is low. These results show that Si self-diffusivity increases with higher B concentration in SiO_2.

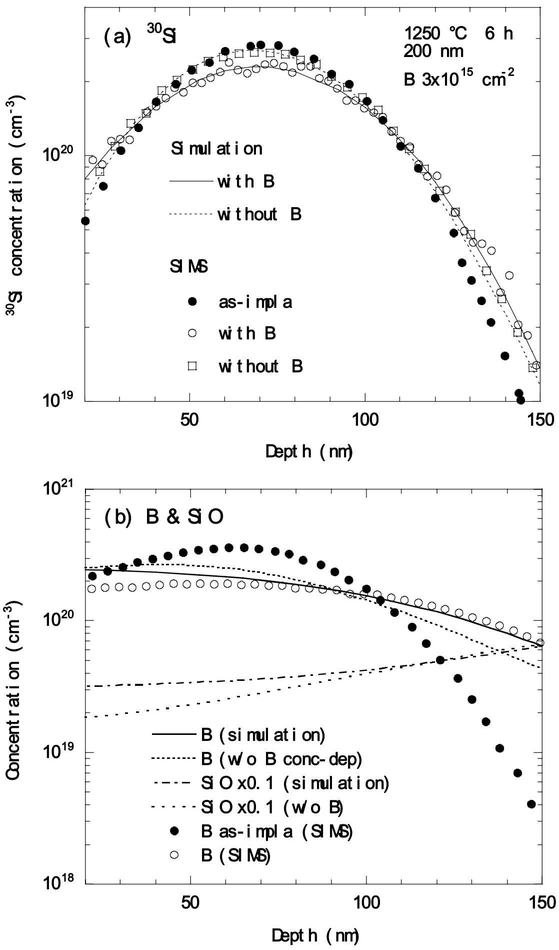

Figure 4: (a) Experimental and simulated ^{30}Si depth profiles with high-dose B implantation (3×10^{15} cm^{-2}) and without B, and (b) experimental and simulated B depth profiles and the simulated SiO profile (multiplied by 0.1) with high B dose in

the 200-nm-thick sample after annealing for 6 h at 1250 ˚C. In (b), the result of simulation without B concentration dependence and the simulated SiO profile (multiplied by 0.1) without B are also shown.

This dependence of B concentration is also seen in B diffusion itself. Figure 4(b) compares the experimental and simulated B profiles in the 200-nm-thick sample with high B dose after annealing at 1250 ˚C for 6 h. With the D_i^{eff} given above, the B diffusion profiles of low-dose samples were well reproduced by the simulation, as described in the previous section. However, the same simulation of the B diffusion for high-dose samples underestimated the results, as shown by the dotted line. This result shows that B diffusion in high-dose samples is faster than that in low-dose samples and that B diffusivity also increases with higher B concentration. The B concentration dependence has been reported in an experiment using a MOS structure, where the B diffusivity abruptly increased above B concentration of 10^{20} cm^{-3} [19], which is consistent with our result.

In order to reproduce the experimentally obtained enhancement of the ^{30}Si and B diffusion in the high-dose sample, we introduced a B concentration dependence of D_{SiO}^{SD} and D_i^{eff} for Si self-diffusion and B diffusion via SiO, of $D_{Si}^{SD(th)}$ for thermal Si self-diffusion, and of $D_B^{eff(th)}$ for thermal B diffusion by multiplying a factor of $\exp(C_B/C_B^{cri})$ to imitate the strong dependence on B concentration, where C_B^{cri} denotes the critical B concentration above which the high-concentration effect occurs. Inclusion of the B concentration dependence [$\times\exp(C_B/C_B^{cri})$] of $D_{Si}^{SD(th)}$ and $D_B^{eff(th)}$ is essential for explaining the enhancement of Si self-diffusion and B diffusion in the 650-nm-thick sample, where very few SiO molecules arrive from the interface. Consequently, the factor $\exp(C_B/C_B^{cri})$ was applied to D_{Si}^{SD} [Eq. (7)] and D_B^{eff} [Eq. (10)], which represent the sum of the two contributions (thermal diffusion and diffusion via SiO) to Si self-diffusion and B diffusion (The value of C_{SiO}^{max} is not changed). Using the value of $C_B^{cri} = 2\times10^{20}$ cm^{-3}, ^{30}Si and B profiles in the high-B-dose samples were fitted by the same set of diffusion parameters as that for low-dose profiles and that without B, as shown in Fig. 4. The profiles of SiO (multiplied by 0.1) obtained from the simulation are also shown in Fig. 4(b). In the near-surface region, the SiO concentration with high B dose is higher than that without B because of the enhanced SiO diffusivity by the B concentration dependence [$\times\exp(C_B/C_B^{cri})$], which leads to the increase of Si self-diffusivity and B diffusivity with higher B concentration. The mechanism of this diffusion enhancement by high-concentration B will be discussed below. The present result indicates that Si and B atoms in SiO_2 diffuse correlatively via SiO; namely, the enhanced SiO diffusion by the existence of B enhances B diffusion and Si self-diffusion. This correlation is consistent with the theoretical result that SiO molecules diffuse predominantly with frequent atomic exchange interactions with substitutional atoms [17].

5 Effect of N on diffusion

In this section, we investigate the effect of N on diffusion in SiO_2 based on the knowledge obtained above and based on the simulation of silicon oxynitridation. We assume that the incorporation of N reduces the SiO diffusivity in SiO_2 because the existence of N retards the B penetration, or B diffusion, which is enhanced by SiO. This assumption is also consistent with the increase of SiO_2 viscosity with N incorporation because diffusion of SiO is closely related to the viscosity of SiO_2 and viscosity is inversely proportional to diffusivity [20]. In order to validate this assumption, we simulate the thickness of Si thermal N_2O oxynitridation based on our interfacial Si emission model, which has successfully simulated Si thermal oxidation [21-24]. In this model, a large amount of SiO molecules (~1% of the oxidized Si) are emitted from the Si/SiO_2 interface during oxidation and most of the emitted SiO molecules diffuse into the oxide. In addition, the oxidation becomes slower with higher SiO concentration near the interface because the existence of high-concentration SiO prevents the emission of new SiO at the interface upon oxidation. Therefore, the oxidation in the oxide, which absorbs the emitted SiO, controls, or modulates, the oxidation rate at the interface. Based on the model, we constructed the diffusion equations of SiO and oxidant with the reaction terms of the SiO oxidation and numerically solved the equations to simulate the oxide thickness.

What has been reported so far about N_2O oxynitridation can be summarized as follows:
(1) The oxynitridation rate is much smaller than the O_2 oxidation rate and becomes smaller as oxynitride grows [25-28].

(2) N_2O thermally decomposes via the reactions of $N_2O \rightarrow N_2 + O$ and $N_2O + O \rightarrow 2NO$, and remaining atomic oxygen rapidly recombines into O_2, resulting in N_2 (64.3%), O_2 (31.0%), and NO (4.7%) at 950 ˚C [26]. Therefore, most of the increase of the thickness occurs via O_2, and NO is the source of N via the reaction with Si at the interface.

(3) Most of the N atoms incorporated during the oxynitridation pile up at the Si/SiO_2 interface with a width of ~2 nm [27] and the N concentration tends to saturate at only ~2 atomic percent (at. %).

Therefore, N_2O oxynitridation can be regarded as O_2 oxidation except that the piled-up N at the Si/SiO_2 interface affects the process. This leads us to apply our interfacial Si emission model to N_2O oxynitridation to simulate the thickness. In our model, therefore, SiO molecules are emitted from the Si/SiO_2 interface upon oxidation and diffuse in SiO_2 containing ~2 at. % N. The oxidation rate constant, k, is reduced as the SiO concentration near the interface, $C_{\mathrm{SiO}}^{\mathrm{I}}$, increases as oxidation proceeds because the existence of high-concentration SiO prevents the emission of new SiO at the interface. This reduction is described by

$$k = k_0 \left(1 - \frac{C_{\mathrm{SiO}}^{\mathrm{I}}}{C_{\mathrm{SiO}}^{\mathrm{max}}} \right), \qquad (11)$$

where k_0 is the maximum oxidation rate constant. Here, we assume that the incorporation of N in SiO_2 reduces the SiO diffusivity. The assumption that the SiO diffusivity exponentially decreases with increasing N concentration was introduced in analogy with B diffusivity in SiO_2, which exponentially increases with B concentration. During oxynitridation, the SiO diffusion is strongly retarded by the N at the interface. This retardation increases the SiO concentration in SiO_2 near the interface as oxynitridation proceeds, which decreases the oxynitridation rate with time.

For the simulation of N_2O oxynitridation, the following three parameters ($C_{\mathrm{N}}^{\mathrm{cri}}$, A_0, $C_{\mathrm{N}}^{\mathrm{max}}$) are newly introduced to our interfacial Si emission model. The other parameter values are the same as those in our previous studies for thermal O_2 oxidation [22,23]. The dependence of the SiO diffusivity on N concentration, C_{N}, is described as

$$D_{\mathrm{SiO}}^{\mathrm{N}} = D_{\mathrm{SiO}} \exp\left(- \frac{C_{\mathrm{N}}}{C_{\mathrm{N}}^{\mathrm{cri}}} \right), \qquad (12)$$

where $C_{\mathrm{N}}^{\mathrm{cri}}$ denotes the critical N concentration above which the N effect occurs. We assume that $C_{\mathrm{SiO}}^{\mathrm{max}}$ is independent of the N concentration. The increase of N concentration with increasing thickness (x) was obtained by

$$\Delta C_{\mathrm{N}} = A \Delta x \qquad (13)$$

for each calculation step. Here, A is the incorporation rate of N and is described by

$$A = A_0 \left(1 - \frac{C_{\mathrm{N}}}{C_{\mathrm{N}}^{\mathrm{max}}} \right), \qquad (14)$$

which describes that the N concentration increases almost linearly with thickness in an early stage and then tends to saturate [25]. The $C_{\mathrm{N}}^{\mathrm{max}}$ is the maximum N concentration. In the present simulation, all the thicknesses can be simulated using $C_{\mathrm{N}}^{\mathrm{max}}$ = 2 at. %. This value is consistent with the saturation of N concentration at ~2 at. %, which indicates that the N concentration dependence of A is reasonable. As mentioned above, most of the N atoms incorporated during the oxynitridation pile up at the Si/SiO_2 interface with a width of ~2 nm. In the simulation, we therefore set an N-containing SiO_2 layer with a width of 2 nm at the interface. The N concentration in this layer increases as oxynitridation proceeds.

The oxynitride thickness simulated in this study and that from experiments [28] are shown in Fig. 5. In the simulation, the thickness increase results from the oxidation by O_2 produced from the thermal decomposition of N_2O, as mentioned above. The proportion of O_2 is ~30 % and therefore the value of 0.3 atm was used as a partial pressure of O_2 in the simulation. Concerning the parameter values introduced for oxynitridation, $C_{\mathrm{N}}^{\mathrm{max}}$ = 2 at. % was used, as previously mentioned. For $C_{\mathrm{N}}^{\mathrm{cri}}$, 0.16 at. % at 950 ˚C, 0.20 at. % at 1050 ˚C, and 0.23 at. % at 1100 ˚C were used to fit the thickness. The temperature dependence of $C_{\mathrm{N}}^{\mathrm{cri}}$ is attributable to lower SiO_2 viscosity, or larger SiO diffusivity, at higher temperatures, which may reduce the effect of N. Concerning the value of A_0, it becomes smaller with smaller N_2O flow rate, and this is attributed to smaller N incorporation with slower flow [26]. Because of the lower N_2O flow rate, it takes longer for the NO to reaches the substrates. With slower flow, therefore, the loss of NO by the reaction $2NO + O_2 \rightarrow 2NO_2$ is more likely to occur during the gas flow, resulting in smaller N incorporation. Therefore, the value of A_0 depends on the flow rate and, in addition, on the dimensions of the furnace used. In the present simulation, however, the thickness was consistently fitted using the same set of parameters when the oxynitride was grown under the same flow, as shown in Fig. 5, where $A_0 = 0.4$ at. %/nm was used to fit the thicknesses. Therefore, the simulation fits the experimental oxynitride thickness in a unified manner, and this indicates the validity of our assumption of the N effect on SiO diffusion.

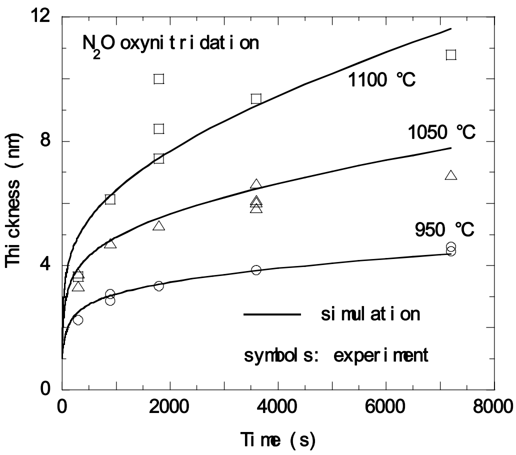

Figure 5: Simulated and experimental oxynitride thickness. Experimental data are from Ref. 28.

The calculated depth profile of SiO deduced from the simulation for 1050 ˚C at 1000 s (Fig. 5) is shown in Fig. 6. N atoms are incorporated in the layer with a width of 2 nm at the interface, as shown by the thick double-headed arrow. For the calculation, the interface is fixed at $x = 0$, while the surface moves as the oxynitridation proceeds. The oxynitride thickness is 5 nm, and the surface position is described by the vertical arrow (The right-hand side of the arrow is the gas phase). For comparison, Fig. 6 also shows the depth profile without N incorporation, that is, in pure O_2 oxidation, where the oxide thickness is 23 nm and the surface is outside the right ordinate. In oxynitridation, SiO diffusion is retarded at the N-containing layer and the SiO concentration almost reaches C_{SiO}^{max} at this temperature. Therefore, the growth rate is significantly reduced [Eq. (11)]. The concentrations of N incorporated after 2-h oxynitridation deduced from the simulation in Fig. 5 are 1.0, 1.5, and 1.8 at. % at 950, 1050, and 1100 ˚C, respectively. From Eq. (12) and the C_N^{cri} values described above, the SiO diffusivity was found to decrease about three orders of magnitude. This result explains why B penetration, which is enhanced by SiO, is suppressed even with a small amount of N (~2 at. %).

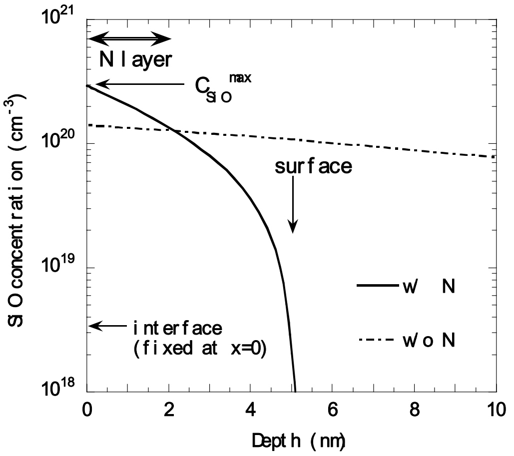

Figure 6: Calculated depth profile of SiO deduced from the simulation for 1050 ˚C at 1000 s in Fig. 5. For comparison, the calculated result without N incorporation is also shown. For the calculation, the interface is fixed at $x = 0$, while the surface moves as the oxynitridation proceeds. The surface position for oxynitridation is indicated by the vertical arrow. The N-containing layer with a width of 2 nm at the interface is also shown by the thick double-headed arrow.

As for the retardation of SiO diffusion by the existence of N, the formation of $Si_3{\equiv}N$ bonds is a possible mechanism. SiO diffuses via the bond exchanges with Si and O atoms of SiO_2, that is, via the reconstruction of Si-O bonds, not via the interstitial mechanism through the open spaces of SiO_2. One N atom forms bonds with three Si atoms and can fix the SiO_2 framework as a brace, and hence, N can effectively block the reconstruction of Si-O bonds in a wide area of the SiO_2 framework. Therefore, SiO diffusion in SiO_2 is significantly reduced even by a small amount of N. In contrast, the existence of B enhances SiO diffusion in SiO_2, as described in the previous section. The difference in the number of valence electrons between B (three) and Si (four) may be the origin of this enhancement. Due to the difference in the valence, substitutional B atoms will produce dangling bonds, which may ease the bond exchanges with Si and O atoms of SiO_2. Therefore, the introduction of B atoms leads to enhanced SiO diffusion in SiO_2. Because diffusion of SiO is closely related to the viscosity of SiO_2 and viscosity is inversely proportional to diffusivity, the present results indicate that the incorporation of B in SiO_2 reduces the viscosity of SiO_2, while that of N increases the viscosity, which is consistent with what has been known so far on the viscosity.

6 Conclusions

We have described the experimental and simulation results of Si self-diffusion and B diffusion in SiO_2, and have examined the effect of B and N on the diffusion. We showed that SiO molecules enhance both Si self-diffusion and B diffusion in SiO_2. In addition, based on the B concentration dependence, the simulation result indicates that B and Si atoms in SiO_2 diffuse correlatively via SiO; namely, the enhanced SiO diffusion by the existence of B enhances both B diffusion and Si self-diffusion. In contrast, the incorporation of N in SiO_2 reduces the SiO diffusivity, which reduces B diffusion in SiO_2.

Acknowledgments

The research on diffusion in SiO_2 was a collaboration with Hiroyuki Kageshima (NTT), Yasuo Takahashi (Hokkaido University), Shigeto Fukatsu, Kohei M. Itoh (Keio University), Kenji Shiraishi (University of Tsukuba), and Ulrich Gösele (Max Planck Institute, Halle).

References

[1] Wilk, G.D., Wallace, R.M., Anthony, J.M.: High-k gate dielectrics: Current status and materials properties considerations. *J. Appl. Phys.*, 89, pp. 5243-5275, 2001.

[2] Pfiester, J.R., Parrillo, L.C., Baker, F.K.: A physical model for boron penetration through thin gate oxides from p+ polysilicon gates. *IEEE Electron. Device Lett.*, 11, pp. 247-249, 1990.

[3] Ma, Z.J., Chen, J.C., Liu, Z.H., Krick, J.T., Cheng, Y.T., Hu, C., Ko, P.K.: Suppression of boron penetration in p^+ polysilicon gate p-MOSFET's using low-temperature gate-oxide N_2O anneal. *IEEE Electron. Device Lett.*, 15, pp. 109-111, 1994.

[4] Morisaki, Y., Aoyama, T., Sugita, Y., Irino, K., Sugii, T., Nakamura, T.: Ultra-thin poly-Si-gate SiN/HfO_2/SiON high-k stack dielectrics with high thermal stability. *IEDM Tech. Dig.*, pp. 861-864, 2002.

[5] Uematsu, M., Kageshima, H., Shiraishi, K.: Two-dimensional simulation of pattern-dependent oxidation of silicon nanostructures on silicon-on-insulator substrates. *Solid State Electron.*, 48, pp. 1073-1078, 2004.

[6] Fukatsu, S., Takahashi, T., Itoh, K.M., Uematsu, M., Fujiwara, A., Kageshima, H., Takahashi, Y., Shiraishi, K., Gösele, U.: Effect of the Si/SiO_2 interface on self-diffusion of Si in semiconductor-grade SiO_2. *Appl. Phys. Lett.*, 83, pp. 3897-3899, 2003.

[7] Uematsu, M., Kageshima, H., Takahashi, Y., Fukatsu, S., Itoh, K.M., Shiraishi, K., Gösele, U.: Modeling of Si self-diffusion in SiO_2: Effect of the Si/SiO_2 interface including time-dependent diffusivity. *Appl. Phys. Lett.*, 84, pp. 876-878, 2004.

[8] Takahashi, T., Fukatsu, S., Itoh, K.M., Uematsu, M., Fujiwara, A., Kageshima, H., Takahashi, Y., Shiraishi, K.: Self-diffusion of Si in thermally grown SiO_2 under equilibrium conditions. *J. Appl. Phys.*, 93, pp. 3674-3676, 2003.

[9] Fukatsu, S., Takahashi, T., Itoh, K.M., Uematsu, M., Fujiwara, A., Kageshima, H., Takahashi, Y., Shiraishi, K.: The effect of partial pressure of oxygen on self-diffusion of Si in SiO_2. *Jpn. J. Appl. Phys.*, 42, pp. L1492-L1494, 2003.

[10] Fukatsu, S., Itoh, K.M., Uematsu, M., Kageshima, H., Takahashi, Y., Shiraishi, K.: Effect of Si/SiO_2 interface on silicon and boron diffusion in thermally grown SiO_2. *Jpn. J. Appl. Phys.*, 43, pp. 7837-7842, 2004.

[11] Tan, T.Y., Gösele, U.: Oxidation-enhanced or retarded diffusion and the growth or shrinkage of oxidation-induced stacking faults in silicon. *Appl. Phys. Lett.*, 40, pp. 616-619, 1982.

[12] Celler, G.K., Trimble, L.E.: Catalytic effect of SiO on thermomigration of impurities in SiO_2. *Appl. Phys. Lett.*, 54, pp. 1427-1429, 1989.

[13] Tsoukalas, D., Tsamis, C., Stoemenos, J.: Investigation of silicon interstitial reaction with insulating films using the silicon wafer

bonding technique. *Appl. Phys. Lett.*, 63, pp. 3167-3169, 1993.

[14] Jüngling, W., Pichler, P., Selberherr, S., Guerrero, E., Pötzel, H.W.: Simulation of critical IC fabrication processes using advanced physical and numerical methods. *IEEE Trans. Electron Devices*, ED-32, pp. 156-167, 1985.

[15] Uematsu, M., Kageshima, H., Takahashi, Y., Fukatsu, S., Itoh, K.M., Shiraishi, K.: Correlated diffusion of silicon and boron in thermally grown SiO_2. *Appl. Phys. Lett.*, 85, pp. 221-223, 2004.

[16] Uematsu, M., Kageshima, H., Takahashi, Y., Fukatsu, S., Itoh, K.M., Shiraishi, K.: Simulation of correlated diffusion of Si and B in thermally grown SiO_2. *J. Appl. Phys.*, 96, pp. 5513-5519, 2004.

[17] Otani, M., Shiraishi, K., Oshiyama, A.: First-principles calculations of boron-related defects in SiO_2. *Phys. Rev. B*, 68, pp. 184112 1-8, 2003.

[18] Aoyama, T., Tashiro, H., Suzuki, K.: Diffusion of boron, phosphorus, arsenic, and antimony in thermally grown silicon dioxide. *J. Electrochem. Soc.*, 146, pp. 1879-1883, 1999.

[19] Aoyama, T., Arimoto, H., Horiuchi, K.: Boron diffusion in SiO_2 involving high-concentration effects. *Jpn. J. Appl. Phys.*, 40, pp. 2685-2687, 2001.

[20] Doremus, R.H.: Viscosity of silica. *J. Appl. Phys.*, 92, pp. 7619-7629, 2002.

[21] Kageshima, H., Shiraishi, K., Uematsu, M.: Universal theory of Si oxidation rate and importance of interfacial Si emission. *Jpn. J. Appl. Phys.*, 38, pp. L971-L974, 1999.

[22] Uematsu, M., Kageshima, H., Shiraishi, K.: Unified simulation of silicon oxidation based on the interfacial silicon emission model. *Jpn. J. Appl. Phys.*, 39, pp. L699-L702, 2000.

[23] Uematsu, M., Kageshima, H., Shiraishi, K.: Simulation of wet oxidation of silicon based on the interfacial silicon emission model and comparison with dry oxidation. *J. Appl. Phys.*, 89, pp. 1948-1953, 2001.

[24] Kageshima, H., Uematsu, M., Akagi, K., Tsuneyuki, S., Akiyama, T., Shiraishi, K.: Theoretical study of excess Si emitted from Si-oxide/Si interfaces. *Jpn. J. Appl. Phys.*, 43, pp. 8223-8226, 2004.

[25] Tang, H.T., Lennard, W.N., Allmang, M.Z.-, Mitchell, I.V., Feldman, L.C., Green, M.L., Brasen, D.: Nitrogen content of oxynitride films on Si(100). *Appl. Phys. Lett.*, 64, pp. 3473-3475, 1994.

[26] Tobin, P.J., Okada, Y., Ajuria, S.A., Lakhotia, V., Feil, W.A., Hedge, R.I.: Furnace formation of silicon oxynitride thin dielectrics in nitrous oxide (N_2O): The role of nitric oxide (NO). *J. Appl. Phys.*, 75, pp. 1811-1817, 1994.

[27] Saks, N.S., Ma, D.I., Fowler, W.B.: Nitrogen depletion during oxidation in N_2O. *Appl. Phys. Lett.*, 67, pp. 374-376, 1995.

[28] Hussey, R.J., Hoffman, T.L., Tao, Y., Graham, M.J.: A study of nitrogen incorporation during the oxidation of Si(100) in N_2O at high temperatures. *J. Electrochem. Soc.*, 143, pp. 221-228, 1996.

Proceedings of The 1st International Conference on **D**iffusion in **S**olids and **L**iquids
DSL-2005, July 6-8, 2005, University of Aveiro, Aveiro, Portugal

OXIDATION OF SUBLIMATES FORMED UPON ELECTRON-BEAM REMELTING OF NIOBIUM

Vladimir M. CHUMAREV, Rosa I. GULYAEVA, Vladimir P. MAR'EVICH,
Alena G. UPOLOVNIKOVA*, Ludmila Y. UDOEVA

Institute of Metallurgy, Ural Division, Russian Academy of Sciences, Ekaterinburg, Russia

*Corresponding author. Email: pcmlab@ky.ru

Abstract

The oxidation of Nb–Al sublimates formed upon electron-beam remelting of niobium was studied upon isothermal and continuous heating in air. Aluminum niobates of the variable compositions $Al_2O_3 \cdot mNb_2O_5$, as well as niobium and aluminum oxides, are the base products formed upon oxidation of the sublimates. The Al-rich sublimates exhibit high oxidation resistance. The $NbAl_3$ compound formed in the sublimates is characterized by the highest heat resistance in comparison with other sublimate components. The oxidation process parameters were determined using an anisothermal kinetic method. The process was found to be multistage and limited by internal diffusion.

Keywords: Oxidation; Nb–Al sublimates; Anisothermal kinetic method; Internal diffusion

---

1 Introduction

Electron-beam remelting of niobium obtained by aluminothermy leads to the formation of sublimates in the form of a sinter of metal condensate having nonuniform chemical and phase compositions. The sublimates consist predominantly of a Nb–Al alloy. The contents of Al and Nb in the alloy vary from 10 to 60 and 20 to 80%, respectively. The sublimates containing metallic impurities, such as 0.5–2.5 % Fe, 0.5–3.0 % Ca, or 0.5–3.0 % Cr, etc., and interstitial impurities, such as oxygen (up to 6 %) or silicon (0.5–1.0 %), etc., are by-products that should be processed if niobium is to be isolated. The available, newly developed technologies for processing sublimates formed upon electron-beam remelting of niobium involve their preliminary oxidation. The oxidation of pure niobium has been studied extensively to date [1].

The oxidation of Nb–Al alloys has been studied only for low-aluminum alloys (containing no more 3.0 % Al). Because of this, studying the chemistry and kinetics of oxidation of Nb–Al sublimates is of not only industrial but also scientific interest.

2 Experimental

The oxidation of Nb–Al sublimates in air was studied under both isothermal and anisothermal conditions. We studied sublimates containing 82.14 % Nb, 11.83 % Al, 1.12 % Fe, 0.20 % Cr, and 0.65 % Si (sample I) and 24.6 % Nb, 50.7 % Al, 1.98 % Ca, 0.83 % Si, 0.8 % Cr, 0.5 % Fe, and 0.8 % C (sample II). Sample I consists predominantly of Nb and $NbAl_3$, and sample II, of $NbAl_3$ and Al.

Oxidation under anisothermal conditions was performed on a Q1500D derivatograph used for differential thermal (DTA) and gravimetric (TGA) analyses. The isothermal oxidation experiments were performed using a tube furnace. The composition of the reaction products was determined using chemical and X-ray diffraction analyses.

3 Results and discussion

Upon heating at a rate of 8 K/min, the oxidation of the milled sublimates (with a particle size smaller than 200 μm) starts at 270–290 °C and isaccompanied by an increase (ΔG) in the weight of the samples. After heating to 1000 and 1430 °C, the increase in the weight of sample I is 22 and 25.5% (relative to the initial weight), respectively. The increase in the weight of sample II is 25 and 40 %

upon heating to 1000 and 1430 °C, respectively. The degree of transformation (calculated with allowance for the formation of the higher oxides of Nab and Al) of the Nb-rich sublimate is 85 and 98 % upon heating to 1000 and 1430 °C, respectively. The degree of transformation of Al-rich sublimates is 40 and 80 % upon heating to 1000 and 1430 °C, respectively. It can be seen that the oxidation is a stepwise process. The multistage character of the oxidation of sample II is most pronounced. According to the DTA curve, the exothermic effect related to the oxidation of sample I begins at ~ 370 °C, and the maxima of the effect correspond to 608 and 865 °C. The oxidation of sample II begins at 270 °C. Upon subsequent heating, three components of the exothermic effect are observed, and their maxima correspond to 650, 970, and 1395 °C. The endothermic effect observed at 615–630 °C is likely to be related to melting of the Al-based solid solution.

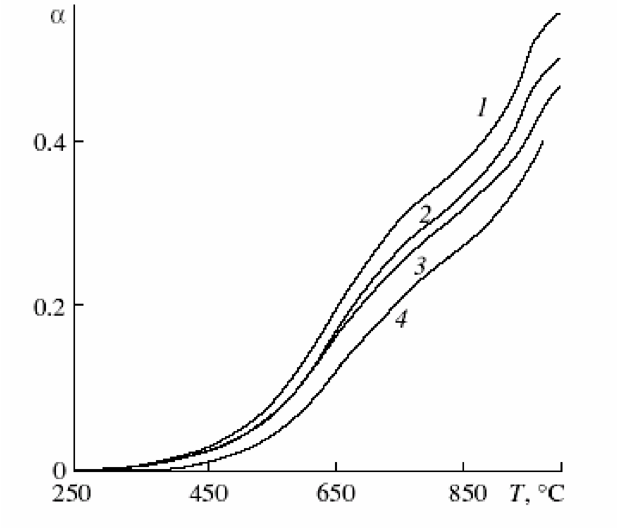

Figure 1: Oxidation polytherms of the Nb–Al sublimates (sample II) upon heating at rates v = (*1*) 2.5, (*2*) 5.0, (*3*) 10.0, and (*4*) 20 K/min.

Using sample II, we studied the effect of the heating rate (v) on the degree of oxidation (α) of a sublimate (Fig. 1). It was found that, as the rate of heating to 1000 °C increases from 2.5 to 20 K/min, α decreases from 0.55 to 0.42. The composition of the reaction products formed during oxidation upon heating in air to 1000 °C was studied by X-ray diffraction analysis using a DRON-2 diffractometer and CoK_α radiation. α-Al_2O_3 and Nb_2O_5 were found to form upon oxidation. As the heating rate decreases, the intensities of the reflections of these phases increase slightly, whereas the intensities of the reflections of $NbAl_3$ and Al decrease. These data indicate that, irrespective of the heating rate, simultaneous oxidation of the initial phase components of the sublimates takes place.

Along with oxidation upon heating in air, we studied the oxidation of sublimates under isothermal conditions. X-ray diffraction analysis of sublimates subjected to oxidation showed that annealing of sample I (with a particle size of less than 100μm) at 400 °C for 300 min leads to the formation of Nb_2O_5, which is present along with the initial phases ($NbAl_3$ and Nb) (see Table 1). After annealing at 600 °C, weak reflections of $NbAl_3$ and pronounced reflections of Nb_2O_5 are observed in X-ray diffraction patterns; in this case, no reflections of Nb are observed. After annealing at 700 °C, a small amount of $NbAl_3$ is present in the reaction product. After annealing at 800 °C, no reflections of $NbAl_3$ were found in X-ray diffraction patterns. It should be noted that, upon annealing at 700 °C, oxidation is accompanied by the formation of aluminum niobates ($Al_2O_3 \cdot Nb_2O_5$), the composition of which becomes more complex ($Al_2O_3 \cdot 11Nb_2O_5$ and $Al_2O_3 \cdot 9Nb_2O_5$) upon heating above 800 °C. After annealing at 1200 °C, the increase in the weight of sample I is equal to 20 % (relative to the initial weight).

Isothermal oxidation of sample II (with a particle size of less than 100 μm) was performed at 1050 °C. Figure 2 shows X-ray diffraction patterns of the reaction products formed. It is seen that, after 200-min holding, α-Al_2O_3 and $Al_2O_3 \cdot Nb_2O_5$ are formed. In this case, the increase in the weight is 33.6 % (relative to the initial weight). The initial phases $NbAl_3$ and Al are found even after 500-min holding at 1050 °C; however, their contents decrease substantially, and the increase in the sample weigh reaches 40.3 %.

The results show that, upon holding in air at 1050–1100 °C for 240–500 min, the milled Nb–Al sublimates are incompletely oxidized, which is likely due to the presence of the $NbAl_3$ intermetallic compound (which is known to be a heat-resistant compound). Its content increases with the Al content in the sublimates.

To determine the oxidation rate of a sublimate containing 99.74 % Nb and 0.25 % Al, we used a cubic sample with a surface area of 1.12 cm^2.

Upon continuous heating, oxidation of the sample begins at 328 °C (Fig. 2) and then takes place at an ever-accelerating rate that reaches ~600 g/(m^2h) at 650–700 °C. This value is higher than that (450 g/(m^2h)) reported in [2] for dense pure niobium subjected to oxidation at 800 °C. It is likely that the sample studied in this work is characterized by a higher porosity and, therefore, has a higher reaction surface. The DTA curve of the sample is characterized by an additional exothermal effect with a maximum corresponding to 550 °C.

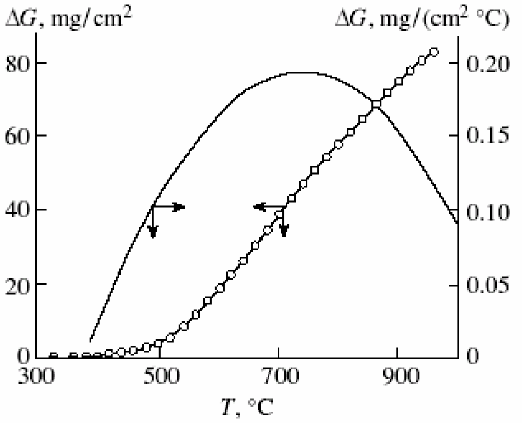

Figure 2: Oxidation polytherms of sublimates containing 99.7 % Nb and 0.25 % Al at a heating rate of 10 K/min.

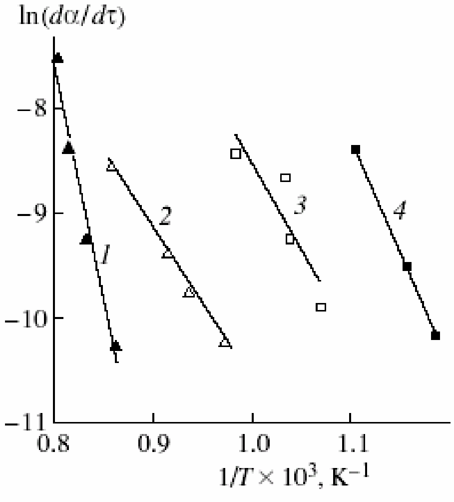

Figure 3: Temperature dependences of the oxidation rate of sample II of the Nb–Al sublimates at . = (*1*) 0.1, (*2*) 0.2; (*3*) 0.3, and (*4*) 0.4.

This effect is likely to be related to crystallization of the amorphous Nb_2O_5 oxide.

Oxidation of pure niobium is known to begin at ~200 °C with the formation of a dense oxide film. Upon heating above 200 °C, oxygen is dissolved in niobium to form metal-like oxides Nb*Ox* and NbOz. Upon heating above 600 °C, a phase transformation of Nb_2O_5 takes place, which leads to the formation of a porous oxide accelerating the oxidation. On the whole, the oxidation process can be represented by the stages [2]

$Nb–(Nb–O)_{sol.sol}–NbO_x–NbO_2–\alpha\text{-}Nb_2O_5–\gamma\text{-}Nb_2O_5$.

The α → γ phase transformation of Nb_2O_5 occurs at 800–850 or 640–800 °C [2]. The presence of Al (5–15 at %) in Nb–Al alloys leads to a decrease in the oxidation rate due to the formation of a dense protective oxide film.

The parameters of the oxidation process of the Nb.Al sublimates (Sample II) were calculated using the anisothermal kinetics method [3, 4] and the equation [10]

$$d\alpha/d\tau = K_0\,(1-\alpha)^n \exp(-E/(RT)),$$

where K_0 is the frequency factor, *E* is the temperature coefficient, *R* is the universal gas constant, and *n* is the reaction order. Taking into account that, upon continuous heating, $v = dT/d\tau$, we determined the oxidation rates $d\alpha/d\tau$ at various temperatures for fixed values of α using the experimental α(*T*) dependences (see Fig. 1). Then, using the equation

$$\ln(d\alpha/d\tau) = -(E/R)\,(1/T) + \text{const}$$

we determined the temperature coefficient *E*. The dependences ln(dα/dτ) versus T^{-1} calculated for the various values of α (0.1–0.4) (Fig. 3) and the dependences dα/dτ versus α show that the oxidation is a multistage process. This is also confirmed by the kinetic parameters of oxidation (Table 2) calculated in the temperature range studied. It was found that the reaction order is $n \approx 1$. The temperature coefficient of oxidation (176.3 kJ/mol) is likely to determine the formation of a protective niobium-oxide film that hinders the diffusion of components to the reaction surface. Above 700 °C, the value of *E* decreases to 119.6 kJ/mol. This can be indicative of disordering and formation of a porous oxide. Above 900 °C, *E* increases abruptly to 358 kJ/mol. In this stage, the oxidation is likely to be retarded because of sintering [2] and the formation of an aluminum oxide with high adhesion to the alloy.

Table 1: Data on the isothermal oxidation of Nb–Al sublimates (sample I) during annealing in air.

№	T, °C	τ, min	ΔG, %	Phase composition of the reaction products
1	400	300	8,0	$NbAl_3$, Nb_2O_5, Nb
2	600	300	15,0	Nb_2O_5, $NbAl_3$
3	700	420	17.0	Nb_2O_5, $NbAl_3$, $Al_2O_3 \cdot Nb_2O_5$
4	800	240	17,6	$Al_2O_3 \cdot Nb_2O_5$, $Al_2O_3 \cdot 11Nb_2O_5$, Nb_2O_5
5	1000	180	17,6	$Al_2O_3 \cdot 9Nb_2O_5$, $Al_2O_3 \cdot 11Nb_2O_5$, $Al_2O_3 \cdot Nb_2O_5$
6	1100	240	19,0	Al_2O_3 $9Nb_2O_5$, $Al_2O_3 \cdot 11Nb_2O_5$, $Al_2O_3 \cdot Nb_2O_5$
7	1200	90	20,0	$Al_2O_3 \cdot 9Nb_2O_5$, $Al_2O_3 \cdot 11Nb_2O_5$, $Al_2O_3 \cdot Nb_2O_5$

Table 2: Kinetic parameters of the oxidation of Nb–Al sublimates (sample II).

v, K/s	$\alpha = 0,1$		$\alpha = 0,2$		$\alpha = 0,3$		$\alpha = 0,4$	
	$d\alpha/d\tau \cdot 10^3$, s^{-1}	T,K	$d\alpha/d\tau \cdot 10^3$, s^{-1}	T,K	$d\alpha/d\tau \cdot 10^3$, s^{-1}	T, K	$d\alpha/d\tau \cdot 10^3$, s^{-1}	T, K
0,0402	0,037	844	0,049	933	0,366	1025	0,034	1159
0,0833	0,073	865	0,095	959	0,059	1064	0,096	1207
0,1609	0,136	865	0,171	964	0,084	1090	0,227	1230
0,2639	0,229	906	0,216	1015	0,198	1168	0,547	1249
E, kJ/mol	176,3		135,5		119,6		358,0	
K_o	$5,0 \cdot 10^6$		$3,5 \cdot 10^3$		64,5		$7,0 \cdot 10^{11}$	

4 Conclusions

The oxidation of Nb–Al sublimates formed upon electron-beam remelting of niobium was studied upon heating to 1000–1430°C in air. The reaction product was found to consist predominantly of niobium and aluminum oxides and aluminum niobates of variable composition ($Al_2O_3 \cdot mNb_2O_5$). It was shown that Al-rich sublimates exhibit high oxidation resistance and that the $NbAl_3$ compound formed in the sublimates has the highest heat resistance.

References

[1] Zelikman, A.N., Korshunov, B.G., Elyutin, A.V., and Zakharov, A.M., *Niobii i tantal* (Niobium and Tantalum), Moscow: Metallurgiya, 1990.

[2] Kubaschewski, O. and Hopkins, B.E., *Oxidation of Metals and Alloys*, London: Butterworths, 1953. Translatedunder the title *Okislenie metallov i splavov*, Moscow: Metallurgiya, 1965.

[3] Merzhanov, A.G., Abramov, V.G., and Abramova, L.T., Thermographic Method for Studying the Heat Evolution Kinetics, *Zh. Fiz. Khim.*, 1967, vol. 41, no. 1, pp. 179–184.

[4] Merzhanov, A.G., Anisothermal Methods in the Chemical Kinetics, *Fiz. Goreniya Vzryva*, 1973, no. 1, pp. 4–36.

Proceedings of The 1st International Conference on **D**iffusion in **S**olids and **L**iquids
DSL-2005, July 6-8, 2005, University of Aveiro, Aveiro, Portugal

TRANSPORT PROPERTIES OF SODIUM DODECYL SULFATE IN CELLULOSE-POLYANILINE BLEND FILMS

Artur J.M. VALENTE[1,*], Hugh D. BURROWS[1], Victor M.M. LOBO[1]

[1]Department of Chemistry, University of Coimbra,
3004-535 Coimbra, Portugal

[*]Corresponding author. Fax: +351 239 827 703; Email: avalente@ci.uc.pt

---

Abstract

Transport properties are reported of sodium dodecyl sulfate (SDS) and water in cellulose acetate and in cellulose acetate-polyaniline (CA- PANi) blend films. With the incorporation of PANi in cellulose acetate the transport, diffusion and permeability coefficients change in a dramatic way. Such a change in transport properties is related to the interaction between SDS and blend film, as suggested by fluorescence measurements. The analysis of blend surface with and without equilibration with SDS, as seen by SEM, also shows a clear alteration in the surface morphology. The interaction which also depends on the amount of PANi present in the blend, has been followed by UV-vis spectroscopy and sorption/desorption processes, and shows that the transport of SDS through the blends is accompanied by a chemisorption process.

Keywords: Diffusion in crystalline and amorphous materials; interfaces; polyaniline; cellulose acetate; sodium dodecyl sulfate

---

1 Introduction

Cellulose acetate has been used as a matrix for a great variety of organic compounds. The neutral properties, capacity for transparent film formation and low cost are the most important advantages of this polymer. Another advantage is that water concentration and water diffusion coefficients in cellulose acetate can be controlled by changing thickness, solvent, etc. [1].

Polyaniline (PANi) is a well known conducting polymer [2] and cellulose acetate-polyaniline blends have been used as selective electrodes [3] and for applications in biochemical processes [4]. The use of surfactants in the polymerisation process of cellulose-acetate blends has been used to check the effect of surfactants in the conductivity properties of the membranes.

The main aim of our study is to contribute for the elucidation of SDS/blend interaction and to use this information to find out new applications for these blends.

2 Experimental

2.1 *Films and solutions*

Cellulose acetate, CA, films were prepared using CA purchased from Aldrich, with a weight-average molecular of 30,000 and degree of substitution by acetyl groups of 39.8 %. The CA (15 % w/v) was dissolved in tetrahydrofuran, with constant stirring during 24 hours. The solution was then deposited on a flat glass support and spread out with a Braive film applicator. After complete evaporation of the solvent at room temperature, the membrane was removed from the glass support with the help of water.

The polymeric blend films of CA and polyaniline were prepared using a similar procedure. Polyaniline as its emeraldine base, and prepared by chemical polymerization was used; two different blend films, named as VBL1 and VBL2 were prepared. The VBL2 film contained double the quantity of PANi than VBL1.

2.2 *Techniques*

The transport of SDS through the polymeric films was measured by using a permeation cell as described previously [5]. This consists of two cells filled with a permeant solution (cell A) and water (cell B). These are connected by two horizontal tubes, and the polymer membrane is placed between them. Silicone was used to seal the membrane to ensure hermetic interfaces. The experiments were carried out ensuring that there is streamlined flow near the membrane, and that there is no hydrostatic pressure influencing the transport.

The variation of concentration of SDS was determined in cell B during permeability experiments by measuring the electrical conductivity using a YSI 3200 instrument.

The flux of SDS, was calculated according to

$$J = (V/A)\ (dc / dt) \qquad (1)$$

where V and A are the volume of the solution in cell B (200 cm^3) and the permeating area (1.54 cm^2), and (dc/dt) is the variation of the concentration of the species, in cell B, with time t.

The conductivity instrument was calibrated (i.e., the dependence of the electrical conductivity on the SDS concentration) prior to each experiment using, at least, four standard solutions, whose concentrations covered the range of experimental values being measured in cell B.

The same experimental conditions were used for calibration and permeability experiments: solutions were stirred at ca. 220 rpm, and constant temperature (25 ± 0.1 ºC) was maintained using a VelpScientifica Multistirrer 6 thermostat bath. Data were recorded over a sufficient time to ensure a steady-state flux, but such that the diffusant concentration in cell B was always well below that in cell A (< 10 %).

Morphology of polymeric films (thickness around 20 µm) was analyzed using a Jeol/Scanning Microscope, model 5310 under low vacuum, operating at 20 and 10 kV.

UV-spectra were obtained over the wavelength range 400-800 nm, with a bandwidth 1.0 nm using a Jasco V-350 spectrophotometer; with the spectra obtained by directly inserting the polymer sample in the spectrophotometer, and using

The diffusion coefficients of water, D_w, in the different polymeric films were measured using a previously described technique [1].

The sorption/desorption cycle experiments were carried out as follows: The films were immersed without stirring in the surfactant solution until they attained equilibrium. The approach to equilibrium, which correspond an alteration in the film colour from blue to green, was monitored by UV-visible spectroscopy. The sorption kinetics were also registered. After that, the polymeric films were immersed in a known volume of water, and desorption was monitored, also by UV-visible spectroscopy.

3 Results and Discussion

Figure 1 shows the permeability and diffusion coefficients of SDS in pure cellulose acetate membranes. There is an increase of D and a decrease of P with an increase of SDS concentration in the pre-micellar region. The magnitude of the permeability coefficients is similar to that obtained in membranes of other cellulose esters [6] and the diffusion coefficients, obtained in steady-state conditions, are five orders of magnitude lower than for aqueous solution, showing the effect of the matrix on the diffusing species. The magnitudes of these parameters (P and D) are also similar to those observed for moderately hydrophilic cellulose derivatives [5], as well as to that reported earlier [7] in gas/polymer systems, and can be expected to be due to specific interactions between the diffusing species and polymer. This suggests that the cellulose acetate structure is the main parameter controlling the diffusion.

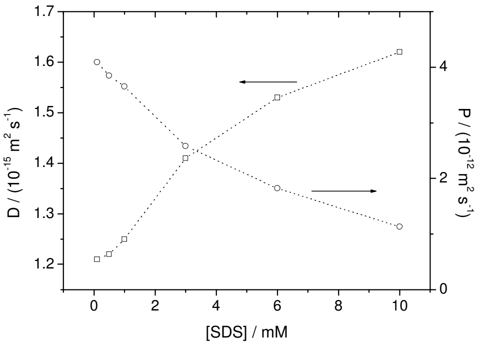

Figure 1: Permeability (o), P, and diffusion (□), D, coefficients of SDS in cellulose acetate films, at 25 ºC. The dot lines are just to guide the eyes.

Previous studies on cellulose acetate/SDS systems have suggested that aggregation, e.g., hemimicelle formation can occur at the CA surface [8]. This surface modification can explain the decrease in the permeability coefficients with an increase of SDS concentration. Two main possibilities are considered to justify this increase of D with SDS concentration, both involving increase in free volume within the membrane: a) the SDS-CA interaction at polymer surface will decrease the amount of diffusing species inside polymeric matrix, and consequently increase the free volume available for diffusion; and b) an increase in free volume may also result from changes in morphology of the CA membrane. Considering the procedure to calculate the polymer volume fraction, φ_P, using the polymer density and the water solubility, described elsewhere [1], it is possible to establish a linear relationship between D and φ_P. (Figure 2). Consequently, we can conclude that the major parameter affecting the diffusion process is the free volume of water in the polymer.

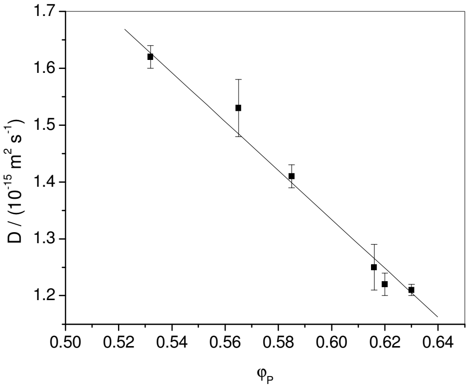

Figure 2: Effect of the polymer volume fraction, φ_P, on the diffusion coefficients, D, of SDS in cellulose acetate membranes.

Figures 3 and 4 show the diffusion and permeability coefficients of SDS through films VBL1 and VBL2, respectively.

The variations of P and D with SDS concentration in polymeric blends are quite different from that obtained in CA membranes.

In the VBL1 system, the transport of SDS shows a sharp decrease of D (approximately two orders of magnitude) followed by a plateau above the cmc, while a continuous decrease is observed in the permeability coefficient. With the increase of PANi content (VBL2 system), D and P follow the same profile with SDS concentration; however the magnitude of D is much lower than in VBL1.

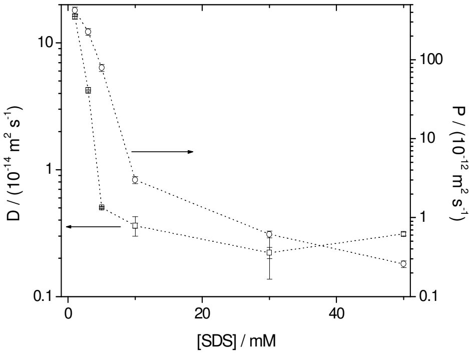

Figure 3: Permeability (o), P, and diffusion (□), D, coefficients of SDS in VBL1 films, at 25 ºC. The dot lines are just to guide the eyes.

In the comparison of permeation through PANi-containing and cellulose acetate films, not only is the time lag extended by the presence of PANi, but the final steady-state permeation is also affected. This steady-state permeation may, therefore, be indicative of interaction between the transported solute and PANi inside matrix. Such an interaction is enhanced in the SDS post-micellar region.

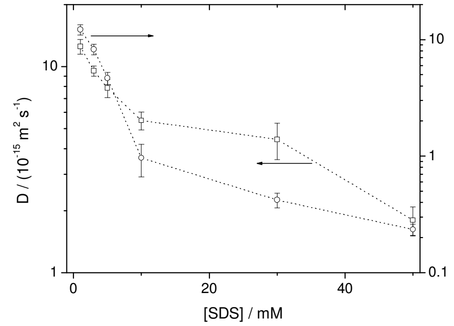

Figure 4: Permeability (o), P, and diffusion (□), D, coefficients of SDS in VBL2 films, at 25 ºC. The dot lines are just to guide the eyes.

However, the magnitude of the diffusion coefficients in VBL1 films, at pre-micellar region, is higher than in cellulose acetate membranes. This is likely to be due to a strong interaction between SDS and PANi, leaving only a low concentration of free unimer available to diffuse (to 0.1 mM SDS the interaction is almost negligible and, as a consequence, a very high D and P). That is the decrease of D upon the increase of SDS concentration can be explained by a reduction in the thermodynamic factor (related to the variation of the activity coefficient with concentration). With the increase of PANi concentration in the polymeric blend, it is expected that once the interactions SDS-blend increases, the tortuosity will tend to increase, thus decreasing surfactant mobility inside the membrane. Therefore, the steric effect becomes predominant and, consequently, not only will the magnitude of D decrease, but the effect of SDS micelles will also contribute to a continuous decrease of the D value.

Such explanations are supported from results obtained by a variety of different techniques.

The analysis of water content shows that with the incorporation of PANi, the water concentration decreases from 0.84 g/g in cellulose acetate [1], to around 0.21 g/g in VBL films. Whilst the water content does not show significant alterations with PANi concentration, it is possible to observe a decrease in the hydrophilicity with an increase of amount of PANi through water diffusion coefficient, D_w, values. That is, doubling of PANi concentration will lead to a decrease in D_w from 2.38×10^{-14} (0.31) $m^2\ s^{-1}$ to 1.34×10^{-14} (0.29) $m^2\ s^{-1}$.

Further arguments to support the above discussion come from SEM and UV-visible spectroscopy.

Figures 5 and 6 show alterations of morphological properties of cellulose acetate without and with (VBL1) the incorporation of PANi. However, following the sorption of SDS (10 mM) by VBL1 (Figure 7), a further change in the surface properties of the polymeric blend film was observed, with the surface structure becoming more diffuse.

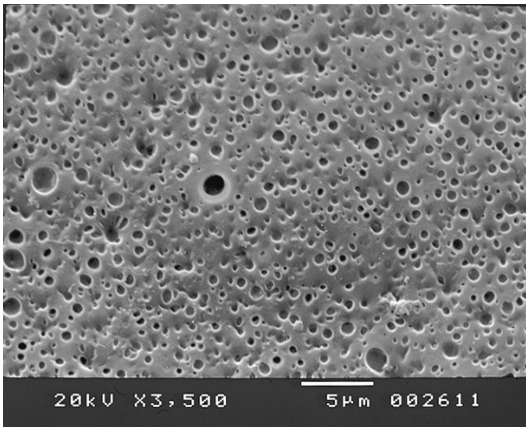

Figure 5: SEM micrograph of cellulose acetate film.

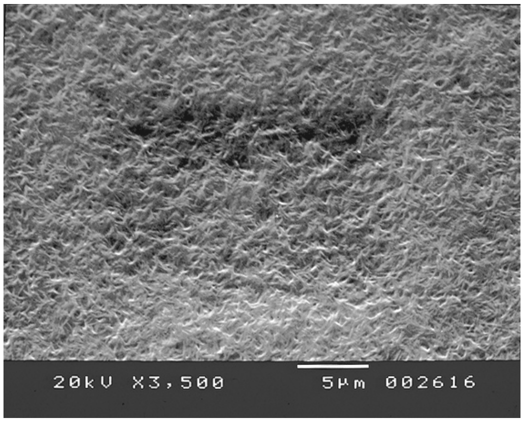

Figure 6: SEM micrograph of VBL 1 film.

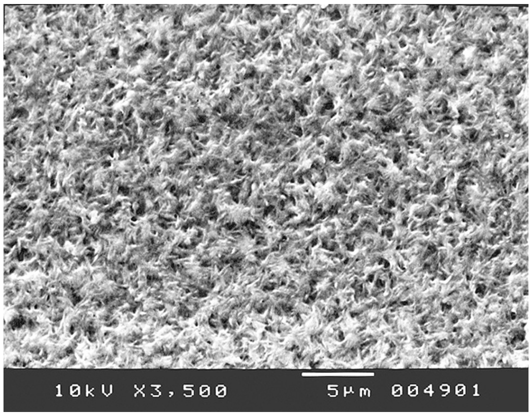

Figure 7: SEM micrograph of VBL 1 film after equilibrium with a SDS 10 mM solution.

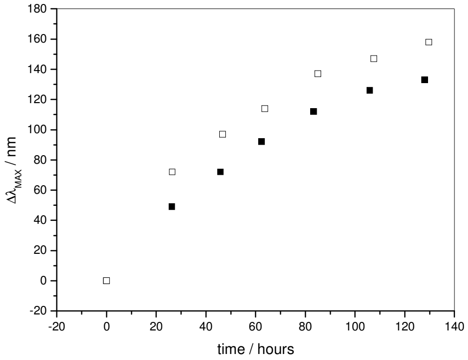

Figure 8: Effect of the sorption of SDS (10 mM) on the variation of the maximum absorbance wavelength, $\Delta\lambda_{MAX}$, of (■)VBL1 and (□) VBL2.

Strong interaction between SDS and PANi is also indicated by changes in color of the membranes from blue to green, and the modification in the visible absorption spectrum, where a clear shift in the absorption maximum is observed (Figure 8).

At low surfactant concentrations only a very small shift is seen. At 10^{-4} M SDS, $\Delta\lambda = 13$ nm. However, this shift increases with concentration, and at [SDS] = 10 mM, $\Delta\lambda$=167 nm. It is also possible to observe that, for the same interval of time, the $\Delta\lambda$ value increases from VBL1 to VBL2.

The alteration of the absorption maximum is, therefore, dependent on the time of sorption of SDS by the polymeric VBL films as well as on the polyaniline concentration in the blend.

Figure 9 shows the effects of sorption and desorption of SDS by VBL1 as seen by UV-visible spectroscopy. Assuming that the concentration of SDS which interacts with VBL1 is responsible for the shift in the maximum wavelength, $\Delta\lambda$ is a direct measure of SDS species linked to polymer structure.

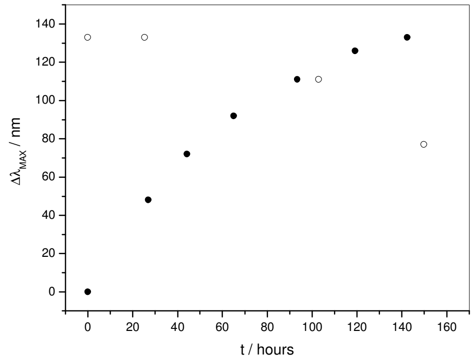

Figure 9: Sorption (•) and desorption (o) of SDS 0.01 M in P(Ani-CA)1 as seen by UV-visible spectroscopy.

As we can observe from the shift, the amount of immobilized SDS, which leads to the formation of the green colour, is approximately one half of the total amount of SDS sorbed by the polymer.

That is, the sorption of SDS by VBL1 can be described as a chemisorption process. The observed interactions help explain the decrease in both permeation of SDS due to steric effects, as well as the decrease in SDS diffusion. The process is partially reversible, but the shift observed on desorption for 160 hours indicates some SDS is still bound to the PANi. Consequently the UV-visible spectroscopy becomes an appropriate technique to check the effect of SDS on sorption/desorption cycles of VBL1.

Two different mechanisms may occur for the interaction between sodium dodecyl sulfate and the conducting polymer in the polymeric blend: a) it acts through electrostatic interactions as a counter ion for conducting-polymer polycations, and b) hydrophobic interactions lead to adsorption on the conducting polymer. These interactions have previously been studied by conductivity [9] in polymers synthesized directly in the presence of the surfactants.

In the present case, it appears that the same interactions are involved between the polymer membrane and SDS, and are a direct consequence of SDS sorption.

Acknowledgments

We thank POCTI, FCT and FEDER for financial support.

References

[1] Valente, A.J.M., Polishchuk, A.Ya., Burrows, H.D., Lobo, V.M.M.: Permeation of water as a tool for characterizing the effect of solvent, film thickness and water solubility in cellulose acetate membranes. *Eur. Polym. J.*, 41, pp. 275-281, 2005.

[2] Pud, A., Ogurtsov, N., Korzhenko, A., Shapoval, G.: Some aspects of preparation methods and properties of polyaniline blends and composites with organic polymers. *Prog. Polym. Sci.*, 28, pp. 1701-1753, 2003.

[3] Lindfors, T., Sjoberg, P., Bobacka, J., Lewenstam, A., Ivaska, A.: Characterization of a single-piece all-solid-state lithium-selective electrode based on soluble conducting polyaniline. *Anal. Chimica Acta*, 385, pp. 163-173, 1999.

[4] Laska, J., Wlodarczyk, J., Zaborska, W.: Polyaniline as support for urease immobilization. *J. Molec. Catalysis B-Enzymatic*, 6, pp. 549-553, 1999.

[5] Valente, A.J.M., Polishchuk, A.Ya., Lobo, V.M.M., Burrows, H.D.: Transport properties of concentrated aqueous solutions of sodium dodecyl sulfate in polymeric membranes derived from cellulose. *Langmuir*, 16, pp. 6475-6479, 2000.

[6] Valente, A.J.M., Burrows, H.D., Polishchuk, A.Ya., Miguel, M.G., Lobo, V.M.M.,: Combined sorption/transport of sodium dodecyl sulfate and hydrochloric acid in a blend of cellulose acetate butyrate with cellulose acetate hydrogen phthalate. *Eur. Polym. J.*, 40, pp. 109-117, 2004.

[7] Hamilton, C.J., Murphy, S.M., Tighe, B.J.: Synthetic Hydrogels (10): anomalous transport behaviour in crown ether-containing hydrogel membranes. *Polymer*, 41, pp. 3651-3658, 2000.

[8] Childress, A.E., Deshmukh, S.S.: Effect of humic substances and anionic surfactants on the surface charge and performance of reverse osmosis membranes. *Desalination*, 118, pp. 167-174, 1998.

[9] Stejskal, J., Omastová, M., Svetlana, F., Prokes, J., Trchová, M.: Polyaniline and polypyrrole prepared in the presence of surfactants: a comparative conductivity study. *Polymer*, 43, pp. 1353-1358, 2003.

Proceedings of The 1st International Conference on **D**iffusion in **S**olids and **L**iquids
DSL-2005, July 6-8, 2005, University of Aveiro, Aveiro, Portugal

PARAMETRIC ANALYSIS OF HEAT TRANSFER IN CLOSED-CELL CELLULAR METALS

Matej VESENJAK[1,*], Zoran ŽUNIČ[1], Andreas ÖCHSNER[2], Matjaž HRIBERŠEK[1], Zoran REN[1]

[1]University of Maribor, Faculty of Mechanical Engineering,
Smetanova 17, SI-2000 Maribor, Slovenia
[2]Department of Mechanical Engineering, University of Aveiro,
Campus Universitário de Santiago, 3810-193 Aveiro, Portugal

[*]Corresponding author. Fax: +386 2 220 7994; E-mail: m.vesenjak@uni-mb.si

---

Abstract

The purpose of this research was to describe the thermal transport properties in closed-cell cellular metals. Influence of cell size variations with different pore gases has been investigated with transient computational simulations. Heat conduction through the base material and gas in pores (cavities) was considered, while the convection and radiation were neglected in the initial stage of this research. First, parametric analysis for defining the proper mesh density and time step were carried out. Then, two-dimensional computational models of the cellular structure, consisting of the base material and the pore gas, have been solved using ANSYS CFX software within the framework of finite volume elements. The results have confirmed the expectations that the majority of heat is being transferred through the metallic base material with almost negligible heat conduction through the gas in pores. The heat conduction in closed-cell cellular metals is therefore extremely depended on the relative density but almost insensitive regarding to the gas inside the pore, unless the relative density is very low.

Keywords: Heat transfer; Cellular metals; Closed-cell; Computational simulations

---

1 Introduction

Foams and other porous materials with a cellular structure have an attractive combination of mechanical, thermal and acoustic properties like high stiffness with regard to low specific weight or high gas permeability combined with high thermal diffusivity [1].
Cellular materials (Figure 1) comprise of a wide range of different arrangements and forms, usually with open or closed cells. The most important structural parameters of cellular materials are the morphology (open or closed cells), topology, cell size and the relative density or volume fraction (the macroscopic density divided by the density of the base material; ρ^*/ρ_s). The advantages of cellular materials are low density (light-weight structures), high acoustic isolation and damping, heat exchange, high impact/blast energy absorption, electromagnetic wave shielding, recyclability etc. The cellular metals (usually referred to as metallic foams) have some further advantages like higher strength and heat permeability [2]. Usually they are made of aluminium alloys or polymer materials, with regular or random cell arrangement. Metallic foams have the potential for application in automotive, rail, naval and aerospace industry as heat exchangers, filters, bearings, acoustic dampers, bio-medical implants and elements for energy absorption.

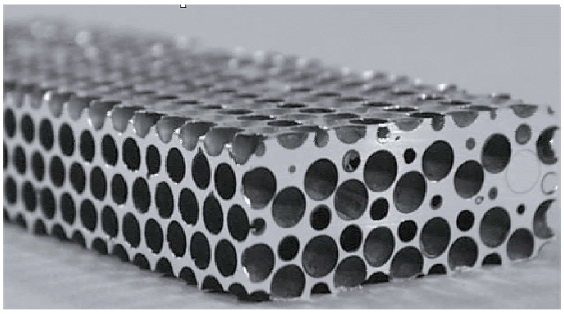

Figure 1: Closed-cell cellular structure [3].

In this paper the heat transfer through a regular closed-cell cellular metal is described. The influence of relative density and pore gases on the heat conduction has been analysed using the ANSYS CFX code within the framework of finite volume elements.

2 Heat transfer in cellular materials

Foams with a low relative density have very low conductivity and are therefore widely used for thermal insulation. There are several parameters that influence the heat flow through the foams: base material, cell size and enclosed gas (only at foams with low relative densities). The coefficient of thermal expansion of cellular material is usually approximately the same as that of the base material. However, their elastic modulus ($E^* = E_s (\rho^*/\rho_s)^2$) is much smaller and consequently the thermal stress generated by thermal load in cellular metals is much lower, which results in good thermal-shock resistance (i.e. ceramic foams) [1].

Several research projects have been initiated in order to develop a comparable analytical model for heat transfer through cellular materials and also its topology optimisation for optimal design to increase the heat dissipation efficiency [4].

In the base material, there are two material properties that define its heat conduction: thermal conductivity (λ) and thermal diffusivity (a). The thermal conductivity is described by Fourier's law, where the heat flux q which is induced due to temperature gradient ∇T is

$$q = -\lambda \nabla \mathrm{T}, \qquad (1)$$

which accounts for infinite speed of heat propagation. When describing unsteady-state conduction, the difference in heat entering and leaving a small element, results in temperature change with time ([1], [5], [6]). Temperature variation in space and time, accounting for heat conduction and heat accumulation, can be described by the following heat conservation equation:

$$\rho c_p \frac{dT}{d\tau} = \frac{d}{dx}\left(\lambda \frac{dT}{dx}\right). \qquad (2)$$

The product of the density (ρ) and the specific heat (c_p) defines the thermal capacity per unit volume of the material. If the density, specific heat and thermal conductivity are geometrically independent (the values are constant over x), the equation (2) reduces to the following unsteady state conduction equation:

$$\frac{dT}{d\tau} = a \frac{d^2T}{dx^2}, \qquad (3)$$

where a is the thermal diffusivity coefficient of the material:

$$a = \frac{\lambda}{\rho c_p}. \qquad (4)$$

The specific heat of a cellular material can be approximated as the sum of each phase multiplied by its volume fraction.

The following four parameters mainly contribute to thermal conduction of cellular materials:

- conduction through the base material (λ_s^*);
- conduction through the gas (λ_g^*);
- convection within the pores (λ_c^*);
- radiation through the pore walls and the cell voids (λ_r^*).

These parameters can be summarised as the conduction coefficient of the whole cellular structure:

$$\lambda^* = \lambda_s^* + \lambda_g^* + \lambda_c^* + \lambda_r^*. \qquad (5)$$

The contribution of the λ_s^* is the product of the conductivity of the full dense solid λ_s and the volume fraction of the cellular material, additionally multiplied by a pore shape factor [1]. The λ_g^* is the product of the gas conductivity multiplied by the gas volume fraction.

The convection is important only when the Grashof number (which describes the ratio of the buoyant force driving convection to the viscous force opposing it) is greater than 1000. Regarding to the definition of Grashof number one can define the minimal pore (cavity) size for which the convection can be neglected [1].

Mills and Gilchrist described the heat transfer in closed cell foams [7]. They found out that there is no convection in small pores and that the heat is transferred through the still gas only by diffusion.

According to Gibson and Ashby the convection can not be neglected, if the size of a pore filled with gas is larger than 10 mm. The cell sizes in real foams and cellular metals are usually much smaller than 10 mm (Alporas - 4 mm, Alulight - 5 mm and Cymat - 8 mm; [8]), therefore the convection might be completely neglected [1].

The radiation heat transfer is defined through Stefan's and Beer's law. However, this form of heat transfer is also neglected in the presented initial analysis.

Heat transfer through the cellular material increases with larger cell sizes, partly because radiation is reflected less often in foams with large cells and partly because, in cells larger than approximately 10 mm in diameter, cell convection starts to contribute.

It is also known that age of the foams can affect its thermal properties. With time, the pore gas diffuses out of the pore while air diffuses in, resulting in increased thermal diffusivity of the foam [1].

There should be an optimum foam or cellular material density for any given insulation problem. It depends on the temperature difference across the insulation and on its thickness. The existence of an optimum can be seen by noting that relatively dense foams conduct well because of the large volume fraction of solid it contain, while the ones with extremely low density allow radiation to pass through it easily. The optimum lies somewhere in between (i.e. for polymer foams it is usually in the range $\rho^*/\rho_s = 0.01 - 0.1$) [1].

In [9], numerical simulations show that the relative conduction appears to be almost independent of the specific shape or topology of the pores (inclusions) and that the morphology has only a minor effect on the thermal diffusivity. In this paper the effect of the cell size and type of gas inside the pore on a cellular structure heat conductivity has been analysed.

3 Numerical model

The numerical approach is in many cases restricted to consideration of few cell units or even only a single cell unit with specific boundary conditions [10]. In this paper an infinite cellular two-dimensional wall is modelled with 7 regular cells through the thickness (Figure 2). The base material of the cellular structure is aluminium and its material properties are listed in Table 1. The influence of the cell size variations (Table 2) with different pore gases (Table 3) has been investigated with transient computational simulations. In Table 2 the relative densities are shown for the two-dimensional (circular pores) and three-dimensional (spherical pores) cellular structure.

Table 1: Aluminium properties.

ρ [kg/m^3]	c [J/kgK]	λ [W/mK]	α [K^{-1}]	a [m^2/s]
2700	896	229	$238\ 10^{-5}$	$9.47\ 10^{-5}$

Table 2: Cell geometry.

s [mm]	r [mm]	ρ_{rp} [%]	ρ_{rv} [%]
1.806	0	100	100
1.806	0.52	74	90
1.806	0.75	46	70
1.806	0.89	24	50

In Table 3 the most commonly used injection gases are listed. For the heat transfer the most important parameter is heat diffusivity (*a*). According to that only air and CO_2 have been used in simulations, because the diffusivity of O_2 and Ar are almost equal to that of air.

Table 3: Pore gases properties.

Gas	ρ [kg/m^3]	c_p [J/kgK]	λ [W/mK]	a [m^2/s]
Air	1.2928	1003	0.02428	$1.87\ 10^{-5}$
O_2	1.4290	931	0.0266	$1.99\ 10^{-5}$
Ar	1.7834	523	0.018	$1.93\ 10^{-5}$
CO_2	1.9768	820	0.014	$0.86\ 10^{-5}$

A constant temperature of 700 K was prescribed at the edge 4 (Figure 2). Boundary conditions for the edge 1, edge 3 and in transversal direction were set as symmetric ($dT/dn = 0$). The edge 2 was specified as insulated ($q = 0$). The initial temperature of the whole model was set to 293 K.

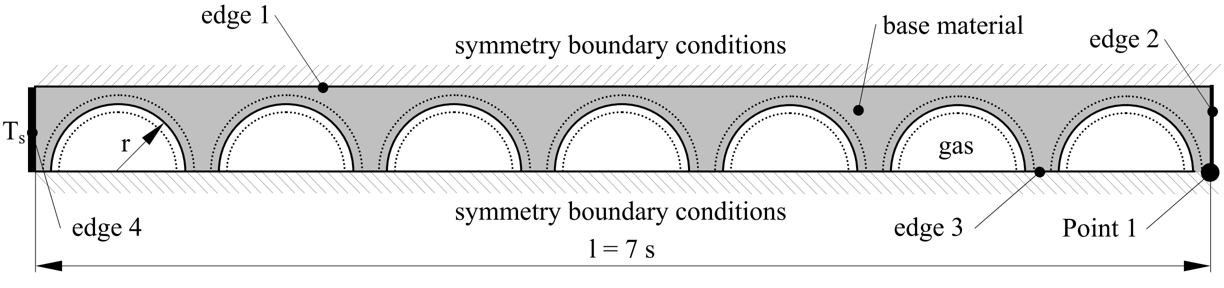

Figure 2: Cellular structure geometry.

For the time dependent thermal analysis the CFX program version 5.7.1 has been used. The program itself is based on the finite volume method and it uses an efficient coupled algebraic multigrid solver to solve transport equations [11].

The effects of fluid motion have been neglected and solid and fluid materials were both modelled as Solid Domain. Within Solid Domains, the conservation of energy equation is simplified since there is no flow inside a solid, thus conduction is the only mode of heat transfer. The heat conduction through the solid has the following transport equation

$$\frac{\partial}{\partial t}(\rho c_p T) = \nabla \cdot (\lambda \nabla T) + S_E . \qquad (6)$$

where S_E is volume source of thermal energy.

This equation is integrated over a control volume, and Gauss' divergence theorem is applied to convert some volume integrals to surface integrals. For control volumes that do not deform in time, the time derivatives can be moved outside of the volume integrals and the equation becomes

$$\frac{\partial}{\partial t}(\int_V \rho c_p T \, dV) = \int_S \lambda \frac{\partial c_p T}{\partial x_j} dn_j + \int_V S_E \, dV , \qquad (7)$$

where V and S respectively denote volume and surface regions of integration, and dn_j are the differential Cartesian components of the outward normal surface vector. The surface integrals are the integrations of the fluxes, whereas the volume integrals represent source or accumulation terms.

The time dependent term (left hand side of Eq. (7)) has been discretised with a second order backward Euler scheme, which approximates the transient term as

$$\frac{\partial}{\partial t}(\int_V \rho \phi \, dV) = \frac{\rho V}{\Delta t}(\frac{3}{2}\phi - 2\phi^0 + \frac{1}{2}\phi^{00}), \qquad (8)$$

where ϕ^o and ϕ^{oo} represent two previous subsequent time step solution fields. This scheme is also robust, implicit, conservative in time, and does not create a time step limitation. It is also second-order accurate in time, but is not bounded and may hence create some nonphysical overshoots or undershoots in the solution.

For the space discretisation the hexahedral (8 node) elements with tri-linear function variation have been used. Diffusive fluxes (first term in right hand side of Eq. (7)) are calculated with derivatives of interpolation functions.

To define a proper mesh size and time step initial parametric analysis has been carried out, considering only one representative volume element (one cell). Tables 4 and 5 show the comparison of time consumption and relative error of the densest mesh and smallest time step versus all other models.

Table 4: Comparison of CPU time [min] for different time steps and mesh densities.

time step [s]	mesh density – number of elements			
	560	1120	2240	4480
10^{-2}	0.7	0.8	1.9	6.9
10^{-3}	7.5	9.2	23.7	61.3
10^{-4}	76.7	90.0	249.5	602.6

Table 5: Relative error for different time steps and mesh densities.

time step [s]	mesh density – number of elements			
	560	1120	2240	4480
10^{-2}	32.9%	4.7%	4.6%	4.6%
10^{-3}	26.4%	0.1%	0.1%	0.1%
10^{-4}	4.7%	0.0	0.0%	0.0%

In Figure 3 the temperature profile at time 0.01 s is shown together with results deviation due to coarse mesh and large time steps.

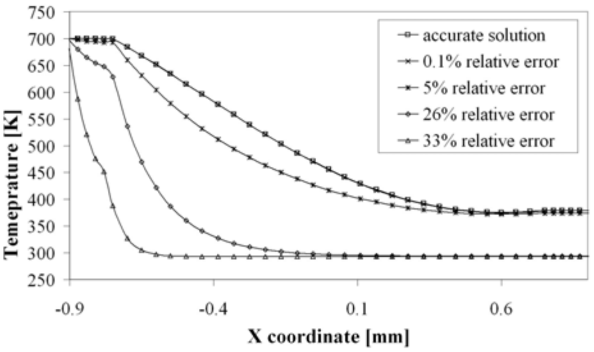

Figure 3: Temperature profile at the time 0.01s.

From these results it can be seen that 1120 elements per cell and a time step of 10^{-3} s provide very accurate results in an acceptable computational time. Consequently, the whole cellular structure model was modelled with 7840 elements. The time dependent analyses run approximately 14 hours on a PC with Intel Pentium IV 3200 MHz processor and 1 GB RAM.

4 Results of computational simulations

The results of the computational simulations are shown in Figures 4 to 7. Figure 4 illustrates the temperature filed in the first three cells at different times. One can observe the difference of heat conduction in the base material and gas.

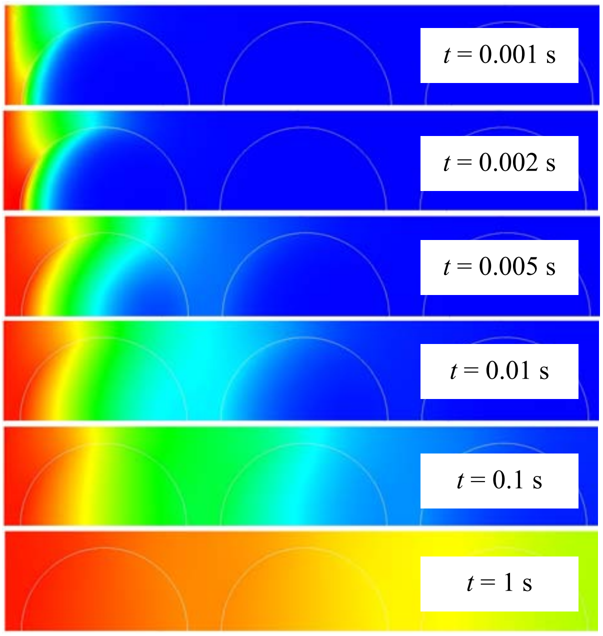

Figure 4: Temperature field for different times.

Figure 5 presents the temperature profile of the cellular material with a relative density 0.46 and air inside the pores for first 4 s.

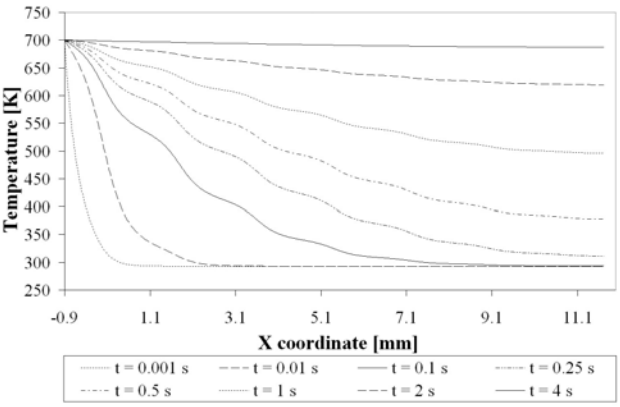

Figure 5: Temperature profile of cellular material ($\rho_{\mathrm{rp}} = 0.46$, pore filled with air) at different times.

The temperature profile of cellular structures with different relative densities shows strong influence on heat transfer through the material (Figure 6).

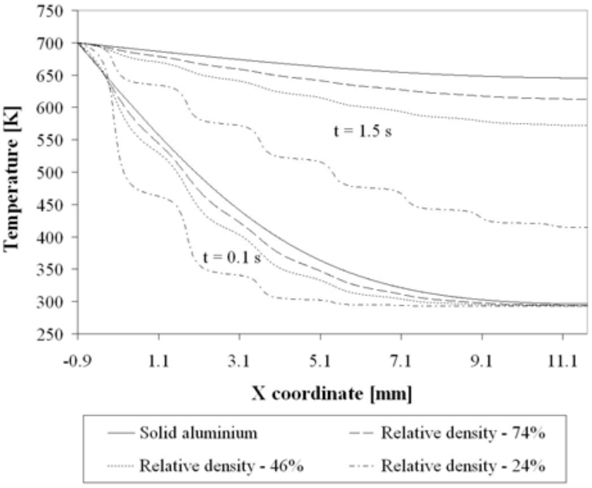

Figure 6: Temperature profile for cellular material with different relative densities.

By decreasing the relative density the heat transfer is also decreased. With a much lower relative density of the cellular material, a much stronger influence of the gas could be observed. However a different cell geometry must be used to achieve that.

Figure 7 illustrates the temperature changes at Point 1 (Figure 2) for different relative densities.

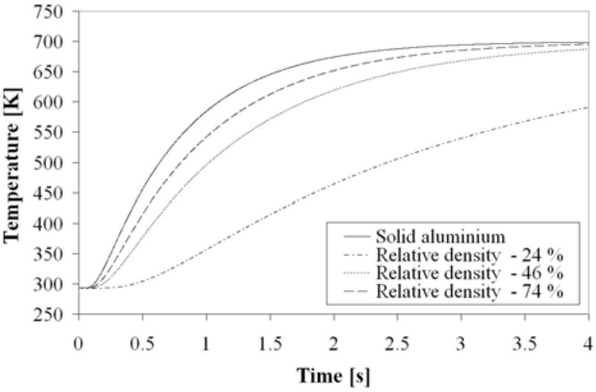

Figure 7: Temperature measured at Point 1 (Figure 2).

According to these results a strong dependence of heat transfer on relative density was confirmed. However the results have also shown that there is a very low influence of gas inside the pore. In Table 6 the temperatures on the outer edge 2 (Figure 2) at time 4 s are listed. It is obvious that for described relative densities the heat conduction through the gas might be neglected. The reason for this is a very high thermal diffusivity of the metallic base material in relation to the gas conductivity properties.

The influence of the gas thermal diffusivity increases in cellular materials with a lower relative density or lover thermal diffusivity of the base material (i.e. polymer, ceramics).

Table 6: Temperature on outer edge 2 (Figure 1) at time 4 s.

Gas in pore	Relative density	Temperature [K]
Air	0.24	590.9
	0.46	687.3
	0.74	695.5
CO_2	0.24	590.7
	0.46	687.3
	0.74	695.5
Void (λ=0)	0.24	587.5
	0.46	687.2
Solid aluminium	1.00	698.7

The results have confirmed that heat conduction in closed-cell cellular metals is strongly depended on the relative density but almost insensitive regarding the gas inside the pore, unless the relative density is very low.

Closed-cell cellular structures have lower thermal diffusivity than fully dense base metal. Therefore the closed-cell cellular structures can be potentially used to provide a certain degree of fire protection.

5 Conclusions

A parametric computational study of heat conduction in closed-cell cellular metal has been presented. First, the basic parameters of the computational model have been determined (mesh density, time step), then transient two-dimensional computational analyses of a chosen cellular structure were performed accounting for different relative densities and pore gases.

The results have shown very strong dependence of the relative density on the cellular material thermal diffusivity. However, the influence of different pore gases is almost negligible, since most of the heat is being transferred through the base material that has a very high thermal diffusivity. The influence of the gas inside the pores would increase with decreasing the relative density.

In further computational simulations, three-dimensional models accounting for the radiation and temperature dependent heat conductivity will be considered. It is envisaged that based on these results a homogenised macroscopic model will be developed, fully describing the thermal effects of filled cellular materials.

References

[1] Gibson, L.J., Ashby, M.F.: Cellular solids: structure and properties. Cambridge University Press, 1997.

[2] Ashby, M.F., Evans, A.G., Fleck, N.A., Gibson, L.S., Hutchinson, J.W., Wadley, H.N.G.: Metal foams: a design rule. Boston, Butterworth-Heinemann, 2000.

[3] Körner, C., Singer, R.F.: Adv. Eng. Mater. Vol. 2, p. 159. 2000.

[4] Wang, B., Cheng, G.D.: The Concurrent Design of Materials and Structures for Cellular Materials on Efficiency of Heat Dissipation. Dalian University of Technology, China.

[5] Alujevič, A., Škerget, L.: Heat Transfer. Tehniška fakulteta, Maribor, 1990. (in Slovenian language)

[6] Hriberšek, M.: Process Engineering – 1. part. Faculty of Mechanical Engineering, Maribor, 2005. (in Slovenian language)

[7] Mills, N.J., Gilchrist, A.: Cell. Polym., 16. 1997.

[8] Lu, T.J., Chen, C.: Therma Transport and Fire Retardance Properties of Cellular Aluminium Alloys. Acta mater., Vol. 47, Elsevier Science Ltd, 1999.

[9] Fiedler, T., Pesetskaya, E., Öchsner, A., Gracio, J.: Determination of the Thermal Conductivity of Porous Materials: Numerical and Mathematical Approaches. University of Aveiro, 2005.

[10] Öchsner, A.: Experimentelle und numerische Untersuchung des elasto-plastischen Verhaltens zellularer Modellwerkstoffe. Düsseldorf, VDI Verlag GmbH, 2003.

[11] ANSYS CFX Users Manual 5.7, 2004.

Proceedings of The 1st International Conference on Diffusion in Solids and Liquids
DSL-2005, July 6-8, 2005, University of Aveiro, Aveiro, Portugal

CODOPING EFFECTS ON THE DIFFUSION OF Ag IN CdTe

F. WAGNER[1,*], H. WOLF[1], Th. WICHERT[1], ISOLDE collaboration[2]

[1] Technische Physik, Universität des Saarlandes, D-66041 Saarbrücken, Germany

[2] CERN, EP Division, CH-1211 Geneve23, Switzerland

Corresponding author. Fax: +49 (0) 681 302 - 43 15; Email: wagner@tech-phys.uni-sb.de

---

Abstract

The influence of Cu, Au and In on the diffusion of Ag in CdTe was investigated using the radiotracer ^{111}Ag. After evaporating a Cu layer on the ^{111}Ag implanted side of a CdTe single crystal and subsequent annealing at 550 K for 30 min most of the radioactive ^{111}Ag atoms was detected in a thin layer of only a few µm at the back of a 500 µm thick crystal. This behaviour is drastically different from the Ag diffusion without an evaporated Cu layer. The qualitatively identical effect is observed if a Au layer is used instead of a Cu-layer. But, the effect of pushing the Ag atoms to the back of the crystal takes place on a significantly longer time scale. In contrast, diffusing the Ag atoms into In doped CdTe results in a penetration of the Ag profile that is strongly retarded as compared to the diffusion of Ag into undoped CdTe.

Keywords: Diffusion; CdTe; Codiffusion; Group I element

---

1 Introduction

The group Ib elements Cu, Ag, and Au are important impurities in II-VI compound semiconductors since they represent potential acceptors. Besides the acceptor like incorporation on substitutional lattice sites, group Ib elements are reported to occupy interstitial lattice sites and to act as donor impurities. For Ag atoms a high diffusivity already at relatively low temperatures is reported [1,2,3]. The fact that the distribution of Ag and Cu in CdTe can be manipulated by varying the partial pressure of Cd or Te during diffusion and thereby changing the stoichiometry of the sample was shown in earlier work [4,5,6]. In this report, it will be shown that the diffusion of Ag is strongly influenced by the presence of an additional group I element, like Cu or Au, and the group III element In.

2 Experimental details

The diffusion of Ag was studied using the radiotracer ^{111}Ag which was implanted into CdTe single crystals. For these experiments, circularly shaped crystals of 6 mm diameter and a thickness of about either 0.5 mm or 0.8 mm were used. The crystals were received polished on both sides from the supplier and were etched in bromine methanol solution before implantation. The implantations were performed with energy of 60 keV at the ISOLDE isotope separator (CERN, Geneva) or with 80 keV at the mass separator of the university of Bonn. Under these conditions the Gaussian like Ag profile is located at a depth of about 30 nm. For the codiffusion experiments, a layer of Cu or Au was evaporated onto the implanted side of the crystal. For diffusion annealing, performed at temperatures between 550 K and 800 K for different times, the crystal was enclosed in an evacuated quartz ampoule. In order to provide a partial pressure of Cd, few mg of Cd metal were added into the quartz ampoule. The concentration profile of ^{111}Ag was determined by mechanical polishing of the crystal and measuring of the γ-activity of the abraded layer using a Ge well-detector. The thickness of the abraded layer was determined by weighing of the polished crystal.

3 Results

Ag Diffusion under Cd pressure

The diffusion of Ag into CdTe under Cd or Te pressure was investigated in earlier work [4,5,6]. It was observed that the diffusion of ^{111}Ag under Cd pressure at 800 K for 60 min into an 800 μm thick crystal leads to a symmetrical, peak shaped concentration profile at the centre of the crystal followed by depletion layers of about 300 μm towards both surfaces (Fig. 1). The experimental data are well described in the framework of a model based on reactions of the dopant atom Ag with intrinsic defects of the Cd sublattice, i.e. Cd interstitials (Cd_i) and Cd vacancies (V_{Cd}). The solid line in Fig. 1 shows a simulation of the corresponding Ag profile based on this defect reaction model. In addition, the corresponding distribution of the intrinsic defects represented by the ratio of the concentrations $[Cd_i]/[V_{Cd}]$ is plotted (dashed line). The CdTe crystals as delivered are expected to be Te rich. Thus, the Cd pressure applied changes the distribution of the intrinsic defects due to chemical self diffusion what is reflected by the increased ratio $[Cd_i]/[V_{Cd}]$ towards both surfaces of the sample. Obviously, the ^{111}Ag profile essentially reflects the actual distribution of the intrinsic defects.

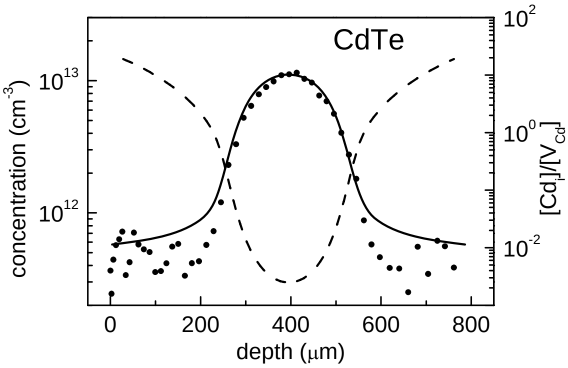

Figure 1: Ag profile in CdTe after diffusion at 800 K for 60 min under Cd pressure. The solid line shows a simulation of the Ag profile and the dashed line the corresponding ratio of intrinsic defects $[Cd_i]/[V_{Cd}]$.

Codiffusion of Cu.

Diffusing Ag into CdTe at 570 K for 30 min under vacuum leads to a monotonously decreasing concentration profile appears and the penetration depth reaches less than 100 μm (open circles in Fig. 2). Whereas such a profile is expected in case of a common diffusion process, the shape of the profile drastically changes if a Cu layers was evaporated onto the implanted side of the crystal before diffusion [6]. After diffusion at 550 K for 30 min under vacuum, the Ag atoms are nearly completely pushed into a thin layer of only few μm at the back of the crystal, while in the interior of the sample the Ag concentration significantly dropped below 10^{12} cm^{-3} (closed circles in Fig. 2).

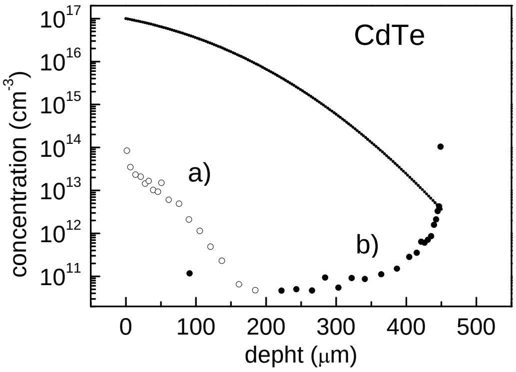

Figure 2: Ag profiles after a) diffusion at 570 K for 30 min and b) 550 K for 30 min obtained upon codiffusion of Cu. The solid line shows the calculated diffusion profile according to Jones et al. [7].

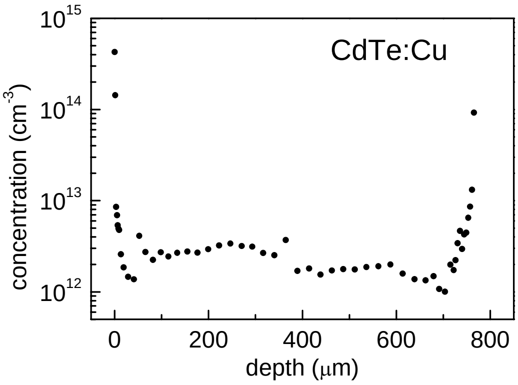

Figure 3: Ag profile after diffusion at 550 K for 30 min in Cu doped CdTe.

The influence of Cu on the diffusion of Ag in CdTe was also investigated in a sample previously doped with Cu. For this purpose, a Cu layer of 30 nm thickness was evaporated onto one side of a CdTe crystal and subsequently heated at 800 K for 2 h under vacuum. After this pre-treatment ^{111}Ag atoms were implanted into the crystal. The Ag profile obtained after diffusion at 550 K for 30 min is shown in Fig. 3. Now, a homogeneous

Ag profile at a concentration of about $3{\cdot}12^{12}$ cm^{-3} is present and the excess Ag is segregated at the surfaces of the crystal. Both experiments in figs. 2 and 3 illustrate that the presence of Cu drastically enhance the diffusion and affects the solubility of Ag in CdTe.

Codiffusion of Au.

Beside the codiffusion of Ag and Cu also the codiffusion of Ag and Au was investigated. In this case, a 30 nm Au layer was evaporated onto the ^{111}Ag implanted side of a CdTe crystal. The ^{111}Ag profiles obtained after diffusion at 550 K for 30 min and 120 min are shown in Fig 4. In contrast to the codiffusion experiment with Cu (closed circles in Fig. 2), now the Ag atoms are not completely pushed to the backside of the crystal but a depletion layer emerges from the Au evaporated side of the crystal. This depletion layer increases with diffusion time extending about 200 μm after 30 min and about 400 μm after 120 min. In case of 30 min diffusion time, the decrease of the Ag profile at depths larger than 200 μm reflects the diffusion range of Ag under these conditions and does not correspond to a depletion layer as observed at smaller depth at the front side of the sample.

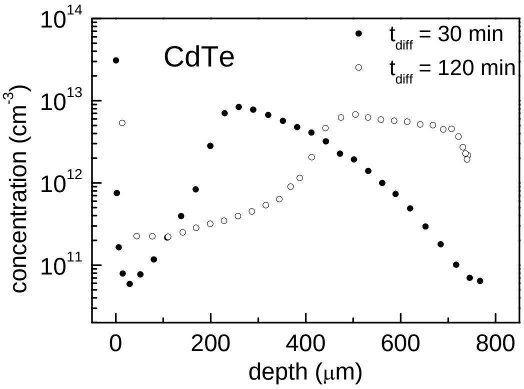

Figure 4: Ag profiles after diffusion at 550 K obtained upon codiffusion of Au for different diffusion times.

Ag diffusion in CdTe:In

Diffusing Ag into a CdTe crystal homogeneously doped with In donors results in drastically different diffusion profiles as it is shown in Fig. 5. Inspecting the Ag-profiles obtained after diffusion at 800 K for 240 min under vacuum (open circles) and under Cd pressure (closed circles) it is evident that the diffusion of Ag is significantly retarded in the In doped material. In particular, the penetration depth of Ag under Cd pressure is only about 300 μm and, therefore, significantly smaller compared to the undoped material shown in fig. 1. In contrast to undoped CdTe also the influence of the external vapour pressure seems to be weak since only a weak depletion layer emerged (closed circles).

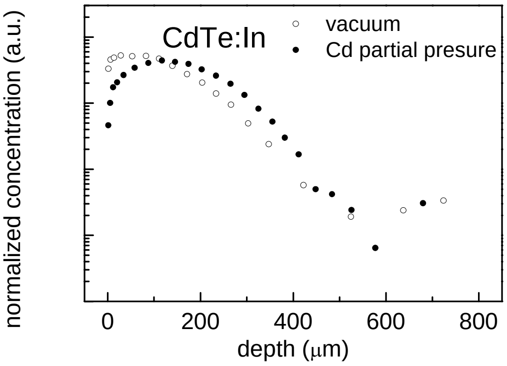

Figure 5: Ag profile after diffusion at 800 K for 240 min in In doped CdTe under vacuum (open circles) and Cd pressure (closed circles). The profiles are normalized to the respective maximum concentration.

4 Discussion

The unusual shape of the Ag profiles, as observed e.g. after diffusion at 800 K for 60 min under Cd pressure (see Fig. 1), has been discussed in earlier publications [4,5] and is well understood in terms of the interaction of Ag dopant atoms with intrinsic defects of the Cd sublattice:

$$\mathrm{Ag_{Cd}} + \mathrm{Cd_i} \rightleftarrows \mathrm{Ag_i} \tag{1a}$$

$$\mathrm{Ag_i} + \mathrm{V_{Cd}} \rightleftarrows \mathrm{Ag_{Cd}} \tag{1b}$$

$$\mathrm{Cd_i} + \mathrm{V_{Cd}} \rightleftarrows \mathrm{Cd_{Cd}} \tag{1c}$$

Assuming local thermal equilibrium, these reactions lead to a relation that connects the concentrations of the extrinsic and the intrinsic defects:

$$\sqrt{\frac{[\mathrm{Cd_i}]}{[\mathrm{V_{Cd}}]}} = k_{\mathrm{Ag}} \cdot \frac{[\mathrm{Ag_i}]}{[\mathrm{Ag_{Cd}}]} \tag{2}$$

Here, k_{Ag} is a temperature dependent equilibrium constant which determines the fraction of substitutionally incorporated Ag atoms. In addition, the model makes the following assumptions: (i) Ag diffuses exclusively interstitially. (ii) The diffusion coefficient $D(Ag_i)$ of the Ag_i defects is larger than the diffusion coefficient $D(Cd_i)$ of Cd_i defects. (iii) The diffusion coefficient $D(V_{Cd})$ of Cd vacancies is much smaller than $D(Cd_i)$. For describing the profile shown in Fig. 1 it is required that the deviation from stoichiometry $\Delta C = [Cd_i] - [V_{Cd}]$ during the diffusion process varies over a sufficiently large range from negative (Te-rich material) to positive (Cd-rich material) values. The dashed line in Fig. 1 shows the ratio $[Cd_i]/[V_{Cd}]$, which is a measure of the deviation from stoichiometry since the product $[Cd_i]\cdot[V_{Cd}]$ is a constant depending only on temperature. According to Eq. (2) the concentration of Ag_{Cd} atoms decreases in favour of Ag_i atoms if the Cd_i concentration is increased. Thus, the depletion layers in the Ag profile of Fig. 1 correspond to regions with an increased ratio $[Cd_i]/[V_{Cd}]$, caused by Cd_i atoms that are created by the Cd partial pressure according to reaction 1c. Most of the Ag atoms in this layer are incorporated at interstitial lattice sites, diffuse rapidly as Ag_i atoms into the V_{Cd}-rich center of the sample and are incorporated on Cd lattice sites according to reaction 1b. Consequently, the Ag distribution is determined by the concentration of the Ag_{Cd} atoms and directly reflects the stoichiometry of the sample after the corresponding diffusion process.

The Ag profile obtained after codiffusion of Cu at 550 K for 30 min (Fig. 2b) shows that the Ag atoms were pushed to the back of the crystal. Obviously the Ag diffusion is strongly enhanced upon codiffusion of Cu compared to Ag diffusion without codoping (Fig. 2a). By comparing the Ag profile, obtained after codiffusion of Cu, with the Cu profile as expected on the basis of the fast diffusing component reported in ref. [7] it turns out that the Ag profile exhibits an inverted behaviour as compared to the Cu profile (solid line in Fig. 2). It is suggested that there exists a seemingly repulsive interaction between Ag and Cu atoms in CdTe. In order to describe the codiffusion of Ag and Cu the following defect reactions have to be added to reactions 1a-1c:

$$Cu_{Cd} + Cd_i \rightleftarrows Cu_i \qquad (3a)$$

$$Cu_i + V_{Cd} \rightleftarrows Cu_{Cd} \qquad (3b)$$

$$Cu_i + Ag_{Cd} \rightleftarrows Cu_{Cd} + Ag_i \qquad (3c)$$

The first two reactions describe the interaction of Cu atoms with the intrinsic defects of the Cd sublattice and are equivalent to the reactions (1a) and (1b); reaction (3c) describes the mutual interaction between Ag and Cu atoms. The corresponding local equilibrium conditions yield

$$\sqrt{\frac{[Cd_i]}{[V_{Cd}]}} = k_{Ag}\cdot\frac{[Ag_i]}{[Ag_{Cd}]} = k_{Cu}\cdot\frac{[Cu_i]}{[Cu_{Cd}]} \qquad (4)$$

where k_{Cu} is, like k_{Ag}, a temperature dependent equilibrium constant. Assuming that Cu like Ag diffuses exclusively interstitially, according to Eq. 4 the codiffusion of Cu_i atoms leads to a change of the distribution of intrinsic defects and thereby to a decrease of the concentration of Ag_{Cd} atoms in favour of Ag_i atoms. As a consequence, the highly mobile Ag_i defects will diffuse into regions with higher V_{Cd} concentrations, i.e. towards the back of the crystal where the Cu concentration is still low, and, according to reaction 1b, they will be incorporated as immobile substitutional Ag_{Cd} defects.

The data obtained after Ag diffusion into a CdTe crystal pre-doped with Cu show that in this case Ag is incorporated only at a low concentration level and the excess of Ag atoms segregates at the surfaces (Fig. 3). Since the pre-doping was performed using a 30 nm Cu layer followed by annealing at 800 K for 120 min a homogeneous Cu concentration of about $4*10^{18}$ cm^{-3} is estimated, which was also verified by an independent diffusion measurement using ^{67}Cu. According to reaction (3b), in this pre-doped crystal a low V_{Cd} concentration is expected to be present if Cu diffuses interstitially into CdTe and, therefore, only a small part of the in-diffusing Ag atoms can be incorporated on substitutional lattice sites. The segregation of Ag atoms at the surfaces becomes understandable if the surface of CdTe acts as a drain for the highly mobile interstitial Ag_i atoms. At present, however, no decision can be made, whether the excess Ag at the surface resides as metal precipitates or has formed a new phase like e.g. Ag_2Te.

The codiffusion of Au shows a depletion layer of the Ag profile, which increases from 200 µm to

400 μm if the diffusion time is increased from 30 min to 120 min (Fig. 4). Obviously there is an apparent repulsive interaction present between Ag and Au atoms, too. But the interaction is significantly weaker than in case of Cu. The width of the depletion layer seems to follow a $\sqrt{t}$ -dependence, suggesting that it is correlated with the diffusion length of Au. Assuming that the width Δx of the depletion layer agrees with the diffusion length of Au, i.e.

$$\Delta x = \sqrt{D(Au) \cdot t}\,, \tag{5}$$

a diffusion coefficient of $D(Au) \approx 2\ 10^{-7}$ cm^2/s for Au at 550 K is obtained. However, this value is in strong contrast to values available in the literature. Interpolating the diffusion coefficient D(Au) from Hage-Ali et al. [8], $D(Au) \approx 2.4 \cdot 10^{-18}$ cm^2/s is obtained and extrapolating the data from Teramoto et al. [9] yields $D(Au) \approx 3.2 \cdot 10^{-18}$ cm^2/s; both values being far off the estimate given above. An explanation might be found in the presence of a second, fast diffusion component like in case of Cu, which was not reported by Hage-Ali and Teramoto. Such an assumption might be supported by the presence of a fast diffusing component reported for Au in $Cd_{0,2}Hg_{0,8}Te$ [10].

Diffusing Ag into In doped CdTe a completely different behaviour is observed. The Ag profile obtained at a diffusion temperature of 800 K for 240 min under vacuum is shown by the open circles in Fig. 5. Performing the same diffusion experiment under Cd pressure the range of the Ag profile extends by about 50 μm further and a weak depletion layer of about 70 μm emerges at the surface (closed circles). In contrast, the profile in Fig. 1 obtained at the same temperature under Cd pressure but for a much shorter time of 60 min in an undoped CdTe crystal shows the symmetric peak shaped Ag profile accompanied by much stronger depletion layers of about 300 μm at both surfaces. Obviously the diffusion of Ag is strongly retarded in In doped CdTe compared to undoped material. A similar observation was made by Lyubomirksky et al., who have investigated the diffusion of Ag in In doped CdTe at 473 K [11]. In this experiment the penetration of Ag reached only about 25 μm after 8 h diffusion time. An explanation might be found in terms of self compensation, i.e. the compensation of the In_{Cd} donors by V_{Cd} defects acting as double acceptors. In case of full compensation the additional concentration of Cd vacancies, which partially might be present as A-centres (In_{Cd}-V_{Cd} paris), essentially agrees with half of the In concentration, being about 10^{17} cm^{-3} in the present case. The V_{Cd} concentration, including A-centres, therefore, might be significantly larger than in the investigated undoped crystals where the V_{Cd} concentration was determined by the initial deviation from stoichiometry. Consequently, compared to undoped material, from the in-diffusing Ag atoms a larger fraction might be incorporated substitutionally being no longer mobile. In addition, Ag atoms that occupy Cd vacancies bound in A-centres will form close donor acceptor pairs In_{Cd}-Ag_{Cd}, which might be still more stable than isolated Ag_{Cd} defects. As a consequence, the equilibrium concentration of mobile Ag_i defects is reduced in favour of Ag_{Cd} atoms, thereby, retarding the diffusion of the Ag atoms. The higher stability of In_{Cd}-Ag_{Cd} pairs might also explain the less pronounced depletion layer since in this case only a smaller fraction of Ag atoms will be moved to interstitial lattice sites by the incorporated Cd_i defects.

5 Summary

The diffusion of Ag in CdTe is strongly influenced by the presence of other impurities. It has been shown that the diffusion of Ag is strongly enhanced upon codiffusion of Cu or Au. At the same time the Ag atoms are driven out of regions of high concentrations of Cu or Au atoms. The enhanced Ag diffusion is more pronounced in case of codiffusion of Cu than of Au. It is concluded that this effect is essentially governed by the diffusion coefficients of Cu and Au. The present data are explained in terms of a replacement of substitutionally incorporated Ag atoms by Cu or Au atoms. In contrast, Ag diffusion is remarkably retarded in In doped CdTe. It is proposed that a higher V_{Cd} concentration exists as compared to undoped material due to self compensation of the In donors. In addition, a higher stability of Ag atoms bound in In_{Cd}-Ag_{Cd} pairs is responsible for this retardation effect.

Acknowledgments

The authors want to thank the Helmholtz Institut für Strahlen und Kernphysik for the implantation of ^{111}Ag, V. Ostheimer for the experimental help, and R. Grill and E. Belas from the Charles University of Prague for the supply of CdTe crystals and fruitful discussions. The financial support by the DFG under contract Wi715/7-1, by the BMBF under contracts 05 KK1TSB/7 and CZE 03/002 is gratefully acknowledged.

References

[1] Woodbury, H. H. and Aven, M.; Some Diffusion and Solubility Measurements of Cu in CdTe, *J. Appl. Phys.* 39, pp. 5485-5488, 1968.

[2] Wartlick, B. O., Blanchard, C., and Barbot, J. F.: Study of silver and copper diffusion in p-type Hg0.3Cd0.7Te and CdTe by capacitance measurements, *Mat. Sci. Eng. B* 71, pp. 254-257, 2000.

[3] Krause-Rehberg, R., Zimmermann, H., Klimakow, A., and Drost, Th.: Occupation of the Cd vacancy site in CdTe by diffusing silver atoms observed by positron annihilation, *Phys. Stat. Sol. A*, 134, pp. K45-K47, 1992.

[4] Wolf, H., Wagner, F., Wichert, Th., and ISOLDE Collaboration: Anomalous Diffusion Profiles of Ag in CdTe due to Chemical Sef-Diffusion, *Phys. Rev. Lett.* 94, 125901, 2005.

[5] Wolf, H., Wagner, F., Wichert, Th., and ISOLDE collaboration: The Role of Intrinsic Defects for the Diffusion of Ag and Cu in CdTe, *Defect and Diffusion Forum*, 237-240, pp. 491-498, 2005.

[6] Wolf, H., Wagner, F., Wichert, Th., and ISOLDE Collaboration: The unusual influence of intrinsic defects on the diffusion of Ag and Cu in CdTe, *Physica B,* 340-342, pp. 275-279, 2003.

[7] Jones, E. D., Stewart, N. M., and Mullin, J. B.: The diffusion of copper in cadmium telluride, *J. Cryst. Growth*, 117, pp. 244-248, 1992.

[8] Hage-Ali, M., Mitchell, I. V., Grob, J. J., and Siffert, P.: Heavy element diffusion in Cadmium Telluride, *Thin Solid Films (Switzerland),* 19, pp. 409-418, 1973.

[9] Teramoto, I. and Takayangi, Sh.: Behavior of Gold in Cadmium Telluride Crystals, *J. Phys. Soc. Jpn (Japan),* 17, pp. 1137-1141, 1962.

[10] Groshkov, A. V., Zatiov, F. A., Shangin, S. B., Shalyapina, G. M., Petrov, I. N., and Asaturova, I. S.: Diffusion of components and impurities in $Cd_xHg_{1-x}Te$ (x=0,2), *Sov. Phys. Solid State*, 26(10), pp. 1787-1791, 1984.

[11] Lyubomirsky, I., Lyakhoviskaya, V. Triboulet, R., and Cahen, D.: Substitutional-Interstitial Silver Diffusion and Drift in Bulk (Cadmium, Mercury) Telluride: Results and Mechanistic Implications, *J. Electron. Mater.*, 26, pp 97 – 105, 1997.

Proceedings of The 1st International Conference on **D**iffusion in **S**olids and **L**iquids
DSL-2005, July 6-8, 2005, University of Aveiro, Aveiro, Portugal

EFFECT OF PRESSURE ON STRUCTURAL EVOLUTION IN METALLIC GLASS

W. K. WANG[1,2*], C. YANG[1,2], L. L. SUN[2], J. Z. JIANG[3] , R. P. LIU[1], J. ZHANG[2]

[1]Key Laboratory of Metastable Materials Science & Technology, Yanshan University, Qinhuangdao 066004, P. R. China
[2]Institute of Physics, Chinese Academy of Science, Beijing 100080, P. R. China
[3]Laboratory of New-Structured Materials, Department of Materials Science and Engineering, Zhejiang University, Hangzhou, 310027, P. R. China

[*]Corresponding author. Fax: 0086-335-8064504; Email: wkwang@aphy.iphy.ac.cn

---

Abstract

Structure evolution of $Fe_{60}Co_{10}Zr_8Mo_5Nb_2B_{15}$ metallic glass under high pressure at room temperature was investigated by utilizing synchrotron radiation x-ray diffraction(SR-XRD). The corresponding coordination number of the atoms for the metallic glass drops from 12 at ambient pressure to 7.44 at 36.8 GPa. Pressure effects on structural evolution of $Zr_{41}Ti_{14}Cu_{12.5}Ni_{10}Be_{22.5}$ bulk metallic glass (BMG) under high-temperature and high-pressure were also studied by *in situ* SR-XRD. Though the primarily precipitated phase is the same at different pressures, the following crystallization sequences are different. In addition, $Zr_{41}Ti_{14}Cu_{12.5}Ni_{10}Be_{22.5}$ BMGs prepared by water quenching and shock-wave quenching were investigated by XRD using synchrotron radiation, differential scanning calorimetry, ultrasonic measurements. Differences in structure, property and thermal stability are found between the two BMGs.

Keywords: Metallic glass; Pressure effect; Shock wave effect; Structural evolution

---

1 Introduction

Multicomponent metallic glasses, with excellent glass forming ability and high thermal stability against crystallization, are a kind of candidate for many functional and engineering applications [1,2]. Unlike polycrystal, their structures are characteristics of short-range order (SRO) and no remarkable long-range order. The structure and property of metallic glasses are profoundly altered under high pressure due to a large change of atom spacing, chemical bonding, and Gibbs free energy. Structural evolution of metallic glasses under high pressure is a long standing issue for disordered materials [2]. This remains a fundamental problem in condensed state physics and is strongly related to a better understanding of the properties and potential applications of metallic glasses.

It is well known that when a glassy system exhibits a negative heat of mixing, the large thermodynamic driving force drives the constituent elements to spontaneous intermixing. Thus, the amorphous structure is degenerated and nonunique on the atomic level, containing a considerable and continuous variation of its microscopic state. Such a microscopic state is defined by the atomic SRO. Theoretical studies [3] indicated that the SRO in metallic glasses is composed of icosahedral configurations whose coordination number (CN) is about 12. Recent experimental investigation shows that this type of icosahedral polyhedra usually exists in binary metallic glasses, which can be considered as parent alloys from which new metallic glasses have been derived [4]. Hence, it is interesting to evaluate how the structural evolutions of multicomponent metallic glasses behave under high pressure.

Structural evolution research of metallic glasses under high pressure and high temperature is of theoretical and applicable significance. Also. In general, metallic glass transforms into equilibrium crystal phases experiencing certain metastable phase stages by heating. Routes for crystallization of metallic glass under pressure, however, may be different because pressure can change its atomic configuration and atomic mobility in the metallic glass. Lots of results show that pressure can restrain crystallization that causes increase of the crystallization temperature (T_x), because the long-range atomic transport required for crystallization is retarded by pressure. It is also reported that pressure can not only affect T_x, but also change crystallization sequence [5]. In the past, much effort was given to the binary metallic glasses (films and ribbons) that possess relatively simple crystallization processes under pressure. For the recently developed multicomponent metallic glasses, the crystallization processes are more complex. Revealing of the crystallization processes under pressure is important for studying the thermal stability of the multicomponent glasses [6,7].

Structure of metallic glass prepared under different melt cooling rates and pressures may possibly be different because pressure and/or cooling rate can exert influences on nucleation and crystal growth both in metallic melt and in metallic glasses. Until now, lots of preparation methods, such as water-quenching, copper mould casting, and melt-spun, *et al.*, have been established to prepare metallic glass. The differences in these methods are mainly related to obtainment of different cooling rates of melt. Eckert *et al.* [8] reported that the SRO of metallic glasses is the same irrespective of these preparation methods. Recently, pressure quenching, especially shock-wave quenching [9] was successfully invented to prepare $Zr_{41}Ti_{14}Cu_{12.5}Ni_{10}Be_{22.5}$ bulk metallic glass (BMG). In this case, metallic melt, treated by extremely high pressure, overheated by extremely high temperature, and then undercooled by rapidly decompression, is quenched into metallic glass by a high cooling rate. Consequently, different SRO for shock-wave quenched BMG in comparison with those for water-quenched one is excepted to be obtained. It is expected that the study of shock-wave quenching may provide insight into the formation mechanism of the BMG and effect of shock wave on structure and physical properties of the BMG.

In this paper, we have studied the structure evolution of $Fe_{60}Co_{10}Zr_8Mo_5Nb_2B_{15}$ metallic glass under high pressure up to 50 GPa at room temperature by utilizing the third generation synchrotron radiation x-ray diffraction (SR-XRD) combined with the diamond anvil cell technique. Structural evolution of $Zr_{41}Ti_{14}Cu_{12.5}Ni_{10}Be_{22.5}$ BMG under high temperature and high pressure was examined by *in situ* SR-XRD x-ray. In addition, shock-wave quenching was used for preparing $Zr_{41}Ti_{14}Cu_{12.5}Ni_{10}Be_{22.5}$ BMG. Different SRO and physical properties between shock-wave quenched BMG and water-quenched one are presented

2 Experimental procedure

$Fe_{60}Co_{10}Zr_8Mo_5Nb_2B_{15}$ metallic glassy ribbons with thickness of 25 μm were prepared by melt spinning in an argon atmosphere. The high pressure x-ray diffraction (XRD) experiments were performed by using a microcolliminated synchrotron radiation source and a diamond anvil cell at the Photon Factory, Tsukuba. The XRD data were collected from an image plate (IP) [10]. For the experiments, an x-ray source of monochromatic radiation with a wavelength of 0.06198 nm was employed. The distance between the sample and the IP is about 180 mm. The exposed IP can be read automatically via an IP reading system (RIGAKU R-AXIS IV). A mixture of methanol, ethanol, and water by proportion 16:4:1 was applied as the pressure-transmitting medium. Pressures inside the diamond anvil cell were determined using the standard ruby fluorescence technique. All measurements were performed at room temperature. Further details regarding the experimental setup can be found in Ref. [11].

In situ high-temperature and high-pressure energy-dispersive XRD patterns (EDXRD) for $Zr_{41}Ti_{14}Cu_{12.5}Ni_{10}Be_{22.5}$ BMG were recorded using synchrotron radiation in HASYLAB in Hamburg, by a multi-anvil pressure apparatus with 8 mm cube pressure cells at the MAX 80 station [12]. A cylindrical boron nitride container with 1 mm in the internal diameter was used. Center of the container was filled with the sample powder filed from $Zr_{41}Ti_{14}Cu_{12.5}Ni_{10}Be_{22.5}$ BMG, and the lower part was filled with NaCl powder for pressure calibration. Electric current was sent through a graphite heater via two appropriate anvils. The temperature was measured by means of thermocouple close to the sample with a stability of ±1K. Pressure of the sample was calculated from the lattice constant of NaCl using the Decker equation of state. Each run of the experiment consisted of isothermal room-temperature compression followed by isobaric heating up to 889 K in steps of 8 K with a recorded EDXRD pattern for every 4 min in order to observe onset T_x in the pressure range up to 6.5 GPa. It was found that only pure metallic phases in the three systems were detected after heat treatment at temperatures up to 889 K under pressure.

The preparation of $Zr_{41}Ti_{14}Cu_{12.5}Ni_{10}Be_{22.5}$ BMG by shock-wave quenching was relatively complicate as shown below. Ingots of the alloy with a nominal composition of $Zr_{41}Ti_{14}Cu_{12.5}Ni_{10}Be_{22.5}$ were prepared from mixture of pure elements (up to 99.9 % wt.) in an arc-melting furnace under Ti-gettered Argon atmosphere. The prepared ingots were re-melted in vacuum-sealed quartz tubes, and then quenched into water to obtain BMG rods, 18 mm in diameter and 55 mm in length. Some of the rods were then crystallized at 923 K for 1 hour. Small cylindrical samples, 17.5 mm in diameter and 10 mm in thickness, were cut from the as-casting and the crystallizing rods. Both kinds of the samples were then shock loaded by a 25-mm two-stage light gas gun. During the shock impacts, the target samples were encapsulated in a recoverable assembly. Copper is chosen as the mould material due to its good ductility and high thermal conductivity, which may benefit the formation of BMG. Copper flyers with 22 mm in diameter and 2 mm in thickness were fired at the speed of 2.9 km/s, which was measured to an accuracy of 0.2% by a magnetic-flyer method.

The recovered samples were sectioned, ground and polished for structural and property analyses. The samples before and after shock-wave quenching were examined with D/max-2500/pc XRD, NETSCH STA449C differential scanning calorimetry (DSC), ultrasonic measurements by a pulse echo overlap method [13] with a MATEC 6600 system at sensitivity of 0.5 ns, and density measurements by the Archimedian principle with an uncertainty of 0.01 mg. XRD measurements for obtainment of radial distribution function (RDF) were performed at experimental station BW5 at HASYLAB DESY using a short wavelength of 0.11271 Å. Samples were measured at room temperature and illumination time was 90 s. XRD patterns were recorded by 2D detector MAR IP in asymmetric mode (for getting high *Q* range). The XRD data were integrated by using Fit2D program. The background was properly subtracted and the image was integrated into *Q*-space. The data were corrected for inelastic scattering and the total structural factor was obtained by using Faber and Ziman formula. The pair correlation function, *g(r)*, from corresponding *S(Q)* were obtained by using MCGR program based on Monte Carlo algorithms [14].

3 Results and discussion

3.1 Structural evolution of $Fe_{60}Co_{10}Zr_8Mo_5Nb_2B_{15}$ metallic glass under high pressure

In order to reveal structural evolution features of $Fe_{60}Co_{10}Zr_8Mo_5Nb_2B_{15}$ metallic glass under high pressure, RDFs were calculated from the IP data by Fourier transformation using a computer program [15].

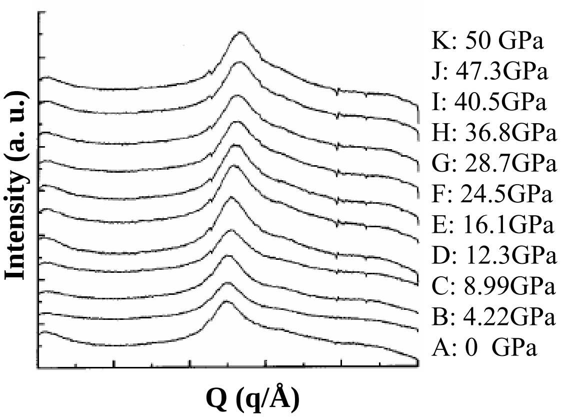

Figure 1: *In situ* SR-XRD patterns of $Fe_{60}Co_{10}Zr_8Mo_5Nb_2B_{15}$ metallic glass at high pressures up to 50 GPa.

The SR-XRD patterns of the metallic glass at high pressures up to 50 GPa are shown in Figure 1. It is apparent that the amorphous halo remains unaltered up to very high pressure, indicating that no crystallization occurs. In other words, the amorphous structure of this material is quite stable in the pressure range investigated. As expected, the amorphous halo of the sample subjected to various pressure shifts towards larger wave vector *Q*, i.e., towards larger two theta values ($Q=4\pi \sin(\theta)/\lambda$, where θ is the scattering angle of the x-ray and λ is the wavelength), reflecting a reduction of the corresponding volume of the sample with increasing pressure. The small peaks appearing in the diffraction patterns are not from the glassy sample since they do not shift with increasing pressure. These small peaks originate from fluorescence of the sample.

To verify the pressure effect on the atomic structure of the sample, we investigated the pressure dependence of the RDF as determined from the *in situ* XRD data. Figure 2 illustrates the typical RDF of the metallic glass at different pressures. The RDF of the sample subjected to a pressure of 4.22 GPa exhibits a double maximum in the first peak (pattern A), indicating that there exists a strong chemical SRO, similar as in other ferromagnetic metallic glasses [16]. Since the studied alloy contains 60 at% Fe, 15 at% B, and 10 at% Co, the main peak at *r*~0.203 nm in the first peak is related to Fe-B correlations, and the subpeak for higher *r* values (*r*~0.276 nm) corresponds to Co-Co correlations. These results are close to the data reported by Imafuku *et al.* [16] and Fukunaga *et al.* [17] With increasing pressure, the intensity of the subpeak becomes weaker. At 16.3 GPa, the subpeak is suppressed by 36% but still visible. When the pressure reaches 36.8 GPa, the subpeak completely disappears, revealing that rearrangement of the amorphous structure occurs under high pressure. It is noteworthy that a double maximum in the second peak in the RDF can also be observed for the sample subjected to 4.22 GPa. For this pressure, the maximum of the second peak is centered at 0.392 nm and the subpeak appears at 0.493 nm. Although we could not clarify their atomic correlations in detail up to now, they might be related to a distinct SRO structure in this multicomponent material. The intensity of this subpeak appears to decrease with increasing pressure. At 36.8 GPa the subpeak has almost vanished. Apparently, increasing pressure eliminates the shoulder of the first peak. These results unambiguously confirmed that the metallic glass undergoes a series of apparent interrelative transitions under high pressure.

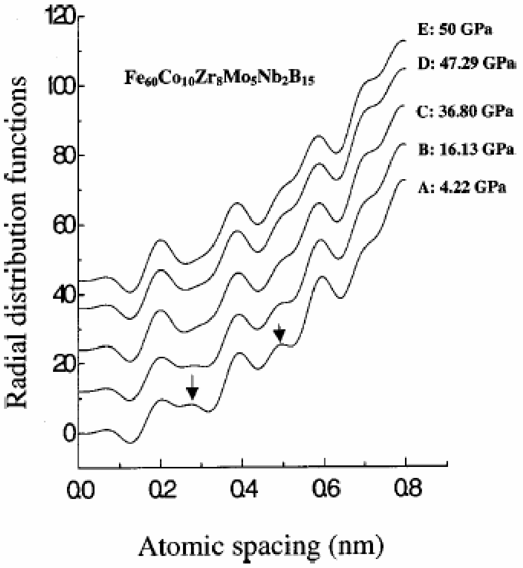

Figure 2: RDFs of $Fe_{60}Co_{10}Zr_8Mo_5Nb_2B_{15}$ metallic glass derived from *in situ* XRD measurements at various pressures.

To understand the pressure dependence of the structure evolution of the metallic glass more clearly, we calculated the CN at various pressures using Gaussian functions (the *r* limit is chosen within 0.126 to 0.241 nm) based on the RDF displayed in Figure 2. The CN of the atoms in the initial metallic glass structure is about 12. With pressure increasing up to 36.8 GPa, the CN drops dramatically, changing from 12 to 7.44. Within this pressure range, the ratio of the average interatomic distance, r_i/r_0 (r_i denotes the average interatomic distance at given pressure and r_0 at ambient pressure), decreases by ~4%. It is interesting that the CN slightly increases with further increasing pressure for values above ~35 GPa, but the r_i/r_0 further continuously decreases.

We believe that the changes in CN under high pressure are associated with the modification of the atomic configuration of the metallic glass. It has been suggested that SRO clusters in metallic glasses are composed of icosahedral configurations with CN of about 12 [3,4]. Such a short-range ordered icosahedral configuration is believed to be an incorporation of tetrahedral configurations in metallic glasses. Our experimental observations that the shoulders of the first and the second peaks in the RDF are removed by pressure, as observed from Figure 2, suggests that the initial configuration collapses and the new configuration forms at high pressure and, as a result, CN drops from 12 to 7.44. From our present data, it can be concluded that the pressure of 36.8 GPa is a threshold driving the initial atomic configuration to collapse. Upon further compressing the sample, the CN slightly increases from 7.44 at 36.8 GPa to 7.58 at 47.3 GPa and 7.691 at 50 GPa. This suggests that the local ordering of the metallic glass increases due to a closer packing of the atoms in local ordering units under higher pressure, so that the CN value slightly increases with increasing pressure.

3.2 Structural evolution of $Zr_{41}Ti_{14}Cu_{12.5}Ni_{10}Be_{22.5}$ BMG under high pressure and high temperature

The primarily precipitated phase appeared under pressure from 0.5 to 6.5 GPa is Zr_2Be_{17}. It is found that the applied pressure strongly affects T_x, as shown in Figure 3. T_x increases largely with pressure, except a sudden drop around 5.6 GPa. In addition, the pressure effect on crystallization process is very complicated as shown in Figs. 4 and 5. Figure 4 exemplifies EDXRD patterns recorded for the $Zr_{41}Ti_{14}Cu_{12.5}Ni_{10}Be_{22.5}$ sample at 0.5 GPa and various temperatures. A broad amorphous peak, located at about E=45 KeV, together with Bragg peaks from BN and fluorescence peaks in the energy range of 31-34 KeV, are observed in the patterns recorded at each temperature. A new tiny crystalline peak (E=41.7 KeV) from Zr_2Be_{17} phase appears at 721 K. At 737K, and another new crystalline peak (E=44.7 KeV) from Zr_2Cu crystals is detected. The peak from $ZrBe_2$ phases, located at E=46.3 KeV is recorded at 769 K. With the increase of temperature, the intensities of peaks from these three phases increase gradually. Up to 873 K, the phase Zr_2Ni_7 (E=37.5 KeV) is detected. Figure 5 shows the EDXRD patterns recorded at 5.6 GPa and at various temperatures. It is found that the primary phase is also Zr_2Be_{17}, but the peak (E=42.2 KeV) appears at 745 K, lower than the T_x of 761 K at 5.3 GPa. The peaks (E=45.1, 47.7 KeV) from Zr_2Cu phases, and other peaks from Zr_2Be_{17} crystals, are recorded at 777K. At 793 k, a new peak from Zr_2Ni (E=43.5 KeV) crystal, another two new peaks from Zr_2Ni_7 (E=38.8, 55.2 KeV), together with other peaks from Zr_2Be_{17} and Zr_2Cu phase, are observed. With the further increase of temperature, the intensities of these peaks continue to increase. Up to 849 K, a new peak from $ZrBe_2$ (E=47.0 KeV) begins to appear.

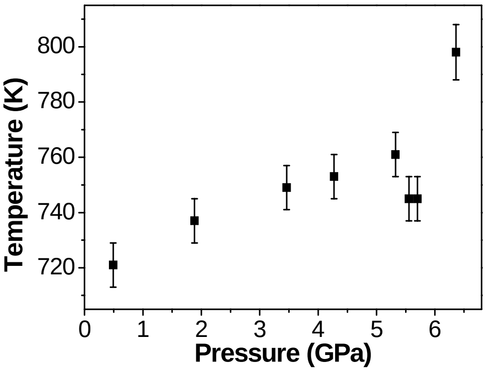

Figure 3: Pressure dependence of crystallization temperature for $Zr_{41}Ti_{14}Cu_{12.5}Ni_{10}Be_{22.5}$ BMG.

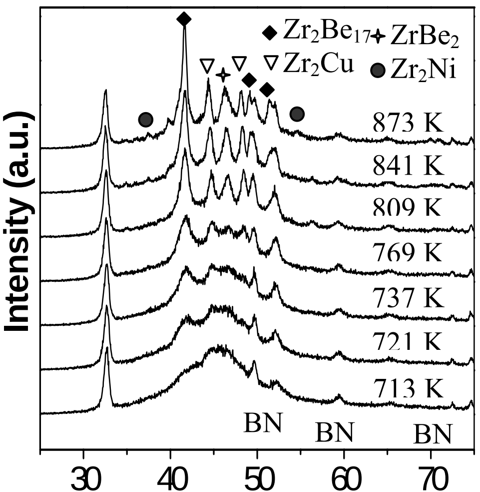

Figure 4: *In situ* EDXRD patterns recorded at various temperatures for $Zr_{41}Ti_{14}Cu_{12.5}Ni_{10}Be_{22.5}$ BMG at 0.5 GPa (Ed=108.34 keV Å). The step of 8 K was used for the temperature range. The fluorescence peaks, located in the energy range of 31-34 KeV, and a few Bragg peaks from BN were detected.

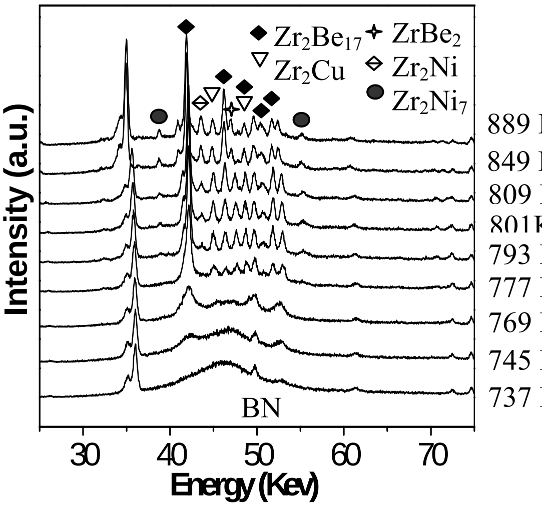

Figure 5: *In situ* EDXRD patterns recorded at various temperatures for $Zr_{41}Ti_{14}Cu_{12.5}Ni_{10}Be_{22.5}$ BMG at 5.6 GPa (Ed=108.24 keV Å). The fluorescence peaks, located in the energy range of 34-37 KeV, and a few Bragg peaks from BN were detected.

Figure 6 further testifies that the crystallization sequence at 4.3 GPa is different from that around 5.6 GPa. The primary crystalline peak from Zr_2Be_{17} appears at 753K, followed by Zr_2Cu phases precipitated at 817K. At 833K, the peak from $ZrBe_2$ appears.

In our present experiments, the primary phase, determined from the EDXRD patterns, is Zr_2Be_{17} at all the pressures applied. But the subsequent crystallization sequences are different.

Prior to crystallization, the BMG decomposes into Zr-rich and Be-rich regions with different SROs, which exhibit higher nucleation probability for the formation of intermetallic compounds compared with the initial homogeneous liquid state [18]. The decomposition in this state is a diffusion-controlled process [18]. Because Be atoms have the biggest diffusivity among the constitute elements of the BMG under high pressure [19], the primary crystal phase will possibly shift to Be-richer side in the Zr-Be binary phase diagram under high pressure. Thus, compared with the primarily precipitated phase $ZrBe_2$ under ambient pressure and annealing conditions [20], the primary crystal phase is Zr_2Be_{17} for $Zr_{41}Ti_{14}Cu_{12.5}Ni_{10}Be_{22.5}$ BMG under high pressure. This is similar to that the primary crystal phase is Fe under ambient pressure, yet Fe_3B, Fe_3C and Fe_3P for $Fe_{83}B_{17}$ and $Fe_{13}P_7C_{80}$ metallic glasses under high pressure [5], respectively. Small changes in composition for metallic glass may cause the dramatic changes in the following crystallization process [20,21]. In addition, pressure and preparation conditions can also lead to different atomic configurations and physical properties for BMGs [9,11,22]. These may possibly explain the present experimental results.

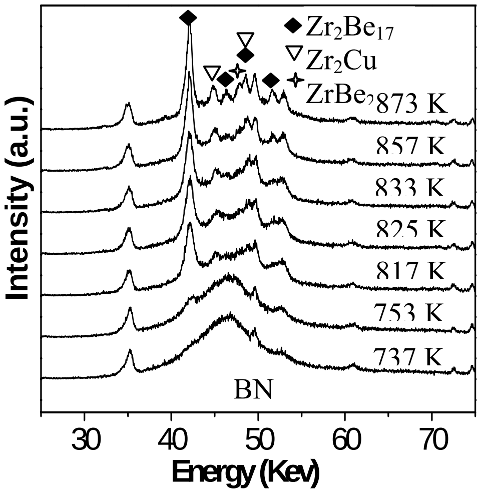

Figure 6: *In situ* EDXRD patterns recorded at various temperatures for $Zr_{41}Ti_{14}Cu_{12.5}Ni_{10}Be_{22.5}$ BMG at 4.3 GPa (*Ed*=108.24 keV Å). The fluorescence peaks, located in the energy range of 33-37 KeV, and a few Bragg peaks from BN were detected.

3.3 Structural evolution of $Zr_{41}Ti_{14}Cu_{12.5}Ni_{10}Be_{22.5}$ BMG after shock-wave quenching

In all shock experiments, symmetric impact method was used. Shock pressure in the samples were calculated to be about 80 GPa by the impedance-match method, and the shock temperatures were calculated to be higher than 3000°. At such high a temperature, the samples were undoubtedly re-melted during shock compression, and solidification was a result of rapid heat dissipation by the copper mould and recoverable assembly. The afterwards recovered samples were in a cake-like shape with the diameter of about 24 mm and the thickness of about 6 mm. Careful observation of the surfaces and sections of the recovered samples revealed that no cracks were found in the samples. Cracking is a typical characteristic of shocked solids without melting. This gives us indirect evidence that the samples were re-melted during the shock-loaded experiment.

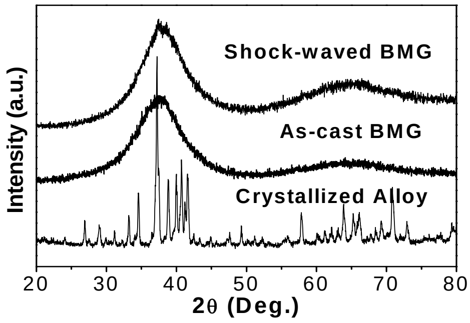

Figure 7: XRD patterns of $Zr_{41}Ti_{14}Cu_{12.5}Ni_{10}Be_{22.5}$ alloys. Shock-waved BMG, as-cast BMG, and crystallized alloy, stand for shock-wave quenched BMG, water-quenched BMG, and the crystallized $Zr_{41}Ti_{14}Cu_{12.5}Ni_{10}Be_{22.5}$ alloy, respectively.

Both the as-cast BMG sample and the crystallized sample were re-solidified into amorphous state after the shock-wave quenching through XRD examination as shown in Figure 7. The DSC traces of the BMG samples prepared by water quenching and by shock-wave quenching were shown in Figure 8, respectively. Both DSC traces of the BMGs reveals endothermic characteristic of a glass transition followed by exothermic crystallization reactions at higher temperature. The glass transition temperature, T_g, of the shock-wave quenched sample is about 10 K higher than that of the water quenched one.

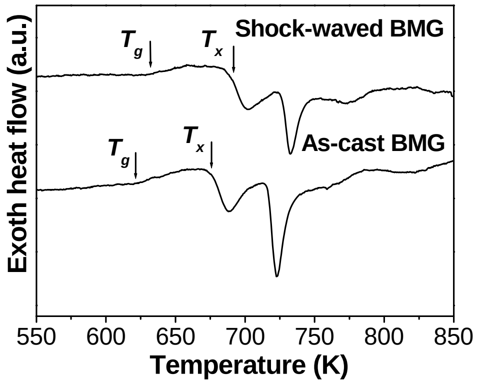

Figure 8: DSC traces for the $Zr_{41}Ti_{14}Cu_{12.5}Ni_{10}Be_{22.5}$ BMG at a heating rate of 10 K/min under a flow of purified argon. As-cast and shock-waved BMG stand for water-quenched BMG and shock-wave quenched BMG, respectively.

Table 1 gives the results of the thermal-elasticity properties measured for both BMGs. Of importance are the decrease in density (ρ) by 0.21%, and the increases in longitudinal acoustic velocity (V_L) by 1.31%, shear acoustic velocity (V_S) by 0.69%, shear modulus by 1.16%, bulk modulus by 3.13%, and Debye temperature by 0.65% for the shock-wave quenched sample relative to the water quenched one. Normally, the acoustic velocities increase with the increase of density [23,24]. But in this experiment, the acoustic velocities increased for the shock-wave quenched sample, which corresponds to a lower density. It implies that difference in structure may exist between the water quenched BMG and the shock-wave quenched BMG, though it is not possible to show exactly this structural difference by XRD patterns. The differences in the density and in the property may find their reasons from the differences in the effect of pressure and cooling rate on the melt.

Table 1: The density ρ, longitudinal acoustic velocity V_L, shear acoustic velocity V_S for the water-quenched $Zr_{41}Ti_{14}Cu_{12.5}Ni_{10}Be_{22.5}$ BMG, sample W, and shock-wave quenched.

Sample	ρ *(g/cm³)*	V_L *(km/s)*	V_S *(km/s)*
Sample W	6.128	5.029	2.463
Sample SW	6.115	5.095	2.480
Difference (%)	-0.21	1.31	0.69

Figures 9 and 10 show atomic pair correlation function, *g(r)*, of $Zr_{41}Ti_{14}Cu_{12.5}Ni_{10}Be_{22.5}$ BMGs prepared by shock-wave quenching and water-quenching in a large range of atomic distance respectively.

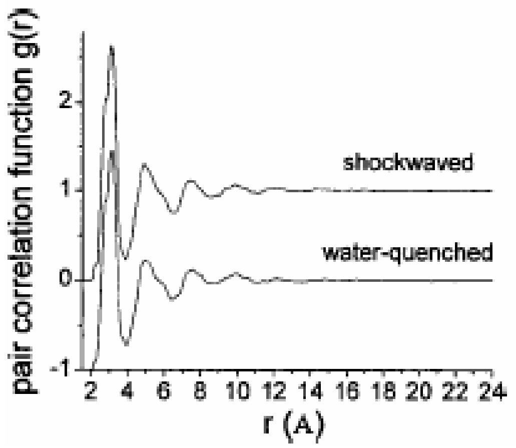

Figure 9: Atomic pair correlation function, *g(r)*, of $Zr_{41}Ti_{14}Cu_{12.5}Ni_{10}Be_{22.5}$ BMGs prepared by shock-wave quenching and water-quenching in a large range of atomic distance.

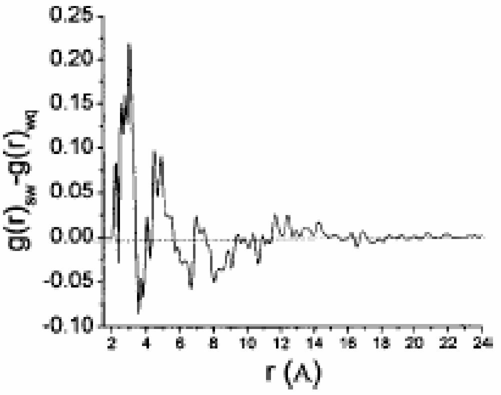

Figure 10: The difference of atomic pair correlation function of $Zr_{41}Ti_{14}Cu_{12.5}Ni_{10}Be_{22.5}$ BMGs prepared by shock-wave quenching, $g(r)_{sw}$, and water-quenching, $g(r)_{wq}$, in a large range of atomic distance.

The fine difference is illustrated in Figure 10. The shock-wave quenched BMG clearly shows a higher g(r) in the first two coordination shells r~2.4-5.6 Å as compared to the water-quenched one. The relative change in the first peak height is about 10 %, but the change in the second peak is of the order of 20 %. In higher coordination shells, r~5.6-9.5 Å, g(r) in water-quenched BMG becomes higher. For r>10 Å, no obvious difference was detected. For a pure structural relaxation effect by annealing treatment at a temperature far below crystallization temperature, the difference in *g(r)* could remain up to r~20 Å.[25]. This indicates that shock-wave quenching mainly modify atomic configuration in the first fourth or fifth coordination shells. In the 5-component $Zr_{41}Ti_{14}Cu_{12.5}Ni_{10}Be_{22.5}$ alloy the measured structure factor $S(q)$ and the estimated $g(r)$ curves represent the weighted sum of the 15 partial functions $S_{ij}(q)$ and $g_{ij}(r)$ [26]:

$$S(q)=\sum_i\sum_j w_{ij}\cdot S_{ij} \text{ and } g(r)=\sum_i\sum_j w_{ij}\cdot g_{ij}$$

$$\text{with } w_{ij}=c_i\cdot c_j\cdot f_i\cdot f_j\Big/\left(\sum_i c_i\cdot f_i\right)^2$$

(1)

where w_{ij}, c_i, and f_i are the weight factor for the *i-j* correlation, the concentration fraction and atomic scattering length of i^{th} atom in the alloy, respectively. An interpretation of the data for the multi-component alloy is therefore difficult and ambiguous. The first CN, N=14.4 and 14.0, was estimated from a distance of 2.1-3.7 Å for $Zr_{41}Ti_{14}Cu_{12.5}Ni_{10}Be_{22.5}$ BMGs prepared by shock-wave quenching and water quenching, respectively. Such higher first CNs strongly indicate a dense packing atomic structure in the BMG. For the higher shells determination of N becomes ambiguous because it is difficult to set the onset and end of shells in *g(r)* curves. However, it is clear that after shock wave treatment, the BMG has higher CNs in the range of r~2.4-5.6 Å and lower ones in the range of r~5.6-9.5 Å than those in the water-quenched BMG in Figure 10.

During shock compression, the pressure in the BMG sample increased instantly by a rate higher than 10^9 GPa/s, accompanied with the increase of shock temperature by 10^{10}-10^{12} K/s. The shock pressure and temperature could reach their peak values within 20 to 100 ns, and the BMG sample was melted immediately under this high temperature and pressure of shock wave, which possessed a short duration of 800-1000 ns. Subsequently, the high pressure was releasing rapidly to ambient by a rate far higher than 10^9 GPa/s. The temperature in the sample promptly equilibrated to ambient by Newton thermal conductive equation. Under high pressure of shock wave, the metallic melt was compressed dramatically and the atomic configuration was possibly changed transiently. The viscosity of the melt increased reciprocally. On the other hand, nucleation in the melt was probably not ready in such a short time. Furthermore, the melting temperature of the alloy was increased by the pressure. According to the Clausius–Clapeyron equation, the pressure dependence of T_m is proportional to volume change, ΔV, between the solid state and melt:

$$\frac{dT_m}{dP}=\frac{T_m\Delta V}{\Delta H_m}$$

(2)

where, P is the pressure, and ΔH_m the heat of fusion. For the $Zr_{41}Ti_{14}Cu_{12.5}Ni_{10}Be_{22.5}$ BMG, T_m=937 K, ΔH_m =6.6 kJ/mol^3, ΔV can be adopted as 1% [27]. Thus, at 80 GPa, dT_m is calculated to be about 1333 K. At extremely high decompression rate and relatively extremely low cooling rate, the metallic melt was overheated dramatically, which will melt completely heterogeneous nuclei (some intermediate compounds with high T_m) and improve the glass forming ability of metallic melt. Furthermore, with a large increase of the T_m, a relatively higher supercooling before crystallization was obtained [28]. The melting of heterogeneous nuclei and suppression in nucleation of crystalline phases may account for the increase of the T_g and T_x during the DSC measurements, and different physical properties and different atomic configuration between the shock-wave quenched BMG and water-quenched one.

4 Conclusion

In conclusion, pressure can change the atomic configurations in melt and solid of metallic glass. Effects of pressure on structural evolution in metallic glasses are very complicated. Through our results, the conclusions can be obtained as follows.

(1) The structural evaluations of $Fe_{60}Co_{10}Zr_8Mo_5Nb_2B_{15}$ metallic glass under high pressure have been investigated by *in situ* XRD measurements using synchrotron radiation in the pressure range of 0-50 GPa at room temperature. The pressure-induced structural evolution was quantified from the characteristic of the RDF which was derived from the *in situ* SR-XRD data via Fourier transformation. The corresponding CN of the atoms changes from 12 at ambient pressure to 7.44 at 36.8 GPa at which the average

interatomic distance has contracted by ~4%. The large drop of the CN suggests that high pressure (~36.8 Gpa) leads to a collapse of the initial atomic configuration of the metallic glass. With further increasing pressure above 37 GPa, the atomic ordering in the local units of the metallic glass is enhanced.

(2) The effect of high pressure on structural evolution of the $Zr_{41}Ti_{14}Cu_{12.5}Ni_{10}Be_{22.5}$ BMG was presented. The same primary crystal phase but with a sudden drop of the crystallization onset temperature and different crystallization sequence at about 5.6 GPa is found in comparison with those at other pressures. This may be attributed to that the BMG possesses different atomic configurations at different pressure.

(3) The $Zr_{41}Ti_{14}Cu_{12.5}Ni_{10}Be_{22.5}$ BMG was prepared by shock-wave quenching. The obtained BMG shows higher thermal stability, acoustic properties, and lower density. The short-range structure of shock-wave quenched BMG was investigated by XRD using synchrotron radiation. It is found that the shock-wave quenched BMG has higher CNs in the range of r~2.4-5.6 Å and lower numbers in the range of r~5.6-9.5 Å than those for the water-quenched one while the shell distances are similar in both glasses. After shock-wave quenching, the atoms in glass are packed even denser in the first two coordination shells and less (or more free volume) in the third and fourth coordination shells as compared to those for conventional water-quenched glass.

Acknowledgments

The author would like to acknowledge cooperation from Prof. J.Z. Jiang, L.L. Sun, R.P. Liu and Mr. C. Yang.

References

[1] Telford, M.: The case for bulk metallic glass. *Materials Today.,* 3, pp. 36-43, 2004.

[2] Inoue, A.: Stabilization of metallic supercooled liquid and bulk amorphous alloy. *Acta Mater.,* 48, pp. 279-306, 2000.

[3] Sachdev, S. Nelson, D.R., Phys. Rev. Lett. 53, 1947, 1984.

[4] Imafuku, M., Sato, S., Koshiba, H., Matsubara, E., Inoue, A.: Structural variation of Fe-Nb-B metallic glasses during crystallization process. *Scr. Mater.,* 44, pp. 2369-2371, 2001.

[5] Wang, W.K., Hiroshi, I., Kazuaki, F.: Effect of high pressure on the crystallization of an amorphous $Fe_{83}B_{17}$ alloy. *J. Mater. Sci.,* 5, pp. 2701-2705, 1980.

[6] Sun, L.L., Kikegawa, T., Wu, Q., Zhan, Z.J., Wang, W.K.: Unusual transition phenomenon in Zr-based bulk metallic glass upon heating at high pressure. *Appl. Phys. Lett.,* 80, pp. 3087-3080, 2002.

[7] Jiang, J.Z., Zhou, T.J., Rasmussen, H., Kuhn, U., Eckert, J., Lathe, C.: Crystallization in $Zr_{41.2}Ti_{13.8}Cu_{12.5}Ni_{10}Be_{22.5}$ bulk metallic glass under pressure. *Appl. Phys. Lett.,* 77, pp. 3553-3555, 2000.

[8] Damonte, L.C., Mendoza-Zélis, L.A., Deledda, S., Eckert, J.: Effect of preparation conditions on the short-range order in Zr-based bulk-forming alloys. *Mater. Sci. Eng. A.,* 343, pp. 194-198, 2003.

[9] Yang, C., Liu, R.P., Zhan, Z.J., Sun, L.L., Zhang, J., Gong, Z.Z, Wang, W.K.: Formation of ZrTiCuNiBe bulk metallic glass by shock-wave quenching. Submitted to *Appl. Phys. Lett.*

[10] Yagi, T., Kikegawa, T., Watanuki, T., Katayama, Y., Shimomura, O.: Laser Heating System at the Photon Factory and Sring-8, Vol. 2: *Proceedings of AIRAPT-17,* University Press, India, 2000.

[11] Sun, L.L., Wang, W.K., Wang, L.M., KiKegawa, T., Wu, Q., Zhang, J., Fan, C.Z., Eckert, J., Schultz, L.: Structural evaluation of $Fe_{60}Co_{10}Zr_8Mo_5Nb_2B_{15}$ metallic glass under high pressure. *Phys. Rev. B.,* 68, pp. 052302(1-4), 2003.

[12] Jiang, J.Z., Roseker, W., Sikorski, M., Cao, Q.P., Xu, F.: Pressureceffect of glass transition temperature in $Zr_{46.8}Ti_{8.2}Cu_{7.5}Ni_{10}Be_{27.5}$ bulk metallic glass. *Appl. Phys. Lett.,* 84, pp. 1871-1873, 2004.

[13] Schreiber, D.: *Elastic Constants and Their Measurement*, McGraw–Hill, New York, 1973.

[14] Pusztai, L., McGreevy, R.L.: MCCR: An inverse method for deriving the pair correlation function from the structure factor. *Physica B.,* 234-236, pp. 357-358, 1997.

[15] Wang, L.M., Wang, W.H., Sun, L.L., Zhao, J.H., Dai, D.Y., Wang, W.K., Sci. China, Ser. A: Math., Phys., Astron., 43, pp. 407, 2000.

[16] Imafuku, M., Yaoita, K., Sato, S., Zhang, W., Inoue, A., Waseda, Y.: Local atomic structure of Fe-Co-Ln-B (Ln=Sm, Tb or Dy) amorphous alloys with supercooled liquid region. *Mater. Sci. Eng. A.,* 304-306, pp. 660-664, 2001.

[17] Fukunaga, T., Misawa, M., Fukamichi, K., Masumoto, T., Suzuki, K., Vol. 2: *Rapidly Quenched Metals III*, The Metal Society, London, 1978.

[18] Busch, R., Schneider, S., Peker, A., Johnson, W.L.: Decomposition and primary crystallization in undercooled $Zr_{41.2}Ti_{13.8}Cu_{12.5}Ni_{10}Be_{22.5}$ melts. *Appl. Phys. Lett.,* 67**,** pp. 1544-1556, 1995.

[19] Geyer, U., Schneider, S., Johnson, W.L., Qiu, Y., Tombrello, T.A., Macht, M.-P.: Atomic diffusion in the supercooled liquid and glassy states of the $Zr_{41.2}Ti_{13.8}Cu_{12.5}Ni_{10}Be_{22.5}$ alloys. *Phys. Rev. Lett.,* 75, pp. 2364-2367, 1995.

[20] Schroers, J., Busch, R., Masuhr, A., Johnson, W. L.: Continuous refinement of the microstructure during crystallization of supercooled $Zr_{41}Ti_{14}Cu_{12}Ni_{10}Be_{23}$ melts. *Appl. Phys. Lett.,* 74, pp. 2806-2808, 1999.

[21] Schneider, S., Thiyagarajan, P., Johnson, W. L.: Formation of nanocrystals based on decomposition in the amorphous $Zr_{41.2}Ti_{13.8}Cu_{12.5}Ni_{10}Be_{22.5}$ alloy. *Appl. Phys. Lett.,* 68, pp. 493-495, 1996.

[22] Yang, L., Yang, C., Saksl, K., Franz, H., Sun, L.L., Wang, W.K., Jiang, N.P., Wu, X.J., Jiang, J.Z.: Short-range structure of $Zr_{41}Ti_{14}Cu_{12.5}Ni_{10}Be_{22.5}$ glass prepared by shock wave. *Appl. Phys. Lett.,* 84, pp. 4998-5000, 2004.

[23] Wang, L.M., Wang, W.H., Wang, R.J., Zhan, Z.J., Dai, D.Y., Sun, L.L., Wang, W.K.: Ultrasonic investigation of PdNiCuP bulk metallic glass upon crystallization. *Appl. Phys. Lett.,* 77, pp. 1147-1149, 2000.

[24] Wang, W.H., Bai, H.Y., Luo, J.L., Wang, R.J., Jin, D.: Supersoftening of transverse phonons in $Zr_{41}Ti_{14}Cu_{12.5}Ni_{10}Be_{22.5}$ bulk metallic glass. *Phys. Rev. B.,* 62, pp. 25-28, 2000.

[25] Egami,T., J. Mater. Sci. 13, 2587, 1978.

[26] Luborsky, F.E.: *Amorphous Metallic Alloys*, Butterworths, London, 1983.

[27] Nagel, C., Rätzke, K., Schmidtke, E., Wolff, J., Geyer, U., Faupel, F.: Free-volume changes in the bulk metallic glass $Zr_{46.7}Ti_{8.3}Cu_{7.5}Ni_{10}Be2_{7.5}$ and the undercooledliquid. *Phys. Rev. B.,* 57, pp. 10224-10227, 1998.

[28] He, D.W., Zhang, F.X., Zhang, M., Liu, R.P., Qin, Z.C., Xu, Y.F., Wang, W.K.: Quenching with rapid decompression-a new method for rapid solidification. *Appl. Phys. Lett.,* 26, pp. 3811-3813, 1997.

Proceedings of The 1st International Conference on **D**iffusion in **S**olids and **L**iquids
DSL-2005, July 6-8, 2005, University of Aveiro, Aveiro, Portugal

APPLICATION OF HYPERSPECTRAL DIGITAL IMAGING TO STUDY OF DIFFUSION PROCESSES IN THE LIQUID SOLUTIONS

Zbigniew GÓRSKI[1,*], Jadwiga MALIŃSKA[1], Ignacy WIERSZYŁŁOWSKI[2]
[1] Technical University Poznan, Institute of Chemistry and Technical Electrochemistry,
Piotrowo 3, 60-965 Poznan, Poland
[2] State College of Leszno, Institute of Technology, Mickiewicza 5, 64-100 Leszno, Poland

[*]Corresponding author. Fax: +48 61 6652571; Email: zgorski_n@wp.pl

Abstract

The concept of the use of hyper spectral digital photography (HSDP) for diffusion studies in solutions absorbing the radiation in the range of UV-Vis-NIR (from 200 to 1100 nm) is presented. One end of capillary filled with a solution and radiation adsorbing substance (RAS) was closed, the other was connected to a vessel without the RAS. The RAS concentration change inside the capillary was photographed by monochromatic radiation camera at certain established intervals. In this way collection of digital images was obtained and used for calculation of radiation changes along the diffusion path (capillary length). For concentration changes according to Beera's law the concentration of diffusing substance and the diffusion coefficients were calculated. The HSDP method can be applied for studies of diffusion in single solutions substances and co-diffusion of substances absorbing radiation.

Keywords: Diffusion profile; Diffusion coefficient; Chemical imaging; Hyper spectral digital imaging; Diffusion

1 Introduction

The investigation of the diffusion processes requires long lasting experiments performed in well defined and stable conditions. In order to decrease experiment error and ensure the bounduary conditions of Fick's second law large capacity of solutions are usually needed and long period of time [1]. From other side it is difficult to keep exactly the same diffusion parameters for a long time.

Application of hyper spectral digital imaging method [2,3] with use matrix detectors [4] and spectral imaging allows significantly decrease time period of experiments and obtain real diffusion profiles with very little error. The use of the hyper spectral imaging method allows for simultaneous multipoint measurement of the optical properties of the system.

The well known and mathematically described dependence of absorbance on concentration allows for use of the photometric results obtained in this way to describe the changes of the physico-chemical properties.

2 Experimental

Measurements and calculation of diffusion coefficient were adapted to the standard capillary method [5] modified for hyper spectral digital imaging. The method is based on diffusion of solution with radiation absorbing substance (RAS) from capillary to vessel with solution without RAS. One end of capillary filled by solution and radiation absorbing substance was closed and another open and connected to a vessel with solution without of the RAS.

In order to obtain photometrical data the capillary and vessel were illuminated by backlighting panel from plastic optical fibres (Luminex USA) [6]. Digital monochromatic light or LED sources was connected with backlighting panel by optical fibre.

Diffusion process was registrated with use WinLight prograne by ultrasensitive, 16 bite, grey scale CCD NightyOWL LB 981 camera (EG&G Berthold Gmbh, Germany). The work parameters of the camera: resolution power 512 x 512 pixels, work temperature CCD, 200 K, radiation range 200-1100nm, quantum efficiency 65 % for = 550 nm, UV (200÷400 nm) 25 %, noise 7e^-,dark current $5*10^{-4}$ e^-/pixel/1s, size of registrated picture 70*70 mm.

The numerical transformation of the images was aided with the set of programming tools of FCT v. 1.1 program [7].

Measuring system worked at constant temperature (1 K accuracy). Digital thermostatic device with Peltier's elements was applied to keep the temperature constant.

The diffusing solution was pumped up into capillary by infusing pump.

Scheme of the apparatus used for investigation of the diffusion process is shown in Fig. 1.

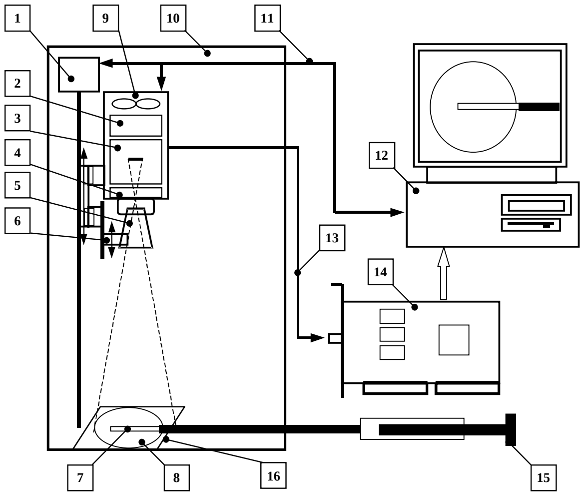

Figure 1: Scheme of measuring system.
1 – camera lift, 2 - Peltier air cooler, 3 – CCD cheep, 4 – vacuum – quartz gate, 5 – quartz lens, 6 – auto focus lift, 7 – sample capillary, 8 – backlight illuminator, 9 – slow scan camera, 10 – dark box, 11 – camera stacking wire (RS 232 J), 12 – IBM PC computer, 13 – imaging wire, 14 – imaging interface, 15 – infusing pomp, 16 – backlighting panel and thermostat.

Wavelength (λ_{max}) of maximum absorbance for diffusing solution was determined with help by JASCO V-530 spectrophotometer (Japan).

Changes of local concentrations caused by diffusion process along the capillary registrated at wavelength λ_{max} was transformed into photometrical data. This photometrical data was applied for calculation of absorbance changes for diffusing solution.

2.1 *Diffusion*

Diffusing solution with RAS was sucked into capillary by numerically controlled infusion pump. In order to block diffusion process certain known amount of air was sucked into capillary at the end of solution sucking. Next the capillary was placed into the vessel with solution. Stirring device and thermostat are switched on. When temperature reached constant value small amount of air is removed and diffusing process starts. Simultaneously starts registration of progress the diffusion process. The photographs were made at 30 s, 1 h or 120 h intervals with help of CCD NightOWL camera. A single image recording time was 50 ms (LED), or 0.5 s (monochromatic light).

2.2 *Photometric data reading*

The radiation intensity passing by capillary containing solution with absorbing substance (RAS) was read from all registrated data using the same rule of region of interest (ROI).

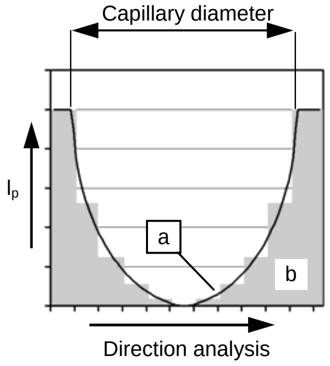

Figure 2: Changes of optical absorption path (l_p) along the direction perpendicular to capillary axis. a – real curve, b –read by the camera.

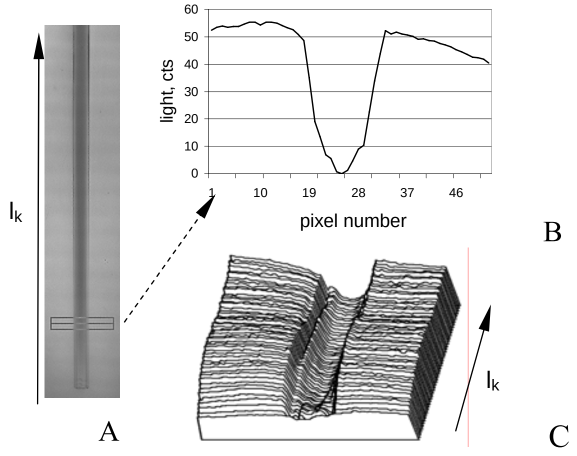

Figure 3: Illustration of the ROI location selection principle on the analysed photographs. A – a photograph of the capillary after 2 h diffusion with marked line of emission intensity analysis, B –passing radiation emission distribution for the indicated line, C –passing radiation emission distribution change along the capillary length.

Since the capillary cross-section is a circle, the optical path of radiation passing by capillary is not constant in every point. It dependence on the location of the measuring point along the analysis direction. (Fig. 2 curve a). In order to minimalized influence of capillary shape on measurements of radiation intensity, ROI was registrated where intensity of path radiation was the smallest.

The lack of parallelism radiation intensity passing by capillary (Fig. 3B, 3C) in the images areas is caused by inner structure of backlighting panel applied.

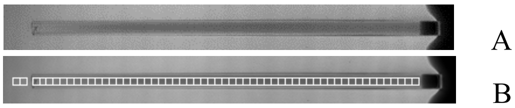

Figure 4: Distribution of the ROI in the photograph. A - Photograph of the capillary after 2h diffusion, B – Photograph of the capillary with overlapped ROIs.

The images obtained were always analysed in the same direction (Fig.4): ROI-1 - initial point – open end of capillary. ROI-n - end point - second end of capillary. Two ROIs located beyond the capillary in the solvent area used to check the maintenance of the condition at which the equation of the Fick's second law was solved (the concentration of the diffusing substance in the solvent area is equal to 0, non-measurably small).

2.3 Calculation of absorbance

Local absorbance (A_i) were calculated by the formula:

$$A_i = \log \frac{I_i}{I_{0i}} \qquad (1)$$

where :

I_i – intensity of radiation passed by capillary with diffusing substance in solution (for $ROI)_i$,

I_{0i} – intensity of radiation passed by capillary with solution without diffusion substance (for ROI_i).

Basing on the Lambert-Beer law, the local concentration (c_i), can be expressed as

$$c_i = \frac{A_i}{\varepsilon l_{pi}} \qquad (2)$$

where: ε – mole absorbance coefficient,

l_{pi} – local optical path for ROI.

Local optical distance of absorbance is constant (in the region of application Lambert-Beer law). Therefore relationship (2) is expressed by simple straight line relationship with $(\varepsilon l_p)^{-1}$ as proportionality factor. The factor, $(\varepsilon l_p)^{-1}$ can be determined from experiments.

2.4 Calculations of the diffusion coefficient

The following formula was used to calculate the diffusion coefficient [5]:

$$D = \frac{4l^2}{\pi^2 t} \ln \frac{8}{\pi^2} \cdot \frac{c_o}{c_t} \qquad (3)$$

where: l – length of the capillary,

t – time of diffusion,

c_o – initial concentration ,

c_t – concentration after t time,

The concentrations, the initial one and after time t, were expressed by means of local absorbances.

Since the momentary concentration of the diffusing substance in capillary (c_k) can be expressed by:

$$c_k = \frac{m_k}{V_k} = \frac{4m_k}{l\pi d_k^2} \qquad (4)$$

where: m_k – mass of the diffusing substance contained in the capillary,

d_k – diameter of the capillary.

The mass (m_k) can be expressed as the sum of the masses of substance in all the elements of the volume (voxels) into which the capillary had been divided (m_{VOXi})

$$m_k = \sum_{i=1}^{n} m_{VOXi} \qquad (5)$$

$$m_{VOXi} = d_k \cdot l_i \cdot c_i = d_k \cdot l_i \cdot \frac{A_i}{\varepsilon l_{pi}}$$

where: l_i – length of the ROI,

Since $d_k = l_{Pi}$, relationship (4) will take the form of:

$$c_k = \frac{4l_i \sum_{i=1}^{n} A_i}{\varepsilon l \pi d_k^2} \qquad (6)$$

If we represent the initial concentration (c_o) and the after time t (c_t), formula (6) for the calculation of the diffusion coefficient will take the form used in calculations, namely:

$$D = \frac{4l^2}{\pi^2 t} \ln \left[\frac{8\left(\sum_{i=1}^{n} A_i\right)_0}{\pi^2 \left(\sum_{i=1}^{n} A_i\right)_t} \right] \qquad (7)$$

The formula can be used provided that $\frac{D \cdot t}{l_k} > 0{,}2$

3 Results

The hyper spectral digital imaging method was tasted for diffusion process of dichromate ions ($Cr_2O_7^{-2}$) to water.

At the start of diffusion concentration of $K_2Cr_2O_7$ was exactly 0.1 mol/dm^3. The solution containing dichromate ions diffused from capillary 5.7 cm long and capacity of 100 µl to water vessel of 55 cm^3.

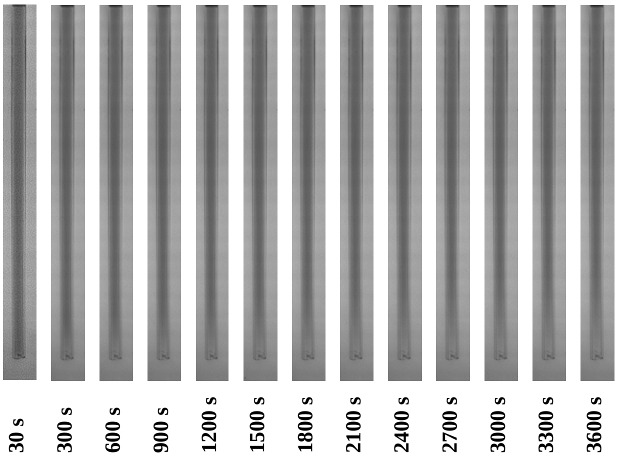

Figure 5: Examples of photographs of the diffusion system (diffusion time 1 h).

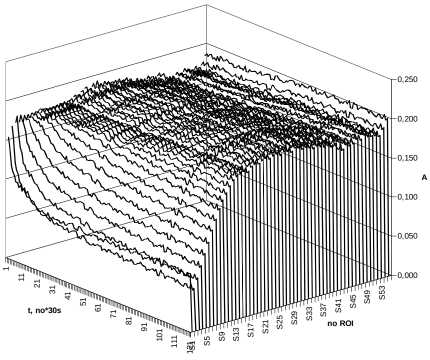

Figure 6: Changes of absorbance for $K_2Cr_2O_7$ solution along capillary (diffusion time 1 h).

The diffusion process was analysed with use photometric analysis. Examples of the diffusion system subjected to photometry analysis are shone in Fig.5. (complete diffusion time 1h). The diffusion profiles understood as the changes of the absorbance of $K_2Cr_2O_7$ solution along the capillary in time, calculated for one-hour experiment, is shown in Fig.6.

The diffusion coefficient calculated basing on the data obtained in both experiments the classic long time and the one-hour experiment is equal 11.9×10^{-10} m^2 s^{-1} conform with literature data [8].

4 Conclusions

Thanks to the digital detector and computer methods of image analysis use, the presented method allows for obtaining precise information about diffusion profile in a classic diffusion experiment in relatively short time. The resolution of the concentration measurements influencing the result of the diffusion coefficient calculation is proportional to the photometric resolution to the camera converter. Sensitivity of the camera depends on stable temperature. Therefore stability work of camera thermostat during experiment is very important. Because of high resolution sensitive camera results are reliable and obtained in relatively short time.

The presented method can be applied for analysis of diffusion processes based on ionization radiation and fluorescence phenomena.

The method can be developed for study of co- and self-diffusion processes of certain elements with application of its ionized radiation.

References

[1] Lobo V.M.M., Ribeiro A.C.F. and Verissimo L.M.P.: Diffusion Coefficients in Aqueous Solutions of Potassium Chloride at High and Low Concentrations. *Journal of Molecular Liquids* 78 (1998) pp.139-149.

[2] Trado P.J.: Chemical imaging reveals more than the microscope. *Laser Focus Word*. October 1995.

[3] Opto-Knowledge Systems Inc.:Hyperspectral imaging. *Spectrosccopy*, vol.14, Number 3, pp. 28-32, March 1999.

[4] Image Sensor Solution. Application Notes. In: CD Estman Kodak Company, 2000 2/00 P/N 6B5226.

[5] Несмеянов Ан., Н.: Радиохимия (Radio-chemistry), Изд. “Химия”, Москва 1972.

[6] www.lumitex.com.

[7] Górski Z., Bembnista T., Floryszak-Wieczorek J., Domanski M., Slawinski J.: Computer-aided photometric analysis of dynamic digital bioluminescent images. *Proceedings of SPIE*, Vol.5064 (2003), pp. 1- 10.

[8] Lakatos I., Lakatos-Szabó J.: Diffusion of chromium ions in polymer/silicate gels. *Colloids Surfaces A: Physicochem. Eng. Aspects* 141 (1008), pp. 425-434, 1998.

Proceedings of The 1st International Conference on **D**iffusion in **S**olids and **L**iquids
DSL-2005, July 6-8, 2005, University of Aveiro, Aveiro, Portugal

KINETICS OF TRANSFORMATION DURING SUPERSATURATION AND AGEING OF THE Al 4.7 % Cu ALLOY. GRAIN SIZE, DILATOMETRIC AND DTA STUDIES

Ignacy WIERSZYŁŁOWSKI [1,*], Sebastian WIECZOREK [2], Andrzej STANKOWIAK [1], Jarosław SAMOLCZYK[3]

[1]State College of Leszno, ul. Mickiewicza 5, 61-100 Leszno, Poland,
[2]Poznań University of Technology, Pl.Marii Skłodowskiej – Curie 5, 60-965 Poznań, Poland,
[3]Institute of Metal Forming , ul. Jana Pawła I I, 14, 61- 139 Poznań, Poland.

[*]Corresponding author. Fax: +48 61 6570 721; Email: JIM@inop.poznan.pl

---

Abstract

The processes taking place during supersaturation of the Al.-4.7 %Cu alloy have been studied by the methods of quantitative metallography and dilatometry. The grain growth activation energy was about 95 kJ/mole, the exponent of time, n, was close to 0.4. Dissolution of precipitates has caused two-stage shrinkage of the sample with activation energies of 90 kJ/mole (first stage, n = 0.8) and 63 kJ/mole (second stage, n = 0.4).The kinetics of the phase transformation during ageing of the Al.-4.7 % Cu alloy has been studied by the dilatometry and DTA. The activation energy of the precipitation processes within the range of 50 – 320 C varied from 50 kJ/mole to about 100 kJ/mole and confirmed the results obtained previously. For the precipitation processes within the range of 320 –462 C, the activation energy varied from 226 – 300 kJ/mole. The results obtained have been compared to the literature data.

Keywords: Transformation kinetics; Grain size; Supersaturation; Ageing

---

1 Introduction

The processes of precipitation in Al.-Cu alloys are well known. After supersaturation consisting of annealing at about 723°C, quick cooling down to room temperature and ageing, G-P zones appear as first, followed by Θ precipitates. Θ nucleates on the most stable G-P zones. The other G-P zones dissolve in the solid solution and the Cu atoms diffuse to the growing Θ. Finally, the equilibrium phase Al2Cu - Θ nucleates at the boundaries of the solid solution grains, Θ dissolves and the Cu atoms diffuse to the growing Θ [1,2,3].

The saturation process precedes ageing and comprises dissolving excess precipitates enriching the solid solution with copper atoms, grain growth and quick cooling to the ambient temperature. The amount of Cu atoms in the solid solution influences the quantity of precipitates during ageing and determines the properties obtained after ageing. The grain boundaries of the solid solution are privileged places of the precipitate nucleation, so the grain size can influence the precipitation kinetics. The processes of dissolving excess equilibrium precipitates and grain growth are interrelated in a sense. Fine grain accelerates precipitate dissolving due to more ways of easy diffusion, the presence of precipitates makes the movement of the grain boundaries and the grain growth difficult. The processes are known but their kinetics has not been described in detail. Since the specific volume of the solid solution decreases during its enrichment with Cu atoms, the process can be studied by means of a dilatometer while the kinetics of the grain growth by the methods of quantitative metallography. During ageing, the processes of precipitation and dissolution overlap each other. That is why they are often difficult to separate when analysing the transformation kinetics The kinetics of phase transformations during the ageing processes can be analysed in isothermal and isochronous experiments. DTA and DSC are applied in isochronous heating because the processes of heat emission during precipitation and heat absorption during dissolving of them are well visible. Precipitation in Al.-Cu alloys is accompanied by the sample volume growth, while dissolution by its decrease. The changes are clearly visible in dilatometric investigation and they can be successfully used for the analysis of the kinetics of the transformations taking place during isothermal ageing. The JMA equation can be applied for the analysis of the kinetics of isothermal transformations. In addition to the determination of activation energy, the equation can be used to find out the value of the n coefficient. The value is helpful in the selection of the nucleation and growth mechanism in the investigated temperature range. The value of the sample elongation can provide some additional information about the quantity of precipitates.

2 Experimental procedure

An Al –4.7% Cu alloy was especially prepared for the studies. Composition the alloy was following: Al -94.85%, Cu-4.69%, Fe-0.2%, Si-0.08%, other elements – 0.15 % Because of decrease of specific volume of the solid solution during its saturation of Cu atoms the process can be studied by dilatometry, whereas grain growth kinetics by quantitative metallography. Presence of the $CuAl_2$ not dissolved during supersaturation was identified by X-ray method.

For ageing kinetics studies two methods were used: dilatometry (for isothermal studies) and DTA (for continuous heating studies).Dilatometric studies were performed with the use of Adamel – Lhomargy LK02 dilatometer. Samples of rod 2mm in diameter and 13mm length were supersaturated at the temperature of 505°C for 10h in preliminary vacuum radiation furnace and quenched to room temperature in helium gas jet. Isothermal ageing was performed also in LK 02 dilatometer in temperature range of 120 – 350°C for time necessary to reach no dilatation change stage. DTA studies were performed with use of Mini DTA M5 Setaram. Samples of truncated cone of 4mm length and diameters of 2 and 3 mm were used. Standard specimen was prepared from electrolytic Al DTA samples were supersaturated in a resistance furnace at 520°C for 6h and quenched in water.

3 Kinetics studies - theoretical basis

a) Grain growth studies

Before annealing structure of Al4.7%Cu consisted of solid solution grains and Al_2Cu. Solid solution grains are big as compared with Al_2Cu gains. Number of the Al_2Cu as compared with number of solid solution gains is small (about 8 %). Therefore the grain growth of the alloy during isothermal annealing at 500- 540 C temperatures range can be treated as one phase (solid solution) grain growth [2,3] and expressed by:

$$\bar{d} = k(T)\cdot t^n \qquad (1)$$

where: d-average grain size

t – time

k(T)- grain growth rate constant

$$k(T) = A\cdot\left(\frac{-Q}{R\cdot T}\right) \qquad (2)$$

where: – A - is a constant

Q- activation energy for analyzed transformation

R- gas constant

T – temperature in K.

b) Precipitation and dissolution studies

For isothermal kinetics studies JMA equation [3, 8] was used in the form of:

$$x(t) = 1 - \exp(-k\cdot t^n) \qquad (3)$$

where: x-is fraction transformed at time t

k- is transformation rate constant for the selected transformation at isothermal temperature

n – is time exponent which is supposed to be constant at the temperature range for certain kind of transformation

Activation energy Q can be determined from equation (2).

For continuous heating kinetic studies of activation energy Q of the transformations, Kissinger method [8, 9] was used:

$$Q = -R\cdot {dC}\Big/{d\left({1}/{T_m}\right)} \qquad (4)$$

where:

$$C = \ln\frac{V}{T_m^2} \qquad (5)$$

V - is constant heating rate

T_m - is temperature of the maximum ΔT curve

4 Results

Examples of structures after annealing at temperatures 510°C and 540°C and quenching are shown on Figures 1 and 2 (510°C) and 3 and 4 (540°C).

Figure1: Annealing 5 h at 510 C. 100 X.

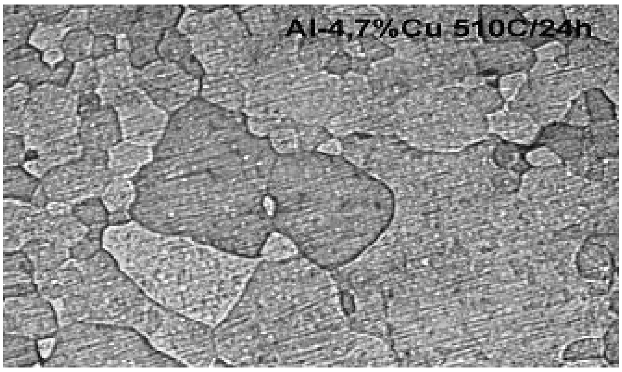

Figure 2: Annealing 24 h at 510 C. 100 X.

Figure 3: Annealing 5 h at 540 C. 100 X.

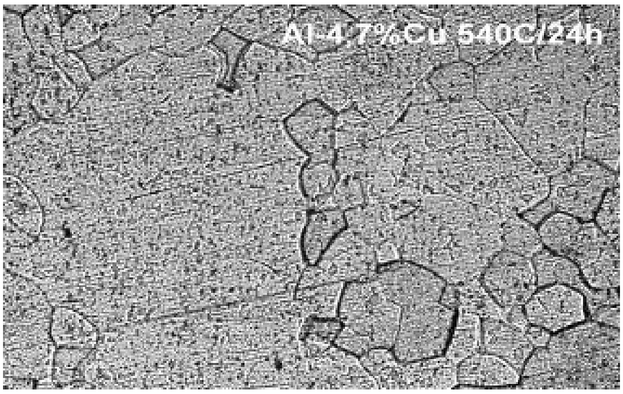

Figure 4: Annealing 24 h at 540 C. 100 X.

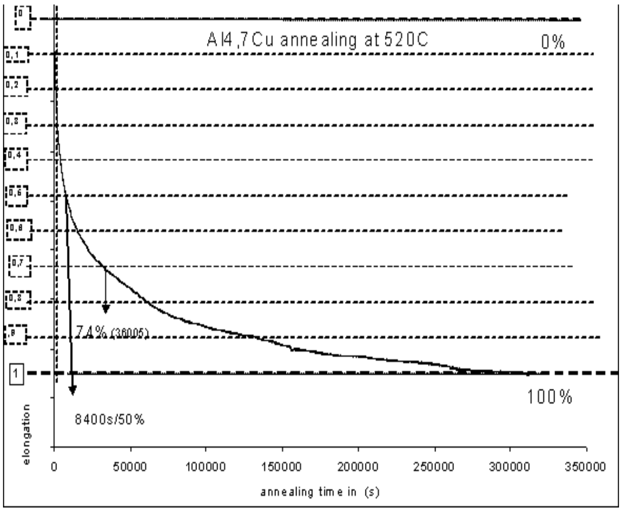

Figure 5: Example of dilatometric diagram of annealing at 520°C.

Changes of average grain size of samples annealed at 510, 525 and 540°C are shown on Figure 6:

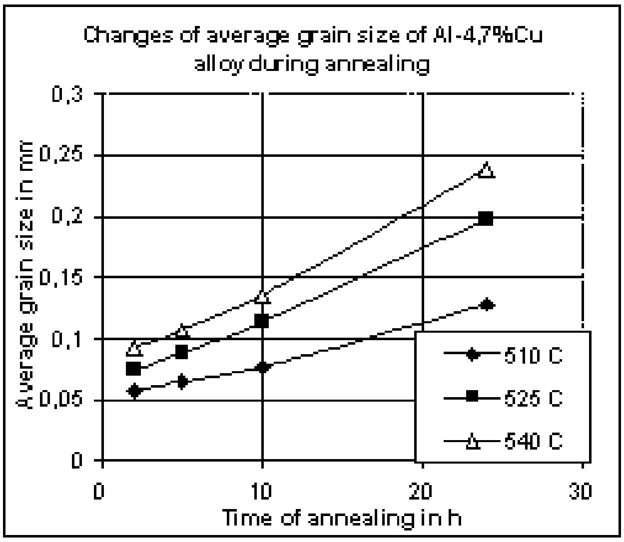

Figure 6: Changes of average grain size during annealing at 510, 525 and 540°C.

Set of dilatometric curves of annealing at temperatures between 480–540°C transformed into lnln[1/(1-x)] vs lnk diagrams is shown on Figure7. Examples of dialatograms of isothermal ageing at temperatures between 125-305 C immediately after supersaturation are collected in Figure 8.

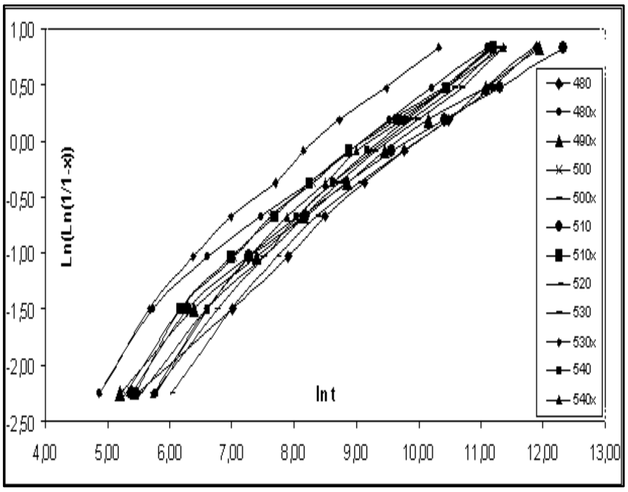

Figure 7: Dilatometric curves of annealing at temperatures range of 480–540°C transformed into lnln[1/(1-x)] vs ln k diagrams.

Table 1: Results of transformation kinetics analysis during annealing. Isothermal studies.

Grain growth kinetics		
Temperature range C	n value	Activation energy kJ/mole
510- 540	0.4 – 0.43	94,432
Contraction kinetics – JMA analysis (dilatometric studies)		
Temperature range °C	n value	Activation energy kJ/mole
480- 540	0.7 -0.8	90,010
480- 540	0.4-0.45	65,854

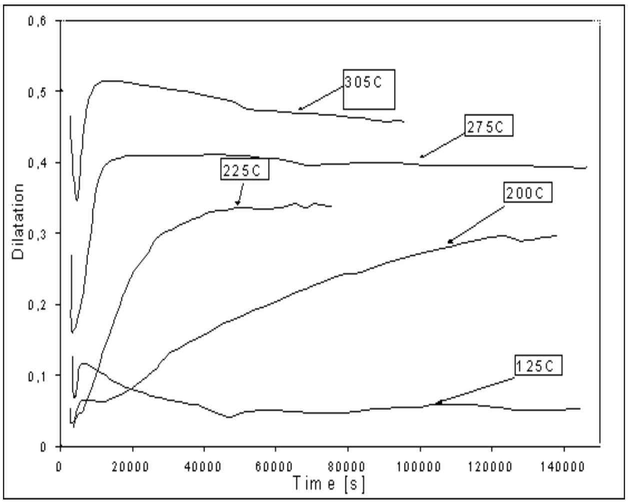

Figure 8: Dilatation changes during isothermal ageing of supersaturated Al-4.7% Cu alloy.

DTA diagrams of isochronal ageing immediately after supersaturation are collected in Figure 9:

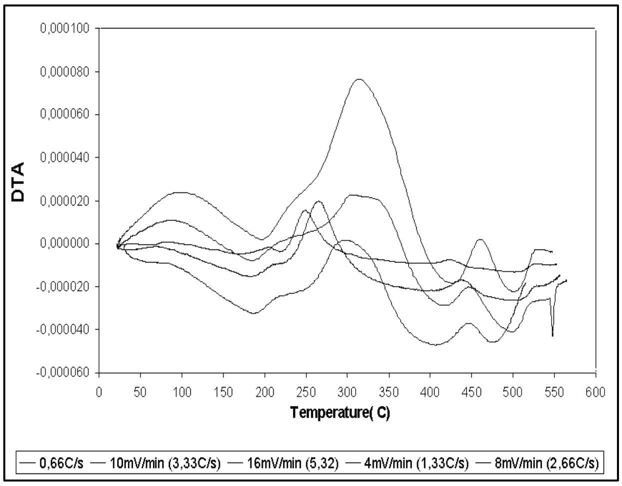

Figure 9: DTA diagrams of isochronal ageing of the Al 4.7% Cu alloy.

One can calculate activation energy if the mechanism of transformation is the same at certain temperature range [10, 11]. That means the same (or nearly the same) the n coefficient. Average values of n for the same mechanism of transformation vary from 1.4 to 1.47 [3]. The temperatures of 523 K and 548 K were excluded from the calculation of activation energy due values of n to different much from 1.4 -1.47.

Results of kinetic analysis of isothermal (dilatometric) ad isochronal (DTA) experiments are collected in Table 1 and shown in Fig. 3

Table 2: Results of transformation kinetics analysis during ageing. Isothermal and isochronal experiments**.**

Temperature range [C]	Experiment	Value of n	Transformation	Activation energy value kJ/mol
124-175	isothermal	1.4	G-P precipitation	60,700
200 -235	isothermal	1.47	Θ” precipitation	100, 767
250 (523K)	isothermal	1.74	Overlap of transformations	
275 (548K)	isothermal	2.08	Overlap of transformations	
290 - 320	isothermal	1.42	Θ’/CuAl$_2$ precipitation	300, 200
51-101	isochronal	-	G-P precipitation	47, 536
168-202	isochronal	-	G-P dissolution	106, 120
205-240	isochronal	-	Θ” precipitation	106, 120
251-316	isochronal	-	Θ”/ Θ’ transformation	67, 830
395-429	isochronal	-	Θ’ dissolution	226, 218
427-462	isochronal	-	CuAl$_2$ precipitation	303. 864

5 Analysis and discussion of results.

Average grain size of solid solution increased during increase of time and temperature of annealing (see Fig. 6). At temperature 540°C grains size increased more than during temperature of 510°C. Time exponent of kinetic equation value was almost the same at each annealing temperature, that means the similar growth mechanism. The activation energy of growth is about 95kJ/mole and is close to that obtained for diffusion of Cu in Al [8,9].

During annealing the samples in the dilatometer at temperature range of 480-540°C a contraction was seen (see Figure 5) because the increase of Cu amount in solid solution [3].

From Figure 7 one can see faster process at the beginning of annealing (more steep slope of diagram) than latter on. The n values are about 0.8 and decrease to about 0.4 when transformation proceeds. The activation energy value at the beginning of transformation is almost the same for that obtained during grain growth. For the next stage of transformation the activation energy decreases, but still is close to that for Cu diffusion in Al. It means that dissolution of $CuAl_2$ particles and the Cu clusters existing at annealing temperatures of 480-540°C limits the grain growth of solid solution. During progress of dissolution $Cu\ Al_2$ particles and Cu clusters gradually disappear but sill limits the decrease of samples.

Dilatometric diagram of supersaturation shows continuous decrease of specimen length caused by saturation of solid solution by Cu atoms. In this the case specific volume of the sample decreases [4].

Dilatometric diagram of ageing at 125°C (Fig. 1) after supersaturation shows a slight increase of specimen length caused by precipitation of small specific volume and small amount of Cu in the G-P zones. After a period of about 40 000s a slight decrease of specific volume appear due to dissolution of precipitates and temporary enrichment of matrix by Cu atoms.

What can be seen in the dilatogram of ageing at 200ºC (Fig. 8) is a slight increase of the sample length due to precipitation followed by a plateau as a result of simultaneous occurrence of changes caused by precipitation and dissolution, and an ultimate sample length growth as a result of formation of precipitates different from the previous ones.

Next dilatometric diagram shows ageing at 225°C (Fig. 8) after supersaturation. Continuous increase of sample length is seen and no changes of length from time about 50 000s. Diagrams of isothermal ageing at 275 and 305°C (Fig. 8) show an increase of sample length because of precipitation. Plateau (or slight decrease of length) for aging at 275°C starts after about 1000s time, for ageing at 305°C after about 1000s time starts decrease of length.

A set of DTA diagrams of ageing with different heating rates after supersaturation is shown in Fig. 9. For heating rate of 0.66 Deg/s all stages of ageing are clearly seen. Below of 100°C G-P zones appear, between 100 C and 150°C dissolution of G-P take place, from about 150 to 225°C transformation of G-P zones to Θ" take place, at about 225 starts dissolution of Θ" and its transformation to Θ'(the biggest pick), dissolution of Θ' begins at about 300°C and ends at about 400°C, and precipitation of $CuAl_2$ starts at about 450°C and at higher temperatures dissolution of precipitates takes place. Similar DTA pick temperatures for precipitation processes were presented by Thomson [7]. Results of dilatometric and DTA studies comply with other; the largest increase of length and the largest heat effect appears at the temperature of 275°C due to precipitation of Θ'. Small changes of length and small heat effects appear at temperatures of G-P precipitation, transformation of G-P into Θ" and precipitation of $CuAl_2$. The smallest activation energy values (47-60 kJ/mol) determined by both methods are relevant to G-P formation and comply with the results obtained by Smith [8,9] (61-73 kJ/mol), the highest (about 300 kJ/mol) is the value of the $CuAl_2$ precipitation that starts sooner in isothermal ageing. Activation energy of dissolution process appearing during G-P zone transformation into Θ" is the order of 100 kJ/mol. Activation energy of the θ" precipitation process is about 100 kJ/mole according to dilatometric and DTA method. The obtained values are somewhat lower than obtained by Smith [8,9] (93-131kJ/mol).

Activation energy of Θ' precipitation determined by DTA is somewhat lower (67,8 kJ/mol) than those that determined by dilatometric method (100,7kJ/mol). The value of activation energy of Cu diffusion in Al without any factors accelerating this process is 135,34 kJ/mol [8,9]. Activation energy of diffusion may be lowered by the presence of quenched in vacancies and dislocations [14]. Therefore decrease of activation energy is expected at low temperatures of the precipitation where G-P zones appear. A certain number of vacancies and dislocations can be produced by dissolution of precipitates and that can be a reason for decrease of the activation energy values during precipitation processes following up dissolution processes. Activation energy values of the $CuAl_2$ precipitation about three times higher than those of precipitation of G-P zones was found by Thomson [7].The increase of the activation energy of the processes taking place above 300ºC is relevant to both experimental methods and is caused by diffusion inhibiting factors. The n values in the JMA equation are close 1.5 and they indicate that, in each of the analyzed processes, nucleation takes place in pre-existing nucleation sites. Those sites are: quenched in dislocations in the case of G-P zones, stable G-P zones which transform into Θ'' for Θ'', grain boundaries of solid solution α for $CuAl_2$. Nucleation of $CuAl_2$ at solid solution grain boundaries may indicate lack of dislocation in solid solution which could be suitable for nucleation, or very small number of dislocations. That can explain high activation energies of Θ' dissolution and $CuAl_2$ precipitation.

6 Conclusion

Dilatometric and quantitative metallography methods can be applied for analysis of grain growth of solid solution and dissolution of precipitates during saturation annealing of Al-4.7% Cu alloy, where both processes overlap each other.

- Activation energy values of grain growth and dissolution of precipitates in Al-4.7% Cu alloy were determined by quantitative metallography and dilatometric method. The values of the activation energy indicates that both processes depends on diffusion of Cu atoms in solid solution. The differences between values obtained by each method are small and acceptable.
- Both methods (dilatometric and DTA) can be applied for analysis of precipitation and dissolution processes during ageing of supersaturated Al-4.7% Cu alloys.
- Activation energy values of precipitation processes in Al-4.7 % Cu alloy were determined by DTA and dilatometric methods. The differences between values obtained by each method are small and acceptable. Results obtained for precipitation of G-P zones and for precipitation of Θ" and Θ' in principle comply with those obtained before by other authors.
- Activation energies of precipitates dissolution were determined by DTA. Activation energy values obtained for dissolution of the G-P zones comply with those obtained before by other authors.

In the case of dissolution of Θ' and $CuAl_2$ precipitation the obtained activation energies were higher than the activation energy of diffusion of Cu in solid solution.

References

[1] D. Altenpohl: *Aluminium und Aluminium-legirungen*. Berlin, Springer Verlag, 1965.

[2] D. A. Porter, K. E. Easterling: *Phase transformations in metals and alloy.* Van Nostrand Reinhold Company, New York, 1981.

[3] J.W.Christian : *The theory of transformations in metals and alloys.* 2nd. Ed. London , Pergamon Press, 1975.

[4] P. Nowak: *Badania procesów starzenia stopów Al-5%Cu. Próba symulacji komputerowej.* Praca dyplomowa. Politechnika Poznańska WBMiZ, 2002.

[7] D. S.Thomson: *The calorimetric observation of solid state reactions in aluminum alloys".* In Thermal analysis ASM 1970 1147-1170.

[8] G. W. Smith: *Thermochimica Acta* 317, 7-23, 1998.

[9] G. W. Smith. *Thermochimica Acta* 313, 27-36, 1998.

[11] W.N.Wendland: *Thermal methods of analysis.* New York ,1974.

[12] E.J.Mittemeijer: *Annual Report*, Delft University of Technology, 6-10, 1990.

[13] I.A. Wierszyłłowski: *Metallurgical Transactions* 22A, 993-999, 1991.

[14] L. Lochte, A.Gitt, G. Gottstein and I.Hurtado, *Acta Materialia* 48, 2969-2984, 2000.

Proceedings of The 1st International Conference on **D**iffusion in **S**olids and **L**iquids
DSL-2005, July 6-8, 2005, University of Aveiro, Aveiro, Portugal

MODELLING OF BULK EVAPORATION AND CONDENSATION IN MULTIPHASE SINGLE FLUID SYSTEM, ENERGY OF FLUID METHOD

Krzysztof WROBEL[1,*], Harry HOEIJMAKERS[1], Gunter SCHNERR[2]

[1]University of Twente; Faculty of Engineering Technology; Engineering Fluid Dynamics;
P.O.Box 217, 7500 AE Enschede, The Netherlands
[2]Technische Universität München; Lehrstuhl für Fluidmechanik - Fachgebiet Gasdynamik;
Boltzmannstraße 15, 85748 Garching, Germany

*Corresponding author. Fax: +31 53 489 3695; Email: k.m.wrobel@ctw.utwente.nl

---

Abstract

A pressure correction algorithm has been developed for predicting two-phase incompressible flow with phase transition, caused by bulk evaporation/condensation. The algorithm is based on the Semi-Implicit Method for Pressure-Linked Equations (SIMPLE), coupled with Energy of Fluid (EOF) procedure allowing for phase transition simulation. EOF uses an energy fraction f indicating amount of a substance undergoing the phase transition. EOF is coupled with Volume of Fluid method (VOF) allowing for indication of phasic regions in a computational domain. VOF uses a volumetric fraction α, which assumes the values 1 and 0 for pure vapor and liquid regimes, respectively. A vapor-liquid interface is thus located within the range (0 , 1) of α. The VOF method belongs to a group of interface capturing procedures, which removes the discontinuity between phasic regimes by a transition layer in space. This allows preserving numerical stability and facilitates mass conservation in a system.

Keywords: Multiphase flow; Phase transition; Energy of fluid; Interface capturing; Heat transfer

---

1 Introduction

Multiphase flows play a huge role in many branches of industry. They are usually accompanied by a phase transition brought about by changing the pressure - temperature circumstances existing in the flow. A phase transition takes place when a flow passes thermodynamically a saturation line, which is a function of temperature and pressure. In case of lower pressures the saturation temperature is also low and saturation conditions are such that a phase change can be observe at a room temperature. This may occur in various kind of flow devices such as pumps, in which vapor structures appear at the suction side of rotor blades. In this case one deals with cavitation phenomena, for which pressure plays the main role as a driving force of the phase transition. Bulk evaporation or condensation also takes place in energy production industry e.g. in nuclear reactors, where fuel rods must be cooled by light water to ensure stability of the entire system. In this situation the pressure of the flow remains approximately on the same level and now temperature is the variable that determines a phase change.

Ability of predicting numerically phase transition opens the possibility to improve the design of the mentioned industrial systems, potentially decreasing costs of their operation and preventing from eventual damage or even destruction of the system. Since the past decades researchers have developed various methods of phase transition simulation, primarily for the case of stratified fluids. In this paper the whole domain is treated as a single field, which allows to implement one set of Navier - Stokes equations for both phases present in a flow.

The widely used phase transition model of Rayleigh and Plesset considers the dynamics of a gaseous sphere surrounded by a liquid. A vapor bubble grows or shrinks in a potential flow in accordance with the equation:

$$R\frac{d^2R}{dt^2}+\frac{3}{2}\left(\frac{dR}{dt}\right)^2=\frac{p_v-p_\infty}{\rho_l}, \qquad (1)$$

where R represents the bubble radius, t time, ρ_l the liquid density, p_v the vapor pressure inside the bubble (or pressure of saturation) and p_∞ the pressure at a point far away from the bubble (or ambience pressure). In case of Eq. (1) the pressure difference is the driving force of the phase transition rate, but utilizing thermodynamical relations it may be easily expressed in terms of temperature difference, see Ref. [1]. The method, called "bubble growth model", may be coupled with the Volume of Fluid (VOF) procedure Ref. [2], which allows for evaluation of a volumetric phase change rate and motion of the vapor structures in a computational domain. However, the above model needs additional user-controlled information in order to determine boundary conditions, namely a number of spherical vapor structures in a control volume, their initial distribution and size. These data can only be obtained from experiments. However, there are many technical barriers, which impede measurement of the variables, see Ref. [3]. Thus, one usually assumes a homogenous distribution of vapor bubbles having equal initial radius, see Ref. [4], which may substantially affect the result.

In order to overcome the obstacle the new method, outlined in this paper, has been developed. The energy fraction f is used to determine an amount of substance, which undergoes transition. The energy fraction f originates from the definition of the internal energy of a flow in a state of thermodynamical imbalance in a control volume:

$$e=Cv_lT_{sat}+\alpha\Delta e+Cv_v\left(T-T_{sat}\right), \qquad (2)$$

where e denotes the specific internal energy, Δe latent heat, Cv the specific heat of constant volume, T is the temperature and α denotes volumetric vapor fraction in a control volume. Subscript sat indicates a variable in the state of saturation and subscripts l, v indicate a physical property assigned to the liquid and vapor phase, respectively. Once a system departs from an equilibrium state a phase transition occurs. The change of energy fraction is defined as:

$$\delta f=\frac{Cv_v\left(T-T_{sat}\right)}{\Delta e}, \qquad (3)$$

where δf represents the change of f caused by the phase transition. However, the transition (depended on its direction) may occur only in the liquid part of a control volume for evaporation and in the vapor part for condensation:

$$\delta f=\begin{cases}\alpha\frac{Cv_v(T-T_{sat})}{\Delta e} & T<T_{sat}\\ (1-\alpha)\frac{Cv_v(T-T_{sat})}{\Delta e} & T>T_{sat}.\end{cases} \qquad (4)$$

The procedure named Energy of Fluid (EOF), see Ref. [5, 6], do not consider single gaseous structures during the phase transition, thus has less user-controlled variables necessary as initial conditions for a calculation process, than a bubble growth method. The EOF approach utilizes a complete set of Navier-Stokes equations including shear stress and body forces (e.g. gravitation). It also incorporates latent heat, which is released or absorbed depending on the phase transition direction and constitutes a heat source in the energy equation.

2 Approach

The set of governing equations used for the present simulations allows to carry out calculations in 2D. For simplicity physical properties such as heat conductivity and viscosity are assumed constant for each phasic component of a flow. Due to the assumed incompressibility of the phases, the densities of each phase are constant. In the region of an interface the physical properties originate from weighted contributions of the two phases, i.e.:

$$\phi=(1-f)\,\phi_l+f\phi_v, \qquad (5)$$

where ϕ denotes any physical variable.

2.1 Momentum

The momentum equations for a two-phase single field flow in a two-dimensional Cartesian coordinate system read:

$$\frac{\partial}{\partial t}\int_\Omega\rho u\,d\Omega+\int_{\partial\Omega}\rho u\left(\vec{u}.\vec{n}\right)\,dS=$$
$$-\int_{\partial\Omega}p\left(\vec{n}.\vec{e}_x\right)\,dS+\int_{\partial\Omega}\vec{\tau}_x.\vec{n}\,dS, \qquad (6)$$

$$\frac{\partial}{\partial t}\int_\Omega\rho v\,d\Omega+\int_{\partial\Omega}\rho v\left(\vec{u}.\vec{n}\right)\,dS=$$
$$-\int_{\partial\Omega}p\left(\vec{n}.\vec{e}_y\right)\,dS+\int_{\partial\Omega}\vec{\tau}_y.\vec{n}\,dS+\int_\Omega\rho g\,d\Omega, \qquad (7)$$

where p denotes static pressure, g gravity acceleration, ρ fuid density, u, v velocity components in x and y directions, respectively, Ω volume of a control volume and τ represents the stress tensor. The incompressibility assumption implies the phasic densities to be thermally independent, thus temperature variations exert no influence on buoyancy force. This has been avoided by implementation of the Boussinesq approximation for effect of density differences in the gravity term of Eq. (7):

$$\rho = (1-f)\,\rho_{0l}\,(1-\beta_l\,(T-T_0)) + f\rho_{0v}\,(1-\beta_v\,(T-T_0))\,, \qquad (8)$$

where the subscript 0 denotes a reference value of the variable and β reads

$$\beta_{l,v} = -\frac{1}{\rho_{l,v}}\left(\frac{\partial\rho_{l,v}}{\partial T}\right). \qquad (9)$$

2.2 *Mass*

The presented model treats a two phase flow as one computational field, thus it uses one continuity equation at every point in the domain. In two phase regimes density is averaged and substituted in the equation of mass conservation:

$$\frac{\partial}{\partial t}\int_{\Omega}\rho\, d\Omega + \int_{\partial\Omega}\rho\,(\vec{u}.\vec{n})\,dS = 0, \qquad (10)$$

where $\vec{n}$ is the control volume boundary normal, a unitary vector pointing outwards and S denotes the boundary surface bounding the control volume. The right hand side of Eq. (10) remains equal to 0 regardless the occurrence of phase transition, thus mass in a system is conserved and a two phase flow with averaged density behaves as quasi-compressible. However, the continuity equation for each phasic component of a flow reveals a source term at its right hand side, what will be utilized for construction of a volumetric source in the transport equation of the volume fraction α. The transport equation for α is necessary for evaluation of the function α in the computational domain. Rearrangement of Eq. (10) leads to finding the system divergence, whose integration yields the phasic volumetric source:

$$\int_{\Omega}\vec{\nabla}.\vec{u}\,d\Omega = -\int_{\Omega}\frac{1}{\rho}\frac{D\rho}{Dt}\,d\Omega = \int_{\Omega}\frac{\rho_l-\rho_v}{\rho}\frac{D\alpha}{Dt}\,d\Omega, \qquad (11)$$

where $\frac{D}{Dt}$ denotes a substantial derivative.

2.3 *Divergence*

Following the above consideration leading to the divergence expression, Eq. (11), one needs to model the substantial derivative of α. It is assumed that the phase transition occurring within a time step is not convected by a flow. Consequently, the substantial derivative become an ordinary time derivative. Translation of Eq. (4) into a volumetric change, its differentiation with respect to time and substitution in Eq. (11) yields the volumetric divergence of a system. This divergence allows for proper modelling the spatial distribution of volume fraction (the transport equation) and the stress term in the momentum equation. It also plays a role in updating the pressure and fluxes distribution in the pressure-correction equation and evaluates the amount of absorbed or released heat originating from heat of vaporization present in the energy equation.

2.4 *Transport equation*

We consider distribution of flow parameters in a domain governed mainly by convection forces. Consequently, the volume fraction α determining phasic regimes, needs to be transported. Therefore it obeys the convection equation derived from the continuity formulation, Eq. (10):

$$\frac{\partial}{\partial t}\int_{\Omega}\alpha\,d\Omega + \int_{\partial\Omega}\alpha\,(\vec{u}.\vec{n})\,dS = \int_{\Omega}\frac{\rho_l-\rho_v}{\rho_l}\vec{\nabla}.\vec{u}\,d\Omega. \qquad (12)$$

The right hand side of Eq. (12) constitutes a source of volume flux, which appears during a phase change. The form of this term comes from consideration of the continuity equation for a fluid mixture, Eq. (10), and the mass conservation equation for a pure substance undergoing a transition, which possesses, opposite to Eq. (10), a source at its right hand side. Combination of these two formulations yields the mentioned term. One should pay attention to the constant factor containing densities at the right hand side of Eq. (12). In the process of phase change one obtains a certain amount of vapor (in case of evaporation), which originates from a portion of liquid of a substantially smaller volume. Thus, the increment of a vapor volume is defined as the difference between the volume of evaporated vapor and the original volume of liquid. Due to the incompressibility assumption of the scheme the relation between the mentioned volumes is constant and controlled by the ratio of liquid and vapor densities.

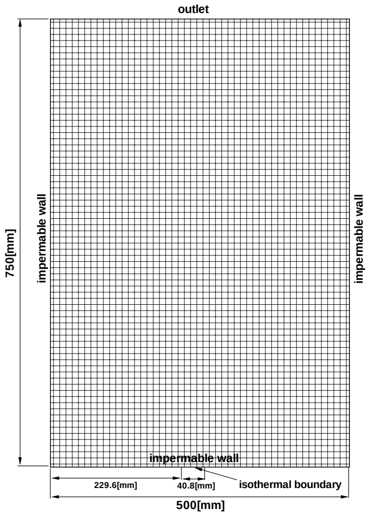

Figure 1: Computational domain.

The VOF system treats a computational domain as one field smearing an interface between vapor and liquid. It helps to maintain numerical stability and mass conservation on an acceptable level, but influences accuracy of phasic distribution and consequently dynamics of the entire system. In order to diminish the problem one has incorporated a special numerical treatment of the convective term of Eq. (12), which ensures high sharpness and a monotonic contour of the interface. The key of the procedure is proper assessment of the α value at each control volume boundary. This value is a function of a spatial distribution of the volume fraction and is estimated using a flux rate represented by the Courant number of the computational cell. The method blends the two procedures - Universal Limiter (ULTIMATE) and Quadratic Upwind Interpolation Estimated (QUICKEST). Following the above consideration a normalized facial value of $\breve{\alpha}_f$ is found based on the formula:

$$\breve{\alpha}_f^{UQ} = \begin{cases} m\left\{ m\left\{1, \frac{\breve{\alpha}_D}{cfl}\right\}^U, m\{1, qc\}^Q \right\}, & \breve{\alpha}_D \in \langle 0,1\rangle \\ \breve{\alpha}_D, & \breve{\alpha}_D \notin \langle 0,1\rangle, \end{cases} \tag{13}$$

where m denotes the minimum function,

$$qc = \frac{8cfl\breve{\alpha}_D + (1 - cfl)(6\breve{\alpha}_D + 3)}{8},$$

cfl is the Courant number and $\breve{\alpha}$ represents the normalized value of α defined by

$$\breve{\alpha} = \frac{\alpha - \alpha_U}{\alpha_A - \alpha_U}. \tag{14}$$

Subscripts U, D and A indicate an upstream, donor and acceptor cell, aligned next to each other ordered from upstream to acceptor cell. The direction of alignment is controlled by the flux direction. A normalized $\breve{\alpha}$ value allows to determine a relation between the α gradient measured somewhere between an acceptor and upstream cell, e.g. at a node of the donor, and the α gradient between an acceptor and upstream control volume. Following a donor cell normalized $\breve{\alpha}_D$ value the most proper method is chosen (ULTIMATE or QUICKEST), which will determine the facial value of $\breve{\alpha}_f$. For details of the approach see Ref. [7, 8]. The described model has been designed for a 1D system, for which the gradient direction coincides with the flux vector. For a 2D scheme the entire procedure needs to be adopted. This has been obtained by employing the Compressive Interface Capturing Scheme for Arbitrary Meshes (CICSAM). The scheme determines a γ factor based on the angle θ between the α gradient direction and the vector connecting the nodes of two adjacent control volumes (for the uniform grid used in the test case illustrated in the paper the connecting vector coincides with a flux vector):

$$\gamma = MIN\left\{\frac{\cos(2\theta) + 1}{2}, 1\right\}. \tag{15}$$

The γ factor delineates a contribution of ULTIMATE-QUICKEST or single ULTIMATE procedures in the evaluation of the normalized face value of $\breve{\alpha}_f$:

$$\breve{\alpha}_f = \gamma\breve{\alpha}_f^U + (1 - \gamma)\,\breve{\alpha}_f^{UQ}. \tag{16}$$

In case the θ angle is small the interface is nearly orthogonal to the flux direction and one may rather expect larger volume fraction gradients and consequently a γ factor obtains higher values giving priority to the ULTIMATE method. In the opposite situation normalized facial values are assessed with a greater contribution of ULTIMATE-QUICKEST, i.e. in case γ is close to 0, the QUICKEST procedure plays a role. CICSAM has been described in detail in Ref. [9].

2.5 *Energy equation*

The energy equation for the specific internal energy is for convenience expressed in terms of the temperature. It has been simplified by the assumption of constant and equal values of specific heat for both phases. Using the definition of internal energy given by Eq. (2) one formulates the expression for energy.

However, the latent heat appearing in Eq. (2) needs to be treated with care - it may not be a part of the unsteady or convective term of the energy equation as long as that it is not a heat influencing the temperature, because it would cause unphysical jumps of the temperature in a system. Consequently, the formulation of energy reads:

$$\frac{\partial}{\partial t}\int_{\Omega}\rho CvT\,d\Omega+\int_{\partial\Omega}\rho CvT\,(\vec{u}.\vec{n})\,dS= \\ =\int_{\partial\Omega}\lambda\left(\vec{\nabla}T\right).\vec{n}\,dS+\int_{\Omega}\left(\bar{\bar{\tau}}\vec{\nabla}\right).\vec{u}\,d\Omega-\Delta e\rho_v\int_{\Omega}\frac{d\alpha}{dt}\,d\Omega, \quad (17)$$

where λ denotes the heat conduction coefficient. The last term at the right hand side of Eq. (17) incorporating the heat of vaporization represents a heat released or absorbed during phase transition.

2.6 *Closure relations*

In order to complete modelling of the governing equation set a closure relation needs to be established. It relates the temperature of saturation to the static pressure present in the control volume. The function has been expressed by a simple Clausius-Clapeyron equation, which reads

$$T_{sat}=\frac{C}{D-ln(p)}, \quad (18)$$

where C and D are constants. In spite of its simplicity the relation gives values of T_{sat} with acceptable small differences from experimental distribution, particularly within the range of pressures including the normal boiling point.

3 Results

The test case carried out concerns simulating the growth of bubble patches as the result of evaporation occurring on the isothermal boundary in the computational domain. The boundary is located at the bottom of the domain. The domain is the lower part of the vessel filled by subcooled water. The 2D domain dimensions are 500x750[mm], the level of subcooling amounts to 81.9[K] and wall superheating 400.09[K] with the local temperature of saturation 375.06[K]. The isothermal boundary of the length 40.8[mm] has been placed in the middle of the domain bottom. The domain has been spatially discretized by the uniform rectangular grid of 50x70 control volumes, Fig. 1. The time step chosen for the calculations has been set to the level of 1e-4[s]. The vapor structures appear periodically, detach and undergo condensation in regions of lower temperatures. A condensation process shrinks a patch. The distribution of the volume fraction illustrating a vapor structure movement is shown on Fig. 2. The patches are convected upwards by natural convection caused by buoyancy forces. They carry higher temperature fields and leave a wake of higher temperature behind, Fig. 3. This decreases the rate of condensation and causes a longer life time of subsequent vapor structures. The behavior of vapor patches, their time and space propagation manifested by their shape, as well as the distribution of other flow parameters caused by the phase transition are in qualitative agreement with results of the experiments described in Ref. [10].

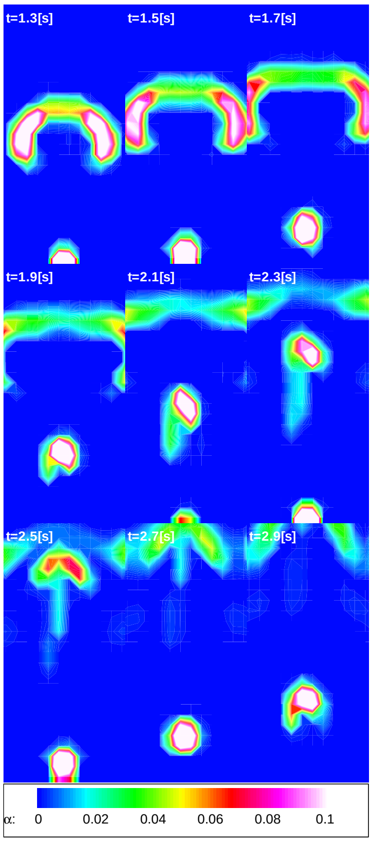

Figure 2: Volume fraction α propagation (the set of pictures is focused on the region of isothermal boundary and zoomed).

4 Conclusions

A phase change involving liquid-vapor transition is always three-dimensional in nature. The scheme used for the present simulation is 2D and contains some simplifications e.g. related to flow physical properties, as mentioned in the text. Thus, one needs to emphasize, that the result may not be quantitatively assessed, but only qualitative comparison with an experiment is allowed. The EOF method assumes that a phase transition reaction occurs up to the moment of thermodynamical equilibrium manifested by an equal value of the temperature in a control volume and the local temperature of saturation. This fact indicates that the method fails in predicting the rate of the reaction. Thus, the vapor-liquid source represented by Eq. (4) needs to be factorized in order to obtain a better approach to real phenomena as well as to maintain numerical stability. Consequently, the purpose of the simulation, which has been performed in this work, has been aimed at the assessment of the feasibility of the method for solving problems with a phase transition. Though EOF avoids the need of user-controlled input data associated with a bubble growth model, lack of a relation with the phase change reaction time is a disadvantage, which challenges a further effort to overcome this weak point of the model. An idea is to combine the EOF procedure and a bubble growth approach, what will be the next step of this project.

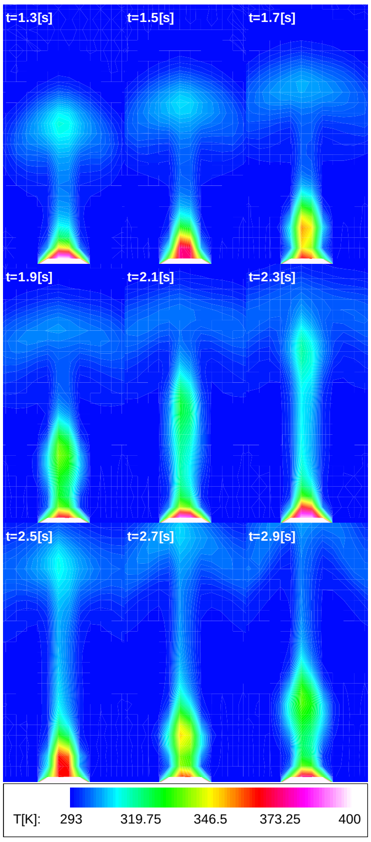

Figure 3: Temperature propagation (the set of pictures is focused on the region of isothermal boundary and zoomed).

Acknowledgments

This work has been performed as a part of the Ph. D. project No 20032122 at University of Twente in The Netherlands.

References

[1] Plesset, M.S., Zwick, S.A.: The growth of vapor bubble in superheated liquid. *J. Appl. Phys.*, 25, pp. 493, 1954.

[2] Hirt, C.W., Nichols, B.D.: Volume of Fluid (VOF) method for the dynamics of free boundaries. *J. Comput. Phys.*, 39, pp. 201-225, 1981.

[3] Schnerr, G.H., Yuan, W.: Numerical simulation of two-phase flow in injection nozzles: interaction of cavitation and external jet formation. *J. Fluid. Eng.*, 125, pp. 963-969, 2003.

[4] Sauer J.: *Instationär Kavitierende Strömungen - Ein Neues Modell, Basierend Auf Front Capturing (VOF) Und Blasendynamik*, Ph. D. Thesis, Universität Karlsruhe, 2000.

[5] Ding Z., Anghaie S.: Numerical modelling of conduction-driven bulk evaporation and condensation processes with constant volume. *Int. J. Numer. Meth. Eng.*, 39, pp. 219-233, 1996.

[6] Ding Z., Anghaie S.: Thermal-hydraulic analysis of bulk evaporation and condensation in a multiphase nuclear fuel cell. *Nucl. Technol.* , 120, pp. 57-70, 1997.

[7] Leonard B.P.: Bounded higher-order upwind multidimensional finite-volume convection-diffusion algorithms. *Advances in Numerical Heat Transfer* , 1, pp. 1-57, 1977.

[8] Leonard B.P.: A stable and accurate convective modelling procedure based om quadratic upstream interpolation. *Comput. Method. Appl. M.* , 19, pp. 59-98, 1979.

[9] Ubbink O.: *Numerical prediction of two fluid systems with sharp interfaces*, Ph. D. Thesis, London University, 1997.

[10] Stralen, S.v., Cole, R.: *Boiling Phenomena, Vol. 2*. First ed., Hemisphere, Washington, 1979.

Proceedings of The 1st International Conference on **D**iffusion in **S**olids and **L**iquids
DSL-2005, July 6-8, 2005, University of Aveiro, Aveiro, Portugal

SELF-DIFFUSION OF P IN Pd-Cu-Ni-P BULK METALLIC GLASS

Yoshihiro YAMAZAKI[1,*], Takayuki NIHEI[1], Junichi KOIKE[1], Tsutomu OHTSUKI[2]
[1]Deparment of Materials Science, Graduate School of Engineering, Tohoku University, Aoba-yama 02, Sendai 980-8579, Japan
[2]Laboratory of Nuclear Science, Graduate School of Science, Tohoku University, Mikamine 1-2-1, Sendai 982-0826, Japan

[*]Corresponding author. Fax: +81 22 795 7338; Email: yamazaki@material.tohoku.ac.jp

---

Abstract

The diffusion coefficients of ^{32}P and ^{67}Cu in $Pd_{42}Cu_{28}Ni_{10}P_{20}$ alloy have been determined in a supercooled liquid state from 573 to 615 K using a serial sputter-microsectioning technique. The diffusion coefficient of ^{32}P in the alloy is found to be two orders of magnitude smaller than that of ^{67}Cu. The small diffusivity of P in comparison with that of Cu is not explained by the size dependence of self-diffusion coefficients in the alloy. This suggests that the local chemical interaction around P is more important for the P diffusion than the atomic radius.

Keywords: Bulk metallic glass; Self-diffusion; Supercooled liquid; Phosphorous; Copper

---

1 Introduction

Pd-Cu-Ni-P bulk metallic glass has an exceptional glass-formability and shows a large supercooled-liquid region of about 100 K[1, 2]. Since the bulk metallic glass is in thermodynamically metastable state, it undergoes various rearrangement processes such as structural relaxation, phase separation and crystallization as a result of diffusion of constituent elements when temperature rises[3, 4]. Therefore, diffusion study is critical to understand and control the phase stability.

Self-diffusion of Ni[5] and P[6], impurity diffusion of Co[7-9], and interdiffusion[10] have been studied in the Pd-Cu-Ni-P bulk metallic glasses. The most detailed diffusion study in the Pd-Cu-Ni-P glass has been carried out by Faupel's group[7-9]. The impurity diffusion of Co and the isotope effect of Co diffusion have been determined in the liquid, supercooled liquid and glassy states. According to them, the diffusion of Co in the supercooled liquid and glassy states occurs via highly collective hopping process. However, the diffusion coefficient of Co[7] in the $Pd_{40}Cu_{30}Ni_{10}P_{20}$ alloy is about one order of magnitude smaller than that of Ni[5]. This suggests that the impurity diffusion of Co does not represent the self-diffusion of Ni. In order to elucidate the diffusion mechanism in the Pd-Cu-Ni-P bulk metallic glass, experimental data on self-diffusion of both metal and metalloid elements in the supercooled liquid state is essential. In the present work, the self-diffusion of P and Cu in the Pd-Cu-Ni-P bulk metallic glass was studied.

2 Experimental procedure

Starting materials were Pd (99.95 mass%), Cu (99.9999 mass%), Ni (99.97 mass%) and P (99.9999 mass%). Cu and Ni were chemically polished. $Pd_{60}P_{40}$ alloy was melted in a SiO_2 tube. $Pd_{42}Cu_{28}Ni_{10}P_{20}$ alloy was induction-melted in a SiO_2 tube and cast into a Cu cold crucible under argon atmosphere. The rod was cut into disc specimens having 1 mm in thickness. The flat face of the specimens was ground on abrasive papers and carefully polished using diamond pastes.

The radioisotope ^{32}P (β-ray 1.711MeV: half-life 14.26days) in the form of chloride in a 1 k $\mathrm{mol \cdot m^{-3}}$ hydrochloric solution was purchased. On the other hand, the radioisotope ^{67}Cu (γ-ray 0.185MeV: half-life 2.58days) was produced by $^{68}\mathrm{Zn}(\gamma,p)^{67}\mathrm{Cu}$ reaction with a linear electron accelerator in Tohoku University. Target material (^{nat}Zn) and radioactive impurities produced as by-products were chemically separated by a solvent extraction method and an anion exchange method. The radioisotopes were electroplated onto the mirror-like surface of the specimen from the solutions. The specimens surrounded by a zirconium foil were held at temperatures in the range from 573 to 615 K for 1.8-9.0 ks under a pressure lower than 10^{-5} Pa.

A serial ion-beam sputter-microsectioning technique was employed to measure the penetration profiles of ^{32}P and ^{67}Cu. Details of the method were described elsewhere[11]. For each specimen 20-40 successive sections were sputtered. The intensity of the β-rays from each section was measured by a plastic scintillation detector in conjunction with a 1024-channel pulse-height analyzer. On the other hand, the intensity of the γ-rays was measured by a well-type Tl-activated NaI scintillation detector.

3 Results and discussion

Experimental results were analyzed using the solution of Fick's second law for one-dimensional volume diffusion of a tracer from an infinitesimally thin surface layer into a sufficiently long rod,

$$I(x,t) \propto C(x,t) = \frac{M}{\sqrt{\pi D t}} \exp\left(\frac{-x^2}{4Dt}\right) \tag{1}$$

where $I(x,t)$ and $C(x,t)$ are the intensity of the radioactivity and the concentration, respectively, of the tracer at a distance x from the original surface after a diffusion time t; D is the volume diffusion coefficient of the tracer; and M is the total amount of the tracer deposited on the surface before the diffusion.

Figure 1 shows the typical plots of $\ln I(x,t)$ vs. x^2 for the diffusion of ^{32}P in the $Pd_{42}Cu_{28}Ni_{10}P_{20}$ alloy. The linear portion follows the Fick's second law. Thus the volume diffusion can be analyzed using Eq. (1). Figure 2 shows the Ahhrenius plot of D_P^* and D_{Cu}^* determined in the alloy together with D_P^* determined in the $Pd_{43}Cu_{27}Ni_{10}P_{20}$ alloy by Rätzke et al.[6] and D_{Ni}^* determined in the $Pd_{40}Cu_{30}Ni_{10}P_{20}$ alloy by Nakajima et al.[5]. The diffusion coefficients of ^{32}P in the $Pd_{42}Cu_{28}Ni_{10}P_{20}$ glass in the supercooled liquid state is approximately equivalent to that reported in the $Pd_{43}Cu_{27}Ni_{10}P_{20}$ by Rätzke et al.[6], suggesting that a small deviation in composition of the Pd-Cu-Ni-P glass does not largely affect the P diffusion. On the other hand, the value of D_P^* in the $Pd_{42}Cu_{28}Ni_{10}P_{20}$ glass is two orders of magnitude smaller than that of D_{Cu}^*. Furthermore, the value of D_{Cu}^* is the same order of that of D_{Ni}^* at the corresponding temperature. This suggests that the diffusion of P which is a metalloid element is largely different from those of metal elements in the alloy.

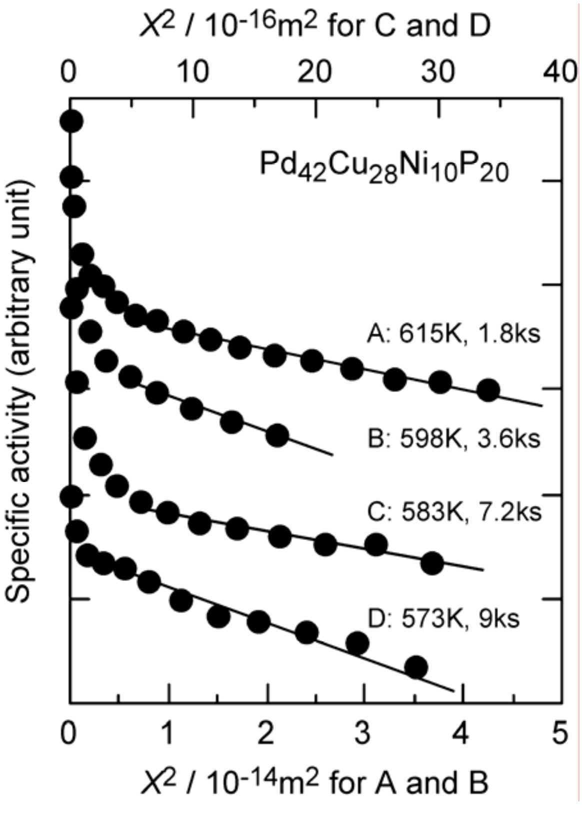

Figure 1: Plots of ln $I(x,t)$ vs. x^2 for diffusion of ^{32}P in supercooled liquid state of $Pd_{42}Cu_{28}Ni_{10}P_{20}$ glass.

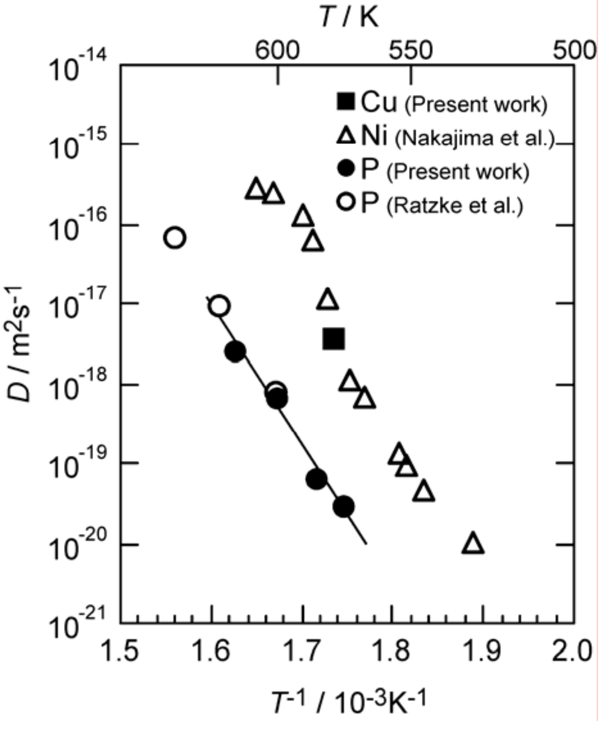

Figure 2: Temperature dependence of self-diffusion coefficients of P and Cu determined in $Pd_{42}Cu_{28}Ni_{10}P_{20}$ glass in comparison with that of P in $Pd_{43}Cu_{27}Ni_{10}P_{20}$ glass and that of Ni in $Pd_{40}Cu_{30}Ni_{10}P_{20}$ glass.

To discuss the slow diffusion of P in the $Pd_{42}Cu_{28}Ni_{10}P_{20}$ bulk metallic glass, we compare this result with the previous diffusion data in metallic glasses. Diffusion behaviour in conventional amorphous alloys has been attributed to the size dependence; smaller atoms diffuse faster than larger ones. This dependence has been mainly discussed for impurity diffusion in the amorphous alloys[3, 12, 13]. However, there are numbers of exceptions from the rule. To simplify the situation, we compare our result with the self-diffusion data reported in the literature.

Diffusion coefficients of more than two constituent elements have been determined in the Fe-Zr[14], Co-Zr[15-17] and Zr-Ti-Cu-Ni-Be[18, 19] (metal-metal type) glasses and the Fe-Ni-B [20-22], Fe-Ni-P-B[23, 24] and Pd-Cu-Ni-P[5, 6] (metal-metalloid type) glasses. The sizes of constituent atoms in the metal-metal type glass are compared on the basis of their metallic radii for a coordination number *CN* of 12 [25]. In the Fe-Zr and Co-Zr conventional amorphous alloys, the diffusion of Zr[14, 17] whose atomic radius r is 0.1602 nm is slower than the diffusion of Fe[14] (r_{Fe} = 0.1274 nm) and Co[15] (r_{Co} = 0.1252 nm), respectively. Furthermore, in the $Zr_{46.7}Ti_{8.3}Cu_{7.5}Ni_{10}Be_{27.5}$ bulk metallic glass (Vit4), the Be atoms with the smallest size (r_{Be} = 0.1128 nm) has the highest diffusion rates followed by those of Ni (r_{Ni} = 0.1246 nm) and Zr. The self-diffusion coefficient decreases with increasing in the atomic radius of the constituent element. These results suggest that the size dependence of D holds in both conventional and bulk metal-metal type glasses.

In the metal-metalloid type glasses, both the metallic radius for a coordination number of 12 and the covalent radius [25] are considered for the comparison. In the Fe-Ni-B system, the diffusion coefficient of small B atoms[20] (r_B = 0.098 nm for *CN* 12 and 0.08 nm for covalent bond) is two orders of magnitude larger than the diffusion coefficients of larger Ni [21] (r_{Ni} = 0.1246 nm) and Fe[22] (r_{Fe} = 0.1274 nm) atoms, suggesting that the size dependence holds also in this system. On the other hand, in the Fe-Ni-P-B system, the diffusion coefficient of P (r_P = 0.128 nm for *CN* 12 and 0.11 nm for covalent bond) is smaller than that of Fe[24] (r_{Fe} = 0.1274 nm). Since the diffusion coefficient of P dose not obey the Arrhenius law [23], the reliability of the diffusion data of P is questioned. However, this implies that the diffusion behavior of P is different from the other metalloid element such as B.

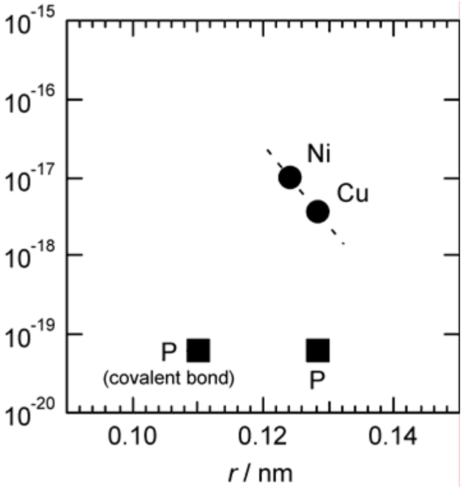

Figure 3: Plot of self-diffusion coefficients of Cu, Ni and P at 580 K in Pd-Cu-Ni-P glass vs. atomic and covalent radii.

The diffusion coefficients of P and Cu determined in the present work and the diffusion coefficient of Ni[5] determined by Nakajima et al. at 580 ± 3 K are plotted against atomic radii and shown in Fig. 3. The same order of diffusion coefficients for Cu and Ni is attributed to the close atomic radii between them (r_{Cu} = 0.1278 nm and r_{Ni} = 0.1246 nm). This is the same trend observed in the Fe-Ni-B conventional amorphous alloy[21, 22] and in the Zr-Ti-Cu-Ni-Be bulk metallic glass[18, 19]. On the other hand, the diffusion coefficient of P is about two orders of magnitude smaller than that of Cu, although the atomic radius of P for CN 12 (r_P = 0.128 nm) and covalent radius (r_P = 0.11 nm) are equivalent to and smaller than that of Cu, respectively. The small diffusivity of P is not explained by the size dependence of self-diffusion coefficients in the alloy. This suggests that the local chemical interaction around P, that is, strong covalent bond of P, is more important for the P diffusion than the size dependence of constituent elements in the alloy.

4 Conclusions

The diffusion coefficients of ^{32}P and ^{67}Cu in $Pd_{42}Cu_{28}Ni_{10}P_{20}$ alloy have been determined in the supercooled liquid state from 573 to 615 K using a serial sputter-microsectioning technique. The diffusion coefficient of ^{32}P in the $Pd_{42}Cu_{28}Ni_{10}P_{20}$ glass is approximately equivalent to that reported in the $Pd_{43}Cu_{27}Ni_{10}P_{20}$ by Rätzke et al., suggesting that a small deviation in composition of the Pd-Cu-Ni-P glass does not largely affect the P diffusion. The diffusion coefficient of P in the alloy is two orders of magnitude smaller than that of Cu. The small diffusivity of P is not explained by the size dependence of self-diffusion coefficients in the alloy but by the strong covalent bond of P.

Acknowledgments

The present work was supported in part by a Grant-in-Aid for Scientific Research of Priority Area A from the ministry of Education, Science, Sports and Culture, Japan.

References

[1] Nishiyama, N. and Inoue, A.: Glass-forming ability of bulk $Pd_{40}Ni_{10}Cu_{30}P_{20}$ alloy: *Mater. Trans. Jim*, 37, pp. 1531-9, 1996.

[2] Lu, I. R., Wilde, G., Görler, G. P. and Willnecker, R.: Thermodynamic properties of Pd-based glass-forming alloys: *J. Non-Cryst. Solids*, 252, pp. 577-81, 1999.

[3] Faupel, F., Frank, W., Macht, M. P., Mehrer, H., Naundorf, V., Rätzke, K., Schober, H. R., Sharma, S. K. and Teichler, H.: Diffusion in metallic glasses and supercooled melts: *Rev. Mod. Phys.*, 75, pp. 237-80, 2003.

[4] Wollgarten, M., Mechler, S., Davidov, E., Wanderka, N. and Macht, M. P.: Decomposition and crystallization of $Pd_{40}Cu_{30}Ni_{10}P_{20}$ and $Zr_{46.8}Ti_{8.2}Cu_{7.5}Ni_{10}Be_{27.5}$ metallic glasses: *Intermetallics*, 12, pp. 1251-5, 2004.

[5] Nakajima, H., Kojima, T., Zumkley, T., Nishiyama, N. and Inoue, A.: Diffusion of Nickel in $Pd_{40}Cu_{30}Ni_{10}P_{20}$: *Proceedings of the International Conference on Solid-Solid Phase Transformations '99 (JIMIC-3)*, Koiwa, M., Otsuka, K. and Miyazaki, T. (Eds), pp. 441-4, 1999.

[6] Rätzke, K., Zöllmer, V., Bartsch, A., Meyer, A. and Faupel, F.: Diffusion in bulk-metallic glass-forming Pd-Cu-Ni-P alloys: from the glass to the equilibrium melt: *J. Non-crystall. Solids*, pp. in press.

[7] Zöllmer, V., Rätzke, K., Faupel, F., Rehmet, A. and Geyer, U.: Evidence of diffusion via collective hopping in metallic supercooled liquids and glasses: *Phys. Rev. B*, 65, pp. 220201-1-3, 2002.

[8] Zöllmer, V., Rätzke, K., Faupel, F. and Meyer, A.: Diffusion in a metallic melt at the critical temperature of mode coupling theory: *Phys. Rev. Lett.*, 90, pp. 195502-1-4, 2003.

[9] Zöllmer, V., Rätzke, K. and Faupel, F.: Diffusion and isotope effect in bulk-metallic glass-forming Pd-Cu-Ni-P alloys from the glass to the equilibrium melt: *J. Mater. Res.*, 18, pp. 2688-96, 2003.

[10] Griesche, A., Zumkley, T., Macht, M. P., Suzuki, S. and Frohberg, G.: Diffusion in PdCuNiP alloys from the amorphous to the liquid state: *Mate. Sci. Eng. a*, 375-77, pp. 285-7, 2004.

[11] Iijima, Y., Yamada, K., Katoh, H., Kim, J. K. and Hirano, K.: Diffusion in iron-base amorphous alloys studied by ion-beam sputter-microsectioning technique: *Proceedings of 13th Symposium on Ion Sources and Ion-assisted Techniques, Ionics*, Takagi, T. (Eds), The Ion Engineering Society of Japan, pp. 179-82, 1990.

[12] Sharma, S. K., Macht, M. P. and Naundorf, V.: A Sims Investigation of Impurity Diffusion in Amorphous $Fe_{40}Ni_{40}B_{20}$: *Acta Metall. Mater.*, 40, pp. 2439-49, 1992.

[13] Sharma, S. K., Macht, M. P. and Naundorf, V.: Impurity-Diffusion Investigations in Amorphous $Ti_{60}Ni_{40}$: *Phys. Rev. B*, 49, pp. 6655-66, 1994.

[14] Horváth, J., Ott, J., Pfahler, K. and Ulfert, W.: Tracer Diffusion in Amorphous-Alloys: *Mater. Sci. Eng.*, 97, pp. 409-13, 1988.

[15] Dorner, W. and Mehrer, H.: Tracer Diffusion and Thermal-Stability in Amorphous Co-Zr and Their Relevance for Solid-State Amorphization: *Phys. Rev. B*, 44, pp. 101-14, 1991.

[16] Klugkist, P., Rätzke, K., Rehders, S., Troche, P. and Faupel, F.: Activation volume of Co-57 diffusion in amorphous $Co_{81}Zr_{19}$: *Phys. Rev. Lett.*, 80, pp. 3288-91, 1998.

[17] Klugkist, P., Rätzke, K. and Faupel, F.: Evidence of defect-mediated zirconium self-diffusion in amorphous $Co_{92}Zr_8$: *Phys. Rev. Lett.*, 81, pp. 614-7, 1998.

[18] Knorr, K., Macht, M., Freitag, K. and Mehrer, H.: Self-diffusion in the amorphous and supercooled liquid state of the bulk metallic glass $Zr_{46.75}Ti_{8.25}Cu_{7.5}Ni_{10}Be_{27.5}$: *J. Non-Cryst. Solids* 252, pp. 669-73, 1999.

[19] Rehmet, a., Rätzke, K., Faupel, F., Eversheim, P. D., Freitag, K., Geyer, U. and Schneider, S.: Be-7 tracer diffusion in a deeply supercooled $Zr_{46.7}Ti_{8.3}Cu_{7.5}Ni_{10}Be_{27.5}$ melt: *Appl. Phys. Lett.*, 79, pp. 2892-4, 2001.

[20] Cahn, R. W., Evetts, J. E., Patterson, J., Somekh, R. E. and Jackson, C. K.: Direct Measurement by Secondary-Ion Mass-Spectrometry of Self-Diffusion of Boron in $Fe_{40}Ni_{40}B_{20}$ Glass: *J. Mater. Sci.*, 15, pp. 702-10, 1980.

[21] Tyagi, a. K., Macht, M. P. and Naundorf, V.: Diffusion-Coefficients of Ni-63 in $Fe_{40}Ni_{40}B_{20}$ Metallic-Glass: *Acta Metall. Mater.*, 39, pp. 609-17, 1991.

[22] Horváth, J. and Mehrer, H.: Tracer Diffusion of Fe-59 in Amorphous $Fe_{40}Ni_{40}B_{20}$: *Crystal Lattice Defects and Amorphous Materials*, 13, pp. 1-14, 1986.

[23] Valenta, P., Maier, K., Kronmüller, H. and Freitag, K.: Self-Diffusion of Phosphorus in the Amorphous Alloy $Fe_{40}Ni_{40}P_{14}B_6$: *Phys. Stat. Sol. B*, 105, pp. 537-42, 1981.

[24] Valenta, P., Maier, K., Kronmüller, H. and Freitag, K.: Self-Diffusion of Iron in the Amorphous-Alloys $Fe_{40}Ni_{40}P_{14}B_6$ and $Fe_{80}B_{20}$: *Phys. Stat. Sol. B*, 106, pp. 129-33, 1981.

[25] Pearson, W. B.: *The Crystal Chemistry and Physics of Metals and Alloys*, Wiley, New York, 1972.

Proceedings of The 1st International Conference on **D**iffusion in **S**olids and **L**iquids
DSL-2005, July 6-8, 2005, University of Aveiro, Aveiro, Portugal

ON APPLICABILITY OF ION EXCHANGE DIFFUSION IN GLASSES FOR PRODUCING DIFFRACTION GRATINGS

Andrey LIPOVSKII, Valentina ZHURIKHINA*

St.-Petersburg State Polytechnic University, Polytechnicheskaja 29, St.-Petersburg, 195251 Russia

*Corresponding author. Fax: +7 812 5345821, Email: zhurikhina@phtf.stu.neva.ru

Abstract

The mode of light diffraction and minimal periodicity are evaluated for graded index diffraction gratings formed in glasses with ion exchange technique. Spontaneous thermal ion exchange can be used only for the formation of gratings demonstrating Raman-Nath mode of light diffraction. Electrically stimulated ion exchange can be applied for the formation of gratings diffracting ~60-80 % of incident light in one diffraction order, however thick diffraction gratings with high angular selectivity can hardly be formed. The relation of glass parameters, the temperature of ion exchange processing and driving electrical field with grating periodicity and the depth of phase modulation is evaluated as well as the magnitude of field, which can be applied to stimulate ion exchange.

Keywords: Diffusion in amorphous materials; Glasses; Ion exchange; Diffraction gratings; Bragg; Modeling

1 Introduction

Ion-exchange technique has recently been implemented in diffractive optics for the formation of periodical phase profiles in glasses [1,2], and the applications of the structures of this kind were reported [3]. Here approximately linear dependence of induced index variation on the concentration of dopants [4] allows to model optical profiles of ion exchange structures using Fick's equations. The interest in the ion-exchanged structures is due to a possibility to have optical elements with flat surfaces, which are more stable comparatively to etched periodical structures, and they can be used for the construction of stacked optical systems. Most of applications need high (> 250 mm^{-1}) periodicity and deep, at least $\varphi = \pi/2$, phase modulation φ of light by the diffractive elements since it is necessary to provide preferable (about 80-90 %) diffraction in the first diffraction order. One more topic of interest is the formation of thick diffraction gratings, which can provide high angular and spectral selectivity of diffraction in a single order (Bragg mode of diffraction) and 100 % effectivity of diffraction [5]. That is why the evaluation of periodicity available for ion-exchanged structures with deep phase modulation is actual.

2 Basics of existing theory

Ion exchange originates from two types of force. The first is due to the concentration gradient of ions, and it leads to the ion flux $\mathbf{J}_D$ proportional to the gradient of concentration C and diffusion coefficient D. The second force is due to the external electric field $\mathbf{E}$, and the ion flux $\mathbf{J}_E$ is proportional to the ionic mobility μ, the field magnitude, and the concentration of ions. In accordance with the relation of Nernst-Einstein modified by Haven ratio [6], diffusion coefficient D and ionic mobility μ are connected as

$$\mu = \frac{eD}{HkT} \tag{1}$$

where e – charge of electron, k – Boltzman coefficient, T – absolute temperature and H – Haven ratio, the coefficient, which takes $H = 1$ for ideal gas systems and can take values between 0.1 and 1 for glasses [6]. Let us consider ion exchange in glass where two types of ions participate in the diffusion process – incoming ions *a* and outcoming *b*. In this case inserting total ion flux $\mathbf{J} = \mathbf{J}_D + \mathbf{J}_E$ into the continuity equation results in interdiffusion equation [6]:

$$\frac{\partial C}{\partial t} = \nabla\left[\frac{D_a}{1-\beta C}\left(\nabla C - \frac{\mathbf{J}_0}{C_0 D_b}C\right)\right], \qquad (2)$$

where t is the time of diffusion, C_0 is the initial concentration of b-type ions in glass, $C = C_a/C_0$, $\mathbf{J_0}$ is the total ionic flux, $\mathbf{J_0} = \mathbf{J_a} + \mathbf{J_b}$, D_a and D_b are the diffusion coefficients of a-type and b-type ions, respectively, and $\beta = 1\text{-}D_a/D_b$. Generally both β and the diffusion coefficients D_a and D_b depend on concentration, and equation (2) is nonlinear. But for rough estimation one can neglect the nonlinearity of diffusion, and further consider the diffusion coefficients to be constant. Moreover, if the radii of a- and b-ions are close, we can assume that $D_a = D_b = D$, and $\beta = 0$. Under these two assumptions equation (2) takes the following form [6]:

$$\frac{\partial C}{\partial t} = D\nabla^2 C - \mu\mathbf{E}\nabla C \cdot \qquad (3)$$

This equation is to be completed with the initial and boundary conditions. In the case of planar ion exchange from molten salt to a glass substrate and **E** parallel to **x**, the initial and boundary conditions are

$$C(0,t) = C_{0a};\ C(\infty,t) = 0;\ C(x,0) = 0, \qquad (4)$$

where we denote the glass surface by x=0. Diffusion equation (3) with boundary conditions (4) has an analytical solution, that is [7]

$$C(x,t) = \frac{C_{0a}}{2}\left\{erfc\left(\frac{x-\mu Et}{2\sqrt{Dt}}\right) + \exp\left(\frac{\mu Ex}{D}\right)\cdot erfc\left(\frac{x+\mu Et}{2\sqrt{Dt}}\right)\right\} \qquad (5)$$

If the diffusion is nonlinear, for rough estimations one can take as D the effective diffusion coefficient, i.e. the coefficient which provides closest complimentary error-function approximation of (5) in case E = 0 [8]. For the formation of a graded-index diffraction grating in glass a mask with periodic openings should be applied to the glass surface (see Fig. 1).

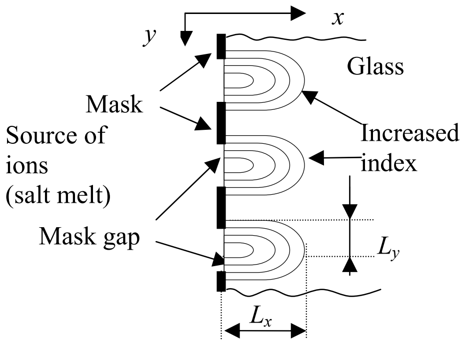

Figure 1: The geometry of the formation of diffractive grating with ion exchange technique.

Equation (3) with corresponding boundary conditions can be solved numerically with the use of finite-difference scheme [9]. This solution will describe spatial distribution of the variation of refractive index $\Delta n(x,y)$, for $\Delta n \sim C$. Periodical distribution of $\Delta n(x,y)$ forms graded index diffraction grating embedded in the glass. This grating diffracts incident light the same way as a hologram or acoustic wave, propagating in a photoelastic medium, and the mode of this diffraction depends on the value of Bragg parameter α [5]:

$$\alpha = \frac{\lambda_o L_x}{n\Lambda^2} \qquad (6)$$

Here λ_o is vacuum wavelength of light, L_x is the thickness of the grating, and n is average index of media refraction. Further in calculations we will take the diffusion depth as the grating thickness. Situation $\alpha \ll 1$ corresponds to Raman-Nath mode of diffraction. This mode has no angular selectivity, and multiple diffraction orders appear. The efficiency of the diffraction in n^{th} order is [5]

$$\eta_n = \frac{I_n}{I_i} = J_n^2(\varphi),\ n = 0, \pm 1, \pm 2, ...$$

where I_i is the intensity of incident light, I_n is the intensity of n^{th} diffraction order, n = 0 corresponds to non-diffracted light, J_n – n^{th} Bessel function, and φ is phase modulation, i.e. the amplitude of phase $\psi(y)$ gained by the index variation:

$$\psi(y) = \frac{2\pi}{\lambda_0}\int_0^\infty \Delta n(x,y)dx;\ \varphi = \frac{1}{2}(\max\psi(y) - \min\psi(y)) \quad (7)$$

Maximal efficiency of Raman-Nath diffraction can be reached in ±1st diffraction orders, and it can not exceed ~33.9%, for $\max(J_1)=0.582$.

If $\alpha >> 1$, angular selective Bragg diffraction mode takes place: incident light diffracts only if it falls at the grating surface (plane $x = 0$) at the angle $\theta/2 = \lambda_0/(2\Lambda)$. In the case of Bragg diffraction the efficiency of the single (first) diffraction order $\eta_1 = \sin^2(\varphi)$, and $\eta_o = \cos^2(\varphi)$. Bragg diffraction mode can provide up to 100% diffraction efficiency. The case of $\alpha \sim 1$, that is intermediate diffraction mode, gives several diffraction orders, and angular selectivity is much worse than that in Bragg diffraction mode. The maximal diffraction efficiency is between ones for Raman-Nath and Bragg modes. This mode requires numerical calculations of the diffraction efficiency, which can reach up to 60-80 % for $\alpha \sim 1$.

3 Discussion

3.1 Thermal ion exchange

Thermal ion-exchange can not be treated as the technique to produce effective highly periodical gratings because isotropic motion of ions in glass is approximately the same in normal (x) and tangential (y) directions, i.e. effective lengths of diffusion L_x (depth) and L_y (lateral) are equal, $L_x \sim L_y$. In case we take as effective length of diffusion the distance where the dopant concentration drops down to 5% of the concentration at the surface, in accordance with (5) we have $L_x \sim 3(Dt)^{1/2}$ - see Figure 2. If we took into account approximately triangle profile of the dopant concentration in depth, the phase modulation φ at the middle of the mask gap can be written as

$$\varphi \approx \frac{1}{2}\left(\frac{2\pi}{\lambda_0}\int_0^\infty \Delta n(x)dx\right) \approx \pi\Delta n\frac{L_x}{2\lambda_0}$$

For relatively high index variation $\Delta n_0 \sim 0.1$ induced by ion exchange (this corresponds to the case of silver-sodium exchange in the glasses good for ion-exchange processing) and wavelengths of light in visible range, $\lambda_o \sim 0.5$ µm, the phase modulation $\varphi = \pi/2$ corresponds to ~5 microns of light propagation in the region with index increase, or to the effective diffusion depth $L_x \sim 5$ µm. For effective diffraction of the grating having equal gap and the distance between gaps (Fig. 1) the period Λ of the structure must about 4 times exceed the value of L_x, $\Lambda \sim 4L_y \sim 4L_x$. If the grating period is less than $4L_x$, the diffraction efficiency in the first order drops since lateral diffusion flows overlap, and effective index variation goes down. This gives us evaluation $\Lambda > 20$ µm for $\pi/2$-phase modulating periodical structures formed with thermal ion exchange.

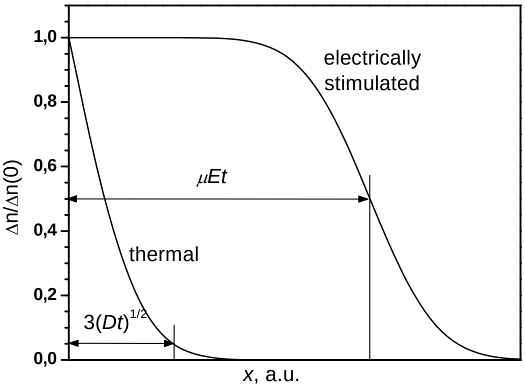

Figure 2: Index profile for thermal and electrically-stimulated ion exchange plotted according to Eq. (5).

The evaluation of Bragg parameter α of the diffraction grating according to (6) gives

$$\alpha = \frac{\lambda_o L_x}{n\Lambda^2} = \frac{\lambda_o L_x}{n(4L_x)^2} \sim \frac{0.02}{L_x} << 1$$

(we took $n \sim 1.5$ for glasses, and $L_x \sim 5$ microns), while for thick gratings $\alpha >> 1$ is necessary. In the case of diffusion mask having narrow openings we have $\Lambda \sim 2L_y \sim 2L_x$. Even in this situation we have $\alpha \sim 0.1/L_x$. Double increase in index variation, $\Delta n_0 \sim 0.2$, could allow double decrease in L_x and provides π/2 phase modulation for L_x ~ 2.5 microns. Anyway we have $\alpha << 1$. This means that thick gratings can not be made with thermal ion exchange, and even the gratings demonstrating intermediate ($\alpha \sim 0.5$–1) mode of diffraction can hardly be formed. Thus, thermal ion exchange technique ought to be used mainly for the formation of graded index diffraction gratings without angular selectivity and with multiple orders of diffraction corresponding to Raman-Nath diffraction mode.

3.2 Field-assisted ion exchange

To make effective gratings with higher periodicity and/or higher value of parameter α it is necessary to provide essential anisotropy of the motion of ions in the glass, or, the same, to provide $L_x >> L_y$. For this it is natural to apply electric voltage and to use field-stimulated drift of ions in *x* direction (depth) as it was proposed by Izawa and Nakogame in 1972 [10] for the formation of optical waveguides. In the case of strong electric field *E* the depth of the diffusion L_x can be evaluated as $L_x \sim \mu E t$, where μ is effective value of ionic mobility of the dopant ions, and *t* – time of the processing (Fig.2). At the same time, for lateral motion of ions we still have approximately the same length $L_y \sim 3(Dt)^{1/2}$, which we had for thermal ion exchange. Using Eq.(1), we can, principally, evaluate the value of electric field, which provides given periodicity Λ of the structure with $\pi/2$ phase modulation. In the case of field-stimulated diffusion we have approximately step profile of dopant concentration and phase shift $\varphi \sim 2\pi \Delta n L_x/\lambda_o$. Thus, taking together relations $\Lambda \sim 4L_y \sim 12(Dt)^{1/2}$, $\pi = 2\pi \Delta n L_x/\lambda_o$, and $L_x \sim \mu E t$, leads to the relation of Λ and *E*:

$$\Lambda \sim \sqrt{\frac{72kTH\lambda_0}{Ee\Delta n}} \approx 8.5\sqrt{\frac{kTH\lambda_0}{Ee\Delta n}}\,.$$

For values of $T \sim 600$K, $\Delta n \sim 0.1$ and $H \sim 0.5$ we have E(in V/μm) $\sim 9/\Lambda^2$(in microns). This means that 2 μm period could be provided by applying electrical field about 2.25 V/μm or, the same, 2250 V/mm, and for 1 μm period it must be about 9000 V/mm. These values are out of practical reasons, at least due to possible electrical breakdown.

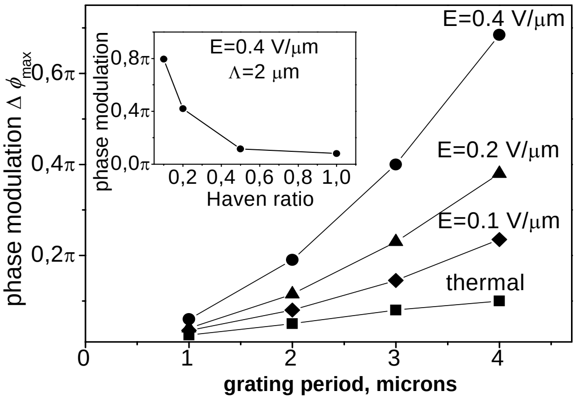

Figure 3: Numerical calculations of maximal phase modulation for thermal and field assisted ion exchange. The influence of Haven ratio is shown in the insertion.

Double increase in Δn allows double decrease of electric field for given grating periodicity, and, in this case, applying electrical field of 1000 V/mm could be used to the formation of gratings having 1.5 μm periodicity. In ion exchange through the mask additional ionic flows arising due to the influence of mask potential are supposedly increasing the necessary field value. Moreover, in the case of strongly nonlinear diffusion, effective value of μ can also go down due to the influence of local charges inducing electrical field slowing the drift. From general point of view it is evident that using glasses with lower value of Haven ratio (see Fig. 3) as well as lower temperatures of processing and higher index variation are preferable in spite of increasing necessary processing time.

The anisotropy of ionic motion can be evaluated using the relation

$$\frac{L_x}{L_y} \sim \frac{\mu E t}{3\sqrt{Dt}} = \frac{eDET}{3HkT\sqrt{Dt}} = \frac{eE\sqrt{Dt}}{3HkT}\,,$$

which gives for depth-to-period ratio

$$\frac{L_x}{\Lambda} \sim \frac{L_x}{4L_y} = \frac{eE\sqrt{Dt}}{12HkT}\,.$$

Here $\Lambda \sim 4L_y$, for this eliminates overlapping of lateral diffusion flows. In the case of electrically stimulated diffusion one can write for Bragg parameter α:

$$\alpha = \frac{\lambda_0 L_x}{n\Lambda^2} \sim \frac{\lambda_0 \mu E t}{n\left(12\sqrt{Dt}\right)^2} = \frac{\lambda_0 e D E t}{144 H k T n D t} = \frac{\lambda_0 e E}{144 H k T n} \approx 0.09E$$

(for H=0.5 and T=600K).

Here E is in V/μm. The evaluation of E for $\alpha >> 1$ (the case of thick grating) gives us $E >> 10000$ V/mm. This value is independent on the diffusion constant, and it looks over practical limits as well. Additional factors, like mentioned above the influence of mask potential, could even increase the magnitude of necessary field. Using masks with narrow windows could allow four-times increasing of α, but even this can not provide $\alpha >> 1$. This means that the formation of thick graded index diffraction gratings by electrically stimulated ion exchange is also hardly possible. Nevertheless periodical structures with $\alpha \sim 0.1\text{-}0.2$, which can diffract 60-80 % of incident light in one diffraction order, could be formed (see Fig. 4).

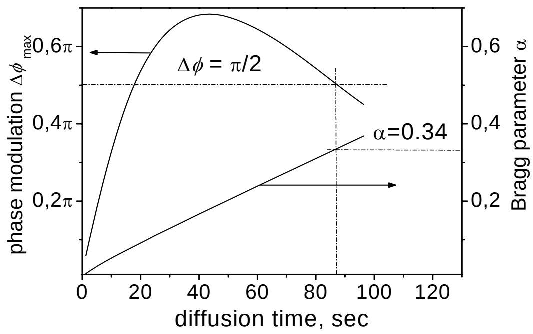

Figure 4: Numerically calculated time dependence of phase modulation and Bragg parameter for 4μm-period grating formed by field-assisted ion exchange. Applied field E = 0.4/μm, Haven ratio H = 0.5.

Practical value of E is additionally limited just due to the resistive heating of glasses by ionic current, which induces local increase of ionic conductivity. Small non-uniformities of the conductivity could induce non-uniformities of ionic current, and this leads to the increase in local conductivity and, finally, to avalanche process, local overheating and glass destruction. The glass sample can also be destroyed due to stresses arising under non-uniform thermal expansion. According to our experience reasonable value of electrical power P, which can be scattered in the glass sample without the sample damage is about several watts per square centimeter of the glass substrate under processing. We can write $P/S = jEd < 10$ W, where j is the density of ionic current ($j = I/S$, I – current), d – thickness of the glass sample and S – area of the sample surface under processing. Since $j = \mu E C_0 e$, where C_0 is the concentration of alkaline ions in the glass, the substitution of μ gives us the evaluation of possible driving field:

$$E_{\max} < \sqrt{\frac{PHkT}{SDC_0 e^2}}$$

The concentration C_0 of alkalines in glasses aimed for ion exchange must be about 10^{22}cm^{-3} to provide necessary high index increase, $\Delta n \sim 0.1$. Taking typical thickness $d \sim 1$ mm we have evaluation for E_{max} value: $E_{\max}$ (in V/mm) < $4 \cdot 10^{-5}$/ (D, in m^2/s)$^{-1/2}$. For glasses with $D \sim 10^{-14}$ m^2/ s [11] at 300 C the evaluation gives $E_{max} \sim 400$ V/mm. For glasses with lower diffusion coefficient, like most industrial glasses, this value is higher. However even 1000 V/mm, that is high for ion exchange processing, is too low for the formation of thick gratings (α >> 1), but the diffractive structures, which provide $\pi/2$ phase modulation and periodicity of several microns as well as the mode of diffraction corresponding to $\alpha \leq 1$ and ~ 80 % efficiency of the diffraction can be formed. The recommendation for producing deep diffractive structures could be only decreasing temperature and, such manner, diffusion coefficient D, and corresponding increasing the duration of the processing. Besides, the same recommendation can be applied to the formation of buried channel optical waveguides if minimal transformation of index profile formed in these waveguides before burying is required.

4 Conclusion

Thermal ion exchange technique ought to be used mainly for the formation of graded index diffraction gratings without angular selectivity and with multiple orders of diffraction corresponding to Raman-Nath diffraction mode. High (more than $\pi/2$) phase modulation by such gratings can be provided only in the case of low periodicity, that is more than 20 microns for ion exchange induced index variation $\Delta n \sim 0.1$. For higher Δn the periodicity can be decreased in inverse proportion. The periodicity of ion-exchanged diffraction gratings can be decreased if electrical field stimulated ion exchange is used. In this case the grating period drops with Haven ratio decrease and the field increase. That is why glasses with lower Haven ratio and lower diffusion coefficient of penetrating ions, which provides prevailing ion drift over thermal diffusion, should be preferably used. For $H = 0.5$ and $\Delta n \sim 0.2$ applying electrical field of 500 V/mm could provide the grating period ~2 microns. This magnitude of the field is close to the critical value, which can induce the damage of the glass substrate in the case of field stimulated ion exchange. The prospective of the formation of highly angular selective thick diffraction gratings by electrically assisted ion exchange is doubtful since necessary electric field exceeds reasonable value of driving field for stimulated ion exchange by order of magnitude. The formation of diffractive structures providing high efficiency in the first diffraction order is real in the case of graded index diffractive gratings with periodicity in the range of several microns.

Acknowledgements

The authors thank CRDF (grant 2530) and Saint-Petersburg government (grant PD05-2.0-45) for the support of this research.

References

[1] Salmio, R.-P., Saarinen, J., Turunen, J., Tervonen, A.: Graded-index diffractive structures fabricated by thermal ion exchange. *Applied Optics*, 36, pp. 2048-2051, 1997.

[2] Lipovskii, A.A., Arvidsson, G.: Application of a gradient index gratings to evaluation of diffusion parameters for waveguide fabrication. *J .Opt. Commun.*, 8, pp. 12-18, 1987.

[3] Bolstad, H.C., Yatagai, T., Seki, M.: Optimization of phase-only computer-generated hologram using an ion-exchange process. *Opt. Eng.*, 31, pp. 1259-1263, 1992.

[4] Messerschmidt, B., Hsieh, C. H., McIntyre, B. L., Houde-Walter, S. N.: Ionic mobility in an ion exchanged silver-sodium boroaluminosilicate glass for micro-optics applications. *J. Non-Cryst. Solids*, 217, pp. 264-271, 1997.

[5] Collier, R.J., Burckhart, C.B., Lin, L.H.: *Optical Holography*. Academic Press, New York, 1971.

[6] Lupasku, A., Kevorkian, A., Boudet, Y., Saint-Andre, F., Persegol, D., Levy, M.: Modeling ion exchange in glass with concentration-dependent diffusion coefficients and mobilities. *Optical Engineering*, 35, pp. 1603-1610, 1996.

[7] Findakly, T.: Glass waveguides by ion exchange: a review. *Opt. Eng.*, 24, pp. 244- 250, 1985.

[8] Lipovskii, A.A., Svistunov, D.V., Tagantsev, D.K., Zhurikhina, V.V., Diffusion nonlinearity in aluminum-boron-silicate glasses for ion-exchanged GRIN structures: A simple technique to evaluate diffusion nonlinearity of glasses. *Optical Materials*, 2005, accepted for publication.

[9] Zhurikhina, V.V.: Diffusion phase diffraction gratings. *Opt. Spectrosc.*, 89, pp. 1000-1005, 2000.

[10] Izawa, T., Nakogame, H., Optical waveguide formed by electrically induced migration of ions in glass plates. *Appl, Phys. Lett.*, 21, pp. 584-590, 1972.

[11] Linares, J., Sotelo, D, Lipovskii, A.A., Zhurihina, V.V., Tagantsev, D.K., Turunen, J., New glasses for graded-index optics: influence of non-linear diffusion on the formation of optical microstructures. *Opt. Materials*, 14, pp. 145-153, 2000.

Proceedings of The 1st International Conference on **D**iffusion in **S**olids and **L**iquids
DSL-2005, July 6-8, 2005, University of Aveiro, Aveiro, Portugal

PHYSICO-CHEMICAL AND MATHEMATICAL MODELING OF PHASE INTERACTION TAKING PLACE DURING FUSION WELDING PROCESSES

Michael ZINIGRAD*, Vladimir MAZUROVSKY, Konstantin BORODIANSKIY

College of Judea & Samaria, Ariel, 44837, Israel

*Corresponding author. Fax: +972 3 9066234; Email: zinigrad@research.yosh.ac.il

Abstract

The quality of metallic materials depends on their composition and structure and these are determined by various physico-chemical and technological factors. To effectively prepare materials with required composition, structure and properties is necessary to carry out research in two parallel directions:

1. Comprehensive analysis of thermodynamics, kinetics and mechanisms of the processes taking place at the solid-liquid-gaseous phase interface during welding processes;
2. Development of mathematical models of the specific welding technologies.

We have developed unique method of mathematical modeling of phase interaction at high temperatures. This method allows us to build models taking into account: thermodynamic characteristics of the processes, influence of the initial composition and temperature on the equilibrium state of the reactions, kinetics of heterogeneous processes, influence of the temperature, composition, hydrodynamic and thermal factors on the velocity of the chemical and diffusion processes. The model can be implemented in optimization of various technological processes in welding, surfacing, casting as well as in manufacturing of steels and non-ferrous alloys, materials refining, alloying with special additives, removing of non-metallic inclusions.

Keywords: Mathematical modelling, Phase transformations

1 Introduction

The development of new flux-cored compositions is the topical area in the current research, especially when we consider such problems as the welding of special-purpose steels and alloys, built-up layers with special properties, or specific maintenance works. The brief review of currently existing calculation techniques for flux-cored compositions demonstrates that they are based on the experimentally deduced dependence which allows to calculate the chemical composition of built-up metal (weld metal) using so called transition coefficients [1] or assimilation coefficients [2] In some cases the attempt is made to take into consideration some redox reactions in the welding zone (on molten metal-slag boundary in the welding pool) [1,3]. Usually, however, the composition of built-up metal (weld metal) is calculated using the mixture method without taking into consideration physico-chemical processes in the welding pool [4]. This approach can be appropriate in order to forecast the chemical composition of built-up metal (weld metal) or to calculate electrode coating for the welding of low-alloy steel and carbon steel, but leads to erroneous results for high-alloy steel and alloys or for built-up layers with special properties. In the latter case the considerable amount of experimental work can be required in order to develop the new composition of electrode coating which can take months or even years.

During the last decade both the increasing potential and the availability of personal computers opened new possibilities for the solution of the above-mentioned problems, and along with it we can consider the computer modeling of physico-chemical processes in the reaction zone connected with technological parameters of the welding process. Computer modeling used now for industrial chemical processes study and for the analysis of real technologies allows us to decrease the amount of time and the amount of labor needed for the research, as well as makes it possible to carry out experiments which cannot be performed or can be performed only with great difficulty on a real object. The development of computer technology and its accessibility have made it possible to solve problems for which there were previously no known methods of solution or these methods were so tedious that they proved to be unsuitable for the practical application. Computer approach is especially valid for physico-chemical processes since their complexity stems from the simultaneous occurrence of a considerable number of physical and chemical processes involving liquid, solid, and gas phases, as well as the high temperatures, the complex character of the hydrodynamic and heat fluxes, and the nonstationary nature of the processes. This complexity is manifested in the large number of parameters determining the course of the processes and in the fact that the variation of a few parameters causes the variation of many others. Such complex physico-chemical objects are studied by constructing models, i.e., simplifying systems, which reflect the most significant aspects of the object under consideration.

2 Computer Modeling as an Up-to-date Approach to New Welding Materials Development

One of the most promising directions of physico-chemical objects computer modeling is the usage of these models for welding technologies analysis which is represented in [5-33]. The first stage of these modeling is generally thermodynamic models construction. This stage is very important both for ascertaining the fundamental possibility of the combined occurrence of particular chemical processes and for listing the most important thermodynamic characteristics. If the rates of the chemical reactions are sufficiently high, the composition of the reactant mixture at the outlet of the chemical reactor should be fairly close to the equilibrium composition and can be found by thermodynamic methods. There are several approaches to the creation of thermodynamic models. They include the employment of polymer theory to model complex multicomponent systems, modeling for the purpose of constructing phase diagrams, the construction of statistical thermodynamic models, the determination of the enthalpy and other thermal characteristics, the modeling of melting processes and structure-building processes.

When there are no or only few theoretical data on the process being modeled, the mathematical description can take the form of a system of empirical equations obtained from a statistical study of the real process. A correlation between the input and output parameters of the object is established as a result of such a study. Naturally, the employment of statistical models is restricted by the width of the range of variation of the parameters studied.

In recent years mathematical modeling has been applied not only to the investigation of theoretical aspects of physicochemical processes, but also to the analysis of actual technologies.

The areas of the prediction and optimization of the composition and properties of materials obtained in different technological processes are especially promising [5-8,21,24-33]. Some of the results were obtained from the modeling of the process of the formation of a weld pool [5,30], from the modeling of metal transfer [28,31,32] and weld metal transformations [22,23,27,30], and from the modeling of temperature distribution [25] and electrode melting [24], from metallurgical modeling of the welding [11,26] and diffusion-controlled kinetics of metallurgical processes [6,20,2].

Important results were obtained from the studies of the physical and chemical parameters of welding processes [20] and development of kinetic model of alloy transfer [21].

By determining the chemical composition of the weld metal researchers have developed the kinetic model [21]. Basing on this model the authors described the transfer of alloying elements between the slag and the metal during flux-shielded welding. The model also takes into consideration the practical welding process parameters such as voltage, current, travel speed, and weld preparation geometry. The model was tested experimentally for transfer Mn, Si, Cr, P, Ni, Cu, and Mo.

In our opinion the problem of modeling complex objects with consideration of the kinetics of the chemical processes occurring them is more complicated. This applies both to diffusion processes [21] and especially to the analysis of the kinetics of complicated heterogeneous reactions.

A more complete, adequate description of actual chemical processes requires the construction of a mathematical model which takes into account the diffusion of all the components in the complex multicomponent system, the kinetics and mechanism of the individual chemical reactions, the special features of their simultaneous occurrence, and the influence of heat transfer and the hydrodynamics, as well as the influence of the engineering parameters and other factors. There is presently a large amount of experimental and theoretical data, which make it possible to solve such problems.

The present research is also intended to be devoted to the development of mathematical models of such a type on the basis of a new method for the kinetic analysis of reactions in multicomponent systems.

The main problem which the technologies cited solve is the production of deposited metal (welds, coatings, etc.) with a required composition and assigned properties. At present time, these problems are generally solved empirically, i.e., either by means of technological experiments or by the statistical treatment of existing experimental data.

Such an approach requires great expenditures of time and resources and the consumption of considerable amounts of expensive materials. In addition, the results of such researches have a random character and are far from optimal.

3 Peculiarities of Proposed Approach, Objects, and Stages of the Research

The approach employed in the present research fundamentally different from the above mentioned ones. The mathematical model of the physicochemical processes developed and the computer program written on its basis will make it possible to “run” a large number of variants within a short time without considerable expenses and to select the optimal variant, which provides products with the required composition and properties. Such a result cannot be obtained, in principle, even after the performance of hundreds of technological experiments.

The use of such a program permits to investigate the possibility of replacing expensive metallic components metal- and oxide-containing industrial waste products, something which is practically impossible to do under the empirical approach.

The research is carried out in three stages: 1) mathematical description of the process being studied, i.e., construction of the mathematical model; 2) development of an algorithm for solving the problem, i.e., a procedure for determining the numerical values of the output parameters; 3) establishment of the equivalence of the model to the process being studied. Special attention was focused on the stage of constructing the model, which was based on a thorough analysis of the physico-chemical essence of the phenomena being described and on constructing based on the model computer program.

From these considerations the following problems of the work were defined:

- to develop a mathematical model of industrial welding processes on the basis of a thermodynamic and kinetic analysis of the metallurgical processes, involving the metal, slag, and gas;
- to use the model and the computer program, written on its basis, to optimize welding technologies employing flux-cored wires;
- to optimize the flux-cored composition which produce welded joints with the preset composition;

The object of modeling for the analysis of the physico-chemical processes, taking place during welding, is a system which includes the following phases: metal, oxide melt (slag), gas, and solid phases, in which various chemical and physical processes take place.

4 Phase Interaction Analysis

Metal-slag interaction in the process of arc welding exerts a substantial impact on the chemical composition of built-up metal (weld metal) which ultimately determines the working characteristics of weld metal or built-up layer. The consideration of this interaction in the process of flux-cored wire development which can ensure the preset composition of weld metal is based on the mathematical modeling of the welding technological process, taking into account the following features of the process:

- metal-slag interaction at two consecutive stages - electrode (drop) and welding pool - which differ in temperature, geometrical and hydrodynamic parameters;
- continual renewal of interacting phases (molten metal and slag) at each stage through the melting and crystallization of base and adding materials;
- simultaneous occurrence of all reactions at each stage and their interplay.

Since it is impossible to built a model describing a process with the absolute adequacy, we offer some assumptions and simplifications. Thus in the model under consideration basing on the experimental data for the stationary welding conditions the following assumptions were made:

- within the phases under consideration there are not any gradients of chemical potential (the ideal mixing of phases);

- while considering the interaction between gas and slag phases we take into account only the reactions with oxygen and carbon oxide;

- metal-slag reactions surfaces for each stage are kinetically homogeneous.

Figure 1 is a scheme showing the interaction of phases with regard to these assumptions.

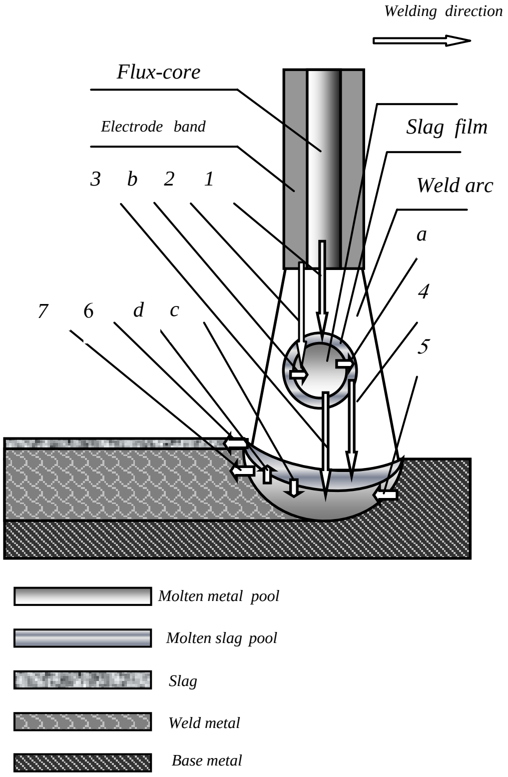

Figure 1: Interaction of phases in FCW-welding process

On the scheme figures denote the direction of material transfer, and letters denote the interaction of phases:

1 - melting of the flux-cored and formation of slag film over the drop;

2 - melting of the electrode band and formation of a drop;

3 - transfer of the drop metal (which has reacted with slag film at the stage of transfer) to the metal pool;

4 – transfer of the slag film (which has reacted with the drop metal at the stage of transfer) to the slag pool;

5 - melting of base metal;

6 - crystallization of slag pool;

7 - crystallization of metal pool;

a, b - redox reaction at slag-metal boundary in a welding drop;

c, d - redox reaction at slag-metal boundary in a welding pool.

5 Development of the Basic Model

The welding process has a stage-like character, and it goes without saying. It should be only specified that the stage of electrode melting as well as the existence of the drop are of considerable importance. At this stage we already observe that the reactions of interaction between phases exert considerable effect on the changes in the chemical composition of molten metal and slag incoming to the welding pool, for which pool they provide the starting chemical composition of incoming electrode metal and slag. Regardless of the process stage and phase type the material balance of elements can be described by the following equation [6]:

$$\sum \boldsymbol{V}_{inp} \frac{[\boldsymbol{E}_i]_{inp}}{100} = \sum \boldsymbol{V}_{out} \frac{[\boldsymbol{E}_i]_{out}}{100} \pm \boldsymbol{I}_{E_{i_j}} \boldsymbol{S}_j \boldsymbol{M}_{E_i} + \frac{\boldsymbol{m}_j}{100} \cdot \frac{\boldsymbol{d}[\boldsymbol{E}_i]}{\boldsymbol{d\tau}} \qquad (1)$$

where:

$\boldsymbol{V}_{inp}$ - the input speed of i-th element incoming to the phase, kg/s;

$\boldsymbol{V}_{out}$ - the output speed of i -th element out of the phase, kg/s;

$[\boldsymbol{E}_i]_{inp}$ - the concentration of i -th element in the incoming flow, wt %;

$[\boldsymbol{E}_i]_{out}$ - the concentration of i -th element in the outgoing flow, wt %;

$\boldsymbol{I}_{E_{i_j}}$ - the rate of mass-transfer of the i -th element through a phase boundary of area $\boldsymbol{S}_j$ at j-th stage, mol / m2 s;

$\boldsymbol{S}_j$ - the area of the reaction surface at j -th stage, m2;

$\boldsymbol{M}_{E_i}$ - element’s molecular (atomic) mass, kg/mol.

$\frac{m_j}{100} \cdot \frac{d[E_i]}{d\tau}$ - the accumulated amount of an element in the phase volume under the non-stationary conditions, and therefore in our case equals to zero;

Thus for each stage of the welding process we can compute the concentration of an element (metal phase) or its oxide (slag phase).

6 The Stage of Electrode Melting (the Drop Stage)

Metal Phase on the Electrode Drop Stage

From (1) follow the material balance equation for the metal phase of the electrode drop:

$$V_e[E_i]_e = V_e[E_i]_d + 100 \cdot S_d I_{E_{i_d}} M_{E_i} \qquad (2)$$

where:

V_e - the speed of electrode melting, kg/s;

$[E_i]_e$ - the element's concentration in the electrode band, wt %;

$[E_i]_d$ - the element's concentration in the drop metal, wt %;

S_d - the area of the drop's reaction surface, m2;

$I_{E_{i_d}}$ - the rate of mass-transfer of the i - th element through a phase boundary of slag – drop metal, mol / m2 s;

M_{E_i} - element's molecular (atomic) mass, g/mol.

Then the concentration of the element in drop metal is defined as:

$$[E_i]_d = [E_i]_e - 100 \cdot \frac{S_d I_{E_{i_d}} M_{E_i}}{V_e} \qquad (3)$$

Slag Phase on the Electrode Drop Stage

By analogy with the preceding:

$$(E_{in}O_m)_d = (E_{in}O_m)_c + 100 \cdot \frac{S_d I_{E_{i_d}} M_{E_{in}O_m}}{nV_c} \qquad (4)$$

where:

$(E_{in}O_m)_d$ - oxide concentration in slag film, wt %;

$(E_{in}O_m)_c$ - oxide concentration in flux-cored, wt %;

V_c - the speed of flux-cored's melting, kg/s .

7 The Stage of the Pool

Metal Phase on the Pool Stage

From (1) follow the material balance equation for the metal phase of the welding pool:

$$V_e[E_i]_e + V_{bm}[E_i]_{bm} = V_{crm}[E_i]_p + 100 \cdot S_p I_{E_{i_p}} M_{E_i} \qquad (5)$$

where:

$[E_i]_{bm}$ - the concentration of i-th element in base metal, wt %;

$[E_i]_p$ - the concentration of i-th element in welding pool, wt %;

V_{crm} - the crystallization speed of metal pool, kg/s;

V_{bm} - the melting speed of base metal, kg/s;

S_p - the area of pool's reactive surface, m2;

$I_{E_{i_p}}$ - the rate of mass-transfer of the i -th element through a phase boundary of slagl – metal pool, mol / m2 s;

Hence the concentration of i-th element in welding pool is:

$$[E_i]_p = \frac{V_e[E_i]_e + V_{bm}[E_i]_{bm} - 100 \cdot S_p I_{E_{i_p}} M_{E_i}}{V_{crm}} \qquad (6)$$

Slag Phase on the Pool Stage

By analogy with the metal phase concentration of i-th oxide in welding pool is

$$(E_{in}O_m)_p = \frac{nV_e(E_{in}O_m)_e + 100S_p I_{E_{i_p}} M_{E_{in}O_m}}{nV_{crs}} \quad (7)$$

where:

V_{crs} - the crystallization speed of slag pool, kg/s;

From (3), (4), (6), (7) one can see that in order to compute the chemical composition of phases we need to know rate of mass-transfer of the i -th reagent through a phase boundary of slag – metal $I_{R_{i_j}}$ (where: Ri - reagent, i.e. Ei or EinOm and j - the stage of the process), which can be computed using the method of kinetic analysis [34] for the reactions at the molten metal-slag boundary, the latter being generalized as:

$$\frac{n}{m}[E_i] + (FeO) = \frac{1}{m}(E_{in}O_m) + [Fe] \quad (8)$$

If stoichiometry coefficient n = 1, the rate of mass-transfer of the i –th element through a phase boundary [34]:

$$I_{E_i} = \frac{x^m K_i^m [E_i] - (E_i O_m)}{\dfrac{x^m K_i^m}{I_{E_i}^{\lim}} + \dfrac{(E_i O_m)}{I_{E_i O_m}^{\lim}}}, \quad (9)$$

with n = 2

$$I_{E_i} = \frac{-\Phi - \sqrt{\Phi^2 - 4\Psi\Theta}}{2\Psi}, \quad (10)$$

where

$$\Psi = \frac{x^m K_i^m [E_i]^2}{I_{E_i}^{\lim\,2}}$$

$$\Phi = -\left(\frac{2x^m K_i^m [E_i]^2}{I_{E_i}^{\lim}} + \frac{2(E_{i2}O_m)}{I_{E_{i2}O_m}^{\lim}}\right)$$

$$\Theta = x^m K_i^m [E_i]^2 - (E_{i2}O_m)$$

$x = \dfrac{(FeO)'}{[Fe]'}$ ([Fe]′ and (FeO)′ are concentrations of iron and iron oxide correspondingly on slag – metal boundary);

Ki - the coefficient, including:

- the equilibrium constant of reaction (8) for i –th element;

- activite's coefficients γ_i ;

- coefficients of recalculation of molar concentration into weight ones.

Limiting diffusion rates of the components in the metal and the slag [35]:

$$I_{R_i}^{lim} = \beta_{R_i} D_{R_i}^{0.5} \frac{C_{R_i}\rho}{100M_{R_i}} \quad (11)$$

where:

β_{R_i} - convection constant, s-0.5

CRi - the concentration of i-th element or oxide, wt %

ρ - metal or slag density, kg/m3;

DRi - reagent's diffusion coefficient, m2/s;

MRi - reagent's molecular (atomic) mass, kg/mol.

For the solution of our task we'll take into account the obvious stoichiometry correlation following from the (8):

$$I_{FeO} = \sum I_i = \sum \frac{m}{n} I_{E_i} = m \sum I_{E_{in}O_m} \quad (12)$$

The system of the above equations (3,4,6,7,9,10,12) presents the general mathematical model of physico-chemical processes of the fusion arc welding.

In actual practice the solution of this problem allows to compute the chemical composition of built-up metal (weld metal) provided that we know the electrode formula and the type of base metal. Rather often, however, we are faced with the inverse problem when it is necessary to compute such an electrode formula that can give us the required chemical composition of built-up metal (weld metal) in the process of welding (or building-up) of specific metal (hereafter, "the inverse problem").

The computation is based on the above model. The initial stage of the solution (the preliminary computation) determines the initial formula of an electrode. Using it as a base one can easily compute the chemical composition of built-up metal (weld metal) and forecast its properties. If the results of this computation do not satisfy the verification criteria, then appropriate corrections are introduced into the initial formula whereupon it becomes "the intermediate formula". The computation is repeated, and the results are again checked. This procedure is repeated until (after n iterations) the desirable results are gained and the final formula of an electrode is obtained

8 Computer Program Implementation

A computer expert system based on the model was designed. This program is based on the mentioned above approach and equations. To make it more obvious, the mathematical modeling results will be illustrated by step-by-step the real life example which shows the optimal electrode coating compositions development.

We assume that our task is to develop a new flux-cored wire(i.e., a new flux-cored composition) for obtaining build-up layers with an assigned composition and required properties. We assume that we are dealing FCAW of carbon steel (as the base metal). The chemical composition of this steel, which is needed for the calculation, is stored in the database together with the compositions of other standard materials.

The technological parameters of the welding process must also be determined. We enter the technological parameters in accordance with the welding procedure selected.

Then we must ensure that the weld metal has a definite composition. We enter the chemical composition of the weld metal that must be obtained.

To solve the problem, the material of the electrode band must be selected and the optimal composition of the flux-cored must be determined, i.e., a new electrode formula must be developed.

We choose, for example, the simple carbon steel as the band material. The choice of a simple carbon steel band is stipulated primarily by economic considerations. Of course, to obtain a weld metal with a high degree of alloying, it will be necessary to use an alloyed band metal.

The next and most important step is optimization (which, in the case at hand, is essentially development) of the flux-cored composition. The required joint composition can clearly be obtained with different combinations of components in the coating. The database contains the chemical compositions of various components (alloying and slag), which should be utilized in selecting the optimal electrode coating composition. We present some of the materials needed for our case (Table 1.).

The program has to determine the flux-cored composition that provides the required weld metal composition and to select the most inexpensive variant among them. This clearly requires a large number of iterations to perform calculations with all the possible component ratios.

In particular, four flux-cored compositions were found for the case under consideration, and one of them was specified as the flux-cored which provides the required joint composition with the lowest production costs. The results of the calculation (both the optimal composition and the other three compositions) are stored in the database of the program.

Such a coating provides the solution for the problem posed, i.e., the required joint composition. This composition agrees well with the composition which we assigned when we posed the problem. Closer agreement between the required and calculated compositions can clearly be provided, but this would require a larger number of iterations and, accordingly, a greater amount of computer time.

The program includes a special module, which provides an evaluation of the weldability and mechanical properties of the joint metal having the composition obtained.

The approximate time for the calculations and optimization was 15-20 min in the case considered. The result is a new formula for an flux-cored electrode that provides assigned build-up layers composition (Table 2). In the Table 3, the compared data of calculated and experimental weld metal compositions are shown.

Table 1: Raw Materials

Material	Type	Main
FeCr-68	Alloy	Cr
FeCr-80	Alloy	Cr
FeMn-77	Alloy	Mn
FeMn-83	Alloy	Mn
FeMn-80	Alloy	Mn
FeSi-45	Alloy	Si
FeSi-85	Alloy	Si
FeTi-88	Alloy	Ti
FeTi-82	Alloy	Ti
FeMo-78	Alloy	Mo
FeMo-75	Alloy	Mo
Graphite (s09)	Alloy	C
Graphite (g17)	Alloy	C
Mrb-bl	Slag	CaO
Mrb-gr	Slag	CaO
Flc123	Slag	CaF_2
Flc016	Slag	CaF_2
Rutil01	Slag	TiO_2
Rutil0156	Slag	TiO_2
Sld1820	Slag	Al_2O_3
Sld2341	Slag	Al_2O_3
BaFF17	Slag	BaF_6
BaFF94	Slag	BaF_6
Qz1003	Slag	SiO_2
Qz1008	Slag	SiO_2
Qz1199	Slag	SiO_2
WG- Sg	Water glass	SiO_2
WG -df	Water glass	SiO_2
WG (Na11123)	Water glass	$SiO_2 \cdot Na_2O$
WG (Na09876)	Water glass	$SiO_2 \cdot Na_2O$

Table 1 displays good agreement between experimental and calculated results (deviation did not exceed 20%).

Table 2 and Table 3 see in appendix

9 Conclusion

The mathematical model of welding technology process on the basis of the kinetic analysis method [34] had been developed.

The model takes into consideration:

- stage-by-stage implementation of the welding process;
- continuous renovation of interacting phases;
- simultaneous running of all reactions and their mutual influence;
- physico-chemical properties of the interaction phases;
- hydrodynamic conditions of the welding process;
- interconnection between welding process parameters (welding conditions) and kinetics of reactions.

The proposed method can be applied to the development of new compositions of welding materials (electric coatings, flux cored wires, welding fluxes). The practical implementation of this approach is considered.

References

[1] A. A. Erokhin: *The Fundamentals of Fusion Welding*, Printing house “Mashinostroenie”, Moscow, (1973), 448 pages.

[2] N. N. Potapov: *Metal Oxidation at Fusion Welding*, Printing house “Mashinostroenie”, Moscow, (1985), 216 pages.

[3] N. N. Potapov: *The Metallurgy of Welding. Welding and Welding Materials.* The Handbook in 3 Vols. Ed. by V.I. Volchenko. Vol.1, Metallurgia, Moscow, (1991), 528 pages.

[4] A. Chasuy, and O. Morigay: *Building up and Spray Coating*, Printing house “Mashinostroenie”, Moscow, (1985), 238 pages.

[5] R. Ducharme, P. Kapadia, J. Dowden, K. Williams and W. Steen: An integrated mathematical model for the welding of thick sheets of metal with a continuous CO2 laser, *Laser Inst. Am.*, (1994), p. 77.

[6] Yu. Davydov, V. Boronenkov, and A. Salamatov: Prediction of the weld formation of variable composition based on modeling of metallurgical processes, *Autom. Svarka*, no. 7-8 (1992), p. 23.

[7] J. Norrish and D. Gray: Computer simulation and off-line programming in integrated welding systems, *Weld. Met. Fabr.*, 60, 3 (1992), p. 119.

[8] S. Kozlovsky: Modeling of the interaction of parts in the contact area in spot welding, *Isv. VUZ. Mashinostr*. No. 9 (1990), p. 89.

[9] V. Grigorenko, O. Kiselev and G. Chernyshov: Mathematical model and its practical evaluation for weld formation, *Svar. Proizvod.*, no. 2 (1994), p. 30.

[10] G. Tsybulkin: Mathematical models in adaptive control of arc welding, *Autom. Svarka*, no. 1 (1994), pp. 24-27.

[11] O. Grong and O. R. Myhr: *Mathematical modeling of weld phenomena*, eds H. Cerjak and K. E. Easterling, The Institute of Materials, London, (1993), p. 300.

[12] J. Vitek, T. Zacharia, S. David, M. Rappaz and H. Boather: *Modeling of single-crystal laser-weld microstructures*, Laser Mater Process., Proc. Symp. TMS, USA, (1994), p. 213.

[13] J. Dowden, R. Ducharme, P. Kapadia, A. Clucas: A mathematical model for the penetration depth in welding with continuous CO2 lasers, *Laser Inst. Am*., 79, (1994), p. 451.

[14] O. Grong, A. O. Kluken, H. K. Nylund, J. Hjelen and Andersen: Mechanisms of cicular ferrite formation in low-alloy steel weld metals, *SINTEF Rep*., (1992).

[15] O. Grong and A. O. Kluken: Microstructure and properties of steel weld metals, *Key Eng. Mater*., (1992) p. 47.

[16] D. L. Olson: *Influence of welding flux on the pyrometallurgical; physical and mechanical behavior of weld metal*, Gov. Rep. Announce. Index (U.S.), no. 86 (21). Abstr. No. 647, 023, (1986).

[17] D. L. Olson, S. Lui and G. R. Edwards: *Role of solidification on HSLA steelweld metal chemistry*, Weldability Mater., Proc. Mater. Weldability Symp., (1990), p. 183.

[18] D. L. Olson and D. K. Matlock: The role of composition and microstructure adiends on weld metal properties and behavior, *Energy Res. Abstr*., no. 12(16), Abstr. No. 33161, (1987).

[19] D. L. Olson and D. K. Matlock: *Compositional* gradient effects on weldment properties, Weldability Mater., Proc. Mater. Weldability Symp., (1990), p. 49.

[20] T. W. Eager: *The physics and chemestry of welding process*, Adv. Weld. Technol., Proc. Int. Conf. Trnds Weld. Res., (1986), p. 281.

[21] U. Mitra and T. W. Eagar: Slag-metal reactions during welding, *Metall. Trans*. (B), vol. 22, No 1, (1991), p. 65.

[22] D. L. Olson, S. Lui and G. R. Edwards: Physical metallurgical concerns in the modeling of weld metal transformations, *Math. Modell. Weld. Phenom*., (1993), p. 89.

[23] F.C. Liao, S. Lui and D. L. Olson: Effect on titanium nitride precipitates on the weldability of nitrogen enhanced Ti-V microalloyed steels, (1994), p. 31.

[24] T. P. Quinn, R. B. Modigan and T. A. Siewert: An electrode extension model for gas metal arc welding. *Weld. J.* 73 (10), (1994), p. 241.

[25] T. P. Quinn, A. Q. Bracarense and S. Lui: A melting rate and temperature distribution model for shielded metal arc welding electrodes. *Weld. J.* 76 (12), (1997), p. 532.

[26] O. Grong: *Metallurgical modelling of welding*. 2nd ed., The Institute of Materials, London, (1997).

[27] K. Mundra, T. Debroy, S. S. Bilu and S. A. Dand: Weld metal microstructure calculation from fundamentals of transport phenomena in the arc welding low-allouy steels. *Weld. J.* 76 (4), (1997), p. 163.

[28] S. W. Simpson, P. Zhu and M. Rados: Simulation and observation of the transfer process in GMWA. *Proc. of 42nd National Welding Conference*, Vol. 2. Paper 31. Welding Technology Institute of Australia, (1994).

[29] P. Zhu, M. Rados and S. W. Simpson: Theoretical prediction of the start-up phase in GMAW. *Weld. J.* 76 (7), (1997), p. 269.

[30] S-Y. Lee and S-J. Na: A numeric analysis of molten pool convection considering geometric parameters of cathode and anode. *Weld. J.* 76 (11), (1997), p. 485.

[31] S. K. Choi, C. D. Yoo and Y-S. Kim: Dynamic simulation of metal transfer in GMAW, Part 1: Globular and Spray transfer modes. *Weld. J.* 77 (1), (1998), p. 38.

[32] S. K. Choi, S. H. Ko, C. D. Yoo and Y-S Kim: Dynamic simulation of metal transfer in GMAW, Part 1: Short-circuit transfer mode. *Weld. J.* 77 (1), (1998), p. 45.

[33] H. Aastroem: Advanced development techniques for coated electrodes. *Weld. Rev. Int*., 12 (2), (1993), p. 72.

[34] V. Boronenkov, S. Shanchurov and M. Zinigrad: Kinetics of the interaction of multicomponent metal with slag under diffusion conditions, *Izvestiya Ac. Nauk USSR. Meta*l, no. 6 (1979), p. 21.

[35] O. Yesin and V. Boronenkov: Kinetic of joint flow of some geterogeeous reactions with common reagents, *Phisicheskaya Chimiy*a, no. 8 (1970), p. 2022.

Appendix

Table 2: New electrode formula obtained using designed computer expert system

Flux - cored electrode(FCE) formula:

Parameters	**Value**
Wide of the electrode band, mm	12
Thickness of the electrode band, mm	0.5
Density of the flux, g/cm3	2.33
Coefficient of fullness, %	27
Deposition rate factor, g/A*h	13

Recomended parameters of the welding(building up) process:

Current, A	Voltage, V	Feed Speed, m/h	Travel speed,m/h	Gas flow, m3/h	Weld output	Polarity
360	26	200	27	-	**CV**	**DCNE**

Coating composition

Component	**Density g/cm3**	**Quantity in 100kg of the FCE, kg**	**Relation in the dray mixture of the flux, %**
Graphite (g17)	0.530	1.220	4.530
FeMn-77	4.300	0.900	3.360
FeCr-80	3.480	6.610	24.620
FeMo-75	6.100	0.840	3.140
FeTi-88	3.150	14.350	53.490
Qz1008	1.900	0.290	1.090
Sld1820	1.290	0.670	2.510
Flc123	2.440	0.290	1.090
Rutil0156	0.670	0.220	0.840
Mrb-gr	1.030	0.870	3.260
BaFF17	1.250	0.560	2.080

Composition of the base materials and the build-up layers, wt%

	C	**Si**	**Mn**	**Cr**	**W**	**V**	**Mo**	**Ti**	**Al**	**Nb**	**B**	**Ni**
Base Metal	0.0800	0.2000	0.3000	0.10	0.0150	0.0100	0.1000	0.0350	0.0200	0.0020	0.0001	0.1000
Electrode band	0.0800	0.0300	0.5000	0.12	0.0150	0.0100	0.1000	0.0100	0.0100	0.0050	0.0001	0.2500
Required weld*	1.3000	0.9500	1.2000	7.00	0.0120	0.0500	0.9500	4.5000	0.2000	0.0040	0.0500	0.2000
Layer 1	0.9985	0.7570	0.9695	5.00	0.0123	0.0842	0.7888	3.4303	0.3425	0.0033	0.0414	0.1649
Layer 2	1.2426	0.9063	1.1474	6.3014	0.0116	0.1039	0.9719	4.3633	0.2995	0.0036	0.0524	0.1822
Layer 3	1.3074	0.9384	1.1948	6.6473	0.0114	0.1091	1.0205	4.6484	0.2413	0.0037	0.0495	0.1867
Layer 4												
Layer 5												

Table 3: Weld metal composition obtained in 3-d layer of build-up metal using new flux-cored electrode

Composition	C	Si	Mn	Cr	Mo	W	V	Ni	Ti	Nb	S	P
	wt %											
Calculated	1.3000	0.9500	1.2000	7.00	0.0120	0.0500	0.9500	4.5000	0.2000	0.0040	0.0500	0.2000
Experiment	1.3074	0.9384	1.1948	6.6473	0.0114	0.1091	1.0205	4.6484	0.2413	0.0037	0.0495	0.1867